

Complexity

# Complexity, Dynamics, Control, and Applications of Nonlinear Systems with Multistability

Lead Guest Editor: Viet-Thanh Pham

Guest Editors: Sundarapandian Vaidyanathan and Tomasz Kapitaniak







---

**Complexity, Dynamics, Control, and  
Applications of Nonlinear Systems with  
Multistability**

Complexity

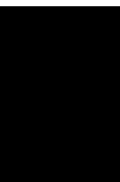
---

**Complexity, Dynamics, Control, and  
Applications of Nonlinear Systems with  
Multistability**

Lead Guest Editor: Viet-Thanh Pham

Guest Editors: Sundarapandian Vaidyanathan and  
Tomasz Kapitaniak





---

Copyright © 2020 Hindawi Limited. All rights reserved.

This is a special issue published in "Complexity." All articles are open access articles distributed under the Creative Commons Attribution License, which permits unrestricted use, distribution, and reproduction in any medium, provided the original work is properly cited.

# Chief Editor

Hiroki Sayama, USA

## Editorial Board

Oveis Abedinia, Kazakhstan  
José Ángel Acosta, Spain  
Carlos Aguilar-Ibanez, Mexico  
Mojtaba Ahmadiéh Khanesar, United Kingdom  
Tarek Ahmed-Ali, France  
Alex Alexandridis, Greece  
Basil M. Al-Hadithi, Spain  
Juan A. Almendral, Spain  
Diego R. Amancio, Brazil  
David Arroyo, Spain  
Mohamed Boutayeb, France  
Átila Bueno, Brazil  
Arturo Buscarino, Italy  
Ning Cai, China  
Eric Campos, Mexico  
Émile J. L. Chappin, The Netherlands  
Yu-Wang Chen, United Kingdom  
Diyi Chen, China  
Giulio Cimini, Italy  
Danilo Comminiello, Italy  
Sergey Dashkovskiy, Germany  
Manlio De Domenico, Italy  
Pietro De Lellis, Italy  
Albert Diaz-Guilera, Spain  
Thach Ngoc Dinh, France  
Jordi Duch, Spain  
Marcio Eisenkraft, Brazil  
Mondher Farza, France  
Thierry Floquet, France  
José Manuel Galán, Spain  
Lucia Valentina Gambuzza, Italy  
Harish Garg, India  
Carlos Gershenson, Mexico  
Peter Giesl, United Kingdom  
Sergio Gómez, Spain  
Xiangui Guo, China  
Lingzhong Guo, United Kingdom  
Sigurdur F. Hafstein, Iceland  
Chittaranjan Hens, India  
Giacomo Innocenti, Italy  
Sarangapani Jagannathan, USA  
Mahdi Jalili, Australia  
Peng Ji, China

Jeffrey H. Johnson, United Kingdom  
Mohammad Hassan Khooban, Denmark  
Toshikazu Kuniya, Japan  
Vincent Labatut, France  
Lucas Lacasa, United Kingdom  
Guang Li, United Kingdom  
Qingdu Li, China  
Chongyang Liu, China  
Xiaoping Liu, Canada  
Xinzhi Liu, Canada  
Rosa M. Lopez Gutierrez, Mexico  
Vittorio Loreto, Italy  
Eulalia Martínez, Spain  
Marcelo Messias, Brazil  
Ana Meštrović, Croatia  
Ludovico Minati, Italy  
Saleh Mobayen, Iran  
Christopher P. Monterola, Philippines  
Marcin Mrugalski, Poland  
Roberto Natella, Italy  
Sing Kiong Nguang, New Zealand  
Irene Otero-Muras, Spain  
Yongping Pan, Singapore  
Daniela Paolotti, Italy  
Cornelio Posadas-Castillo, Mexico  
Mahardhika Pratama, Singapore  
Matilde Santos, Spain  
Michele Scarpiniti, Italy  
Enzo Pasquale Scilingo, Italy  
Dan Selișteanu, Romania  
Dimitrios Stamovlasis, Greece  
Shahadat Uddin, Australia  
Gaetano Valenza, Italy  
Jose C. Valverde, Spain  
Alejandro F. Villaverde, Spain  
Dimitri Volchenkov, USA  
Christos Volos, Greece  
Qingling Wang, China  
Wenqin Wang, China  
Zidong Wang, United Kingdom  
Yan-Ling Wei, Singapore  
Yong Xu, China  
Honglei Xu, Australia  
Xinggang Yan, United Kingdom







---

Zhile Yang, China  
Baris Yuce, United Kingdom  
Massimiliano Zanin, Spain  
Hassan Zargarzadeh, USA  
Rongqing Zhang, China  
Xianming Zhang, Australia  
Xiaopeng Zhao, USA  
Quanmin Zhu, United Kingdom

# Contents

## **Complexity, Dynamics, Control, and Applications of Nonlinear Systems with Multistability**

Viet-Thanh Pham , Sundarapandian Vaidyanathan , and Tomasz Kapitaniak

Editorial (7 pages), Article ID 8510930, Volume 2020 (2020)

## **Nonlinear Dynamics and Power Generation on a New Bistable Piezoelectric-Electromagnetic Energy Harvester**

Minghui Yao , Pengfei Liu, and Hongbo Wang



Research Article (29 pages), Article ID 5681703, Volume 2020 (2020)

## **Coexistence of Multiple Points, Limit Cycles, and Strange Attractors in a Simple Autonomous Hyperjerk Circuit with Hyperbolic Sine Function**

M. Fouodji Tsotsop , J. Kengne, G. Kenne , and Z. Tabekoueng Njitacke 





Research Article (24 pages), Article ID 6182183, Volume 2020 (2020)

## **Analyses and Encryption Implementation of a New Chaotic System Based on Semitensor Product**

Rui Wang , Peifeng Du, Wenqi Zhong, Han Han, and Hui Sun 

Research Article (13 pages), Article ID 1230804, Volume 2020 (2020)

## **A Luenberger-Like Observer for Multistable Kapitaniak Chaotic System**

J. Humberto Pérez-Cruz , Jacobo Marcos Allende Peña, Christian Nwachiona , Jose de Jesus Rubio , Jaime Pacheco, Jesus Alberto Meda-Campaña , David Ávila-González, Olivia Guevara Galindo, Ignacio Adrian Romero, and Salvador Isidro Belmonte Jiménez



Research Article (12 pages), Article ID 9531431, Volume 2020 (2020)

## **A Fractional-Order Discrete Noninvertible Map of Cubic Type: Dynamics, Control, and Synchronization**

Xiaojun Liu , Ling Hong , Lixin Yang , and Dafeng Tang

Research Article (21 pages), Article ID 2935192, Volume 2020 (2020)

## **Parallel Encryption of Noisy Images Based on Sequence Generator and Chaotic Measurement Matrix**

Jiayin Yu , Yaqin Xie, Shiyu Guo, Yanqi Zhou, and Erfu Wang 


Research Article (18 pages), Article ID 1987670, Volume 2020 (2020)

## **Circuit Realization of a 3D Multistability Chaotic System and Its Synchronization via Linear Resistor and Linear Capacitor in Parallel Coupling**

Xikui Hu and Ping Zhou 

Research Article (10 pages), Article ID 9846934, Volume 2020 (2020)



## **Complexity Analysis of a 3-Player Game with Bounded Rationality Participating in Nitrogen Emission Reduction**

Jixiang Zhang and Xuan Xi 



Research Article (16 pages), Article ID 2069614, Volume 2020 (2020)





**Heterogeneous and Homogenous Multistabilities in a Novel 4D Memristor-Based Chaotic System with Discrete Bifurcation Diagrams**

Lilian Huang , Wenju Yao, Jianhong Xiang , and Zefeng Zhang  
Research Article (15 pages), Article ID 2408460, Volume 2020 (2020)

**Symmetry Breaking, Coexisting Bubbles, Multistability, and Its Control for a Simple Jerk System with Hyperbolic Tangent Nonlinearity**

Léandre Kamdjeu Kengne , Jacques Kengne, Justin Roger Mboupda Pone, and Hervé Thierry Kamdem Tagne   
Research Article (24 pages), Article ID 2340934, Volume 2020 (2020)




**An Efficient and Cost-Effective Power Scheduling in Zero-Emission Ferry Ships**

Armin Letafat, Mehdi Rafiei, Masoud Ardeshiri, Morteza Sheikh, Mohsen Banaei , Jalil Boudjadar, and Mohammad Hassan Khooban   
Research Article (12 pages), Article ID 6487873, Volume 2020 (2020)



**Multistable Systems with Hidden and Self-Excited Scroll Attractors Generated via Piecewise Linear Systems**

R. J. Escalante-González and Eric Campos   
Research Article (12 pages), Article ID 7832489, Volume 2020 (2020)


**Dynamic Analysis of a Heterogeneous Diffusive Prey-Predator System in Time-Periodic Environment**

Chuanjun Dai , He Liu, Zhan Jin, Qing Guo, Yi Wang, Hengguo Yu , Qi Wang, Zengling Ma, and Min Zhao   
Research Article (13 pages), Article ID 7134869, Volume 2020 (2020)


**The Diffusive Model for West Nile Virus on a Periodically Evolving Domain**

Abdelrazig K. Tarboush  and Zhengdi Zhang   
Research Article (18 pages), Article ID 6280313, Volume 2020 (2020)










**Control of Near-Grazing Dynamics in the Two-Degree-of-Freedom Vibroimpact System with Symmetrical Constraints**

Zihan Wang, Jieqiong Xu , Shuai Wu, and Quan Yuan  
Research Article (12 pages), Article ID 7893451, Volume 2020 (2020)

**Data-Driven Learning-Based Fault Tolerant Stability Analysis**





Lei Ge and Shun Chen   
Research Article (7 pages), Article ID 1891273, Volume 2020 (2020)

**Chaos-Based Application of a Novel Multistable 5D Memristive Hyperchaotic System with Coexisting Multiple Attractors**

Fei Yu , Li Liu , Shuai Qian, Lixiang Li , Yuanyuan Huang , Changqiong Shi , Shuo Cai , Xianming Wu , Sichun Du , and Qiuzhen Wan   
Research Article (19 pages), Article ID 8034196, Volume 2020 (2020)


# Contents

## **Global Dynamics of the Chaotic Disk Dynamo System Driven by Noise**

Chunsheng Feng , Lijie Li , Yongjian Liu , and Zhouchao Wei 


Research Article (9 pages), Article ID 8375324, Volume 2020 (2020)

## **CCII and FPGA Realization: A Multistable Modified Fourth-Order Autonomous Chua's Chaotic System with Coexisting Multiple Attractors**

Fei Yu , Hui Shen , Li Liu , Zinan Zhang , Yuanyuan Huang , Binyong He , Shuo Cai , Yun Song , Bo Yin, Sichun Du , and Quan Xu 




Research Article (17 pages), Article ID 5212601, Volume 2020 (2020)

## **The Impact of Service and Channel Integration on the Stability and Complexity of the Supply Chain**

Jianheng Zhou and Xingli Chen 




Research Article (27 pages), Article ID 8178947, Volume 2020 (2020)

## **The Impacts of Fairness Concern and Different Business Objectives on the Complexity of Dual-Channel Value Chains**

Qiuxiang Li , Yuhao Zhang , and Yimin Huang 

Research Article (15 pages), Article ID 1716084, Volume 2020 (2020)

## **Dynamical Complexity and Multistability in a Novel Lunar Wake Plasma System**

Bo. Yan, Punam K. Prasad , Sayan Mukherjee, Asit Saha , and Santo Banerjee 


Research Article (11 pages), Article ID 5428548, Volume 2020 (2020)

## **Symmetry Breaking Soliton, Breather, and Lump Solutions of a Nonlocal Kadomtsev–Petviashvili System**

Hong-Yu Wu , Jin-Xi Fei, Zheng-Yi Ma , Jun-Chao Chen , and Wen-Xiu Ma 



Research Article (13 pages), Article ID 6423205, Volume 2020 (2020)

## **On a Thermoelastic Laminated Timoshenko Beam: Well Posedness and Stability**

Baowei Feng 


Research Article (13 pages), Article ID 5139419, Volume 2020 (2020)

## **Hopf Bifurcation and Dynamic Analysis of an Improved Financial System with Two Delays**

G. Kai, W. Zhang , Z. Jin , and C. Z. Wang

Research Article (13 pages), Article ID 3734125, Volume 2020 (2020)

## **Navigating Deeply Uncertain Tradeoffs in Harvested Predator-Prey Systems**

Antonia Hadjimichael , Patrick M. Reed, and Julianne D. Quinn

Research Article (18 pages), Article ID 4170453, Volume 2020 (2020)



## **Mixed-Mode Oscillation in a Class of Delayed Feedback System and Multistability Dynamic Response**

Youhua Qian  and Wenjing Meng

Research Article (18 pages), Article ID 4871068, Volume 2020 (2020)



**Stability and Hopf Bifurcation of Three-Species Prey-Predator System with Time Delays and Allee Effect**

F. A. Rihan , H. J. Alsakaji , and C. Rajivganthi




Research Article (15 pages), Article ID 7306412, Volume 2020 (2020)

**A New Proof of Existence of Positive Weak Solutions for Sublinear Kirchhoff Elliptic Systems with Multiple Parameters**

Salah Mahmoud Boulaaras , Rafik Guefaifa , Bahri Cherif , and Sultan Alodhaibi 











Research Article (6 pages), Article ID 1924085, Volume 2020 (2020)

**Existence of Positive Solutions for a Class of  $\Delta$ -Laplacian Elliptic Systems with Multiplication of Two Separate Functions**

Youcef Bouizem , Salah Mahmoud Boulaaras , and Ali Allahem 

Research Article (10 pages), Article ID 3756406, Volume 2020 (2020)

**Secure Communication Scheme Based on a New 5D Multistable Four-Wing Memristive Hyperchaotic System with Disturbance Inputs**

Fei Yu , Zinan Zhang , Li Liu , Hui Shen , Yuanyuan Huang , Changqiong Shi , Shuo Cai , Yun Song , Sichun Du , and Quan Xu 

Research Article (16 pages), Article ID 5859273, Volume 2020 (2020)

**Investigations of Nonlinear Triopoly Models with Different Mechanisms**

S. S. Askar  and A. Al-khedhairi 

Research Article (15 pages), Article ID 4252151, Volume 2019 (2019)

**Abundant Coexisting Multiple Attractors' Behaviors in Three-Dimensional Sine Chaotic System**

Huagan Wu , Han Bao , Quan Xu , and Mo Chen 

Research Article (11 pages), Article ID 3687635, Volume 2019 (2019)

## Editorial

# Complexity, Dynamics, Control, and Applications of Nonlinear Systems with Multistability

**Viet-Thanh Pham** <sup>1,2,3</sup>, **Sundarapandian Vaidyanathan** <sup>4</sup>, and **Tomasz Kapitaniak**<sup>3</sup>

<sup>1</sup>Faculty of Electrical and Electronic Engineering, Phenikaa Institute for Advanced Study (PIAS), Phenikaa University, Yen Nghia, Ha Dong District, Hanoi 100000, Vietnam

<sup>2</sup>Phenikaa Research and Technology Institute (PRATI), A&A Green Phoenix Group, 167 Hoang Ngan, Hanoi 100000, Vietnam

<sup>3</sup>Division of Dynamics, Lodz University of Technology, Stefanowskiego 1/15, Lodz 90-924, Poland

<sup>4</sup>Research and Development Centre, Vel Tech University, No. 42, Avadi-Vel Tech Road, Avadi, Chennai, Tamil Nadu 600062, India

Correspondence should be addressed to Viet-Thanh Pham; thanh.phamviet@phenikaa-uni.edu.vn

Received 4 June 2020; Accepted 5 June 2020; Published 4 September 2020

Copyright © 2020 Viet-Thanh Pham et al. This is an open access article distributed under the Creative Commons Attribution License, which permits unrestricted use, distribution, and reproduction in any medium, provided the original work is properly cited.

Multistability is a critical property of nonlinear dynamical systems, where a variety of phenomena such as coexisting attractors can appear for the same parameters but with different initial conditions. The flexibility in the system's performance can be achieved without changing parameters. Complex dynamics have been observed in multistable systems, and we have witnessed systems with multistability in numerous fields ranging across physics, biology, chemistry, electronics, and mechanics, as well as reported applications in oscillators and secure communications. It is now well established from a variety of studies that multistable systems are very sensitive to both random noise and perturbations. Numerous studies such as open-loop control, feedback control, adaptive control, intelligent control, and stochastic control have been attempted to control multistable systems.

Recent attention has focused more on extraordinary cases of systems with multistability, such as systems with megastability and extreme multistability. A megastable system can display countably infinite number of coexisting attractors, whereas an extreme multistable system can exhibit an uncountably infinite number of coexisting attractors. However, there are still various theoretical and technical issues which should be investigated in such multistable systems. Circuit design (numerical and hardware) of multistable systems is a related research problem with real-world applications, and fractional-order modelling and realization of multistable systems also constitute a

complex and challenging task. Furthermore, circuit realizations (simulations and hardware design) of multistable systems are useful for various practical applications in engineering.

This special issue aims to introduce and discuss novel results, control techniques, and circuit simulations for complex nonlinear systems with multistability. We had received a total of 94 submissions. After the review process, the acceptance rate is approximately 35.1%. This special issue contains 33 articles, the contents of which are summarized as follows.

In the article by M. F. Tsotsop et al., a new elegant hyperjerk system with three equilibria and hyperbolic sine nonlinearity is investigated. In contrast to other models of hyperjerk systems where either hidden or self-excited attractors are obtained, the case reported in this work represents a unique one which displays the coexistence of self-excited chaotic attractors and stable fixed points. The dynamic properties of the new system are explored in terms of equilibrium point analyses, symmetry, and dissipation and existence of attractors as well. Common analysis tools (i.e., bifurcation diagram, Lyapunov exponents, phase portrait, etc.) are used to highlight some important phenomena such as period-doubling bifurcation, chaos, periodic windows, and symmetric restoring crises. More interestingly, the system under consideration shows the coexistence of several types of stable states, including the

coexistence of two, three, four, six, eight, and ten coexisting attractors. In addition, the system is shown to display antimonotonicity and offset boosting. Laboratory experimental measurements show very good coherence with the theoretical predictions.

The objective of the article by J. H. Pérez-Cruz is to estimate the unmeasurable variables of a multistable chaotic system using a Luenberger-like observer. First, the observability of the chaotic system is analyzed. Next, a Lipschitz constant is determined on the attractor of this system. Then, the methodology proposed by Raghavan and the result proposed by Thau are used to try to find an observer. Both attempts are unsuccessful. In spite of this, a Luenberger-like observer can still be used based on a proposed gain. The performance of this observer is tested by numerical simulation showing the convergence to zero of the estimation error. Finally, the chaotic system and its observer are implemented using 32-bit microcontrollers. The experimental results confirm good agreement between the responses of the implemented and simulated observers.

Semitenor product theory can deal with matrix multiplication with different number of columns and rows. Therefore, a new chaotic system for different high dimensions can be created by employing a semitenor product of chaotic systems with different dimensions so that more channels can be selected for encryption. R. Wang et al. propose a new chaotic system generated by the semitenor product applied on Qi and Lorenz systems. The corresponding dynamic characteristics of the new system are discussed in this article to verify the existences of different attractors. The detailed algorithm is illustrated in this article. The FPGA hardware encryption implementations are also elaborated and conducted. Correspondingly, the randomness tests are realized as well, and compared with those of the individual Qi system and Lorenz system, the proposed system in this article owns the better randomness characteristic. The statistical analyses, differential analyses, and correlation analyses are also discussed.

The article by M. Yao et al. focuses on power generation and nonlinear dynamic behaviors on a new bistable piezoelectric-electromagnetic energy harvester. Three different kinds of piezoelectric cantilever beam structures, which include the monostable piezoelectric cantilever beam, the bistable piezoelectric cantilever beam with the spring and the magnet, and the bistable piezoelectric cantilever beam with the spring, magnet and coil, are designed. The power generation efficiency and dynamic behaviors for each structure are experimentally studied, respectively. Due to the spring introduced, the system easily goes through the potential barrier. Experimental results show that the power generation structure of the bistable piezoelectric-electromagnetic harvester can vibrate between two steady states in a wider range of the frequency. Therefore, the effective frequency bandwidth is broadened about 2 Hz when the spring is introduced under the condition of the suitable magnetic distance. Comparing with the power generation efficiency for three different kinds of structures, it is found that the bistable piezoelectric-electromagnetic harvester has the optimum characteristics, which include the optimal magnetic distance

of 15 mm, the optimal load of  $8\text{ M}\Omega$ , and the parameter variation law of coils. For this structure, the influences of the external excitation and the magnetic distance on the output voltage and dynamic behaviors of the system are examined.

In the article by X. Liu et al., a new fractional-order discrete noninvertible map of cubic type is presented. Firstly, the stability of the equilibrium points for the map is examined. Secondly, the dynamics of the map with two different initial conditions are studied by numerical simulation when a parameter or a derivative order is varied. A series of attractors are displayed in various forms of periodic and chaotic ones. Furthermore, bifurcations with the simultaneous variation of both the parameter and the order are also analyzed in the three-dimensional space. Interior crises are found in the map as a parameter or an order varies. Thirdly, based on the stability theory of fractional-order discrete maps, a stabilization controller is proposed to control the chaos of the map, and the asymptotic convergence of the state variables is determined. Finally, the synchronization between the proposed map and the fractional-order discrete Loren map is investigated. Numerical simulations are used to verify the effectiveness of the designed synchronization controllers.

Aiming at the problem of weak security of compressed sensing, J. Yu et al. combine the cryptographic characteristics of chaotic systems with compressed sensing technology. In the actual research process, the existing image encryption technology needs to be applied to hardware. This article focuses on the combination of image encryption based on compressed sensing and digital logic circuits. The authors propose a novel technology of parallel image encryption based on a sequence generator. It uses a three-dimensional chaotic map with multiple stability to generate a measurement matrix. This study also analyzes the effectiveness, reliability, and security of the parallel encryption algorithm for source noise pollution with different distribution characteristics. Simulation results show that parallel encryption technology can effectively improve the efficiency of information transmission and greatly enhance its security through key space expansion.

In the article by X. Hu and P. Zhou, a 3D multistability chaotic system with two coexisting conditional symmetric attractors is studied by using a circuit block diagram and realized by using an electronic circuit. The simulation results show that two coexisting conditional symmetric attractors are emerged in this electronic circuit. Furthermore, synchronization of this 3D multistability chaotic system and its electronic circuit is studied. It shows that the linear resistor and the linear capacitor in parallel coupling can achieve synchronization in this chaotic electronic circuit. That is, the output voltage of the chaotic electronic circuit is coupled via one linear resistor and one linear capacitor in parallel coupling. The simulation results verify that synchronization of the chaotic electronic circuit can be achieved.

In the article by J. Zhang and X. Xi, a decision-making competition game model concerning governments, agricultural enterprises, and the public, all of which participate in the reduction of nitrogen emissions in the watersheds, is established based on bounded rationality. First, the stability

conditions of the equilibrium points in the system are discussed, and the stable region of the Nash equilibrium is determined. Then, the bifurcation diagram, maximal Lyapunov exponent, strange attractor, and sensitive dependence on the initial conditions are shown through numerical simulations. The research shows that the adjustment speed of three players' decisions may alter the stability of the Nash equilibrium point and lead to chaos in the system. Among these decisions, a government's decision has the largest effect on the system. In addition, authors found that some parameters will affect the stability of the system; when the parameters become beneficial for enterprises to reduce nitrogen emissions, the increase in the parameters can help control the chaotic market. Finally, the delay feedback control method is used to successfully control the chaos in the system and stabilize it at the Nash equilibrium point. The research of this article is of great significance to the environmental governance decisions and nitrogen reduction management.

L. Huang et al. have constructed a new 4D memristor-based chaotic system by using a smooth flux-controlled memristor to replace a resistor in the realization circuit of a 3D chaotic system. Compared with general chaotic systems, the chaotic system can generate many coexisting attractors. The proposed chaotic system not only possesses heterogeneous multistability but also possesses homogenous multistability. When the parameters of the system are fixed, the chaotic system only generates two kinds of chaotic attractors with different positions in a very large range of initial values. Different from other chaotic systems with continuous bifurcation diagrams, this system has discrete bifurcation diagrams when the initial values change. In addition, this article reveals the relationship between the symmetry of coexisting attractors and the symmetry of initial values in the system. The dynamic behaviors of the new system are analyzed by the equilibrium point and stability, bifurcation diagrams, Lyapunov exponents, and phase orbit diagrams. Finally, the chaotic attractors are captured through circuit simulation, which verifies numerical simulation.

L. K. Kengne et al. investigate the dynamics of a simple jerk system with a hyperbolic tangent whose symmetry is broken by adding a constant term modelling an external excitation force. They demonstrate that the modified system experiences several unusual and striking nonlinear phenomena including coexisting bifurcation branches, hysteretic dynamics, coexisting asymmetric bubbles, critical transitions, and multiple (i.e., up to six) coexisting asymmetric attractors for some suitable ranges of system parameters. These features are highlighted by exploiting common nonlinear analysis tools such as graphs of the largest Lyapunov exponent, bifurcation diagrams, phase portraits, and basins of attraction. The control of multistability is investigated by using the method of linear augmentation. The authors demonstrate that the multistable system can be converted to a monostable state by smoothly adjusting the coupling parameter. The theoretical results are confirmed by performing a series of PSpice simulations based on an electronic analogue of the system.

The article by A. Letafat et al. introduces an energy management strategy (EMS) for a hybrid energy system (HES) of a ferry boat with the goal to optimize the performance and reduce the operation cost. HES considered for the ferry boat consists of different devices such as the proton-exchange membrane fuel cell (PEMFC), LI-ION battery bank, and cold ironing (CI). PEMFC systems are appropriate to employ as they are not polluting. The battery bank compensates for the abrupt variations of the load as the fuel cell has a slow dynamic against sudden changes of the load. Also, CI systems can improve the reduction of the expenses of energy management, during hours where the ferry boat is located at the harbor. To study the performance, the cost, and the pollution contribution ( $\text{CO}_2$ ,  $\text{NO}_x$ , and  $\text{SO}_x$ ) of the proposed hybrid energy management strategy (HEMS), we compare it against three various types of HEM from the state-of-the-art and also available rule-based methods in the literature. The analysis results show a high applicability of the proposed HES. All results in this article have been obtained in the MATLAB software environment.

The article by R. J. Escalante-González and E. Campos presents an approach to design a multistable system with the one-directional (1D), two-directional (2D), and three-directional (3D) hidden multiscroll attractor by defining a vector field on  $\mathbb{R}^3$  with an even number of equilibria. The design of multistable systems with hidden attractors remains a challenging task. Current design approaches are not as flexible as those that focus on self-excited attractors. To facilitate a design of hidden multiscroll attractors, they propose an approach that is based on the existence of self-excited double-scroll attractors and switching surfaces whose relationship with the local manifolds associated to the equilibria leads to the appearance of the hidden attractor. The multistable systems produced by the approach could be explored for potential applications in cryptography since the number of attractors can be increased by design in multiple directions while preserving the hidden attractor allowing a bigger key space.

In the article by C. Dai et al., a heterogeneous diffusive prey-predator system is first proposed and then studied analytically and numerically. Some sufficient conditions are derived, including permanence and extinction of the system and the boundedness of the solution. The existence of the periodic solution and its stability are discussed as well. Furthermore, numerical results indicate that both the spatial heterogeneity and the time-periodic environment can influence the permanence and extinction of the system directly. The numerical results are consistent with the analytical analysis.

A. K. Tarboush and Z. Zhang investigate the impact of a periodically evolving domain on the dynamics of the diffusive West Nile virus. A reaction-diffusion model on a periodically and isotropically evolving domain which describes the transmission of the West Nile virus is proposed. In addition to the classical basic reproduction number, the spatial-temporal basic reproduction number depending on the periodic evolution rate is introduced, and its properties are discussed. Under some conditions, they explore the long-time behavior of the virus. The virus will go extinct if the



spatial-temporal basic reproduction number is less than or equal to one. The persistence of the virus happens if the spatial-temporal basic reproduction number is greater than one. They consider a special case when the periodic evolution rate is equivalent to one to better understand the impact of the periodic evolution rate on the persistence or extinction of the virus. Some numerical simulations are performed in order to illustrate the analytical results. The theoretical analysis and numerical simulations show that the periodic change of the habitat range plays an important role in the West Nile virus transmission; in particular, the increase in periodic evolution rate has a positive effect on the spread of the virus.

The stability of grazing bifurcation is lost in three ways through the local analysis of the near-grazing dynamics using the classical concept of discontinuity mappings in the two-degree-of-freedom vibroimpact system with symmetrical constraints. For this instability problem, Z. Wang et al. presented a control strategy for the stability of grazing bifurcation by controlling the persistence of local attractors near the grazing trajectory in this vibroimpact system with symmetrical constraints. Discrete-in-time feedback controllers designed on two Poincaré sections are employed to retain the existence of an attractor near the grazing trajectory. The implementation relies on the stability criterion under which a local attractor persists near a grazing trajectory. Based on the stability criterion, the control region of the two parameters is obtained, and the control strategy for the persistence of near-grazing attractors is designed accordingly. Especially, the chaos near codimension-two grazing bifurcation points was controlled by the control strategy. In the end, the results of numerical simulation are used to verify the feasibility of the control method.

In the article by L. Ge and S. Chen, a new data-driven learning method is investigated based on the dynamical data of the system. A regularized regression wavelet (RRW) approach is proposed to optimize the learning result for the system fault. Based on the optimizing results, a fault tolerant stability scheme is given. Then, the efficiency of the proposed technique is verified by a vertical take-off and landing (VTOL) aircraft stability example.

F. Yu et al. have introduced a novel multistable 5D memristive hyperchaotic system and its application. The interesting aspect of this chaotic system is that it has different types of coexisting attractors, chaos, hyperchaos, periods, and limit cycles. First, a novel 5D memristive hyperchaotic system is proposed by introducing a flux-controlled memristor with quadratic nonlinearity into an existing 4D four-wing chaotic system as a feedback term. Then, the phase portraits, Lyapunov exponential spectrum, bifurcation diagram, and spectral entropy are used to analyze the basic dynamics of the 5D memristive hyperchaotic system. For a specific set of parameters, we find an unusual metastability, which shows the transition from chaotic to periodic (period-2 and period-3) dynamics. Moreover, its circuit implementation is also proposed. By using the chaoticity of the novel hyperchaotic system, they have developed a random number generator (RNG) for practical image encryption

applications. Furthermore, security analyses are carried out with the RNG and image encryption designs.

The disk dynamo system, which is capable of chaotic behaviours, is obtained experimentally from two disk dynamos connected together. It models the geomagnetic field and is used to explain the reversals in its polarity. Actually, the parameters of the chaotic systems exhibit random fluctuation to a greater or lesser extent, which can carefully describe the disturbance made by environmental noise. In the article by C. Feng et al., the global dynamics of the chaotic disk dynamo system with random fluctuating parameters are concerned, and some new results are presented. Based on the generalized Lyapunov function, the globally attractive and positive invariant set is given, including a two-dimensional parabolic ultimate boundary and a four-dimensional ellipsoidal ultimate boundary. Furthermore, a set of sufficient conditions is derived for all solutions of the stochastic disk dynamo system being global convergent to the equilibrium point. Finally, numerical simulations are presented for verification.

In the article by F. Yu et al., multistable modified fourth-order autonomous Chua's chaotic system is investigated. In addition to the dynamic characteristics of third-order Chua's chaotic system itself, what interests authors is that this modified fourth-order autonomous Chua's chaotic system has five different types of coexisting attractors: double-scroll, single-band chaotic attractor, period-4 limit cycle, period-2 limit cycle, and period-1 limit cycle. Then, inductorless modified fourth-order autonomous Chua's chaotic circuit is proposed. The active elements as well as the synthetic inductor employed in this circuit are designed using second-generation current conveyors (CCII). The reason for using CCII is that they have high conversion rate and operation speed, which enable the circuit to work at a higher frequency range. The Multisim simulations confirm the theoretical estimates of the performance of the proposed circuit. Finally, using the RK-4 numerical algorithm of VHDL 32-bit IQ-Math floating-point number format, inductorless modified fourth-order autonomous Chua's chaotic system is implemented on FPGA for the development of embedded engineering applications based on chaos. The system is simulated and synthesized on the Virtex-6 FPGA chip. The maximum operating frequency of modified Chua's chaotic oscillator based on FPGA is 180.180 MHz. This study demonstrates that hardware-based multistable modified fourth-order autonomous Chua's chaotic system is a very good source of entropy and can be applied to various embedded systems based on chaos, including secure communication, cryptography, and random number generator.

J. Zhou and X. Chen construct a supply chain consisting of a manufacturer and a retailer. Considering channel integration and service cooperation, two dynamic Stackelberg game models are established: one without unit profit allocation ( $M$ ) and the other one with unit profit allocation ( $M^\epsilon$ ). In two dynamic models, the authors analyze the influence of relevant parameters on the stability and complexity of the dynamic system and system profit by nonlinear system theory and numerical simulation. They found that the higher adjustment parameters can cause the system to

lose stability, showing double-period bifurcation or wave-shape chaos. The stable region becomes larger with increase in service value and value of unit profit sharing. Besides, when the system is in the chaotic state, the authors found that the profit of the system will fluctuate or even decline sharply; however, keeping the parameters in a certain range is helpful in maintaining the system stability and is conducive to decision makers to obtain steady profits. In order to control the chaos phenomenon, the state feedback method is employed to control the chaotic system well. This study provides some valuable significance to supply chain managers in channel integration and service cooperation.

Q. Li et al. consider a Stackelberg game model in a dual-channel supply chain, which is composed of a manufacturer and a retailer. The manufacturer and the retailer consider fairness concern in the market competition, and the manufacturer takes market share and profit as his/her business objectives. The entropy complexity and the dynamic characteristic of the dual-channel system are analyzed through mathematical analysis and numerical simulation, such as local stability, bifurcation, entropy, and chaos. The results show that, with the increase of price adjustment speed, the dual-channel supply chain is more complex and falls into a chaotic state in which system entropy increases; the stability of the dual-channel supply chain will be robust with the increase of weight of market share and weaken with the increase of the fairness concern level of the manufacturer and the retailer. The high level of fairness concern of the manufacturer and the retailer is always disadvantageous to the leading manufacturer but not always bad for the follower retailer. The performance of the dual-channel supply chain is improved with a high level of the manufacturer's fairness concern and reduced with a high level of the retailer's fairness concern. They also found that the retailer will gain more profits in the chaotic state than the stable state in the Stackelberg game model. The variable feedback control method is applied to control the chaos of the dual-channel supply chain, and choosing appropriate control parameters can make the dual-channel supply chain system return to the stable state from the chaotic state or delay the system to enter the bifurcation state. The research results can provide a guideline for enterprise decision-making.

In the article by B. Yan et al., dynamical complexity and multistability of electrostatic waves are investigated in four-component homogenous and magnetized lunar wake plasma constituting beam electrons, heavier ions (alpha particles,  $\text{He}^{++}$ ), protons, and suprathermal electrons. The unperturbed dynamical system of the considered lunar wake plasma supports nonlinear and supernonlinear trajectories which correspond to nonlinear and supernonlinear electrostatic waves. On the contrary, the perturbed dynamical system of lunar wake plasma shows different types of coexisting attractors including periodic, quasi-periodic, and chaotic, investigated by phase plots and Lyapunov exponents. To confirm chaotic and nonchaotic dynamics in the perturbed lunar wake plasma, 0-1 chaos test is performed. Furthermore, a weighted recurrence-based entropy is implemented to investigate the dynamical complexity of the

system. Numerical results show the existence of chaos with variation of complexity in the perturbed dynamics.

The Kadomtsev–Petviashvili equation is one of the well-studied models of nonlinear waves in dispersive media and in multicomponent plasmas. In the article by H.-Y. Wu et al., the coupled Alice–Bob system of the Kadomtsev–Petviashvili equation is first constructed via the parity with a shift of the space variable  $x$  and time reversal with a delay. By introducing an extended Bäcklund transformation, symmetry-breaking soliton, symmetry-breaking breather, and symmetry-breaking lump solutions for this system are presented through the established Hirota bilinear form. According to the corresponding constants in the involved ansatz function, a few fascinating symmetry-breaking structures of the presented explicit solutions are shown.

B. Feng is concerned with a linear thermoelastic laminated Timoshenko beam, where the heat conduction is given by Cattaneo's law. B. Feng firstly proves the global well-posedness of the system. For stability results, the author establishes exponential and polynomial stabilities by introducing a stability number  $\chi$ .

G. Kai et al. study the influence of two-delay feedback on the nonlinear dynamics behavior of the financial system, considering the linear stability of the equilibrium point under the condition of single delay and two delays. The system undergoes Hopf bifurcation near the equilibrium point. The stability and bifurcation directions of Hopf bifurcation are studied by using the normal form method and central manifold theory. The theoretical results are verified by numerical simulation. Furthermore, one feature of the proposed financial chaotic system is that its multistability depends extremely on the memristor initial condition and the system parameters. It is shown that the nonlinear dynamics of the financial chaotic system can be significantly changed by changing the values of time delays.

Results of A. Hadjimichael et al. show that classical assumptions for fisheries management can yield severe instabilities in the quantified views of socioecological tradeoffs, making their ability to inform stakeholder preferences questionable. The complex ecological interactions implied by different parameterizations of such systems yield highly complex and nonlinear dynamic properties with multiple distinct basins of attraction. The authors show that small changes in the deeply uncertain representations of predator-prey systems can fundamentally shift their dynamics and the validity of candidate management strategies for harvest. Insights from this study highlight the importance of ensuring models capture deep uncertainties, as well as a breadth of financial and ecological criteria, when searching for robust management options for resilient fisheries.

A class of two-parameter mixed-mode oscillation with time delay under the action of amplitude modulation is studied by Y. Qian and W. Meng. The investigation is from four aspects. Firstly, a parametric equation is considered as a slow variable. By the time-history diagram and phase diagram, the authors can find that the system generates a cluster discovery image. Secondly, the Euler method is used

to discrete the system and obtain the discrete equation. Thirdly, the dynamic characteristics of the system at different time scales are discussed when the ratio of the natural frequency and the excitation frequency of the system is integer and noninteger. Fourthly, the authors discuss the influence of time delay on the discovery of clusters of this kind of system. The research shows that the time lag does not interfere with the influence of the cluster image, but the dynamics of the upper and lower parts of the oscillation in each period will be delayed. So, they can improve peak performance by adjusting the time lag and obtain the desired peak. Finally, the authors explore the multistate dynamic response of a two-dimensional non-autonomous Duffing system with higher order. According to the bifurcation diagram and the time-history curve, bistable state will appear in the system within the critical range. With the gradual increase of parameters, the chaotic attractor will suddenly disappear which will lead to the destruction of the bistable state.

F. A. Rihan et al. study the dynamics of a two-prey one-predator system, where the growth of both prey populations is subject to Allee effects, and there is a direct competition between the two-prey species having a common predator. Two discrete time delays  $\tau_1$  and  $\tau_2$  are incorporated into the model to represent the reaction time of predators. Sufficient conditions for local stability of positive interior equilibrium and existence of Hopf bifurcations in terms of threshold parameters  $\tau_1^*$  and  $\tau_2^*$  are obtained. A Lyapunov functional is deduced to investigate the global stability of positive interior equilibrium. Sensitivity analysis to evaluate the uncertainty of the state variables to small changes in the Allee parameters is also investigated. Presence of Allee effect and time delays in the model increases the complexity of the model and enriches the dynamics of the system. Some numerical simulations are provided to illustrate the effectiveness of the theoretical results. The model is highly sensitive to small changes in Allee parameters at the early stages and with low population densities, and this sensitivity decreases with time.

The article by S. M. Boulaaras et al. deals with the study of the existence of weak positive solutions for sublinear Kirchhoff elliptic systems with the zero Dirichlet boundary condition in the bounded domain  $\Omega \subset \mathbb{R}^N$  by using the sub-supersolution method.

The article by Y. Bouizem et al. deals with the study of the existence of weak positive solutions for a new class of the system of elliptic differential equations with respect to the symmetry conditions and the right-hand side which has been defined as multiplication of two separate functions by using the sub-supersolution method.

By introducing a flux-controlled memristor model with absolute value function, a 5D multistable four-wing memristive hyperchaotic system (FWMHS) with linear equilibrium points is proposed in the article by F. Yu et al. The dynamic characteristics of the system are studied in terms of the equilibrium point, perpetual point, bifurcation diagram, Lyapunov exponential spectrum, phase portraits, and spectral entropy. This system is of the group of systems that have coexisting attractors. In addition, the

circuit implementation scheme is also proposed. Then, a secure communication scheme based on the proposed 5D multistable FWMHS with disturbance inputs is designed. Based on parametric modulation theory and Lyapunov stability theory, synchronization and secure communication between the transmitter and the receiver are realized, and two message signals are recovered by a convenient robust high-order sliding mode adaptive controller. Through the proposed adaptive controller, the unknown parameters can be identified accurately, the gain of the receiver system can be adjusted continuously, and the disturbance inputs of the transmitter and the receiver can be suppressed effectively. Thereafter, the convergence of the proposed scheme is proven by means of an appropriate Lyapunov functional, and the effectiveness of the theoretical results is testified via numerical simulations.

The article by S. S. Askar and A. Al-khedhairi studies the dynamic characteristics of triopoly models that are constructed based on a 3-dimensional Cobb–Douglas utility function. The article presents two parts. The first part introduces a competition among three rational firms on which their prices are isoelastic functions. The competition is described by a 3-dimensional discrete dynamical system. The authors examine the impact of rationality on the system's steady-state point. The stability/instability of this point is illustrated. Numerically, the authors give some global analysis of the Nash point and its stability. The second part deals with heterogeneous scenarios. It consists of two different models. In the first model, the authors assume that one competitor adopts the local monopolistic approximation mechanism (LMA), while the other opponents are rational. The second model assumes two heterogeneous players with the LMA mechanism against one rational firm. Studies show that the stability of the NE point of those models is not guaranteed. Furthermore, simulation shows that when firms behave rational with symmetric costs, the stability of the NE point is achievable.

The article by H. Wu et al. presents a novel and simple three-dimensional (3D) chaotic system by introducing two sine nonlinearities into a simple 3D linear dynamical system. The presented sine system possesses nine equilibrium points consisting of five index-2 saddle foci and four index-1 saddle foci which allow the coexistence of various types of disconnected attractors, also known as multistability. The coexisting multiple attractors are depicted by the phase plots and attraction basins. Coexisting bifurcation modes triggered by different initial values are numerically simulated by two-dimensional bifurcation and complexity plots under two sets of initial values and one-dimensional bifurcation plots under three sets of initial values, which demonstrate that the abundant coexisting multiple attractors' behaviors in the presented sine system are related not only to the system parameters but also to the initial values. A simulation-oriented circuit model is synthesized, and PSIM (power simulation) screen captures well validate the numerical simulations.

### **Conflicts of Interest**

The editors declare that they have no conflicts of interest.

### **Acknowledgments**

The editorial team would like to express their appreciation to all authors for their valuable contributions. In addition, the editors would like to thank the Complexity Journal's Editorial Board for their valuable help and support regarding this special issue.

*Viet-Thanh Pham  
Sundarapandian Vaidyanathan  
Tomasz Kapitaniak*



## Research Article

# Nonlinear Dynamics and Power Generation on a New Bistable Piezoelectric-Electromagnetic Energy Harvester

Minghui Yao <sup>1</sup>, Pengfei Liu,<sup>2</sup> and Hongbo Wang<sup>3</sup>

<sup>1</sup>*School of Artificial Intelligence, Tiangong University, Tianjin 300387, China*

<sup>2</sup>*School of Mechanical Engineering, Tiangong University,*

*Tianjin Key Laboratory of Modern Mechatronics Equipment Technology, Tianjin 300387, China*

<sup>3</sup>*College of Mechanical Engineering, Beijing University of Technology,*

*Beijing Key Laboratory of Nonlinear Vibrations and Strength of Mechanical Structures, Beijing 100124, China*

Correspondence should be addressed to Minghui Yao; merry\_mingming@163.com

Received 5 January 2020; Revised 5 April 2020; Accepted 29 May 2020; Published 4 September 2020

Guest Editor: Viet-Thanh Pham

Copyright © 2020 Minghui Yao et al. This is an open access article distributed under the Creative Commons Attribution License, which permits unrestricted use, distribution, and reproduction in any medium, provided the original work is properly cited.

This paper focuses power generation and nonlinear dynamic behaviors on a new bistable piezoelectric-electromagnetic energy harvester. Three different kinds of piezoelectric cantilever beam structures, which include the monostable piezoelectric cantilever beam, the bistable piezoelectric cantilever beam with spring and magnet, and the bistable piezoelectric cantilever beam with spring, magnet, and coil, are designed. The power generation efficiency and dynamic behaviors for each structure are experimentally studied, respectively. Due to the spring introduced, the system easily goes through the potential barrier. Experimental results show that the power generation structure of the bistable piezoelectric-electromagnetic harvester can vibrate between two steady states in a wider range of the frequency. Therefore, the effective frequency bandwidth is broadened about 2 Hz when the spring is introduced under the condition of the suitable magnetic distance. Comparing with the power generation efficiency for three different kinds of structures, it is found that the bistable piezoelectric-electromagnetic harvester has the optimum characteristics, which include the optimal magnetic distance of 15 mm, the optimal load of 8 M $\Omega$ , and the parameters variation law of coils. For this structure, the influences of the external excitation and the magnetic distance on the output voltage and dynamic behaviors of the system are examined.

## 1. Introduction

The energy harvesting technology is a way to convert the energy of the environment into electrical energy, for example, solar energy, heat energy, sound energy, wind energy, and vibration energy. Based on much research results, the conversion efficiency of the environmental vibration energy is the best. Therefore, the vibration energy harvester has been widely studied. At present, there are three kinds of the vibration energy harvesters, such as the electrostatic type, the piezoelectric type, and the electromagnetic type. Since the electrostatic type of the energy harvester requires the external power supply and has usually the complex structure, there are few studies. Because the piezoelectric structure and the electromagnetic structure have great harvesting

efficiencies and do not need the external power supply, these two structures have been widely investigated. In recent years, scholars have theoretically and experimentally studied the power generation efficiency and dynamic behaviors of the piezoelectric beam structure and the electromagnetic power generation structure. A number of innovative structures have been proposed. The study on energy harvesters of piezoelectric type, electromagnetic type, and piezoelectric-electromagnetic combined type is introduced as follows.

The first type of the vibration energy harvesting is the piezoelectric type, which utilizes the piezoelectric effect of materials to convert the vibration energy of the environment into the electrical energy. The piezoelectric power generation has advantages of the great output voltage, the simple structure, no electromagnetic interference, and no pollution.

The piezoelectric power generation structures do not need the external power supply, so it has been widely investigated. Researchers have designed many kinds of the piezoelectric energy harvesters. Roundy et al. [1] studied a method of power supply for wireless sensor nodes based on low amplitude vibrations. The results of simulations showed that the output power of the piezoelectric structure was obviously great. Leland and Wright [2] designed and tested a vibration energy harvester with the tunable resonance frequency. This structure reduced its resonance frequency by using the novel method of an axially compressing piezoelectric beam. Beeby et al. [3] did a review of the vibration energy harvesting for the wireless and self-powered microsystems applications. There were three main approaches that could be used to capture the vibration energy of the environment. The advantages and disadvantages of each technology were described in this review. Mann and Owens [4] investigated a nonlinear energy harvester, which used magnetic interactions to design a generator with a bistable potential well. Both theoretical and experimental results showed that the potential well-escaped phenomenon broadened the effective frequency bandwidth of the energy harvester. Stanton et al. [5] examined a bistable nonlinear piezoelectric generator, which could respond in a wide range of the frequencies. Erturk and Inman [6] explored the relation between the power generation efficiency and nonlinear vibration of the bistable piezoelectric cantilever beam. They found that the magnetic piezoelectric structure had a larger vibration amplitude and a greater output power than the piezoelectric structure without magnet. Ferrari et al. [7] established a nonlinear energy harvesting system of the single magnet. The experimental results indicated that the bistable motion significantly improved the output voltage and the output power. Ma et al. [8] theoretically and experimentally investigated a magnetic piezoelectric energy harvester. The frequency bandwidth of the magnetic piezoelectric structure was broadened effectively compared with the piezoelectric structure without magnet. Arrieta et al. [9] examined a novel piezoelectric energy harvester with the bistable cantilevered structure. The bistable cantilevered structure enhanced the harvesting efficiency of the system. Al-Ashtari et al. [10] introduced a new design of the energy harvester, which improved the output power without changing the resonance frequency of the structure. The stiffness of the structure was added by the attractive force between two permanent magnets. Theoretical and experimental results showed that the great output power was generated when the piezoelectric cantilever beam only had a slight deformation. Ali and Kyle [11] explored a vibration energy harvester based on a miniature asymmetric air-spaced cantilever beam, which can generate the great power density. It was sufficient to support the electric power of the most wireless sensor nodes. Fan et al. [12] designed a roller to actuate vibration of the piezoelectric beam, which can capture the energy from both sway and bidirectional vibrations. Yao et al. [13] investigated complicated nonlinear dynamic behaviors of the simply supported laminated composite piezoelectric beam subjected to the axial load and the transverse load. Numerical results showed that the periodic motions and the chaotic

motions existed in nonlinear vibrations of the system. Jemai et al. [14] studied parameter optimization of a vibration energy harvester by using piezocomposite material and interdigitated electrode. Arkadiusz et al. [15] exploited the snap-through phenomenon between two stable states of a bistable energy harvesting device. Xie and Wang [16] examined a high efficient cylinder composite piezoelectric energy harvester. The newly designed cylinder piezoelectric energy harvester can provide more efficient energy harvesting under a higher dimension and a higher rotating speed of the roller.

The second type of the vibration energy harvesting is the electromagnetic type, which uses Faraday's law of electromagnetic induction to convert the vibration energy of the environment into the electrical energy. The power generation structure of the electromagnetic induction does not require the external power supply. It has been widely used in the field of the power generation. Galchev et al. [17] investigated an electromagnetic vibration power generator, which can efficiently harvest the energy from low-frequency excitations and nonlinear vibrations. Sari et al. [18] examined a wideband electromagnetic vibration generator. The microgenerator generated the stable output power in a wide range of the external excitation frequencies. Mann and Sims [19] experimentally and theoretically investigated a novel energy harvesting device, which used the magnetic levitation to design an oscillator with the tunable resonance frequency. The results showed that the nonlinear phenomenon can be exploited to improve the effectiveness of the energy harvesting devices. Sardini and Serpelloni [20] experimentally studied a nonlinear electromagnetic energy harvester for capturing the vibration energy of the low frequency. The effectiveness of harvesting of the nonlinear structure was greater than that of the linear structure. Zorlu et al. [21] presented a new electromagnetic energy harvester based on vibration, which harvested the energy from low-frequency vibration within a range of 1–10 Hz. The electromagnetic energy harvester with the magnet and the spring was proposed by Faisal et al. [22]. The friction between the magnet and the tube was reduced by using the lubricant in order to improve the output voltage. Ramlan et al. [23] carried out an experimental study to illustrate the dynamic characteristic of the dual mode and the bistable nonlinear energy harvester under the harmonic excitation. The nonlinear device had a greater power generation efficiency than that of the linear device. Kremer and Liu [24] investigated the energy harvester with the nonlinear energy sink. It had the capacity of absorbing the energy in a wide range of frequencies. Seol et al. [25] studied the combined energy harvester with simultaneous triboelectric and electromagnetic power generation. Resali and Salleh [26] investigated the performance of two types of the electromagnetic power generation devices, which one used the wound coil wire and the other used the printed circuit board coil.

The third type of the vibration energy harvesting is the piezoelectric-electromagnetic combined power generation structure. In order to improve the power generation efficiency of the energy harvester, there is a new trend towards simultaneously using the piezoelectric type, the

electromagnetic type, the photovoltaic type, and other energy conversion types. Since the electromechanical coupling coefficient of the electromagnetic and piezoelectric power generation structure is great, the piezoelectric-electromagnetic combined power generation structures are paid more attention. The prospects of the combined power generation devices are valued by many experts. Wacharasindhu and Kwon [27] experimentally dug into a novel microenergy harvester, which can harvest the energy from typing motions on the computer keyboard. Tadesse et al. [28] analyzed a multimode energy harvesting device, which combined electromagnetic and piezoelectric energy harvesting mechanism. The harvesting efficiency of the device was improved in a wide range of the frequencies. Challa et al. [29] studied a coupled piezoelectric-electromagnetic energy harvesting technique for improving the performance of the power generation devices. Karami and Inman [30] proposed a novel combined energy harvester, which used the nonlinear harvesting mechanisms to improve the output power and broaden the frequency bandwidth. A novel piezoelectric and electromagnetic combined energy harvester was investigated by Yang et al. [31]. When the polarization direction of magnets was perpendicular to the plane of coils, coils generated the maximum output voltage. Wang et al. [32] examined a two-degree-of-freedom combined energy harvester based on the piezoelectric and electromagnetic conduction. They concluded that the power generation efficiency of the combined energy harvester was greater than that of the single energy harvester. Mahmoudi et al. [33] validated the enhancement of the performance of a combined nonlinear energy harvester by theoretical investigation, which is based on the piezoelectric and electromagnetic transduction. Hamid and Yuce [34] designed a new wearable energy harvesting system combined piezoelectric and electromagnetic energy harvesters. It harvested the energy from low-frequency vibrations of the human motion. It showed that the combined power generation structure could be applied to the life. Yao et al. [35, 36] studied carefully power generations of the bistable energy harvester with L-shaped piezoelectric cantilever beam.

The piezoelectric power generation structures combined with electromagnetic induction were studied by a few scholars. At present, most of investigations were focused on the monostable piezoelectric-electromagnetic combined power generation structure. There were few investigations on the bistable piezoelectric-electromagnetic combined power generation structures. A multimode vibration generator, which combines the piezoelectric power generation, the electromagnetic power generation, and the bistable structure, is designed. This multimode vibration generator has been applied for the international patent (PCT/CN2015/077888), and the patent has been public. In the next study, the power generation efficiency of the bistable piezoelectric-electromagnetic combined power generation structure is explored, and dynamic behaviors of it are analyzed.

In this paper, the power generation efficiency and dynamic behaviors of the bistable piezoelectric-electromagnetic combined energy harvester based on vibration are mainly studied. The design of both bistable and multimode

structure improves the power generation efficiency of the piezoelectric part and the electromagnetic part. The magnet at the end of the spring does the telescopic reciprocating motion in the tube so that the magnetic flux of the coil is constantly changing to induce electromotance. The influence of external excitation frequencies, external excitation amplitudes, magnetic distances, loads, and coils on the power generation efficiency of the bistable piezoelectric-electromagnetic combined power generation structure is explored. Dynamic behaviors of the system under the different external excitation are studied. Comparing with the earlier studies given by Yao et al. [37], this paper is extended to add the analysis of the potential energy for the bistable power generation structure and explore the influences of the magnetic distance, the optimal external load, and coils on the power generation.

## 2. Experimental Setups

In the experiment, the piezoelectric cantilever beam, coils, magnets, and the spring are fixed on the fixture. The fixture is fixed on the vibration exciter. The signals are sent to the power amplifier by the signal generator to control vibration of the piezoelectric cantilever beam. The displacement of vibration of the piezoelectric cantilever beam is captured by using the high precision laser detector, and the time-displacement data are obtained. Then, data are sent to computer by the LK-G controller. The output voltage of the system is measured by multimeter. Finally, time-displacement data are analyzed by the LK-Navigator and Origin software. The experimental setups include the YE1311 signal generator, the YE5874 power amplifier, the JZK series of the electric vibration exciter, the high precision laser detector, the multimeter, and the LK-Navigator, as shown in Figure 1(a). The experiment fixture and the circuit are shown in Figure 1(b).

## 3. Experimental Materials

The materials used in the experiment are the piezoelectric beam, coils, resistances, springs, magnets, and wires, as shown in Figure 2. The piezoelectric material used in the experiment is the PVDF. The PVDF material is not easily damaged when the cantilever beam vibrates with a large vibration amplitude. The base layer of the piezoelectric beam is the brass. The PVDF layers and the brass are combined by the conductive adhesive. The length of the piezoelectric beam is 90 mm, the width is 10 mm, and the thickness is 0.51 mm, respectively. The thickness of the PVDF layer is 30 microns. The piezoelectric materials on the upper and lower layers are fully covered. The piezoelectric strain constant is 17 PC/N. The piezoelectric voltage constant is 0.2 Vm/N. The size of the square magnet at the end of the piezoelectric beam is 8 mm × 5 mm × 2 mm. The diameter of the cylindrical magnet at the end of the spring is 10 mm, and the thickness is 8 mm. The coil is the copper wire. The length of the soft spring is 20 mm, and the initial wire diameter of the spring is 0.5 mm. The initial spring stiffness is 1018 N/m, as calculated by the formula  $k = (Gd^4/8D^3)$ , where  $k$  indicates the spring stiffness;  $G$  denotes the shear module of the spring and



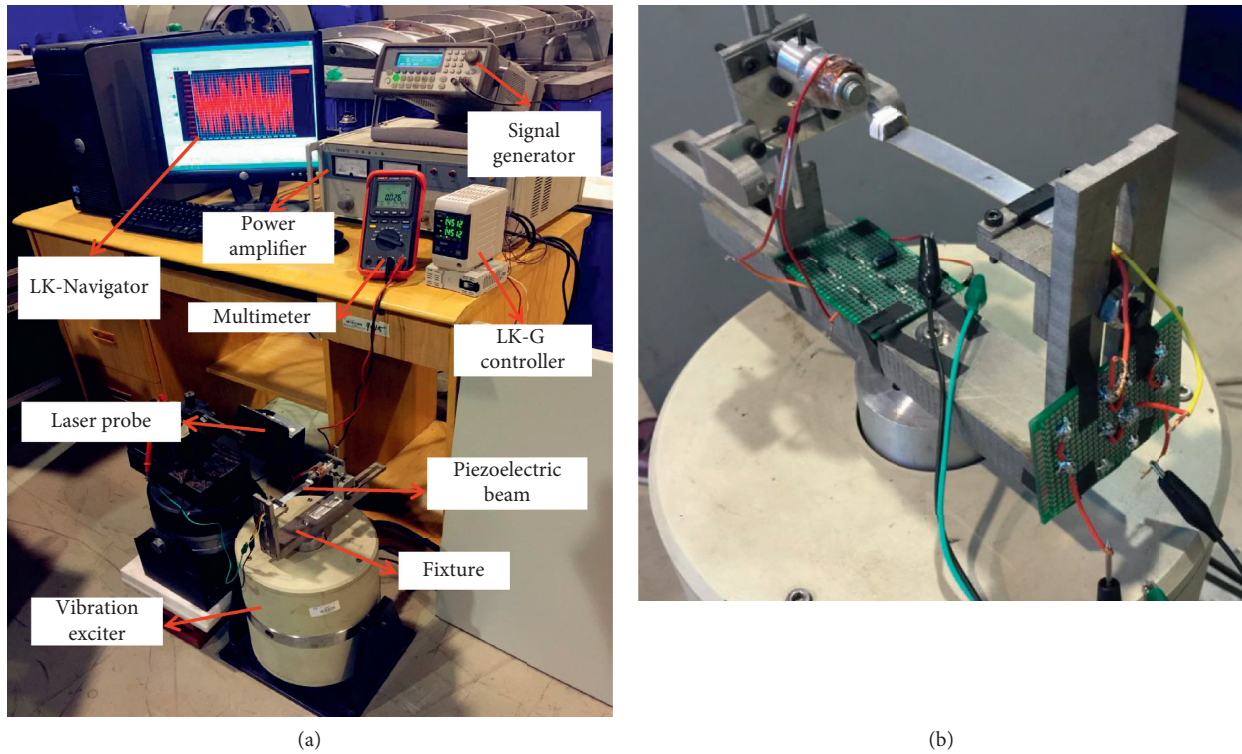


FIGURE 1: Experimental setups: (a) experimental apparatus; (b) experimental fixture and circuit.

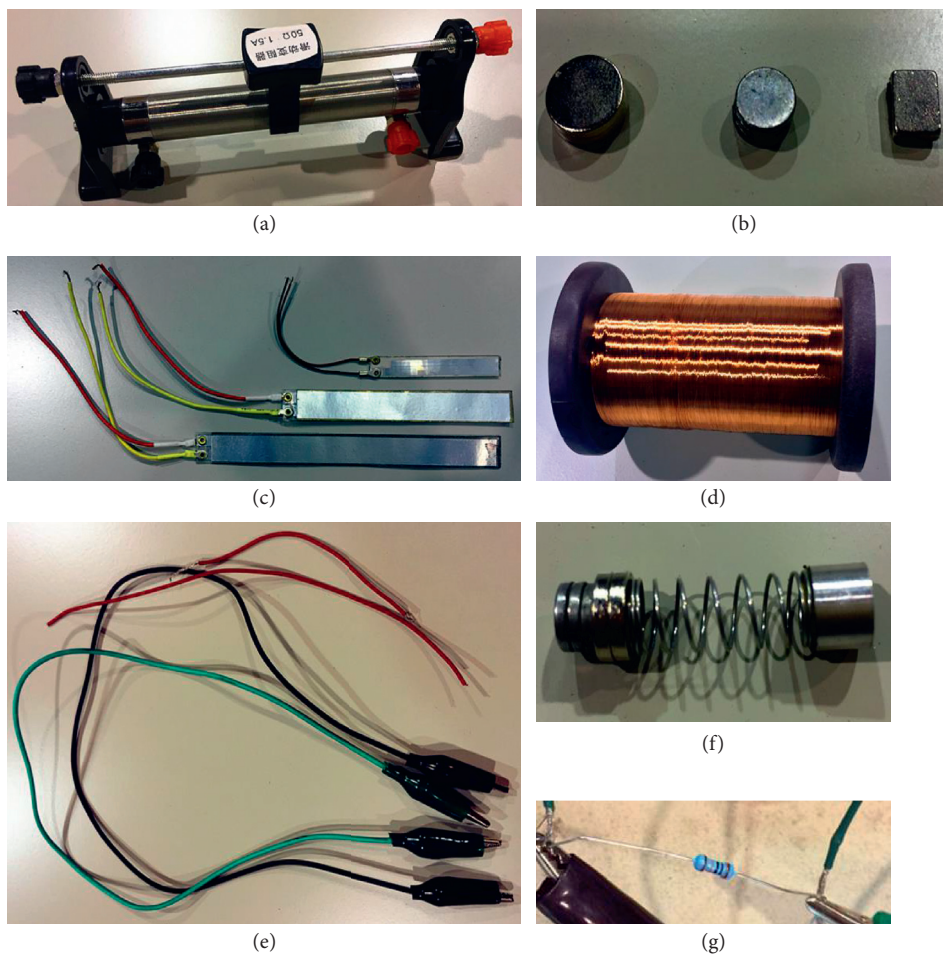


FIGURE 2: Experimental materials: (a) variable resistance; (b) magnet; (c) PVDF piezoelectric beam; (d) coil; (e) wire; (f) spring and magnet connection; (g) load.

$G = 8 \times 10^{10}$  Pa;  $d$  is the initial wire diameter of the spring and  $d = 0.5$  mm; and  $D$  represents the initial diameter of the spring and  $D = 8.5$  mm. The spring does the telescopic movement with a large amplitude when the magnetic force is weak.

#### 4. Potential Energy of the Bistable Experimental Model

At present, most of scholars have investigated the monostable piezoelectric-electromagnetic combined power generation structure. Since the monostable structure has some disadvantages, a bistable model for the piezoelectric cantilever beam power generation structure is proposed. Moreover, a coil is added to introduce the electromagnetic induction power generation. The model of the structure in this paper is shown in Figure 3. There is a magnet on the opposite position of the piezoelectric cantilever beam, which is fixed at the end of the soft spring in the sleeve. The inner surface of the sleeve is smooth. The magnet does the reciprocating motion in the sleeve. So, the magnetic flux changes continuously through the coil, which results in generating the electromotance.

Since the formation of the bistable structure is mainly caused by the magnetic potential energy of the system, the analysis of the potential energy for the bistable power generation structure needs to be performed. The bistable beam has two stable positions and an unstable position, as shown in Figure 4(a). The potential function of the bistable piezoelectric-electromagnetic combined generator is established as follows:

$$U = U_S + U_M + U_E, \quad (1)$$

where  $U_S$  indicates the structural potential energy,  $U_M$  is the magnetic potential energy, and  $U_E$  denotes the elastic potential energy.

Based on the von Karman nonlinear strain displacement relation, the strain displacement relation of the  $x$  direction is given as follows:

$$S = \frac{\partial u_0}{\partial x} + \frac{1}{2} \left( \frac{\partial w_0}{\partial x} \right)^2 - z \frac{\partial^2 w_0}{\partial x^2}. \quad (2)$$

The constitutive equations of the piezoelectric layer are described as follows:

$$\begin{aligned} T &= CS - dE, \\ D &= dS + \varepsilon E, \end{aligned} \quad (3)$$

where  $T$  indicates the stress,  $D$  is the electric displacement,  $C$  denotes the modulus of the elasticity,  $S$  represents the strain,  $d$  is the piezoelectric constant,  $E$  indicates the electric field intensity, and  $\varepsilon$  denotes the dielectric constant.

Therefore, the structural potential energy of the system is expressed as follows:

$$\begin{aligned} U_S &= \frac{1}{2} \int_v S(CS - dE) dv - \frac{1}{2} \int_v E(dS - \varepsilon E) dv, \\ E &= \frac{V}{(h_3 - h_4)}, \end{aligned} \quad (4)$$

where  $v$  is the volume of the piezoelectric beam,  $V$  indicates the electric potential difference, and  $(h_3 - h_4)$  represents the thickness of piezoelectric layer.

The structural potential energy is obtained as follows:

$$\begin{aligned} U_S &= \frac{1}{2} \int_v \left[ C \left( \frac{\partial u_0}{\partial x} + \frac{1}{2} \left( \frac{\partial w_0}{\partial x} \right)^2 - z \frac{\partial^2 w_0}{\partial x^2} \right)^2 \right. \\ &\quad \left. + \frac{Vd}{h_3 - h_4} \left( \frac{\partial u_0}{\partial x} + \frac{1}{2} \left( \frac{\partial w_0}{\partial x} \right)^2 - z \frac{\partial^2 w_0}{\partial x^2} \right) \right] dv \\ &\quad - \frac{1}{2} \int_v \left[ \frac{Vd}{h_3 - h_4} \left( \frac{\partial u_0}{\partial x} + \frac{1}{2} \left( \frac{\partial w_0}{\partial x} \right)^2 \right. \right. \\ &\quad \left. \left. - z \frac{\partial^2 w_0}{\partial x^2} \right) + \frac{\varepsilon V^2}{(h_3 - h_4)^2} \right] dv. \end{aligned} \quad (5)$$

Next, the magnetic potential energy of the system is established in this section. First of all, the repulsive force of two magnets can be described as follows [38]:

$$\begin{aligned} F_0 &= \frac{3}{2(1 + 3d_m)} \times \frac{w_m h_m}{2\mu_k} \times \frac{B_r^2}{\pi^2} \times \left( \tan^{-1} \frac{w_m h_m}{2d_m \sqrt{w_m^2 + h_m^2 + 4d_m^2}} \right. \\ &\quad \left. - \tan^{-1} \frac{w_m h_m}{2d_m (l_m + d_m) \sqrt{w_m^2 + h_m^2 + 4(l_m + d_m)^2}} \right)^2, \end{aligned} \quad (6)$$

where  $l_m$  indicates the length of the magnet,  $w_m$  is the width of the magnet,  $h_m$  denotes the height of the magnet,  $\mu_k$  represents the magnetic permeability,  $B_r$  indicates the magnetic flux density on the magnet polarity surface, and  $d_m$  is the distance between two magnets.

The vertical component force  $F_z$  of the repulsive force  $F_0$  is related to the displacement  $w_0$  along the vertical direction of the magnet, and it can be written as follows:

$$F_z = F_0 \times \frac{w_0}{\sqrt{w_0^2 + d_m^2}}. \quad (7)$$

The magnetic potential energy is expressed as follows:

$$\begin{aligned} U_M &= \int_0^z F_z dz \\ &= \frac{k_p}{2d_m} \left( w_0^2 - \frac{1}{4\sqrt{d_m}} w_0^4 \right), \end{aligned} \quad (8)$$

where  $k_p$  represents the repulsive force  $F_0$ .

Finally, the elastic potential energy of the system is calculated. The expression for the deformation of the spring is obtained as follows:

$$\Delta x = \frac{F_x}{k_s} = \frac{k_p d_m}{k_s \sqrt{w_0^2 + d_m^2}}, \quad (9)$$

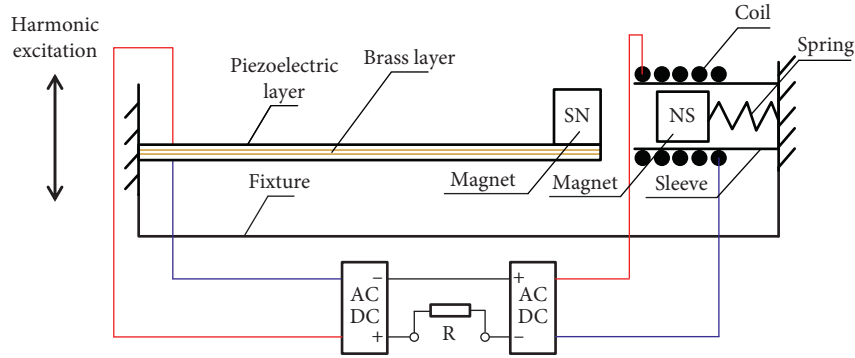


FIGURE 3: Model of the generator.

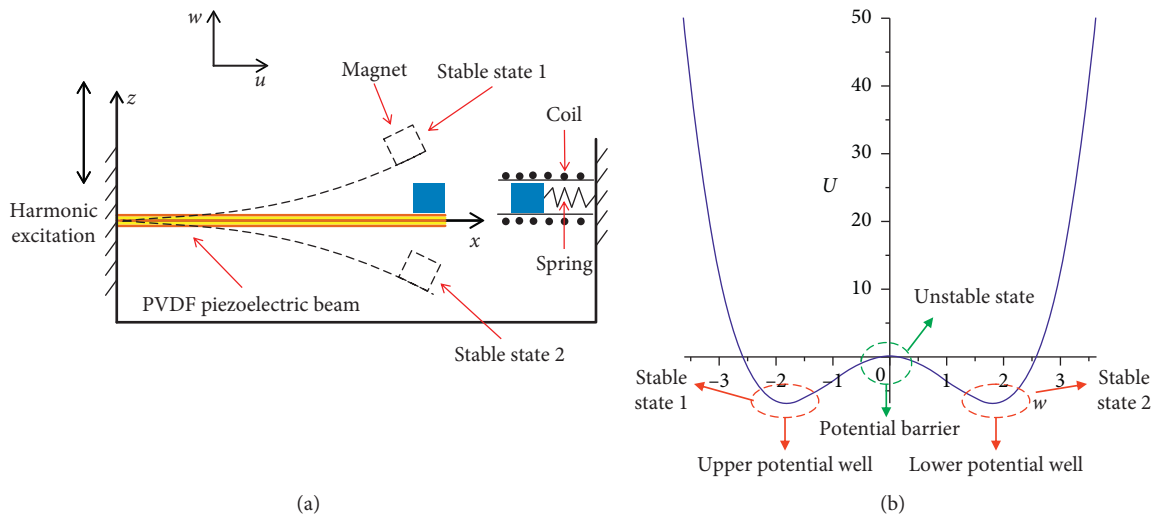


FIGURE 4: Bistable model and the potential curve of the structure: (a) mechanical model of the structure; (b) the relation of the potential well and the bistable state.

where  $k_s$  indicates the stiffness coefficient of the spring.

The elastic potential energy of the system is written as follows:

$$U_E = \frac{1}{2} k_s \Delta x^2 = \frac{k_p^2 d_m^2}{2k_s(w_0^2 + d_m^2)}. \quad (10)$$

Substituting equations (5), (8), and (10) into equation (1), the potential function is obtained as follows:

$$\begin{aligned}
 U = & \frac{1}{2} \int_v \left[ C \left( \frac{\partial u_0}{\partial x} + \frac{1}{2} \left( \frac{\partial w_0}{\partial x} \right)^2 - z \frac{\partial^2 w_0}{\partial x^2} \right)^2 + \frac{Vd}{h_3 - h_4} \left( \frac{\partial u_0}{\partial x} + \frac{1}{2} \left( \frac{\partial w_0}{\partial x} \right)^2 - z \frac{\partial^2 w_0}{\partial x^2} \right) \right] dv \\
 & - \frac{1}{2} \int_v \left[ \frac{Vd}{h_3 - h_4} \left( \frac{\partial u_0}{\partial x} + \frac{1}{2} \left( \frac{\partial w_0}{\partial x} \right)^2 - z \frac{\partial^2 w_0}{\partial x^2} \right) + \frac{\epsilon V^2}{(h_3 - h_4)^2} \right] dv \\
 & + \frac{k_p}{2d_m} \left( w_0^2 - \frac{1}{4\sqrt{d_m}} w_0^4 \right) + \frac{k_p^2 d_m^2}{2k_s(w_0^2 + d_m^2)}. \quad (11)
 \end{aligned}$$

Based on the practical working condition of the structure and theoretical and numerical studies given by Arrieta et al.

[9, 10], it is known that vibrations of the first-order mode for the beam play an important role during vibration. The power



generation of the bistable piezoelectric-electromagnetic combined structure mainly depends on vibration of the first-order mode in the beam. Galerkin approach is applied to obtain ordinary differential equations for the potential of the system. Galerkin approach is derived by the Taylor expansion method, which is a mathematically convergent method. Thus, the first-order discretization of equation (11) is expressed as follows:

$$w_0 = \phi_1(x)w_1(t), \quad (12)$$

where  $\phi_1(x) = ch\lambda_1x - \cos\lambda_1x + ((sh\lambda_1l - \sin\lambda_1l)/(ch\lambda_1l + \cos\lambda_1l))(sh\lambda_1x - \sin\lambda_1x)$ .

Substituting equation (12) into equation (11), the potential function is obtained by calculating as follows:

$$U = I_1w_1^4 - I_2w_1^3 + I_3w_1^2 - 2I_4w_1 + I_5\left(\frac{I_6}{w_1^2 + I_6}\right) - I_7, \quad (13)$$

where  $I_0 = (1/l) \int_0^1 [\phi_1'(x)]^2 dx$ ,  $I_1 = (1/2) \int_0^1 \int_V CI_0^2 \phi_1(x) dv dx - \int_0^1 (k_p/8d\sqrt{d}) \phi_1^5(x) dx$ ,  $I_2 = \int_0^1 \int_V CI_0 \phi_1(x) \phi_1''(x) z dv dx$ ,  $I_3 = (1/2) \int_0^1 \int_V C \phi_1(x) [\phi_1''(x)]^2 z dv dx + \int_0^1 \int_V (V d I_0 / (h_3 - h_4)) \phi_1(x) dv dx + \int_0^1 (k_p/2d_m) [\phi_1(x)]^3 dx$ ,  $I_4 = (1/2) \int_0^1 \int_V (V d / (h_3 - h_4)) \phi_1(x) \phi_1''(x) z dv dx$ ,  $I_5 = (1/2) \int_0^1 (k_p^2/2k_s) \phi_1(x) dx$ ,  $I_6 = (d_m^2/\phi_1^2(x))$ , and  $I_7 = (1/2) \int_0^1 \int_V (\epsilon V^2 / (h_3 - h_4)^2) \phi_1(x) dv dx$ .

Bistable states of the system exist in a certain practical physical parameter range. The potential energy equation (13) of the system is derived from the practical bistable model. Since we have conducted a series of experimental studies in this paper, in the process of experiments, we need to compare experimental results by changing the practical parameters, such as magnetic distances, coils, and loads. Thus, parameters of the model are not unique. In order to ensure the universality of the study, dimensionless parameters were used. The parameters of equation (13) are selected as  $I_1 = 0.6$ ,  $I_2 = 0.06$ ,  $I_3 = -4$ ,  $I_4 = -0.1$ ,  $I_5 = 0.2$ ,  $I_6 = 0.3$ , and  $I_7 = 0.1$ , and Figure 4(b) is obtained by Maple software. Conclusions can be drawn from Figures 4(a) and 4(b) that the structure has two stable states, which correspond to the upper potential well and the lower potential well. The structure has one unstable state, which corresponds to the potential barrier. Therefore, the generator is the bistable structure. When the piezoelectric cantilever beam obtains the enough large energy to go through the potential barrier, the structure can vibrate between the two stable states. Thus, the frequency bandwidth of the power generation for the structure is broadened. The power generation efficiency of the structure is greatly improved. The schematic diagram of the overall experimental model is shown in Figure 5.

The power generation structure with the bistable states and multimode generates much larger energy when the beam produces a large amplitude vibration. Since the spring is soft, the magnet moves fast inside the coil when the piezoelectric beam vibrates between two stable positions. When the piezoelectric cantilever beam moves from each

stable position to the unstable position, the repulsive force between magnets increases gradually. Based on the bistable structure, the spring component is introduced. When the spring is compressed, the repulsive force of the structure with the spring is smaller than that of the structure without the spring. Under the case of the spring, the energy required to pass through the barrier is reduced in the structure. The piezoelectric cantilever beam is easier to go through the potential barrier. The combination of the bistable states and multimode structure makes the piezoelectric beam vibrate between two stable positions easily, and the power generation efficiency of the system is greatly improved. Therefore, the piezoelectric-electromagnetic combined generator has much a greater power generation efficiency.

## 5. Experimental Result Analysis

The power generation efficiency and dynamic behaviors of the piezoelectric-electromagnetic combined generator are investigated. The power generation efficiency of the single piezoelectric cantilever beam structure and the piezoelectric-electromagnetic combined power generation structure is compared. Then, magnetic distances, coils, and loads of the structure are optimized. The diagrams of experimental setups are shown in Figure 6. Figures 6(a) and 6(b) indicate the piezoelectric cantilever beam placed in the upper potential well and the lower potential well, respectively. In the experiment, three different kinds of power generation structures are studied, as shown in Figure 7. The structure A is the conventional monostable piezoelectric cantilever beam structure. The structure B indicates the bistable piezoelectric cantilever beam structure introduced the spring and the magnet. The structure C is the bistable piezoelectric-electromagnetic combined power generation structure, which introduced the spring, the magnet, and the coil.

### 5.1. Power Generation Efficiency of Structures

**5.1.1. Influence of Excitation Frequencies on the Power Generation of Structures.** Firstly, the power generation of the structure A and the structure B is investigated. In order to ensure the reliability of the experimental results, four groups of experiments are performed under the conditions of different magnetic distances. The external excitation is given in the form of the sinusoidal signal  $A \sin \omega t$ . The external excitation amplitude is selected as 2.5 V. The external excitation frequency increases from 5 Hz to 20 Hz with 0.2 Hz step size. In the experiment, the effective output voltage is defined to compare the effective frequency bandwidth of different structures. Thus, it is assumed that the effective output voltage is greater than or equal to 3 V. The effective frequency bandwidth is the difference between the maximum external excitation frequency and the minimum external excitation frequency in the range of the effective voltage. In the experiment, the maximum output voltage of the structure A is 12.337 V, and the effective frequency bandwidth of structure A is 4 Hz.

In the first group, the magnetic distance of structure B is 15 mm. The experimental results are shown in Figure 8, in

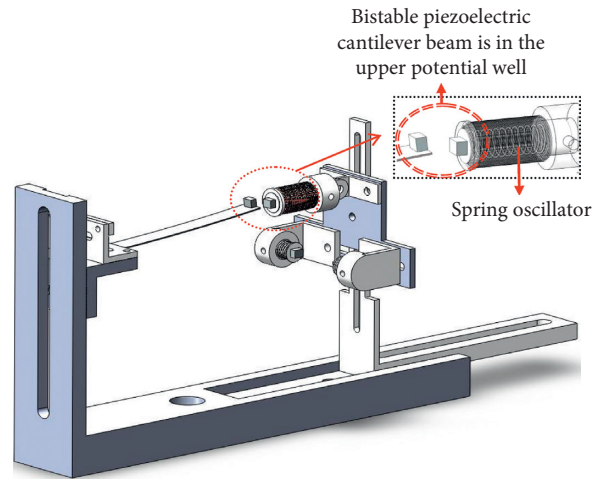


FIGURE 5: Schematic diagram of the experimental model.

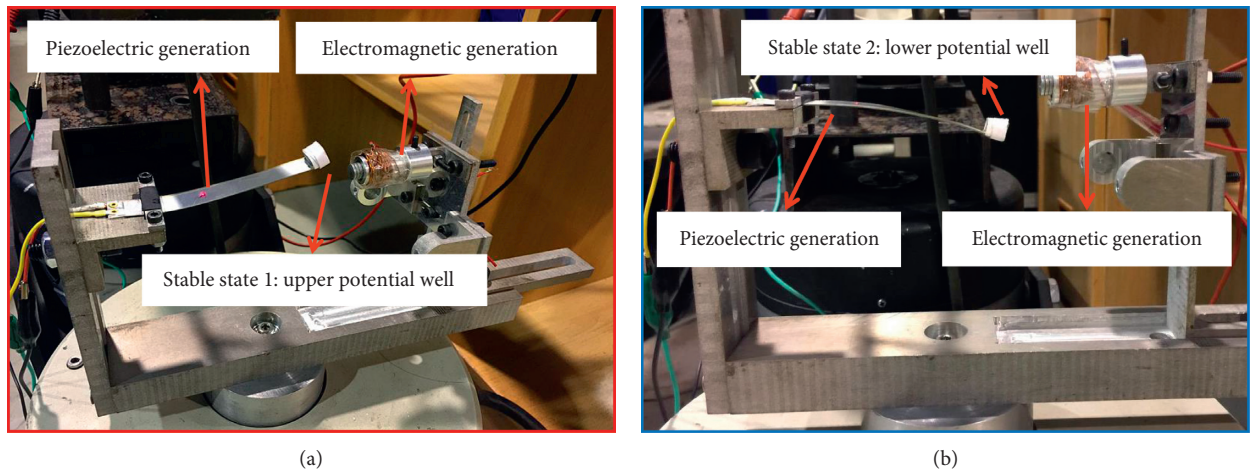


FIGURE 6: Diagrams of experimental setups: (a) structure is placed in the upper potential well; (b) structure is placed in the lower potential well.

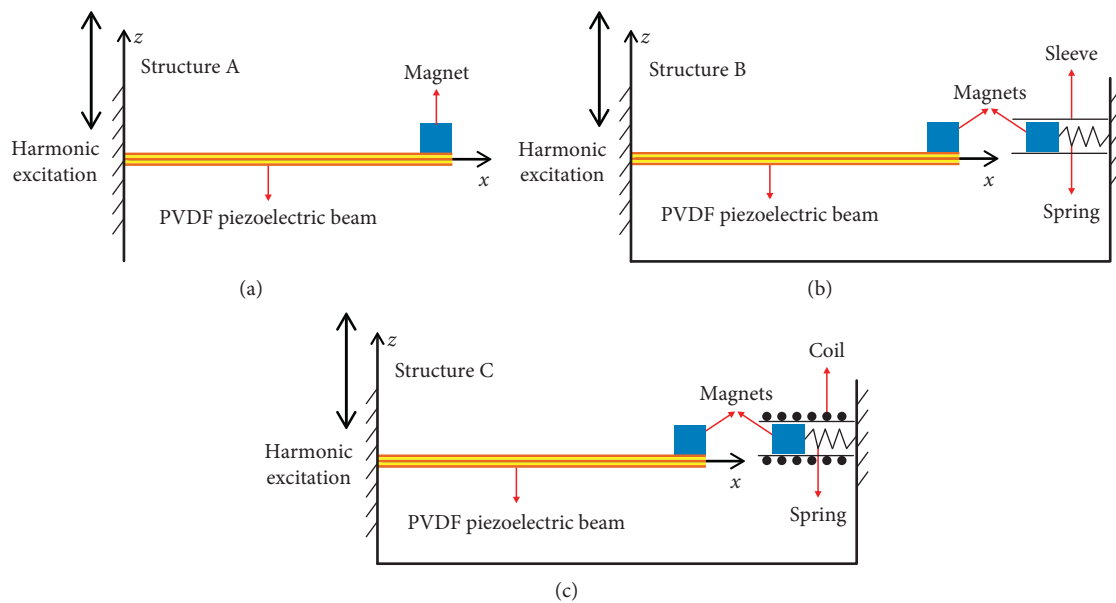


FIGURE 7: Three kinds of structures: (a) structure A; (b) structure B; (c) structure C.



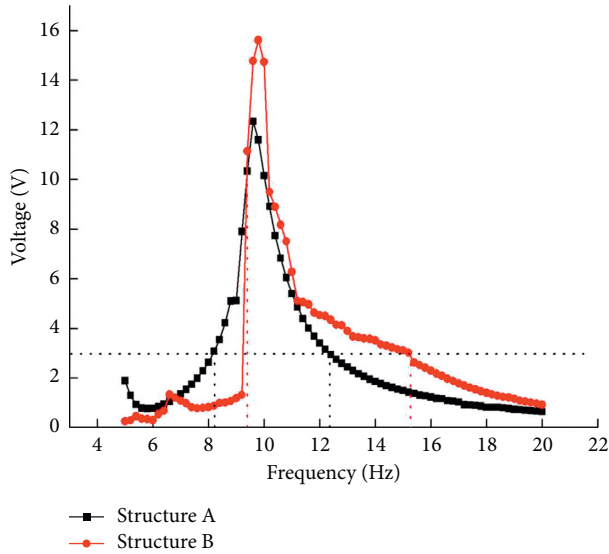


FIGURE 8: Relation of the frequency-voltage of the structure A and the structure B is given when the initial magnetic distance of the structure B is 15 mm.

which the maximum output voltage of structure B is 15.214 V. The output voltage of structure B is greater than that of structure A. The range of two black dashed lines, which are vertical to the horizontal axis, is the effective frequency bandwidth of structure A, as shown in Figure 8. The range of two red dashed lines is the effective frequency bandwidth of structure B, as shown in Figure 8. The effective frequency bandwidth of structure B is 5.8 Hz. The effective frequency bandwidth of structure B is wider than that of structure A.

In the second group, the magnetic distance of structure B is 14 mm. The results can be seen from Figure 9 that the maximum output voltage of structure B is 14.882 V. The maximum output voltage of the bistable structure B is greater than that of the monostable structure A. The effective frequency bandwidth of structure B is 5.8 Hz. Comparing with structure A, the effective frequency bandwidth of structure B is broadened.

In the third group, the magnetic distance of structure B is 13 mm. It can be shown from Figure 10 that the maximum output voltage of structure B is 12.478 V. The maximum output voltage of the system is improved. The effective frequency bandwidth of structure B is 6.2 Hz. The effective frequency bandwidth of the system is broadened.

In the fourth group, the magnetic distance of structure B is 12 mm. The effective frequency bandwidth of the system is 4 Hz. Since the magnetic distance of 12 mm is too small, the repulsive force between two magnets is too great. The piezoelectric cantilever beam cannot go through the potential barrier so that the beam cannot conduct a large amplitude vibration. The results show that the magnetic distance is too small to generate the large output voltage.

Based on the above experiments, it is found that the piezoelectric cantilever beam is easier to go through the potential barrier when the spring and the magnet are introduced under the condition of a suitable magnetic

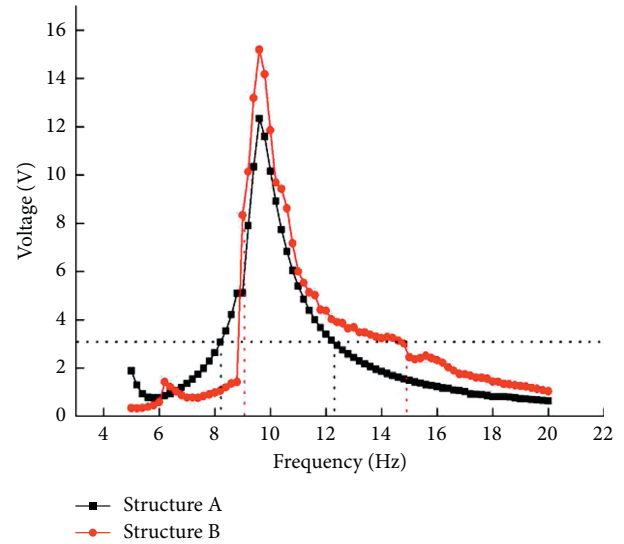


FIGURE 9: Relation of the frequency-voltage of the structure A and the structure B is given when the initial magnetic distance of the structure B is 14 mm.

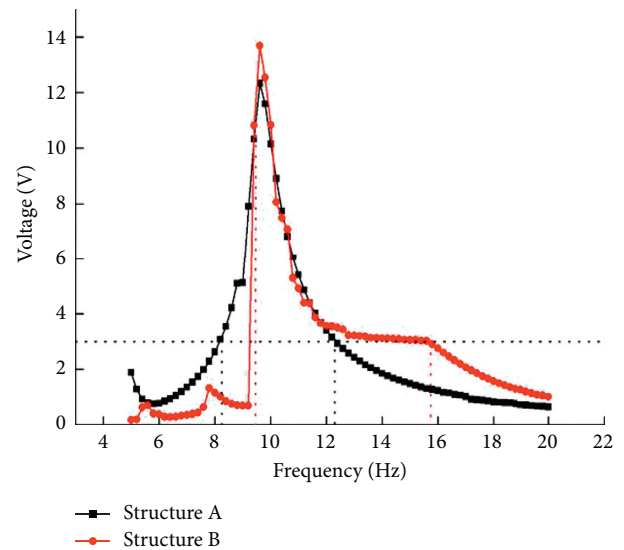


FIGURE 10: Relation of the frequency-voltage of the structure A and the structure B is given when the initial magnetic distance of the structure B is 13 mm.

distances. Therefore, the cantilever beam produces large amplitude vibrations in a wide range of frequencies. The effective frequency bandwidth of the system is broadened under the case of a suitable magnetic distance after the spring is introduced.

In the following experiment, the power generation of structure B and structure C is studied. Experiments are carried out to confirm what the range of magnetic distances is good for the power generation of structure B and structure C. It is found that the power generation efficiency of the system is relatively great when the magnetic distance is from 11 mm to 16 mm. Therefore, the magnetic distances of this experiment are 11 mm, 12 mm, 13 mm, 14 mm, 15 mm, and

16 mm. The comparison of the power generation efficiency of structure B and structure C under the different magnetic distances is given, as shown in Table 1. Based on the bistable piezoelectric cantilever beam structure with the spring and the magnet, it is found that the output voltage is improved, and the effective frequency bandwidth is broadened when the coil is introduced. According to Table 1, the maximum output voltage of structure B and structure C is further compared, as shown in Figure 11. It can be seen in Figure 11 that the introduction of the coil improves the maximum output voltage of structure C. The conclusion is drawn that the power generation efficiency of structure C is the best among three kinds of structures.

Subsequently, the influence of excitation frequencies on the power generation of structure C under the different magnetic distances is studied. Figure 12 is obtained when magnetic distances are 12 mm, 13 mm, 14 mm, and 15 mm, respectively. It can be observed from Figure 12 that the output voltage of the system is quite small when the structure just starts to vibrate in the low-frequency range. When the external excitation frequency increases to 9.5 Hz, the piezoelectric cantilever beam goes through the potential barrier to perform a larger amplitude vibration. The output voltage of the system improves sharply. The structure generates the maximum output voltage when the external excitation frequency is about 9.8 Hz. When the external excitation frequency continues to increase, the output voltage decreases gradually. Therefore, the power generation efficiency of the structure is the best when the external excitation frequency is near the frequency of passing through the potential barrier.

It is found from Figure 12 that the power generation efficiency of the structure is very small when the magnetic distance is 12 mm. Since the magnetic distance is less than 12 mm, the magnetic force is too great. The energy required becomes greatly when the cantilever beam goes through the potential barrier. So, the cantilever beam cannot go through the potential barrier easily. The cantilever beam only conducts small amplitude vibration near the one stable position, and the power generation efficiency of the system is not good. The conclusion can be obtained that the power generation efficiency of structure C can be improved under suitable magnetic distances.

*5.1.2. Influence of External Excitation Amplitudes on the Power Generation of Structures.* In the above experiment, the piezoelectric cantilever beam goes through the potential barrier when the external excitation frequency is about 9.5 Hz. So, the external excitation frequency is selected as 9.5 Hz. The external excitation amplitude increases from 0.5 V to 2.5 V with 0.1 V step size. The magnetic distances are 13 mm, 14 mm, and 15 mm, respectively. The experimental results are shown in Table 2. Compared with the output voltage of structure B, the output voltage of structure C improves 6.2% when the magnetic distance is 15 mm. The output voltage of structure C is improved 8.29% than that of structure B when the magnetic distance is 14 mm. Compared with structure B, the output voltage of structure C improves 1.72% when the magnetic distance is 13 mm.

In this section, we mainly discuss the influence of external excitation amplitudes on the power generation of three different kinds of structures. Conclusions are obtained from Figure 13 that the power generation efficiency of structure B and structure C is worse than that of structure A when the external amplitude is less than 1.3 V. Since the cantilever beam cannot go through the potential barrier, the structures show the monostable vibration behaviors and the power generation efficiency of the structures are quite small. When the cantilever beam goes through the potential barrier, the output voltage of structure B and structure C improves greatly. The output voltages of structure B and structure C are greater than that of structure A. It is found from Figure 13 that the output voltage of structure B and structure C improves rapidly when the external excitation amplitude is greater than 2.3 V.

*5.2. Dynamic Behaviors of Structures.* The power generation efficiency of structures mainly depends on two factors, which one is the output frequency bandwidth and the other is the output voltage of the structure. In the above experimental studies, we mainly analyze the influence of external excitation frequencies and amplitudes on the power generation of structures in order to determine what structure produces the most largest power generation. Based on the experimental results, we have drawn the following conclusions:

- (1) From the opinion of the output frequency bandwidth, the power generation of structure B is better than that of structure A, and the power generation of structure C is better than that of structure B. The output frequency bandwidth of structure C is the best among three kinds of structures.
- (2) From the opinion of the output voltage, the output voltages of structure B and structure C are greater than that of structure A when the external excitation amplitude is greater than 2.3 V. Structure B and structure C produce almost the same amount of the output voltage.
- (3) In a word, the power generation efficiency of the structure C is the best among three kinds of structures, and the power generation of the structure A is the worst. Structure A is the monostable structure, and both structure B and structure C are bistable structures. Since the output frequency bandwidth of the bistable structure is wider than that of the monostable structure, the power generation efficiency of structures B and C is better than that of structure A.
- (4) The power generation capacity of the bistable structure depends on the nonlinear dynamic characteristics of the structure. So, complicated dynamical behaviors of structures A and C need to be further analyzed. In order to find the advantages of dynamical characteristics for the bistable structure, dynamic behaviors of the monostable structure and the bistable structure are comparatively studied.

TABLE 1: Comparison of the power generation efficiency of the structure A, the structure B, and the structure C is given when the external excitation frequency is studied.

Magnetic distance (mm)	Structure	Freq (Hz)	V (V)	V%	$\bar{V}$ %
—	A	4	12.337	—	—
16	B	4.4	10.127	13.8	9.14
	C	5.4	11.521		
15	B	5.8	15.214	6.71	10.11
	C	6.8	15.806		
14	B	5.8	14.882	3.47	7.81
	C	7.2	15.399		
13	B	6.2	12.478	10.44	19.24
	C	7.0	13.781		
12	B	4	6.634	7.21	4.14
	C	4.2	7.112		
11	B	1.6	4.26	13.8	8.21
	C	1.8	4.85		

A is the conventional monostable piezoelectric cantilever beam; B indicates the bistable piezoelectric cantilever beam with the spring and the magnet; C indicates the bistable piezoelectric cantilever beam with the spring, the magnet, and the coil. Freq indicates the effective frequency bandwidth of structures; V indicates the maximum output voltage; V% indicates the growth rate of the maximum output voltage;  $\bar{V}$ % indicates the average growth rate of the output voltage.

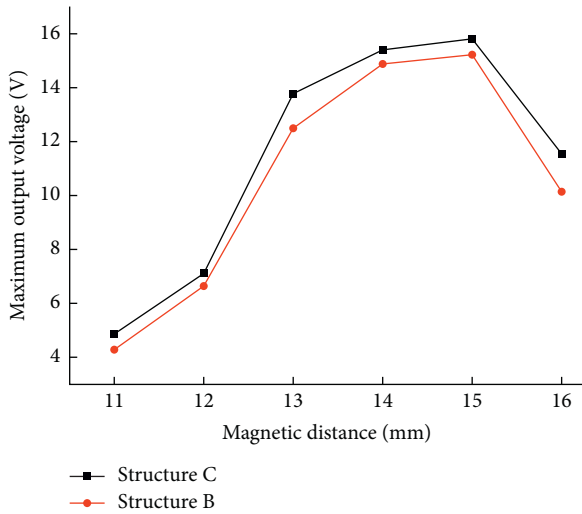


FIGURE 11: Maximum output voltage of the structure B and the structure C.

According to the above experiment of the influence of external excitation amplitudes on the power generation of structures, it is found that the output voltage of structure C improves rapidly when the external excitation amplitude is greater than 2.3 V. But, the maximum excitation amplitude, which the experimental equipment can provide, is 2.5 V. Thus, the external excitation amplitude is selected as 2.5 V in this experiment. In the previous experiment, the power generation efficiency of the structures is worse when the excitation frequency is greater than 30 Hz. Therefore, the external excitation frequency increases from 5 Hz to 30 Hz. Dynamic behaviors of the piezoelectric cantilever beam are analyzed when magnetic distances are 13 mm, 14 mm, and

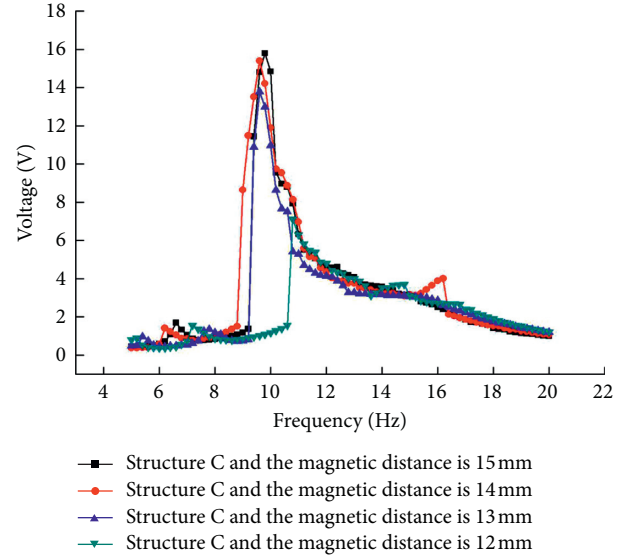


FIGURE 12: Relation of the voltage-frequency of different magnetic distances.

TABLE 2: Comparison of the power generation efficiency of the structure A, the structure B, and the structure C is given when the external excitation amplitude is studied.

Magnetic distance (mm)	Structure	V (V)	$\bar{V}$ %
—	A	12.281	—
15	B	15.096	6.2
	C	15.246	
14	B	15.065	8.29
	C	15.217	
13	B	13.426	1.72
	C	13.451	

A is the conventional monostable piezoelectric cantilever beam; B indicates the bistable piezoelectric cantilever beam with the spring and the magnet; C indicates the bistable piezoelectric cantilever beam with the spring, the magnet, and the coil. V indicates the maximum output voltage;  $\bar{V}$ % indicates the average growth rate of the output voltage.

15 mm, respectively. Based on the above experiment, we find that the output voltage becomes larger with the increase in the vibration amplitude of the piezoelectric beam. The value of the output voltage relies on the amplitude of vibration for the structure.

5.2.1. *Dynamic Behaviors of the Structure A.* When the external excitation frequency is changed from 5 Hz to 20.6 Hz, dynamic behaviors of the cantilever beam show the period-1 motion, as shown in Figure 14. When the external excitation frequency is changed from 20.6 Hz to 30 Hz, dynamic behaviors of the quasiperiod motion are obtained, as shown in Figure 15. In the experimental study of this paper, the material of the piezoelectric cantilever beam is PVDF, which is relatively flexible and prone to the large deformation. At the same time, the length-width ratio of the piezoelectric cantilever beam is larger, which is easy to produce the large deformation. Although structure A is a

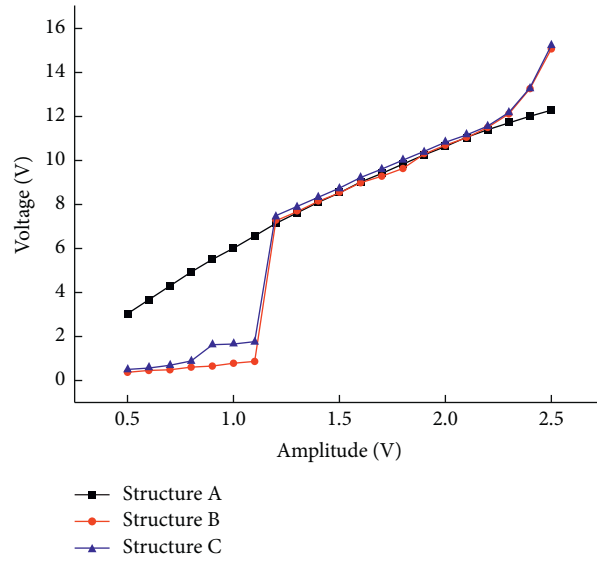


FIGURE 13: Relation of the voltage-amplitude of three structures is given when magnetic distances of the structure B and the structure C are both 14 mm.

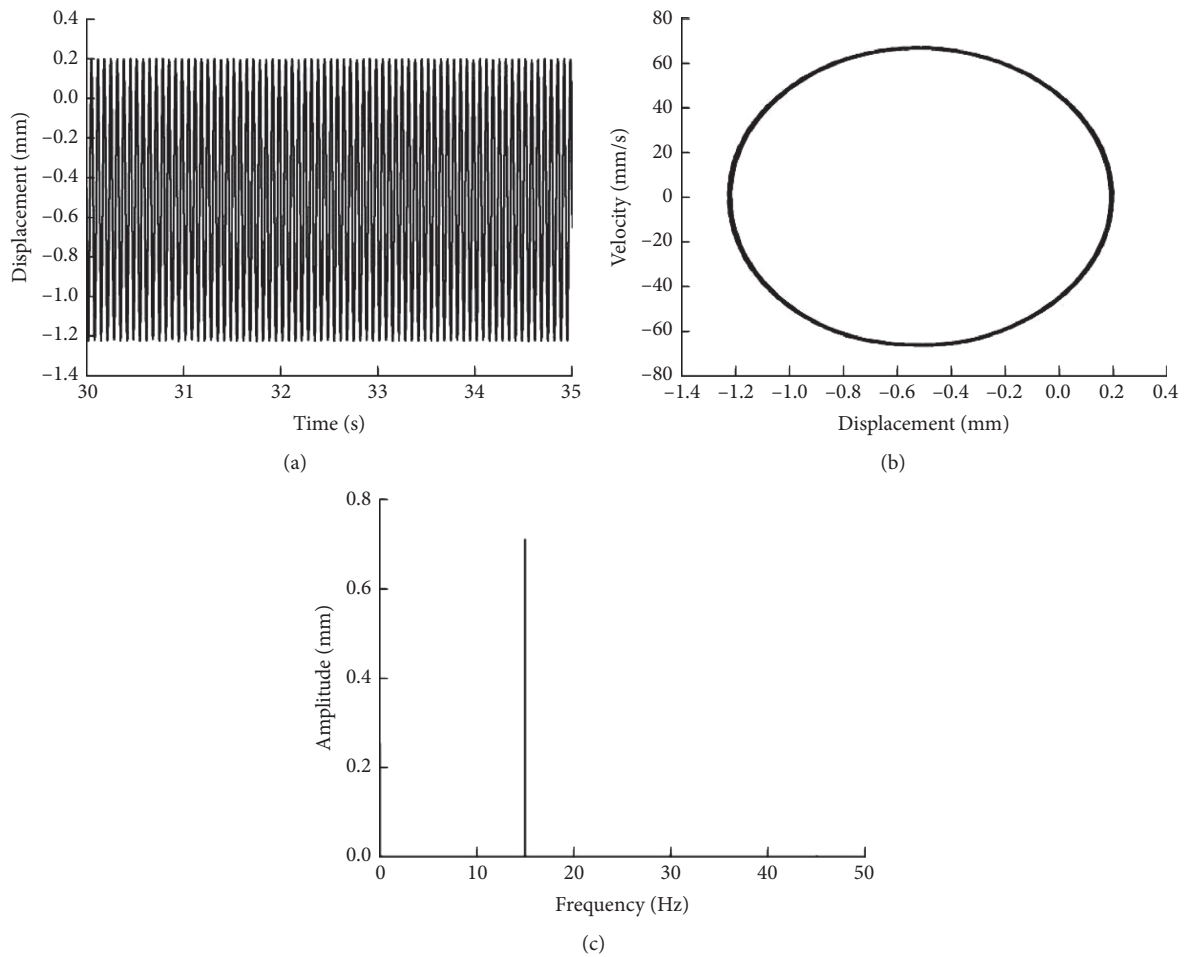


FIGURE 14: Period-1 motion of the structure A is obtained for the external excitation amplitude  $W = 2.5$  V and the external excitation frequency  $\Omega = 15$  Hz: (a) waveform; (b) phase portrait; (c) amplitude spectrum.

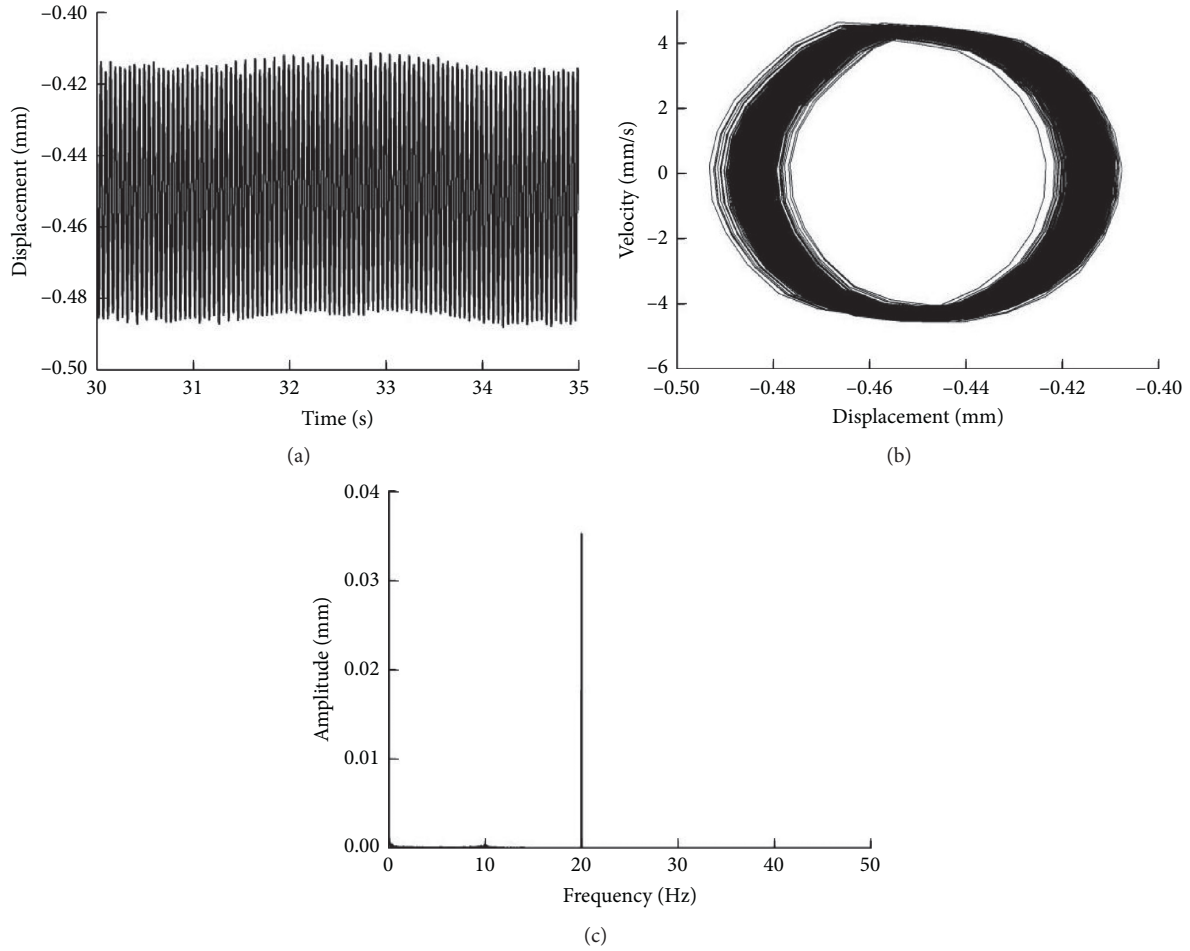


FIGURE 15: Quasiperiodic motion of the structure A is obtained for the external excitation frequency  $\Omega = 20.8$  Hz: (a) waveform; (b) phase portrait; (c) amplitude spectrum.

conventional monostable system, it has nonlinear phenomena. Thus, the quasiperiod motion in structure A is caused by geometric nonlinearity with the large deformation. Dynamic behaviors of structure A are given as follows: period-1 motion  $\rightarrow$  quasiperiod motion. It can be seen from experimental results that nonlinear dynamic behaviors of the conventional monostable piezoelectric cantilever beam are not obvious. The vibration amplitude of the quasiperiod motion for structure A is smaller than that of the period-1 motion. Therefore, the power generation efficiency of the period-1 motion for structure A is better than that of the quasiperiod motion.

**5.2.2. Dynamic Behaviors of the Structure C.** Dynamic behaviors of structure C are analyzed in this section. When the magnetic distance is chosen as 15 mm, dynamic behaviors of the system change 10 times. When the magnetic distance is selected as 14 mm, dynamic behaviors of the system change 12 times. When the magnetic distance is 13 mm, dynamic behaviors of the system change 10 times. The chaotic motion occurs in vibration of the structure under the conditions of three different magnetic distances. It is observed that rich

and complex nonlinear dynamic behaviors occur in vibration of the system when the spring and the magnet are introduced.

Dynamic behaviors of structure C are shown in Figures 16–27 when the magnetic distance is selected as 14 mm. In these figures, (a) is the waveform diagram of the system, (b) is the phase portrait of the system, and (c) is the amplitude spectrum of the system. When the external excitation frequency is from 5 Hz to 10.4 Hz, the period-1 motion appears in the system, as shown in Figure 16. When the external excitation frequency is less than 9.5 Hz, the cantilever beam vibrates only in the upper potential well so that the vibration amplitude of the beam is small and increases slowly. When the external excitation frequency increases to 9.8 Hz, the piezoelectric cantilever beam goes through the potential barrier, and the vibration amplitude of the beam increases sharply. A snap-through phenomenon occurs in the output voltage of the system, in which the output voltage of the system reaches the maximum value. Existence of a snap-through phenomenon corresponds to the period-1 motion in vibration of the system.

When the external excitation frequency increases to 10.4 Hz, Figure 17 shows the occurrence of the chaotic



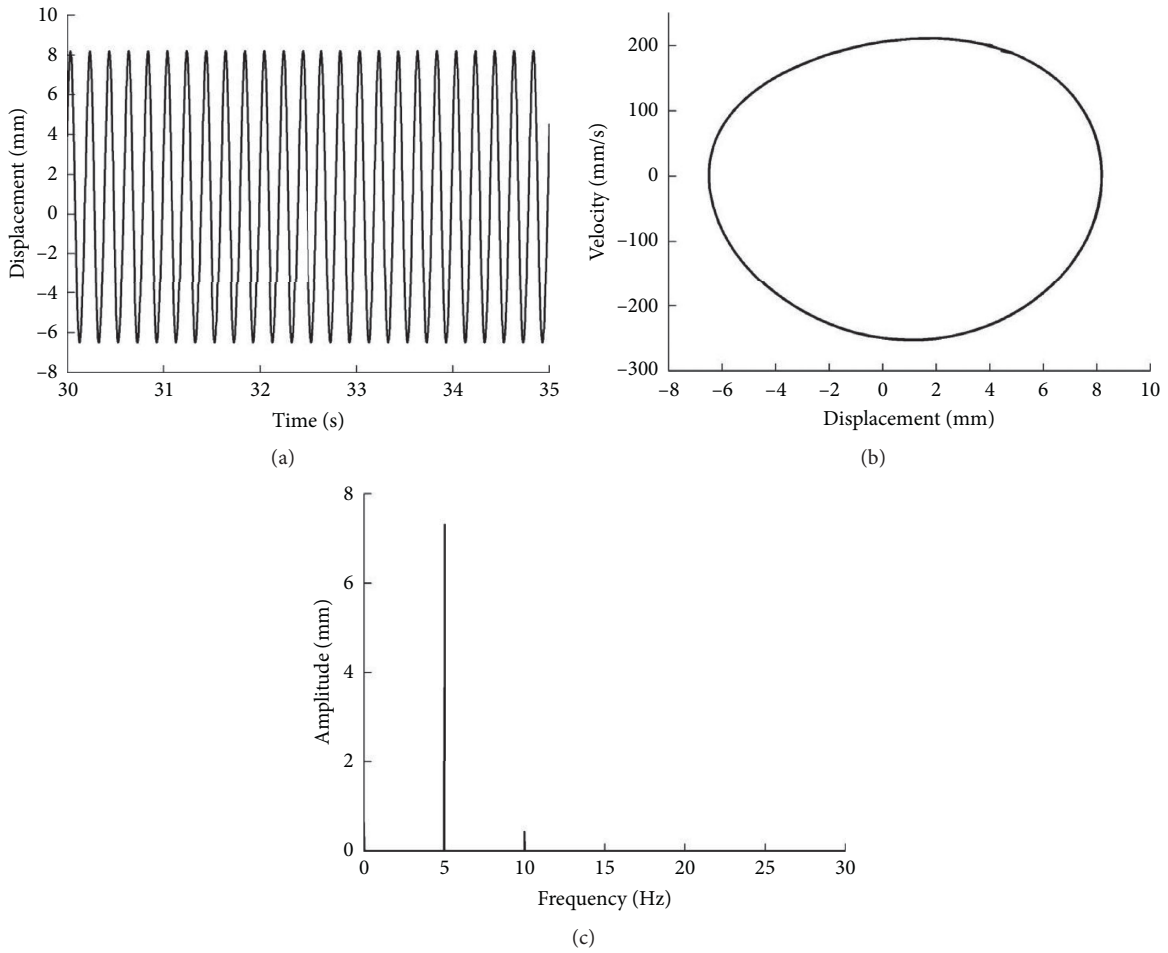


FIGURE 16: Period-1 motion of the structure C is obtained for the external excitation amplitude  $W = 2.5$  V, the external excitation frequency  $\Omega = 5$  Hz, and the magnetic distance 14 mm: (a) waveform; (b) phase portrait; (c) amplitude spectrum.

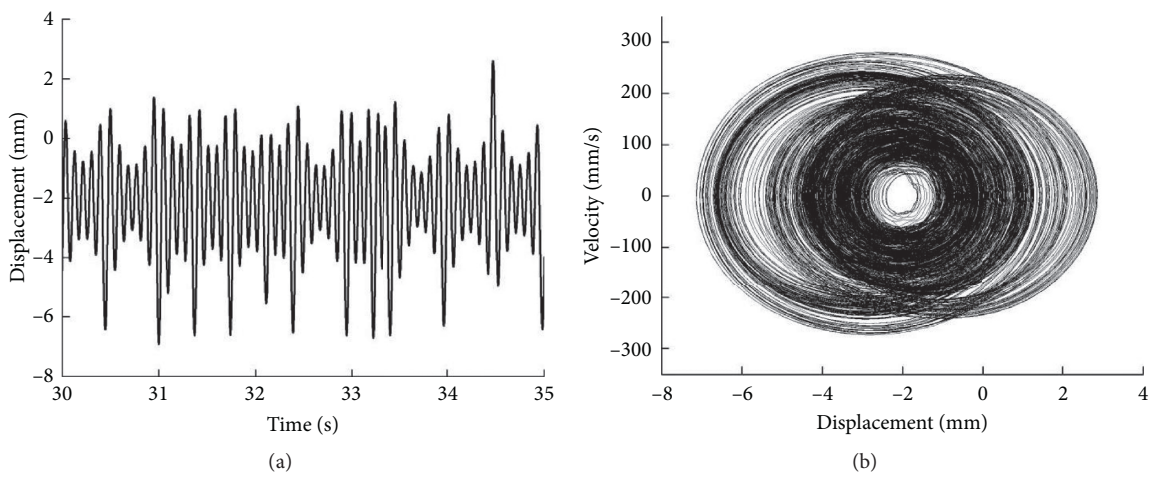


FIGURE 17: Continued.

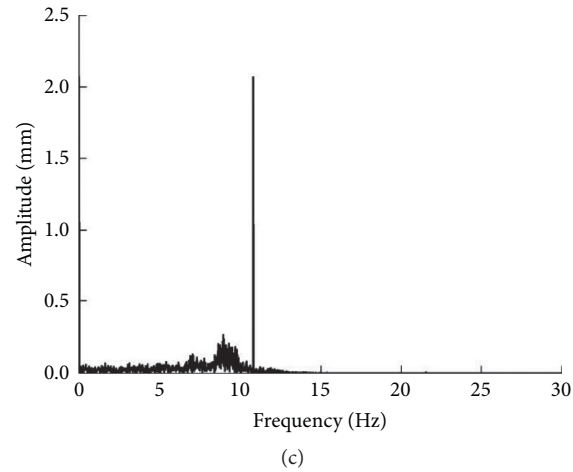


FIGURE 17: Chaotic motion of the system is obtained for the external excitation frequency  $\Omega = 10.8$  Hz: (a) waveform; (b) phase portrait; (c) amplitude spectrum.

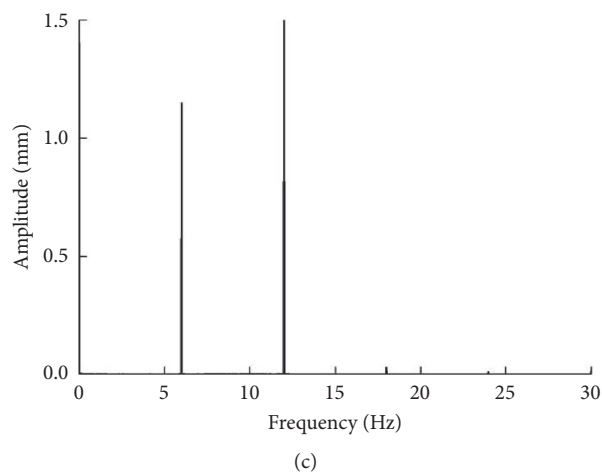
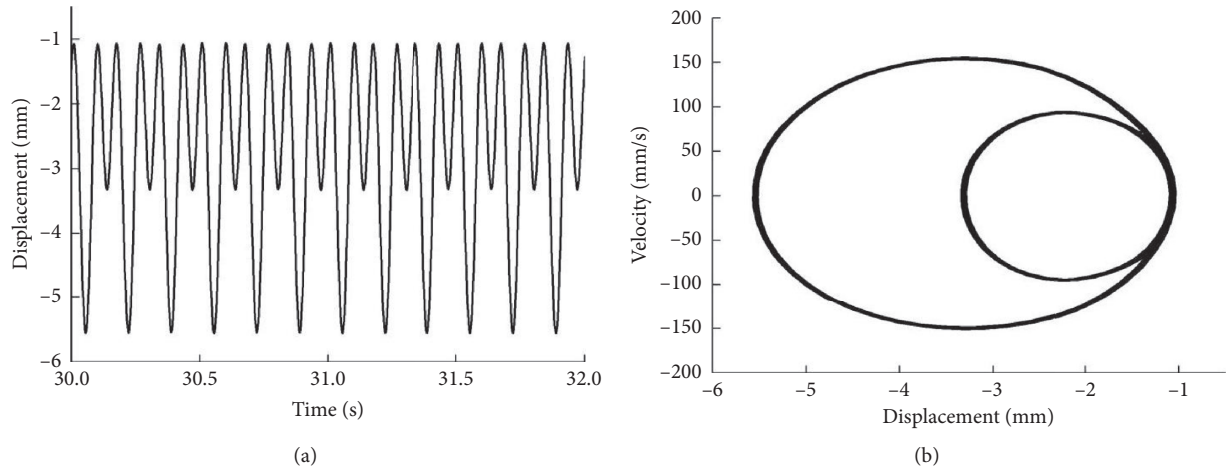


FIGURE 18: Period-2 motion of the system is obtained for the external excitation frequency  $\Omega = 12$  Hz: (a) waveform; (b) phase portrait; (c) amplitude spectrum.

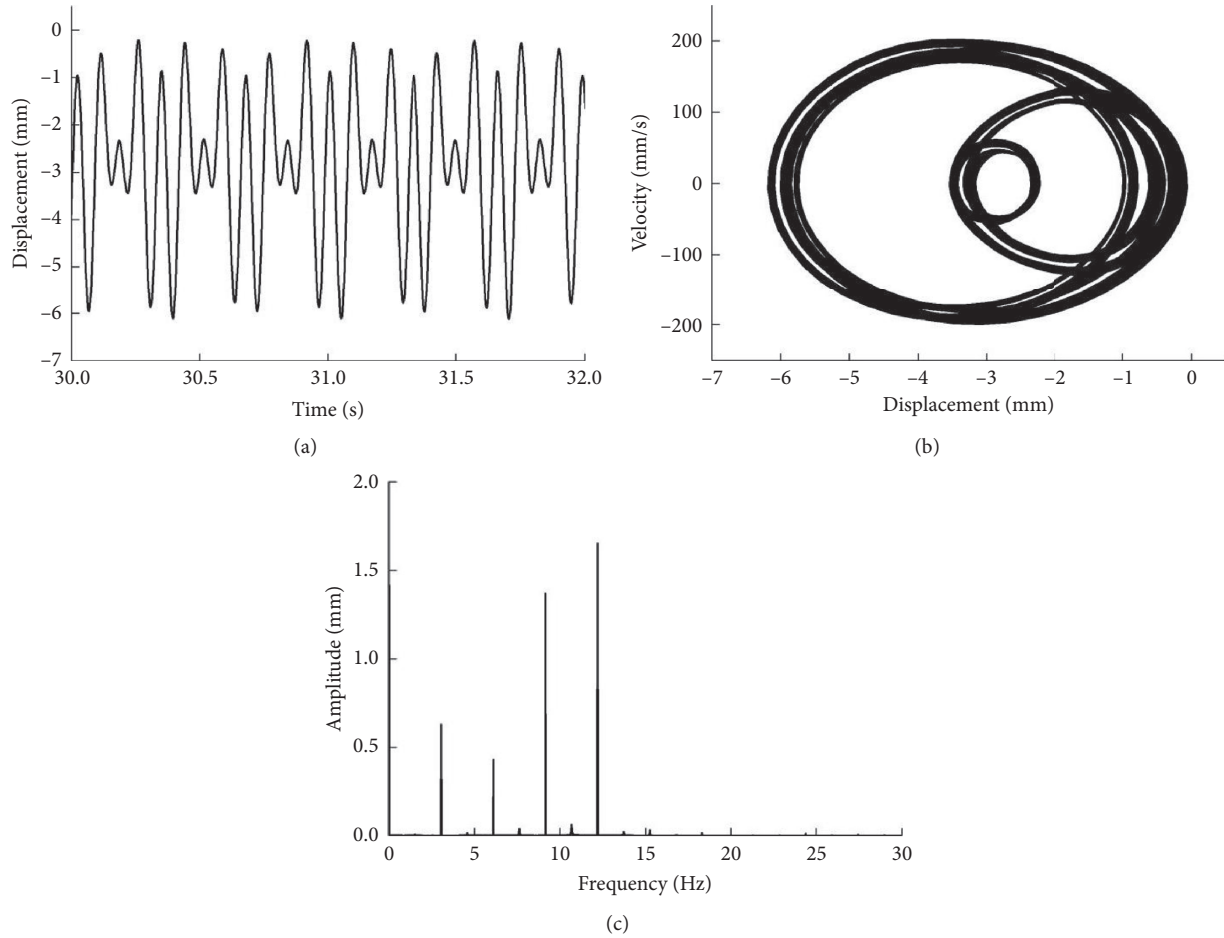


FIGURE 19: Multiperiod motion of the system is obtained for the external excitation frequency  $\Omega = 12.2$  Hz: (a) waveform; (b) phase portrait; (c) amplitude spectrum.

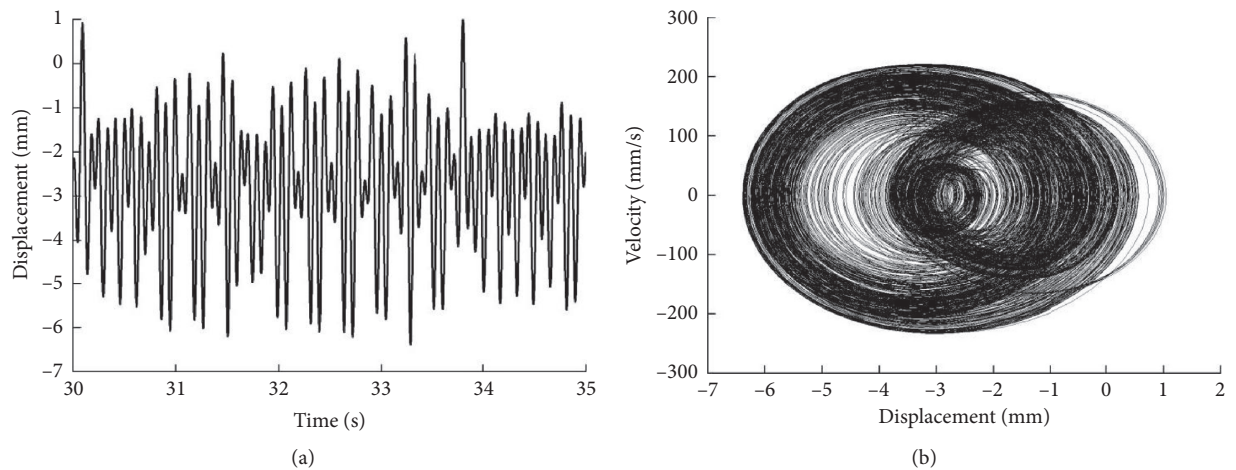


FIGURE 20: Continued.





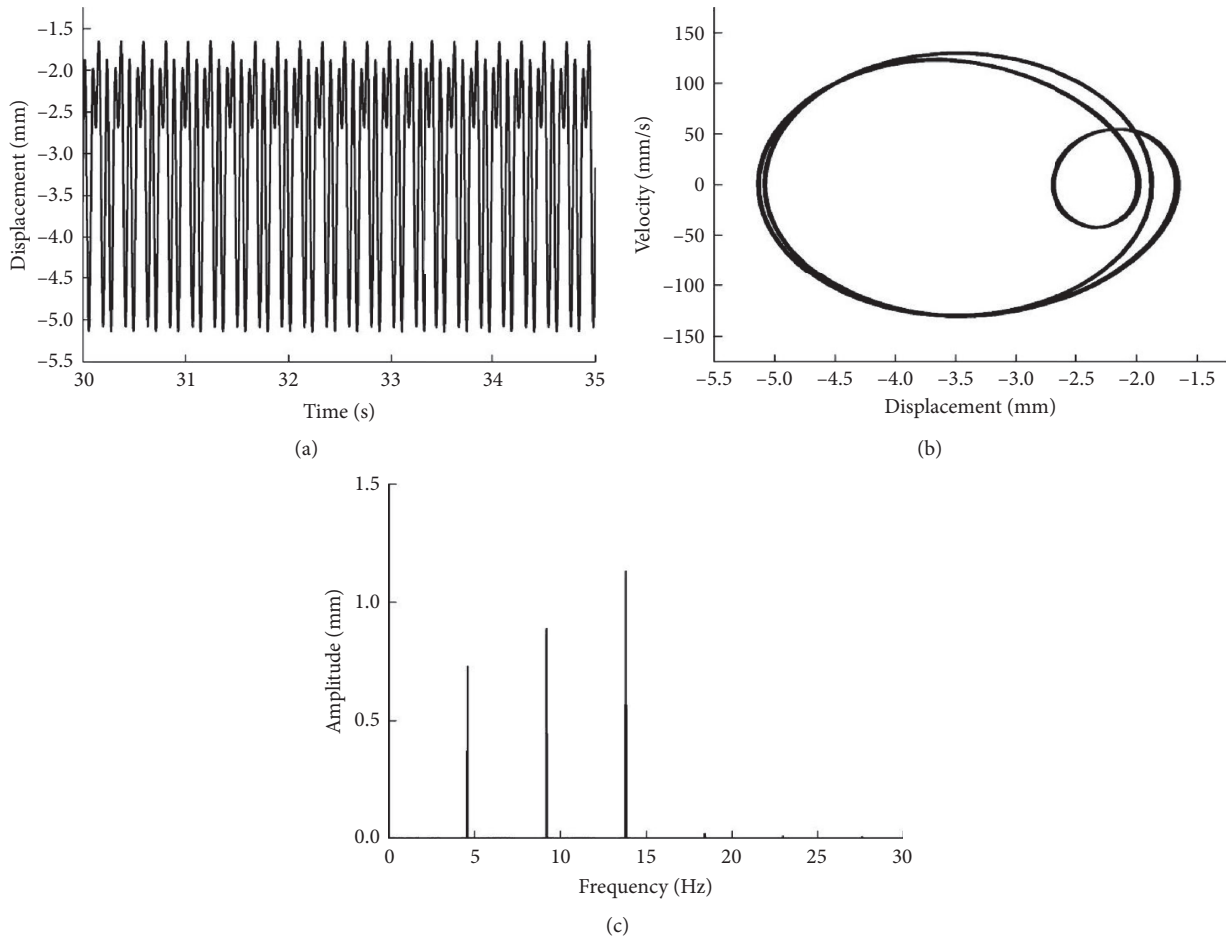


FIGURE 22: Period-3 motion of the system is obtained for the external excitation frequency  $\Omega = 13.8$  Hz: (a) waveform; (b) phase portrait; (c) amplitude spectrum.

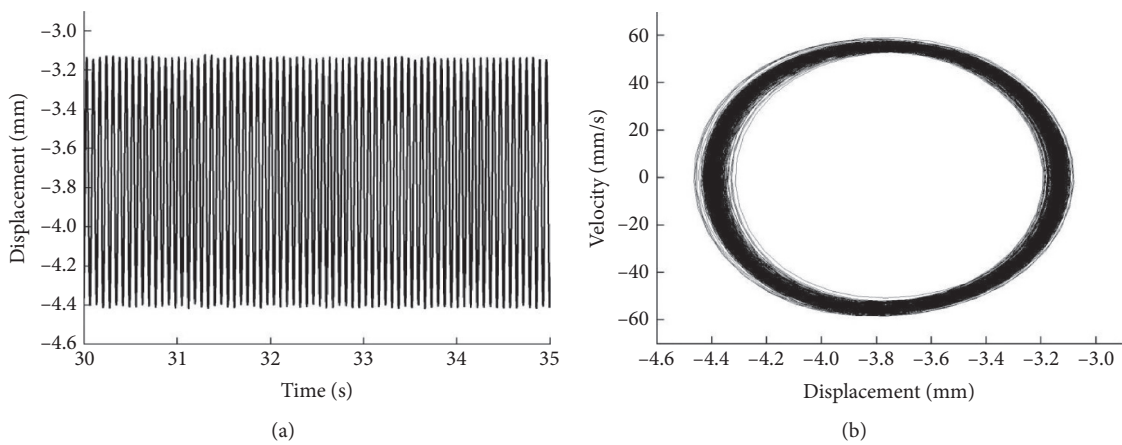
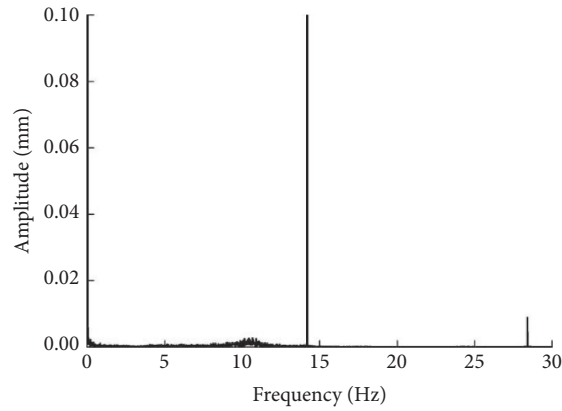
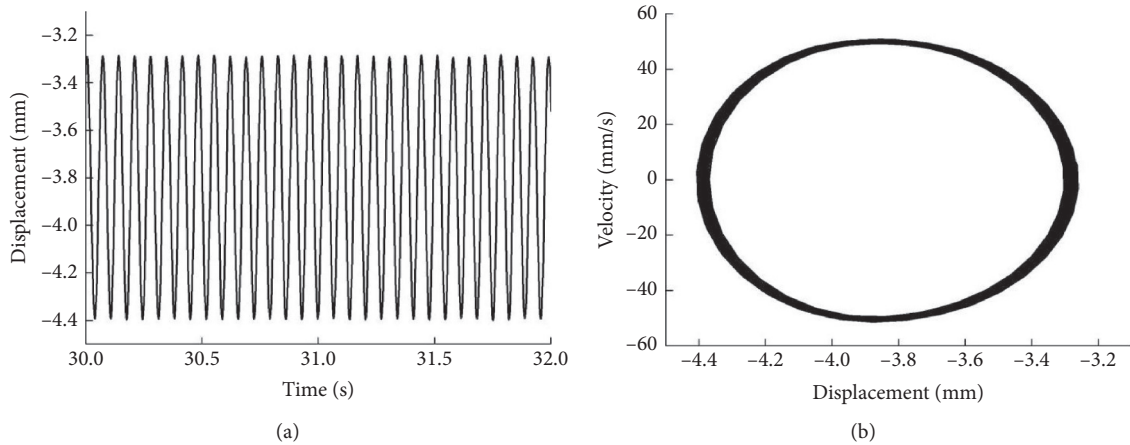


FIGURE 23: Continued.



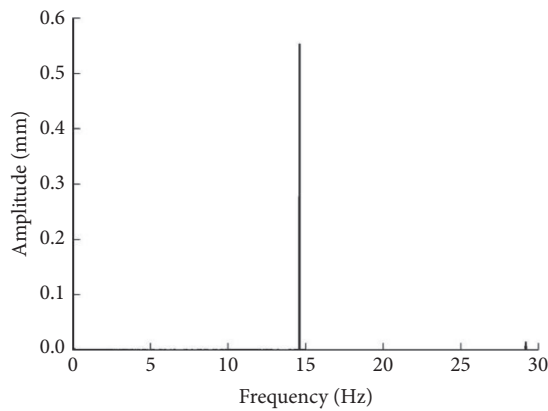
(c)

FIGURE 23: Quasiperiod motion of the system is obtained for the external excitation frequency  $\Omega = 14.2$  Hz: (a) waveform; (b) phase portrait; (c) amplitude spectrum.



(a)

(b)



(c)

FIGURE 24: Period-1 motion of the system is obtained for the external excitation frequency  $\Omega = 14.6$  Hz: (a) waveform; (b) phase portrait; (c) amplitude spectrum.

motion in vibration of the cantilever beam. Since the vibration amplitude of the chaotic motion becomes small, the output voltage of the system decreases. When the external excitation frequency changes from 12 Hz to 12.2 Hz, the

dynamic behavior of the system shows the period-2 motion, as shown in Figure 18. The vibration amplitude of the period-2 motion is larger than that of the chaotic motion. When the external excitation frequency changes from

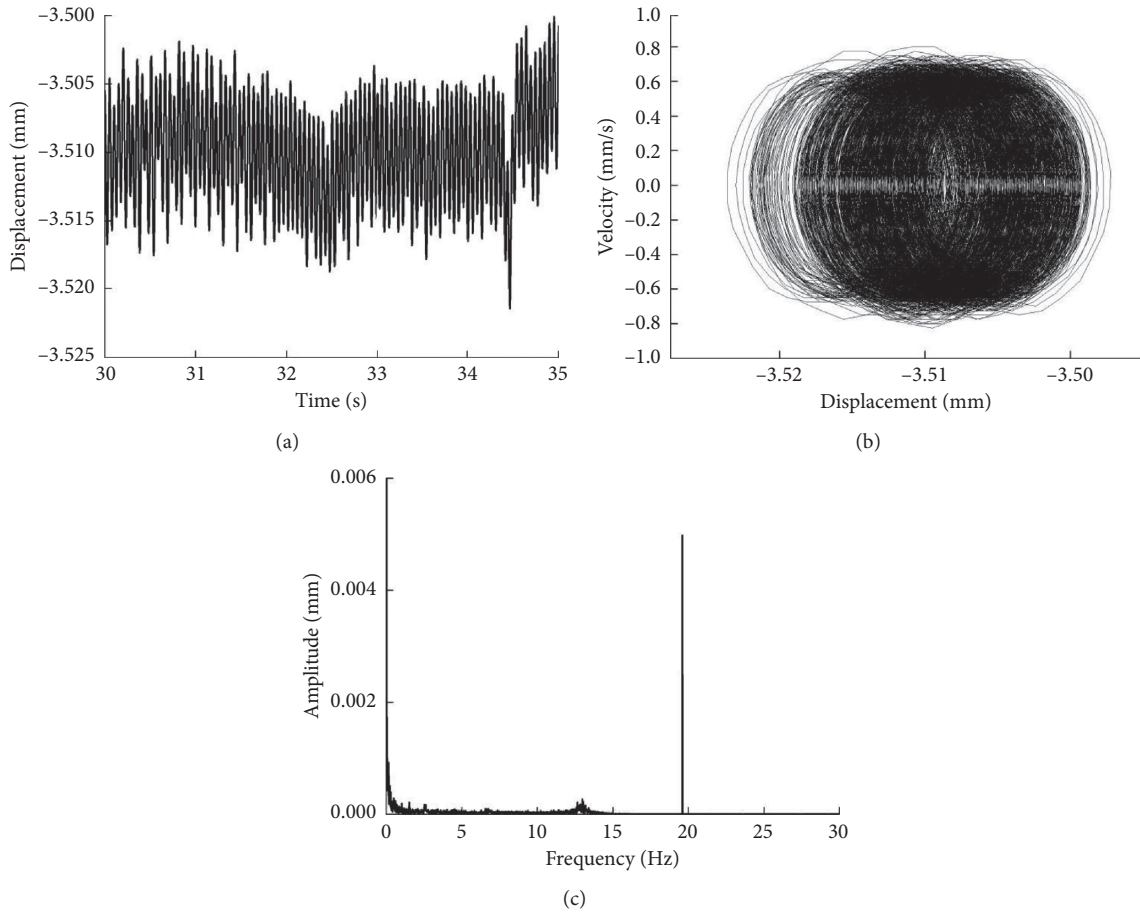


FIGURE 25: Chaotic motion of the system is obtained for the external excitation frequency  $\Omega = 19.6$  Hz: (a) waveform; (b) phase portrait; (c) amplitude spectrum.

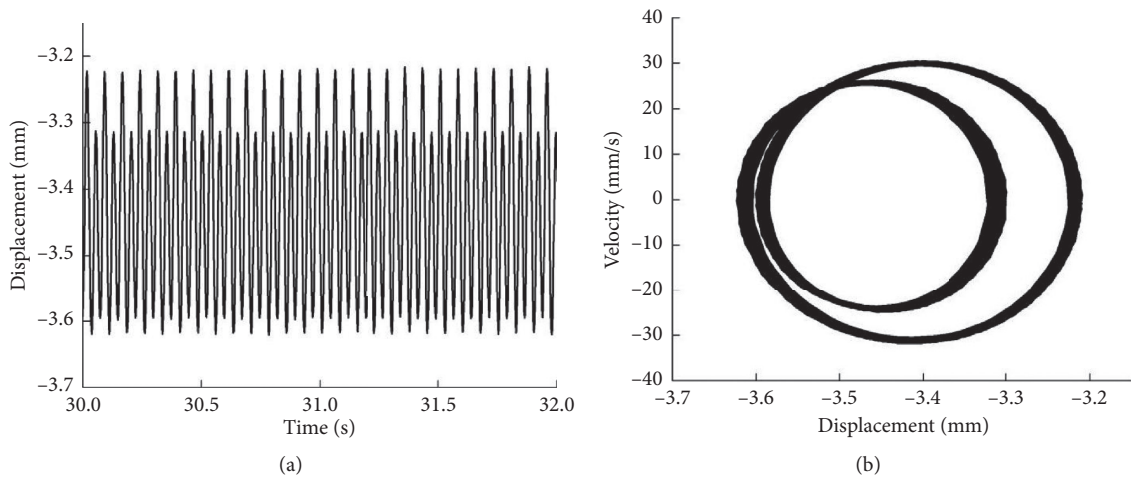


FIGURE 26: Continued.

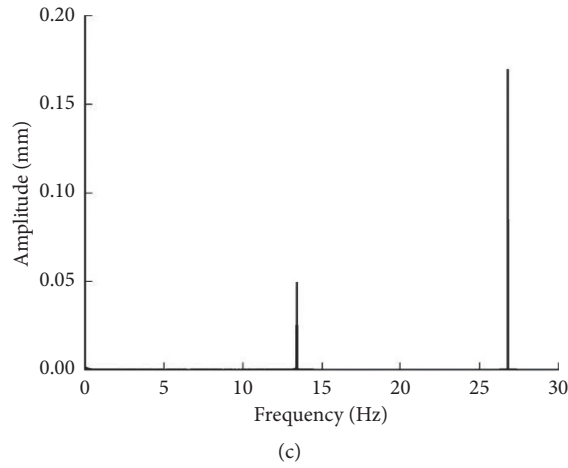


FIGURE 26: Period-2 motion of the system is obtained for the external excitation frequency  $\Omega = 26.8$  Hz: (a) waveform; (b) phase portrait; (c) amplitude spectrum.

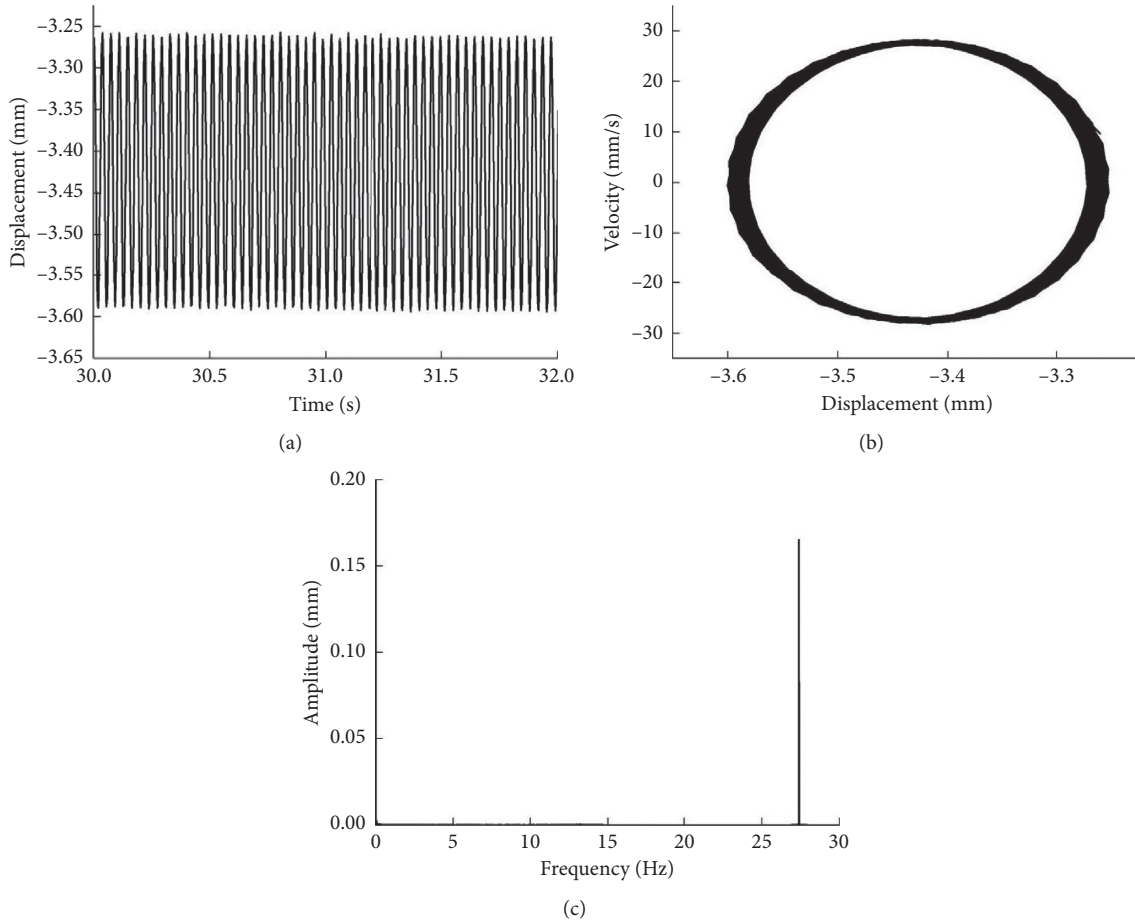


FIGURE 27: Period-1 motion of the system is obtained for the external excitation frequency  $\Omega = 27.4$  Hz: (a) waveform; (b) phase portrait; (c) amplitude spectrum.

12.2 Hz to 12.4 Hz, the dynamic behavior of the system illustrates the multiple period motion, as shown in Figure 19. The vibration amplitude becomes large in the external

excitation frequency range of 0.2 Hz. When the external excitation frequency changes from 12.4 Hz to 13 Hz, the dynamic behavior of the chaotic motion is obtained, as

shown in Figure 20. The nonlinear dynamic behavior is obvious, and the piezoelectric cantilever beam continues to vibrate between two stable states. When the external excitation frequency changes from 13 Hz to 13.4 Hz, the dynamic behavior of the system shows the multiple period motion, as shown in Figure 21. When the external excitation frequency changes from 13.4 Hz to 14.2 Hz, the dynamic behavior of the system displays the period-3 motion, as shown in Figure 22. When the external excitation frequency changes from 14.2 Hz to 14.6 Hz, the dynamic behavior of the system demonstrates the quasiperiod motion, as shown in Figure 23. The piezoelectric cantilever beam cannot go through the potential barrier, and the output voltage of the system decreases significantly. According to the above dynamical analysis, it is found that the system can go through the potential barrier to realize the bistable structure at the appropriate frequency range when the magnetic distance is given. The repulsive force between two magnets can be self-tuning by introducing the spring, and the energy going through the potential barrier decreases. The system can vibrate between two stable states, and the output voltage is greater in a wide range of frequencies.

When the external excitation frequency gradually becomes larger, the system can only vibrate in the one stable state. When the external excitation frequency is chosen from 14.6 Hz to 19.6 Hz, the dynamic behavior of the period-1 motion is obtained, as shown in Figure 24. When the external excitation frequency changes from 19.6 Hz to 23 Hz, there is the appearance of the chaotic motion in the system, as shown in Figure 25. When the external excitation frequency changes from 23 Hz to 26 Hz, the dynamic behavior of the system shows the period-1 motion. The vibration amplitude of the system increases slightly, and the output voltage improves slightly.

When the external excitation frequency continues to increase, the piezoelectric cantilever beam vibrates between two stable states again. When the external excitation frequency changes from 26 Hz to 27.4 Hz, the dynamic behavior of the system demonstrates the period-2 motion and the output voltage of the system improves, as shown in Figure 26.

When the external excitation frequency is increased continuously, the system comes back to the one stable state again. When the external excitation frequency changes from 27.4 Hz to 30 Hz, the dynamic behavior of the period-1 motion is obtained, as shown in Figure 27. The vibration amplitude of the cantilever beam is quite small when the external excitation frequency is larger than 30 Hz. The phenomenon of two stable states cannot appear in vibration of the piezoelectric cantilever beam.

According to the above analysis of the experimental results, the law of dynamic behaviors for the system is given as follows: period-1 motion  $\rightarrow$  chaotic motion  $\rightarrow$  period-2 motion  $\rightarrow$  multiple period motion  $\rightarrow$  chaotic motion  $\rightarrow$  multiple period motion  $\rightarrow$  period-3 motion  $\rightarrow$  quasiperiod motion  $\rightarrow$  period-1 motion  $\rightarrow$  chaotic motion  $\rightarrow$  period-1 motion  $\rightarrow$  period-2 motion  $\rightarrow$  period-1 motion.

When external excitation frequencies are 10.4 Hz, 12 Hz, and 19.6 Hz, respectively, the chaotic motion occurs in vibration of structure C under the case of the magnetic distance of 15 mm. There is the existence of the chaotic motion in structure C under the case of the magnetic distance of 13 mm when the external excitation frequency is 11.8 Hz, 12.4 Hz, and 14 Hz, respectively. The experimental results show that dynamic behaviors of the system are complex when the structure is introduced the spring and the magnet. The bistable phenomenon and the self-tuning magnetic distance are beneficial to broaden the effective frequency bandwidth of the structure.

*5.3. Influence of the Magnetic Distance on the Power Generation.* The purpose of investigating the magnetic distance is to improve the performance of the multimode power generation device. The problem proposed is whether there is an optimum range of the initial magnetic distances, which make the power generation efficiency of the structure greater. Since the optimum range of the initial magnetic distances exist in the system, the energy through the potential barrier is reduced. The piezoelectric beam easily produces large amplitude vibration between two stable states. In order to obtain an optimum range of the initial magnetic distances, the experiments are conducted under the case of the different magnetic distances. Through further analysis, the optimal initial magnetic distance is found, which makes the power generation efficiency of the system greatest.

In the experiment, the external excitation amplitude is selected as 2.5 V, and the external excitation frequency increases from 5 Hz to 20 Hz. It is obtained from previous experiments that the power generation efficiency of the system is great when the initial magnetic distances are selected from 11 mm to 16 mm. Figure 28 shows that the power generation efficiency of the system is greater when the initial magnetic distances are 13 mm, 14 mm, and 15 mm, respectively. Therefore, the optimum range of the initial magnetic distances is from 13 mm to 15 mm. When the initial magnetic distances are too small, the piezoelectric beam cannot go through the potential barrier, which results in the smaller output voltage. When the initial magnetic distances are too large, it is difficult to realize the bistable structure. The cantilever beam cannot produce large amplitude vibration in a wide range of frequencies. Therefore, the performance of the power generation for the system is improved effectively in an optimum range of the initial magnetic distances.

In the following experiment, the optimal magnetic distance is studied in the optimum range of the initial magnetic distances, which are changed from 11 mm to 16 mm. It is observed from Figure 29 that the optimal initial magnetic distance is 15 mm.

*5.4. Optimal External Load of the Structure.* In fact, the power generation device is required to connect with the external load. The external load must affect the output power of the system. So, there is the optimal external load, which makes



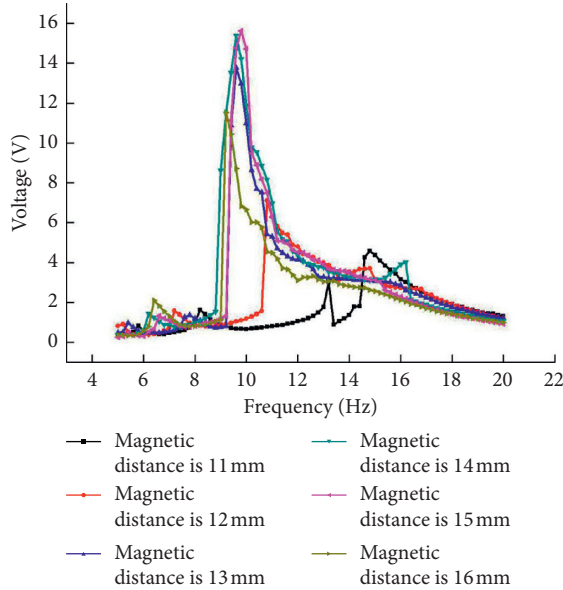


FIGURE 28: Relation of the voltage-frequency of the structure C is given when initial magnetic distances are selected as 11 mm, 12 mm, 13 mm, 14 mm, 15 mm, and 16 mm, respectively.

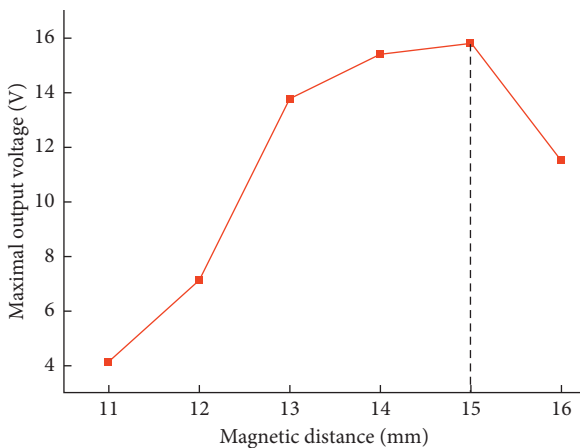


FIGURE 29: Relation of initial magnetic distances and the maximum output voltage of the structure C.

the output power of the system greatest. In this experiment, the external loads are connected at the end of the generator. The output power of structure C is calculated by measuring the output voltage of each external load. Through the experimental analysis, the optimal external load of the system is obtained.

In the experiment, the external excitation amplitude is 2 V. The external excitation frequency increases from 5 Hz to 30 Hz. Experimental results show that the output power of the system is very low when external loads are less than 1 MΩ, as shown in Figure 30. Firstly, the output power is examined when external loads are 1 MΩ, 3 MΩ, and 5 MΩ, respectively, as shown in Figure 31(a). The output power of the system increases with the increase in external loads. Then, external loads are chosen as 6 MΩ, 8 MΩ, and 10 MΩ. It is shown in Figure 31(b) that the output power of the

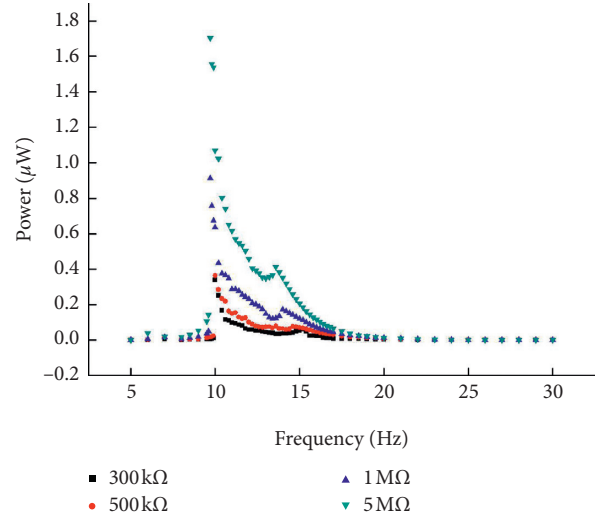


FIGURE 30: Relation of the power-frequency of the system is given when external loads are selected as 300 kΩ, 500 kΩ, 1 MΩ, and 5 MΩ, respectively.

external load 8 MΩ is greater than that of the external load 6 MΩ. When the external load is 8 MΩ, the output power is maximum. When the external load increases to 10 MΩ, the output power decreases. Figure 31(c) illustrates that the output power of the system decreases with the increase in external loads when external loads of 11 MΩ and 12 MΩ are studied. In order to analyze whether the optimal external load of the system is about 8 MΩ, the output power of the system is further studied when external loads are from 7 MΩ to 9 MΩ. Experimental results show that the output power of the system with the external load of 8 MΩ is the greatest, as shown in Figure 31(d). Based on Figure 31, the conclusion is drawn that the optimal external load of the system is about 8 MΩ. Figure 32 further exhibits the relationship between the output power and the external load of the system.

Based on the above experiment, we have obtained the optimal external load of the system is 8 MΩ. It is further studied whether different initial magnetic distances affect the optimal load of the system. In the experiment, the initial magnetic distances are selected as 12 mm and 15 mm, respectively. The external excitation amplitude of two groups of experiments is both selected as 2 V. It can be seen from Figure 33 that optimal external loads are both 8 MΩ under two different initial magnetic distances. Therefore, the initial magnetic distance cannot have an effect on the optimal external load of the system.

**5.5. Influence of Coils on the Power Generation.** In the above experiment, the influence of external excitation frequencies, external excitation amplitudes, magnetic distances, and loads on the power generation of the system is studied. In the following experimental investigation, the influence of coils from the electromagnetic induction generator on power generation of the system is examined. The coil is the copper wire. The main parameters of coils include the height, turns, and the wire diameter. Since the power generation efficiency

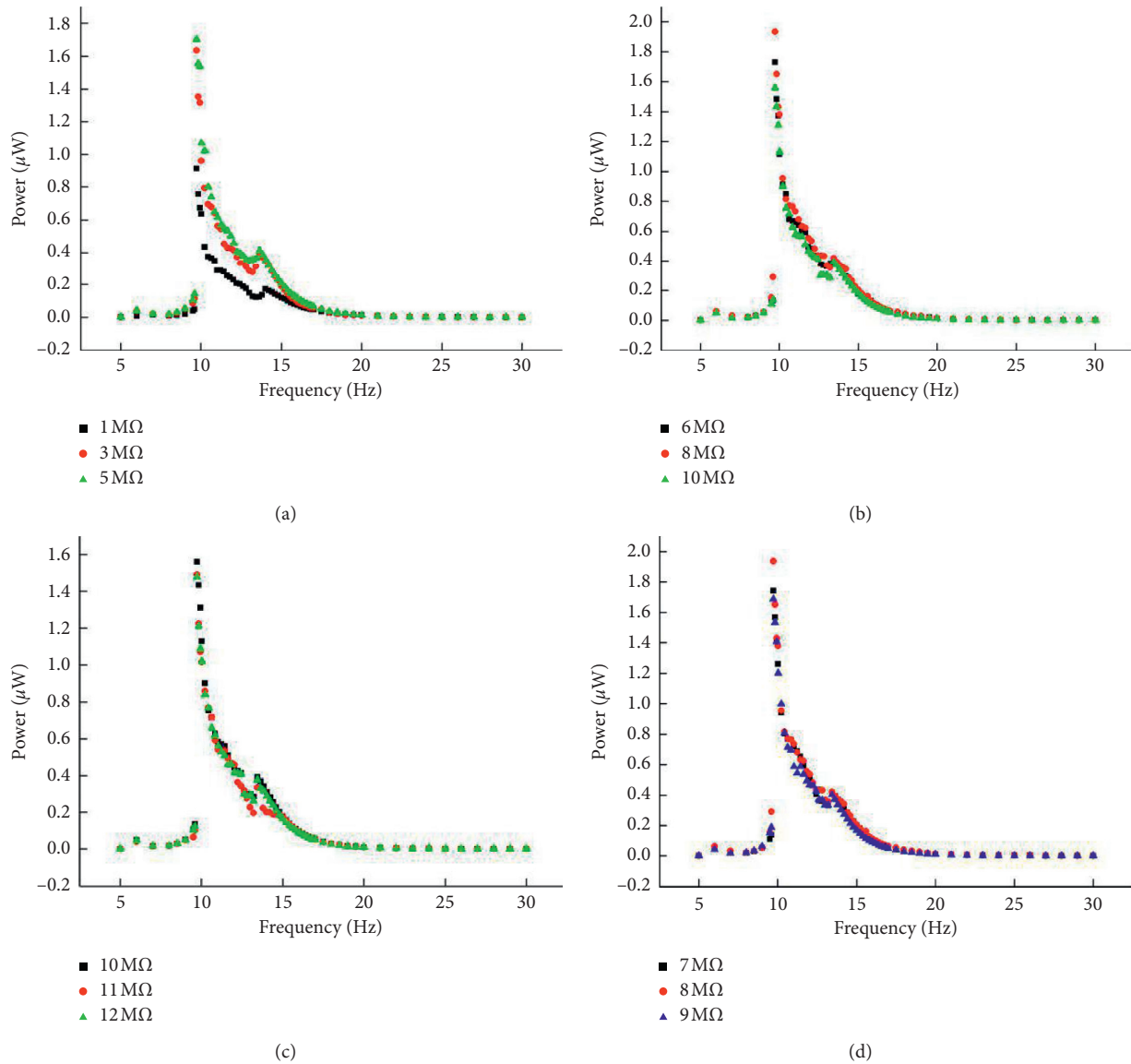


FIGURE 31: Relation of the power-frequency of different external loads is given: (a) external loads are 1 M $\Omega$ , 3 M $\Omega$ , and 5 M $\Omega$ , respectively; (b) external loads are 6 M $\Omega$ , 8 M $\Omega$ , and 10 M $\Omega$ , respectively; (c) external loads are 10 M $\Omega$ , 11 M $\Omega$ , and 12 M $\Omega$ , respectively; (d) external loads are 7 M $\Omega$ , 8 M $\Omega$ , and 9 M $\Omega$ , respectively.

of structure C is the greatest, the influence of parameters of coils on the power generation efficiency of structure C is studied. In the experiment, the external excitation amplitude is selected as 2 V. The influence of heights, turns, and wire diameters of the coil on the power generation efficiency is investigated. Experimental results are shown in Figures 34–37.

In the first step, the influence of the coil height on the power generation efficiency of the system is examined. When the effect of the coil height is studied, the other parameters of coils remain unchanged in the same group of the experiment. The relationship between the output voltage and the external excitation frequency is investigated under the different coil heights. Two different turns of coils are selected to prove that the coil height has a universal effect on power generation of structure C. When turns of coils are

selected as 100, Figure 34(a) is obtained. Figure 34(a) demonstrates the comparison of the power generation of the system when heights of coils are selected as 10 mm and 20 mm, respectively. When heights of coils are not changed and turns of coils are chosen as 200, Figure 34(b) is given. It can be obtained from Figures 34(a) and 34(b) that the output voltage of the system, whose the coil height is 10 mm, is greater than that of the system, whose coil height is 20 mm. Therefore, the power generation efficiency of the system decreases when the coil height increases.

Secondly, the influence of the coil turns on the power generation of the system is analyzed, as shown in Figures 35 and 36. The turns of coils are 50 turns, 100 turns, 150 turns, and 200 turns, respectively. The power generation efficiency of the coil of 100 turns is greater than that of the coil of 50 turns, as shown in Figure 35(a). It can be seen from



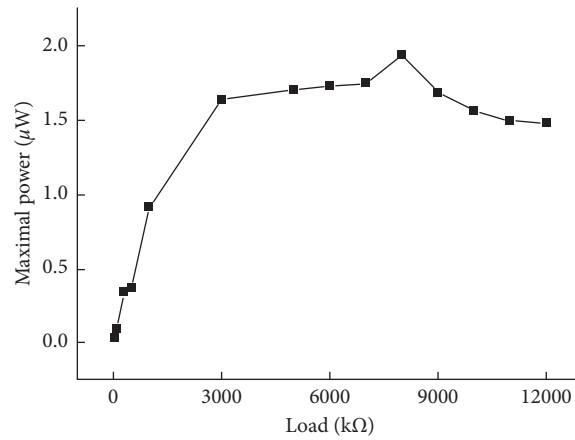


FIGURE 32: Relation of the maximum power and external loads of the system.

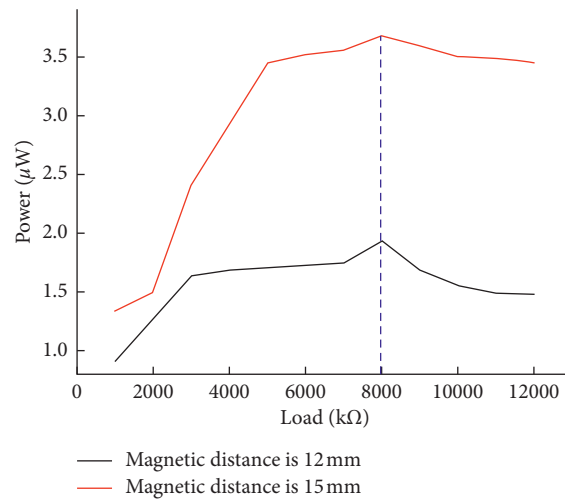


FIGURE 33: Relation of the power-loads of the system is given when the initial magnetic distances are selected as 12 mm and 15 mm, respectively.

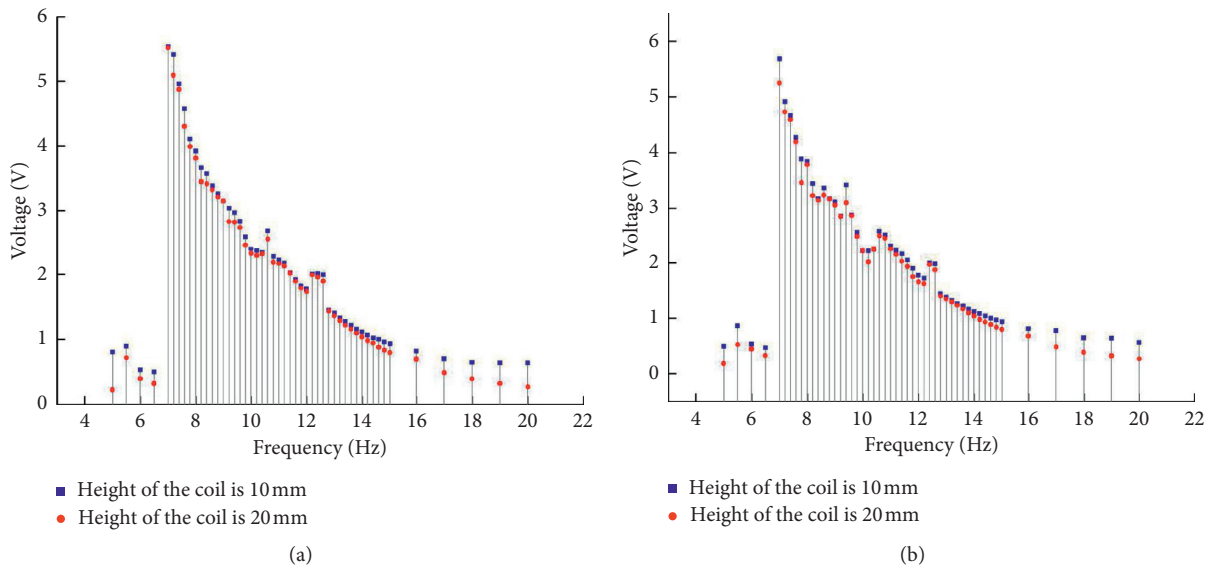


FIGURE 34: Relation of the voltage-frequency of the system is given when heights of coils are selected as 10 mm and 20 mm, respectively: (a) turns of coils are 100 turns; (b) turns of coils are 200 turns.

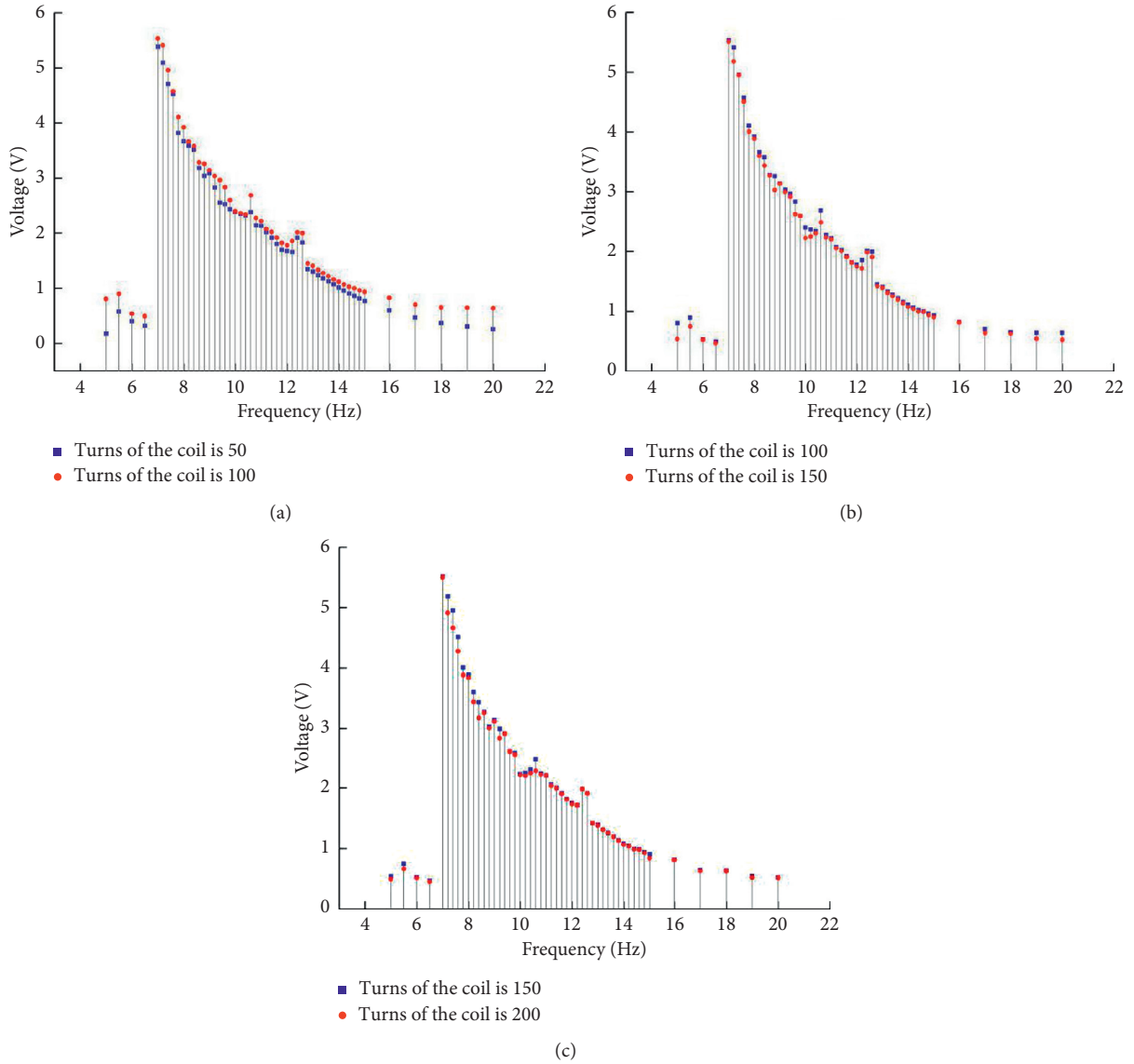


FIGURE 35: Relation of the voltage-frequency of the system is given when turns of coils are selected as 50, 100, 150, and 200, respectively: (a) coil turns are 50 and 100, respectively; (b) coil turns are 100 and 150, respectively; (c) coil turns are 150 and 200, respectively.

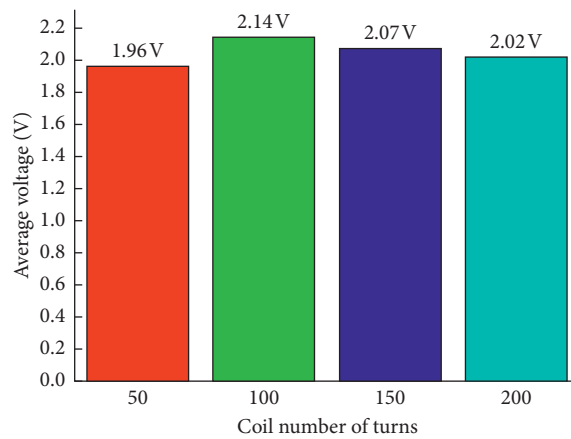


FIGURE 36: Relation of the average voltage and turns of coils.

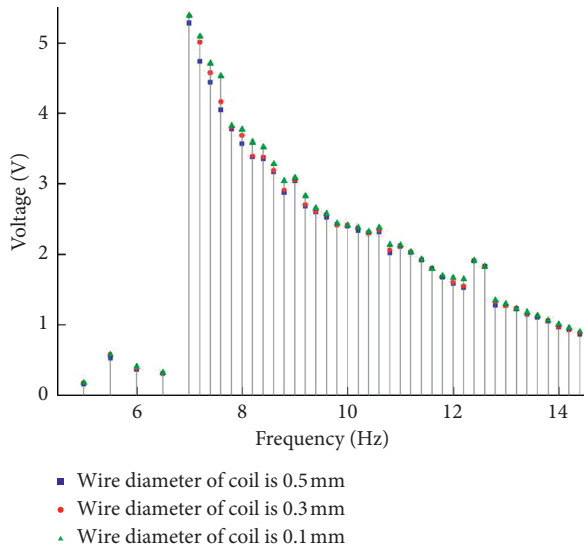


FIGURE 37: Relation of the voltage-frequency of the system is given when wire diameters of coils are selected as 0.1 mm, 0.3 mm, and 0.5 mm, respectively.

Figure 35(b) that the power generation efficiency of the system decreases when turns of coils increase from 100 turns to 150 turns. It can be obtained from Figure 35(c) that the power generation efficiency of the system decreases when turns of coils increase from 150 turns to 200 turns. Therefore, the power generation efficiency of the system is the greatest when turns of the coil are 100 turns. The result also can be drawn from Figure 36 that the coil has optimal turns, which make the power generation efficiency of the system greatest.

Finally, the influence of wire diameters of the coil on the power generation efficiency of the system is investigated, as shown in Figure 37. The output voltage of the system improves with the decrease in wire diameters of coils. Therefore, the power generation efficiency of the system is improved when wire diameters of coils are increased.

## 6. Conclusions and Discussion

In this paper, three different kinds of generators are designed: one is the monostable piezoelectric cantilever beam structure (structure A), and other two kinds of structures are bistable piezoelectric cantilever beam structures (structures B and C). The power generation and dynamic behaviors of the different structures are investigated. Following conclusions are drawn:

- (1) Comparing the monostable structure with the bistable structure, the power generation of structures B and C is better. The bistable structure is easier to go through the potential barrier by introducing the spring so that the cantilever beam vibrates between two stable states in a wide range of frequencies when the magnetic distance is suitable. When the magnetic distance is very small, the structure produces the larger magnetic force. So, the cantilever beam is difficult to go through the potential barrier, and the nonlinear dynamic

behavior is not obvious. When the magnetic distance is too large, the system makes the magnetic force quiet small. The bistable phenomenon of the cantilever beam disappears. Thus, the system improves the output voltage and broadens the effective frequency bandwidth under the condition of the suitable magnetic distance. When the bistable structure is introduced in the electromagnetic power generation, the output voltage of the system can be further improved. Therefore, the power generation of structure C is the best among three kinds of generators.

- (2) The power generation capacity of the bistable structure depends on the nonlinear dynamic characteristics of the structure. So, dynamical behaviors of structure C have been studied in detail. The experimental results show that dynamic behaviors of the system are rich and complex when the spring and the magnet are introduced. The repulsive force between two magnets can be self-tuning, and the energy through the potential barrier decreases when the spring is introduced. The system can vibrate between two stable states and the output voltage is greater. The bistable phenomenon and the self-tuning magnetic distance are beneficial to broaden the effective frequency bandwidth of the structure.
- (3) The smaller the energy passes through the potential barrier, the greater the power generation efficiency is produced by structure C. Since the magnetic distance affects the energy through the potential barrier, it is needed to find the optimal magnetic distance. In the experiment, the optimum range of the initial magnetic distance and the optimal magnetic distance is investigated in detail. It is found that the optimal initial magnetic distance is 15 mm, which makes the power generation efficiency of the system greatest.
- (4) In fact, the power generation of structure C is required to connect with the external load, which can affect the output power of the system. So, there is the optimal external load, which makes the output power of the system greatest. In the experiment, the influence of the external loads on the output power is studied under different initial magnetic distances. It is found that the optimal external load is 8 M $\Omega$ . In addition, the initial magnetic distance cannot have an effect on the optimal external load of the system.
- (5) Since structure C includes the electromagnetic induction generator, the influence of coils on power generation is needed to further examine. In the experiment, the influence of heights, turns, and wire diameters of the coil on the power generation efficiency is investigated in detail. It is found that the power generation efficiency of the system decreases when heights of coils increase. The optimal turns of coils are found, which makes the power generation efficiency of the system greatest. It is also observed that the wire diameter of the coil is too large to improve the power generation efficiency of the system.

## Data Availability

The data used to support the findings of this study are included within the article. Any reader can access the data supporting the conclusions of the study.

## Conflicts of Interest

The authors declare that there are no conflicts of interest regarding the publication of this paper.

## Acknowledgments

The authors gratefully acknowledge the support of the National Natural Science Foundation of China (NNSFC) (grant nos. 11772008, 11172009, 11372015, 11232009, 10872010, 11290152, and 10732020), Tianjin Natural Science Foundation (grant no. 19JCZDJC32300), and the ASME/IDETC-CIE Conference.

## References

- [1] S. Roundy, P. K. Wright, and J. Rabaey, "A study of low level vibrations as a power source for wireless sensor nodes," *Computer Communications*, vol. 26, no. 11, pp. 1131–1144, 2003.
- [2] E. S. Leland and P. K. Wright, "Resonance tuning of piezoelectric vibration energy scavenging generators using compressive axial preload," *Smart Materials and Structures*, vol. 15, no. 5, pp. 1413–1420, 2006.
- [3] S. P. Beeby, M. J. Tudor, and N. M. White, "Energy harvesting vibration sources for microsystems applications," *Measurement Science and Technology*, vol. 17, no. 12, pp. 175–195, 2006.
- [4] B. P. Mann and B. A. Owens, "Investigations of a nonlinear energy harvester with a bistable potential well," *Journal of Sound and Vibration*, vol. 329, no. 9, pp. 1215–1226, 2009.
- [5] S. C. Stanton, C. C. McGehee, and B. P. Mann, "Nonlinear dynamics for broadband energy harvesting: investigation of a bistable piezoelectric inertial generator," *Physica D: Nonlinear Phenomena*, vol. 239, no. 10, pp. 640–653, 2010.
- [6] A. Erturk and D. J. Inman, "Broadband piezoelectric power generation on high-energy orbits of the bistable duffing oscillator with electromechanical coupling," *Journal of Sound and Vibration*, vol. 330, no. 10, pp. 2339–2353, 2010.
- [7] M. Ferrari, V. Ferrari, M. Guizzetti, B. Andò, S. Baglio, and C. Trigona, "Improved energy harvesting from wideband vibrations by nonlinear piezoelectric converters," *Sensors and Actuators A: Physical*, vol. 162, no. 2, pp. 425–431, 2010.
- [8] H. A. Ma, J. Q. Liu, G. Tang, C. S. Yang, and Y. G. Li, "A magnetic structure for broadband piezoelectric vibration energy harvester," *Transducer and Micro-system Technologies*, vol. 30, no. 4, pp. 66–68, 2011.
- [9] A. F. Arrieta, T. Delpero, A. E. Bergamini, and P. Ermanni, "Broadband vibration energy harvesting based on cantilevered piezoelectric bi-stable composites," *Applied Physics Letters*, vol. 102, no. 17, Article ID 173904, 2013.
- [10] W. Al-Ashtari, M. Hunstig, T. Hemsell, and W. Sestro, "Increasing the power of piezoelectric energy harvesters by magnetic stiffening," *Journal of Intelligent Material Systems and Structures*, vol. 24, no. 11, pp. 1332–1342, 2013.
- [11] E. K. Ali and J. Kyle, "Efficiency enhancement of a cantilever-based vibration energy harvester," *Sensors*, vol. 14, pp. 188–211, 2014.
- [12] K. Fan, J. Chang, F. Chao, and W. Pedrycz, "Design and development of a multipurpose piezoelectric energy harvester," *Energy Conversion and Management*, vol. 96, pp. 430–439, 2015.
- [13] M. H. Yao, W. Zhang, and Z. G. Yao, "Nonlinear vibrations and chaotic dynamics of the laminated composite piezoelectric beam," *Journal of Vibration and Acoustics*, vol. 137, no. 1, Article ID 011002, 2015.
- [14] A. Jemai, F. Najjar, M. Chafra, and Z. Ounaies, "Modeling and parametric analysis of a unimorph piezocomposite energy harvester with interdigitated electrodes," *Composite Structures*, vol. 135, pp. 176–190, 2016.
- [15] S. Arkadiusz, R. B. Christopher, H. A. Kim, R. Andrzej, and L. Grzegorz, "Responses of bistable piezoelectric-composite energy harvester by means of recurrences," *Mechanical Systems and Signal Processing*, vol. 76–77, pp. 823–832, 2016.
- [16] X. D. Xie and Q. Wang, "A study on a high efficient cylinder composite piezoelectric energy harvester," *Composite Structures*, vol. 161, pp. 237–245, 2017.
- [17] T. Galchev, H. Kim, and K. Najafi, "Micro power generator for harvesting low-frequency and nonperiodic vibrations," *Journal of Microelectromechanical System*, vol. 20, no. 4, pp. 852–866, 2011.
- [18] I. Sari, T. Balkan, and H. Kulah, "An electromagnetic micro power generator for wideband environmental vibrations," *Sensors and Actuators*, vol. 11, pp. 1–9, 2007.
- [19] B. P. Mann and N. D. Sims, "Energy harvesting from the nonlinear oscillations of magnetic levitation," *Journal of Sound and Vibration*, vol. 319, no. 1–2, pp. 515–530, 2009.
- [20] E. Sardini and M. Serpelloni, "An efficient electromagnetic power harvesting device for low-frequency applications," *Sensors and Actuators A-Physical*, vol. 172, no. 2, pp. 475–482, 2010.
- [21] Ö. Zorlu, E. T. Topal, and H. Kulah, "A vibration-based electromagnetic energy harvester using mechanical frequency up-conversion method," *IEEE Sensors Journal*, vol. 11, no. 2, pp. 481–488, 2011.
- [22] A. R. M. Faisal, C. Hong, and G.-S. Chung, "Multi-frequency electromagnetic energy harvester using a magnetic spring cantilever," *Sensors and Actuators A: Physical*, vol. 182, pp. 106–113, 2012.
- [23] R. Ramlan, M. J. Brennan, B. R. Mace, and S. G. Burrow, "On the performance of a dual-mode non-linear vibration energy harvesting device," *Journal of Intelligent Material Systems and Structures*, vol. 23, no. 13, pp. 1423–1432, 2012.
- [24] D. Kremer and K. Liu, "A nonlinear energy sink with an energy harvester: transient responses," *Journal of Sound and Vibration*, vol. 333, no. 20, pp. 4859–4880, 2014.
- [25] M.-L. Seol, J.-W. Han, S.-J. Park, S.-B. Jeon, and Y. K. Choi, "Hybrid energy harvester with simultaneous triboelectric and electromagnetic generation from an embedded floating oscillator in a single package," *Nano Energy*, vol. 23, pp. 50–59, 2016.
- [26] M. Resali and H. Salleh, "Comparison of an electromagnetic energy harvester performance using wound coil wire and PCB coil," *Earth and Environmental Science*, vol. 32, Article ID 012059, 2016.
- [27] T. Wacharasindhu and J. W. Kwon, "A micromachined energy harvester from a keyboard using combined electromagnetic and piezoelectric conversion," *Journal of*

- Micromechanics and Microengineering*, vol. 18, no. 10, Article ID 104016, 2008.
- [28] Y. Tadesse, S. J. Zhang, and S. Priya, "Multimodal energy harvesting system: piezoelectric and electromagnetic," *Journal of Intelligent Material Systems and Structures*, vol. 20, no. 5, pp. 625–632, 2009.
- [29] V. R. Challa, M. G. Prasad, and F. T. Fisher, "A coupled piezoelectric electromagnetic energy harvesting technique for achieving increased power output through damping matching," *Smart Materials and Structures*, vol. 18, Article ID 095029, 2009.
- [30] M. A. Karami and D. J. Inman, "Nonlinear hybrid energy harvesting utilizing piezo-magneto-elastic spring," in *Proceedings of the 2010 Conference on Active and Passive Smart Structures and Integrated Systems*, San Diego, CA, USA, March 2010.
- [31] B. Yang, C. K. Lee, W. L. Kee, and S. P. Lim, "Hybrid energy harvester based on piezoelectric and electromagnetic mechanisms," *Journal of Micro/Nanolithography, MEMS, and MOEMS*, vol. 9, no. 2, Article ID 023002, 2010.
- [32] H.-y. Wang, L.-h. Tang, Y. Guo, X.-b. Shan, and T. Xie, "A 2DOF hybrid energy harvester based on combined piezoelectric and electromagnetic conversion mechanisms," *Journal of Zhejiang University SCIENCE A*, vol. 15, no. 9, pp. 711–722, 2014.
- [33] S. Mahmoudi, N. Kacem, and N. Bouhaddi, "Enhancement of the performance of a hybrid nonlinear vibration energy harvester based on piezoelectric and electromagnetic transductions," *Smart Materials and Structures*, vol. 23, no. 7, Article ID 075024, 2014.
- [34] R. Hamid and M. R. Yuce, "A wearable energy harvester unit using piezoelectric-electromagnetic hybrid technique," *Sensors and Actuators A: Physical*, vol. 257, pp. 198–207, 2017.
- [35] M. H. Yao, L. Ma, and W. Zhang, "Study on power generations and dynamic responses of the bistable straight beam and the bistable L-shaped beam," *Science China Technological Sciences*, vol. 61, no. 9, pp. 1404–1416, 2018.
- [36] M. H. Yao, P. F. Liu, L. Ma, H. B. Wang, and W. Zhang, "Experimental study on broadband bistable energy harvester with L-shaped piezoelectric cantilever beam," *Acta Mechanica Sinica*, vol. 36, no. 3, pp. 557–577, 2020.
- [37] M. H. Yao, P. F. Liu, W. Zhang, and D. X. Cao, "The experimental study on a bistable piezoelectric-electromagnetic combined vibration energy harvester," in *Proceedings of the ASME International Design Engineering Technical Conferences and Computers and Information in Engineering Conference (IDETC/CIE 2017)*, Cleveland, OH, USA, August 2017.
- [38] M. Getzlaff, *Fundamentals of Magnetism*, Springer, Berlin, Germany, 2008.

## Research Article

# Coexistence of Multiple Points, Limit Cycles, and Strange Attractors in a Simple Autonomous Hyperjerk Circuit with Hyperbolic Sine Function

M. Fouodji Tsotsop <sup>1,2</sup>, J. Kengne,<sup>1</sup> G. Kenne <sup>1</sup> and Z. Tabekoueng Njitacke <sup>1,2</sup>

<sup>1</sup>Unité de Recherche d'Automatique et Informatique Appliquée (UR-AIA), Department of Electrical Engineering, IUT-FV Bandjoun, University of Dschang (Cameroon), Dschang, Cameroon

<sup>2</sup>Unité de Recherche de Matière Condensée, d'Electronique et de Traitement du Signal (UR-MACETS), Department of Physics, University of Dschang, P.O. Box 67, Dschang, Cameroon

Correspondence should be addressed to M. Fouodji Tsotsop; [tsotsopmerlinefouodji@yahoo.com](mailto:tsotsopmerlinefouodji@yahoo.com)

Received 18 December 2019; Revised 8 March 2020; Accepted 28 March 2020; Published 29 July 2020

Academic Editor: Oveis Abedinia

Copyright © 2020 M. Fouodji Tsotsop et al. This is an open access article distributed under the Creative Commons Attribution License, which permits unrestricted use, distribution, and reproduction in any medium, provided the original work is properly cited.

In this contribution, a new elegant hyperjerk system with three equilibria and hyperbolic sine nonlinearity is investigated. In contrast to other models of hyperjerk systems where either hidden or self-excited attractors are obtained, the case reported in this work represents a unique one which displays the coexistence of self-excited chaotic attractors and stable fixed points. The dynamic properties of the new system are explored in terms of equilibrium point analyses, symmetry and dissipation, and existence of attractors as well. Common analysis tools (i.e., bifurcation diagram, Lyapunov exponents, and phase portraits) are used to highlight some important phenomena such as period-doubling bifurcation, chaos, periodic windows, and symmetric restoring crises. More interestingly, the system under consideration shows the coexistence of several types of stable states, including the coexistence of two, three, four, six, eight, and ten coexisting attractors. In addition, the system is shown to display anti-monotonicity and offset boosting. Laboratory experimental measurements show a very good coherence with the theoretical predictions.

## 1. Introduction

Most authors have been interested in chaotic systems because of their sensitivity to the initial conditions and also to the variation of system parameters. Since the discovery of this phenomenon by Lorenz [1], many classical chaotic systems have emerged. We can mention the Rossler system [2], Chen system [3], Jafari system [4], Pham system [5], and Lü system just to name a few [6]. In the last few years, special attention has been given to “jerk systems” because of their simplicity and complex dynamics [7–12]. From a mathematical point of view, a generalization of the jerk dynamics is usually given in the following form:

$$\frac{d^n x}{dt^n} = f\left(\frac{d^{n-1}x}{dt^{n-1}}, \dots, \frac{dx}{dt}, x\right). \quad (1)$$

When  $n = 3$ , we have  $(d^3x/dt^3) = f((d^2x/dt^2), (dx/dt), x)$ , which is called “jerk system” [13]. For  $n \geq 4$ , (1) turns to “hyperjerk system” or “snap system” [14]. In the literature, several authors have studied the latter. Generally, these systems exhibit multistability phenomenon which are the coexistence of multiple attractors solely depending on the initial conditions. These attractors are generally classified into two categories, namely, self-excited and hidden attractors [15–20]. Remember that self-excited attractors exist in systems with unstable equilibrium points [21–23]. In contrast, hidden attractors are characterized by the systems with no equilibrium [24–29], either by a line or a curve of



equilibrium points, or system with stable equilibrium points [24, 25]. In addition, hidden attractors have a basin of attraction which does not intersect with the neighborhoods of equilibria.

Interested by the self-excited attractors, many authors applied different techniques to hyperjerk systems. Some of these authors introduced different types of nonlinearities. For instance, in 2006, Cklouverakis and Sprott [22] presented a numerical study of a simple subclass of hyperjerk systems and showed that the 4<sup>th</sup> and 5<sup>th</sup> order hyperjerk systems developed some simple chaotic behaviors. In 2015, Sundiarapandian and coworkers [23] presented a new hyperchaotic 4-D hyperjerk system by adding a quadratic nonlinearity to the hyperjerk system of Chlouverakis–Sprott system. The authors present some qualitative and quantitative analyses of the new system. In 2017, Daltzis et al. [13] introduced a new hyperjerk system with two nonlinearities (absolute value and quintic term) and showed that the new system can develop hyperchaotic behaviors. Recently, Leutcho et al. [21] presented a new hyperjerk circuit with hyperbolic sine function and demonstrated that the novel proposed system is the unique one which is capable to exhibit the coexistence of nine periodic and chaotic attractors.

Motivated by the above mentioned results, we present a new hyperjerk system with nonlinear position feedback involving a hyperbolic sine function. Our circuit is derived from the hyperjerk system proposed by Dalkirian and Sprott [7] by replacing the exponential nonlinearity by the hyperbolic sine function. The striking aspect of the proposed system is its ability to develop the coexistence of up to ten disconnected attractors including periodic, chaotic, and point attractors. The objectives of this work are as follows: (a) to present an analytical study of the proposed hyperjerk system; (b) to highlight regions in which we observe the coexistence of multiple attractors; (c) to point out some striking features like anti-monotonicity and offset boosting; and (d) to verify the feasibility of the proposed model through an experimental study.

This research is organized as follows. Section 2 deals with the modeling process. The electronic consuration of the hyperjerk circuit is presented and the suitable mathematical model is derived to describe the dynamics of the novel hyperjerk, wherein some basic properties of the model are equally presented. In Section 3, the bifurcation structures of the system are investigated numerically. Also, in this section, some tools are used to show multistability observed in the novel system. Section 4 contains experimental study, and at the end of this section, it appears that coherence is observed between the theoretical and experimental analysis. Finally, Section 5 presents conclusion.

## 2. Description and Analysis of the Model

**2.1. Circuit Description.** It is important to know that the new circuit proposed here derives from the hyperjerk system proposed by Dalkirian and Sprott [7]. It is obtained by substituting the exponential nonlinearity by the hyperbolic sine function. Figure 1 represents the schematic diagram of the novel hyperjerk circuit. The circuit consists of four successive integrators associated to several feedback loops. In addition, the

nonlinear feedback loop linked with the pair of semiconductor diodes ( $D_1, D_2$ ) is applied to the first integrator. The symmetrical nature [30] of the system is due to the antiparallel configuration of the diodes. In such type of configuration, the voltage across each diode is equal to the voltage of the resulting two-terminal device, while the current is the addition of the currents flowing through each diode. The symmetrical property of the nonlinearity is necessary for the occurrence of symmetric attractors [30]. We would like to recall that the pair of semiconductor diodes is the only nonlinear element responsible for the chaotic behavior displayed by the whole electronic circuit.

**2.2. State Equations.** The following assumptions will be adopted throughout our analysis. Firstly, we considered that capacitors and operational amplifiers are ideal with the latter operating in linear domains. Secondly, the current-voltage characteristic (3) of the pair of semiconductor diodes ( $D_1$  and  $D_2$ ) is obtained from the Shockley diode equation [31, 32] as follows:

$$I_d = I_{D_1} - I_{D_2} = I_S [\exp(V_d/\eta V_T) - 1] - I_S [\exp(-V_d/\eta V_T) - 1] = 2I_S \sinh(V_d/\eta V_T), \quad (2)$$

where  $I_S$ ,  $V_T = (k_b T/q)$ ,  $k_b$ ,  $T$ ,  $q$ , and  $\eta$  ( $1 < \eta < 2$ ) are the intrinsic parameters of the diodes. By applying Kirchhoff's laws to Figure 1 and considering the above assumptions, it can be shown that the voltages  $V_1$ ,  $V_2$ ,  $V_3$ , and  $V_4$  satisfy the following set of four coupled first-order nonlinear differential equations:

$$\begin{cases} C_1 \frac{dV_1}{dt} = \frac{V_2}{R}, \\ C_2 \frac{dV_2}{dt} = \frac{V_3}{R_m}, \\ C_3 \frac{dV_3}{dt} = \frac{V_4}{R_d}, \\ C_4 \frac{dV_4}{dt} = \frac{V_1}{R_c} - \frac{V_2}{R_b} - \frac{V_3}{R_e} - \frac{V_4}{R_a} - I_d. \end{cases} \quad (3)$$

Applying the following change of variables:

$$\begin{aligned} t &= \tau RC, \\ V_{\text{ref}} &= 10\eta V_T, \\ x_j V_{\text{ref}} &= V_j \quad (j = 1, 2, 3, 4), \\ a &= R/R_a, \\ b &= R/R_b, \\ c &= R/R_c, \\ d &= R/R_d, \\ m &= R/R_m, \\ e &= R/R_e, \\ \gamma &= 2RI_S/V_{\text{ref}}, \end{aligned} \quad (4)$$



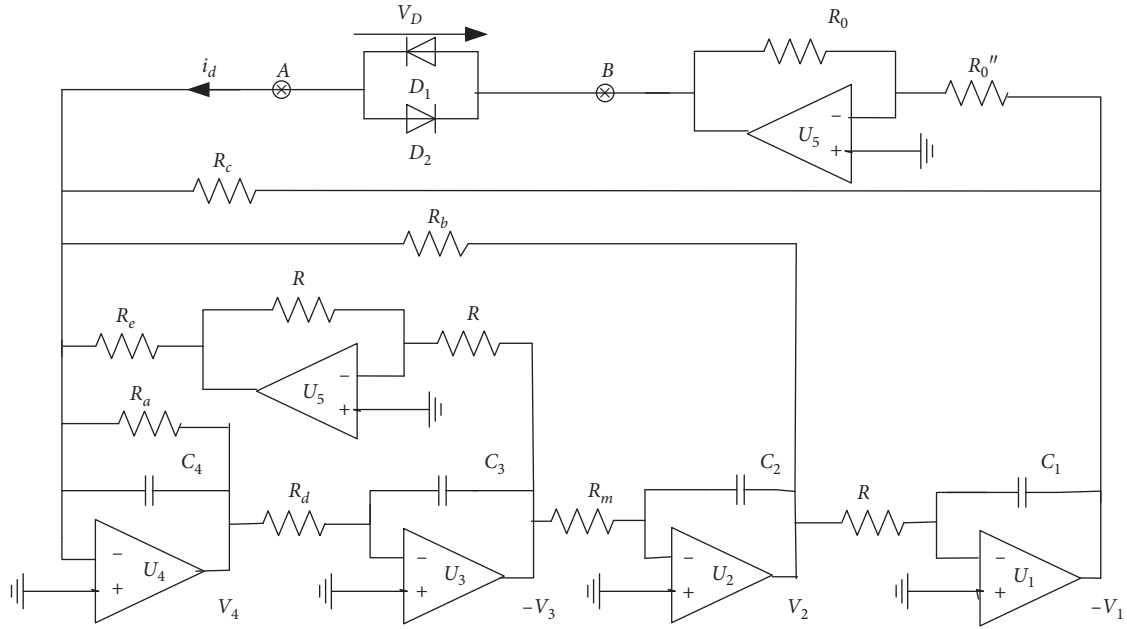


FIGURE 1: Electronic circuit realization of the novel 4-D hyperjerk system with hyperbolic sine nonlinearity. Its simplicity is remarkable. The pair of semiconductor diodes implements the hyperbolic nonlinearity of the model.

we get the normalized circuit equations which are expressed by the following smooth nonlinear fourth-order differential equations easy for numerical integration:

$$\begin{cases} \dot{x}_1 = x_2, \\ \dot{x}_2 = mx_3, \\ \dot{x}_3 = dx_4, \\ \dot{x}_4 = cx_1 - bx_2 - ex_3 - ax_4 - \gamma \sinh(x_1), \end{cases} \quad (5)$$

where the dot represents differentiation concerning the dimensionless time  $\tau$ . Note that the nonlinear function only depends on the state variable  $x_1$  in system (5).  $\gamma$  will be kept constant throughout the numerical analysis:  $\gamma = 0.0011$ . Therefore, during the bifurcation analysis of the 4-D system,  $c$  is considered like the control parameter (i.e., with respect to  $R_c$ ). The values of electronic components used for both the numerical and experimental analyses are listed in Table 1. System (5) can be expressed equivalently in the general hyperjerk form as follows:

$$\ddot{x}_1 = mbcx_1 - d\gamma \sinh(x_1) - mbd\dot{x}_1 - dex_1 - a\dot{x}_1. \quad (6)$$

By observing equation (6), it can be noticed that our model belongs to the wider class of “elegant” hyperjerk dynamical systems defined in [14]. More interestingly, our model (5) represents one of the simplest autonomous 4-D systems reported recently, displaying the coexistence of up to ten fixed points, periodic and chaotic attractors.

**2.3. Symmetry, Dissipation, and Existence of Attractors.** Equation (5) being invariant following the transformation  $(x_1, x_2, x_3, x_4) \iff (-x_1, -x_2, -x_3, -x_4)$ , we can conclude that we will have a couple of solutions for a given parameter

TABLE 1: List of electronic components used during the analyses.

Components	Values	
	Case A	Case B
$R_a$	$300\Omega - 1.7k\Omega$	$5.555k\Omega$
$R_b$	$1.666k\Omega$	$2.631k\Omega$
$R_c$	$10k\Omega$	$4k\Omega - 6k\Omega$
$R_d$	$2k\Omega$	$7.407k\Omega$
$R_e$	$5k\Omega$	$673.4\Omega$
$R_m$	$10k\Omega$	$4.545k\Omega$
$R, R_0, R_0'$ (numerical study)	$10k\Omega$	$10k\Omega$
$R, R_0$ (experimental study)	$10k\Omega$	$10k\Omega$
$R_0''$ (experimental study)	$100k\Omega$	$100k\Omega$
$C_1, C_2, C_3, C_4$	$10nF$	$10nF$
$D_1, D_2$	1N4148	1N4148

range. So, if  $(x_1, x_2, x_3, x_4)$  is a solution of our system, then its symmetry  $(-x_1, -x_2, -x_3, -x_4)$  will also be a solution. All these makes it possible to highlight the symmetrical nature of our system. In order to verify the dissipation property of our system, it is necessary to calculate the volume contraction rate ( $\Lambda = (V^{-1}dV/dt)$ ). For every point of space  $(x_1, x_2, x_3, x_4)^T$  [33, 34], it is given by the following expression:

$$\Lambda = \frac{\partial \dot{x}_1}{\partial x_1} + \frac{\partial \dot{x}_2}{\partial x_2} + \frac{\partial \dot{x}_3}{\partial x_3} + \frac{\partial \dot{x}_4}{\partial x_4} = -a < 0. \quad (7)$$

The above expression is negative and does not depend on the space coordinates of the system, and thus we can conclude that the introduced system is dissipative.

**2.4. Fixed Point Analysis.** By canceling the right side of equation (5), it is possible to determine the equilibrium

points of the system which play a crucial role in the study of the system dynamics. The resolution of equation (8) permits to obtain different equilibrium points of the system.

$$\begin{cases} x_2 = 0, \\ x_3 = 0, \\ x_4 = 0, \\ cx_1 - bx_2 - ex_3 - ax_4 - \gamma \sinh(x_1) = 0. \end{cases} \quad (8)$$

Note that the point  $E_0(0, 0, 0, 0)$  is a trivial equilibrium point, while  $E_1$  and  $E_2$  are the solutions of the transcendental equation:

$$cx_1 - \gamma \sinh(x_1) = 0. \quad (9)$$

By fixing  $c = 2.442$  and maintaining  $\gamma$  at the same previous value, we obtain the other nontrivial equilibrium points  $(E_1, E_2) = (\pm 10.79, 0, 0, 0)$ . The stability of the system in the neighborhood of those equilibrium points is studied by resolving the characteristic equation (12), resulting from the below equation:

$$\det(M_J - \lambda I_d) = 0, \quad (10)$$

where  $I_d$  represents the  $4 \times 4$  identity matrix and  $M_J$  the Jacobian matrix defined as follows:

$$M_J = \begin{bmatrix} 0 & 1 & 0 & 0 \\ 0 & 0 & m & 0 \\ 0 & 0 & 0 & d \\ c - \gamma \cosh(x_1^0) & -b & -e & -a \end{bmatrix}. \quad (11)$$

The characteristic equation obtained is  $\lambda^4 + c_3\lambda^3 + c_2\lambda^2 + c_1\lambda + c_0 = 0$ , with

$$\begin{aligned} c_0 &= -md(c - \gamma \cosh(x_1^0)), \\ c_1 &= mdb, \\ c_2 &= ed, \\ c_3 &= a. \end{aligned} \quad (12)$$

By applying the Lyapunov stability theory, it is shown that at the equilibrium point  $E_0(0, 0, 0, 0)$ ,  $c - \gamma > 0 \implies c_0 < 0$ , and thus the equilibrium  $E_0$  is unstable since the characteristic equation has coefficients with different signs. In contrast, the stability of the nonzero equilibrium points  $(E_{1,2}(\pm 10.79, 0, 0, 0))$  depends on the control parameters  $m$  and  $b$ . By applying the Routh–Hurwitz criterion [32, 33], we have shown that for  $b < b_{c1} = 3.4397$  and  $b > b_{c2} = 5.56$ , the nontrivial equilibrium points are unstable, but for  $b_{c1} < b < b_{c2}$ , they are stable. These critical values are obtained from the calculation of the Hopf bifurcation conditions:

$$\begin{aligned} \omega_{\text{Hopf}} &= \sqrt{mdb/a}, \\ b_{c1,c2} &= \frac{1}{2} \left( \frac{ea}{m} \pm \sqrt{\Delta} \right), \end{aligned} \quad (13)$$

with  $\Delta = (ea/m)^2 + (4a^2/md)(c - \cosh(10.79))$ .

Equation (13) provides the frequency of stable oscillations as well as the critical values of  $b_{c1,c2}$  corresponding to the Hopf bifurcation of the system. From Table 2, it follows that in the regime of (periodic or chaotic) oscillations, the three equilibria are unstable, and thus the system generates self-excited oscillations. For the following parameters  $a = 1.8$ ,  $d = 1.35$ ,  $e = 15$ ,  $m = 3$ , and  $c = 2.442$ , the equilibrium point  $E_0(0, 0, 0, 0)$  remains unstable for all values of control parameter  $b$ . Moreover, for some values of bifurcation parameter  $b$ , the nontrivial equilibria have pure imaginary roots, and thus the system presents the Hopf bifurcation. In order to verify the existence of the Hopf bifurcation in the system, eigenvalue locus is plotted. It shows the existence of Hopf bifurcation in the system which is characterized by the intersection of the eigenvalue locus with the imaginary axis. By observing Figures 2(a) and 2(b), we can certify that the new hyperjerk system presents Hopf bifurcation.

### 3. Numerical Computation

**3.1. Numerical Techniques.** System (5) is resolved numerically in order to highlight the rich variety of bifurcation that can be observed in a new hyperjerk system. The dynamic properties of the model were numerically simulated in Turbo Pascal using the fourth-order Runge–Kutta method with a constant time step size of  $2 \times 10^{-3}$ , and parameters are taken in extended precision mode. The transient phase is canceled by integrating the system for a long time. The bifurcation diagram and the Lyapunov exponent are the traditional tools that measure the dependence of the system on the initial conditions as well as the sequence that leads to chaos in the system. The algorithms of Wolf and his collaborators [35] are used for calculating the Lyapunov exponents.

**3.2. Bifurcation, Chaos in a Novel Hyperjerk Circuit.** Different scenarios exhibited by the proposed hyperjerk system are obtained by plotting the bifurcation diagrams. The bifurcation diagram of Figure 3(a) is obtained by plotting the local maxima of the variable  $x_1$  according to the bifurcation parameter  $a$ , the other parameters being fixed at  $c = 1$ ,  $b = 6$ ,  $d = 5$ ,  $e = 2$ , and  $m = 1$ . It can be noted that it is a period-doubling route to chaos because the transition from period-1 attractor to double-band chaos is as follows: period-1  $\rightarrow$  period-2  $\rightarrow$  period-4  $\rightarrow$  single-band chaos  $\rightarrow$  period-5  $\rightarrow$  single-band chaos  $\rightarrow$  double-band chaos. Figure 4 clearly shows the above transition. It is obtained by progressively varying the control parameter. The exact nature of the attractors mentioned above is defined by the graphs of the four largest Lyapunov exponents shown in Figure 3(b). We can observe in Figure 3(b) that periodic attractors are characterized by  $\lambda_1 = 0$ ,  $\lambda_2, \lambda_3$ , and  $\lambda_4 < 0$ , while chaotic attractors have the following characteristics:  $\lambda_1 > 0$ ,  $\lambda_2 = 0$ ,  $\lambda_3$ , and  $\lambda_4 < 0$ . A perfect coherence is observed between the bifurcation diagram and the corresponding graphs of the four largest Lyapunov exponents. In order to show the complexity of the new hyperjerk circuit, the chaotic attractor has been projected on several planes (Figures 5(a)–5(f)), as well

TABLE 2: Corresponding eigenvalues of each equilibrium point according to the bifurcation parameter  $b$ .

Values of bifurcation parameter $b$	Eigenvalues at nontrivial fixed $(E_1, E_2), \lambda_1, \lambda_2, \lambda_3, \lambda_4$	Eigenvalues at the origin $E_0(0, 0, 0, 0)$ $\lambda_1, \lambda_2, \lambda_3, \lambda_4$
3.1	$-0.9641 \pm 3.4906i$ $0.0641 \pm 2.7165i$ (unstable)	$-0.5719 \pm 4.4347i$ $-1.1041$ $0.4478$ (unstable)
3.2	$-0.9461 \pm 3.4712i$ $0.0461 \pm 2.7346i$ (unstable)	$-0.5618 \pm 4.4350i$ $-1.1185$ $0.4422$ (unstable)
3.4397	$-0.9000 \pm 3.4206i \pm 2.7820i$ (neutral, Hopf bifurcation)	$-0.5378 \pm 4.4358i$ $-1.1536$ $0.4292$ (unstable)
3.5	$-0.0023 \pm 3.5339i$ $-0.8977 \pm 2.6358i$ (stable)	$-0.5318 \pm 4.4361i$ $-1.1625$ $0.4260$ (unstable)
5.55	$-0.0093 \pm 3.5246i$ $-0.8907 \pm 2.6459i$ (stable)	$-0.3297 \pm 4.4591i$ $-1.4757$ $0.3351$ (unstable)
5.56	$\pm 3.5370i$ $-0.9000 \pm 2.6324i$ (neutral, Hopf bifurcation)	$-0.3287 \pm 4.4593i$ $-1.4772$ $0.3347$ (unstable)
5.59	$-0.9476 \pm 3.2070i$ $0.0476 \pm 3.0071i$ (unstable)	$-0.3258 \pm 4.4598i$ $-1.4819$ $0.3336$ (unstable)
9.12	$0.3784 \pm 4.0088i$ $-1.2784 \pm 2.0827i$ (unstable)	$-0.0077 \pm 4.5497i$ $-2.0210$ $0.2363$ (unstable)

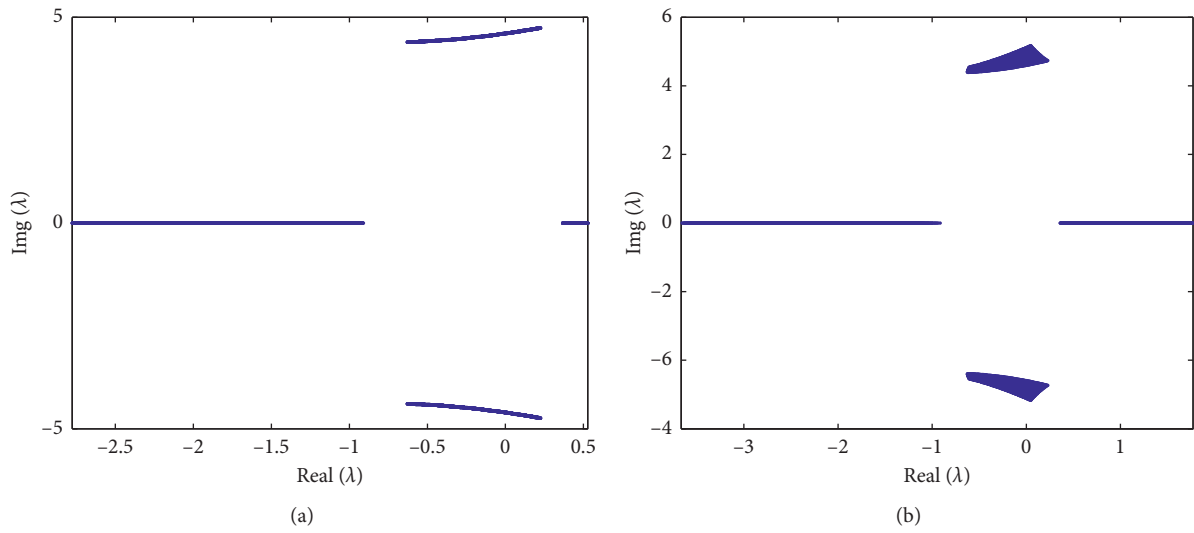


FIGURE 2: Representation of eigenvalue locus in the complex plan  $(\text{Re}(\lambda), \text{Im}(\lambda))$  with the following parameter values: (a)  $a = 1.8, b = 3.8, c = 2.442, d = 1.35, e = 14.85$ , and  $2 \leq m \leq 10$ ; (b)  $a = 1.8, b = 3.8, d = 1.35, e = 14.85, 2 \leq m \leq 10$ , and  $2.34 \leq c \leq 12.985$ . The appearance of eigenvalues in complex conjugate pairs justifies the symmetry observed in the system and intersection of the curve with imaginary axis shows the presence of the Hopf bifurcation in the system.

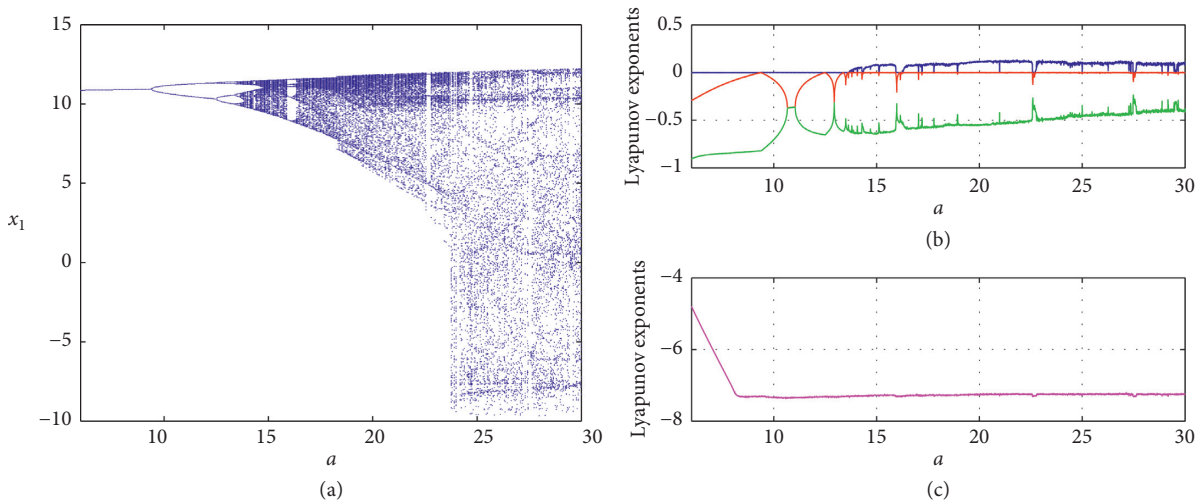


FIGURE 3: (a) Bifurcation diagram showing local maxima of the coordinate  $x_1$  versus  $c$  and (b, c) the corresponding graphs of four largest Lyapunov exponents plotted in the range  $6 \leq a \leq 30$ , with  $c = 1, b = 6, d = 5, e = 2$ , and  $m = 1$  and initial conditions  $(x_1(0), x_2(0), x_3(0), x_4(0)) = (0, 0, 2.4, 0)$ .

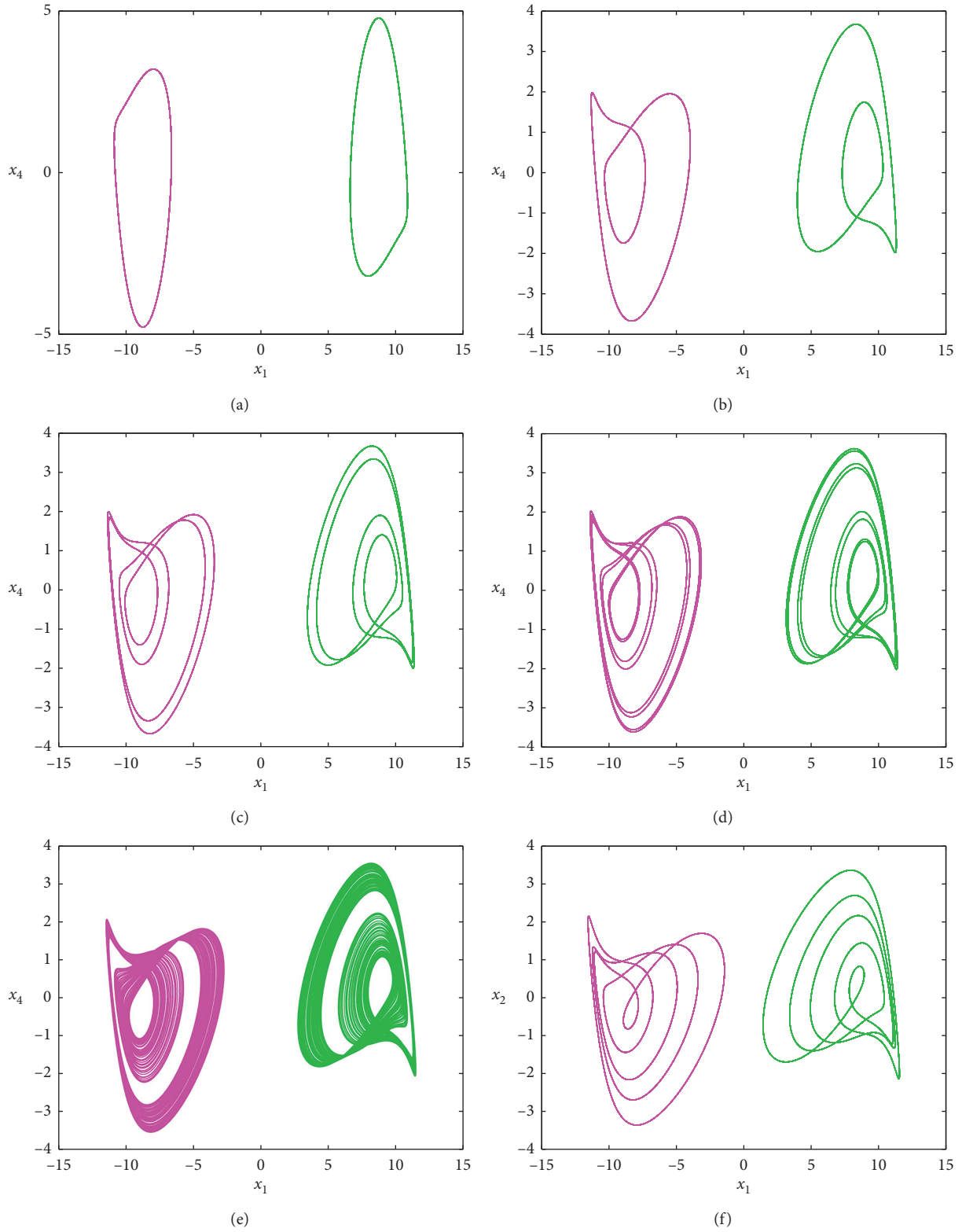


FIGURE 4: Continued.

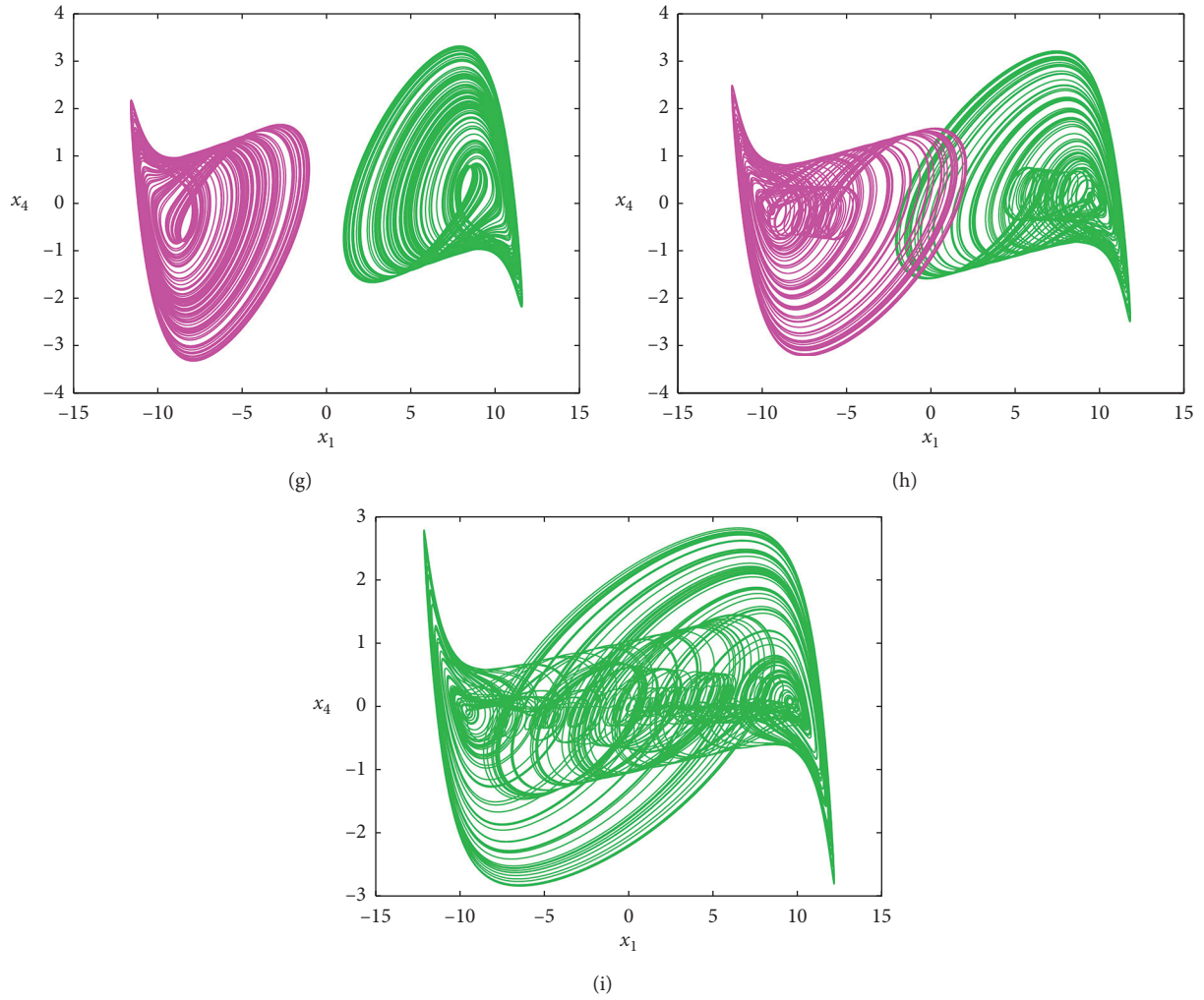


FIGURE 4: Numerical phase space trajectories showing routes to chaos in the system when varying the control parameter  $c$ : (a) period-1 for  $a = 7$ , (b) period-2 for  $a = 12.38$ , (c) period-4 for  $a = 13$ , (d) period-8 for  $a = 13.49$ , (e) single-band chaos for  $a = 14.6$ , (f) period-5 for  $a = 16.08$ , (g) single-band chaos for  $a = 16.7$ , (h) single-band chaos for  $a = 20$ , and (i) double-band chaos for  $a = 30$ . Initial conditions  $(x_1(0), x_2(0), x_3(0), x_4(0))$  are  $(0, 0, 2.4, 0)$ . The others parameters are fixed as follows:  $c = 1$ ,  $b = 6$ ,  $d = 5$ ,  $e = 2$ , and  $m = 1$ .

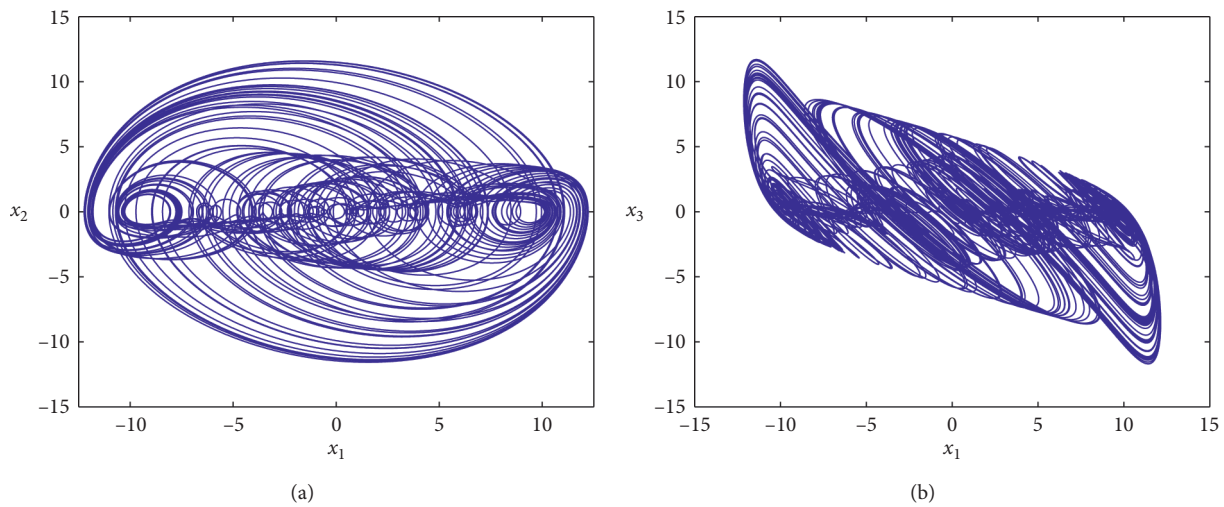


FIGURE 5: Continued.



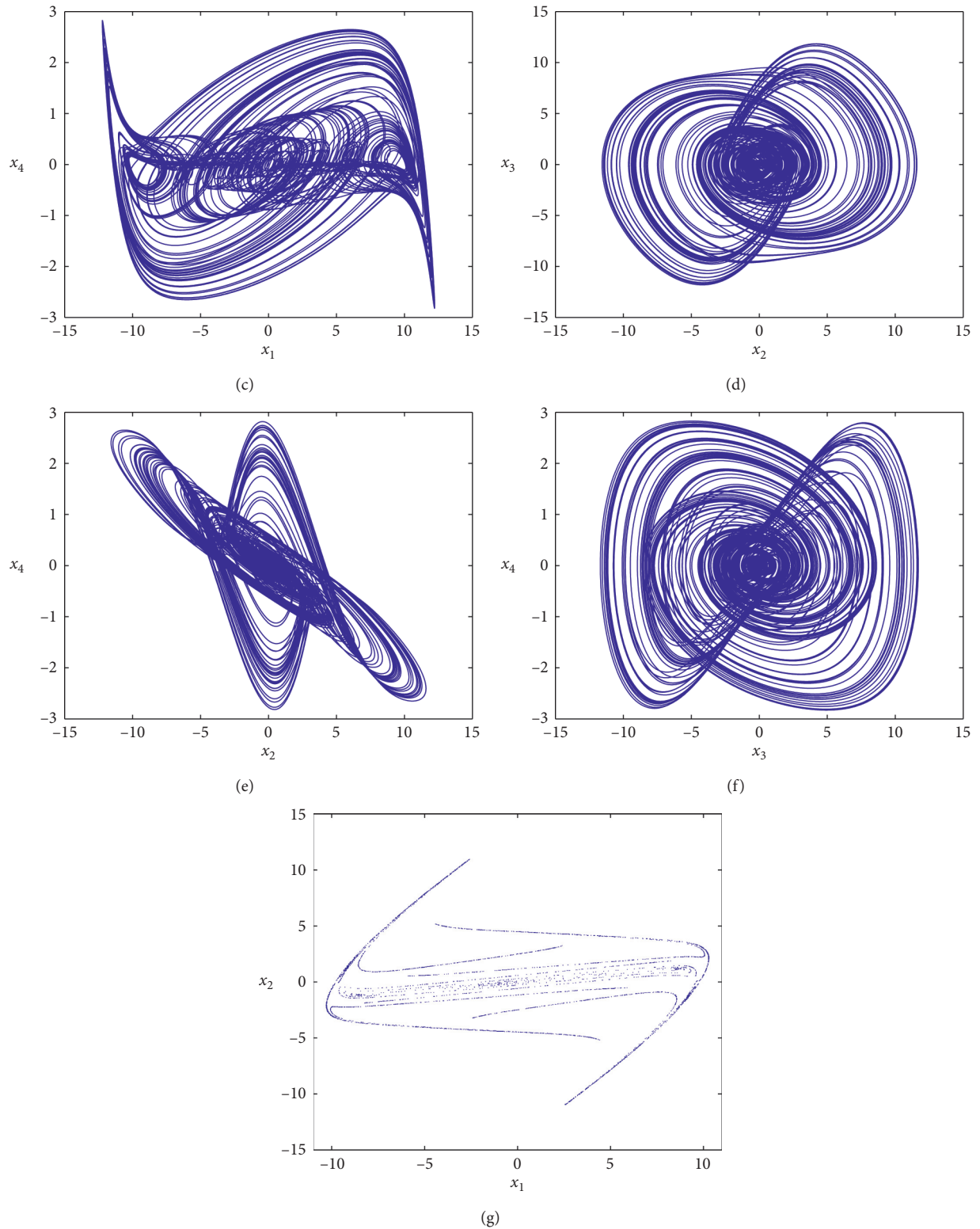


FIGURE 5: 2-D projection of the phase portraits of symmetric double-band chaotic attractors (a-f) of system (3) plotted into planes  $(x_1 - x_4)$ ,  $(x_2 - x_3)$ ,  $(x_2 - x_4)$ ,  $(x_3 - x_4)$  and corresponding double-sided Poincaré section (e) in the plane  $x_1 = 0$ . Parameters are the same as those in Figure 4.

as the Poincaré section (Figure 5(g)). We can observe that the double-band chaos completely changes when moving from one plane to another. For the value of the bifurcation parameter

$a = 17.04$ , the coexistence of four periodic and chaotic attractors is observed in the novel proposed system (see Figure 6). In order to illustrate the Hopf bifurcation previously



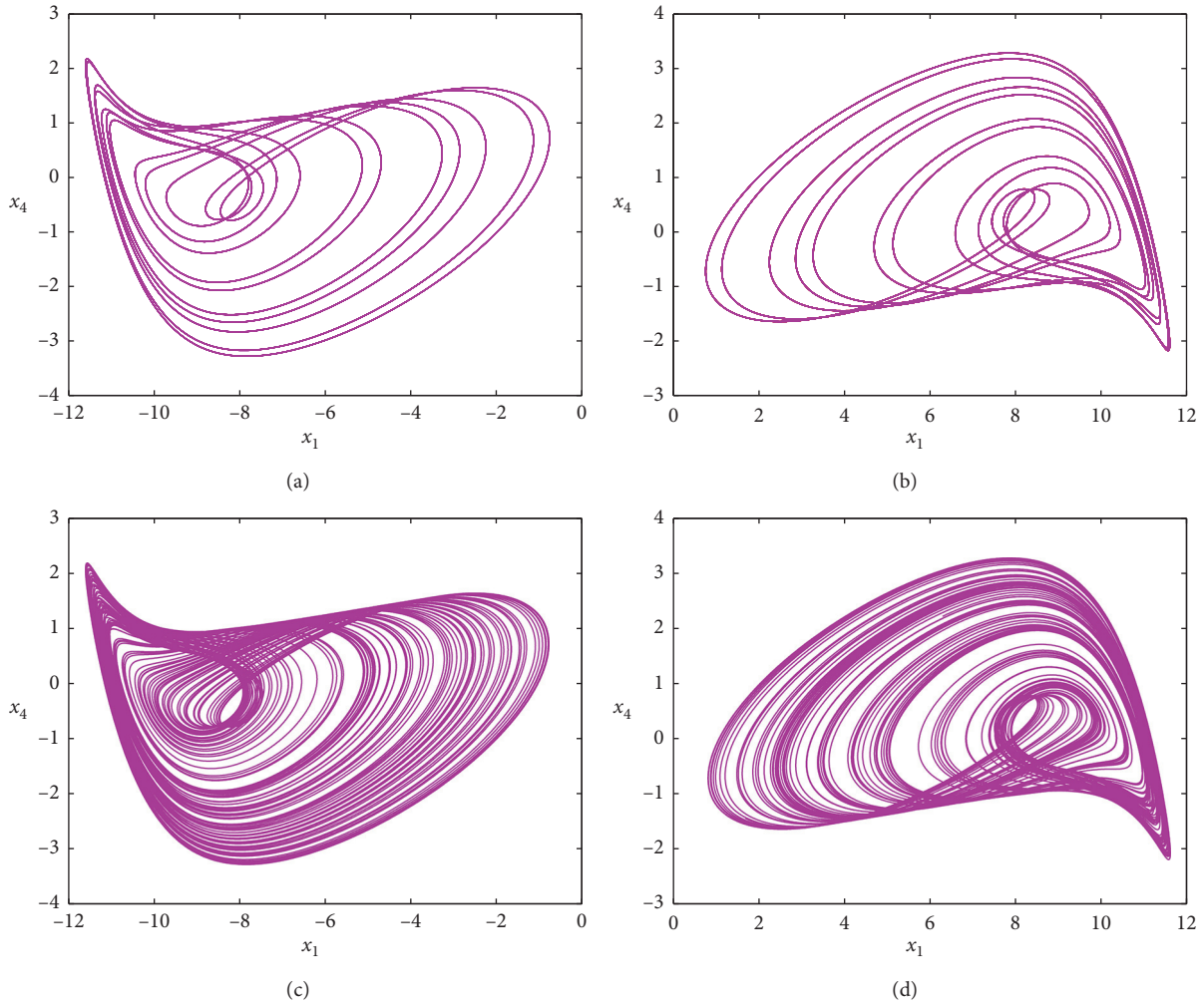


FIGURE 6: Coexistence of four attractors (a pair of period-11 limit cycle and a pair of chaotic attractors) with  $a = 17.04$ , and their corresponding initial conditions are  $(\pm 4.8, 0, 0, 0)$  and  $(\pm 1.2, 0, 0, 0)$ .

proved by theoretical calculations, the bifurcation diagram of Figure 7 has been represented. Stable state is characterized by a fixed point with  $\lambda_{\max} < 0$ , while oscillatory state is characterized by  $\lambda_{\max} \geq 0$ .

**3.3. Multistability.** In this section, we demonstrate the variety of dynamical regimes in the new 4-D system. We show that depending on the values of the system parameters, the system exhibits very rich dynamics and bifurcation scenarios. A multistable system is a system with various coexisting stable states (chaotic, point, and periodic state) under the same system parameters, with different initial conditions. In recent years, the phenomenon of multistability phenomenon has been reported in many nonlinear dynamic systems [13, 36–46].

**3.3.1. Coexistence of Attractors with respect to Bifurcation Parameter  $c$ .** By changing the system parameters and considering  $c$  as bifurcation parameter, we observe a completely different behavior. In addition, a very interesting

phenomenon which is the coexistence of multiple attractors appears in the new 4-D hyperjerk. For this phenomenon to be illustrated, the bifurcation diagrams of Figure 8 are plotted using the following method:

- (i) The blue diagram is obtained by simultaneously increasing the value of the control parameter  $c$  as well as the initial condition  $x(0)$ . At each iteration, we assign to  $x(0)$  the new value of the control parameter  $c$ .
- (ii) The red diagram is obtained by incrementing  $c$  from its minimum value 2.34 to its maximum value 2.985, with a carefully chosen step. Note that the solutions of the system at each iteration are considered as the initial condition of the next iteration.
- (iii) The cyan diagram respects the previous procedure, with the initial condition  $(-10.67, 0, 0, 0)$ , whereas the black diagram follows the same procedure as previously described but the only difference is the decrease of the control parameter  $c$ . The initial condition is  $(10, 0, 0, 0)$ .

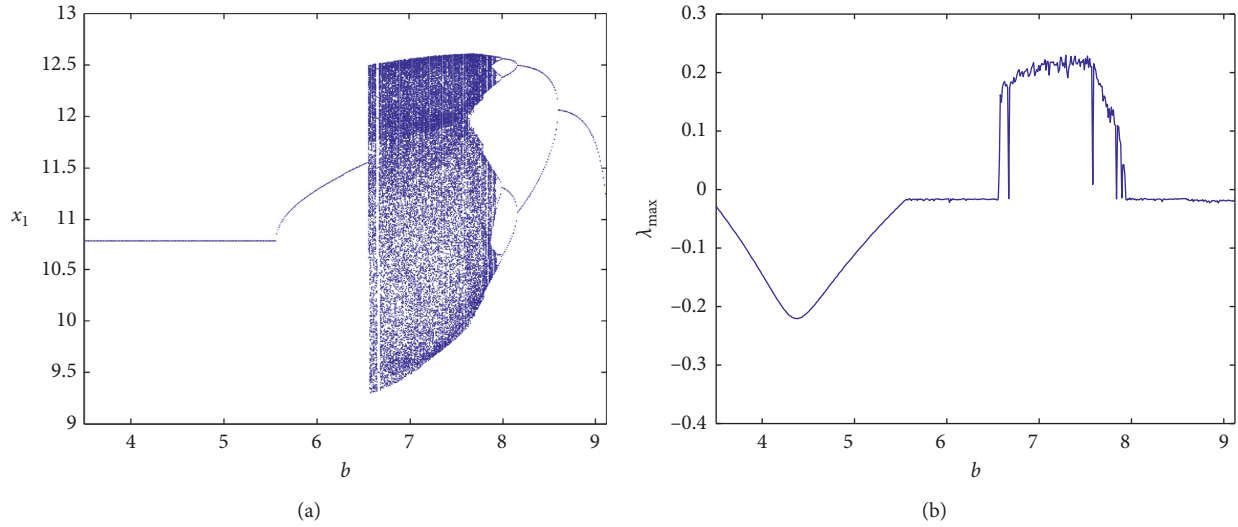


FIGURE 7: (a) Bifurcation diagram showing local maxima of the coordinate  $x_1$  versus  $b$  and (b) the corresponding graph of largest Lyapunov exponent ( $\lambda_{\max}$ ) plotted by decreasing  $b$  in the range  $3.5 \leq b \leq 9.12$ , with  $a = 1.8$ ,  $m = 3$ ,  $c = 2.442$ ,  $d = 1.35$ , and  $e = 15$  and initial conditions  $(x_1(0), x_2(0), x_3(0), x_4(0)) = (0, 0, 9.333, 0)$ .

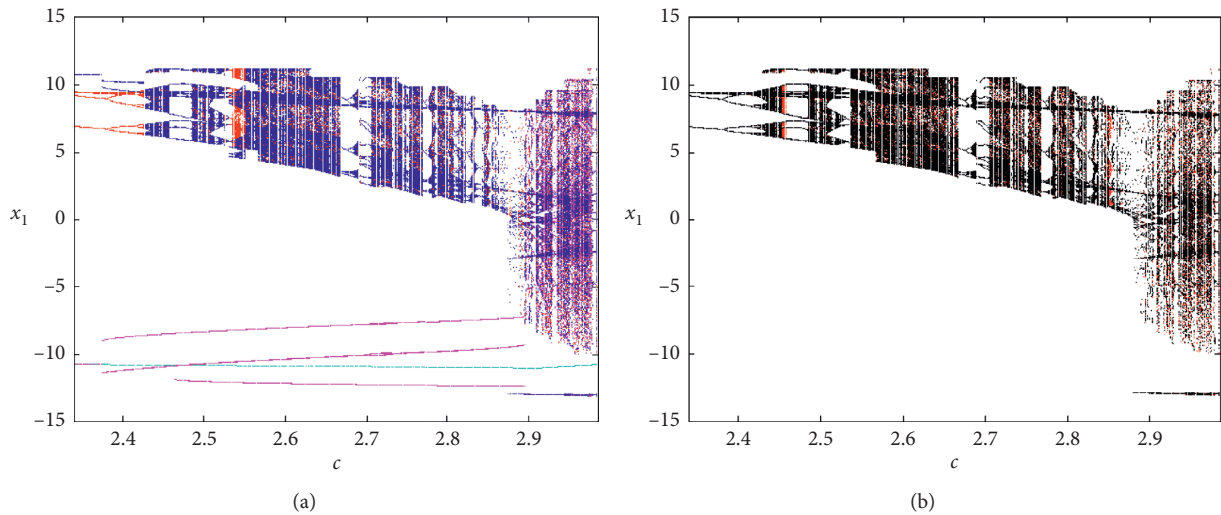


FIGURE 8: symmetric coexisting bifurcation diagrams showing complex structure of the new hyperjerk for  $a = 1.8$ ,  $b = 3.8$ ,  $d = 1.35$ ,  $e = 14.85$ , and  $m = 2.2$ . Initial conditions  $y(0) = z(0) = w(0) = 0$  and  $x(0)$  are fixed as follows for obtaining these diagrams: red diagrams for increasing  $c$  with  $x(0) = 5.25$ , black diagram for decreasing  $c$  with  $x(0) = -10$ , cyan diagrams for increasing  $c$  with  $x(0) = -10.67$ , magenta diagram for increasing and decreasing, started at  $c = 2.5442$  with  $x(0) = -4$ , and blue diagram for starting  $c$  with same initial condition  $x(0) = c$ . For more information, see Table 3.

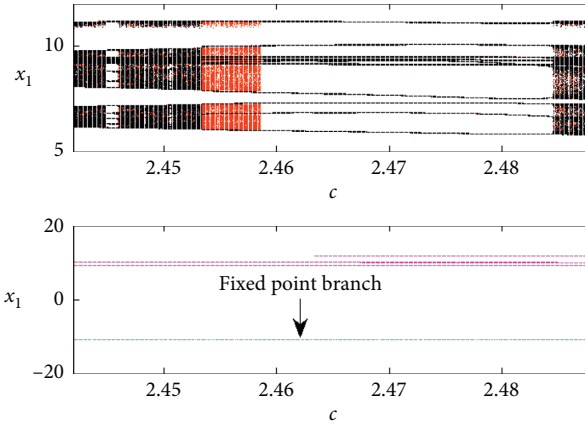
- (iv) The magenta diagram is obtained by increasing the control parameter  $c$  from 2.398 to 2.985, followed by decreasing the bifurcation parameter  $c$  from 2.398 to 2.34.

We can observe in Figure 8 several windows of coexisting attractors. For more details about the methods used to plot the bifurcation diagrams of Figure 8, see Table 3. The enlarged bifurcation diagram of Figure 9 shows the hysteretic domain, plotted in the range  $2.442 \leq c \leq 2.488$ , and the techniques used to plot the diagrams are also presented in

Table 3. Figure 9 shows the coexistence of six and eight different limit cycles, chaotic and point attractors. Some sample phase portraits showing the coexistence of six and eight attractors are presented in Figures 10 and 11, respectively. Some basins of attractions showing the initial conditions domains of the coexisting attractors are presented in Figure 12. The coexistence of four attractors is clearly denoted (a pair of periodic attractors (black and yellow) and a pair of chaotic attractors (blue and green)). Note that there is a perfect symmetry between the different cross sections of the competing attractors.

TABLE 3: Techniques used to obtain coexisting bifurcation diagrams and corresponding initial conditions.

$Fig.n^o$	Color graph	Parameter range	Sweeping direction	Initial condition $(x_1(0), x_2(0), x_3(0), x_4(0))$
Figure 8	Blue	$2.34 \leq c \leq 2.985$	Upward	$(c, 0, 0, 0)$
	Red	$2.34 \leq c \leq 2.985$	Upward	$(5.25, 0, 0, 0)$
	Cyan	$2.34 \leq c \leq 2.985$	Upward	$(-10.67, 0, 0, 0)$
	Black	$2.985 \leq c \leq 2.34$	Downward	$(-10, 0, 0, 0)$
	Magenta	$2.398 \leq c \leq 2.985$	Upward	$(-4, 0, 0, 0)$
		$2.398 \leq c \leq 2.34$	Downward	$(-4, 0, 0, 0)$
Figure 9	Red	$2.442 \leq c \leq 2.488$	Upward	$(5, 0, 0, 0)$
	Black	$2.488 \leq c \leq 2.442$	Downward	$(5, 0, 0, 0)$
	Cyan	$2.442 \leq c \leq 2.488$	Upward	$(-10.67, 0, 0, 0)$
	Magenta	$2.442 \leq c \leq 2.488$	Upward	$(12, 0, 0, 0)$
Figure 13	Blue	$2.802 \leq m \leq 2.865$	Upward	$(-5.5, 0, 0, 0)$
		$2.738 \leq m \leq 2.802$	Downward	
	Red	$2.802 \leq m \leq 2.865$	Upward	$(12.8, 0, 0, 0)$
		$2.738 \leq m \leq 2.802$	Downward	
	Magenta	$2.802 \leq m \leq 2.865$	Upward	$(-10.1, 0, 0, 0)$
		$2.738 \leq m \leq 2.802$	Downward	

FIGURE 9: Enlargement of bifurcation diagram of Figure 8 plotted in the range  $2.442 \leq c \leq 2.488$  showing the region in which the system exhibits multiple coexisting attractors. The system parameters are the same as the one of Figure 8.

The initial conditions of the coexistence of ten attractors exhibited by the proposed hyperjerk system are presented in Figure 13. The bifurcation like sequence of Figure 13 shows the variation of  $x_3(0)$  in terms of the control parameter  $c$ , and the other initial conditions are set to zero ( $x_1(0) = x_2(0) = x_4(0) = 0$ ). Note that chaotic attractors are characterized by an unlimited number of points, while periodic attractors are characterized by a finite number of points. In the same line, the basin of attraction shows the different domains of convergence of similar attractors. The phase portrait of Figure 14 illustrates the coexistence of ten attractors. The initials conditions of the coexisting attractors are given in Table 4.

**3.3.2. Coexistence of Attractors with respect to Bifurcation Parameters  $m$  and  $b$ .** In order to investigate the sensitivity of the new hyperjerk system in terms of the bifurcation parameter  $m$ , the other parameters are fixed as follows:  $a = 1.8$ ,  $b = 3.8$ ,  $c = 2.442$ ,  $d = 1.35$ , and  $e = 14.85$ . We found that

the novel hyperjerk system can exhibit striking bifurcation sequences when varying the control parameter  $m$  in the range  $2 \leq m \leq 4.18$ . With reference to Figure 11, the bifurcation diagram in black and the one in blue are obtained by increasing and decreasing the values of the parameter  $m$ , while the one in red is obtained by fixing the initial conditions at  $(x_1(0), x_2(0), x_3(0), x_4(0)) = (-4, 0, 0, 0)$ . A window of hysteretic dynamics can be identified in the range  $2.6 \leq m \leq 2.9$ . The enlarged bifurcation diagram of Figure 12 clearly illustrates the domain of the coexistence of multiple attractors observed in the new hyperjerk system according to the bifurcation parameter  $m$ . Different methods used to plot these bifurcation diagrams are presented in Table 3. Up to six different periodic, chaotic, and point attractors can be obtained by only changing the initial conditions. For instance, sample phase portraits of the coexistence of six distinct attractors are presented in Figure 13.

During the mathematical analyses, it has been shown that the Hopf bifurcation was depending on the control parameter  $m$ . The bifurcation diagram of Figure 13(a) clearly illustrates this

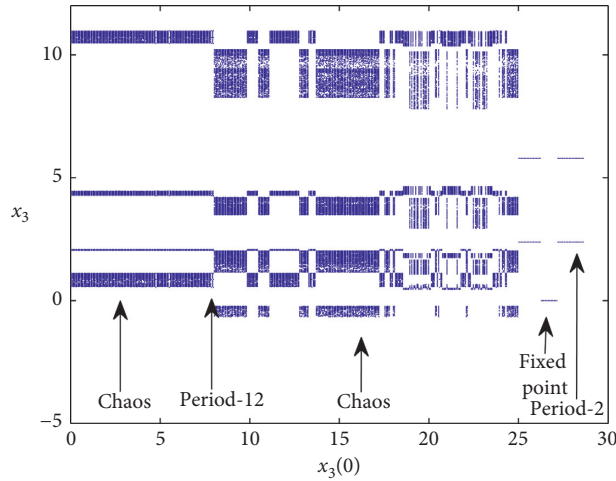


FIGURE 10: Bifurcation like sequence showing local maxima of the coordinate  $x_3$  versus the initial condition  $x_3(0)$ , plotted in the range  $0 \leq x_3(0) \leq 30$ , with  $a = 1.8, b = 3.8, c = 2.5442, d = 1.35$ , and  $e = 14.85$ . It can be observed the coexistence of ten periodic, chaotic, and point attractors.

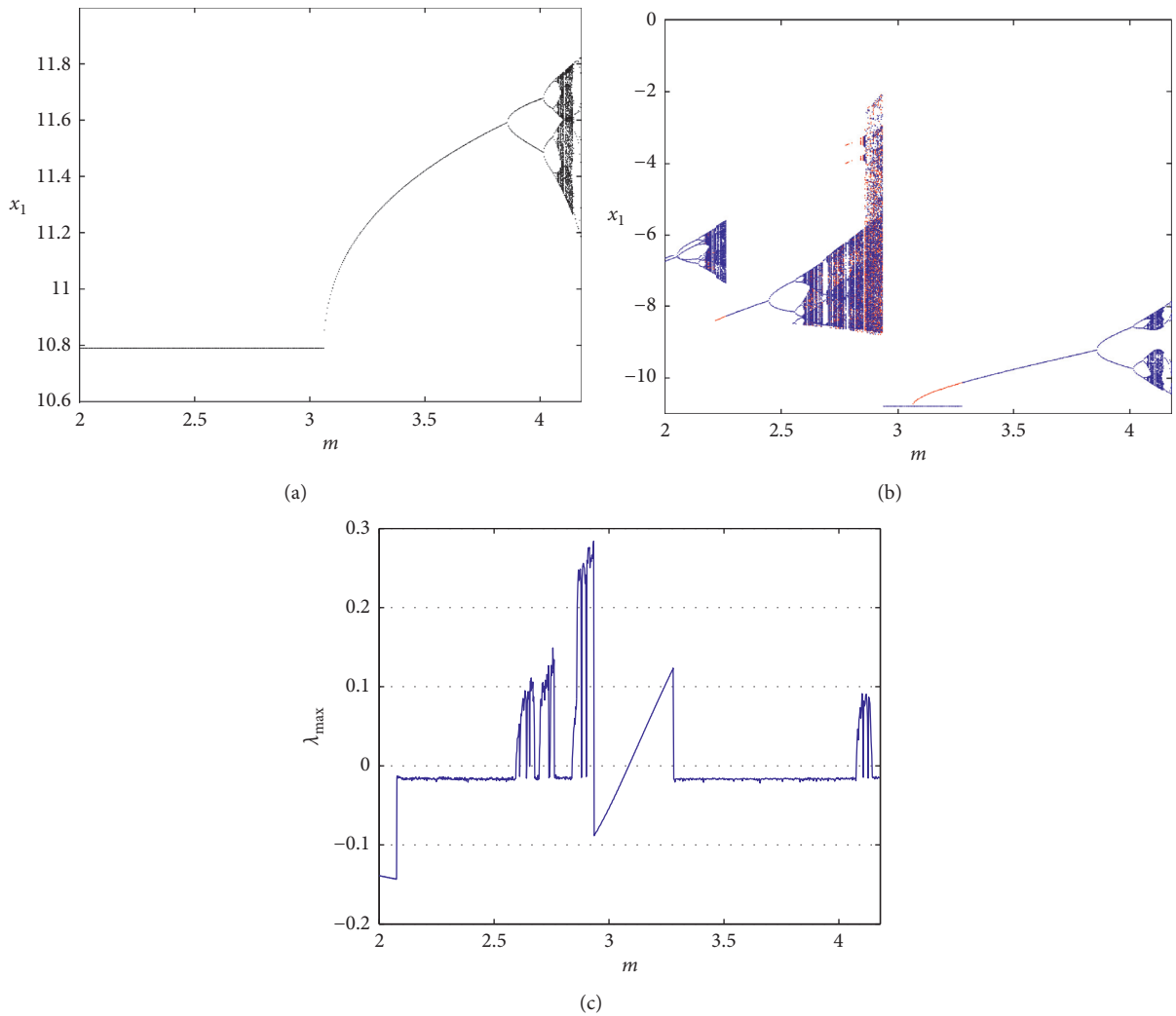


FIGURE 11: (a, b) Bifurcation diagrams showing local maxima of the coordinate  $x_1$  versus  $m$  and (c) the corresponding graph of largest Lyapunov exponent ( $\lambda_{\max}$ ) plotted in the range  $2 \leq m \leq 4.18$ , with  $a = 1.8, b = 3.8, c = 2.442$ , and  $d = 1.35$ .

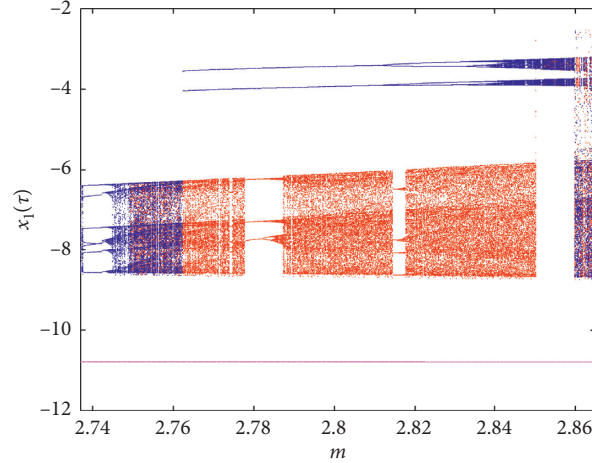


FIGURE 12: Enlargement of the bifurcation diagram of Figure 11(a) showing the region in which the system exhibits multiple coexisting attractors. This region corresponds to values of  $m$  in the range:  $2.735 \leq m \leq 2.865$ . Three sets of data are superimposed. For more information about the methods used to plot, see Table 3.

phenomenon characterized by the stable state followed by the unstable state. Moreover, this control parameter also highlights the coexistence of multiple attractors exhibited by the new 4-D system. By considering the following sets of the parameters:  $a = 1.8$ ,  $b = 3.5$ ,  $c = 2.442$ ,  $d = 1.35$ ,  $e = 15$ , and  $m = 3$ , we discover that the new 4-D system displays the coexistence of four distinct chaotic and point attractors. The phase portraits of the Figure 14 and their corresponding cross section of the basin of attraction clearly show the coexistence phenomenon and also give the initial condition domain of each attractor. The green and black domains represent the initial conditions regions of the pair of chaotic attractors, while the yellow domain represents the initial condition regions of the pair of point attractors.

**3.4. Offset Boosting Scenario.** Another property of system (3) is the possibility to develop an offset boosting effect. In our model,  $x_1$  appears only in the fourth line of equation (3), and thus this variable is a bootable variable [47–52]. Assuming the transformation  $x_1 \rightarrow x_1 + k$  where  $k$  is a constant, equation (5) can be rewritten accordingly as

$$\begin{cases} \dot{x}_1 = x_2, \\ \dot{x}_2 = mx_3, \\ \dot{x}_3 = dx_4, \\ \dot{x}_4 = c(x_1 + k) - bx_2 - ex_3 - ax_4 - \gamma \sinh(x_1 + k). \end{cases} \quad (14)$$

Figure 19 clearly presents offset boosting of the double-band chaotic attractor. The following values of parameter:  $k = 0$  (blue),  $k = 10$  (red) and  $k = -10$  (green) are used to plot them in  $x_1$ - $x_4$  and  $x_1$ - $x_3$  planes.

**3.5. Antimonotonicity.** By decreasing the value of the control parameter  $e$  ( $15 \leq e \leq 20$ ), we can observe the

formation and destruction of periodic orbits via reverse period-doubling bifurcation sequences. This interesting phenomenon has been reported in the literature. It is reported in various nonlinear systems such as Duffing oscillator [12], Chua circuit [53], and second-order nonlinear nonautonomous circuit [54, 55]. This phenomenon was reported for the first time in the hyperjerk system by Leutcho et al. [21]. The creation of periodic seas in the parameter space is the necessary requirement for a nonlinear system to experience forward and reverse period-doubling cascade [21]. Sample illustrations are represented in Figure 20, where some bifurcation diagrams are shown. These diagrams are obtained for each discrete value of the control parameter  $c$ . In Figure 20, note that for  $c = 2.5442$ , we have period-2 bubble and for a slight adjustment of the control parameter  $c$ , period-4 bubble is observed for  $c = 2.8442$ , whereas for  $c = 2.9$ , we have a period-8 bubble. In the same order, chaotic bubbles are formed for  $c = 2.97$ , and  $c = 2.99$ . The increase of control parameter  $c$  causes the creation of other bubbles, and it finally results in an infinite tree (like chaos).

## 4. Experimental Study

The objective of this section is to confirm the above theoretical results by realizing a laboratory experimental study. For this purpose to be achieved, several approaches have been proposed in the literature to implement chaotic circuit (by using many types of off-the-shelf electronic components [56] or field-programmable gate array (FPGA) technology [57–60] or field-programmable-analog-array (FPAA) technology [61, 62] just to name a few). Only off-the-shelf electronic components (i.e., resistors, capacitors, pair of semiconductor diodes ( $D_1 = D_2 = 1N4148$ ), and TL084 operational amplifiers types with a power supply of  $\pm 15$  VDC) are used to realize



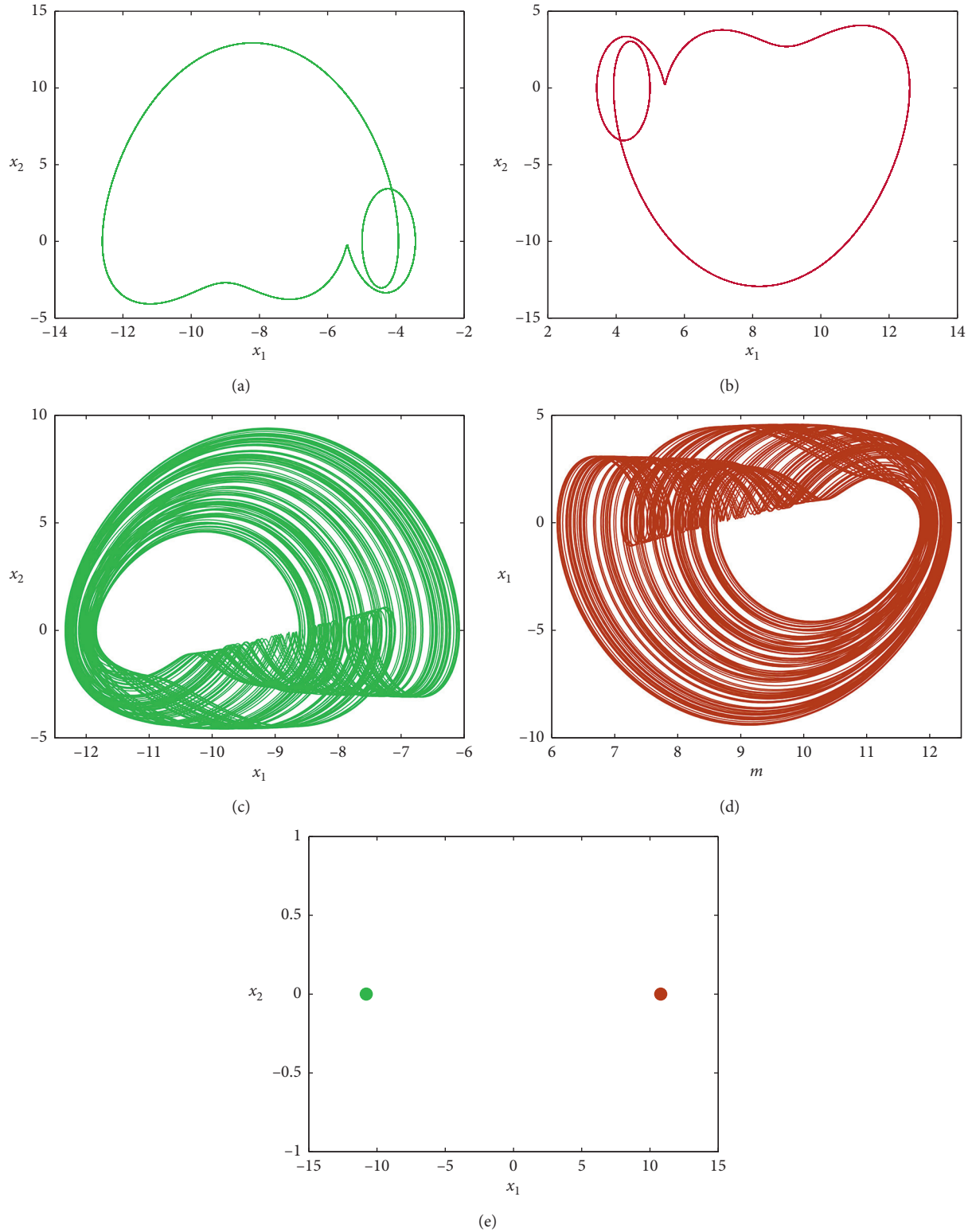


FIGURE 13: Coexistence of six different attractors (a pair of period-2 limit cycle, a pair of chaotic attractors, and a pair of fixed point attractor) for the following values of system parameters:  $a = 1.8$ ,  $b = 3.8$ ,  $c = 2.442$ ,  $d = 1.35$ ,  $e = 14.85$ , and  $m = 2.802$ . Initial conditions  $(x_1(0), x_2(0), x_3(0), x_4(0))$  are, respectively,  $(\pm 5.5, 0, 0, 0)$ ,  $(\pm 12.8, 0, 0, 0)$ , and  $(\pm 10.1, 0, 0, 0)$ .

the schematic diagram of Figure 1. The following values of electronic circuit components are used during the experimental process:  $R_c = R_m = R = 10\text{ k}\Omega$ ,  $R_b = 1.67\text{ k}\Omega$ ,

$R_e = 5\text{ k}\Omega$ , and  $R_d = 2.941\text{ k}\Omega$  (for the other parameters, see Table 1 case A). The complete sequence of phase portraits plotted in  $(x_1, x_4)$  plan is obtained by adjusting



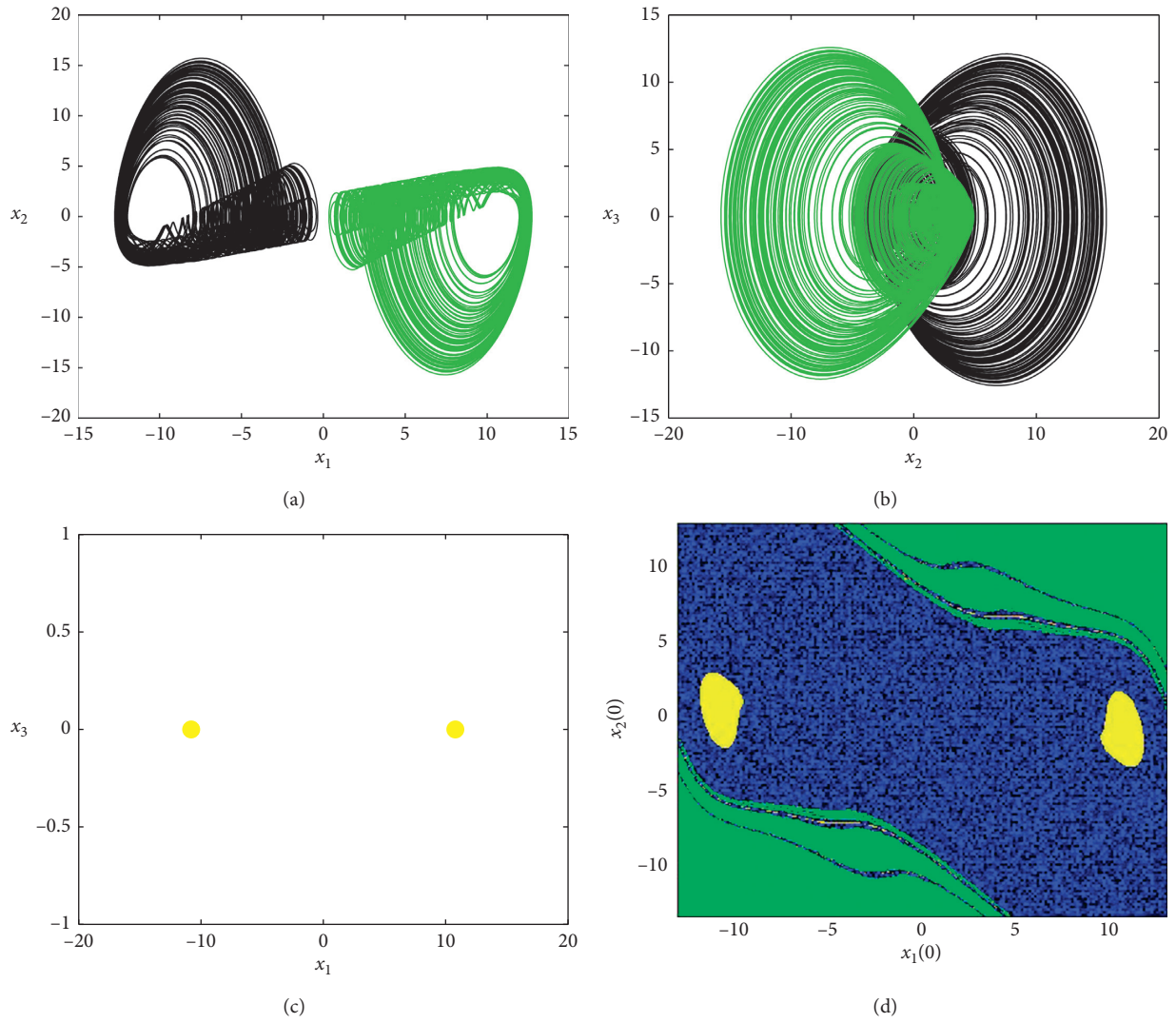


FIGURE 14: (a, b) Coexistence of four distinct attractors (a pair of chaotic attractors represented in  $x_1 - x_2$  and  $x_2 - x_3$  plans), (c) a pair of fixed point attractor) and their corresponding basin of attraction. Initial conditions  $(x_1(0), x_2(0), x_3(0), x_4(0))$  are, respectively,  $(\pm 7.15, 0, \pm 8.613, 0)$  and  $(\pm 12.8, 0, 0, 0)$ . The rest of the parameters are  $a = 1.8, b = 3.5, c = 2.442, d = 1.35, e = 15$ , and  $m = 3$ .

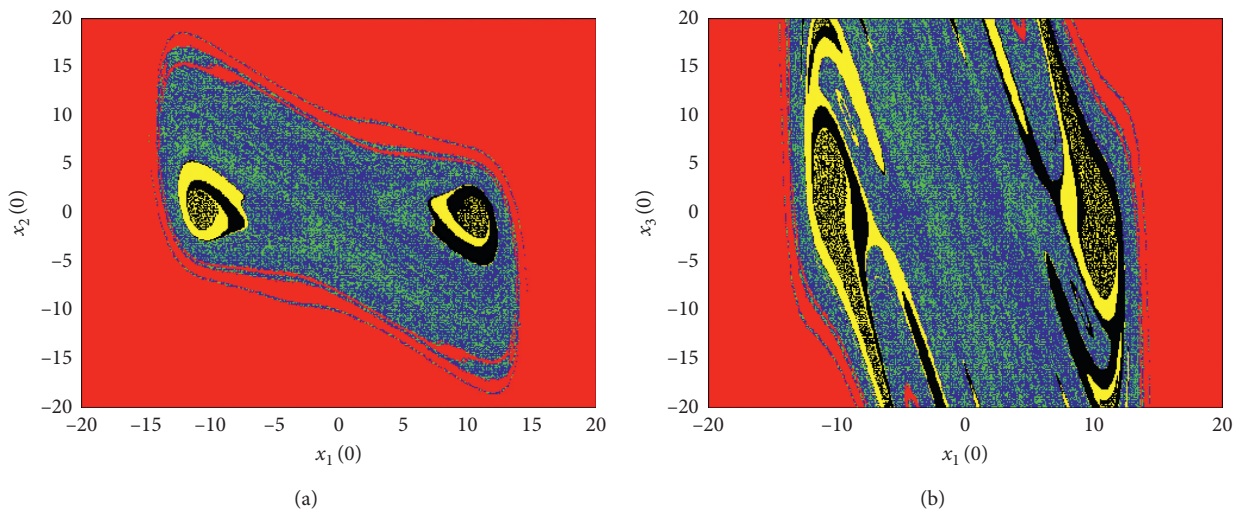


FIGURE 15: Continued.

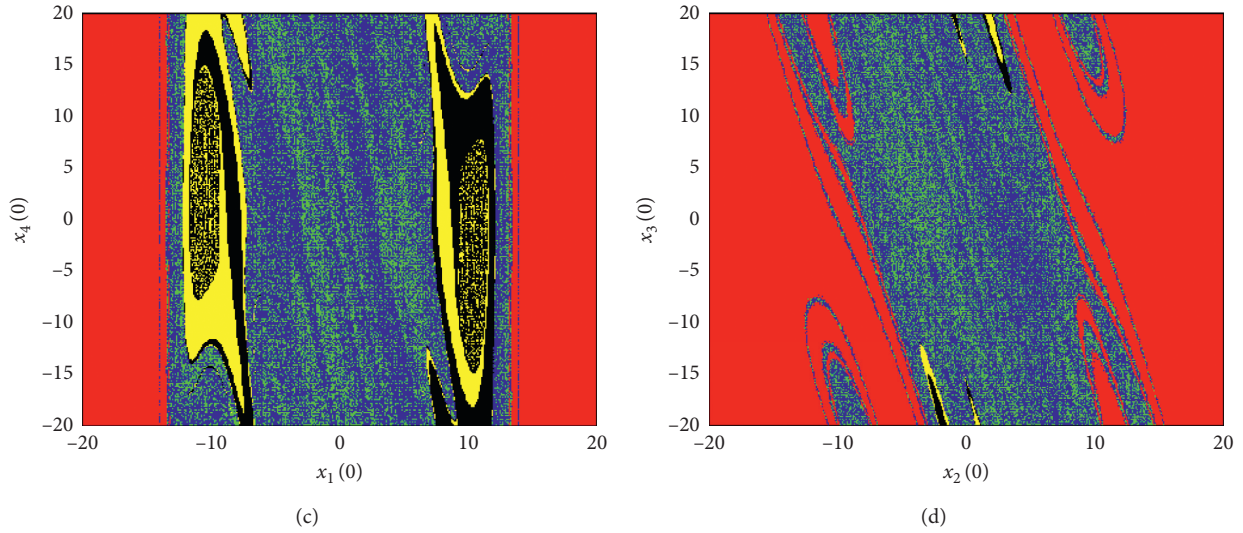


FIGURE 15: Cross sections of basin of attraction for  $x_3(0) = x_4(0) = 0$ ,  $x_2(0) = x_4(0) = 0$ ,  $x_2(0) = x_3(0) = 0$ , and  $x_1(0) = x_4(0) = 0$  corresponding to the asymmetric pair of chaotic (blue and green) and period-2 attractors (yellow and black) obtained for  $c = 2.44$ . Red regions correspond to unbounded motion.

TABLE 4: Details of the coexistences observed in the novel hyperjerk system.

<i>Fig.n<sup>o</sup></i>	Type of coexistences	Values of control parameter	Initial condition $(x_1(0), x_2(0), x_3(0), x_4(0))$
<b>Figure 16</b>	A symmetric pair of period-2 attractors, a symmetric pair of chaotic attractors, and a pair of fixed point.	$c = 2.44$	(a) $(0, 0, \pm 44.4, 0)$ (b) $(0, 0, \pm 48, 0)$ (c) $(0, 0, \pm 26.4, 0)$
<b>Figure 17</b>	A symmetric pair of period-2 attractors, a symmetric pair of chaotic attractors, a symmetric pair of period-9 attractors, and a pair of fixed point.	$c = 2.454$	(a) $(0, 0, \pm 25.2, 0)$ (b) $(0, 0, \pm 48, 0)$ (c) $(0, 0, \pm 10.8, 0)$ (d) $(0, 0, \pm 26.4, 0)$
<b>Figure 18</b>	A symmetric pair of period-2 attractors, a fixed point, a symmetric pair of period-12 attractors, 2 symmetric pairs of chaotic attractors, and a pair of fixed point.	$c = 2.5442$	(A <sup>n</sup> A <sub>1</sub> , A <sub>2</sub> <sup>n</sup> ) $(0, 0, \pm 45.6, 0)$ (b) $(0, 0, \pm 18, 0)$ (c) $(0, 0, \pm 49.2, 0)$ (d) $(0, 0, \pm 48, 0)$ (e) $(0, 0, \pm 26.4, 0)$

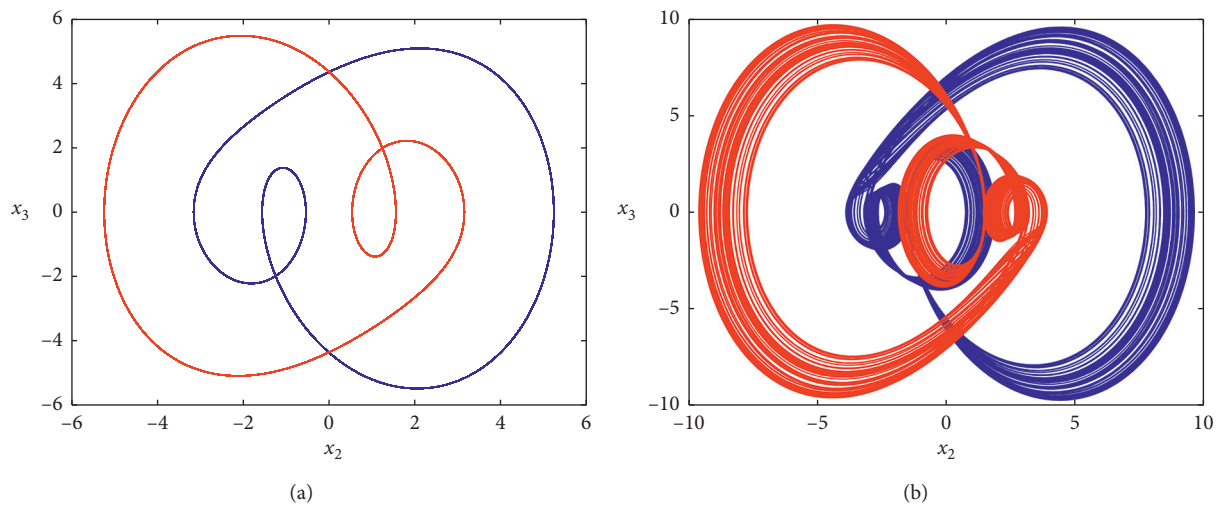
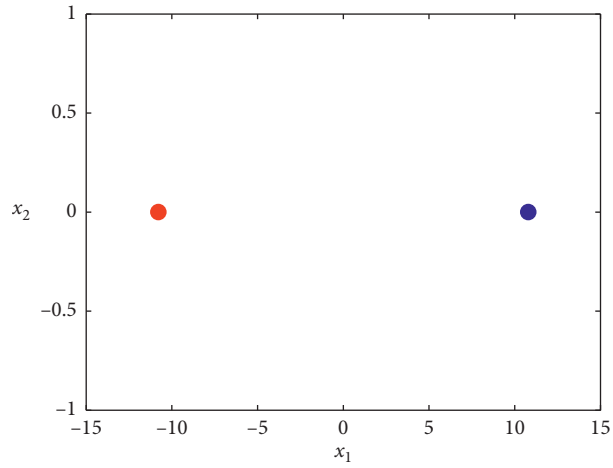
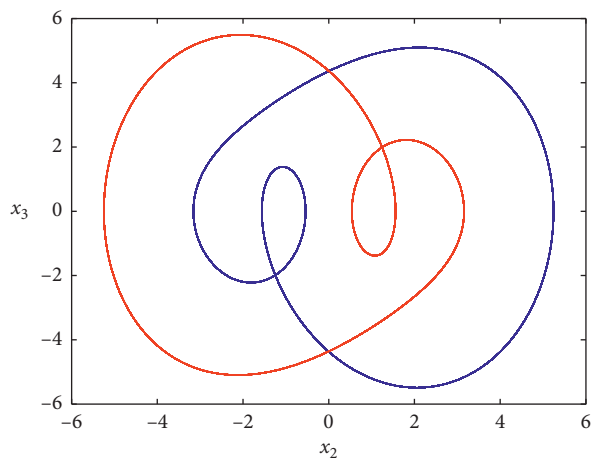


FIGURE 16: Continued.

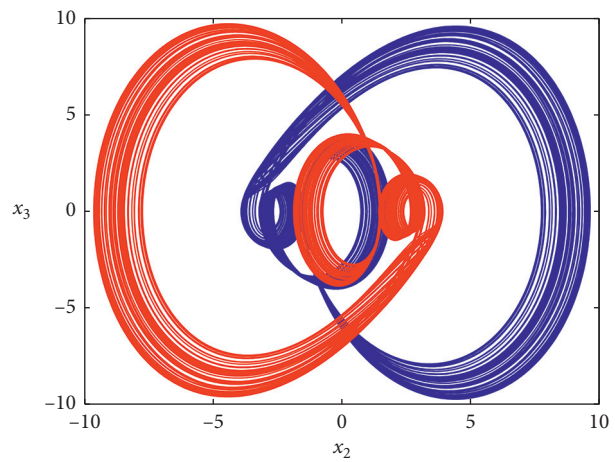


(c)

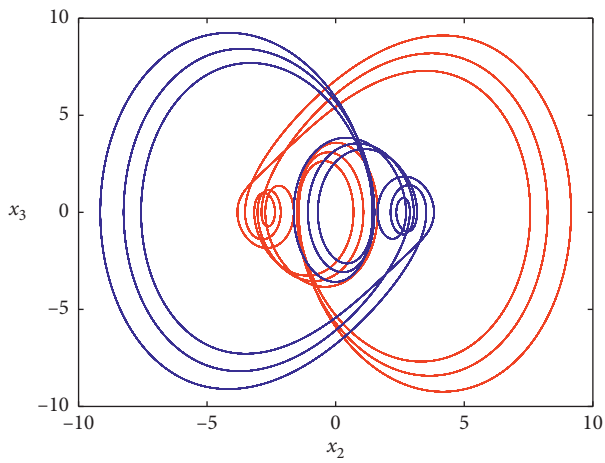
FIGURE 16: Coexistence of six different attractors (a pair of symmetric period-2 limit cycle, a pair of symmetric period-9 limit cycle, a pair of symmetric chaotic attractors, and a pair of point attractors). The values of others system parameters are fixed as follows:  $a = 1.8$ ,  $b = 3.8$ ,  $d = 1.35$ ,  $e = 14.85$ , and  $m = 2.2$ . Initial conditions are given in Table 4.



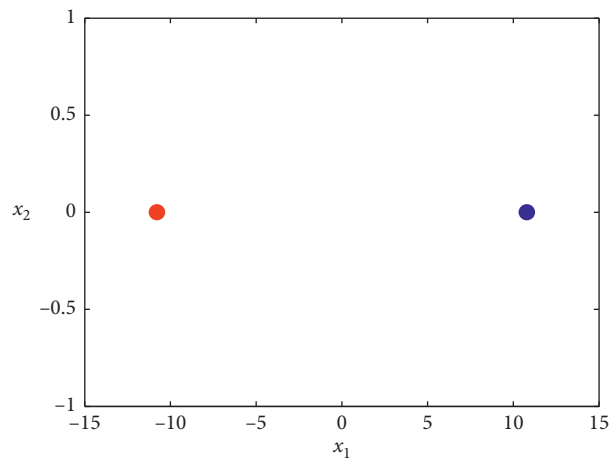
(a)



(b)



(c)



(d)

FIGURE 17: Coexistence of eight different attractors (a pair of symmetric period-2 limit cycle, a pair of symmetric chaotic attractors, and a pair of point attractors). The parameters are the same as those in Figure 16. Initial conditions are given in Table 4.

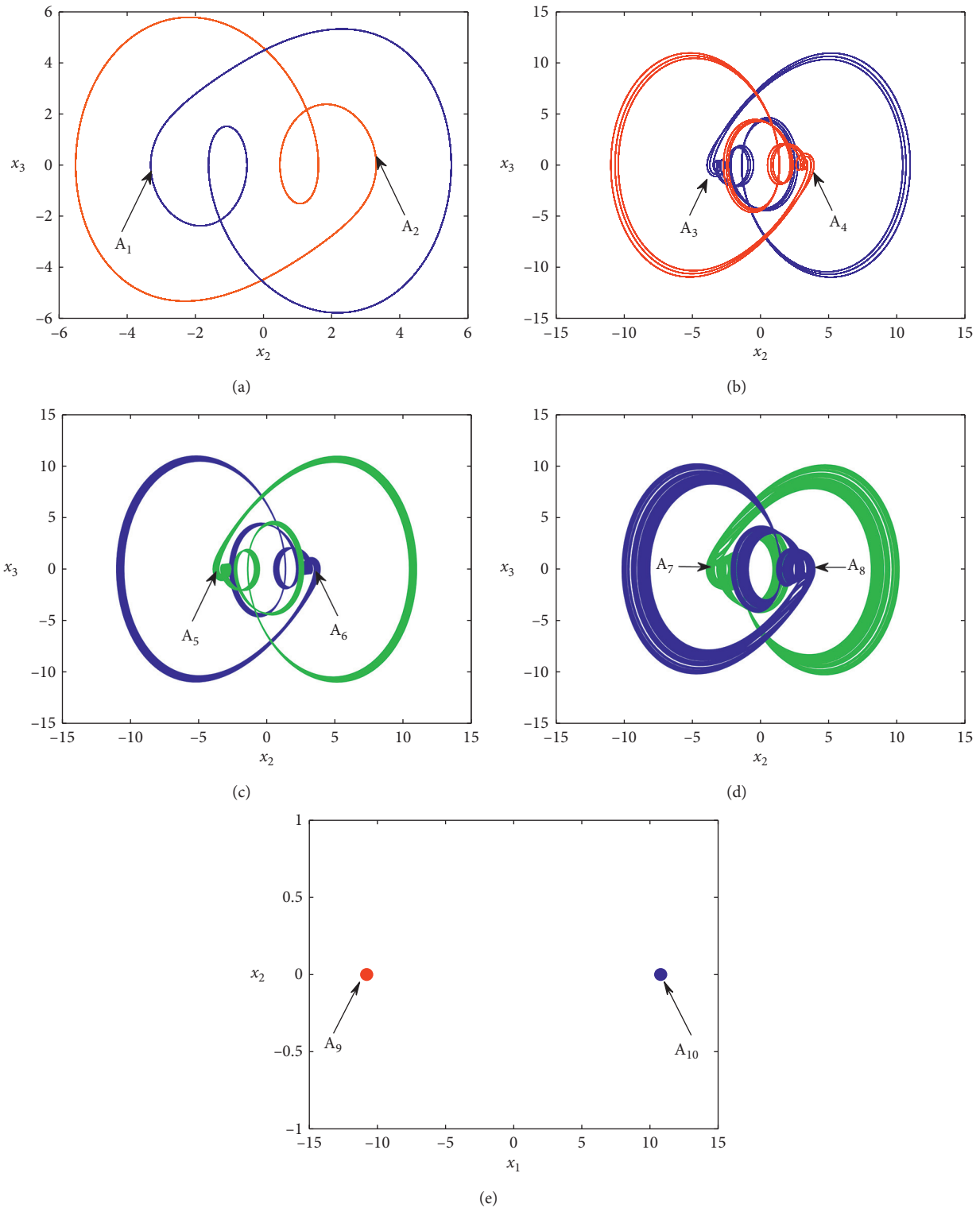


FIGURE 18: Coexistence of ten different attractors (a pair of symmetric period-2 limit cycle, 2 pair of symmetric chaotic attractors, a pair of symmetric period-9 limit cycle, and a pair of point attractors). The parameters are the same as those in Figure 16. Initial conditions are given in Table 4.

the control resistor  $R_a$  in the range  $333, 33 \Omega \leq R_a \leq 1.66 \text{ k}\Omega$ . It can be seen in Figure 21 a good coherence between the numerical results (left side) and the experimental ones (right side). By changing the values

of electronic components:  $R_e = 600 \Omega$ ,  $R_a = 2.116 \text{ k}\Omega$ ,  $R_b = 4.21 \text{ k}\Omega$ ,  $R_m = 784 \Omega$ ,  $R_d = 3.234 \text{ k}\Omega$ , and  $R_c = 5.16 \text{ k}\Omega$  (for the other parameters, see Table 1 case B), the coexistence of attractors emerges. Figure 22 clearly illustrates the

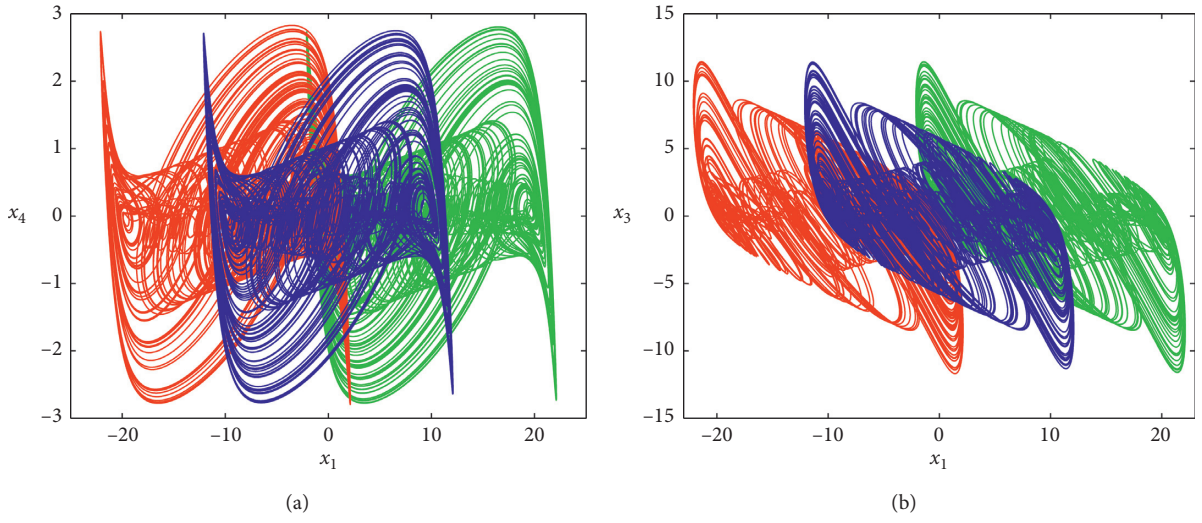


FIGURE 19: Offset boosting of the double-band chaotic attractor with the following values of parameter:  $k = 0$ (blue),  $k = 10$ (red), and  $k = -10$ (green). The other parameters are the same as those in Figure 4.

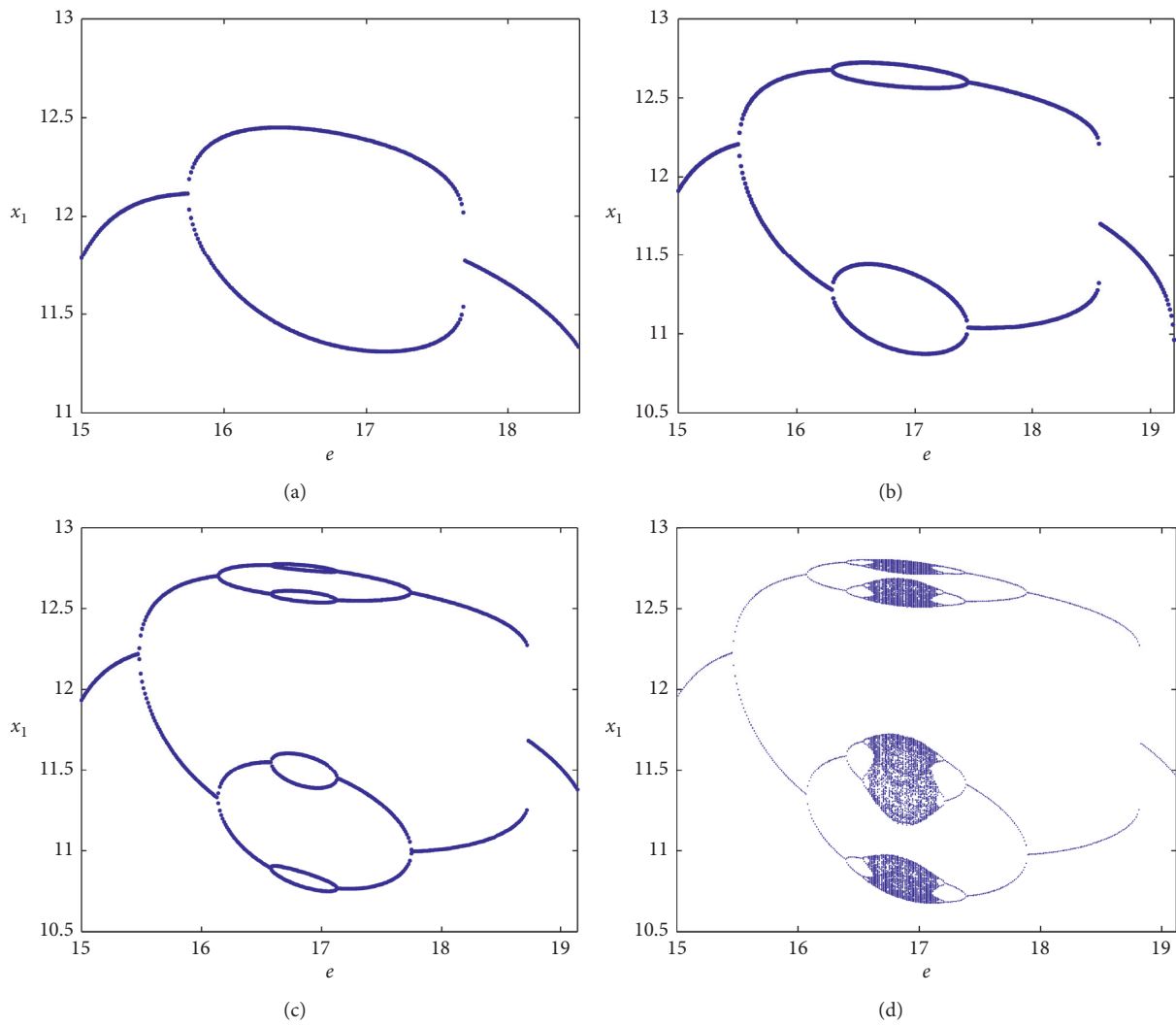


FIGURE 20: Continued.



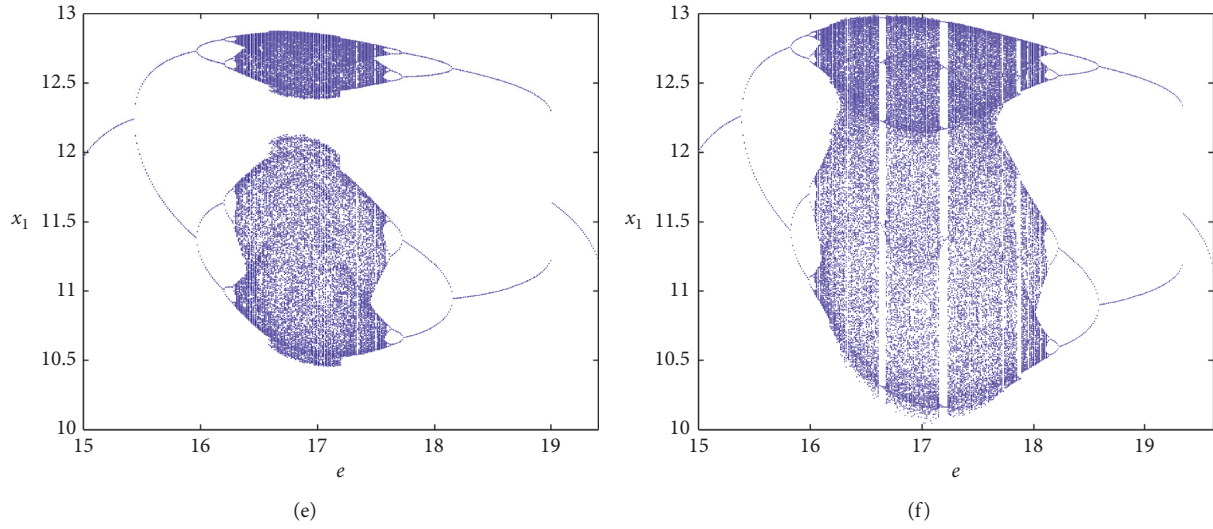


FIGURE 20: Bifurcation diagrams showing local maxima of the coordinate  $x_1$  of the attractor in Poincaré cross section in terms of the control parameter  $a$  (bubbling): (a) period-2 bubble for  $c = 2.5442$ , (b) period-4 bubble for  $c = 2.8442$ , (c) period-8 bubble for  $c = 2.9$ , (d) single-band chaos bubble for  $c = 2.93$ , (e) single-band chaos bubble for  $c = 2.99$ , and (f) double-band chaos bubble for  $c = 3.0$ .

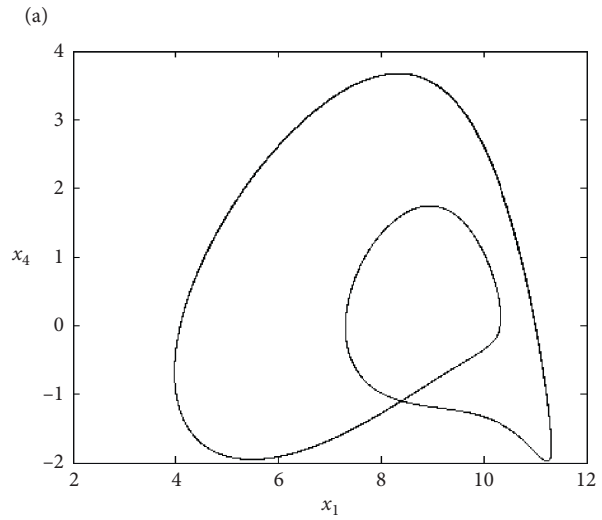
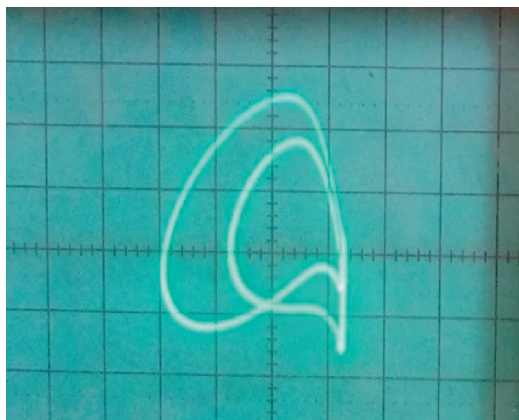
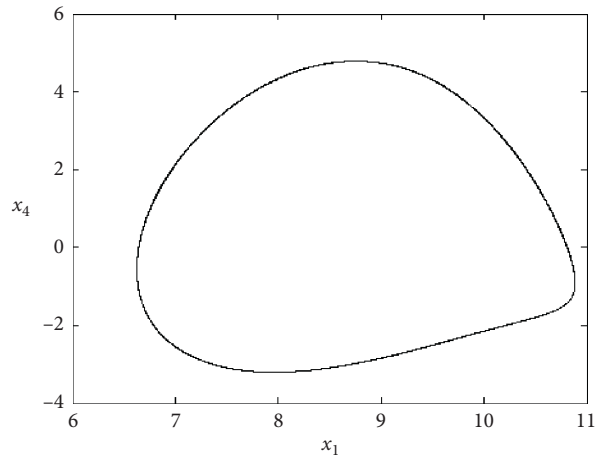
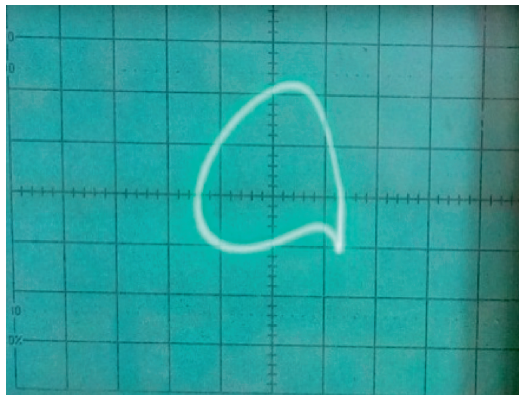


FIGURE 21: Continued.



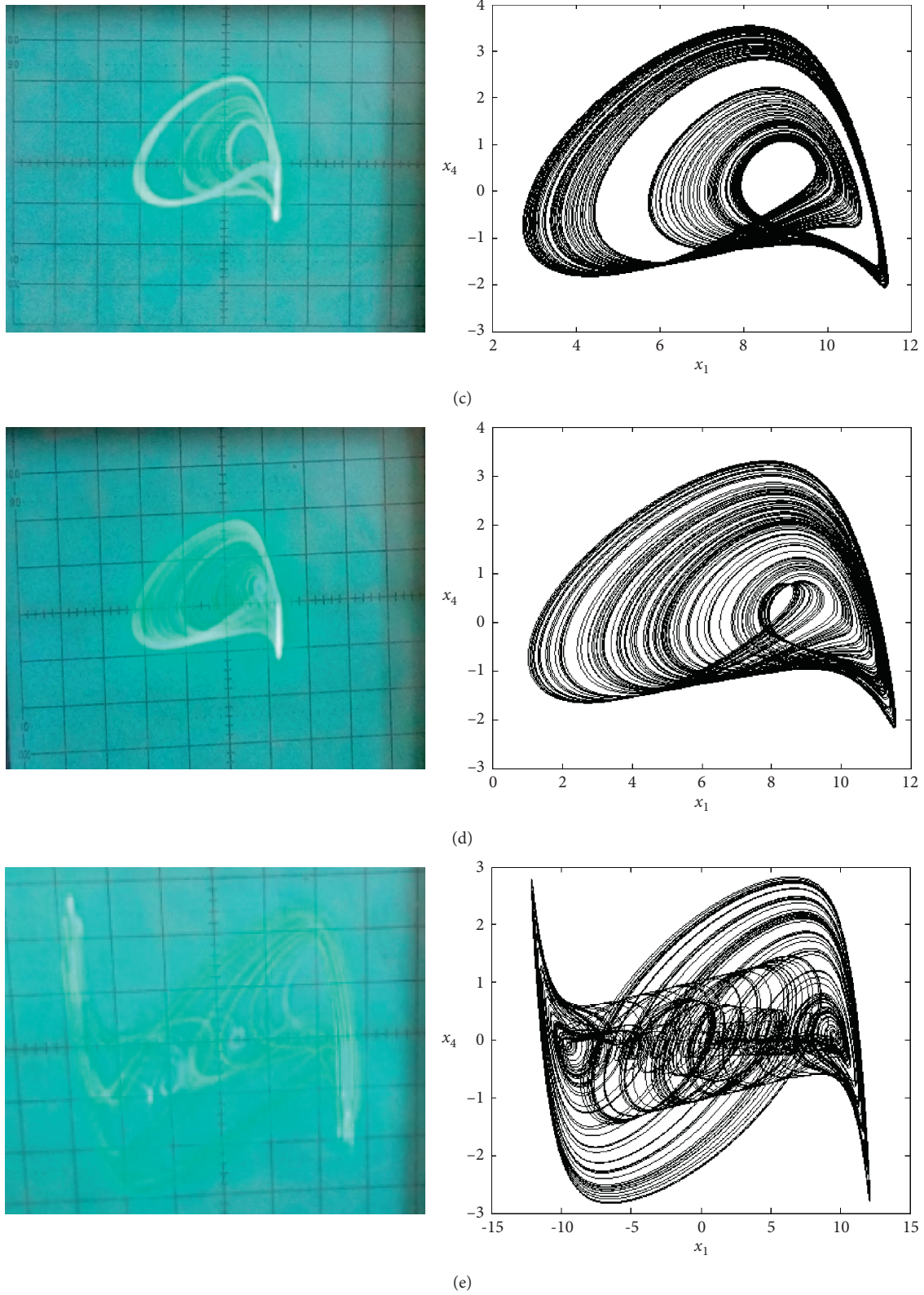


FIGURE 21: Experimental phase portraits (right column) and corresponding numerical ones (left column) obtained by a direct integration of the system (1) confirming the scenario to chaos in the system for varying  $Ra$  (i.e., parameter  $a$ ): (a) period-1 for  $Ra = 1.428$ , (b) period-2 for  $Ra = 807$ , (c) single-band chaos for  $Ra = 684$ , (d) single-band chaos for  $Ra = 500$ , and (e) double-band chaos for  $Ra = 333, 33$ . The scales are  $X = 0.2 V/div$  and  $Y = 0.5 V/div$ .

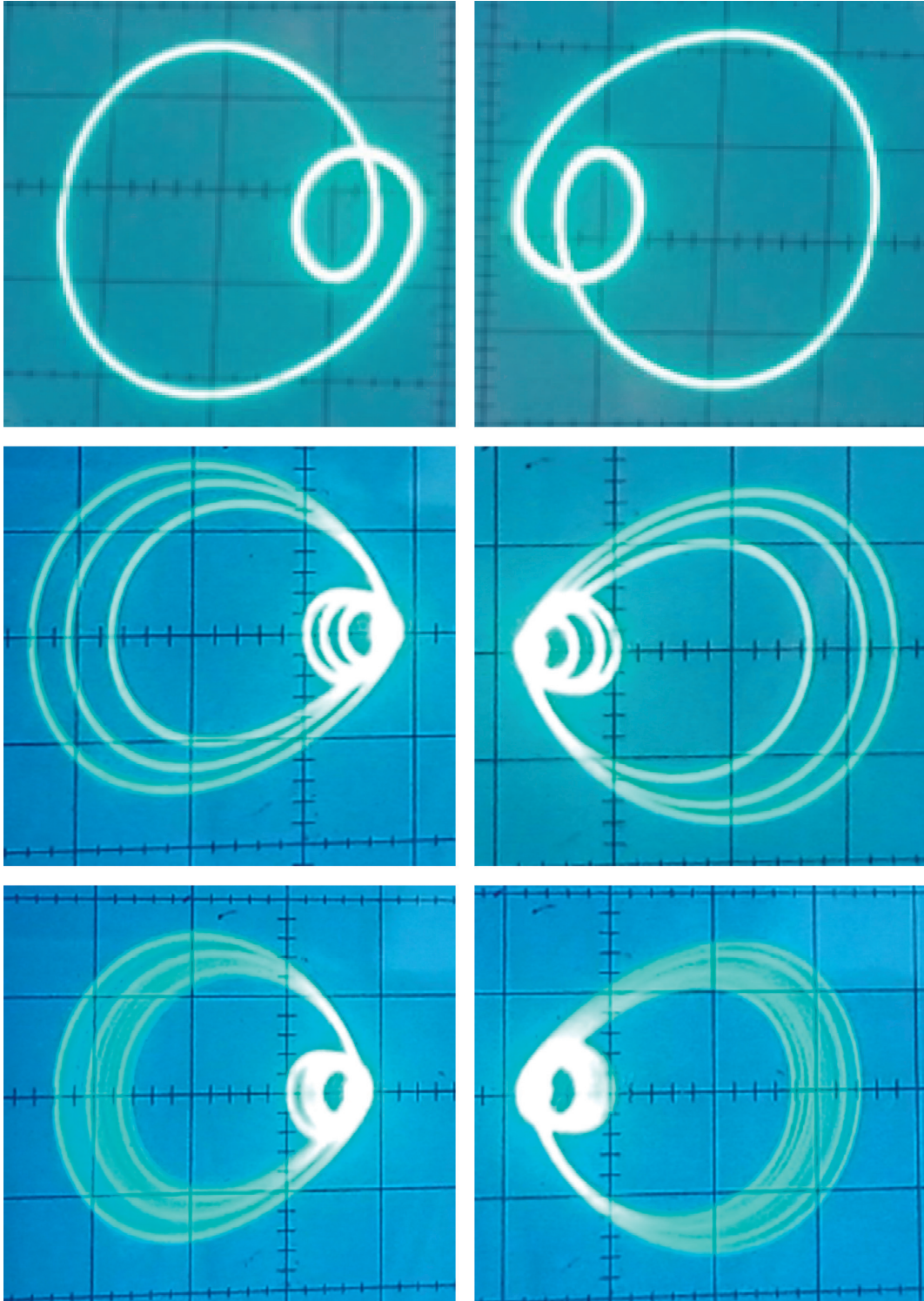


FIGURE 22: Coexistence of multiples attractors for  $R_c = 5.16 k\Omega$ . Both periodic and chaotic attractors appear randomly in the experiment when switching on and off the power supply. The scales are  $X = 5V/div$  and  $Y = 2V/div$  for all pictures.

coexistence of fixed points, period-2 attractor, and chaotic attractor. Those attractors appear randomly by switching on and off the power supply. We can conclude that the mathematical model proposed in this work perfectly describes the real behavior of the novel hyperjerk circuit.

## 5. Conclusion

This work has proposed and investigated a new chaotic hyperjerk circuit with three equilibrium points having hyperbolic sine nonlinearity. The chaotic behavior observed in the system is due to the nonlinear component formed by two



antiparallel diodes. Classical nonlinear analysis tools have been used to study the complete dynamics of the system. The bifurcation analysis of the new circuit shows that the chaotic double-band attractor arises from the period-doubling scenario followed by the symmetry recovering crisis event. In addition, some properties of the system such as antimonotonicity and offset boosting have been revealed. In particular, various regions in the parameter space in which the system develops the coexistence of up to ten disconnected attractors consisting of stable fixed points, limit cycles, and strange attractors have been reported. The coexistence of periodic, chaotic, and stable fixed points discovered in this work has not yet been reported in a hyperjerk system (at least as simple as the case discussed) and thus merits dissemination. To validate the theoretical study presented in this work, the new chaotic hyperjerk circuit has been realized and used for the investigations. Experimental results agree well with those obtained during the numerical experiment, thus confirming the feasibility of the proposed model. Owing to its extreme simplicity coupled with extremely rich dynamics, the new hyperjerk circuit introduced in this work has potential utility for information encryption as well as for other chaos-based applications [62].

## Data Availability

No data were used in this study.

## Conflicts of Interest

The authors declare that they have no conflicts of interest.

## References

- [1] E. N. Lorenz, "Deterministic nonperiodic flow," *Journal of the Atmospheric Sciences*, vol. 20, no. 2, pp. 130–141, 1963.
- [2] O. E. Rössler, "An equation for continuous chaos," *Physics Letters A*, vol. 57, no. 5, pp. 397–398, 1976.
- [3] G. R. Chen, *Controlling Chaos and Bifurcations in Engineering Systems*, CRC Press, Boca Raton, FL, USA, 1999.
- [4] S. Jafari and J. C. Sprott, "Simple chaotic flows with a line equilibrium," *Chaos, Solitons & Fractals*, vol. 57, pp. 79–84, 2013.
- [5] V.-T. Pham, C. Volos, S. Jafari, Z. Wei, and X. Wang, "Constructing a novel no-equilibrium chaotic system," *International Journal of Bifurcation and Chaos*, vol. 24, no. 5, p. 1450073, 2014.
- [6] J. Lü and G. Chen, "A new chaotic attractor coined," *International Journal of Bifurcation and Chaos*, vol. 12, no. 03, pp. 659–661, 2002.
- [7] F. Y. Dalkiran and J. C. Sprott, "Simple chaotic hyperjerk system," *International Journal of Bifurcation and Chaos*, vol. 26, no. 11, p. 1650189, 2016.
- [8] S. J. Linz, "Nonlinear dynamical models and jerky motion," *American Journal of Physics*, vol. 65, no. 6, pp. 523–526, 1997.
- [9] J. Kengne, Z. T. Njitacke, A. N. Negou, M. Fouodji Tsostop, and H. B. Fotsin, "Coexistence of multiple attractors and crisis route to chaos in a novel chaotic jerk circuit," *International Journal of Bifurcation and Chaos*, vol. 26, no. 5, p. 1650081, 2016.
- [10] J. Kengne, A. N. Negou, and D. Tchiotso, "Antimonotonicity, chaos and multiple attractors in a novel autonomous memristor-based jerk circuit," *Nonlinear Dynamics*, vol. 88, no. 4, pp. 2589–2608, 2017.
- [11] J. Kengne, V. R. F. Signing, J. C. Che djou, and G. D. Leutcho, "Nonlinear behavior of a novel chaotic jerk circuit: antimonotonicity, crisis and multiple coexisting attractors," *International Journal of Dynamics and Control*, vol. 6, pp. 1–18, 2017.
- [12] Z. T. Njitacke, J. Kengne, and L. K. Kengne, "Antimonotonicity, chaos and multiple coexisting attractors in a simple hybrid diode-based jerk circuit," *Chaos, Solitons & Fractals*, vol. 105, pp. 77–91, 2017.
- [13] P. Daltzis, S. Vaidyanathan, V. T. Pham, C. Volos, E. Nistazakis, and G. Tombras, "Hyperchaotic attractor in a novel hyperjerk system with two nonlinearities," *Circuits, Systems, and Signal Processing*, vol. 37, no. 2, pp. 613–635, 2018.
- [14] J. C. Sprott, *Elegant Chaos: Algebraically Simple Chaotic Flows*, World Scientific Publishing, Singapore, 2010.
- [15] A. P. Kuznetsov, S. P. Kuznetsov, and N. V. Stankevich, "A simple autonomous quasiperiodic self-oscillator," *Communications in Nonlinear Science and Numerical Simulation*, vol. 15, no. 6, pp. 1676–1681, 2010.
- [16] N. V. Kuznetsov, G. A. Leonov, and V. I. Vagaitsev, "Analytical-numerical method for attractor localization of generalized Chua's system\*," *IFAC Proceedings Volumes*, vol. 43, no. 11, pp. 29–33, 2010.
- [17] N. V. Kuznetsov, O. A. Kuznetsova, G. A. Leonov, and V. I. Vagaitsev, "Hidden attractor in chua's circuits," in *Proceedings of the 8th International Conference Informatics in Control, Automation and Robotics*, pp. 279–283, ICINCO, Noordwijkerhout, The Netherlands, 2011.
- [18] N. V. Kuznetsov, G. A. Leonov, and S. M. Seledzhi, "Hidden oscillations in nonlinear control systems," *IFAC Proceedings Volumes*, vol. 44, no. 1, pp. 2506–2510, 2011.
- [19] G. A. Leonov, N. V. Kuznetsov, and V. I. Vagaitsev, "Hidden attractor in smooth Chua systems," *Physica D: Nonlinear Phenomena*, vol. 241, no. 18, pp. 1482–1486, 2012.
- [20] G. A. Leonov and N. V. Kuznetsov, "Hidden attractors in dynamical systems. From hidden oscillations in hilbert-Kolmogorov, aizerman, and kalman problems to hidden chaotic attractor in chua circuits," *International Journal of Bifurcation and Chaos*, vol. 23, no. 1, pp. 1330002–1330011, 2013.
- [21] G. D. Leutcho, J. Kengne, and L. K. Kengne, "Dynamical analysis of a novel autonomous 4-D hyperjerk circuit with hyperbolic sine nonlinearity: chaos, antimonotonicity and a plethora of coexisting attractors," *Chaos, Solitons & Fractals*, vol. 107, pp. 67–87, 2018.
- [22] K. E. Chlouverakis and J. C. Sprott, "Chaotic hyperjerk systems," *Chaos, Solitons & Fractals*, vol. 28, no. 3, pp. 739–746, 2006.
- [23] V. Sundarapandian, C. Volos, V. T. Pham, and K. Madhavan, "Analysis, adaptive control and synchronization of a novel 4-D hyperchaotic hyperjerk system and its SPICE implementation," *Archives of Control Sciences*, vol. 25, no. 1, pp. 135–158, 2015.
- [24] C. Li, "Coexisting hidden attractors in a 4-D simplified Lorenz System," *International Journal of Bifurcation and Chaos in Applied Sciences and Engineering*, vol. 24, p. 1450034, 2013.
- [25] B. Bao, X. Zou, Z. Liu, and F. Hu, "Generalized memory element and chaotic memory system," *International Journal of Bifurcation and Chaos*, vol. 23, no. 8, p. 1350135, 2013.
- [26] S. Ren, S. Panahi, K. Rajagopal, K. Akgul, V. T. Pham, and S. Jafari, "A new chaotic flow with hidden attractor: the first hyperjerk system with no-equilibrium," *Zeitschrift für Naturforschung A*, vol. 73, 2018.

- [27] S. Vaidyanathan, S. Jafari, V. T. Pham, A. T. Azar, and F. Alsaadi, "A 4-D chaotic hyperjerk system with a hidden attractor, adaptive backstepping control and circuit design" *Archive of Control Sciences*, vol. 28, no. 2, pp. 239–254, 2018.
- [28] J. Kengne, S. Jafari, and Z. T. Njitacke, "Dynamic analysis and electronic circuit implementation of a novel 3D autonomous system without linear terms," *Communications in Nonlinear Science and Numerical Simulation*, vol. S1007-5704, no. 17, pp. 30126–30130, 2017.
- [29] J. C. Sprott, "A proposed standard for the publication of new chaotic systems," *International Journal of Bifurcation and Chaos*, vol. 21, no. 9, pp. 2391–2394, 2011.
- [30] A. Buscarino, L. Fortuna, M. Frasca, and L. V. Gambuzza, "A chaotic circuit based on Hewlett-Packard memristor," *Chaos*, vol. 22, no. 2, Article ID 023136, 2012.
- [31] M. P. Haniyas, G. Giannaris, A. Spyridakis, and A. Rigas, "Time series analysis in chaotic diode resonator circuit," *Chaos, Solitons & Fractals*, vol. 27, no. 2, pp. 569–573, 2006.
- [32] D. W. Sukow, M. E. Bleich, J. Gauthier, and J. E. S. Socolar, "Controlling chaos in a fast diode resonator using extended time-delay auto-synchronization: experimental observations and theoretical analysis," *Chaos*, vol. 7, no. 4, pp. 560–576, 1997.
- [33] S. H. Strogatz, *Nonlinear Dynamics and Chaos*, Addison-Wesley, Boston, MA, USA, 1994.
- [34] N. ah and B. Balachandran, *Applied Nonlinear Dynamics: Analytical, Computational and Experimental Methods*, John Wiley & Sons, Hoboken, NJ, USA, 1995.
- [35] A. Wolf, J. B. Swift, H. L. Swinney, and J. A. Vastano, "Determining Lyapunov exponents from a time series," *Physica D: Nonlinear Phenomena*, vol. 16, no. 3, pp. 285–317, 1985.
- [36] L. Chunbiao and J. C. Sprott, "An infinite 3-D periodic lattice of chaotic attractors," *Physics Letters A*, vol. 382, no. 8, pp. 581–587, 2017.
- [37] L. Chunbiao, J. C. Sprott, T. Kapitaniak, and T. Lu, "Infinite lattice of hyperchaotic strange attractors," *Chaos, Solitons and Fractals*, vol. 109, pp. 76–82, 2018.
- [38] F. T. Fozin, J. Kengne, and F. B. Pelab, "Dynamical analysis and multistability in autonomous hyperchaotic oscillator with experimental verification," *Nonlinear Dynamics*, vol. 93, no. 2, pp. 653–669, 2018.
- [39] N. Z. Tabekoueng, D. I. Sami, J. Kengne, and Cheukem, "Coexistence of firing patterns and its control in two neurons coupled through an asymmetric electrical synapse," *Chaos*, vol. 30, Article ID 023101, 2020.
- [40] K. L. Kamdjeu, J. Kengne, P. R. J. Mboupda, and T. T. H. Kamdem, "Dynamics, control and symmetry breaking aspects of an infinite equilibrium chaotic system," *International Journal of Dynamics and Control*, 2020.
- [41] H. Chang, Y. Li, and F. Yuan, "Extreme multistability with hidden attractors in a simple memristor-based circuit," *International Journal of Bifurcation and Chaos in Applied Sciences and Engineering*, vol. 29, no. 6, 2019.
- [42] Q. Lai, C. Chen, X. W. Zhao, J. Kengne, and C. Volos, "Constructing chaotic system with multiple coexisting attractors," *IEEE Access*, vol. 7, 2019.
- [43] Q. Lai, K. D. P. Kuate, F. Liu, and H. C. H. Iu, "An extremely simple chaotic system with infinitely many coexisting attractors," *IEEE Transactions on Circuits and Systems II: Express Briefs*, vol. 1, 2019.
- [44] K. Rajagopal, P. J. Singh, K. B. Roy, and A. Karthikeyan, "Dissipative and conservative chaotic nature of a new quasi-periodically forced oscillator with megastability," *Chinese Journal of Physics*, vol. 58, 2019.
- [45] Y. Li and J. Zeng, "A unique jerk system with abundant dynamics: symmetric or asymmetric bistability, tristability, and coexisting bubbles," *Brazilian Journal of Physics*, vol. 50, 2020.
- [46] M. Tuna, A. Karthikeyan, K. Rajagopal, M. Alçın, and I. Koyuncu, "Hyperjerk multiscroll oscillators with megastability: analysis, FPGA implementation and A novel ANN-ring-based true random number generator," *International Journal of Electronics and Communications*, vol. 112, 2019.
- [47] C. Li, X. Wang, and G. Chen, "Diagnosing multistability by offset boosting," *Nonlinear Dynamics*, vol. 90, 2017.
- [48] C. Li, J. C. Sprott, A. Akgul, H. H. C. Lu, and Y. Zhao, "A new chaotic oscillator with free control," *Chaos*, vol. 27, Article ID 083101, 2017.
- [49] C. Li, J. C. Sprott, and Y. Mei, "An infinite 2-D lattice of strange attractors," *Nonlinear Dynamics*, vol. 89, 2017.
- [50] C. Li, J. C. Sprott, W. Hu, and Y. Xu, "Infinite multistability in a self-reproducing chaotic system," *International Journal of Bifurcation and Chaos*, vol. 27, no. 10, Article ID 1750160, 2017.
- [51] C. Li, J. C. Sprott, T. Kapitaniak, and T. Lu, "Infinite lattice of hyperchaotic strange attractors," *Chaos, Solitons & Fractals*, vol. 109, pp. 76–82, 2018.
- [52] C. Li and J. C. Sprott, "An infinite 3-D quasiperiodic lattice of chaotic attractors," *Physics Letters A*, vol. 382, no. 8, pp. 581–587, 2018.
- [53] S. P. Dawson, C. Grebogi, J. A. Yorke, I. Kan, and H. Koçak, "Antimonotonicity: inevitable reversals of period-doubling cascades," *Physics Letters A*, vol. 162, no. 3, pp. 249–254, 1992.
- [54] L. Kocarev, K. S. Halle, K. Eckert, and L. O. Chua, "Experimental observation of antimonotonicity in Chua's circuit," *International Journal of Bifurcation and Chaos*, vol. 3, no. 4, pp. 1051–1055, 1993.
- [55] I. Manimehan and P. Philominathan, "Composite dynamical behaviors in a simple series-parallel LC circuit," *Chaos, Solitons & Fractals*, vol. 45, no. 12, pp. 1501–1509, 2012.
- [56] I. M. Kyprianidis, I. N. Stouboulos, P. Haralabidis, and T. Bountis, "Antimonotonicity and chaotic dynamics in a fourth-order autonomous nonlinear electric circuit," *International Journal of Bifurcation and Chaos*, vol. 10, no. 08, pp. 1903–1915, 2000.
- [57] S. P. Dawson, C. Grebogi, and H. Koçak, "Mechanism for antimonotonicity in scalar maps with two critical points," *Physical Review E*, vol. 48, no. 3, pp. 1676–1682, 1993.
- [58] V.-T. Pham, A. Akgul, C. Volos, S. Jafari, and T. Kapitaniak, "Dynamics and circuit realization of a no-equilibrium chaotic system with a boostable variable," *AEU-International Journal of Electronics and Communications*, vol. 78, pp. 134–140, 2017.
- [59] E. Tlelo-Cuautle, A. D. Pano-Azucena, J. J. Rangel-Magdaleno, V. H. Carbajal-Gomez, and G. Rodriguez-Gomez, "Generating a 50-scroll chaotic attractor at 66 MHz by using FPGAs," *Nonlinear Dynamics*, vol. 85, no. 4, pp. 2143–2157, 2016.
- [60] B. Muthuswamy and S. Banerjee, *A Route to Chaos Using FPGAs*, Complexity and Computation Springer International Publishing, Berlin, Germany, 2015.
- [61] E. Tlelo-Cuautle, J. J. Rangel-Magdaleno, A. D. Pano-Azucena, P. J. Obeso-Rodelo, and J. C. Nunez-Perez, "FPGA realization of multi-scroll chaotic oscillators," *Communications in Nonlinear Science and Numerical Simulation*, vol. 27, no. 1-3, pp. 66–80, 2015.
- [62] I. Koyuncu, A. T. Ozcerit, and I. Pehlivan, "Implementation of FPGA-based real time novel chaotic oscillator," *Nonlinear Dynamics*, vol. 77, no. 1-2, pp. 49–59, 2014.

## Research Article

# Analyses and Encryption Implementation of a New Chaotic System Based on Semitensor Product

Rui Wang <sup>1,2</sup> Peifeng Du,<sup>2,3</sup> Wenqi Zhong,<sup>2,4</sup> Han Han,<sup>2,5</sup> and Hui Sun <sup>2</sup>

<sup>1</sup>Tianjin Key Laboratory for Civil Aircraft Airworthiness and Maintenance, Civil Aviation University of China, Tianjin 300300, China

<sup>2</sup>College of Information Engineering and Automation, Civil Aviation University of China, Tianjin 300300, China

<sup>3</sup>School of Electronics and Communication Engineering (SECE), Sun Yat-sen University, Guangzhou 510006, China

<sup>4</sup>School of Automation, Northwestern Polytechnical University, Xi'an 710072, China

<sup>5</sup>North China Research Institute of Electro-Optics, Beijing 100015, China

Correspondence should be addressed to Rui Wang; wrhappyfuture@hotmail.com and Hui Sun; shhappy1@hotmail.com

Received 4 January 2020; Revised 27 April 2020; Accepted 21 May 2020; Published 17 July 2020

Guest Editor: Viet-Thanh Pham

Copyright © 2020 Rui Wang et al. This is an open access article distributed under the Creative Commons Attribution License, which permits unrestricted use, distribution, and reproduction in any medium, provided the original work is properly cited.

Semitensor product theory can deal with matrices multiplication with different numbers of columns and rows. Therefore, a new chaotic system for different high dimensions can be created by employing a semitensor product of chaotic systems with different dimensions, so that more channels can be selected for encryption. This paper proposes a new chaotic system generated by semitensor product applied on Qi and Lorenz systems. The corresponding dynamic characteristics of the new system are discussed in this paper to verify the existences of different attractors. The detailed algorithms are illustrated in this paper. The FPGA hardware encryption implementations are also elaborated and conducted. Correspondingly, the randomness tests are realized as well, and compared to that of the individual Qi system and Lorenz system, the proposed system in this paper owns the better randomness characteristic. The statistical analyses and differential and correlation analyses are also discussed.

## 1. Introduction

With the coming of 5G technology, more and more information is transformed by video, and video information security becomes more and more important in practical applications especially for long-distance transmission [1, 2]. The existing traditional encryption methods, such as DES and AES, however, cannot meet the high requirements for real time [3]. Therefore, it is necessary to focus on making progresses in the encryption technology in order to meet the real-time requirements.

People never stop studying the chaotic systems since Lorenz proposed the first chaotic system. Except for the typical chaotic systems, such as Chen, Lv, and Qi systems, some new different types of chaotic systems are generated as well, such as multistable chaotic hyperjerk system [4], a class of fractional-order partial differential systems [5], multistable modified fourth-order autonomous Chua's system [6],

coexisting chaotic attractors chaotic systems [7–9], and chaotic system generation with memristors [10]. The authors in reference [11] present a MDMBCAs design method without reconstructing nonlinear function. Correspondingly, chaotic systems are employed in different areas such as modeling neurodegenerative disease [12] and image and video encryptions [13–18]. It is known that the characteristics of chaotic systems, such as pseudorandomness and sensitivity to initial values, meet the requirements of encryption discussed in the Shannon's epoch-making paper "Communication Theory of Secrecy Systems." Consequently, it is hot for researchers to focus on the image and video data encryption, where the encrypted sequences are generated by chaotic systems in order to satisfy the need for remote communications and other applications. Multiple hardware platforms are implemented on encryptions such as FPGA, ARM, or circuits implementation [19–32]. Thus, different encryption methods based on various hardware



platforms are proposed in many articles [19]. The authors in reference [20] propose chaos encryption and decryption operated on FPGA and tested by TESTU01. The study in [21, 22] implements scrambling and antisqueezing of RGB three primary color pixel position and video chaotic encryption and decryption of pixel value on arm and a digital programmable audio encryption based on chaos system on FPGA. The effectiveness of chaotic secure communication system method is proved by using adder and multiplier of FPGA [23]. A generalized improved chaotic transformation mapping is proposed in [24]. Based on this mapping, the speech encryption of position transformation network is implemented on FPGA. Meanwhile, [25] realizes FPGA circuit output of three-dimensional chaotic system without balancing points on FPGA. The study in [26] implements the multibutterfly chaotic attractor problem on FPGA. The study in [27] proposes a Kolmogorov-type three-dimensional chaotic system and implements the chaotic system on FPGA. The study in [28] implements an application of high-dimensional digital chaos system (HDDCS) in image encryption in a limited precision range on FPGA. The study in [29] proposes a fractional order three-dimensional chaotic system with four wing chaotic attractors implemented on FPGA. The study in [30] proposes a sinusoidal chaotic model (SCM) and uses FPGA to implement chaotic mapping to verify its complexity and larger chaotic range. SOPC technology is used to realize the video processing of FPGA and the data receiving and sending of ARM [15]. A method of generating pseudorandom number based on chaotic system is proposed and implemented on FPGA [31]. In addition to FPGA and arm, [32, 33] also use improved modular circuit design in hyperchaotic system. The study in [34] studies the security of the latest three-dimensional chaotic self-synchronization flow secret key and a single secret key algorithm. The study in [35] proposes a method for a high-dimension chaotic system implemented on FPGA and also provides comparison among different methods, such as Real Domain Chaotic System (RDCS), Integer Domain Chaotic System (IDCS), Chaotic Bitwise Dynamical System (CBDS), and Higher-Dimensional Digital Chaotic Systems (HDDCS) implemented on FPGA. Compared to these methods, the proposed method can solve the dynamical degradation issue. The study in [36] discusses the Orthogonal Frequency Division Multiplexing-Passive Optical Network (OFDM-PON) method which initiates a method for real-time video encryption with chaotic systems. Chen. et al. design an encryption algorithm using chaotic control methods and implement this method on FPGA and ARM hardware platforms. Furthermore, the comparisons of the encryption method based on ARM and FPGA are discussed by mixing the advantages of each platform to achieve better real-time performance [15, 23, 24].

Semitensor product is a matrix operation first proposed by Cheng et al. [37]. This method breaks the restriction of matrix product; that is, the column dimension of the front matrix must be the same with the row dimension of the back matrix. Then semitensor product realizes the multiplication for matrices with different dimensions. Therefore, this method makes the matrices product more easily and can be

applied in much wider areas. Semitensor product method is also extended in nonlinear issues and multiple areas such as Boolean network control, game theory, compressed sensing, and data fusion [38–40]. The study in [41] provides the literature review for the applications of semitensor product in engineering areas. This paper is inspired by the typical characteristics of semitensor product method mentioned previously which provides a new idea to generate chaotic systems. The new chaotic systems can be employed in real-time video encryption areas as well.

The main contribution of this paper is to employ the unique characteristic of the semitensor product to form a new chaotic system with different-order chaotic systems, Qi and Lorenz systems, in order to enhance the randomness of the sequence. Then the dynamic characteristics of the new chaotic system are analyzed, and the system is applied in video encryption. When compared to the individual chaotic system, the new one constructed by semitensor product has the overwhelmed pseudorandomness.

The rest of the paper is arranged as follows. Section 2 presents a new chaotic system formed by semitensor product theory. Furthermore, the corresponding dynamic characteristics of the system are analyzed. Section 3 provides the detailed encryption implementation based on FPGA with the new chaotic system. NIST test and the corresponding stochastic analysis are conducted as well in this section. The conclusion of the paper is drawn in Section 4.

## 2. A New Chaotic System Based on the Semitensor Product Theory

*2.1. Preliminaries of Semitensor Product.* Normally, the semitensor product operation includes left semitensor product operation and right semitensor product operation. Left semitensor product operation meets the multiple-dimension condition; that is,  $n = t \times p$  ( $t \in \mathbb{N}^+$ ). Or if  $p = s \times n$  ( $s \in \mathbb{N}^+$ ), the operation is right semitensor product operation.

**Lemma 1.** *Assume matrix  $A$  is  $m \times n$ , matrix  $B$  is  $p \times q$ , and  $n = t \times p$  ( $t \in \mathbb{N}^+$ ) [42]. Let  $A$  be divided into a blocking matrix  $[A_1, \dots, A_t]$ , where  $A_i$  ( $i = 1, \dots, t$ ) is an  $m \times p$  matrix. Then the left semitensor product is defined as*

$$A^{m \times n} \ltimes B^{p \times q} = (A_1^{m \times p} B^{p \times q}, A_2^{m \times p} B^{p \times q}, A_3^{m \times p} B^{p \times q}, \dots, A_t^{m \times p} B^{p \times q})^{m \times tq}, \quad (1)$$

where “ $\ltimes$ ” is the left semitensor product.

**Lemma 2.** *If  $A \in M_{m \times tp}$  and  $B \in M_{p \times q}$ , then*

$$A \ltimes B = A(B \otimes I_t), \quad (2)$$

where  $\otimes$  is the Kronecker product of matrices [42].

*2.2. A New Chaotic System Generated by Semitensor Product Theory.* Qi system is a hyperchaotic system with two positive Lyapunov exponents, 3 and 13, under certain conditions [28]. And it could be used for secure communication due to its large positive Lyapunov exponents. It is known that Qi system is described as follows:



$$\begin{cases} \dot{x}_{Q1} = a(x_{Q2} - x_{Q1}) + x_{Q2}x_{Q3}, \\ \dot{x}_{Q2} = b(x_{Q1} + x_{Q2}) - x_{Q1}x_{Q3}, \\ \dot{x}_{Q3} = -cx_{Q3} - ex_{Q4} + x_{Q1}x_{Q2}, \\ \dot{x}_{Q4} = -dx_{Q4} + fx_{Q3} + x_{Q1}x_{Q2}, \end{cases} \quad (3)$$

where  $x_{Qi}$  ( $i = 1, 2, 3, 4$ ) is the state variable and  $a, b, c, d,$  and  $f$  are the related system parameters. System (3) is a hyperchaotic system, when  $49 \leq a \leq 55$ ,  $20 \leq b \leq 24$ ,  $c = 13$ ,  $d = 8$ ,  $e = 33$ , and  $f = 30$ .

The first chaotic system under study is a Lorenz chaotic system [28]. The dynamics of the system are shown in

$$\begin{cases} \dot{x} = \sigma(y - x), \\ \dot{y} = rx - y - xz, \\ \dot{z} = xy - \beta z, \end{cases} \quad (4)$$

where  $x, y,$  and  $z$  are state variables and  $\sigma, r,$  and  $\beta$  are the related system parameters. The typical system parameters for Lorenz chaotic system are selected as  $\sigma = 10$ ,  $r = 28$ , and  $\beta = 8/3$ .

It is relaxed for semitensor product operation only to satisfy the multiple-dimension condition. Therefore, different numbers state variables of systems can be selected and conduct semitensor operation. For example, this paper selects a two-dimension state variable  $(xy)^T$  of Lorenz system and a four-dimension state variable  $(x_{Q1}x_{Q2}x_{Q3}x_{Q4})$

$^T$  of  $Q_i$  system to operate semitensor product. The result is shown as follows:

$$\begin{bmatrix} x \\ y \end{bmatrix} \times \begin{bmatrix} x_{Q1} \\ x_{Q2} \\ x_{Q3} \\ x_{Q4} \end{bmatrix} = \begin{bmatrix} x \\ y \end{bmatrix} \begin{bmatrix} x_{Q1} \\ x_{Q2} \\ x_{Q3} \\ x_{Q4} \end{bmatrix}^T \begin{bmatrix} x_{Q1} \\ x_{Q2} \\ x_{Q3} \\ x_{Q4} \end{bmatrix}^T. \quad (5)$$

It is observed that the result of equation (5) is eight-dimension column vector which is equivalent to the new system state variable vector  $(x_1x_2x_3x_4x_5x_6x_7x_8)^T$ ; that is,

$$\begin{bmatrix} x_1 \\ x_2 \\ x_3 \\ x_4 \\ x_5 \\ x_6 \\ x_7 \\ x_8 \end{bmatrix} = \begin{bmatrix} xx_{Q1} \\ xx_{Q2} \\ xx_{Q3} \\ xx_{Q4} \\ yx_{Q1} \\ yx_{Q2} \\ yx_{Q3} \\ yx_{Q4} \end{bmatrix}. \quad (6)$$

Differentiate each state variable in equation (6), and substitute equations (3) and (4) into the result. Then the following equation can be derived:

$$\begin{bmatrix} \dot{x}_1 \\ \dot{x}_2 \\ \dot{x}_3 \\ \dot{x}_4 \\ \dot{x}_5 \\ \dot{x}_6 \\ \dot{x}_7 \\ \dot{x}_8 \end{bmatrix} = \begin{bmatrix} \dot{xx}_{Q1} + x\dot{x}_{Q1} \\ \dot{xx}_{Q2} + x\dot{x}_{Q2} \\ \dot{xx}_{Q3} + x\dot{x}_{Q3} \\ \dot{xx}_{Q4} + x\dot{x}_{Q4} \\ \dot{yx}_{Q1} + y\dot{x}_{Q1} \\ \dot{yx}_{Q2} + y\dot{x}_{Q2} \\ \dot{yx}_{Q3} + y\dot{x}_{Q3} \\ \dot{yx}_{Q4} + y\dot{x}_{Q4} \end{bmatrix} = \begin{bmatrix} \sigma(y-x)x_{Q1} + ax(x_{Q2} - x_{Q1}) + xx_{Q2}x_{Q3} \\ \sigma(y-x)x_{Q2} + bx(x_{Q1} + x_{Q2}) - xx_{Q1}x_{Q3} \\ \sigma(y-x)x_{Q3} - cxx_{Q3} - exx_{Q4} + xx_{Q1}x_{Q2} \\ \sigma(y-x)x_{Q4} - dx_{Q4} + fx_{Q3} + xx_{Q1}x_{Q2} \\ (rx - y - xz)x_{Q1} + ay(x_{Q2} - x_{Q1}) + yx_{Q2}x_{Q3} \\ (rx - y - xz)x_{Q2} + by(x_{Q1} + x_{Q2}) - yx_{Q1}x_{Q3} \\ (rx - y - xz)x_{Q3} - cyx_{Q3} - eyx_{Q4} + yx_{Q1}x_{Q2} \\ (rx - y - xz)x_{Q4} - dyx_{Q4} + fyx_{Q3} + yx_{Q1}x_{Q2} \end{bmatrix} = \begin{bmatrix} \sigma(x_5 - x_1) + a(x_2 - x_1) + \frac{x_2x_3}{x} \\ \sigma(x_6 - x_2) + b(x_2 + x_1) - \frac{x_1x_3}{x} \\ \sigma(x_7 - x_3) - cx_3 - ex_4 + \frac{x_1x_2}{x} \\ \sigma(x_8 - x_4) - dx_4 + fx_3 + \frac{x_1x_2}{x} \\ rx_1 - x_5 - x_1z + a(x_6 - x_5) + \frac{x_6x_7}{x} \\ rx_2 - x_6 - x_2z + b(x_5 + x_6) - \frac{x_5x_7}{x} \\ rx_3 - x_7 - x_3z - cx_7 - ex_8 + \frac{x_5x_6}{x} \\ rx_4 - x_8 - x_4z - dx_8 + fx_7 + \frac{x_5x_6}{x} \end{bmatrix}. \quad (7)$$

It is obvious that the dynamics of (7) still include three state variables of Lorenz system,  $x, y,$  and  $z$ . Therefore, insert

equation (4) into equation (7) and then form a complete eleven-dimension system as illustrated in the following:

$$\left. \begin{aligned}
 \dot{x}_1 &= \sigma(x_5 - x_1) + a(x_2 - x_1) + \frac{x_2 x_3}{x}, \\
 \dot{x}_2 &= \sigma(x_6 - x_2) + b(x_2 + x_1) - \frac{x_1 x_3}{x}, \\
 \dot{x}_3 &= \sigma(x_7 - x_3) - cx_3 - ex_4 + \frac{x_1 x_2}{x}, \\
 \dot{x}_4 &= \sigma(x_8 - x_4) - dx_4 + fx_3 + \frac{x_1 x_2}{x}, \\
 \dot{x}_5 &= rx_1 - x_5 - x_1 z + a(x_6 - x_5) + \frac{x_6 x_7}{y}, \\
 \dot{x}_6 &= rx_2 - x_6 - x_2 z + b(x_5 + x_6) - \frac{x_5 x_7}{y}, \\
 \dot{x}_7 &= rx_3 - x_7 - x_3 z - cx_7 - ex_8 + \frac{x_5 x_6}{y}, \\
 \dot{x}_8 &= rx_4 - x_8 - x_4 z - dx_8 + fx_7 + \frac{x_5 x_6}{y}, \\
 \dot{x} &= \sigma(y - x), \\
 \dot{y} &= rx - y - xz, \\
 \dot{z} &= xy - \beta z.
 \end{aligned} \right\} \quad (8)$$

As seen from equation (8), if one substitutes  $x \rightarrow -x$ ,  $y \rightarrow -y$ , and  $z \rightarrow z$ ,  $\dot{z} = (-x)(-y) - \beta z = xy - \beta z$ , it proves that it is symmetric with respect to  $z$  variable for  $x$  and  $y$ .

**2.3. Numerical Analysis of the New System.** The paper analyzes some dynamics characteristics of the new system including symmetry, dissipativity, equilibrium point, equilibria, bifurcation diagram, Lyapunov diagram, and phase portraits.

**2.3.1. Symmetry.** As described in system (8), the system is symmetry with respect to  $z$ -axis since the system is invariant under the coordinate transformations:  $(x_1, x_2, x_3, x_4, x_5, x_6, x_7, x_8, x, y, z) \rightarrow (-x_1, -x_2, -x_3, -x_4, -x_5, -x_6, -x_7, -x_8, -x, -y, z)$ .

**2.3.2. Dissipativity.** The divergence of system (12) is given by

$$\begin{aligned}
 \nabla \cdot f &= \frac{\partial f_1}{\partial x_1} + \frac{\partial f_2}{\partial x_2} + \dots + \frac{\partial f_8}{\partial x_8} + \frac{\partial f_9}{\partial x} + \frac{\partial f_{10}}{\partial y} + \frac{\partial f_{11}}{\partial z} \\
 &= -5\sigma - 2a + 2b - 2c - 2d - 5 - \beta,
 \end{aligned} \quad (9)$$

and when  $-5\sigma - 2a + 2b - 2c - 2d - 5 - \beta < 0$ , the system undergoes dissipation.

**2.3.3. Equilibria.** As shown in system (8),  $x$ ,  $y$ , and  $z$  could not be zero when calculating equilibria. Then the equilibria of system (8) are  $(0, 0, 0, 0, 0, 0, 0, 0, \pm\sqrt{\beta(r-1)}, \pm\sqrt{\beta(r-1)}, r-1)$ . One has

$$J_{1,2} = \begin{bmatrix}
 -\sigma - a & a & 0 & 0 & \sigma & 0 & 0 & 0 & 0 & 0 & 0 \\
 b & b - \sigma & 0 & 0 & 0 & \sigma & 0 & 0 & 0 & 0 & 0 \\
 0 & 0 & -\sigma - c & -e & 0 & 0 & \sigma & 0 & 0 & 0 & 0 \\
 0 & 0 & f & -\sigma - d & 0 & 0 & 0 & \sigma & 0 & 0 & 0 \\
 1 & 0 & 0 & 0 & -1 - a & a & 0 & 0 & 0 & 0 & 0 \\
 0 & 1 & 0 & 0 & b & b - 1 & 0 & 0 & 0 & 0 & 0 \\
 0 & 0 & 1 & 0 & 0 & 0 & -1 - c & -e & 0 & 0 & 0 \\
 0 & 0 & 0 & 1 & 0 & 0 & f & -1 - d & 0 & 0 & 0 \\
 0 & 0 & 0 & 0 & 0 & 0 & 0 & 0 & -\sigma & 0 & 0 \\
 0 & 0 & 0 & 0 & 0 & 0 & 0 & 0 & 1 & -1 & 0 \\
 0 & 0 & 0 & 0 & 0 & 0 & 0 & 0 & \pm\sqrt{\beta(r-1)} & \pm\sqrt{\beta(r-1)} & \beta \Big|_{\text{equilibria}}
 \end{bmatrix} \quad (10)$$

The corresponding polynomial is

$$f(\lambda) = \lambda(\lambda + \beta)(\lambda - 1)f_1(\lambda) \quad (11)$$

where  $f_1(\lambda)$  is an eighth-order polynomial. It is obvious that at least 0, 1, and  $-\beta$  are eigenvalues of system (8) for the these equilibrium points; therefore, not each real part of the

eigenvalues is negative. Then it can be concluded that these are not stable equilibrium points.

**2.3.4. Bifurcation Diagram, Lyapunov Diagram, and Phase Portraits.** It is known that when  $49 \leq a \leq 55$ ,  $20 \leq b \leq 24$ ,  $c = 13$ ,  $d = 8$ ,  $e = 33$ , and  $f = 30$ , Qi system is a hyperchaotic system. When  $\sigma = 10$ ,  $r = 28$ , and  $\beta = 8/3$ , Lorenz system is a chaotic system. Therefore, the paper selects the parameters  $a = 50$ ,  $c = 13$ ,  $d = 8$ ,  $e = 33$ ,  $f = 30$ ,  $\sigma = 10$ ,  $r = 28$ , and  $\beta = 8/3$  and varies  $b$  to analyze the bifurcation of system (12) as shown in Figure 1(a). As the bifurcation diagram shows, the system demonstrates the chaotic characteristics when  $b \in [-5, 26]$ . The corresponding Lyapunov diagram is illustrated in Figure 1(b). Furthermore, partial phase portraits of system (7) for different initials when  $b = 24$  are shown in Figures 1(c). One has

$$\left\{ \begin{array}{l} \dot{x}_1 = 10(x_5 - x_1) + 50(x_2 - x_1) + \frac{x_2 x_3}{x}, \\ \dot{x}_2 = 10(x_6 - x_2) + b(x_2 + x_1) - \frac{x_1 x_3}{x}, \\ \dot{x}_3 = 10(x_7 - x_3) - 13x_3 - 33x_4 + \frac{x_1 x_2}{x}, \\ \dot{x}_4 = 10(x_8 - x_4) - 8x_4 + 30x_3 + \frac{x_1 x_2}{x}, \\ \dot{x}_5 = 28x_1 - x_5 - x_1 z + 50(x_6 - x_5) + \frac{x_6 x_7}{y}, \\ \dot{x}_6 = 28x_2 - x_6 - x_2 z + b(x_5 + x_6) - \frac{x_5 x_7}{y}, \\ \dot{x}_7 = 28x_3 - x_7 - x_3 z - 13x_7 - 33x_8 + \frac{x_5 x_6}{y}, \\ \dot{x}_8 = 28x_4 - x_8 - x_4 z - 8x_8 + 30x_7 + \frac{x_5 x_6}{y}, \\ \dot{x} = 10(y - x), \\ \dot{y} = 28x - y - xz, \\ \dot{z} = xy - \frac{8}{3z}. \end{array} \right. \quad (12)$$

Figures 1(c)–1(f) illustrate different phase portraits including  $x_1$  versus  $x_2$ ,  $x_2$  versus  $x_4$ ,  $x_3$  versus  $x$ , and  $x$  versus  $z$  when  $b = 24$  for two initial value sets, the initial values for the blue line phase portraits are 0.01418, 0.04217, 0.09157, 0.07922, 0.09594, 0.06557, 0.00357, 0.08491, 0.09339, 0.06787, and 0.07577, and those for the red line phase

portraits are 0.01417, 0.04218, 0.09156, 0.07921, 0.09593, 0.06558, 0.00356, 0.08492, 0.09338, 0.06788, and 0.07576. These portraits demonstrate that system (12) has obvious chaotic attractors and approaches periodic characteristics as initial values changes.

### 3. Encryption Implementation with the New Chaotic System Based on FPGA

This paper employs the random sequence of system (12) as the random sequence to encrypt video data and realize the hardware implement on FPGA. Figure 2 is the FPGA hardware diagram used for the encryption. The main components are HDMI, ZYNQ, JTAG, and source interface. The video is collected from JTAG, then the encryption algorithm is performed in ZYNQ powered by 5 V DC, and the outputs will be shown in the monitor through HDMI.

The encryption algorithm is described in the following, and the corresponding block diagram is demonstrated in Figure 3:

Step 1: to generate the random sequences for each state variable for both discretized Qi system and Lorenz system, respectively.

Step 2: to generate the random sequence for the new system (12) constructed by semitensor product operation on  $(x_{Q1} \ x_{Q2} \ x_{Q3} \ x_{Q4})^T$  and  $(x \ y)^T$ .

Step 3: to generate the sequence  $x_i = (x_{i1}, x_{i2}, x_{i3}, \dots, x_{i32})$  by the new system ( $i = 1, 2, \dots, 8, j = 1, 2, \dots, 32$ ), where  $x_{ij}$  is a binary number,  $i$  represents the number of state variables, and  $j$  is the bit number for each state variable. Choose a sequence  $x_i$  with fixed bits from  $t$  to  $q$ ; that is,

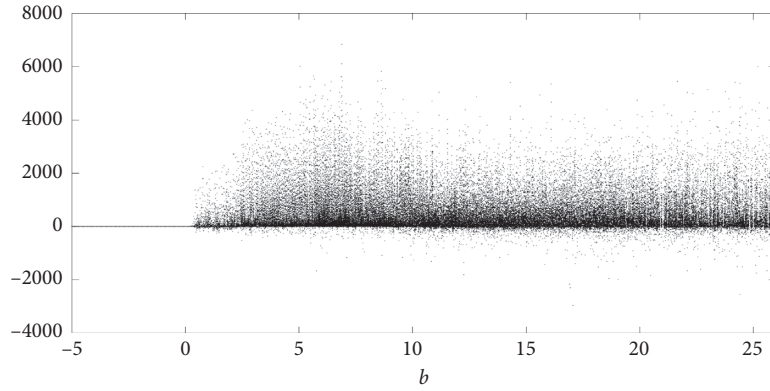
$$c_i(n) = ((x_i \bmod 2^q) \bmod 2^{t-q}), \quad (i = 1, 2, \dots, 8, 1 \leq t < q \leq 32). \quad (13)$$

Make an XOR operation on  $c_i(n)$  and divide video data based on pixels; that is,

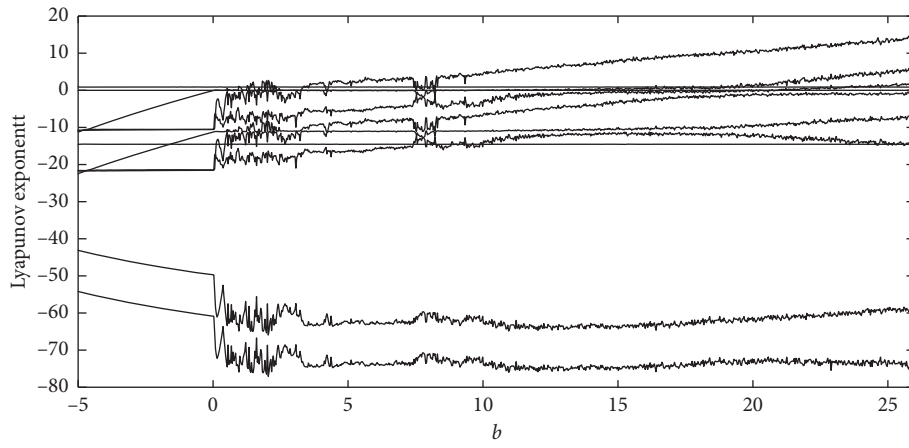
$$m(n) = ((x_i \bmod 2^{t-1}) \bmod 2^{t-q}) \oplus (m), \quad (14)$$

where  $\oplus$  is the XOR operation.

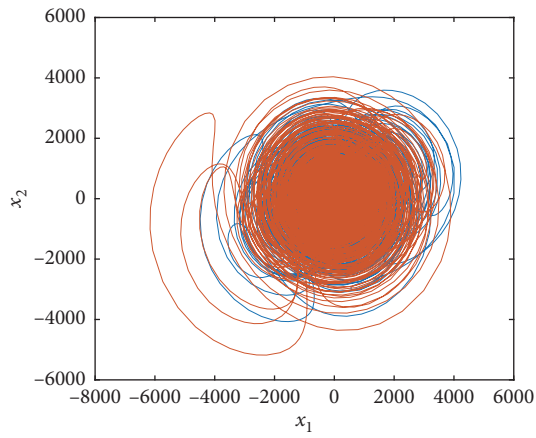
**3.1. Discretization for the New System and Its Implementation Based on FPGA.** In the hardware experiment, it is impossible to implement the continuous Lorenz and Qi chaotic systems because of limitation of the bit width in FPGA. Therefore, it is necessary to discretize continuous system first. Multiple methods can be used to discretize a differential equation such as Euler method, improved Euler method, and Runge-Kutta method. To meet the requirement of real-time performance and the limitation of hardware implementation, Euler method is used to discretize the differential equations due to its low computation complexity. First, Euler method is used to discretize Qi and Lorenz systems, respectively. The corresponding process of Qi system is proposed as follows:



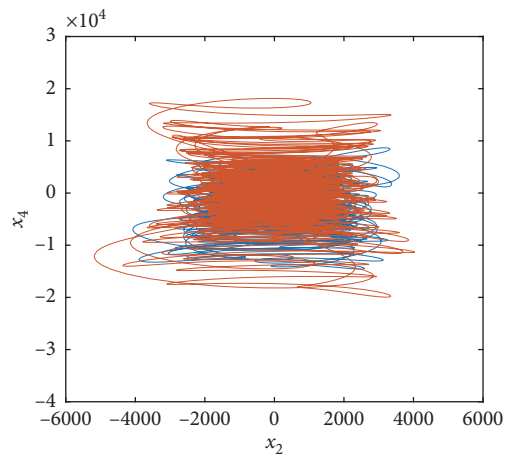
(a)



(b)



(c)



(d)

FIGURE 1: Continued.

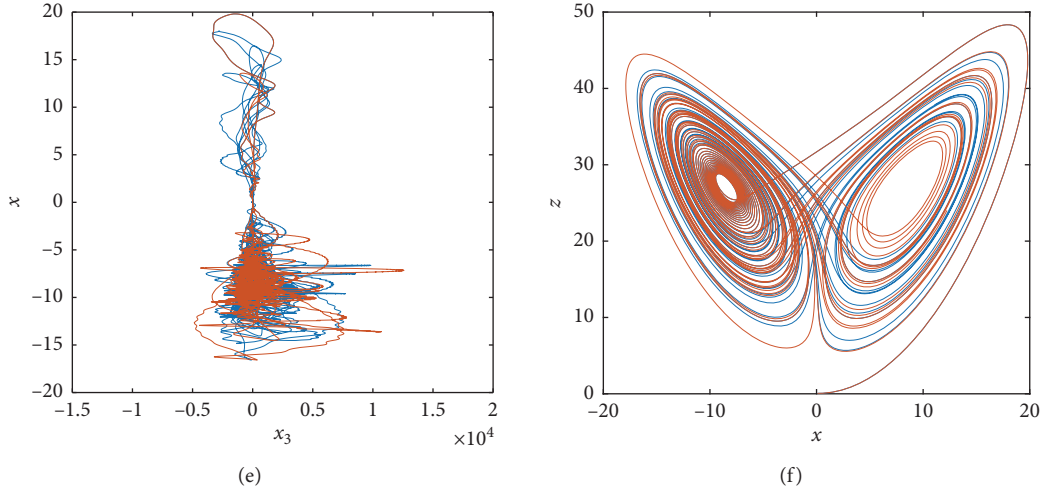


FIGURE 1: Bifurcation diagram along with  $b$  variation and partial phase portraits for different initial values (blue line for the first initial value set and red line for the second initial value set).

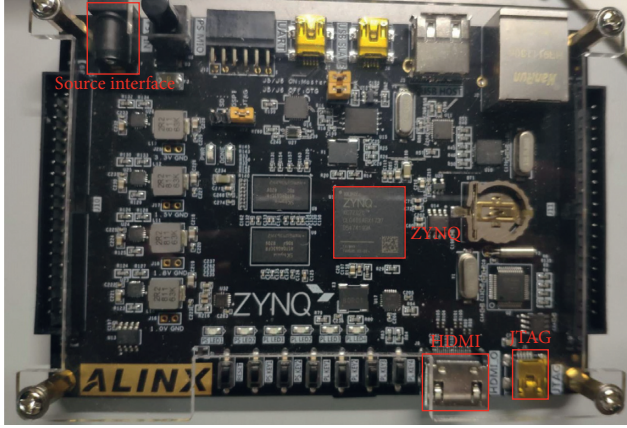


FIGURE 2: FPGA hardware diagram.

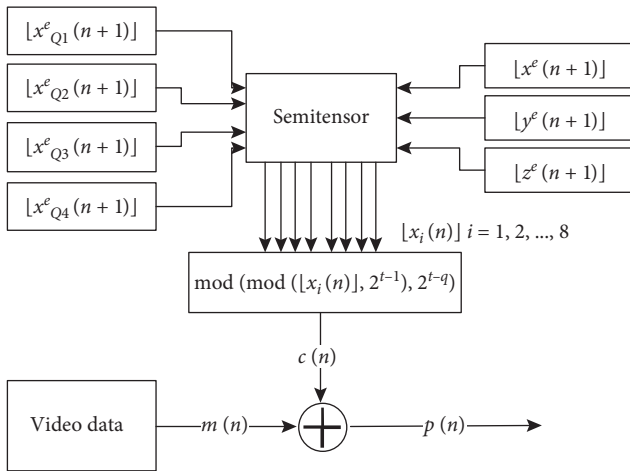


FIGURE 3: Block diagram of encryption algorithm.

$$\begin{cases} \frac{(x_{Q1}(n+1) - x_{Q1}(n))}{\tau} = a(x_{Q2}(n) - x_{Q1}(n)) + x_{Q2}(n)x_{Q3}(n), \\ \frac{(x_{Q2}(n+1) - x_{Q2}(n))}{\tau} = b(x_{Q1}(n) + x_{Q2}(n)) - x_{Q1}(n)x_{Q3}(n), \\ \frac{(x_{Q3}(n+1) - x_{Q3}(n))}{\tau} = -cx_{Q3}(n) - ex_{Q4}(n) + x_{Q1}(n)x_{Q2}(n), \\ \frac{(x_{Q4}(n+1) - x_{Q4}(n))}{\tau} = -dx_{Q4}(n) + fx_{Q3}(n) + x_{Q1}(n)x_{Q2}(n). \end{cases} \quad (15)$$

Then, the iteration equations of Qi system are shown in

$$\begin{cases} x_{Q1}(n+1) = atx_{Q2}(n) + (1-at)x_{Q1}(n) + \tau x_{Q2}(n)x_{Q3}(n), \\ x_{Q2}(n+1) = b\tau x_{Q1}(n) + (1+b\tau)x_{Q2}(n) - \tau x_{Q1}(n)x_{Q3}(n), \\ x_{Q3}(n+1) = (1-c\tau)x_{Q3}(n) - e\tau x_{Q4}(n) + \tau x_{Q1}(n)x_{Q2}(n), \\ x_{Q4}(n+1) = (1-d\tau)x_{Q4}(n) + f\tau x_{Q3}(n) + \tau x_{Q1}(n)x_{Q2}(n). \end{cases} \quad (16)$$

Similarly, the discrete Lorenz system is

$$\begin{cases} \frac{x(n+1) - x(n)}{\tau} = \sigma(y(n) - x(n)), \\ \frac{y(n+1) - y(n)}{\tau} = rx(n) - y(n) - x(n)z(n), \\ \frac{z(n+1) - z(n)}{\tau} = x(n)y(n) - \beta z(n). \end{cases} \quad (17)$$

Correspondingly, the iteration equations of Lorenz system are

$$\begin{cases} x(n+1) = \sigma\tau y(n) + (1 - \sigma\tau)x(n), \\ y(n+1) = r\tau x(n) + (1 - \tau)y(n) - \tau x(n)z(n), \\ z(n+1) = \tau x(n)y(n) + (1 - \beta\tau)z(n). \end{cases} \quad (18)$$

In general, FPGA can store float data and fixed-point data. Since fixed-point data require less computing resources than that of float data, this paper uses 64-bit fixed-point

number to represent the data. The detailed data format of 64-bit fixed-point numbers is shown in Figure 4.

In Figure 4,  $I$  represents the integer part of 64-bit fixed-point numbers, and  $f$  is the fractional part.

As mentioned before, because of the limitation of bit width in FPGA, all data are truncated numbers in hardware implementation. Therefore, the Qi and Lorenz system becomes

$$\begin{cases} \lfloor x_{Q1}(n+1) \rfloor = a\tau \lfloor x_{Q2}(n) \rfloor + (1 - a\tau) \lfloor x_{Q1}(n) \rfloor + \tau \lfloor x_{Q2}(n) \rfloor \lfloor x_{Q3}(n) \rfloor, \\ \lfloor x_{Q2}(n+1) \rfloor = b\tau \lfloor x_{Q1}(n) \rfloor + (1 + b\tau) \lfloor x_{Q2}(n) \rfloor - \tau \lfloor x_{Q1}(n) \rfloor \lfloor x_{Q3}(n) \rfloor, \\ \lfloor x_{Q3}(n+1) \rfloor = (1 - c\tau) \lfloor x_{Q3}(n) \rfloor - e\tau \lfloor x_{Q4}(n) \rfloor + \tau \lfloor x_{Q2}(n) \rfloor \lfloor x_{Q1}(n) \rfloor, \\ \lfloor x_{Q4}(n+1) \rfloor = (1 - d\tau) \lfloor x_{Q4}(n) \rfloor + f\tau \lfloor x_{Q3}(n) \rfloor + \tau \lfloor x_{Q1}(n) \rfloor \lfloor x_{Q2}(n) \rfloor, \end{cases} \quad (19)$$

$$\begin{cases} \lfloor x(n+1) \rfloor = \sigma\tau \lfloor y(n) \rfloor + (1 - \sigma\tau) \lfloor x(n) \rfloor, \\ \lfloor y(n+1) \rfloor = r\tau \lfloor x(n) \rfloor + (1 - \tau) \lfloor y(n) \rfloor - \tau \lfloor x(n) \rfloor \lfloor z(n) \rfloor, \\ \lfloor z(n+1) \rfloor = \tau \lfloor x(n) \rfloor \lfloor y(n) \rfloor + (1 - \beta\tau) \lfloor z(n) \rfloor. \end{cases} \quad (20)$$

Let the iteration step be  $\tau=0.00001$  and use the same parameters in system (12). Then substitute them into (19)

and (20), respectively. Therefore, Qi system and Lorenz system are changed as follows:

$$\begin{cases} \lfloor x_{Q1}(n+1) \rfloor = 0.9995 \lfloor x_{Q2}(n) \rfloor + 0.0005 \lfloor x_{Q1}(n) \rfloor + 0.00001 \lfloor x_{Q2}(n) \rfloor \lfloor x_{Q3}(n) \rfloor, \\ \lfloor x_{Q2}(n+1) \rfloor = 0.0002 \lfloor x_{Q1}(n) \rfloor + 1.0002 \lfloor x_{Q2}(n) \rfloor - 0.00001 \lfloor x_{Q1}(n) \rfloor \lfloor x_{Q3}(n) \rfloor, \\ \lfloor x_{Q3}(n+1) \rfloor = 0.99987 \lfloor x_{Q3}(n) \rfloor - 0.00033 \lfloor x_{Q4}(n) \rfloor + 0.00001 \lfloor x_{Q2}(n) \rfloor \lfloor x_{Q1}(n) \rfloor, \\ \lfloor x_{Q4}(n+1) \rfloor = 0.00008 \lfloor x_{Q4}(n) \rfloor + 0.9997 \lfloor x_{Q3}(n) \rfloor + 0.00001 \lfloor x_{Q1}(n) \rfloor \lfloor x_{Q2}(n) \rfloor, \end{cases} \quad (21)$$

$$\begin{cases} \lfloor x(n+1) \rfloor = 0.0001 \lfloor y(n) \rfloor + 0.9999 \lfloor x(n) \rfloor, \\ \lfloor y(n+1) \rfloor = 0.00028 \lfloor x(n) \rfloor + 0.99999 \lfloor y(n) \rfloor - 0.00001 \lfloor x(n) \rfloor \lfloor z(n) \rfloor, \\ \lfloor z(n+1) \rfloor = 0.00001 \lfloor x(n) \rfloor \lfloor y(n) \rfloor + 0.9999733 \lfloor z(n) \rfloor. \end{cases} \quad (22)$$

To iterate Qi system and Lorenz system and make semitensor product operation on these two systems after each iteration, respectively, the discretized first 8 state variables of the new system are obtained:

$$\begin{cases} x_1(n+1) = \lfloor x(n+1) \rfloor \times \lfloor x_{Q1}(n+1) \rfloor, \\ x_2(n+1) = \lfloor x(n+1) \rfloor \times \lfloor x_{Q2}(n+1) \rfloor, \\ x_3(n+1) = \lfloor x(n+1) \rfloor \times \lfloor x_{Q3}(n+1) \rfloor, \\ x_4(n+1) = \lfloor x(n+1) \rfloor \times \lfloor x_{Q4}(n+1) \rfloor, \\ x_5(n+1) = \lfloor y(n+1) \rfloor \times \lfloor x_{Q1}(n+1) \rfloor, \\ x_6(n+1) = \lfloor y(n+1) \rfloor \times \lfloor x_{Q2}(n+1) \rfloor, \\ x_7(n+1) = \lfloor y(n+1) \rfloor \times \lfloor x_{Q3}(n+1) \rfloor, \\ x_8(n+1) = \lfloor y(n+1) \rfloor \times \lfloor x_{Q4}(n+1) \rfloor, \end{cases} \quad (23)$$

where  $x_i(n+1)$  and  $x_i(n)$  are system state variables.  $\lfloor y(n+1) \rfloor$  is the approximate value of  $y(n+1)$  using fixed-point number.

**3.2. Implementation and Analysis of Encryption Algorithm of the New Chaotic System.** In order to ensure the randomness of the random sequence, therefore, select the low bits from  $t$  to  $q$  as shown in Figure 5. The positions of these bits are not close to those of sign and exponent bits. Then the chosen random encryption sequence,  $c_i(n)$ , is shown in equation (17). This paper selects  $t=1$  and  $q=6$ :

$$c_i(n) = \text{mod} \left( \left( \frac{\lfloor x_i(n) \rfloor}{2^{t-1}} \right), 2^{q-t+1} \right), \quad i = 1, 2, \dots, 8. \quad (24)$$

Random sequences which are selected from eight states based on the method mentioned previously are combined to generate the random sequence,  $c(n)$ :

$$c(n) = (c_1(n), c_2(n), \dots, c_8(n)). \quad (25)$$

In order to resist the differential attack and decrease the correlation between adjacent random sequences, the paper selects the very first iteration sequence among every  $N$  iterations and stacks these selected sequences to construct a



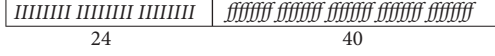


FIGURE 4: Data format for 64-bit fixed-point numbers.

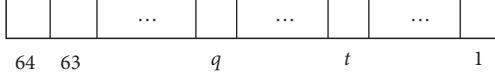


FIGURE 5: The schematics of numbered data bits.

random sequence,  $c(n)$ , as shown in equation (18). This can improve the randomness of the random sequence.

Next, the random sequence,  $c(n)$ , conducts XOR operation with the divided video data. Since a frame video data includes tricolor integer sequences,  $R(n)$ ,  $G(n)$ , and  $B(n)$ , these three sequences will be encrypted simultaneously after changing the random sequence,  $c(n)$ , into three columns evenly,  $c^1(n)$ ,  $c^2(n)$ , and  $c^3(n)$ :

$$\begin{aligned} p_1(n) &= c^1(n) \oplus R(n), \\ p_2(n) &= c^2(n) \oplus G(n), \\ p_3(n) &= c^3(n) \oplus B(n), \end{aligned} \quad (26)$$

where  $p_1(n)$ ,  $p_2(n)$ , and  $p_3(n)$  are encrypted sequences and  $\oplus$  is an XOR operation. One has

$$\begin{aligned} \hat{R}(n) &= \text{mod}\left(\frac{\lfloor \hat{x}_1(n) \rfloor}{2^t}, 2^{q-t+1}\right) \oplus p_1(n) \\ &= \text{mod}\left(\frac{\lfloor \hat{x}_1(n) \rfloor}{2^t}, 2^{q-t+1}\right) \oplus c^1(n) \oplus R(n), \\ \hat{G}(n) &= \text{mod}\left(\frac{\lfloor \hat{x}_2(n) \rfloor}{2^t}, 2^{q-t+1}\right) \oplus p_2(n) \\ &= \text{mod}\left(\frac{\lfloor \hat{x}_2(n) \rfloor}{2^t}, 2^{q-t+1}\right) \oplus c^1(n) \oplus G(n), \\ \hat{B}(n) &= \text{mod}\left(\frac{\lfloor \hat{x}_3(n) \rfloor}{2^t}, 2^{q-t+1}\right) \oplus p_3(n) \\ &= \text{mod}\left(\text{mod}\left(\lfloor \hat{x}_3(n) \rfloor, 2^t\right), 2^{t-q}\right) \oplus c^3(n) \oplus B(n), \end{aligned} \quad (27)$$

where  $\lfloor \hat{x}_{p'}(n) \rfloor$ ,  $p' = 1, 2, 3$  are receiver terminal sequences.

**3.3. Analysis for NIST Test.** NIST test is provided by National Institute of Standards and Technology, and it is a standard to test the randomness of a random sequence. According to the encryption algorithm in this paper,  $c(n)$  in equation (25) should be tested by NIST standard. The comparisons of the random sequence among the new system, Qi system, and Lorenz system,  $c(n)$ ,  $c_L(n)$ , and  $c_Q(n)$ , are conducted which are obtained from serial interfaces. The results of the tests are shown in Table 1.

As shown in Table 1, all the test results for the random sequences of the new system meet the NIST test index

standards. Partial test results are larger than 0.8, which means these random indexes are quite close to those of the real random sequences. The randomness indexes and some other test results are better than those generated from Lorenz system and Qi system, such as frequency, block frequency, cumulative sums, nonoverlapping template, approximate entropy, random excursions, random excursions variant, and linear complexity.

**3.4. Statistical Analyses.** Vivado IDE is used to conduct the hardware simulation. The paper also performs the statistics analysis for the encrypted video data generated by hardware. Figure 6(a) is one picture of a video before encryption. Figure 6(b) is the encrypted picture of a video.

Figure 7 demonstrates the comparisons of statistics histogram between the original and encrypted pictures.

Figure 7 demonstrates the comparisons of statistics histograms between the original and encrypted pictures. As illustrated in Figure 7(a), the difference of the pixels distribution is obvious. However, distribution of different pixels for the encrypted picture shown in Figure 7(b) is the approximately uniform distribution. It can be concluded that the proposed encryption algorithm for the new system can better resist statistic attack effectively.

**3.5. Differential Analysis.** Differential attack is used to measure the sensitivity of plaintext change for the encryption algorithm and commonly uses NPCR (Number of Pixels Change Rate) and UACI (Unified Average Changing Intensity) as indexes defined as follows:

$$\begin{cases} \text{NPCR} = \frac{\sum_{e,f} D(e,f)}{W \times H} \times 100\%, \\ \text{UACI} = \frac{1}{W \times H} \times \sum_{e,f} \frac{|C(e,f) - C'(e,f)|}{255} \times 100\%, \end{cases} \quad (28)$$

$$\begin{cases} \overline{\text{NPCR}} = \sum_m \text{NPCR}(m), \\ \overline{\text{UACI}} = \sum_m \text{UACI}(m), \end{cases} \quad (29)$$

where  $C(e, f)$  is the pixel value before encryption and  $C'(e, f)$  is the pixel value after encryption. If  $C(e, f) = C'(e, f)$ ,  $D(e, f) = 0$ , else 1.  $\overline{\text{NPCR}}$  and  $\overline{\text{UACI}}$  calculated by (29) and the proposed system and encryption algorithm are 99.60% and 12.28% for the first-time encryption, respectively. Therefore, the ability to resist differential attack improves to some extent. In video encryption application, the requirement for encryption speed is more concerned.

**3.6. Correlation Analysis.** Correlation analysis is used to check whether the neighbor pixels are close or not. This paper analyzes the correlation for Figure 6. The paper selects 5000 random pixels from the original and the encrypted images and analyzes the correlation among these random-pixel pairs as shown in Figure 8. As Figure 8 illustrates, the

TABLE 1: NIST test results for the random sequences of the new system, Lorenz system, and Qi system (the number of sequences is 100, and their lengths are 1000000).

Statistical test	$P$ value of $c_L(n)$	$P$ value of $c_Q(n)$	$P$ value of $c(n)$	Test results of $c(n)$	Proportion
Frequency	0.000000	0.236810	0.474986	√	100/100
Block frequency ( $m = 128$ )	0.289667	0.699313	0.946308	√	99/100
Cumulative sums	0.000000	0.108791	0.779188	√	100/100
Runs	0.000000	0.554420	0.075719	√	100/100
Longest run	0.419021	0.383827	0.289667	√	100/100
Rank	0.851383	0.996335	0.289667	√	100/100
FFT	0.911413	0.911413	0.213309	√	99/100
Nonoverlapping template ( $m = 9$ )	0.000003	0.181557	0.983453	√	100/100
Overlapping template ( $m = 9$ )	0.181557	0.935716	0.924076	√	100/100
Universal	0.616305	0.289667	0.014550	√	97/100
Approximate entropy ( $m = 10$ )	0.000000	0.798139	0.816537	√	99/100
Random excursions	0.008879	0.319084	0.739918	√	64/64
Random excursions variant	0.213309	0.289667	0.949602	√	64/64
Linear complexity ( $M = 500$ )	0.010988	0.013569	0.108791	√	99/100
Serial ( $m = 16$ )	0.616305	0.028817	0.262249	√	100/100

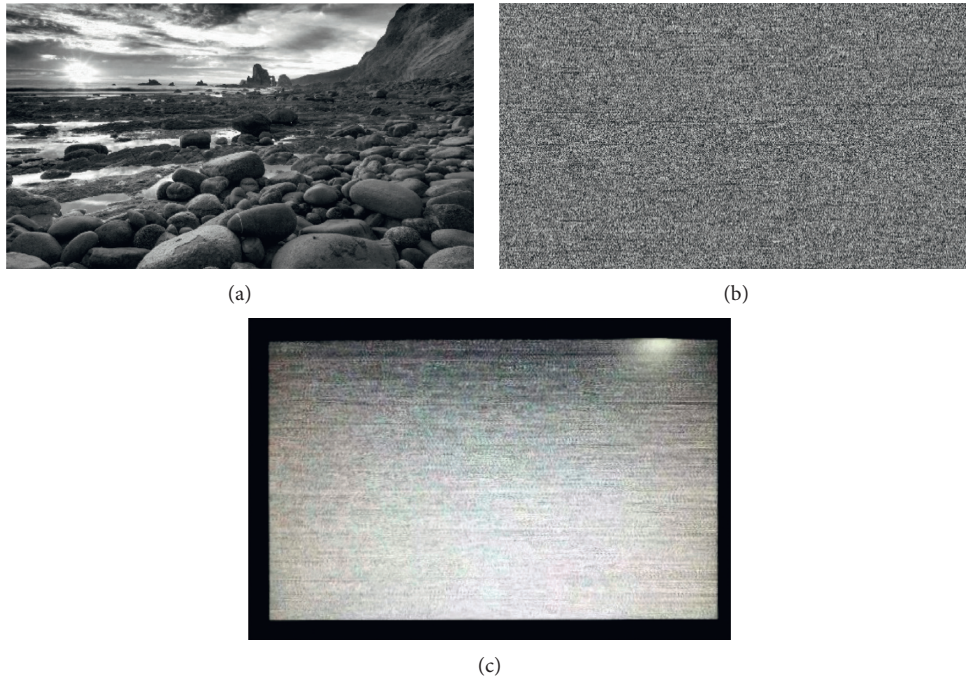


FIGURE 6: The original and encrypted pictures of a video and the corresponding encrypted video data through FPGA. (a) The original picture of a video. (b) The encrypted picture of a video. (c) Encrypted video data shown on a monitor.

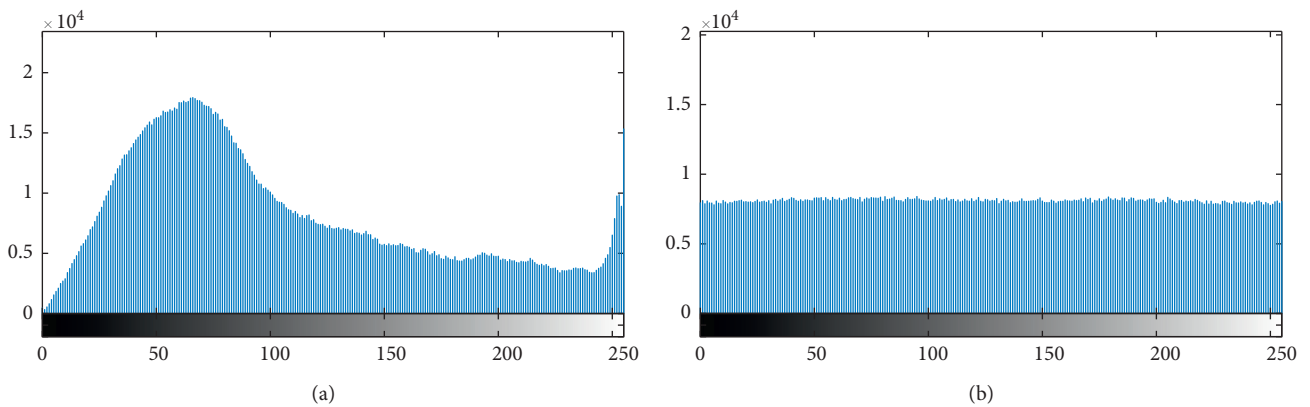


FIGURE 7: Histogram between the original and encrypted pictures. (a) Histogram of the original picture. (b) Histogram of the encrypted picture.

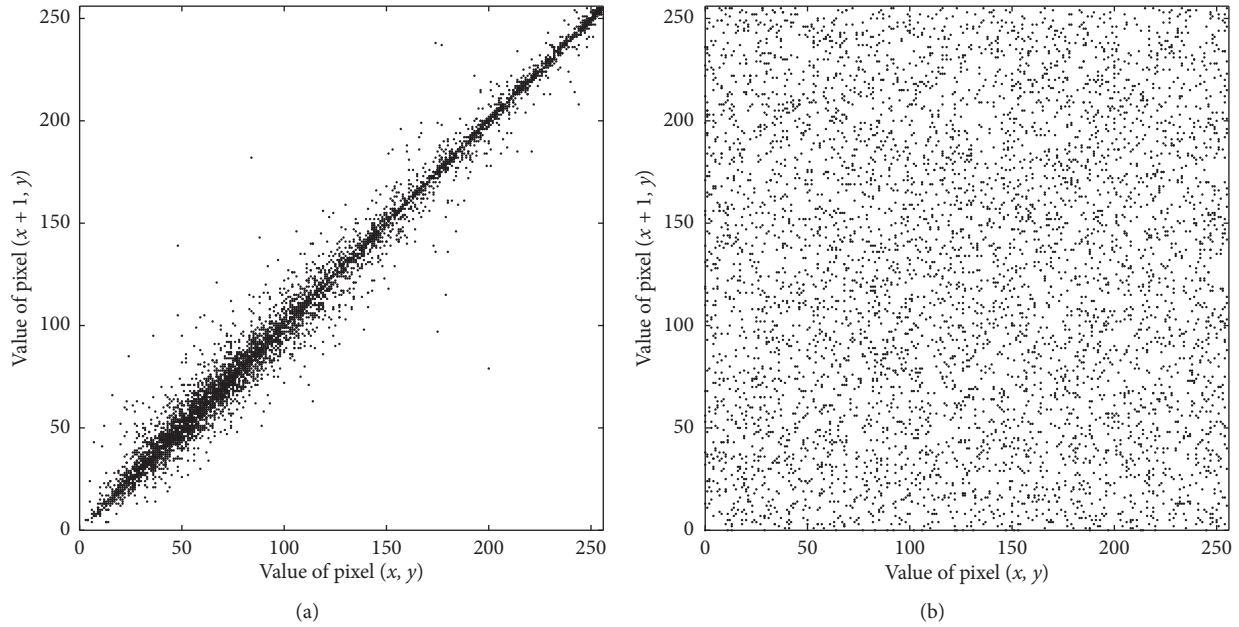


FIGURE 8: Correlation analyses for the original and encrypted figures in Figure 6. (a) Correlation analysis for the original figure as shown in Figure 6(a). (b) Correlation analysis for the encrypted figure as shown in Figure 6(b).

correlation dramatically decreases when comparing two figures before and after encryption as shown in Figure 6.

#### 4. Conclusions

This paper proposed a new chaotic system generated by using semitensor product on two chaotic systems, and the related dynamic characteristics are analyzed. The new system is employed in video encryption as well, and the proposed method can generate 8 or even 12 state variables when compared to Qi system and Lorenz system which only generate 7 state variables at most in one iteration period. The proposed method can improve the speed of random sequence generation. The NIST test results demonstrate that the pseudorandomness of new system is better than that of single Qi system and single Lorenz system.

The proposed encryption algorithm based on semitensor product can be used in other chaotic systems. The synchronization of the new system can be implemented by synchronizing two original chaotic systems separately. In this paper, FPGA is used to implement the generation of the new chaotic system and to encrypt video data. The corresponding statistics and differential and correlation analyses were also conducted which demonstrates that the new system has obvious advantages, such as better random features, better resistance to differential attacks, and lower pixel correlation for encrypted images. The future work will focus on the decryption of video information by the proposed chaotic system generated by the semitensor product method in hardware.

#### Data Availability

The figures' .zip data used to support the findings of this study are available from the corresponding author upon request.

#### Conflicts of Interest

The authors declare that there are no conflicts of interest regarding the publication of this paper.

#### Acknowledgments

This work was supported by the Fundamental Research Funds for the Central Universities-Civil Aviation University of China (3122019044).

#### References

- [1] J. Li, J. Li, X. Chen, C. Jia, and W. Lou, "Identity-based encryption with outsourced revocation in cloud computing," *IEEE Transactions on Computers*, vol. 64, no. 2, pp. 425–437, 2015.
- [2] J. Li, Y. K. Li, X. Chen, P. P. C. Lee, and W. Lou, "A hybrid cloud approach for secure authorized deduplication," *IEEE Transactions on Parallel and Distributed Systems*, vol. 26, no. 5, pp. 1206–1216, 2015.
- [3] M. Feki, B. Robert, G. Gelle, and M. Colas, "Secure digital communication using discrete-time chaos synchronization," *Chaos, Solitons & Fractals*, vol. 18, no. 4, pp. 881–890, 2003.
- [4] V. T. Pham, S. Vaidyanathan, C. Volos, S. Jafari, and T. Kapitaniak, "A new multi-stable chaotic hyperjerk system, its special features, circuit realization, control and synchronization," *Archives of Control Sciences*, vol. 30, no. 1, pp. 23–45, 2020.
- [5] A. Ouannas, X. Wang, V. T. Pham, G. Grassi, and V. V. Huynh, "Synchronization results for a class of fractional-order spatiotemporal partial differential systems based on fractional lyapunov approach," *Boundary Value Problems*, vol. 2019, no. 1 2019.
- [6] F. Yu, H. Shen, L. Liu et al., "CCII and FPGA realization: a multistable modified fourth-order autonomous Chua's

- chaotic system with coexisting multiple attractors,” *Complexity*, vol. 2020, Article ID 5212601, 17 pages, 2020.
- [7] Q. Lai, P. D. K. Kuate, F. Liu, and H. H. Lu, “An extremely simple chaotic system with infinitely many coexisting attractors,” *IEEE Transactions on Circuits and Systems II: Express Briefs*, vol. 67, no. 6, 2019.
  - [8] Q. Lai, A. Akgul, C. B. Li, G. H. Xu, and U. Cavusoglu, “A new chaotic system with multiple attractors: dynamic analysis, circuit realization and s-box design,” *Entropy*, vol. 20, no. 1, 2018.
  - [9] Q. Lai, B. Norouzi, and F. Liu, “Dynamic analysis, circuit realization, control design and image encryption application of an extended Lü system with coexisting attractors,” *Chaos, Solitons & Fractals*, vol. 114, pp. 230–245, 2018.
  - [10] R. Wang, M. Li, Z. Gao, and H. Sun, “A new memristor-based 5D chaotic system and circuit implementation,” *Complexity*, vol. 2018, Article ID 6069401, 12 pages, 2018.
  - [11] Q. Hong, Y. Li, X. Wang, and Z. Zeng, “A versatile pulse control method to generate arbitrary multidirection multi-butterfly chaotic attractors,” *IEEE Transactions on Computer-Aided Design of Integrated Circuits and Systems*, vol. 38, no. 8, pp. 1480–1492, 2019.
  - [12] P. S. Shabestari, Z. Rostami, V. T. Pham, F. E. Alsaadi, and T. Hayat, “Modeling of neurodegenerative diseases using discrete chaotic systems,” *Communications in Theoretical Physics*, vol. 71, no. 10, pp. 1241–1245, 2019.
  - [13] Q. Jiang, J. Jiang, and J. Li, “An image encryption algorithm based on high-dimensional chaotic systems,” in *Proceedings of the IEEE International Conference on Signal Processing, Communications and Computing*, pp. 1–4, Hong Kong, China, August 2016.
  - [14] S. Singh, M. Ahmad, and D. Malik, “Breaking an image encryption scheme based on chaotic synchronization phenomenon,” in *Proceedings of the 2016 Ninth International Conference on Contemporary Computing (IC3)*, Noida, India, August 2016.
  - [15] P. Chen, S. Yu, B. Chen, L. Xiao, and J. Lu, “Design and SOPC-based realization of a video chaotic secure communication scheme,” *International Journal of Bifurcation and Chaos*, vol. 28, no. 13, Article ID 1850160, 24 pages, 2018.
  - [16] P. R. Sankpal and P. A. Vijaya, “Image encryption Using chaotic maps: a survey,” in *Proceedings of the 2014 Fifth International Conference on Signal and Image Processing*, pp. 102–107, IEEE, Bangalore, India, January 2014.
  - [17] A. Rani and B. Raman, “An image copyright protection system using chaotic maps,” *Multimedia Tools and Applications*, vol. 76, no. 2, pp. 3121–3138, 2016.
  - [18] N. Shyamala and K. Anusudha, “Reversible chaotic encryption techniques for images,” in *Proceedings of the 2017 Fourth International Conference on Signal Processing, Communication and Networking (ICSCN)*, Chennai, India, March 2017.
  - [19] S. Chen, S. Yu, J. Lu, G. Chen, and J. He, “Design and FPGA-based realization of a chaotic secure video communication system,” *IEEE Transactions on Circuits and Systems for Video Technology*, vol. 28, no. 9, pp. 2359–2371, 2018.
  - [20] Z. Lin, S. Yu, J. Lu, S. Cai, and G. Chen, “Design and ARM-embedded implementation of a chaotic map-based real-time secure video communication system,” *IEEE Transactions on Circuits and Systems for Video Technology*, vol. 25, no. 7, pp. 1203–1216, 2015.
  - [21] D. Chang, Z. Li, M. Wang, and Y. Zeng, “A novel digital programmable multi-scroll chaotic system and its application in FPGA-based audio secure communication,” *AEU—International Journal of Electronics and Communications*, vol. 88, pp. 20–29, 2018.
  - [22] F. J. Farsana and K. Gopakumar, “Private key encryption of speech signal based on three dimensional chaotic map,” in *Proceedings of the International Conference on Communication & Signal Processing*, pp. 2197–2201, Chennai, India, April 2017.
  - [23] H. Jia, Z. Guo, S. Wang, and Z. Chen, “Mechanics analysis and hardware implementation of a new 3D chaotic system,” *International Journal of Bifurcation and Chaos*, vol. 28, no. 13, Article ID. 1850161, 14 pages, 2018.
  - [24] E. Tlelo-Cuautle, L. G. De La Fraga, V.-T. Pham, C. Volos, S. Jafari, and A. D. J. Quintas-Valles, “Dynamics, FPGA realization and application of a chaotic system with an infinite number of equilibrium points,” *Nonlinear Dynamics*, vol. 89, no. 2, pp. 1129–1139, 2017.
  - [25] A. Akgul, H. Calgan, I. Koyuncu, I. Pehlivan, and A. Istanbulu, “Chaos-based engineering applications with a 3D chaotic system without equilibrium points,” *Nonlinear Dynamics*, vol. 84, no. 2, pp. 481–495, 2016.
  - [26] Q. Lai, X. Zhao, K. Rajagopal, G. Xu, A. Akgul, and E. Guleryuz, “Dynamic analyses, FPGA implementation and engineering applications of multi-butterfly chaotic attractors generated from generalised spott c system,” *Pramana*, vol. 90, no. 1, p. 12, 2018.
  - [27] W. S. Sayed, M. F. Tolba, A. G. Radwan, and S. K. Abd-El-Hafiz, “FPGA realization of a speech encryption system based on a generalized modified chaotic transition map and bit permutation,” *Multimedia Tools and Applications*, vol. 78, no. 12, pp. 16097–16127, 2019.
  - [28] Q. Wang, S. Yu, C. Li et al., “Theoretical design and FPGA-based implementation of higher-dimensional digital chaotic systems,” *IEEE Transactions on Circuits and Systems I: Regular Papers*, vol. 63, no. 3, pp. 401–412, 2016.
  - [29] E. Dong, Z. Wang, Z. Chen, and Z. Wang, “Topological horseshoe analysis and field-programmable gate array implementation of a fractional-order four-wing chaotic attractor,” *Chinese Physics B*, vol. 27, no. 1, pp. 300–306, 2018.
  - [30] Z. Hua, B. Zhou, and Y. Zhou, “Sine chaotification model for enhancing chaos and its hardware implementation,” *IEEE Transactions on Industrial Electronics*, vol. 66, no. 2, pp. 1273–1284, 2019.
  - [31] İ. Öztürk and R. Kılıç, “A novel method for producing pseudo random numbers from differential equation-based chaotic systems,” *Nonlinear Dynamics*, vol. 80, no. 3, pp. 1147–1157, 2015.
  - [32] R. Wang, Q. Xie, Y. Huang, H. Sun, and Y. Sun, “Design of a switched hyperchaotic system and its application,” *International Journal of Computer Applications in Technology*, vol. 57, no. 3, pp. 207–218, 2018.
  - [33] R. Wang, H. Sun, J. Wang, L. Wang, and Y. Wang, “Applications of modularized circuit designs in a new hyper-chaotic system circuit implementation,” *Chinese Physics B*, vol. 24, no. 4, Article ID 020501, 2015.
  - [34] Z. Lin, S. Yu, and J. Li, “Chosen ciphertext attack on a chaotic stream cipher,” in *Proceedings of the 30th Chinese Control and Decision Conference*, pp. 1238–1242, Shenyang, China, June 2018.
  - [35] G. Qi, G. Chen, M. A. Van Wyk, and B. J. Van Wyk, “On a new hyperchaotic system,” *Physics Letters A*, vol. 372, no. 2, pp. 124–136, 2008.
  - [36] Z. Hu and C.-K. Chan, “A real-valued chaotic orthogonal matrix transform-based encryption for OFDM-PON,” *IEEE*







- Photonics Technology Letters*, vol. 30, no. 16, pp. 1455–1458, 2018.
- [37] D. Cheng, H. Qi, and Y. Zhao, *An Introduction to Semi-Tensor Product of Matrices and Its Applications*, World Scientific, Singapore, 2012.
- [38] T. Akutsu, M. Hayashida, W.-K. Ching, and M. K. Ng, “Control of boolean networks: hardness results and algorithms for tree structured networks,” *Journal of Theoretical Biology*, vol. 244, no. 4, pp. 670–679, 2007.
- [39] D. Cheng, “On finite potential games,” *Automatica*, vol. 50, no. 7, pp. 1793–1801, 2014.
- [40] X. Liu and J. Zhu, “On potential equations of finite games,” *Automatica*, vol. 68, pp. 245–253, 2016.
- [41] H. Li, G. Zhao, M. Meng, and J. Feng, “A survey on applications of semi-tensor product method in engineering,” *Science China Information Sciences*, vol. 61, no. 1, pp. 24–40, 2018.
- [42] D. Cheng and H. Qi, *Semi-Tensor Product of Matrices-Theory and Applications*, Science Publication, Washington, DC, USA, 2nd edition, 2011.



## Research Article

# A Luenberger-Like Observer for Multistable Kapitaniak Chaotic System

**J. Humberto Pérez-Cruz** <sup>1</sup>, **Jacobo Marcos Allende Peña**,<sup>1</sup> **Christian Nwachioma** <sup>1,2</sup>,  
**Jose de Jesus Rubio** <sup>1</sup>, **Jaime Pacheco**,<sup>1</sup> **Jesus Alberto Meda-Campana** <sup>3</sup>,  
**David Ávila-González**,<sup>1</sup> **Olivia Guevara Galindo**,<sup>1</sup> **Ignacio Adrian Romero**,<sup>1</sup>  
and **Salvador Isidro Belmonte Jiménez**<sup>4</sup>

<sup>1</sup>SEPI, ESIME Azcapotzalco, Instituto Politécnico Nacional, Ciudad de México 02250, Mexico

<sup>2</sup>CIDETEC, Instituto Politécnico Nacional, Ciudad de México 07700, Mexico

<sup>3</sup>SEPI, ESIME Zacatenco, Instituto Politécnico Nacional, Ciudad de México 07738, Mexico

<sup>4</sup>CIIDIR-Oaxaca, Instituto Politécnico Nacional, Oaxaca 71230, Mexico

Correspondence should be addressed to J. Humberto Pérez-Cruz; [jhperez@ipn.mx](mailto:jhperez@ipn.mx)

Received 4 January 2020; Revised 6 April 2020; Accepted 1 May 2020; Published 14 July 2020

Guest Editor: Viet-Thanh Pham

Copyright © 2020 J. Humberto Pérez-Cruz et al. This is an open access article distributed under the Creative Commons Attribution License, which permits unrestricted use, distribution, and reproduction in any medium, provided the original work is properly cited.

The objective of this paper is to estimate the unmeasurable variables of a multistable chaotic system using a Luenberger-like observer. First, the observability of the chaotic system is analyzed. Next, a Lipschitz constant is determined on the attractor of this system. Then, the methodology proposed by Raghavan and the result proposed by Thau are used to try to find an observer. Both attempts are unsuccessful. In spite of this, a Luenberger-like observer can still be used based on a proposed gain. The performance of this observer is tested by numerical simulation showing the convergence to zero of the estimation error. Finally, the chaotic system and its observer are implemented using 32-bit microcontrollers. The experimental results confirm good agreement between the responses of the implemented and simulated observers.

## 1. Introduction

Due to the absence or high cost of sensors, some of the variables associated with the dynamics of a system could not be available for measurement. Nevertheless, if the system must be monitored or a state feedback controller implemented, such unmeasurable variables should be estimated. Consequently, an aggregated dynamic system (observation scheme) based on the system model and the measurable states must be incorporated to reconstruct the unavailable variables. In 1996, Luenberger proposed for the first time, an observer and a design methodology for linear systems [1]. Currently, the problem of state estimation for a linear system is well understood, and the solution is well established. However, the nonlinear case is more challenging. For this case, a first proposal of a solution was provided by Thau in [2] in which structure of the

Luenberger observer was applied to Lipschitz nonlinear systems. In this context, the structure is known as the Luenberger-like observer. Based on this observer, Thau presented sufficient conditions to guarantee the asymptotic convergence to zero of the estimation error. However, no design procedure to find the observer gain was provided. In [3], Xia and Gao showed a necessary condition for the existence of an exponential observer. Tsiniias provided sufficient conditions and a simple approach for the observer design [4]. In fact, this approach was a direct extension of the observer design in the linear case. Based on the off-line solution of an algebraic Riccati equation, Raghavan and Hedrick proposed an iterative procedure of observer design for a class of Lipschitz nonlinear systems [5]. In [6–11], different kinds of observers were studied for chaotic systems. The main use of an observer in chaotic systems is for synchronization [12–19].

A chaotic system is a dynamical system with the following properties: (1) high sensitivity to initial conditions, (2) dense periodic orbits, and (3) topological mixing. Consequently, it is impossible to carry out accurate predictions about its long-term dynamic behavior [20–23]. In spite of that, the boundedness of its states can be guaranteed. Chaotic systems can be classified according to the nature of its equilibrium points as (a) no-equilibrium systems; in this kind of systems, there are no real equilibrium points, (b) stable equilibrium systems [24]; in this case, the real parts of all eigenvalues associated with the equilibrium point are negative, (c) line equilibrium systems [25]; there is an infinite number of equilibrium points along a straight line, and (d) curve equilibrium systems; the equilibrium points form a locus such as a circle [26], square [27], and three-leaved clover [28]. All these aforementioned systems belong to the general class of chaotic systems with hidden attractors.

Some chaotic systems have an additional very interesting property: they can have two or more coexisting attractors [29–37]. For the same set of parameters, each attractor can be reached depending on the selected initial condition. Such systems are known as multistable chaotic systems [38–41], and they have received increasing attention during the last decade due to their potential applications [42–44].

In this paper, the attention is focused on the state estimation of a multistable chaotic system proposed by Kapitaniak and coauthors in [45] using a Luenberger-like observer. The system has two attractors for the same set of parameters. The main contribution of this paper is as follows: for the first time, the Kapitaniak system has (a) its basins of attraction thoroughly studied, (b) its observability analyzed, (c) an observer is proposed for it, and (d) the system and its corresponding observer are implemented using 32-bit microcontrollers.

## 2. Multistable Kapitaniak Chaotic System

A three-dimensional chaotic system with a fixed point attractor and a hidden strange attractor was presented in [45]. Each one of these attractors can be reached depending on the selected initial condition. The mathematical model of the system is given as follows:

$$\begin{cases} \dot{x}_1 = x_3, \\ \dot{x}_2 = -x_1 - x_3, \\ \dot{x}_3 = 0.1x_1 + 5x_2 - x_3 + x_1x_2 - 0.3x_1x_3 + 1, \end{cases} \quad (1)$$

where  $x_1, x_2$ , and  $x_3$  are the system's states. By using Wolf's algorithm, the Lyapunov exponents of system (1) can be calculated as  $L_1 = 0.1501, L_2 = 0$ , and  $L_3 = -1.1501$ . As  $L_1 > 0$ , it can be confirmed that system (1) is chaotic. Additionally, the Kaplan–Yorke dimension can be determined as  $D_{KY} = 2.1305$ . By inspection, the equilibrium point is given by  $(0, -0.2, 0)$ . The eigenvalues associated with it are  $\lambda_1 = -0.9835$  and  $\lambda_{2,3} = -0.0082 \pm 2.2547i$ . Thus, it can be concluded that this equilibrium is stable. This equilibrium point can be reached, for example, by taking the initial condition as  $(2, 3, 0)$ . With respect to the strange attractor, this can be reached, for example, by using the initial condition  $(5.4, -1.8, 3.3)$  (see [45]). The projections of this attractor on  $x_1 - x_2, x_2 - x_3$ , and  $x_1 - x_3$  planes are presented in Figure 1.

The attractor was obtained by simulation of equation (1) using Simulink® with solver ode45 (Dormand–Prince), relative tolerance  $1e-6$ , absolute tolerance  $1e-7$ , start time 0, and stop time 500 sec. If the stop time is increased to 1,000,000 sec, it can be determined that the chaotic states of system (1) belong to the following set:

$$\Omega = \{(x_1, x_2, x_3) \mid x_1 \in [-4.9150, 10.8287], x_2 \in [-5.3136, 13.7184], x_3 \in [-14.6249, 22.3794]\}. \quad (2)$$

Thus, the following bounds for  $x_1, x_2$ , and  $x_3$  can be established:

$$\begin{cases} |x_1| \leq x_{1, \max} = 11, \\ |x_2| \leq x_{2, \max} = 14, \\ |x_3| \leq x_{3, \max} = 22.5. \end{cases} \quad (3)$$

Finally, it is important to mention that system (1) can briefly be represented as

$$\dot{\mathbf{x}} = \mathbf{A}\mathbf{x} + \mathbf{f}(\mathbf{x}), \quad (4)$$

where

$$\begin{aligned} \mathbf{x} &:= [x_1 \ x_2 \ x_3]^T, \\ \mathbf{A} &:= \begin{bmatrix} 0 & 0 & 1 \\ -1 & 0 & -1 \\ 0.1 & 5 & -1 \end{bmatrix}, \\ \mathbf{f}(\mathbf{x}) &:= \begin{bmatrix} 0 \\ 0 \\ x_1x_2 - 0.3x_1x_3 + 1 \end{bmatrix}. \end{aligned} \quad (5)$$

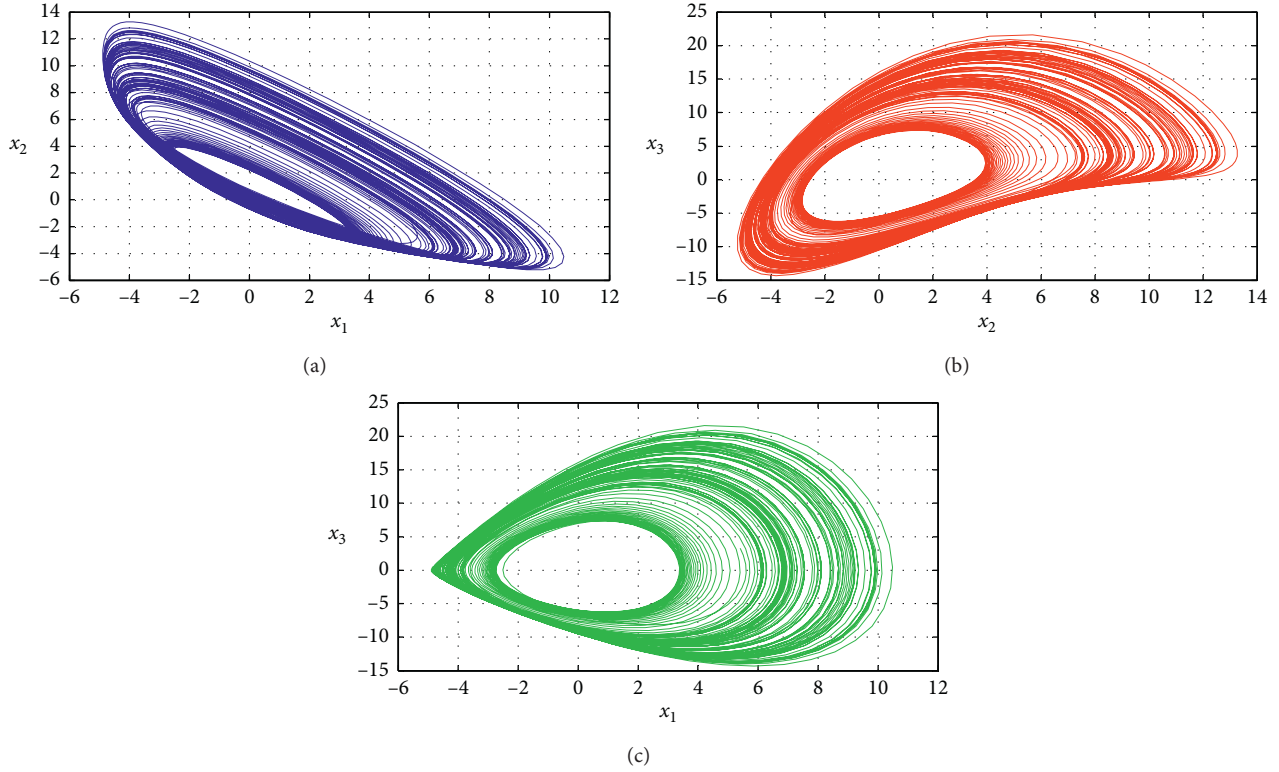


FIGURE 1: Projections of the strange attractor of system (1) with the initial condition  $(5.4, -1.8, 3.3)$ : (a)  $x_1 - x_2$  phase plane, (b)  $x_2 - x_3$  phase plane, and (c)  $x_1 - x_3$  phase plane.

### 3. Basin of Attraction

The basin of attraction of an attractor comprises the set of points in the state space that leads to the attractor [46, 47]. The current system (1) has two attractors including a fixed point attractor and a chaotic hidden strange attractor. The basin of attraction of both attractors is shown in Figure 2 on the  $x_1 - x_2$  plane (Figure 2(a)) and on the  $x_1 - x_3$  plane (Figure 2(b)). In the first case, the plane is chosen such that  $x_3 = 0$ . Orbits are started at every pixel in a region of interest and followed until they return to the Poincare section or diverge to infinity, and the corresponding initial point is colored accordingly: red, if it identifies the chaotic attractor, light green, if it identifies the fixed point attractor, and white, otherwise. Similarly, for completeness, we choose the plane containing the equilibrium  $x_2 = -0.2$  and perform similar operations as before. The resultant basin of attraction can be appreciated, as shown in Figure 2(b).

Moreover, it is important to classify and quantify the basin of attraction based on the work reported in [48]. According to the results, a probability function considered at large distances is the basis for classifying and quantifying chaotic attractors' basins. The function at large distances, has power law scaling:

$$P(r) = \frac{P_0}{r^\gamma}, \quad (6)$$

where  $P(r)$  is the probability that an initial condition at a distance  $r$  from the attractor lies within the basin of attraction, and  $P_0$  and  $\gamma$  are the classification and

quantification parameters. Based on these parameters, the basin of a chaotic system can be grouped into one of four classes [48]. As Figure 3 shows, system (1) has a class 3 fractal basin with noninteger power law scaling. The basin of attraction of the chaotic attractor extends to infinity, but since the codimension of the basin is almost 2, the basin most likely has a narrow width.

### 4. Problem Formulation

Let us focus on the case when not all the states of system (1) are available for measurement because the corresponding sensors do not exist or they are very expensive. In this case, we can represent system (4) as

$$\begin{cases} \dot{\mathbf{x}} = \mathbf{Ax} + \mathbf{f}(\mathbf{x}), \\ \mathbf{y} = \mathbf{Cx}, \end{cases} \quad (7)$$

where  $\mathbf{y}$  is the output vector and  $\mathbf{C}$  is the constant output matrix with appropriate dimension. Throughout this work, we consider that the output is simply given by

$$y = x_1. \quad (8)$$

This means that

$$\mathbf{C} = [1 \ 0 \ 0]. \quad (9)$$

To reproduce the unavailable states  $x_2$  and  $x_3$ , we need to use a dynamic system known as an observer. For the linear case, Luenberger proposed a well-known structure of an observer. For the nonlinear case, we could use a

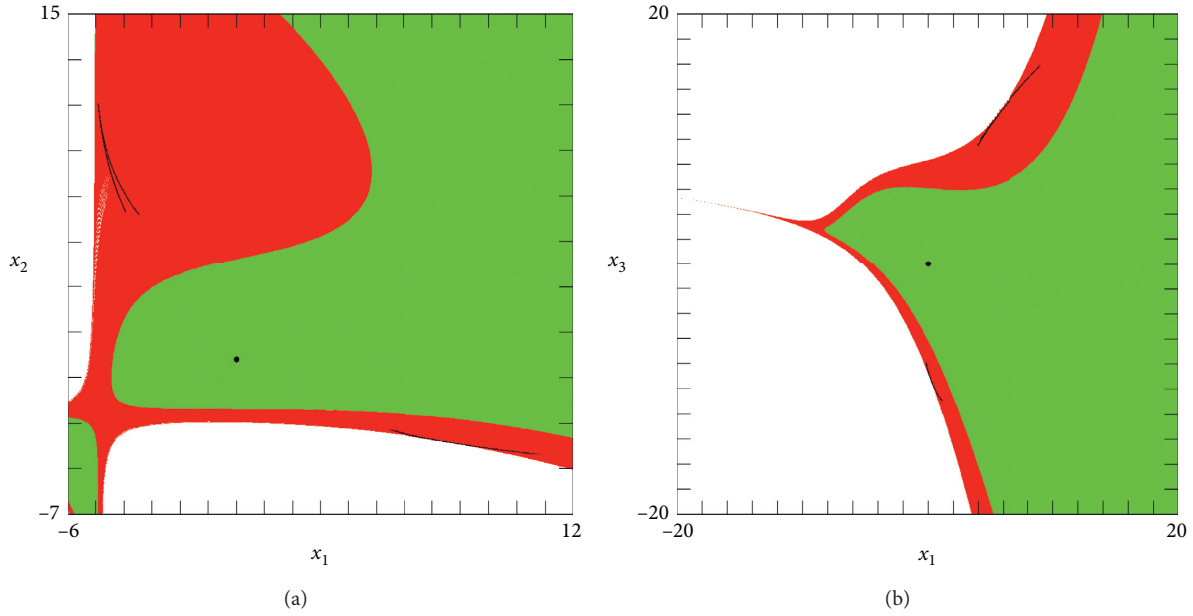


FIGURE 2: Basin of attraction of the chaotic system (1) viewed along the plane  $x_3 = 0$  (a) and along the plane  $x_2 = -0.2$  (b).

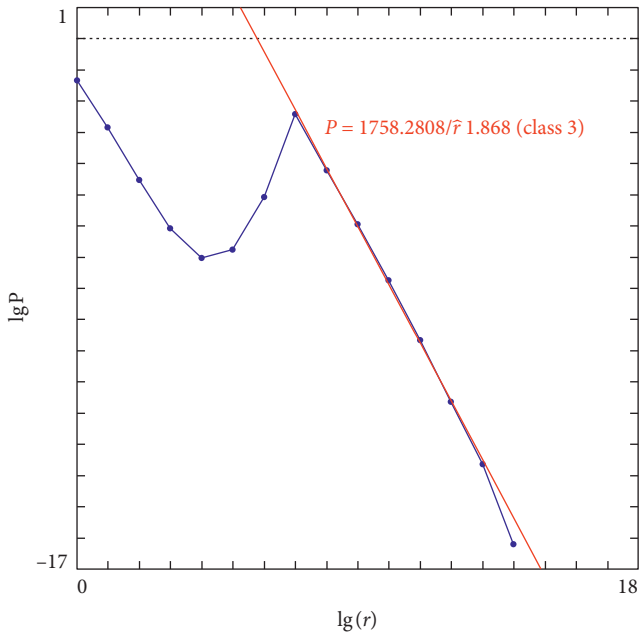


FIGURE 3: The chaotic system (1) has a class 3 fractal basin that extends to infinity and with a noninteger power law scaling.

generalization of this structure called the Luenberger-like observer. For system (7), this observer is given by

$$\begin{cases} \dot{\hat{\mathbf{x}}} = \mathbf{A}\hat{\mathbf{x}} + \mathbf{f}(\hat{\mathbf{x}}) + \mathbf{L}(\mathbf{y} - \hat{\mathbf{y}}), \\ \hat{\mathbf{y}} = \mathbf{C}\hat{\mathbf{x}}, \end{cases} \quad (10)$$

where  $\hat{\mathbf{x}}$  is the observer's state and  $\mathbf{L}$  is a constant gain matrix. The Luenberger-like observer is formed by the model of the original system (with the true state  $\mathbf{x}$  replaced by the estimated state  $\hat{\mathbf{x}}$ ), plus a linear correction term.

The difference between the states of the observer (10) and the system (7) is called the estimation error which is defined as

$$\mathbf{e} := \mathbf{x} - \hat{\mathbf{x}}. \quad (11)$$

The problem of state estimation consists of finding an appropriate gain matrix  $\mathbf{L}$  in such a way that  $\lim_{t \rightarrow \infty} \mathbf{e} = \mathbf{0}$ , that is,  $\mathbf{e}$  converges asymptotically to zero.

### 5. Observability Analysis

Before attempting to find the observer gain, or in general, to use any observation scheme, a fundamental question must be resolved. That is, what are the conditions under which the reconstruction problem of the unmeasurable states of a system has a solution?

*Definition 1* (see [49, 50]). System (7) is said to be observable over the time interval  $[t_0, t_1], t_1 > t_0$ , if the knowledge of the output  $\mathbf{y}$  over  $[t_0, t_1]$  suffices to uniquely determine the initial state  $\mathbf{x}(t_0)$  completely.

The observability analysis for linear systems is a well-understood problem. However, the case for nonlinear systems is subtler and more complicated. Results on the observability of nonlinear systems are discussed in [51] and references therein. In this work, these results are summarized for an unforced system with a unique output like system (7).

Consider the extended output vector as

$$\mathbf{Y} = \begin{bmatrix} \mathbf{y} \\ \dot{\mathbf{y}} \\ \ddot{\mathbf{y}} \end{bmatrix}. \quad (12)$$

The observability matrix for the nonlinear case is defined as

$$\mathbf{Q} = \frac{\partial \mathbf{Y}}{\partial \mathbf{x}}. \quad (13)$$

**Corollary 1** (see [50]). *System (7) is locally observable in a neighbourhood of the point  $\mathbf{x}$  at time  $t$ , if*

$$\det(\mathbf{Q}) \neq 0. \quad (14)$$

*Remark 1.* Although the Kalman condition for observability of linear systems is necessary and sufficient, condition expressed in (14) is only sufficient.

To begin with the observability analysis for system (7), the extended output vector is calculated as

$$\mathbf{Y} = \begin{bmatrix} y \\ \dot{y} \\ \ddot{y} \end{bmatrix} = \begin{bmatrix} x_1 \\ \dot{x}_1 \\ \ddot{x}_1 \end{bmatrix} = \begin{bmatrix} x_1 \\ x_3 \\ 0.1x_1 + 5x_2 - x_3 + x_1x_2 - 0.3x_1x_3 + 1 \end{bmatrix}. \quad (15)$$

Next, the observability matrix can be determined as

$$\mathbf{Q} = \frac{\partial \mathbf{Y}}{\partial \mathbf{x}} = \begin{bmatrix} 1 & 0 & 0 \\ 0 & 0 & 1 \\ 0.1 + x_2 - 0.3x_3 & 5 + x_1 & -1 - 0.3x_1 \end{bmatrix}. \quad (16)$$

It is easy to show that

$$\det(\mathbf{Q}) = -5 - x_1. \quad (17)$$

Thus, system (7) loses its observability only when  $x_1 = -5$ .

## 6. Raghavan Observer

In this section, observer gain  $\mathbf{L}$  is tried to be determined using the Raghavan procedure. First, the Lipschitz constant of system (7) must be found.

$$\bar{\Omega} = \{(x_1, x_2, x_3) \mid |x_1| \leq x_{1,\max} = 11, |x_2| \leq x_{2,\max} = 14, |x_3| \leq x_{3,\max} = 22.5\}. \quad (21)$$

Thus,  $\mathbf{F}$  is a matrix whose elements are the maximum absolute values of each corresponding element in the Jacobian matrix (19) on the set  $\bar{\Omega}$ . Next,  $\mathbf{F}$  can be determined as

$$\mathbf{F} = \begin{bmatrix} 0 & 0 & 0 \\ 0 & 0 & 0 \\ 20.75 & 11 & 3.3 \end{bmatrix}. \quad (22)$$

Finally, the Lipschitz constant for  $\mathbf{f}$  on the set  $\bar{\Omega}$  is given by

$$\gamma = \|\mathbf{F}\| = 23.7161, \quad (23)$$

where  $\|\mathbf{F}\|$  denotes the two-norm of  $\mathbf{F}$ , that is,  $\|\mathbf{F}\| = \sqrt{\lambda_{\max}(\mathbf{F}^T \mathbf{F})}$ , and  $\lambda_{\max}(\mathbf{F}^T \mathbf{F})$  denotes the maximum eigenvalue of  $\mathbf{F}^T \mathbf{F}$ .

### 6.1. Lipschitz Constant Determination

*Definition 2* (see [49, 52]). A function  $\mathbf{f}(\mathbf{x}): \mathfrak{R}^n \rightarrow \mathfrak{R}^n$  is said to be locally Lipschitz on  $\Omega \subset \mathfrak{R}^n$  if there exists a constant  $\gamma$  (known as the Lipschitz constant) such that for all  $\mathbf{x}_1, \mathbf{x}_2 \in \Omega$ , the following inequality holds:

$$\|\mathbf{f}(\mathbf{x}_1) - \mathbf{f}(\mathbf{x}_2)\| \leq \gamma \|\mathbf{x}_1 - \mathbf{x}_2\|. \quad (18)$$

Finally,  $\mathbf{f}$  is said to be globally Lipschitz if it satisfies (18) with  $\Omega = \mathfrak{R}^n$ .

**Lemma 1** (see [49, 52]). *If a function  $\mathbf{f}: \mathfrak{R}^n \rightarrow \mathfrak{R}^n$  is continuously differentiable on a set  $\Omega \subset \mathfrak{R}^n$ , then it is locally Lipschitz on  $\Omega$ .*

Taking into account Lemma 1, Khalil [52] proposed a procedure to calculate the Lipschitz constant  $\gamma$  [53]. Although this procedure produces conservative results, it is enough for the purpose of this work. First, for the function  $\mathbf{f}$  given in (5), let us calculate its Jacobian matrix as

$$\frac{\partial \mathbf{f}(\mathbf{x})}{\partial \mathbf{x}} = \begin{bmatrix} 0 & 0 & 0 \\ 0 & 0 & 0 \\ x_2 - 0.3x_3 & x_1 & -0.3x_1 \end{bmatrix}. \quad (19)$$

Let us define the matrix  $\mathbf{F}$  as

$$\mathbf{F} = \max_{\mathbf{x} \in \bar{\Omega}} \left| \frac{\partial \mathbf{f}}{\partial \mathbf{x}} \right|, \quad (20)$$

where

*6.2. Raghavan Design Procedure.* The procedure proposed by Raghavan is based on the following result.

**Theorem 1** (see [5]). *Given system (7) and its observer (10), if there exists  $\varepsilon > 0$  such that the following algebraic Riccati equation (ARE) has a symmetric, positive definite solution  $\mathbf{P}$ :*

$$\mathbf{A}\mathbf{P} + \mathbf{P}\mathbf{A}^T + \mathbf{P}\left(\gamma^2 \mathbf{I} - \frac{1}{\varepsilon} \mathbf{C}^T \mathbf{C}\right)\mathbf{P} + \mathbf{I} + \varepsilon \mathbf{I} = \mathbf{0}, \quad (24)$$

*then, by selecting the observer gain as  $\mathbf{L} = (1/2\varepsilon)\mathbf{P}\mathbf{C}^T$ , the estimation error  $\mathbf{e} = \mathbf{x} - \hat{\mathbf{x}}$  converges asymptotically to zero for all  $\mathbf{f}$  with a Lipschitz constant  $\gamma$ .*

*Remark 2.* A necessary condition for the existence of a symmetric, positive definite solution  $\mathbf{P}$  is that the pair  $(\mathbf{A}, \mathbf{C})$  be detectable.



Let us apply Algorithm 1 to our problem. We must verify that  $(\mathbf{A}, \mathbf{C})$  is detectable. Let us define the observability matrix  $\mathbf{O}$  using (6) and (9) as

$$\mathbf{O} = \begin{bmatrix} \mathbf{C} \\ \mathbf{CA} \\ \mathbf{CA}^2 \end{bmatrix} = \begin{bmatrix} 1 & 0 & 0 \\ 0 & 0 & 1 \\ 0.1 & 5 & -1 \end{bmatrix}. \quad (25)$$

The rank of  $\mathbf{O}$  is 3, that is, the pair  $(\mathbf{A}, \mathbf{C})$  is observable, a stronger condition than detectability. Now, by setting  $\varepsilon = 10.9227$ , we use Algorithm 1 implemented in Matlab<sup>®</sup> with command “are” for the solution of equation (24). The algorithm gives a result until the 14th iteration when  $\varepsilon = 1/1500$ . With this value, the corresponding solution of equation (24) is

$$\mathbf{P} = \begin{bmatrix} 0.0326 & 0.0003 & 0.0000 \\ -0.0015 & 0.0002 & -0.0419 \\ -0.0012 & 0.0425 & 0.0016 \end{bmatrix}. \quad (26)$$

However, as can be easily verified,  $\mathbf{P}$  is not a symmetric matrix. Besides, smaller values for  $\varepsilon$  do not produce a symmetric matrix either. Thus, the algorithm has failed.

**6.3. Scaling of System.** If Algorithm 1 does not work, a possible solution could be to scale the chaotic system (1).

Consider the variables  $z_1$ ,  $z_2$ , and  $z_3$  defined as

$$\begin{cases} z_1 = \frac{x_1}{k_1}, \\ z_2 = \frac{x_2}{k_2}, \\ z_3 = \frac{x_3}{k_3}, \end{cases} \quad (27)$$

where  $k_1$ ,  $k_2$ , and  $k_3$  are the positive constants. By taking the first derivative of (27) with respect to time and substituting (1), after some algebraic operations, can be found that

$$\begin{cases} \dot{z}_1 = \frac{k_3 z_3}{k_1}, \\ \dot{z}_2 = \frac{k_1}{k_2} z_1 - \frac{k_3}{k_2} z_3, \\ \dot{z}_3 = 0.1 \frac{k_1}{k_3} z_1 + 5 \frac{k_2}{k_3} z_2 - z_3 + \frac{k_1 k_2}{k_3} z_1 z_2 - 0.3 k_1 z_1 z_3 + \frac{1}{k_3}. \end{cases} \quad (28)$$

Succinctly, system (28) can be represented as

$$\begin{cases} \dot{\mathbf{z}} = \bar{\mathbf{A}}\mathbf{z} + \bar{\mathbf{f}}(\mathbf{z}), \\ \bar{\mathbf{y}}_1 = \mathbf{C}\mathbf{z}, \end{cases} \quad (29)$$

where

$$\mathbf{z} := [z_1 \ z_2 \ z_3]^T,$$

$$\bar{\mathbf{A}} := \begin{bmatrix} 0 & 0 & \frac{k_3}{k_1} \\ \frac{k_1}{k_2} & 0 & \frac{k_3}{k_2} \\ 0.1 \frac{k_1}{k_3} & 5 \frac{k_2}{k_3} & -1 \end{bmatrix}, \quad (30)$$

$$\bar{\mathbf{f}}(\mathbf{z}) := \begin{bmatrix} 0 \\ 0 \\ \frac{k_1 k_2}{k_3} z_1 z_2 - 0.3 k_1 z_1 z_3 + \frac{1}{k_3} \end{bmatrix},$$

and  $\bar{\mathbf{y}}_1$  is the output of system (29), that is,  $\bar{\mathbf{y}}_1 = z_1$ .

To find the Lipschitz constant of scaled system (29), the Jacobian matrix of  $\bar{\mathbf{f}}$  is determined as

$$\frac{\partial \bar{\mathbf{f}}(\mathbf{z})}{\partial \mathbf{z}} = \begin{bmatrix} 0 & 0 & 0 \\ 0 & 0 & 0 \\ \frac{k_1 k_2}{k_3} z_2 - 0.3 k_1 z_3 & \frac{k_1 k_2}{k_3} z_1 & -0.3 k_1 z_1 \end{bmatrix}, \quad (31)$$

and the matrix  $\mathbf{F}$  for (31), that is,  $\bar{\mathbf{F}}$ , is given by

$$\bar{\mathbf{F}} = \begin{bmatrix} 0 & 0 & 0 \\ 0 & 0 & 0 \\ \frac{k_1}{k_3} 14 + 0.3 \frac{k_1}{k_3} 22.5 & \frac{k_2}{k_3} 11 & 3.3 \end{bmatrix}. \quad (32)$$

Thus, the scaled Lipschitz constant can be calculated as

$$\bar{\gamma} = \|\bar{\mathbf{F}}\|. \quad (33)$$

To try to find a positive result for Algorithm 1, it is important to reduce  $\bar{\gamma}$ . This can be achieved by reducing  $k_1$  and  $k_2$  and increasing  $k_3$ . The minimum value for  $\bar{\gamma}$  is 3.3. Although different values for  $k_1$ ,  $k_2$ ,  $k_3$ , and  $\varepsilon$  are tested, Algorithm 1 does not work on the scaled system (28). Thus, it can be inferred that there does not exist a Raghavan observer for Kapitaniak system (1).

## 7. Thau Observer

In [2], Thau provided a sufficient condition to guarantee the asymptotic convergence to zero of the estimation error. However, a systematic procedure of design was not provided. That is, to use this result, first, the user must propose a value of gain for the observer by trial and error.

Step 1. Set  $\varepsilon$  to a positive value.  
 Step 2. Solve ARE (24).  
 Step 3. If  $\mathbf{P}$  is symmetric and positive definite, then  $\mathbf{L} = (1/2\varepsilon)\mathbf{P}\mathbf{C}^T$  and the process is terminated.  
 Step 4. If not, set  $\varepsilon = \varepsilon/2$ , and go to Step 2. If  $\varepsilon$  is below some precision value, abandon the method.

ALGORITHM 1: Procedure to obtain the observer gain [5].

**Theorem 2** (see [2, 49]). *Given system (7), the corresponding observer (10), a symmetric positive definite matrix  $\mathbf{Q}_1$ , and an observer gain  $\mathbf{L}$ , proposed by the user, such that  $\mathbf{A} - \mathbf{L}\mathbf{C}$  is Hurwitz, if the following Lyapunov equation:*

$$(\mathbf{A} - \mathbf{L}\mathbf{C})^T \mathbf{P}_1 + \mathbf{P}_1 (\mathbf{A} - \mathbf{L}\mathbf{C}) = -\mathbf{Q}_1, \quad (34)$$

has a symmetric positive definite solution  $\mathbf{P}_1$  which satisfies the following inequality:

$$\gamma < \frac{\lambda_{\min}(\mathbf{Q}_1)}{2\lambda_{\max}(\mathbf{P}_1)}, \quad (35)$$

where  $\lambda_{\min}(\mathbf{Q}_1)$  and  $\lambda_{\max}(\mathbf{P}_1)$  are the minimum eigenvalues of  $\mathbf{Q}_1$  and the maximum eigenvalue of  $\mathbf{P}_1$ , respectively; then, the estimation error  $\mathbf{e}$  converges asymptotically to zero.

It should be noted that relation in (35) can be increased if the minimum eigenvalue of  $\mathbf{Q}_1$  is increased and/or the maximum eigenvalue of  $\mathbf{P}_1$  is reduced. According to [54, 55], the ratio in (35) can be maximized if  $\mathbf{Q}_1 = \mathbf{I}$ . To apply Theorem 2 to our problem, several values for the gain observer  $\mathbf{L}$  are proposed. In spite of the exhaustive search, the inequality (35) cannot be satisfied. In this case, the scaled system (28) is considered. Several combinations of values for  $k_1$ ,  $k_2$ ,  $k_3$ , and observer gain are tested. However, attempts are again unsuccessful. Thus, it can be inferred that the Thau observer does not exist for Kapitaniak system (1).

## 8. Luenberger-Like Observer

In spite of the negative results of the previous sections, it is important to take into account that Theorems 1 and 2 provide only sufficient conditions. If these conditions are not satisfied, this does not mean the nonexistence of the Luenberger-like observer. In fact, in this section, the existence of a Luenberger-like observer (10) for Kapitaniak chaotic system (1) is verified by numerical simulation. Consider the following value for the observer gain  $\mathbf{L}$ :

$$\mathbf{L} = \begin{bmatrix} 24.4844 \\ -1.0968 \\ -0.9137 \end{bmatrix}. \quad (36)$$

Once the gain  $\mathbf{L}$  has been proposed, the observer (10) can easily be simulated. Models for the chaotic system (7) and for the corresponding observer (10) are built on Simulink<sup>®</sup>. The initial condition for the chaotic system is again (5.4, -1.8, 3.3) as in Section 2. As the states are not available, it is reasonable to propose the initial condition of the observer simply as (0, 0, 0). For a fair comparison with respect to the experimental results of the following section, the simulation is

accomplished using solver ode4 (Runge–Kutta) with a fixed step size of 0.0004 sec, a start time 0, and a stop time 10 sec. In Figure 4, the observation process is shown, whereas in Figure 5, the signal of the estimation error  $\mathbf{e}$  is presented.

As can be appreciated from Figure 5, the estimation error converges asymptotically to zero.

## 9. Microcontroller Implementation and Experimental Results

The implementation is accomplished using two Teensy USB Development Board based on the 72 MHz Cortex-M4 3.3 V signal microcontroller. The chaotic system (7) is implemented on the first board, whereas the corresponding Luenberger-like observer (10) is implemented on the second board. A block diagram of this implementation is shown in Figure 6.

Both systems are implemented using solver ode4 (Runge–Kutta) with a fixed step size of 0.0004 sec. Since the observer requires signal  $x_1$  as an input, a unidirectional communication between the microcontrollers must be set. The communication is achieved using an analog to digital conversion based on PWM and a digital to analog converter built on the microcontroller. The following process is accomplished: (1) the first microcontroller with the chaotic system provides the states  $x_1, x_2$ , and  $x_3$ , (2) the states are sent by the PWM port (10-bit resolution and 5 Mhz frequency), and also the states are scaled, (3) the PWM signals go to a low-pass RC filter with a cutoff frequency of 30 Hz, (4) the output of this filter is taken by an analog to digital converter of the second microcontroller. This converter has a 10-bit resolution and a sample frequency of 5 MHz, (5) the digital signal is scaled to the original range, (6) the second microcontroller with the Luenberger-like observer produces the states  $\hat{x}_1, \hat{x}_2$ , and  $\hat{x}_3$ , (7) the observer states are scaled, (8) these states are sent to the PWM port, and (9) such signals go to a second low-pass filter. The states of the chaotic systems and the states of the observer are sent by serial communication to a computer for visualization (see Figure 7). At the same time, the outputs of both low-pass filters are sent to an oscilloscope to verify the measurements.

To facilitate the implementation process and the reproduction of our results, the pseudocodes for the master microcontroller and the slave microcontroller are as follows:

Pseudocode of the master microcontroller:

```
BEGIN
Initial conditions of states
define step time
```

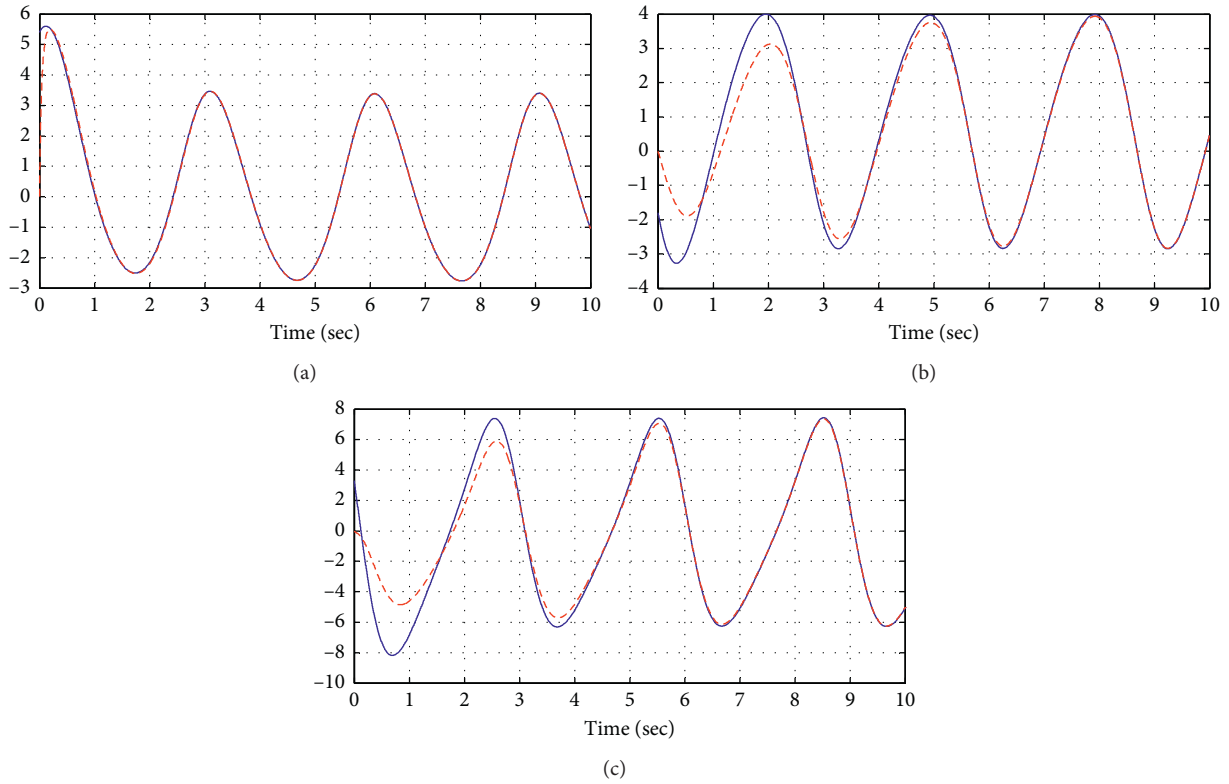


FIGURE 4: Observation process (true state, solid line; estimated state, dashed line) for (a)  $x_1$  and  $\hat{x}_1$ , (b)  $x_2$  and  $\hat{x}_2$ , and (c)  $x_3$  and  $\hat{x}_3$ .

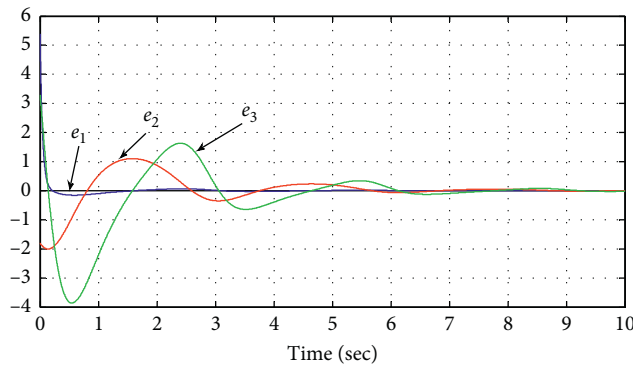


FIGURE 5: Time evolution of the estimation error  $e$ .

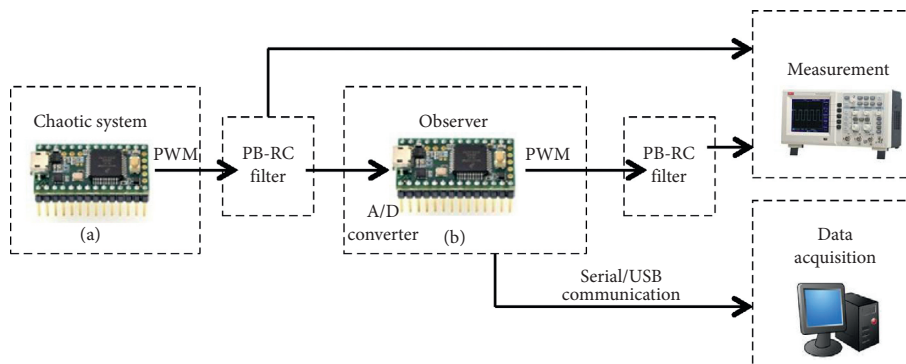


FIGURE 6: Block diagram of the implementation.

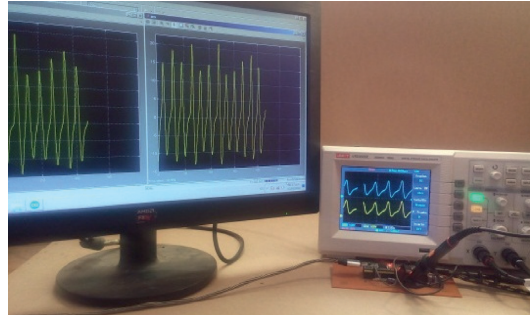
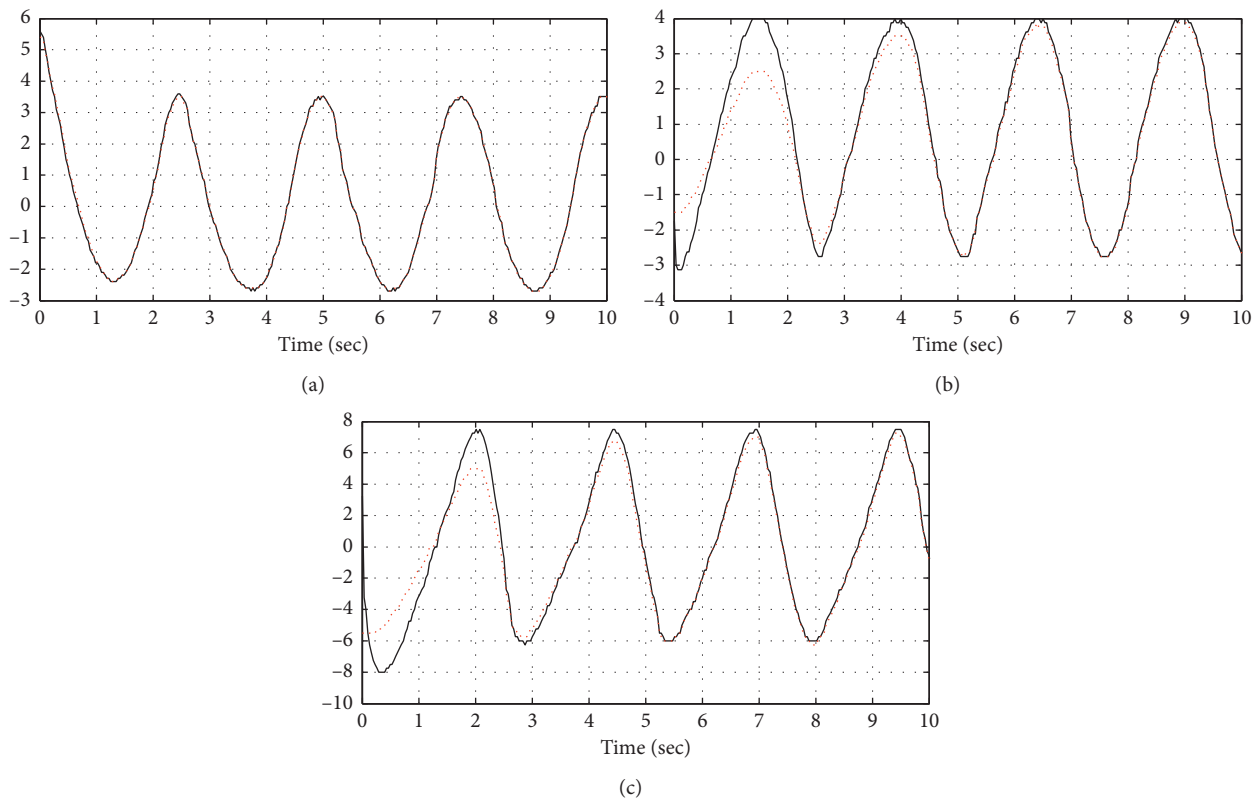


FIGURE 7: Data visualization on the computer screen.

FIGURE 8: Observation process for the implemented systems (true state, solid line; estimated state, dashed line) for (a)  $x_1$  and  $\hat{x}_1$ , (b)  $x_2$  and  $\hat{x}_2$ , and (c)  $x_3$  and  $\hat{x}_3$ .

```
main loop function ()
```

```
{
```

```
Calculate states through the Runge-Kutta method
```

```
{ x1
```

```
  x2
```

```
  x3
```

```
}
```

Applied offset to states of the original system to get positives values in the PWM port and the scale factor for distributing the values in all range of the PWM port

```
Sx1 = (x1 + offset)* scale factor
```

```
Sx2 = (x2 + offset)* scale factor
```

```
Sx3 = (x3 + offset)* scale factor
```

```
Send values through the PWM port
```

```
PWM output ← (Sx1)
```

```
PWM output ← (Sx2)
```

```
PWM output ← (Sx3)
```

```
Calculate time delay for the sample time
```

```
}
```

Pseudocode of the observer microcontroller:

```
BEGIN
```

```
Initial conditions of states
```

```
define step time
```

```
main loop function ()
```

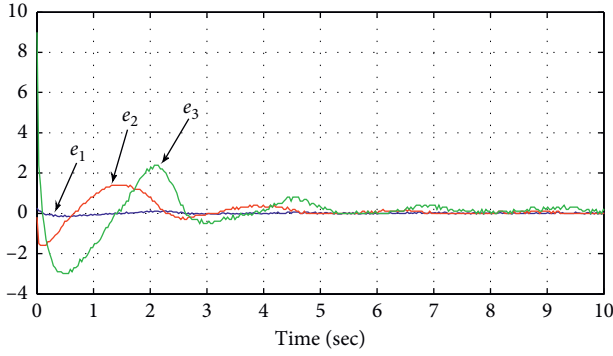


FIGURE 9: Time evolution of the estimation error  $e$  for the implemented systems.

```

{
  Read values of the real system through the analog to
  digital converter and remove the offset and the scale
  factor
   $x1_r \leftarrow (\text{analog input}/\text{scale factor})-\text{offset}$ 
   $x2_r \leftarrow (\text{analog input}/\text{scale factor})-\text{offset}$ 
   $x3_r \leftarrow (\text{analog input}/\text{scale factor})-\text{offset}$ 
  Calculate observer states, using the  $x1_r$  state and the
  Runge–Kutta method
  {  $x1_O$ 
     $x2_O$ 
     $x3_O$ 
  }
  Calculate error between the real or original system and
  the observer system
  Applied offset to observer states to get positives values
  in the PWM port and the scale factor for distributing
  the values in all range of the PWM port
   $Sx1_O = (x1_O + \text{offset}) * \text{scale factor}$ 
   $Sx2_O = (x2_O + \text{offset}) * \text{scale factor}$ 
   $Sx3_O = (x3_O + \text{offset}) * \text{scale factor}$ 
  Send values through the PWM port
  PWM output  $\leftarrow (Sx1_O)$ 
  PWM output  $\leftarrow (Sx2_O)$ 
  PWM output  $\leftarrow (Sx3_O)$ 
  Send states of real system, states of observer system, and
  error of systems through the serial/USB port
  Calculate time delay for the sample time
}

```

In Figures 8 and 9, the experimental results are presented. The observation process is shown in Figure 8 for the first states, second states, and third states, respectively, of the implemented systems. Finally, the estimation error between the implemented chaotic system and the implemented observer can be appreciated in Figure 9.

## Data Availability

The experimental microcontroller data used to support this study are available from the second author upon request to the e-mail: jacobmarcoap@gmail.com.

## Conflicts of Interest

The authors declare that there are no conflicts of interest regarding the publication of this paper.

## Acknowledgments

The authors are very grateful to Dr. J. C. Sprott for his invaluable help. Figures 2 and 3 are courtesy of him. This work was financed by SIP, Instituto Politécnico Nacional, under Grant (20200083). The authors also acknowledge the support of EDI-IPN and SNI-Conacyt.

## References

- [1] D. G. Luenberger, "Observers for multivariable systems," *IEEE Transactions on Automatic Control*, vol. 11, no. 2, 1966.
- [2] F. E. Thau, "Observing the state of non-linear dynamic systems," *International Journal of Control*, vol. 17, no. 3, pp. 471–479, 1973.
- [3] X.-h. Xia and W.-b. Gao, "On exponential observers for nonlinear systems," *Systems & Control Letters*, vol. 11, no. 4, pp. 319–325, 1988.
- [4] J. Tsiniias, "Observer design for nonlinear systems," *Systems & Control Letters*, vol. 13, no. 2, pp. 135–142, 1989.
- [5] S. Raghavan and J. K. Hedrick, "Observer design for a class of nonlinear systems," *International Journal of Control*, vol. 59, no. 2, pp. 515–528, 1994.
- [6] H. R. Sabouhi, A. A. Gharaveisi, S. M. R. Rafiei, and S. M. A. Mohammadi, "Design of A Novel sliding mode observer for chaotic systems," in *Proceedings of the World Congress on Engineering 2008*, pp. 1–6, London, UK, July 2008.
- [7] R. Aguilar-López and J. L. Mata-Machuca, "A new finite-time observer for nonlinear systems: applications to synchronization of lorenz-like systems," *The Scientific World Journal*, vol. 2016, Article ID 8342089, 7 pages, 2016.
- [8] S. Vaidyanathan, "Nonlinear observer design for chaotic systems," in *Studies in Computational Intelligence*, pp. 19–41, Springer-Verlag, Berlin, Germany, 2016.
- [9] H. Saadaoui, M. Djemai, N. Manamanni, and J. P. Barbot, "Observer for hybrid chaotic systems," *IFAC Proceedings Volumes*, vol. 39, no. 8, pp. 166–171, 2006.
- [10] S. Vaidyanathan, "Nonlinear observer design for population biology systems," in *Studies in Computational Intelligence*, pp. 43–57, Springer-Verlag, Berlin, Germany, 2016.
- [11] L. Moysis, C. Volos, V.-T. Pham et al., "Analysis of a chaotic system with line equilibrium and its application to secure communications using a descriptor observer," *Technologies*, vol. 7, pp. 1–16, 2019.
- [12] T. Youssef, M. Chadli, H. R. Karimi, and M. Zelmat, "Chaos synchronization based on unknown input proportional multiple-integral fuzzy observer," *Abstract and Applied Analysis*, vol. 2013, 2013.



- [13] S. Beyhan, "Runge-Kutta model-based nonlinear observer for synchronization and control of chaotic systems," *ISA Transactions*, vol. 52, no. 4, pp. 501–509, 2013.
- [14] Ö. Morgül and E. Solak, "Observer based synchronization of chaotic systems," *Physical Review E: Statistical Physics, Plasmas, Fluids, and Related Interdisciplinary Topics*, vol. 54, no. 5, 1996.
- [15] S. Čelikovský and G. Chen, "Secure synchronization of a class of chaotic systems from a nonlinear observer approach," *IEEE Transactions on Automatic Control*, vol. 50, no. 1, 2005.
- [16] M. Chen, Q. Wu, and C. Jiang, "Disturbance-observer-based robust synchronization control of uncertain chaotic systems," *Nonlinear Dynamics*, vol. 70, pp. 2421–2432, 2012.
- [17] M. Boutayeb, M. Darouach, and H. Rafaralahy, "Generalized state-space observers for chaotic synchronization and secure communication," *IEEE Transactions on Circuits and Systems I: Fundamental Theory and Applications*, vol. 49, no. 3, 2002.
- [18] Y. Zhao, X. Li, and P. Duan, "Observer-based sliding mode control for synchronization of delayed chaotic neural networks with unknown disturbance," *Neural Networks*, vol. 117, pp. 268–273, 2019.
- [19] Z. Cheng, G. Xue, C. Wang, and Q. Chen, "Adaptive chaos synchronization control of nonlinear PMSM system using extended state observer," *Mathematical Problems in Engineering*, vol. 2016, Article ID 3976586, 10 pages, 2016.
- [20] J. H. Pérez-Cruz, E. A. Portilla-Flores, P. A. Niño-Suárez, and R. Rivera-Blas, "Design of a nonlinear controller and its intelligent optimization for exponential synchronization of a new chaotic system," *Optik*, vol. 130, pp. 201–212, 2017.
- [21] Y.-j. Xian, C. Xia, T.-t. Guo, K.-r. Fu, and C.-b. Xu, "Dynamical analysis and FPGA implementation of a large range chaotic system with coexisting attractors," *Results in Physics*, vol. 11, pp. 368–376, 2018.
- [22] P. Zhou and M. Ke, "A new 3D autonomous continuous system with two isolated chaotic attractors and its topological horseshoes," *Complexity*, vol. 2017, Article ID 4037682, 7 pages, 2017.
- [23] L. Xiong, Y. Lu, Y. Zhang, and X. Zhang, "A novel memductor-based chaotic system and its applications in circuit design and experimental validation," *Complexity*, vol. 2019, Article ID 3870327, 17 pages, 2019.
- [24] X. Wang, V.-T. Pham, S. Jafari, C. Volos, J. M. Munoz-Pacheco, and E. Tlelo-Cuautle, "A new chaotic system with stable equilibrium: from theoretical model to circuit implementation," *IEEE Access*, vol. 5, pp. 8851–8858, 2017.
- [25] S. Jafari and J. C. Sprott, "Simple chaotic flows with a line equilibrium," *Chaos, Solitons & Fractals*, vol. 57, pp. 79–84, 2013.
- [26] T. Gotthans and J. Petřžela, "New class of chaotic systems with circular equilibrium," *Nonlinear Dynamics*, vol. 81, pp. 1143–1149, 2015.
- [27] T. Gotthans, J. C. Sprott, and J. Petřžela, "Simple chaotic flow with circle and square equilibrium," *International Journal of Bifurcation and Chaos*, vol. 26, no. 8, Article ID 1650137, 2016.
- [28] S. Mobayen, C. K. Volos, S. Kaçar, and Ü. Çavuşoğlu, "New class of chaotic systems with equilibrium points like a three-leaved clover," *Nonlinear Dynamics*, vol. 91, pp. 939–956, 2018.
- [29] S. Jafari, K. Rajagopal, T. Hayat, A. Alsaedi, and V. T. Pham, "Simplest megastable chaotic oscillator," *International Journal of Bifurcation and Chaos in Applied Sciences and Engineering*, vol. 29, 2019.
- [30] A. Sambas, S. Vaidyanathan, S. Zhang, Y. Zeng, M. A. Mohamed, and M. Mamat, "A new double-wing chaotic system with coexisting attractors and line equilibrium: bifurcation analysis and electronic circuit simulation," *IEEE Access*, vol. 7, pp. 115454–115462, 2019.
- [31] K. Rajagopal, S. Jafari, A. Akgul, A. Karthikeyan, S. Çiçek, and Y. Shekofteh, "A simple snap oscillator with coexisting attractors, its time-delayed form, physical realization, and communication designs," *Zeitschrift Fur Naturforschung A*, vol. 73, no. 5, 2018.
- [32] K. Rajagopal, A. Akgul, V. T. Pham et al., "Multistability and coexisting attractors in a new circulant chaotic system," *International Journal of Bifurcation and Chaos in Applied Sciences and Engineering*, vol. 29, 2019.
- [33] A. N. Pisarchik and B. K. Goswami, "Annihilation of one of the coexisting attractors in a bistable system," *Physical Review Letters*, vol. 84, no. 7, 2000.
- [34] A. Sambas, S. Vaidyanathan, E. Tlelo-Cuautle et al., "A novel chaotic system with two circles of equilibrium points: multistability, electronic circuit and fpga realization," *Electron*, vol. 8, no. 11, p. 1211, 2019.
- [35] N. V. Kuznetsov and G. A. Leonov, "Hidden attractors in dynamical systems: systems with no equilibria, multistability and coexisting attractors," *IFAC Proceedings Volumes*, vol. 47, no. 3, pp. 5445–5454, 2014.
- [36] Q. Lai, T. Nestor, J. Kengne, and X.-W. Zhao, "Coexisting attractors and circuit implementation of a new 4D chaotic system with two equilibria," *Chaos, Solitons & Fractals*, vol. 107, pp. 92–102, 2018.
- [37] Y. Tang, H. R. Abdolmohammadi, A. J. M. Khalaf, Y. Tian, and T. Kapitaniak, "Carpet oscillator: a new megastable nonlinear oscillator with infinite islands of self-excited and hidden attractors," *Pramana*, vol. 91, 2018.
- [38] B. C. Bao, H. Bao, N. Wang, M. Chen, and Q. Xu, "Hidden extreme multistability in memristive hyperchaotic system," *Chaos, Solitons and Fractals*, vol. 94, pp. 102–111, 2017.
- [39] A. N. Pisarchik and U. Feudel, "Control of multistability," *Physics Reports*, vol. 540, no. 4, pp. 167–218, 2014.
- [40] C. Li, W. Hu, J. C. Sprott, and X. Wang, "Multistability in symmetric chaotic systems," *The European Physical Journal Special Topics*, vol. 224, no. 8, pp. 1493–1506, 2015.
- [41] J. C. Sprott, S. Jafari, A. J. M. Khalaf, and T. Kapitaniak, "Megastability: coexistence of a countable infinity of nested attractors in a periodically-forced oscillator with spatially-periodic damping," *The European Physical Journal Special Topics*, vol. 226, pp. 1979–1985, 2017.
- [42] A. Ahmadi, K. Rajagopal, F. E. Alsaadi, V. T. Pham, F. E. Alsaadi, and S. Jafari, "A novel 5D chaotic system with extreme multi-stability and a line of equilibrium and its engineering applications: circuit design and FPGA implementation," *Iranian Journal of Science and Technology, Transactions of Electrical Engineering*, vol. 44, pp. 59–67, 2019.
- [43] C. Li, F. Min, Q. Jin, and H. Ma, "Extreme multistability analysis of memristor-based chaotic system and its application in image decryption," *AIP Advances*, vol. 7, no. 12, 2017.
- [44] A. Sambas, S. Vaidyanathan, S. Zhang, W. T. Putra, M. Mamat, and M. A. Mohamed, "Multistability in a novel chaotic system with perpendicular lines of equilibrium: analysis, adaptive synchronization and circuit design," *Engineering Letters*, vol. 27, no. 4, pp. 1–8, 2019.
- [45] T. Kapitaniak, S. A. Mohammadi, S. Mekhilef, F. E. Alsaadi, T. Hayat, and V. T. Pham, "A new chaotic system with stable equilibrium: entropy analysis, parameter estimation, and circuit design," *Entropy*, vol. 20, 2018.
- [46] P. Brzeski, J. Wojewoda, T. Kapitaniak, J. Kurths, and P. Perlikowski, "Sample-based approach can outperform the

- classical dynamical analysis - experimental confirmation of the basin stability method,” *Scientific Reports*, vol. 7, 2017.
- [47] D. Dudkowski, K. Czołczyński, and T. Kapitaniak, “Multi-stability and basin stability in coupled pendulum clocks,” *Chaos*, vol. 29, 2019.
- [48] J. C. Sprott and A. Xiong, “Classifying and quantifying basins of attraction,” *Chaos*, vol. 25, no. 8, 2015.
- [49] H. Márquez, *Nonlinear Control Systems: Analysis and Design*, Wiley-Interscience, Hoboken, NJ, USA, 1st edition, 2003.
- [50] J. H. Pérez-Cruz, J. S. Benítez-Read, and A. Poznyak, “On the observability of the point kinetic equations of a nuclear reactor,” in *Proceedings of the International Atomic Energy Agency (IAEA)*, México, Mexico, July 2007.
- [51] A. Poznyak, “Deterministic output noise effects in sliding mode observation,” in *Variable Structure Systems: from Principles to Implementation*, pp. 45–80, IET Publications, London, UK, 2011.
- [52] H. K. Khalil, *Nonlinear Systems*, Prentice. Hall, Upper Saddle River, NJ, USA, 3rd edition, 2002.
- [53] J. H. Pérez-Cruz, P. A. Tamayo-Meza, M. Figueroa et al., “Exponential synchronization of chaotic xian system using linear feedback control,” *Complexity*, vol. 2019, Article ID 4706491, 10 pages, 2019.
- [54] R. V. Patel and M. Toda, “Quantitative measures of robustness for multivariable systems,” in *Proceedings of the Joint Automatic Control Conference*, San Francisco, CA, USA, 1980.
- [55] R. Rajamani, “Observers for Lipschitz nonlinear systems,” *IEEE Transactions on Automatic Control*, vol. 43, no. 3, 1998.

## Research Article

# A Fractional-Order Discrete Noninvertible Map of Cubic Type: Dynamics, Control, and Synchronization

Xiaojun Liu <sup>1</sup>, Ling Hong <sup>2</sup>, Lixin Yang <sup>3</sup>, and Dafeng Tang<sup>4</sup>

<sup>1</sup>School of Sciences, Xi'an University of Posts and Telecommunications, Xi'an 710061, China

<sup>2</sup>State Key Laboratory for Strength and Vibration of Mechanical Structures, Xi'an Jiaotong University, Xi'an 710049, China

<sup>3</sup>School of Arts and Sciences, Shaanxi University of Science and Technology, Xi'an 710021, China

<sup>4</sup>School of Automation, Xi'an University of Posts and Telecommunications, Xi'an 710061, China

Correspondence should be addressed to Xiaojun Liu; flybett3952@126.com

Received 6 December 2019; Revised 24 February 2020; Accepted 1 April 2020; Published 22 May 2020

Guest Editor: Viet-Thanh Pham

Copyright © 2020 Xiaojun Liu et al. This is an open access article distributed under the Creative Commons Attribution License, which permits unrestricted use, distribution, and reproduction in any medium, provided the original work is properly cited.

In this paper, a new fractional-order discrete noninvertible map of cubic type is presented. Firstly, the stability of the equilibrium points for the map is examined. Secondly, the dynamics of the map with two different initial conditions is studied by numerical simulation when a parameter or a derivative order is varied. A series of attractors are displayed in various forms of periodic and chaotic ones. Furthermore, bifurcations with the simultaneous variation of both a parameter and the order are also analyzed in the three-dimensional space. Interior crises are found in the map as a parameter or an order varies. Thirdly, based on the stability theory of fractional-order discrete maps, a stabilization controller is proposed to control the chaos of the map and the asymptotic convergence of the state variables is determined. Finally, the synchronization between the proposed map and a fractional-order discrete Lorenz map is investigated. Numerical simulations are used to verify the effectiveness of the designed synchronization controllers.

## 1. Introduction

In the recent several decades, chaos is an attractive phenomenon in nonlinear dynamical systems, which has been extensively analyzed and studied deeply. It is well known that chaos was first detected in continuous nonlinear systems. Its characteristics and the existence in discrete dynamical maps have also been the interesting topics. Many discrete maps with chaotic attractors have been proposed, such as the Logistic map, Hénon map, and Lozi map [1–5]. With the rapid development of fractional calculus, many works including chaos, control, and synchronization for fractional-order continuous systems have been reported [6–18]. It should be pointed out that the fractional discrete maps were not paid enough attention and properly explored until recently [19].

In 1974, Diaz and Olser first put forward the fractional difference [20]. Up to now, fractional-order discrete maps have obtained more and more attention. In [21], a discrete

fractional Hénon map was introduced, and its chaotic behavior was discussed. Dynamics, stabilization, and synchronization for several fractional-order maps, such as the Ikeda map, Lorenz map, and Lozi map, were studied in [22–28]. The discrete fractional calculus can avoid the tedious information or calculation error of the numerical discretization for the continuous ones due to the nonlocal property [29]. Therefore, more and more discrete maps with fractional operators need to be presented, and more abundant and complex dynamics behaviors need to be explored. Besides, it is well known that fractional-order discrete maps are sensitive not only to the small disturbance of parameters and initial conditions but also to the variation of fractional orders [30], which are the unique advantages of fractional-order systems. For this reason, a fractional-order discrete map is more suitable for data encryption and secure communications. Furthermore, fractional-order discrete maps have simple forms and rich dynamics, which are good for system analysis and numerical computation. Based on

these, investigation of a new fractional-order discrete map including dynamics, stabilization, and synchronization is necessary and important for the development of fractional calculus.

In [31, 32], a two-dimensional noninvertible map with cubic order nonlinearity, which was taken as a chaotic cryptosystem, was proposed and studied. The evolution of attractors and their basins have been analyzed deeply and explained thoroughly. A noncyclic chaotic attractor for the map was displayed in [33]. Based on these, we extend the map to the fractional case and study its dynamics. The stability of the equilibrium points for the map is examined. By the bifurcation graphs and phase diagrams, the dynamics of the fractional-order discrete map with two different initial conditions is displayed as a parameter or a derivative order varies. Furthermore, bifurcations with the simultaneous variation of both a parameter and the order are also analyzed in the three-dimensional space. Interior crises occur in the map with the variation of a parameter or the order.

The main motivation of our work is to know whether bifurcations and chaos, which the integer-order discrete map possesses, also exist in the fractional-order counterpart. In fact, these dynamics behaviors do exist in the fractional-order map, and multifaceted complex dynamics is observed by means of the numerical simulations. For a chaotic system, control and synchronization are very important for its application in practical problems. In our work, we are also interested in studying the control and synchronization for the fractional-order map. Based on the stability theory of fractional-order discrete maps, a stabilization controller is proposed to control the chaos of the map. The synchronization between the proposed map and a fractional-order discrete Loren map is studied and realized.

## 2. Discrete Fractional Calculus

In this section, we will recall the definition and related theories for the discrete fractional calculus. In the following, the symbol  ${}^C\Delta_a^\nu X(t)$  represents the  $\nu$  order Caputo type delta fractional calculus of a function  $X(t): N_a \rightarrow R$  with  $N_a = \{a, a+1, a+2, \dots\}$  [34], which is expressed as follows:

$${}^C\Delta_a^\nu X(t) = \Delta_a^{-(n-\nu)} X(t) = \frac{1}{\Gamma(n-\nu)} \sum_{s=a}^{t-(n-\nu)} (t-s-1)^{(n-\nu-1)} \Delta^n X(s), \quad (1)$$

where  $\nu \notin N$  is the order,  $t \in N_{a+n-\nu}$ , and  $n = \lceil \nu \rceil + 1$ . In formula (1), the  $\nu$ th fractional sum of  $\Delta_s^n X(t)$  is defined as [35, 36]

$$\Delta_a^{-\nu} X(t) = \frac{1}{\Gamma(\nu)} \sum_{s=a}^{t-\nu} (t-s-1)^{(\nu-1)} X(s), \quad (2)$$

where  $t \in N_{a+\nu}$ ,  $\nu > 0$ .  $t^{(\nu)}$  represents the falling function which is defined according to the Gamma function  $\Gamma$  as

$$t^{(\nu)} = \frac{\Gamma(t+1)}{\Gamma(t+1-\nu)}. \quad (3)$$

Generally speaking, the following method is employed to compute the numerical solutions for a fractional-order discrete map.

$$\begin{cases} {}^C\Delta_a^\nu u(t) = f(t+\nu-1, u(t+\nu-1)), \\ \Delta^k u(a) = u_k, n = \lceil \nu \rceil + 1, \quad k = 0, 1, 2, \dots, n-1, \end{cases} \quad (4)$$

the equivalent discrete integral one is

$$u(t) = u_0(t) + \frac{1}{\Gamma(\nu)} \sum_{s=a+n-\nu}^{t-\nu} (t-s-1)^{(\nu-1)} f(s+\nu-1, u(s+\nu-1)), \quad t \in N_{a+n}, \quad (5)$$

where  $u_0(t) = \sum_{k=0}^{n-1} ((t-a)^{(k)}/\Gamma(k+1)) \Delta^k u(a)$ .

The following theorem is used to analyze the stabilization and synchronization for fractional discrete maps. For the proof of the theorem, please refer to the literature [37].

**Theorem 1.** *The zero equilibrium of a linear fractional discrete system:*

$${}^C\Delta_a^\nu X(t) = \mathbf{M}X(t+\nu-1), \quad (6)$$

where  $X(t) = (x_1(t), x_2(t), \dots, x_n(t))^T$ ,  $0 < \nu \leq 1$ ,  $\mathbf{M} \in R^{n \times n}$  and  $\forall t \in N_{a+1-\nu}$ , is asymptotically stable if

$$|\lambda_i| < \left( 2 \cos \frac{|\arg \lambda_i| - \pi}{2 - \nu} \right)^\nu, \quad (7)$$

$$|\arg \lambda_i| > \frac{\nu\pi}{2}, \quad i = 1, 2, \dots, n,$$

for all the eigenvalues  $\lambda$  of  $\mathbf{M}$ .

## 3. A Fractional-Order Discrete Map

**3.1. Description of the Map.** Firstly, the two-dimensional discrete map with cubic nonlinearity in [31–33] is described as follows:

$$\begin{cases} x(n+1) = y(n), \\ y(n+1) = b(-x^3(n) + x(n)) + c(-y^3(n) + y(n)), \end{cases} \quad (8)$$

where  $x(n)$  and  $y(n)$  are the state variables and  $b$  and  $c$  parameters. The first-order difference of (8) is formulated as

$$\begin{cases} x(n+1) = y(n) - x(n), \\ y(n+1) = b(-x^3(n) + x(n)) + c(-y^3(n) + y(n)) - y(n). \end{cases} \quad (9)$$

By employing the Caputo-like delta difference given in (1) with the starting point  $a$ , the corresponding fractional map is

$$\begin{cases} {}^C\Delta_a^\nu x(t) = y(t-1+\nu) - x(t-1+\nu), \\ {}^C\Delta_a^\nu y(t) = b(-x^3(t-1+\nu) + x(t-1+\nu)) + c(-y^3(t-1+\nu) + y(t-1+\nu)) - y(t-1+\nu). \end{cases} \quad (10)$$

Based on equations (4) and (5), we can obtain

$$\begin{cases} x(t) = x(a) + \frac{1}{\Gamma(\nu)} \sum_{s=a+1}^{t-\nu} (t-s-1)^{(\nu-1)} (y(t-1+\nu) - x(t-1+\nu)), \\ y(t) = y(a) + \frac{1}{\Gamma(\nu)} \sum_{s=a+1}^{t-\nu} (t-s-1)^{(\nu-1)} (b(-x(t-1+\nu)^3 + x(t-1+\nu)) \\ + c(-y(t-1+\nu)^3 + y(t-1+\nu)) - y(t-1+\nu)), \end{cases} \quad (11)$$

where  $(t-s-1)^{(\nu-1)}/\Gamma(\nu)$  is the discrete kernel function and  $((t-s-1)^{(\nu-1)}/\Gamma(\nu)) = (\Gamma(t-s)/(\Gamma(\nu)\Gamma(t-s-\nu+1)))$ .

Based on this, the numerical solution for the fractional discrete map (10) can be obtained, which is as follows:

$$\begin{cases} x(n) = x(a) + \frac{1}{\Gamma(\nu)} \sum_{j=1}^n \frac{\Gamma(n-j+\nu)}{\Gamma(n-j+1)} (y(j-1) - x(j-1)), \\ y(n) = y(a) + \frac{1}{\Gamma(\nu)} \sum_{j=1}^n \frac{\Gamma(n-j+\nu)}{\Gamma(n-j+1)} (b(-x^3(j-1) + x(j-1)) + c(-y^3(j-1) + y(j-1)) - y(j-1)). \end{cases} \quad (12)$$

In the rest of the paper, the low limit  $a$  is fixed as 0.

**3.2. Stability of Equilibrium Points.** Now, we turn to study the stability of equilibrium points for map (10). By the simple computation, we can get the three equilibrium points:

$$\begin{aligned} E_1(0, 0), \\ E_{2,3} \left( \pm \sqrt{1 - \frac{1}{b+c}}, \pm \sqrt{1 - \frac{1}{b+c}} \right), \end{aligned} \quad (13)$$

when  $b+c > 1$ . The map has only one equilibrium point  $E_1(0, 0)$  when  $b+c \leq 1$ . The Jacobian matrix of map (10) evaluated at an equilibrium point  $E_* = (x^*, y^*)$  is

$$J_1 = \begin{bmatrix} -1 & 1 \\ b(-3x^* + 1) & c(-3y^* + 1) - 1 \end{bmatrix}. \quad (14)$$

The corresponding eigenvalues for the equilibrium point  $E_1(0, 0)$  are  $\lambda_{1,2} = (c/2) \pm (\sqrt{4b+c^2}/2)$ . In this paper, we only consider the case of map (10) with positive parameters.

Therefore, the zero equilibrium point  $E_1$  is unstable due to  $|\arg \lambda_1| = 0 < (\nu\pi/2)$  on the basis of Theorem 1.

For a fractional-order discrete map, the stability of a zero equilibrium point can be determined easily based on Theorem 1. Therefore, we will use a very simple method proposed in [38] for handling with the nonzero equilibrium points. For more special details about the method, please refer to Remark 2.5 in the literature [38].

In order to analyze the stability of the nonzero equilibrium points  $E_{2,3}$ , let  $x_2 = \sqrt{1 - (1/(b+c))}$ ,  $y_2 = \sqrt{1 - (1/(b+c))}$ ,  $x_3 = -\sqrt{1 - (1/(b+c))}$ , and  $y_3 = -\sqrt{1 - (1/(b+c))}$ . Through the following variable transforms,

$$\begin{cases} z_{21}(t-1+\nu) = x(t-1+\nu) - x_2, \\ z_{22}(t-1+\nu) = y(t-1+\nu) - y_2, \\ z_{31}(t-1+\nu) = x(t-1+\nu) - x_3, \\ z_{32}(t-1+\nu) = y(t-1+\nu) - y_3, \end{cases} \quad (15)$$

we can get two newly maps with a zero equilibrium point:



$$\begin{cases} {}^C\Delta_a^v(z_{21}(t) + x_2) = {}^C\Delta_a^v z_{21}(t) = z_{22}(t-1+v) + y_2 - z_{21}(t-1+v) - x_2, \\ {}^C\Delta_a^v(z_{22}(t) + y_2) = {}^C\Delta_a^v z_{22}(t) = b(-(z_{21}(t-1+v) + x_2)^3 + z_{21}(t-1+v) + x_2) \\ + c(-(z_{22}(t-1+v) + y_2)^3 + z_{22}(t-1+v) + y_2) - z_{22}(t-1+v) - y_2, \end{cases} \quad (16)$$

$$\begin{cases} {}^C\Delta_a^v(z_{31}(t) + x_3) = {}^C\Delta_a^v z_{31}(t) = z_{32}(t-1+v) + y_3 - z_{31}(t-1+v) - x_3, \\ {}^C\Delta_a^v(z_{32}(t) + y_3) = {}^C\Delta_a^v z_{32}(t) = b(-(z_{31}(t-1+v) + x_3)^3 + z_{31}(t-1+v) + x_3) \\ + c(-(z_{32}(t-1+v) + y_3)^3 + z_{32}(t-1+v) + y_3) - z_{32}(t-1+v) - y_3, \end{cases} \quad (17)$$

which are corresponding to  $E_{2,3}$ , respectively. The Jacobian matrix of maps (16) and (17) evaluated at the zero equilibrium point is

$$\begin{aligned} J_2 &= \begin{bmatrix} -1 & 1 \\ -3bx_2^2 + b & -3cy_2^2 + c - 1 \end{bmatrix} \\ &= \begin{bmatrix} -1 & 1 \\ -3bx_3^2 + b & -3cy_3^2 + c - 1 \end{bmatrix}. \end{aligned} \quad (18)$$

The corresponding eigenvalues of  $J_2$  for the zero equilibrium point are

$$\lambda_{3,4} = \frac{2b - c \pm \sqrt{-(2b + 2c - 3)(4b^2 - 2bc^2 + 4bc - 2c^3 + 3c^2)} + 2bc + 2c^2}{2(b + c)}. \quad (19)$$

When the parameters of map (10) are chosen as  $b = 2.2$  and  $c = 0.95$  and the order is taken as  $v = 0.98$ , the corresponding eigenvalues are  $\lambda_{3,4} = -1.4976 \pm 1.4343i$ . By simple computation, we can obtain

$$\begin{aligned} |\arg \lambda_i| &= 2.3788 > \frac{v\pi}{2} = 1.5379, \quad i = 3, 4, \\ |\lambda_i| &= 2.0736 > \left(2 \cos \frac{|\arg \lambda_i| - \pi}{2 - v}\right)^v = 1.4538, \quad i = 3, 4, \end{aligned} \quad (20)$$

which means the equilibrium point  $E_{2,3}$  is unstable in this case according to Theorem 1.

#### 4. Dynamics Analysis

In this section, the dynamics of the fractional-order discrete map (10) with the variation of a parameter or the fractional order and the bifurcations with the simultaneous variation of both a parameter and the order  $v$  will be analyzed in detail.

**4.1. Dynamics as the Parameter  $b$  Varies.** When the order  $v = 0.98$  and parameter  $c = 0.95$ , the dynamics of map (10) with the variation of the parameter  $b$  is analyzed. The bifurcation diagrams and the corresponding largest Lyapunov exponents (LLE) spectrums with two different initial conditions  $x_{01} = (0.8, -0.4)$  and  $x_{02} = (0.8, 0.4)$  are displayed in Figure 1. From which we can see that the dynamics of the

map is abundant and shows a symmetry with different initial conditions in this case.

The evolution of the trajectories for different  $b$  with  $x_{01}$  is depicted in Figure 2. In the phase plane, there is a fixed point which means the map is period-1 for  $b = 1$  (Figures 2(a) and 2(b)). The map has a limit cycle attractor for  $b = 1.5$ , see Figure 2(c), which means a Hopf bifurcation occurs as the parameter  $b$  increases from 1 to 1.5. The shape of the limit cycle changes as  $b$  increases further (Figures 2(d) and 2(e)). The map keeps chaotic when  $b$  varies from 1.75 to 2.2. In Figure 2(g), three small chaotic attractors appear in the phase plane when  $b = 1.9$  and convert to one large attractor when  $b = 1.95$  (Figure 2(h)). From Figures 2(i) and 2(j), we can see that the chaotic attractor becomes a large one suddenly, which implies that an interior crisis occurs as  $b$  increases from 2 to 2.2.

The dynamics of the map with the initial condition  $x_{02}$ , which is similar to Figure 2, is displayed in Figure 3. From the global dynamics perspective, the two chaotic attractors, which are depicted in Figures 2(i) and 3(i), collide with each other and convert to a large one (Figures 2(j) and 3(j)).

**4.2. Dynamics as the Parameter  $c$  Varies.** The fractional order  $v$  is fixed as 0.98 and the parameter  $b = 2.2$ , and the dynamics of map (10) when  $c$  is varied in the interval of  $[0.2, 1]$  with two initial conditions  $x_{01}$  and  $x_{02}$  are studied. Firstly, the bifurcation diagrams and the corresponding LLE spectrums with  $x_{01}$  and  $x_{02}$  are plotted in Figure 4. From

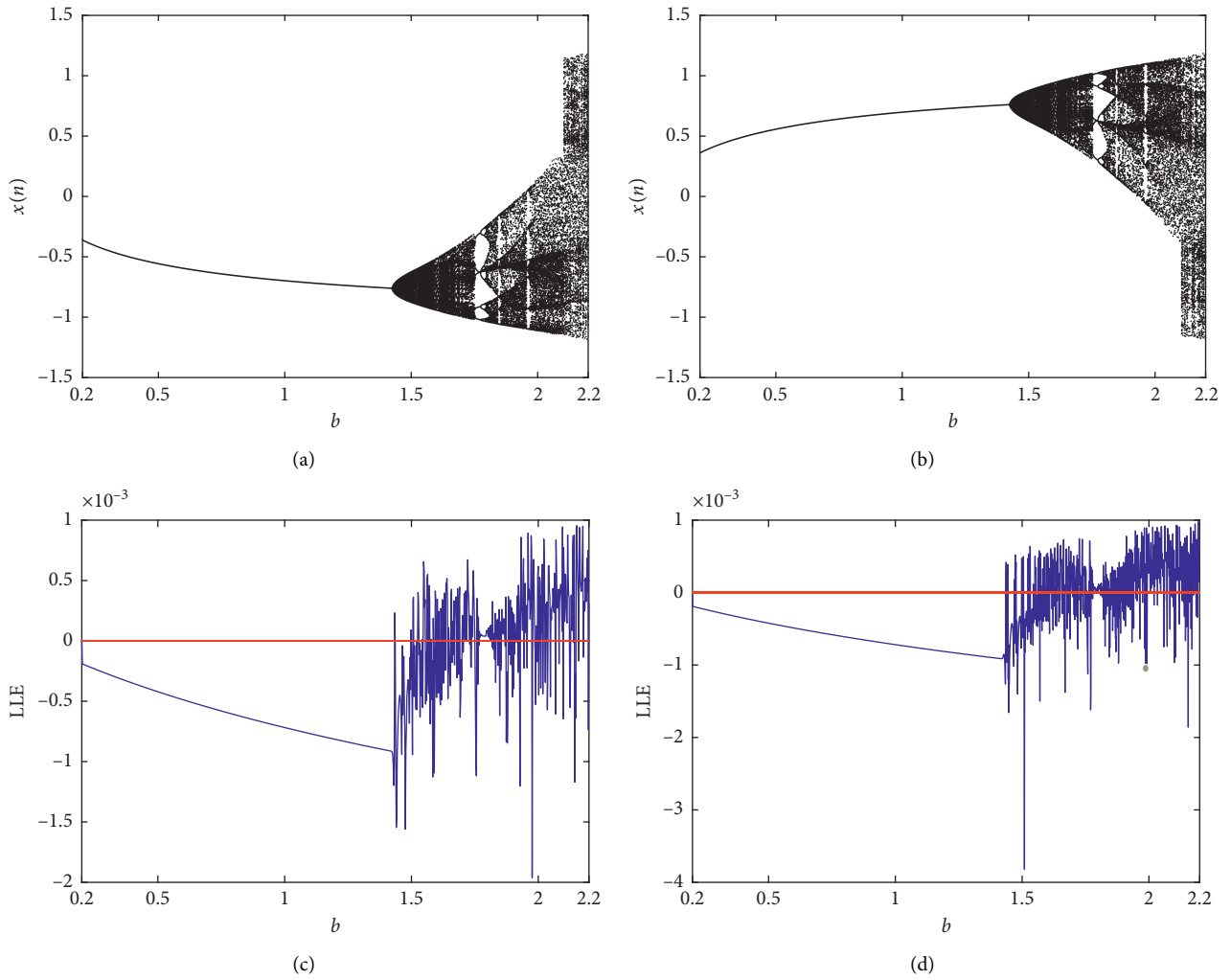


FIGURE 1: Bifurcation diagrams and corresponding LLE spectra for the map with different initial values as the parameter  $b$  varies: (a) the bifurcation diagram with  $x_{01}$ , (b) the bifurcation diagram with  $x_{02}$ , (c) the LLE spectrum with  $x_{01}$ , and (d) the LLE spectrum with  $x_{02}$ .

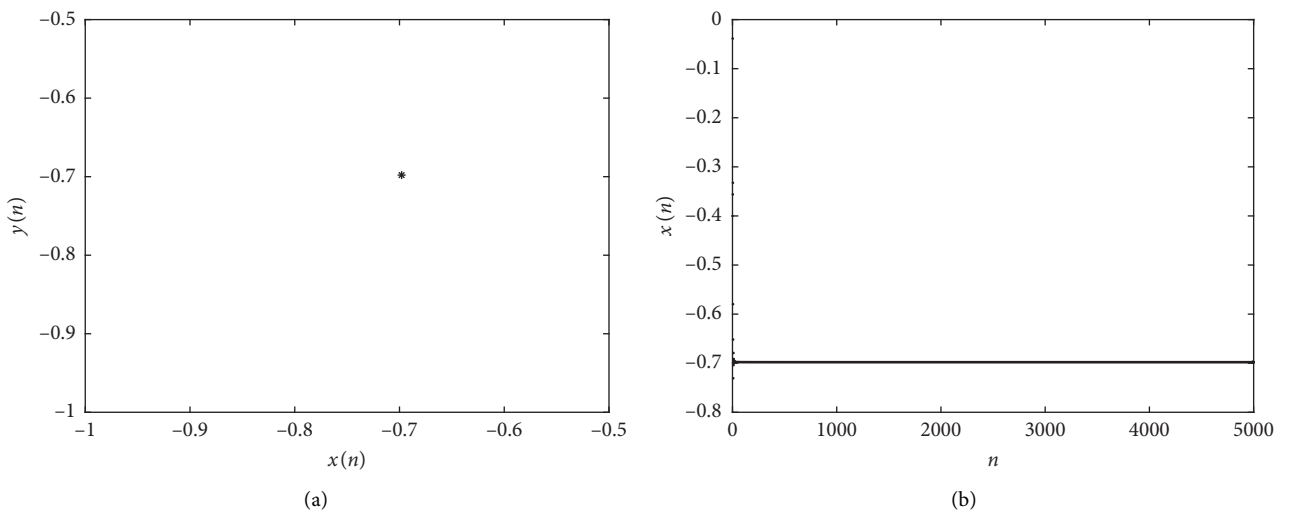


FIGURE 2: Continued.

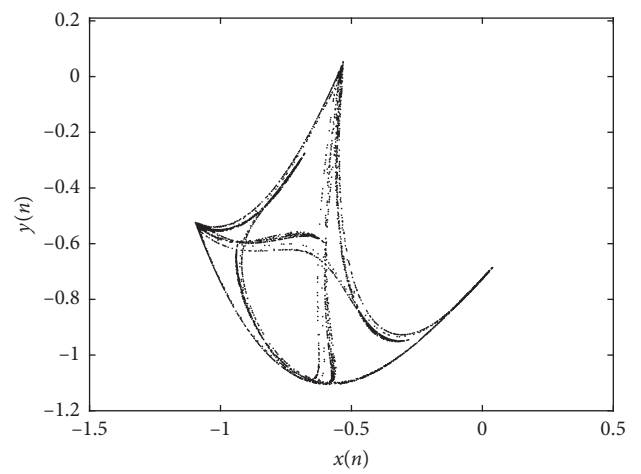
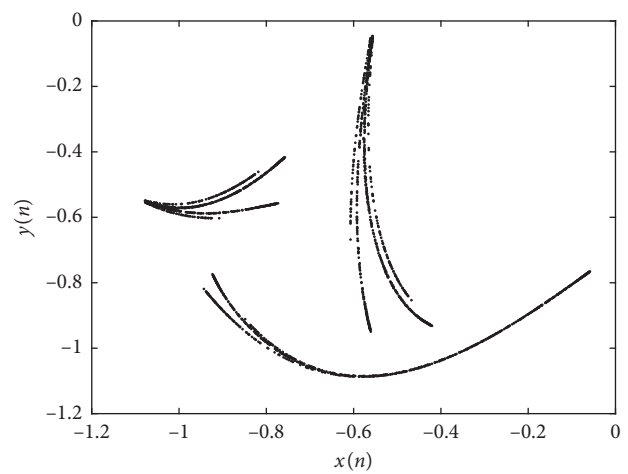
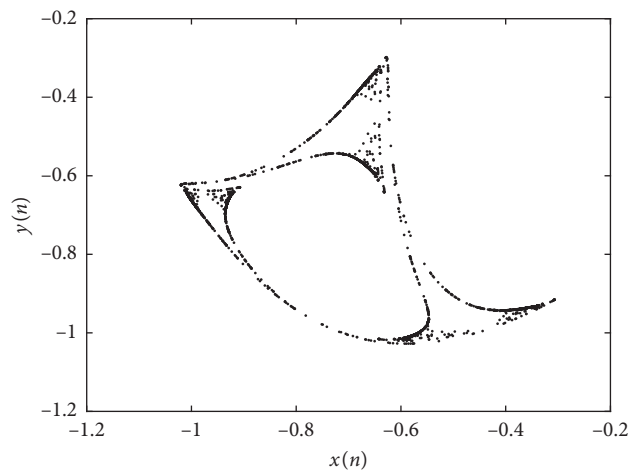
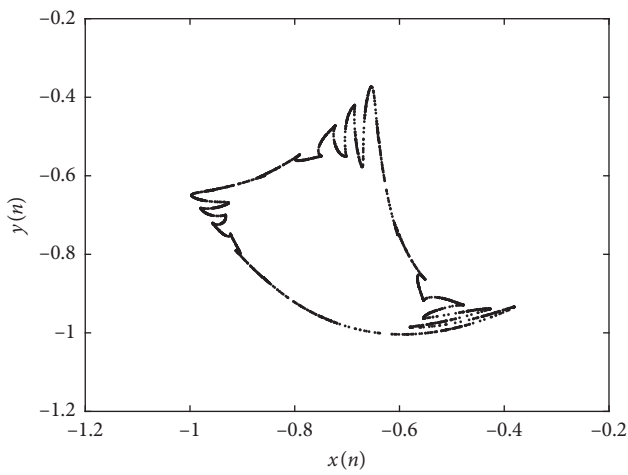
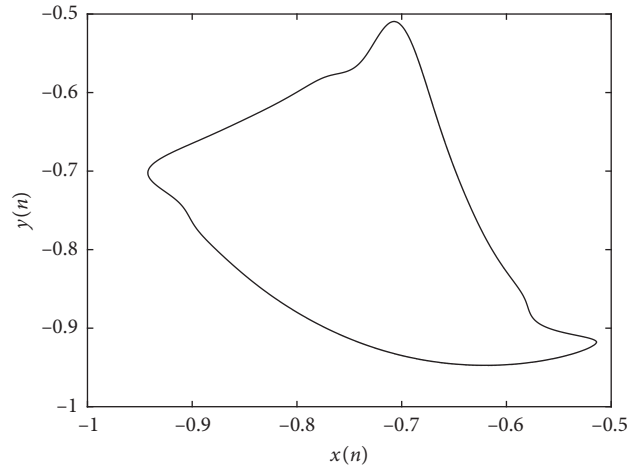
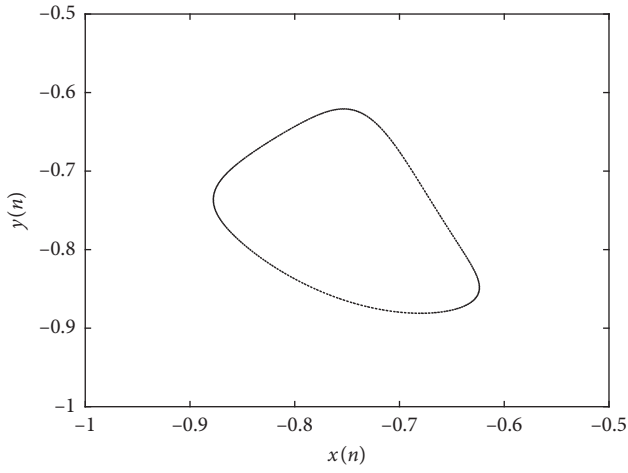


FIGURE 2: Continued.

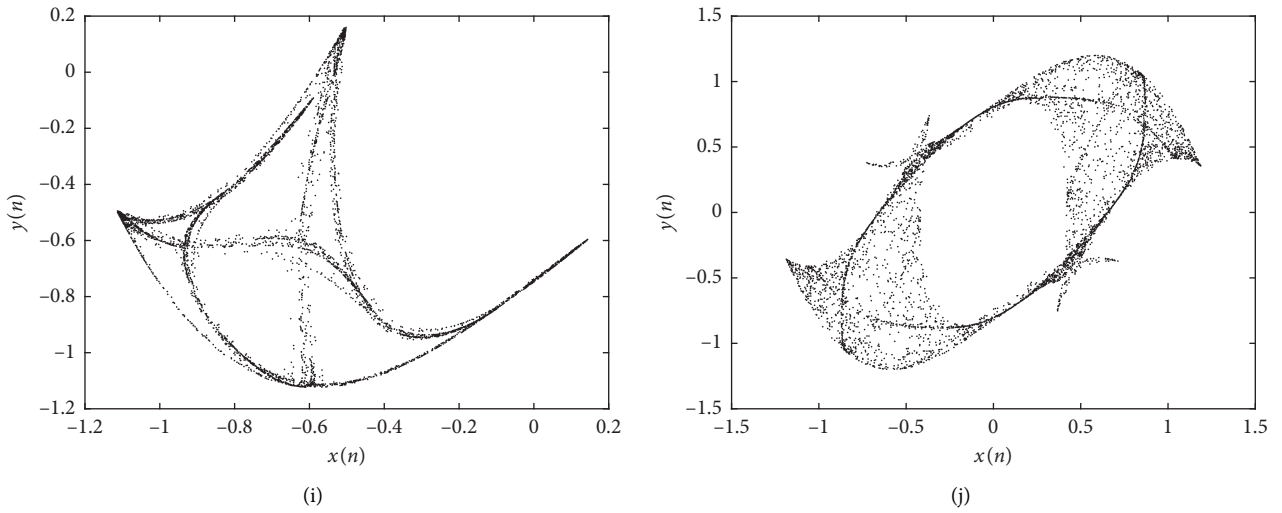


FIGURE 2: The phase diagrams of map (10) with the initial condition  $x_{01}$ : (a)  $b = 1$ , (b) the discrete time evolution of the state variable  $x(n)$  with  $b = 1$ , (c)  $b = 1.5$ , (d)  $b = 1.6$ , (e)  $b = 1.7$ , (f)  $b = 1.75$ , (g)  $b = 1.9$ , (h)  $b = 1.95$ , (i)  $b = 2$ , and (j)  $b = 2.2$ .

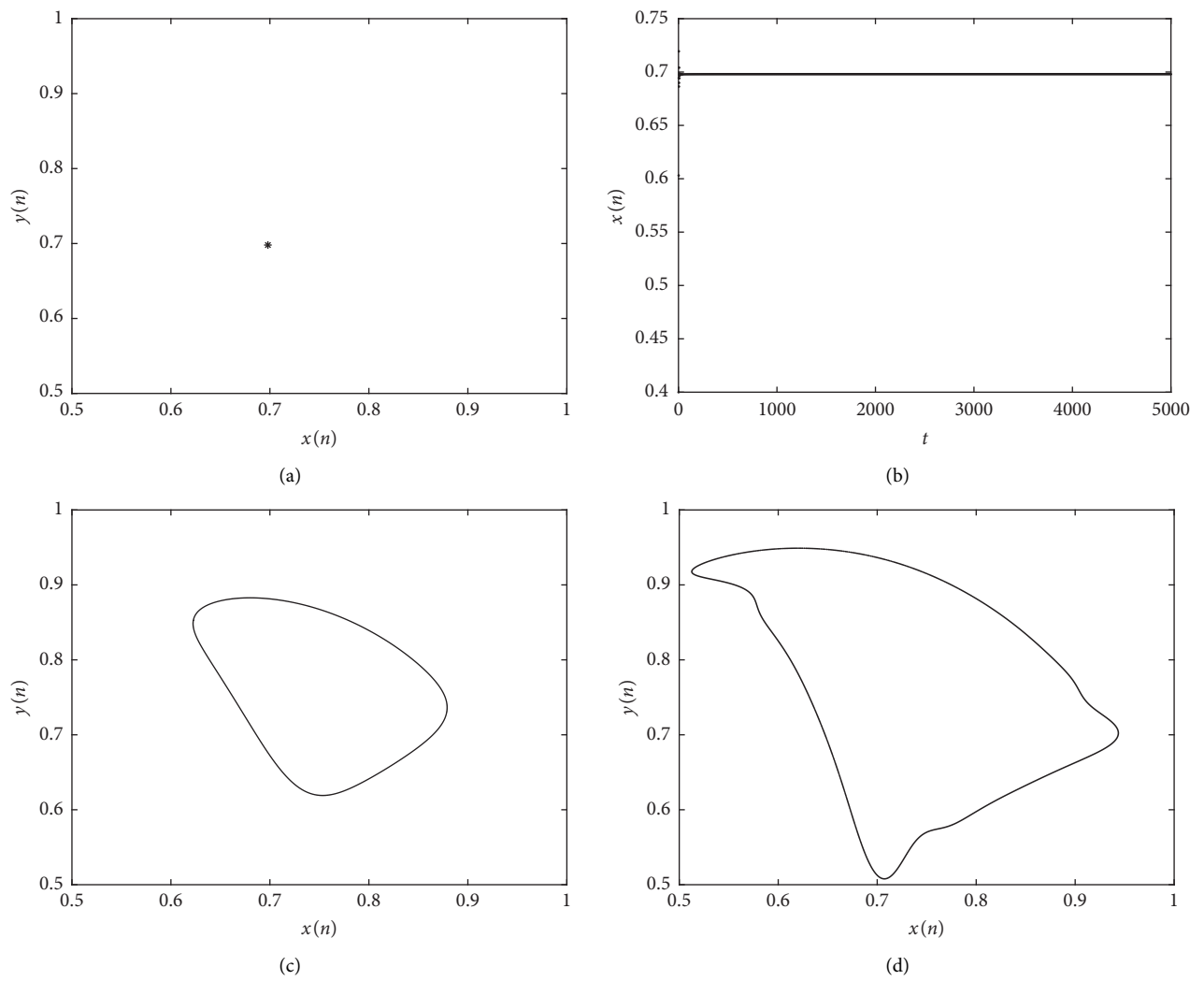


FIGURE 3: Continued.

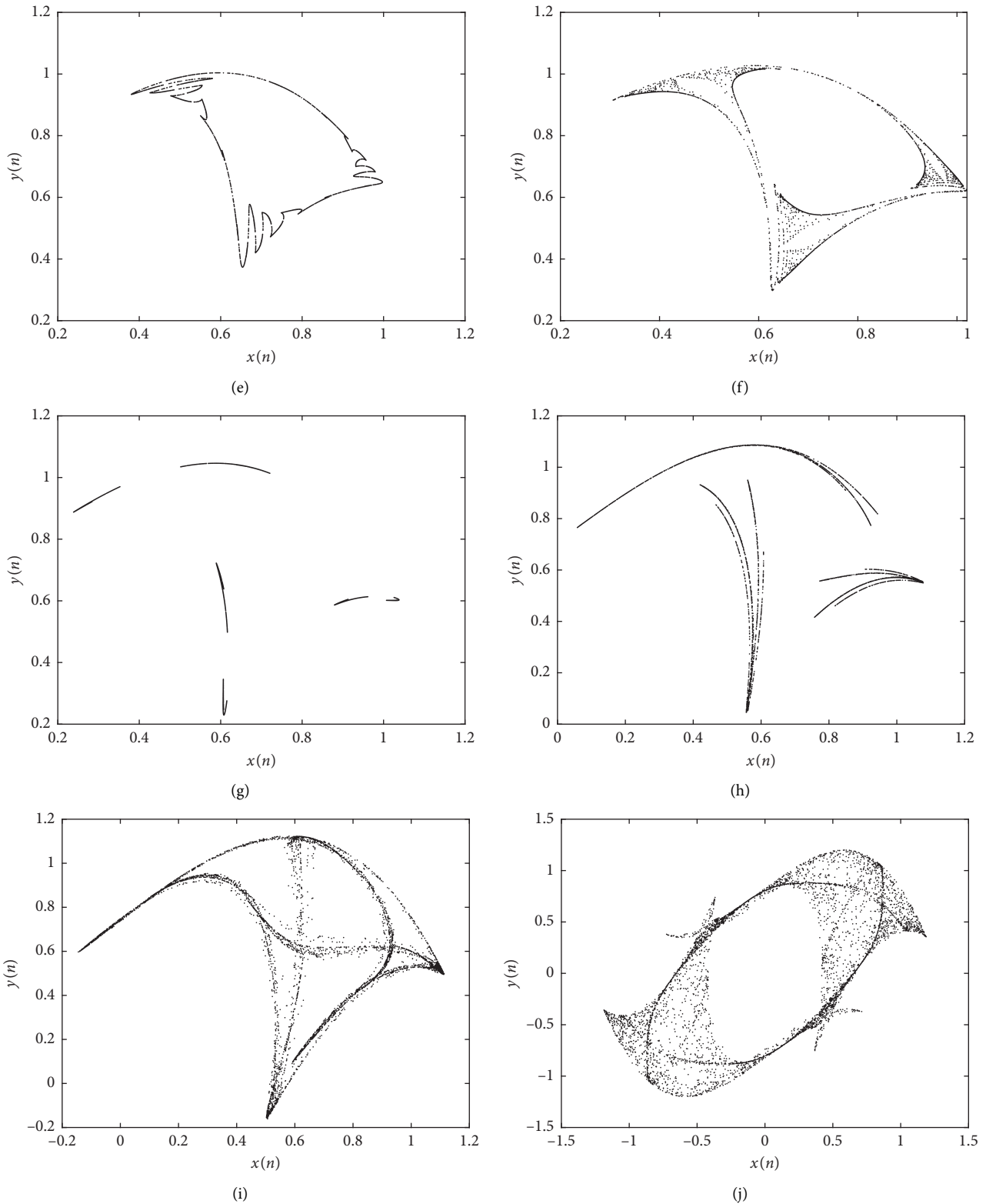


FIGURE 3: The phase diagrams of map (10) with the initial condition  $x_{02}$ : (a)  $b = 1$ , (b) the discrete time evolution of the state variable  $x(n)$  with  $b = 1$ , (c)  $b = 1.5$ , (d)  $b = 1.6$ , (e)  $b = 1.7$ , (f)  $b = 1.75$ , (g)  $b = 1.8$ , (h)  $b = 1.9$ , (i)  $b = 2$ , and (j)  $b = 2.2$ .

which we can see that the dynamics of the map is different from that of the map as the parameter  $b$  varies and lost the symmetry.

The phase diagrams for the map with  $x_{01}$  are shown in Figure 5. The map is period-2 when  $c = 0.2$  (Figures 5(a) and 5(b)), and the periodic behavior persists for a long time until



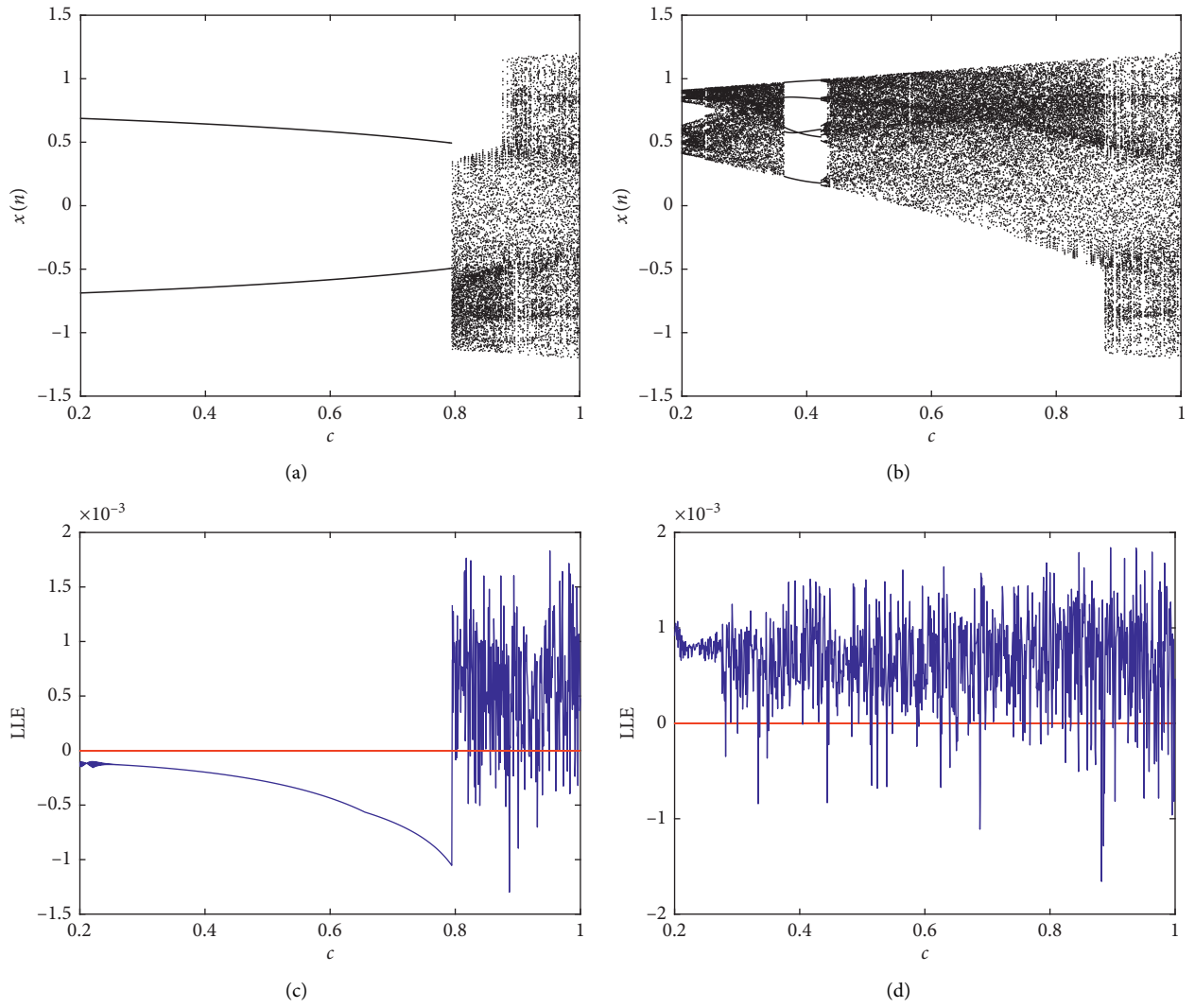


FIGURE 4: Bifurcation diagrams and corresponding LLE spectra for the map with different initial values as the parameter  $c$  varies: (a) the bifurcation diagram with  $x_{01}$ , (b) the bifurcation diagram with  $x_{02}$ , (c) the LLE spectrum with  $x_{01}$ , and (d) the LLE spectrum with  $x_{02}$ .

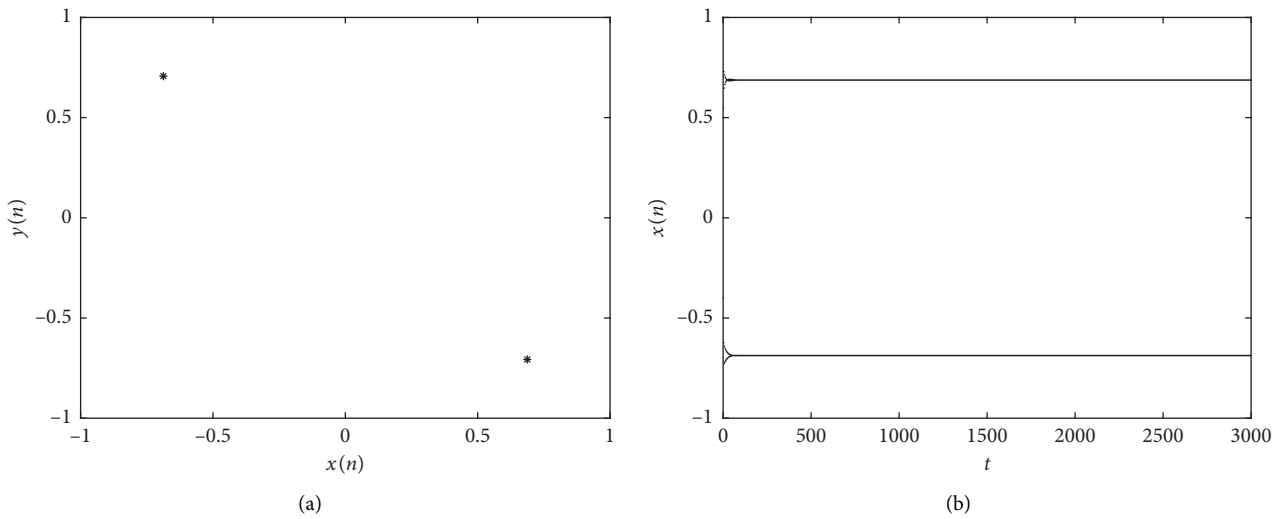


FIGURE 5: Continued.

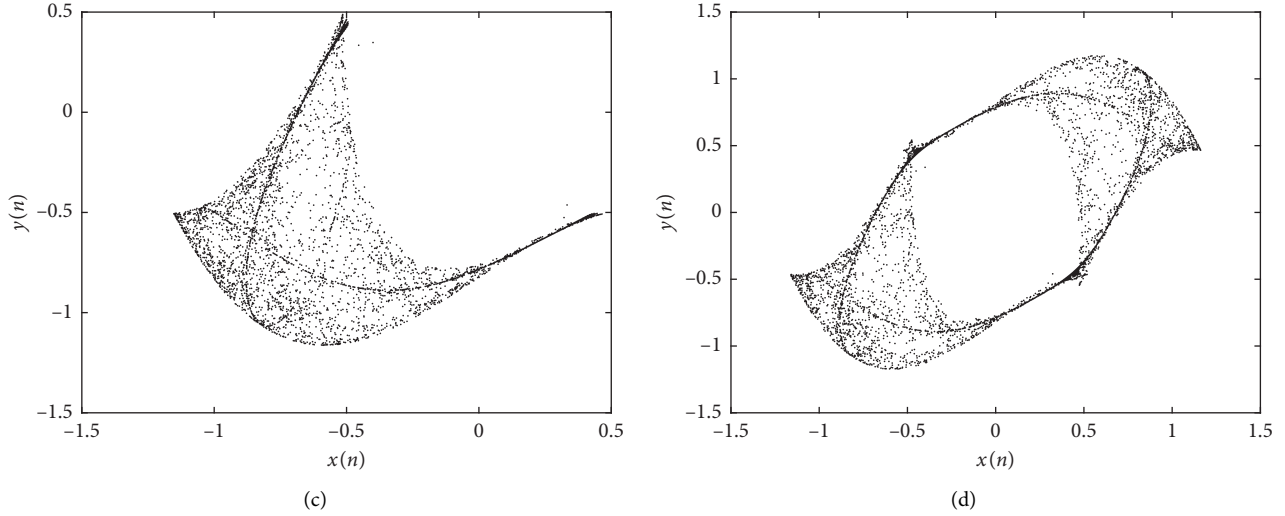


FIGURE 5: The phase diagrams of system (10) with the initial condition  $x_{01}$ : (a)  $c = 0.20$ , (b) the discrete time evolution of the state variable  $x(n)$  with  $c = 0.20$ , (c)  $c = 0.80$ , and (d)  $c = 0.88$ .

$c = 0.79$ . When  $c = 0.8$ , the system is chaotic and the chaotic attractor is depicted in Figure 5(c). As  $c$  increases from 0.87 to 0.88, the chaotic attractor becomes a large one, which means an interior crisis occurs.

The dynamics of the map with the initial condition  $x_{02}$  is displayed in Figure 6. The map keeps chaotic as the parameter  $c$  changes in the interval of  $[0.2, 1]$ , and the chaotic attractor has different formations. A chaotic attractor consists of four small parts in the phase space when the parameter  $c$  increases from 0.2 to 0.28 (Figures 6(a)–6(c)) and converts to a whole one when  $c = 0.29$  (Figure 6(d)). The system is period-5 when  $c = 0.4$ , and the phase diagram and the discrete time evolution of the state variable  $x(n)$  are plotted in Figures 6(e) and 6(f). When the parameter  $c$  increases from 0.87 to 0.88, the chaotic attractor becomes a large one suddenly (Figures 6(g) and 6(h)), which implies that an interior crisis occurs.

The stable region for the map in the  $b - c$  parameter plane with  $v = 0.98$  is plotted in Figure 7 in order to give a guidance of choosing values of the parameters. From this figure, we can see that map (10) is chaotic when  $b = 2.2$  and  $c = 0.95$ .

**4.3. Dynamics as the Order  $v$  Varies.** The parameters are fixed as  $b = 2.2$  and  $c = 0.95$ , the dynamics of map (10) is studied when the order  $v$  is varied in this section. The bifurcation diagrams and the corresponding LLE spectrums with  $x_{01}$  and  $x_{02}$  are plotted in Figure 8. From which it can be seen that the dynamics of the map also shows a symmetry with different initial conditions in this case.

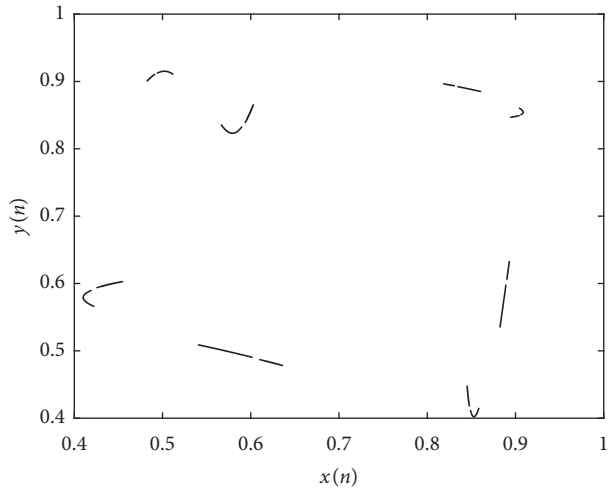
For different values of the  $v$ , the phase diagrams with  $x_{01}$  are shown in Figure 9. The map has period-1 attractor for  $v = 0.7$  (Figure 9(a)), and a limit cycle for  $v = 0.71$  (Figure 9(b)), which means a Hopf bifurcation, occurs as the order  $v$  increases. The shape of the limit cycle changes

as  $v$  increases (Figure 9(c)). The map exists as a multicycle attractor for  $v = 0.83$ , see Figure 9(d). As the order increases to 0.84, the attractor becomes a chaotic one which is consisted by several small parts (Figure 9(e)). The small parts combine into one attractor when  $v = 0.86$  (Figure 9(f)). From Figures 9(g) and 9(h), it is clear that the chaotic attractor has three small parts in the phase plane when  $v = 0.89$ , and these parts become a whole one when  $v = 0.9$ . The chaotic attractor in Figure 9(i) becomes a large one (Figure 9(j)) when the order varies from 0.95 to 0.96.

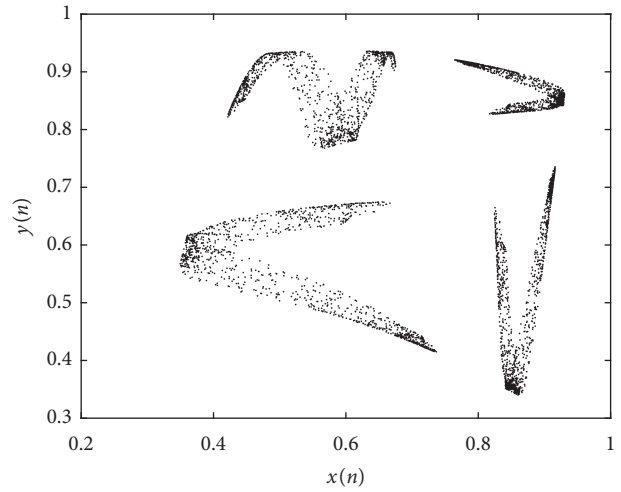
The phase diagrams with initial condition  $x_{02}$  as the order varies from 0.7 to 0.96 are shown in Figure 10, which are symmetric with those of the map with  $x_{01}$ . From the global dynamics perspective, the two chaotic attractors, which are depicted in Figures 9(i) and 10(i), collide with each other and convert to a large one (Figures 9(j) and 10(j)).

**4.4. Bifurcation with the Simultaneous Variation of Both Parameter and Order  $v$ .** In this section, the bifurcations of map (10) as a parameter and the order variation with the initial conditions  $x_{01}$  and  $x_{02}$  are studied. Firstly, the value of parameter  $c$  is fixed as 0.95. The bifurcation diagram of the map is depicted in Figure 11, when the parameter  $b \in [0.2, 2.2]$  and the order  $v \in [0.5, 1]$  change simultaneously. Secondly, the value of parameter  $b$  is set as 2.2. Figure 12 shows the bifurcation diagram of the map with the variation of the parameter  $b \in [0.2, 2.2]$  and the order  $v \in [0.5, 1]$ . From these figures, it can be seen that map (10) is periodic when the order is less than a certain threshold and appears chaotic behavior when the order is greater than the certain threshold.

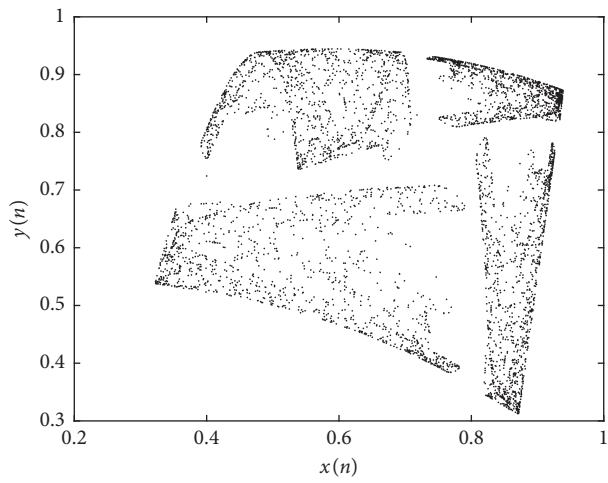
In other words, the dynamics of map (10) becomes regular as the derivate order  $v$  decreases from 1 to 0.5 and complex as the derivate order  $v$  increases from 0.5 to 1.



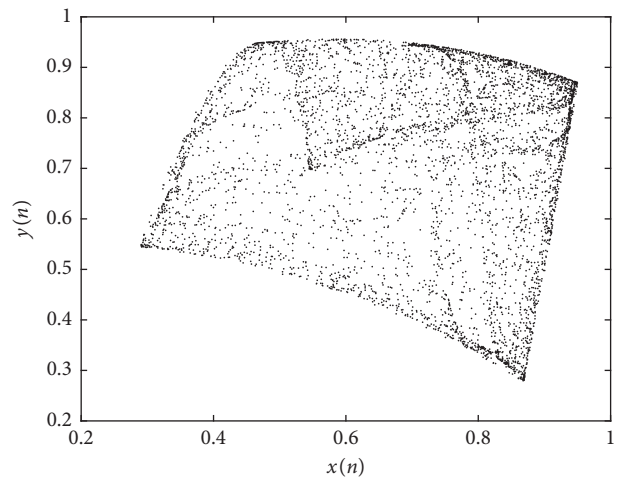
(a)



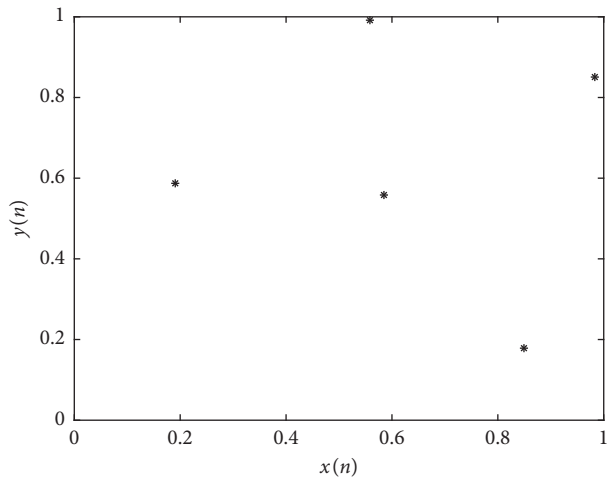
(b)



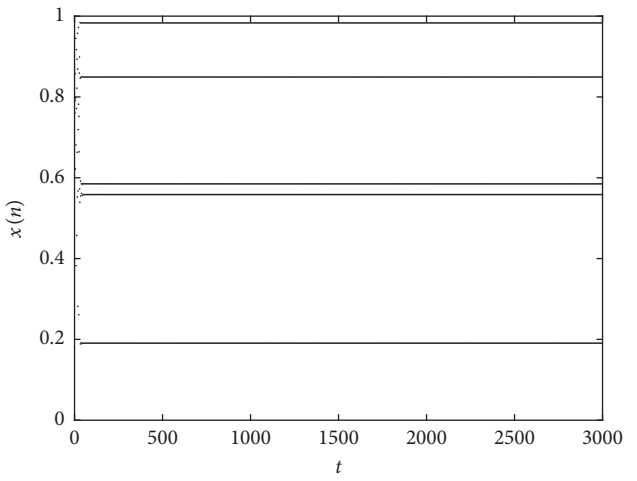
(c)



(d)



(e)



(f)

FIGURE 6: Continued.

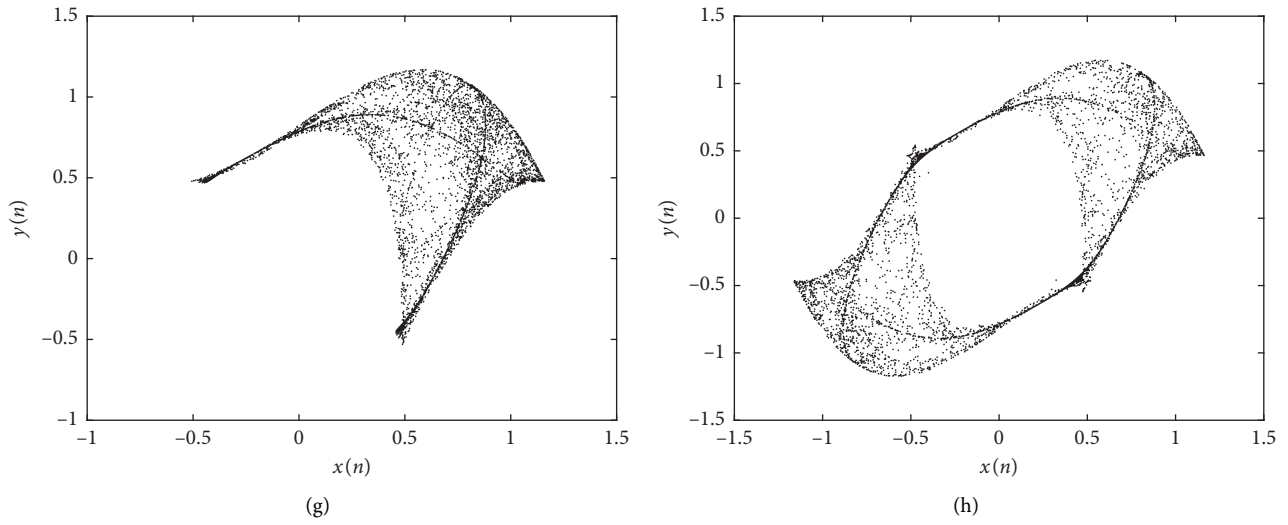


FIGURE 6: The phase diagrams of system (10) with the initial condition  $x_{02}$ : (a)  $c = 0.20$  (b)  $c = 0.25$ , (c)  $c = 0.28$ , (d)  $c = 0.29$ , (e)  $c = 0.40$ , (f) discrete time evolution of the state variable  $x(n)$  with  $c = 0.40$ , (g)  $c = 0.87$ , and (h)  $c = 0.88$ .

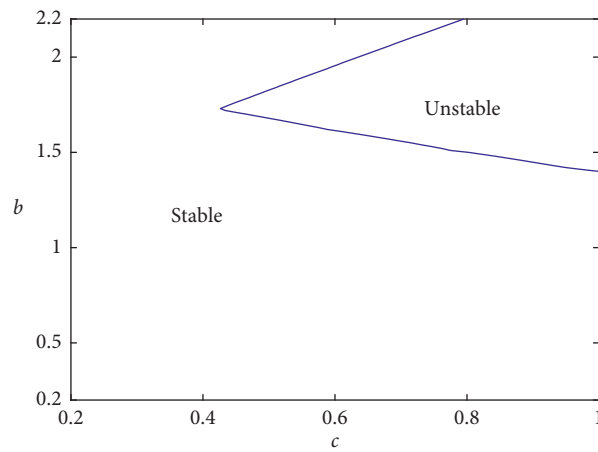


FIGURE 7: The stable region of the map for the two parameters.

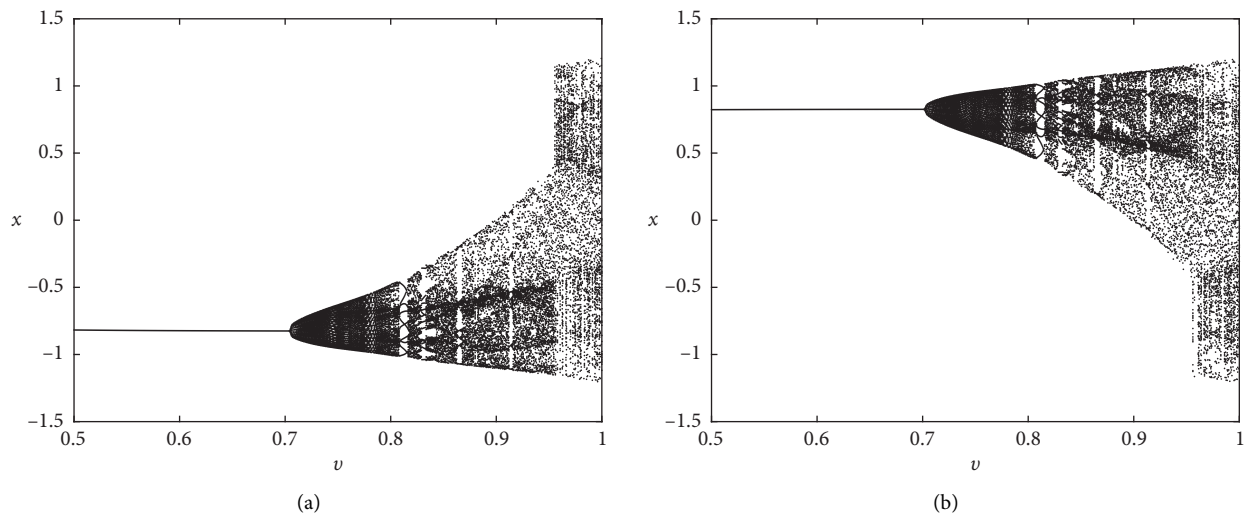


FIGURE 8: Continued.

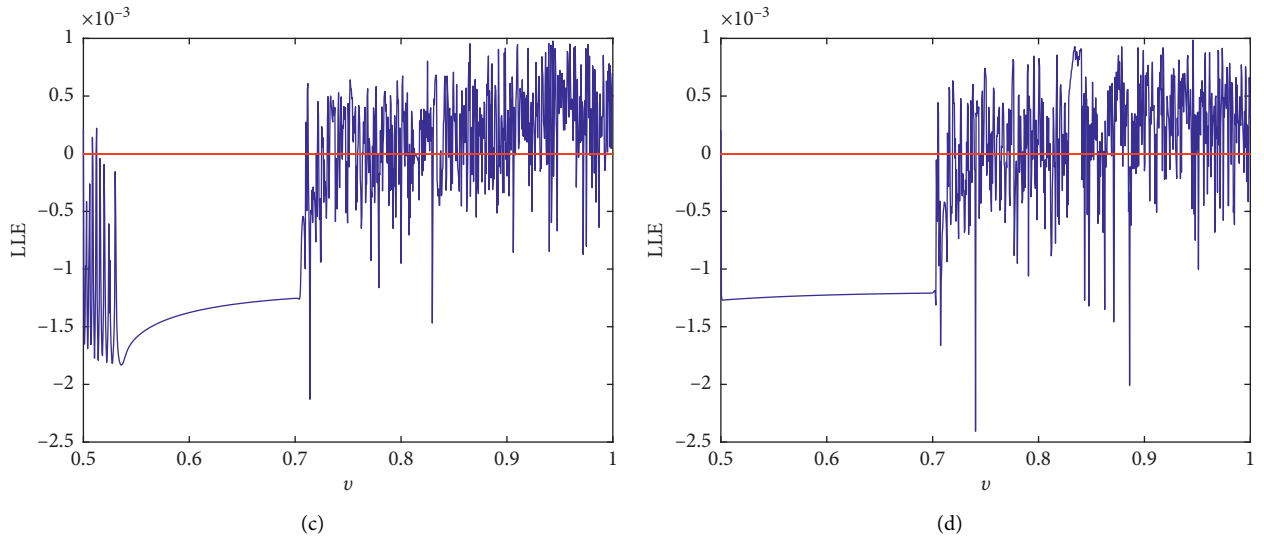


FIGURE 8: Bifurcation diagrams and corresponding LLE spectrums for the map with different initial values as the order  $\nu$  varies: (a) the bifurcation diagram with  $x_{01}$ , (b) the bifurcation diagram with  $x_{02}$ , (c) the LLE spectrum with  $x_{01}$ , and (d) the LLE spectrum with  $x_{02}$ .

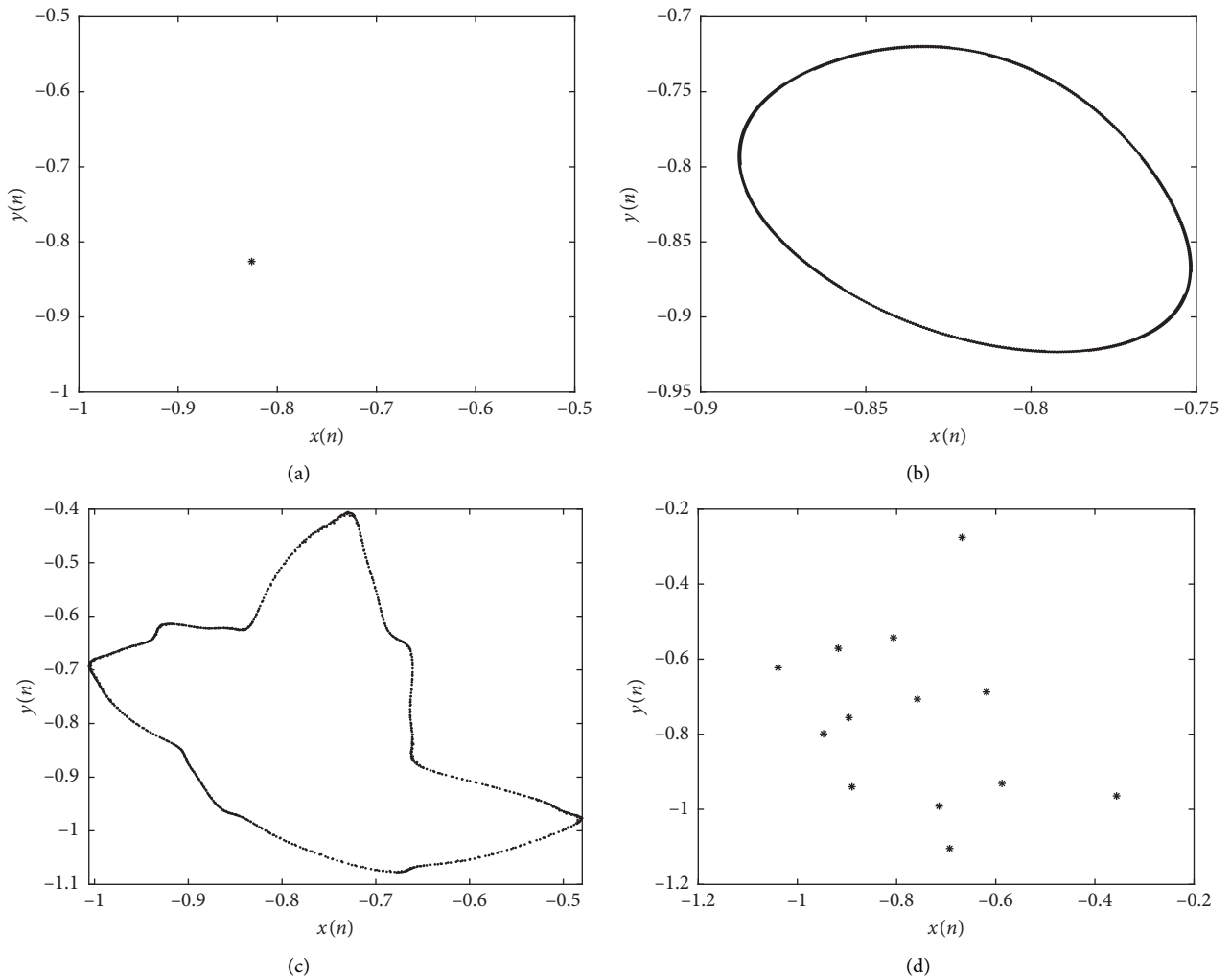


FIGURE 9: Continued.



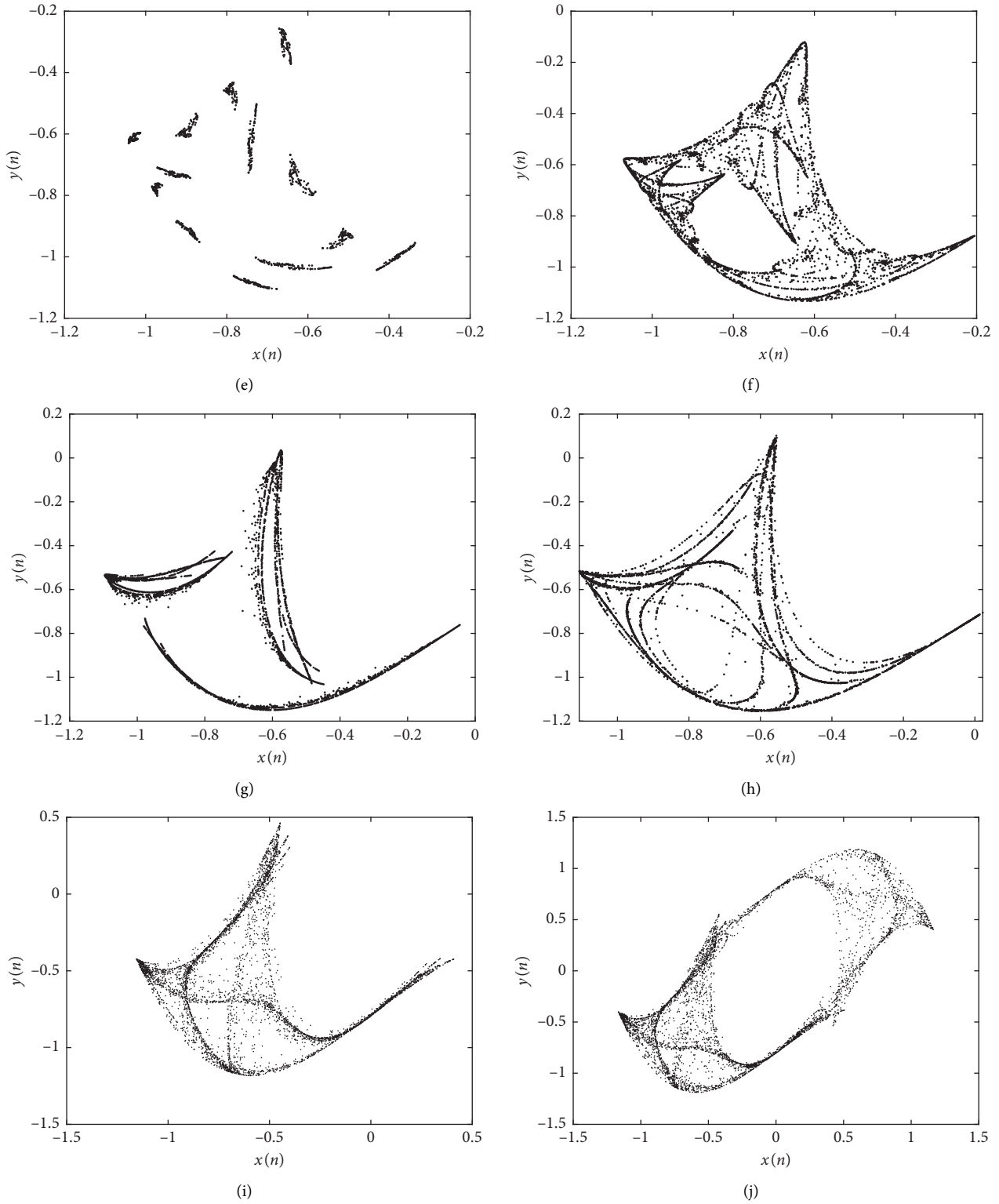
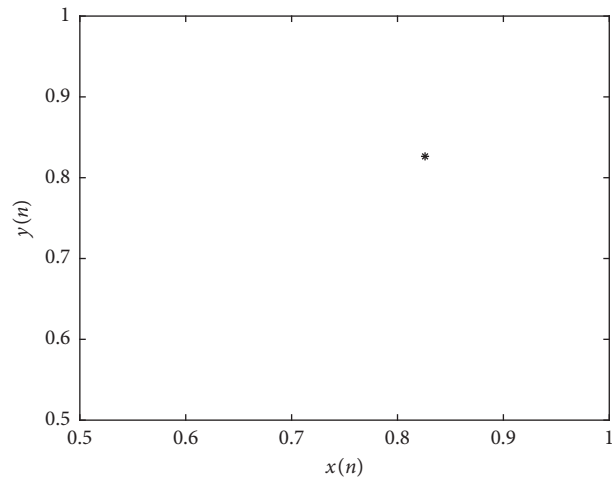
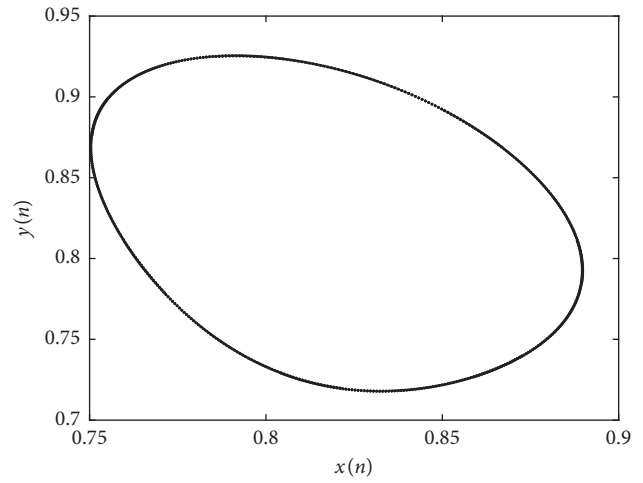


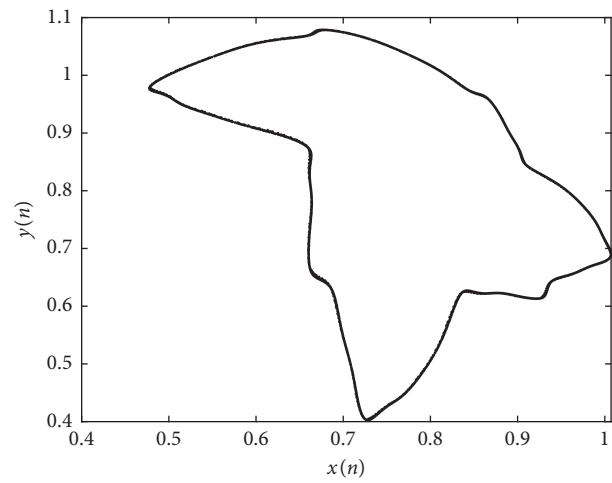
FIGURE 9: The phase diagrams of system (10) with the initial condition  $x_{01}$ : (a)  $\nu = 0.70$ , (b)  $\nu = 0.71$ , (c)  $\nu = 0.81$ , (d)  $\nu = 0.83$ , (e)  $\nu = 0.84$ , (f)  $\nu = 0.86$ , (g)  $\nu = 0.89$ , (h)  $\nu = 0.90$ , (i)  $\nu = 0.95$ , and (j)  $\nu = 0.96$ .



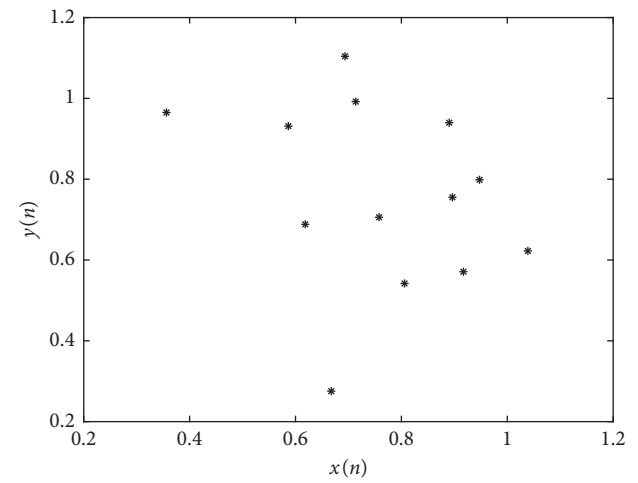
(a)



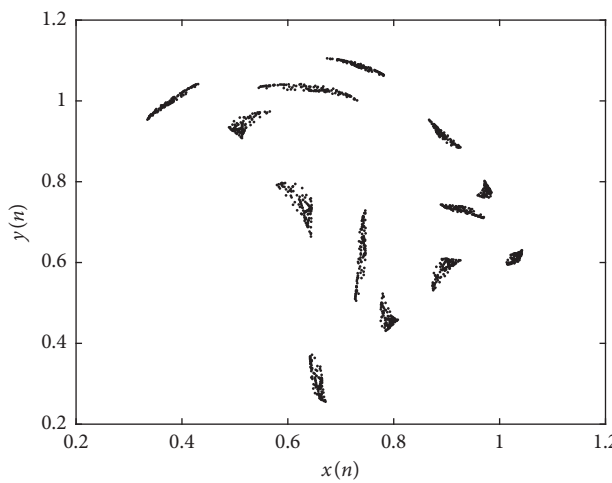
(b)



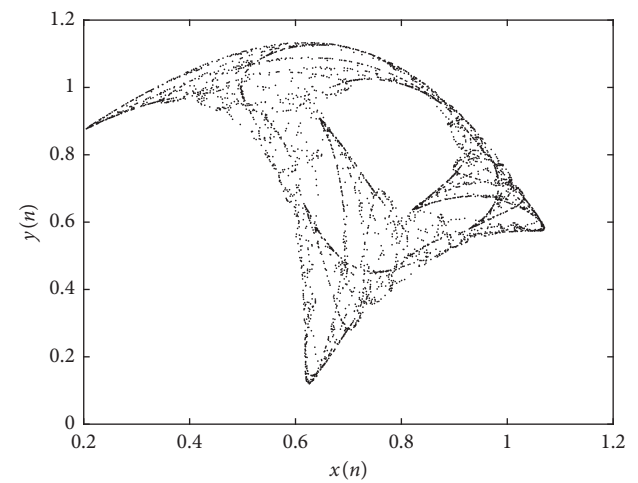
(c)



(d)



(e)



(f)

FIGURE 10: Continued.

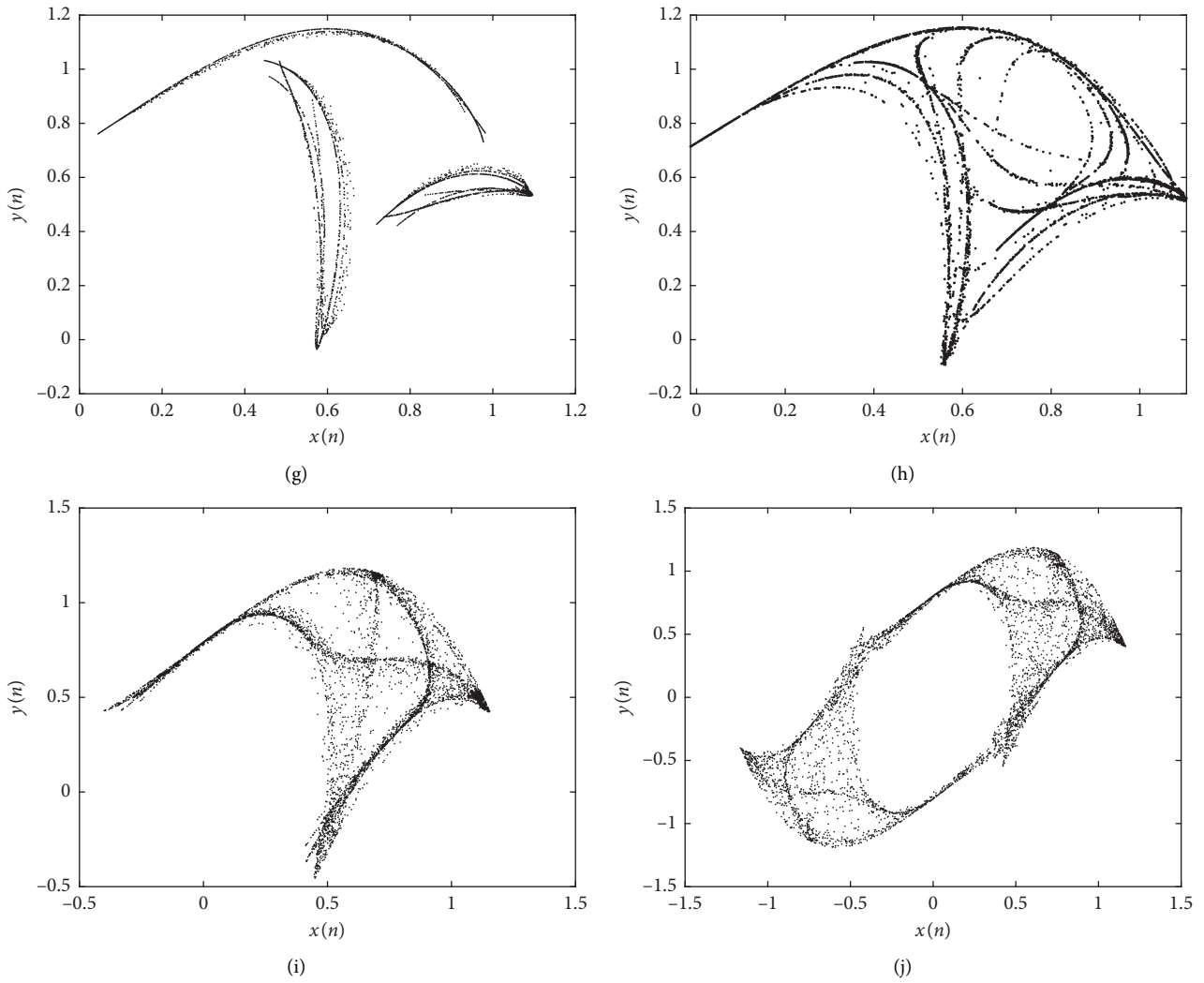


FIGURE 10: The phase diagrams of system (10) with the initial condition  $x_{02}$ : (a)  $\nu = 0.70$ , (b)  $\nu = 0.71$ , (c)  $\nu = 0.80$ , (d)  $\nu = 0.83$ , (e)  $\nu = 0.84$ , (f)  $\nu = 0.86$ , (g)  $\nu = 0.89$ , (h)  $\nu = 0.90$ , (i)  $\nu = 0.95$ , and (j)  $\nu = 0.96$ .

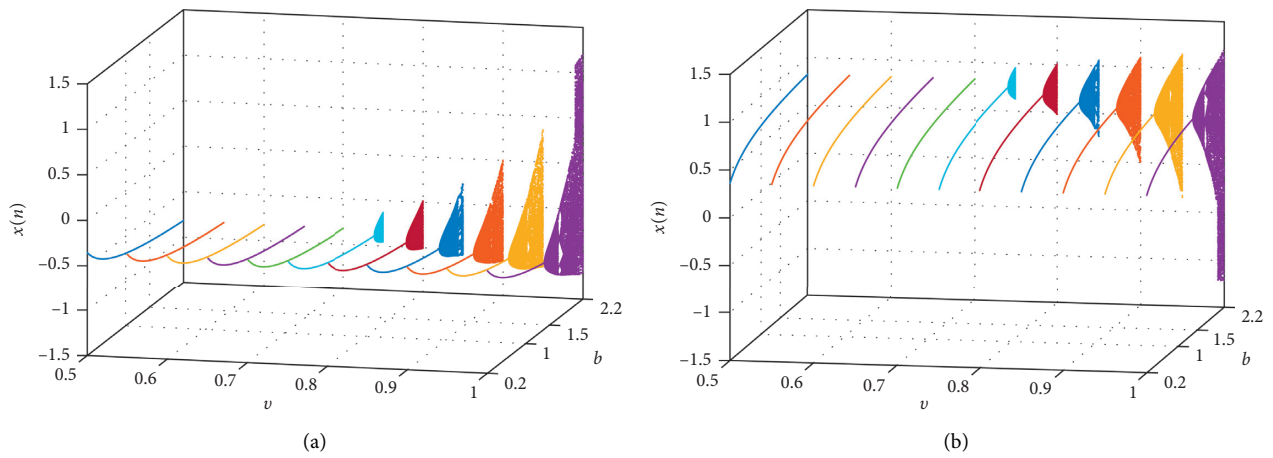


FIGURE 11: Bifurcation diagrams for map (10) with different initial values as the parameter  $b$  and the order  $\nu$  vary: (a) the bifurcation diagram with  $x_{01}$  and (b) the bifurcation diagram with  $x_{02}$ .

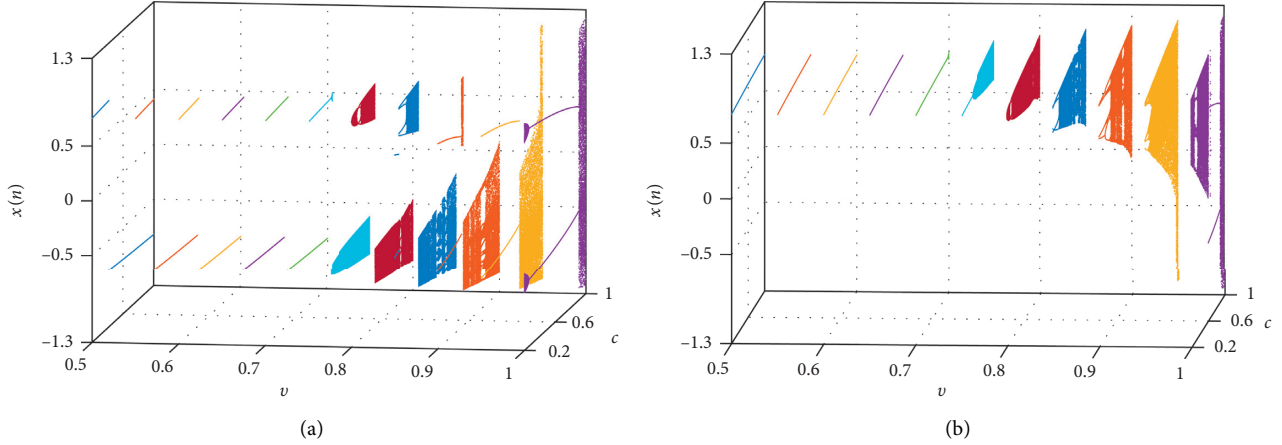


FIGURE 12: Bifurcation diagrams for map (10) with different initial values as the parameter  $c$  and the order  $v$  vary: (a) the bifurcation diagram with  $x_{01}$  and (b) the bifurcation diagram with  $x_{02}$ .

## 5. Stabilization

The stabilization of map (10) will be studied in this section. From here, the case of the equilibrium to be at the origin is considered. For convenience, the controlled map (10) is rewritten as the following form:

$$\begin{cases} {}^C\Delta_a^\nu x(t) = y(\omega) - x(\omega) + u_1(\omega), \\ {}^C\Delta_a^\nu y(t) = b(-x^3(\omega) + x(\omega)) + c(-y^3(\omega) + y(\omega)) - y(\omega) + u_2(\omega), \end{cases} \quad (21)$$

where  $\omega = t - 1 + v$  and  $u_1$  and  $u_2$  are the stabilization controllers.

**Theorem 2.** *The fractional-order map (10) can be stabilized when the controllers are designed as the following form:*

$$\begin{cases} u_1(t) = -y(t), \\ u_2(t) = -b(-x^3(t) + x(t)) - c(-y^3(t) + y(t)). \end{cases} \quad (22)$$

*Proof.* Through substituting (22) into (21), map (21) becomes

$$\begin{cases} {}^C\Delta_a^\nu x(t) = -x(\omega), \\ {}^C\Delta_a^\nu y(t) = -y(\omega). \end{cases} \quad (23)$$

Map (23) can be rewritten in the compact form:

$${}^C\Delta_a^\nu (x(t), y(t))^T = \mathbf{A} \times (x(\omega), y(\omega))^T, \quad (24)$$

where  $\mathbf{A} = \begin{pmatrix} -1 & 0 \\ 0 & -1 \end{pmatrix}$ . Based on Theorem 1, it is easy to see that the eigenvalues of  $\mathbf{A}$  satisfy the conditions

$$\begin{cases} {}^C\Delta_a^\nu x_r(t) = y_r(\omega) - x_r(\omega) + u_1(\omega), \\ {}^C\Delta_a^\nu y_r(t) = b(-x_r^3(\omega) + x_r(\omega)) + c(-y_r^3(\omega) + y_r(\omega)) - y_r(\omega) + u_2(\omega), \end{cases} \quad (26)$$

where the subscript  $r$  denotes the response system. The error state variables are defined as  $e_x(t) = x_r(t) - x_d(t)$

$|\arg \lambda_i| = \pi$  and  $|\lambda_i| = 2^v$ , for  $i = 1, 2$ , which implies that the chaos of map (10) can be controlled and the zero equilibrium of (24) is globally asymptotically stable.

In the numerical simulations, the values of the parameters are fixed as  $b = 2.2$  and  $c = 0.95$ , and the fractional order  $v = 0.98$ . The controllers are used to stabilize map (10) when the iterations are chosen as  $n = 1000$ . The stabilization results are displayed in Figure 13. It is clear that the state variables  $x(n)$  and  $y(n)$  toward to zeros, which means the chaos of map (10) is stabilized and the results confirm the theoretical control results presented in Theorem 2.  $\square$

## 6. Synchronization

Now, we consider the synchronization of map (10). Firstly, a fractional Lorenz map is taken as the drive system:

$$\begin{cases} {}^C\Delta_a^\nu x_d(t) = \gamma \delta x_d(\omega) - \delta y_d(\omega) x_d(\omega), \\ {}^C\Delta_a^\nu y_d(t) = \delta (-y_d(\omega) + x_d^2(\omega)), \end{cases} \quad (25)$$

where  $0 < v < 1$  and state subscript  $d$  denotes the drive system. Map (25) is chaotic when the parameters  $\gamma = 1.25$  and  $\delta = 0.75$  and the derivative order  $v = 0.98$ . For more details about the dynamics of map (25), please refer to the literature [23]. Map (10) with synchronization controllers  $u_1(\omega)$  and  $u_2(\omega)$ , which can be described by the following equations:

and  $e_y(t) = y_r(t) - y_d(t)$ . If all the error states variables tend to 0 as the time  $t \rightarrow \infty$ , then maps (25) and (26) are

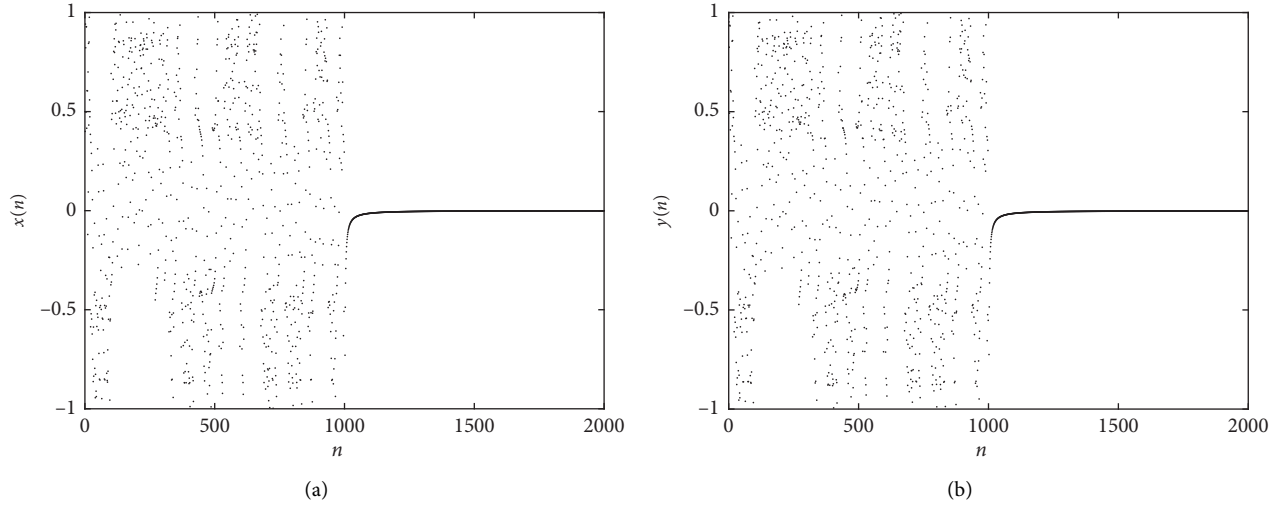


FIGURE 13: The results of the stabilization of system (10): (a) the variation of  $x(n)$  with  $n$  and (b) the variation of  $y(n)$  with  $n$ .

synchronized. The following theorem is given to ensure the synchronization between the two maps can be realized.

**Theorem 3.** *The drive and response maps (25) and (26) are synchronized when the controllers are designed as follows:*

$$\begin{cases} u_1(\omega) = \gamma \delta x_d(\omega) - \delta y_d(\omega) x_d(\omega) - y_d(\omega) + x_d(\omega), \\ u_2(\omega) = \delta(-y_d(\omega) + x_d^2(\omega)) - b(-x_r^3(\omega) + x_r(\omega)) - c(-y_r^3(\omega) + y_r(\omega)) + y_d(\omega). \end{cases} \quad (27)$$

*Proof.* The error dynamical system with fractional Caputo difference is

$$\begin{cases} {}^C \Delta_a^v e_1(t) = y_r(\omega) - x_r(\omega) - \gamma \delta x_d(\omega) + \delta y_d(\omega) x_d(\omega) + u_1(\omega), \\ {}^C \Delta_a^v e_2(t) = b(-x_r^3(\omega) + x_r(\omega)) + c(-y_r^3(\omega) + y_r(\omega)) - y_r(\omega) - \delta(-y_d(\omega) + x_d^2(\omega)) + u_2(\omega). \end{cases} \quad (28)$$

By substituting controllers (27) into (28), we can obtain the error dynamical system:

$$\begin{cases} {}^C \Delta_a^v e_1(t) = e_2(\omega) - e_1(\omega), \\ {}^C \Delta_a^v e_2(t) = -e_2(\omega). \end{cases} \quad (29)$$

System (29) is rewritten in the compact form:

$${}^C \Delta_a^v (e_1(t), e_2(t)) = \mathbf{M} \times (e_1(\omega), e_2(\omega))^T, \quad (30)$$

where  $\mathbf{M} = \begin{bmatrix} -1 & 1 \\ 0 & -1 \end{bmatrix}$ . It can be seen that the eigenvalues of the matrix  $\mathbf{M}$  satisfy the following stability condition:

$$|\lambda_i| < \left( 2 \cos \frac{|\arg \lambda_i| - \pi}{2 - v} \right)^v, \quad (31)$$

$$|\arg \lambda_i| > \frac{v\pi}{2}, \quad i = 1, 2.$$

Based on Theorem 1, we can get that the zero equilibrium of (29) is globally asymptotically stable, which implies the two maps (25) and (26) are synchronized.

In the numerical simulations, the parameters are fixed as  $\gamma = 1.25$ ,  $\delta = 0.75$ ,  $b = 2.2$ , and  $c = 0.95$  and the order is  $v = 0.98$ . The initial conditions of the two systems (25) and (26) are  $(x_{d0}, y_{d0}) = (0.1, 0.1)$  and  $(x_{r0}, y_{r0}) = (0.8, 0.4)$ .



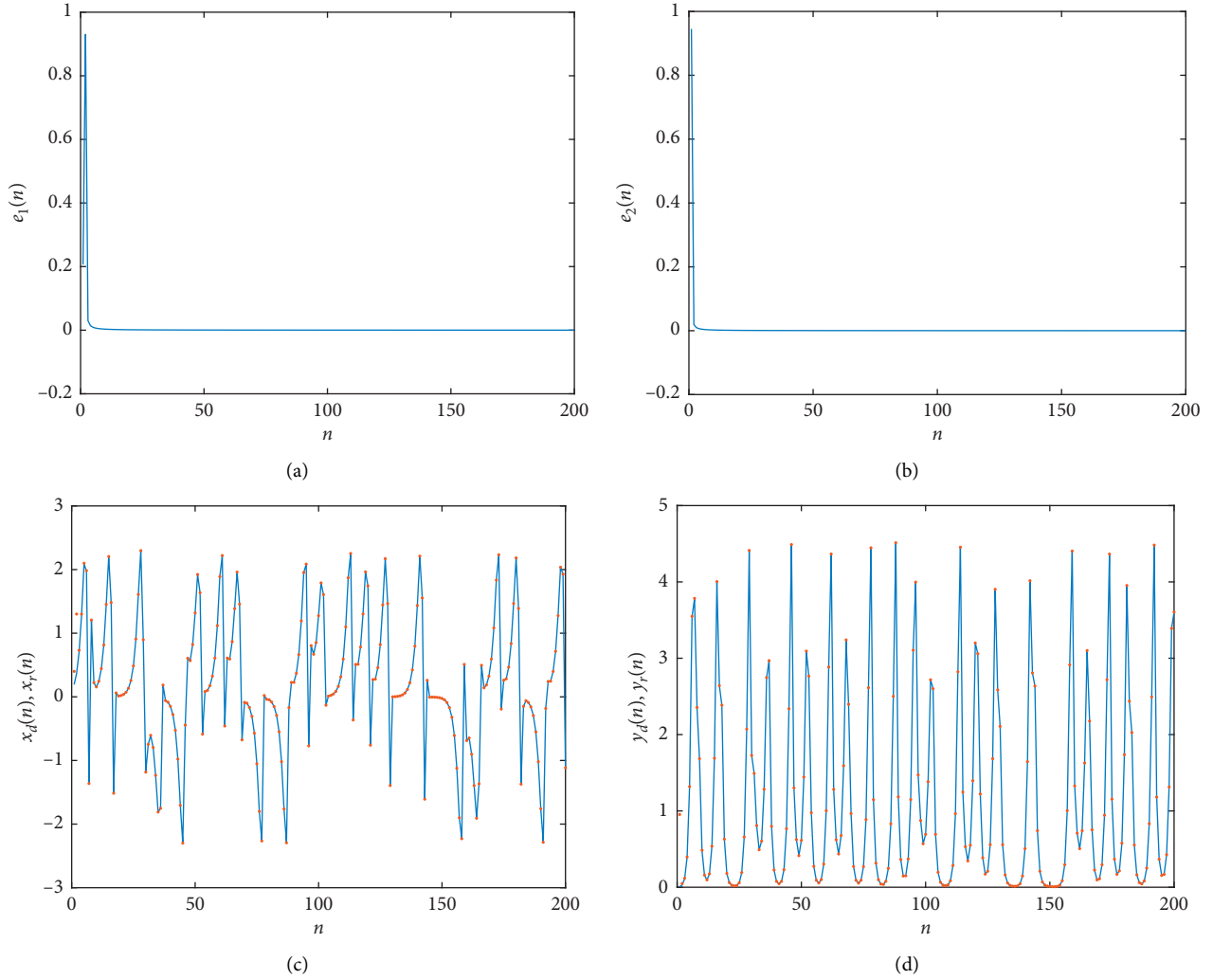


FIGURE 14: The simulation results for the synchronization of map (10): (a) the error state variable  $e_1(n)$  with the variation of  $n$ , (b) the error state variable  $e_2(n)$  with the variation of  $n$ , (c) the state variables  $x_d(n)$  and  $x_r(n)$  with the variation  $n$ , and (d) the state variables  $y_d(n)$  and  $y_r(n)$  with the variation  $n$ .

The results of numerical simulations are depicted in Figure 14. From which, we can see that the error variables  $e_1$  and  $e_2$  converge to zero rapidly as  $n$  increases (Figures 14(a) and 11(b)). Meanwhile, the evolution of the state variables with time  $n$  for the two maps (25) and (26) are synchronized under the designed controllers (27) (Figures 14(c) and 14(d)).  $\square$

## 7. Conclusions and Discussion

A fractional-order discrete noninvertible map with cubic nonlinearity is proposed in this paper. Firstly, the stability of the equilibrium points for the map is analyzed. Secondly, the dynamics of the map with two different initial conditions is studied by numerical simulation. Bifurcation diagrams and phase plots are obtained as a parameter or the fractional order varies. A series of attractors of the map in different forms, including equilibrium points, limit cycles, and chaotic attractors, are plotted. Furthermore, bifurcations with the

simultaneous variation of both parameter and order are also analyzed in the three-dimensional space. From the global dynamics perspective, interior crises occur in the map as a parameter or the order varies. Thirdly, based on the stability theory of fractional-order discrete maps, the chaos of the map is controlled by the stabilization controllers. Finally, the synchronization between the proposed map and a fractional-order discrete Lorenz map is investigated. Numerical simulations are implemented to verify the effectiveness of the designed controllers. The results obtained in this paper reveal that chaos really exists in the fractional-order formation for the map proposed in [31–33]. More abundant local and global dynamics are found in the fractional-order map.

It is worth mentioning that the mechanism of interior crises occur in map (10) cannot be displayed from a global perspective due to the absence of effective global dynamics computation methods for fractional-order discrete maps. Therefore, developing the effective computation methods of global analysis for this kind of systems is our following work.

## Data Availability

The data for the bifurcation diagrams used to support the findings of this study are included within the supplementary information files (available here). For the large of the data, we will supply the bifurcation data calculated by the software Matlab.

## Conflicts of Interest

The authors declare that they have no conflicts of interest.

## Acknowledgments

This work was supported by the National Natural Science Foundation of China (nos. 11702194 and 11702195) and Natural Science Preparatory Study Foundation of Xi'an University of Posts and Telecommunications (no. 106/205020030).

## Supplementary Materials

(1) discretosanweiN1q098b and discretesanweiN2q098b: the data of Figures 1(a) and 1(b). (2) discretesanweiN1q098c and discretesanweiN2q098c: the data of Figures 4(a) and 4(b). (3) discretesanweiqIN1 and discretesanweiqIN2: the data of Figures 8(a) and 8(b). (*Supplementary Materials*)

## References

- [1] R. M. May, "Simple mathematical models with very complicated dynamics," *Nature*, vol. 261, no. 21, pp. 459–467, 1976.
- [2] H. Sakaguchi and K. Tomita, "Bifurcations of the coupled Logistic map," *Progress of Theoretical Physics*, vol. 78, no. 2, pp. 305–315, 1987.
- [3] M. J. Feigenbaum, "Quantitative universality for a class of nonlinear transformations," *Journal of Statistical Physics*, vol. 19, no. 1, pp. 25–52, 1978.
- [4] M. Hénon, "A two-dimensional mapping with a strange attractor," *Communications in Mathematical Physics*, vol. 50, no. 1, pp. 69–77, 1976.
- [5] P. R. Lozi, "Un attracteur étrange du type attracteur de Hénon," *Journal de Physique*, vol. 39, pp. 9–10, 1978.
- [6] C. P. Li, W. H. Deng, and D. Xu, "Chaos synchronization of the Chua system with a fractional order," *Physica A: Statistical Mechanics and Its Applications*, vol. 360, no. 2, pp. 171–185, 2006.
- [7] J. G. Lu and G. Chen, "A note on the fractional-order Chen system," *Chaos, Solitons & Fractals*, vol. 27, no. 3, pp. 685–688, 2006.
- [8] C. Zeng, Q. Yang, and J. Wang, "Chaos and mixed synchronization of a new fractional-order system with one saddle and two stable node-foci," *Nonlinear Dynamics*, vol. 65, no. 4, pp. 457–466, 2011.
- [9] R. Behinfaraz and M. A. Badamchizadeh, "Synchronization of different fractional order chaotic systems with time-varying parameter and orders," *ISA Transactions*, vol. 80, pp. 399–410, 2018.
- [10] D. Cafagna and G. Grassi, "Bifurcation and chaos in the fractional-order Chen system via a time-domain approach," *International Journal of Bifurcation and Chaos*, vol. 18, no. 7, pp. 1845–1863, 2008.
- [11] J. Huo, H. Zhao, and L. Zhu, "The effect of vaccines on backward bifurcation in a fractional order HIV model," *Nonlinear Analysis: Real World Applications*, vol. 26, pp. 289–305, 2015.
- [12] X. Li and R. Wu, "Hopf bifurcation analysis of a new commensurate fractional-order hyperchaotic system," *Nonlinear Dynamics*, vol. 78, no. 1, pp. 279–288, 2014.
- [13] A. Y. T. Leung, H. X. Yang, and P. Zhu, "Bifurcation of a Duffing oscillator having nonlinear fractional derivative feedback," *International Journal of Bifurcation and Chaos*, vol. 24, no. 3, Article ID 1450028, 2014.
- [14] A. M. A. El-Sayed, A. Elsonbaty, A. A. Elsadany, and A. E. Matouk, "Dynamical analysis and circuit simulation of a new fractional-order hyperchaotic system and its discretization," *International Journal of Bifurcation and Chaos*, vol. 26, no. 13, Article ID 1650222, 2016.
- [15] A. E. Matouk and A. A. Elsadany, "Dynamical analysis, stabilization and discretization of a chaotic fractional-order GLV model," *Nonlinear Dynamics*, vol. 85, no. 3, pp. 1597–1612, 2016.
- [16] X. Rui, W. Yin, Y. Dong, L. Lin, and X. Wu, "Fractional-order sliding mode control for hybrid drive wind power generation system with disturbances in the grid," *Wind Energy*, vol. 22, no. 1, pp. 49–64, 2019.
- [17] R. Behinfaraz, S. Ghaemi, and S. Khanmohammadi, "Adaptive synchronization of new fractional order chaotic systems with fractional adaption laws based on risk analysis," *Mathematical Methods in the Applied Sciences*, vol. 42, no. 6, pp. 1772–1785, 2019.
- [18] R. Behinfaraz, S. Ghaemi, and S. Khanmohammadi, "Risk assessment in control of fractional-order coronary artery system in the presence of external disturbance with different proposed controllers," *Applied Soft Computing*, vol. 77, pp. 290–299, 2019.
- [19] C. Goodrich and A. C. Peterson, *Discrete Fractional Calculus*, Springer, New York, NY, USA, 2015.
- [20] J. B. Diaz and T. J. Osler, "Differences of fractional order," *Mathematics of Computation*, vol. 28, no. 125, pp. 185–202, 1974.
- [21] Y. Liu, "Discrete chaos in fractional Hénon maps," *International Journal of Nonlinear Science*, vol. 18, no. 3, pp. 170–175, 2014.
- [22] A. Ouannas, A.-A. Khennaoui, Z. Odibat, V.-T. Pham, and G. Grassi, "On the dynamics, control and synchronization of fractional-order Ikeda map," *Chaos, Solitons & Fractals*, vol. 123, pp. 108–115, 2019.
- [23] A. A. Khennaoul, A. Ouannas, S. Bendoukha, G. Grassi, P. R. Lozi, and V. T. Pham, "On fractional-order discrete-time systems: chaos, stabilization and synchronization," *Chaos, Solitons and Fractals*, vol. 119, pp. 150–162, 2019.
- [24] J. Mumkhamar, "Chaos in a fractional order logistic map," *Fractional Calculus and Applied Analysis*, vol. 16, no. 3, pp. 511–519, 2013.
- [25] G. C. Wu, D. Baleanu, and S. D. Zeng, "Discrete chaos in fractional sine and standard maps," *Physics Letters A*, vol. 378, no. 5–6, pp. 484–487, 2014.
- [26] A. A. Khennaoul, A. Ouannas, S. Bendoukha, G. Grassi, X. Wang, and V. T. Pham, "Generalized and inverse generalized synchronization of fractional-order discrete-time chaotic systems with non-identical dimension," *Advances Difference Equations*, vol. 2018, Article ID 303, 2018.

- [27] O. Megherbi, H. Hamiche, S. Djennoune, and M. Bettayeb, "A new contribution for the impulsive synchronization of fractional-order discrete-time chaotic systems," *Nonlinear Dynamics*, vol. 90, no. 3, pp. 1519–1533, 2017.
- [28] Y. Ji, L. Lai, S. Zhong, and L. Zhang, "Bifurcation and chaos of a new discrete fractional-order logistic map," *Communications in Nonlinear Science and Numerical Simulation*, vol. 57, pp. 352–358, 2018.
- [29] H. Sun, Y. Zhang, D. Baleanu, W. Chen, and Y. Chen, "A new collection of real world applications of fractional calculus in science and engineering," *Communications in Nonlinear Science and Numerical Simulation*, vol. 64, pp. 213–231, 2018.
- [30] G.-C. Wu and D. Baleanu, "Discrete chaos in fractional delayed logistic maps," *Nonlinear Dynamics*, vol. 80, no. 4, pp. 1697–1703, 2015.
- [31] C. Mira, D. Fournier-Prunaret, L. Gardini, H. Kawakami, and J. C. Cathala, "Basin bifurcations of two-dimensional non-invertible maps: fractalization of basins," *International Journal of Bifurcation and Chaos*, vol. 4, no. 2, pp. 342–382, 1994.
- [32] D. Fourier-Prunaret and V. Guglielmi, "Bifurcations and attractors in two-dimensional maps of cubic type," in *Proceedings of the international conference on nonlinear theory and applications 1999*, Hawai, USA, November–December 1999.
- [33] V. Guglielmi, H. Poonith, D. Fourier-Prunaret, and A. K. Taha, "Security performances of a chaotic cryptosystem," in *Proceedings of the 2004 IEEE International Symposium on Industrial Electronics*, vol. 1, Ajaccio, France, May 2004.
- [34] T. Abdeljawad, "On Riemann and Caputo fractional differences," *Computers & Mathematics with Applications*, vol. 62, no. 3, pp. 1602–1611, 2011.
- [35] H. L. Gray and N. F. Zhang, "On a new definition of the fractional difference," *Mathematics of Computation*, vol. 50, no. 182, p. 513, 1988.
- [36] K. S. Miller and B. Ross, *Univalent Functions, Fractional Calculus, and Their Applications*, Eills Howard, Chichester, UK, 1989.
- [37] J. Čermák, I. Györi, and L. Néchvátal, "On explicit stability condition for a linear fractional difference system," *Fractional Calculus and Applied Analysis*, vol. 18, no. 3, pp. 651–672, 2015.
- [38] D. Baleanu, G. C. Wu, Y. R. Bai, and F. L. Chen, "Stability analysis of Caputo-like discrete fractional systems," *Communications in Nonlinear Science and Numerical Simulation*, vol. 48, pp. 520–530, 2017.

## Research Article

# Parallel Encryption of Noisy Images Based on Sequence Generator and Chaotic Measurement Matrix

Jiayin Yu , Yaqin Xie, Shiyu Guo, Yanqi Zhou, and Erfu Wang 

*Electrical Engineering College, Heilongjiang University, Harbin 150080, China*

Correspondence should be addressed to Erfu Wang; [wangerfu@hlju.edu.cn](mailto:wangerfu@hlju.edu.cn)

Received 23 December 2019; Revised 20 February 2020; Accepted 26 February 2020; Published 7 May 2020

Guest Editor: Viet-Thanh Pham

Copyright © 2020 Jiayin Yu et al. This is an open access article distributed under the Creative Commons Attribution License, which permits unrestricted use, distribution, and reproduction in any medium, provided the original work is properly cited.

With the rapid development of information technology in today's society, the security of transmission and the storage capacity of hardware are increasingly required in the process of image transmission. Compressed sensing technology can achieve data sampling and compression at the rate far lower than that of the Nyquist sampling theorem and can effectively improve the efficiency of information transmission. Aiming at the problem of weak security of compressed sensing, this study combines the cryptographic characteristics of chaotic systems with compressed sensing technology. In the actual research process, the existing image encryption technology needs to be applied to the hardware. This paper focuses on the combination of image encryption based on compressed sensing and digital logic circuits. We propose a novel technology of parallel image encryption based on a sequence generator. It uses a three-dimensional chaotic map with multiple stability to generate a measurement matrix. This study also analyzes the effectiveness, reliability, and security of the parallel encryption algorithm for source noise pollution with different distribution characteristics. Simulation results show that parallel encryption technology can effectively improve the efficiency of information transmission and greatly enhance its security through key space expansion.

## 1. Introduction

Nowadays, the rapid evolution of information technology and data networks has brought great convenience to people's productivity and lives [1]. As the main carrier of information transmission, a network must store and forward a significant amount of information at any moment [2]. Among them, digital information is easy to store and forward, and noise does not accumulate, which makes it easy to store and transmit widely in the network. As an important information carrier in digital information, the digital image is widely used in national defense, education, medical treatment, finance, and other fields [3]. Effective encryption of digital image information can resist illegal attacks, malicious destruction, and destruction of information by criminals and realize the safe transmission of information [4]. In the traditional process of information transmission and encryption, the Nyquist sampling theorem is applied, which indicates that the sampling frequency must be more than twice the highest frequency when sampling a signal with

limited bandwidth in order to ensure the complete recovery of the original signal from the sampling value [5]. In recent years, compressed sensing as a cryptosystem has attracted much attention owing to its low complexity and compressibility in the sampling process [6]. Compressed sensing can sample the compressible signal at the frequency far lower than that specified by Nyquist's sampling theorem and can ensure that the receiver can accurately reconstruct the original signal [7]. However, the encryption system under the traditional compressed sensing framework is vulnerable to plaintext attacks. To reduce the correlation between adjacent pixels of the encrypted image [8], an efficient image compression and encryption algorithm based on a chaotic system and compressed sensing was proposed in [9]. At the same time, owing to the use of diffusion and scrambling operations, the chaotic system has the characteristics of cryptography in order to achieve more effective encryption of image information.

Compressed sensing (CS), as a new signal sampling and compression technology [10], has been widely used in the

field of image processing since it was proposed [11]. Orsdemir et al. studied the robustness and security of CS-based encryption algorithms [12]. Schulz et al. analyzed the distortion performance of compressed sensing in image compression and compared it with traditional algorithms [13]. Fridrich discussed the relationship between discretization and chaotic cryptosystems and proposed a two-dimensional Baker-based symmetric image encryption algorithm. This algorithm uses image chaos to scramble and diffuse images to achieve image encryption [14]. Zhang proposed an image encryption algorithm about plaintext-related shuffling. This algorithm combines two types of diffusion operations and plaintext-related transformations to encrypt the image and uses hyper chaos to generate a keystream [15]. Enayatifar et al. proposed an image encryption scheme based on synchronous scrambling diffusion, using chaos mapping and a DNA encryption algorithm to diffuse and scramble pixels [16]. An image encryption algorithm based on two-dimensional sinusoidal coupled mapping and chaotic diffusion was proposed in the literature [17]. Chen et al. proposed an optical image conversion and encryption scheme based on a phase detection algorithm and incoherent superposition that can realize the conversion and encryption of color images and gray images [18]. Hua et al. used high-speed scrambling and pixel adaptation to encrypt an image. This can protect certain impulse noise and prevent data loss [19]. Gong et al. proposed an image encryption method combining a hyperchaotic system with a fractional-order discrete transform [20]. Zhang et al. [21] proposed an image encryption method combining orthogonal coding and double-random phase coding that can compress all images into random signals and diffuse them into stationary white noise. Wang et al. studied CS-based image optimization technology in three main aspects [22]. The signal after compressed sensing processing is optimized.

To improve the computational efficiency of compressed sensing and the security of image encryption, a parallel image encryption technique based on a sequence signal generator was proposed. Regarding information security, the algorithm aims to provide a new data fusion processing technology, design a new encryption scheme, create a plan under the premise of guaranteeing the safety of image encryption, and minimize the decryption time to reduce information storage. This indirectly reduces the cost of information transmission and storage. Owing to the sensitivity of the initial value and the complex dynamic behavior of chaotic systems, pseudo-random sequences with randomness, relevance, and complexity can be provided. When designing a CS measurement matrix, this algorithm introduces a chaotic system, which has cryptographic characteristics achieved through scrambling and diffusion [23]. Li et al. [24] proposed an image communication system for IOT monitoring combined with CS model which helps reduce the image encryption/decryption time. Zhou et al. [25] proposed an algorithm by using double random-phase encoding and compressed sensing to enhance the security of digital image encryption with authentication capability. Shi et al. [26] proposed an image CS framework using convolutional neural network. The sampling network adaptively learns the sampling matrix from the training

image. This study combines compressed sensing with chaotic cryptography to optimize the encryption effect and transmission efficiency of compressed sensing and greatly improve the key space.

In the actual information transmission process, noise cannot be avoided, and the existence of noise seriously affects the image quality. Aiming at the problem of noise-contaminated signals and whether the original signal can be reconstructed effectively after being encrypted and compressed by the compressed sensing algorithm, Section 4 of this article will focus on presenting the analysis of the encrypted observation when the plaintext contains noise. Whether the image can meet the encryption requirements and whether the reconstructed image is accurate will be assessed.

## 2. Compressed Sensing and Chaos Theory

Compressed sensing technology was originally developed using the sparsity or compressibility of signals, and its theory includes three key technologies [27]. The first is the sparse representation of the target signal in order to thin the signal to the extent possible [28]. In this, we need to obtain the transform domain that matches the target signal  $\psi$ . The second is the construction process of measurement matrix. The target signal is compressed and sampled after passing through the measurement matrix, so the design of the measurement matrix needs to ensure that the effective information contained in the target signal is not lost [29]. The receiver can effectively recover the target signal by using the sampling value. The third is the design of the reconstruction algorithm. The reconstruction algorithm finds the optimal solution of the target signal by solving the optimization problem [30]. Whether the reconstruction algorithm has accuracy, efficiency, and stability is also key in algorithm design.

Chaos used in this study is a new three-dimensional map with self-excited structures as proposed by Jiang et al. in 2016 [31]. This kind of chaotic system has hidden chaotic dynamics, which is a new topic in nonlinear science and has attracted extensive attention from mathematical and engineering researchers in recent years. This kind of self-excited three-dimensional mapping can provide a deeper understanding of the complex behavior of chaotic dynamics hidden in discrete mapping. At the same time, the stability of these chaotic systems can be analyzed based on the existence of fixed points. In this algorithm, a three-dimensional system with a single fixed point is used. The stability of the system will be analyzed by calculating the fixed point of the system.

*2.1. Mathematical Representation of Compressed Sensing.* Suppose that a two-dimensional signal  $X$  of size  $N \times N$  is needed in the process of achieving compressed sensing to make the signal sparse. Under the corresponding sparse space of the signal, CS can achieve effective compression and sampling. Using equation (1), CS can generate the sparse representation of the signal  $X$  under  $\psi$  [32]:

$$X = \sum_{n=1}^N \psi_n s_n = \psi s, \quad (1)$$

where  $\psi$  is the sparse basis matrix and  $s$  is the projection under the sparse basis  $\psi$ . In equation (1), if there exist  $K$  ( $K \ll N$ ) nonzero coefficients, the signal  $X$  is said to be compressible under a sparse basis  $\psi$ , and the sparsity is  $K$  [25]. If there is a two-dimensional matrix  $\phi$  of size  $M \times N$  ( $M < N$ ), then the original signal  $X$  can be converted into a signal of size  $M \times N$  by the following equation:

$$Y = \phi X = \phi \psi s, \quad (2)$$

where  $Y$  is the measurement value and  $\phi$  is the measurement matrix. On the basis of the known measurement value  $Y$  and measurement matrix  $\phi$ , CS can reconstruct the signal  $X$  by solving the equation which is underdetermined. In the traditional underdetermined equation, there should be infinite solutions [33]; however, because  $s$  is sparse, conversion to an optimization problem is possible. The unique optimal solution of the underdetermined equation can be arrived at by obtaining the minimum norm  $L_0$  in the following equation:

$$\begin{aligned} \min \quad & \|s\|_0 \\ \text{s.t.} \quad & Y = \phi \psi s, \end{aligned} \quad (3)$$

where  $\|m\|$  represents the  $L_0$  norm,  $s$  is recovery signal, and  $Y$  is the measurement signal. Because  $s$  is obtained using a sparse-basis transformation, the signal  $X$  can be recovered from the signal  $s$  through a single inverse transformation.

**2.2. Three-Dimensional Map with Single Fixed Point.** From the computational point of view, if the attractor domain of the attractor does not intersect with a small balanced neighborhood, then the former can be classified as a hidden attractor; otherwise, it is called a self-excited attractor [34]. Classical chaotic attractors, such as the Lorenz, Chua, Chen, and other chaotic systems, are self-excited attractors with one or more unstable equilibrium points. Self-excited attractors can be predicted by a standard calculation program, but there is no effective method to predict the existence of hidden attractors owing to the unpredictability of hidden attractor [35]. Hidden attractors can determine the success or failure of a project in engineering. It has become a new trend to study the continuous chaotic systems with implicit and multistable attractors.

This algorithm uses a three-dimensional chaotic map (SF1) with a single fixed point. The map was proposed in [31], which used a computer exhaustive search program to mine the hidden attractors contained in the map with stability. The mathematical expression is as follows:

$$\text{SFI} = \begin{cases} x_{k+1} = y_k, \\ y_{k+1} = z_k, \\ z_{k+1} = 0.6x_k + 0.39y_k + 0.65x_k^2 - 0.65y_k^2. \end{cases} \quad (4)$$

In order to solve the fixed points of the three-dimensional mapping above, it is first assumed that there are fixed

points  $(x^*, y^*, z^*)$  in equation (4). The Jacobian matrix at the fixed point is shown as follows:

$$J = \begin{bmatrix} 0 & 1 & 0 \\ 0 & 0 & 1 \\ 0.6 + 1.3x^* & 0.39 - 1.3y^* & 0 \end{bmatrix}. \quad (5)$$

The characteristic equation of the above equation is shown in the following equation:

$$\det(\lambda I - J) = \lambda^3 + p\lambda^2 + q\lambda + r = 0, \quad (6)$$

where  $p = -\text{tr}(J) = 0$ ,  $q = -(0.39 + 1.35y^*)$ ,  $r = \det(J) = -(0.6 + 1.3x^*)$ , and  $\text{tr}$  is the trace of the Jacobian matrix. We can determine the unique fixed point  $x^* = y^* = z^* = 0$  based on the definition of the fixed point. According to equation (6), the eigenvalues  $|\lambda_1| = 0.7761$ ,  $|\lambda_2| = 0.7761$ , and  $|\lambda_3| = 0.9962$  of the three-dimensional system shown in (4) can be obtained. The eigenvalues of the Jacobian matrix at this fixed point  $\lambda_1$ ,  $\lambda_2$ , and  $\lambda_3$  are all in the unit circle, that is,  $|\lambda_i| < 1$ . Therefore, the fixed point of the three-dimensional chaotic map is stable, that is, the chaotic map has the hidden chaotic attractor of the stable fixed point. Attractors of the chaotic maps are shown in Figure 1.

### 3. Parallel Compressed Sensing Encryption Algorithm Based on Sequence Generator

In the image encryption and transmission process, the complete image can be transmitted directly or by row or column. The efficiency of image transmission depends on the dimensions of the image information. In order to improve the efficiency of encryption and transmission, this study designs a block and parallel compressed sensing encryption algorithm. We study this problem in detail and introduce a logic circuit-based compressed sensing encryption method in [36]. Based on this algorithm, this paper makes a further study. By selecting appropriate block dimensions, the image is divided into blocks, and the blocks are encrypted and transmitted in parallel. This method can greatly improve the transmission efficiency of the image. In the process of designing the measurement matrix, this algorithm is based on the sensitivity and pseudorandom performance of chaotic signals to initial values, as well as the cryptographic characteristics of chaos under the mechanism of diffusion and scrambling. Combined with the feature that compressed sensing needs to rely on a measurement matrix for compressed sampling, the security of a traditional compressed sensing framework is not high, and the reconstruction wastes a large amount of storage resources.

**3.1. Algorithm Principle.** This algorithm adopts a combination of a digital logic circuit and compressed sensing theory. First, the binary sequence signal of the length is generated through the sequence signal generator, and the binary sequence signal is taken as the “modulation signal.” Based on chaotic system’s sensitivity to the “tiny disturbance” of the initial conditions, for chaotic systems, the initial value of any small changes can directly affect the entire



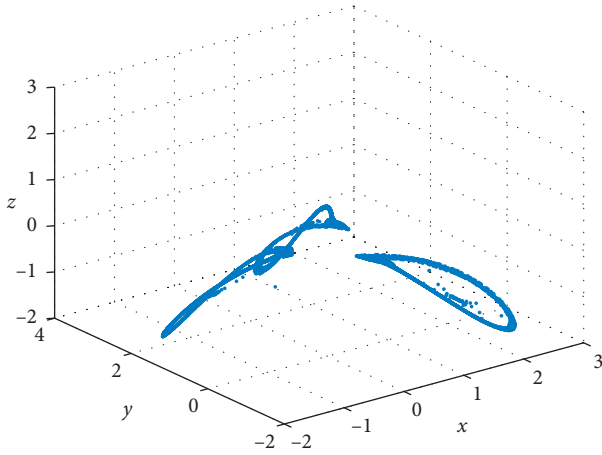


FIGURE 1: SF1 attractor.

chaos matrix generation. In this way, the security of image encryption can be improved. Second, the chaos matrix disturbed by the initial value is taken as the measurement matrix, and the compressed sensing process is used to encrypt the image. In this study, a  $256 \times 256$  image is segmented into eight blocks by columns, and the image is segmented and compressed in parallel. In order to better present the chaotic cryptographic characteristics, this algorithm diffuses and scrambles the compressed sampled cipher text image so that the energy blocks gathered in blocks in the cipher text image after block encryption can be evenly distributed. This is distributed on the entire image to achieve effective encryption and efficient transmission of the image information. The realization principle diagram of this algorithm is shown in Figure 2.

**3.2. Sequence Signal Generator Mode.** In this study, a shift register with feedback logic circuit is designed, as shown in Figure 3. If the number of bits of the sequence signal is  $m$  and the number of bits of the shift register is  $n$ , then  $2^n \geq m$  should be used. For example, to generate a set of 8 bit sequence signals such as 00101110 (time sequence from left to right), a 3 bit shift register and a feedback logic circuit can be used to form the required signal generator. The shift register outputs the serial output signal from end  $Q_2$ , that is, the required sequence signal.

The sequence signal generated according to the requirements can list the state transition table that the shift register should have, as shown in Table 1. Starting from the requirements of state transition, the requirements for the value of input  $D_0$  of the shift register are obtained. According to the value requirements, the functional relationship between  $D_0$  and  $Q_2$  and  $Q_1$  and  $Q_0$  can be obtained as shown in the following formula:

$$D_0 = Q_2 Q_1' Q_0 + Q_2' Q_1 + Q_2' Q_0'. \quad (7)$$

The state transition table is shown in Table 1.

The clock signal is continuously added to the counter, and the state of  $Q_2 Q_1 Q_0$  circulates continuously according to the order given in Table 1.  $Q_2$  is the output end of the

sequence signal, and the feedback logic circuit in the generator can be used as the key to modulate the initial value of the chaotic system. It should be noted that the purpose of generating different sequence signals can be realized only by modifying the functional relationship of the feedback logic circuit, so this circuit possesses the characteristics of flexibility and convenience.

**3.3. Parallel Compressed Sensing.** In this study, the initial value of the chaotic system is fine-tuned by the binary sequence signal generated in the previous section, and different chaotic matrices are generated as the measurement matrices to realize the compressed sensing process. In the image process compression and encryption using compressed sensing, it is necessary to set the compression ratio, adjust the dimensions of the measurement matrix according to the size of the compression ratio, and realize the compression sampling process of the sparse image. In this algorithm, the sparse plaintext image is evenly divided into eight blocks according to the column, and the size of each block is  $256 \times 32$ . Compared with the transmission by column, eight-block parallel transmission can effectively improve the efficiency. The parallel compression sampling process is shown in Figure 4.

It should be noted that although the parallel compressed sensing image encryption scheme can effectively and reliably encrypt the image, it is not bereft of some defects. Since the plaintext image is sampled as a block, the energy of each block in the measured value is stored centrally. To overcome this defect, we adopt diffusion and scrambling operations to evenly distribute the energy of the cipher text image in the entire image. The reference formula for the diffusion process is as follows:

$$Q^*(n) = Q(n) \oplus k_d(n) \oplus Q^*(n-1), \quad (8)$$

where  $Q(n)$  is the current operated element,  $Q^*(n)$  is the output cipher element,  $Q^*(n-1)$  is the previous cipher element, and  $k_d(n)$  is the corresponding key stream.

**3.4. Encryption Performance Analysis.** We select a  $256 \times 256$  gray image "Pepper" from the standard test gallery. The image is sparsified by using a discrete wavelet transform, and the sparse image is divided into eight parts. Each part has dimensions of  $256 \times 32$ . The initial value of the chaotic system is as follows:  $x(1) = 0.17$ ,  $y(1) = 1.63$ , and  $z(1) = -1.18$ . According to the method detailed in Section 3.1, the sequence signal generator is designed to generate the binary signal 00101110. When the sequence signal is 1, the initial value of chaos is fine-tuned to a step size of  $10^{-8}$ . When the sequence signal is 0, the initial value at this point is kept unchanged to generate the chaotic signal. The chaos matrix is used as the measurement matrix, and eight sub-blocks of the image are compressed and sampled in parallel by means of compressed sensing. The dimensions of the measurement matrix in the encryption process are  $190 \times 256$ , so the compression ratio is 74.2%. Finally, the encrypted cipher text image is diffused. Figure 5 shows the

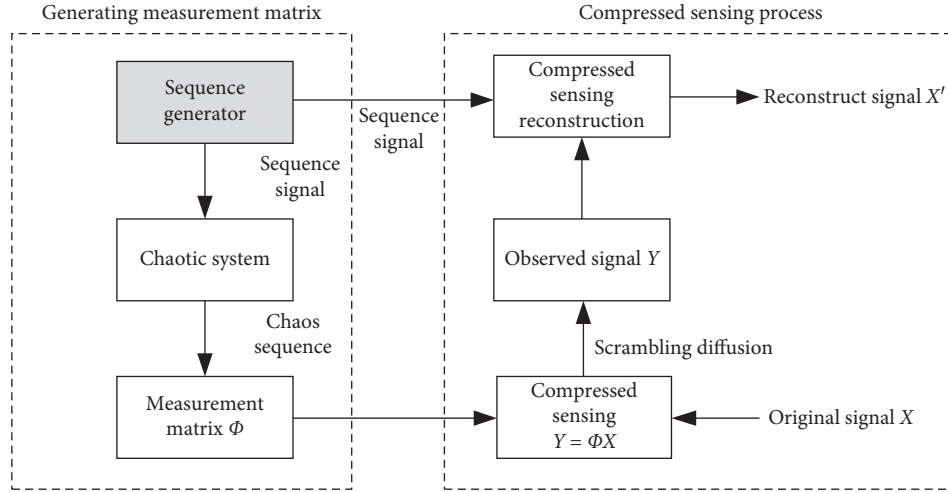


FIGURE 2: Parallel compression sensing encryption algorithm based on sequence generator.

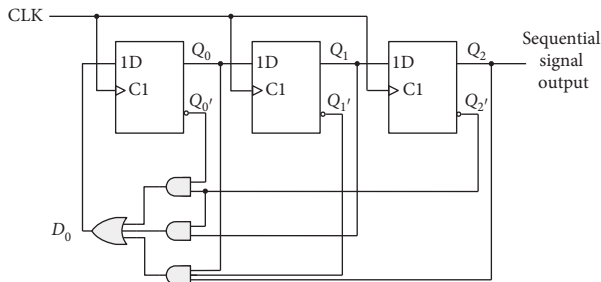


FIGURE 3: Signal generator based on shift register.

TABLE 1: Circuit state transition.

CLK	$Q_2$	$Q_1$	$Q_0$	$D_0$
0	0	0	0	1
1	0	0	1	0
2	0	1	0	1
3	1	0	1	1
4	0	1	1	1
5	1	1	1	0
6	1	1	0	0
7	1	0	0	0
8	0	0	0	1

original image, encrypted image, diffused image, and difference between the encrypted image and diffused image.

As can be seen from Figure 5, the algorithm described in this study presents a snowflake shape after encrypting sparse images, and it is unable to distinguish any information related to plaintext by the naked eye. From a subjective perspective, it can be considered that this algorithm achieves effective encryption of plaintext. Next, the encryption effect and reconstruction effect are analyzed from an objective perspective to verify that this algorithm can achieve the secure encryption and effective decryption of plaintext images. Figure 6 shows the original image, diffused image, and their histograms.

The histogram in Figure 6(c) can clearly reflect the distribution of pixel values, from which we can obtain relevant information of the image. However, the pixel values in Figure 6(d) are evenly distributed within the range  $[0, 255]$ . Different from the normal image, the attacker cannot obtain any valid information of the original image from the encrypted image. From the perspective of the histogram, this algorithm achieves effective encryption of the plaintext image.

Information entropy is an index used in information theory to measure the amount of information. Conversely, the more chaotic the system, the higher the information entropy. For image information, the image information entropy with high information is lower, while the image information entropy with low effective information is higher. The higher the entropy is, the more evenly the energy distribution in the image is and the less information the attacker can obtain. Table 2 shows the change of information entropy with the compression ratio when the compression rate changes.

As can be seen from the table, the entropy value of the image encrypted by the algorithm in this study is close to 8, indicating that the algorithm achieves secure encryption of the image.

### 3.5. Decryption (Reconstruction) Effect and Performance.

This algorithm uses compressed sensing to encrypt the image. The decryption process can be regarded as the inverse operation of the encryption process. The decryption process can also be seen as the reconstruction process of the image. First, the cipher text is antidiffused, and the formula is shown as (9). The receiving end generates sequence signals according to the key it holds and generates the initial value control parameters of the measurement matrix. The chaotic matrix is restored according to the control parameters, and the measurement matrix is obtained. The sparse signal is reconstructed by solving the optimization problem. The formula for solving the optimization problem is shown in (10). Finally, the plaintext image is restored by using equation (11).

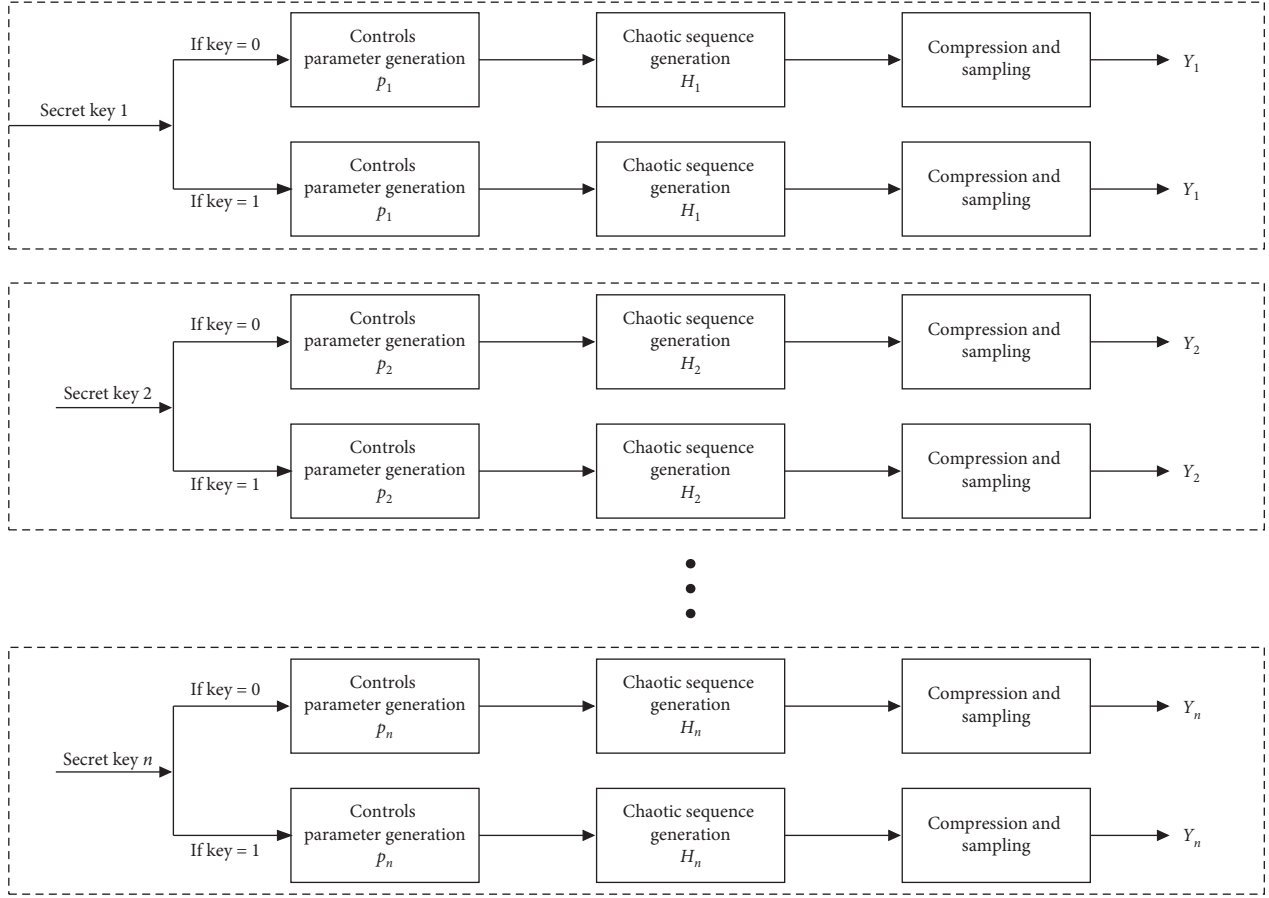


FIGURE 4: Parallel sampling compression of compressed sensing process.

$$Q(n) = Q^*(n) \oplus Q^*(n-1) \oplus k_d(n), \quad (9)$$

$$\begin{aligned} \hat{s}_i &= \arg \min_{s_i \in \mathbb{R}^N} \|s_i\|_1 \\ \text{s.t. } \hat{y}_i &= \phi_i x_i = \phi_i \psi_i s_i, \end{aligned} \quad (10)$$

$$i = 1, \dots, N,$$

$$\hat{x}_i = \psi \hat{s}_i. \quad (11)$$

According to the above process, the original image, reconstructed image, and their histograms are shown in Figure 7.

According to Figure 7(b), we see that this algorithm can achieve reconstruction of cipher text. The image reconstruction reflects a clear image of effective information. Comparing Figures 7(c) and 7(d) of the histogram, the reconstructed image can be found in the original image and the pixel distribution is basically similar, and we can assume that this algorithm can realize image reconstruction.

Structural similarity is an index that measures the similarity of two images, and the value ranges from 0 to 1. The closer the similarity to 1, the higher the similarity of two images; otherwise, the greater the difference. Table 3 shows the structural similarity between the original image and reconstructed image at different compression rates.

As can be seen from Table 3, with an increasing compression rate, the image similarity also increases. When the compression rate is about 74.2%, the image can recover over 90%. However, the similarity of cipher text is very low, which indicates that this algorithm can achieve the image encryption requirements.

#### 4. Encryption and Decryption Algorithms for Noisy Images and Performance Analysis

In the process of actual transmission, the information is composed of different kinds of noise pollution. Noise may be derived from the source with the noise of the signal, from the transmission channel through additive noise, or can be derived from the actual produced physical noise. The existence of noise affects the accuracy of information transmission. This section will present the analysis of whether the algorithm can still effectively encrypt and successfully reconstruct the image when the noise is mixed at the source.

*4.1. Encryption and Reconstruction Results.* This study intends to add Gaussian noise and salt-and-pepper noise to the original image, sparse the original image containing noise, and compress and perceive the sampling encryption. This is used to verify whether the compressed sensing image encryption technology optimized by this algorithm has the

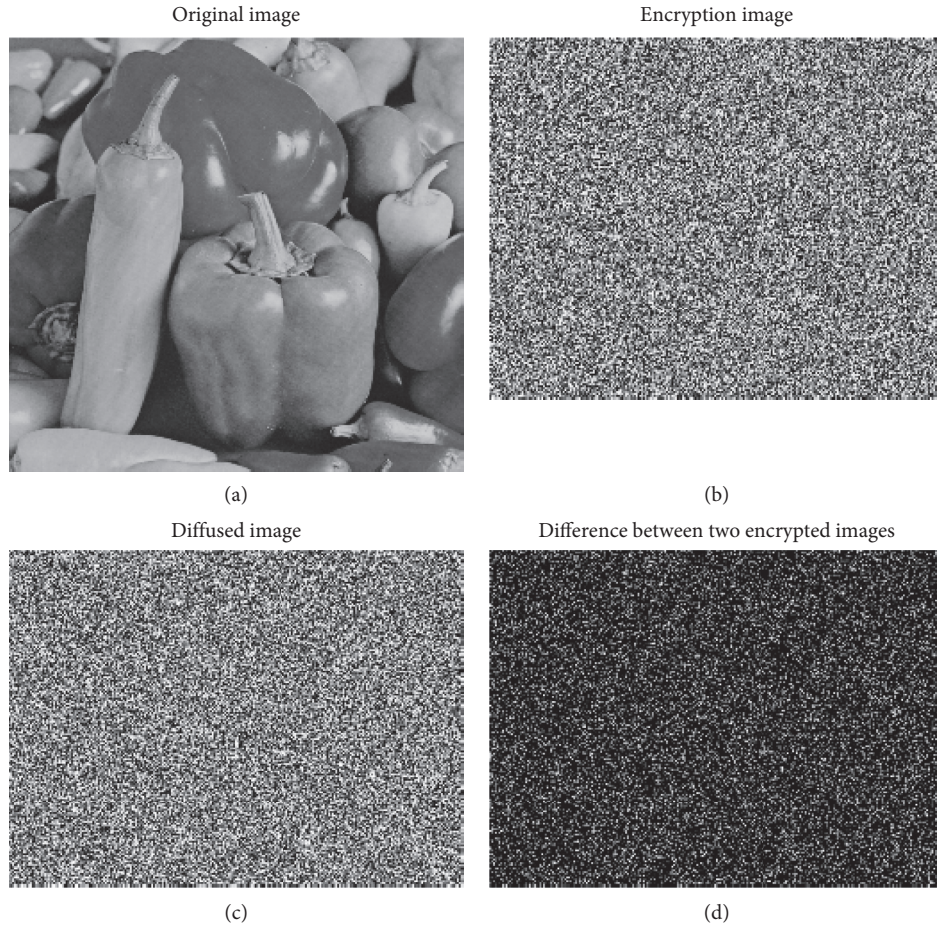


FIGURE 5: Results of gray image parallel compression perception encryption: (a) original image, (b) compressed sensing encrypted image, (c) diffused cipher text image, and (d) difference between (b) and (c).

ability to resist source noise. The salt-and-pepper noise used in this section has a noise density of 0.02, average Gaussian noise of 0, variance of 0.01, and compression ratio of 0.8. First, it is determined whether the image with noise can be reconstructed at the receiving end. The simulation results and histogram of adding salt-and-pepper noise to the original image are shown in Figure 8, and the simulation results and histogram of adding Gaussian noise are shown in Figure 9.

As can be seen from Figures 8(b) and 9(b), after adding noise to the original signal, the cipher text image encrypted by the algorithm in this study still resembles a snowflake, and the useful information in the image cannot be identified by observation. The histograms of Figures 8(e) and 9(e) are evenly distributed, indicating that we have successfully hidden the effective information of the original image, and the attacker cannot attack the algorithm using a statistical attack. Figures 8(c) and 9(c) show the recovered images of the encrypted image after the reconstruction algorithm. It can be seen that although the image still contains noise, the reconstructed image can be restored to the original image after filtering. It shows that the algorithm has a certain ability to resist the source noise. Since the intensity and variance of the noise we added to the original picture are both low, by

comparing Figures 8(d), 8(f), 9(d), and 9(f), we can see that the image is polluted with salt-and-pepper noise. The reconstructed image has a better restoration effect after reconstruction, the image is clear, the histogram distribution is similar to the original image, and the signal contaminated by Gaussian noise is greatly affected, but it can still effectively recover the original information.

**4.2. Encryption Performance Analysis.** When the information entropy of the image is low, it is vulnerable to malicious attacks and tampering by criminals. For encrypted images, the higher the information entropy is, the more uniform the energy distribution in the image is and the less useful information an attacker can obtain from the grayscale distribution. Table 4 shows the changes in the entropy of the encrypted image when the compression ratio changes during the compression and encryption process. The noise intensity of the salt-and-pepper noise selected during the experiments in this section is 0.02; the mean and variance of the Gaussian noise are 0.2 and 0.01, respectively; and the compression rate of the compressed sensing process is 74.2%. In the table,  $I$  represents the noise intensity,  $M$  represents the mean, and  $V$  represents the variance.



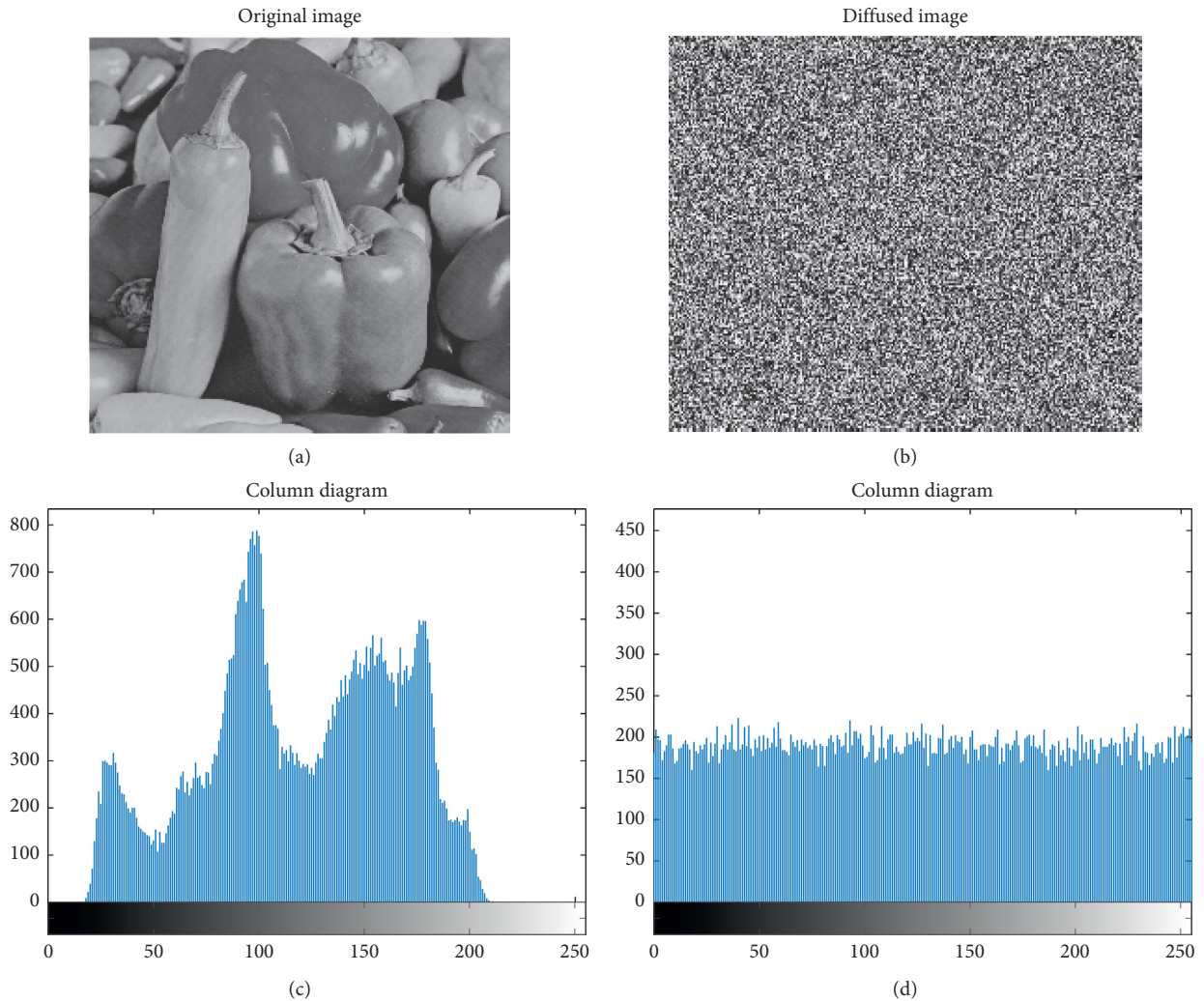


FIGURE 6: Histogram of original and encryption image: (a) original image, (b) cipher image, (c) histogram of plaintext image, (d) and histogram of cipher text image.

TABLE 2: Information entropy of encrypted images.

Entropy	Compression ratio							
	0.3	0.4	0.5	0.6	0.7	0.8	0.9	1
Cipher image	7.9920	7.9936	7.9937	7.9954	7.9960	7.9965	7.9972	7.9970

The table lists the cipher text entropies under the influence of salt-and-pepper noise and Gaussian noise with different parameters. It shows that the entropy value of the image after encryption in this study is close to 8, which can achieve effective encryption.

The correlation between adjacent pixels in an image can reflect the degree of diffusion of pixels in the image. The correlation between adjacent pixels in an encrypted image should be close to zero. In [33], a fractional-order Mellin transform is used to compress the image from two directions to obtain the encrypted image. Meanwhile, in [37], a discrete fractional-order random measurement matrix is used to encrypt the image from orthogonal directions. In this study, the correlation of adjacent pixels is compared with the above

two studies to prove the effectiveness of this algorithm. Table 5 shows the correlation of adjacent pixels under the influence of salt-and-pepper noise and Gaussian noise, respectively.

Figure 10 shows the adjacent pixel correlation distribution between the plaintext image and the encrypted image when the original signal is polluted by salt-and-pepper noise with a noise intensity of 0.02. From the figure, we can see that the plaintext image has a high degree of correlation, while the adjacent pixels in the cipher text image are evenly distributed in the pixel interval, and the correlation is very weak. Therefore, according to the data and image results, it can be seen that the algorithm in this study can still achieve a good encryption effect when the signal source is polluted by noise.

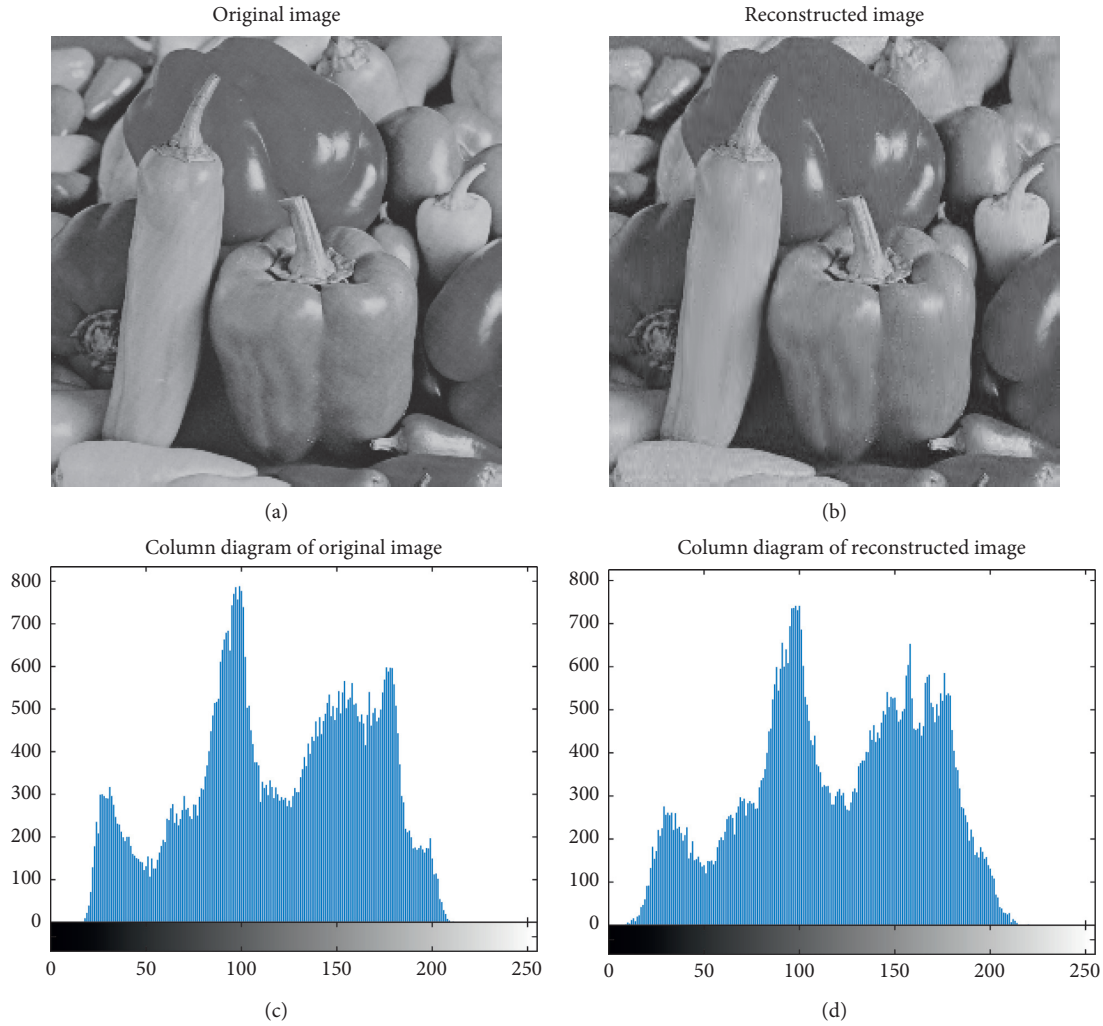


FIGURE 7: Histogram of original and reconstructed image: (a) original image, (b) reconstructed image, (c) histogram of original image, and (d) histogram of reconstructed image.

TABLE 3: Structural similarity between original image and reconstructed image.

SSIM	Compression ratio							
	0.3	0.4	0.5	0.6	0.7	0.8	0.9	1
Reconstructed image	0.4528	0.6356	0.7761	0.8592	0.9059	0.9453	0.9607	0.9813
Cipher image	0.0025	0.0034	0.0043	0.0055	0.0066	0.0070	0.0079	0.0092

Structural similarity is an index that can measure the similarity of two images. The structural similarity of natural images is very high, which is reflected in the strong correlation between the pixels of images. The value range of structural similarity is 0 to 1. When the similarity is close to 1, the more similar the two pictures, the more different the two pictures. Table 6 shows the structural similarity between the encrypted image and the original image under the influence of salt-and-pepper noise and Gaussian noise.

As can be seen from the table, the structural similarity of cipher text images affected by any noise is less than 0.2, which can achieve a satisfactory encryption effect.

*4.3. Decryption (Reconstruction) Performance Analysis.* The peak signal-to-noise ratio (PSNR) refers to the ratio between the maximum possible power of a signal and the destructive noise power that affects its signal accuracy. It can be defined by the mean square error (MSE), and its expression is shown as follows:

$$\text{PSNR} = 10 \log_{10} \left( \frac{L^2}{\text{MSE}} \right), \quad (12)$$

where  $L$  is the value range of grayscale in the image. For the 8 bit image,  $L = 256$ . In general, the higher the PSNR, the lower the distortion.



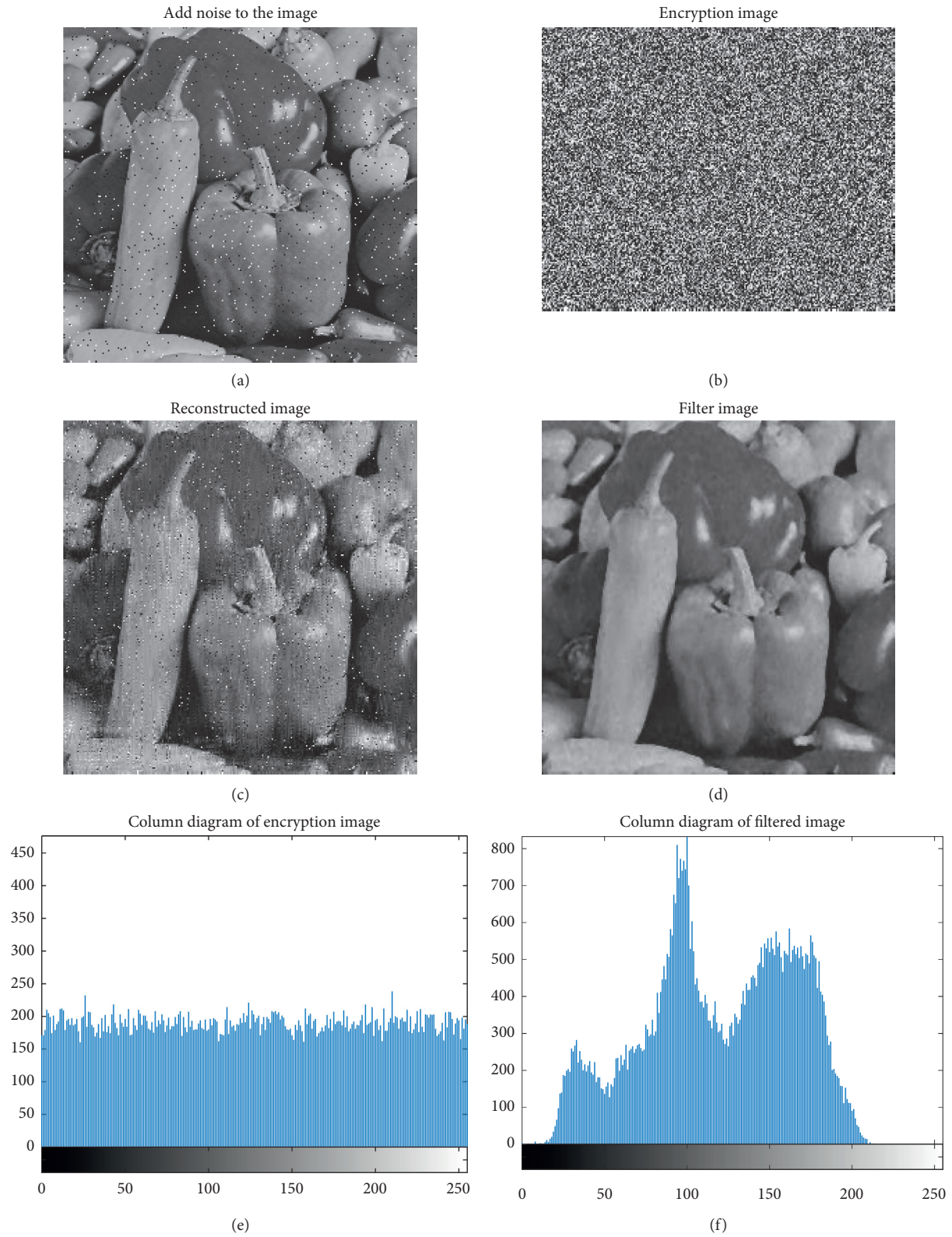


FIGURE 8: Encryption and reconstruction of noisy images: (a) image with noise, (b) cipher image, (c) reconstructed image, (d) filtered image, (e) histogram of cipher text image, and (f) histogram of filtered image.

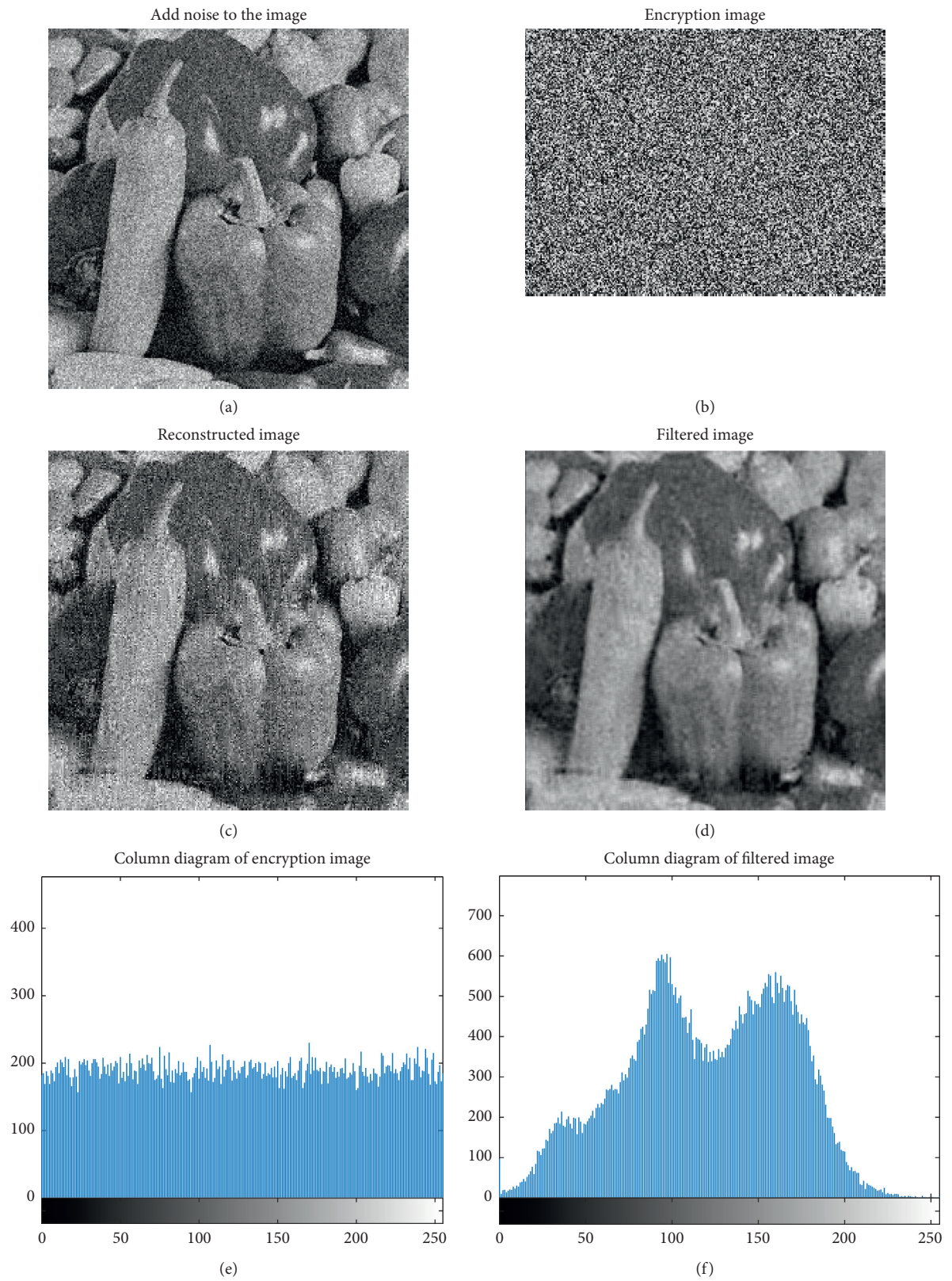


FIGURE 9: Encryption and reconstruction of noisy images: (a) image with noise, (b) cipher image, (c) reconstructed image, (d) filtered image, (e) histogram of cipher text image, and (f) histogram of filtered image.

TABLE 4: Information entropy of encrypted images.

Entropy		Compression ratio						
		0.3	0.4	0.5	0.6	0.7	0.8	0.9
Salt-and-pepper noise	$I = 0.02$	7.9918	7.9934	7.9948	7.9948	7.9962	7.9964	7.9970
	$I = 0.05$	7.9913	7.9933	7.9936	7.9955	7.9957	7.9966	7.9971
	$I = 0.1$	7.9921	7.9930	7.9944	7.9962	7.9957	7.9965	7.9971
Gaussian noise	$M = 0, V = 0.01$	7.9902	7.9939	7.9951	7.9954	7.9962	7.9955	7.9970
	$M = 0, V = 0.02$	7.9901	7.9928	7.9946	7.9956	7.9962	7.9969	7.9967
	$M = 0.2, V = 0.01$	7.9901	7.9925	7.9950	7.9951	7.9960	7.9961	7.9971

TABLE 5: Correlation between adjacent pixels of cipher text image.

Algorithm	Horizontal direction	Vertical direction	Diagonal direction
Proposed algorithm (impulse noise)	0.0498	-0.0035	0.0032
Proposed algorithm (Gaussian noise)	-0.0398	0.0051	0.0042
Reference [30]	0.0586	-0.0021	0.0269
Reference [25]	0.0597	0.0766	0.0083

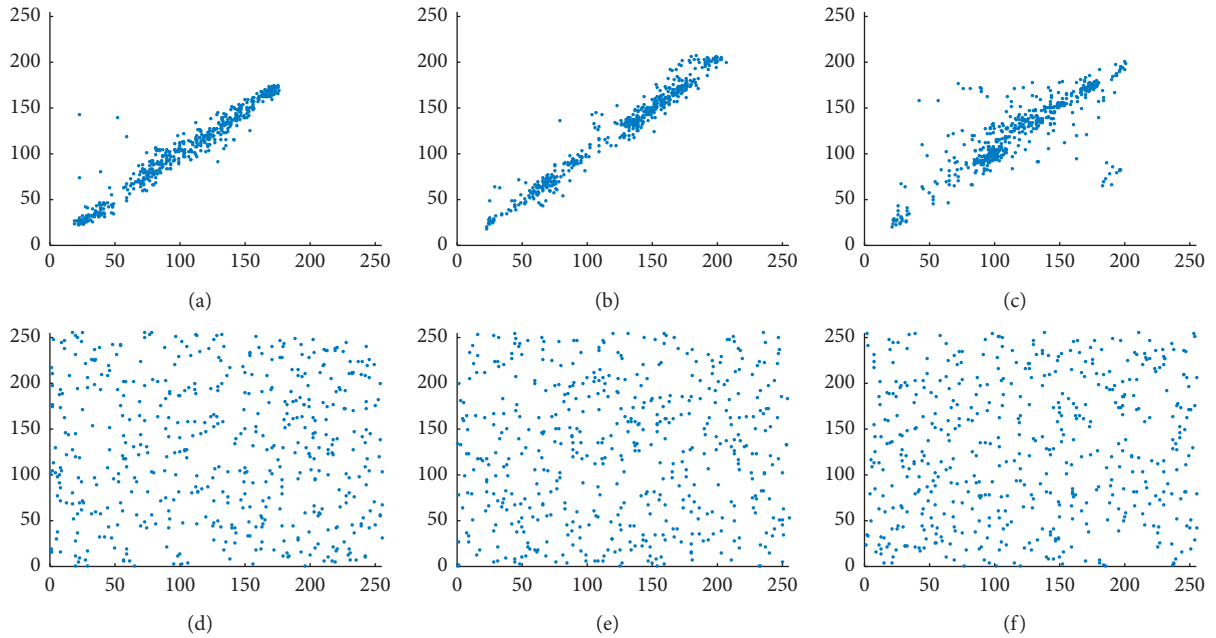


FIGURE 10: Distribution of adjacent pixels: (a) plaintext horizontal adjacent pixels, (b) plaintext vertical adjacent pixels, (c) plaintext diagonal adjacent pixels, (d) cipher text horizontal adjacent pixels, (e) cipher text vertical adjacent pixels, and (f) cipher text diagonal adjacent pixels.

TABLE 6: Structural similarity between original image and cipher image.

SSIM (cipher image)		Compression ratio						
		0.3	0.4	0.5	0.6	0.7	0.8	0.9
Impulse noise	$I = 0.02$	0.0042	0.0044	0.0064	0.0085	0.0071	0.0067	0.0074
	$I = 0.05$	0.0024	0.0018	0.0049	0.0036	0.0041	0.0047	0.0052
	$I = 0.1$	0.0020	0.0026	0.0020	0.0035	0.0074	0.0066	0.0076
Gaussian noise	$M = 0, V = 0.01$	0.0017	0.0024	0.0031	0.0054	0.0053	0.0113	0.0104
	$M = 0, V = 0.02$	0.0022	0.0020	0.0041	0.0031	0.0051	0.0063	0.0120
	$M = 0.2, V = 0.01$	0.0023	0.0022	0.0039	0.0068	0.0089	0.0112	0.0063

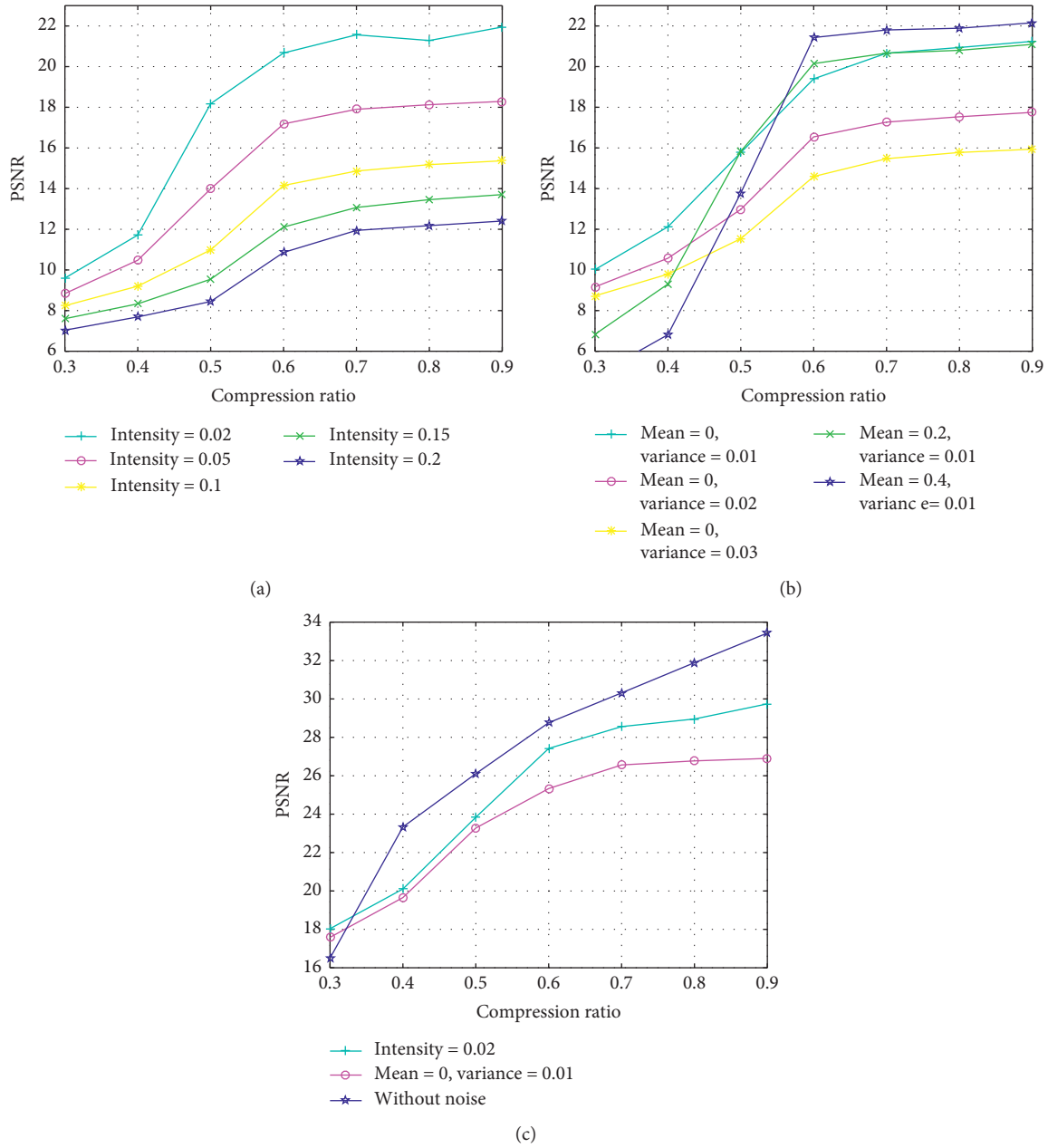


FIGURE 11: PSNR of reconstructed image: (a) PSNR of impulse noise, (b) PSNR of Gaussian noise, and (c) PSNR of filtered image.

Figure 11 shows a line chart of the peak signal-to-noise ratio of the restored picture under the salt-and-pepper noise with different noise intensities and Gaussian noise pollution with different mean variances.

It can be seen from Figure 11(a) that the PSNR of the reconstructed image increases with the reduction of salt-and-pepper noise intensity, and the curve trend in the figure is relatively consistent. In Figure 11(b), there are two variables (mean value and variance), and the curve in the figure has a large fluctuation. Since it has not been filtered, the reconstructed image still contains noise. When calculating PSNR, the noise in the image will have a certain impact on the calculated value. The PSNR value after filtering can be improved effectively. It can be seen from the performance

analysis of encrypted images in Tables 4–6 that the images encrypted by the algorithm in this paper can meet the encryption requirements of images. In Figure 11(c), PSNR values under the condition of filtering salt-and-pepper noise, filtering Gaussian noise, and no noise are given, respectively, and it can be seen that the image quality has been significantly improved after filtering. In Figure 11(c), the curve at the top represents the PSNR value of the proposed algorithm under the circumstance of no noise. When processing the image without noise, the peak signal noise is higher, which can meet the safety requirements.

In reference [38], Zhou et al. proposed an algorithm based on hyperchaotic system and 2D compressive sensing without any noise. Table 7 shows the comparison results



TABLE 7: Comparison of PSNR.

	Proposed algorithm		Reference [38]	
	Impulse noise $I=0.02$	Gaussian noise $M=0, V=0.01$	Picture 1	Picture 2
PSNR	28.5603	26.5630	30.6881	26.3460

between the algorithms in this paper and those in the literature [38] for which the compression rate is 76.5625%.

The PSNR of the two pictures in reference [38] is 30.6881 and 26.3460, respectively. In the algorithm in this paper, when the noise type is pepper-and-salt noise, the PSNR is 28.5603. When the noise type is Gaussian noise, the PSNR is 26.5630. It can be seen from the comparison that the image encrypted by the algorithm in this paper can also achieve effective decryption under the influence of noise.

In practical application, noise parameters are selected according to the size of the compression rate. From the figure above, we find that although this algorithm can recover the original image at the receiving end owing to the noise at the source, the effect of image reconstruction is still affected to some extent. In this paper, we think we can use compression rate as a measure of throughput. As can be seen from Table 3 and Figure 11, the similarity coefficient and PSNR of reconstructed images will increase with the increase of compression rate. However, when the compression rate reaches about 70%, the performance of reconstructed images can be stable. When the compression rate is more than 70%, the growth curve is relatively flat. Therefore, in the process of encryption and decryption, a better reconstruction effect can be achieved by setting the compression rate at around 60%–70%. Table 8 shows the structural similarity between the reconstructed image and the original image under the influence of noise of different parameters when the compression ratio is 74.2%.

It can be seen from Table 8 that under the influence of different parameter noises, the receiving end can reconstruct the original signal and can subjectively determine the effective information in the restored image. The structural similarity under each parameter mostly exceeds 0.5, indicating that the algorithm in this study can effectively recover the effective information of the signal when processing the signal polluted by noise and has the certain ability to resist the source noise.

**4.4. Key Sensitivity and Key Space Analysis.** Because the encryption algorithm is highly sensitive to the key, when the key changes slightly, this leads to the failure of decryption and other processes. Key sensitivity refers to the degree to which the cipher text changes when the initial key changes slightly. Owing to the sensitivity of the initial value of the chaotic system, we can verify the key sensitivity of this algorithm based on this characteristic. When the chaotic system changes initial value slightly, the reconstructed image will be greatly different. This section studies whether the original signal has good key sensitivity after being encrypted by the algorithm in this study. The superimposed noise in the original signal is salt-and-pepper noise with a noise intensity of 0.02, and the compression rate in the image encryption process is 74.2%.

Figure 12(a) is the recovery image when the key changes by an order of magnitude of  $10^{-14}$ , Figure 12(b) is the recovery image when the key changes by  $10^{-15}$ , and Figure 12(c) is the recovery image when the key changes by  $10^{-16}$ . It can be seen that although the initial value changed only very slightly, the reconstructed image could not recognize any effective information, proving that the algorithm has good key sensitivity.

In the process of image encryption, the size of the key space reflects the difficulty and complexity of attacking the cryptographic system. The above experiments on key sensitivity verification also show that the encryption algorithm needs to have a strong dependence on the key. When the decryption key changes slightly, the decrypted image will be very different from the original image. As an important reference to evaluate the encryption algorithm, the key space directly determines whether the algorithm can resist exhaustive attacks. For the algorithm proposed in this study, without considering the diffusion process or scrambling, only the following are considered: a measurement matrix to decrypt, nine-chaotic-sequence signal generator, and the control parameters of the system. According to the international standard IEEE 754, in order to simplify the comparison, a positive indices section is represented. The double-precision floating-point type of valid number is 52. Table 9 lists the key spaces of the algorithm in this study and the key spaces of different schemes proposed by others. It can be seen from the table that the key space in this study is at least  $2^{52 \times 9} = 2^{468}$ . In other words, the attacker needs  $2^{468}$  attacks to build the correct matrix, so the image encryption algorithm proposed in this study is safe enough to resist brute-force attacks.

The sensitivity intensity of the plaintext can determine the ability to resist differential attacks. The parameters used to measure the sensitivity of the encryption algorithm to plaintext can be described by either the number of pixels change rate (NPCR) or the unified average changing intensity (UACI). The calculation formulas of NPCR and UACI are as follows:

$$\text{NPCR} = \frac{1}{N \times M} \sum_{i=1}^M \sum_{j=1}^N E(i, j) \times 100\%, \quad (13)$$



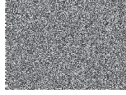





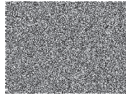



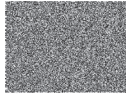







$$\text{UACI} = \frac{1}{N \times M} \sum_{i=1}^M \sum_{j=1}^N \frac{|M_1(i, j) - M_2(i, j)|}{255} \times 100\%, \quad (14)$$

where  $M$  and  $N$  are the number of rows and columns of the image pixel and  $n$  is the color bit depth of the image. The NPCR and UACI of the encrypted image are listed in Tables 10 and 11, respectively, and are compared with the critical value.

In [42], the key generated through chaos is used as the index of row and column replacement in the image encryption process, and the encryption method of row and column replacement is adopted to encrypt the image. In [43], a hyperchaotic system based on closed-loop modulation is used to replace image pixels. In [44], piecewise linear chaotic mapping is used to exchange binary elements in the original image sequence with a chaotic sequence to scramble and encrypt the image. Table 12 shows a comparison



TABLE 8: Structural similarity between original image and decryption image.

Original image	Image with noise	Noise parameter	Cipher image	Decrypted image	SSIM
 (impulse noise)		$I = 0.02$			0.7433
		$I = 0.05$			0.5275
		$I = 0.1$			0.3981
 (Gaussian noise)		$M = 0$ $V = 0.01$			0.5895
		$M = 0$ $V = 0.02$			0.4853
		$M = 0.2$ $V = 0.01$			0.5883

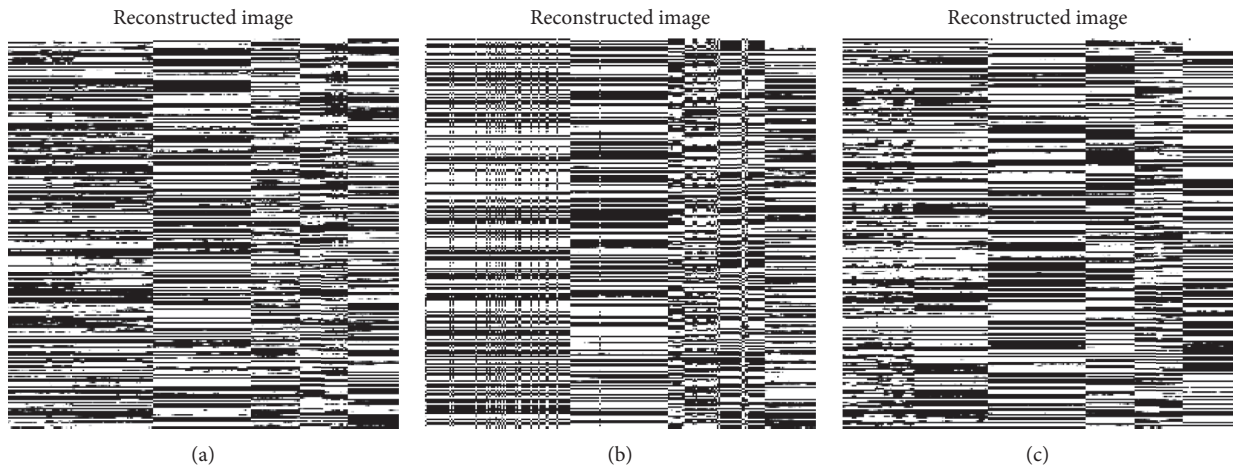
FIGURE 12: Key sensitivity analysis: (a) initial value change of  $10^{-14}$ , (b) initial value change of  $10^{-15}$ , and (c) initial value change of  $10^{-16}$ .

TABLE 9: Comparison of key spaces.

Algorithm	Proposed algorithm	Reference [12]	Reference [39]	Reference [40]	Reference [41]
Key space	$2^{468}$	$2^{16}$	$2^{78}$	$2^{128}$	$2^{96}$

TABLE 10: NPCR analysis of test image.

NPCR (%)	Ideal NPCR critical values		
	$N_{0.05}^* = 99.5693\%$	$N_{0.01}^* = 99.5527\%$	$N_{0.001}^* = 99.5341\%$
99.6085	Pass	Pass	Pass

TABLE 11: UACI analysis of test image.

UACI (%)	Ideal UACI critical values		
	$U_{0.05}^{*-} = 33.2824\%$	$U_{0.01}^{*-} = 33.2255\%$	$U_{0.001}^{*-} = 33.1594\%$
33.4632	Pass	Pass	Pass

TABLE 12: NPCR and UACI.

Index	Our scheme	Reference [42]	Reference [43]	Reference [44]
NPCR (%)	99.6094	99.6075	99.6063	97.6198
UACI (%)	33.4635	33.4195	33.3437	32.8014

between the NPCR and UACI obtained by the algorithm in this study and the above studies. The evaluation criteria of NPCR and UACI are given in [45].

The results show that the encrypted image can reach the threshold standard, which verifies that the compression and encryption algorithm proposed in this study can resist a differential attack to some extent.

## 5. Conclusions

In this study, the parallel encryption technology of a sequence generator and chaos measurement matrix based on noisy images is proposed. The purpose is to solve how to combine compressed sensing technology with chaotic cryptography for image encryption in actual hardware encryption. At the same time, due to the flexibility of the hardware circuit in this algorithm, the key in the encryption process is easy to change, which enhances the security of the encryption algorithm to a greater extent. This combines a compressed sensing algorithm with the random characteristics of chaotic signals from the perspective of security and efficiency of information transmission. Because chaotic signals are sensitive to initial values, this algorithm can greatly expand the key space and effectively resist violent attacks. Through a simulation, the feasibility of the algorithm was verified. The algorithm can still achieve effective encryption and decryption under the condition that the original information contains noise. In Section 4, the experimental results were analyzed in detail. Through the analysis, it could be seen that the algorithm proposed in this study has a very high key sensitivity, and the encryption effect of the image is ideal. In the process of restoring the original image, it was found that this algorithm can resist a certain degree of source noise pollution and effectively recover the original signal. In terms of operational efficiency, the algorithm encryption process needs 0.24 s, and the use of common compression perception algorithm encryption requires about 1 s. The decryption algorithm in this study

requires 8 s and the ordinary compression perception algorithm decryption needs about 10 s, so the algorithm in this study using parallel transmission can effectively improve the efficiency of information transmission. In the following research, we will focus on whether the algorithm can resist the influence of channel noise and realize the image encryption and effective decryption.

## Data Availability

The data used to support the findings of this study are included within the article.

## Conflicts of Interest

The authors declare that they have no conflicts of interest.

## Acknowledgments

This study was supported by the National Natural Science Foundation of China (nos. 61571181 and 61801173) and the Natural Science Foundation of Heilongjiang Province, China (no. LH2019F048).

## References

- [1] A. Hasheminejad and M. J. Rostami, "A novel bit level multiphase algorithm for image encryption based on PWLCM chaotic map," *Optik*, vol. 184, pp. 205–213, 2019.
- [2] N. Zhou, A. Zhang, F. Zheng, and L. Gong, "Novel image compression-encryption hybrid algorithm based on key-controlled measurement matrix in compressive sensing," *Optics & Laser Technology*, vol. 62, pp. 152–160, 2014.
- [3] G. Hu, D. Xiao, Y. Wang, and T. Xiang, "An image coding scheme using parallel compressive sensing for simultaneous compression-encryption applications," *Journal of Visual Communication and Image Representation*, vol. 44, pp. 116–127, 2017.
- [4] R. Gao, "A novel track control for Lorenz system with single state feedback," *Chaos, Solitons and Fractals*, vol. 122, pp. 236–244, 2019.
- [5] S. Zhu, C. Zhu, and W. Wang, "A novel image compression-encryption scheme based on chaos and compression sensing," *IEEE Access*, vol. 6, pp. 67095–67107, 2018.
- [6] R. Ponuma and R. Amutha, "Compressive sensing based image compression-encryption using Novel 1D-Chaotic map," *Multimedia Tools and Applications*, vol. 4, pp. 1–26, 2017.
- [7] L. Gong, K. Qiu, C. Deng, and N. Zhou, "An image compression and encryption algorithm based on chaotic system and compressive sensing," *Optics & Laser Technology*, vol. 115, pp. 257–267, 2019.
- [8] L. Gong, K. Qiu, C. Deng, and N. Zhou, "An optical image compression and encryption scheme based on compressive sensing and RSA algorithm," *Optics and Lasers in Engineering*, vol. 121, pp. 169–180, 2019.
- [9] S. Hassanzadeh and A. Karami, "Compression and noise reduction of hyperspectral images using non-negative tensor decomposition and compressed sensing," *European Journal of Remote Sensing*, vol. 49, no. 1, pp. 587–598, 2017.
- [10] D. Donoho, "Compressed sensing," *IEEE Transactions on Information Theory*, vol. 52, no. 4, pp. 1289–1306, 2016.

- [11] Y. Gu and Y. D. Zhang, "Compressive sampling optimization for user signal parameter estimation in massive MIMO systems," *Digital Signal Processing*, vol. 94, pp. 105–113, 2019.
- [12] A. Orsdemir, H. Altun, G. Sharma et al., "On the security and robustness of encryption via compressed sensing," in *Proceedings of the Military Communications Conference, 2008. MILCOM 2008*, IEEE, San Diego, CA, USA, November 2008.
- [13] A. Schulz, L. Velho, and E. Silva, "On the empirical rate-distortion performance of compressive sensing," in *Proceedings of the IEEE International Conference on Image Processing*, IEEE, Cairo, Egypt, November 2009.
- [14] J. Fridrich, "Symmetric ciphers based on two-dimensional chaotic maps," *International Journal of Bifurcation and Chaos*, vol. 8, no. 6, pp. 1259–1284, 1998.
- [15] Y. Zhang, "The image encryption algorithm with plaintext-related shuffling," *IETE Technical Review*, vol. 33, no. 3, pp. 310–322, 2015.
- [16] R. Enayatifar, A. H. Abdullah, I. F. Isnin, A. Altameem, and M. Lee, "Image encryption using a synchronous permutation-diffusion technique," *Optics and Lasers in Engineering*, vol. 90, pp. 146–154, 2017.
- [17] Z. Hua, F. Jin, B. Xu, and H. Huang, "2D Logistic-Sine-coupling map for image encryption," *Signal Processing*, vol. 149, pp. 148–161, 2018.
- [18] L. Chen, G. Chang, B. He, H. Mao, and D. Zhao, "Optical image conversion and encryption by diffraction, phase retrieval algorithm and incoherent superposition," *Optics and Lasers in Engineering*, vol. 88, pp. 221–232, 2017.
- [19] Z. Hua, S. Yi, and Y. Zhou, "Medical image encryption using high-speed scrambling and pixel adaptive diffusion," *Signal Processing*, vol. 144, pp. 134–144, 2018.
- [20] L. Gong, C. Deng, S. Pan, and N. Zhou, "Image compression-encryption algorithms by combining hyper-chaotic system with discrete fractional random transform," *Optics & Laser Technology*, vol. 103, pp. 48–58, 2018.
- [21] L. Zhang, Y. Zhou, D. Huo, J. Li, and X. Zhou, "Multiple-image encryption based on double random phase encoding and compressive sensing by using a measurement array preprocessed with orthogonal-basis matrices," *Optics & Laser Technology*, vol. 105, pp. 162–170, 2018.
- [22] G. Wang, R. Zhou, and Y. Zou, "Research on image optimization technology based on compressed sensing," *Journal of Electronics & Information Technology*, vol. 42, pp. 222–233, 2020.
- [23] A.-A. Khennaoui, A. Ouannas, S. Bendoukha, G. Grassi, R. P. Lozi, and V.-T. Pham, "On fractional-order discrete-time systems: chaos, stabilization and synchronization," *Chaos, Solitons & Fractals*, vol. 119, pp. 150–162, 2019.
- [24] L. Li, G. Wen, Z. Wang, and Y. Yang, "Efficient and secure image communication system based on compressed sensing for IOT monitoring applications," *IEEE Transactions on Multimedia*, vol. 22, no. 1, pp. 82–95, 2020.
- [25] K. Zhou, J. Fan, H. Fan, and M. Li, "Secure image encryption scheme using double random-phase encoding and compressed sensing," *Optics and Laser Technology*, vol. 121, Article ID 105769, 2020.
- [26] W. Shi, F. Jiang, S. Liu, and D. Zhao, "Image compressed sensing using convolutional neural network," *IEEE Transactions on Image Processing*, vol. 29, pp. 375–388, 2020.
- [27] J. Chen, Y. Zhang, L. Qi, C. Fu, and L. Xu, "Exploiting chaos-based compressed sensing and cryptographic algorithm for image encryption and compression," *Optics & Laser Technology*, vol. 99, pp. 238–248, 2018.
- [28] L. Weizhi, L. Weiyu, K. Kpalma, and J. Ronsin, "Compressed sensing performance of random Bernoulli matrices with high compression ratio," *IEEE Signal Processing Letters*, vol. 22, no. 8, pp. 1074–1078, 2015.
- [29] L. Zeng, X. Zhang, L. Chen, T. Cao, and J. Yang, "Deterministic construction of toeplitzed structurally chaotic matrix for compressed sensing," *Circuits, Systems, and Signal Processing*, vol. 34, no. 3, pp. 797–813, 2014.
- [30] L. Y. Zhang, K.-W. Wong, Y. Zhang, and J. Zhou, "Bi-level protected compressive sampling," *IEEE Transactions on Multimedia*, vol. 18, no. 9, pp. 1720–1732, 2016.
- [31] H. Jiang, Y. Liu, Z. Wei, and L. Zhang, "A new class of three-dimensional maps with hidden chaotic dynamics," *International Journal of Bifurcation and Chaos*, vol. 26, no. 12, Article ID 1650206, 2016.
- [32] T. Zhang, S. Li, R. Ge, M. Yuan, and Y. Ma, "A novel 1D hybrid chaotic map-based image compression and encryption using compressed sensing and Fibonacci-Lucas transform," *Mathematical Problems in Engineering*, vol. 2016, Article ID 7683687, 15 pages, 2016.
- [33] N. Zhou, H. Li, D. Wang, S. Pan, and Z. Zhou, "Image compression and encryption scheme based on 2D compressive sensing and fractional Mellin transform," *Optics Communications*, vol. 343, pp. 10–21, 2015.
- [34] E. F. Doungmo Goufo, "On chaotic models with hidden attractors in fractional calculus above power law," *Chaos, Solitons & Fractals*, vol. 127, pp. 24–30, 2019.
- [35] H. Jahanshahi, A. Yousefpour, Z. Wei, R. Alcaraz, and S. Bekiros, "A financial hyperchaotic system with coexisting attractors: dynamic investigation, entropy analysis, control and synchronization," *Chaos, Solitons & Fractals*, vol. 126, pp. 66–77, 2019.
- [36] J. Yu, S. Guo, X. Song, Y. Xie, and E. Wang, "Image parallel encryption technology based on sequence generator and chaotic measurement matrix," *Entropy*, vol. 22, no. 1, p. 76, 2020.
- [37] J. Deng, S. Zhao, Y. Wang, L. Wang, H. Wang, and H. Sha, "Image compression-encryption scheme combining 2D compressive sensing with discrete fractional random transform," *Multimedia Tools and Applications*, vol. 76, no. 7, pp. 10097–10117, 2017.
- [38] N. Zhou, S. Pan, S. Cheng, and Z. Zhou, "Image compression-encryption scheme based on hyper-chaotic system and 2D compressive sensing," *Optics & Laser Technology*, vol. 82, pp. 121–133, 2016.
- [39] R. Huang and K. Sakurai, "A robust and compression-combined digital image encryption method based on compressive sensing," in *Proceedings of the Seventh International Conference on Intelligent Information Hiding and Multimedia Signal Processing*, Dalian, China, October 2011.
- [40] S. George and D. Pattathil, "A secure LFSR based random measurement matrix for compressive sensing," *Sensing and Imaging*, vol. 15, no. 1, pp. 85–240, 2014.
- [41] S. N. George, N. Augustine, and D. P. Pattathil, "Audio security through compressive sampling and cellular automata," *Multimedia Tools and Applications*, vol. 74, no. 23, pp. 10393–10417, 2014.
- [42] X. Wang, Q. Wang, and Y. Zhang, "A fast image algorithm based on rows and columns switch," *Nonlinear Dynamics*, vol. 79, no. 2, pp. 1141–1149, 2015.
- [43] W. Liu, K. Sun, and C. Zhu, "A fast image encryption algorithm based on chaotic map," *Optics and Lasers in Engineering*, vol. 84, pp. 26–36, 2016.

- [44] L. Xu, Z. Li, J. Li, and W. Hua, "A novel bit-level image encryption algorithm based on chaotic maps," *Optics and Lasers in Engineering*, vol. 78, pp. 17–25, 2016.
- [45] Q. Xu, K. Sun, C. Cao, and C. Zhu, "A fast image encryption algorithm based on compressive sensing and hyperchaotic map," *Optics and Lasers in Engineering*, vol. 121, pp. 203–214, 2019.

## Research Article

# Circuit Realization of a 3D Multistability Chaotic System and Its Synchronization via Linear Resistor and Linear Capacitor in Parallel Coupling

Xikui Hu<sup>1</sup> and Ping Zhou<sup>1,2</sup> 

<sup>1</sup>Center of System Theory and Its Applications, Chongqing University of Posts and Telecommunications, Chongqing 400065, China

<sup>2</sup>Key Laboratory of Network Control and Intelligent Instrument of Ministry of Education, Chongqing University of Posts and Telecommunications, Chongqing 400065, China

Correspondence should be addressed to Ping Zhou; [zhouping@cqupt.edu.cn](mailto:zhouping@cqupt.edu.cn)

Received 5 December 2019; Revised 9 February 2020; Accepted 13 March 2020; Published 30 April 2020

Guest Editor: Viet-Thanh Pham

Copyright © 2020 Xikui Hu and Ping Zhou. This is an open access article distributed under the Creative Commons Attribution License, which permits unrestricted use, distribution, and reproduction in any medium, provided the original work is properly cited.

In this paper, a 3D multistability chaotic system with two coexisting conditional symmetric attractors is studied by using a circuit block diagram and realized by using an electronic circuit. The simulation results show that two coexisting conditional symmetric attractors are emerged in this electronic circuit. Furthermore, synchronization of this 3D multistability chaotic system and its electronic circuit is studied. It shows that linear resistor and linear capacitor in parallel coupling can achieve synchronization in this chaotic electronic circuit. That is, the output voltage of chaotic electronic circuit is coupled via one linear resistor and one linear capacitor in parallel coupling. The simulation results verify that synchronization of the chaotic electronic circuit can be achieved.

## 1. Introduction

There are many nonlinear systems known to obtain coexistence of multiple attractors [1–10]. The coexistence of multiple attractors indicates that the attractor depends crucially on the initial condition (IC). These nonlinear systems are referred to as multistability systems. Multistability has been found in various systems, including Lorenz system [11], Rössler oscillators [12], neuronal oscillator [13], lasers [14], DC/DC converter [15], and permanent magnet synchronous motor [16]. Meanwhile, many multistability chaotic systems have been reported in recent years. Kengne et al. [17] reported a multistability chaotic system via van der Pol oscillator and suggested an appropriate electronic simulator. Peng and Min [18] proposed a novel multistability memristive chaotic circuit and applied it to image encryption. Chen et al. [19] introduced a multistability modified canonical Chua's circuit and obtained three sets of

topologically different and disconnected attractors. Pham et al. [2] suggested a multistability chaotic system with no equilibrium.

On the other hand, synchronous behavior, which ensures that the states track the desired trajectory, has attracted much research attention for its potential applications especially in secure communication and image encryption [20]. Many chaotic electronic circuits reconstructed for chaotic attractors in nonlinear systems have been proposed. Therefore, synchronization of nonlinear chaotic systems can be converted to synchronization of chaotic electronic circuits. In recent years, linear capacitor coupling, linear resistor coupling, and linear inductor coupling have been used to achieve synchronization of two identical chaotic electronic circuits, in which many interesting results have been obtained. Liu et al. [21, 22] realized synchronization control for Chua's chaotic circuits and synchronization of neural circuits. Yao et al. [23]



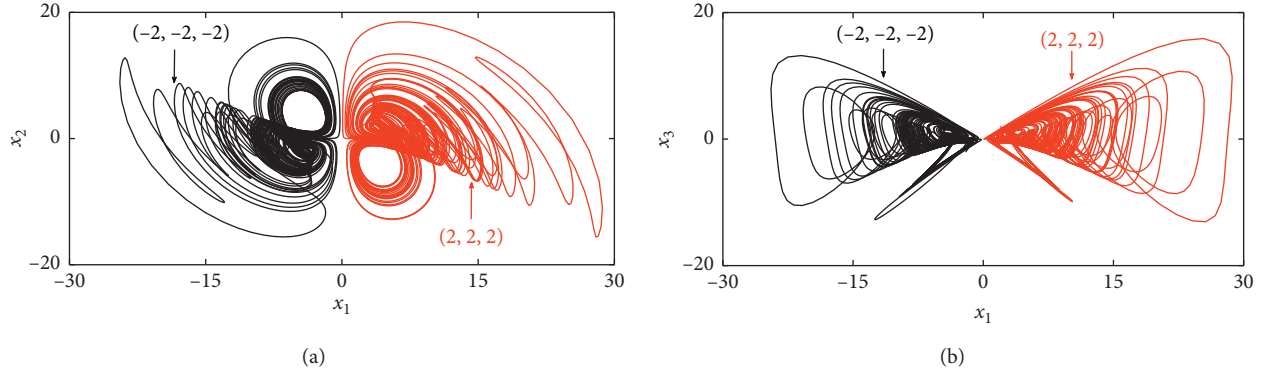


FIGURE 1: A symmetric pair of coexisting attractors in system (1) with  $a = 2.5$ . IC =  $(2, 2, 2)$  is red in the positive- $x$  region and IC =  $(-2, -2, -2)$  is black in the negative- $x$  region. (a) The  $x_1x_2$  phase diagram and (b) the  $x_1x_3$  phase diagram.

proposed a synchronization scheme for nonlinear circuits via induction coil coupling. Feng et al. [24] studied synchronization and electronic circuit application of a hidden hyperchaos system without equilibria. Singh and Roy [25] used adaptive contraction theory to research synchronization of a Lorenz hyperchaotic system and its circuit realization. He et al. [26] studied the dynamics and synchronization of conformable fractional-order hyperchaotic systems. Ma et al. [27] realized crack synchronization for chaotic circuits via field coupling. When the chaotic systems transform to nonlinear electronic circuits, direct linear variable coupling between chaotic systems can be implemented as a linear resistor coupling, and first derivative of state variable linear coupling can be implemented as a linear capacitive coupling or a linear inductor coupling. In fact, the synchronization of chaotic systems by resistor coupling is based on the consumption of Joule heat, and the synchronization of chaotic systems by capacitive coupling or inductor coupling is based on electric field energy exchange or magnetic field energy exchange.

Based on the 3D multistability chaotic system [1] reported by Zhou and Ke, in which there are two coexisting conditional symmetric chaotic attractors with different initial conditions, the chaos synchronization achieved by linear resistor and capacitor coupling is studied in this paper. First, the 3D multistability chaotic system [1] is studied by using a block diagram, and its electronic circuit is realized. The circuit simulation results are given. Second, the synchronization between two 3D multistability chaotic circuits is discussed, and we obtain that chaos synchronization can be achieved by using only one linear capacitor and one linear resistor in parallel coupling.

## 2. A 3D Multistability Chaotic System with Two Coexisting Conditional Symmetric Attractors and Its Circuit Realization

Based on the 3D Lü chaotic system [28], a multistability chaotic system with two coexisting conditional symmetric attractors has been reported by Zhou and Ke [1], which is shown as follows:

$$\begin{cases} \dot{x}_1 = -x_1 + 0.5x_1x_3 + x_2x_3, \\ \dot{x}_2 = ax_2 - 1.2x_1x_3, \\ \dot{x}_3 = x_1x_2 - 6x_3. \end{cases} \quad (1)$$

When  $0 \leq a \leq 4$ , there are two coexisting conditional symmetric attractors in the positive- $x$  region and negative- $x$  region separately [1] with different initial conditions. For example, let  $a = 2.5$ , the maximum Lyapunov exponent is 0.5758 [1]. The positive- $x$  region chaotic attractor with initial conditions  $(2, 2, 2)$  and negative- $x$  region chaotic attractor with initial conditions  $(-2, -2, -2)$  are shown in Figure 1, respectively.

Next, using the MATLAB Simulink module, circuit implementation of system (1) can be realized by block diagram in which all the blocks are standard basic operational circuits. Integrators marked as “Integrator” blocks are employed to obtain output voltage signal  $v_i$  with input voltage signal  $\dot{v}_i$ . Without loss of generality, the value of resistor in each integrator is  $R_0 = 100 \text{ k}\Omega$  and the value of capacitor is  $C_0 = 10 \text{ nF}$  for dimensionless. The voltage signals  $v_i$  are thus converted to dimensionless parameter  $x_i$ . All nonlinear terms  $x_ix_j$  are obtained by using multipliers marked as “Product” blocks. For example, multiplier “Product  $x_1x_2$ ” is employed to produce output signal  $x_1x_2$  with the input signals  $x_1$  and  $x_2$ . All coefficients except “1” are implemented by using gain converters marked as “Gain” blocks. The gain converter is composed of an inverse proportional circuit with coefficient “ $K = R_f/R_K$ ” and an inverter is linked together. Similarly, the reference resistance is  $R_f = 100 \text{ k}\Omega$  for dimensionless. Therefore, the resistance with respect to the coefficient is  $R_K = 100/K \text{ k}\Omega$ . The output signal is  $x_o = Kx_i$  with respect to the input signal  $x_i$  in the “Gain” blocks, and  $K$  is the gain coefficient marked inside the block. Adders marked as “Add” blocks are employed to realize addition and subtraction between the input signals. Finally, all the blocks can form three circuit loops as shown in Figure 2. Each loop corresponds to a dimensionless nonlinear equation in system (1).

In the implementation of system (1) with blocks, the properties of the chaotic system (1) can be studied by computer simulation experiment. The evolution of each signal  $x_i$  ( $i = 1, 2, 3$ ) with respect to time  $t$  can be demonstrated by “Scope” block connected with corresponding

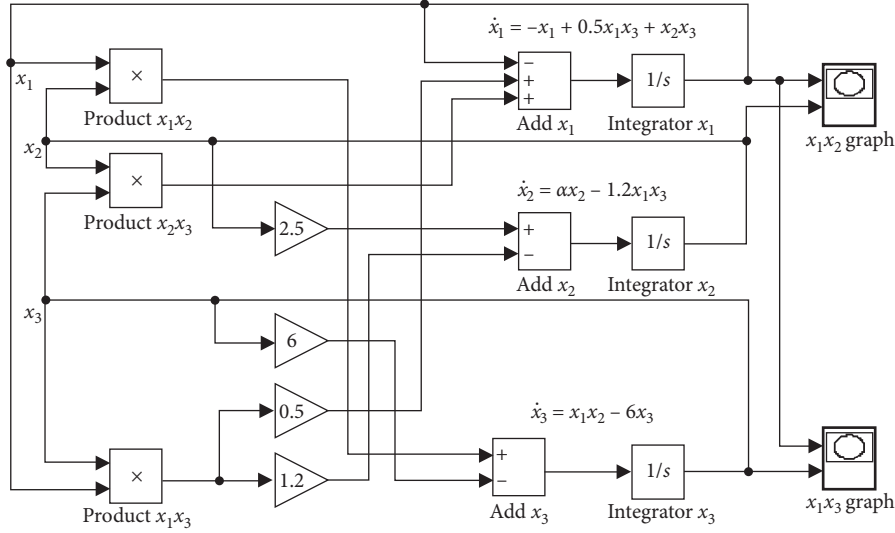


FIGURE 2: Implementation of system (1) realized by using the block diagram in the MATLAB Simulink module.

signal. “XY Graph” blocks, which play the part of an oscilloscope with two vertical input signals at the same time, are employed in plotting the phase diagrams of two arbitrarily different signals  $x_i$  and  $x_j$ . As shown in Figure 3, the phase diagrams of positive- $x$  region attractors are observed with the “ $x$  Initial = [ 2 2 2 ]” input into the MATLAB workspace, and the phase diagrams of negative- $x$  region attractors are observed with the “ $x$  Initial = [ -2 -2 -2 ].” The results of circuit simulation by the MATLAB Simulink module fit well with that of nonlinear dynamic system (1).

The circuit simulation system based on the standard circuit described as blocks by the MATLAB Simulink module has the advantages of intuitionistic design, simple parameter setting, and easy debugging. In practical circuits, however, some blocks can be combined for economy. Multiple signals with parallel connection are adopted at the input terminal of the integrator in order to remove adders. The resistance of each branch in the input terminal is properly selected to remove gains. Finally, the electronic circuit can be obtained for practical application and the usage of electronic components can be greatly reduced. The electronic circuit of system (1) is shown in Figure 4. Without loss of generality, nonlinear terms  $x_i x_j$  are obtained by using a multiplier with two signals  $x_i$  and  $x_j$  input at the same time and the minus of the signals is realized by using an inverter.  $u$  represents the input terminal of the coupling signal which is suspended herein. It means that there is no coupling signal at this condition.

Nonlinear equations from the electronic circuit are derived as follows:

$$\begin{cases} C_1 \frac{dv_1}{d\tau} = -\frac{v_1}{R_{11}} + \frac{v_2 v_3}{R_{12}} + \frac{v_1 v_3}{R_{13}}, \\ C_2 \frac{dv_2}{d\tau} = \frac{v_2}{R_{21}} - \frac{v_1 v_3}{R_{22}}, \\ C_3 \frac{dv_3}{d\tau} = \frac{v_1 v_2}{R_{31}} - \frac{v_3}{R_{32}}. \end{cases} \quad (2)$$

Note that we set  $R_0 = 100 \text{ k}\Omega$ ,  $C_0 = 10 \text{ nF}$ , and the time scaling as  $t_0 = R_0 C_0 = 10^{-3} \text{ S}$ . Let  $x_1 = v_1$ ,  $x_2 = v_2$ ,  $x_3 = v_3$ , and  $t = \tau/t_0$ . A dimensionless dynamical system (3) mapped from the circuit equations can be approached as follows:

$$\begin{cases} \frac{C_1}{C_0} \frac{dx_1}{dt} = -\frac{R_0}{R_{11}} x_1 + \frac{R_0}{R_{12}} x_2 x_3 + \frac{R_0}{R_{13}} x_1 x_3, \\ \frac{C_2}{C_0} \frac{dx_2}{dt} = \frac{R_0}{R_{21}} x_2 - \frac{R_0}{R_{22}} x_1 x_3, \\ \frac{C_3}{C_0} \frac{dx_3}{dt} = \frac{R_0}{R_{31}} x_1 x_2 - \frac{R_0}{R_{32}} x_3. \end{cases} \quad (3)$$

It indicates that the resistance  $R$  is scaled in  $100 \text{ k}\Omega$ , capacitance  $C$  is scaled in  $10 \text{ nF}$ , and time  $t$  is scaled in  $1 \text{ ms}$  when circuit equations are dimensionless.

### 3. Synchronization of Multistability Chaotic System (1) by Using One Linear Capacitor and One Linear Resistor in Parallel Coupling

In this section, synchronization of multistability chaotic system (1) is discussed. Let system (1) be the driving system. The response system with signals  $y_1$ ,  $y_2$ , and  $y_3$  is shown as follows:

$$\begin{cases} \dot{y}_1 = -y_1 + 0.5y_1 y_3 + y_2 y_3, \\ \dot{y}_2 = a y_2 - 1.2y_1 y_3, \\ \dot{y}_3 = y_1 y_2 - 6y_3. \end{cases} \quad (4)$$

Analogous to system (1), the corresponding circuit schematic diagram of response system (2) can be obtained by the MATLAB Simulink model as shown in Figure 5.

In order to study the chaotic synchronization between driving system (1) and response system (4), the state variable  $x_2$  of driving system (1) (i.e., the output voltage signal  $x_2$  in

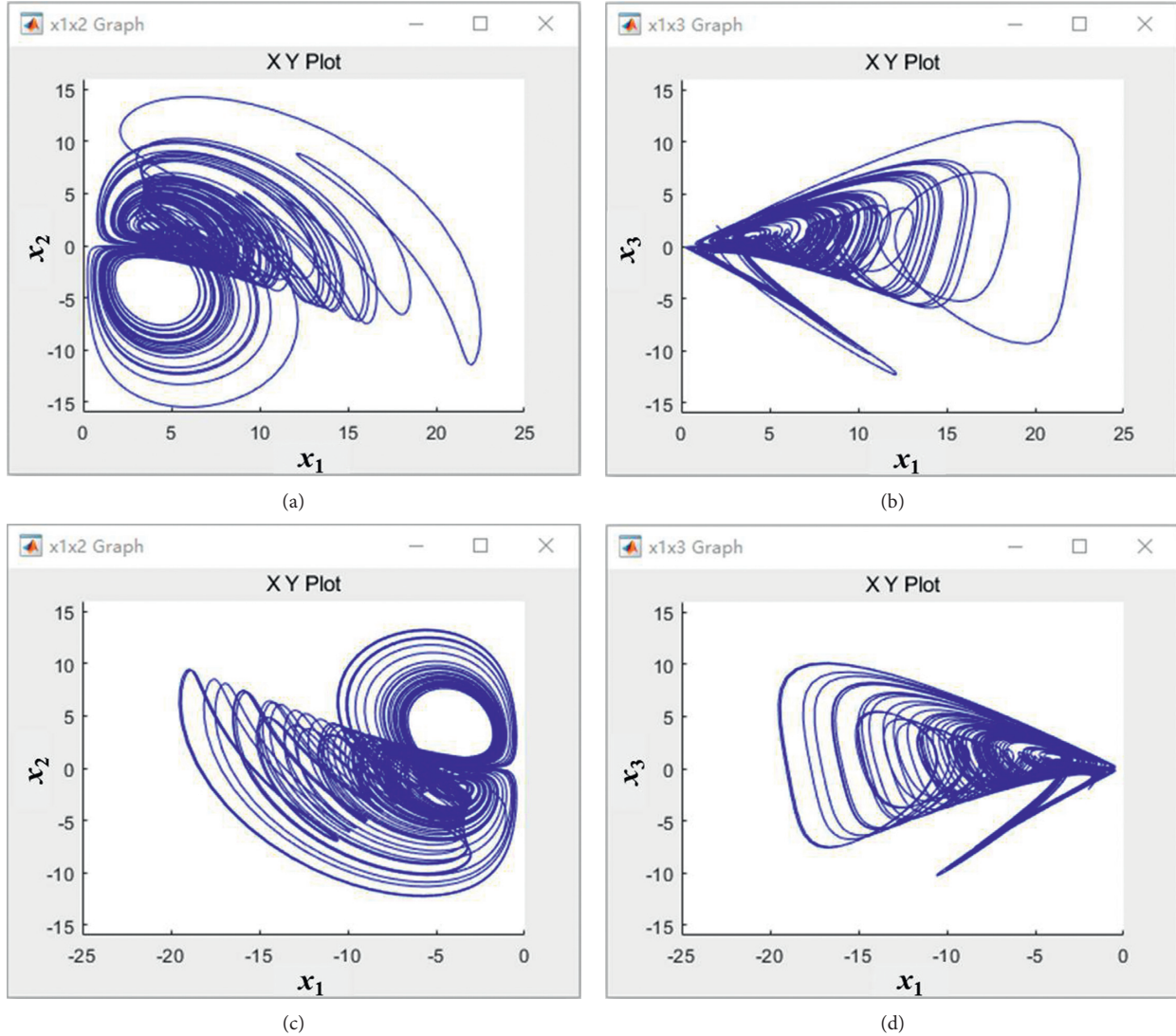


FIGURE 3: Formations of the phase diagrams that are plotted by “XY Graph” in the MATLAB Simulink module block diagram. (a)  $x_1x_2$  phase diagram and (b)  $x_1x_3$  phase diagram with IC = (2, 2, 2); (c)  $x_1x_2$  phase diagram and (d)  $x_1x_3$  phase diagram with IC = (-2, -2, -2).

Figure 2) and the state variable  $y_2$  of response system (2) (i.e., the output voltage signal  $y_2$  in Figure 5) are coupled in this paper. They are coupled via one linear resistor  $R$  and one linear capacitor  $C$  in parallel to form a new six-dimensional system in this paper. In order to obtain the dimensionless nonlinear equations of the coupled system, the unit of the coupling resistance  $R$  is 100 k $\Omega$  and the unit of the coupling capacitance  $C$  is 10 nF. The circuit implementation by blocks in the MATLAB Simulink module is shown in Figure 6. First, the subtraction circuit with  $x_2$  and  $y_2$  in the input terminal is used to obtain the output signal  $x_2 - y_2$ . Second, the  $x_2 - y_2$  signal is divided into two branches. One branch is processed by a Gain block “ $K_R$ ” with the coefficient  $K_R = 100 \text{ k}\Omega/R$ , which is equivalent to the resistive coupling. The corresponding output signal is  $u_R = K_R(x_2 - y_2)$ . The other branch is processed by the combination of a Differentiator block and a Gain block “ $K_C$ ” with the coefficient  $K_C = C/10 \text{ nF}$ , which is equivalent to the capacitive coupling. The corresponding output signal is  $u_C = K_C(\dot{x}_2 - \dot{y}_2)$ .

After that, the two branches are combined together by an Add block to realize the parallel connection between the resistor and capacitor. The final output signal  $u = K_R(x_2 - y_2) + K_C(\dot{x}_2 - \dot{y}_2)$ , right now, is the coupling signal between driving system (1) and response system (4). The coupling strength is proportional to  $K_R$  and  $K_C$ , which is inversely proportional to the value of coupling resistance  $R$  and proportional to the value of coupling capacitance  $C$ , respectively. If the coupling resistance is close to zero, it is equivalent to a direct connection between  $x_2$  and  $y_2$ . If the coupling resistance approaches infinity, it is equivalent to the coupling of a linear capacitor. If the coupling capacitance is close to zero, it is equivalent to the coupling of a linear resistor. At last, coupling signal  $u$  is inverse feedback input to the adder of the second loop in the driving system and direct feedback input to the adder of the second loop in the response system, respectively. In this case, the second nonlinear equations of system (1) and system (4) are separately rewritten as

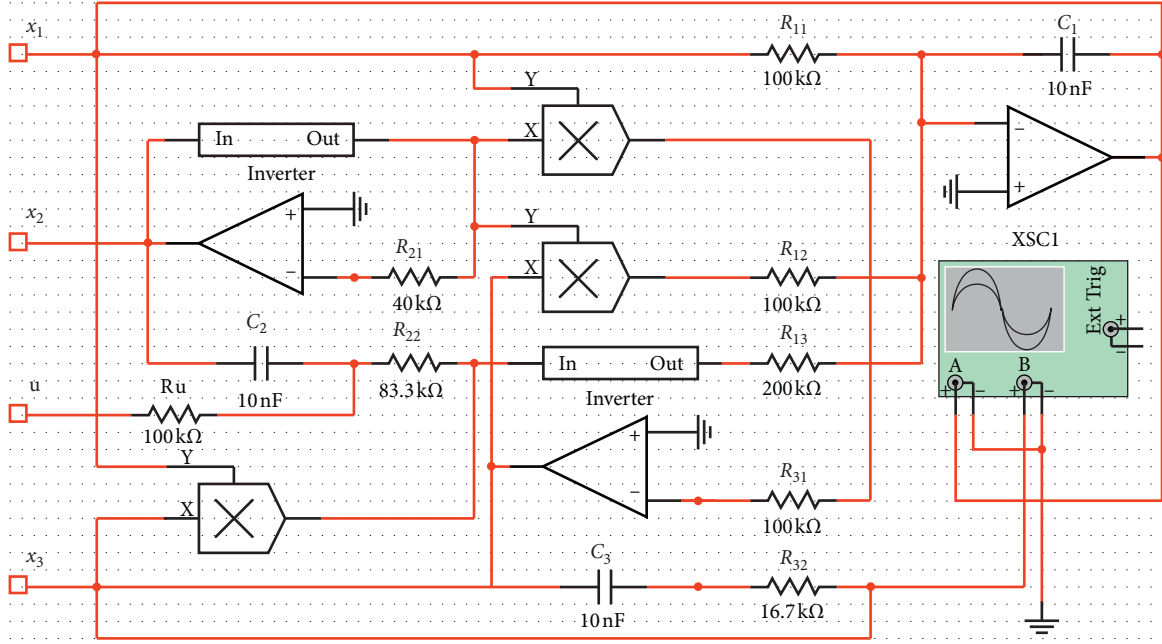


FIGURE 4: Schematic diagram of the electronic circuit realization of system (1).

$$\begin{cases} \dot{x}_2 = ax_2 - 1.2x_1x_3 - u, \\ \dot{y}_2 = ay_2 - 1.2y_1y_3 + u. \end{cases} \quad (5)$$

The electronic circuit described by using the block diagram in the MATLAB Simulink module can also be realized for practical applications as shown in Figure 7. Herein, the driving circuit and response circuit are represented by subcircuit blocks whose formations are shown in Figure 4. The signals  $x_2$  and  $y_2$  are connected to two input terminals of a subtraction circuit at the same time. The value of all the resistors is  $100 \text{ k}\Omega$ . The output signal of the subtraction circuit is  $x_2 - y_2$ , which is then applied to both the resistor and capacitor concurrently. Without loss of generality, the unit of resistance  $R$  is  $100 \text{ k}\Omega$  and the unit of capacitance  $C$  is  $10 \text{ nF}$  in order to nondimensionalize the nonlinear equations of circuits. Besides, the coupling terminal in the driving system and response system connects with the feedback signals  $u$  and  $-u$ , respectively.

When the coupled system is regarded as a new six-dimensional combined system, the dimensionless nonlinear state equations of coupled circuit (Figure 7) are described as

$$\begin{cases} \dot{x}_1 = -x_1 + 0.5x_1x_3 + x_2x_3, \\ \dot{x}_2 = ax_2 - 1.2x_1x_3 - \frac{(x_2 - y_2)}{R} - C(\dot{x}_2 - \dot{y}_2), \\ \dot{x}_3 = x_1x_2 - 6x_3, \\ \dot{y}_1 = -y_1 + 0.5y_1y_3 + y_2y_3, \\ \dot{y}_2 = ay_2 - 1.2y_1y_3 + \frac{(x_2 - y_2)}{R}R + C(\dot{x}_2 - \dot{y}_2), \\ \dot{y}_3 = y_1y_2 - 6y_3. \end{cases} \quad (6)$$

Herein, the parameter  $a = 2.5$ , the unit of coupled resistance  $R$  is  $100 \text{ k}\Omega$ , and the unit of coupled capacitance  $C$  is  $10 \text{ nF}$  for dimensionless as mentioned above. The nonlinear system (6) can be rewritten as nonlinear system:

$$\begin{cases} \dot{x}_1 = -x_1 + 0.5x_1x_3 + x_2x_3, \\ \dot{x}_2 = \frac{((1+C)f_x + Cf_y)}{(1+2C)}, \\ \dot{x}_3 = x_1x_2 - 6x_3, \\ \dot{y}_1 = -y_1 + 0.5y_1y_3 + y_2y_3, \\ \dot{y}_2 = \frac{(Cf_x + (1+C)f_y)}{(1+2C)}, \\ \dot{y}_3 = y_1y_2 - 6y_3. \end{cases} \quad (7)$$

Herein,  $f_x$  and  $f_y$  are introduced to simplify the form of the nonlinear equations of system (6). Their expressions are as follows:

$$\begin{cases} f_x = ax_2 - 1.2x_1x_3 - \frac{(x_2 - y_2)}{R}, \\ f_y = ay_2 - 1.2y_1y_3 + \frac{(x_2 - y_2)}{R}. \end{cases} \quad (8)$$

In order to study the chaotic evolution of system (7), especially the synchronization between the driving system and response system, the difference  $e$  should be employed as follows:

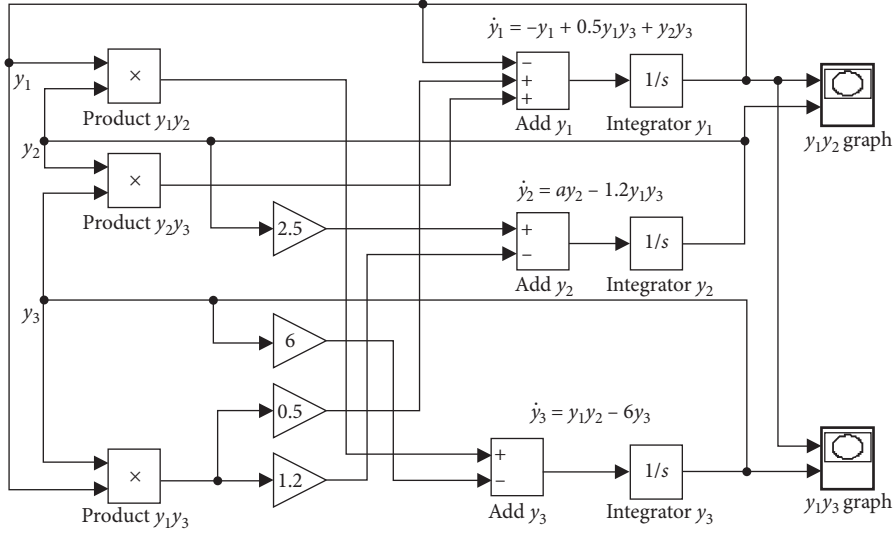


FIGURE 5: Implementation of response system (2) realized by block diagram in the MATLAB Simulink module.

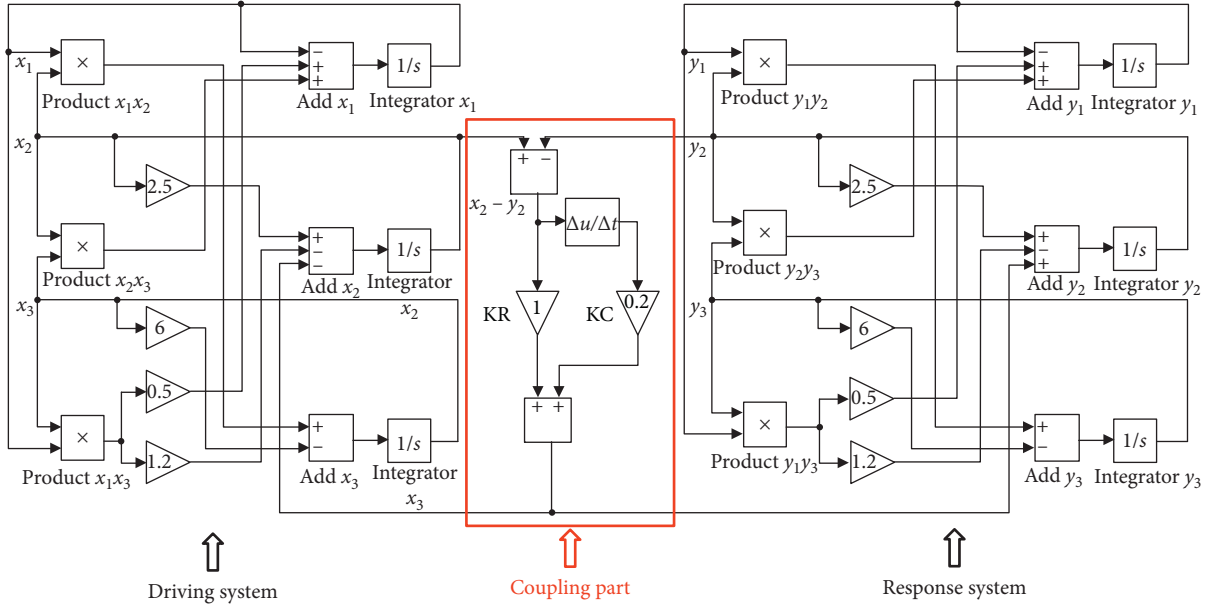


FIGURE 6: Implementation of the coupled system realized by block diagram in the MATLAB Simulink module.

$$\begin{aligned}
 e_1 &= x_1 - y_1, \\
 e_2 &= x_2 - y_2, \\
 e_3 &= x_3 - y_3.
 \end{aligned} \tag{9}$$

The corresponding error functions with respect to difference  $e$  and driving signal  $x$  are described as error system:

$$\begin{cases}
 \dot{e}_1 = (-1 + 0.5x_3)e_1 + x_3e_2 + (0.5x_1 + x_2)e_3 - 0.5e_1e_3 - e_2e_3, \\
 \dot{e}_2 = \frac{(-1.2x_3e_1 + (a - 2/R)e_2 - 1.2x_1e_3 + 1.2e_1e_3)}{(1 + 2C)}, \\
 \dot{e}_3 = x_2e_1 + x_1e_2 - 6e_3 - e_1e_2.
 \end{cases} \tag{10}$$

It is obvious that  $e = 0$  is the equilibrium point of error system (10). If equilibrium point  $e = 0$  is asymptotic stability, then chaotic synchronization between driving system (1) and response system (4) can be achieved. It indicates that there exists a synchronized state  $x = y$  for driving system (1) and response system (4). In general, the synchronization can be checked numerically by conditional Lyapunov exponents (CLEs). This is that synchronization occurs only if all CLEs of error system (10) are negative.

Therefore, the CLEs of system (10) are studied by MATLAB based on the QR decomposition method to analyse the synchronization with respect to the variable parameters  $R$  and  $C$ . The Jacobi matrix of the error system (10) is



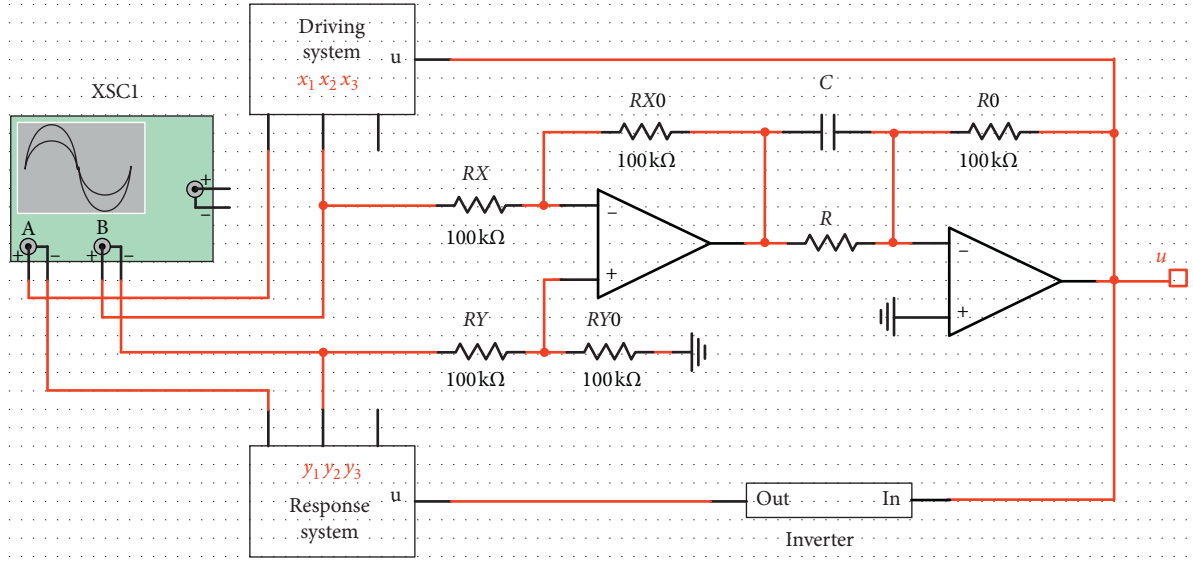


FIGURE 7: Schematic diagram of the electronic circuit realization of the coupled system.

$$J = \begin{bmatrix} -1 + 0.5(x_3 - e_3) & x_3 - e_3 & 0.5(x_1 - e_1) + (x_2 - e_2) \\ \frac{-1.2(x_3 - e_3)}{1 + 2C} & \frac{a - 2/R}{1 + 2C} & \frac{-1.2(x_1 - e_1)}{1 + 2C} \\ x_2 - e_2 & x_1 - e_1 & -6 \end{bmatrix}. \quad (11)$$

All the CLEs have been calculated by MATLAB numerical simulation with initial driving signals  $x_0 = (2, 2, 2)$  and initial difference  $e_0 = (-1, -1, -1)$ . The maximum CLEs distribution with respect to  $R$  and  $C$  is shown in Figure 8. It can be pointed out that the maximum CLEs are negative in the blue area and the maximum CLEs are positive in the yellow area. Therefore, the synchronization is realizable when the values of the coupling resistor and coupling capacitor are located in the blue area, while it is irrealizable when their values are in the yellow area. With the increase of capacitance, the range of resistance synchronization achieved is decreasing. When the capacitance  $C > 10$  nF, synchronization scarcely exists. Synchronization also disappears when the resistance  $R$  is much larger, e.g.,  $R > 160$  k $\Omega$ .

Take  $R = 1.0$  and  $C = 0.2$ ; namely, the value of coupling resistance is 100 k $\Omega$  and coupling capacitance is 2 nF as an example. In this case, the corresponding coefficients are  $K_R = 1$  and  $K_C = 0.2$ . All the three CLEs of error system (10) are negative as  $\lambda_1 = -0.19$ ,  $\lambda_2 = -1.05$ , and  $\lambda_3 = -5.50$ . The equilibrium point  $e = 0$  in error system (10) is asymptotic stability. Therefore, synchronization exists in the coupled system (6). It is proved by circuit simulation of the MATLAB Simulink module as shown in Figure 9. Herein, the coefficient in the Gain block " $K_R$ " is 1 and the coefficient in the Gain block " $K_C$ " is 0.2. Subtraction block is employed to obtain the difference signal. The input terminals are connected with  $x_i$  and  $y_i$ , respectively; thus, the output signal of

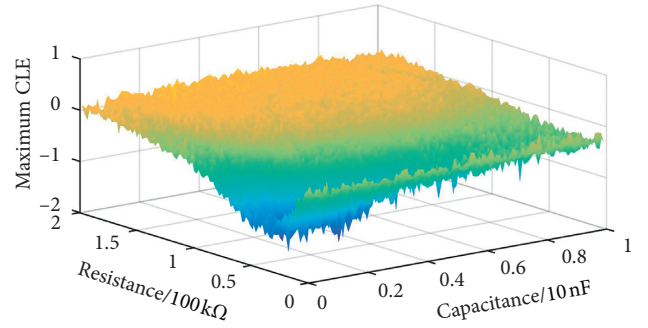


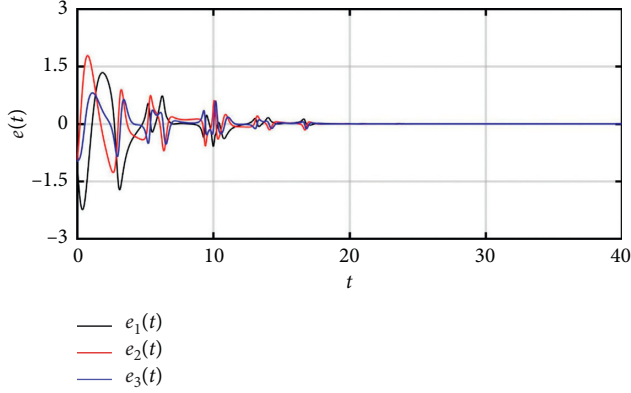
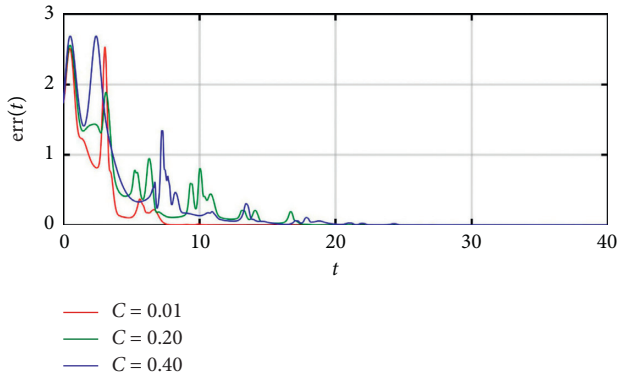
FIGURE 8: Maximum CLEs of error system (10) with resistive and capacitive coupling by parallel connection.

the Subtraction block is  $e_i = x_i - y_i$ . Scope block connected with the output terminal of the Subtraction block is used to plot the variation of difference signal  $e_i$  with respect to  $t$ . As shown in Figure 9, it is obvious that all the three difference signals  $e_i(t)$  gradually approach zero over some time with " $x$  Initial = [2 2 2]" and " $y$  Initial = [3 3 3]" are input into the MATLAB workspace. Therefore, it is confirmed that system (6) can achieve complete synchronization.

Generally, the synchronization performance varies with coupling parameters. As shown in Figure 8, the maximum CLEs of system (8) increase with respect to  $C$  approximately when  $R$  is determined. It means that the synchronization process slows down as  $C$  increases. Absolute error  $err(t)$  is employed to estimate the synchronization process:

$$err(t) = \sqrt{e_1^2 + e_2^2 + e_3^2}. \quad (12)$$

As shown in Figure 10, absolute errors of the synchronization process with different  $C$  values and  $R = 1.0$  are calculated. It can be verified that the larger the capacitance is, the longer the time will be taken to achieve synchronization.

FIGURE 9: Variation of the difference  $e$  with  $R=1.0$  and  $C=0.2$ .FIGURE 10: Variation of the absolute error  $err(t)$  with different  $C$  values and  $R=1.0$ .

In addition, the only resistive coupling is also studied. In this condition, the coupling capacitance  $C=0$  and the nonlinear system (6) are changed as follows:

$$\begin{cases} \dot{x}_1 = -x_1 + 0.5x_1x_3 + x_2x_3, \\ \dot{x}_2 = ax_2 - 1.2x_1x_3 - \frac{(x_2 - y_2)}{R}, \\ \dot{x}_3 = x_1x_2 - 6x_3, \\ \dot{y}_1 = -y_1 + 0.5y_1y_3 + y_2y_3, \\ \dot{y}_2 = ay_2 - 1.2y_1y_3 + \frac{(x_2 - y_2)}{R}, \\ \dot{y}_3 = y_1y_2 - 6y_3. \end{cases} \quad (13)$$

The corresponding error system is

$$\begin{cases} \dot{e}_1 = (-1 + 0.5x_3)e_1 + x_3e_2 + (0.5x_1 + x_2)e_3 - 0.5e_1e_3 - e_2e_3, \\ \dot{e}_2 = -1.2x_3e_1 + \left(a - \frac{2}{R}\right)e_2 - 1.2x_1e_3 + 1.2e_1e_3, \\ \dot{e}_3 = x_2e_1 + x_1e_2 - 6e_3 - e_1e_2. \end{cases} \quad (14)$$

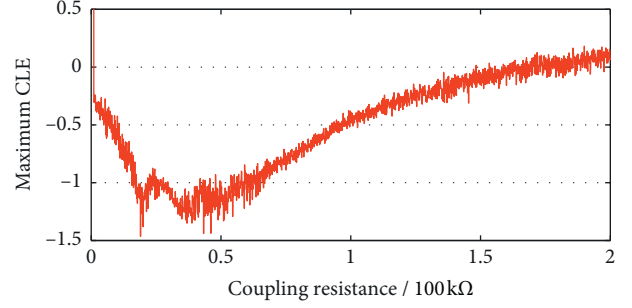
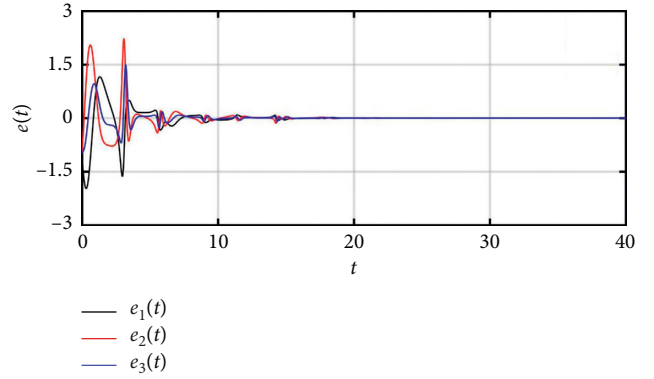


FIGURE 11: Maximum CLEs of the error system (14) with only resistive coupling.

FIGURE 12: Variation of the difference  $e$  with  $R=1.0$ .

The Jacobi matrix is

$$J = \begin{bmatrix} -1 + 0.5(x_3 - e_3) & x_3 - e_3 & 0.5(x_1 - e_1) + (x_2 - e_2) \\ -1.2(x_3 - e_3) & a - \frac{2}{R} & -1.2(x_1 - e_1) \\ x_2 - e_2 & x_1 - e_1 & -6 \end{bmatrix}. \quad (15)$$

All the CLEs have been calculated by MATLAB numerical simulation with initial driving signals  $x_0 = (2, 2, 2)$  and initial difference  $e_0 = (-1, -1, -1)$  similarly. The maximum CLEs distribution with respect to  $R$  is shown in Figure 11. It can be obtained that the maximum CLEs are negative when  $R < 1.6$ . It means that synchronization is achieved when the value of coupling resistance is less than 160 k $\Omega$  for only resistance coupling condition.

Take  $R=1.0$ ; namely, the value of coupling resistance is 100 k $\Omega$  as an example. In this case, the corresponding coefficients of Gain block " $K_R$ " is  $K_R = 1$ , while the corresponding coefficients of Gain block " $K_C$ " is  $K_C = 0$  which means the branch of capacitive coupling can even be removed. All the three CLEs of error system (14) are negative as  $\lambda_1 = -0.49$ ,  $\lambda_2 = -0.71$ , and  $\lambda_3 = -5.30$ . It indicates that synchronization exists in coupled system (13). As shown in Figure 12, it is obvious that all the three difference signals  $e_i(t)$  gradually approach zero over some time with " $x$  Initial = [ 2 2 2 ]" and " $y$  Initial = [ 3 3 3 ]" input into the MATLAB workspace.

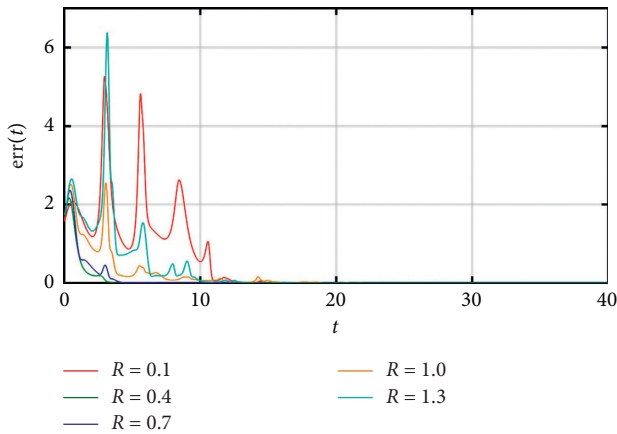


FIGURE 13: Variation of the absolute error  $\text{err}(t)$  with different  $R$ .

Therefore, it is confirmed that system (6) can achieve complete synchronization with suitable values (Figure 12).

Furthermore, the synchronization performance varies with  $R$ . As shown in Figure 11, the maximum CLEs of system (14) decrease at first and then increase with  $R$  increasing approximately. Therefore, the synchronization process speeds up at first and then slows down as  $R$  increases. As shown in Figure 13, absolute errors of the synchronization process with different  $R$  values are calculated. It can be found out that the time taken to achieve synchronization reduces first and then increases when  $R$  increases.

#### 4. Conclusions

Based on a 3D multistability chaotic system [1] reported by Zhou and Ke, an electronic circuit is proposed in this paper. The circuit simulation results show that there are two coexisting conditional symmetric chaotic attractors for different initial conditions, which are consistent with the findings in the reference [1]. Meanwhile, the chaotic synchronization between two 3D multistability chaotic systems with only one linear resistor and one linear capacitor in parallel coupling is discussed. The maximum condition Lyapunov exponents (CLEs) of the coupled system are studied. The negative maximum CLEs indicate that chaotic synchronization can be achieved with a capacitor and resistor in parallel coupling in the appropriate range. Furthermore, an electronic circuit is given to verify the synchronization scheme. Circuit simulation results confirm that the chaos synchronization for the 3D multistability chaotic system can be realized. Our work provides a method to realize the electronic circuit of the 3D multistability chaotic system and its synchronization, which has application prospect in secret communications and adaptive control. Future work can include the analysis of the synchronization between positive- $x$  region attractors and negative- $x$  region attractors.

#### Data Availability

The data used in our manuscript are obtained by MATLAB program and MATLAB Simulink module (MSM) and are available from the corresponding author upon request.

#### Conflicts of Interest

The authors declare that there are no conflicts of interest regarding the publication of this paper.


#### References

- [1] P. Zhou and M. Ke, "A new 3D autonomous continuous system with two isolated chaotic attractors and its topological horseshoes," *Complexity*, vol. 2017, Article ID 4037682, 7 pages, 2017.
- [2] V.-T. Pham, C. Volos, S. Jafari, and T. Kapitaniak, "Coexistence of hidden chaotic attractors in a novel no-equilibrium system," *Nonlinear Dynamics*, vol. 87, no. 3, pp. 2001–2010, 2017.
- [3] S. Cang, Y. Li, R. Zhang, and Z. Wang, "Hidden and self-excited coexisting attractors in a Lorenz-like system with two equilibrium points," *Nonlinear Dynamics*, vol. 95, no. 1, pp. 381–390, 2019.
- [4] Q. Lai and S. Chen, "Coexisting attractors generated from a new 4D smooth chaotic system," *International Journal of Control, Automation and Systems*, vol. 14, no. 4, pp. 1124–1131, 2016.
- [5] N. Stankevich and E. Volkov, "Multistability in a three-dimensional oscillator: tori, resonant cycles and chaos," *Nonlinear Dynamics*, vol. 94, no. 4, pp. 2455–2467, 2018.
- [6] J. Kengne, Z. T. Njitacke, and H. B. Fotsin, "Dynamical analysis of a simple autonomous jerk system with multiple attractors," *Nonlinear Dynamics*, vol. 83, no. 1-2, pp. 751–765, 2016.
- [7] C. B. Li, T. A. Lu, G. R. Chen, and H. Y. Xing, "Doubling the coexisting attractors," *Chaos: An Interdisciplinary Journal of Nonlinear Science*, vol. 29, no. 5, Article ID 051102, 2019.
- [8] İ. Pehlivan, E. Kurt, Q. Lai, A. Basaran, and M. C. Kutlu, "A multiscroll chaotic attractor and its electronic circuit implementation," *Chaos Theory and Applications*, vol. 1, no. 1, pp. 29–37, 2019.
- [9] C. K. Volos, A. Akgul, V. T. Pham, and M. S. Baptista, "Antimonotonicity, crisis and multiple attractors in a simple memristive circuit," *Journal of Circuits, Systems and Computers*, vol. 27, no. 2, Article ID 1850026, 2018.
- [10] K. Rajagopal, J. P. Singh, B. K. Roy, and A. Karthikeyan, "Dissipative and conservative chaotic nature of a new quasi-periodically forced oscillator with megastability," *Chinese Journal of Physics*, vol. 58, pp. 263–272, 2019.
- [11] C. B. Li and J. C. Sprott, "Multistability in the Lorenz system: a broken butterfly," *International Journal of Bifurcation and Chaos*, vol. 24, no. 10, Article ID 1450131, 2014.
- [12] P. Jaros, P. Perlikowski, and T. Kapitaniak, "Synchronization and multistability in the ring of modified Rössler oscillators," *The European Physical Journal Special Topics*, vol. 224, no. 8, pp. 1541–1552, 2015.
- [13] E. B. M. Ngounkadi, H. B. Fotsin, P. L. Fotso, V. K. Tamba, and H. A. Cerdeira, "Bifurcations and multistability in the extended Hindmarsh-Rose neuronal oscillator," *Chaos, Solitons & Fractals*, vol. 85, pp. 151–163, 2016.
- [14] R. Meucci, E. Allaria, F. Salvadori, and F. T. Arecchi, "Attractor selection in chaotic dynamics," *Physical Review Letters*, vol. 95, no. 18, Article ID 184101, 2005.
- [15] Z. T. Zhusubaliyev and E. Mosekilde, "Multistability and hidden attractors in a multilevel DC/DC converter," *Mathematics and Computers in Simulation*, vol. 109, pp. 32–45, 2015.

- [16] J. P. Singh, B. K. Roy, and N. V. Kuznetsov, "Multistability and hidden attractors in the dynamics of permanent magnet synchronous motor," *International Journal of Bifurcation and Chaos*, vol. 29, no. 4, Article ID 1950056, 2019.
- [17] J. Kengne, J. C. Chedjou, M. Kom, K. Kyamakya, and V. K. Tamba, "Regular oscillations, chaos, and multistability in a system of two coupled van der Pol oscillators: numerical and experimental studies," *Nonlinear Dynamics*, vol. 76, no. 2, pp. 1119–1132, 2014.
- [18] G. Peng and F. Min, "Multistability analysis, circuit implementations and application in image encryption of a novel memristive chaotic circuit," *Nonlinear Dynamics*, vol. 90, no. 3, pp. 1607–1625, 2017.
- [19] M. Chen, Q. Xu, Y. Lin, and B. Bao, "Multistability induced by two symmetric stable node-foci in modified canonical Chua's circuit," *Nonlinear Dynamics*, vol. 87, no. 2, pp. 789–802, 2017.
- [20] Q. Xu, K. Sun, C. Cao, and C. Zhu, "A fast image encryption algorithm based on compressive sensing and hyperchaotic map," *Optics and Lasers in Engineering*, vol. 121, pp. 203–214, 2019.
- [21] Z. Liu, J. Ma, G. Zhang, and Y. Zhang, "Synchronization control between two Chua's circuits via capacitive coupling," *Applied Mathematics and Computation*, vol. 360, pp. 94–106, 2019.
- [22] Z. Liu, C. Wang, W. Jin, and J. Ma, "Capacitor coupling induces synchronization between neural circuits," *Nonlinear Dynamics*, vol. 97, no. 4, pp. 2661–2673, 2019.
- [23] Z. Yao, J. Ma, Y. Yao, and C. Wang, "Synchronization realization between two nonlinear circuits via an induction coil coupling," *Nonlinear Dynamics*, vol. 96, no. 1, pp. 205–217, 2019.
- [24] Y. Feng, Z. Wei, U. E. Kocamaz, A. Akgül, and I. Moroz, "Synchronization and electronic circuit application of hidden hyperchaos in a four-dimensional self-exciting homopolar disc dynamo without equilibria," *Complexity*, vol. 2017, Article ID 7101927, 11 pages, 2017.
- [25] J. P. Singh and B. K. Roy, "Hidden attractors in a new complex generalised Lorenz hyperchaotic system, its synchronisation using adaptive contraction theory, circuit validation and application," *Nonlinear Dynamics*, vol. 92, no. 2, pp. 373–394, 2018.
- [26] S. He, K. Sun, and H. Wang, "Dynamics and synchronization of conformable fractional-order hyperchaotic systems using the Homotopy analysis method," *Communications in Nonlinear Science and Numerical Simulation*, vol. 73, pp. 146–164, 2019.
- [27] J. Ma, F. Wu, A. Alsaedi, and J. Tang, "Crack synchronization of chaotic circuits under field coupling," *Nonlinear Dynamics*, vol. 93, no. 4, pp. 2057–2069, 2018.
- [28] J. Lü and G. Chen, "A new chaotic attractor coined," *International Journal of Bifurcation and Chaos*, vol. 12, no. 3, pp. 659–661, 2002.

## Research Article

# Complexity Analysis of a 3-Player Game with Bounded Rationality Participating in Nitrogen Emission Reduction

Jixiang Zhang and Xuan Xi 

College of Economics and Management, Nanjing University of Aeronautics and Astronautics, Nanjing 211106, China

Correspondence should be addressed to Xuan Xi; 372952184@qq.com

Received 14 December 2019; Revised 5 March 2020; Accepted 26 March 2020; Published 27 April 2020

Guest Editor: Viet-Thanh Pham

Copyright © 2020 Jixiang Zhang and Xuan Xi. This is an open access article distributed under the Creative Commons Attribution License, which permits unrestricted use, distribution, and reproduction in any medium, provided the original work is properly cited.

In this paper, a decision-making competition game model concerning governments, agricultural enterprises, and the public, all of which participate in the reduction of nitrogen emissions in the watersheds, is established based on bounded rationality. First, the stability conditions of the equilibrium points in the system are discussed, and the stable region of the Nash equilibrium is determined. Then, the bifurcation diagram, maximal Lyapunov exponent, strange attractor, and sensitive dependence on the initial conditions are shown through numerical simulations. The research shows that the adjustment speed of three players' decisions may alter the stability of the Nash equilibrium point and lead to chaos in the system. Among these decisions, a government's decision has the largest effect on the system. In addition, we find that some parameters will affect the stability of the system; when the parameters become beneficial for enterprises to reduce nitrogen emissions, the increase in the parameters can help control the chaotic market. Finally, the delay feedback control method is used to successfully control the chaos in the system and stabilize it at the Nash equilibrium point. The research of this paper is of great significance to the environmental governance decisions and nitrogen reduction management.

## 1. Introduction

According to the European Nitrogen Assessment, the total economic loss caused by the reactive nitrogen in 27 countries of the European Union amount to 70–320 billion euros per year. The economic cost of the reactive nitrogen pollution is about twice that of Europe's "willingness" to pay for carbon controls. To integrate the research on global nitrogen emissions and nitrogen pollution, the European Union puts forward the "nitrogen and Europe" research plan, and all countries of the world were invited to participate. Due to the intensification of nonpoint source nitrogen pollution in agriculture enterprises, the problem of nitrogen pollution in river basins is becoming more and more serious. Two-thirds of the coastal rivers and bays in the United States are degraded from nutrient pollution, and nitrogen inputs in these waters continue to increase [1]. Therefore, controlling the input of nitrogen and phosphorus from human activities is essential in reducing eutrophication in watersheds [2]. As

the reduction of nitrogen emission starts to attract the attention of the whole world, the nitrogen emission trading market and the nitrogen emission limits of various industries are gradually being formed, and agricultural enterprises will face this major challenge. At the same time, governments should not only consider the environmental benefits but also control the normal operation of the whole market. Therefore, as the main players in the reduction of nitrogen emissions in the river basin, any party in government and agricultural enterprises and the social public decisions will be influenced by the other two parties.

Some literature mainly focuses on watershed pollution based on game theory. Initially, there has been much discussion on the treatment of environmental problems. Ni and Wang [3] used a cooperative game to analyze the allocation of pollution control costs in watershed pollution and explored a reasonable allocation method. Gao et al. [4] analyzed the interaction among upstream governments, downstream governments, and the central government in



the Eastern Route of South-to-North Water Transfer Project based on evolutionary game theory. Secondly, there is cross-border water pollution in the river basin. Jorgensen [5] took the upstream and downstream areas in the river basin as the main body of the game and analyzed whether the cooperation between the upstream and downstream could solve the problem of unreasonable pollution through the differential game method. Frisvold and Caswell [6] used the static bargaining game method to study the impact of pollution control policies on the game relationship between two countries in terms of environmental pollution control. Third, there is a conflict of interest between subjects in the river basin. Bárcena-Ruiz [7] used the idea of a differential game to analyze whether two governments should solve the problem of river basin pollution by setting environmental taxes to be the same.

The majority of nitrogen emission reduction in the watershed is based on bounded rationality. At present, the research on dynamic competitive game with bounded rationality comes mainly from the following authors. Puu [8] first found a variety of complex dynamic phenomena in the Cournot duopoly model such as the singular attractor with a fractal dimension. Yali [9] studied a delayed duopoly game considering increasing marginal costs based on bounded rationality and demonstrated that state delay is helpful in enlarging the stability region of the system. Peng et al. [10] and Elsadany [11] discussed the correction of a duopoly game with bounded rationality based on the strategy of maximizing the output expectations of enterprises. Yao and Xu [12] established an advertising market competition model that considered the bounded rationality of participants and analyzed the complex decision-making behaviors of decision-makers in the dynamic game process. Ding et al. [13] proposed a linear dynamic system in a duopoly game involving renewable resource extraction with the strategy of bounded rationality. Yao et al. [14] and Elabbasy et al. [15] both constructed a nonlinear triopoly game model with heterogeneous players, and the three different decision-makers were bounded rational, adaptive, and naive. Research by Zhao [16] investigated a novel Cournot duopoly game model of carbon emission reduction based on the hypothesis of participant's bounded rationality.

Our study is closely related to reduction mechanism, which can be divided into mandatory emission reduction mechanism [17, 18] and incentive emission reduction mechanism [19, 20]. Wang et al. [21] analyzed the relationship between supply chain enterprise operation and government policy. A three-stage Stackelberg game model of decentralized supply chain and a two-stage Stackelberg game model of centralized supply chain were used to study the government's carbon emission tax policy. De Jonge [22] proposed that the instruments of legislation, subsidies, green taxation, and emission trading can help achieve reduction targets for  $\text{NO}_x$ . Research by Svensson and Elofsson [23] showed that the net nitrogen reductions achieved through environmental policy efforts and the costs of the nitrogen reductions should be considered. According to previous research, most scholars mainly focused on the decision-

making game of emission reduction, price, or output of enterprises, whereas seldom discussed the decisions of government policies and the public. However, when the government and the public are involved in nitrogen emission reduction work, under a series of environmental policies and public supervision, studying the complex dynamic behavior of a game involving governments, agricultural enterprises, and the public with bounded rationality will have great practical significance.

The contributions of this study are as follows: first, a reasonable decision-making mechanism for nitrogen emission reduction is proposed considering the influence of government and the public decisions in emission reduction. Second, how to establish a reasonable adjustment strategy of output, supervision intensity, and policy intensity is explored. Third, the integration of nonlinear dynamic theory and nitrogen emission reduction management is fulfilled. Moreover, the effects of the market price of nitrogen trading and the subsidy standard of nitrogen emission reductions on the decisions of three players are simulated, and it is important to adjust the parameters that will become beneficial for enterprises to reduce nitrogen emissions. This study can provide a theoretical guidance for reducing nitrogen pollution in the watersheds.

The organization of the paper is as follows: in Section 2, a competition model concerning governments, agricultural enterprises, and the public is formulated; in Section 3, we analyze the equilibrium point of the game model and give the existence condition and local stability range of the equilibrium point. In Section 4, the complex dynamic behavior under a change in the adjustment speed of three players' decisions is analyzed. In Section 5, we apply the delay feedback method to control chaos in the system. Finally, some research conclusions are summarized in Section 6.

## 2. Model

This main purpose of this chapter was to introduce the aforementioned dynamic game model. Considering nitrogen emission trading, nitrogen emission reduction subsidies, and marginal emission reduction costs, this paper analyzes whether governments, agricultural enterprises, and the public make an optimal decision according to their own decision rules in the game. Lanoie et al. [24] discussed the impact of environmental policies on environmental innovation performance, and the intensity of environmental policies was divided into three categories: weak, narrow, and strong. Thus, the optimal goal of the government is to choose the appropriate policy intensity to maximize the total utility, and the optimal goal of the agricultural enterprise is to make the appropriate output decision to maximize its profit when the pollution situation meets the government's policy intensity. In terms of the public, the best goal is to choose the appropriate supervision intensity to maximize its total utility. The meanings of specific parameters and variables are shown in Table 1.

TABLE 1: Major notations.

Notations	Description
$x(t)$	The government's policy intensity at period $t$
$z(t)$	The public's supervision intensity at period $t$
$y(t)$	The agricultural enterprises' output at period $t$
$A$	The highest price of the product in the market
$C$	The marginal production cost
$d$	The consumer losses caused by the unit emission of nitrogen
$E$	Initial unit amount of nitrogen emissions
$p_e$	The price of emission permits
$N$	The marginal abatement costs
$y_0$	The initial nitrogen emission permits
$\gamma_1$	The impact coefficient of policy intensity on emission reduction
$\gamma_2$	The emission reduction coefficient
$\gamma_3$	The impact coefficient of supervision intensity on emission reduction
$G$	The emission reduction subsidy coefficient
$T$	The government's various tax revenues
$\delta$	The treatment cost of per unit nitrogen emission
$h$	The government's marginal supervisory cost
$u$	The base value of the product
$M$	The initial supervision cost of the public
$M$	The impact coefficient of policy intensity on supervision cost

The following assumptions are made to develop the model:

- (1) This paper is mainly aimed at agricultural enterprises, and the price  $p$  of the enterprises in the period  $t$  is determined by  $y(t)$  through the inverse demand function  $p = a - by$ , where  $a$  and  $b$  are positive constants; the production cost of the enterprise is a linear function, namely,  $C = cy$ .

The nitrogen emissions generated in the production process of an enterprise are linearly related to its output, denoted as  $E = ey$ . The emission reduction of enterprises is related to their own technical level of nitrogen emission reduction, the government policy intensity, and the public's supervision intensity. Wu et al. [25] proposed that public participation had significant positive effects on the reduction of both binding and nonbinding environmental pollutant emissions. Therefore, the emission reduction of enterprises is [21, 26] as follows:

$$Q_e = \gamma_1 x + \gamma_2 y + \gamma_3 z, \quad (1)$$

where  $\gamma_i > 0$  ( $i = 1, 2, 3$ ); thus, the final nitrogen emission of enterprises is  $ey - Q_e$ . The cost of nitrogen emission reduction is  $nQ_e$ . When participating in nitrogen emission trading, the tradable emission permits that enterprises need can be described as  $ey - Q_e - y_0$ ; then, the fee for nitrogen emission trading is  $p_e(ey - Q_e - y_0)$ .

- (2) In terms of governments, the revenue function of the government in this paper mainly includes four parts:

tax, nitrogen pollution treatment costs, supervision cost, and subsidy expense. According to Wang et al. [21] and Alexeev et al. [26], the nitrogen pollution treatment costs are  $\delta(ey - Q_e)$ . The government provides subsidies and incentives for enterprises to reduce nitrogen emissions, so the subsidy expense can be described as  $xgQ_e$ .

- (3) Regarding the public, the research of Carreira et al. [27] showed that the degree of public participation in corporate environmental behavior depended on government's policy intensity. The supervision cost of the public on enterprises is negatively correlated with the government's policy intensity [28], so we assume the supervision cost is  $H(z) = z(M - mx)$ . Based on Newig et al. [29], the utility function of the consumer can be described as

$$U = u - p - H(z) - d(ey - Q_e). \quad (2)$$

Therefore, the profit function of a government, agricultural enterprise, and the public is

$$\begin{aligned} \pi_1(x, y, z) &= T - \delta(ey - \gamma_1 x + \gamma_2 y + \gamma_3 z) - xh - xg\gamma_1 x \\ &\quad + \gamma_2 y + \gamma_3 z, \end{aligned}$$

$$\begin{aligned} \pi_2(x, y, z) &= (a - by)y - cy - \gamma_1 x + \gamma_2 y + \gamma_3 zn \\ &\quad + p_e[y_0 - (ey - \gamma_1 x + \gamma_2 y + \gamma_3 z)] \\ &\quad + xg\gamma_1 x + \gamma_2 y + \gamma_3 z, \end{aligned}$$

$$\pi_3(x, y, z) = u - p - z(M - mx) - d[ey - \gamma_1 x + \gamma_2 y + \gamma_3 z]. \quad (3)$$

Then, the marginal profit of a government, enterprise, and the public in period  $t$  is

$$\frac{\partial \pi_1(t)}{\partial x(t)} = \gamma_1 \delta - h - 2\gamma_1 gx(t) - g(\gamma_2 y(t) + \gamma_3 z(t)),$$

$$\frac{\partial \pi_2(t)}{\partial y(t)} = a - c - \gamma_2 n - p_e(e - \gamma_2) + \gamma_2 gx(t) - 2by(t),$$

$$\frac{\partial \pi_3(t)}{\partial z(t)} = mx(t) - M + d\gamma_3. \quad (4)$$

Due to incomplete market information and limitations of their own conditions in reality, when governments, agricultural enterprises, and the public make decisions with bounded rationality, they cannot fully predict the future market demand. Therefore, it is assumed that they can only determine their decisions based on the local estimation of marginal profit. If the marginal profit is positive in period  $t$ , they will increase their decision quantity in period  $t+1$ . Thus, a three-dimensional discrete dynamic game model in the  $t+1$  period is set up as follows [30]:

$$\begin{cases} x(t+1) = x(t) + \alpha_1 x(t) \frac{\partial \pi_1(t)}{\partial x(t)}, \\ y(t+1) = y(t) + \alpha_2 y(t) \frac{\partial \pi_2(t)}{\partial y(t)}, \\ z(t+1) = z(t) + \alpha_3 z(t) \frac{\partial \pi_3(t)}{\partial z(t)}, \end{cases} \quad (5)$$

where  $\alpha_i > 0$  ( $i = 1, 2,$  and  $3$ ), respectively, represents the adjustment speed of each bounded rational player. For the convenience of calculation, we assume  $T_1 = \gamma_1 \delta - h$ ,  $a_1 = a - c - \gamma_2 n - p_e(e - \gamma_2)$ , and  $M_1 = M - d\gamma_3$ , so the dynamic adjustment mechanism of the government, enterprises, and the public with bounded rationality is simplified as

$$\begin{cases} x(t+1) = x(t) + \alpha_1 x(t) [T_1 - 2\gamma_1 g x(t) - g(\gamma_2 y(t) + \gamma_3 z(t))], \\ y(t+1) = y(t) + \alpha_2 y(t) [a_1 + \gamma_2 g x(t) - 2b y(t)], \\ z(t+1) = z(t) + \alpha_3 z(t) [m x(t) - M_1]. \end{cases} \quad (6)$$

### 3. Equilibrium Points and Local Stability

In order to study the dynamic behavior of the game model, the nonnegative equilibrium point will be discussed in this chapter. In system (6), equilibrium points are obtained by setting  $x(t+1) = x(t)$ ,  $y(t+1) = y(t)$ , and  $z(t+1) = z(t)$ , so we can obtain six equilibrium points:

$$\begin{aligned} E_0 &= (0, 0, 0), \\ E_1 &= \left(0, \frac{a_1}{2b}, 0\right), \\ E_2 &= \left(\frac{T_1}{2\gamma_1 g}, 0, 0\right), \\ E_3 &= \left(\frac{M_1}{m}, 0, \frac{T_1 m - 2\gamma_1 g M_1}{2\gamma_3 g m}\right), \\ E_4 &= \left(\frac{2T_1 b - \gamma_2 g a_1}{g(4\gamma_1 b + \gamma_2^2 g)}, \frac{2a_1 \gamma_1 + T_1 \gamma_2}{4\gamma_1 b + \gamma_2^2 g}, 0\right), \\ E_5 &= (x^*, y^*, z^*) \end{aligned} \quad (7)$$

Obviously,  $E_0, E_1, E_2, E_3,$  and  $E_4$  are bounded equilibrium points. When  $M_1 > 0, m a_1 + \gamma_2 g M_1 > 0,$  and  $m(2T_1 b - \gamma_2 g a_1) - g M_1(4\gamma_1 b + \gamma_2^2 g) > 0,$   $E_5$  is a Nash equilibrium point. To discuss the local stability of the above equilibrium points, we must consider the Jacobian matrix of system (6):

$$J = \begin{bmatrix} 1 + \alpha_1 [T_1 - 4\gamma_1 g x - g(\gamma_2 y + \gamma_3 z)] & -\alpha_1 \gamma_2 g x & -\alpha_1 \gamma_3 g x \\ \alpha_2 \gamma_2 g y & 1 + \alpha_2 (a_1 + \gamma_2 g x - 4b y) & 0 \\ \alpha_3 m z & 0 & 1 + \alpha_3 (m x - M_1) \end{bmatrix}. \quad (8)$$

**Theorem 1.** *If the Nash equilibrium point  $E_5$  is strictly nonnegative, the boundary equilibrium points  $E_0, E_1, E_2, E_3,$  and  $E_4$  of system (6) are unstable equilibrium points.*

*Proof.* In order to prove this result, we find the eigenvalues of the Jacobian matrix  $J(x, y, z)$  at each boundary equilibria  $E_0, E_1, E_2, E_3,$  and  $E_4$ . The Jacobian matrix at  $E_0$  is

$$J(E_0) = \begin{bmatrix} 1 + \alpha_1 T_1 & 0 & 0 \\ 0 & 1 + \alpha_2 a_1 & 0 \\ 0 & 0 & 1 - \alpha_3 M_1 \end{bmatrix}, \quad (9)$$

whose eigenvalues are  $\lambda_1 = 1 + \alpha_1 T_1,$   $\lambda_2 = 1 + \alpha_2 a_1,$  and  $\lambda_3 = 1 - \alpha_3 M_1.$  Since  $T_1 = \gamma_1 \delta - h,$   $h$  is the government's marginal supervisory cost, and  $\gamma_1 \delta$  represents the increase in environmental benefits with an increase in  $x(t),$  so we can

get  $\gamma_1\delta - h > 0$ . Otherwise, the government's policy improvement will not make any sense, namely,  $T_1 > 0$ . Since  $a_1 = a - c - \gamma_2n - p_e(e - \gamma_2)$ ,  $a$  is the highest price of the product in the market, while  $c + \gamma_2n + p_e(e - \gamma_2)$  can be regarded as the total variable costs of the enterprise. In the actual market, the highest price of the product must be higher than its total variable costs, namely,  $a_1 > 0$ . With conditions where  $T_1 > 0$  and  $a_1 > 0$ ,  $|\lambda_1| > 1$  and  $|\lambda_2| > 1$  can be obtained. Therefore,  $E_0$  is an unstable equilibrium point.

The Jacobian matrix at  $E_1$  is

$$J(E_1) = \begin{bmatrix} \frac{1 + \alpha_1(2T_1b - \gamma_2ga_1)}{2b} & 0 & 0 \\ 0 & 1 - \alpha_2a_1 & 0 \\ 0 & 0 & 1 - \alpha_3M_1 \end{bmatrix}, \quad (10)$$

whose eigenvalues are  $\lambda_1 = 1 + \alpha_1(2T_1b - \gamma_2ga_1)/2b$ ,  $\lambda_2 = 1 - \alpha_2a_1$ , and  $\lambda_3 = 1 - \alpha_3M_1$ . Since  $z^* > 0$ , it is clear that when the condition  $2T_1b - \gamma_2ga_1 > 0$ ,  $|\lambda_1| > 1$  is obtained. Then,  $E_1$  is an unstable equilibrium point.

The Jacobian matrix at  $E_2$  is

$$J(E_2) = \begin{bmatrix} 1 - \alpha_1T_1 & \frac{\alpha_1T_1\gamma_2}{2\gamma_1} & \frac{\alpha_1T_1\gamma_3}{2\gamma_1} \\ 0 & 1 + \alpha_2(a_1 + T_1\gamma_2/2\gamma_1) & 0 \\ 0 & 0 & \frac{1 + \alpha_3(T_1m - 2\gamma_1gM_1)}{2\gamma_1g} \end{bmatrix}, \quad (11)$$

whose eigenvalues are  $\lambda_1 = 1 - \alpha_1T_1$ ,  $\lambda_2 = 1 + \alpha_2(a_1 + T_1\gamma_2/2\gamma_1)$ , and  $\lambda_3 = 1 + \alpha_3(T_1m - 2\gamma_1gM_1)/2\gamma_1g$ . It is clear that when the condition  $a_1 + T_1\gamma_2/2\gamma_1 > 0$ ,  $|\lambda_2| > 1$ . Then,  $E_2$

is an unstable equilibrium point. Similarly, we can prove that  $E_3$  and  $E_4$  are also unstable.

The Jacobian matrix at  $E_3(x_3, 0, z_3)$  is

$$J(E_3) = \begin{bmatrix} 1 + \alpha_1(T_1 - 4\gamma_1gx_3 - \gamma_3gz_3) & -\alpha_1\gamma_2gx_3 & -\alpha_1\gamma_3gz_3 \\ 0 & 1 + \alpha_2(a_1 + \gamma_2gx_3) & 0 \\ \alpha_3mz_3 & 0 & 1 \end{bmatrix}. \quad (12)$$

By calculating the eigenvalue of the Jacobian matrix  $J(E_3)$ , we can find  $|\lambda_2 = 1 + \alpha_2(a_1 + \gamma_2gM_1/m)| > 1$ . Thus,  $E_3$  is an unstable equilibrium point.

The Jacobian matrix at  $E_4(x_4, y_4, 0)$  is

$$J(E_4) = \begin{bmatrix} 1 - 2\alpha_1\gamma_1gx_4 & -\alpha_1\gamma_2gx_4 & -\alpha_1\gamma_3gx_4 \\ \alpha_2\gamma_2gy_4 & 1 - 2\alpha_2by_4 & 0 \\ 0 & 0 & 1 + \alpha_3(mx_4 - M_1) \end{bmatrix}. \quad (13)$$

By calculating the eigenvalue of the Jacobian matrix  $J(E_4)$ ,  $\lambda_3 = 1 + \alpha_3[m(2T_1b - \gamma_2ga_1)/g(4\gamma_1b + \gamma_2^2g) - M_1]$ . It is clear that when the condition  $m(2T_1b - \gamma_2ga_1) - gM_1(4\gamma_1b + \gamma_2^2g) > 0$ ,  $|\lambda_3| > 1$ . Thus,  $E_4$  is an unstable equilibrium point.  $\square$

**Theorem 2.** *If the system parameters satisfy  $M_1 > 0$ ,  $ma_1 + \gamma_2gM_1 > 0$ ,  $m(2T_1b - \gamma_2ga_1) - gM_1(4\gamma_1b + \gamma_2^2g) > 0$ , and when the following Jury conditions are performed, the Nash equilibrium point  $E_5$  is locally asymptotically stable.*

*Proof.* In order to investigate the local stability of the Nash equilibrium point  $E_5 = (x^*, y^*, z^*)$ , the Jacobian matrix at  $E_5$  is

$$J(E_5) = \begin{bmatrix} 1 - 2\alpha_1\gamma_1gx^* & -\alpha_1\gamma_2gx^* & -\alpha_1\gamma_3gx^* \\ \alpha_2\gamma_2gy^* & 1 - 2\alpha_2by^* & 0 \\ \alpha_3mz^* & 0 & 1 \end{bmatrix}. \quad (14)$$

The characteristic equation of the matrix  $J(E_5)$  is

$$f\lambda = \lambda^3 + A_1\lambda^2 + A_2\lambda + A_3, \quad (15)$$

where

$$\begin{aligned}
A_1 &= -3 + 2\alpha_1\gamma_1gx^* + 2\alpha_2by^*, \\
A_2 &= 3 - 4\alpha_2by^* + \alpha_1\alpha_2\gamma_2^2g^2x^*y^* + \alpha_1\alpha_3\gamma_3gmx^*z^* \\
&\quad - 4\alpha_1\gamma_1gx^* + 4\alpha_1\alpha_2\gamma_1gbx^*y^*, \\
A_3 &= -1 + 2\alpha_2by^* + 2\alpha_1\gamma_1gx^* - 4\alpha_1\alpha_2\gamma_1gbx^*y^* \\
&\quad - \alpha_1\alpha_2\gamma_2^2g^2x^*y^* - \alpha_1\alpha_3\gamma_3gmx^*z^* + 2\alpha_1\alpha_2\alpha_3\gamma_3gmbx^*y^*z^*.
\end{aligned} \tag{16}$$

The local stability conditions of the Nash equilibrium are given by Jury's conditions, which are the sufficient and necessary conditions  $|\lambda_i| < 1, i = 1, 2, 3$ :

$$\begin{cases}
1 + A_1 + A_2 + A_3 > 0, \\
(A_3^2 - 1)^2 - (A_2 - A_1A_3)^2 > 0, \\
1 - A_1 + A_2 - A_3 > 0, \\
A_3^2 - 1 < 0.
\end{cases} \tag{17}$$

Obviously, the Nash equilibrium point  $E_5$  is a stable node in the stability region defined by (17). However, if  $\alpha_1, \alpha_2$ , and  $\alpha_3$  go beyond the stability region, more complex phenomena in terms of the evolution of outputs will occur such as bifurcation and chaos. Moreover, we found that the local stability of the system in the Nash equilibrium point can be decided by every parameter in (17). Based on inequalities (17), the three-dimensional stability domains of the system (6) are simulated when  $p_e$  and  $g$  take different values (as shown in Sections 4.2 and 4.3).  $\square$

#### 4. Numerical Simulations

In this section, we analyzed the dynamic behaviors of the bounded rational players through various numerical simulations. They could observe the influence of the adjustment speed of  $\alpha_1, \alpha_2$ , and  $\alpha_3$ , the market price of nitrogen trading  $p_e$ , and the subsidy standard of nitrogen emission reduction  $g$  on the model. In order to study the local stability properties of the equilibrium point, it is convenient to take the parameter values as follows:  $a = 10, b = 3, c = 1, d = 0.42, \gamma_1 = 3, \gamma_2 = 0.5, \gamma_3 = 1, n = 0.5, p_e = 1, e = 0.6, g = 0.3, \delta = 1, h = 0.5, m = 0.55$ , and  $M = 1$ .

**4.1. The Impact of the Adjustment Speed on the Stability of the System.** Figure 1 shows the bifurcation diagram with respect to the adjustment speed  $\alpha_1$  of a government's policy intensity while  $\alpha_2 = 0.21$  and  $\alpha_3 = 0.5$ . The corresponding largest Lyapunov exponents with respect to  $\alpha_1$  are drawn in Figure 2. In the range  $\alpha_1 < 1.1057$ , the Lyapunov exponents are negative, which means that the Nash equilibrium point  $E_5$  is stable. When  $\alpha_1 = 1.1057$ , the first bifurcation point in Figure 1 corresponds to the first peak (1.1057, -0.008) in Figure 2, leading to the system gradually entering a period-doubling bifurcation. Finally, when  $\alpha_1 > 1.2340$ , the maximal Lyapunov exponents are almost greater than zero, indicating that chaotic behavior is occurring and the Nash equilibrium point is becoming very unstable.

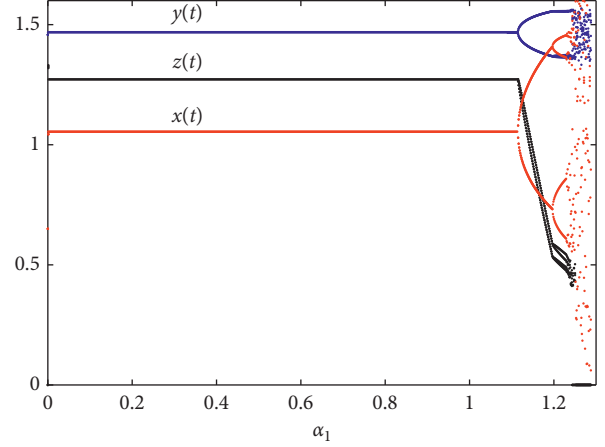


FIGURE 1: Bifurcation diagram for  $\alpha_2 = 0.21$  and  $\alpha_3 = 0.5$ .

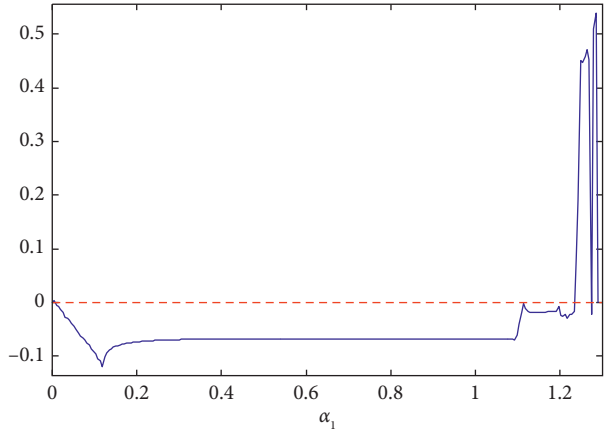


FIGURE 2: Maximal Lyapunov exponent for  $\alpha_2 = 0.21$  and  $\alpha_3 = 0.5$ .

Figure 3 shows the bifurcation diagram with respect to the adjustment speed  $\alpha_2$  of the enterprises' output while  $\alpha_1 = 0.7$  and  $\alpha_3 = 0.5$ . The corresponding largest Lyapunov exponents with respect to  $\alpha_2$  are drawn in Figure 4. As can be seen from Figures 3 and 4, in the range  $\alpha_2 < 0.2279$ , the Lyapunov exponents are negative, which means that the Nash equilibrium point  $E_5$  is stable. When  $\alpha_2 = 0.2279$ , the first bifurcation point in Figure 3 corresponds to the first peak (0.2279, -0.0282) in Figure 4. With  $\alpha_2$  increasing to 0.2792, the second bifurcation point in Figure 3 corresponds to the second peak (0.2792, -0.0473) in Figure 4, and the system then gradually enters a period-doubling bifurcation. Finally, when  $\alpha_2 > 0.2928$ , the maximal Lyapunov exponents are almost greater than zero, indicating that chaotic behavior is occurring and the Nash equilibrium point is becoming very unstable.

Figure 5 shows the bifurcation diagram with respect to the adjustment speed  $\alpha_3$  of the public's supervision intensity while  $\alpha_1 = 0.7$  and  $\alpha_2 = 0.21$ . The corresponding largest Lyapunov exponents with respect to  $\alpha_3$  are drawn in Figure 6. From Figures 5 and 6, when  $\alpha_3 < 8.493$ , the Lyapunov exponents are negative, which means that the Nash equilibrium point  $E_5$  is locally stable for small values of  $\alpha_3$ .



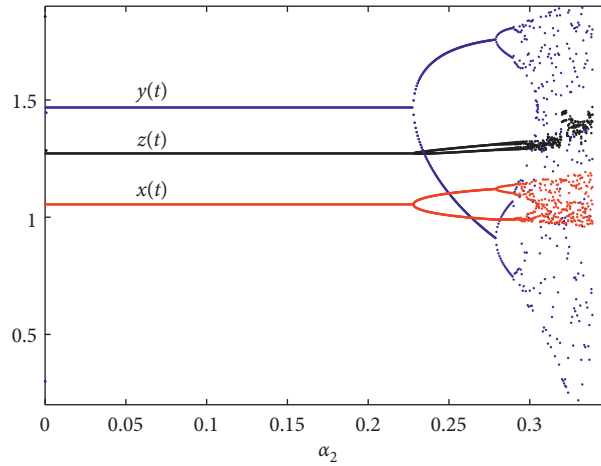


FIGURE 3: Bifurcation diagram for  $\alpha_1 = 0.7$  and  $\alpha_3 = 0.5$ .

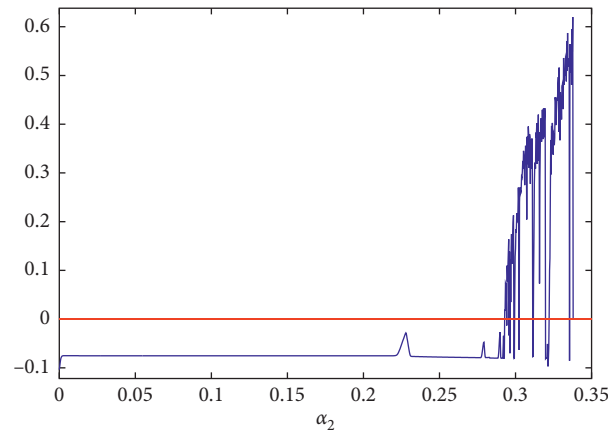


FIGURE 4: Maximal Lyapunov exponent for  $\alpha_1 = 0.7$  and  $\alpha_3 = 0.5$ .

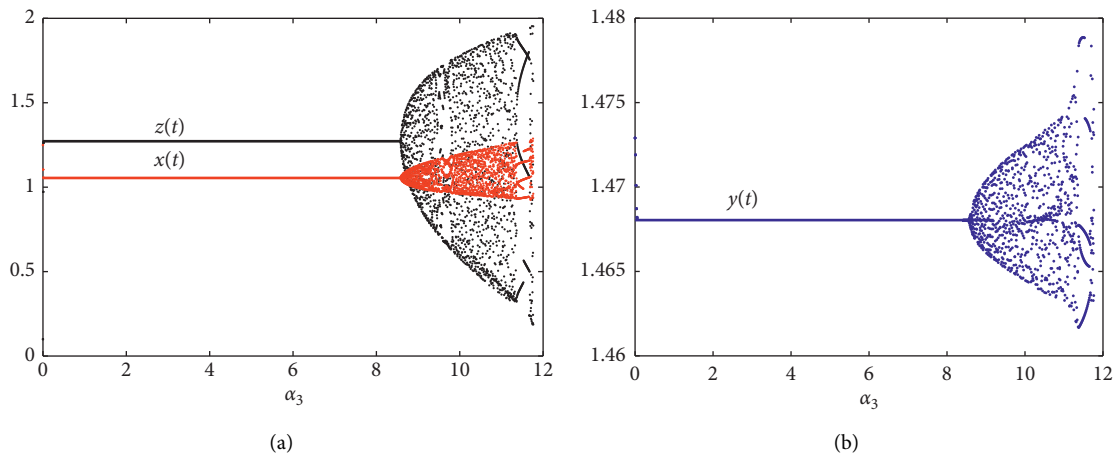


FIGURE 5: Bifurcation diagram for  $\alpha_1 = 0.7$  and  $\alpha_2 = 0.21$ : (a)  $x(t)$  and  $z(t)$ ; (b)  $y(t)$ .

However, in the range  $\alpha_3 > 8.493$ , the system starts to enter into the chaotic state and complex dynamic behavior occurs.

The strange attractors corresponding to Figure 1 are shown in Figures 7–10, which shows the changing situation for strange attractors at different values of  $\alpha_1$  while  $\alpha_2 = 0.21$

and  $\alpha_3 = 0.5$ . When  $\alpha_1 = 0.008$ , the decision-making behavior of the government, enterprises, and the public forms a spiral trajectory map and finally forms a gradual stability point. However, with the finiteness of market information and the bounded rationality of the game players, when  $\alpha_1 > 1.1057$ ,

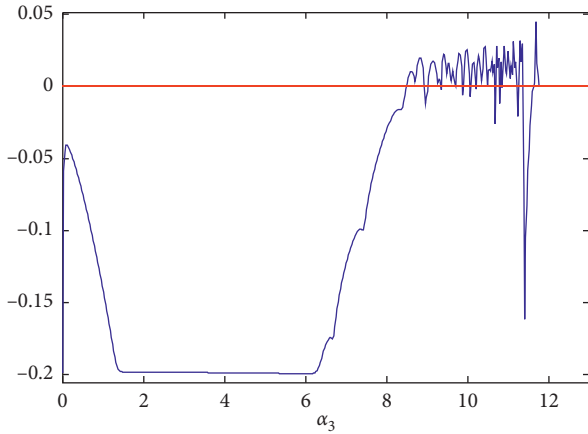


FIGURE 6: Maximal Lyapunov exponent for  $\alpha_1 = 0.7$  and  $\alpha_2 = 0.21$ .

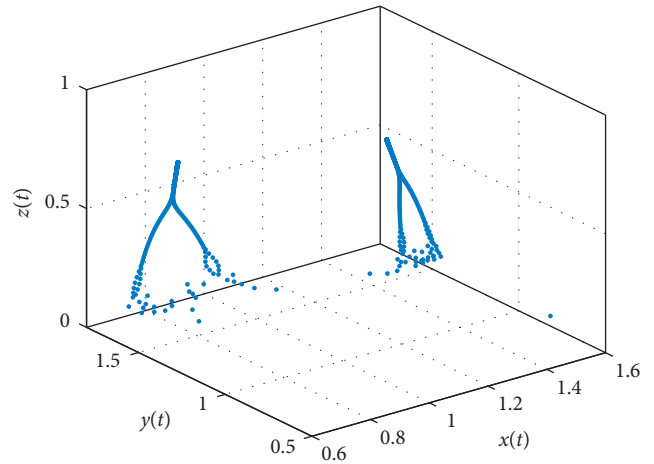


FIGURE 8: Strange attractors for  $\alpha_1 = 1.18$ .

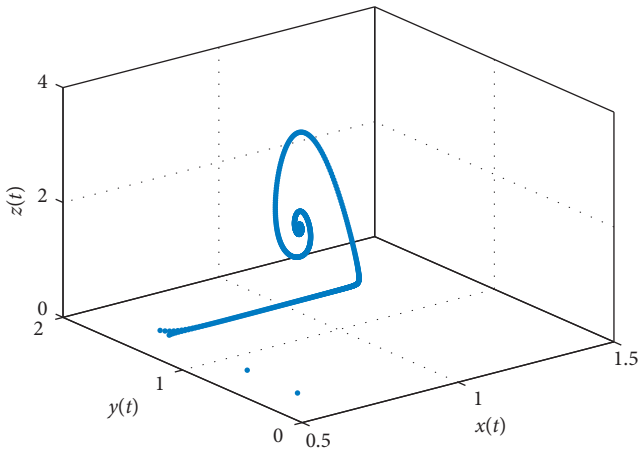


FIGURE 7: Strange attractors for  $\alpha_1 = 0.008$ .

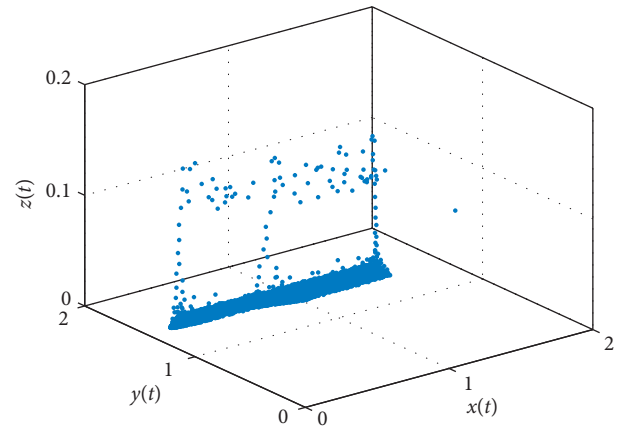


FIGURE 9: Strange attractors for  $\alpha_1 = 1.25$ .

the stable point gradually appears as a branch state, as shown in Figure 8. When  $\alpha_1 > 1.2340$ , it was found that the point was no longer stable and chaos began to appear until a chaos phenomenon in Figure 9 appeared.

Figure 10 shows the strange attractor in a chaotic state while  $\alpha_1 = 0.7$ ,  $\alpha_2 = 0.31$ , and  $\alpha_3 = 0.5$ . At this time, the decision-making behavior of players appears to be a complex chaos phenomenon. The strange attractors corresponding to Figure 5 are shown in Figures 11 and 12, which shows the change situation for strange attractors at different values of  $\alpha_3$  while  $\alpha_1 = 0.7$  and  $\alpha_2 = 0.21$ . When  $\alpha_3$  increases to 8.5, chaos has occurred and a vortex shaped attractor appears, as shown in Figure 11. When  $\alpha_3 > 8.5$ , it was found that the vortex had evolved into an annular phase diagram, as shown in Figure 12.

In order to further explore the chaotic phenomenon caused by a change in the decision-making adjustment speed, we investigated the sensitivity at the initial value of the system (6). These numerical simulations are performed by setting  $\alpha_1 = 1.28$ ,  $\alpha_2 = 0.21$ , and  $\alpha_3 = 0.5$  (the system is in a chaotic state at this time). It can be seen from Figure 13 that two orbits of  $x(t)$ ,  $y(t)$ , or  $z(t)$  are indistinguishable at the beginning, but after several iterations, the separation

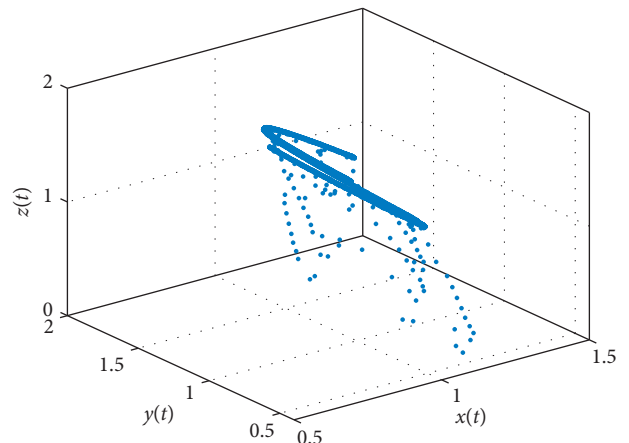


FIGURE 10: Strange attractors for  $\alpha_2 = 0.31$ .

between them builds up rapidly; that is, subtle changes in the initial conditions will greatly affect the results.

Through the above numerical simulation analysis, it can be concluded that the adjustment speeds  $\alpha_1$ ,  $\alpha_2$ , and  $\alpha_3$  of the bounded rational players may greatly affect the stability of system (6) and lead to complex chaos phenomena in the

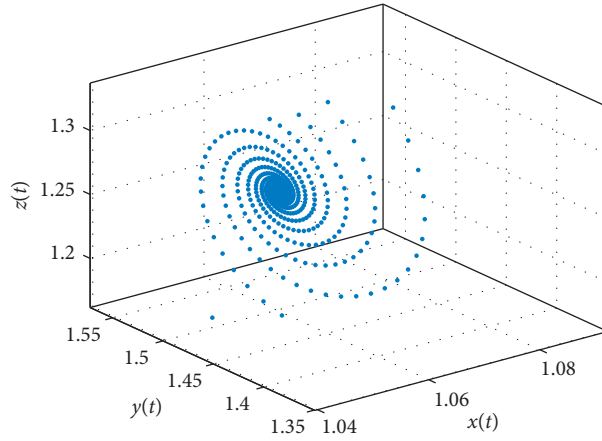


FIGURE 11: Strange attractors for  $\alpha_3 = 8.5$ .

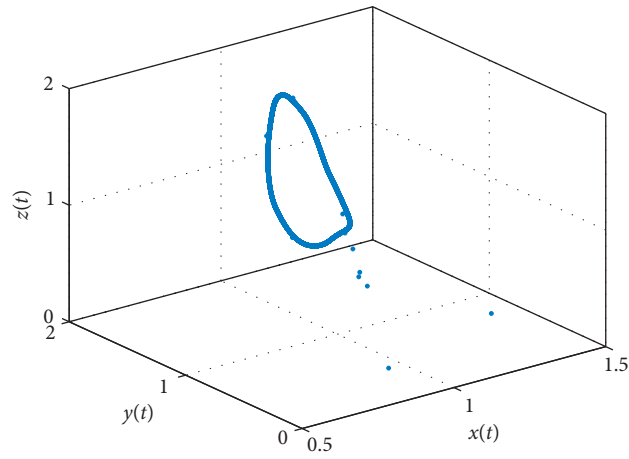
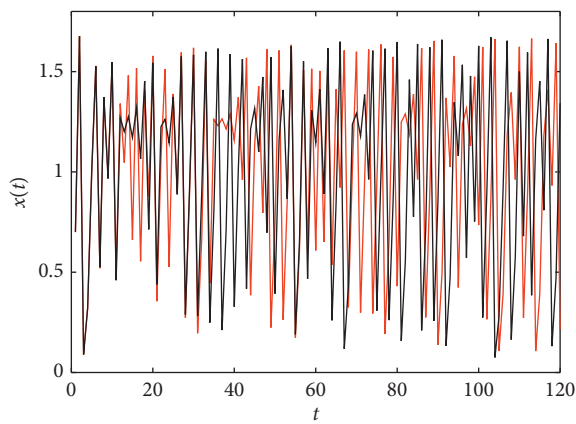
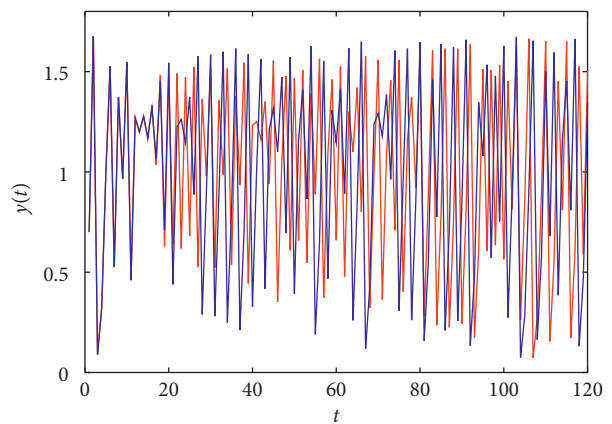


FIGURE 12: Strange attractors for  $\alpha_3 = 10.5$ .



—  $x_1 = 0.7001$   
—  $x_0 = 0.7$

(a)



—  $y_1 = 0.4001$   
—  $y_0 = 0.4$

(b)

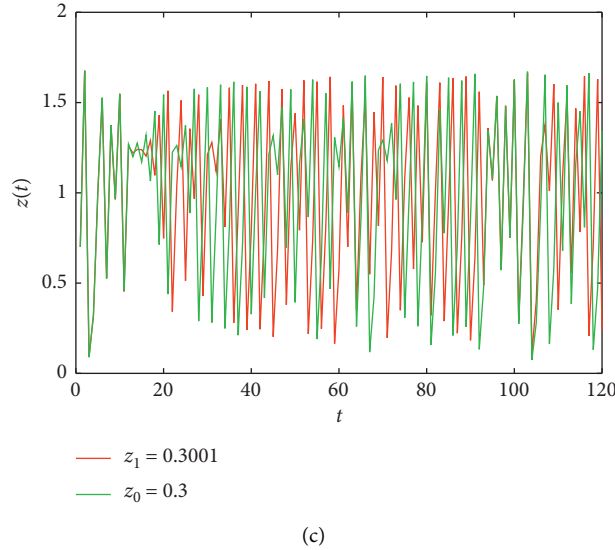


FIGURE 13: Sensitive dependence on initial conditions: (a) two orbits of  $x(t)$  with initial values  $x_1 = 0.7001$  and  $x_0 = 0.7$ ; (b) two orbits of  $y(t)$  with initial values  $y_1 = 0.4001$  and  $y_0 = 0.4$ ; (c) two orbits of  $z(t)$  with initial value  $z_1 = 0.3001$  and  $z_0 = 0.3$ .

system. Once trapped in a chaotic market, slight changes in various initial conditions of the government, agricultural enterprises, and the public will greatly affect the final results. In addition, the players cannot effectively predict various changes in reality, which will result in their decisions not being effectively implemented.

**4.2. The Impact of the Market Price of Nitrogen Trading on the Stability of the System.** When enterprises decide whether to trade emission permits based on their own nitrogen emissions, it is necessary to compare the market price of nitrogen trading with the cost of nitrogen emission reductions. The emission level  $e$  and emission reduction technology level of enterprises  $\gamma_2$  are determined by their production equipment and technology, which cannot be changed quickly. The variable cost of nitrogen emissions  $p_e \epsilon \gamma_2$  can affect the decision-making behavior of enterprises; therefore, it is the market price of nitrogen trading that affects the stability of the system.

Inequalities (17) define the stable range of the Nash equilibrium point of the system under the adjustment speeds  $\alpha_1$ ,  $\alpha_2$ , and  $\alpha_3$ . When the initial values of each parameter are fixed, the region of stability for the Nash equilibrium point  $E_5$  under different values of  $p_e$  is shown as in Figure 14. When the trading price of nitrogen emissions  $p_e = 1$  increases to  $p_e = 10$ , the stability of the system will decrease. In addition, the Nash equilibrium point will evolve from  $E_5$  (1.0545, 1.4680, 1.2720) to  $E'_5$  (1.0545, 1.3180, 1.3470), indicating that, with an increase in  $p_e$ , the government's policy intensity will remain unchanged, while the enterprises' output will be reduced and the public's supervision intensity will increase.

Figure 15(a) shows the bifurcation diagram with respect to the market price of nitrogen trading  $p_e$  while  $\alpha_1 = 0.7$ ,  $\alpha_2 = 0.21$ , and  $\alpha_3 = 0.5$  (the system is stable). The Nash equilibrium point  $E_5$  then becomes  $E^* = (x^*, y^*, z) = (1.0545, 1.4847 -$

$0.0167 p_e, 1.2637 + 0.0083 p_e)$ . From this Figure 15(a), it can be observed that the equilibrium point is locally stable for the small values of the parameter  $p_e$ . When  $p_e$  increases, the Nash equilibrium point  $E^*$  becomes unstable, and even complex dynamics phenomena such as period-doubling bifurcation and chaos appear. The main reason behind this is that an increase in  $p_e$  increases the variable cost for enterprises. When the technical level remains unchanged, enterprises have to reduce their output.

Figure 15(b) shows the bifurcation diagram with respect to  $p_e$  while  $\alpha_1 = 1.25$ ,  $\alpha_2 = 0.21$ , and  $\alpha_3 = 0.5$  (the system being in chaos). The research shows that when the adjustment speed of policy intensity  $\alpha_1$  is too large, the public's supervision intensity will decrease to zero with an increase in  $p_e$ , and the system still remains in a chaotic state. Figure 15(c) shows the bifurcation diagram with respect to  $p_e$  while  $\alpha_1 = 0.7$ ,  $\alpha_2 = 0.315$ , and  $\alpha_3 = 0.5$  (the system being in chaos). It can be seen that when the adjustment speed of enterprises' output  $\alpha_2$  is too large, as  $p_e$  increases, the system gradually evolves from chaos to period-doubling bifurcation until reaching a state of equilibrium. However, when  $p_e$  continues to increase, a complex evolution similar to that shown in Figure 15(a) will appear and eventually enter chaos. Figure 15(d) shows the bifurcation diagram with respect to  $p_e$  while  $\alpha_1 = 0.7$ ,  $\alpha_2 = 0.21$ , and  $\alpha_3 = 10$  (the system being in chaos). When the adjustment speed of the public's supervision intensity  $\alpha_3$  is too large, each player is still in chaotic state with an increase in  $p_e$ . The main reason for this is that  $p_e$  has an influence on the decision of enterprises' output  $y(t)$  by affecting the marginal profit of enterprises. Therefore, when  $\alpha_2$  is too large, increasing  $p_e$  can control chaos.

**4.3. The Impact of Subsidizing Nitrogen Emission on the Stability of the System.** The subsidy of nitrogen emission reductions is proportional to the amount of emission

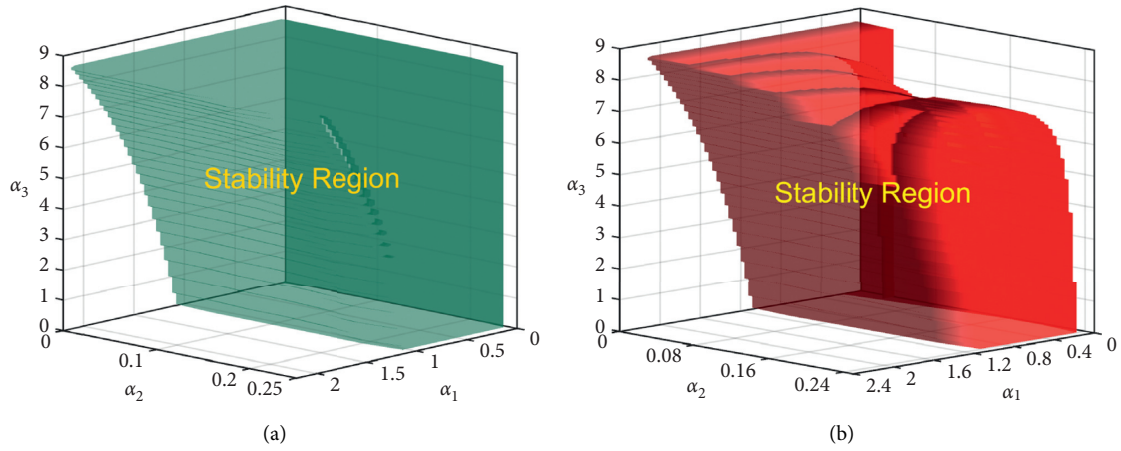


FIGURE 14: The stability region of  $E_3$  in  $\alpha_1$ ,  $\alpha_2$ , and  $\alpha_3$ -plane under different values of  $p_e$ : (a)  $p_e = 1$ ; (b)  $p_e = 10$ .

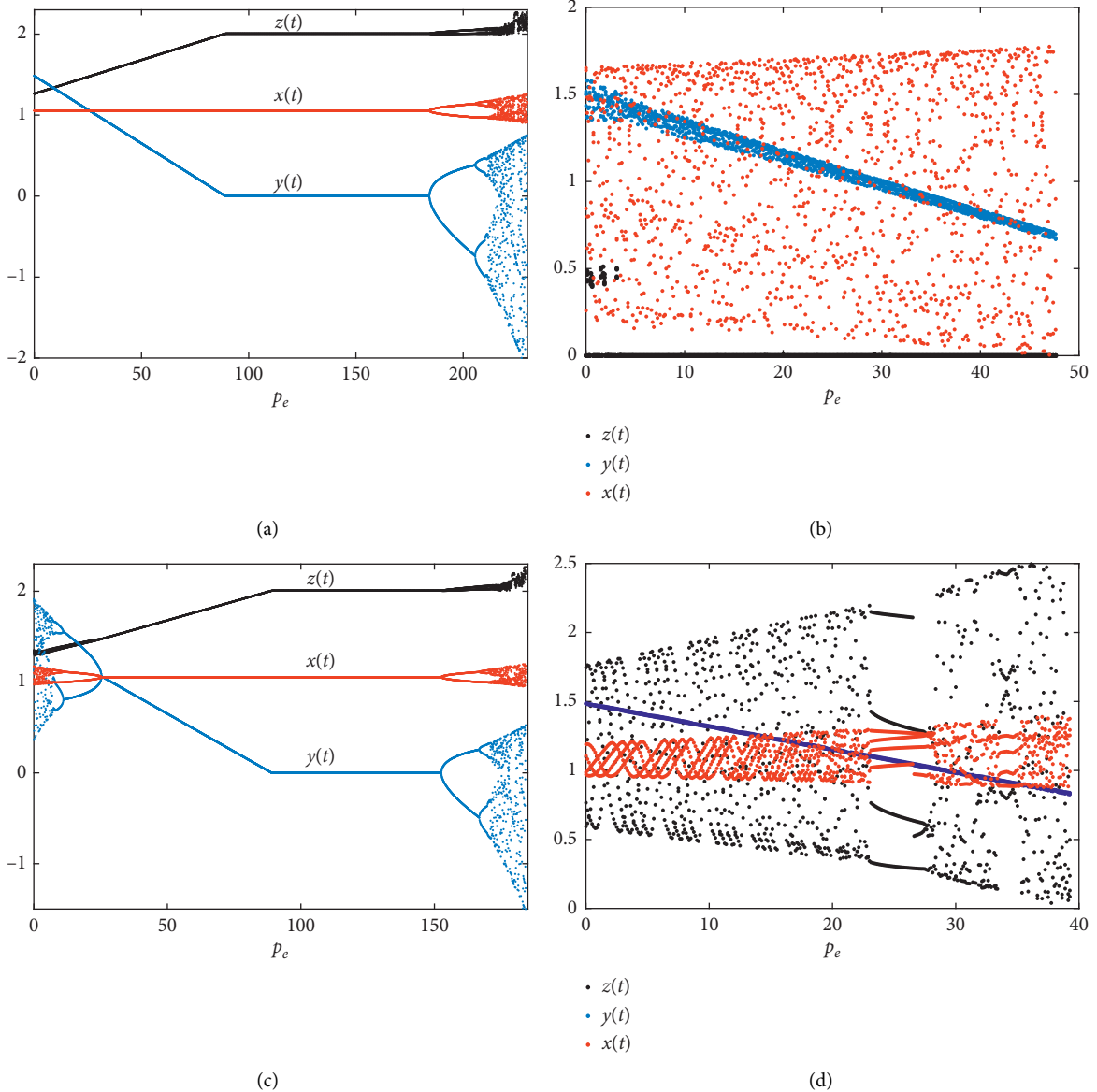


FIGURE 15: Bifurcation diagram with respect to  $p_e$ : (a)  $\alpha_1 = 0.7$ ,  $\alpha_2 = 0.21$ , and  $\alpha_3 = 0.5$ ; (b)  $\alpha_1 = 1.25$ ,  $\alpha_2 = 0.21$ , and  $\alpha_3 = 0.5$ ; (c)  $\alpha_1 = 0.7$ ,  $\alpha_2 = 0.315$ , and  $\alpha_3 = 0.5$ ; (d)  $\alpha_1 = 0.7$ ,  $\alpha_2 = 0.21$ , and  $\alpha_3 = 10$ .



reductions. The subsidy of emission reductions is not only a source of income for an enterprise but also the government's fiscal expenditure to encourage enterprises to reduce emissions. Therefore, the subsidy standard of the reduction of nitrogen emissions  $g$  will affect the system.

When the subsidy standard of the reduction of nitrogen emissions  $g=0.3$ , the stable region of the Nash equilibrium point is shown as in Figure 14(a). If other parameters are fixed, the nitrogen emission reduction subsidy standard  $g$  varies to  $g=0.32$  from  $g=0.3$ , and we can see that the area of the stable region increases in the direction of  $\alpha_2$  and  $\alpha_3$ , as shown in Figure 16. Therefore, the stability of the system will increase with an increase in  $g$ ; in addition, the Nash equilibrium point will evolve from  $E_5$  (1.0545, 1.468, 1.272) to  $E'_5$  (1.0545, 1.4698, 0.7503), which means that, as  $g$  increases, the government's policy intensity will remain unchanged, while the enterprises' output will increase and the public's supervision intensity will decrease.

Figure 17(a) shows the bifurcation diagram with regard to the subsidy standard of the nitrogen emission reduction  $g$  while  $\alpha_1 = 0.7$ ,  $\alpha_2 = 0.21$ , and  $\alpha_3 = 0.5$  (the system being stable) because the Nash equilibrium point  $E_5$  at this time becomes  $E^* = (x^*, y^*, z) = (1.0545, 1.4417 + 0.0879g, (2.5/g - 7.0481 - 0.0439g))$ . From Figure 18, it can be observed that the equilibrium point is locally stable for small values of the parameter  $g$ . When  $g$  increases, the Nash equilibrium point  $E^*$  becomes unstable, and even complex dynamic phenomena appear such as period-doubling bifurcation and chaos. The main reason is that the increase in  $g$  increases the government's variable cost, and the government has to reduce its policy intensity. When other conditions remain unchanged, enterprises can obtain more subsidies by increasing their output. At this time, the public will reduce their supervision intensity due to the increase in enterprises' emission reduction. When  $g$  becomes too large, the market cannot be balanced, and the decision-making of the government, enterprises, and the public cannot reach an equilibrium point any more until chaos appears.

Figure 17(b) shows the bifurcation diagram with regard to  $g$  while  $\alpha_1 = 1.25$ ,  $\alpha_2 = 0.21$ , and  $\alpha_3 = 0.5$  (the system being in chaos). The research shows that when the adjustment speed of policy intensity  $\alpha_1$  is too large, as  $g$  increases, the public's supervision intensity will decrease to zero, and the system gradually evolves from chaos to period-doubling bifurcation until reaching an equilibrium state. However, when  $g$  continues to increase, a complex evolution similar to that shown in Figure 17(a) will appear and eventually enter chaos. Figure 17(c) shows the bifurcation diagram with respect to  $g$  while  $\alpha_1 = 0.7$ ,  $\alpha_2 = 0.315$ , and  $\alpha_3 = 0.5$  (the system being in chaos). It can be seen that when the adjustment speed of enterprises' output  $\alpha_2$  is too large, as  $g$  increases, the government and enterprises are still in a chaotic state. Figures 17(d) and 17(e) show the bifurcation diagram with respect to  $g$  while  $\alpha_1 = 0.7$ ,  $\alpha_2 = 0.21$ , and  $\alpha_3 = 10$  (the system being in chaos). When the adjustment speed of the public's supervision intensity  $\alpha_3$  is too large, the system gradually evolves from chaos to an equilibrium state

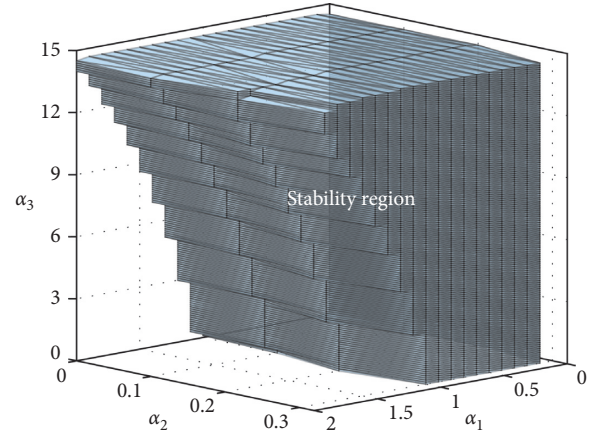


FIGURE 16: The stability region of  $E_5$  in  $\alpha_1$ ,  $\alpha_2$ , and  $\alpha_3$ -plane for  $g=0.32$ .

with an increase in  $g$ . Therefore, when  $\alpha_1$  or  $\alpha_3$  is too large, increasing  $g$  can control chaos.

The above numerical simulation shows that the market price of nitrogen trading  $p_e$  and the subsidy standard for the reduction of nitrogen emission  $g$  are important factors in the dynamic game among governments, enterprises, and the public participating in the reduction of nitrogen emissions in the basin. They not only influence the Nash equilibrium point of the system but also affect the stable region of the system.

## 5. Chaos Control

Through model analysis and numerical simulation, it is found that when  $\alpha_1$ ,  $\alpha_2$ , or  $\alpha_3$  exceeds the critical value, the system (6) will lose stability. At this time, the chaotic system will have a sensitive dependence on the initial conditions, which means that the government, enterprises, and the public would not be able to predict the market development and any small adjustment of the initial conditions. Therefore, it is very important to perform chaotic control on the system (6) to ensure that it is in a stable equilibrium state.

There are many chaos control methods. This section uses the delayed feedback control method proposed by Pyragas [31] to control the chaos of the system (6). It is expressed as  $u(t) = k(y(t+1-\tau) - y(t+1))$ ,  $t > \tau$ , where  $k$  is the controlling factor and  $\tau$  is the length of the time delay. Substituting  $\tau = 1$  into the second equation of the system (6), the controlled system can be modeled as

$$\begin{aligned} x(t+1) &= x(t) + \alpha_1 x(t) [T_1 - 2\gamma_1 g x(t) - g(\gamma_2 y(t) + \gamma_3 z(t))], \\ y(t+1) &= y(t) + \frac{\alpha_2}{(k+1)} y(t) [a_1 + \gamma_2 g x(t) - 2b y(t)], \\ z(t+1) &= z(t) + \alpha_3 z(t) [m x(t) - M_1], \end{aligned} \quad (18)$$

and the Jacobian matrix of (17) at the Nash equilibrium point  $E_5$  is

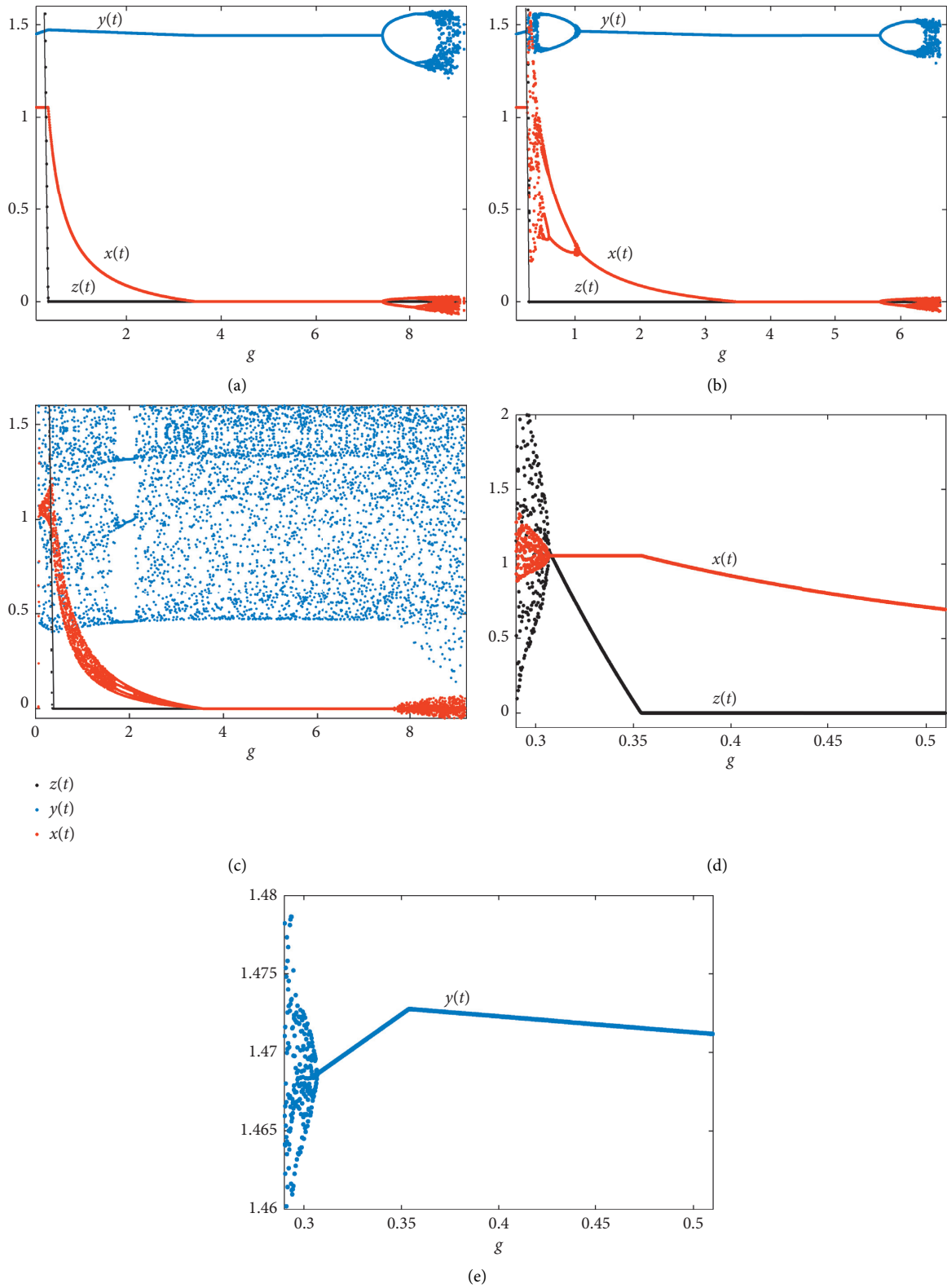


FIGURE 17: Bifurcation diagram with respect to  $g$ : (a)  $\alpha_1 = 0.7$ ,  $\alpha_2 = 0.21$ , and  $\alpha_3 = 0.5$ ; (b)  $\alpha_1 = 1.25$ ,  $\alpha_2 = 0.21$ , and  $\alpha_3 = 0.5$ ; (c)  $\alpha_1 = 0.7$ ,  $\alpha_2 = 0.315$ , and  $\alpha_3 = 0.5$ ; (d)  $\alpha_1 = 1.25$ ,  $\alpha_2 = 0.21$ , and  $\alpha_3 = 10$  ( $x(t)$ ,  $z(t)$ ); (e)  $\alpha_1 = 1.25$ ,  $\alpha_2 = 0.21$ , and  $\alpha_3 = 10$  ( $y(t)$ ).

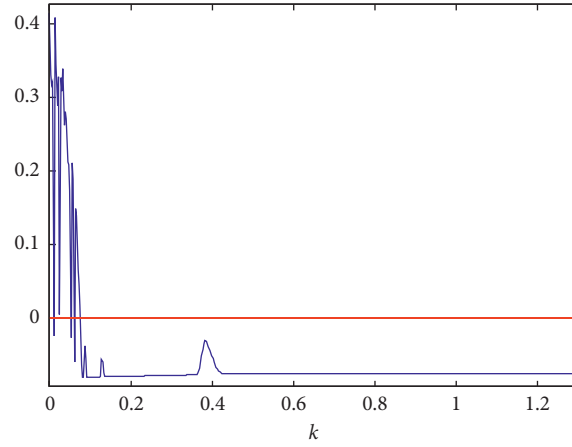


FIGURE 18: Maximal Lyapunov exponent with respect to  $k$ .

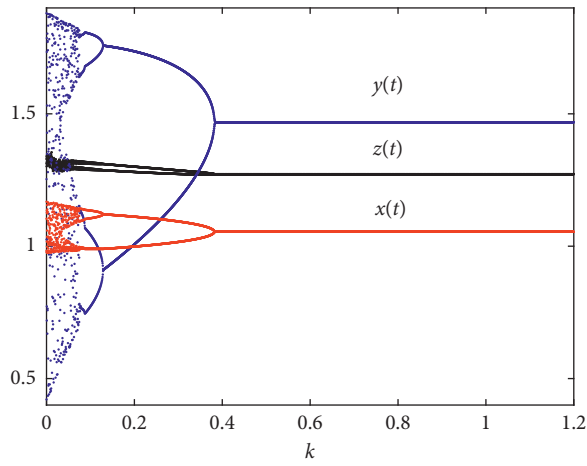


FIGURE 19: Bifurcation diagram with respect to  $k$ .

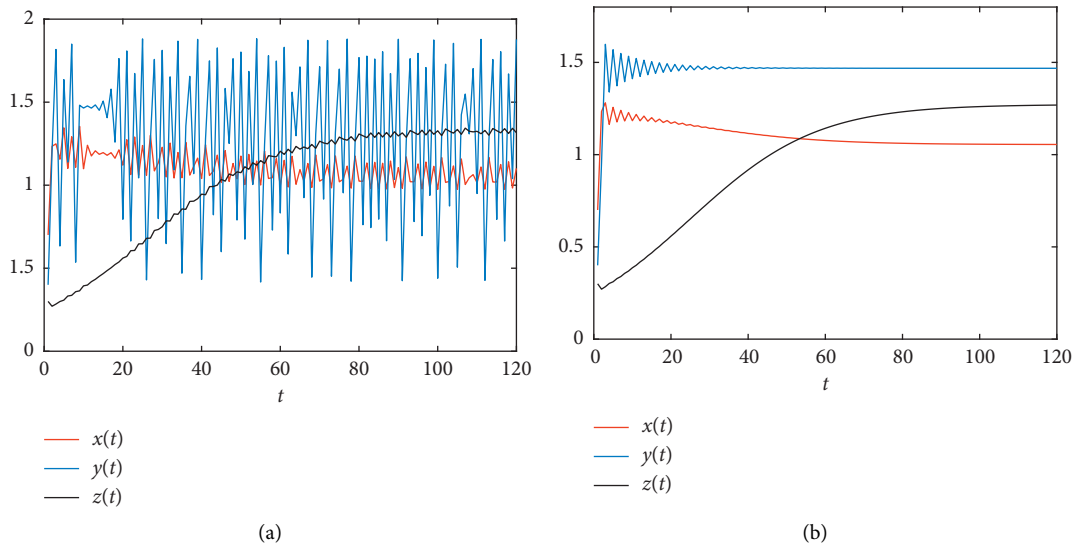


FIGURE 20: Effects of control factor  $k$  on  $x(t)$ ,  $y(t)$ , and  $z(t)$ : (a)  $k=0$ ; (b)  $k=0.45$ .

$$J'(E_5) = \begin{bmatrix} 1 - 2\alpha_1\gamma_1gx^* & -\alpha_1\gamma_2gx^* & -\alpha_1\gamma_3gx^* \\ \frac{\alpha_2}{(k+1)}\gamma_2gy^* & 1 - \frac{\alpha_2}{(k+1)}2by^* & 0 \\ \alpha_3mz^* & 0 & 1 \end{bmatrix}. \quad (19)$$

Figure 19 shows the bifurcation diagram with regard to the control factor  $k$ , while the initial values of the other parameters are fixed, and  $\alpha_1 = 0.7$ ,  $\alpha_2 = 0.315$ , and  $\alpha_3 = 0.5$ . Figure 18 shows the largest Lyapunov exponents with regard to the control factor  $k$ . From Figure 19, with the increase in  $k$ , the decision variables  $x(t)$ ,  $y(t)$ , and  $z(t)$  can evolve from chaos to periodic bifurcation and finally stabilize at the Nash equilibrium levels. With a gradual increase in  $k$ , in the range  $k > 0.384$ , the controlled system (18) becomes stable without chaotic behaviors. The effects of the control factor  $k$  on the controlled system before and after chaos are shown in Figure 20 when  $k = 0.45$ , and this figure depicts the change process of the controlled system from chaos to a stable state when the initial values of the bounded rational players are  $(x_0, y_0, z_0) = (0.7, 0.4, 0.3)$ .

## 6. Conclusions

In this paper, bounded rationality, nitrogen emission trading, and the subsidy of reductions in nitrogen emissions are considered in terms of a dynamic game involving the government, enterprises, and the public, and a decision-making game model is established based on bounded rationality. At the same time, we analyzed the dynamic behavior of players with bounded rationality, the equilibrium points of the model are discussed, and a three-dimensional stability region of the Nash equilibrium point is presented. Through the discussion, it can be concluded that many parameters such as the market price of nitrogen trading  $p_e$  and the subsidy standard of nitrogen emission reductions  $g$  would affect the stability of the system; when the parameters become beneficial for enterprises to reduce nitrogen emissions, the chaotic market will restore, and the regional stability of the system will decrease with the increase in the parameters. Furthermore, the numerical simulation shows the dynamic evolution process of the decisions of the participants. The results show that when the adjustment speed values of the bounded rational player  $\alpha_1$ ,  $\alpha_2$ , and  $\alpha_3$  are small, the system is stable. If one of  $\alpha_1$ ,  $\alpha_2$ , and  $\alpha_3$  increases beyond the stability region of the Nash equilibrium point, bifurcation, chaos, and other dynamic behaviors will occur. Finally, it is proven that the delayed feedback control method can effectively control the system in a chaos state to restore the stable equilibrium market.

## Data Availability

Some or all data, models, or code generated or used during the study are available from the corresponding author by request.

## Disclosure

Jixiang Zhang and Xuan Xi should be regarded as the co-first authors.

## Conflicts of Interest

The authors declare that they have no conflicts of interest.

## Authors' Contributions

Jixiang Zhang and Xuan Xi contributed to the work equally.

## Acknowledgments

This work was supported by the Fundamental Research Funds for the Central Universities (Grant no. NS2019045).

## References

- [1] R. W. Howarth, "The development of policy approaches for reducing nitrogen pollution to coastal waters of the USA," *Science in China Series C Life Sciences*, vol. 48, pp. 791–806, 2005.
- [2] K. E. Havens, R. T. James, T. L. East, and V. H. Smith, "N:P ratios, light limitation, and cyanobacterial dominance in a subtropical lake impacted by non-point source nutrient pollution," *Environmental Pollution*, vol. 122, no. 3, pp. 379–390, 2003.
- [3] D. Ni and Y. Wang, "Sharing a polluted river," *Games and Economic Behavior*, vol. 60, no. 1, pp. 176–186, 2007.
- [4] X. Gao, J. Shen, W. He et al., "An evolutionary game analysis of governments' decision-making behaviors and factors influencing watershed ecological compensation in China," *Journal of Environmental Management*, vol. 251, Article ID 109592, 2019.
- [5] S. Jorgensen, "A dynamic game of waste management," *Journal of Economic Dynamics & Control*, vol. 34, no. 2, pp. 258–265, 2010.
- [6] G. Frisvold and M. F. Caswell, "Transboundary water management game-theoretic lessons for projects on the US-Mexico border," *Agricultural Economics*, vol. 24, no. 1, pp. 101–111, 2000.
- [7] J. C. Bárcena-Ruiz, "Environmental taxes and first-mover advantages," *Environmental & Resource Economics*, vol. 35, no. 1, pp. 19–39, 2006.
- [8] T. Puu, "Chaos in duopoly pricing," *Chaos Solitons Fractals*, vol. 1, no. 1, pp. 573–581, 1991.
- [9] L. U. Yali, "Dynamics of a delayed duopoly game with increasing marginal costs and bounded rationality strategy," *Procedia Engineering*, vol. 15, pp. 4392–4396, 2011.
- [10] Y. Peng, Q. Lu, and Y. Xiao, "A dynamic Stackelberg duopoly model with different strategies," *Chaos, Solitons & Fractals*, vol. 85, pp. 128–134, 2016.
- [11] A. A. Elsadany, "Dynamics of a Cournot duopoly game with bounded rationality based on relative profit maximization," *Applied Mathematics and Computation*, vol. 294, pp. 253–263, 2017.
- [12] H.-X. Yao and F. Xu, "Complex dynamics analysis for a duopoly advertising model with nonlinear cost," *Applied Mathematics and Computation*, vol. 180, no. 1, pp. 134–145, 2006.

- [13] Z. Ding, Q. Li, D. Ge, and S. Jiang, "Research on dynamics in a resource extraction game with bounded rationality," *Applied Mathematics and Computation*, vol. 236, pp. 628–634, 2014.
- [14] H. Yao, X. Yang, and Z. Jiang, "Dynamic analysis of nonlinear triopoly game with heterogeneous players in finance invest model," *International Journal of Nonlinear Science*, vol. 13, no. 2, pp. 252–256, 2012.
- [15] E. M. Elabbasy, H. N. Agiza, and A. A. Elsadany, "The dynamics of triopoly game with heterogeneous players," *International Journal of Nonlinear Science*, vol. 3, no. 2, pp. 83–90, 2007.
- [16] L. Zhao, "Nonlinear complex dynamics of carbon emission reduction Cournot game with bounded rationality," *Complexity*, vol. 2017, Article ID 8301630, 10 pages, 2017.
- [17] T. Sterner and L. Höglund Isaksson, "Refunded emission payments theory, distribution of costs, and Swedish experience of NOx abatement," *Ecological Economics*, vol. 57, no. 1, pp. 93–106, 2006.
- [18] W. Harrington, R. D. Morgenstern, and P. Nelson, "On the accuracy of regulatory cost estimates," *Journal of Policy Analysis and Management*, vol. 19, no. 2, pp. 297–322, 2000.
- [19] R. Fan and L. Dong, "The dynamic analysis and simulation of government subsidy strategies in low-carbon diffusion considering the behavior of heterogeneous agents," *Energy Policy*, vol. 117, pp. 252–262, 2018.
- [20] C. Liu, W. Huang, and C. Yang, "The evolutionary dynamics of China's electric vehicle industry-taxes vs. subsidies," *Computers & Industrial Engineering*, vol. 113, pp. 103–122, 2017.
- [21] C. Wang, W. Wang, and R. Huang, "Supply chain enterprise operations and government carbon tax decisions considering carbon emissions," *Journal of Cleaner Production*, vol. 152, pp. 271–280, 2017.
- [22] L. De Jonge, "Policies and instruments for reducing nitrogen oxide emissions from stationary sources in The Netherlands," *Environmental Pollution*, vol. 102, no. 1, pp. 671–675, 1998.
- [23] T. H. Svensson and K. Elofsson, "The ex-post cost-effectiveness of nitrogen load reductions from nine countries to the Baltic sea between 1996 and 2010," *Water Resources Research*, vol. 55, no. 6, pp. 5119–5134, 2019.
- [24] P. Lanoie, J. Laurent-Lucchetti, N. Johnstone, and S. Ambec, "Environmental policy, innovation and performance: new insights on the Porter hypothesis," *Journal of Economics & Management Strategy*, vol. 20, no. 3, pp. 803–842, 2011.
- [25] J. Wu, M. Xu, and P. Zhang, "The impacts of governmental performance assessment policy and citizen participation on improving environmental performance across Chinese provinces," *Journal of Cleaner Production*, vol. 184, pp. 227–238, 2018.
- [26] A. Alexeev, D. H. Good, and K. Krutilla, "Environmental taxation and the double dividend in decentralized jurisdictions," *Ecological Economics*, vol. 122, no. 2, pp. 90–100, 2016.
- [27] V. Carreira, J. R. Machado, and L. Vasconcelos, "Legal citizen knowledge and public participation on environmental and spatial planning policies: a case study in Portugal," *International Journal of Humanities and Social Science Research*, vol. 2, no. 7, pp. 22–33, 2016.
- [28] S.-F. Ji, D. Zhao, and R.-J. Luo, "Evolutionary game analysis on local governments and manufacturers' behavioral strategies: impact of phasing out subsidies for new energy vehicles," *Energy*, vol. 189, Article ID 116064, 2019.
- [29] J. Newig and O. Fritsch, "Environmental governance: participatory, multi-level-and effective?" *Environmental Policy and Governance*, vol. 19, no. 3, pp. 197–214, 2009.
- [30] Y. M. Huang, Q. X. Li, and Y. H. Zhang, "The complexity analysis for price game model of risk-averse supply chain considering fairness concern," *Complexity*, vol. 2018, Article ID 9216193, 15 pages, 2018.
- [31] K. Pyragas, "Continuous control of chaos by self-controlling feedback," *Physics Letters A*, vol. 170, no. 6, pp. 421–428, 1992.



## Research Article

# Heterogeneous and Homogenous Multistabilities in a Novel 4D Memristor-Based Chaotic System with Discrete Bifurcation Diagrams

Lilian Huang , Wenju Yao, Jianhong Xiang , and Zefeng Zhang

*College of Information and Communication Engineering, Harbin Engineering University, Harbin 150001, China*

Correspondence should be addressed to Jianhong Xiang; [xiangjianhong@hrbeu.edu.cn](mailto:xiangjianhong@hrbeu.edu.cn)

Received 25 December 2019; Revised 20 February 2020; Accepted 11 March 2020; Published 25 April 2020

Guest Editor: Viet-Thanh Pham

Copyright © 2020 Lilian Huang et al. This is an open access article distributed under the Creative Commons Attribution License, which permits unrestricted use, distribution, and reproduction in any medium, provided the original work is properly cited.

In this paper, a new 4D memristor-based chaotic system is constructed by using a smooth flux-controlled memristor to replace a resistor in the realization circuit of a 3D chaotic system. Compared with general chaotic systems, the chaotic system can generate coexisting infinitely many attractors. The proposed chaotic system not only possesses heterogeneous multistability but also possesses homogenous multistability. When the parameters of system are fixed, the chaotic system only generates two kinds of chaotic attractors with different positions in a very large range of initial values. Different from other chaotic systems with continuous bifurcation diagrams, this system has discrete bifurcation diagrams when the initial values change. In addition, this paper reveals the relationship between the symmetry of coexisting attractors and the symmetry of initial values in the system. The dynamic behaviors of the new system are analyzed by equilibrium point and stability, bifurcation diagrams, Lyapunov exponents, and phase orbit diagrams. Finally, the chaotic attractors are captured through circuit simulation, which verifies numerical simulation.

## 1. Introduction

Memristor was first proposed by Chua [1] in 1971 and is the fourth basic electronic component manufactured by HP Labs in 2008 [2]. The discovery of memristors has caused an upsurge in studying and applying memristors. Due to the nonlinearity of memristor, it has been applied in many fields, such as flash memory [2, 3], neuromorphic computing [4, 5], neural network [6, 7], and chaotic system [8–11] based on chaos synchronization for encryption algorithms [12, 13] and secure communication [14, 15].

Memristor is a nonlinear element, and its resistance depends on the voltage or current signal, so it has been widely used in the construction of chaotic circuits in recent years [16–19]. In 2008, Itoh and Chua proposed together a Chua's chaotic circuit based on memristor. The dynamic analysis results show that Chua's chaotic circuit based on memristors has more complex dynamic characteristics than classic Chua's chaotic circuit [17]. In 2010, a Chua's chaotic

circuit based on memristance was proposed by replacing Chua's diode with a smooth flux-controlled memristor and a negative conductance [18]. In 2017, a multiscroll hyperchaotic system was proposed by introducing the memristor into the jerk multiscroll system, and the numbers of scrolls can be controlled by adjusting the coefficient before the term related to memristor [19].

In recent years, multistability [20–25] and extreme multistability [26–32] have become research hotspots in the field of chaotic systems. Multistability means that when the system parameters remain unchanged, the system can generate more than one attractor with different initial values. When the number of attractors is infinite, this phenomenon is called extreme multistability. Coexisting attractors and hidden coexisting attractors are shown in a memristive system with many equilibrium points in reference [23]. A wing-variable chaotic system with coexisting twin-wing attractors is proposed by replacing one of the resistors of the pseudo-four-wing chaotic system with a memristor in

reference [24]. In the same year, a memristor-based chaotic system is constructed by introducing an ideal flux-controlled memristor with absolute value nonlinearity into an existing hypogenetic chaotic jerk system, which can exhibit the extreme multistability phenomenon in reference [31]. A simplest third-order memristive chaotic system with hidden attractors is proposed, which exhibits the extreme multistability phenomenon of coexisting infinitely many attractors in reference [32].

Although multistability and extreme multistability in memristive chaotic systems had been reported in many existing papers, most of them researched the heterogeneous multistability of chaotic systems, and homogenous multistability was rarely reported. Heterogeneous multistability means that under the same parameters, the chaotic system has some chaotic attractors with different structures, while homogenous multistability means the chaotic system can generate attractors with the same structure, but the amplitudes and positions of their attractors can be different. In this article, the mathematical model of a memristor is employed to construct the chaotic system owning heterogeneous and homogenous multistabilities. Besides, the presented memristor-based system displays other complex dynamic characteristics, including constant Lyapunov exponents, discrete bifurcation diagrams, the symmetry of coexisting attractors, and so on.

The rest of this paper is organized as follows. In Section 2, a new chaotic system based on the model of a memristor is studied. And basic properties of the proposed system are investigated, including symmetry and dissipation, equilibrium, and stability. In Section 3, complex dynamic behaviors of the memristor-based chaotic system are analyzed. In Section 4, extreme multistability of the chaotic system is investigated by bifurcation diagrams and Lyapunov exponent spectra, and the dynamic analysis results show that the chaotic system possesses not only heterogeneous multistability but also homogenous multistability. In Section 5, the presented chaotic system is realized by analog circuit and the experimental results are given. Finally, some conclusions are drawn.

## 2. Basic Properties of the Memristive Chaotic System

A 3D pseudo-four-wing chaotic system was proposed by Liu and Chen [33, 34]. Actually, it is a coexisting two-wing system, and it can be described as follows:

$$\begin{cases} \dot{x} = ax - byz, \\ \dot{y} = -cy + xz, \\ \dot{z} = -dz + xy, \end{cases} \quad (1)$$

where  $a$ ,  $b$ ,  $c$ , and  $d$  are all constants and  $x$ ,  $y$ , and  $z$  are the state variables.

By utilizing a smooth flux-controlled memristor to substitute a resistor in realization circuit of system (1), a novel 4D memristor-based chaotic system is given by

$$\begin{cases} \dot{x} = ax - byz, \\ \dot{y} = -cy + xz + eW(w)x, \\ \dot{z} = -dz + xy, \\ \dot{w} = hx, \end{cases} \quad (2)$$

where  $e$  and  $h$  are positive parameters and  $W(w)$  is a memductance function.

The memductance function  $W(w)$  is shown as

$$W(w) = f + 3gw^2, \quad (3)$$

where  $f$  and  $g$  are two positive constants and  $w$  is the state variable.

**2.1. Symmetry and Dissipativity.** The symmetry property of chaotic systems is an important property. The memristive chaotic system (2) is invariant if we do the transformation  $(x, y, z, w) \rightarrow (-x, -y, z, -w)$ , which means system (2) has to be symmetric with respect to  $z$  axis in state space.

The dissipativity of system (2) is expressed by the following formula:

$$\nabla V = \frac{\partial \dot{x}}{\partial x} + \frac{\partial \dot{y}}{\partial y} + \frac{\partial \dot{z}}{\partial z} + \frac{\partial \dot{w}}{\partial w} = a - c - d. \quad (4)$$

When  $a$ ,  $c$ , and  $d$  satisfy condition  $a - c - d < 0$ , the system is dissipative. It means that the volume of phase space will be contracted to zero in exponential form  $e^{-(a-c-d)t}$  and all trajectories of the system are confined to zero volume.

**2.2. Equilibria and Stability.** Let the terms on left-hand side of system (2) be zero, and we can easily observe that the system has a line equilibrium

$$O = \{(x, y, z, w) \mid x = y = z = 0, w = k\}, \quad (5)$$

where  $k$  is any real constant.

By linearizing system (2) at point  $O$ , we can obtain the Jacobian matrix of the equation on  $O$ .

$$J_o = \begin{pmatrix} a & 0 & 0 & 0 \\ eW(k) & -c & 0 & 0 \\ 0 & 0 & -d & 0 \\ h & 0 & 0 & 0 \end{pmatrix}. \quad (6)$$

According to the Jacobian matrix (6), the characteristic equation can be obtained as follows:

$$\lambda(\lambda - a)(\lambda + c)(\lambda + d) = 0. \quad (7)$$

We can solve its eigenvalues easily, and they can be expressed by

$$\begin{aligned} \lambda_1 &= 0, \\ \lambda_2 &= a, \\ \lambda_3 &= -c, \\ \lambda_4 &= -d. \end{aligned} \quad (8)$$

The values of  $a$ ,  $c$ , and  $d$  are all positive, so  $\lambda_3$  and  $\lambda_4$  are always negative, and  $\lambda_2$  is always positive. Therefore, system (2) has an unstable saddle point.

### 3. Dynamics of the Memristor-Based Chaotic System

**3.1. Phase Portraits and Lyapunov Exponents.** The Lyapunov exponent spectra are an effective way of judging whether the system has chaotic behavior. The main characteristics of nonlinear dynamical systems can be described by the number of positive Lyapunov exponents. When the system has only one Lyapunov exponent greater than zero, the system has chaotic dynamic behavior. When a nonlinear system has more than two or equal to two Lyapunov exponents greater than zero, the system has hyperchaotic dynamic behavior.

When the parameters of the chaotic system are set as  $a = 4$ ,  $b = 6$ ,  $c = 20$ ,  $d = 5$ ,  $e = 0.01$ ,  $f = 1$ ,  $3g = 0.1$ , and  $h = 0.1$  and the initial conditions are set to  $(1, 1, 0, 0)$ , system (2) can generate chaotic attractor as shown in Figure 1. The corresponding Lyapunov exponents are computed as 0.5161,  $-0.0104$ ,  $-0.0645$ , and  $-21.5665$ , and the Lyapunov dimension  $dL = 3.0204$ , which indicates the system has chaotic behavior.

**3.2. Poincaré Projection.** The Poincaré projection is another effective way of judging whether the system has chaotic behaviour. Take projections  $x = 0$ ,  $y = 0$ ,  $z = 6$ , and  $w = 1.4$ , respectively, and the system obtains the Poincaré projections as shown in Figure 2. A large area of points can be observed in these pictures, which indicate that the system has chaotic behaviour.

### 4. Extreme Multistability in the Memristor-Based Chaotic System

**4.1. Dynamic Analysis of Heterogeneous Multistability.** Heterogeneous multistability means under the same parameters, a system can generate several or even infinitely many coexisting attractors with different structures, while homogenous multistability means that a chaotic system can generate the same structure coexisting attractors but with different positions or amplitudes.

In system (2), when the parameters are set as  $a = 4$ ,  $b = 6$ ,  $c = 20$ ,  $d = 5$ ,  $e = 0.01$ ,  $f = 1$ ,  $3g = 0.1$ , and  $h = 0.1$  and initial conditions are set as  $(1, 0, 0, w(0))$ , the system can generate various coexisting attractors depending on  $w(0)$ . The typical chaotic attractors are shown in Figure 3. Besides, system (2) can generate other kinds of coexisting attractors, coexisting limit cycle attractors, and symmetric limit cycle attractor as shown in Figures 4, 5, and 6, respectively.

When  $w(0)$  is changed in the region  $[-50, 50]$ , the bifurcation diagram of the state variable  $w$  and Lyapunov exponent spectra are shown in Figures 7(a) and 7(b), respectively. As shown in Figure 7(a), the bifurcation diagram of the state variable  $w$  is almost linear. It can be seen from Figure 7(b) that the chaotic attractor with a positive

Lyapunov exponent is mainly located at the region  $[-36, -32]$ ,  $[-22, 22]$ , and  $[32, 35]$  (the last Lyapunov exponent is not displayed because it is always a big negative number). And system (2) can also generate other kinds of attractors and limit cycle attractors, which means the system has heterogeneous multistability.

**4.2. Dynamic Analysis of Homogenous Multistability.** The parameters of system (2) remain unchanged, and the initial conditions are set as  $(x(0), 1, 0, 0)$ . When  $x(0)$  is varied in the region  $[-10^4, 10^4]$ , the bifurcation diagrams of the state variable  $z$ , the state variable  $w$ , and its Lyapunov exponent spectra are plotted in Figures 8(a), 8(b), and 8(c), respectively. Besides, when  $x(0)$  is varied in the region  $[-0.1, 0.1]$ , Lyapunov exponent spectra are plotted in Figure 8(d).

It can be seen from Figure 8(a) that when the initial condition  $x(0)$  is varied in the region  $[-10^4, 10^4]$ , the state variable  $z$  shows two kinds of steady chaotic states. When  $x(0)$  is varied in the region  $[-10^4, 0]$ , state variable  $z$  is located below or above the  $z$  axis, while  $x(0)$  is varied in the region  $(0, 10^4]$ , the state variable  $z$  is all located above the  $z$  axis. From Figure 8(b), when the initial condition  $x(0)$  is varied in the region  $[-10^4, 10^4]$ , there are many discrete small line segments in bifurcation diagram of the state variable  $w$ , which means the state variable  $w$  exists in infinite steady chaotic states. And this phenomenon also indicates the system can generate coexisting infinitely many attractors, which means system (2) has the extreme multistability. Different from other systems possessing extreme multistability, system (2) only generates two kinds of chaotic attractors with different positions in a very large range of initial values, which are distributed along the  $w$  axis parallelly. As shown in Figure 8(c), it is obvious that the four Lyapunov exponents are always approximately constant and the largest Lyapunov exponent is always positive except for the zero point when  $x(0)$  is varied in the region  $[-10^4, 10^4]$ , which means system (2) can exhibit chaotic behavior except zero point. Figure 8(d) shows that the region cannot exhibit chaotic behavior which is very small.

Considering the particularity of system (2), it is necessary to discuss the system when  $x(0) = 1$ . The control parameters of system (2) remain unchanged, and the initial conditions are set as  $(0, 1, 0, 0)$ . The LEs are 4.0002,  $-0.2034$ ,  $-5.0005$ , and  $-19.8272$ , which means system (2) cannot exhibit chaotic behavior under this circumstance.

It has been confirmed that there are coexisting infinitely many attractors in chaotic system (2) according to the above analysis. When  $x(0)$  is set to 10,  $-10$ , 50,  $+50$ , 100,  $-100$ , and 1, respectively, the phase portraits of coexisting infinitely many attractors in the  $x - w$  plane, the  $y - w$  plane, the  $z - w$  plane, and the  $w - z - x$  space are shown in Figures 9(a), 9(b), 9(c), and 9(d), respectively. Figure 9 clearly reveals the coexistence of a large number of same attractors with different positions, which implies the emergence of homogenous multistability. This result of the phase portraits is consistent with the bifurcation diagrams and Lyapunov spectrum with respect to initial condition  $x(0)$ .

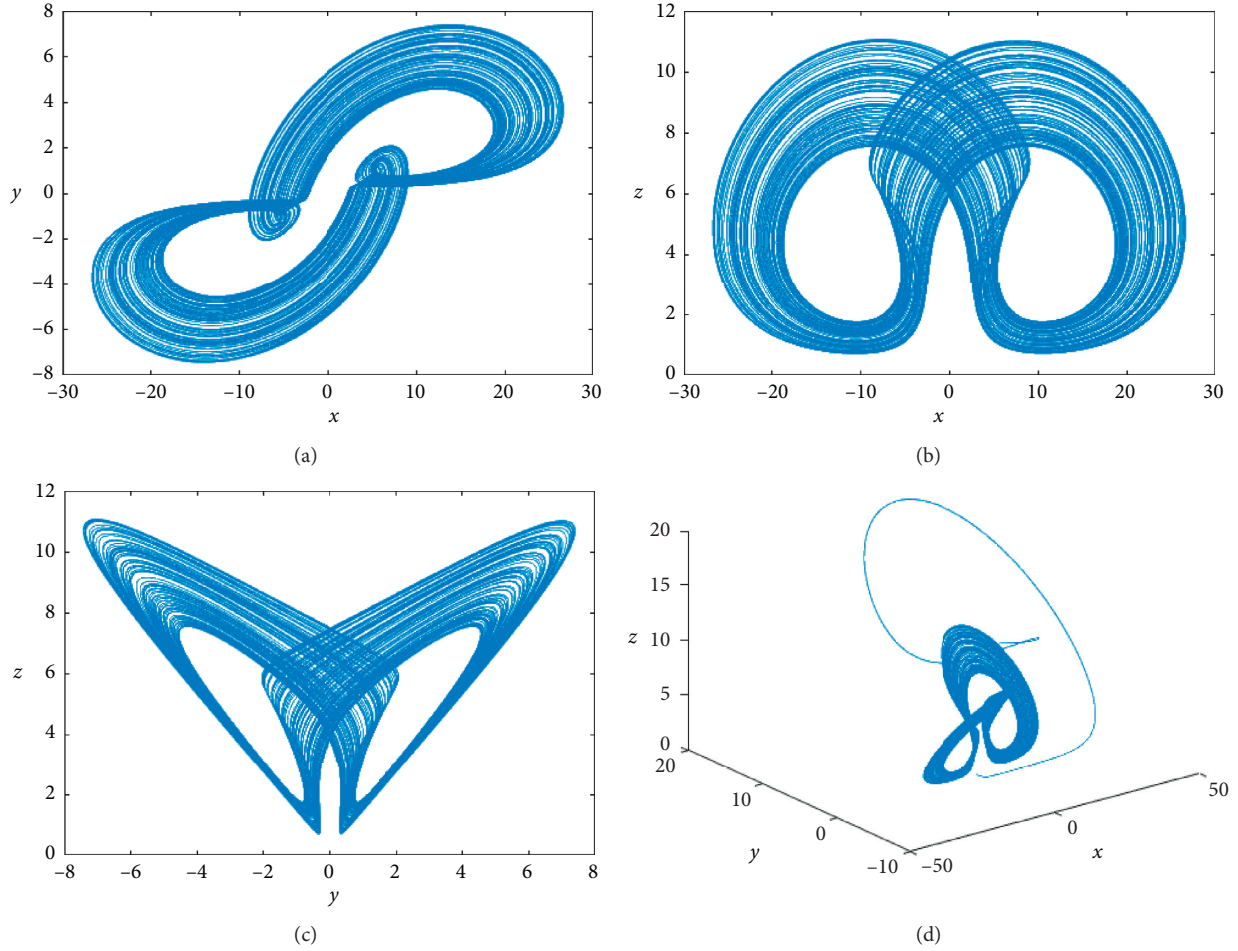


FIGURE 1: Phase portraits of system (2) when  $a = 4, b = 6, c = 20, d = 5, e = 0.01, f = 1, 3g = 0.1,$  and  $h = 0.1$ : (a) projection on  $x - y$  plane, (b) projection on  $x - z$  plane, (c) projection on  $y - z$  plane, and (d) 3D view in the  $x - y - z$  space.

The parameters of system (2) are set as  $a = 4, b = 6, c = 20, d = 5, e = 0.01, f = 1, 3g = 0.1,$  and  $h = 0.1,$  the initial conditions are set as  $(1, y(0), 0, 0),$  and the initial condition  $y(0)$  is used as the independent variable of bifurcation diagram. When  $y(0)$  is changed in the region  $[-10^4, 10^4],$  the bifurcation diagram of the state variable  $w$  and its Lyapunov exponent spectra are plotted in Figures 10(a) and 10(b), respectively. As can be seen from Figure 10(a), when the initial condition  $y(0)$  is changed in the region  $[-10^4, 10^4],$  there are many discrete small line segments in bifurcation diagram of the state variable  $w,$  which implies that there are coexisting infinitely many attractors in system (2). It can be clearly seen from Figure 10(b) that four Lyapunov exponents are always approximately constant and largest Lyapunov exponent is always positive when  $y(0)$  is changed in the region  $[-10^4, 10^4],$  which means system (2) only exhibits chaotic behavior.

The parameters of system (2) are set as  $a = 4, b = 6, c = 20, d = 5, e = 0.01, f = 1, 3g = 0.1,$  and  $h = 0.1,$  the initial conditions are set as  $(1, 0, z(0), 0),$  and the initial condition  $z(0)$  is used as the independent variable of bifurcation diagram. When  $z(0)$  is changed in the region

$[-10^4, 10^4],$  the bifurcation diagram of the state variable  $w$  and its Lyapunov exponent spectra are plotted in Figures 11(a) and 11(b), respectively. The bifurcation diagram of the state variable  $w$  and its Lyapunov exponent spectra are similar with those with the initial conditions set as  $(1, y(0), 0, 0).$  Many discrete small line segments are more closely clustered in the bifurcation diagram of the state variable  $w$  for the initial conditions set as  $(1, 0, z(0), 0)$  compared with the one for the initial conditions set as  $(1, y(0), 0, 0).$  And Lyapunov exponent spectra for the initial conditions set as  $(1, 0, z(0), 0)$  are similar with the ones for the initial conditions set as  $(1, y(0), 0, 0),$  and four Lyapunov exponents are always approximately constant and largest Lyapunov exponent is always positive when  $z(0)$  is changed in the region  $[-10^4, 10^4].$

**4.3. Symmetry in Infinitely Many Coexisting Attractors.** Obviously, system (2) is invariant if we do the transformation  $(x, y, z, w) \rightarrow (-x, -y, z, -w),$  which means that  $(x, y, z, w)$  and  $(-x, -y, z, -w)$  are all solutions to the equation of the system. This symmetry characteristic of system (2) could be served to explain the presence of symmetric coexisting attractors in state space.

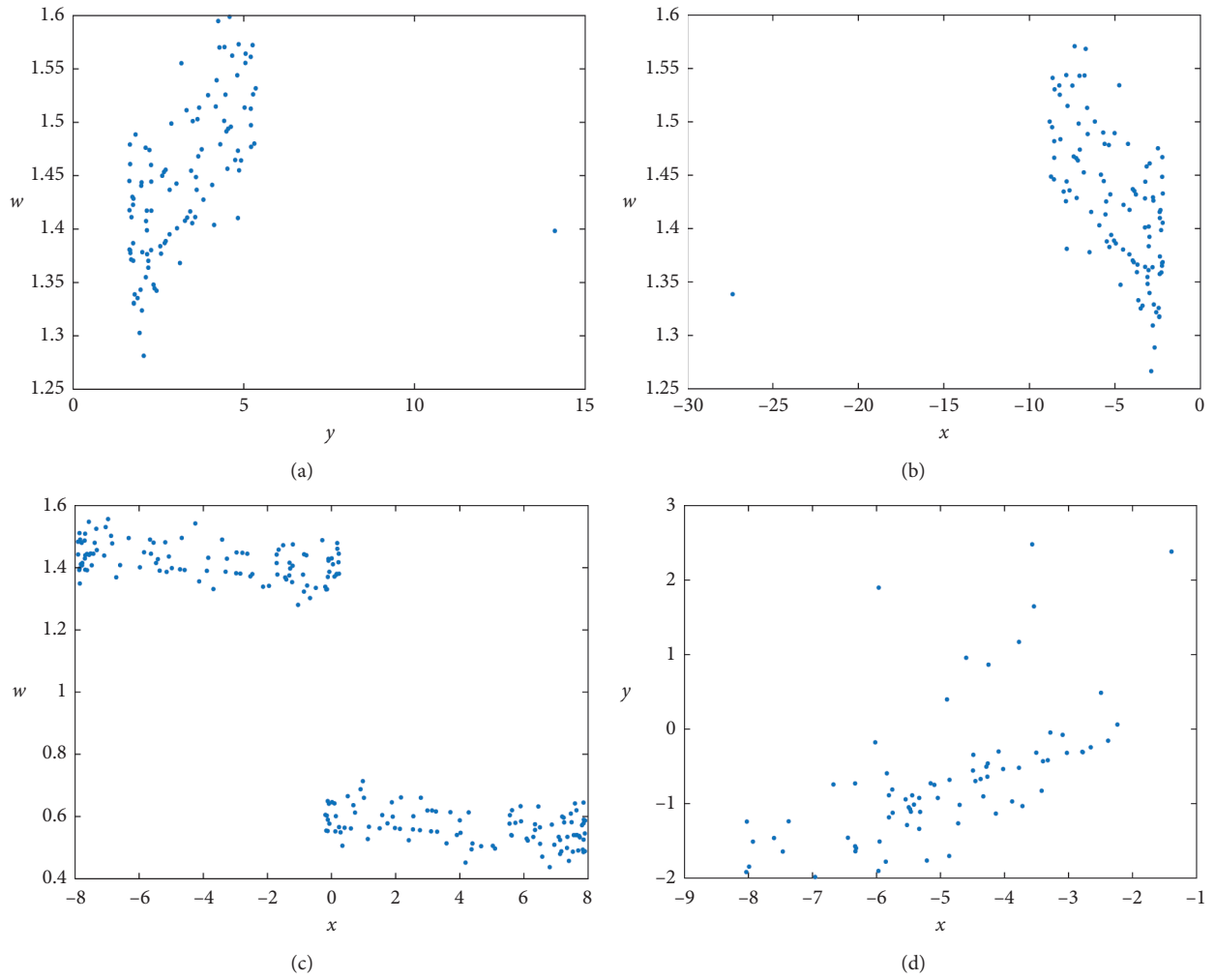


FIGURE 2: Poincaré sections of system (2): (a) projection on  $y - w$  plane when Poincaré section is  $x = 0$ , (b) projection on  $x - w$  plane when Poincaré section is  $y = 0$ , (c) projection on  $x - w$  plane when Poincaré section is  $z = 6$ , and (d) projection on  $x - y$  plane when Poincaré section is  $w = 1.4$ .

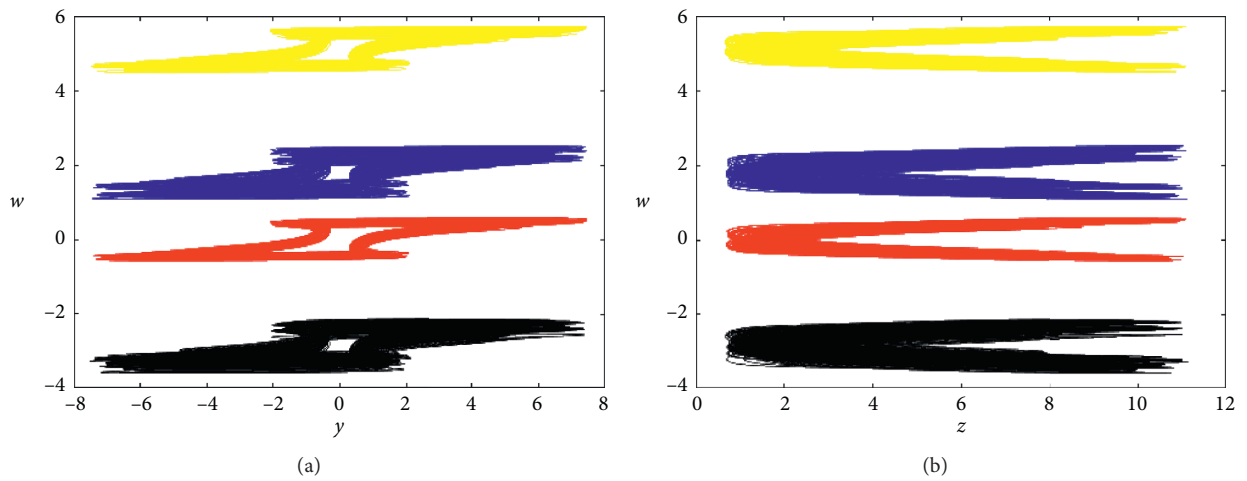


FIGURE 3: Phase portraits of coexisting infinitely many attractors in (a)  $y - w$  and (b)  $w - z$  planes (the blue one starts from initial conditions  $(1, 0, 0, 1)$ , the red one starts from  $(1, 0, 0, -1)$ , the yellow one starts from  $(1, 0, 0, 4)$ , and the black one starts from  $(1, 0, 0, -4)$ ).



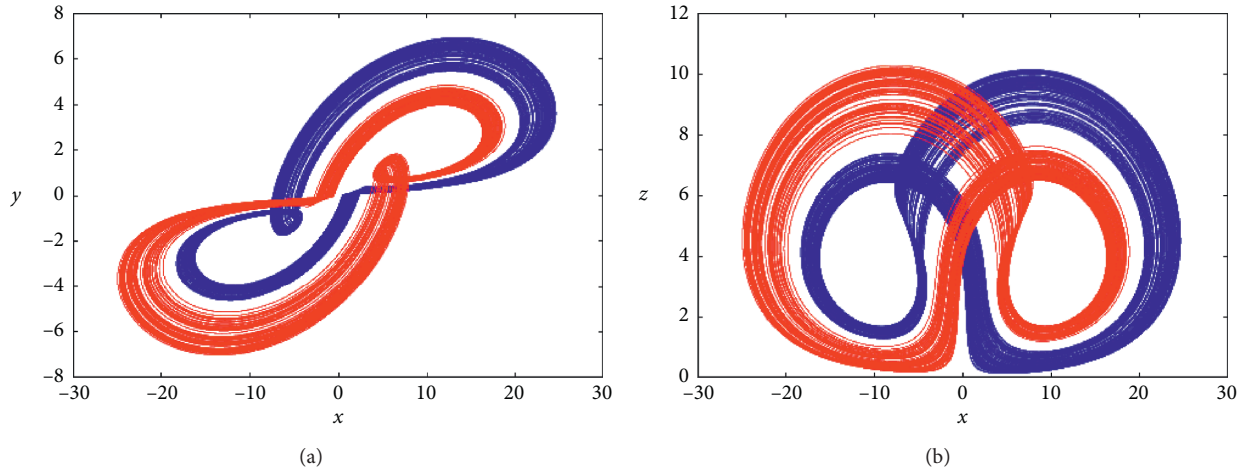


FIGURE 4: Phase portraits of coexisting attractors in (a)  $x - y$  and (b)  $x - z$  planes (the blue one starts from initial conditions  $(1, 0, 0, 22)$  and the red one starts from  $(1, 0, 0, -22)$ ).

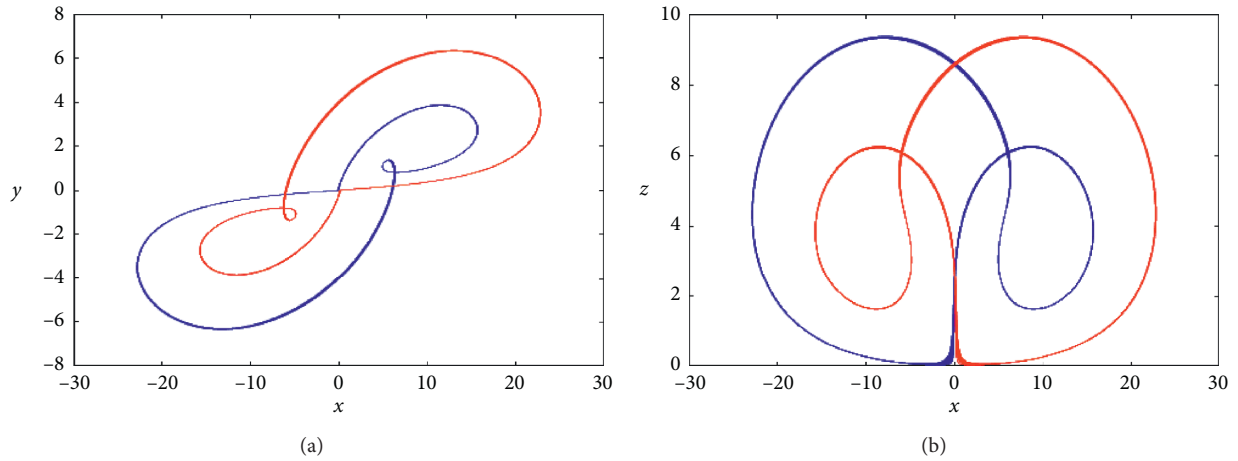


FIGURE 5: Phase portraits of coexisting limit cycle attractors in (a)  $x - y$  and (b)  $x - z$  planes (the blue one starts from initial conditions  $(1, 0, 0, 26)$  and the red one starts from  $(1, 0, 0, -26)$ ).

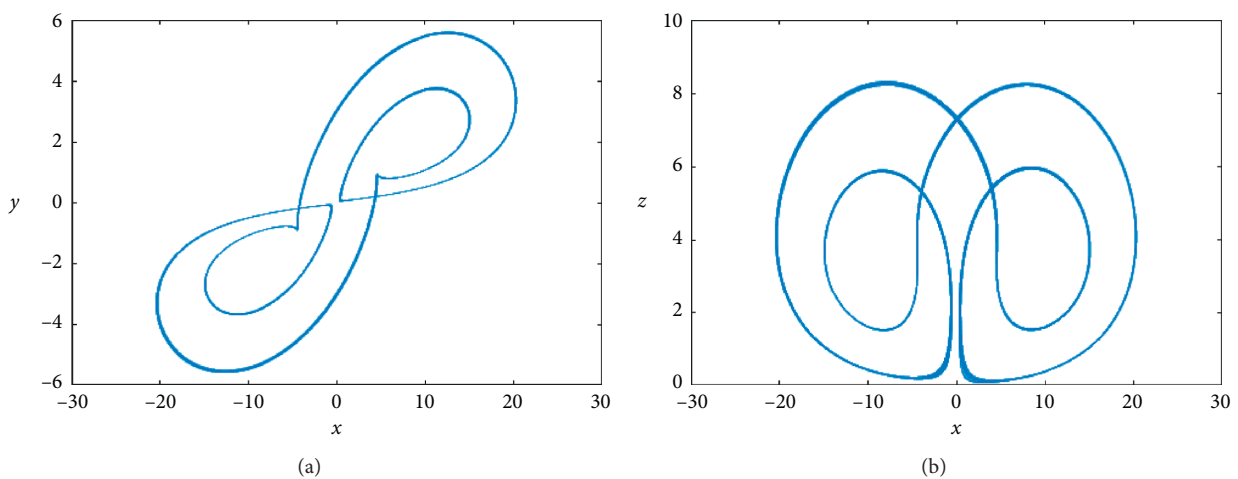


FIGURE 6: Phase portraits of limit cycle in (a)  $x - y$  and (b)  $x - z$  planes for initial conditions set as  $(1, 0, 0, 30)$ .

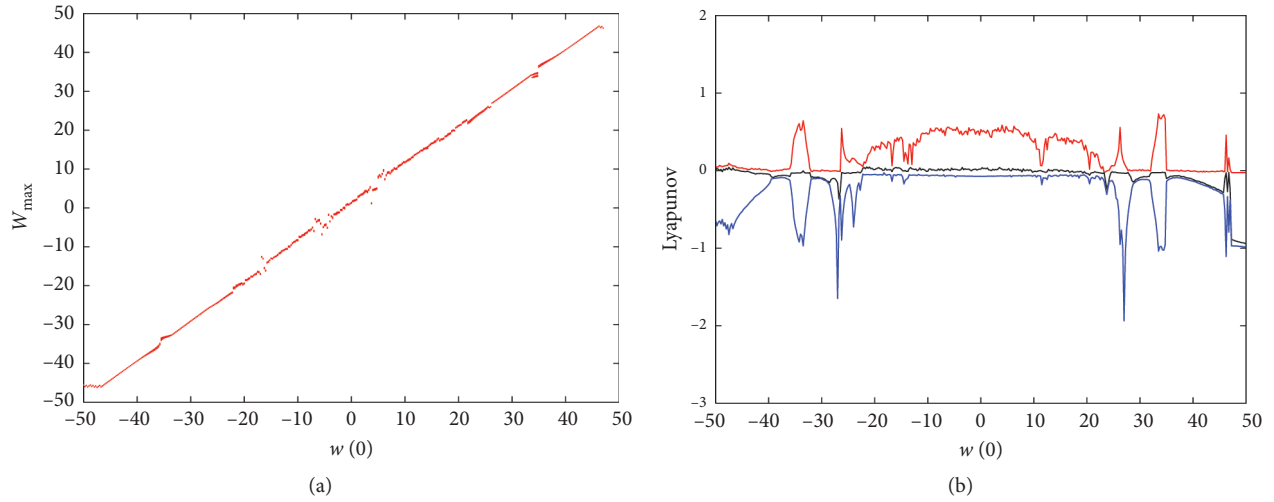


FIGURE 7: (a) Bifurcation diagram of the state variable  $w$  and (b) Lyapunov spectrum with respect to memristor initial condition  $w(0)$ .

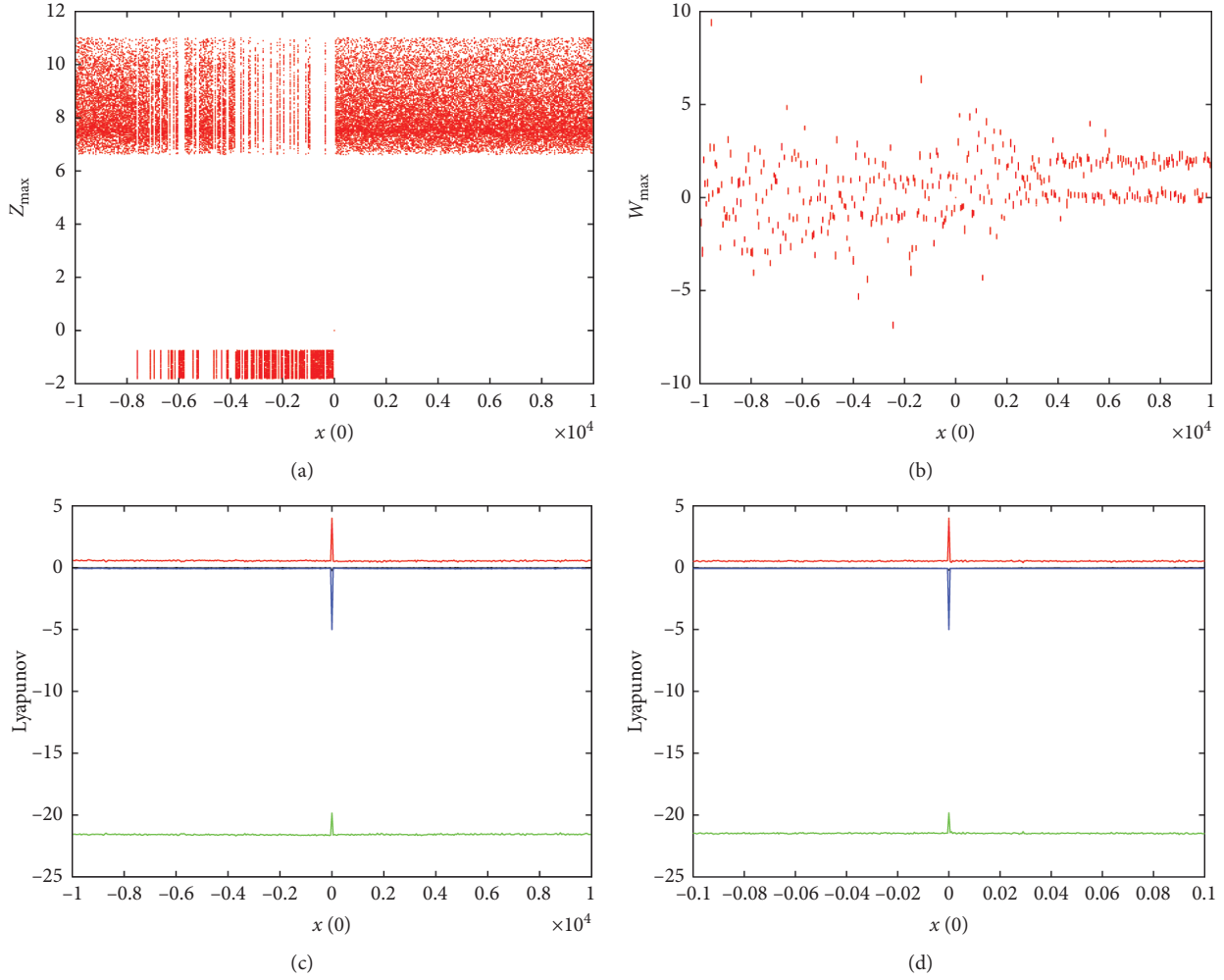


FIGURE 8: (a) Bifurcation diagram of the state variable  $z$ , (b) bifurcation diagram of the state variable  $w$ , (c) Lyapunov spectrum with respect to initial condition  $x(0)$  in the region  $[-10^4, 10^4]$ , and (d) Lyapunov spectrum with respect to initial condition  $x(0)$  in the region  $[-0.1, 0.1]$ .

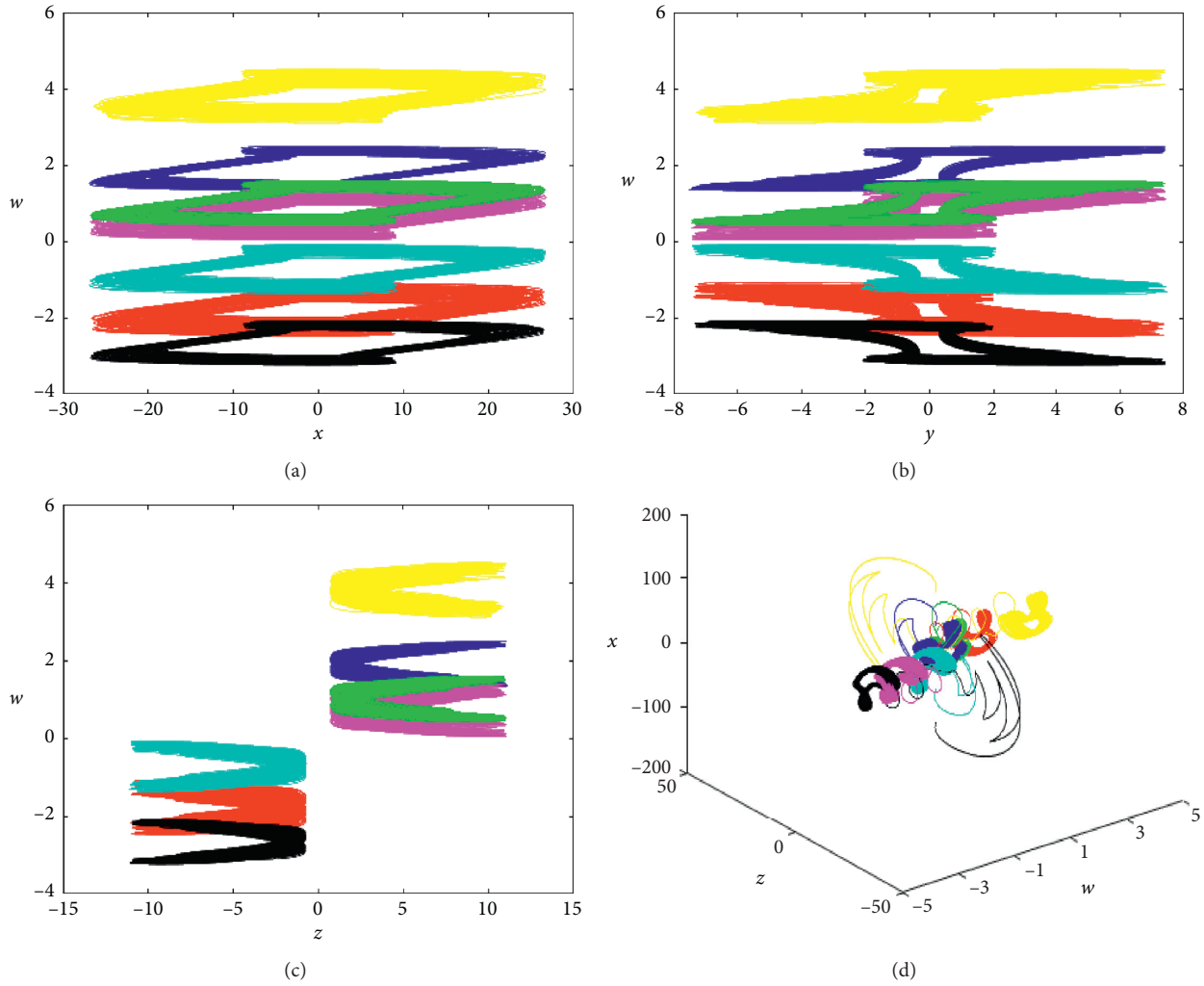


FIGURE 9: Phase portraits of coexisting infinitely many attractors on (a)  $x-w$  plane, (b)  $y-w$  plane, (c)  $z-w$  plane, and (d)  $w-z-x$  plane in chaotic system (2) (the blue one starts from initial conditions  $(10, 1, 0, 0)$ , the red one starts from  $(-10, 1, 0, 0)$ , the pink one starts from  $(50, 1, 0, 0)$ , the cyan one starts from  $(-50, 1, 0, 0)$ , the yellow one starts from  $(100, 1, 0, 0)$ , the black one starts from  $(-100, 1, 0, 0)$ , and the green one starts from  $(1, 1, 0, 0)$ ).

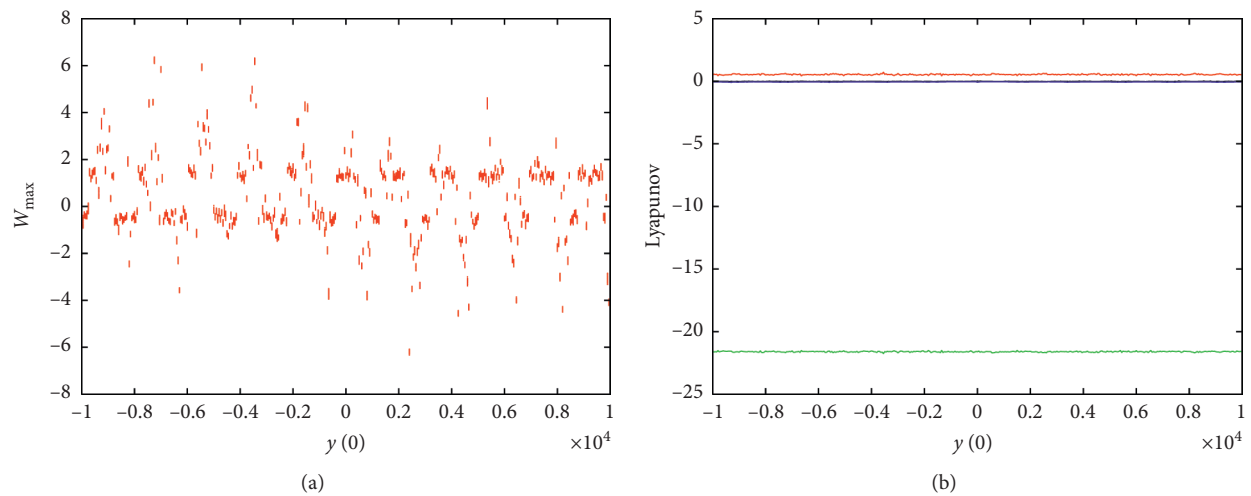


FIGURE 10: (a) Bifurcation diagram of the state variable  $w$  and (b) Lyapunov spectrum with respect to initial condition  $y(0)$  in the region  $[-10^4, 10^4]$ .

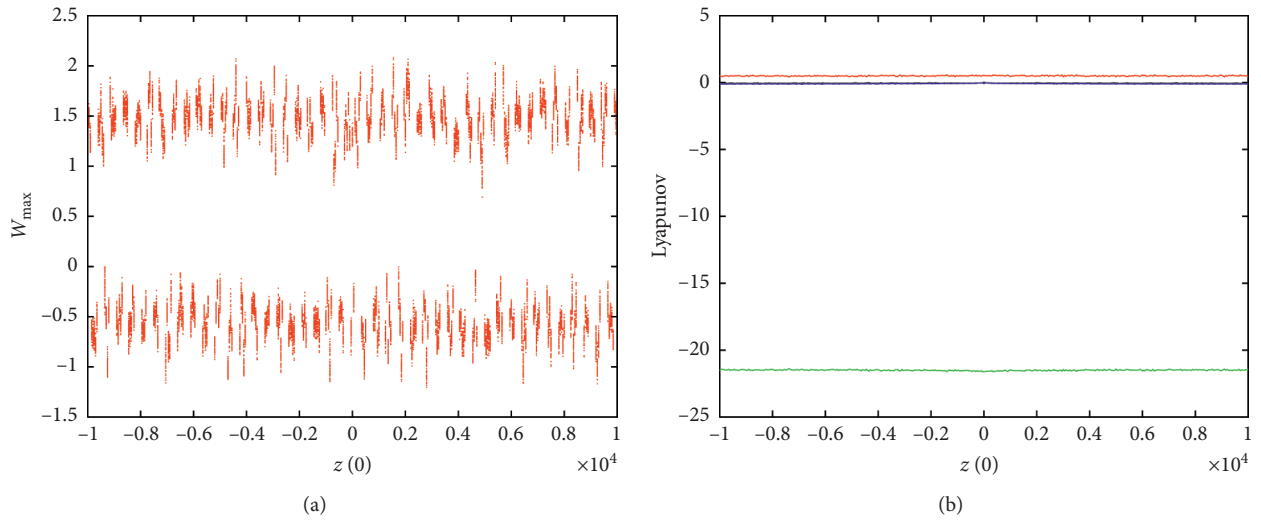


FIGURE 11: (a) Bifurcation diagram of the state variable  $w$  and (b) Lyapunov spectrum with respect to initial condition  $z(0)$  in the region  $[-10^4, 10^4]$ .

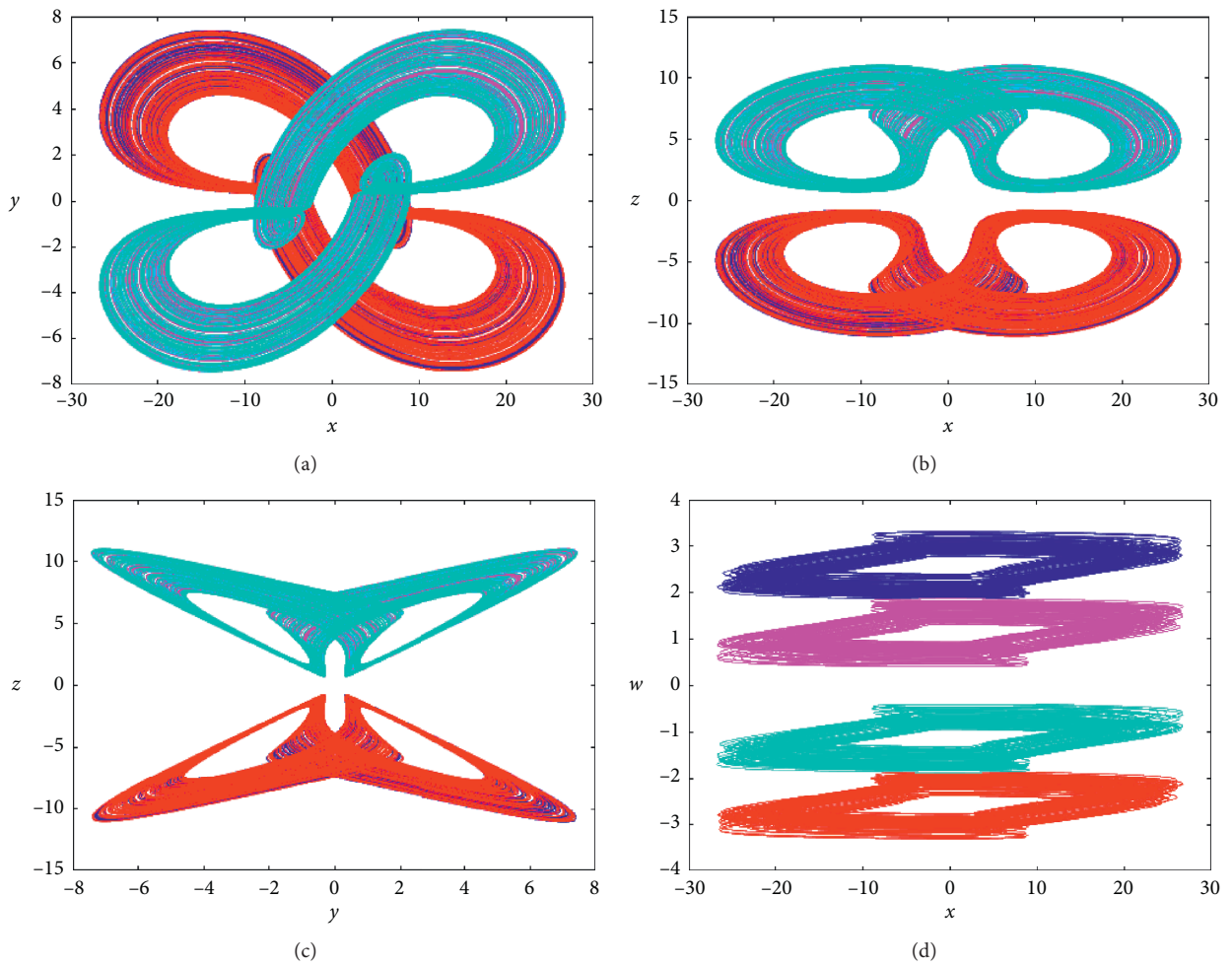


FIGURE 12: Continued.

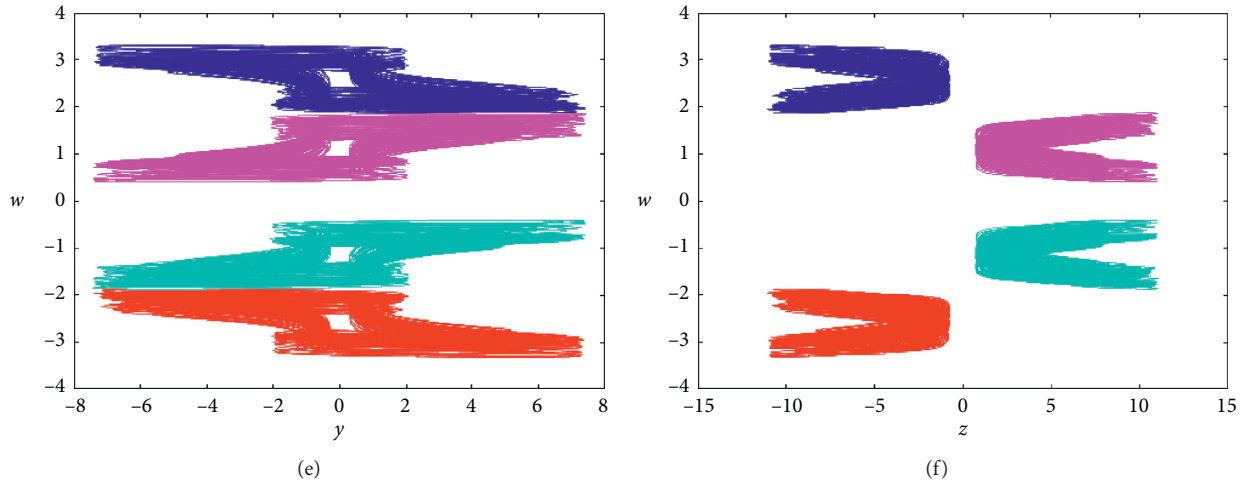


FIGURE 12: Phase portraits of symmetric coexisting infinitely many attractors in chaotic system (2) (the blue one starts from initial conditions  $(1, 1, -10, 1)$ , the red one starts from  $(-1, -1, -10, -1)$ , the pink one starts from  $(10, 20, 15, 2)$ , and the cyan one starts from  $(-10, -20, 15, -2)$ ).

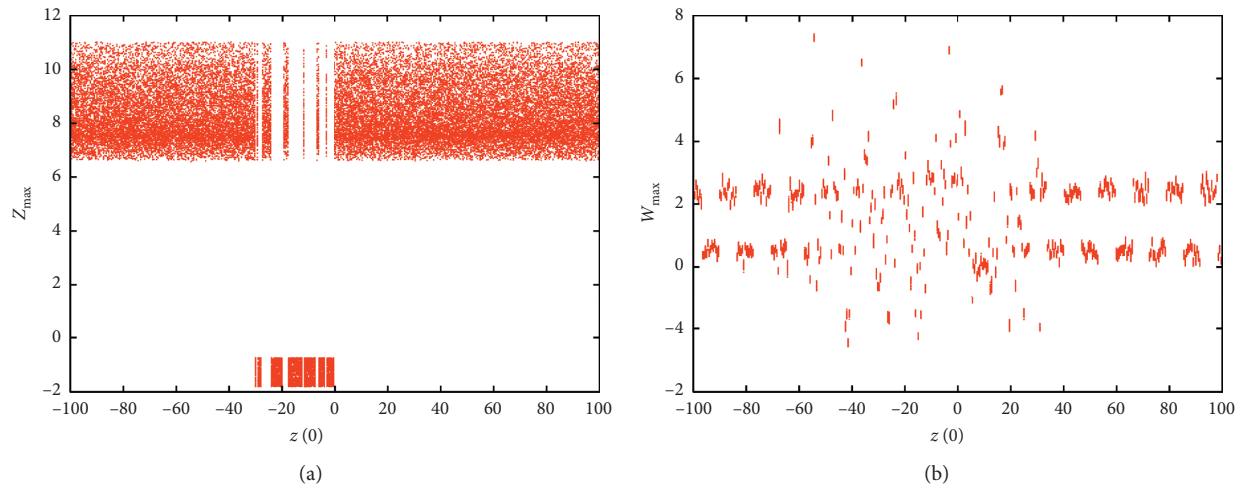


FIGURE 13: (a) Bifurcation diagram of the state variable  $z$  and (b) bifurcation diagram of the state variable  $w$  with respect to initial conditions  $(1, 1, z(0), 1)$ .

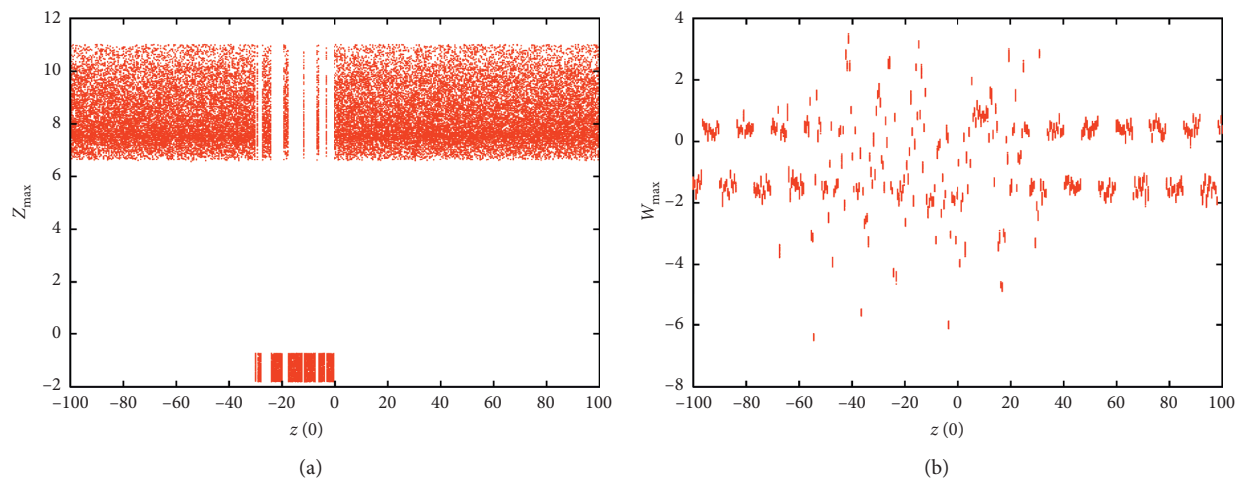


FIGURE 14: (a) Bifurcation diagram of the state variable  $z$  and (b) bifurcation diagram of the state variable  $w$  with respect to initial conditions  $(-1, -1, z(0), -1)$ .



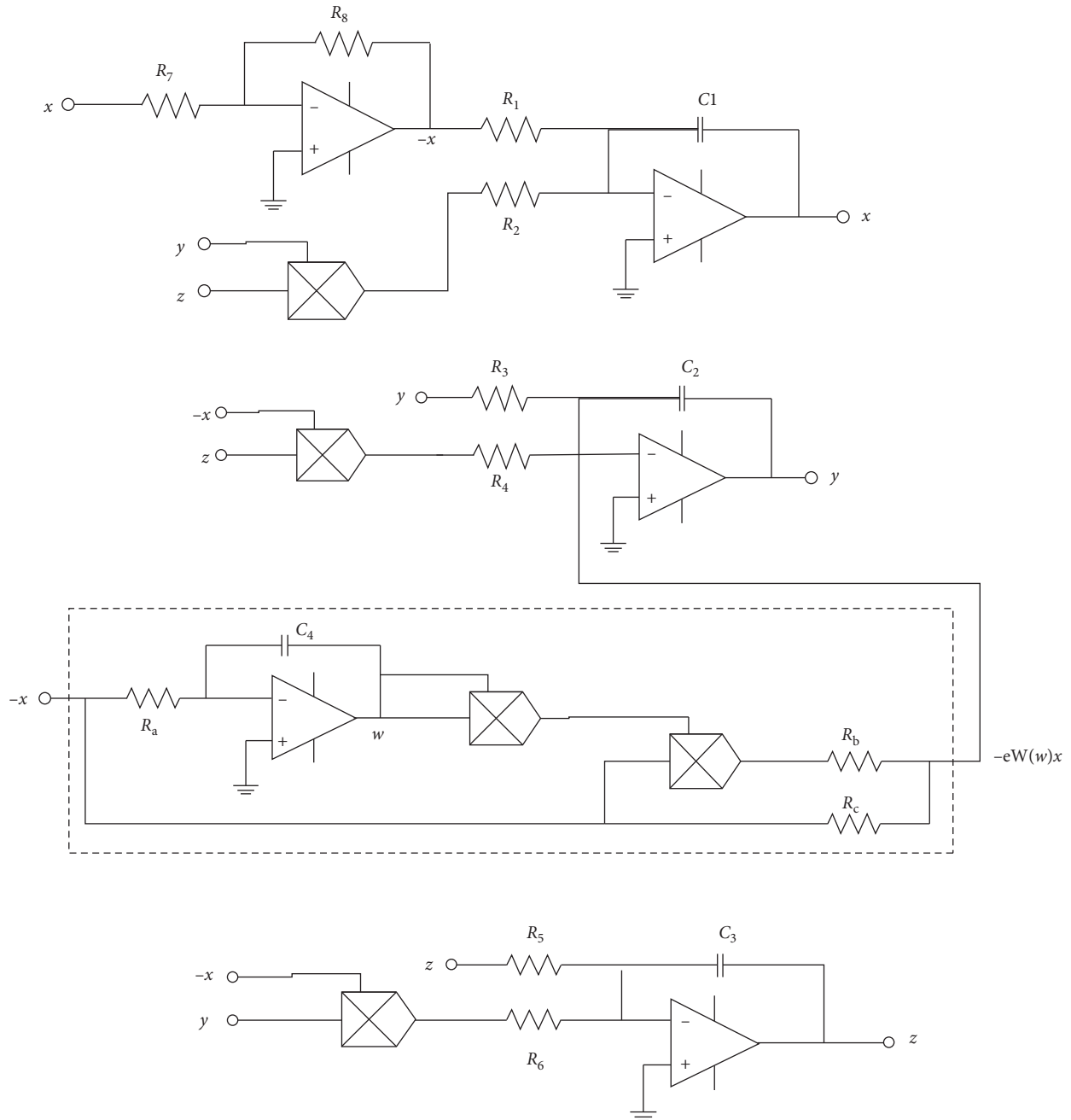


FIGURE 15: Circuit diagram of memristive system (2).

If we set parameters as  $a = 4$ ,  $b = 6$ ,  $c = 20$ ,  $d = 5$ ,  $e = 0.01$ ,  $f = 1$ ,  $3g = 0.1$ , and  $h = 0.1$ , the system can generate many pairs of symmetric coexisting attractors for the corresponding conditions set as  $(x(0), y(0), z(0), w(0))$  and  $(-x(0), -y(0), z(0), -w(0))$ . And two pairs of symmetric coexisting attractors of these are shown in Figure 12, where the blue one and the red one are a pair of symmetric attractors and the pink one and the cyan one are another pair of symmetric attractors. The projections of the symmetric attractors on the coordinate planes can be shown in the form of central symmetry or axial symmetry. In system (2), it is centrosymmetric on the  $x - y$  plane, the  $x - w$  plane, and the  $y - w$  plane and axisymmetric on the  $x - z$  plane, the

$y - z$  plane, and the  $z - w$  plane. It is worth noting that the structures of many coexisting attractors in Figure 9 are the same roughly, and there are differences in the details. But the structures of each pairs of coexisting attractors in Figure 12 are symmetric exactly.

In order to further verify symmetry of coexisting infinitely many attractors in chaotic system (2), bifurcation diagrams of the state variable  $z$  and the state variable  $w$  are given. The parameters of system (2) are assigned as  $a = 4$ ,  $b = 6$ ,  $c = 20$ ,  $d = 5$ ,  $e = 0.01$ ,  $f = 0.1$ ,  $3g = 0.1$ , and  $h = 0.1$ , and the initial conditions are set as  $(1, 1, z(0), 1)$ , and the initial condition  $z(0)$  is used as the independent variable of bifurcation diagram. When  $z(0)$  is varied in the region

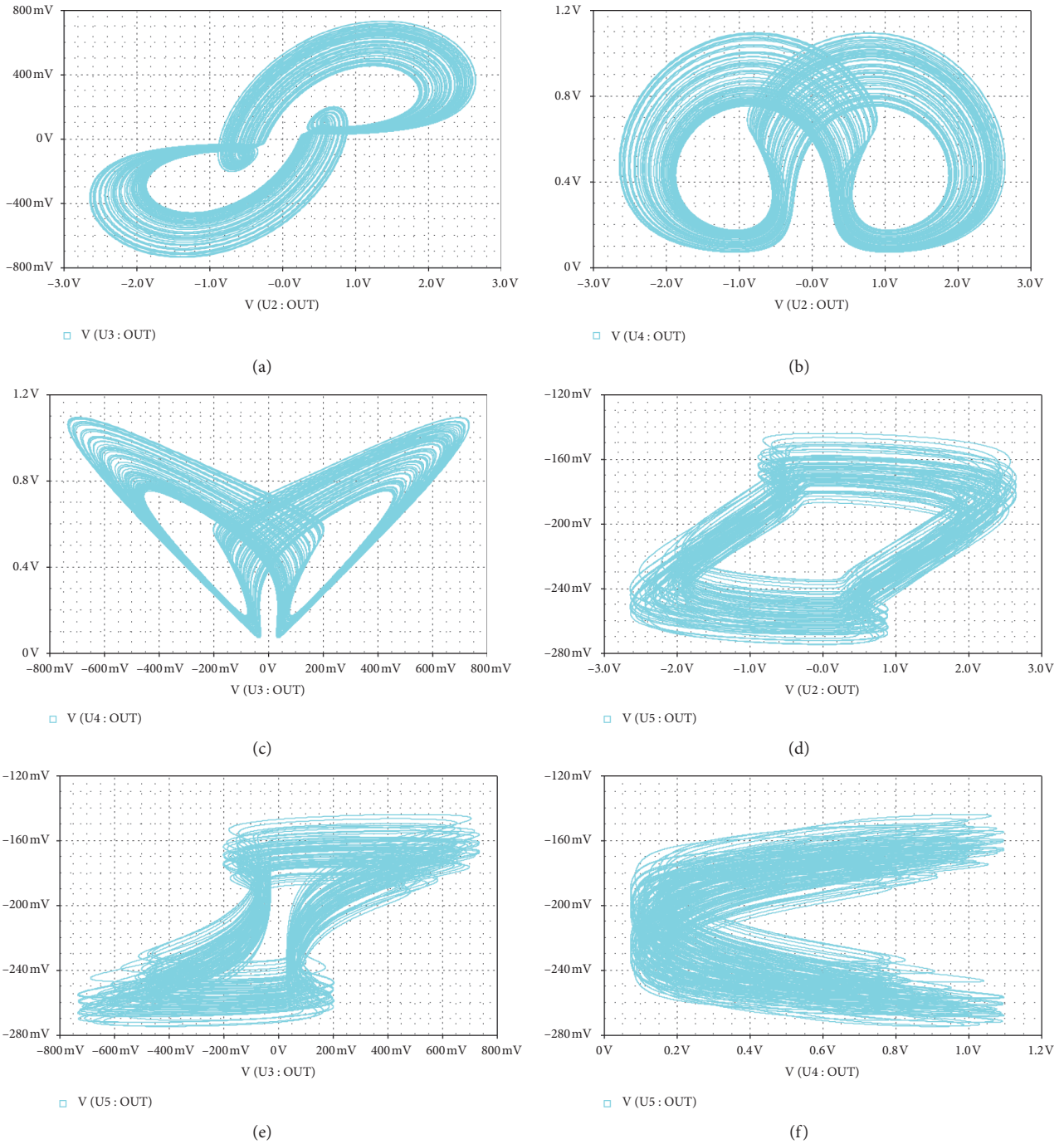


FIGURE 16: PSpice simulated phase portraits of chaotic attractors with initial voltages (1 V, 0.1 V, 0 V, 0 V).

$[-100, 100]$ , the bifurcation diagrams of the state variable  $z$  and the state variable  $w$  are plotted in Figures 13(a) and 13(b), respectively. Similarly, the parameters of system (2) remain unchanged, the initial conditions are set as  $(-1, -1, z(0), -1)$ , and the initial condition  $z(0)$  is used as the independent variable. When  $z(0)$  is varied in the region  $[100, -100]$ , the bifurcation diagrams of the state variable  $z$  and the state variable  $w$  are plotted in Figures 14(a) and 14(b), respectively.

A comparison of the Figures 13(a) and 14(a) indicates that bifurcation diagrams of the state variable  $z$  for the initial conditions set as  $(1, 1, z(0), 1)$  and  $(-1, -1, z(0), -1)$  are the same exactly. And a comparison of the Figures 13(b) and 14(b) shows that they are symmetric about the horizontal axis. This phenomenon reflects the fact that when the parameters of system (2) set as  $a = 4, b = 6, c = 20, d = 5, e = 0.01, f = 1, 3g = 0.1, h = 0.1$ , the structures of coexisting attractors with conditions set as  $(1, 1, z(0), 1)$  and

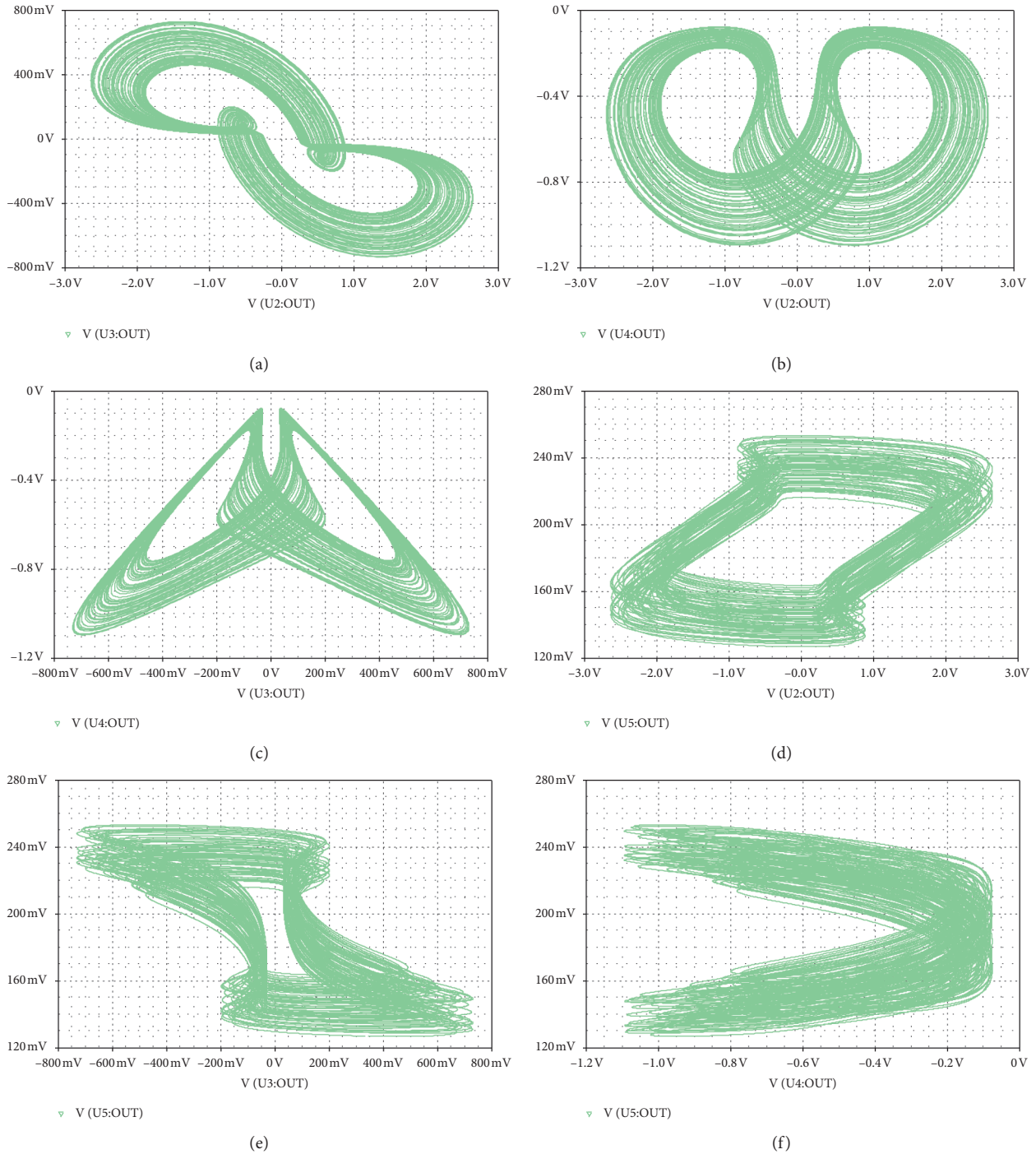


FIGURE 17: PSpice simulated phase portraits of chaotic attractors with initial voltages  $(-1\text{ V}, 0.1\text{ V}, 0\text{ V}, 0\text{ V})$ .

$(-1, -1, z(0), -1)$  are symmetric with respect to  $z$  coordinate axis.

We compared the advantages and disadvantages of this system with other improved Liu-and-Chen systems in the literature [11, 23, 24]. The system proposed in reference [11] is a three-dimensional chaotic system without memristor. And it can generate three-scroll and four-scroll chaotic attractors. The system in reference [23] is a four-dimensional chaotic system with two memristors, which can generate

various kinds of attractors and hidden attractors. The system in reference [24] is a four-dimensional chaotic system with a memristor, which can generate three-wing, four-wing, and coexisting two-wing chaotic attractors. It has line equilibrium points. This system has a line equilibrium, within which the attractors generated are hidden. The new system is a four-dimensional chaotic system with a memristor, which can generate coexisting infinitely many attractors distributed along the  $w$  axis parallelly. It produces hidden attractors

because it has a line equilibrium. In addition, the system has discrete bifurcation diagrams and many symmetrical coexisting attractors. Compared with above improved Liu-and-Chen systems, we can find that chaotic systems with memristor have more complex dynamic behaviors than chaotic systems without memristor and are more likely to have extreme multistability.

## 5. Circuit Implementation

In this section, complex dynamic behaviors of the proposed chaotic system can be observed by analog circuit, where integrated operational amplifiers and multipliers are used to construct the circuit for generating chaotic attractors. Supply voltages of operational amplifiers are  $E = \pm 15\text{ V}$ . The input and output range of all the multipliers is between  $-15\text{ V}$  to  $15\text{ V}$ . However, the values of the state variables  $x$ ,  $y$ ,  $z$ , and  $w$  may be out of this range. Thus, it is necessary that state variables  $x$ ,  $y$ ,  $z$ , and  $w$  are compressed to the 1/10 of original system to be limited in the region of  $(-15\text{ V}, 15\text{ V})$ , which is the reference voltage of the operational amplifiers. At the same time, taking the time scale factor  $RC$  into account, system (2) after scale transformation can be represented as follows:

$$\begin{cases} RC\dot{x} = ax - 10byz, \\ RC\dot{y} = -cy + 10xz + e(f + 300gw^2)x, \\ RC\dot{z} = -dz + 10xy, \\ RC\dot{w} = hx. \end{cases} \quad (9)$$

A flux-controlled memristor depicted in the dashed box of Figure 15 is applied to construct the chaotic circuit. The analog circuit of system (2) is shown in Figure 15. The state equations can be obtained as follows:

$$\begin{cases} C_1\dot{v}_x = \frac{v_x}{R_1} - \frac{v_y v_z}{R_2}, \\ C_2\dot{v}_y = -\frac{v_y}{R_3} + \frac{v_x v_z}{R_4} + \left( \frac{v_x}{R_c} + \frac{v_x v_w^2}{R_b} \right), \\ C_3\dot{v}_z = -\frac{v_z}{R_5} + \frac{v_x v_y}{R_6}, \\ C_4\dot{v}_w = \frac{v_x}{R_a}, \end{cases} \quad (10)$$

where  $v_x$ ,  $v_y$ ,  $v_z$ , and  $v_w$  are the voltages on capacitors. Compared with (9) and (10), the parameters are taken as follows:  $C_1 = C_2 = C_3 = C_4 = C$ ,  $R_1 = (R/a)$ ,  $R_2 = (R/10b)$ ,  $R_3 = (R/c)$ ,  $R_4 = (R/10)$ ,  $R_5 = (R/d)$ ,  $R_6 = (R/10)$ ,  $R_a = (R/h)$ ,  $R_b = (R/(e*3g*100))$ , and  $R_c = (R/ef)$ .

System (2) can generate coexisting infinitely many attractors when the parameters are set as  $a = 4$ ,  $b = 6$ ,  $c = 20$ ,  $d = 5$ ,  $e = 0.01$ ,  $f = 1$ ,  $3g = 0.1$ , and  $h = 0.1$ . Let us take  $R = 100\text{ k}\Omega$  and  $C = 10000\text{ nF}$ , and the resistance parameters can be obtained as  $R_1 = 25\text{ k}\Omega$ ,  $R_2 = 1.67\text{ k}\Omega$ ,  $R_3 = 5\text{ k}\Omega$ ,  $R_4 = 10\text{ k}\Omega$ ,  $R_5 = 20\text{ k}\Omega$ ,  $R_6 = 10\text{ k}\Omega$ ,  $R_a = 1000\text{ k}\Omega$ ,  $R_b = 1000\text{ k}\Omega$ , and  $R_c = 10000\text{ k}\Omega$ . Also, the initial voltages

of all capacitors are set as  $(1\text{ V}, 0.1\text{ V}, 0\text{ V}, 0\text{ V})$  (initial voltages of all capacitors should be compressed to the 1/10 of original values). According to the above parameter settings, circuit simulation of chaotic attractor can be obtained by PSpice as shown in Figure 16. Similarly, when the initial voltages of all capacitors are set as  $(-1\text{ V}, 0.1\text{ V}, 0\text{ V}, 0\text{ V})$ , circuit simulation of chaotic attractor can be obtained by PSpice as shown in Figure 17. Obviously, the chaotic attractors obtained in the analog circuit well verify those shown by numerical simulations.

## 6. Conclusion

A new memristor-based chaotic system with coexisting infinitely many attractors is proposed by using a smooth flux-controlled memristor to replace a resistor in the analog circuit of the three-dimensional chaotic system. The system has a line equilibrium and exhibits homogenous and heterogeneous multistabilities. The dynamical behaviors of the system are analyzed by equilibrium point and stability, phase portraits, bifurcation diagrams and Lyapunov exponent spectra, and so on. Compared with general chaotic systems, this chaotic system has some special properties. When the parameters of system are fixed, the chaotic system only generates two kinds of chaotic attractors with different positions in a very large range of initial values and has constant Lyapunov exponent spectra. In addition, the system has discrete bifurcation diagrams, which has not been found in existing chaotic systems. Further, the relationship between the symmetry of the coexisting attractors and the symmetry of initial values in the system is explored and verified by phase portraits and bifurcation diagrams. Finally, the chaotic system is realized by analog circuit, and the numerical simulation results are verified by the simulation results of the analog circuit. The complex dynamical behaviors of the proposed system are very useful for various chaos-based information encryption and secure communication applications.

## Data Availability

The data used to support the findings of this study are included within the article.

## Conflicts of Interest

The authors declare that there no conflicts of interest.

## Acknowledgments

This research was funded by the National Natural Science Foundation of China (nos. 61203004 and 61306142), Natural Science Foundation of Heilongjiang Province (grant no. F201220), and Fundamental Research Funds for the Central Universities (no. 3072019CFG0802).

## References

- [1] L. Chua, "Memristor-the missing circuit element," *IEEE Transactions on Circuit Theory*, vol. 18, no. 5, pp. 507–519, 1971.



- [2] D. B. Strukov, G. S. Snider, D. R. Stewart, and R. S. Williams, "The missing memristor found," *Nature*, vol. 453, no. 7191, pp. 80–83, 2008.
- [3] S. Hamdioui, M. Taouil, and N. Z. Haron, "Testing open defects in memristor-based memories," *IEEE Transactions on Computers*, vol. 64, no. 1, pp. 247–259, 2015.
- [4] S. Kumar, J. P. Strachan, and R. S. Williams, "Chaotic dynamics in nanoscale NbO<sub>2</sub> Mott memristors for analogue computing," *Nature*, vol. 548, no. 7667, pp. 318–321, 2017.
- [5] Z. Wang, S. Joshi, S. E. Savel'ev et al., "Memristors with diffusive dynamics as synaptic emulators for neuromorphic computing," *Nature Materials*, vol. 16, no. 1, pp. 101–108, 2017.
- [6] S. Wen, Z. Zeng, M. Z. Q. Chen, and T. Huang, "Synchronization of switched neural networks with communication delays via the event-triggered control," *IEEE Transactions on Neural Networks and Learning Systems*, vol. 28, pp. 2334–2343, 2017.
- [7] G. Zhang, F. Wu, T. Hayat, and J. Ma, "Selection of spatial pattern on resonant network of coupled memristor and Josephson junction," *Communications in Nonlinear Science and Numerical Simulation*, vol. 65, pp. 79–90, 2018.
- [8] L. L. Huang, Z. F. Zhang, J. H. Xiang, and S. M. Wang, "A new 4D chaotic system with two-wing, four-wing, and coexisting attractors and its circuit simulation," *Complexity*, vol. 2019, Article ID 5803506, 13 pages, 2019.
- [9] C. Li, X. Wang, and G. Chen, "Diagnosing multistability by offset boosting," *Nonlinear Dynamics*, vol. 90, no. 2, pp. 1335–1341, 2017.
- [10] V.-T. Pham, A. Akgul, C. Volos, S. Jafari, and T. Kapitaniak, "Dynamics and circuit realization of a no-equilibrium chaotic system with a boostable variable," *AEU-International Journal of Electronics and Communications*, vol. 78, pp. 134–140, 2017.
- [11] L. Wang, "3-Scroll and 4-scroll chaotic attractors generated from a new 3-D quadratic autonomous system," *Nonlinear Dynamics*, vol. 56, no. 4, pp. 453–462, 2009.
- [12] G. Grassi and S. Mascolo, "A system theory approach for designing cryptosystems based on hyperchaos," *IEEE Transactions on Circuits and Systems I: Fundamental Theory and Applications*, vol. 46, no. 9, pp. 1135–1138, 1999.
- [13] B. Wang, F. C. Zou, and J. Cheng, "A memristor-based chaotic system and its application in image encryption," *Optik*, vol. 154, pp. 538–544, 2018.
- [14] M. F. Hassan, "A new approach for secure communication using constrained hyperchaotic systems," *Applied Mathematics and Computation*, vol. 246, pp. 711–730, 2014.
- [15] R. L. Filali, M. Benrejeb, and P. Borne, "On observer-based secure communication design using discrete-time hyperchaotic systems," *Communications in Nonlinear Science and Numerical Simulation*, vol. 19, no. 5, pp. 1424–1432, 2014.
- [16] Y. Zhang, M. Guo, G. Dou, Y. Li, and G. Chen, "A physical SBT-memristor-based Chua's circuit and its complex dynamics," *Chaos: An Interdisciplinary Journal of Nonlinear Science*, vol. 28, no. 8, Article ID 083121, 2018.
- [17] M. Itoh and L. O. Chua, "Memristor oscillators," *International Journal of Bifurcation and Chaos*, vol. 18, no. 11, pp. 3183–3206, 2008.
- [18] B. C. Bao, Z. Liu, and J. P. Xu, "Transient chaos in smooth memristor oscillator," *Chinese Physics B*, vol. 19, no. 3, Article ID 030510, 2010.
- [19] C. Wang, H. Xia, and L. Zhou, "A memristive hyperchaotic multiscroll jerk system with controllable scroll numbers," *International Journal of Bifurcation and Chaos*, vol. 27, no. 6, Article ID 1750091, 2017.
- [20] N. Stankevich and E. Volkov, "Multistability in a three-dimensional oscillator: tori, resonant cycles and chaos," *Nonlinear Dynamics*, vol. 94, no. 4, pp. 2455–2467, 2018.
- [21] K. Rajagopal, S. Jafari, A. Karthikeyan, A. Srinivasan, and B. Ayele, "Hyperchaotic memcapacitor oscillator with infinite equilibria and coexisting attractors," *Circuits, Systems, and Signal Processing*, vol. 37, no. 9, pp. 3702–3724, 2018.
- [22] S. Zhang, Y. Zeng, Z. Li, M. Wang, X. Zhang, and D. Chang, "A novel simple no-equilibrium chaotic system with complex hidden dynamics," *International Journal of Dynamics and Control*, vol. 6, no. 4, pp. 1465–1476, 2018.
- [23] F. Yuan, G. Wang, and X. Wang, "Extreme multistability in a memristor-based multi-scroll hyper-chaotic system," *Chaos: An Interdisciplinary Journal of Nonlinear Science*, vol. 26, no. 7, Article ID 073107, 2016.
- [24] L. Zhou, C. Wang, and L. Zhou, "Generating four-wing hyperchaotic attractor and two-wing, three-wing, and four-wing chaotic attractors in 4D memristive system," *International Journal of Bifurcation and Chaos*, vol. 27, no. 2, Article ID 1750027, 2017.
- [25] Q. Xu, Y. Lin, B. Bao, and M. Chen, "Multiple attractors in a non-ideal active voltage-controlled memristor based Chua's circuit," *Chaos, Solitons & Fractals*, vol. 83, pp. 186–200, 2016.
- [26] J. Kengne, Z. Njitacke Tabekoueng, V. Kamdoum Tamba, and A. Nguomkam Negou, "Periodicity, chaos, and multiple attractors in a memristor-based Shinriki's circuit," *Chaos: An Interdisciplinary Journal of Nonlinear Science*, vol. 25, no. 10, Article ID 103126, 2015.
- [27] B. C. Bao, H. Bao, N. Wang, M. Chen, and Q. Xu, "Hidden extreme multistability in memristive hyperchaotic system," *Chaos, Solitons & Fractals*, vol. 94, pp. 102–111, 2017.
- [28] H. Bao, T. Jiang, K. B. Chu, M. Chen, Q. Xu, and B. C. Bao, "Memristor-based canonical Chua's circuit: extreme multistability in voltage-current domain and its controllability in flux-charge domain," *Complexity*, vol. 2018, Article ID 5935637, 13 pages, 2018.
- [29] M. Chen, M. Sun, B. Bao, H. Wu, Q. Xu, and J. Wang, "Controlling extreme multistability of memristor emulator-based dynamical circuit in flux-charge domain," *Nonlinear Dynamics*, vol. 91, no. 2, pp. 1395–1412, 2018.
- [30] G. Y. Wang, C. B. Shi, X. W. Wang, and F. Yuan, "Coexisting oscillation and extreme multistability for a memcapacitor-based circuit," *Mathematical Problems in Engineering*, vol. 2017, Article ID 6504969, 13 pages, 2017.
- [31] H. Bao, N. Wang, B. Bao, M. Chen, P. Jin, and G. Wang, "Initial condition-dependent dynamics and transient period in memristor-based hypogenetic jerk system with four line equilibria," *Communications in Nonlinear Science and Numerical Simulation*, vol. 57, pp. 264–275, 2018.
- [32] F. Yuan, Y. Deng, Y. Li, and G. Wang, "The amplitude, frequency and parameter space boosting in a memristor-meminductor-based circuit," *Nonlinear Dynamics*, vol. 96, no. 1, pp. 389–405, 2019.
- [33] W. Liu and G. Chen, "A new chaotic system and its generation," *International Journal of Bifurcation and Chaos*, vol. 13, no. 1, pp. 261–267, 2003.
- [34] W. Liu and G. Chen, "Can a three-dimensional smooth autonomous quadratic chaotic system generate a single four-scroll attractor?" *International Journal of Bifurcation and Chaos*, vol. 14, no. 4, pp. 1395–1403, 2004.



## Research Article

# Symmetry Breaking, Coexisting Bubbles, Multistability, and Its Control for a Simple Jerk System with Hyperbolic Tangent Nonlinearity

Léandre Kamdjeu Kengne <sup>1,2</sup>, Jacques Kengne,<sup>1</sup> Justin Roger Mboupda Pone,<sup>1</sup> and Hervé Thierry Kamdem Tagne <sup>3</sup>

<sup>1</sup>Unité de Recherche d'Automatique et Informatique Appliquée (UR-AIA), Department of Electrical Engineering, IUT-FV Bandjoun, University of Dschang, P.O. Box 134, Bandjoun, Cameroon

<sup>2</sup>Unité de Recherche de Matière Condensée, d'Electronique et de Traitement du Signal (UR-MACETS), Department of Physics, University of Dschang, P.O. Box 67, Dschang, Cameroon

<sup>3</sup>Unité de Recherche de Mécanique et de Modélisation des Systèmes Physiques (UR-2MSP), Department of Physics, University of Dschang, P.O. Box 67, Dschang, Cameroon

Correspondence should be addressed to Léandre Kamdjeu Kengne; [lkamdjeu@gmail.com](mailto:lkamdjeu@gmail.com)

Received 31 December 2019; Revised 20 February 2020; Accepted 26 February 2020; Published 23 April 2020

Academic Editor: Dimitri Volchenkov

Copyright © 2020 Léandre Kamdjeu Kengne et al. This is an open access article distributed under the Creative Commons Attribution License, which permits unrestricted use, distribution, and reproduction in any medium, provided the original work is properly cited.

Symmetry is an important property found in a large number of nonlinear systems. The study of chaotic systems with symmetry is well documented. However, the literature is unfortunately very poor concerning the dynamics of such systems when their symmetry is altered or broken. In this paper, we investigate the dynamics of a simple jerk system with hyperbolic tangent nonlinearity (Kengne et al., *Chaos Solitons, and Fractals*, 2017) whose symmetry is broken by adding a constant term modeling an external excitation force. We demonstrate that the modified system experiences several unusual and striking nonlinear phenomena including coexisting bifurcation branches, hysteretic dynamics, coexisting asymmetric bubbles, critical transitions, and multiple (i.e., up to six) coexisting asymmetric attractors for some suitable ranges of system parameters. These features are highlighted by exploiting common nonlinear analysis tools such as graphs of largest Lyapunov exponent, bifurcation diagrams, phase portraits, and basins of attraction. The control of multistability is investigated by using the method of linear augmentation. We demonstrate that the multistable system can be converted to a monostable state by smoothly adjusting the coupling parameter. The theoretical results are confirmed by performing a series of PSpice simulations based on an electronic analogue of the system.

## 1. Introduction

Recently, a particular attention has been paid to the study of nonlinear and chaotic dynamic systems. This is due to the rapid development of increasingly powerful computers on the one hand and on the other hand to the many potential applications in several fields of science and engineering. These systems are capable of several forms of complexity such as chaos, hyperchaos, multirhythmicity, bifurcations, intermittency, hysteresis, and multistability [1–3]. Concerning the latter feature, it should be noted that a

multistable dynamic system is capable of displaying two or more attractors for the same set of parameters. In this situation, each of the coexisting attractors is connected with an attraction basin that represents all the initial conditions leading to the underlined attractor [4]. Fixed points, limit cycles, toruses, and chaotic attractors can coexist in the same system, in various combinations depending on the choice of parameters. The term extreme multistability refers to the situation where an infinite number of attractors coexist [5–9]. Multistability is relevant from the view point of practical application as it may give rise to unexpected and

even disastrous consequences [10]. If the phenomenon of multistability is encountered in dynamic systems with no symmetry property, it should be noted that symmetric systems are much more likely to develop this phenomenon [10]. Concerning the symmetry property, it should be mentioned that it is shared by many systems in several fields of science and engineering [2, 4]. In addition to multistability mentioned above, symmetric dynamic systems exhibit interesting behaviors such as period doubling, spontaneous symmetry breaking, merging crisis, hysteresis, and intermittency [1]. The study of symmetrical systems is well documented. However, to the best of the authors' knowledge, the literature is very poor concerning the behavior of these systems when their symmetry is altered or broken. The symmetry break purposefully induced in a nonlinear dynamical system may be adjusted to discover many complex nonlinear phenomena (e.g., multi-rhythmicity, bursting, coexisting bubbles, hysteresis, critical transitions, and coexisting multiple asymmetric attractors) as previously discussed in several nonlinear systems [11–17].

In this work, we consider a simple jerk system with hyperbolic tangent nonlinearity [18] whose symmetry is broken by the introduction of an additive constant  $k$ . We address the chaos generation mechanism, the formation of bubbles of bifurcation, and the coexistence of multiple attractors in both the symmetric ( $k = 0$ ) and the asymmetric ( $k \neq 0$ ) regimes of operation. For convenience, recall that jerk dynamic systems [19–23] refer to 3D ordinary differential equations (ODEs) in the form  $\ddot{x} = J(x, \dot{x}, \ddot{x})$  where the nonlinear vector function  $J(\cdot)$  indicates the “jerk” (i.e., the time derivative of the acceleration). The hyperbolic tangent function is relevant in numerous problems such as nonideal operational amplifiers, activation function in neural network, magnetization in ferromagnetic systems, and solar wind-driven magnetosphere-ionosphere systems [24–28]. Multistability in simple jerk dynamic systems has recently drained tremendous research interest in varied fields of science and technology resulting in several publications. On this line, Kengne and colleagues reported the coexistence of four self-excited mutually symmetric attractors in a jerk system possessing a cubic nonlinearity [23] based on both numerical and experimental methods. This striking feature of multiple attractors is mainly due to the system's symmetry and thus is also obtained with a hyperbolic sine [29], a hyperbolic tangent [18], a composite tanh-cubic nonlinearity [21], or a voltage controlled memristor [30], whose intrinsic current-voltage characteristics has the form of a pinched hysteresis loop. Despite the pertinence and the importance of the abovementioned results, we would like to stress that all cases of multistability discussed so far is restricted to symmetric jerk systems; also, multistability in jerk dynamic systems in case of a broken symmetry is very little studied. Motivated by previous results on jerk dynamical systems, this paper focuses on the effects engendered by symmetry break in a simple autonomous jerk system with hyperbolic tangent nonlinearity previously analyzed in [18]. Thus, the novel chaotic flow is smoothly tuned to behave either symmetrically or to develop no symmetry property using a single parameter. Importantly, the investigations clearly

reveal that the modified system can experience coexisting bubbles of bifurcation, coexisting multiple (symmetric or asymmetric) attractors, and crises phenomena not found in the original symmetric system [18]. Despite the fact that the addition of a constant term may be viewed as a purely mathematical technique to induce new nonlinear phenomena, one of the key motivations is that symmetries are rarely exact in real physical systems, and some symmetry-breaking imperfections are always present [31–33].

The structure of the paper is as follows. Section 2 describes the evolution equations of the modified jerk system with hyperbolic tangent and analyses possible symmetries. Analytical conditions for the occurrence of Hopf-type bifurcations are established, and the stability of the equilibrium points is investigated with respect to parameters. In Section 3, numerical results concerning the bifurcation behaviour of the model, the coexistence of numerous attractors, and the coexistence of bubbles of bifurcation are presented. The control of multistability based on the linear augmentation scheme is described in Section 4. Section 5 is concerned with the experimental study of the modified system. A convenient electronic circuit (i.e., the analogue simulator) is designed for investigating the extremely complex dynamics of the system. PSpice simulation experiment supports the results of the theoretical study. Finally, Section 6 presents the conclusions of the whole work.

## 2. Description and Analysis of the Model

**2.1. The Model.** The state equation of the autonomous jerk system, which is considered in this work, is expressed by the following third-order nonlinear system (ODEs) with a single nonlinear function:

$$\begin{cases} \dot{x}_1 = x_2, \\ \dot{x}_2 = ax_3, \\ \dot{x}_3 = -\gamma x_2 - \mu x_3 + \varphi_k(x_1), \end{cases} \quad (1a)$$

$$\varphi_k(x_1) = -k - 3(x_1 - 2 \tanh(x_1)), \quad (1b)$$

where  $a$ ,  $\mu$ , and  $\gamma$  denote (real) positive control parameters. Notice that the nonlinearity is smooth and involves only one state variable (i.e.,  $x_1$ ). Here,  $k$  is the symmetry control parameter of the model. Specifically, for  $k = 0$ , system (1) exhibits a perfect symmetry and reduces to the case previously studied by Kengne and coworkers [18]. The case  $k \neq 0$  corresponds to an asymmetric model for which more complex nonlinear phenomena arise (that cannot be explained by using the symmetry arguments) including, for instance, the presence of multiple coexisting asymmetric attractors, coexisting bifurcation branches, and crisis events (see Section 4). The graphical representations of the nonlinear function  $\varphi_k(\cdot)$  are provided in Figure 1 for several discrete values of parameter  $k$ . Interestingly, we would like to quote that the hyperbolic tangent nonlinearity has also been considered in many problems related to neural networks and Chua's system as well [24–28]. The inclusion of this nonlinear term in model (1) engenders the extremely complex

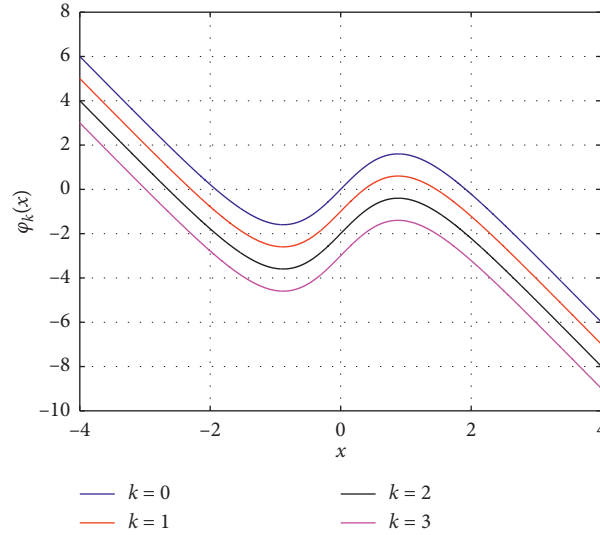


FIGURE 1: Graphical representation of the nonlinear function  $\varphi_k(x) = -k - 3x + 6 \tanh(x)$  for four discrete values of the symmetry parameter  $k$ . Notice that the number (one, two, or three) of zeros of  $\varphi_k(\cdot)$  depends crucially on the value of parameter  $k$ .

and striking bifurcation patterns developed by the whole system. The most “elegant” form [4] of system (1) is achieved by expressing it as a jerk equation:

$$\ddot{x} = -a\gamma\dot{x} - \mu\ddot{x} + a\varphi_k(x). \quad (2)$$

Finally, it should be remarked that the state variable  $x_1$  appears solely in the third equation and, consequently, represents an offset boosted variable [34, 35].

**2.2. Symmetry and Dissipation.** As previously indicated above, it can easily be seen that systems (1a) and (1b) are symmetric with respect to the origin of the coordinates for the special case  $k = 0.0$ . For this singular case, systems (1a) and (1b) represent an inversion invariant nonlinear dynamic system, provided that it remains unchanged when performing the coordinate substitution:  $(x_1(t), x_2(t), x_3(t)) \iff (-x_1(t), -x_2(t), -x_3(t))$ . As a result, all attractors of systems (1a) and (1b) occur either as individual symmetric attractors or as mutually symmetric couples. This property is the key ingredient to justify the presence of multiple coexisting stable states appearing for some suitable sets of system parameters. More importantly, a suitable exploitation of the symmetry property of the evolution equation simplifies considerably the numerical experiment (e.g., the stability analysis, the calculation of phase space trajectory, and the basins of attraction as well).

More generally, systems (1a) and (1b) are nonsymmetric for any value of  $k \neq 0.0$ . However, we notice the invariance of systems (1a) and (1b) following the coordinate transformation  $(x_1(t), x_2(t), x_3(t), k) \iff (-x_1(t), -x_2(t), -x_3(t), -k)$ . Consequently, we restrict our analysis for positive values of parameter  $k$  all over this work. The dynamics for negative values of  $k$  can be deduced from the latter transformation.

The divergence of the vector field (1a) and (1b) is computed as follows:

$$\begin{aligned} \Lambda &= \frac{\partial \dot{x}_1}{\partial x_1} + \frac{\partial \dot{x}_2}{\partial x_2} + \frac{\partial \dot{x}_3}{\partial x_3}, \\ &= \frac{\partial(x_2)}{\partial x_1} + \frac{\partial(ax_3)}{\partial x_2} + \frac{\partial(-k - \gamma x_2 - \mu x_3 - 3x_1 + 6 \tanh(x_1))}{\partial x_3}, \\ &= -\mu < 0. \end{aligned} \quad (3)$$

It follows that, for any point  $x = (x_1, x_2, x_3)$  in phase space, the divergence is always negative. Accordingly, system (1) is dissipative and consequently can develop attractors [1–3].

**2.3. Fixed Point Analysis.** The study of equilibria always represents the first issue to be addressed when performing the investigation of a nonlinear dynamic system. Their study yields preliminary insights into the dynamics of complete system [1–4]. By equating to zero all the derivatives in system (5), we found that (see Figure 1), for  $|k| < k_{\max} \approx 7.57$ , there exist three different rest points  $E_n = (x_n, 0, 0)$  ( $n = 0, 1, 2$ ), where  $x_j$  verifies the following transcendental equation:

$$k + 3(x - 2 \tanh(x)) = 0. \quad (4)$$

In view of the graph presented in Figure 1, we notice that, for  $|k| = k_{\max}$ , the system has two fixed points, while a single equilibrium point exists in case  $|k| > k_{\max}$ . Throughout the rest of this work, we restrict our analysis for values of  $k$  where the system exhibits three fixed points. It should be remarked that, for  $k = 0.0$ , the system displays three symmetric fixed points amongst which the origin [18]. Using the set of parameters defined above, the roots equation (4) have been numerically obtained for two discrete values of  $k$  (i.e.,  $k = 0.00$  and  $k = 0.25$ ) by using the “fzero” build in function of Matlab. Recall that the “fzero” function is a MATLAB subroutine to search for the zeros of a single variable real-value function. As

sample results, we have obtained the following fixed points: (i)  $E_0(0, 0, 0)$  and  $E_{1,2}(\pm 1.915, 0, 0)$  for  $k = 0.0$ ; (ii)  $E_0(0.083, 0, 0)$ ,  $E_1(1.813, 0, 0)$ , and  $E_2(-2.013, 0, 0)$  for  $k = 0.25$ . We notice that the positions of the equilibrium points in state space are defined solely by the value of parameter  $k$ . Evaluated at any given fixed point  $E(\bar{x}, 0, 0)$ , the Jacobian matrix of system (1) takes the following form:

$$M_J = \begin{bmatrix} 0 & 1 & 0 \\ 0 & 0 & a \\ 3 - 6 \tanh^2(\bar{x}) & -\gamma & -\mu \end{bmatrix}. \quad (5)$$

We obtain the related eigenvalues  $\lambda_j (j = 1, 2, 3)$  by searching for the zeros of the characteristic polynomial:

$$P(\lambda) = \det(M_J - \lambda I_d) = \lambda^3 + \mu\lambda^2 + a\gamma\lambda - 3a(1 - 2 \tanh^2(\bar{x})), \quad (6)$$

where  $I_d$  refers to the  $3 \times 3$  identity matrix. From the graphs in Figure 1, we notice that the equilibrium point  $E_0$  has its  $x$ -coordinate with magnitude smaller than unity. Also, the related characteristic polynomial possesses coefficients with different signs, and thus,  $E_0$  is always unstable according to the Routh stability theorem. The stability of the pair of fixed points ( $E_1$  and  $E_2$ ) changes with the values of parameters  $\alpha$  and  $\gamma$ . From both the Routh–Hurwitz stability criterion [1, 2] and the Hopf bifurcation theorem, we derived the following results about the stability of the above pair of equilibrium points. Each of the fixed points  $E_n (n = 1, 2)$  remains stable only for values of  $\gamma > \gamma_c(x_n) = \gamma_{cn} = 3(2 \tanh^2(x_n) - 1)/\mu$ . If the parameter  $\gamma$  is brought beyond the critical value  $\gamma_{cn}$ , the fixed point  $E_j$  becomes unstable. We now investigate the Hopf bifurcation related to the fixed point  $E_n (n = 1, 2)$  when  $\gamma$  is considered as the bifurcation control parameter. The following analytical conditions have been derived:

$$\gamma_H(x_n) = \gamma_{cn} = \frac{3(2 \tanh^2(x_n) - 1)}{\mu}, \quad (7a)$$

$$\omega_H(x_n) = \sqrt{a\gamma_{cn}}, \quad (7b)$$

$$\operatorname{Re}\left(\frac{d\lambda}{d\gamma}\bigg|_{\gamma=\gamma_c}\right) = \frac{-a}{2 + 2a\gamma_{cn}} \neq 0. \quad (7c)$$

As a result, systems (1a) and (1b) exhibit a Hopf bifurcation from  $E_n (n = 1, 2)$  when  $\gamma = \gamma_H(x_n)$ , and a limit cycle will develop around the point  $E_n (n = 1, 2)$ . Equation (7b) defines the frequency of oscillations ( $\omega_H$ ), while the transversality condition is expressed by equation (7c). As sample numerical results, both equilibrium points  $E_1$  and  $E_2$  undergo a Hopf bifurcation at  $\gamma = \gamma_{c1} = \gamma_{c2} \approx 2.496$  for  $k = 0.0$  and  $\mu = 1.0$ . In contrast, for  $k = 0.25$  and  $\mu = 1.0$ , the Hopf bifurcation values are  $\gamma_{c1} \approx 2.40$  and  $\gamma_{c2} \approx 2.58$ , respectively, for  $E_1$  and  $E_2$ . From the study presented above, we conclude that both three equilibriums are unstable in any regime (periodic or chaotic oscillations) of operation, and systems (1a) and (1b) exhibit self-excited attractors accordingly [36,37].

### 3. Numerical Study

**3.1. Scenario to Chaos.** To highlight the influence of system parameters on the dynamics of the system, we keep  $a = 10.0$  and use  $\gamma$  and  $k$  as control parameters. Figure 2 provides the bifurcation diagrams of the coordinate  $x_1$  against  $\gamma$  and related plots of largest Lyapunov exponent [38] for two different values of  $k$  (i.e.,  $k = 0.00$  and  $k = 0.25$ ). These diagrams are obtained by scanning the parameter downward without resetting the values of initial conditions, starting the system from the initial state  $(\pm 0.5, 0, 0)$ , respectively. We know that, for  $k = 0.0$  (see Figure 2), the system is symmetric as well as related dynamical structures (i.e., equilibrium points, attractors, and basins of attractions). For this particular case, it can be seen from the diagram of Figure 2 (left panel) that there exist two symmetric bifurcation branches (blue and magenta), exhibiting a period doubling sequence to chaos for decreasing  $\gamma$ . These branches merge at approximately  $\gamma = 1.0$  via the well-known symmetry recovering the crisis process. At this point, two mutually symmetric mono-scroll chaotic attractors (corresponding to the blue and magenta branches) combine to form a double-scroll strange attractor (see Figure 3). Completely different routes are found in the nonsymmetric system (i.e.,  $k \neq 0.0$ ). In fact, for a nonzero value of parameter  $k$  (e.g.,  $k = 0.25$ ), it can be captured from Figure 2 (right panel) that a pair of asymmetric limit cycles with different periodicity experiences each its own route of period doubling cascade to chaos when the control parameter  $\gamma$  is decreased in small steps. Accordingly, blue and magenta bifurcation branches display a horizontal shift which increases with parameter  $k$ . For example, in the bifurcation plot of Figure 2 (right panel), the first period doubling takes place at  $\gamma = 0.15$  for the blue branch and  $\gamma = 0.25$  for the red one. Here, the merging process never occurs. Instead, the series of period doublings of coexisting asymmetric cycles yields an asymmetric double-scroll strange attractor (see Figure 4). Moreover, most fascinating properties of the asymmetric system is the sudden disappearance (via a critical transition) of one of the bifurcation branches (i.e., the magenta branch; see Figure 2) when decreasing the control parameter  $\gamma$  for any nonzero value of  $k$ . Past this crisis event, the system experiences a single attractor that metamorphoses to an asymmetric double-scroll chaotic attractor as  $\gamma$  is further decreased.

**3.2. Coexistence of Multiple Attractors.** The coexistence of multiple stable states [10] is one of the most attractive properties the jerk system considered in this work. This intriguing feature has been deeply investigated for the symmetric system (i.e.,  $k = 0.00$ ) in the reference work [18]. In this section, we investigate the impact of the excitation term ( $k$ ) on the mechanism governing the generation of multiple solutions. In this regard, several bifurcation plots are produced following appropriate numerical techniques [18] in order to track parameter domains corresponding to the presence of multiple coexisting stable states. As sample results, Figure 5 shows the bifurcation diagrams of local maxima of  $x_1$  variable, obtained when varying parameter  $a$



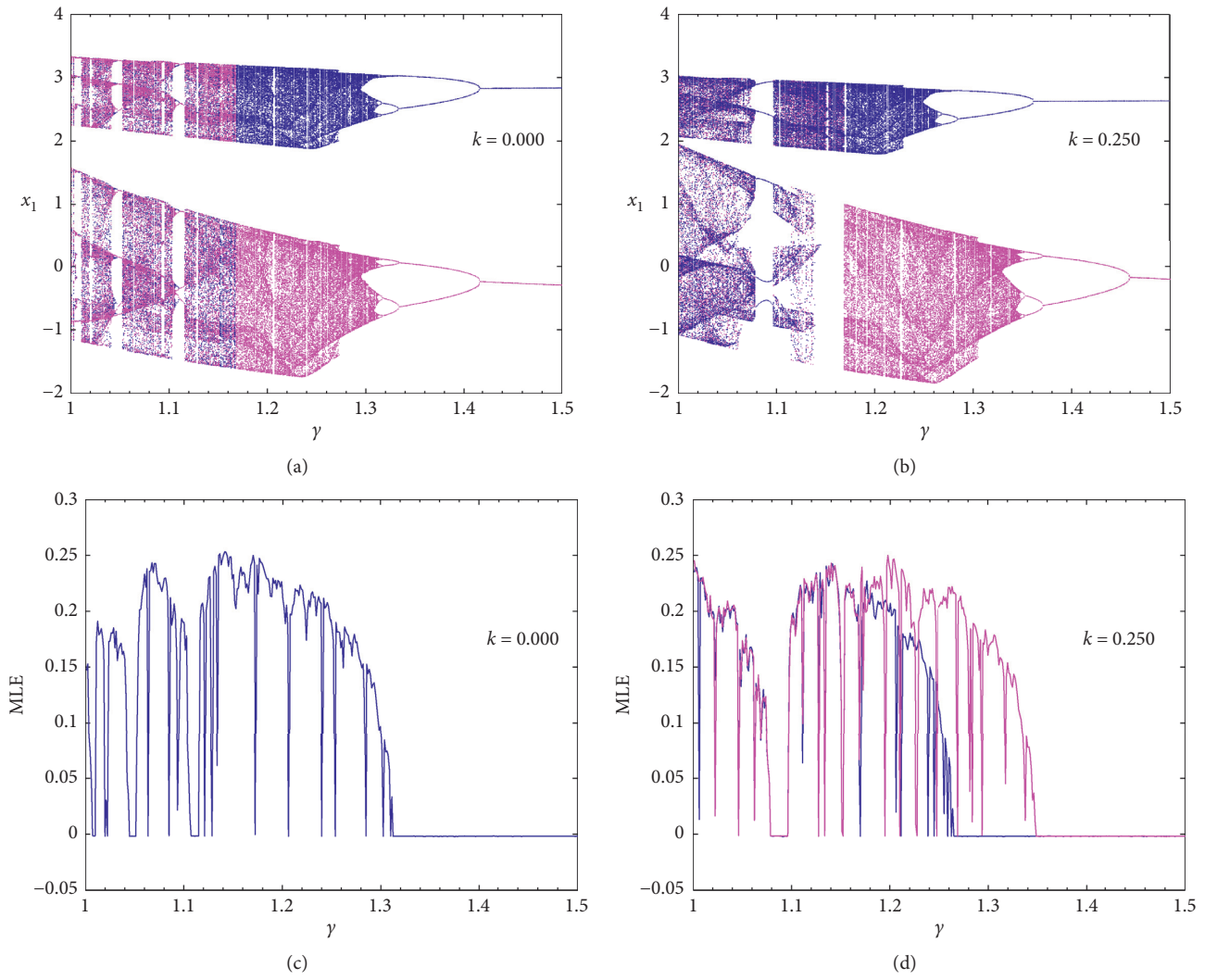


FIGURE 2: Bifurcation diagrams (a, b) of the system showing local maxima of the coordinate  $x_1$  versus parameter  $\gamma$  computed for  $a = 5$  both for the symmetric ( $k=0.000$ ) and the asymmetric ( $k=0.250$ ) modes of oscillations. The corresponding graph of maximal Lyapunov exponent is shown in the lower panel (c, d).

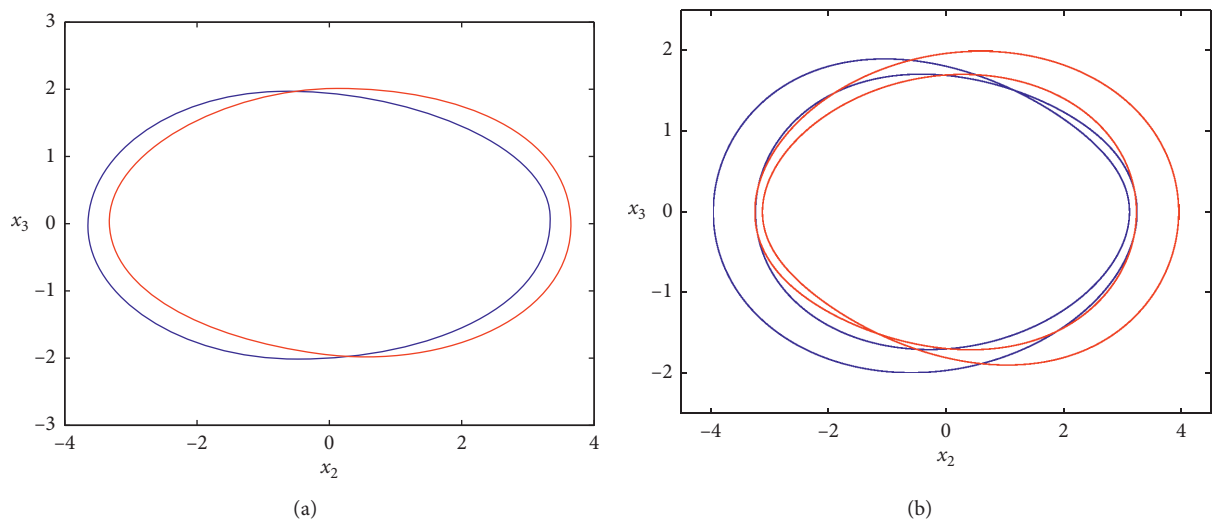


FIGURE 3: Continued.



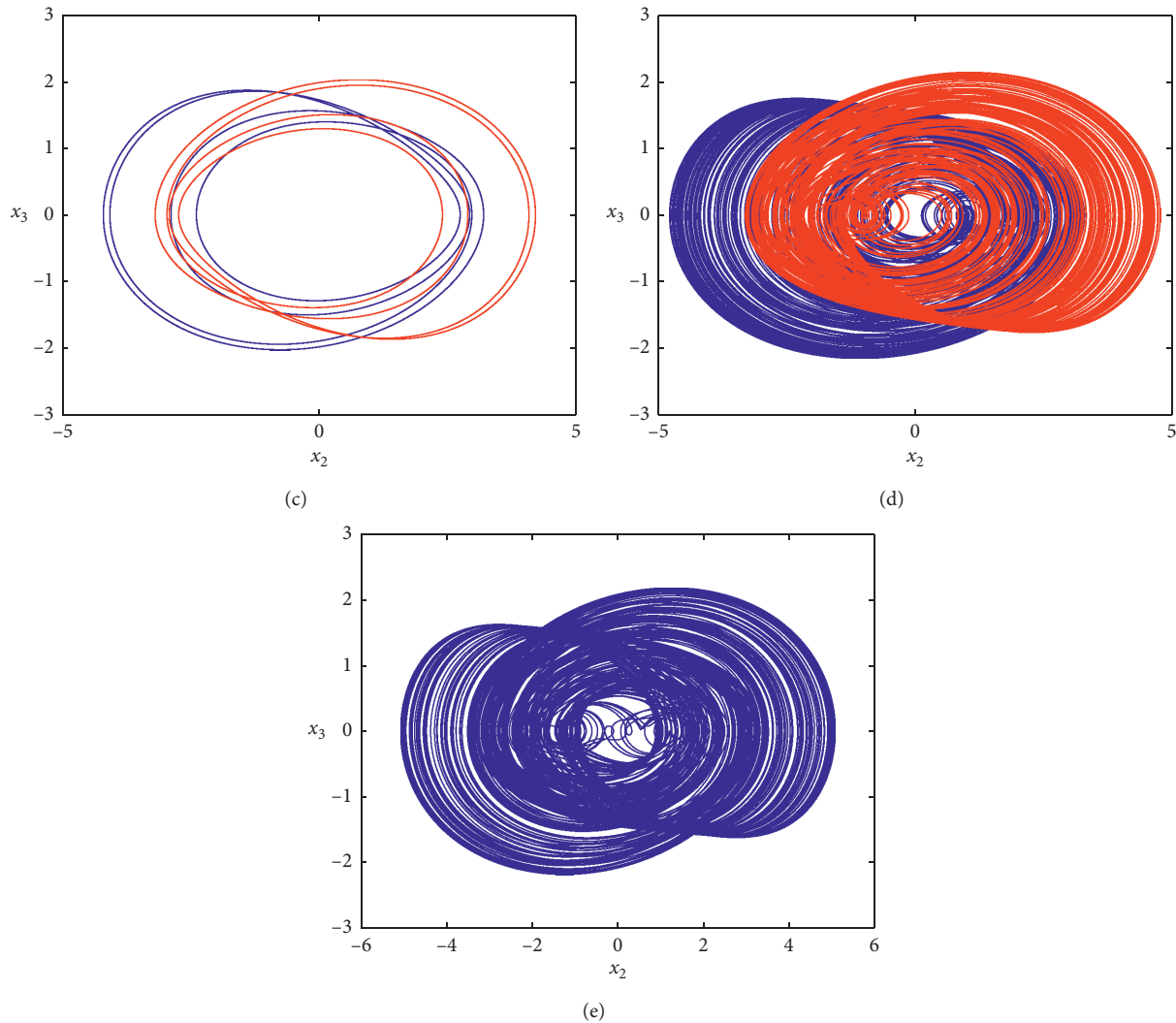


FIGURE 3: Sample chaotic phase portraits of the symmetric system: (a) a pair of period-1 cycles for  $\gamma = 1.6$ ; (b) a pair of period-2 cycles for  $\gamma = 1.4$ ; (c) a pair of period-4 cycles for  $\gamma = 1.323$ ; (d) two mutually symmetric spiraling strange attractors for  $\gamma = 1.18$ ; (e) a double-scroll strange attractor for  $\gamma = 1.078$ . Initial conditions are not critical but fixed as  $(x(0), y(0), z(0)) = (1, 0, 0)$ . The rest of parameters are  $k = 0.0$ ,  $a = 5.0$ , and  $\mu = 1.0$ .

in the range  $5 \leq a \leq 30$  for four discrete values of  $k$ . Details of numerical procedures employed to produce these plots are described in Table 1. These diagrams display the intricate phenomenon of parallel branches and hysteresis which justify the occurrence of multiple attractors for several parameter sets. More importantly, notice that the merging process does occur for the symmetric system (i.e.,  $k = 0.00$ ). In contrast, one of the branches undergoes a critical transition and collapses for nonzero values of parameter  $k$  when the control parameter  $\gamma$  is slowly decreased. The numerical techniques used to obtain those diagrams are provided in Table 1. A close examination of Figure 5 reveals that various combinations of coexisting attractors can be obtained when suitably selecting the system parameters. For example, Figure 6 presents the coexistence of two different chaotic attractors (a, b) computed for  $a = 15.0$  using two different values of initial conditions. The corresponding cross section

of the basins of attraction is provided in (c) using the same colors as the relevant attractors. In this figure, the red zone indicates unbounded dynamics. In the same line, Figure 7 depicts three different asymmetric coexisting attractors and corresponding cross sections of the basin of attraction. More interestingly, by choosing appropriately the values of system parameters and initial conditions, four asymmetric coexisting attractors can be found as exemplified in Figure 8. A more intriguing situation is depicted in Figure 9 where up to five different asymmetric attractors coexist. The corresponding bifurcation like sequence of local maxima of the coordinate  $x_1$  versus initial condition  $x_1(0)$  is provided in the graph of Figure 9(f). The cases reported above relate to the asymmetric mode of operation, and a different configuration of coexisting attractors occurs in the symmetric regime where coexisting attractors now appear only in mutually symmetric pairs (see Figure 10).

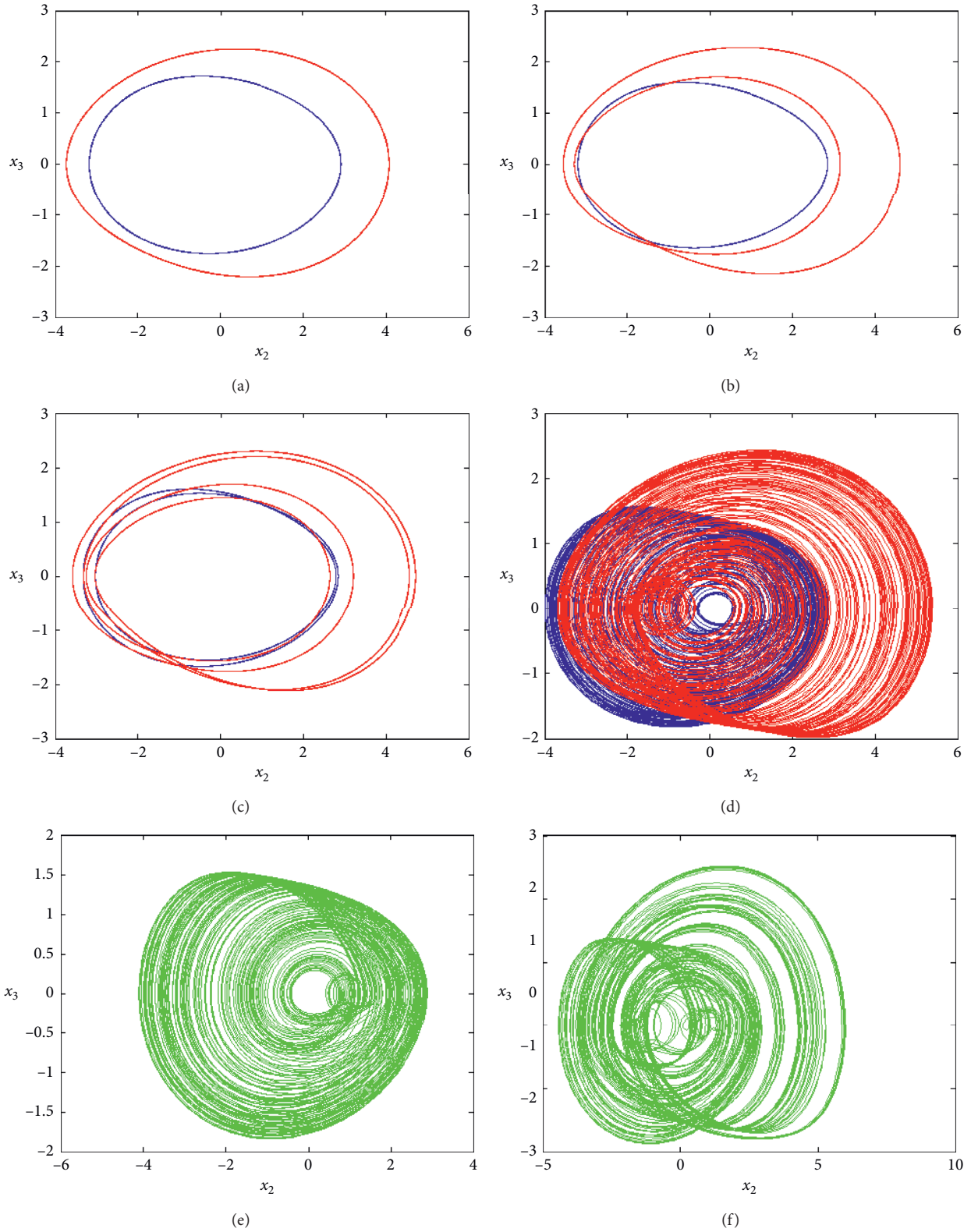


FIGURE 4: Computer-generated phase space trajectories of the system projected onto the  $y$ - $z$  planes obtained for some discrete values of parameter  $\gamma$ : (a) coexistence of two period-1 limit cycles for  $\gamma = 1.6$ ; (b) coexistence of period-1 and period-2 cycles for  $\gamma = 1.4$ ; (c) coexistence of period-4 and period-2 cycles for  $\gamma = 1.359$ ; (d) coexistence of two nonsymmetric strange attractors for  $\gamma = 1.2$ ; (e) a nonsymmetric strange attractor for  $\gamma = 1.16$ ; (f) an asymmetric double-scroll strange attractor for  $\gamma = 1.0$ . The computations are done with  $k = 0.25$ ,  $\mu = 1.0$ , and  $a = 5.0$ . Initial conditions are  $(x(0), y(0), z(0)) = (\pm 1, 0, 0)$ .

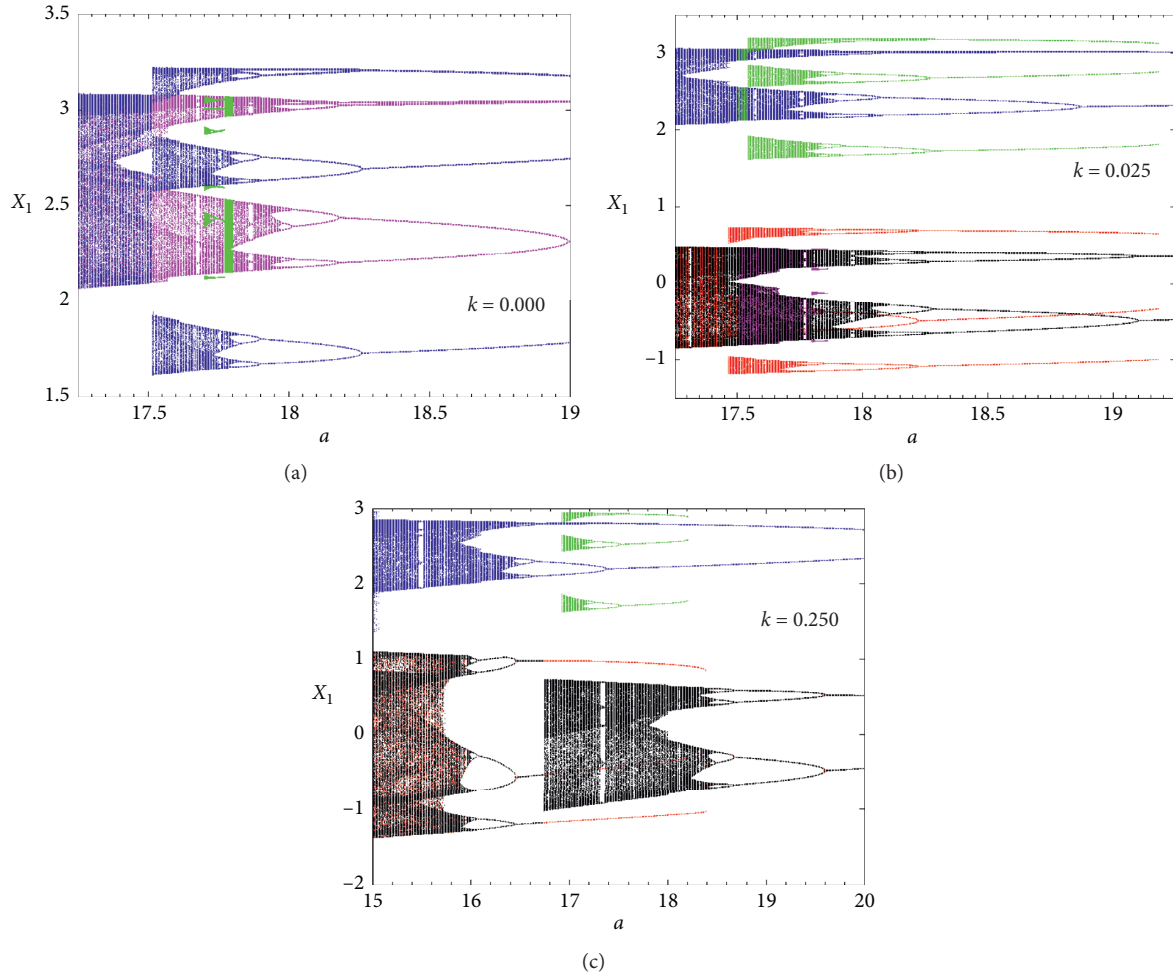


FIGURE 5: Enlargements of the bifurcation diagrams of the system showing various coexisting bifurcation branches and hysteresis, computed for three different values of parameter  $k$ , namely,  $k = 0.000$ ,  $k = 0.025$ , and  $k = 0.250$ . Detail numerical procedures used to obtain those diagrams are provided in Table 1. The rest of parameters are same as in Figure 5.

TABLE 1: Detailed numerical procedures used to obtain the bifurcation diagrams of Figure 5.

Graph identification	Color data	Parameter range	Sweeping direction	Initial condition ( $x_1(0), x_2(0), x_3(0)$ )
$k = 0.000$	Magenta	$17.25 \leq a \leq 19$	Upward	(0.1, 0, 0)
	Green	$17.70 \leq a \leq 19$	Upward	(0.2, 0, 0)
	Blue	$5 \leq a \leq 19$	Downward	(0.6, 0, 0)
$k = 0.025$	Blue	$17.25 \leq a \leq 19.25$	Upward	(+2, 0, 0)
	Red	$17.5 \leq a \leq 19.18$	Downward	(-2, 0, 0)
	Black	$17.25 \leq a \leq 19.25$	Upward	(-5, 0, 0)
	Magenta	$17.25 \leq a \leq 17.86$	Downward	(-0.8, 0, 0)
	Green	$17.5 \leq a \leq 19.18$	Downward	(1, 0, 0)
$k = 0.250$	Blue	$15 \leq a \leq 20$	Downward	(5, 0, 0)
	Black	$15 \leq a \leq 20$	Downward	(-5, 0, 0)
	Red	$15 \leq a \leq 20$	Upward	(-5, 0, 0)
	Green	$16.92 \leq a \leq 18.20$	Upward	(3, 0, 0)

From the above investigations, we notice that the occurrence of multiple attractors is possible both in the unforced (i.e.,  $k = 0.0$ ) and the forced ( $k \neq 0.0$ ) regimes. The latter situation is being much more challenging for analysis provided that the occurrence of multiple solutions cannot be

explained based on symmetry arguments. At this point, we would like to stress that the occurrence of multiple attractors has reported numerous other problems from diverse fields of science and technology. This feature can be advantageously exploited in engineering applications such as image

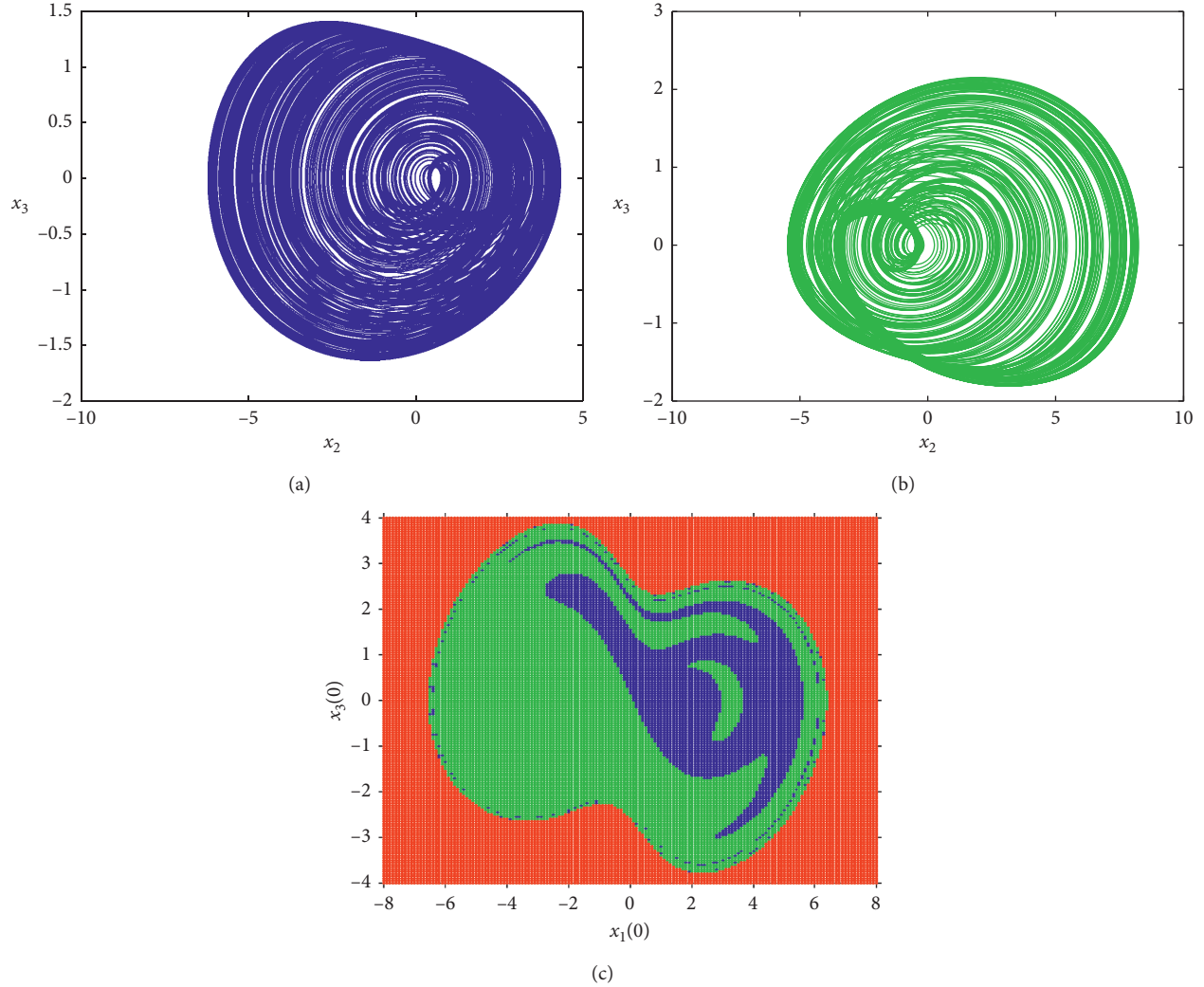


FIGURE 6: Coexistence of two different attractors for  $a = 12.0$ ,  $\gamma = 1.0$ ,  $\mu = 0.95$ , and  $k = 0.25$ . Initial conditions  $(x_1(0), x_2(0), x_3(0))$  are  $(0.4, 0, 0)$  and  $(-0.4, 0, 0)$  for (a) and (b), respectively. The corresponding cross section of the basins of attraction is provided in (c) using the same colors as the relevant attractors. The red zone denotes unbounded dynamics.

encryption and random signal generation as well. However, in cases where only a single stable attractor is desired, some control strategies may be developed. Detailed analysis concerning this point is out of the scope of this paper. Accordingly, interested readers may obtain precious information from the review work of [10].

**3.3. Coexisting Bubbles of Bifurcation.** Another interesting and striking event revealed monitoring the parameters of system (1) is the phenomenon of antimonotonicity [39–44]. In fact, the period doubling transition to chaos followed by the reverse bifurcation scenario is found when varying the control parameter  $a$  for several values of  $\gamma$  in case of a zero forcing term (i.e.,  $k = 0.0$ ). Sample results are depicted in Figure 11 which presented five bifurcation plots of the coordinate  $x$  versus  $a$  for five discrete values of  $\gamma$ . In each case of the diagrams in Figure 11, there are two symmetric bifurcation diagrams due to the symmetry of the model. From Figure 11, we note that a period-1 bubble is obtained

for  $\mu = 1.0$ . As  $\gamma$  decreases the sequence  $P_1$  bubble  $\rightarrow P_2$  bubbles  $\rightarrow P_4$  bubble  $\rightarrow P_8$  bubbles  $\rightarrow$  full, Feigenbaum tree takes place. This behavior corresponds to the symmetric system ( $k = 0.0$ ) and much more complex nonlinear dynamics arise in the presence of a nonzero excitation force (i.e.,  $k \neq 0.0$ ), as exemplified in Figure 12. This latter figure depicts the bifurcation plots of the coordinate  $x$  against parameter  $a$  obtained for several discrete values of  $k$  while maintaining  $\gamma = 1.475$  and  $\mu = 0.875$ . In contrast to the situation presented in Figure 11, lower and upper bifurcation branches are nonsymmetric, depicting a horizontal shift and exhibiting different periodicities. This striking behavior (engendered by symmetry break) is rarely reported and thus represents an enriching contribution to the behavior of these types of systems.

#### 4. Control of Multistability

Recently, a control method referred to as linear augmentation is described which is suitable to control the dynamics



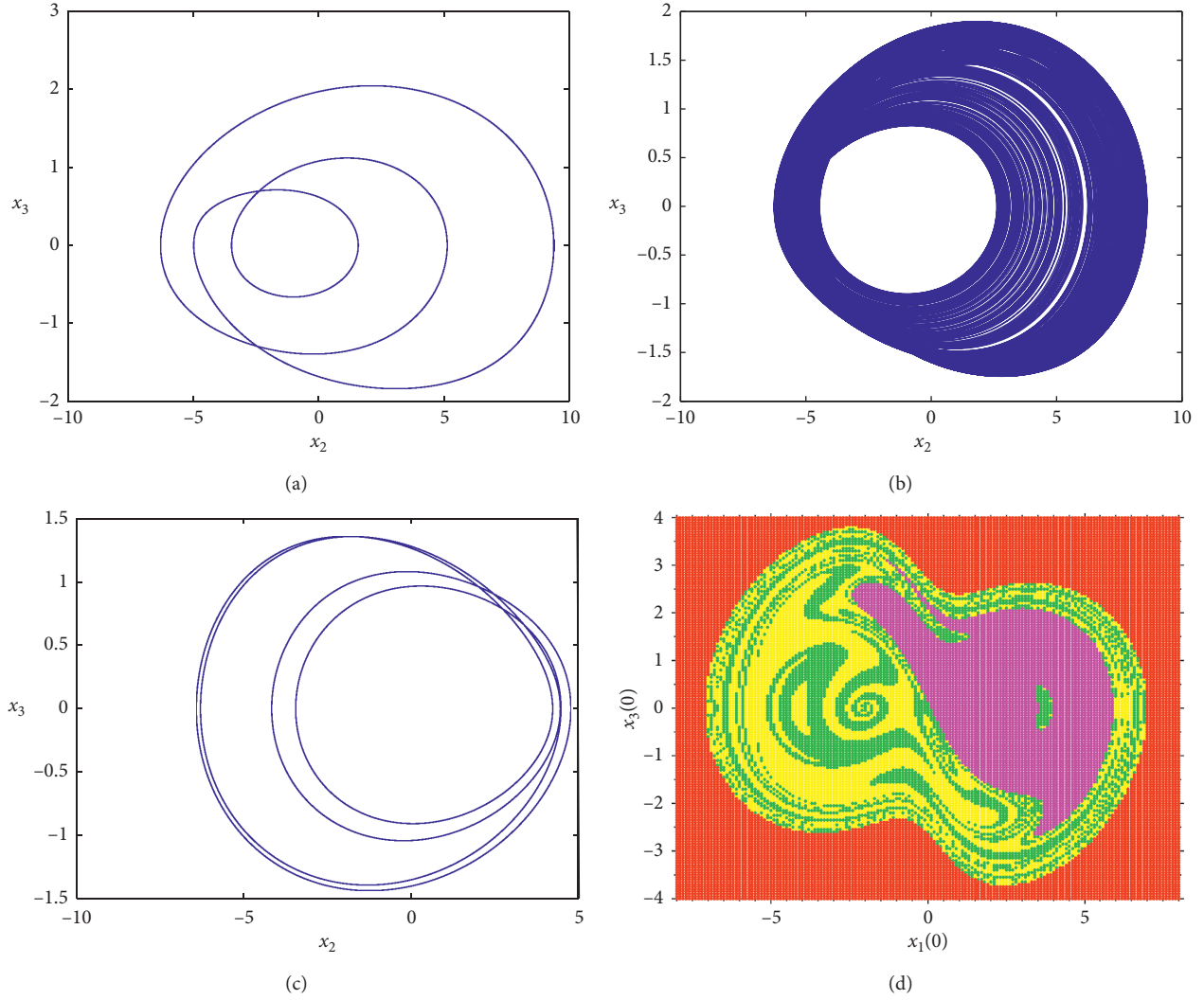


FIGURE 7: Coexistence of three different attractors for  $a = 16.85$ ,  $\gamma = 1.0$ ,  $\mu = 0.95$ , and  $k = 0.25$ . Initial conditions  $(x_1(0), x_2(0), x_3(0))$  are  $(-1.8, 0, 0)$  for attractor in (a),  $(-1.6, 0, 0)$  for attractor in (b), and  $(0.4, 0, 0)$  for attractor in (c). Green, magenta, and yellow colors correspond to the attractors in (a), (b), and (c), respectively. The red zone corresponds to unbounded dynamics.

of a nonlinear system without perturbing the system's parameters [45–47]. In this strategy, a nonlinear dynamic system is coupled with a linear one. The motivations of this coupling scheme are twofold: (a) to stabilize the steady state in a given nonlinear oscillator; (b) to adjust the number of coexisting attractors for a multistable system. Accordingly, the dynamics of the jerk system with hyperbolic tangent nonlinearity coupled to a linear system is described by the following fourth-order system:

$$\begin{cases} \dot{x}_1 = x_2, \\ \dot{x}_2 = ax_3, \\ \dot{x}_3 = -\gamma x_2 - \mu x_3 - k - 3x_1 + 6 \tanh(x_1) + \delta u, \\ \dot{u} = -\sigma u - \delta(x - \beta). \end{cases} \quad (8)$$

Here,  $\sigma \geq 0$  represents the decay parameter of the linear system  $u$ ,  $\delta$  denotes the coupling strength, and  $\beta$  is the control parameter, which serves to locate the position of the

equilibrium points. For  $\delta = 0$ , both oscillators evolve independently, and the linear system exhibits a fixed-point motion. For a nonzero coupling coefficient (i.e.,  $\delta \neq 0$ ), there is a mutual influence between the nonlinear oscillator and the linear system resulting in the symmetry breaking of the whole system even for  $k = 0.0$ . The fixed points of the coupled system are yielded by the following nonlinear algebraic system:

$$\begin{cases} -k - 3x_1 + 6 \tanh(x_1) + \delta u = 0, \\ -\sigma u - \delta(x - \beta) = 0. \end{cases} \quad (9)$$

System (9) clearly shows that the fixed points are asymmetrically located in state space, and their number strongly depends on the values of the linear system parameters as well as the coupling strength. Considering the case where the system develops six distinct periodic and chaotic attractors, we examine the range of coupling parameter corresponding to a monostable behavior of the



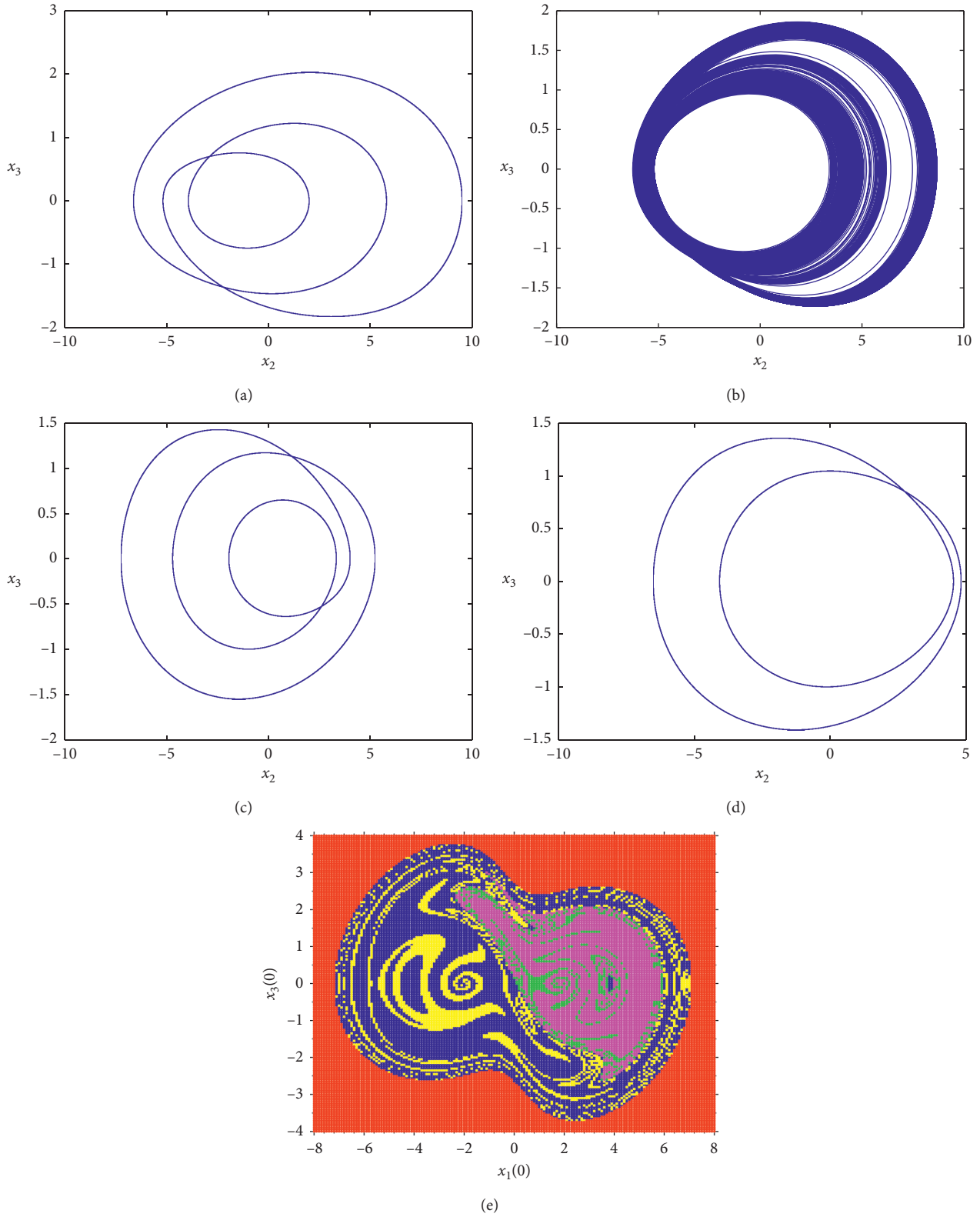


FIGURE 8: Coexistence of four different attractors for  $a = 18.0$ ,  $\gamma = 1.0$ ,  $\mu = 0.95$ , and  $k = 0.25$ . Initial conditions  $(x_1(0), x_2(0), x_3(0))$  are  $(-1.8, 0, 0)$  for the period-3 cycle in (a) with blue basin,  $(-1.6, 0, 0)$  for the chaotic attractor in (b) with green basin,  $(0.2, 0, 0)$  for attractor in (c) with magenta basin, and  $(0.4, 0, 0)$  for attractor in (d) with yellow basin. (e) Red zones indicate unbounded dynamics.

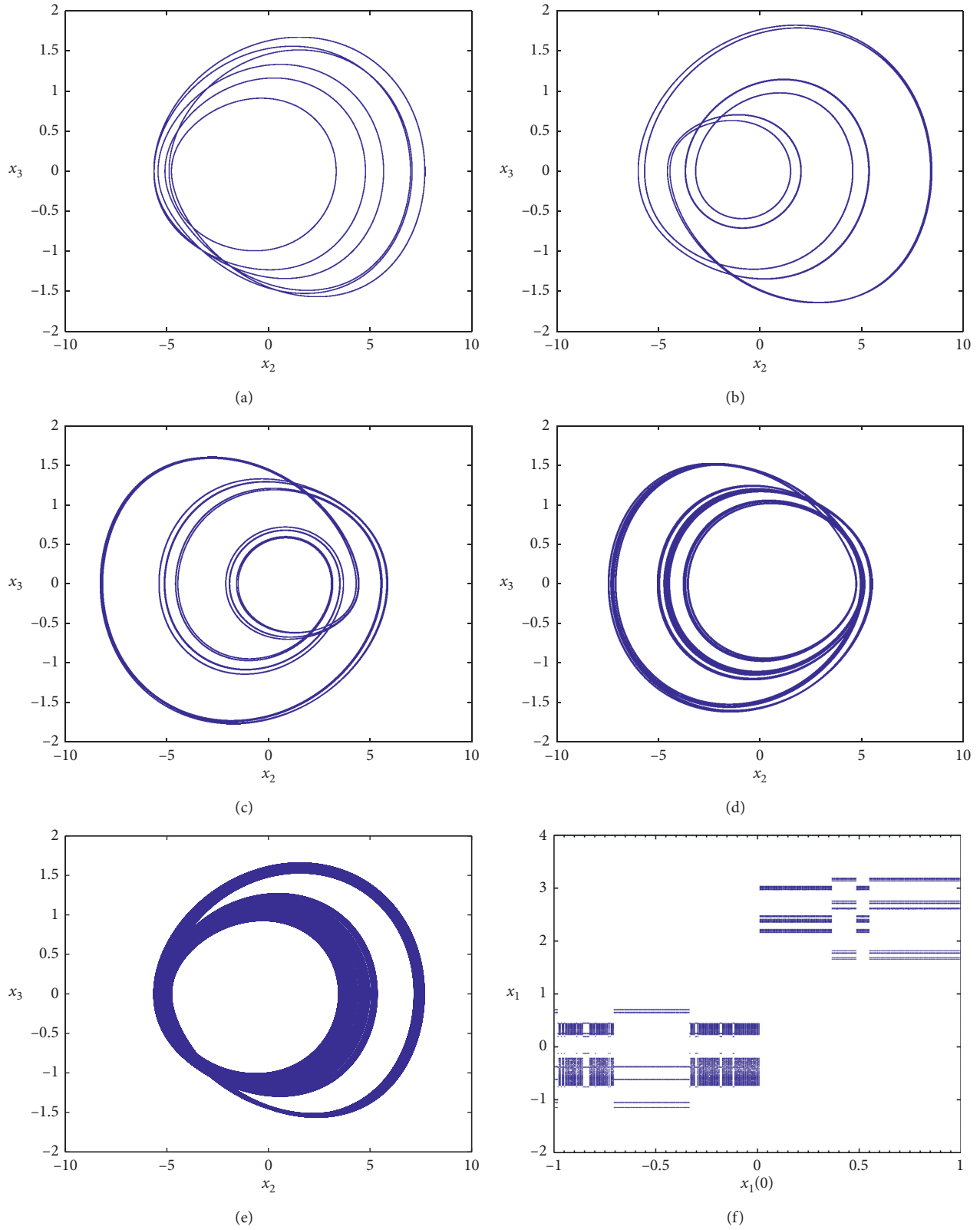


FIGURE 9: Coexistence of five different attractors for  $a = 17.85$ ,  $\gamma = 1.0$ ,  $\mu = 0.95$ , and  $k = 0.025$ . Initial conditions  $(x_1(0), x_2(0), x_3(0))$  are  $(-0.12, 0, 0)$  for (a),  $(-1.12, 0, 0)$  for (b),  $(0.648, 0, 0)$  for (c),  $(0.128, 0, 0)$  for (d), and  $(-0.048, 0, 0)$  for (e). The bifurcation-like sequence of local maxima of the coordinate  $x_1$  versus initial condition  $x_1(0)$  obtained with  $(x_1(0), x_2(0)) = (0, 0)$  is provided in graph in (f).

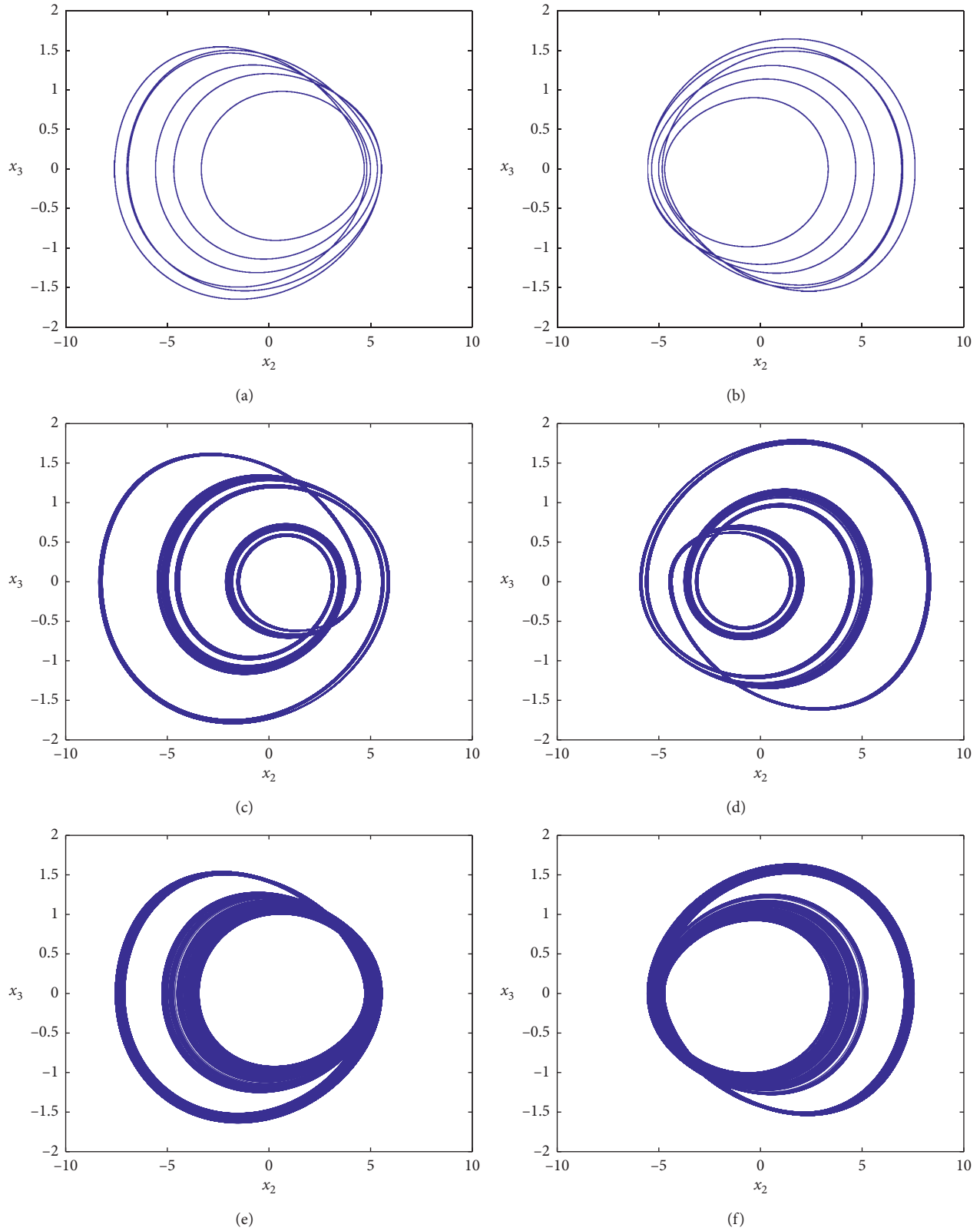


FIGURE 10: Coexistence of six different attractors for  $a = 17.77$ ,  $\gamma = 1.0$ ,  $\mu = 0.95$ , and  $k = 0.0$ . Initial conditions  $(x_1(0), x_2(0), x_3(0))$  are  $(\pm 0.104, 0, 0)$  for the pair of period-6 cycles (a, b),  $(\pm 0.4, 0, 0)$  for the pair of three-band chaotic attractors (c, d), and  $(\pm 0.2, 0, 0)$  for two-band chaotic attractors (e, f).

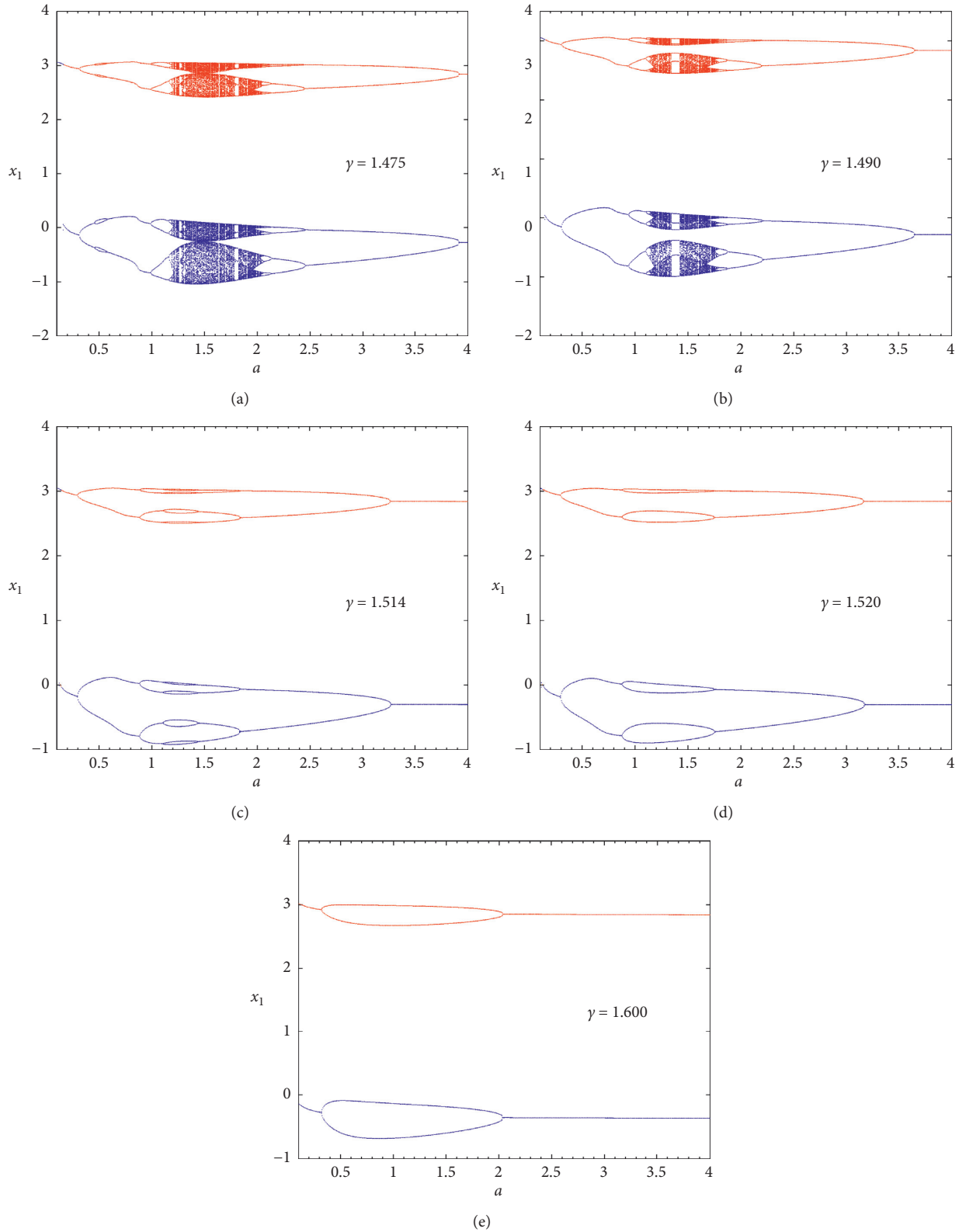


FIGURE 11: Bifurcation diagrams of the system showing local maxima of the coordinate  $x_1$  versus the control parameter  $a$  computed for some discrete values of  $\gamma$  keeping  $\mu = 1.0$  and  $k = 0.00$ . In each diagram, the blue and red branches are obtained by scanning the parameter downward (i.e., downward continuation) starting with initial conditions  $(-0.5, 0, 0)$  and  $(0.5, 0, 0)$ , respectively.

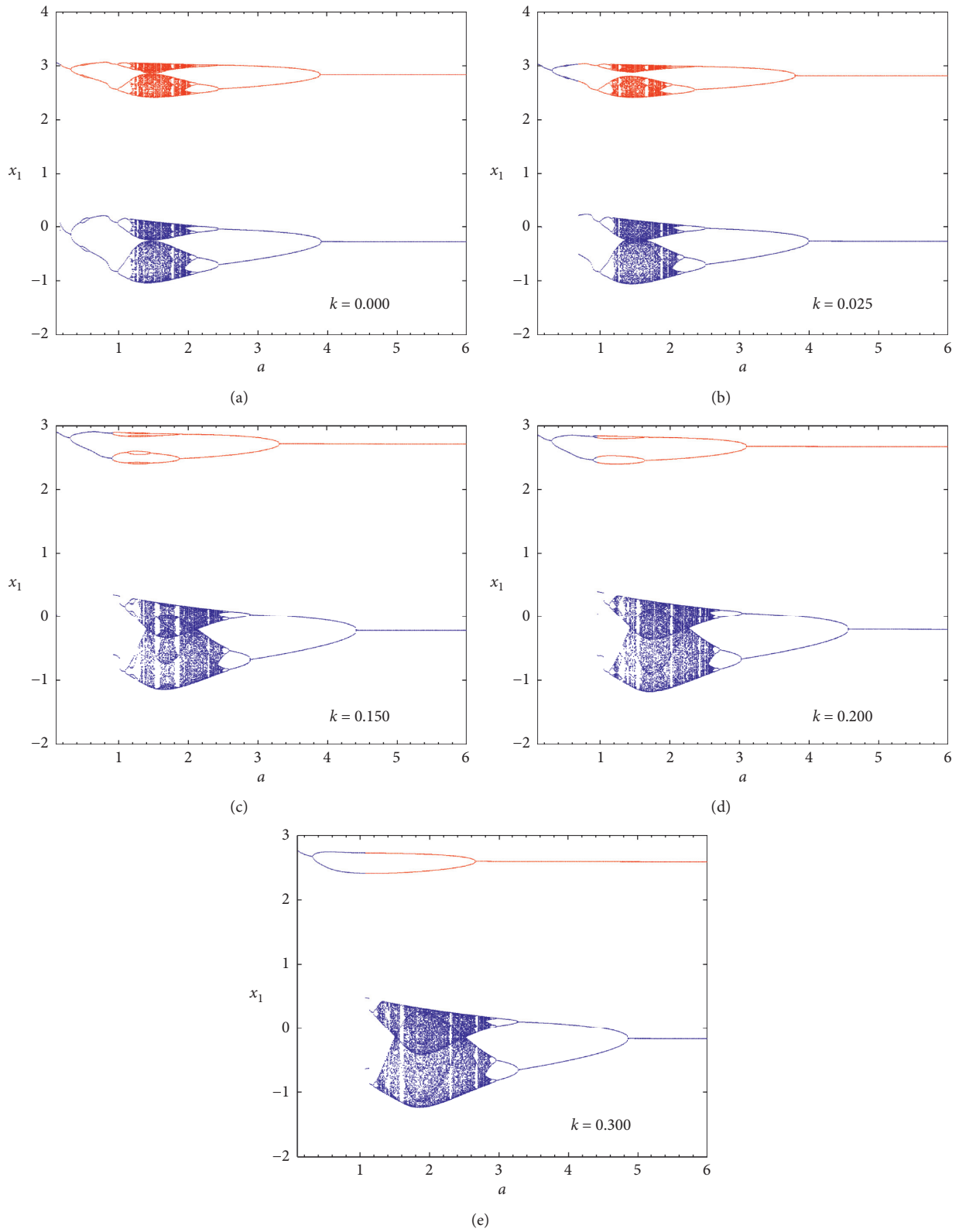


FIGURE 12: Bifurcation diagrams of the coordinate  $x_1$  versus  $a$  showing coexisting bubbles of bifurcation computed for five discrete value of  $k$ , keeping  $\gamma = 1.475$  and  $\mu = 1.0$ . In each diagram, the blue and red branches are obtained by scanning the parameter downward (i.e., downward continuation) starting with initial conditions  $(-0.5, 0, 0)$  and  $(0.5, 0, 0)$ , respectively.



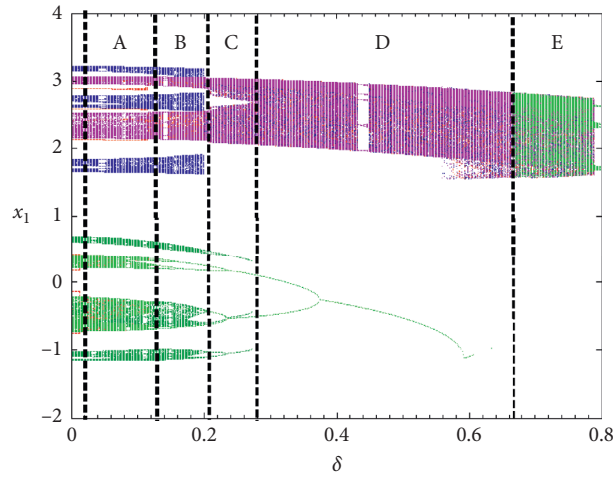


FIGURE 13: Bifurcation diagram illustrating the transition from a multistable state to monostability when smoothly varying the coupling strength in the range  $0 \leq \delta \leq 0.80$ . The rest of parameters are  $a = 17.77$ ,  $\gamma = 1.0$ , and  $\mu = 0.95$ . Regions A, B, C, and D correspond to the coexistence of five, four, three, and two attractors, respectively, while a single attractor is observed in region E. Six sets of data are superimposed. These data are obtained by scanning the parameter upward starting from each of the six coexisting attractors (see text).

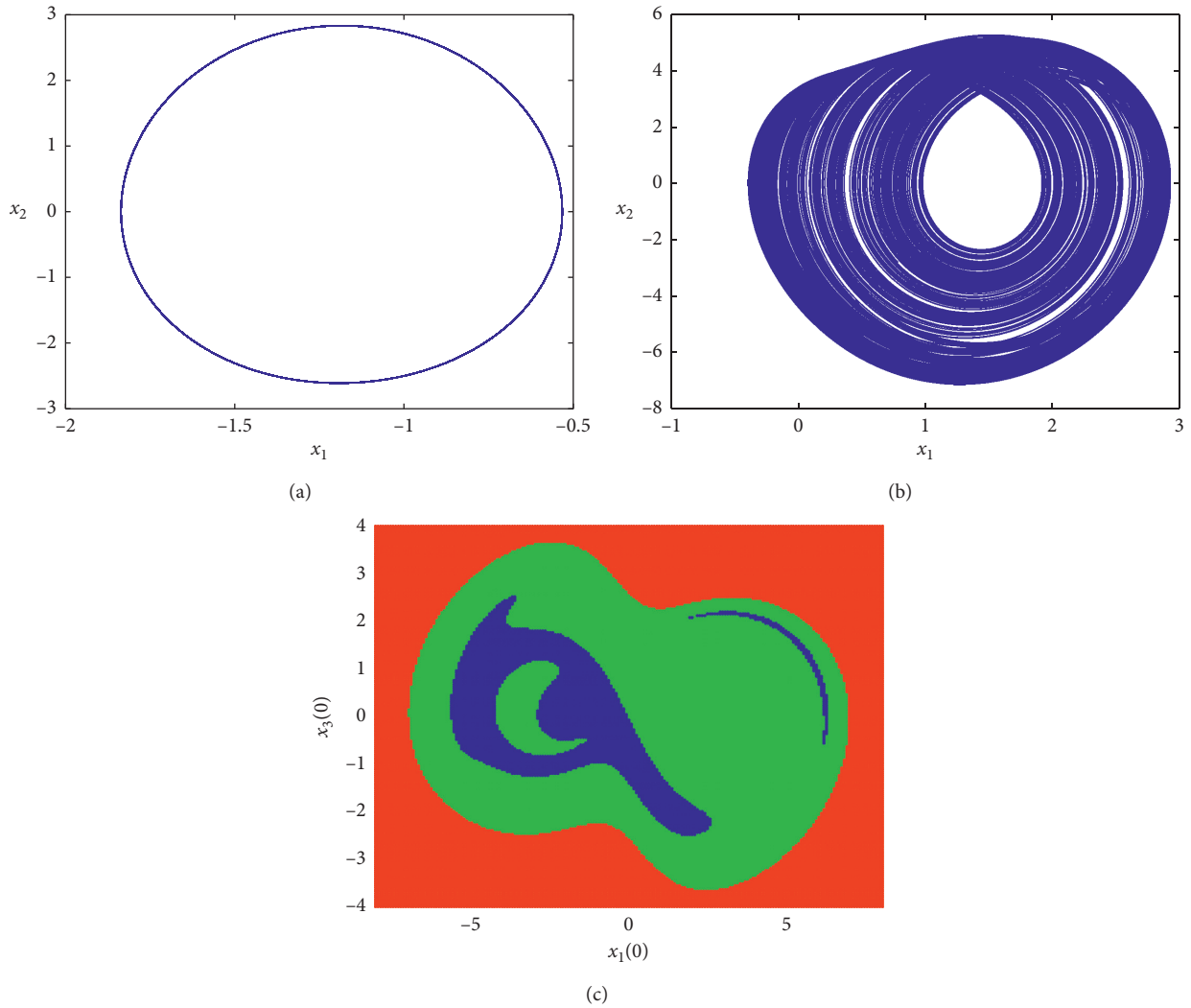


FIGURE 14: Coexistence of two different attractors for  $\delta = 0.50$  using two different initial conditions and corresponding cross section of the basins of attraction. Blue and green basins correspond, respectively, to the period-1 and the chaotic attractor, respectively, while red zone denotes unbounded dynamics. The rest of parameters are same as in Figure 18.

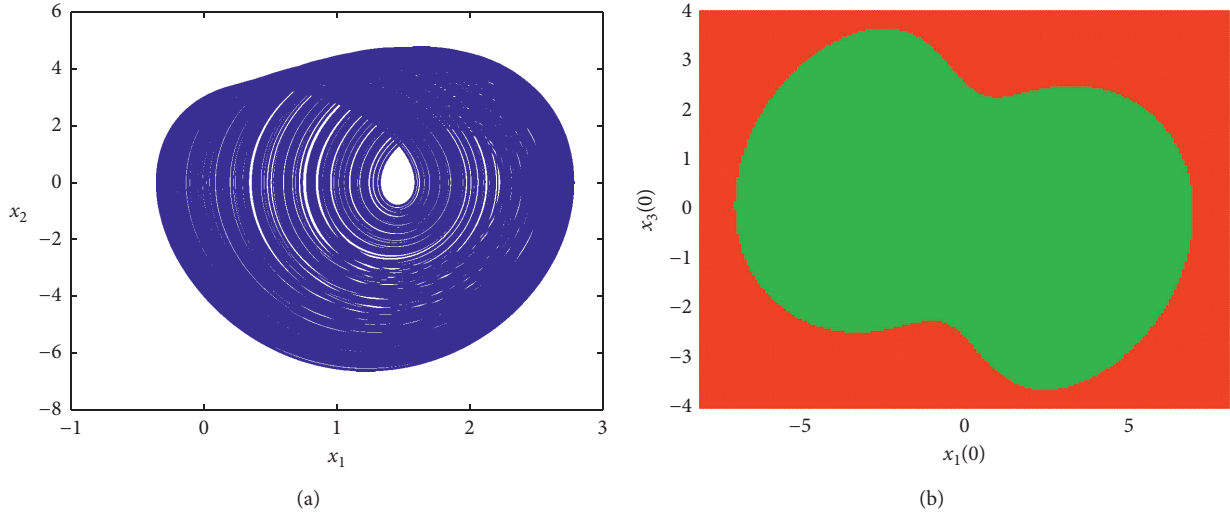


FIGURE 15: A single attractor (a) for  $\delta = 0.75$  and corresponding cross section of the basins of attraction (b). Green zones represent the basin of attraction of the chaotic attractor, while red zone denotes unbounded dynamics. The rest of parameters are same as in Figure 18.

coupled system. To this end, the parameters are fixed as in the caption of Figure 13. The latter figure shows the bifurcation diagrams illustrating the transition from a multistable state (see Figure 10) to monostability when smoothly varying the coupling strength in the range  $0 \leq \delta \leq 0.80$ . Regions A, B, C, and D correspond to the coexistence of five, four, three, and two attractors, respectively, while a single attractor is observed in region E. Six sets of data are superimposed. These data are obtained by scanning the parameter upward starting from each of the six coexisting attractors without resetting the initial conditions. We present in Figures 15 and 16 sample phase portraits of the system (corresponding cross sections of the basins of attraction), highlighting the transition of the system to a monostable state.

## 5. PSpice Simulations

It is predicted from the above results that the jerk system with a single hyperbolic tangent function can undergo extremely varied dynamic behaviors. The design and implementation of a convenient electrical circuit (i.e., the analogue simulator) for the experimental study of the model are presented in this section. PSpice simulation [48] investigations are carried out to check the results of analytical and numerical analyses. The possibility of monitoring capacitors initial voltages and evaluating the corresponding impact on the behavior of the whole circuit represents one of the main advantages of using of PSpice. Interestingly, evidence of several coexisting stable solutions [49–54] in the system may easily be demonstrated both in the symmetric and the asymmetric modes of operation. Moreover, the hardware realization of theoretical chaotic mathematical models is convenient for engineering utilization including, for instance, random signal generation, chaos-based communications, and image encryption.

**5.1. Design of the Experimental Circuit.** The circuit diagram of the proposed electronic simulator is shown in Figures 16(a) and 16(b). The hyperbolic tangent nonlinearity module [53, 54] whose detailed schematic diagram is depicted in Figure 16(b) consists of resistors, a dual-transistor pair, a pair of operational amplifiers, and a dc current source. A detailed analysis of the hyperbolic tangent circuit can be found in [53, 54]. Operational amplifiers and related circuitry (in Figure 16(a)) implement the basic operations of addition, subtraction, and integration. By choosing a suitable time scaling, the simulator outputs can directly be displayed on the screen of a double trace oscilloscope by feeding the output voltage of  $X_1$  to the X input and the output voltage of  $X_2$  to the Y input. With the hypothesis of ideal operational amplifiers operating in their linear regime, upon applying Kirchhoff current and voltage laws to the circuit diagram in Figure 16(a), it can be established that the voltages  $X_1$ ,  $X_2$ , and  $X_3$  satisfy the set of three coupled first-order nonlinear differential equations:

$$\begin{cases} \frac{dX_1}{dt_e} = \frac{X_2}{RC}, \\ \frac{dX_2}{dt_e} = \frac{X_3}{R_a C}, \\ \frac{dX_3}{dt_e} = -\frac{V_{cc}}{R_k C} - \frac{3X_1}{RC} - \frac{X_2}{R_\gamma C} - \frac{X_3}{R_\mu C} + \frac{6 \tanh(X_1)}{RC}. \end{cases} \quad (10)$$

Choosing the following rescale of time and variables:  $t_e = tRC$ ;  $X_k = x_k \times 1V$  ( $k = 1, 2, 3$ ), system (10) is identical to system (1) with the following definition of parameters:

$$a = R/R_a; \quad \gamma = R/R_\gamma; \quad \mu = R/R_\mu; \quad k = \frac{R}{R_k} \frac{V_{cc}}{1V}. \quad (11)$$

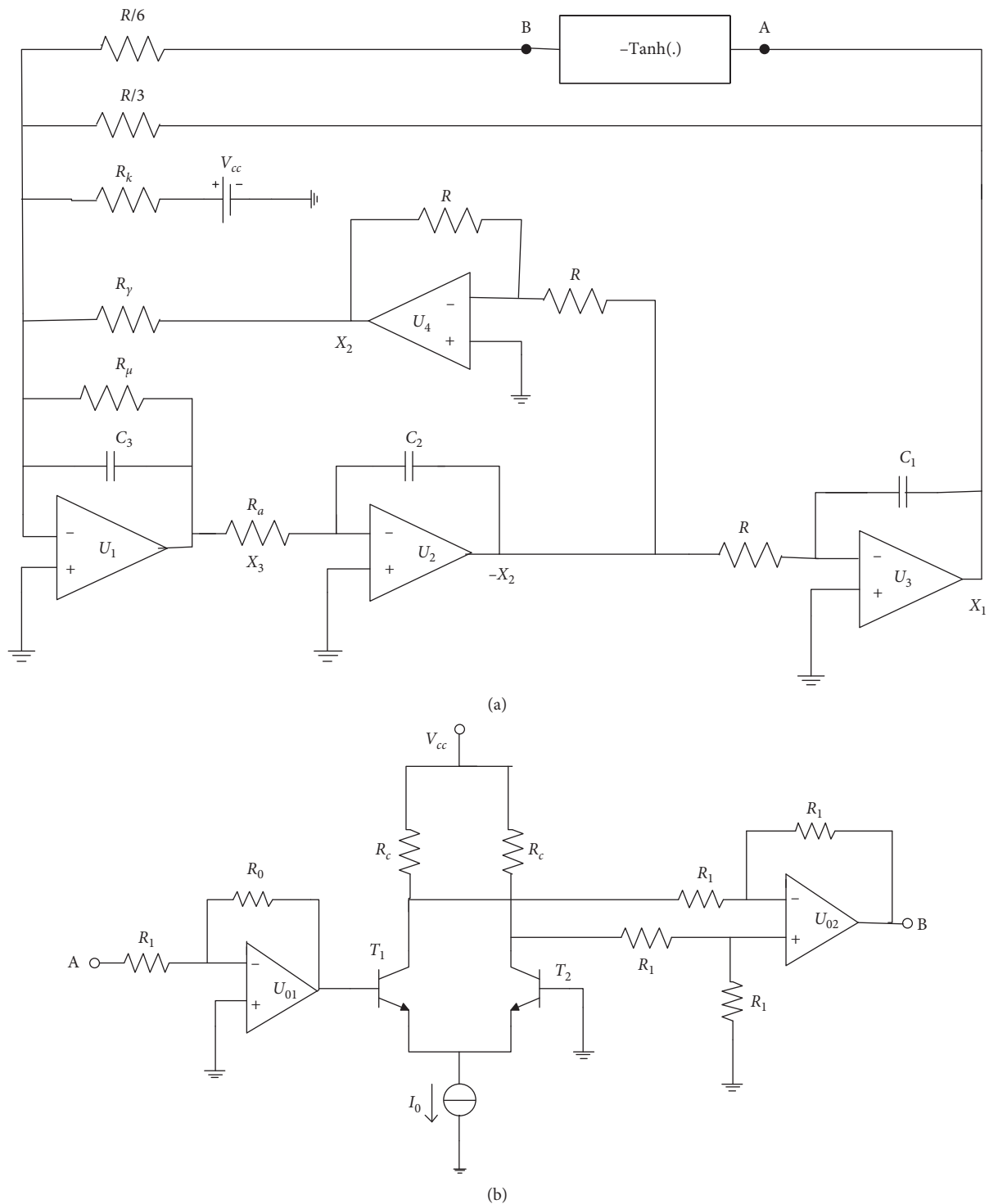


FIGURE 16: Electronic circuit implementation (a) of system. The circuit realization of tangent hyperbolic values function is shown in (b). The values of electronic circuit components used for the analysis are listed in Table 2.

From the above equations, it follows that the dynamics of system (1(a) and 1(b)) can be simulated at any desired frequency (within the bandwidth of op. amplifiers) by choosing the value of the three capacitors.

5.2. PSpice Simulation Results. The behavior of the circuit shown in Figure 16 is studied in PSpice by employing the values of parameters provided in Table 2 in order to check the theoretically predicted results of Section 3, in particular

TABLE 2: The values of electronic components used for PSpice simulations.

Parameters	Signification	Values
$R_0$	Resistance	$0.52K\Omega$
$R_C$	Resistance	$1K\Omega$
$R_1$	Resistance	$10K\Omega$
$R$	Resistance	$12K\Omega$
$R_a$	Tunable resistance	Tunable
$R_\mu$	Resistance	Tunable
$R_y$	Resistance	Tunable
$C_1, C_2, C_3$	Capacitance	$10nF$
$V_{CC}$	Voltage source	$15V_{DC}$
$I_0$	Current source	$1.1mA$
$T_1, T_2$	Amplifier transistors NPN	Q2N2222
$U_i (i = 1, 2, 3, 4)$	Operational amplifiers	TL084
$U_{01}, U_{02}$	Operational amplifiers	TL082

Figure 16 is partially reproduced from (f) [18].

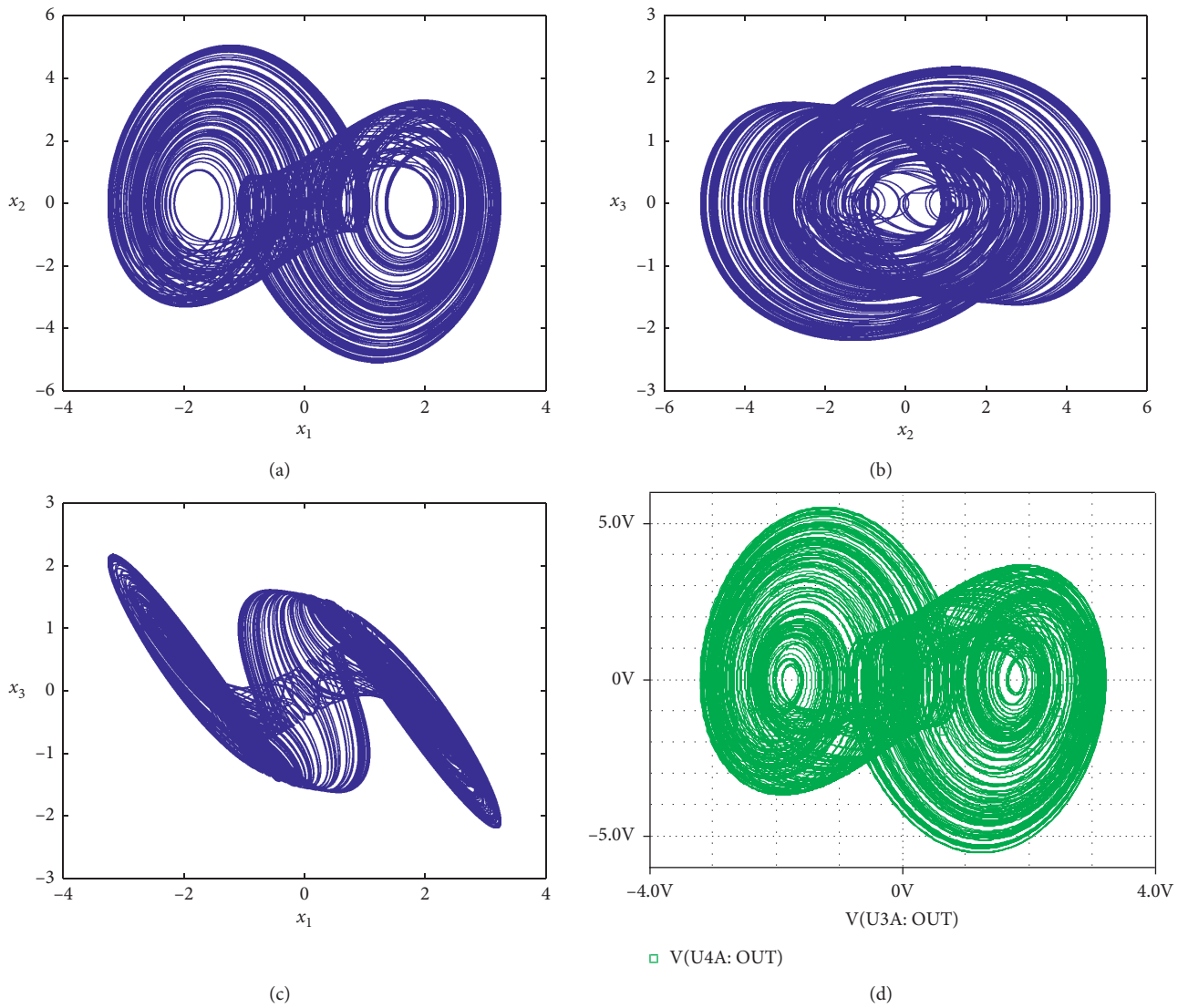


FIGURE 17: Continued.

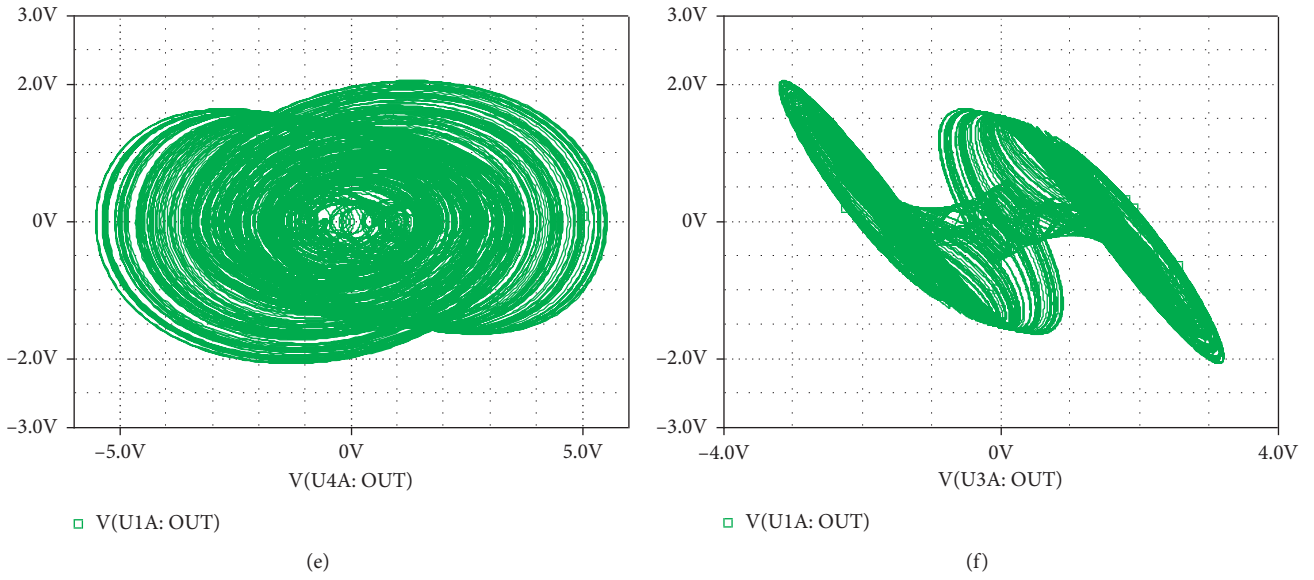


FIGURE 17: Two-dimensional views (left panel) of the symmetric double-scroll chaotic attractors computed for  $a = 5.0$ ,  $\mu = 1.0$ , and  $k = 0.00$  and the corresponding PSpice simulation results (right panel) obtained for  $R_\gamma = 11.13 \text{ k}\Omega$  and  $R_\kappa = \infty$  with the initial point  $(0.5, 0, 0)$ .

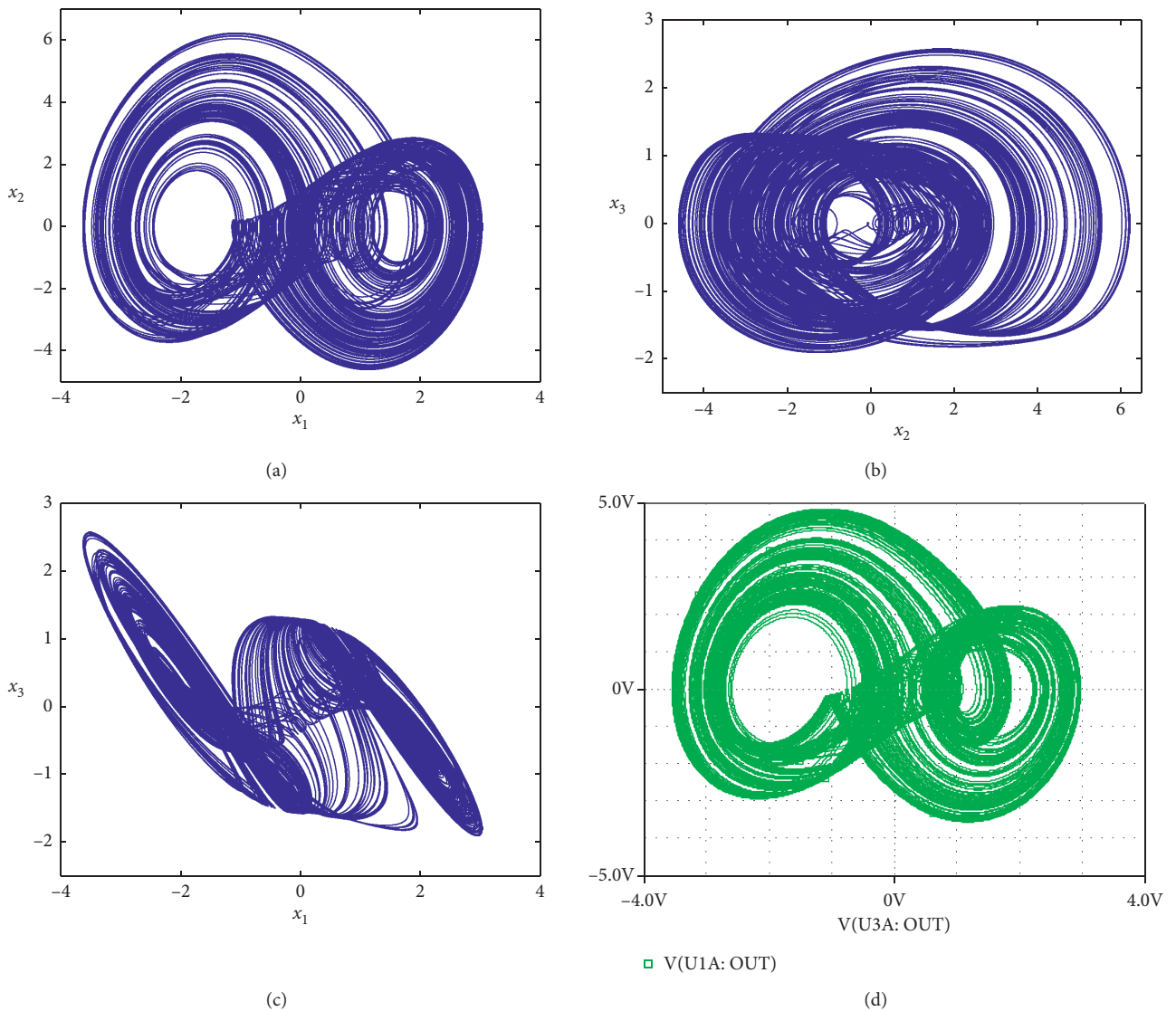


FIGURE 18: Continued.



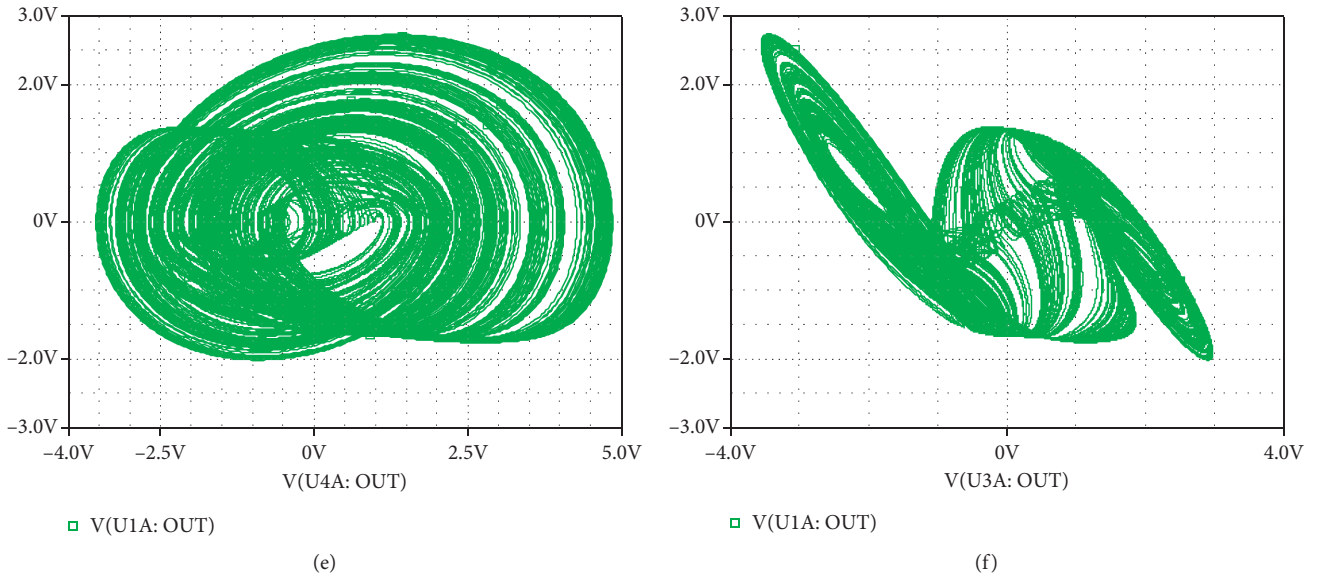


FIGURE 18: Two-dimensional views (left panel) of the asymmetric double-scroll chaotic attractors computed for  $a = 5.0$  and  $k = 0.25$  and the corresponding PSpice simulation results (right panel) obtained for  $R_\gamma = 12\text{ k}\Omega$ ,  $R_k = 576\text{ k}\Omega$ , and  $R_\mu = 12\text{ k}\Omega$  with the initial point  $(0.5, 0, 0)$ .

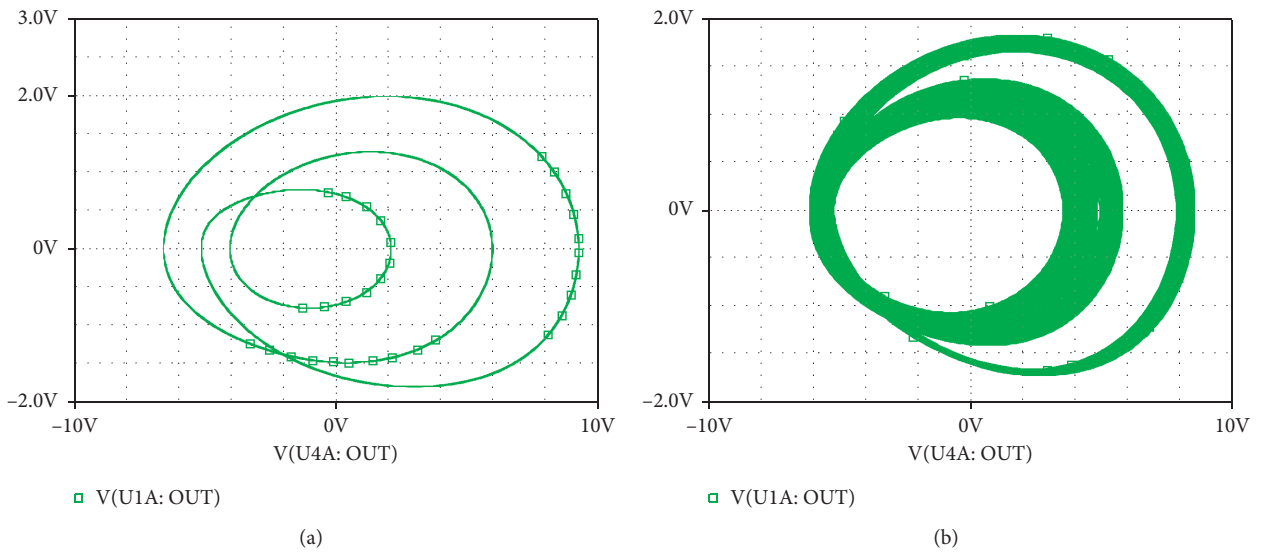


FIGURE 19: Continued.

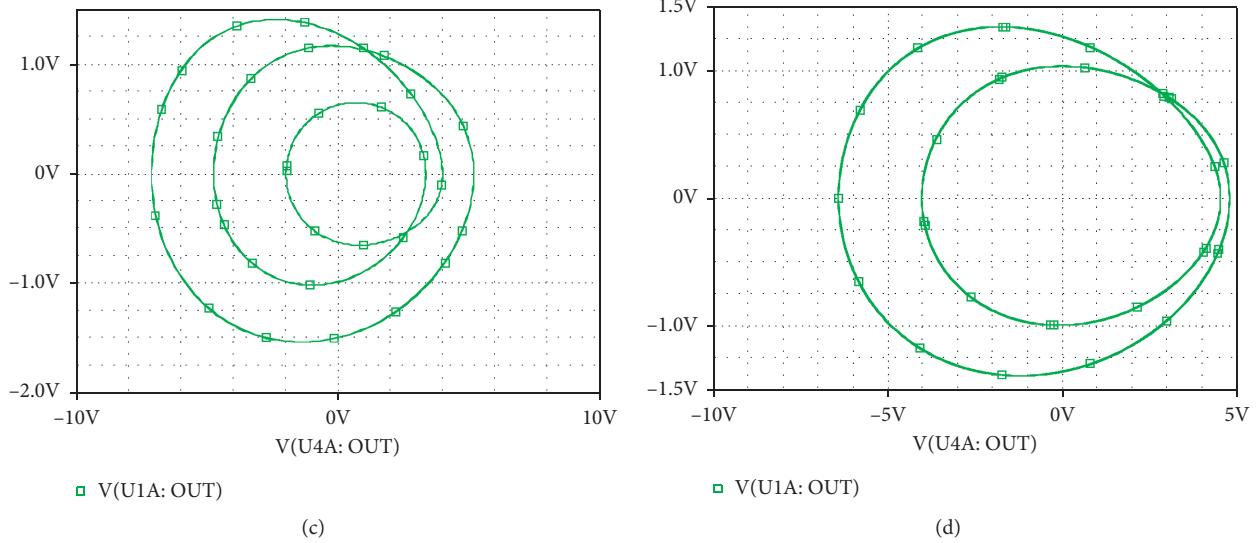


FIGURE 19: PSpice simulation results showing the coexistence of four different asymmetric attractors for  $R_a = 666 \Omega$ ,  $R_\mu = 12.631 \text{ k}\Omega$ ,  $R_\gamma = 12 \text{ k}\Omega$ , and  $R_k = 576 \text{ k}\Omega$  obtained with four different initial conditions  $(v_{c_1}(0), v_{c_2}(0), v_{c_3}(0))$ : (a) a period-3 limit cycle for  $(0.4, 0.0, 0.0)$ ; (b) a chaotic attractor for  $(0.2, 0.0, 0.0)$ ; (c) a period-3 limit cycle for  $(-0.303, 0.0, 0.0)$ ; (d) a period-2 limit cycle for  $(-1.8, 0.0, 0.0)$ .

the period doubling route to chaos and the presence of coexisting bifurcation branches.  $R_\gamma$  (i.e., equivalently parametry) is chosen as main bifurcation control resistor. The electronic components' values ( $R = 12 \text{ k}\Omega$ ,  $R_\mu = 12 \text{ k}\Omega$ ,  $R_a = 2.4 \text{ k}\Omega$ , and  $R_k = \infty$ ; see Table 2) are selected so as to match the dimensionless values ( $a = 5.0$  and  $\mu = 1.00$ ) of Section 3 in view of allowing the comparison between theory and PSpice results. When varying progressive resistor  $R_\gamma$ , we observe the same sequence of bifurcations described in PSpice. Sample results showing the projections of the double-scroll attractor emanating from the merging crisis of coexisting asymmetric mono-scroll chaotic attractors for  $R_\gamma = 11.13 \text{ k}\Omega$  are provided in Figure 17 along with corresponding theoretical ones. Similarly, Figure 18 depicts various projections of the asymmetric double-scroll chaotic attractor obtained in PSpice (right panel) and the corresponding theoretically obtained ones (left panel) when the control resistors are fixed as  $R_\gamma = 12 \text{ k}\Omega$ ,  $R_k = 576 \text{ k}\Omega$ ,  $R_a = 2.4 \text{ k}\Omega$ , and  $R_\mu = 12 \text{ k}\Omega$ . The bifurcation sequences observed in PSpice perfectly agree with those of theoretical studies carried out in Section 3. On the contrary, using the electronic component values fixed as  $R_\gamma = 12 \text{ k}\Omega$ ,  $R_k = 576 \text{ k}\Omega$ ,  $R_a = 666 \Omega$ , and  $R_\mu = 12.631 \text{ k}\Omega$ , we have observed the coexistence of four different asymmetric attractors, namely, a pair of asymmetric period-3 cycles, a period-2 cycle, and a chaotic attractor when starting the system from four different initial conditions (see Figure 19). The latter situation is identical to the case reported in Figure 8 during the theoretical analysis. We have avoided the inclusion of other cases of multistability obtained in PSpice for the sake of brevity. We would like to point out the existence of some small shifts in the values of the control resistor  $R_\gamma$  in PSpice in comparison to the theoretically predicted values. Such discrepancies are mainly due to the

unavoidable simplifications adopted during the modeling step of the analogue simulator (e.g., ideal bipolar junction transistor model and ideal op. amplifier model, in comparison with more realistic/complex models implemented in PSpice).

## 6. Concluding Remarks

In summary, this paper has explored the dynamics of a simple chaotic jerk system with hyperbolic tangent non-linearity whose symmetry is destroyed by the adding a constant term acting as an external excitation force. We have shown that the modified system exhibits several unusual and interesting nonlinear patterns such as coexisting bifurcation branches, hysteretic behaviors, coexisting symmetric and asymmetric bubbles, critical phenomena, and multiple (i.e., two, three, four, five, or six) coexisting asymmetric attractors for some appropriately chosen sets of its parameters. These features were illustrated by exploiting common nonlinear analysis tools such as graphs of largest Lyapunov exponent, bifurcation diagrams, phase portraits, and basins of attraction. The control of multistability based on the linear augmentation scheme is exploited to tune the system from the state of six coexisting attractors to monostability. An appropriate electronic analogue of the system was designed and simulated in PSpice. The theoretical results show a very good agreement with the PSpice simulation investigations.

The model considered in this work can be regarded as prototypal autonomous 3D system with three rest points and an odd symmetry. Also, we conjecture that the dynamics induced by symmetry break observed in this work may also be found when using the jerk equation with other types of nonlinearities (e.g., cubic, quintic, hyperbolic sine, and piece-wise quadratic). Moreover, the extension of the

analysis presented in this paper to cases of other chaotic oscillators such as Chua's, Shinriki, autonomous van der Pol-Duffing, and hyperjerk circuits is under consideration.

## Data Availability

The data used to support the findings of this study are available from the corresponding author upon request.

## Conflicts of Interest

The authors declare that there are no conflicts of interest.

## References

- [1] S. H. Strogatz, *Nonlinear Dynamics and Chaos Reading*, Addison-Wesley, Boston, MA, USA, 1994.
- [2] Y. A. Kuznetsov, *Elements of Applied Bifurcation Theory*, Springer-Verlag, New York, NY, USA, 1995.
- [3] A. H. Nayfeh and B. Balachandran, *Applied Nonlinear Dynamics: Analytical, Computational and Experimental Methods*, John Wiley & Sons, New York, NY, USA, 1995.
- [4] J. C. Sprott, *Elegant Chaos: Algebraically Simple Flow*, World Scientific Publishing, Singapore, 2010.
- [5] S. Jafari and J. C. Sprott, "Simple chaotic flows with a line equilibrium," *Chaos, Solitons & Fractals*, vol. 57, pp. 79–84, 2013.
- [6] S. Jafari, J. C. Sprott, and M. Molaie, "A simple chaotic flow with a plane of equilibria," *International Journal of Bifurcation and Chaos*, vol. 26, no. 6, p. 1650098, 2016.
- [7] V. T. Pham, S. Jafari, C. Volos, A. Giakoumis, S. Vaidyanathan, and T. Kapitaniak, "A chaotic system with equilibria located on the rounded square loop and its circuit implementation," *IEEE Transactions on Circuits and Systems II: Express Briefs*, vol. 63, no. 9, pp. 878–882. In Press, 2016.
- [8] V.-T. Pham, S. Jafari, C. Volos, S. Vaidyanathan, and T. Kapitaniak, "A chaotic system with infinite equilibria located on a piecewise linear curve," *Optik*, vol. 127, no. 20, pp. 9111–9117, 2016.
- [9] V.-T. Pham, S. Jafari, J. Ma, X. Wang, and J. Ma, "A Chaotic system with different shapes of equilibria," *International Journal of Bifurcation and Chaos*, vol. 26, no. 4, p. 1650069, 2016.
- [10] A. N. Pisarchik and U. Feudel, "Control of multistability," *Physics Reports*, vol. 540, no. 4, pp. 167–218, 2014.
- [11] C. Kahlert, "The effects of symmetry breaking in Chua's circuit and related piecewise-linear dynamical systems," *Int. J. of Bif. and Chaos*, vol. 3, no. 4, pp. 963–979, 1993.
- [12] S. K. Dana, S. Chakraborty, and G. Ananthakrishna, "Homoclinic bifurcation in Chua's circuit," *Pramana Journal of Physics*, vol. 64, no. 3, p. 44344, 2005.
- [13] A. Sofroniou and S. R. Bishop, "Breaking the symmetry of the parametrically excited pendulum," *Chaos, Solitons & Fractals*, vol. 28, no. 3, pp. 673–681, 2006.
- [14] S. R. Bishop, A. Sofroniou, and P. Shi, "Symmetry-breaking in the response of the parametrically excited pendulum model," *Chaos Solitons and Fractals*, vol. 25, no. 2, pp. 27–264, 2005.
- [15] R. Rynio and A. Okniński, "Symmetry breaking and fractal dependence on initial conditions in dynamical systems: ordinary differential equations of thermal convection," *Chaos, Solitons & Fractals*, vol. 9, no. 10, pp. 1723–1732, 1998.
- [16] H. Cao and Z. Jing, "Chaotic dynamics of Josephson equation driven by constant dc and ac forcings," *Chaos, Solitons & Fractals*, vol. 12, no. 10, pp. 1887–1895, 2001.
- [17] M. Henrich, T. Dahms, V. Flunkert, S. W. Teitsworth, and E. Scholl, "Symmetry breaking transitions in networks of nonlinear circuits elements," *New Journal of Physics*, vol. 12, Article ID 113030, 2010.
- [18] J. Kengne, S. M. Njikam, and V. R. F. Signing, "A plethora of coexisting strange attractors in a simple jerk system with hyperbolic tangent nonlinearity," *Chaos, Solitons & Fractals*, vol. 106, pp. 201–213, 2018.
- [19] J. C. Sprott, "A new chaotic jerk circuit," *IEEE Transactions on Circuits and Systems II: Express Briefs*, vol. 58, no. 4, pp. 240–243, 2011.
- [20] P. Louodop, M. Kountchou, H. Fotsin, and S. Bowong, "Practical finite-time synchronization of jerk systems: theory and experiment," *Nonlinear Dynamics*, vol. 78, no. 1, pp. 597–607, 2014.
- [21] J. Kengne and R. L. T. Mogue, "Dynamic analysis of a novel jerk system with composite tanh-cubic nonlinearity: chaos, multi-scroll, and multiple coexisting attractors," *International Journal of Dynamics and Control*, vol. 7, no. 1, pp. 112–133, 2018.
- [22] J. Kengne, V. R. F. Signing, J. C. Chedjou, and G. D. Leutcho, "Nonlinear behavior of a novel chaotic jerk system: anti-monotonicity, crises, and multiple coexisting attractors," *International Journal of Dynamics and Control*, vol. 6, no. 2, pp. 468–485, 2017.
- [23] J. Kengne, Z. T. Njitacke, and H. B. Fotsin, "Dynamical analysis of a simple autonomous jerk system with multiple attractors," *Nonlinear Dynamics*, vol. 83, no. 1-2, pp. 751–765, 2016.
- [24] S. Sedra and K. C. Smith, *Microelectronic Circuits*, Oxford University Press, London, UK, 2003.
- [25] N. Özkurt, F. A. Savaci, and M. Gündüzalp, "The circuit implementation of a wavelet function approximator," *Analog Integrated Circuits and Signal Processing*, vol. 32, no. 2, pp. 171–175, 2002.
- [26] D. Biswas and T. Banerjee, "A simple chaotic and hyperchaotic time-delay system: design and electronic circuit implementation," *Nonlinear Dynamics*, vol. 83, no. 4, pp. 2331–2347, 2016.
- [27] W. Horton, R. S. Weigel, and J. C. Sprott, "Chaos and the limits of predictability for the solar-wind-driven magnetosphere-ionosphere system," *Physics of Plasmas*, vol. 8, no. 6, pp. 2946–2952, 2001.
- [28] F. R. Tahir, R. S. Ali, V.-T. Pham, A. Buscarino, M. Frasca, and L. Fortuna, "A novel 4D autonomous 2  $\vec{n}$  -butterfly wing chaotic attractor," *Nonlinear Dynamics*, vol. 85, no. 4, pp. 2665–2671, 2016.
- [29] J. Kengne, Z. T. Njitacke, N. A. Nguomkam, T. M Fouodji, and H. B. Fotsin, "Coexistence of multiple attractors and crisis route to chaos in a novel chaotic jerk circuit," *International Journal of Bifurcation and Chaos*, vol. 25, no. 4, Article ID 1550052, 2015.
- [30] Z. T. Njitacke, J. Kengne, H. B. Fotsin, A. N. Negou, and D. Tchiotop, "Coexistence of multiple attractors and crisis route to chaos in a novel memristive diode bidge-based Jerk circuit," *Chaos, Solitons & Fractals*, vol. 91, pp. 180–197, 2016.
- [31] V. Kirk and A. M. Rucklidge, "The effect of symmetry breaking on the dynamics near a structurally stable heteroclinic cycle between equilibria and a periodic orbit," *Dynamical Systems*, vol. 23, no. 1, pp. 43–74, 2008.
- [32] J. Porter and E. Knobloch, "Dynamics in the 1:2 spatial resonance with broken reflection symmetry," *Physica D: Nonlinear Phenomena*, vol. 201, no. 3-4, pp. 318–344, 2005.

- [33] R. Lauterbach, "Symmetry breaking in dynamical systems," in *Nonlinear Dynamical Systems and Chaos 1996; Progress in Nonlinear Differential Equations and Their Applications*, H. W. Broer, S. A. van Gils, I. Hoveijn, and F. Takens, Eds., Vol. 19, Birkhäuser, Basel, Switzerland, 1996.
- [34] C. Li and J. C. Sprott, "Amplitude control approach for chaotic signals," *Nonlinear Dynamics*, vol. 73, no. 3, pp. 1335–1341, 2013.
- [35] C. Li, J. C. Sprott, A. Akgul, H. C. Lu, and Y. Zhao, "A new chaotic oscillator with free control," *Chaos*, vol. 27, Article ID 083101, 2017.
- [36] G. A. Leonov and N. V. Kuznetsov, "Hidden attractors in dynamical systems. From hidden oscillations in Hilbert-Kolmogorov, Aizerman, and Kalman problems to hidden chaotic attractor in Chua circuits," *International Journal of Bifurcation and Chaos*, vol. 23, no. 1, Article ID 1330002, 2013.
- [37] G. A. Leonov, N. V. Kuznetsov, and T. N. Mokaev, "Hidden attractor and homoclinic orbit in Lorenz-like system describing convective fluid motion in rotating cavity," *Communications in Nonlinear Science and Numerical Simulation*, vol. 28, no. 1-3, pp. 166–174, 2015.
- [38] A. Wolf, J. B. Swift, H. L. Swinney, and J. A. Vastano, "Determining Lyapunov exponents from a time series," *Physica D: Nonlinear Phenomena*, vol. 16, no. 3, pp. 285–317, 1985.
- [39] S. P. Dawson, C. Grebogi, J. A. Yorke, I. Kan, and H. Koçak, "Antimonotonicity: inevitable reversals of period-doubling cascades," *Physics Letters A*, vol. 162, no. 3, pp. 249–254, 1992.
- [40] U. Parlitz and W. Lauterborn, "Period-doubling cascades and devil's staircases of the driven van der Pol oscillator," *Physical Review A*, vol. 36, no. 3, pp. 1428–1434, 1987.
- [41] L. Kocarev, K. S. Halle, K. Eckert, and L. O. Chua, "Experimental observation of antimonotonicity in chua's circuit," *International Journal of Bifurcation and Chaos*, vol. 3, no. 4, pp. 1051–1055, 1993.
- [42] I. M. Kyprianidis, I. N. Stouboulos, P. Haralabidis, and T. Bountis, "Antimonotonicity and chaotic dynamics in a fourth-order autonomous nonlinear electric circuit," *International Journal of Bifurcation and Chaos*, vol. 10, no. 8, pp. 1903–1915, 2000.
- [43] M. Bier and T. C. Bountis, "Remerging Feigenbaum trees in dynamical systems," *Phys Lett A*, vol. 104, pp. 239–244, 1994.
- [44] B. Bao, L. Xu, N. Wang, H. Bao, Q. Xu, and M. Chen, "Third-order RLCM-four-elements-based chaotic circuit and its coexisting bubbles," *AEU - International Journal of Electronics and Communications*, vol. 94, pp. 26–35, 2018.
- [45] P. R. Sharma, A. Singh, A. Prasad, and M. D. Shrimali, "Controlling dynamical behavior of drive-response system through linear augmentation," *The European Physical Journal Special Topics*, vol. 223, pp. 1531–1539, 2015.
- [46] P. R. Sharma, M. D. Shrimali, A. Prasad, N. V. Kuznetsov, and G. A. Leonov, "Control of multistability in hidden attractors," *The European Physical Journal Special Topics*, vol. 224, no. 8, pp. 1485–1491, 2015.
- [47] P. R. Sharma, M. D. Shrimali, A. Prasad, N. V. Kuznetsov, and G. A. Leonov, "Controlling dynamics of hidden attractors," *International Journal of Bifurcation and Chaos*, vol. 25, no. 4, pp. 1–7, 2015.
- [48] D. C. Hamill, "Learning about chaotic circuits with SPICE," *IEEE Transactions on Education*, vol. 36, no. 1, pp. 28–35, 1993.
- [49] Z.-H. Guan, Q. Lai, M. Chi, X.-M. Cheng, and F. Liu, "Analysis of a new three-dimensional system with multiple chaotic attractors," *Nonlinear Dynamics*, vol. 75, no. 1-2, pp. 331–343, 2014.
- [50] Q. Lai and S. Chen, "Generating multiple chaotic attractors from sprott B system," *International Journal of Bifurcation and Chaos*, vol. 26, no. 11, p. 1650177, 2016.
- [51] Q. Lai, A. Akgul, X.-W. Zhao, and H. Pei, "Various types of coexisting attractors in a new 4D autonomous chaotic system," *International Journal of Bifurcation and Chaos*, vol. 27, no. 9, p. 1750142, 2017.
- [52] B. C. Bao, Q. D. Li, N. Wang, and Q. Xu, "Multistability in Chua's circuit with two stable node-foci," *Chaos*, vol. 26, no. 4, Article ID 043111, 2016.
- [53] S. Duan and X. Liao, "An electronic implementation for Liao's chaotic delayed neuron model with non-monotonous activation function," *Physics Letters A*, vol. 369, no. 1-2, pp. 37–43, 2007.
- [54] S. Duan and L. Wang, "A novel delayed chaotic neural model and its circuitry implementation," *Computers & Mathematics with Applications*, vol. 57, no. 11-12, pp. 1736–1742, 2009.

## Research Article

# An Efficient and Cost-Effective Power Scheduling in Zero-Emission Ferry Ships

Armin Letafat,<sup>1</sup> Mehdi Rafiei,<sup>2</sup> Masoud Ardehshiri,<sup>1</sup> Morteza Sheikh,<sup>2</sup> Mohsen Banaei ,<sup>3</sup> Jalil Boudjadar,<sup>4</sup> and Mohammad Hassan Khooban <sup>4</sup>

<sup>1</sup>Department of Electronics and Electrical Engineering, Islamic Azad University, Kazerun Branch, Kazerun, Iran

<sup>2</sup>Department of Electrical and Electronic Engineering, Shiraz University of Technology, Shiraz, Iran

<sup>3</sup>Faculty of Engineering, Ferdowsi University of Mashhad, P.O. Box 91775-1111, Mashhad, Iran

<sup>4</sup>Department of Engineering, Aarhus University, Aarhus 8200, Denmark

Correspondence should be addressed to Mohammad Hassan Khooban; mhkhoban@gmail.com

Received 7 November 2019; Revised 6 February 2020; Accepted 25 February 2020; Published 17 April 2020

Guest Editor: Viet-Thanh Pham

Copyright © 2020 Armin Letafat et al. This is an open access article distributed under the Creative Commons Attribution License, which permits unrestricted use, distribution, and reproduction in any medium, provided the original work is properly cited.

Today's remarkable challenge of maritime transportation industry is the detrimental contamination generation from fossil fuels. To tackle such a challenge and reduce the contribution into air pollution, different power solutions have been considered; among others, hybrid energy-based solutions are powering many ferry boats. This paper introduces an energy management strategy (EMS) for a hybrid energy system (HES) of a ferry boat with the goal to optimize the performance and reduce the operation cost. HES considered for the ferry boat consists of different devices such as proton exchange membrane fuel cell (PEMFC), LI-ION battery bank, and cold ironing (CI). PEMFC systems are appropriate to employ as they are not polluting. The battery bank compensates for the abrupt variations of the load as the fuel cell has a slow dynamic against sudden changes of the load. Also, CI systems can improve the reduction of the expenses of energy management, during hours where the ferry boat is located at the harbor. To study the performance, cost and the pollution contribution ( $\text{CO}_2$ ,  $\text{NO}_x$ ,  $\text{SO}_x$ ) of the proposed hybrid energy management strategy (HEMS), we compare it against three various types of HEM from the state-of-the-art and also available rule-based methods in the literature. The analysis results show a high applicability of the proposed HES. All results in this paper have been obtained in the MATLAB software environment.

## 1. Introduction

Renewable energy resources (RESs) have received growing attention in supplying the required energy of different systems during the last years. The marine industry has also been affected by this trend. Application of renewable and clean energies for supplying the required energy of the marine vessels like small ships and boats is growing and this has led to introducing the concept of Electric Ferry Boats (EFBs) in the marine industry. Different combinations of fossil fuel-based resources and RESs such as diesel generators (DGs), fuel cells (FCs), solar panels, storage batteries (SBs), and cold ironing (CI) [1–3] can be used in the EFBs for supplying the demand and providing the propulsion force of these boats. In this situation, optimal energy management of

the EFB is an important subject from the viewpoint of both ship owners and reliability concerns that should be considered to reduce the operation cost while considering the operation constraints of the equipment.

Optimal energy management of the marine vessels has been studied before in the literature. The authors of [4] provided an energy management schedule in the electric ship according to the Model Predictive Control (MPC) to optimize the concordance between power generators and batteries' energy-saving under high-power ramp rate loads. The authors of [5] proposed manner-based energy management by means of Fuzzy Logic (FL) and Proportional-Integration (P-I) control in an all-electric ship with only electric storage devices. Abkenar et al. [6] apply a genetic algorithm to find the proper and safe operation of fuel cells



in an electric ship with fuel cells and energy storage system. A subhourly energy management technique based on MPC has been employed for electric ships in an integrated power network having a variety of equipment such as FC, battery, photovoltaic cells, and two DGs [7]. Tang et al. [8] propose an optimal energy resources scheduling model for a large green ship supplied with diesel, battery, photovoltaic, and cold ironing. Different constraints of the model are involved in the objective function and hence, an unconstrained, large-scale, global optimization method is applied to solve the optimization problem. In [9], a nonlinear programming approach is used to find the optimal energy management of an all-electric ship supplied with a hybrid storage system. Optimal power resources scheduling of a ship with diesel generators and batteries alongside a combined cooling and heat power plant is formulated in [10]. The dynamic programming approach is used in [11] to solve the energy management problem of EFB with an energy storage system. Rule-based is applied in [12] to perform the energy management for a ship with a hybrid FC and battery energy system. Applying this method leads to a straightforward lookup table method which cannot necessarily lead to an optimal solution. Particle Swarm Optimization (PSO) algorithm is utilized in [13] for energy management of the shipboard loads. Hou et al. [14] solve the optimal energy management of a hybrid energy storage system for tracking the energy fluctuations of the shipboard loads. In [15], integrated perturbation analysis and sequential programming algorithms and MPC methods are used to solve the energy management problem of a boat with hybrid ultracapacitors and batteries. Optimal power allocation for a hybrid diesel engine and electric motor is performed for a ship without an energy storage system in [16].

There are also some studies in the literature that focus on each equipment of the EFBs such as CI possibility, pollution control, FCs characteristics, and application of solar panels and wind turbines in the EFBs. CI is one of the practical, beneficial energy generation sources to supply power during the ship berthing onshore or harbor where the energy requirements of the ship are provided through the port's connection of the ship to the Microgrids (MGs) or power networks located onshore. Nevertheless, CI has a low pollution rate [17, 18]. Over recent years, different studies have been conducted to optimize the utilization of CI. For instance, in [19], significant effects of the CI on the bus voltages and power quality of the Electrical and Distribution Network around Coast Zone have been investigated. The authors of [20] introduce a CI technology to assess the air pollution due to the presence of a ferry boat in port and a cost-benefit analysis to evaluate the profit quantity of the socioeconomic "Copenhagen-Denmark."

To minimize the perilous air pollutant, suspended particles ( $CO_2$ ,  $NO_x$ , and  $SO_x$ ), particularly the sulfur reduction rate, as well as component expenses of the system, a combined coast-side power source CI with liquefied natural gas (LNG) has been provided in [21]. Furthermore, in [21], an optimization algorithm based on a nonlinear model was implemented to find the best way for costs and emission terms.

FC is another energy generation source to satisfy the load demand of EMSs [22, 23]. Generally, the system operation of the FCs is based on a transform process, wherein the chemical energy is converted into electrical power [24]. Universally, FCs with various chemical fuels and distinguishing features have been deployed in maritime transportation and power electrical industry including low and high-temperature polymer membrane fuel cell (LT-HT-PEMFC), phosphoric acid fuel cell (PAFC), and solid oxide fuel cell (SOFC) [25]. Nonetheless, multiple disparate works have been carried out in previous studies on FCs. For instance, proton exchange membrane fuel cell (PEMFC) is a process, in which two elements such as oxygen and hydrogen are used for anode and cathode electrodes of the FC's cells to generate power. Zero emission, fast launch, high productivity and power density, low noise and operating temperature, and solid electrolyte are the several important features of the PEMFC.

In order to increase the ship power efficiency, a hybrid fuel cell system by considering several schedules is provided in [26] to decrease the rate of fuel or total energy consumption of the hybrid system. The authors of [27] studied the level of safety and hazardous operability of the molten carbonate fuel cell tanker in nautical systems. Moreover, FL approach has been applied for Failure Mode and Effect Analysis (FMEA) in the presence of FC with molten carbon fuel and gas turbine system for liquefied hydrogen tanker in the marine driven technology [28].

Considering the environmental protection as another important issue in the maritime transportation industry, many research efforts have been devoted to reduce the underlying pollution during recent years. The use of renewable energy sources, such as photovoltaic (PV) and wind turbine, is one of the alternatives that have been proposed. On the contrary, these sources, due to the weather dependency, cannot handle the total power of the ship during peak loads. Thus, to deal with this scenario, other renewable or fossil fuel resources must be used to provide energy. Batteries can also be used parallel to the PV and wind turbines to increase the efficiency of the systems with renewable energy resources [29]. This process will be accompanied by operation cost and environmental contamination.

Reviewing the abovementioned studies shows that there is a gap in the literature in the field of optimal daily energy management of EFBs with FCs as the main source of energy and batteries alongside with the CI. Most of the research studies that are performed in the field of marine vessels are focused on the ships with diesel generators such as [4, 7, 8] and [10], which are not categorized in the field of zero-emission boats. Some of the studies in the field of energy management for zero-emission EFBs consider only the energy storage systems as the main energy resource of the boats like [5, 9] and [11]. On the contrary, the design and application of zero-emission EFBs with the hybrid of FCs and batteries as the main energy resources have received growing attention during the last years. While there are some studies in the field of this type of ships such as [6, 12], these studies perform the energy management for short time intervals and their main goals are satisfying the dynamic constraints of the equipment.

In this paper, an optimal hybrid energy management strategy (HEMS) for an EFB with the FCs as the main energy resource, batteries, and possibility of CI at the harbors is proposed. The goal is obtaining an optimal power scheduling for the FCs, batteries, and CI that minimizes the total operation cost while considering the different operation constraints of the equipment. The characteristics of the proposed test system are adopted from practical research performed in [30, 31]. The capacities of FC systems are considered such that they can supply the total load power of the ship at any weather condition independently. The battery banks installed on the ship will compensate for the unexpected variations of the load because of the FC system slow dynamic. Moreover, the CI system can supply the ship's load power during the existence of the ship at the harbor, at hours where the price of CI system energy is lower than the price of FC system energy. In order to compare the simulation results of the proposed test system with other available hybrid energy systems for the boats, three different types of the energy systems that are based on the fossil fuel as the main energy resource are modeled and compared with the proposed model in this paper. Plus, the rule-based method introduced in [12] is also modeled and its results are compared with the proposed method.

The rest of this paper is organized as follows. Section 2 describes the topology of the electrical ferry boat. Section 3 expresses the hybrid energy management of the ship, including FC, battery, and CI. Finally, simulation results and conclusion are presented in Sections 4 and 5, respectively.

## 2. The Topology of the Electrical Ferry Boat Description

The topology of the proposed hybrid energy system for the considered ferry boat is illustrated in Figure 1 [30, 31]. This work considers a ferry boat equipped with two PEMFC systems with 200 kW and a PEMFC system with 100 kW capacity. In addition, 20 hydrogen reservoirs with 18.8 kg content from Luxer-GMT with 5,000 psi equivalent to 350 bar at high-pressure gas have been embedded on the ship which are adequate for one operational day without refueling. Also, the mentioned ferry boat has two electromotors with 250 kW rated power for each one. Furthermore, a room consisting of batteries is necessary to save and manage the power generation surplus of FC output after setting up the FC system on the ship. LI-ION batteries with 200 kWh charge capacity (two 100 kWh units) are utilized in the ferry boat to load power compensation. The FCs can continuously produce power along with the 24-hour duration because the FC installation on the ship is without any affiliation to the weather conditions. Therefore, no other renewable energy or fossil fuel sources are needed to supply the ship's loads. Since the total load demand of the ferry boat is met by FCs on an hourly basis, the battery bank installed on the ship requires low power for load supply. This has led to using a small size battery. Thus, employing the battery bank with a small size and not using the fossil fuel resource lead to a significant reduction in the exploitation cost of ship's hybrid energy system and air pollution as well. Ergo, the hybrid energy management strategy (HEMS), is carried out in the presence of FC and battery bank, while the

ship is in sailing conditions. Nevertheless, the electric load requirement of the vessel is directly supplied through FC output and the excess of FC power is utilized to feed the battery room. FCs have slow dynamics; therefore, they cannot supply the unanticipated overload in hours with load abrupt variation. Hereupon, the batteries with a fast dynamic can be an appropriate choice to compensate for the power shortage caused by load variation. In this regard, the batteries can receive the energy through the surplus energy of FC and deliver the power to feed the vessel's load.

Table 1 represents the high-speed ferry boat technical specifications. However, all this information may not be necessary for performing the daily energy management of this boat. In order to model the different equipment in the energy management system, (1) the PEMFC systems are considered as a single FC system with a capacity equal to the sum of the generation capacities of all PEMFC systems, (2) all the batteries are considered as a single battery with the capacity of the sum of the capacities of available batteries in the boat, and (3) total load including electromotor load and shipboard loads are modeled as a single load.

## 3. Hybrid Energy Management Strategy of the Ship

As mentioned before, the goal of this paper is proposing an optimal energy management model for the understudy EFB that minimizes the operation cost and satisfies the operation constraints of the equipment. To this end, first, the objective function is presented, and then the operation constraints of FCs, batteries, and CI are modeled separately. Before starting the formulation, the power flow of the ship in the case that the boat is sailing and the case that the boat is at the harbor is described. Figure 2 indicates the power flow of the system when the boat is sailing.  $P_1$  is the generated power by the FCs that is consumed by the boat loads.  $P_2$  is the generated power of the FCs that is charged in the batteries. The sum of  $P_1$  and  $P_2$  represents the total generated power by the FCs.  $P_3$  is the discharged power by the batteries to the boat loads.

When the ship is at the harbor, the CI can also be performed. Figure 3 represents this situation.  $P_4$  is the consumed power the boat loads through the CI and  $P_5$  represents the stored energy in the batteries through CI.

**3.1. Objective Function.** Operation costs of the understudy zero-emission EFB are the cost of buying the required hydrogen for FCs plus the cost of the CI in the hours that the ship is at harbor. Moreover, a cost related to the degradation rate of the batteries is also considered in the models [8]. This cost is modeled by multiplying a predefined price ( $C_b$ ) by the amount of discharged power of the batteries during the operation horizon. So, the total operation cost of the EFB is formulated as follows:

$$C_T = \sum_{t=1}^{24} (C_H \times M_H(t) + \rho(t) \times (P_4(t) + P_5(t)) + C_b \times P_3(t)). \quad (1)$$

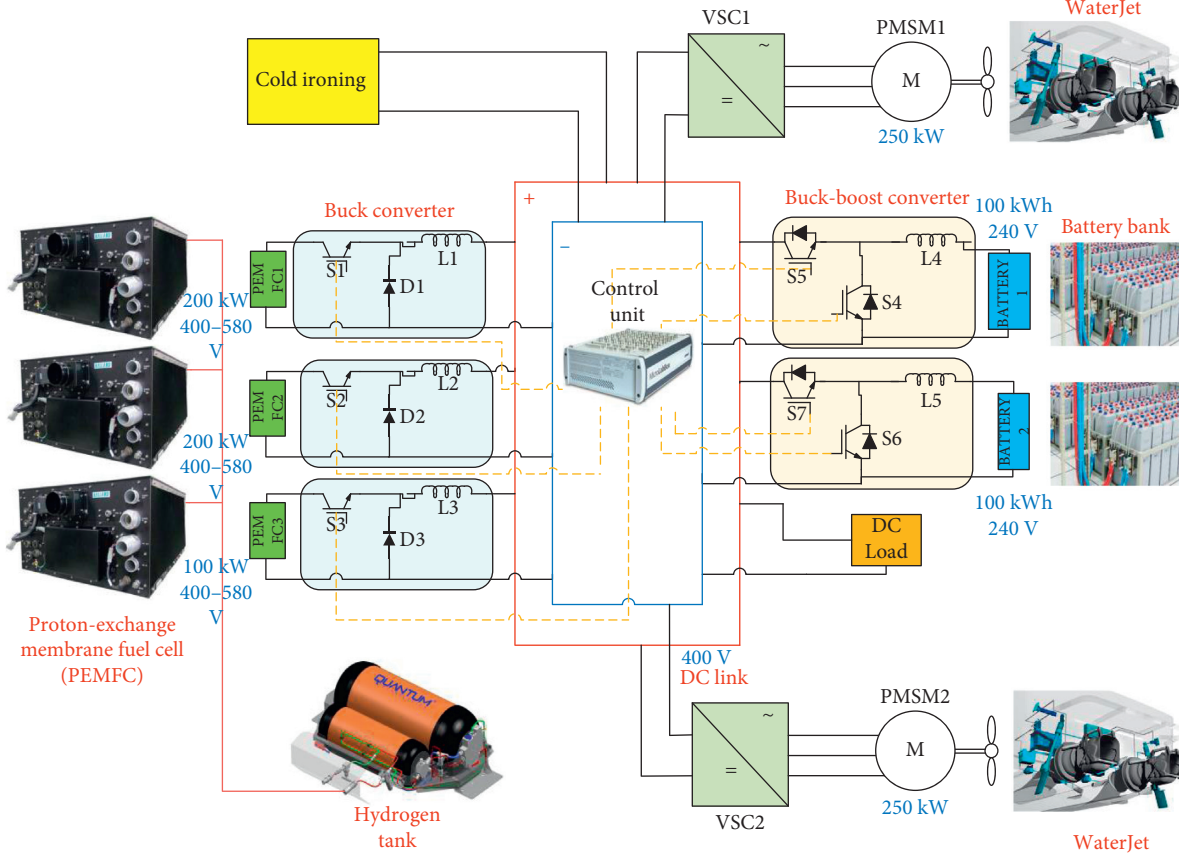


FIGURE 1: The proposed circuit of the hybrid energy system.

TABLE 1: Technical characteristics of the PEM fuel cell-battery hybrid system.

Type	High-speed passenger ferry
Overall length	24.5 m
Beam	8 m
Average speed	25.3 knots (47.2 km/h)
Maximum speed	32.5 knots (60.67 km/h)
Distance	8 nm
Total voyage time	9 hours
Fuel cell power	2 PEMFC of 200 kW each and a PEMFC of 100 kW
Hydrogen price	1.35 (\$/kg)
Average shaft power	235.41 kW
Main engine power (MEP)	500 kW
Hydrogen fuel (kg)	376
Hydrogen per tank (kg)	18.8
Number of tanks	20
Battery capacity (kWh)	200
Battery charge efficiency	85%
Battery discharge efficiency	100%
Initial state of charge	85 kWh
Minimum allowable capacity ( $S_{\min}$ )	60 kWh (30% of the battery capacity)
Maximum allowable capacity ( $S_{\max}$ )	170 kWh (85% of the battery capacity)
Total investment cost of battery banks ( $F$ )	3562 \$

First term of objective function is the cost of consuming  $M_H(t)$  mass of hydrogen in the price of  $C_H$ . Second term is the cost of buying  $(P_4(t) + P_5(t))$  kWh energy in the price of  $\rho(t)$  through the CI and third term refers to the degradation rate of the batteries.

3.2. Fuel Cell Operation Cost and Constraints. The price of buying hydrogen is assumed to be known. The mass of consumed hydrogen in each hour of the day should be found. To this end, the relation between the generated power and output power of the FCs and the relation between the

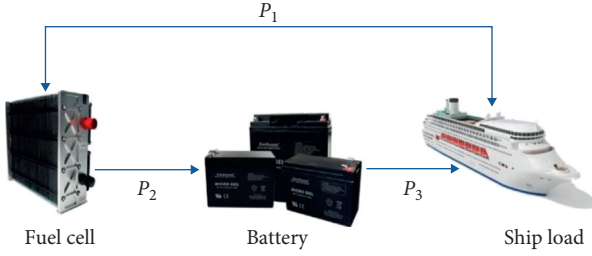


FIGURE 2: FC/battery/ship's load topology.

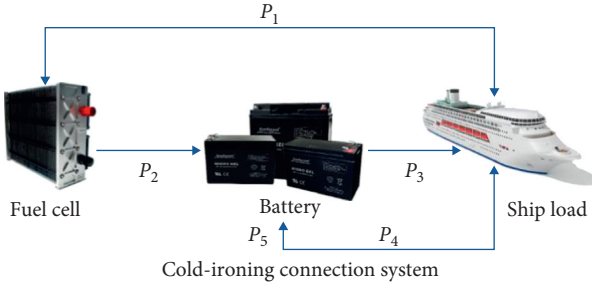


FIGURE 3: The topology of the fuel cell-battery-cold ironing.

generated power of the FCs and consumed mass of hydrogen are used. The efficiency formula is used to find the relation between the generated power and output power of the FCs. The efficiency curve of the FCs is presented in Figure 4. According to Figure 4, the efficiency of the FCs varies by changing the loading of the FCs. For the sake of simplicity, this curve is estimated by a fixed value for efficiency that according to references [32, 33] is 0.45. The relation between the generated power of the FCs and the consumed mass of hydrogen is written using the conversion coefficient that is equal to 0.03 (kg/kWh). So, the relation between the total output power of the FCs, i.e.,  $P_1 + P_2$ , and the consumed mass of the hydrogen is written as follows:

$$M_H(t) = \frac{P_1(t) + P_2(t)}{0.45} \times 0.03. \quad (2)$$

The output power of the FCs is limited to the maximum nominal output power of all FCs. In addition, the output power of the FCs is positive. Below constraint is defined to consider these limitations:

$$0 \leq P_1(t) + P_2(t) \leq P_{FC}^{\max}, \quad (3)$$

$$P_1(t) \geq 0, \quad (4)$$

$$P_2(t) \geq 0. \quad (5)$$

**3.3. Cold-Ironing Cost and Constraints.** CI is an electrical energy transmission system which is used to supply the required power of the ship equipment. The power is transmitted from the coast outlet to the ship and devices such as batteries. So, CI is considered in the aforesaid power flow dispatching, when the ferry ship or vessel is at the harbor.

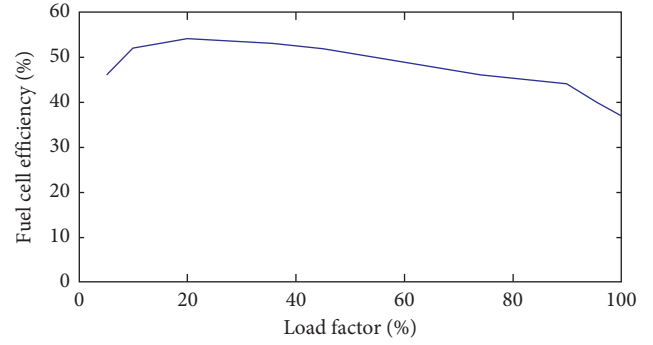


FIGURE 4: PEMFC efficiency curve.

In this work, the electricity price changes in the CI system are given over different hours of the day. The high, average, and low prices are considered for the peak, standard, and off-peak hours, respectively. In this regard, the workaday electricity price of CI is defined in equation (6) as follows:

$$\rho(t) = \begin{cases} \rho_p, & t \in [7.10) \cup [18.20), \\ \rho_s, & t \in [6.7) \cup [10.18) \cup [20.22), \\ \rho_o, & t \in [0.6) \cup [22.24), \end{cases} \quad (6)$$

where the CI system price at  $t^{\text{th}}$  hour is denoted by  $\rho(t)$ . The  $\rho_p$ ,  $\rho_s$ , and  $\rho_o$  demonstrate the price for peak, standard, and off-peak hours and are presented in Table 2.

Since the CI is possible just in the case that the boat is at the harbor, the injected power by CI is considered equal to zero when the boat is sailing. So, the constraint below is considered in the model:

$$P_4(t) = 0 \text{ in hours that the boat is sailing,} \quad (7)$$

$$P_5(t) = 0 \text{ in hours that the boat is sailing.} \quad (8)$$

**3.4. Batteries Degradation Cost and Operation Constraints.** Charging and discharging power of the battery bank are determined through the FC power generated and load demand at given hour  $t$ .  $t$  is an integer demonstrating the  $t^{\text{th}}$  hour. One of the main challenges for modeling the batteries' operation is determining the value of the price that is considered for the batteries in (1), i.e.,  $C_b$ . This cost refers to the degradation rate of the batteries and tries to reduce the aging rate of the batteries as much as possible. Studies show that this cost is mostly dependent on the discharged power of the batteries. Hence, only discharged power is considered in the objective function (1). In many studies in the literature, a constant value is assigned to this cost [18, 34]. This paper also considers a constant value for this price. The proposed method in [8] is used to determine the proper value for  $C_b$ . In [8], the concept of Depth of Discharge (DoD) and rainflow approach is used to calculate the  $C_b$ . In this method, first, for a dispatching plan, the SOC profile of the batteries is estimated. Then, the cycles of SOC profile is determined, and the DoD of each cycle ( $D_{w_i}$ ) is calculated using the proposed

TABLE 2: HEMS assessed parameter.

Parameter	Value
Cold ironing price for peak period ( $\rho_p$ )	0.31538 \$/kWh
Cold ironing price for standard period ( $\rho_s$ )	0.15948 \$/kWh
Cold ironing price for low period ( $\rho_o$ )	0.06558 \$/kWh

method in [35]. Finally, the formulations below are used to calculate the  $C_b$ :

$$C_b = \sum_{w=1}^l \frac{F}{N_w}, \quad (9)$$

wherein  $F$  is the total investment cost of battery banks.  $N_w$  is calculated by equation (10) as follows:

$$N_w = -3278D_W^4 - 5D_W^3 + 12823D_W^2 - 14122D_W + 5112, \quad (10)$$

$l$  is the number of charging and discharging cycles calculated through the rainflow approach, and  $D$  and  $N_w$  are the discharge depth and cycle lifetime, respectively [35].  $C_b$  obtained in (9) is used in (1) as a constant to consider the operation cost related to the batteries.

The batteries state of charge (SOC) at any hour  $t$ ,  $S(t)$ , depends on the SOC at the prior hour  $S(t-1)$ . The following situation must be considered for the energy flows from  $t-i$  to  $t$ . The hourly battery SOC will be achieved via equations (11) and (12) [34].

Under sail,

$$S(t) = S(t-1) + \eta_c P_2(t) - \frac{1}{\eta_d} P_3(t). \quad (11)$$

At anchor,

$$S(t) = S(t-1) + \eta_c [P_2(t) + P_5(t)] - \frac{1}{\eta_d} P_3(t), \quad (12)$$

wherein both  $\eta_c$  and  $\eta_d$  represent the charging and discharging efficiency of the batteries, respectively. Considering equations (12) and (13), the current SOC can be expressed through the initial SOC  $S(0)$  of a day in equations (13) and (14).

Under sail,

$$S(t) = S(0) + \eta_c \sum_{W=0}^{t-1} P_2(W) - \frac{1}{\eta_d} \sum_{W=0}^{t-1} P_3(W). \quad (13)$$

At anchor,

$$S(t) = S(0) + \eta_c \sum_{W=0}^{t-1} [P_2(W) + P_5(W)] - \frac{1}{\eta_d} \sum_{W=0}^{t-1} P_3(W). \quad (14)$$

The total energy storage of the battery bank should not be less than the minimum  $S_{\min}$  and higher than the maximum  $S_{\max}$  permissible capacity. This theorem is described in relation (15) as follows:

$$S_{\min} \leq S(t) \leq S_{\max}. \quad (15)$$

**3.5. Power Generation and Consumption Balance Constraints.** Equations (16) and (17) define the power flow when the ship is at anchorage and under sail.

Under sail,

$$P_1(t) + P_3(t) + P_5(t) = PL(t), \quad (t = 1, 2, \dots, N). \quad (16)$$

At anchor,

$$P_1(t) + P_3(t) = PL(t), \quad (t = 1, 2, \dots, N). \quad (17)$$

In equations (16) and (17),  $PL(t)$  is the electrical load demand of the vessel at  $t^{\text{th}}$  hour.

Proposed formulation (1)–(17) represents a linear model for the optimization problem of energy management in the zero-emission EFB. MATLAB software is used to solve this problem. By solving this problem, optimal hourly scheduling of FCs, batteries, and CI systems is obtained.

## 4. Simulation Results and Analysis

In this section, first, the proposed case study results are compared with the results of the four different case studies of hybrid energy systems of ferry boats. Then, the proposed optimization method is compared with the proposed rule-based method in reference [12] for hybrid FC/battery ferry boat.

**4.1. Comparing the Energy Management Results for Different Case Studies.** In this section, energy management, operation cost, and pollution rate results of the proposed hybrid FC/battery ferry boat are compared with three other hybrid energy system cases presented in [8]. The energy resources related to the first case study include diesel generator/cold ironing (CI). The energy systems used in the second case study are diesel generator/battery and CI. The third case study consists of hybrid energy systems such as the photovoltaic (PV)/battery/diesel generator/CI. These cases are modeled using the proposed method in [8]. In order to formulate the models in cases 1–3, optimization problems similar to the proposed formulation (1)–(17) in this paper are used considering the fact that FCs' variables, cost, and constraints are replaced by the variables, cost, and constraints of diesel generators and PV similar to the proposed method in [8]. The proposed model in this paper is also considered as the fourth case in the following simulations. It is well worth mentioning that the 24-hour profile of the ship's load power considered for four case studies is the same. Figure 5 shows the profile of the load power of the ship. The traveling scenario (including under-sail and at-anchor hours) is the same for all four cases. The ferry boat is located in the anchor at hours (1 to 8), (13 to 16), and (20 to 24), and for the rest of the hours the ship is patrolling on the sea.

In the first case study, since the ferry boat is just equipped with a diesel generator, CI will supply a portion of the load power of the ferry boat during the hours where the ship is at anchor and receive the energy from the diesel generator while the ship is patrolling on the sea. However, this scenario leads to cost and air pollution enhancement. The results of case 1 are depicted in Figure 6.



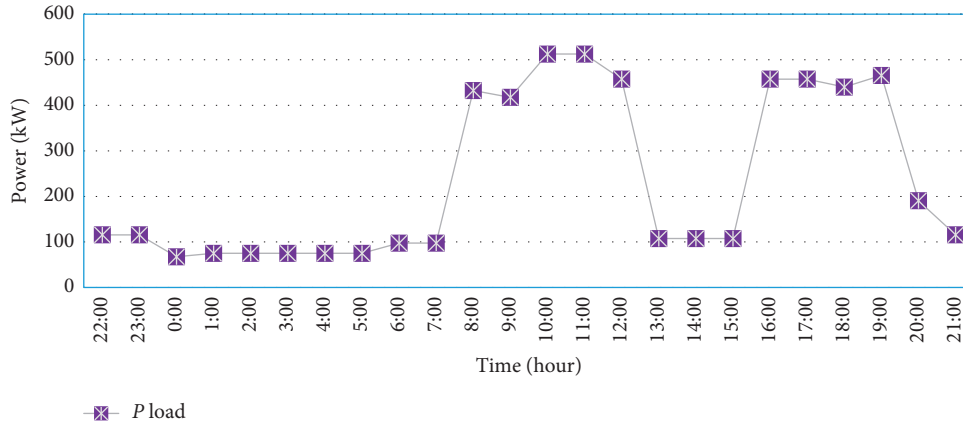


FIGURE 5: Ship's load power profile for 24 hours.

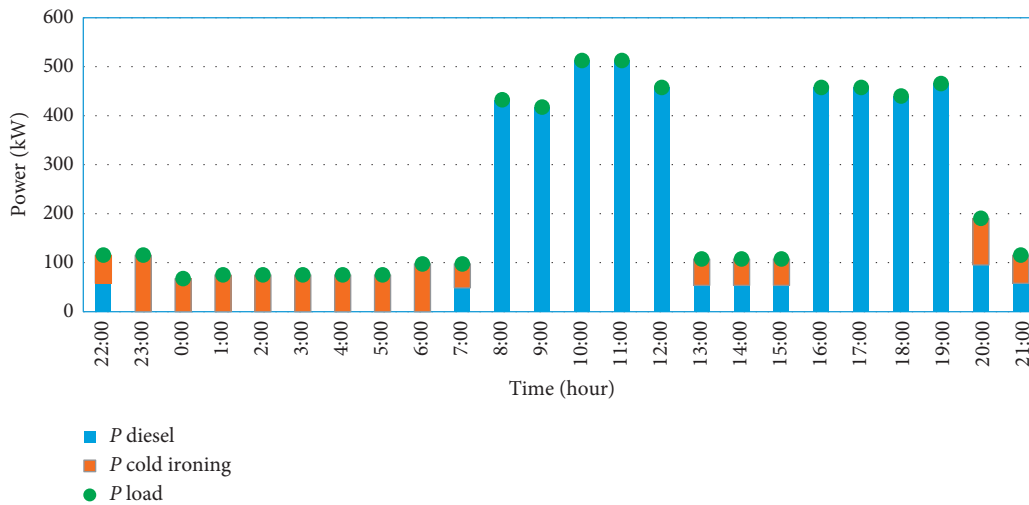


FIGURE 6: Hybrid energy management system case 1.

The battery bank considered for the second case study provides the part of the load power of the ship at some hours, wherein the pollution rate and cost have been reduced in comparison to the first case study, although the total operation cost due to the battery bank installation will increase. Figure 7 demonstrates the simulation results of case 2. As shown in Figure 7, in this case, the battery charges in hour 1:00 and discharges in hour 7:00.

The PV available in the third case study covers the part of the consumption power of the ship without using the fossil fuel which leads to decrease in the generated power rate through the diesel generator. Under such condition, the total cost of the energy supply and ecological contamination will decrease compared to the first and second cases, although the generated pollution rate due to the energy management used in the third case is high. The size of PV is considered equal to 7 kWh. Figure 8 shows the results related to case 3.

The management strategy applied for cases 1–3 is according to the process wherein the needed load of the ship is provided through the CI system at hours, and the energy price received from the CI system is cheaper than the diesel system, during the presence of the ship at anchor. On the

other hand, if the energy price received from the diesel generator is cheaper than CI system, at least 50% of the load power is supplied via CI system because of the ecological contamination diesel generator function. Under such conditions, the rest of the load power is provided by the diesel generator.

HEMS of case 4 is investigated and related results are depicted in Figures 9–12. Figure 9 illustrates the generated power of all resources in the boat. Except for the hours when the ship is at anchor in port, the power generated by FC ( $P_1$ ) provides all needed load power of the ship at per hours without the use of renewable energy resources or other fossil fuel to handle the ship's load power. In addition, a part of generated power by FC system is used for the charging of the battery banks ( $P_2$ ). Since the FC systems have slow dynamics against the unexpected variations of the load power, ergo, the battery banks embedded on the ship, because of their fast dynamic, should compensate and cover the load abrupt changes. In this respect, the energy management strategy is considered somehow; at least 10 percent of the ship's load power is provided through the battery banks discharging power ( $P_3$ ), during the hours that FC is supplying the needed

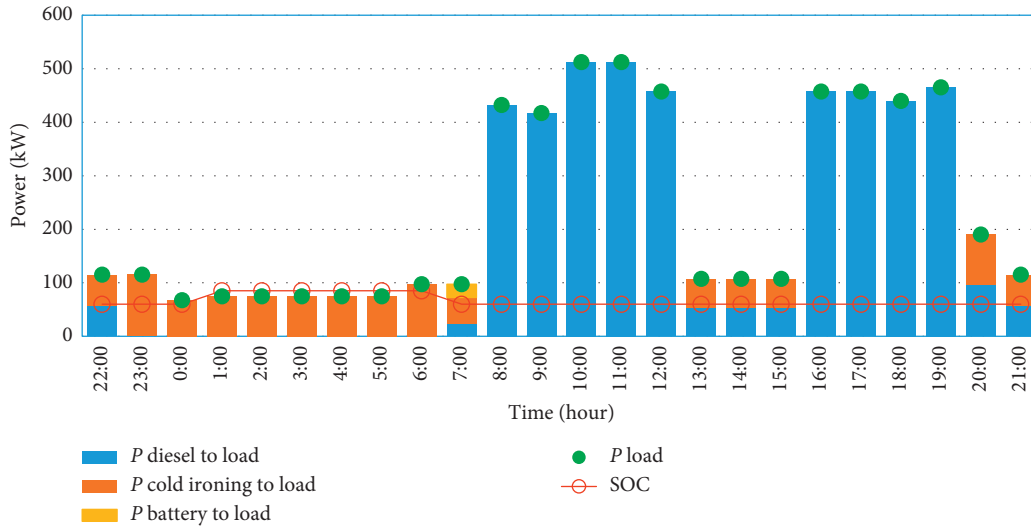


FIGURE 7: Hybrid energy management system case 2.

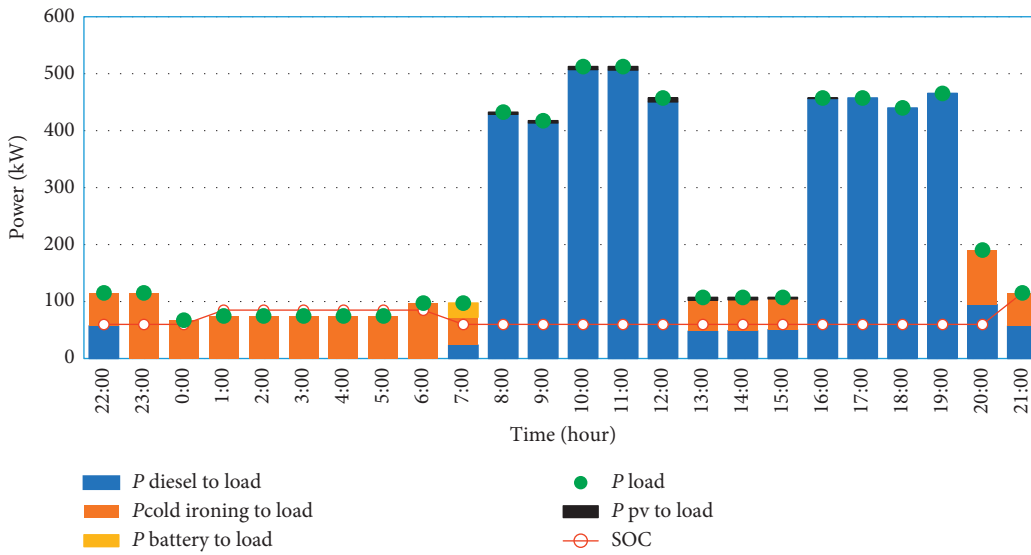


FIGURE 8: Hybrid energy management system case 3.

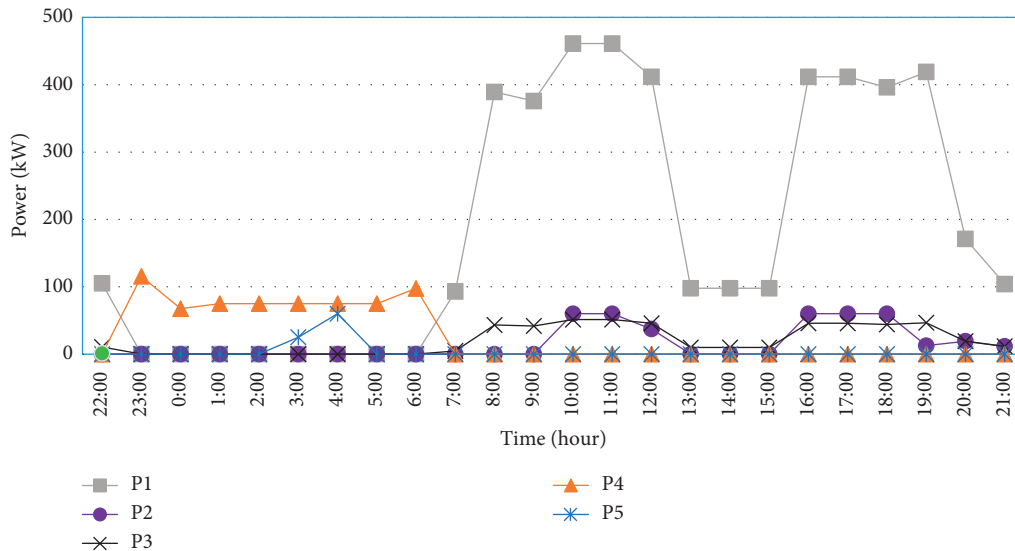


FIGURE 9: Hybrid energy management system in case 4.  $P_1$  and  $P_4$  illustrate the power flow from the fuel cell and cold ironing to feed the load and  $P_2$  and  $P_5$  demonstrate the power flow from the fuel cell and cold ironing to charge the battery bank and the  $P_3$  is discharge power of the battery.

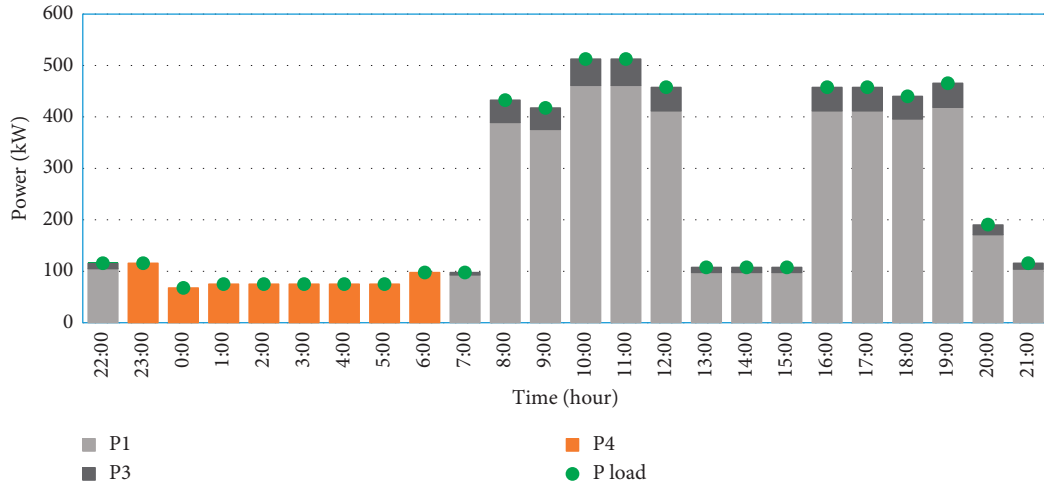


FIGURE 10: Injected power to the load by different resources in case 4.

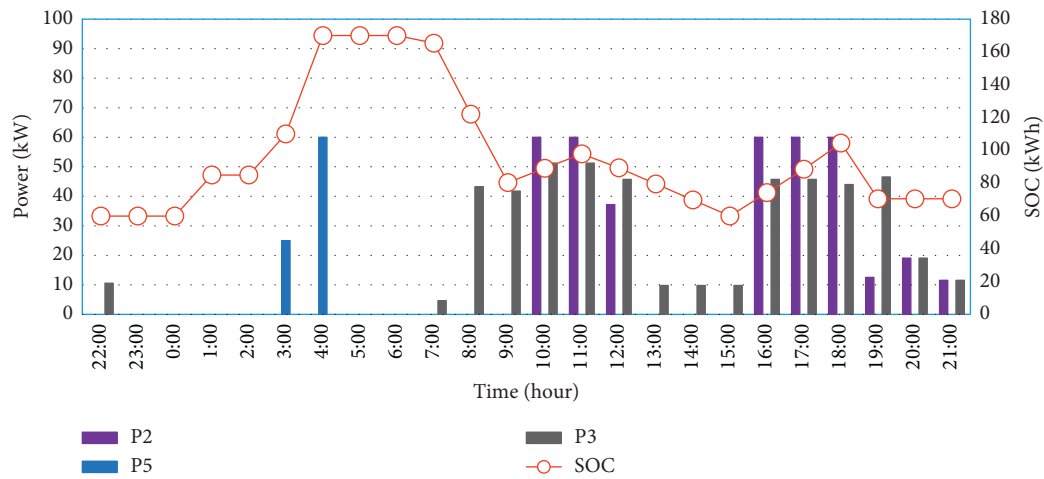


FIGURE 11: Batteries operation in case 4.

ship's load power as shown in Figure 10. Due to the lower energy price of CI system compared with the FC system at (1–6) and (23–24) hours, the ship will receive the required energy from the CI system ( $P_4$ ) while being at anchor in port; also the battery bank can be charged from CI system ( $P_5$ ) if needed. This fact is shown in both Figures 9 and 10. For the rest of the hours, while the ship is at the harbor, FC covers the load power of the ship due to the cheaper price of FC system compared with CI, although a small part of ship's load power is compensated by the battery banks because of FC system weak dynamic. The charging and discharging process of the batteries is depicted in Figure 11. Since the batteries should supply at least 10 percent of the load in hours that the FCs are active, batteries are frequently charged and discharged in different hours to have enough stored energy for covering 10 percent of the load in the next hours.

The hydrogen consumption process is presented in Figure 12. In hours that the FCs are not active, the mass of hydrogen consumption is zero. But in other hours, hydrogen is consumed and mass of remained hydrogen in the tank reduces.

All expenses value and pollution rate related to each of the four cases are listed in Table 3 separately. According to Table 3, the total costs and contamination rate ( $\text{CO}_2$ ,  $\text{NO}_x$ , and  $\text{SO}_x$ ) obtained from the energy management of case 1 are in high range. In case 2, the rate of total cost and ecological contamination is less than case 1 because of less fossil fuel usage. The use of PV in the energy management process of case 3 leads to reducing the total cost and pollution rate compared with case 1 and case 2, whereas the rate of costs and pollution is still high. Moreover, the installation of PV systems on the ship leads to the operation cost enhancement in this respect. As can be seen from Table 3 as the proposed case can satisfy the main objective of this paper which is to eliminate the emissions of  $\text{CO}_2$ ,  $\text{NO}_x$ , and  $\text{SO}_x$ , the energy management considered for case 4 has a completely acceptable cost compared to the other three cases.

*4.2. Comparing the Proposed Optimization Method with the Rule-Based Method in [12].* In order to compare the efficiency of the proposed method with available methods in the

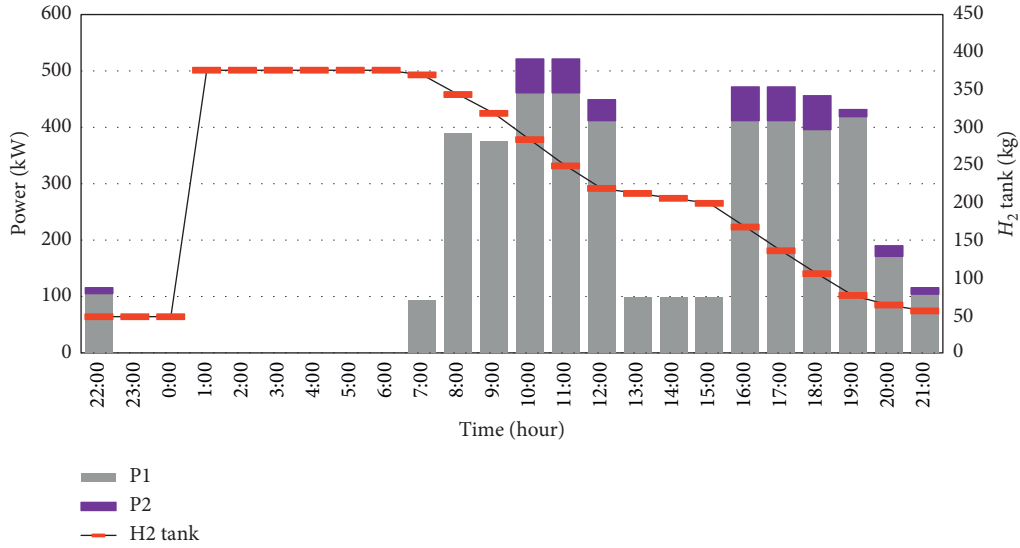


FIGURE 12: Output power of FCs and consumed hydrogen in case 4.

TABLE 3: Comparison of total costs and emission factors for different energy management strategy.

Case type	Under-sail cost (\$)	At-anchor cost (\$)	Total cost (\$)	CO <sub>2</sub> (kg)	NO <sub>x</sub> (kg)	SO <sub>x</sub> (kg)
Case 1	395.497	117.672	477.179	3123.871	11.434	8.141
Case 2	357.532	117.682	475.214	3106.796	11.372	8.097
Case 3	354.682	117.682	472.081	3079.572	11.272	8.026
Case 4	426.486	69.530	496.016	0	0	0

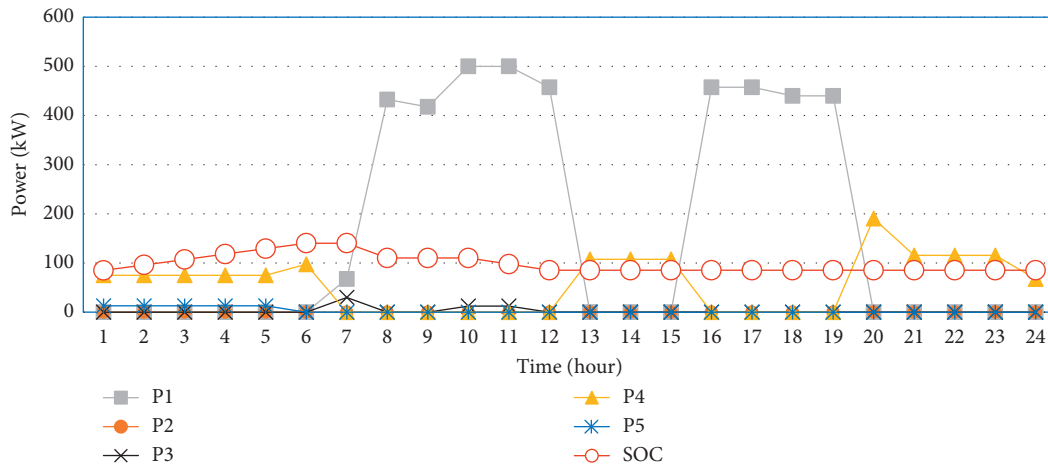


FIGURE 13: Hybrid energy management system rule-based method.

TABLE 4: Total costs and emission factors for rule-based method.

Case type	Under-sail cost (\$)	At-anchor cost (\$)	Total cost (\$)	CO <sub>2</sub> (kg)	NO <sub>x</sub> (kg)	SO <sub>x</sub> (kg)
Proposed method	426.486	69.530	496.016	0	0	0
Rule-based	438.655	72.309	510.964	0	0	0

literature, the proposed rule-based method in [12] that is the available method for energy management of the hybrid FC/battery boat is modeled for the understudy case system. More information about the rules and assumptions of this

rule-based method is presented in [12]. HEMS results are illustrated in Figure 13. The operation cost of the rule-based method is also presented in Table 4. Comparing the simulation results indicates that the operation cost of the rule-

based method in both under-sail and at-anchor situations is more than the operation cost obtained in this paper by the proposed method. This results in 4% increase in total operation cost at the rule-based method compared to the proposed method in this paper.

## 5. Conclusion

Hybrid energy management system (HEMS) installation on the ships with optimal energy management can have a remarkable impact on the maritime industry to supply the power of the ship's load demand. The nautical industry targets, such as environmental protection, are not satisfied if the hybrid energy system applied for the ship is considered without optimal energy management. In this paper, four different case studies based on HEMS have been considered for the ferry boat, wherein each case study is along with optimal energy management. Also, all cases were analyzed and compared in terms of total costs and the generated rate of contamination. The total cost obtained from case 1 (diesel generator/cold ironing) is 477.179 \$ and the rate of pollution ( $\text{CO}_2$ ,  $\text{NO}_x$ , and  $\text{SO}_x$ ) is 3123.871 kg, 11.434 kg, and 8.141 kg. The results of the total expenses and pollution rate ( $\text{CO}_2$ ,  $\text{NO}_x$ , and  $\text{SO}_x$ ), regarding the energy sources used in case 2 (diesel generator/cold ironing/battery) are 475.214 \$ and 3106.796 kg, 11.372 kg, and 8.097 kg, respectively. The obtained results of costs and pollution rate ( $\text{CO}_2$ ,  $\text{NO}_x$ , and  $\text{SO}_x$ ), from the hybrid energy system utilized in case 3 (diesel generator/cold ironing/battery/PV), are 472.081 \$ and 3079.572 kg, 11.272 kg, and 8.026 kg. Finally, case 4 is the major case study proposed in this literature. The hybrid energy system used for this case includes fuel cell/battery and cold ironing. Although the total cost obtained from case 4 is 496.016 \$, the rate of generated contamination ( $\text{CO}_2$ ,  $\text{NO}_x$ , and  $\text{SO}_x$ ) is zero. Thus, by comparing the obtained results from case 4, although the HEMS proposed in this paper acceptably enhances the expenses compared with other cases, it drastically reduces the environmental contamination ( $\text{CO}_2$ ,  $\text{NO}_x$ , and  $\text{SO}_x$ ). The proposed method in this paper is also compared with the proposed rule-based method in the literature. Simulation results show that applying the proposed method in this paper reduces the total operation cost by about 4% compared to the rule-based method. Thereupon, the proposed test system and optimization method can be useful for the maritime transportation industry and improve the clean air as well.

## Data Availability

The data used to support the findings of this study are available from the corresponding author upon request.

## Conflicts of Interest

The authors declare that they have no conflicts of interest.

## References

- [1] M. M. Mardani, M. H. Khooban, A. Masoudian, and T. Dragicevic, "Model predictive control of DC-DC

- converters to mitigate the effects of pulsed power loads in naval DC microgrids," *IEEE Transactions on Industrial Electronics*, vol. 66, no. 7, pp. 5676–5685, 2019.
- [2] M.-H. Khooban, T. Dragicevic, F. Blaabjerg, and M. Delimar, "Shipboard microgrids: a novel approach to load frequency control," *IEEE Transactions on Sustainable Energy*, vol. 9, no. 2, pp. 843–852, 2018.
- [3] M. Gheisarnejad, M. H. Khooban, T. Dragicevic, and J. Boudjadar, *Shipboard Secondary Load Frequency Control Based on PPLs and Communication Degradations*, IECON, Singapore, 2019.
- [4] T. V. Vu, D. Gonsoulin, F. Diaz, C. S. Edrington, and T. El-Mezyani, "Predictive control for energy management in ship power systems under high-power ramp rate loads," *IEEE Transactions on Energy Conversion*, vol. 32, no. 2, pp. 788–797, 2017.
- [5] M. M. S. Khan, M. O. Faruque, and A. Newaz, "Fuzzy logic based energy storage management system for MVDC power system of all electric ship," *IEEE Transactions on Energy Conversion*, vol. 32, no. 2, pp. 798–809, 2017.
- [6] A. T. Abkenar, A. Nazari, S. D. G. Jayasinghe, A. Kapoor, and M. Negnevitsky, "Fuel cell power management using genetic expression programming in all-electric ships," *IEEE Transactions on Energy Conversion*, vol. 32, no. 2, pp. 779–787, 2017.
- [7] M. R. Banaei and R. Alizadeh, "Simulation-based modeling and power management of all-electric ships based on renewable energy generation using model predictive control strategy," *IEEE Intelligent Transportation Systems Magazine*, vol. 8, no. 2, pp. 90–103, 2016.
- [8] R. Tang, X. Li, and J. Lai, "A novel optimal energy-management strategy for a maritime hybrid energy system based on large-scale global optimization," *Applied Energy*, vol. 228, pp. 254–264, 2018.
- [9] F. Balsamo, C. Capasso, G. Miccione, and O. Veneri, "Hybrid storage system control strategy for all-electric powered ships," *Energy Procedia*, vol. 126, pp. 1083–1090, 2017.
- [10] L. Zhengmao, X. Yan, F. Sidun, and W. Yu, "Multi-objective coordinated energy dispatch and voyage scheduling for a multi-energy cruising ship," in *Proceedings of the IEEE/IAS 55th Industrial and Commercial Power Systems Technical Conference (I&CPS)*, Calgary, Canada, May 2019.
- [11] F. D. Kanellos, "Optimal power management with GHG emissions limitation in all-electric ship power systems comprising energy storage systems," *IEEE Transactions on Power Systems*, vol. 29, no. 1, pp. 330–339, 2014.
- [12] J. Han, J.-F. Charpentier, and T. Tang, "An energy management system of a fuel cell/battery hybrid boat," *Energies*, vol. 7, no. 5, pp. 2799–2820, 2014.
- [13] S. Paran, T. V. Vu, T. E. Mezyani, and C. S. Edrington, "MPC-based power management in the shipboard power system," in *Proceedings of the IEEE Electric Ship Technologies Symposium (ESTS)*, Old Town Alexandria, VA, USA, June 2015.
- [14] J. Hou, J. Sun, and H. Hofmann, "Control development and performance evaluation for battery/flywheel hybrid energy storage solutions to mitigate load fluctuations in all-electric ship propulsion systems," *Applied Energy*, vol. 212, pp. 919–930, 2018.
- [15] J. Hou, Z. Song, H. Park, H. Hofmann, and J. Sun, "Implementation and evaluation of real-time model predictive control for load fluctuations mitigation in all-electric ship propulsion systems," *Applied Energy*, vol. 230, pp. 62–77, 2018.
- [16] G. Papalambrou, S. Samokhin, S. Topaloglou, N. Planakis, N. Kyrtatos, and K. Zenger, "Model predictive control for



- hybrid diesel-electric marine propulsion,” *IFAC-PapersOn-Line*, vol. 50, no. 1, pp. 11064–11069, 2017.
- [17] D. Paul, K. Peterson, and P. R. Chavdarian, “Designing cold ironing power systems: electrical safety during ship berthing,” *IEEE Industry Applications Magazine*, vol. 20, no. 3, pp. 24–32, 2014.
- [18] R. Tang, Z. Wu, and X. Li, “Optimal operation of photovoltaic/battery/diesel/cold-ironing hybrid energy system for maritime application,” *Energy*, vol. 162, pp. 697–714, 2018.
- [19] E. A. Sciberras, B. Zahawi, and D. J. Atkinson, “Electrical characteristics of cold ironing energy supply for berthed ships,” *Transportation Research Part D: Transport and Environment*, vol. 39, pp. 31–43, 2015.
- [20] F. Ballini and R. Bozzo, “Air pollution from ships in ports: the socio-economic benefit of cold-ironing technology,” *Research in Transportation Business & Management*, vol. 17, pp. 92–98, 2015.
- [21] E. A. Sciberras, B. Zahawi, D. J. Atkinson, A. Juandó, and A. Sarasquete, “Cold ironing and onshore generation for airborne emission reductions in ports,” *Proceedings of the Institution of Mechanical Engineers, Part M: Journal of Engineering for the Maritime Environment*, vol. 230, no. 1, pp. 67–82, 2016.
- [22] M. Gheisarnejad, J. Boudjadar, and M.-H. Khooban, “A new adaptive type-II fuzzy-based deep reinforcement learning control: fuel cell air-feed sensors control,” *IEEE Sensors Journal*, vol. 19, no. 20, pp. 9081–9089, 2019.
- [23] M. H. Khooban, N. Vafamand, and J. Boudjadar, “Tracking control for hydrogen fuel cell systems in zero-emission ferry ships,” *Complexity*, vol. 2019, Article ID 5358316, 9 pages, 2019.
- [24] S. C. Singhal, “Advances in solid oxide fuel cell technology,” *Solid State Ionics*, vol. 135, no. 1–4, pp. 305–313, 2000.
- [25] L. Van Biert, M. Godjevac, K. Visser, and P. V. Aravind, “A review of fuel cell systems for maritime applications,” *Journal of Power Sources*, vol. 327, pp. 345–364, 2016.
- [26] A. M. Bassam, A. B. Phillips, S. R. Turnock, and P. A. Wilson, “Development of a multi-scheme energy management strategy for a hybrid fuel cell driven passenger ship,” *International Journal of Hydrogen Energy*, vol. 42, no. 1, pp. 623–635, 2017.
- [27] J. Ahn, Y. Noh, T. Joung et al., “Safety integrity level (SIL) determination for a maritime fuel cell system as electric propulsion in accordance with IEC 61511,” *International Journal of Hydrogen Energy*, vol. 44, no. 5, pp. 3185–3194, 2019.
- [28] J. Ahn, Y. Noh, S. H. Park, B. I. Choi, and D. Chang, “Fuzzy-based failure mode and effect analysis (FMEA) of a hybrid molten carbonate fuel cell (MCFC) and gas turbine system for marine propulsion,” *Journal of Power Sources*, vol. 364, pp. 226–233, 2017.
- [29] F. Zaouche, D. Rekioua, J.-P. Gaubert, and Z. Mokrani, “Supervision and control strategy for photovoltaic generators with battery storage,” *International Journal of Hydrogen Energy*, vol. 42, no. 30, pp. 19536–19555, 2017.
- [30] M. H. Khooban, M. Gheisarnejad, H. Farsizadeh, A. Masoudian, and J. Boudjadar, “A new intelligent hybrid control approach for DC/DC converters in emission-free ferry ships,” *IEEE Transactions on Power Electronics*, vol. 35, no. 6, 2020.
- [31] M. Banaei, M. Rafiei, J. Boudjadar, and M. H. Khooban, “A comparative analysis of optimal operation scenarios in hybrid emission-free ferry ships,” *IEEE Transactions on Transportation Electrification*, vol. 6, no. 1, 2020.
- [32] J. J. Minnehan and J. W. Pratt, *Practical Application Limits of Fuel Cells and Batteries for Zero Emission Vessels*, Sandia National Laboratories, Albuquerque, NM, USA, 2017.
- [33] A. Letafat, M. Rafiei, Mo. Sheikh et al., “Simultaneous energy management and optimal components sizing of a zero emission ferry boat,” *Journal of Energy Storage*, vol. 28, 2020.
- [34] M. Banaei and B. Rezaee, “Fuzzy scheduling of a non-isolated micro-grid with renewable resources,” *Renewable Energy*, vol. 123, pp. 67–78, 2018.
- [35] L. Zhang and J. Zhang, “Capacity optimal research of hybrid energy storage systems for stand-alone wind/PV micro-grid,” *DEStech Transactions on Environment, Energy and Earth Sciences*, vol. 1, 2016.

## Research Article

# Multistable Systems with Hidden and Self-Excited Scroll Attractors Generated via Piecewise Linear Systems

R. J. Escalante-González and Eric Campos 

*Division of Applied Mathematics, Institute for Scientific and Technological Research of San Luis Potosí, Camino a la Presa San José 2055, Lomas 4 Sección 78216, San Luis Potosí, Mexico*

Correspondence should be addressed to Eric Campos; [eric.campos@ipicyt.edu.mx](mailto:eric.campos@ipicyt.edu.mx)

Received 4 January 2020; Revised 26 February 2020; Accepted 23 March 2020; Published 14 April 2020

Guest Editor: Sundarapandian Vaidyanathan

Copyright © 2020 R. J. Escalante-González and Eric Campos. This is an open access article distributed under the Creative Commons Attribution License, which permits unrestricted use, distribution, and reproduction in any medium, provided the original work is properly cited.

In this work, we present an approach to design a multistable system with one-directional (1D), two-directional (2D), and three-directional (3D) hidden multiscroll attractor by defining a vector field on  $\mathbb{R}^3$  with an even number of equilibria. The design of multistable systems with hidden attractors remains a challenging task. Current design approaches are not as flexible as those that focus on self-excited attractors. To facilitate a design of hidden multiscroll attractors, we propose an approach that is based on the existence of self-excited double-scroll attractors and switching surfaces whose relationship with the local manifolds associated to the equilibria lead to the appearance of the hidden attractor. The multistable systems produced by the approach could be explored for potential applications in cryptography, since the number of attractors can be increased by design in multiple directions while preserving the hidden attractor allowing a bigger key space.

## 1. Introduction

Piecewise linear systems that display scroll attractors have been studied since the publication of the well-known Chua's circuit. The attractor exhibited by Chua's circuit is an example of chaotic attractor whose chaotic nature has been explained through the Shilnikov method. Some works have extended this system in order to obtain a greater number of scrolls or different geometries. According to [1], an attractor with three or more scrolls in the attractor is considered a multiscroll attractor. Recently in [2], the generation of scroll attractors via multistable systems have been observed.

According to [3], there are two classes of attractors, one of them is a class called self-excited attractors that includes all the attractors excited by unstable equilibria, *i.e.*, the basin of attraction intersects with an arbitrarily small open neighborhood of equilibria [4]. Examples of this class are the well-known Lorenz attractor [5] and the scroll attractor of Chua's circuit [6]. The other class is called hidden attractors and their basins of attractions do not contain neighborhoods of equilibria. Some hidden attractors have been studied in

[7–19]. There are some works focused on control systems with hidden attractors, as in references [20, 21]. Most works related to multiscroll attractors are based on the first class. Multiscroll attractors have been reported in [12, 13, 18, 19, 22–26]. In [27], a system with a multiscroll chaotic sea was introduced.

Multistability can be considered undesirable for some applications, so some works focus on how to avoid this behavior. For example, in [28], a method that allows to transform a periodic or chaotic multistable system into a monostable was studied, and some experiments were carried out with a fiber laser doped with erbium. However, for some applications it may be considered desirable to be able to switch from monostable to bistable behavior, for example, in [29], a parameterized method to design multivibrator circuits with stable, monostable, and bistable regimes was proposed.

Some works deal with multistable systems with infinite number of equilibria and their electronic realization [30, 31].

A study on the widening of the basin of attraction of a class of piecewise linear (PWL) systems was recently

performed in [2]. In this work, a bifurcation from a bistable system with two self-excited double-scroll attractors to a multistable system with two self-excited attractors and one hidden attractor was reported. Other study on the emergence of hidden double-scroll attractors in a class of PWL systems is reported in [32].

Based on the observations made in previous works, a question of whether or not it is possible to generate a hidden multiscroll attractor with scrolls along more than one direction emerges. Depending on the number of directions in which the scrolls in the attractor extend, they are usually referred to as one-directional (1D), two-directional (2D), and three-directional (3D) grid scroll attractors.

Here, we introduce an approach for the construction of multistable PWL systems that exhibit hidden multiscroll attractors with 1D, 2D, and 3D grid arrangements. In Section 2, a system with a chaotic double-scroll self-excited attractor is introduced. In Section 3, the construction is extended to 1D grid scroll self-excited attractor; then, the equilibria are separated by pairs to generate multistable systems with hidden and self-excited attractors. In Section 4, the construction is generalized to 1D grid scroll hidden attractor. In Section 5, the construction is generalized to 2D and 3D grid scroll hidden attractors; in Section 6, conclusions are given.

## 2. Heteroclinic Chaos

Let  $P = \{P_1, \dots, P_\eta\}$  ( $\eta > 1$ ) be a finite partition of  $X \subset \mathbb{R}^3$ , that is,  $X = \cup_{1 \leq i \leq \eta} P_i$ , and  $P_i \cap P_j = \emptyset$  for  $i \neq j$ . The approach to generate hidden attractors is based on the existence of self-excited attractors; thus, the class of systems considered in this work are those that present a saddle equilibrium point in each element of the partition  $P$  that is called an atom.

We denote the closure of a set  $P_i$  as  $cl(P_i)$ . For each pair of adjacent atoms  $P_i$  and  $P_j$ ,  $i \neq j$ ,  $SW_{i,j} = cl(P_i) \cap cl(P_j)$  is the switching surface.

Consider a dynamical system  $T: X \rightarrow X$  whose dynamic is given by

$$\dot{\mathbf{x}} = A\mathbf{x} + f(\mathbf{x})B, \quad (1)$$

where  $\mathbf{x} = (x_1, x_2, x_3)^T \in \mathbb{R}^3$  is the state vector and  $A = \{\alpha_{ij}\} \in \mathbb{R}^{3 \times 3}$  is a linear operator whose matrix is as follows:

$$A = \begin{pmatrix} \frac{a}{3} + \frac{2c}{3} & b & \frac{2c}{3} - \frac{2a}{3} \\ -\frac{b}{3} & a & \frac{2b}{3} \\ \frac{c}{3} - \frac{a}{3} & -b & \frac{2a}{3} + \frac{c}{3} \end{pmatrix}, \quad (2)$$

where  $a, b \in \mathbb{R}^+$ , and  $c \in \mathbb{R}^-$ . Thus, the linear operator  $A$  has a negative real eigenvalue  $\lambda_1 = c$  with the corresponding eigenvector  $v_1$  and a pair of complex conjugate eigenvalues with positive real part,  $\lambda_2 = a + ib$  and  $\lambda_3 = a - ib$ , with the

corresponding eigenvectors  $v_2$  and  $v_3$ , respectively. The eigenvectors are given by

$$\begin{aligned} v_1 &= \begin{pmatrix} 1 \\ 0 \\ \frac{1}{2} \end{pmatrix}, \\ v_2 &= \begin{pmatrix} 0 \\ -1 \\ 0 \end{pmatrix}, \\ v_3 &= \begin{pmatrix} -1 \\ 0 \\ 1 \end{pmatrix}. \end{aligned} \quad (3)$$

$B = (\beta_1, \beta_2, \beta_3)^T \in \mathbb{R}^3$  is a constant vector, and  $f: X \rightarrow \mathbb{R}$  is a functional such that  $f(\mathbf{x})B$  is a constant vector in each atom  $P_i$ , and there exists an equilibrium point  $\mathbf{x}_{eq_i}^* = (x_{1_{eq_i}}^*, x_{2_{eq_i}}^*, x_{3_{eq_i}}^*)^T = -f(\mathbf{x})A^{-1}B$ , with  $i = 1, \dots, \eta$ , in each atom  $P_i$ . Thus, in each atom  $P_i$  there exists a saddle equilibrium point with a local stable manifold of dimension one given by  $W_{\mathbf{x}_{eq_i}^*}^s = \{\mathbf{x} + \mathbf{x}_{eq_i}^* : \mathbf{x} \in \text{span}\{v_1\}\}$ . A two-dimensional local unstable manifold is given by  $W_{\mathbf{x}_{eq_i}^*}^u = \{\mathbf{x} + \mathbf{x}_{eq_i}^* : \mathbf{x} \in \text{span}\{v_2, v_3\}\}$ .

We begin to explain the generation of chaotic attractors by first considering a partition with two atoms  $P = \{P_1, P_2\}$  and the constant vector  $B \in \mathbb{R}^3$  given by

$$B = \begin{pmatrix} \frac{a}{3} - \frac{2c}{3} \\ \frac{b}{3} \\ \frac{a}{3} - \frac{c}{3} \end{pmatrix}, \quad (4)$$

and the functional  $f$  given by

$$f(\mathbf{x}) = \begin{cases} -\alpha, & \mathbf{x} \in P_1, \\ \alpha, & \mathbf{x} \in P_2, \end{cases} \quad (5)$$

with  $0 < \alpha \in \mathbb{R}$ .

Please note that the vector  $-B$  is the first column of the linear operator  $A$ , and thus, system (1) can be rewritten as  $\dot{\mathbf{x}} = A(x_1 - f(\mathbf{x}), x_2, x_3)^T$ . Then, the functional  $f(\mathbf{x})$  determines the location of the equilibria along the  $x_1$ -axis. So,  $\mathbf{x}_{eq_i}^* = (x_{1_{eq_i}}^*, x_{2_{eq_i}}^*, x_{3_{eq_i}}^*)^T \in P_i$ ,  $i = 1, 2$ .

**Proposition 1.** *If the PWL system (1) is given by (2), (4), and (5), then the functional  $f(\mathbf{x})$  determines the location of the equilibria along the  $x_1$ -axis.*

*Proof.* Let  $A = [A_1, A_2, A_3]$  be the linear operator so that each  $A_i$ ,  $i = 1, 2, 3$ , is a column vector. Since  $B = -A_1$ , then  $\dot{\mathbf{x}} = A\mathbf{x} + f(\mathbf{x})B$  can be rewritten as

$$\dot{\mathbf{x}} = (x_1 - f(\mathbf{x}))A_1 + x_2A_2 + x_3A_3, \quad (6)$$

and then

$$\dot{x} = A(x_1 - f(\mathbf{x}), x_2, x_3)^T. \quad (7)$$

Now, in order to find the equilibria, we equate the vector field to zero:

$$\mathbf{0} = A(x_1 - f(\mathbf{x}), x_2, x_3)^T. \quad (8)$$

Since  $A \neq 0$ , it follows that

$$\mathbf{x}_{eq}^* = (f(\mathbf{x}), 0, 0)^T. \quad (9)$$

Thus, the equilibria is determined by  $f(\mathbf{x})$  given by (5) along the  $x_1$ -axis.

According to  $f(\mathbf{x})$ , the first components of the equilibria fulfill that  $x_{1_{eq_1}}^* < x_{1_{eq_2}}^*$ .

The switching plane  $SW$  has associated an equation  $\widehat{A}x_1 + \widehat{B}x_2 + \widehat{C}x_3 + D = \mathbf{N} \cdot \mathbf{x}^T + D = 0$ , with  $\widehat{A} > 0$ , and  $\mathbf{N} = (\widehat{A}, \widehat{B}, \widehat{C})$  is the normal vector. Then, the atoms  $P_i$ ,  $i = 1, 2$ , are defined as follows:

$$\begin{aligned} P_1 &= \{\mathbf{x} \in \mathbb{R}^3 : x_3 > 0, \quad \mathbf{N} \cdot \mathbf{x}^T \leq -D\} \cup \{\mathbf{x} \in \mathbb{R}^3 : x_3 \leq 0, \quad \mathbf{N} \cdot \mathbf{x}^T < -D\}, \\ P_2 &= \{\mathbf{x} \in \mathbb{R}^3 : x_3 > 0, \quad \mathbf{N} \cdot \mathbf{x}^T > -D\} \cup \{\mathbf{x} \in \mathbb{R}^3 : x_3 \leq 0, \quad \mathbf{N} \cdot \mathbf{x}^T \geq -D\}. \end{aligned} \quad (10)$$

*Assumption 1.* The switching plane  $SW$  intersects the  $x_1$ -axis at the midpoint between the equilibrium points  $\mathbf{x}_{eq_1}^*$  and  $\mathbf{x}_{eq_2}^*$ .

**Proposition 2.** Under Assumption 1, each atom  $P_i$  given by (10),  $i = 1, 2$ , contains an equilibrium point of the PWL system (1) given by (2), (4), and (5).

*Proof.* We want to prove that if a system is given by (1), (2), (4), and (5), then  $\exists \mathbf{x}_{eq_1}^* \in P_1$  and  $\exists \mathbf{x}_{eq_2}^* \in P_2$ . From (9) and (5), the two equilibrium points are

$$\mathbf{x}_{eq_1}^* = (-\alpha, 0, 0)^T \quad \text{and} \quad \mathbf{x}_{eq_2}^* = (\alpha, 0, 0)^T. \quad (11)$$

From Assumption 1, the parameter  $D$  can be defined as  $D = -x_{sw_1}\widehat{A}$ , where  $x_{sw_1}$  in  $(x_{1_{eq_1}}^*, x_{1_{eq_2}}^*)$  is the intersection of  $SW$  with the  $x_1$ -axis:

$$\begin{aligned} \mathbf{N} \cdot \mathbf{x}_{eq_1}^* &= -\alpha\widehat{A}, \\ \mathbf{N} \cdot \mathbf{x}_{eq_2}^* &= \alpha\widehat{A}. \end{aligned} \quad (12)$$

Thus,

$$\begin{aligned} \mathbf{N} \cdot \mathbf{x}_{eq_1}^* &< -D, \\ \mathbf{N} \cdot \mathbf{x}_{eq_2}^* &> -D, \end{aligned} \quad (13)$$

from (10)  $\mathbf{x}_{eq_1}^* \in P_1$  and  $\mathbf{x}_{eq_2}^* \in P_2$ .  $\square$

**Proposition 3.** If  $SW = cl(P_1) \cap cl(P_2) = \{\mathbf{x} \in \mathbb{R}^3 : 2x_1 - x_3 = 0\}$ , the stable and unstable manifolds of the PWL system (1) given by (2), (4), and (5) intersect at two points given by  $\mathbf{x}_{in_1} = ((\alpha/3), 0, (2\alpha/3))^T$  and  $\mathbf{x}_{in_2} = (-(\alpha/3), 0, -(2\alpha/3))^T$ .

*Proof.* The equilibrium points are located at  $\mathbf{x}_{eq_1}^* = (-\alpha, 0, 0)^T$  and  $\mathbf{x}_{eq_2}^* = (\alpha, 0, 0)^T$ . In each atom  $P_i$ , the equilibrium point  $\mathbf{x}_{eq_i}^*$  has a local stable manifold (14) of dimension one given by  $W_{\mathbf{x}_{eq_i}^*}^s = \{\mathbf{x} + \mathbf{x}_{eq_i}^* : \mathbf{x} \in \text{span}\{\nu_1\}\}$  and a two-dimensional local unstable manifold given by

$W_{\mathbf{x}_{eq_i}^*}^u = \{\mathbf{x} + \mathbf{x}_{eq_i}^* : \mathbf{x} \in \text{span}\{\nu_2, \nu_3\}\}$ . Thus, the local manifolds are given as follows:

$$W_{\mathbf{x}_{eq_1}^*}^s = \{\mathbf{x} \in P_1 : x_1 + \alpha = 2x_3, x_2 = 0\}, \quad (14)$$

$$W_{\mathbf{x}_{eq_1}^*}^u = \{\mathbf{x} \in P_1 : x_1 + x_3 = -\alpha\}, \quad (15)$$

$$W_{\mathbf{x}_{eq_2}^*}^s = \{\mathbf{x} \in P_2 : x_1 - \alpha = 2x_3, x_2 = 0\}, \quad (16)$$

$$W_{\mathbf{x}_{eq_2}^*}^u = \{\mathbf{x} \in P_2 : x_1 + x_3 = \alpha\}. \quad (17)$$

According to (18), the stable and unstable manifolds, and the intersection points are given by

$$\mathbf{x}_{in_1} = cl\left(W_{\mathbf{x}_{eq_1}^*}^s\right) \cap cl\left(W_{\mathbf{x}_{eq_2}^*}^u\right) = ((\alpha/3), 0, (2\alpha/3))^T, \quad (18)$$

$$\mathbf{x}_{in_2} = cl\left(W_{\mathbf{x}_{eq_2}^*}^s\right) \cap cl\left(W_{\mathbf{x}_{eq_1}^*}^u\right) = (-(\alpha/3), 0, -(2\alpha/3))^T. \quad (19)$$

These points belong to  $SW$ .  $\square$

*Assumption 2.* The parameters  $a$  and  $b$  control the oscillation around the equilibrium point  $\mathbf{x}_{eq_i}^*$ , and we consider  $b/a > 10$ .

**Proposition 4.** The hyperbolic system given by (1), (2), (4), and (5) generates a pair of heteroclinic orbits if the switching surface between the atoms  $P_1$  and  $P_2$  is given by the plane  $SW = cl(P_1) \cap cl(P_2) = \{\mathbf{x} \in \mathbb{R}^3 : 2x_1 - x_3 = 0\}$ .

*Proof.* We want to show that there exist initial conditions  $\mathbf{x}_{01}, \mathbf{x}_{02} \in SW$ , such that two solution curves  $\varphi(\mathbf{x}_{01}, t)$  and  $\varphi(\mathbf{x}_{02}, t)$  of the hyperbolic system given by (1), (2), (4), and (5) fulfill that  $\varphi(\mathbf{x}_{01}, t) \rightarrow \mathbf{x}_{eq_1}^*$  and  $\varphi(\mathbf{x}_{02}, t) \rightarrow \mathbf{x}_{eq_2}^*$  as  $t \rightarrow \infty$  and  $\varphi(\mathbf{x}_{01}, t) \rightarrow \mathbf{x}_{eq_2}^*$  and  $\varphi(\mathbf{x}_{02}, t) \rightarrow \mathbf{x}_{eq_1}^*$  as  $t \rightarrow -\infty$ ; in particular, these initial conditions correspond to the intersection points  $cl(W_{\mathbf{x}_{eq_1}^*}^s) \cap cl(W_{\mathbf{x}_{eq_2}^*}^u)$  and  $cl(W_{\mathbf{x}_{eq_2}^*}^s) \cap cl(W_{\mathbf{x}_{eq_1}^*}^u)$ .

From (2), the linear operator  $A$  can be expressed as

$$A = QEQ^{-1}, \quad (20)$$

where  $Q = [v_1 \ v_2 \ v_3]$  and

$$E = \begin{pmatrix} c & 0 & 0 \\ 0 & a & -b \\ 0 & b & a \end{pmatrix}. \quad (21)$$

The intersection points  $\mathbf{x}_{in_1}$  and  $\mathbf{x}_{in_2}$  belong to  $SW$  and  $\mathbf{x}_{in_1} \in P_1$  and  $\mathbf{x}_{in_2} \in P_2$ . Because these points  $\mathbf{x}_{in_1}$  and  $\mathbf{x}_{in_2}$  belong to the stable manifolds  $W_{\mathbf{x}_{eq_1}^*}^s$  and  $W_{\mathbf{x}_{eq_2}^*}^s$ , respectively, they are points whose trajectories remain in atoms  $P_1$  and  $P_2$ , respectively.

By definition,  $\mathbf{x}_{1_{eq_1}^*} = -\mathbf{x}_{1_{eq_2}^*}$ ; then, the  $x_2$ -axis belongs to the plane  $SW$ . The sets  $cl(W_{\mathbf{x}_{eq_i}^*}^s) \cap SW$ , for  $i = 1, 2$ , can be written as follows:

$$\{(0, \epsilon, 0)^T + \mathbf{x}_{in_i} : \epsilon \in \mathbb{R}\}, \text{ for } i = 1, 2. \quad (22)$$

Consider the following changes of coordinates  $\mathbf{z}^{(i)} = Q^{-1}(\mathbf{x} - \mathbf{x}_{eq_i}^*)$ , for  $i = 1, 2$ . Then, the vector field in  $\mathbf{z}^{(i)}$  coordinates for the space given by the atom  $P_i$  is given by  $\dot{\mathbf{z}}^{(i)} = E\mathbf{z}^{(i)}$ , with  $i = 1, 2$ .

Since  $Q^{-1}(0, \epsilon, 0)^T = (0, -\epsilon, 0)^T$ , the sets given by (22) in  $\mathbf{z}^{(i)}$  coordinates are given as follows:

$$\{(0, \epsilon, 0)^T + Q^{-1}(\mathbf{x}_{in_i} - \mathbf{x}_{eq_i}^*) : \epsilon \in \mathbb{R}\}, \text{ for } i = 1, 2, \quad (23)$$

where  $\mathbf{z}_{in_i}^{(i)} = Q^{-1}(\mathbf{x}_{in_i} - \mathbf{x}_{eq_i}^*) = ((-1)^{i+1}4\alpha/3, 0, 0)^T$  is a point on the  $z_1^{(i)}$ -axis that corresponds to the transformation of the intersection points  $\mathbf{x}_{in_i} \in P_i$  to  $\mathbf{z}_{in_i}^{(i)} \in \{Q^{-1}(\mathbf{x} - \mathbf{x}_{eq_i}^*) : \mathbf{x} \in P_i\}$ , for  $i = 1, 2$ .

When  $t > 0$ ,  $\varphi(\mathbf{x}_{in_i}, t)$  remains in the atom  $P_1$ , the transformation of  $\mathbf{x}_{in_1}$  under  $Q^{-1}(\mathbf{x}_{in_1} - \mathbf{x}_{eq_1}^*)$  is  $\mathbf{z}_{in_1}^{(1)} = (4\alpha/3, 0, 0)^T$ . In a similar way, when  $t > 0$ ,  $\varphi(\mathbf{x}_{in_2}, t)$ , remains in the atom  $P_2$ , the transformation of  $\mathbf{x}_{in_2}$  under  $Q^{-1}(\mathbf{x}_{in_2} - \mathbf{x}_{eq_2}^*)$  is  $\mathbf{z}_{in_2}^{(2)} = (-4\alpha/3, 0, 0)^T$ . So,  $\mathbf{z}_{in_i}^{(i)}$  belongs to the stable manifold  $W_{\mathbf{z}_{eq_i}^*}^s$ , for  $i = 1, 2$ ; then, the trajectories  $\mathbf{z}^{(i)}(t) = e^{Et}\mathbf{z}_{in_i}^{(i)} \rightarrow 0$  when  $t \rightarrow \infty$ . This implies that

$$\begin{aligned} \lim_{t \rightarrow \infty} \varphi(\mathbf{x}_{in_1}, t) &= \mathbf{x}_{eq_1}^*, \\ \lim_{t \rightarrow \infty} \varphi(\mathbf{x}_{in_2}, t) &= \mathbf{x}_{eq_2}^*. \end{aligned} \quad (24)$$

When  $t < 0$ ,  $\varphi(\mathbf{x}_{in_i}, t)$  leaves the atom  $P_1$  and enters to atom  $P_2$ , the transformation of  $\mathbf{x}_{in_1}$  under  $Q^{-1}(\mathbf{x}_{in_1} - \mathbf{x}_{eq_2}^*)$  to  $\mathbf{z}_{in_1}^{(2)} \in \{Q^{-1}(\mathbf{x} - \mathbf{x}_{eq_2}^*) : \mathbf{x} \in cl(P_2)\}$  is  $\mathbf{z}_{in_1}^{(2)} = (0, 0, 2\alpha/3)^T$ . In a similar way, when  $t < 0$ ,  $\varphi(\mathbf{x}_{in_2}, t)$  leaves the atom  $P_2$  and enters to atom  $P_1$ , the transformation of  $\mathbf{x}_{in_2}$  under  $Q^{-1}(\mathbf{x}_{in_2} - \mathbf{x}_{eq_1}^*)$  to  $\mathbf{z}_{in_2}^{(1)} \in \{Q^{-1}(\mathbf{x} - \mathbf{x}_{eq_1}^*) : \mathbf{x} \in cl(P_1)\}$  is  $\mathbf{z}_{in_2}^{(1)} = (0, 0, -2\alpha/3)^T$ . Thus,  $\mathbf{z}_{in_i}^{(j)} = (0, 0, (-1)^j 2\alpha/3)^T$  is a point on the axis  $z_3^{(j)}$  and belongs to  $cl(W_{\mathbf{z}_{eq_j}^*}^u)$  for  $i, j \in \{1, 2\}$  and  $i \neq j$ .

With the uncoupled system in  $\mathbf{z}^{(i)}$  coordinates, we can analyze the flow on the plane  $z_2^{(i)} - z_3^{(i)}$  and see how the flow converges at the equilibrium point  $\mathbf{z}_{eq_j}^*(i)$  when  $t \rightarrow -\infty$ :

$$\begin{aligned} \dot{z}_2^{(i)} &= az_2^{(i)} - bz_3^{(i)}, \\ \dot{z}_3^{(i)} &= bz_2^{(i)} + az_3^{(i)}, \\ z_2^{(i)}\dot{z}_2^{(i)} + z_3^{(i)}\dot{z}_3^{(i)} &= a\left((z_2^{(i)})^2 + (z_3^{(i)})^2\right). \end{aligned} \quad (25)$$

If  $r^2 = (z_2^{(i)})^2 + (z_3^{(i)})^2$ , then  $rr' = ar^2$

$$\dot{r} = ar, \quad (26)$$

$$r = r_0 e^{at}. \quad (27)$$

As  $0 < a \in \mathbb{R}$ , so  $r \rightarrow 0$  when  $t \rightarrow -\infty$ . Then, the trajectories  $\mathbf{z}^{(i)}(t) = e^{Et}\mathbf{z}_{in_i}^{(i)} \rightarrow 0$  when  $t \rightarrow -\infty$ . This implies that

$$\lim_{t \rightarrow -\infty} \varphi(\mathbf{x}_{in_1}, t) = \mathbf{x}_{eq_2}^*, \quad \text{and} \quad \lim_{t \rightarrow -\infty} \varphi(\mathbf{x}_{in_2}, t) = \mathbf{x}_{eq_1}^*, \quad (28)$$

Thus, the heteroclinic orbits are defined as

$$\begin{aligned} HO_1 &= \{\mathbf{x} \in \varphi(\mathbf{x}_{in_1}, t) : t \in (-\infty, \infty)\}, \\ HO_2 &= \{\mathbf{x} \in \varphi(\mathbf{x}_{in_2}, t) : t \in (-\infty, \infty)\}. \end{aligned} \quad (29)$$

As example, consider systems (1), (2), (4), and (5) with the parameters  $a = 0.2, b = 5, c = -3, \alpha = 1$ , which fulfills (10) with the switching surface  $SW = cl(P_1) \cap cl(P_2) = \{\mathbf{x} \in \mathbb{R}^3 : 2x_1 - x_3 = 0\}$ . Then, heteroclinic chaos emerges from this system, a double-scroll attractor is exhibited, as it is shown in Figure 1(b), for the initial condition  $\mathbf{x}_0 = (0, 0, 0)^T$ .  $\square$

### 3. Multiple Self-Excited Attractors

A study on the widening of the basins of attraction of multistable switching dynamical system with symmetrical equilibria is performed in [2]. In this study, the increment of distance between the equilibria of the self-excited double-scroll attractors increases the basin of attraction of both attractors. The study also reveals that, for the system under study, there is a distance at which a hidden double-scroll attractor emerges.

Based on the idea of generating hidden scroll attractors from sufficiently separated self-excited attractors, we consider now a partition with more atoms  $P = \{P_1, P_2, P_3, P_4\}$  along with the PWL system (1), with  $A$  and  $B$  given by (2) and (4), respectively. For this partition, the functional  $f(\mathbf{x})$  is defined in the four atoms as follows:

$$f(\mathbf{x}) = \begin{cases} -\alpha - \gamma, & \mathbf{x} \in P_1, \\ \alpha - \gamma, & \mathbf{x} \in P_2, \\ -\alpha + \gamma, & \mathbf{x} \in P_3, \\ \alpha + \gamma, & \mathbf{x} \in P_4, \end{cases} \quad (30)$$



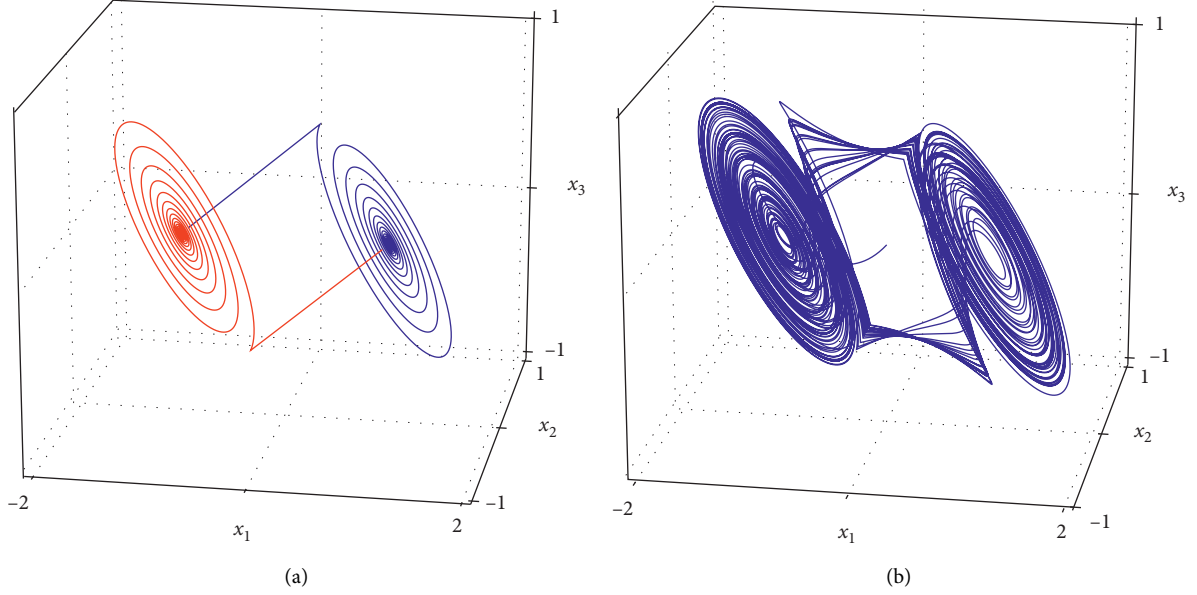


FIGURE 1: In (a) the heteroclinic loop of system (1), (2), (4), and (5) with the switching surface  $\{x \in \mathbb{R}^3 : 2x_1 - x_3 = 0\}$  and the parameters  $a = 0.2, b = 5, c = -3, \alpha = 1$  and in (b) a double-scroll attractor that emerges from an heteroclinic loop using the following initial condition  $\mathbf{x}_0 = (0, 0, 0)^T$ .

where  $0 < \alpha, \gamma \in \mathbb{R}$  and  $\gamma > \alpha$ . Now, there are four atoms and each atom contains an equilibrium point,  $\mathbf{x}_{eq_i}^* = (x_{1_{eq_i}}^*, x_{2_{eq_i}}^*, x_{3_{eq_i}}^*)^T \in P_i$ ,  $i = 1, 2, 3, 4$ . The first components of the equilibrium points fulfill that  $x_{1_{eq_i}}^* < x_{1_{eq_{i+1}}}^*$ ,  $i = 1, 2, 3$ .

There are three switching planes and each switching plane  $SW_{i,i+1}$  crosses the  $x_1$ -axis and is located between the equilibrium points  $\mathbf{x}_{eq_i}^*$  and  $\mathbf{x}_{eq_{i+1}}^*$ ,  $i = 1, 2, 3$ .

The switching plane  $SW_{ij}$  with  $i, j \in \{1, \dots, \eta\}$  has associated an equation  $A_{ij}x_1 + B_{ij}x_2 + C_{ij}x_3 + D_{ij} = \mathbf{N}_{ij} \cdot \mathbf{x}^T + D_{ij} = 0$ , where  $A_{ij} > 0$  and  $\mathbf{N}_{ij} = (A_{ij}, B_{ij}, C_{ij})$  is the normal vector. Then, in order to know if a point  $\mathbf{x}$  belongs to a  $P_i$  the following conditions are considered:

$$\begin{aligned}
 & \text{If } x \in \{\mathbf{x} \in \mathbb{R}^3 : x_3 > 0, \mathbf{N}_{ij} \cdot \mathbf{x}^T \leq -D_{ij}\}, \\
 & \text{then } x \in P_k \text{ for a } k \leq i, \\
 & \text{If } x \in \{\mathbf{x} \in \mathbb{R}^3 : x_3 > 0, \mathbf{N}_{ij} \cdot \mathbf{x}^T > -D_{ij}\}, \\
 & \text{then } x \in P_k \text{ for a } k \geq j, \\
 & \text{If } x \in \{\mathbf{x} \in \mathbb{R}^3 : x_3 \leq 0, \mathbf{N}_{ij} \cdot \mathbf{x}^T \geq -D_{ij}\}, \\
 & \text{then } x \in P_k \text{ for a } k \geq j, \\
 & \text{If } x \in \{\mathbf{x} \in \mathbb{R}^3 : x_3 \leq 0, \mathbf{N}_{ij} \cdot \mathbf{x}^T < -D_{ij}\}, \\
 & \text{then } x \in P_k \text{ for a } k \leq i.
 \end{aligned} \tag{31}$$

If  $\mathbf{x} \in P_k$  for a  $k \geq i$  and  $\mathbf{x} \in P_k$  for a  $k \leq i$ , it follows that  $\mathbf{x} \in P_i$ .

The equilibria are located on the  $x_1$ -axis at

$$\begin{aligned}
 \mathbf{x}_{eq_1}^* &= \begin{bmatrix} -(\gamma + \alpha) \\ 0 \\ 0 \end{bmatrix}, \\
 \mathbf{x}_{eq_2}^* &= \begin{bmatrix} -(\gamma - \alpha) \\ 0 \\ 0 \end{bmatrix}, \\
 \mathbf{x}_{eq_3}^* &= \begin{bmatrix} (\gamma - \alpha) \\ 0 \\ 0 \end{bmatrix}, \\
 \mathbf{x}_{eq_4}^* &= \begin{bmatrix} (\gamma + \alpha) \\ 0 \\ 0 \end{bmatrix},
 \end{aligned} \tag{32}$$

so  $\mathbf{x}_{eq_1}^* \in P_1$ ,  $\mathbf{x}_{eq_2}^* \in P_2$ ,  $\mathbf{x}_{eq_3}^* \in P_3$ , and  $\mathbf{x}_{eq_4}^* \in P_4$ .

*Assumption 3.* The distance between the self-excited attractors should be big enough to allow the existence of a hidden double-scroll attractor, so we consider  $(\gamma/\alpha) \geq 10$ .

Consider three switching surfaces with the following orientation:

$$\begin{aligned}
 SW_{1,2} &= cl(P_1) \cap cl(P_2) = \{\mathbf{x} \in \mathbb{R}^3 : 2x_1 - x_3 = -2\gamma\}, \\
 SW_{2,3} &= cl(P_2) \cap cl(P_3) = \{\mathbf{x} \in \mathbb{R}^3 : 2x_1 - x_3 = 0\}, \\
 SW_{3,4} &= cl(P_3) \cap cl(P_4) = \{\mathbf{x} \in \mathbb{R}^3 : 2x_1 - x_3 = 2\gamma\},
 \end{aligned} \tag{33}$$

which fulfill that

$$\begin{aligned} SW_{i,(i+1)} \cap \{\mathbf{x} \in \mathbb{R}^3 : x_3 > 0\} &\in P_i, \\ SW_{i,(i+1)} \cap \{\mathbf{x} \in \mathbb{R}^3 : x_3 \leq 0\} &\in P_{i+1}. \end{aligned} \quad (34)$$

The switching surfaces given in (33) along with the condition given in (34) ensure the existence of the four heteroclinic orbits. Moreover,  $cl(W_{\mathbf{x}_{eq_2}^u}) \cap W_{\mathbf{x}_{eq_3}^s} \neq \emptyset$  and  $cl(W_{\mathbf{x}_{eq_3}^u}) \cap W_{\mathbf{x}_{eq_2}^s} \neq \emptyset$ .

As example, consider the system with parameters  $a = 0.2, b = 5, c = -3, \alpha = 1$ , and  $\gamma = 10$ , the system presents two self-excited attractors; however, the hidden double-scroll attractor is not present and a transitory double-scroll oscillation is exhibited instead. Figure 2(a) shows in blue the trajectory for the initial condition  $\mathbf{x}_0 = (0, 0, 0)^T$  for a time  $t \in [0, 150]$  a.u. (arbitrary units). Thus, an enough separation of the self-excited double-scroll attractors is not sufficient to produce a hidden double-scroll attractor.

The absence of a hidden attractor is related to the switching plane  $SW_{2,3}$  and how the trajectories of the transitory double-scroll cross it near the stable manifolds. Consider now the following switching surfaces:

$$\begin{aligned} SW_{1,2} &= cl(P_1) \cap cl(P_2) = \{\mathbf{x} \in \mathbb{R}^3 : 2x_1 - x_3 = -2\gamma, x_3 < 0\}, \\ SW_{2,3} &= cl(P_2) \cap cl(P_3) = \{\mathbf{x} \in \mathbb{R}^3 : x_1 = 0\}, \\ SW_{3,4} &= cl(P_3) \cap cl(P_4) = \{\mathbf{x} \in \mathbb{R}^3 : 2x_1 - x_3 = 2\gamma, x_3 > 0\}. \end{aligned} \quad (35)$$

With the change in  $SW_{2,3}$ , the intersections  $cl(W_{\mathbf{x}_{eq_2}^u}) \cap W_{\mathbf{x}_{eq_3}^s} = \emptyset$  as well as  $cl(W_{\mathbf{x}_{eq_3}^u}) \cap W_{\mathbf{x}_{eq_2}^s} = \emptyset$ . Furthermore, the distance from  $cl(W_{\mathbf{x}_{eq_2}^u}) \cap SW_{2,3}$  to  $W_{\mathbf{x}_{eq_3}^s} \cap SW_{2,3}$  and by symmetry from  $cl(W_{\mathbf{x}_{eq_3}^u}) \cap SW_{2,3}$  to  $W_{\mathbf{x}_{eq_2}^s} \cap SW_{2,3}$  allow the trajectories to cross  $SW_{2,3}$  far from the stable manifolds and allowing the existence of the hidden double-scroll attractor.

As example, consider the system given by (1), (2), (4), and (30) with  $a = 0.2, b = 5, c = -3, \alpha = 1$ , and  $\gamma = 10$  and the new switching surfaces given by (35). Figure 2(b) shows in blue the trajectory for the initial condition  $\mathbf{x}_0 = (0, 0, 0)^T$  for a time  $t \in [50000, 51000]$  a.u. The trajectory reaches the hidden double-scroll instead of converging to one of the self-excited attractors. A trajectory has been simulated for a time  $t > 1000000$  to verify that the double-scroll oscillation is not a transitory behavior and that the trajectory does not converge to a self-excited attractor.

The construction can be further extended to the number of scrolls desired just by adding two atoms for each scroll; for instance, for a triple scroll attractor the partition is  $P = \{P_1, \dots, P_6\}$  and a possible set of switching surfaces is given by

$$\begin{aligned} SW_{1,2} &= cl(P_1) \cap cl(P_2) = \{\mathbf{x} \in \mathbb{R}^3 : 2x_1 - x_3 = -4\gamma, x_3 < 0\}, \\ SW_{2,3} &= cl(P_2) \cap cl(P_3) = \{\mathbf{x} \in \mathbb{R}^3 : x_1 = -\gamma\}, \\ SW_{3,4} &= cl(P_3) \cap cl(P_4) = \{\mathbf{x} \in \mathbb{R}^3 : 2x_1 - x_3 = 0, x_3 > 0\}, \\ SW_{4,5} &= cl(P_4) \cap cl(P_5) = \{\mathbf{x} \in \mathbb{R}^3 : x_1 = \gamma\}, \\ SW_{5,6} &= cl(P_5) \cap cl(P_6) = \{\mathbf{x} \in \mathbb{R}^3 : 2x_1 - x_3 = 4\gamma, x_3 > 0\}, \end{aligned} \quad (36)$$

with

$$f(\mathbf{x}) = \begin{cases} -\alpha - 2\gamma, & \mathbf{x} \in P_1, \\ \alpha - 2\gamma, & \mathbf{x} \in P_2, \\ -\alpha, & \mathbf{x} \in P_3, \\ \alpha, & \mathbf{x} \in P_4, \\ -\alpha + 2\gamma, & \mathbf{x} \in P_5, \\ \alpha + 2\gamma, & \mathbf{x} \in P_6. \end{cases} \quad (37)$$

Then, the equilibria are located at the  $x_1$ -axis with  $x_{1eq_1}^* = -2\gamma - \alpha$ ,  $x_{1eq_2}^* = -2\gamma + \alpha$ ,  $x_{1eq_3}^* = -\alpha$ ,  $x_{1eq_4}^* = \alpha$ ,  $x_{1eq_5}^* = 2\gamma - \alpha$ , and  $x_{1eq_6}^* = 2\gamma + \alpha$ .

#### 4. Generalization

The number of scrolls for a hidden scroll attractor exhibited by the system from the previous section depends on the number of self-excited attractors. In order to simplify the description for a large number of scrolls, a generalization is introduced in this section. Consider a dynamical system  $T: X \rightarrow X$  whose dynamic is given by

$$\dot{\mathbf{x}} = A\mathbf{x} + BF(\mathbf{x}), \quad (38)$$

where  $\mathbf{x} = (x_1, x_2, x_3)^T \in \mathbb{R}^3$  is the state vector,  $A = \{\alpha_{ij}\} \in \mathbb{R}^{3 \times 3}$  is the linear operator given by (2), and  $F$  is a functional such that  $BF(\mathbf{x})$  is a constant vector in each atom  $P_i$ . The saddle equilibrium point of each atom is given by  $\mathbf{x}_{eq_i}^* = (x_{1eq_i}^*, x_{2eq_i}^*, x_{3eq_i}^*)^T = (F(\mathbf{x}), 0, 0)^T$ , with  $i = 1, \dots, \eta$ .  $F(\mathbf{x})$  is defined as follows:

$$F(\mathbf{x}) = \alpha g(2(x_1 - f_1(x_1)) - x_3, x_3) + f_1(x_1), \quad (39)$$

where

$$f_1(x_1) = \sum_{j=1}^{N_{x_1}} \gamma u(x_1 + 2\gamma(j-1) - \gamma(N_{x_1} - 1)), \quad (40)$$

with  $N_{x_1} \in \mathbb{Z}^+$ . The parameters  $\alpha$  and  $\gamma$  fulfill Assumption 3. The function  $u(y)$  is the Heaviside step function:

$$u(y) = \begin{cases} 1, & \text{if } y \geq 0, \\ -1, & \text{if } y < 0, \end{cases} \quad (41)$$

and  $g$  is a step function defined as follows:

$$g(y, z) = \begin{cases} 1, & \text{if } y > 0 \text{ and } z \geq 0, \\ -1, & \text{if } y \leq 0 \text{ and } z \geq 0, \\ 1, & \text{if } y \geq 0 \text{ and } z < 0, \\ -1, & \text{if } y < 0 \text{ and } z < 0. \end{cases} \quad (42)$$

Note that  $g(y, z)$  is equal to  $u(y)$ , when  $z < 0$ ; while, for  $z \geq 0$ , it is similar to  $u(y)$  with the only difference that 0 is mapped to 1 instead of -1.

Please note that  $-B$  is the first column of the operator  $A$  and therefore system (38) can be rewritten as follows:

$$\dot{\mathbf{x}} = A\mathbf{x} - AB(\mathbf{x}), \quad (43)$$

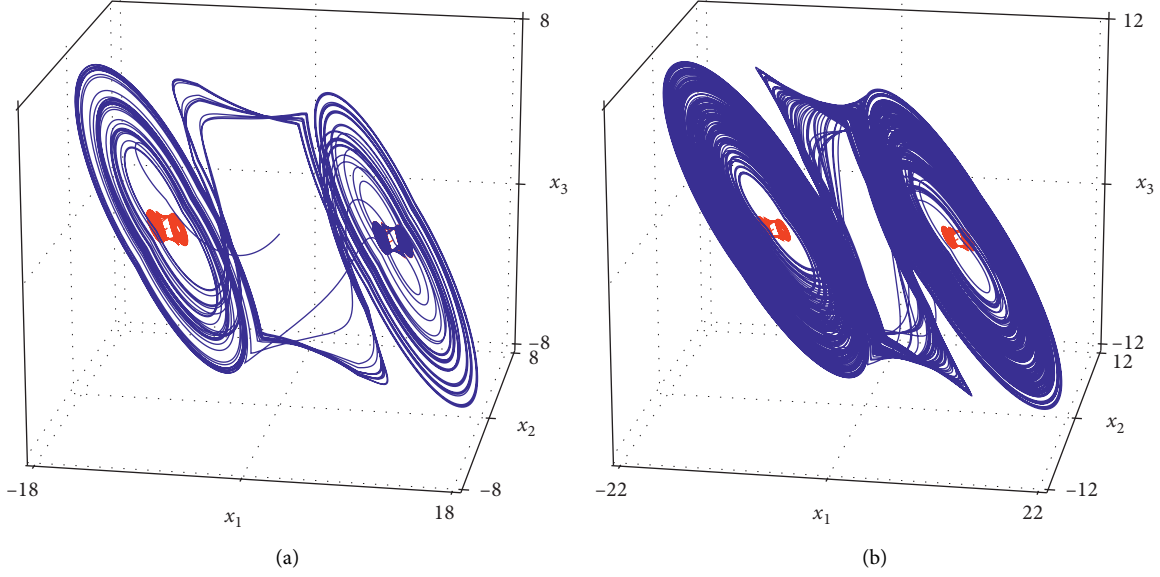


FIGURE 2: Simulation of the system given by (1), (2), (4), and (30) with  $a = 0.2, b = 5, c = -3, \alpha = 1, \gamma = 10$ , and  $\alpha = 1$  for the initial condition  $\mathbf{x} = (0, 0, 0)^T$  in blue. In (a) the surfaces are defined by (33) and (34), the simulation is shown for  $t \in [0, 300]a \cdot u.$  (arbitrary units), and the trajectory converges to one of the self-excited attractors in red. In (b) the surfaces are defined by (35) and the simulation is shown for  $t \in [50000, 51000]a \cdot u.,$  and the hidden attractor emerges.

where  $B: X \rightarrow X$  is a vector valued function defined as follows:

$$B(\mathbf{x}) = \begin{pmatrix} B_1 \\ B_2 \\ B_3 \end{pmatrix} = \begin{pmatrix} \alpha g(2(x_1 - f_1(x_1)) - x_3, x_3) + f_1(x_1) \\ 0 \\ 0 \end{pmatrix}, \quad (44)$$

such that  $AB(x)$  is a constant vector in each atom  $P_i$ . The saddle equilibrium point of each atom is now given by  $\mathbf{x}_{eq_i}^* = (x_{1,eq_i}^*, x_{2,eq_i}^*, x_{3,eq_i}^*)^T = B(\mathbf{x})$ , with  $i = 1, \dots, \eta$ .

To understand the form of  $B(\mathbf{x})$ , it is useful to separate  $B_1$  and analyze the effect of each term of the sum, i.e., the effect of the term  $\alpha g(2(x_1 - f_1(x_1)) - x_3, x_3)$  and the effect of  $f_1(x_1)$ .

First, consider the function  $f_1(x_1)$  whose plot resembles a stair centered at the origin whose plateaus are of  $2\gamma$  in height and width. Two examples for  $N_{x_1} = 3$  and  $N_{x_1} = 6$  are shown in Figure 3.

Thus,  $f_1(x_1)$  generates  $N_{x_1}$  switching planes of the form  $\{\mathbf{x} \in \mathbb{R}^3 : x_1 = e \in \mathbb{R}\}$ , which are parallel to the plane  $x_2 - x_3$ .

Then,  $f_1(x_1)$  generates a partition  $R = \{R_1, \dots, R_{N_{x_1}+1}\}$  of  $X$ .

Now, consider the term  $\alpha g(2(x_1 - f_1(x_1)) - x_3, x_3)$ , and this term generates a switching plane  $\{\mathbf{x} \in R_i : 2(x_1 - f_1(x_1)) - x_3 = 0\}$  for  $i = 1, \dots, N_x + 1$ . Since  $f_1(x_1)$  takes  $N_{x_1} + 1$  values, then  $\alpha g(2(x_1 - f_1(x_1)) - x_3, x_3)$  generates  $N_{x_1} + 1$  switching planes, one for each element of the partition  $R$ . Thus, the elements  $R_i$  are split and the partition  $P = \{P_1, \dots, P_{2N_{x_1}+2}\}$  is generated.

In this way,  $B(\mathbf{x})$  locates two equilibrium points with a separation of  $2\alpha$  in the middle of each element  $R_i$  (along  $x_1$ ) for  $i = 1, \dots, N_{x_1} + 1$ . In the partition  $P$ ,  $B(\mathbf{x})$  locates an equilibrium point in each  $P_i$  for  $i = 1, \dots, 2N_{x_1} + 2$ .

Thus, the equilibria along the  $x_1$ -axis is located in  $N_{x_1}$  pairs, each pair of nearby equilibrium points have a separation of  $2\alpha$ . Let us denote the midpoint of the line that joins a pair  $\mu$  of nearby equilibria as  $cp_\mu$  with  $\mu = 1, \dots, (N_{x_1} + 1)$ . Then, the distance from  $cp_i$  to  $cp_{i+1}$  is  $2\gamma$ . The purpose of this distribution for the equilibria is to allow the existence of double-scroll self-excited attractors that are separated enough from other double-scroll self-excited attractors in a way that these resemble equilibria for the generation of a bigger scroll attractor at a larger scale. This larger scroll attractor is indeed the hidden scroll attractor.

The equilibria are located along the  $x_1$ -axis as follows:

$$\begin{aligned} x_{1,eq_1}^* &= (0)2\gamma - \gamma(N_{x_1}) - \alpha, \\ x_{1,eq_3}^* &= (1)2\gamma - \gamma(N_{x_1}) - \alpha, \\ x_{1,eq_5}^* &= (2)2\gamma - \gamma(N_{x_1}) - \alpha, \\ &\vdots \\ x_{1,eq_{2N_{x_1}-1}}^* &= (N_{x_1} - 1)2\gamma - \gamma(N_{x_1}) - \alpha, \\ x_{1,eq_{2N_{x_1}+1}}^* &= (N_{x_1})2\gamma - \gamma(N_{x_1}) - \alpha, \\ x_{1,eq_2}^* &= (0)2\gamma - \gamma(N_{x_1}) + \alpha, \\ x_{1,eq_4}^* &= (1)2\gamma - \gamma(N_{x_1}) + \alpha, \\ x_{1,eq_6}^* &= (2)2\gamma - \gamma(N_{x_1}) + \alpha, \\ &\vdots \\ x_{1,eq_{2N_{x_1}}}^* &= (N_{x_1} - 1)2\gamma - \gamma(N_{x_1}) + \alpha, \\ x_{1,eq_{2N_{x_1}+2}}^* &= (N_{x_1})2\gamma - \gamma(N_{x_1}) + \alpha. \end{aligned} \quad (45)$$

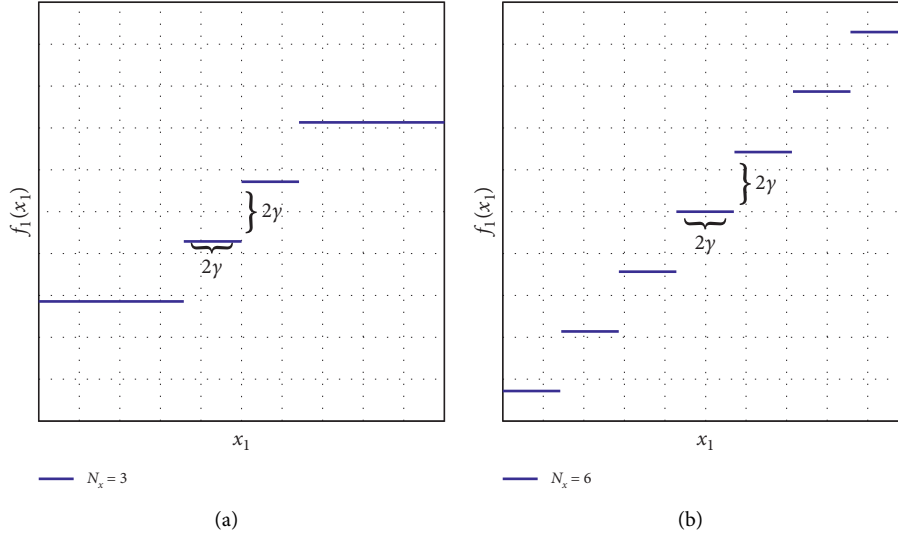


FIGURE 3: The plot of the function  $f_1(x_1)$  for (a)  $N_{x_1} = 3$  and (b)  $N_{x_1} = 6$ .

The switching planes located in the middle of the self-excited attractors are given as follows:

$$\begin{aligned}
 SW_{1,2} &= \{ \mathbf{x} \in \mathbb{R}^3 : 2(x_1 - (x_{1eq_1}^* + \alpha)) - x_3 = 0, \quad x_1 < x_{1eq_2}^* + (\gamma - \alpha) \}, \\
 SW_{3,4} &= \{ \mathbf{x} \in \mathbb{R}^3 : 2(x_1 - (x_{1eq_3}^* + \alpha)) - x_3 = 0, \quad x_{1eq_3}^* - (\gamma - \alpha) \leq x_1 < x_{1eq_4}^* + (\gamma - \alpha) \}, \\
 &\vdots \\
 SW_{2N_{x_1}+1, 2N_{x_1}+2} &= \{ \mathbf{x} \in \mathbb{R}^3 : 2(x_1 - (x_{1eq_{N_{x_1}+1}}^* + \alpha)) - x_3 = 0, \quad x_{1eq_{N_{x_1}+1}}^* - (\gamma - \alpha) \leq x_1 \}.
 \end{aligned} \tag{46}$$

The rest of the switching surfaces are

$$\begin{aligned}
 SW_{2,3} &= \{ \mathbf{x} \in \mathbb{R}^3 : x = x_{1eq_2}^* + (\gamma - \alpha) \}, \\
 SW_{4,5} &= \{ \mathbf{x} \in \mathbb{R}^3 : x = x_{1eq_4}^* + (\gamma - \alpha) \}, \\
 &\vdots \\
 SW_{2N_{x_1}-2, 2N_{x_1}-1} &= \{ \mathbf{x} \in \mathbb{R}^3 : x = x_{1eq_{2N_{x_1}-2}}^* + (\gamma - \alpha) \}, \\
 SW_{2N_{x_1}, 2N_{x_1}+1} &= \{ \mathbf{x} \in \mathbb{R}^3 : x = x_{1eq_{2N_{x_1}}}^* + (\gamma - \alpha) \}.
 \end{aligned} \tag{47}$$

To illustrate the construction, consider the parameters  $a = 0.2$ ,  $b = 5$ ,  $c = -7$ , and  $N_{x_1} = 1$ , the system presents two self-excited attractors and a hidden double-scroll attractor, which is shown in Figure 4(a).

According to the definition, the attraction basin of a hidden attractor does not intersect neighborhoods of equilibria. Figure 5 shows the cut of the numerically evaluated basins of attraction given by the plane  $x_3 = 0$ . Each double-scroll self-excited attractor has its own attraction basin shown in red and green. Also, the attractor around these double-scroll self-excited attractors has its own attraction basin shown in blue and the intersection of this basin with the attraction basins of the self-excited attractor is

the empty set. Because all equilibria of the system belong to the attraction basin of the self-excited attractors, the attraction basin of the attractor around the self-excited attractors does not contain an equilibrium point. So, the attractor around the self-excited attractors is a hidden attractor.

Another numerical approach to verify that it is a hidden attractor consist in performing a long-time simulation of a trajectory and make sure that the trajectory does not converge to a self-excited attractor. In Figure 6, it is shown that the simulation for the initial condition  $\mathbf{x}_0 = (0, 0, 0)^T$  with  $t \in [1000000, 10001000]$ . This last approach requires less computing time, so it was the approach used in all the examples in the manuscript.

For a second example, consider  $N_{x_1} = 4$ ; then, the system presents five self-excited attractors and a hidden 5-scroll attractor shown in Figure 4(b). Thus, the number of scrolls is equal to the number of self-excited attractors, which is  $N_{x_1} + 1$ .

## 5. Extension for 2D and 3D Grid Scroll Hidden Attractors

The approach presented in Section 4 can be further extended for 2D and 3D grid scroll hidden attractors. The idea is to

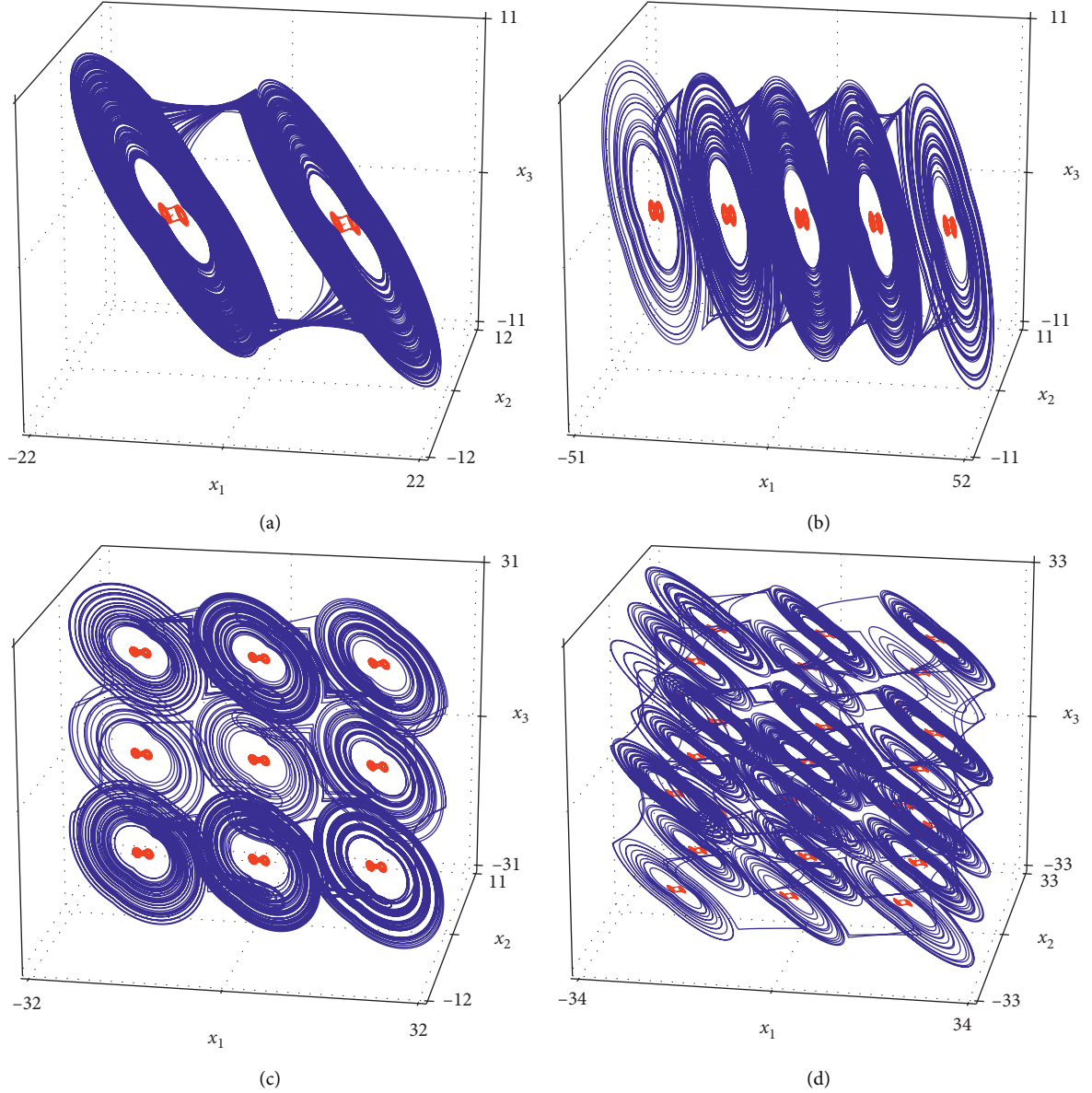


FIGURE 4: Simulation of the hidden attractor (in blue) and the self-excited attractors (in red) exhibited by system (43) with parameters  $a = 0.2$ ,  $b = 5$ , and  $c = -7$ . In (a) and (b)  $B(\mathbf{x})$  is given by (44) with  $N_{x_1} = 1$  and  $N_{x_1} = 4$ , respectively. In (c)  $B(\mathbf{x})$  is given by (48) with  $E_2 = 0, E_3 = 1, N_{x_1} = 2$ , and  $N_{x_3} = 2$ . In (d)  $B(\mathbf{x})$  is given by (48) with  $E_2 = 1, E_3 = 1, N_{x_1} = 2, N_{x_2} = 2, N_{x_3} = 2$ , and  $w = 0.2$ .

add switching surfaces, which are parallel to the planes  $x_1 - x_2$  and  $x_1 - x_3$ .

This requires the modification on  $B(\mathbf{x})$ , for simplicity, the functions  $f_i(\cdot)$  are written as  $f_i$ :

$$B(\mathbf{x}) = \begin{pmatrix} f_4 + f_1 - \frac{wf_2}{\gamma} \\ f_2 \\ f_3 + \frac{wf_2}{\gamma} \end{pmatrix}, \quad (48)$$

$$f_2 = E_2 \left( \sum_{k=1}^{N_{x_2}} \gamma u \left( x_2 + 2\gamma(k-1) - \gamma(N_{x_2} - 1) \right) \right), \quad (49)$$

$$f_3 = E_3 \left( \sum_{l=1}^{N_{x_3}} \gamma u \left( \left( x_3 - \frac{wf_2}{\gamma} \right) + 2\gamma(l-1) - \gamma(N_{x_3} - 1) \right) \right), \quad (50)$$

$$f_1 = \sum_{j=1}^{N_{x_1}} \gamma u \left( \left( x_1 + \frac{wf_2}{\gamma} \right) + 2\gamma(j-1) - \gamma(N_{x_1} - 1) \right), \quad (51)$$

where

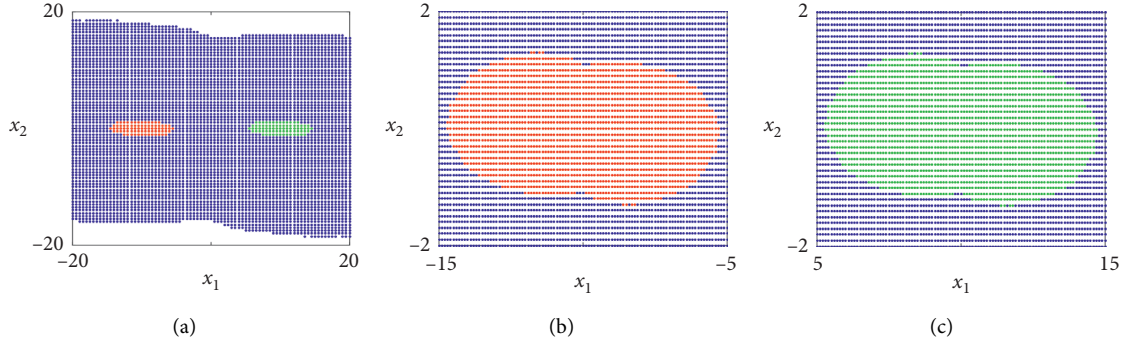


FIGURE 5: Cut of basins of attraction of system (43) with parameters  $a = 0.2$ ,  $b = 5$ ,  $c = -7$ , and  $N_{x_1} = 1$  at  $x_3 = 0$ . Red and green dots belong to the basins of attraction of self-excited attractors, and blue dots belong to the basin of attraction of the hidden attractor. In (a) grid of 0.5 and in (b) and (c) grid of 0.1.

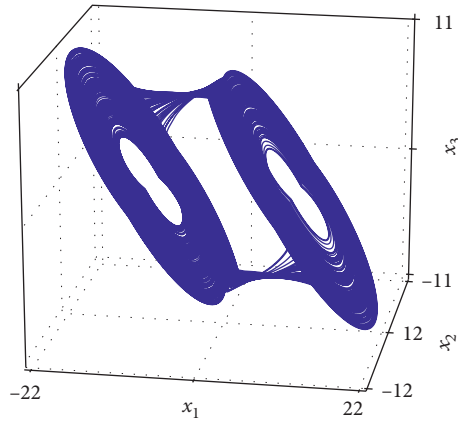


FIGURE 6: Simulation of the hidden attractor exhibited by system (43) with parameters  $a = 0.2$ ,  $b = 5$ ,  $c = -7$ , and  $N_{x_1} = 1$  for  $t \in [1000000, 10001000]$ .

$$f_4 = \alpha g \left( 2 \left( x_1 + \frac{w f_2}{\gamma} - f_1 \right) - \left( x_3 - \frac{w f_2}{\gamma} - f_3 \right), \right. \\ \left. \left( x_3 - \frac{w f_2}{\gamma} - f_3 \right) \right), \quad (52)$$

where (52)  $w \geq 0$ ,  $E_2, E_3 \in \{0, 1\}$ , and  $N_{x_1}, N_{x_2}, N_{x_3} \in \mathbb{Z}^+$ .

Let us denote the equilibria found in Section 4 as  $\mathbf{x}_{eq_j}^{*1D} = (x_{1eq_j}^{*1D}, x_{2eq_j}^{*1D}, x_{3eq_j}^{*1D})^T$  for  $j = 1, \dots, 2N_{x_1} + 2$ . Then, the new equilibria for the new  $B(\mathbf{x})$  in (48) are found from

$$\mathbf{x}_{jkl}^{*3D} = \mathbf{x}_{eq_j}^{*1D} + \begin{pmatrix} 0 \\ 0 \\ (E_1 l)2\gamma - \gamma N_{x_3} \end{pmatrix} + \begin{pmatrix} 0 \\ (E_2 k)2\gamma - \gamma N_{x_2} \\ 0 \end{pmatrix} + \begin{pmatrix} \frac{w f_2(\gamma)}{\gamma} \\ 0 \\ \frac{w f_2(\gamma)}{\gamma} \end{pmatrix}, \quad (53)$$

where  $k = 1, \dots, 2N_{x_2} + 2$  and  $l = 1, \dots, 2N_{x_3} + 2$ . The switching surfaces are now restricted on  $x_2$  and  $x_3$  and located according to the new equilibria.

As example, consider the parameters  $a = 0.2$ ,  $b = 5$ ,  $c = -7$ , and  $w = 0.2$  with  $E_2 = 0$ ,  $E_3 = 1$ ,  $N_{x_1} = 2$ , and  $N_{x_3} = 2$  for a 2D-grid scroll hidden attractor shown in Figure 4(c) and  $E_2 = 1$ ,  $E_3 = 1$ ,  $N_{x_1} = 2$ ,  $N_{x_3} = 2$ , and  $N_{x_3} = 2$  for a 3D-grid scroll hidden attractor shown in Figure 4(d).

## 6. Conclusions

In this work, the question of whether or not it is possible to generate a hidden multiscroll attractor with an arrangement of scrolls along more than one direction from multiple self-excited attractors was addressed. It was found that the separation between self-excited double-scroll attractors and the switching plane between these self-excited attractors lead



to the emergence of a hidden attractor. A generalized construction was proposed for the generation of multistable systems with self-excited double-scroll chaotic attractors and a hidden multiscroll/grid attractor. The coexistence of self-excited attractors and a hidden attractor is presented via PWL systems and the approach considers for each scroll in the hidden attractors a self-excited attractor inside the scroll. As future work, we envision working on the answer to the following question: is it possible to generate multistability with more than one hidden attractor?

## Data Availability

The data used to support the findings of this study are included within the article.

## Conflicts of Interest

The authors declare that there are no conflicts of interest regarding the publication of this paper.

## Acknowledgments

R.J. Escalante-González is thankful to CONACYT for the scholarships granted. Eric Campos acknowledges CONACYT for the financial support through Project no. A1-S-30433.

## References

- [1] E. Campos-Cantón, J. G. Barajas-Ramírez, G. Solís-Perales, and R. Femat, "Multiscroll attractors by switching systems. *Chaos, An Interdisciplinary Journal of Nonlinear Science*, vol. 20, no. 1, 2010.
- [2] L. J. Ontañón-García and E. Campos-Cantón, "Widening of the basins of attraction of a multistable switching dynamical system with the location of symmetric equilibria," *Nonlinear Analysis: Hybrid Systems*, vol. 26, pp. 38–47, 2017.
- [3] G. A. Leonov, N. V. Kuznetsov, and V. I. Vagaitsev, "Localization of hidden Chua's attractors," *Physics Letters A*, vol. 375, no. 23, pp. 2230–2233, 2011.
- [4] D. Dudkowski, S. Jafari, T. Kapitaniak, N. V. Kuznetsov, G. A. Leonov, and A. Prasad, "Hidden attractors in dynamical systems," *Physics Reports*, vol. 637, no. 1, p. 50, 2016.
- [5] E. N. Lorenz, "Deterministic nonperiodic flow," *Journal of the Atmospheric Sciences*, vol. 20, pp. 130–141, 1963.
- [6] T. Matsumoto, "A chaotic attractor from Chua's circuit," *IEEE Transactions on Circuits and Systems*, vol. 31, no. 12, pp. 1055–1058, 1984.
- [7] S. Jafari, J. C. Sprott, and S. M. R. Hashemi Golpayegani, "Elementary quadratic chaotic flows with no equilibria," *Physics Letters A*, vol. 377, no. 9, pp. 699–702, 2013.
- [8] D. Cafagna and G. Grassi, "Chaos in a new fractional-order system without equilibrium points," *Communications in Nonlinear Science and Numerical Simulation*, vol. 19, no. 9, pp. 2919–2927, 2014.
- [9] Z. Wang, S. Cang, E. O. Ochola, and Y. Sun, "A hyperchaotic system without equilibrium," *Nonlinear Dynamics*, vol. 69, no. 1–2, pp. 531–537, 2012.
- [10] C. Li, J. C. Sprott, W. Thio, and H. Zhu, "A new piecewise linear hyperchaotic circuit," *IEEE Transactions on Circuits and Systems II: Express Briefs*, vol. 61, no. 12, pp. 977–981, 2014.
- [11] J. M. Muñoz-Pacheco, E. Zambrano-Serrano, C. Volos, S. Jafari, J. Kengne, and K. Rajagopal, "A new fractional-order chaotic system with different families of hidden and self-excited attractors," *Entropy*, vol. 20, no. 8, 2018.
- [12] X. Hu, C. Liu, L. Liu, J. Ni, and S. Li, "Multi-scroll hidden attractors in improved Sprott A system," *Nonlinear Dynamics*, vol. 86, no. 3, pp. 1725–1734, 2016.
- [13] X. Hu, C. Liu, L. Liu, Y. Yao, and G. Zheng, "Multi-scroll hidden attractors and multi-wing hidden attractors in a 5-dimensional memristive system," *Chinese Physics B*, vol. 26, no. 11, p. 110502, 2017.
- [14] F. R. Tahir, S. Jafari, V.-T. Pham, C. Volos, and X. Wang, "A novel no-equilibrium chaotic system with multiwing butterfly attractors," *International Journal of Bifurcation and Chaos*, vol. 25, no. 04, p. 1550056, 2015.
- [15] M. A. Kiseleva, N. V. Kuznetsov, and G. A. Leonov, "Hidden attractors in electromechanical systems with and without equilibria," *IFAC-PapersOnLine*, vol. 49, no. 14, pp. 51–55, 2016.
- [16] M.-F. Danca, N. Kuznetsov, and G. Chen, "Unusual dynamics and hidden attractors of the Rabinovich-Fabrikant system," *Nonlinear Dynamics*, vol. 88, no. 1, pp. 791–805, 2017.
- [17] R. J. Escalante-González and E. Campos-Cantón, "Generation of chaotic attractors without equilibria via piecewise linear systems," *International Journal of Modern Physics C*, vol. 28, no. 1, 2017.
- [18] R. J. Escalante-González, E. Campos-Cantón, and M. Nicol, "Generation of multi-scroll attractors without equilibria via piecewise linear systems," *Chaos: An Interdisciplinary Journal of Nonlinear Science*, vol. 27, no. 5, 2017.
- [19] R. J. Escalante-González and E. Campos-Cantón, "A class of piecewise linear systems without equilibria with 3-d grid multiscroll chaotic attractors," *IEEE Transactions on Circuits and Systems II: Express Briefs*, vol. 66, no. 8, pp. 1456–1460, 2019.
- [20] J. Ma, F. Wu, W. Jin, P. Zhou, and T. Hayat, "Calculation of Hamilton energy and control of dynamical systems with different types of attractors," *Chaos: An Interdisciplinary Journal of Nonlinear Science*, vol. 27, no. 5, 2017.
- [21] G. Zhang, F. Wu, C. Wang, and J. Ma, "Synchronization behaviors of coupled systems composed of hidden attractors," *International Journal of Modern Physics B*, vol. 31, no. 26, p. 1750180, 2017.
- [22] J. A. K. Suykens, A. Huang, and L. O. Chua, "A family of n-scroll attractors from a generalized Chua's circuit," *Archiv Fur Elektronik und Ubertragungstechnik*, vol. 51, no. 3, pp. 131–138, 1997.
- [23] W. K. S. Tang, G. Q. Zhong, G. Chen, and K. F. Man, "Generation of N-Scroll attractors via sine function," *IEEE Transactions on Circuits and Systems I: Fundamental Theory and Applications*, vol. 48, no. 11, pp. 1369–1372, 2001.
- [24] M. E. Yalçın, J. A. K. Suykens, J. Vandewalle, and S. Özoğuz, "Families of scroll grid attractors," *International Journal of Bifurcation and Chaos*, vol. 12, no. 1, pp. 23–41, 2002.
- [25] B. Aguirre-Hernández, E. Campos-Cantón, J. A. López-Rentería, and E. C. Díaz González, "A polynomial approach for generating a monoparametric family of chaotic attractors via switched linear systems," *Chaos, Solitons & Fractals*, vol. 71, no. 1, pp. 100–106, 2015.
- [26] E. Campos-Cantón, "Chaotic attractors based on unstable dissipative systems via third-order differential equation," *International Journal of Modern Physics C*, vol. 27, no. 1, 2016.

- [27] S. Jafari, V.-T. Pham, and T. Kapitaniak, "Multiscroll chaotic sea obtained from a simple 3d system without equilibrium," *International Journal of Bifurcation and Chaos*, vol. 26, no. 2, 2016.
- [28] R. Sevilla-Escoboza, A. N. Pisarchik, R. Jaimes-Reátegui, and G. Huerta-Cuellar, "Selective monostability in multi-stable systems," *Proceedings of the Royal Society A: Mathematical, Physical and Engineering Sciences*, vol. 471, 2015.
- [29] E. Campos-cantón, R. Femat, J. G. Barajas-ramírez, and I. Campos-cantón, "A multivibrator circuit based on chaos generation," *International Journal of Bifurcation and Chaos*, vol. 22, no. 1, 2012.
- [30] A. Sambas, S. Vaidyanathan, E. Tlelo-Cuautle et al., "A novel chaotic system with two circles of equilibrium points: multistability, electronic circuit and fpga realization," *Electronics*, vol. 8, no. 11, 2019.
- [31] A. Sambas, S. Vaidyanathan, S. Zhang, M. Mamat, and M. A. Mohamed, "Multistability in a novel chaotic system with perpendicular lines of equilibrium: analysis, adaptive synchronization and circuit design," *Engineering Letters*, vol. 27, 2019.
- [32] R. J. Escalante-González and E. Campos-Cantón, "Coexistence of hidden attractors and self-excited attractors through breaking heteroclinic-like orbits of switched systems," *Engineering Letters*, vol. 27, 2019.

## Research Article

# Dynamic Analysis of a Heterogeneous Diffusive Prey-Predator System in Time-Periodic Environment

Chuanjun Dai <sup>1,2</sup>, He Liu,<sup>3</sup> Zhan Jin,<sup>1,2</sup> Qing Guo,<sup>3</sup> Yi Wang,<sup>4,5</sup> Hengguo Yu <sup>2</sup>, Qi Wang,<sup>1,2</sup> Zengling Ma,<sup>1,2</sup> and Min Zhao <sup>1,2</sup>

<sup>1</sup>School of Life and Environmental Science, Wenzhou University, Wenzhou, Zhejiang 325035, China

<sup>2</sup>Zhejiang Provincial Key Laboratory for Water Environment and Marine Biological Resources Protection, Wenzhou University, Wenzhou, Zhejiang 325035, China

<sup>3</sup>Environmental Engineering Program, University of Northern British Columbia, Prince George, British Columbia V2N 4Z9, Canada

<sup>4</sup>Department of Applied Mathematics, Northwestern Polytechnical University, Xi'an, Shanxi 710129, China

<sup>5</sup>Division of Applied Mathematics, Brown University, Providence, Rhode Island 02912, USA

Correspondence should be addressed to Min Zhao; [zmcnzj@sina.com](mailto:zmcnzj@sina.com)

Received 12 December 2019; Revised 29 February 2020; Accepted 16 March 2020; Published 14 April 2020

Guest Editor: Viet-Thanh Pham

Copyright © 2020 Chuanjun Dai et al. This is an open access article distributed under the Creative Commons Attribution License, which permits unrestricted use, distribution, and reproduction in any medium, provided the original work is properly cited.

In this paper, a heterogeneous diffusive prey-predator system is first proposed and then studied analytically and numerically. Some sufficient conditions are derived, including permanence and extinction of system and the boundedness of the solution. The existence of periodic solution and its stability are discussed as well. Furthermore, numerical results indicate that both the spatial heterogeneity and the time-periodic environment can influence the permanence and extinction of the system directly. Our numerical results are consistent with the analytical analysis.

## 1. Introduction

Due to the complexity of ecosystems, prey-predator dynamics have always drawn interest among mathematical ecologists, as well as experimental ecologists [1–3]. The significance of studying prey-predator dynamics is to gain insights into the complex ecological processes. Prey-predator models, as the base of researching prey-predator dynamics, have attracted increasing attention [4–7]. Since Holling [8] introduced the concept of the functional response, a lot of studies have been devoted to the understanding of the effect of functional response on prey-predator dynamics [9]. Usually, the functional response is assumed to be either prey dependent or ratio dependent in prey-predator models [10, 11].

A classical general prey-predator system can be written as follows [12]:

$$\frac{dN}{dt} = f(N)N - g(N, P)P, \quad (1a)$$

$$\frac{dP}{dt} = h(g(N, P), P)P, \quad (1b)$$

where  $N$  and  $P$  denote the prey and predator densities, respectively,  $f(N)$  is the prey growth rate,  $g(N, P)$  is the functional response, and  $h(g(N, P), P)$  is the per capita growth rate of predators. Let  $h(g(N, P), P) = eg(N, P) - m(P)$ , then equation (1b) can be rewritten as follows:

$$\frac{dP}{dt} = (eg(N, P) - m(P))P, \quad (2)$$

where  $e$  is the conversion efficiency and  $m(P)$  is the specific mortality of predators in absence of prey. For the function  $m(P)$ , the most widely accepted assumption [13] is

$m(P) = \mu$ , where  $\mu$  is a constant describing the death rate of the predator. However, Cavani and Farkas [14] introduced another function for  $m(P)$ :

$$m(P) = \frac{\gamma + \delta P}{1 + P}, \quad (3)$$

where  $\gamma$  is the mortality at low density and  $\delta$  is the limiting, maximal mortality (obviously,  $\gamma < \delta$ ). The specific mortality (3) depends on the quantity of predators, which suggests that the predator mortality is neither a constant nor an unbounded function, and increasing with quantity. Obviously, when  $\gamma = \delta$ , equation (3) can be simplified to a constant death rate type. Prey-predator systems with this nonconstant death rate have been studied by some researchers [15–17].

Additionally, in order to understand patterns and the mechanisms of spatial distribution of interacting species, the dispersal process is taken into consideration [18–20]. Thus, the spatiotemporal dynamics of a prey-predator system can be presented by a couple of reaction-diffusion equations based on equations (1a) and (2) [10, 21, 22]:

$$\frac{\partial N}{\partial t} = f(N)N - g(N, P)P + D_N \Delta N, \quad (4a)$$

$$\frac{\partial P}{\partial t} = (eg(N, P) - m(P))P + D_P \Delta P, \quad (4b)$$

where  $D_N$  and  $D_P$  are the prey and predator diffusion coefficients, respectively, and the Laplace operator  $\Delta$  describes the spatial dispersal.

Because of the emergence of Lotka–Volterra models [23, 24], a logistic type growth  $f(N)$  is usually assumed for the prey species in the models. Some functional response  $g(N, P)$  are taken into account in many works, such as Holling type [25], Michaelis–Menten type [26, 27], and Beddington–DeAngelis type [28, 29]. Especially, many biologists argued that the ratio-dependent theory is more suitable for describing prey-predator systems in many situations [13, 30–32]. Since Ardini and Ginzburg proposed the ratio-dependent prey-predator system, the prey-predator systems with ratio-dependent functional response are widely studied [13, 33–36], and many interesting results are obtained.

Based on model (4a) and (4b), in this paper, we employ the ratio-dependent functional response and the nonconstant death rate (i.e., equation (3)) and assume that the growth rate of prey population follows the logistic growth type. Moreover, let  $u$  and  $v$  be the prey density and the predator density, respectively. Then, the resulting system is

$$\frac{\partial u}{\partial t} = ru \left(1 - \frac{u}{K}\right) - \frac{auv}{bv + u} + \mu_1 \Delta u, \quad x \in \Omega, t > 0, \quad (5a)$$

$$\frac{\partial v}{\partial t} = \frac{euv}{bv + u} - \frac{c + \delta v}{1 + v} v + \mu_2 \Delta v, \quad x \in \Omega, t > 0, \quad (5b)$$

$$\frac{\partial u}{\partial n} = \frac{\partial v}{\partial n} = 0, \quad x \in \partial \Omega, t > 0, \quad (5c)$$

where  $\Omega \in \mathbb{R}^n$  is a bounded domain with smooth boundary  $\partial \Omega$ .

In system (5a)–(5c), when  $c = \delta = \mu$ , the system without diffusion is so-called the Michaelis–Menten ratio-dependent predator-prey system, which has been studied by many researchers. Kuang and Beretta [37] systematically studied the global behaviors of solutions and obtained some new and significant results, but many important open questions remain to be unsolved. For these open questions, Hsu et al. [38] resolved the global stability of all equilibria in various cases and the uniqueness of limit cycles by transforming the Michaelis–Menten-type ratio-dependent model. Xiao and Ruan [39] investigated the qualitative behavior of the Michaelis–Menten-type ratio-dependent model at the origin in the interior of the first quadrant and confirmed that the origin is indeed a critical point inducing rich and complicated dynamics. Additionally, when the diffusion process is considered, the Michaelis–Menten ratio-dependent predator-prey system with diffusion can produce rich spatial patterns, which makes it a widely studied system for pattern formation [10, 40–43].

While  $c < \delta$ , Kovács et al. [44] incorporated delays into system (5a)–(5c) and studied the qualitative behaviour of the system without diffusion. Yun et al. [45] presented an efficient and accurate numerical method for solving system (5a)–(5c) with a Turing instability and studied the existence of nonconstant stationary solutions. Aly et al. [46] studied Turing instability for system (5a)–(5c) and showed that diffusion-driven instability occurs at a certain critical value analytically. In these works, parameters in system (5a)–(5c) are always considered as constants.

However, it seems that there is no research for considering spatial heterogeneity and time-periodic environment in system (5a)–(5c). It is well known that spatial heterogeneity occurs at all scales of the environment [47]. Additionally, interactive populations often live in a fluctuating environment [48], where some environmental conditions such as temperature, light, availability of food, and other resources usually vary in time. Specially, some data depending on season in systems may be periodic functions of time. Thus, more realistic models to describe ecosystem should be nonautonomous systems with spatial heterogeneity. With this mind, we propose the following system to study effects of spatial heterogeneity and time-periodic environment on prey-predator dynamics:

$$\frac{\partial u(t, x)}{\partial t} = r(t, x)u(t, x) \left(1 - \frac{u(t, x)}{K(t, x)}\right) - \frac{a(t, x)u(t, x)v(t, x)}{b(t, x)v(t, x) + u(t, x)} + \mu_1 \Delta u(t, x), \quad (6a)$$

$$\frac{\partial v(t, x)}{\partial t} = \frac{e(t, x)u(t, x)v(t, x)}{b(t, x)v(t, x) + u(t, x)} - \frac{c(t, x) + \delta(t, x)v(t, x)}{1 + v(t, x)} v(t, x) + \mu_2 \Delta v(t, x), \quad (6b)$$

$$\frac{\partial u(t, x)}{\partial n} = \frac{\partial v(t, x)}{\partial n} = 0, \quad x \in \partial \Omega, t > 0, \quad (6c)$$

where  $u(t, x)$  and  $v(t, x)$  represent the densities of the prey and predator, respectively, at a space point  $x$  and time  $t$ ; for simplification,  $u(t, x)$  and  $v(t, x)$  are rewritten as  $u$  and  $v$  in the rest of this paper, respectively;  $r(t, x)$  is the intrinsic growth rate of prey population;  $K(t, x)$  denotes the environmental carrying capacity of prey population;  $a(t, x)$  is the capturing rate of the predator;  $b(t, x)$  is the half saturation; and  $e(t, x)$  denotes the conversion rate. The term  $c(t, x) + \delta(t, x)v(t, x)/1 + v(t, x)$  describes the specific mortality of predators in absence of prey population, where  $c(t, x)$  is the mortality at low density and  $\delta(t, x)$  is the limiting, maximal mortality. The terms  $\mu_1\Delta u(t, x)$  and  $\mu_2\Delta v(t, x)$  with positive diffusion coefficients  $\mu_1$  and  $\mu_2$  represent the nonhomogeneous dispersion of the prey and the predator, respectively. Neumann boundary conditions (see equation (6c)) are employed, which characterize the absence of migration. Here, we assume that prey and predator populations are confined to a fixed bounded space domain  $\Omega \in \mathbb{R}^n$  with smooth boundary  $\partial\Omega$  and  $\bar{\Omega} = \Omega \cup \partial\Omega$ .

The rest of the paper is organized as follows. In Section 2, some conditions and definitions are given. In Section 3, dynamics of system (6a)–(6c) are studied, including boundedness, permanence, extinction, and periodic solution. Moreover, a series of numerical simulations are carried out for further study of the dynamics of system (6a)–(6c) in Section 4. Finally, the paper ends with conclusion in Section 5.

## 2. Preliminaries

Let  $\mathbb{R}$ ,  $\mathbb{Z}$ , and  $\mathbb{N}$  be the sets of all real numbers, integers, and positive integers, respectively, and  $\mathbb{R}_+ = [0, +\infty)$ . We assume that the following condition holds throughout the paper:

(H) The functions  $r(t, x)$ ,  $K(t, x)$ ,  $a(t, x)$ ,  $b(t, x)$ ,  $c(t, x)$ ,  $e(t, x)$ ,  $\delta(t, x)$  are bounded positive-valued functions on  $\mathbb{R} \times \bar{\Omega}$ , continuously differentiable in  $t$  and  $x$ , and are periodic in  $t$  with period  $\tau > 0$ .

Moreover, for a continuous function  $\phi(t, x)$ , we denote  $\phi^L = \inf_{(t,x)} \phi(t, x)$  and  $\phi^M = \sup_{(t,x)} \phi(t, x)$ .

**Definition 1.** Solutions of system (6a)–(6c) are ultimately bounded if there exist positive constants  $N_1$  and  $N_2$  such that for every solution  $(u(t, x, u_0, v_0), v(t, x, u_0, v_0))$ , there exists a moment of time  $T = T(u_0, v_0) > 0$  such that

$$\begin{aligned} u(t, x, u_0, v_0) &\leq N_1, \\ v(t, x, u_0, v_0) &\leq N_2, \end{aligned} \quad (7)$$

for all  $x \in \bar{\Omega}$  and  $t \geq T$ .

**Definition 2.** System (6a)–(6c) is permanent if there exist positive constants  $\zeta$  and  $\eta$  such that for every solution with nonnegative initial functions  $u_0(x) \neq 0$  and  $v_0(x) \neq 0$ , there exists a moment of time  $\hat{t} = \hat{t}(u_0, v_0)$  such that

$$\begin{aligned} \zeta &\leq u(t, x, u_0, v_0) \leq \eta, \\ \zeta &\leq v(t, x, u_0, v_0) \leq \eta, \end{aligned} \quad (8)$$

for all  $x \in \bar{\Omega}$  and  $t \geq \hat{t}$ .

Consider the following equations:

$$\frac{\partial u}{\partial t} - d\Delta u + f(t, x, u) = 0, \quad (t, x) \in (0, T] \times \Omega, \quad (9a)$$

$$\frac{\partial u}{\partial n} = 0, \quad (t, x) \in (0, T] \times \partial\Omega. \quad (9b)$$

Then, we have the following definition.

**Definition 3.** A function  $\hat{u}: (0, T] \times \Omega \rightarrow \mathbb{R}$  is called a lower solution of equations (9a) and 9b if it satisfies

$$\frac{\partial \hat{u}}{\partial t} - d\Delta \hat{u} + f(t, x, \hat{u}) \leq 0, \quad (t, x) \in (0, T] \times \Omega, \quad (10a)$$

$$\frac{\partial \hat{u}}{\partial n} \leq 0, \quad (t, x) \in (0, T] \times \partial\Omega. \quad (10b)$$

To analyze dynamics of system (6a)–(6c), the following results will be needed.

**Theorem 1** (Walter [49]). *Suppose that vector-functions  $v(t, x) = (v_1(t, x), \dots, v_m(t, x))$  and  $w(t, x) = (w_1(t, x), \dots, w_m(t, x))$ ,  $m \geq 1$ , satisfy the following conditions:*

(i) *They are of class  $C^2$  in  $x$ ,  $x \in \Omega$  and of class  $C^1$  in  $(t, x) \in [a, b] \times \bar{\Omega}$ , where  $\Omega \in \mathbb{R}^n$  is a bounded domain with a smooth boundary;*

(ii)  *$v_i - \mu\Delta v - g(t, x, v) \leq w_i - \mu\Delta w - g(t, x, w)$ , where  $(t, x) \in [a, b] \times \Omega$ ,  $\mu = (\mu_1, \dots, \mu_m) > 0$  (inequalities between vectors are satisfied coordinate-wise), and vector function  $g(t, x, u) = (g_1(t, x, u), \dots, g_m(t, x, u))$  is continuously differentiable and quasimonotonically increasing with respect to  $u = (u_1, \dots, u_m)$ :*

$$\frac{\partial g_i(t, x, u_1, \dots, u_m)}{\partial u_j} \geq 0, \quad i, j = 1, \dots, m, i \neq j; \quad (11)$$

(iii)  $\partial v / \partial n = \partial w / \partial n = 0$ ,  $(t, x) \in [a, b] \times \partial\Omega$ .

Then,  $v(t, x) \leq w(t, x)$  for  $(t, x) \in [a, b] \times \bar{\Omega}$ .

**Theorem 2** (Smith [50]). *Assume that  $T$  and  $d$  are positive real numbers, a function  $u(t, x)$  is continuous on  $[0, T] \times \bar{\Omega}$ , continuously differentiable in  $x \in \bar{\Omega}$ , with continuous derivatives  $\partial^2 u / \partial x_i \partial x_j$  and  $\partial u / \partial t$  on  $(0, T] \times \Omega$ , and  $u(t, x)$  satisfies the following inequalities:*

$$\frac{\partial u}{\partial t} - d\Delta u + c(t, x)u \geq 0, \quad (t, x) \in (0, T] \times \Omega,$$

$$\frac{\partial u}{\partial n} \geq 0, \quad (t, x) \in (0, T] \times \partial\Omega, \quad (12)$$

$$u(0, x) \geq 0, \quad x \in \Omega,$$

where  $c(t, x)$  is bounded on  $(0, T] \times \Omega$ . Then,  $u(t, x) \geq 0$  on  $(0, T] \times \bar{\Omega}$ .

Moreover,  $u(t, x)$  is strictly positive on  $(0, T] \times \bar{\Omega}$  if  $u(t, x)$  is not identically zero.

### 3. Main Results

**3.1. Boundedness.** From the biological and ecological viewpoint, we are always interested in the nonnegative solutions. Thus, the following theorem is given first in system (6a)–(6c).

**Theorem 3.** *Suppose that the condition (H) holds, then nonnegative and positive quadrants of  $\mathbb{R}^2$  are positively invariant for system (6a)–(6c).*

*Proof.* Let  $(u(t, x, u_0, v_0), v(t, x, u_0, v_0))$  be a solution of system (6a)–(6c) with initial condition  $u_0(x) \geq 0 (\neq 0)$ ,  $v_0(x) \geq 0 (\neq 0)$ . Additionally,  $\hat{u}$  is a solution of the following system:

$$\frac{\partial \hat{u}}{\partial t} - \mu_1 \Delta \hat{u} - \hat{u} \left( r^L - \frac{a^M}{b^L} - \frac{r^M}{K^L} \hat{u} \right) = 0, \quad \hat{u}(0, x) = u_0(x). \quad (13)$$

From system (6a), we can obtain

$$\begin{aligned} \frac{\partial u}{\partial t} - \mu_1 \Delta u - r(t, x)u \left( 1 - \frac{u}{K(t, x)} \right) + \frac{a(t, x)uv}{b(t, x)v + u} \\ \leq \frac{\partial u}{\partial t} - \mu_1 \Delta u - u \left( r^L - \frac{a^M}{b^L} - \frac{r^M}{K^L} u \right), \end{aligned} \quad (14)$$

which implies  $\hat{u}(t, x)$  is a lower solution of system (6a). According to Theorem 2, it is obvious that  $\hat{u}(t, x) \geq 0$  for all  $x \in \bar{\Omega}$  and  $t > 0$ . Furthermore, due to  $u_0(x) \geq 0 (\neq 0)$ ,  $\hat{u}(t, x) > 0$  holds for all  $x \in \bar{\Omega}$  and  $t > 0$ . Thus,  $u(t, x) > 0$  holds because  $u(t, x)$  is bounded from below by positive function  $\hat{u}(t, x)$ .

For system (6b), it can be simply verified that  $\hat{v}(t, x)$  is a lower solution of system (6b), where  $\hat{v}(t, x)$  satisfies

$$\begin{aligned} \frac{\partial \hat{v}}{\partial t} - \mu_2 \Delta \hat{v} + \delta^M \hat{v} = 0, \\ \hat{v}(0, x) = v_0(x). \end{aligned} \quad (15)$$

By the similar argument to  $u(t, x)$ , we can prove the positiveness of  $v(t, x)$ .

This completes the proof.

Based on Theorem 3, we will discuss ultimate boundedness of solutions in system (6a)–(6c), and then the following theorem can be obtained.  $\square$

**Theorem 4.** *If the condition (H) holds, then all solutions of system (6a)–(6c) with nonnegative initial conditions are ultimately bounded.*

*Proof.* From system (6a), it can be found that the following inequality holds:

$$\begin{aligned} 0 = \frac{\partial u}{\partial t} - \mu_1 \Delta u - r(t, x)u \left( 1 - \frac{u}{K(t, x)} \right) + \frac{a(t, x)uv}{b(t, x)v + u} \\ \geq \frac{\partial u}{\partial t} - \mu_1 \Delta u - u \left( r^M - \frac{r^L}{K^M} u \right). \end{aligned} \quad (16)$$

Let  $\bar{u}(t, x, u_0)$  be a solution of

$$\frac{\partial \bar{u}}{\partial t} - \mu_1 \Delta \bar{u} - \bar{u} \left( r^M - \frac{r^L}{K^M} \bar{u} \right) = 0, \quad (17)$$

then

$$\begin{aligned} \frac{\partial \bar{u}}{\partial t} - \mu_1 \Delta \bar{u} - \bar{u} \left( r^M - \frac{r^L}{K^M} \bar{u} \right) = 0 \\ \geq \frac{\partial u}{\partial t} - \mu_1 \Delta u - u \left( r^M - \frac{r^L}{K^M} u \right). \end{aligned} \quad (18)$$

According to Theorem 1, we can get  $u(t, x, u_0, v_0) \leq \bar{u}(t, M_u)$ , where  $M_u$  satisfies  $\|u_0(x)\|_C = \max_{x \in \bar{\Omega}} |u_0(x)| \leq M_u$ . By the uniqueness theorem, it is obvious that the solution  $\bar{u}(t, M_u)$  with initial conditions independent of  $x$  does not depend on  $x$  for  $t > 0$ . Therefore,  $\bar{u}(t, M_u)$  is the solution of the following ordinary differential equation:

$$\frac{d\bar{u}}{dt} = \bar{u} \left( r^M - \frac{r^L}{K^M} \bar{u} \right), \quad \bar{u}(0, M_u) = M_u. \quad (19)$$

Hence, we have

$$u(t, x, u_0, v_0) \leq \bar{u}(t, M_u) \longrightarrow \frac{r^M K^M}{r^L}, \quad \text{as } t \longrightarrow \infty. \quad (20)$$

Thus, there exists a positive constant  $M_1$  in system (6a)–(6c) such that  $u(t, x) \leq M_1$ , starting with some moment of time.

For predator population  $v$ , by system (6b), we have

$$\begin{aligned} 0 = \frac{\partial v}{\partial t} - \mu_2 \Delta v - v \left( \frac{e(t, x)u}{b(t, x)v + u} - \frac{c(t, x) + \delta(t, x)v}{1 + v} \right) \\ = \frac{\partial v}{\partial t} - \mu_2 \Delta v - v \left( \frac{e(t, x)u}{b(t, x)v + u} - \delta(t, x) - \frac{c(t, x) - \delta(t, x)}{1 + v} \right) \\ \geq \frac{\partial v}{\partial t} - \mu_2 \Delta v + c^L v - \frac{e^M M_1}{b^L}, \end{aligned} \quad (21)$$

which implies that  $v(t, x, u_0, v_0) \leq \bar{v}(t, M_v)$ , where  $\bar{v}(t, M_v)$  is a solution of the following initial value problem:

$$\frac{d\bar{v}}{dt} = -c^L \bar{v} + \frac{e^M M_1}{b^L}, \quad \bar{v}(0, M_v) = M_v, \quad (22)$$

and  $M_v$  satisfies  $\|v_0(x)\|_C = \max_{x \in \bar{\Omega}} |v_0(x)| \leq M_v$ . Obviously, we can obtain that

$$\bar{v}(t, M_v) = M_v e^{-c^L t} + \frac{e^M M_1}{b^L c^L} \longrightarrow \frac{e^M M_1}{b^L c^L}, \quad \text{as } t \longrightarrow \infty. \quad (23)$$

Therefore,  $v(t, x, u_0, v_0)$  is also ultimately bounded.

This completes the proof.  $\square$



### 3.2. Permanence

**Theorem 5.** Under the condition (H), if the following inequalities

$$r^L - \frac{a^M}{b^L} > 0, \quad (24a)$$

$$e^L - \delta^M > 0, \quad (24b)$$

hold, then system (6a)–(6c) is permanent, i.e., there exist positive constants  $m_i$  and  $M_i$  ( $i = 1, 2$ ) such that any solution of system (6a)–(6c) with nonnegative initial functions  $u_0(x) (\neq 0)$  and  $v_0(x) (\neq 0)$  satisfies  $(u(t, x), v(t, x)) \in S = \{(u, v): m_1 \leq u(t, x) \leq M_1, m_2 \leq v(t, x) \leq M_2\}$ , starting with a certain time.

*Proof.* Under the condition (H), we can know from Theorem 4 that there exists  $M_i$  ( $i = 1, 2$ ) such that  $u(t, x) \leq M_1, v(t, x) \leq M_2$ , starting with some moment of time. By comparison principle, if  $u_0(x) \geq 0 (\neq 0)$  and  $v_0(x) \geq 0 (\neq 0)$ , then  $u(t, x, u_0, v_0) > 0$  and  $v(t, x, u_0, v_0) > 0$  for all  $x \in \bar{\Omega}$  and  $t > 0$ .

Thus, for some small  $\varepsilon > 0$ , we can get initial conditions  $(u(\varepsilon, x, u_0, v_0), v(\varepsilon, x, u_0, v_0))$  separated from zero by the solution on the interval  $t \geq \varepsilon$ . Without loss of generality, we assume that  $\min_{x \in \bar{\Omega}} u_0(x) = m_u, \min_{x \in \bar{\Omega}} v_0(x) = m_v$ . Then, the following inequality holds:

$$\begin{aligned} 0 &= \frac{\partial u}{\partial t} - \mu_1 \Delta u - u \left( r(t, x) - \frac{r(t, x)}{K(t, x)} u \right) + \frac{a(t, x)uv}{b(t, x)v + u} \\ &\leq \frac{\partial u}{\partial t} - \mu_1 \Delta u - u \left( r^L - \frac{a^M}{b^L} - \frac{r^M}{K^L} u \right). \end{aligned} \quad (25)$$

Obviously, we can get

$$\begin{aligned} 0 &= \frac{\partial \hat{u}}{\partial t} - \mu_1 \Delta \hat{u} - \hat{u} \left( r^L - \frac{a^M}{b^L} - \frac{r^M}{K^L} \hat{u} \right) \\ &\leq \frac{\partial \hat{u}}{\partial t} - \mu_1 \Delta \hat{u} - \hat{u} \left( r^L - \frac{a^M}{b^L} - \frac{r^M}{K^L} \hat{u} \right). \end{aligned} \quad (26)$$

Consequently, for  $t \geq 0$ , we have

$$u(t, x, u_0, v_0) \geq \hat{u}(t, m_u). \quad (27)$$

Thus, the solution  $u(t, x, u_0, v_0)$  is bounded from below by a solution of the following logistic equation:

$$\frac{d\hat{u}}{dt} = \hat{u} \left( r^L - \frac{a^M}{b^L} - \frac{r^M}{K^L} \hat{u} \right), \quad \hat{u}(0) = m_u. \quad (28)$$

Thus, by Theorem 1 and condition (24a) and (24b), we have

$$u(t, x, u_0, v_0) \geq \hat{u}(t, x) \longrightarrow \frac{K^L (r^L - a^M/b^L)}{r^M}, \quad \text{as } t \longrightarrow \infty \quad (29)$$

Therefore, there exists a positive constant  $m_1$  such that  $u(t, x, u_0, v_0) \geq m_1$  for  $t$  large enough.

By system (6b), the following inequality holds:

$$\begin{aligned} \frac{\partial v}{\partial t} - \mu_2 \Delta v - v \left( \frac{e(t, x)u}{b(t, x)v + u} - \frac{c(t, x) + \delta(t, x)v}{1 + v} \right) \\ \leq \frac{\partial v}{\partial t} - \mu_2 \Delta v + (\delta^M - e^L)v + \frac{b^M e^L}{m_1} v^2. \end{aligned} \quad (30)$$

By a similar analysis to  $u$ , we have  $v(t, x, u_0, v_0) \geq \hat{v}(t, m_v)$ , where  $\hat{v}(t, m_v)$  is a solution of the following system:

$$\frac{\partial \hat{v}}{\partial t} - \mu_2 \Delta \hat{v} + (\delta^M - e^L)\hat{v} + \frac{b^M e^L}{m_1} \hat{v}^2, \quad \hat{v}(0) = m_v. \quad (31)$$

According to condition (24b), we can obtain that there exists a positive  $m_2$  such that  $v(t, x, u_0, v_0) \geq m_2$  for  $t$  large enough. Thus, system (6a)–(6c) is permanent, starting with a certain time.

This completes the proof.  $\square$

**3.3. Extinction.** In this section, we will discuss the extinction of predator species, and then the following theorem arrives in system (6a)–(6c).

**Theorem 6.** If the condition (H) holds, and

$$e^M - c^L < 0, \quad (32)$$

then,  $v(t, x) \longrightarrow 0$  as  $t \longrightarrow \infty$ .

*Proof.* Suppose  $M_v$  is a fixed positive constant guaranteeing  $M_v \leq v_0(x)$ , and  $\bar{v}(t, M_v)$  is the solution of the following initial value problem:

$$\frac{\partial \bar{v}}{\partial t} = \bar{v}(e^M - c^L), \quad (33)$$

$$\bar{v}(0, M_v) = M_v.$$

By system (6b), we have

$$\begin{aligned} 0 &= \frac{\partial v}{\partial t} - \mu_2 \Delta v + v \left( -\frac{e(t, x)u}{b(t, x)v + u} + \frac{c(t, x) + \delta(t, x)v}{1 + v} \right) \\ &\geq \frac{\partial v}{\partial t} - \mu_2 \Delta v + (c^L - e^M)v. \end{aligned} \quad (34)$$

Thus, according to Theorem 1, we can deduce that  $v(t, x, u_0, v_0) \leq \bar{v}(t, M_v) \longrightarrow 0$  as  $t \longrightarrow \infty$  if inequality (32) holds.

This completes the proof.  $\square$

**3.4. Periodic Solution.** In this section, we will study the periodic solutions in system (6a)–(6c) by constructing a proper Lyapunov function.

**Theorem 7.** Under the condition (H), assume that system (6a)–(6c) is permanent, that is, there exist positive constants  $N$  and  $M$  such that an arbitrary solution of system (6a)–(6c)

with nonnegative initial functions not identically equal to zero satisfies the condition:

$$(u(t, x), v(t, x)) \in E = \{(u, v): N \leq u(t, x) \leq M, \\ N \leq v(t, x) \leq M\}, \quad (35)$$

starting with a certain moment of time. If

$$\lambda_M(W) < 0, \quad (36)$$

where  $\lambda_M$  is the maximal eigenvalue of the following matrix:

$$\begin{pmatrix} E_{11} & E_{12} \\ E_{21} & E_{22} \end{pmatrix}, \quad (37)$$

where

$$E_{11} = 2 \left( r^M - \frac{r^L}{K^M} N - \frac{a^L b^L N^2}{(b^M M + M)^2} \right),$$

$$E_{22} = 2 \left( -\delta^L + \frac{\delta^M - c^L}{(1 + N)^2} + \frac{e^M M^2}{(b^L N + N)^2} \right), \quad (38)$$

$$E_{12} = E_{21} = a^M + \frac{e^M}{b^L}.$$

Then system (6a)–(6c) has a unique and strictly positive  $\tau$ -periodic solution, which is globally asymptotically stable.

*Proof.* Let  $(u(t, x), v(t, x))$  and  $(\bar{u}(t, x), \bar{v}(t, x))$  be two solutions of system (6a)–(6c) bounded by constants  $N$  and

$M$  from below and above, respectively. Consider the following function:

$$L(t) = \int_{\Omega} [(u(t, x) - \bar{u}(t, x))^2 + (v(t, x) - \bar{v}(t, x))^2] dx. \quad (39)$$

By system (6a)–(6c), we can get its derivative:

$$\begin{aligned} \frac{dL(t)}{dt} &= 2 \int_{\Omega} (u - \bar{u}) \left( \frac{\partial u}{\partial t} - \frac{\partial \bar{u}}{\partial t} \right) dx + 2 \int_{\Omega} (v - \bar{v}) \left( \frac{\partial v}{\partial t} - \frac{\partial \bar{v}}{\partial t} \right) dx \\ &= 2\mu_1 \int_{\Omega} (u - \bar{u}) \Delta(u - \bar{u}) dx + 2\mu_2 \int_{\Omega} (v - \bar{v}) \Delta(v - \bar{v}) dx \\ &\quad + 2 \int_{\Omega} (u - \bar{u}) \left[ \left( u \left( r - \frac{r}{K} u \right) - \frac{auv}{bv+u} \right) - \left( \bar{u} \left( r - \frac{r}{K} \bar{u} \right) - \frac{a\bar{u}\bar{v}}{b\bar{v}+\bar{u}} \right) \right] dx \\ &\quad + 2 \int_{\Omega} (v - \bar{v}) \left[ \left( \frac{euv}{bv+u} - \frac{c+\delta v}{1+v} \right) - \left( \frac{e\bar{u}\bar{v}}{b\bar{v}+\bar{u}} - \frac{c+\delta\bar{v}}{1+\bar{v}} \right) \right] dx \\ &= I_1 + I_2 + I_3 + I_4. \end{aligned} \quad (40)$$

Then, from the boundary condition (6c),

$$\begin{aligned} I_1 + I_2 &= -2\mu_1 \int_{\Omega} \nabla^2(u - \bar{u}) dx - 2\mu_2 \int_{\Omega} \nabla^2(v - \bar{v}) dx \\ &\leq -2\mu_1 \int_{\Omega} |\nabla(u - \bar{u})|^2 dx - 2\mu_2 \int_{\Omega} |\nabla(v - \bar{v})|^2 dx \leq 0. \end{aligned} \quad (41)$$

For other terms  $I_3$  and  $I_4$ ,

$$\begin{aligned} I_3 + I_4 &= 2 \int_{\Omega} (u - \bar{u}) \left( r(u - \bar{u}) - \frac{r}{K} (u - \bar{u})(u + \bar{u}) + \frac{a\bar{u}\bar{v}}{b\bar{v}+\bar{u}} - \frac{auv}{bv+u} \right) dx \\ &\quad + 2 \int_{\Omega} (v - \bar{v}) \left( -\delta(v - \bar{v}) + \frac{c - \delta}{1 + \bar{v}} \bar{v} - \frac{c - \delta}{1 + v} v + \frac{euv}{bv+u} - \frac{e\bar{u}\bar{v}}{b\bar{v}+\bar{u}} \right) dx \\ &= 2 \int_{\Omega} (u - \bar{u})^2 \left( r - \frac{r}{K} (u - \bar{u}) - \frac{abv\bar{v}}{(bv+u)(b\bar{v}+\bar{u})} \right) dx \\ &\quad + 2 \int_{\Omega} (v - \bar{v})^2 \left( \frac{e\bar{u}\bar{v}}{(bv+u)(b\bar{v}+\bar{u})} - \frac{c - \delta}{(1+v)(1+\bar{v})} - \delta \right) dx \\ &\quad + 2 \int_{\Omega} (u - \bar{u})(v - \bar{v}) \left( \frac{ebv\bar{v}}{(bv+u)(b\bar{v}+\bar{u})} - \frac{a\bar{u}\bar{v}}{(bv+u)(b\bar{v}+\bar{u})} \right) dx \\ &\leq 2 \int_{\Omega} (u - \bar{u})^2 \left( r^M - \frac{r^L}{K^M} N - \frac{a^L b^L N^2}{(b^M M + M)^2} \right) dx \\ &\quad + 2 \int_{\Omega} (v - \bar{v})^2 \left( \frac{e^M M^2}{(b^L N + N)^2} + \frac{\delta^M - c^L}{(1 + N)^2} - \delta^L \right) dx \\ &\quad + 2 \int_{\Omega} |u - \bar{u}| |v - \bar{v}| \left( a^M + \frac{e^M}{b^L} \right) dx \\ &\leq \lambda_M \int_{\Omega} [(u - \bar{u})^2 + (v - \bar{v})^2] dx. \end{aligned} \quad (42)$$

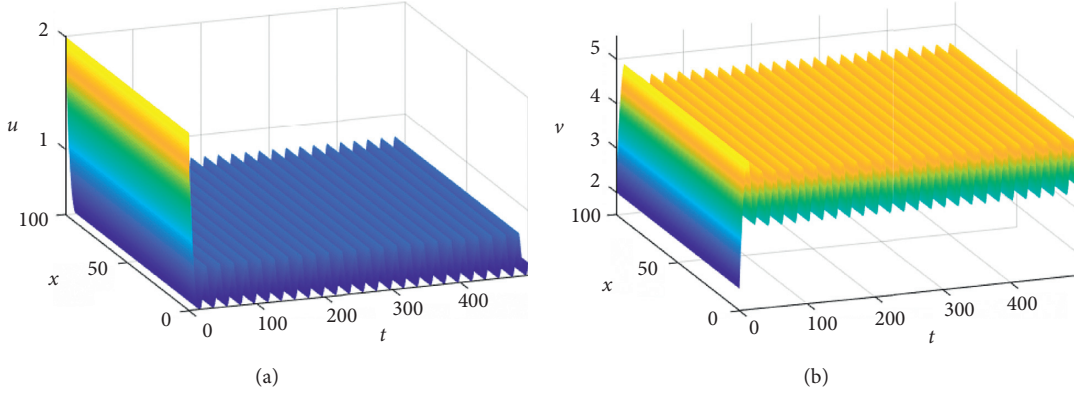


FIGURE 1: Numerical solutions of system (6a)–(6c): (a) prey population  $u$  and (b) predator population  $v$ , where  $r(t, x) = 1.1 + 0.1 \sin(\pi * t/10)$ ,  $K(t, x) = 2 + 0.5 * \cos(\pi * t/10)$ ,  $a(t, x) = 0.8 + 0.005 * \cos(\pi * t/10)$ ,  $b(t, x) = 0.9 + 0.005 * \cos(\pi * t/10)$ ,  $e(t, x) = 0.7 - 0.002 * \cos(\pi * t/10)$ ,  $c(t, x) = 0.02 + 0.005 * \cos(\pi * t/10)$ ,  $\delta(t, x) = 0.12 + 0.05 * \cos(\pi * t/10)$ ,  $\mu_1 = 1$ , and  $\mu_2 = 1$ .

By condition (36), we have

$$L(t) \leq L(0)e^{\lambda_M t} \rightarrow 0, \quad \text{as } t \rightarrow \infty, \quad (43)$$

which implies that  $\|u(t, x) - \bar{u}(t, x)\| \rightarrow 0$  and  $\|v(t, x) - \bar{v}(t, x)\| \rightarrow 0$  as  $t \rightarrow \infty$ , where  $\|\cdot\|$  is the norm of the space  $L_2(\Omega)$ . Additionally, by condition (35), solutions of system (6a)–(6c) are bounded in the space  $C^{1+\nu}(\bar{\Omega}, \mathbb{R}^2)$ , where  $0 < \nu < 2l - (n/p)$  and  $(1/2) + (n/2p) < l < 1$ .

Therefore,

$$\begin{aligned} \lim_{t \rightarrow \infty} \sup_{x \in \bar{\Omega}} |u(t, x) - \bar{u}(t, x)| &= 0, \\ \lim_{t \rightarrow \infty} \sup_{x \in \bar{\Omega}} |v(t, x) - \bar{v}(t, x)| &= 0. \end{aligned} \quad (44)$$

Consider the sequence  $(u(k\tau, x, u_0, v_0), v(k\tau, x, u_0, v_0)) = W(k\tau, W_0)$ ,  $k \in \mathbb{N}$ . Then,  $\{W(k\tau, W_0), k \in \mathbb{N}\}$  is compact in the space  $C(\bar{\Omega}) \times C(\bar{\Omega})$ . Let  $\bar{W}$  be a limit of this sequence, then  $W(\tau, \bar{W}) = \bar{W}$ .

Actually, because  $W(\tau, W(k_n\tau, W_0)) = W(k_n\tau, W(\tau, W_0))$  and  $W(k_n\tau, W(\tau, W_0)) - W(k_n\tau, W_0) \rightarrow 0$  as  $k_n \rightarrow \infty$ , we have

$$\begin{aligned} \|W(\tau, \bar{W}) - \bar{W}\|_C &\leq \|W(\tau, \bar{W}) - W(\tau, W(k_n\tau, W_0))\|_C \\ &+ \|W(\tau, W(k_n\tau, W_0)) - W(k_n\tau, W_0)\|_C \\ &+ \|W(k_n\tau, W_0) - \bar{W}\|_C \rightarrow 0 \text{ as } n \rightarrow \infty. \end{aligned} \quad (45)$$

Thus, the sequence  $\{W(k\tau, W_0), k \in \mathbb{N}\}$  has a unique limit point. Otherwise, suppose that the sequence has two limit points  $\bar{W} = \lim_{n \rightarrow \infty} W(k_n\tau, W_0)$  and  $\tilde{W} = \lim_{n \rightarrow \infty} W(k'_n\tau, W_0)$ , then we can get the following result from (45) and  $\bar{W} = W(k_n\tau, \bar{W})$ :

$$\begin{aligned} \|\bar{W} - \tilde{W}\|_C &\leq \|\bar{W} - W(k_n\tau, W_0)\|_C \\ &+ \|W(k_n\tau, W_0) - \tilde{W}\|_C \rightarrow 0, \quad n \rightarrow \infty. \end{aligned} \quad (46)$$

Hence,  $\bar{W} = \tilde{W}$ . The solution  $(u(t, x, \bar{u}, \bar{v}), v(t, x, \bar{u}, \bar{v}))$  is the unique periodic solution of system (6a)–(6c), and it is asymptotically stable using equation (44).

This completes the proof.  $\square$

## 4. Numerical Results

In the previous section, we have obtained some interesting results of system (6a)–(6c). However, due to the complexity of system (6a)–(6c), it becomes much more difficult to provide in-depth analysis. Thus, here, we perform some numerical simulations to investigate prey-predator dynamics further.

According to Theorem 5, when  $r^L - a^M/b^L > 0$  and  $e^L - \delta^M > 0$  holds, system (6a)–(6c) is permanent under condition (H). Figure 1 shows that system (6a)–(6c) is permanent, where  $r^L - a^M/b^L \approx 0.1 > 0$  and  $e^L - \delta^M = 0.528 > 0$ . When  $e = 0.005 - 0.002 \sin(\pi * t/10)$ , other parameters are the same as the ones in Figure 1, and we can get a numerical solution of system (6a)–(6c) (see Figure 2). It is obvious that predator population  $v$  is extinct ultimately, which is consistent with Theorem 6 because  $e^M - c^L = -0.008 < 0$ .

In section 3.4, the existence of periodic solution was discussed, and its stability and uniqueness were analyzed as well. In fact, Figure 1 has shown the existence of a periodic solution. Yet, we here take another set of function corresponding to the parameters of system (6a)–(6c), which is only the periodic function of time  $t$  with period 200. The corresponding numerical solutions are shown in Figure 3. Clearly, the numerical solution is periodic in  $t$  with the period of 200 (see Figures 3(c) and 3(d)), but it is homogeneous in space (see Figures 3(a) and 3(b)). Compared to Figure 3, we consider another situation that the parameters of system (6a)–(6c) are functions with respect to both time  $t$  and space  $x$ . We find the solution is still periodic, but it is heterogeneous in space (see Figure 4). It is evident that the spatial heterogeneity is the reason giving rise to the oscillation of the solution in space.

Additionally, we find that the spatial heterogeneity can promote the permanence of the system. Figure 5 indicates that the extinction occurs in system (6a)–(6c). However,

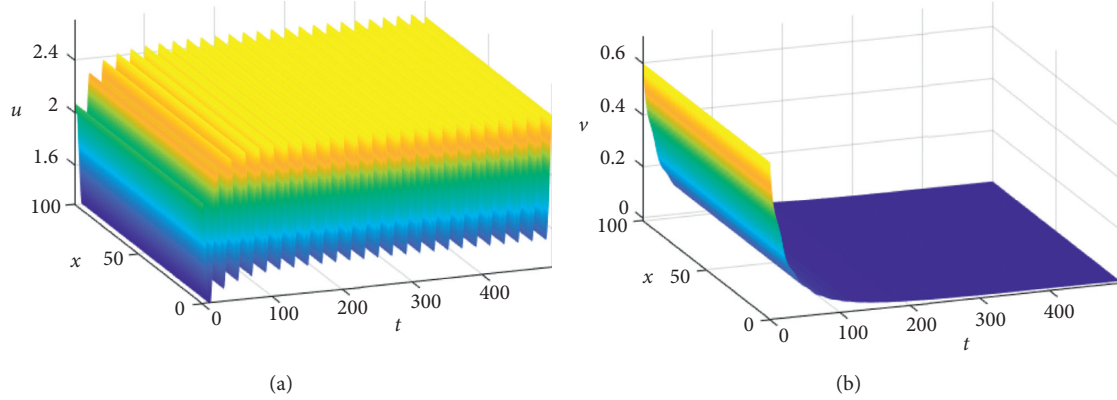


FIGURE 2: Numerical solutions of system (6a)–(6c): (a) prey population  $u$  and (b) predator population  $v$ .

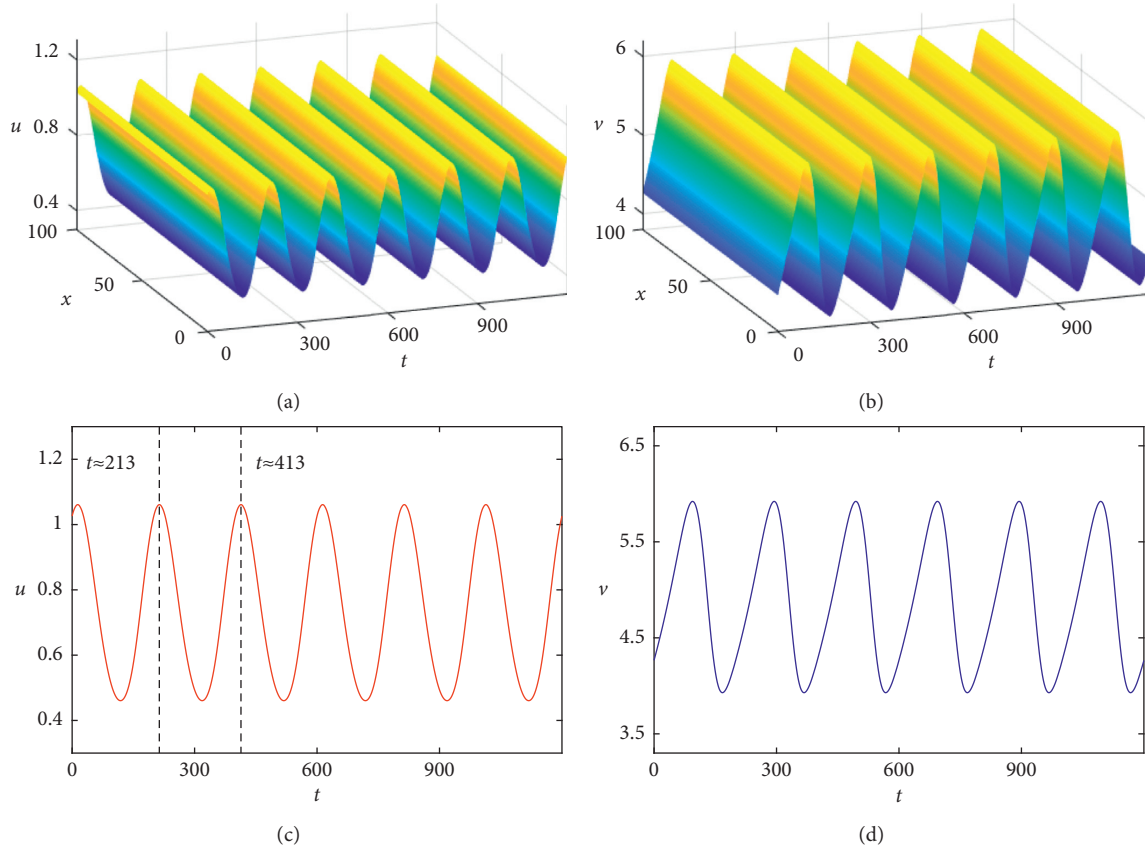


FIGURE 3: Numerical solutions of system (6a)–(6c): (a) prey population  $u$ , (b) predator population  $v$ , (c) profile of  $u(t)$  at  $x = 50$ , and (d) profile of  $v(t)$  at  $x = 50$ . Here,  $r(t, x) = 1.2 + 0.1 \sin(\pi * t/100)$ ,  $K(t, x) = 2 + 0.5 \cos(\pi * t/100)$ ,  $a(t, x) = 0.8 + 0.005 \cos(\pi * t/100)$ ,  $b(t, x) = 0.9 + 0.005 \cos(\pi * t/100)$ ,  $e(t, x) = 0.7 - 0.005 \sin(\pi * t/100)$ ,  $c(t, x) = 0.02 + 0.01 \cos(\pi * t/100)$ ,  $\delta(t, x) = 0.12 + 0.05 \cos(\pi * t/100)$ ,  $\mu_1 = 1$ , and  $\mu_2 = 1$ .

when we set  $r(t, x) = 0.9 + 0.001 \sin(5 * \pi * t/100) + 0.1 \cos(5 * \pi * x/100)$  (other parameters are the same as the ones in Figure 5), we get a very interesting result, that is, system (6a)–(6c) becomes permanent (see Figure 6). Likewise, other parameters are explored by repeating the same procedure, and similar results are obtained, which are

omitted here. Obviously, the spatial heterogeneity plays an important role in dynamics of system (6a)–(6c).

Let all the parameters be constant, then there exists a nonconstant stationary solution in system (6a)–(6c), as shown in Figure 7. Furthermore, we consider the parameters depending on time  $t$  based on Figure 7, but the result shows

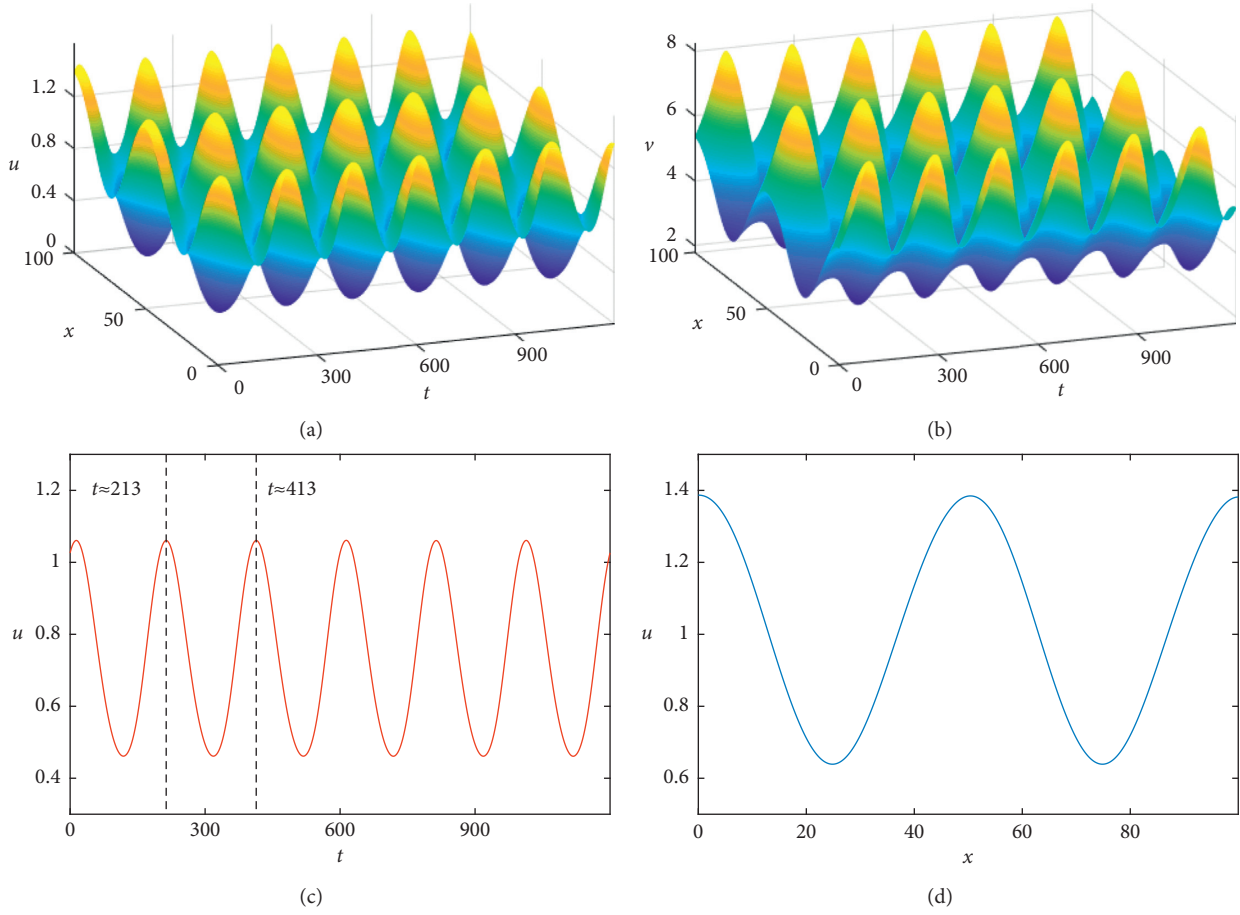


FIGURE 4: Numerical solutions of system (6a)–(6c): (a) prey population  $u$ , (b) predator population  $v$ , (c) profile of  $u(t)$  at  $x = 50$ , and (d) profile of  $u(x)$  at  $t = 1200$ . Here,  $r(t, x) = 1.2 + 0.1 \sin(\pi * t/100) + 0.01 \cos(4 * \pi * x/100) * \sin(4 * \pi * x/100)$ ,  $K(t, x) = 2 + 0.5 \cos(\pi * t/100) + \cos(4 * \pi * x/100)$ ,  $a(t, x) = 0.8 + 0.005 \cos(\pi * t/100) + 0.1 \cos(4 * \pi * x/100)$ ,  $b(t, x) = 0.9 + 0.005 \cos(\pi * t/100) + 0.1 \cos(4 * \pi * x/100)$ ,  $e(t, x) = 0.7 - 0.005 \sin(\pi * t/100) + 0.1 \cos(4 * \pi * x/100)$ ,  $c(t, x) = 0.02 + 0.01 \cos(\pi * t/100) + 0.001 \cos(4 * \pi * x/100)$ ,  $\delta(t, x) = 0.12 + 0.05 \cos(\pi * t/100) + 0.01 \cos(4 * \pi * x/100)$ ,  $\mu_1 = 1$ , and  $\mu_2 = 1$ .

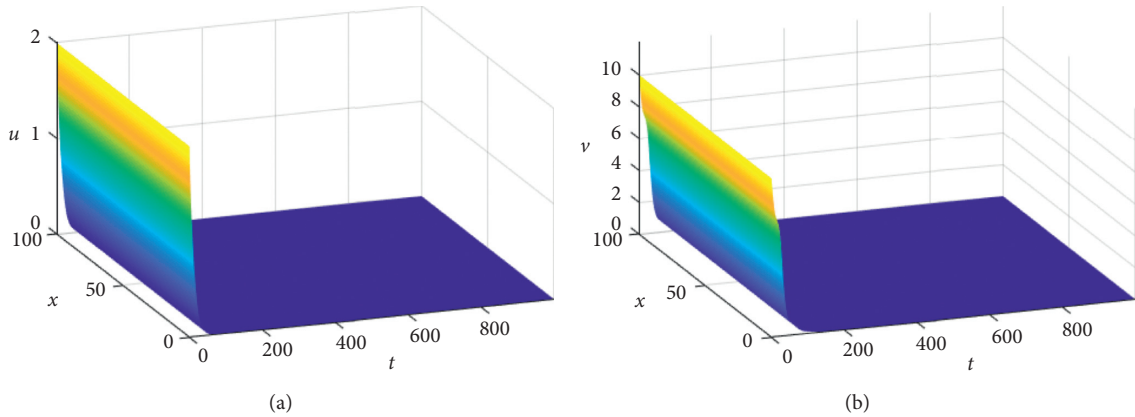


FIGURE 5: Numerical solutions of system (6a)–(6c): (a) prey population  $u$  and (b) predator population  $v$ , where  $r(t, x) = 0.9 + 0.001 \sin(5 * \pi * t/100)$ ,  $K(t, x) = 10 + 0.5 \cos(5 * \pi * t/100)$ ,  $a(t, x) = 0.8 + 0.005 \cos(5 * \pi * t/100)$ ,  $b(t, x) = 0.78 + 0.005 \cos(5 * \pi * t/100)$ ,  $e(t, x) = 0.7 - 0.005 \sin(5 * \pi * t/100)$ ,  $c(t, x) = 0.02 + 0.001 \cos(5 * \pi * t/100)$ ,  $\delta(t, x) = 0.12 + 0.05 \cos(5 * \pi * t/100)$ ,  $\mu_1 = 1$ , and  $\mu_2 = 1$ .

that the extinction of both prey and predator occurs (see Figure 8). However, when the parameter  $r$  depends on space  $x$  except for time  $t$ , it can be found from Figure 9 that system

(6a)–(6c) is still permanent. Although both Figures 7 and 9 show the spatial heterogeneity of population distribution, their natures are different. The spatial heterogeneity in



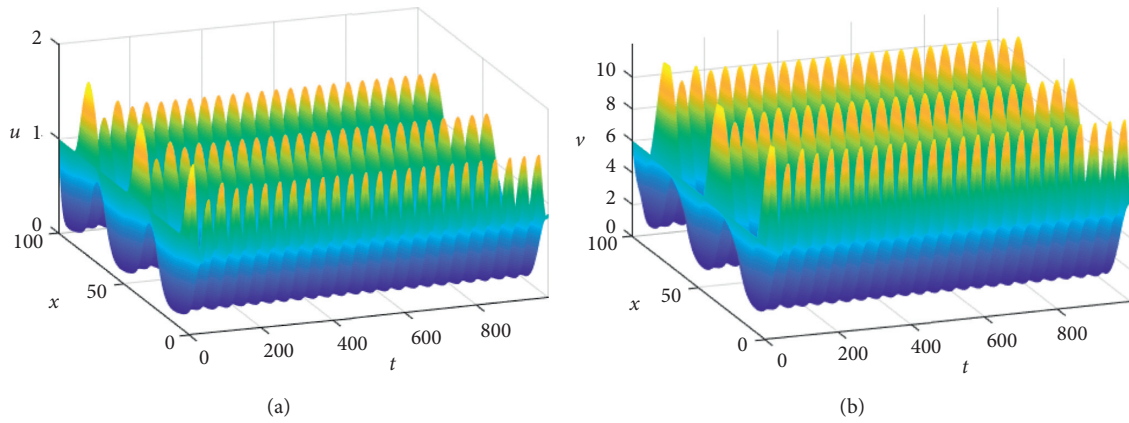


FIGURE 6: Numerical solutions of system (6a)–(6c): (a) prey population  $u$  and (b) predator population  $v$ .

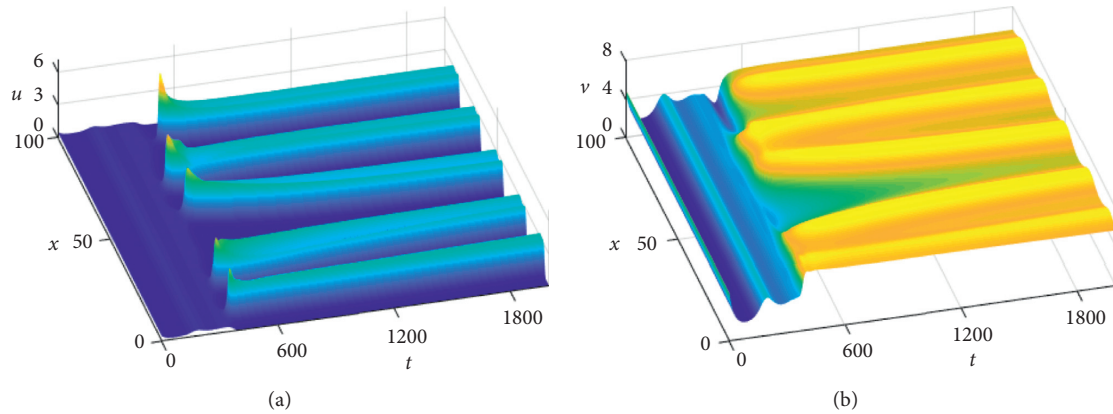


FIGURE 7: Numerical solutions of system (6a)–(6c): (a) prey population  $u$  and (b) predator population  $v$ , where  $r(t, x) = 0.9$ ,  $K(t, x) = 10$ ,  $a(t, x) = 0.8$ ,  $b(t, x) = 0.8$ ,  $e(t, x) = 0.7$ ,  $c(t, x) = 0.02$ ,  $\delta(t, x) = 0.12$ ,  $\mu_1 = 0.01$ , and  $\mu_2 = 20$ .

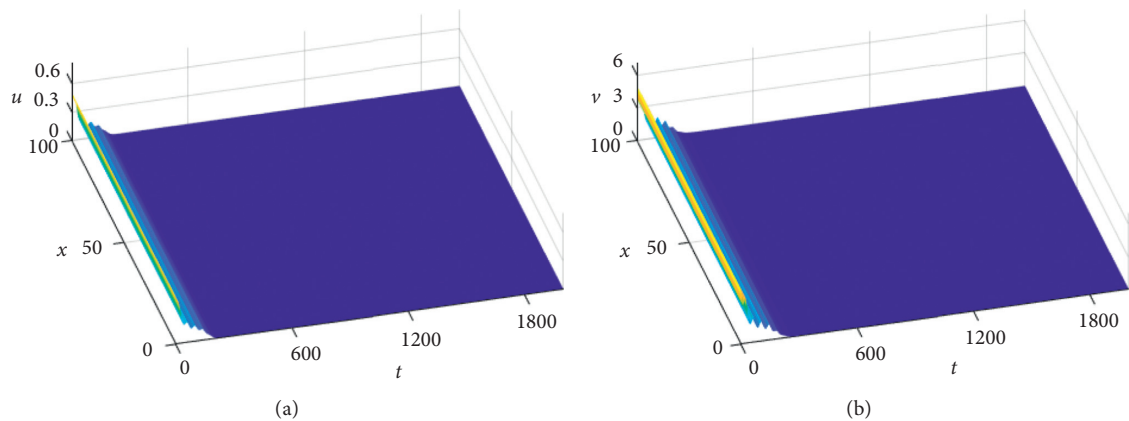


FIGURE 8: Numerical solutions of system (6a)–(6c): (a) prey population  $u$  and (b) predator population  $v$ , where  $r(t, x) = 0.9 + 0.001 \sin(5 * \pi * t/100)$ ,  $K(t, x) = 10 + 0.5 \sin(5 * \pi * t/100)$ ,  $a(t, x) = 0.8 + 0.005 \sin(5 * \pi * t/100)$ ,  $b(t, x) = 0.8 + 0.005 \sin(5 * \pi * t/100)$ ,  $e(t, x) = 0.7 - 0.005 \sin(5 * \pi * t/100)$ ,  $c(t, x) = 0.02 + 0.001 \sin(5 * \pi * t/100)$ ,  $\delta(t, x) = 0.12 + 0.05 \sin(5 * \pi * t/100)$ ,  $\mu_1 = 0.01$ , and  $\mu_2 = 20$ .



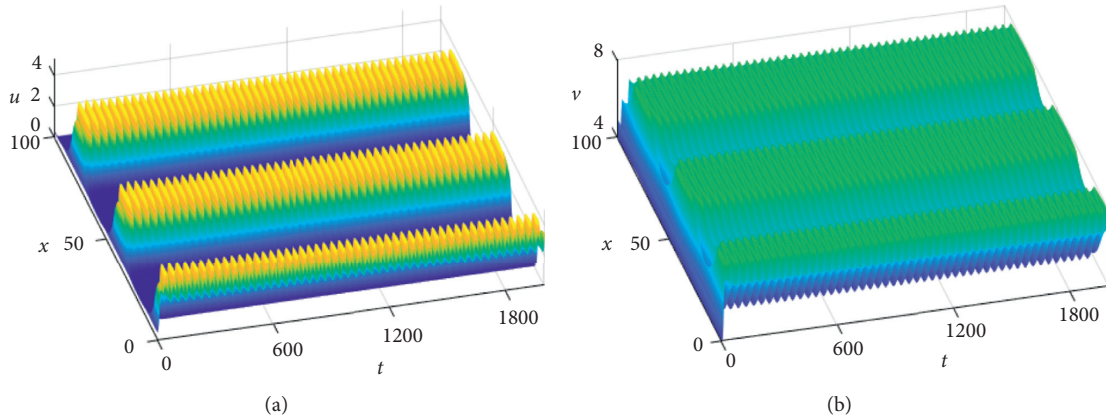


FIGURE 9: Numerical solutions of system (6a)–(6c): (a) prey population  $u$  and (b) predator population  $v$ , where  $r(t, x) = 0.9 + 0.001 \sin(5 * \pi * t/100) + 0.1 \cos(t * \pi * x/100)$  and other parameters are the same as the ones in Figure 8.

Figure 7 is induced by the diffusion, while in Figure 9 it depends on the space variation of parameters. For other parameters of system (6a)–(6c), we can obtain similar results, which are omitted here.

## 5. Conclusion

In this paper, we first propose a reaction-diffusion system (6a)–(6c) to describe the interaction between the prey and the predator, where the spatial heterogeneity and the time-periodic environment are considered. In order to study the boundedness of solution, the positive invariance of system (6a)–(6c) is discussed, and the results demonstrate that nonnegative and positive quadrants of  $\mathbb{R}^2$  are always positively invariant for system (6a)–(6c) when the condition (H) holds. Based on this, we find that all solutions of system (6a)–(6c) are ultimately bounded as long as the initial conditions are nonnegative. Also, we discuss the permanence of system (6a)–(6c) and obtain the sufficient conditions. Moreover, we derive the sufficient conditions for the extinction of predator population. Obviously, these conditions are very significant for studies of permanence and extinction of the system. When system (6a)–(6c) is permanent, we discuss the existence of a periodic solution, which suggests that a unique and strictly positive periodic solution with fixed period exists under certain conditions.

According to theoretical analysis, some numerical results are given, which show further dynamics in system (6a)–(6c). Results from literature [45, 46] indicate that Turing patterns can exist in system (5a)–(5c) (i.e., system (6a)–(6c) without spatial heterogeneity and time-periodic environment). After taking time-periodic environment into account, we find that both prey population and predator population are extinct. However, when the combination of spatial heterogeneity and time-periodic environment is considered, it is demonstrated that both prey population and predator population are permanent, which means that spatial heterogeneity tends to enhance the persistence of prey and predator population. Additionally, when prey population and predator population are permanent, our results show that solutions of system (6a)–(6c) seem to be periodic

because of the time-periodic environment and the spatial heterogeneity. Thus, we want to emphasize that spatial heterogeneity and time-periodic environment indeed play a significant role in prey-predator dynamics.

## Data Availability

The data used to support the findings of this study are included within the article.

## Conflicts of Interest

The authors declare that there are no conflicts of interest.

## Acknowledgments

This work was supported by the Zhejiang Provincial Natural Science Foundation of China (Grant no. LQ18C030002), the National Key Research and Development Program of China (Grant no. 2018YFE0103700), the National Natural Science Foundation of China (Grant nos. 61871293, 61901303, and 41876124), and the Science and Technology Major Program of Wenzhou, China (Grant no. 2018ZG002).

## References

- [1] R. M. May, "Limit cycles in predator-prey communities," *Science*, vol. 177, no. 4052, pp. 900–902, 1972.
- [2] G. F. Fussmann, S. P. Ellner, K. W. Shertzer, and N. G. Hairston Jr., "Crossing the hopf bifurcation in a live predator-prey system," *Science*, vol. 290, no. 5495, pp. 1358–1360, 2000.
- [3] E. McCauley, R. M. Nisbet, W. W. Murdoch, A. M. de Roos, and W. S. C. Gurney, "Large-amplitude cycles of *Daphnia* and its algal prey in enriched environments," *Nature*, vol. 402, no. 6762, pp. 653–656, 1999.
- [4] P. J. Wangersky and W. J. Cunningham, "Time lag in prey-predator population models," *Ecology*, vol. 38, no. 1, pp. 136–139, 1957.
- [5] M. Wang and Y. Zhang, "Dynamics for a diffusive prey-predator model with different free boundaries," *Journal of Differential Equations*, vol. 264, no. 5, pp. 3527–3558, 2018.

- [6] T. Antal and M. Droz, "Phase transitions and oscillations in a lattice prey-predator model," *Physical Review E*, vol. 63, Article ID 056119, 2001.
- [7] C. J. Dai, H. G. Yu, Q. Guo et al., "Dynamics induced by delay in a nutrient-phytoplankton model with multiple delays," *Complexity*, vol. 2019, Article ID 3879626, 16 pages, 2019.
- [8] C. S. Holling, "The components of predation as revealed by a study of small-mammal predation of the European pine sawfly," *The Canadian Entomologist*, vol. 91, no. 5, pp. 293–320, 1959.
- [9] M. U. Akhmet, M. Beklioglu, T. Ergenc, and V. I. Tkachenko, "An impulsive ratio-dependent predator-prey system with diffusion," *Nonlinear Analysis: Real World Applications*, vol. 7, no. 5, pp. 1255–1267, 2006.
- [10] D. Alonso, F. Bartumeus, and J. Catalan, "Mutual interference between predators can give rise to Turing spatial patterns," *Ecology*, vol. 83, no. 1, pp. 28–34, 2002.
- [11] L. R. Ginzburg and H. R. Akcakaya, "Consequences of ratio-dependent predation for steady-state properties of ecosystems," *Ecology*, vol. 73, no. 5, pp. 1536–1543, 1992.
- [12] P. A. Abrams and L. R. Ginzburg, "The nature of predation: prey dependent, ratio dependent or neither?" *Trends in Ecology & Evolution*, vol. 15, no. 8, pp. 337–341, 2000.
- [13] R. Arditi and L. R. Ginzburg, "Coupling in predator-prey dynamics: ratio-Dependence," *Journal of Theoretical Biology*, vol. 139, no. 3, pp. 311–326, 1989.
- [14] M. Cavani and M. Farkas, "Bifurcations in a predator-prey model with memory and diffusion. I: andronov-Hopf bifurcation," *Acta Mathematica Hungarica*, vol. 63, no. 3, pp. 213–229, 1994.
- [15] M. Cavani and M. Farkas, "Bifurcations in a predator-prey model with memory and diffusion II: Turing bifurcation," *Acta Mathematica Hungarica*, vol. 63, no. 4, pp. 375–393, 1994.
- [16] R. Yang, "Hopf bifurcation analysis of a delayed diffusive predator-prey system with nonconstant death rate," *Chaos, Solitons & Fractals*, vol. 81, pp. 224–232, 2015.
- [17] C. Duque and M. Lizana, "Partial characterization of the global dynamic of a predator-prey model with non constant mortality rate," *Differential Equations and Dynamical Systems*, vol. 17, no. 1-2, pp. 63–75, 2009.
- [18] C. J. Dai, M. Zhao, H. G. Yu, and Y. P. Wang, "Delay-induced instability in a nutrient-phytoplankton system with flow," *Physical Review E*, vol. 91, no. 6, Article ID 032929, 2015.
- [19] X. Tang and Y. Song, "Cross-diffusion induced spatiotemporal patterns in a predator-prey model with herd behavior," *Nonlinear Analysis: Real World Applications*, vol. 24, pp. 36–49, 2015.
- [20] X. Tang, Y. Song, and T. Zhang, "Turing-Hopf bifurcation analysis of a predator-prey model with herd behavior and cross-diffusion," *Nonlinear Dynamics*, vol. 86, no. 1, pp. 73–89, 2016.
- [21] A. B. Medvinsky, S. V. Petrovskii, I. A. Tikhonova, H. Malchow, and B.-L. Li, "Spatiotemporal complexity of plankton and fish dynamics," *SIAM Review*, vol. 44, no. 3, pp. 311–370, 2002.
- [22] J. Wang, J. Shi, and J. Wei, "Dynamics and pattern formation in a diffusive predator-prey system with strong Allee effect in prey," *Journal of Differential Equations*, vol. 251, no. 4-5, pp. 1276–1304, 2011.
- [23] A. J. Lotka, *Elements of Physical Biology*, Williams & Wilkins, Baltimore, ND, USA, 1925.
- [24] V. Volterra, "Fluctuations in the abundance of a species considered Mathematically1," *Nature*, vol. 118, no. 2972, pp. 558–560, 1926.
- [25] C. S. Holling, "The functional response of predators to prey density and its role in mimicry and population regulation," *Memoirs of the Entomological Society of Canada*, vol. 97, no. 45, pp. 1–60, 1965.
- [26] Z. Lin and M. Pedersen, "Stability in a diffusive food-chain model with Michaelis-Menten functional response," *Nonlinear Analysis: Theory, Methods & Applications*, vol. 57, no. 3, pp. 421–433, 2004.
- [27] C. Dai, M. Zhao, and H. Yu, "Dynamics induced by delay in a nutrient-phytoplankton model with diffusion," *Ecological Complexity*, vol. 26, pp. 29–36, 2016.
- [28] R. S. Cantrell and C. Cosner, "On the dynamics of predator-prey models with the Beddington-DeAngelis functional response," *Journal of Mathematical Analysis and Applications*, vol. 257, no. 1, pp. 206–222, 2001.
- [29] X. Guan and F. Chen, "Dynamical analysis of a two species amensalism model with Beddington-DeAngelis functional response and Allee effect on the second species," *Nonlinear Analysis: Real World Applications*, vol. 48, pp. 71–93, 2019.
- [30] R. Arditi, L. R. Ginzburg, and H. R. Akcakaya, "Variation in plankton densities among lakes: a case for ratio-dependent predation models," *The American Naturalist*, vol. 138, no. 5, pp. 1287–1296, 1991.
- [31] R. Arditi, N. Perrin, H. Saiah, and H. Saiah, "Functional responses and heterogeneities: an experimental test with cladocerans," *Oikos*, vol. 60, no. 1, pp. 69–75, 1991.
- [32] R. Arditi and H. Saiah, "Empirical evidence of the role of heterogeneity in ratio-dependent consumption," *Ecology*, vol. 73, no. 5, pp. 1544–1551, 1992.
- [33] M. Fan and K. Wang, "Periodicity in a delayed ratio-dependent predator-prey system," *Journal of Mathematical Analysis and Applications*, vol. 262, no. 1, pp. 179–190, 2001.
- [34] T. Huang, H. Zhang, X. Cong, G. Pan, X. Zhang, and Z. Liu, "Exploring spatiotemporal complexity of a predator-prey system with migration and diffusion by a three-chain coupled map lattice," *Complexity*, vol. 2019, Article ID 3148323, 19 pages, 2019.
- [35] Z. Liu, S. Zhong, Z. Teng, and L. Zhang, "Permanence and global attractivity of an impulsive ratio-dependent predator-prey system in a patchy environment," *Applied Mathematics and Computation*, vol. 219, no. 18, pp. 9791–9804, 2013.
- [36] Z. Liu, S. Zhong, C. Yin, and W. Chen, "On the dynamics of an impulsive reaction-diffusion predator-prey system with ratio-dependent functional response," *Acta Applicandae Mathematicae*, vol. 115, no. 3, pp. 329–349, 2011.
- [37] Y. Kuang and E. Beretta, "Global qualitative analysis of a ratio-dependent predator-prey system," *Journal of Mathematical Biology*, vol. 36, no. 4, pp. 389–406, 1998.
- [38] S.-B. Hsu, T.-W. Hwang, and Y. Kuang, "Global analysis of the Michaelis-Menten-type ratio-dependent predator-prey system," *Journal of Mathematical Biology*, vol. 42, no. 6, pp. 489–506, 2001.
- [39] D. Xiao and S. Ruan, "Global dynamics of a ratio-dependent predator-prey system," *Journal of Mathematical Biology*, vol. 43, no. 3, pp. 268–290, 2001.
- [40] F. Bartumeus, D. Alonso, and J. Catalan, "Self-organized spatial structures in a ratio-dependent predator-prey model," *Physica A: Statistical Mechanics and Its Applications*, vol. 295, no. 1-2, pp. 53–57, 2001.
- [41] Y. Song and X. Zou, "Spatiotemporal dynamics in a diffusive ratio-dependent predator-prey model near a Hopf-Turing bifurcation point," *Computers & Mathematics with Applications*, vol. 67, no. 10, pp. 1978–1997, 2014.

- [42] M. Banerjee and S. Petrovskii, "Self-organised spatial patterns and chaos in a ratio-dependent predator-prey system," *Theoretical Ecology*, vol. 4, no. 1, pp. 37–53, 2011.
- [43] W. W. Wang, Q. X. Liu, and Z. Jin, "Spatiotemporal complexity of a ratio-dependent predator-prey system," *Physical Review E*, vol. 75, Article ID 051913, 2007.
- [44] S. Kovács, K. Kiss, and M. Farkas, "Qualitative behaviour of a ratio-dependent predator-prey system," *Nonlinear Analysis: Real World Applications*, vol. 10, no. 3, pp. 1627–1642, 2009.
- [45] A. Yun, D. Jeong, and J. Kim, "An efficient and accurate numerical scheme for turing instability on a predator-prey model," *International Journal of Bifurcation and Chaos*, vol. 22, Article ID 1250139, 11 pages, 2012.
- [46] S. Aly, I. Kim, and D. Sheen, "Turing instability for a ratio-dependent predator-prey model with diffusion," *Applied Mathematics and Computation*, vol. 217, no. 17, pp. 7265–7281, 2011.
- [47] B. E. Kendall and G. A. Fox, "Spatial structure, environmental heterogeneity, and population dynamics: analysis of the coupled logistic map," *Theoretical Population Biology*, vol. 54, no. 1, pp. 11–37, 1998.
- [48] X. Liang, Y. Yi, and X.-Q. Zhao, "Spreading speeds and traveling waves for periodic evolution systems," *Journal of Differential Equations*, vol. 231, no. 1, pp. 57–77, 2006.
- [49] W. Walter, "Differential inequalities and maximum principles: theory, new methods and applications," *Nonlinear Analysis: Theory, Methods & Applications*, vol. 30, no. 8, pp. 4695–4711, 1997.
- [50] L. H. Smith, "Dynamics of competition," *Lecture Notes in Mathematics*, vol. 1714, pp. 192–240, Springer, Berlin, Germany, 1999.

## Research Article

# The Diffusive Model for West Nile Virus on a Periodically Evolving Domain

Abdelrazig K. Tarboush <sup>1,2</sup> and Zhengdi Zhang <sup>1</sup>

<sup>1</sup>Faculty of Science, Jiangsu University, Zhenjiang 212013, China

<sup>2</sup>Department of Mathematics, Faculty of Education, University of Khartoum, Khartoum 321, Sudan

Correspondence should be addressed to Zhengdi Zhang; [dzyzhang@ujs.edu.cn](mailto:dzyzhang@ujs.edu.cn)

Received 28 October 2019; Revised 1 March 2020; Accepted 6 March 2020; Published 11 April 2020

Guest Editor: Viet-Thanh Pham

Copyright © 2020 Abdelrazig K. Tarboush and Zhengdi Zhang. This is an open access article distributed under the Creative Commons Attribution License, which permits unrestricted use, distribution, and reproduction in any medium, provided the original work is properly cited.

In this paper, we investigate the impact of a periodically evolving domain on the dynamics of the diffusive West Nile virus. A reaction-diffusion model on a periodically and isotropically evolving domain which describes the transmission of the West Nile virus is proposed. In addition to the classical basic reproduction number, the spatial-temporal basic reproduction number depending on the periodic evolution rate is introduced and its properties are discussed. Under some conditions, we explore the long-time behavior of the virus. The virus will go extinct if the spatial-temporal basic reproduction number is less than or equal to one. The persistence of the virus happens if the spatial-temporal basic reproduction number is greater than one. We consider special case when the periodic evolution rate is equivalent to one to better understand the impact of the periodic evolution rate on the persistence or extinction of the virus. Some numerical simulations are performed in order to illustrate our analytical results. Our theoretical analysis and numerical simulations show that the periodic change of the habitat range plays an important role in the West Nile virus transmission, in particular, the increase of periodic evolution rate has positive effect on the spread of the virus.

## 1. Introduction

West Nile virus (WNV) is an arbovirus with natural transmission cycle between mosquitoes and birds. When infected mosquitoes bite birds or other animals including humans, they transmit the virus [1]. WNV is different from other arbovirus since it involves a cross infection between birds (hosts) and mosquitoes (vector) and those birds might travel with spatial boundaries. Also, WNV can be passed via vertical transmission from mosquito to its offspring which increases the survival of the virus [2]. WNV was first isolated and identified in 1937 from the blood of a febrile woman in the West Nile province of Uganda during research on yellow fever virus [3]. It is worth mentioning that WNV is endemic in some temperate and tropical regions such as Africa and the Middle East; it has now spread to North America; the first epidemic case was introduced in New York City in 1999 and then propagated across the USA [4–6]. The USA had experienced one of its worst epidemics in 2012; there were 5387 cases of infections in humans [7]. As we know, there are no

indications that the spread of the virus has stopped. Consequently, it is very necessary to acquire some insights into the propagation of WNV in the mosquito-bird population.

Mathematical nonspatial models have been proposed and analyzed in an attempt to study the transmission dynamics of WNV, in order to elucidate control strategies [2, 6, 8, 9]. It is essential to study and understand its temporal and spatial spread, but most of the models are focused on the nonspatial transmission dynamics of the virus between birds and mosquitoes.

With respect to spatial models of WNV, Lewis et al. [4] studied the spatial spread of WNV to describe the movement of birds and mosquitoes, established the existence of travelling waves, and calculated the spatial spreading rate of the infection. The effects of vertical transmission in the spatial dynamics of the virus for different bird species were proposed by Maidana and Yang in [10], and they studied the travelling wave solutions of the model to determine the speed of virus dissemination. Liu et al. [11] presented the directional dispersal of birds and impact on spatial spreading



of WNV. Likewise, Lin and Zhu studied spatial spreading model and dynamics of WNV in birds and mosquitoes with free boundary [12].

To investigate the existence of travelling wave and calculate the spatial spread rate of infection, Lewis et al. in [4] proposed the following simplified WNV model:

$$\begin{cases} \frac{\partial I_b}{\partial t} = D_1 \Delta I_b + \alpha_b \beta_b \frac{(N_b - I_b)}{N_b} I_m - \gamma_b I_b, & (x, t) \in \Omega \times (0, +\infty), \\ \frac{\partial I_m}{\partial t} = D_2 \Delta I_m + \alpha_m \beta_b \frac{(A_m - I_m)}{N_b} I_b - d_m I_m, & (x, t) \in \Omega \times (0, +\infty), \end{cases} \quad (1)$$

where the positive constants  $N_b$  and  $A_m$  denote the total population of birds and adult mosquitoes;  $I_b(x, t)$  and  $I_m(x, t)$  represent the populations of infected birds and mosquitoes at the location  $x$  in the habitat  $\Omega \subset \mathbb{R}^N$  and at time  $t \geq 0$ , respectively, and  $I_b(x, 0) + I_m(x, 0) > 0$ . The parameters in the above system are defined as follows:

- (i)  $\alpha_m, \alpha_b$ : WNV transmission probability per bite to mosquitoes and birds, respectively
- (ii)  $\beta_b$ : biting rate of mosquitoes on birds
- (iii)  $d_m$ : adult mosquito death rate
- (iv)  $\gamma_b$ : bird recovery rate from WNV
- (v)  $D_1, D_2$ : diffusion coefficients for birds and mosquitoes, respectively

As in [13], throughout this paper, we assume that the mosquitoes' population does not diffuse ( $D_2 = 0$ ).

For the corresponding spatially independent model of (1), the basic reproduction number is

$$R_0 = \sqrt{\frac{\alpha_m \alpha_b \beta_b^2 A_m}{d_m \gamma_b N_b}}, \quad (2)$$

such that for  $0 < R_0 < 1$ , the virus always vanishes, while for  $R_0 > 1$ , a nontrivial epidemic level appears, which is globally asymptotically stable in the positive quadrant [4]. As pointed out in [14], the basic reproduction number  $R_0$  is a very important concept in epidemiology and it defined as an expected number of secondary cases produced by a typical infected individual during its entire period of infectiousness in a completely susceptible population, and mathematically it is introduced as the dominant eigenvalue of a positive linear operator. It is important to mention that usually the basic reproduction numbers for the nonspatial models are calculated by the next generation matrix method [15], while for the spatially dependent systems, the numbers could expressed in terms of the principal eigenvalue of related eigenvalue problem [16] or the spectral radius of next infection operator [17].

The dynamics of the spatial dependence model (1) has been studied. The existence and nonexistence of the coexistence states in a heterogeneous environment have been investigated in [18]. The impact of the environmental heterogeneity and seasonal periodicity on the transmission of WNV was considered in [19].

In recent years, the impact of change of the habitat range on biological population has attracted much attention. We know there are two aspects: one is the domain changing with unknown boundary, which describes the domain change induced by the activity of population itself, and the other is the domain changing with known boundary, which characterizes the domain change induced by objective environments. For the domain changing with unknown boundary, many researchers have proposed and considered the free boundary problem, for example, [20–23] for the persistence of invasive species and [24, 25] for the transmission of diseases. In addition, Tarboush et al. [13] discussed the corresponding free boundary problem to model (1). Wang et al. investigated the spreading speed for a WNV model with free boundary in a homogeneous environment [26]. Their results indicated that the asymptotic spreading speed of the WNV model with free boundary is strictly less than that of the corresponding model in Lewis et al. [4]. For the domain changing with known boundary, there are also some papers, for instance, [27–30] for a growing domain and [31–34] for a periodically evolving domain. In [31], the authors introduced the periodically evolving domain into a single-species diffusion logistic model and studied the influence of periodic evolution on the survival and extinction of species. Recently, Zhang and Lin considered the diffusive model for *Aedes aegypti* mosquito on a periodically evolving domain in order to explore the diffusive dynamics of *Aedes aegypti* mosquito [32]. Their results indicated that the periodic domain evolution has a significant impact on the dispersal of *Aedes aegypti* mosquito. To investigate the impact of periodically evolving domain on the mutualism interaction of two species, Adam et al. [33] studied a mutualistic model on the periodic evolving domain. They suggested that the periodic evolution of domain places significant influence on the interaction of two species. Zhu et al. [34] used a periodic evolving domain to investigate the gradual transmission of a dengue fever model. They found that the periodic domain evolution has a significant effect on the transmission of dengue.

In this paper, we will consider the impact of the periodic evolving domain on the dynamics of a diffusive WNV model corresponding to system (1). We followed the methods of Adam et al. [33], Zhang and Lin [32], and Zhu et al. [34].

The rest of this paper is organized as follows. We will present the formulation of our problem in Section 2. In Section 3, we introduce the spatial-temporal basic

reproduction number and present its properties. The existence and nonexistence of the periodic solutions on a periodically evolving domain  $\Omega_t$  are discussed in Section 4. Section 5 is devoted to the attractivity of periodic solutions on a periodically evolving domain  $\Omega_t$ . In Section 6, we deal with the existence, nonexistence, and attractivity of the periodic solutions on a fixed domain  $\Omega_0$ . Some numerical simulations are given in Section 7. Section 8 provides some conclusions.

## 2. Model Formulation

Motivated by [27], we let  $\Omega_t \subset \mathcal{R}^n$  ( $n \geq 1$ ) be a periodically evolving domain and  $\partial\Omega_t$  be the evolving boundary. For any

point,  $x(t) \in \Omega_t$  satisfies  $x(t+T) = x(t)$  for some positive constant  $T$ . Also, we assume that the domain  $\Omega_t$  grows uniformly and isotropically, that is,

$$x(t) = \rho(t), \quad \text{for all } x(t) \in \Omega_t \text{ and } (y, t) \in \Omega_0 \times [0, T], \quad (3)$$

where  $\rho(t) \in C^1[[0, T]; (0, \infty)]$  and  $y$  represents the spatial coordinates of the initial domain  $\Omega_0$ . Moreover,  $\rho(t)$  is  $T$ -periodic in time, i.e.,  $\rho(t+T) = \rho(t)$ ,  $\rho(0) = 1$  and  $\dot{\rho}(t) \geq 0$  for  $t > 0$ .

According to the principle of mass conservation and Reynolds transport theorem [35], in this paper, we will focus on the following problem:

$$\left\{ \begin{array}{l} \frac{\partial I_b}{\partial t} + \mathbf{a} \cdot \nabla I_b + I_b (\nabla \cdot \mathbf{a}) = D_1 \Delta I_b + \alpha_b(x(t), t) \beta_b(x(t), t) \frac{(N_b - I_b)}{N_b} I_m - \gamma_b(x(t), t) I_b, \quad \text{in } \Omega_t, \\ \frac{\partial I_m}{\partial t} + \mathbf{a} \cdot \nabla I_m + I_m (\nabla \cdot \mathbf{a}) = \alpha_m(x(t), t) \beta_b(x(t), t) \frac{(A_m - I_m)}{N_b} I_b - d_m(x(t), t) I_m, \quad \text{in } \Omega_t, \\ I_b(x(t), t) = I_m(x(t), t) = 0, \quad \text{on } \partial\Omega_t, \\ I_b = I_{b,0}(x), I_m = I_{m,0}(x), \quad \text{in } \Omega_0, \end{array} \right. \quad (4)$$

where  $I_b(x(t), t)$  and  $I_m(x(t), t)$  represent the densities of infected birds and mosquitoes at position  $x(t) \in \Omega_t$  and time  $t$ , respectively, and  $I_{b,0}(x)$  and  $I_{m,0}(x)$  are positive smooth functions in  $\Omega_0$ . The functions  $\alpha_b(x(t), t)$ ,  $\beta_b(x(t), t)$ ,  $\gamma_b(x(t), t)$ ,  $\alpha_m(x(t), t)$ , and  $d_m(x(t), t)$  are all sufficiently smooth,  $T$ -periodic, and strictly positive when  $t \geq 0$ . According to [36, 37], the evolution of domain  $\Omega_t$  generates a flow velocity  $\mathbf{a}(x(t), t)$ . In addition, the evolving domain  $\Omega_t$  represents two kinds of extra terms into the problem, one of which is the advection terms  $\nabla I_b \cdot \mathbf{a}$  and  $\nabla I_m \cdot \mathbf{a}$  representing the transport of material around  $\Omega_t$  at a rate determined by the flow  $\mathbf{a}$ , and the other is the dilution terms  $(\nabla \cdot \mathbf{a}) I_b$  and  $(\nabla \cdot \mathbf{a}) I_m$  due to local volume expansion.

Since problem (4) is involving the terms of advection and dilution, it is not easy to study the long-time behavior of its solutions; therefore, we will transform the continuously

deforming domain in problem (4) to a fixed domain by using Lagrangian transformations [29, 36].

We suppose that  $\mathbf{a}(x(t), t) = \dot{x}(t)$  is the flow velocity, which is identical to the domain velocity.

This means that  $\mathbf{a} = \dot{x}(t) = \dot{\rho}(t)y = (\dot{\rho}(t)/\rho(t))x(t)$ .

Define

$$\begin{aligned} I_b(x(t), t) &\equiv u(y, t), \\ I_m(x(t), t) &\equiv v(y, t), \end{aligned} \quad (5)$$

and assume

$$\begin{aligned} \alpha_b(x(t), t) &\equiv \alpha_b(y, t), \alpha_m[x(t), t] \equiv \alpha_m(y, t), \\ \beta_b(x(t), t) &\equiv \beta_b(y, t), \\ \gamma_b(x(t), t) &\equiv \gamma_b(y, t), d_m(x(t), t) \equiv d_m(y, t). \end{aligned} \quad (6)$$

Therefore, problem (4) is transformed to

$$\left\{ \begin{array}{l} \frac{\partial u}{\partial t} - \frac{D_1(y, t)}{\rho^2(t)} \Delta u + \frac{n\dot{\rho}(t)}{\rho(t)} u = \alpha_b(y, t) \beta_b(y, t) \frac{(N_b - u)}{N_b} v - \gamma_b(y, t) u, \quad y \in \Omega_0, t > 0, \\ \frac{\partial v}{\partial t} + \frac{n\dot{\rho}(t)}{\rho(t)} v = \alpha_m(y, t) \beta_b(y, t) \frac{(A_m - v)}{N_b} u - d_m(y, t) v, \quad y \in \Omega_0, t > 0, \\ u(y, t) = v(y, t) = 0, \quad y \in \partial\Omega_0, t > 0, \end{array} \right. \quad (7)$$



with the periodic condition

$$\begin{aligned} u(y, 0) &= u(y, T), \\ v(y, 0) &= v(y, T), \end{aligned} \quad (8)$$

$$y \in \Omega_0,$$

and under the initial condition

$$\begin{aligned} u(y, 0) &= \eta_1(y) = I_{b,0}(y), \\ v(y, 0) &= \eta_2(y) = I_{m,0}(y), \end{aligned} \quad (9)$$

$$y \in \Omega_0.$$

Moreover, we assume that the functions  $\alpha_b(y, t)$ ,  $\alpha_m(y, t)$ ,  $\beta_b(y, t)$ ,  $\gamma_b(y, t)$ , and  $d_m(y, t) \in C^{\alpha, \alpha/2}(\overline{\Omega_0} \times [0, \infty))$  for some  $\alpha \in (0, 1)$ ; all are positive bounded in the

sense that there exist constants  $\alpha_b^*$ ,  $\alpha_b^*$ ,  $\alpha_m^*$ ,  $\alpha_m^*$ ,  $\beta_b^*$ ,  $\beta_b^*$ ,  $\gamma_b^*$ ,  $\gamma_b^*$ ,  $d_m^*$ , and  $d_m^*$  such that  $\alpha_b^* \leq \alpha_b(y, t) \leq \alpha_b^*$ ,  $\alpha_m^* \leq \alpha_m(y, t) \leq \alpha_m^*$ ,  $\beta_b^* \leq \beta_b(y, t) \leq \beta_b^*$ ,  $\gamma_b^* \leq \gamma_b(y, t) \leq \gamma_b^*$ , and  $d_m^* \leq d_m(y, t) \leq d_m^*$ . Furthermore,  $\alpha_b(y, t) = \alpha_b(y, t + T)$ ,  $\alpha_m(y, t) = \alpha_m(y, t + T)$ ,  $\beta_b(y, t) = \beta_b(y, t + T)$ ,  $\gamma_b(y, t) = \gamma_b(y, t + T)$ , and  $d_m(y, t) = d_m(y, t + T)$  for all  $t > 0$ .

### 3. Spatial-Temporal Basic Reproduction Number

In this section, we will introduce the spatial-temporal basic reproduction number  $R_0(\rho)$  and exhibit its properties. To address this, we consider the following linearized periodic reaction-diffusion problem:

$$\begin{cases} \frac{\partial u}{\partial t} - \frac{D_1}{\rho^2(t)} \Delta u = \alpha_b(y, t) \beta_b(y, t) v - \left( \gamma_b(y, t) + \frac{n\dot{\rho}(t)}{\rho(t)} \right) u, & y \in \Omega_0, t > 0, \\ \frac{\partial v}{\partial t} = \alpha_m(y, t) \beta_b(y, t) \frac{A_m}{N_b} u - \left( d_m(y, t) + \frac{n\dot{\rho}(t)}{\rho(t)} \right) v, & y \in \Omega_0, t > 0, \\ u(y, t) = v(y, t) = 0, & y \in \partial\Omega_0, t > 0, \\ u(y, 0) = u(y, T), v(y, 0) = v(y, T), & y \in \Omega_0. \end{cases} \quad (10)$$

Employing the ideas go back to [17, 32, 38], and we let  $C_T$  be the ordered Banach space consisting of all  $T$ -periodic and continuous functions from  $R$  to  $C(\overline{\Omega_0}, R)$  with the maximum norm  $C_T^+ = \{\eta \in C_T : \eta(t)y \geq 0, \text{ for all } t \in R, y \in \overline{\Omega_0}\}$  and the positive cone  $\eta \in C_T^+$ . For any given  $\eta(y, t) = \eta(t)y$ , we have  $m = (m_1, m_2) \in C_T \times C_T$ . Next, we suppose that is the density distribution at the spatial location  $y \in \Omega_0$  and time  $s$  and let  $\{\Phi(t, s), t \geq s\}$  be the evolution family determined by

$$\begin{cases} \frac{\partial u}{\partial t} - \frac{D_1}{\rho^2(t)} \Delta u = - \left( \gamma_b(y, t) + \frac{n\dot{\rho}(t)}{\rho(t)} \right) u, & y \in \Omega_0, t > 0, \\ \frac{\partial v}{\partial t} = - \left( d_m(y, t) + \frac{n\dot{\rho}(t)}{\rho(t)} \right) v, & y \in \Omega_0, t > 0, \\ u(y, t) = v(y, t) = 0, & y \in \partial\Omega_0, t > 0, \\ u(y, 0) = u(y, T), v(y, 0) = v(y, T), & y \in \Omega_0. \end{cases} \quad (11)$$

Define the operator  $G(t)$  by

$$G(t)\phi = [G_1(t)\phi_2, G_2(t)\phi_1], \quad \text{for all } \phi \in C_T \times C_T, t > 0, \quad (12)$$

where

$$\begin{aligned} G_1(t)\phi_2 &= \alpha_b(\cdot, t) \beta_b(\cdot, t) \phi_2, \\ G_2(t)\phi_1 &= \alpha_m(\cdot, t) \beta_b(\cdot, t) \frac{A_m}{N_b} \phi_1. \end{aligned} \quad (13)$$

Now under the same boundary conditions in problem (11), we let  $\{\Phi_1(t, s), t \geq s\}$  and  $\{\Phi_2(t, s), t \geq s\}$  be the evolution families determined by the first equation and second equation in problem (11), respectively. Moreover, let  $A$  and  $B$  be two bounded linear operator defined by

$$\begin{aligned} Am &= (A_1 m_1, A_2 m_2), \\ Bm &= (B_1 m_2, B_2 m_1), \end{aligned} \quad (14)$$

for  $m \in C_T \times C_T$ , where  $[A_1 m_1](t) = \int_0^\infty \Phi_1(t, t-s) m_1(t-s) ds$  and  $[A_2 m_2](t) = \int_0^\infty \Phi_2(t, t-s) m_2(t-s) ds$ ,  $[B_1 m_2] = G_1(t) m_2$ ,  $[B_2 m_1] = G_2(t) m_1$ , and define

$$Lm = ABm = (A_1 B_1 m_2, A_2 B_2 m_1). \quad (15)$$

Consequently, we define the spatial-temporal basic reproduction number of system (10), that is,

$$R_0(\rho) = r(L), \quad (16)$$

where  $r(L)$  is spectral radius of the operator  $L$ .

With the above discussion, we have the following result (see [19, 32] for more details).

**Lemma 1.**  $\text{sign}[1 - R_0(\rho)] = \text{sign}(\lambda_0)$ , where  $R_0(\rho) = \mu_0$  is the principal eigenvalue of the eigenvalue problem

$$\left\{ \begin{array}{l} \frac{\partial \phi}{\partial t} - \frac{D_1}{\rho^2(t)} \Delta \phi = \frac{\alpha_b(y,t)\beta_b(y,t)}{\mu} \psi - \left( \gamma_b(y,t) + \frac{n\dot{\rho}(t)}{\rho(t)} \right) \phi, \quad y \in \Omega_0, t > 0, \\ \frac{\partial \psi}{\partial t} = \alpha_m(y,t)\beta_b(y,t) \frac{A_m}{N_b \mu} \phi - \left( d_m(y,t) + \frac{n\dot{\rho}(t)}{\rho(t)} \right) \psi, \quad y \in \Omega_0, t > 0, \\ \phi(y,t) = \psi(y,t) = 0, \quad y \in \partial\Omega_0, t > 0, \\ \phi(y,0) = \phi(y,T), \psi(y,0) = \psi(y,T), \quad y \in \Omega_0, \end{array} \right. \quad (17)$$

and  $\lambda_0$  is the principal eigenvalue of the eigenvalue problem

$$\left\{ \begin{array}{l} \frac{\partial \phi}{\partial t} - \frac{D_1}{\rho^2(t)} \Delta \phi = \alpha_b(y,t)\beta_b(y,t)\psi - \left[ \gamma_b(y,t) + \frac{n\dot{\rho}(t)}{\rho(t)} \right] \phi + \lambda \phi, \quad y \in \Omega_0, t > 0, \\ \frac{\partial \psi}{\partial t} = \alpha_m(y,t)\beta_b(y,t) \frac{A_m}{N_b} \phi - \left( d_m(y,t) + \frac{n\dot{\rho}(t)}{\rho(t)} \right) \psi + \lambda \psi, \quad y \in \Omega_0, t > 0, \\ \phi(y,t) = \psi(y,t) = 0, \quad y \in \partial\Omega_0, t > 0, \\ \phi(y,0) = \phi(y,T), \psi(y,0) = \psi(y,T), \quad y \in \Omega_0. \end{array} \right. \quad (18)$$

In what follows, we will present the properties of the spatial-temporal basic reproduction number  $R_0(\rho)$ , that is,  $\mu_0$ . Note that problem (17) is degenerate, so we will not be able to derive the existence of the principal eigenvalue by using Krein–Rutman theorem [39] because of the lack of compactness for the solution semigroup. Therefore, we first transform the equations of (17) to one equation. To achieve this, let

$$\begin{aligned} g_1(y,t) &= \gamma_b(y,t) + \frac{n\dot{\rho}(t)}{\rho(t)}, \\ g_2(y,t) &= d_m(y,t) + \frac{n\dot{\rho}(t)}{\rho(t)}, \end{aligned} \quad (19)$$

and then the second equation of (17) can be written as

$$\frac{\partial \psi}{\partial t} = \alpha_m \beta_b(y,t) \frac{A_m}{N_b \mu} \phi - g_2(y,t) \psi, \quad (20)$$

which gives rise to

$$\left\{ \begin{array}{l} \frac{\partial \phi}{\partial t} - \frac{D_1}{\rho^2(t)} \Delta \phi = \frac{\alpha_b(y,t)\beta_b(y,t)}{\mu^2} G[\phi(y,t)] - \left[ \gamma_b(y,t) + \frac{n\dot{\rho}(t)}{\rho(t)} \right] \phi, \quad y \in \Omega_0, t > 0, \\ \phi(y,t) = 0, \quad y \in \partial\Omega_0, t > 0, \\ \phi(y,0) = \phi(y,T), \quad y \in \Omega_0. \end{array} \right. \quad (23)$$

$$\left( e^{\int_0^t g_2(y,s) ds} \psi \right)_t = \alpha_m \beta_b(y,t) \frac{A_m}{N_b \mu} \phi e^{\int_0^t g_2(y,s) ds}. \quad (21)$$

Together with the periodic condition  $\psi(y,0) = \psi(y,T)$ , direct computations yield

$$\begin{aligned} \psi(y,t) &= \frac{e^{-\int_0^t g_2(y,s) ds}}{1 - e^{-\int_0^T g_2(y,s) ds}} \int_0^T \alpha_m \beta_b(y,\tau) \frac{A_m}{N_b \mu} \phi(y,\tau) e^{-\int_\tau^t g_2(y,s) ds} \\ &\quad + \int_0^t \alpha_m \beta_b(y,\tau) \frac{A_m}{N_b \mu} \phi(y,\tau) e^{-\int_\tau^t g_2(y,s) ds} \\ &:= \frac{1}{\mu} G[\phi(y,t)]. \end{aligned} \quad (22)$$

Here, one can easily see that the function  $G(\phi(y,t))$  is monotonically nondecreasing with respect to  $\beta_b(y,t)$  and decreasing with respect to  $d_m(y,t)$ . Hence, problem (17) reduces to the following form:

By employing the integration by parts to problem (23) and denoting the principal eigenvalue of (17) as  $\mu_0$ , we obtain

$$\mu_0 \leq \sup_{\phi \in G_1, \phi \neq 0} \left\{ \frac{\int_0^T \int_{\Omega_0} \alpha_m(y, t) \beta_b(y, t) A_m / N_b G(\phi) dy dt}{\sqrt{\int_0^T \int_{\Omega_0} D_1 / \rho^2(t) |\nabla \phi|^2 dy dt + \int_0^T \int_{\Omega_0} g_1(y, t) \phi^2 dy dt}} \right\}, \quad (24)$$

where

$$G_1 = \left\{ \phi \in \mathcal{C}^{2+\alpha, 1+(\alpha/2)}(\overline{\Omega_0} \times [0, +\infty)) : \phi(y, t) = 0, \text{ for } y \in \partial\Omega_0, t \in [0, +\infty), \phi \text{ is } T\text{-periodic in } t \right\}. \quad (25)$$

For formula (24), in some special cases, we can replace the sign of inequality ( $\leq$ ) by equality sign by using the variational methods [40–42].

In order to give the relationship between the spatial-temporal basic reproduction number  $R_0(\rho)$  and the periodic evolution rate  $\rho(t)$ , we adopt the notation  $\overline{\rho^{-2}} = 1/T \int_0^T (1/\rho^2(t)) dt$ .  $\lambda^*$  is the principal eigenvalue of the following eigenvalue problem:

$$\begin{cases} -\Delta \varphi = \lambda^* \varphi, & y \in \Omega_0, \\ \varphi = 0, & y \in \partial\Omega_0. \end{cases} \quad (26)$$

Consequently, we have the following result.

**Theorem 1.** *The following assertions are valid:*

(a) If  $\alpha_b(y, t) = \alpha_b(t)$ ,  $\alpha_m(y, t) = \alpha_m(t)$ ,  $\beta_b(y, t) = \beta_b(t)$ ,  $\gamma_b(y, t) = \gamma_b(t)$ , and  $d_m(y, t) = d_m(t)$ , then the principal eigenvalue  $R_0(\rho)$  for (17) is expressed by

$$R_0(\rho) \geq \sqrt{\frac{\left[ \frac{1}{T} \int_0^T \sqrt{\alpha_b(t) \alpha_m(t) \beta_b^2(t) (A_m / N_b)} dt \right]^2}{\frac{1}{T} \int_0^T d_m(t) dt \left[ \frac{1}{T} \int_0^T \gamma_b(t) dt + \lambda^* D_1 \overline{\rho^{-2}} \right]}}. \quad (27)$$

(b) Moreover, if  $\alpha_b(y, t) = \alpha_b^*$ ,  $\alpha_m(y, t) = \alpha_m^*$ ,  $\beta_b(y, t) = \beta_b^*$ ,  $\gamma_b(y, t) = \gamma_b^*$ , and  $d_m(y, t) = d_m^*$ , then we have

$$R_0(\rho) \geq \sqrt{\frac{A_m \alpha_b^* (\beta_b^*)^2 \alpha_m^*}{N_b d_m^* [D_1 \lambda^* \overline{\rho^{-2}} + \gamma_b^*]}}. \quad (28)$$

Furthermore,

$$R_0(1) = \sqrt{\frac{A_m \alpha_b^* (\beta_b^*)^2 \alpha_m^*}{N_b d_m^* [D_1 \lambda^* + \gamma_b^*]}}. \quad (29)$$

in the sense that  $\rho(t) = 1$ .

*Proof.* Let

$$\begin{aligned} \phi(y, t) &= p(t) \varphi(y), \\ \psi(y, t) &= q(t) \varphi(y), \\ (y, t) &\in \Omega_0 \times (0, \infty), \end{aligned} \quad (30)$$

where  $p(t)$  and  $q(t)$  are functions to be determined later and  $[\lambda^*, \varphi(y)]$  is the principal eigenpair of the eigenvalue problem

$$\begin{cases} -\Delta \varphi = \lambda^* \varphi, & y \in \Omega_0, \\ \varphi = 0, & y \in \partial\Omega_0. \end{cases} \quad (31)$$

Together with (17), we obtain

$$\begin{cases} \frac{dp(t)}{dt} = \frac{\alpha_b(t) \beta_b(t)}{R_0(\rho)} q(t) - \left( \frac{D_1 \lambda^*}{\rho^2(t)} + \gamma_b(t) + \frac{n\dot{\rho}(t)}{\rho(t)} \right) p(t), \\ \frac{dq(t)}{dt} = \alpha_m(t) \beta_b(t) \frac{A_m}{N_b R_0(\rho)} p(t) - \left( d_m(t) + \frac{n\dot{\rho}(t)}{\rho(t)} \right) q(t), \end{cases} \quad (32)$$

where

$$\begin{aligned} p(t) &= p(t+T), \\ q(t) &= q(t) \\ t &= [0, \infty), \end{aligned} \quad (33)$$

and  $(R_0(\rho); p(t)\varphi(y), q(t)\varphi(y))$  is the unique principal eigenpair of problem (17).

Rewriting (32) as

$$\begin{cases} \frac{1}{p(t)} \frac{dp(t)}{dt} = \frac{\alpha_b(t) \beta_b(t)}{R_0(\rho)} \frac{q(t)}{p(t)} - \left( \frac{D_1 \lambda^*}{\rho^2(t)} + \gamma_b(t) + \frac{n\dot{\rho}(t)}{\rho(t)} \right), \\ \frac{1}{q(t)} \frac{dq(t)}{dt} = \alpha_m(t) \beta_b(t) \frac{A_m}{N_b R_0(\rho)} \frac{p(t)}{q(t)} - \left( d_m(t) + \frac{n\dot{\rho}(t)}{\rho(t)} \right), \end{cases} \quad (34)$$

and integrating from 0 to  $T$  yield

$$\begin{cases} \frac{1}{R_0(\rho)} \int_0^T \alpha_b(t) \beta_b(t) \frac{q(t)}{p(t)} dt = \int_0^T \left( \frac{D_1 \lambda^*}{\rho^2(t)} + \gamma_b(t) + \frac{n\dot{\rho}(t)}{\rho(t)} \right) dt, \\ \frac{A_m}{N_b R_0(\rho)} \int_0^T \alpha_m(t) \beta_b(t) \frac{p(t)}{q(t)} dt = \int_0^T \left( d_m(t) + \frac{n\dot{\rho}(t)}{\rho(t)} \right) dt. \end{cases} \quad (35)$$

By using Hölder inequality, one can easily obtain that

$$R_0(\rho)^2 \geq \frac{\left( (1/T) \int_0^T \sqrt{\alpha_b(t) \alpha_m(t) \beta_b^2(t) (A_m/N_b)} dt \right)^2}{(1/T) \int_0^T d_m(t) dt \left( (1/T) \int_0^T \gamma_b(t) dt + \lambda^* D_1 \rho^{-2} \right)}. \quad (36)$$

The proof of assertion (a) is completed.

For assertion (b), since we assumed that all coefficients are constants, we can get

$$R_0(\rho) \geq \sqrt{\frac{A_m \alpha_b^* (\beta_b^*)^2 \alpha_m^*}{N_b d_m^* [D_1 \lambda^* \rho^{-2} + \gamma_b^*]}}, \quad (37)$$

directly from (27).

To prove the rest of assertion (b), let  $\rho(t) \equiv 1$ , that is,  $\Omega_t = \Omega_0$  is a fixed domain and rewrite (32) as

$$\begin{cases} \frac{dp(t)}{dt} = \frac{\alpha_b^* \beta_b^*}{R_0(1)} q(t) - (D_1 \lambda^* + \gamma_b^*) p(t), \\ \frac{dq(t)}{dt} = \alpha_m^* \beta_b^* \frac{A_m}{N_b R_0(1)} p(t) - d_m^* q(t), \end{cases} \quad (38)$$

which are explicitly given by

$$\begin{cases} p(t) = e^{(-D_1 \lambda^* - \gamma_b^* + (C \alpha_b^* \beta_b^*/R_0(1)))t}, \\ q(t) = C e^{(-D_1 \lambda^* - \gamma_b^* + (C \alpha_b^* \beta_b^*/R_0(1)))t}, \end{cases} \quad (39)$$

with

$$C = \frac{-d_m^* + D_1 \lambda^* + \gamma_b^* + \sqrt{(d_m^* - D_1 \lambda^* - \gamma_b^*)^2 + 4(A_m \alpha_b^* (\beta_b^*)^2 \alpha_m^*/N_b R_0^2(1))}}{2(\alpha_b^* \beta_b^*/R_0(1))}. \quad (40)$$

According to (38), direct computations yield

$$R_0(1) = \sqrt{\frac{A_m \alpha_b^* (\beta_b^*)^2 \alpha_m^*}{N_b d_m^* [D_1 \lambda^* + \gamma_b^*]}}, \quad (41)$$

which is consistent with the result given from the variational method.  $\square$

#### 4. Periodic Solutions on Evolving Domain

In this section, we discuss the existence and nonexistence of  $T$ -periodic solutions. To begin, we first consider the  $T$ -periodic boundary problem corresponding to (7) and (8):

$$\begin{cases} \frac{\partial u}{\partial t} - \frac{D_1}{\rho^2(t)} \Delta u = f_1(t, u, v), & y \in \Omega_0, t > 0, \\ \frac{\partial v}{\partial t} = f_2(t, u, v), & y \in \Omega_0, t > 0, \\ u(y, t) = v(y, t) = 0, & y \in \partial\Omega_0, t > 0, \\ u(y, 0) = u(y, T), v(y, 0) = v(y, T), & y \in \bar{\Omega}_0, \end{cases} \quad (42)$$

where

$$\begin{aligned} f_1(t, u, v) &= \alpha_b(y, t) \beta_b(y, t) \frac{(N_b - u)}{N_b} v - \left( \gamma_b(y, t) + \frac{n\dot{\rho}(t)}{\rho(t)} \right) u, \\ f_2(t, u, v) &= \alpha_m(y, t) \beta_b(y, t) \frac{(A_m - v)}{N_b} u - \left( d_m(y, t) + \frac{n\dot{\rho}(t)}{\rho(t)} \right) v. \end{aligned} \quad (43)$$

For later analysis, we give the following definition of upper and lower solutions.

*Definition 1.* A pair of functions  $(\tilde{u}, \tilde{v}), (\hat{u}, \hat{v})$  in  $\mathcal{C}^{2,1}[\Omega_0 \times (0, \infty) \cap \mathcal{E}(\bar{\Omega}_0 \times [0, \infty))]$  is called ordered upper and lower solutions of problem (42), if  $(0, 0) \leq (\hat{u}, \hat{v}) \leq (\tilde{u}, \tilde{v}) \leq (N_b, A_m)$  and

$$\left\{ \begin{array}{ll} \frac{\partial \tilde{u}}{\partial t} - \frac{D_1}{\rho^2(t)} \Delta \tilde{u} \geq f_1(t, \tilde{u}, \tilde{v}), & y \in \Omega_0, t > 0, \\ \frac{\partial \tilde{v}}{\partial t} \geq f_2(t, \tilde{u}, \tilde{v}), & y \in \Omega_0, t > 0, \\ \frac{\partial \hat{u}}{\partial t} - \frac{D_1}{\rho^2(t)} \Delta \hat{u} \leq f_1(t, \hat{u}, \hat{v}), & y \in \Omega_0, t > 0, \\ \frac{\partial \hat{v}}{\partial t} \leq f_2(t, \hat{u}, \hat{v}), & y \in \Omega_0, t > 0, \\ \tilde{u}(y, t) \geq 0 \geq \hat{u}(y, t), \tilde{v}(y, t) \geq 0 \geq \hat{v}(y, t), & y \in \partial\Omega_0, t > 0, \\ \tilde{u}(y, 0) \geq \tilde{u}(y, T), \hat{u}(y, 0) \leq \hat{u}(y, T), & y \in \Omega_0, \\ \tilde{v}(y, 0) \geq \tilde{v}(y, T), \hat{v}(y, 0) \leq \hat{v}(y, T), & y \in \Omega_0. \end{array} \right. \quad (44)$$

Now we are in a position to state the existence and nonexistence of  $T$ -periodic solutions to problem (42) as well as problems (7) and (8). To begin with, in the following result we give the existence of  $T$ -periodic solution.

**Theorem 2.** *If  $R_0(\rho) > 1$ , then problem (42) admits at least one positive  $T$ -periodic solution  $(u(y, t), v(y, t))$ .*

*Proof.* Since  $R_0(\rho) > 1$ , one can easily verify that  $(\bar{u}, \bar{v}) = (N_b, A_m)$  and  $(\hat{u}, \hat{v}) = (\delta\phi, \delta\psi)$  are ordered upper and lower solutions of problem (42), where  $\delta$  is positive constant and small enough,  $(\phi, \psi) \equiv (\phi(y, t), \psi(y, t))$  is (normalized) positive eigenfunction corresponding to  $\lambda_0$ , and  $\lambda_0$  is the principal eigenvalue of periodic-parabolic eigenvalue problem (11) (for more details, see [19]).

To establish the nonexistence of a  $T$ -periodic solution to problem (42), we have the following result.  $\square$

**Theorem 3.** *If  $R_0(\rho) \leq 1$ , then problem (42) has no positive  $T$ -periodic solution.*

*Proof.* Suppose that  $(u^*(y, t), v^*(y, t))$  is a positive  $T$ -periodic solution of problem (42), that is,  $(u^*(y, t), v^*(y, t)) > (0, 0)$  in  $\Omega_0 \times (0, \infty)$  and satisfies

$$\left\{ \begin{array}{ll} \frac{\partial u^*}{\partial t} - \frac{D_1}{\rho^2(t)} \Delta u^* + \frac{n\dot{\rho}(t)}{\rho(t)} u^* = \alpha_b(y, t)\beta_b(y, t) \frac{(N_b - u^*)}{N_b} v^* - \gamma_b(y, t)u^*, & y \in \Omega_0, t > 0, \\ \frac{\partial v^*}{\partial t} + \frac{n\dot{\rho}(t)}{\rho(t)} v^* = \alpha_m(y, t)\beta_b(y, t) \frac{(A_m - v^*)}{N_b} u^* - d_m(y, t)v^*, & y \in \Omega_0, t > 0, \\ u^*(y, t) = v^*(y, t) = 0, & y \in \partial\Omega_0, t > 0, \\ u^*(y, 0) = u^*(y, T), v^*(y, 0) = v^*(y, T), & y \in \Omega_0. \end{array} \right. \quad (45)$$

From the above equations, we have

$$\left\{ \begin{array}{ll} \frac{\partial u^*}{\partial t} - \frac{D_1}{\rho^2(t)} \Delta u^* < \alpha_b(y, t)\beta_b(y, t)v^* - \left[ \gamma_b(y, t) + \frac{n\dot{\rho}(t)}{\rho(t)} \right] u^*, & y \in \Omega_0, t > 0, \\ \frac{\partial v^*}{\partial t} < \alpha_m(y, t)\beta_b(y, t) \frac{A_m}{N_b} u^* - \left( d_m(y, t) + \frac{n\dot{\rho}(t)}{\rho(t)} \right) v^*, & y \in \Omega_0, t > 0, \\ u^*(y, t) = v^*(y, t) = 0, & y \in \partial\Omega_0, t > 0, \\ u^*(y, 0) = u^*(y, T), v^*(y, 0) = v^*(y, T), & y \in \Omega_0. \end{array} \right. \quad (46)$$

Recalling (17), one can easily deduce from the monotonicity of the principal eigenvalue  $R_0(\rho)$  that  $R_0(\rho) > 1$  by comparing (17) and (46), which contradicts the fact  $R_0(\rho) \leq 1$ .  $\square$

## 5. Attractivity of Periodic Solutions

In this section, we first construct the true solutions of problem (42) and then present the attractivity of  $T$ -periodic solutions to problems (8) and (9) in relation to the minimal and maximal  $T$ -periodic solution of problems (8) and (9). In what follows, we construct the true solutions of problem (42) by using the monotone iterative scheme. Let

$$\begin{aligned} k_1 &= \gamma_b^M + \alpha_b^M \rho_b^M \frac{A_m}{N_b} + n \left( \frac{\dot{\rho}(t)}{\rho(t)} \right)^M, \\ k_2 &= d_m^M + \alpha_m^M \rho_b^M + n \left( \frac{\dot{\rho}(t)}{\rho(t)} \right)^M, \end{aligned} \quad (47)$$

$$F_1 = k_1 u + f_1(t, u, v),$$

$$F_2 = k_2 v + f_2(t, u, v),$$

where  $f^m = \min_{(-\infty, \infty) \times [0, T]} f(t)$  and  $f^M = \max_{(-\infty, \infty) \times [0, T]} f(t)$  for any given continuous  $T$ -periodic function  $f$ . It is easy to verify that both  $F_1$  and  $F_2$  are nondecreasing with respect to  $u$  and  $v$ . Then, problem (42) is equivalent to

$$\begin{cases} \frac{\partial u}{\partial t} - \frac{D_1}{\rho^2(t)} \Delta u + k_1 u = F_1(t, u, v), & y \in \Omega_0, t > 0, \\ \frac{\partial v}{\partial t} + k_2 v = F_2(t, u, v), & y \in \Omega_0, t > 0, \\ u(y, t) = v(y, t) = 0, & y \in \partial\Omega_0, t > 0, \\ u(y, 0) = u(y, T), v(y, 0) = v(y, T), & y \in \Omega_0. \end{cases} \quad (48)$$

Using  $(\bar{u}^{(0)}, \bar{v}^{(0)}) = (N_b, A_m)$  and  $(\underline{u}^{(0)}, \underline{v}^{(0)}) = (\delta\phi, \delta\psi)$  as an initial iteration, one can construct a sequence  $\{(u^{(i)}, v^{(i)})\}$  from the iteration process

$$\begin{cases} \bar{u}_t^{(i)} - \frac{D_1}{\rho^2(t)} \Delta \bar{u}^{(i)} + k_1 \bar{u}^{(i)} = F_1(t, \bar{u}^{(i-1)}, \bar{v}^{(i-1)}), & y \in \Omega_0, t > 0, \\ \bar{v}_t^{(i)} + k_2 \bar{v}^{(i)} = F_2(t, \bar{u}^{(i-1)}, \bar{v}^{(i-1)}), & y \in \Omega_0, t > 0, \\ \underline{u}_t^{(i)} - \frac{D_1}{\rho^2(t)} \Delta \underline{u}^{(i)} + k_1 \underline{u}^{(i)} = F_1\left(t, \underline{u}^{(i-1)}, \underline{v}^{(i-1)}\right), & y \in \Omega_0, t > 0, \\ \underline{v}_t^{(i)} + k_2 \underline{v}^{(i)} = F_2(t, \underline{u}^{(i-1)}, \underline{v}^{(i-1)}), & y \in \Omega_0, t > 0, \\ \bar{u}^{(i)}(y, t) = \underline{u}^{(i)}(y, t) = \bar{v}^{(i)}(y, t) = \underline{v}^{(i)}(y, t) = 0, & y \in \partial\Omega_0, t > 0, \end{cases} \quad (49)$$

with the periodic condition

$$\begin{cases} \bar{u}^{(i)}(y, 0) = \bar{u}^{(i-1)}(y, T), \bar{v}^{(i)}(y, 0) = \bar{v}^{(i-1)}(y, T), & y \in \Omega_0, \\ \underline{u}^{(i)}(y, 0) = \underline{u}^{(i-1)}(y, T), \underline{v}^{(i)}(y, 0) = \underline{v}^{(i-1)}(y, T), & y \in \Omega_0, \end{cases} \quad (50)$$

where  $i = 1, 2, \dots$

Under condition  $R_0(\rho) > 1$ , we know that  $(N_b, A_m)$  and  $(\delta\phi, \delta\psi)$  are ordered upper and lower solution of problem (42). Taking  $(N_b, A_m)$  and  $(\delta\phi, \delta\psi)$  as initial iteration and employing ideas of [43] with the monotonicity of  $f_1$  and  $f_2$ , it follows that the well-defined sequences governed by (49) and (50) possess the monotone property

$$\begin{aligned} (\bar{u}, \bar{v}) &\leq (\underline{u}^{(i-1)}, \underline{v}^{(i-1)}) \leq (\underline{u}^{(i)}, \underline{v}^{(i)}) \leq (\bar{u}^{(i)}, \bar{v}^{(i)}) \\ &\leq (\bar{u}^{(i-1)}, \bar{v}^{(i-1)}) \leq (\bar{u}, \bar{v}). \end{aligned} \quad (51)$$

Therefore, the pointwise limits

$$\begin{aligned} \lim_{i \rightarrow \infty} (\bar{u}^{(i)}, \bar{v}^{(i)}) &= (\bar{u}, \bar{v}), \\ \lim_{i \rightarrow \infty} (\underline{u}^{(i)}, \underline{v}^{(i)}) &= (\underline{u}, \underline{v}), \end{aligned} \quad (52)$$

exist and their limits possess the relation

$$(\hat{u}, \hat{v}) \leq (\underline{u}^{(i)}, \underline{v}^{(i)}) \leq (\underline{u}, \underline{v}) \leq (\bar{u}, \bar{v}) \leq (\bar{u}^{(i)}, \bar{v}^{(i)}) \leq (\bar{u}, \bar{v}). \quad (53)$$

Therefore,  $(\bar{u}, \bar{v})$  and  $(\underline{u}, \underline{v})$  are the true positive  $T$ -periodic solutions of problem (42). Moreover,  $(\bar{u}, \bar{v})$  and  $(\underline{u}, \underline{v})$  in respect are the maximal and minimal solutions in the sense that  $(u, v)$  is any other solution of (42) in  $\langle (\hat{u}, \hat{v}), (\bar{u}, \bar{v}) \rangle$ , and then  $(\underline{u}, \underline{v}) \leq (u, v) \leq (\bar{u}, \bar{v})$ . Furthermore, if  $\bar{u}(y, 0) = \underline{u}(y, 0)$  or  $\bar{v}(y, 0) = \underline{v}(y, 0)$ , then  $(\bar{u}, \bar{v}) =$



$(\underline{u}, \underline{v}) := (u^*, v^*)$  and  $(u^*, v^*)$  is the unique solution of (42) in  $\bar{\Omega}_0$ .

From the above conclusions, we have the following result.

**Theorem 4.** *Let  $(\bar{u}, \bar{v})$  and  $(\hat{u}, \hat{v})$  be a pair of ordered upper and lower solutions of (42), respectively, and then the sequences  $\{(\bar{u}^{(i)}, \bar{v}^{(i)})\}$  and  $\{(\underline{u}^{(i)}, \underline{v}^{(i)})\}$  provided from (49), (50) converge monotonically from above to a maximal solution  $(\bar{u}, \bar{v})$  and from below to a minimal solution  $(\underline{u}, \underline{v})$  in  $\bar{\Omega}_0$ , respectively, and satisfy the relation*

$$\begin{aligned} (\hat{u}, \hat{v}) &\leq \begin{pmatrix} (i) & (i) \\ \underline{u} & \underline{v} \end{pmatrix} \leq \begin{pmatrix} (i+1) & (i+1) \\ \underline{u} & \underline{v} \end{pmatrix} \leq \begin{pmatrix} (i+1) & (i+1) \\ \bar{u} & \bar{v} \end{pmatrix} \\ &\leq \begin{pmatrix} (i) & (i) \\ \bar{u} & \bar{v} \end{pmatrix} \leq (\bar{u}, \bar{v}) \\ &\leq \begin{pmatrix} (i) & (i) \\ \underline{u} & \underline{v} \end{pmatrix} \leq (\underline{u}, \underline{v}). \end{aligned} \quad (54)$$

Moreover, if  $\bar{u}(y, 0) = \underline{u}(y, 0)$  or  $\bar{v}(y, 0) = \underline{v}(y, 0)$ , then  $(\bar{u}, \bar{v}) = (\underline{u}, \underline{v}) = (u^*, v^*)$  and  $(u^*, v^*)$  is the unique solution of (42) in  $\bar{\Omega}_0$ .

For problems (8) and (9),  $(\bar{u}, \bar{v})$  and  $(\hat{u}, \hat{v})$  defined in (44) are also the ordered upper and lower solutions provided the initial condition is replaced by

$$(\hat{u}, \hat{v}) \leq [(\eta_1(y), \eta_2(y) \leq (\bar{u}, \bar{v}))], \quad \text{in } \Omega_0. \quad (55)$$

Applying  $(\bar{u}^{(0)}, \bar{v}^{(0)}) = (\bar{u}, \bar{v})$  and  $(\underline{u}^{(0)}, \underline{v}^{(0)}) = (\hat{u}, \hat{v})$  as an initial iteration again, we denote the sequences generated by (49) as  $\{(\underline{u}_A^{(i)}, \underline{v}_B^{(i)})\}$  and  $\{(\bar{u}_A^{(i)}, \bar{v}_B^{(i)})\}$  such that

$$(\underline{u}_A^{(i)}, \underline{v}_B^{(i)})(y, 0) = (\bar{u}_A^{(i)}, \bar{v}_B^{(i)})(y, 0) = [(\eta_1(y), \eta_2(y))], \quad y \in \bar{\Omega}_0. \quad (56)$$

The following three lemmas follow from [43], so we omit their proofs here.

**Lemma 2.** *The sequences  $\{(\underline{u}_A^{(i)}, \underline{v}_B^{(i)})\}$  and  $\{(\bar{u}_A^{(i)}, \bar{v}_B^{(i)})\}$  converge monotonically to a unique solution  $(u(y, t), v(y, t))$  of problems (7) and (8) and satisfy the relation*

$$\begin{aligned} (\hat{u}, \hat{v}) &\leq \begin{pmatrix} (i-1) & (i-1) \\ \underline{u}_A & \underline{v}_B \end{pmatrix} \leq \begin{pmatrix} (i) & (i) \\ \underline{u}_A & \underline{v}_B \end{pmatrix} \leq (u, v) \\ &\leq \begin{pmatrix} (i) & (i) \\ \bar{u}_A & \bar{v}_B \end{pmatrix} \leq \begin{pmatrix} (i-1) & (i-1) \\ \bar{u}_A & \bar{v}_B \end{pmatrix} \leq (\bar{u}, \bar{v}), \end{aligned} \quad (57)$$

on  $\bar{\Omega}_0 \times [0, \infty)$ .

**Lemma 3.** *For any  $i$  and  $j$ , if the pairs  $(\bar{u}^{(i)}, \bar{v}^{(i)})$  and  $(\underline{u}^{(j)}, \underline{v}^{(j)})$  are ordered upper and lower solutions to problem (42), then they are also ordered upper and lower solutions of (7) and (9) provided that  $(\underline{u}^{(j)}, \underline{v}^{(j)})(y, 0) \leq [(\eta_1(y), \eta_2(y))] \leq (\bar{u}^{(i)}, \bar{v}^{(i)})(y, 0)$  in  $\Omega_0$ .*

**Lemma 4.** *Let  $(u, v)(y, t; \eta_1, \eta_2)$  be the solution of (7) and (9) with any*

$$(\eta_1(y), \eta_2(y)) \in S_0, \quad (58)$$

where

$$\begin{aligned} S_0 &= \{(\eta_1, \eta_2) \in \mathcal{C}(\bar{\Omega}_0) : (\hat{u}, \hat{v})(y, 0) \leq (\eta_1, \eta_2) \\ &\leq (\bar{u}, \bar{v})(y, 0) \text{ on } \bar{\Omega}_0\}. \end{aligned} \quad (59)$$

Then,

$$\begin{pmatrix} (i) & (i) \\ \underline{u} & \underline{v} \end{pmatrix} (y, t) \leq (u, v)(y, t + iT; \eta_1, \eta_2) \leq \begin{pmatrix} (i) & (i) \\ \bar{u} & \bar{v} \end{pmatrix} (y, t), \quad (60)$$

on  $\bar{\Omega}_0 \times [0, \infty)$ .

In the next theorem, we present the attractivity of  $T$ -periodic solutions to problems (7) and (9) in relation to the maximal and minimal  $T$ -periodic solution of problems (7) and (8).

**Theorem 5.** *Let  $(u, v)(y, t; \eta_1, \eta_2)$  be any solution of problems (7) and (9). The following assertions hold:*

(a) *If  $R_0(\rho) > 1$ , then*

$$\begin{aligned} \lim_{i \rightarrow \infty} (u(y, t + iT; \eta_1, \eta_2), v(y, t + iT; \eta_1, \eta_2)) \\ = \begin{cases} (\underline{u}, \underline{v})(y, t) & \text{if } (\hat{u}, \hat{v}) \leq (\eta_1, \eta_2) \leq (\underline{u}, \underline{v}) \text{ in } \Omega_0, \\ (\bar{u}, \bar{v})(y, t) & \text{if } (\bar{u}, \bar{v}) \leq (\eta_1, \eta_2) \leq (\bar{u}, \bar{v}) \text{ in } \Omega_0. \end{cases} \end{aligned} \quad (61)$$

In addition, for any  $(\eta_1, \eta_2) \in S_0$ ,

$$\begin{aligned} (\underline{u}, \underline{v})(y, t) \leq (u(y, t + iT), v(y, t + iT))(\eta_1, \eta_2) \\ \leq (\bar{u}, \bar{v})(y, t), \quad \text{on } \bar{\Omega}_0 \times [0, \infty), \end{aligned} \quad (62)$$

as  $i \rightarrow \infty$ . Furthermore, if  $(\underline{u}, \underline{v})(y, t) = (\bar{u}, \bar{v})(y, t) = (u^*, v^*)$ , then

$$\begin{aligned} \lim_{i \rightarrow \infty} (u, v)(y, t + iT; \eta_1, \eta_2) = (u^*, v^*), \\ \text{on } \bar{\Omega}_0 \times [0, \infty). \end{aligned} \quad (63)$$

(b) *If  $R_0(\rho) \leq 1$ , then for any  $(\eta_1, \eta_2)$ ,*

$$\lim_{t \rightarrow \infty} (u, v)(y, t; \eta_1, \eta_2) = (0, 0). \quad (64)$$

*Proof.* Let  $(u_i, v_i)(y, t) = (u, v)(y, t + iT; \eta_1, \eta_2)$  for every  $i = 1, 2, \dots$ , where  $(\eta_1, \eta_2) \in S_0$  (see Lemma 4). It follows from Lemma 2 that the solution  $(u_i, v_i)$  is in  $\bar{\Omega}_0 \times [0, \infty)$  and, in particular,  $(\hat{u}, \hat{v})(y, t + T) \leq (u_1, v_1) \leq (\bar{u}, \bar{v})(y, t + T)$  on  $\bar{\Omega}_0 \times [0, \infty)$ . Next, we consider (7) with the initial condition  $[(\eta_1(y), \eta_2(y))]$  in  $\Omega_0$ . By the iteration process in (49) for  $i = 1$ , we have

$$\begin{aligned} (\bar{u}^{(1)}, \bar{v}^{(1)})(y, 0) &= (\bar{u}^{(0)}, \bar{v}^{(0)})(y, T) = (\bar{u}, \bar{v})(y, T), \\ \begin{pmatrix} (1) & (1) \\ \underline{u} & \underline{v} \end{pmatrix} (y, 0) &= \begin{pmatrix} (1) & (1) \\ \underline{u} & \underline{v} \end{pmatrix} (y, T) = (\hat{u}, \hat{v})(y, T). \end{aligned} \quad (65)$$

Therefore, one can see that

$$\left( \begin{matrix} (1) & (1) \\ \underline{u} & \underline{v} \end{matrix} \right) (y, 0) \leq (u_1, v_1)(y, 0) \leq (\overline{u}^{(1)}, \overline{v}^{(1)})(y, 0), \quad (66)$$

in  $\Omega_0$ .

According to Lemma 2,  $(\overline{u}^{(1)}, \overline{v}^{(1)})(y, t)$  and  $(\underline{u}^{(1)}, \underline{v}^{(1)})(y, t)$  are ordered upper and lower solutions of (7), respectively, when  $[\eta_1(y), \eta_2(y)] = (u_1, v_1)(y, 0)$  in  $\Omega_0$ . With respect to Theorem 4, we can see that

$$\left( \begin{matrix} (1) & (1) \\ \underline{u} & \underline{v} \end{matrix} \right) (y, t) \leq (u_1, v_1)(y, t) \leq (\overline{u}^{(1)}, \overline{v}^{(1)})(y, t), \quad (67)$$

on  $\overline{D}$ . By the principle of induction,

$$\left( \begin{matrix} (i) & (i) \\ \underline{u} & \underline{v} \end{matrix} \right) (y, t) \leq (u_i, v_i)(y, t) \leq (\overline{u}^{(i)}, \overline{v}^{(i)})(y, t) \quad (68)$$

holds on  $\overline{\Omega}_0 \times [0, \infty)$ . On the other hand, relation (63) directly follows from (62) with the assumption that  $(\underline{u}, \underline{v})(y, t) = (\overline{u}, \overline{v})(y, t) = (u^*, v^*)$ . The proof of assertion (a) is completed.

When it comes to assertion (b), in fact, it is easy to see that  $(N_b, A_m)$  and  $(0, 0)$  are a pair of ordered upper and lower solutions of problems (7) and (8). Using the same argument as in assertion (a), as well as the fact that  $(0, 0)$  is the unique solution to problems (7) and (8), we can conclude that the solution  $(u, v)(y, t; \eta_1, \eta_2)$  of problem (7), associated with any nonnegative initial function pair  $(\eta_1(y), \eta_2(y))$ , possesses the convergence property

$$\lim_{i \rightarrow \infty} (u, v)(y, t + iT; \eta_1, \eta_2) = (0, 0), \quad (69)$$

which is equivalent to

$$\lim_{t \rightarrow \infty} (u, v)(y, t; \eta_1, \eta_2) = (0, 0). \quad (70)$$

□

## 6. The Impact of Evolving Domain

To better understand the impact of periodic evolving domain, in this section, we assume that  $\rho(t) \equiv 1$ , that is,  $\Omega_t = \Omega_0$  is a fixed domain, and then problem (7) becomes

$$\begin{cases} \frac{\partial U}{\partial t} - D_1(y, t)\Delta U = \alpha_b(y, t)\beta_b(y, t)\frac{(N_b - U)}{N_b}V - \gamma_b(y, t)U, & y \in \Omega_0, t > 0, \\ \frac{\partial V}{\partial t} = \alpha_m(y, t)\beta_b(y, t)\frac{(A_m - V)}{N_b}U - d_m(y, t)V, & y \in \Omega_0, t > 0, \\ U(y, t) = V(y, t) = 0, & y \in \partial\Omega_0, t > 0, \end{cases} \quad (71)$$

with the periodic condition

$$\begin{aligned} U(y, 0) &= U(y, T), \\ V(y, 0) &= V(y, T), \end{aligned} \quad (72)$$

$y \in \Omega_0,$

and under the initial condition

$$\begin{aligned} U(y, 0) &= \eta_1(y) = I_{b,0}(y), \\ V(y, 0) &= \eta_2(y) = I_{m,0}(y), \end{aligned} \quad (73)$$

$y \in \Omega_0.$

By the similar arguments as in Section 2, we have the following eigenvalue problem corresponding to problems (71) and (72):

$$\begin{cases} \Phi_t - D_1\Delta\Phi = \alpha_b(y, t)\beta_b(y, t)\Psi - \gamma_b(y, t)\Phi + \lambda\Phi, & y \in \Omega_0, t > 0, \\ \Psi_t = \alpha_m(y, t)\beta_b(y, t)\frac{A_m}{N_b}\Phi - d_m(y, t)\Psi + \lambda\Psi, & y \in \Omega_0, t > 0, \\ \Phi(y, t) = \Psi(y, t) = 0, & y \in \partial\Omega_0, t > 0, \\ \Phi(y, 0) = \Phi(y, T), \Psi(y, 0) = \Psi(y, T), & y \in \Omega_0, \end{cases} \quad (74)$$

where  $(\Phi, \Psi)$  is the eigenfunction corresponding to the principal eigenvalue and  $R_0^* = R_0(1)$  is the principal eigenvalue of the eigenvalue problem

$$\left\{ \begin{array}{l} \Phi_t - D_1 \Delta \Phi = \frac{\alpha_b(y,t)\beta_b(y,t)}{R_0^*} \Psi - \gamma_b(y,t)\Phi, \quad y \in \Omega_0, t > 0, \\ \Psi_t = \alpha_m(y,t)\beta_b(y,t) \frac{A_m}{N_b R_0^*} \Phi - d_m(y,t)\Psi, \quad y \in \Omega_0, t > 0, \\ \Phi(y,t) = \Psi(y,t) = 0, \quad y \in \partial\Omega_0, t > 0, \\ \Phi(y,0) = \Phi(y,T), \Psi(y,0) = \Psi(y,T), \quad y \in \Omega_0. \end{array} \right. \quad (75)$$

Moreover,  $(\tilde{U}, \tilde{V}) = (N_b, A_m)$  and  $(\hat{U}, \hat{V}) = (\delta\Phi, \delta\Psi)$  are ordered upper and lower solutions of problems (71) and (73), where  $\delta$  is positive constant and small enough.

The main results of this section are given in the following two theorems which are parallel to Theorems 2–5.

**Theorem 6.** *The following statements are valid:*

- (a) If  $R_0^* > 1$ , then problems (71) and (72) possess a maximal positive  $T$ -periodic solution  $(\bar{U}, \bar{V})$  and a minimal positive  $T$ -periodic solution  $(\underline{U}, \underline{V})$ . Besides, if  $(\bar{U}, \bar{V})(y, 0) = (\underline{U}, \underline{V})(y, 0)$ , then  $(\bar{U}, \bar{V}) = (\underline{U}, \underline{V}) := (U^*, V^*)$  and  $(U^*, V^*)$  is the unique  $T$ -periodic solution of problems (71) and (72).
- (b) If  $R_0^* \leq 1$ , then problems (71) and (72) have no positive  $T$ -periodic solution.

**Theorem 7.** *Let  $(U, V)(y, t; \eta_1, \eta_2)$  be the solution of problems (71) and (73).*

- (a) If  $R_0^* > 1$ , then

$$\lim_{i \rightarrow \infty} (U, V)(y, t + iT; \eta_1, \eta_2) = \begin{cases} (\underline{U}, \underline{V})(y, t) & \text{if } (\hat{U}, \hat{V}) \leq (\eta_1, \eta_2) \leq (\underline{U}, \underline{V}), \quad \text{in } \Omega_0, \\ (\bar{U}, \bar{V})(y, t) & \text{if } (\bar{U}, \bar{V}) \leq (\eta_1, \eta_2) \leq (\tilde{U}, \tilde{V}), \quad \text{in } \Omega_0. \end{cases} \quad (76)$$

Moreover, for any  $(\eta_1, \eta_2) \in S_0^*$ ,

$$(\underline{U}, \underline{V})(y, t) \leq (U, V)(y, t + iT; \eta_1, \eta_2) \leq (\bar{U}, \bar{V})(y, t), \quad \text{on } \bar{\Omega}_0 \times [0, \infty), \quad (77)$$

as  $i \rightarrow \infty$ . Additionally, if  $(\underline{U}, \underline{V})(y, t) = (\bar{U}, \bar{V})(y, t) := (U^*, V^*)$ , then

$$\lim_{i \rightarrow \infty} (U, V)(y, t + iT; \eta_1, \eta_2) = (U^*, V^*)(y, t), \quad \text{on } \bar{\Omega}_0 \times [0, \infty). \quad (78)$$

- (b) If  $R_0^* \leq 1$ , then for any  $(\eta_1, \eta_2)$ ,

$$\lim_{t \rightarrow \infty} (U, V)(y, t + iT; \eta_1, \eta_2) = (0, 0), \quad (79)$$

uniformly for  $y \in \Omega_0$ , where

$$S_0^* = [(\eta_1, \eta_2) \in \mathcal{C}(\bar{\Omega}_0) : (\tilde{U}, \tilde{V})(y, 0) \leq (\eta_1, \eta_2) \leq (\bar{U}, \bar{V})(y, 0), \quad \text{in } \bar{\Omega}_0]. \quad (80)$$

Thanks to the above analysis, here we adopt the integral average value  $\bar{\rho}^{-2} = 1/T \int_0^T (1/\rho^2(t))dt$  generated by the evolution rate  $\rho(t)$ . It is easy to see that the spreading or vanishing of the virus on periodically evolving domain depends on the spatial-temporal basic reproduction number  $R_0(\rho)$ , while on the fixed domain, it depends on  $R_0^*$ . When  $\bar{\rho}^{-2} < 1$ , we have  $R_0(\rho) > 1$ , which means that the spreading of the virus has increased. Meanwhile, if  $\bar{\rho}^{-2} > 1$ , then  $R_0(\rho) \leq 1$ , which implies that the spreading of the virus has decreased. When the domain is fixed, the parallel results hold with  $R_0^* = R_0(1)$ , then the virus in the case of vanishing.

## 7. Numerical Simulation and Discussion

In this section, we first carry out numerical simulations to illustrate the theoretical results obtained in previous sections. Our focus is the impact of periodic evolving domain on the transmission of the West Nile virus (WNV).

For simplicity, first we fix

$$\begin{aligned} \frac{A_m}{N_b} &= 20, \\ \alpha_b &= 0.88, \\ \alpha_m &= 0.16, \\ \gamma_b &= 0.01, \\ D_1 &= 0.06, \\ \lambda^* &= \pi^2, \\ \Omega_0 &= (0, 1), \end{aligned} \quad (81)$$

$$I_{b,0}(x) = 0.3 \sin(\pi x),$$

$$I_{m,0}(x) = 0.2 \sin(\pi x) + 0.1 \sin(3\pi x),$$

and then change the value of the evolution rate  $\rho(t)$  to observe the long time behavior of problems (7) and (9).

*Example 1.* In systems (7) and (9), we fix  $\beta_b = 0.3$  and  $d_m = 0.029$  with  $\rho(t) = 1$ . Direct calculations show that

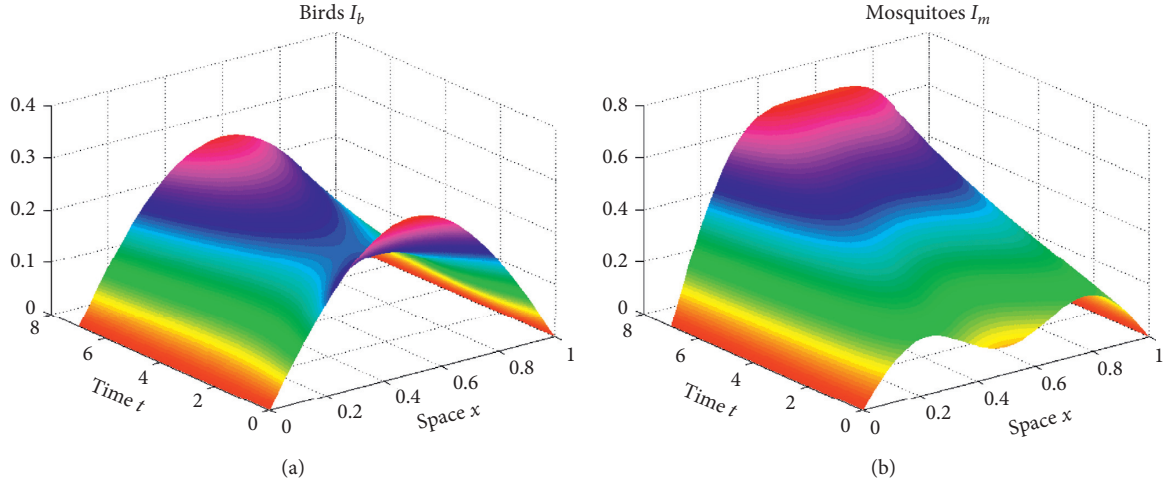


FIGURE 1:  $\rho(t) = 1$ .  $R_0(1) > 1$ , which implies that the solution tends to steady state in a fixed domain.

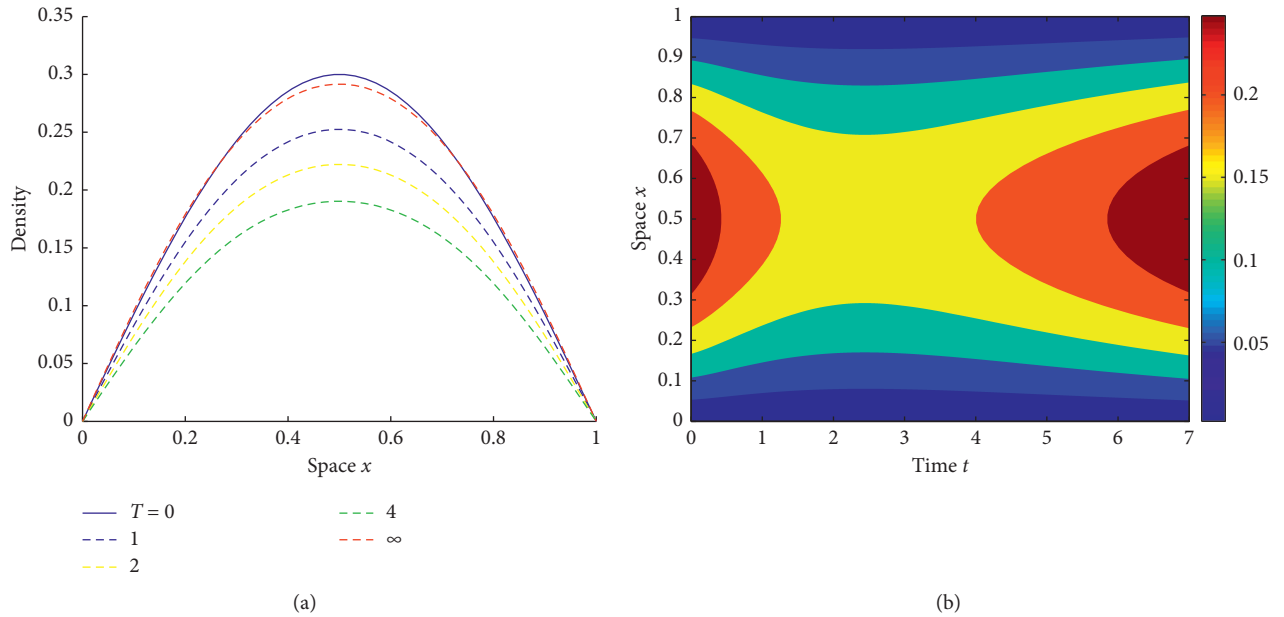


FIGURE 2: The corresponding cross-sectional view (a) and contour one (b) for the solution of problems (7) and (9), which means that the domain is fixed when the evolution rate  $\rho(t) = 1$ .

$$\begin{aligned}
 R_0(1) &= \sqrt{\frac{A_m/N_b\alpha_b(\beta_b)^2\alpha_m}{d_m^*(D_1\lambda^* + \gamma_b)}} \\
 &= \sqrt{\frac{20 \times 0.88 \times 0.09 \times 0.16}{0.029 \times (0.06 \times 9.8596 + 0.01)}} > 1.
 \end{aligned} \tag{82}$$

Hence, the solution of problems (7) and (9) tends to positive steady states (see Figures 1 and 2), which implies that the virus will persist in a fixed domain.

*Example 2.* In systems (7) and (9), we choose  $\beta_b = 0.09$  and  $d_m = 0.29$  with  $\rho(t) = 1$ . Direct calculations show that

$$\begin{aligned}
 R_0(1) &= \sqrt{\frac{A_m/N_b\alpha_b(\beta_b)^2\alpha_m}{d_m(D_1\lambda^* + \gamma_b)}} \\
 &= \sqrt{\frac{20 \times 0.88 \times 0.0081 \times 0.16}{0.29 \times (0.06 \times 9.8596 + 0.01)}} < 1.
 \end{aligned} \tag{83}$$

It is easy to see that the solution of problems (7) and (9) decays to zero quickly (see Figures 3 and 4), which implies that the virus will be extinct in a fixed domain.

*Example 3.* In systems (7) and (9), we set  $\beta_b = 0.3$  and  $d_m = 0.029$  with  $\rho(t) = e^{0.1(1-\cos(4t))}$ . Direct calculations show that

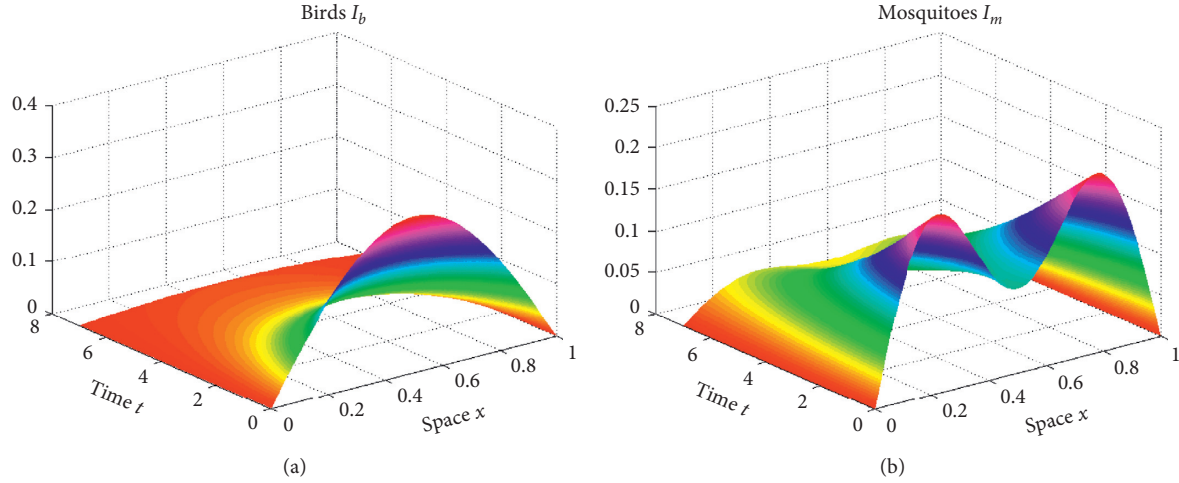


FIGURE 3:  $\rho(t) = 1$ .  $R_0(1) < 1$ , which implies that the solution decays quickly to zero in a fixed domain.

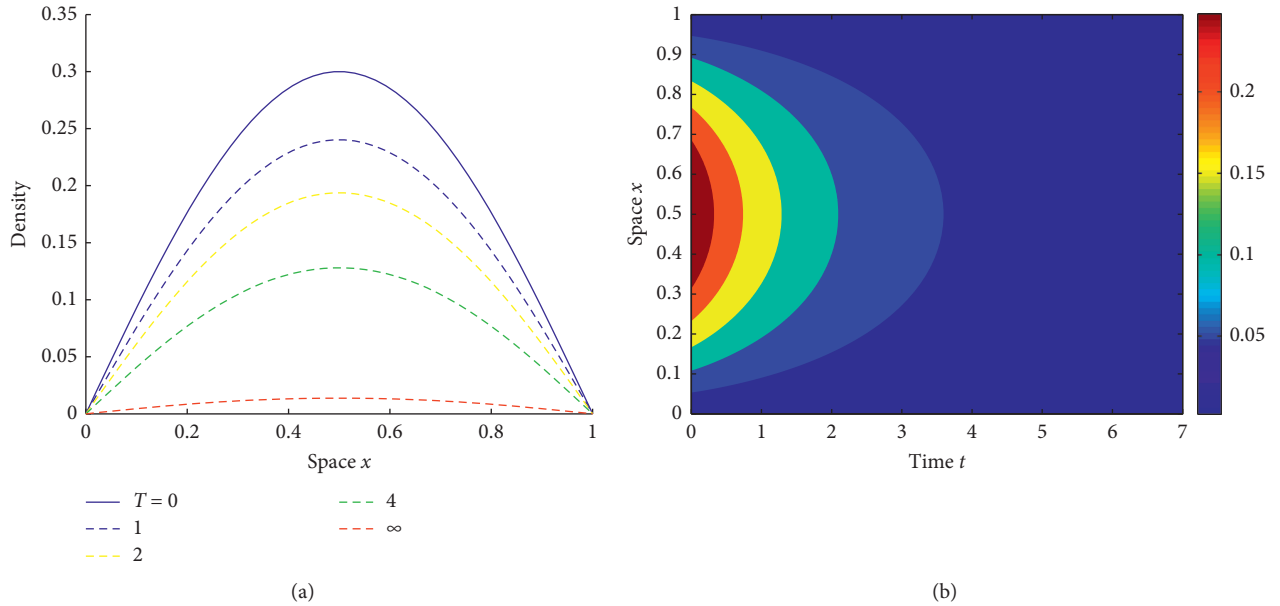


FIGURE 4: The corresponding cross-sectional view (a) and contour one (b) for the solution of problems (7) and (9), which implies that the domain is fixed when the evolution rate  $\rho(t) = 1$ .

$$\overline{\rho^{-2}} = \frac{2}{\pi} \int_0^{\pi/2} e^{0.1(1-\cos(4t))} dt \approx 0.8269 < 1,$$

$$\begin{aligned} R_0(\rho) &\geq \sqrt{\frac{A_m/N_b \alpha_b (\beta_b)^2 \alpha_m^*}{d_m (D_1 \lambda^* \overline{\rho^{-2}} + \gamma_b)}} \\ &= \sqrt{\frac{20 \times 0.88 \times 0.09 \times 0.16}{0.029 \times (0.06 \times 9.8596 \times 0.8269 + 0.01)}} > 1. \end{aligned} \quad (84)$$

Therefore, it is easy to see that the solution of problems (7) and (9) converges to a positive periodic steady state (see Figures 5 and 6), which means that the virus with periodically

evolving domain will persist. Consequently, we can see that  $\overline{\rho^{-2}} < 1$  has positive effect on the persistence of WNv.

*Example 4.* In systems (7) and (9), we set  $\beta_b = 0.09$  and  $d_m = 0.29$  with  $\rho(t) = e^{0.2(\cos(4t)-1)}$ . Direct calculations show that

$$\overline{\rho^{-2}} = \frac{2}{\pi} \int_0^{\pi/2} e^{0.2(\cos(4t)-1)} dt \approx 1.5221 > 1,$$

$$\sqrt{\frac{A_m/N_b \alpha_b (\beta_b)^2 \alpha_m^*}{d_m (D_1 \lambda^* \overline{\rho^{-2}} + \gamma_b)}} = \sqrt{\frac{20 \times 0.88 \times 0.0081 \times 0.16}{0.29 \times (0.06 \times 9.8596 \times 1.5221 + 0.01)}} < 1. \quad (85)$$

Therefore, one can easily see that the solution of problems (7) and (9) tends to zero quickly (see Figures 7 and 8), which

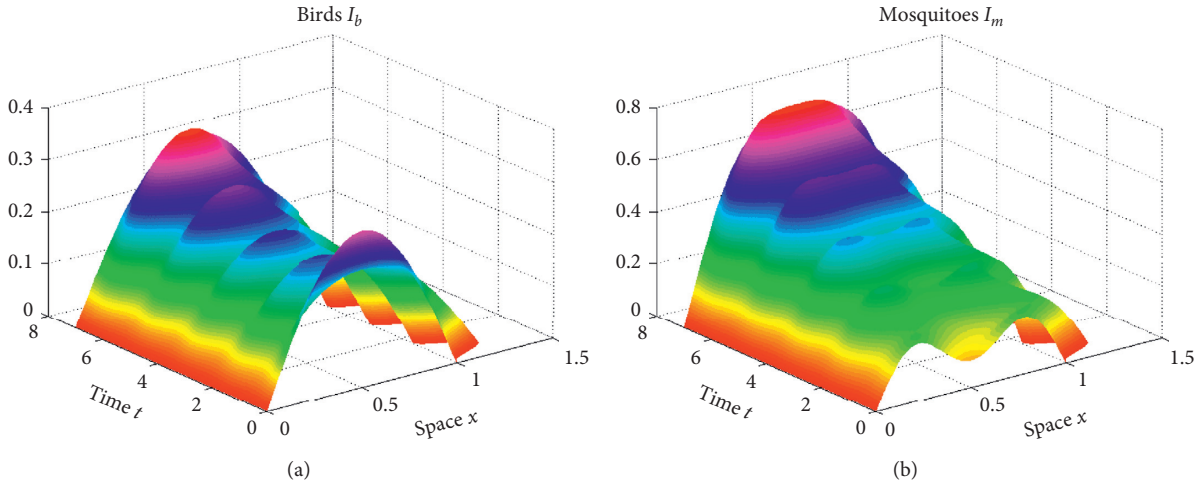


FIGURE 5:  $\rho(t) = e^{0.1(1-\cos(4t))}$ ,  $\overline{\rho^{-2}} < 1$ ,  $R_0(\rho) > 1$ , which means that the solution of problems (7) and (9) converges to a positive periodic steady state.

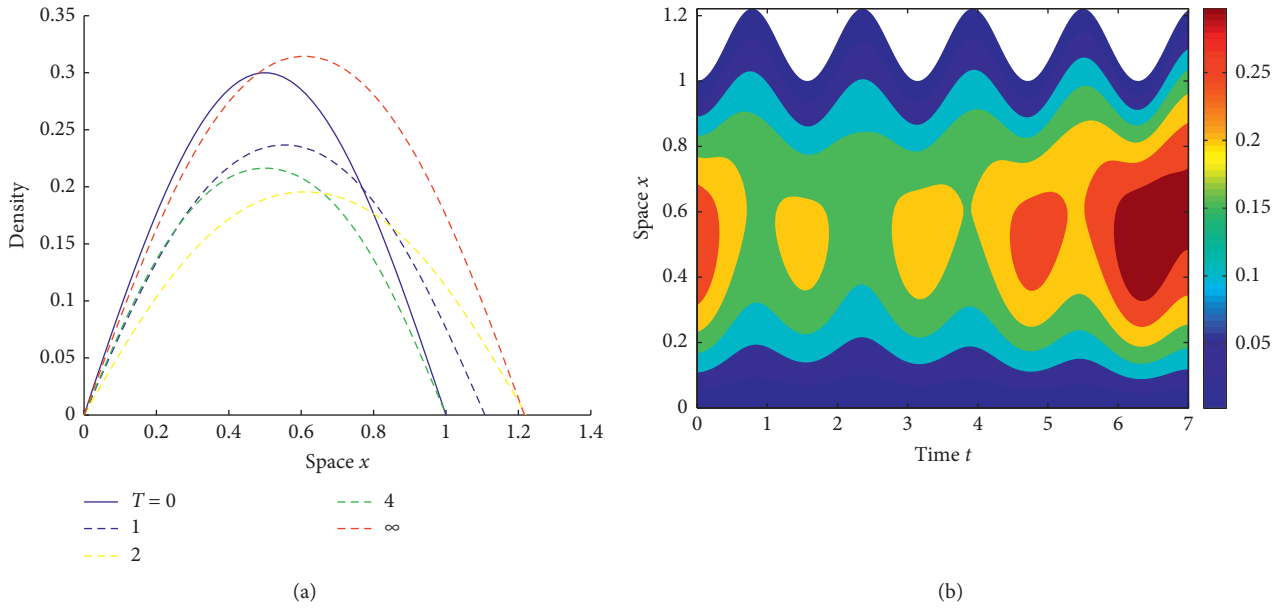


FIGURE 6: The corresponding cross-sectional view (a) and contour one (b) for the solution of problems (7) and (9), which implies that the domain is periodically evolving when the evolution rate  $\rho(t) = e^{0.1(1-\cos(4t))}$ .

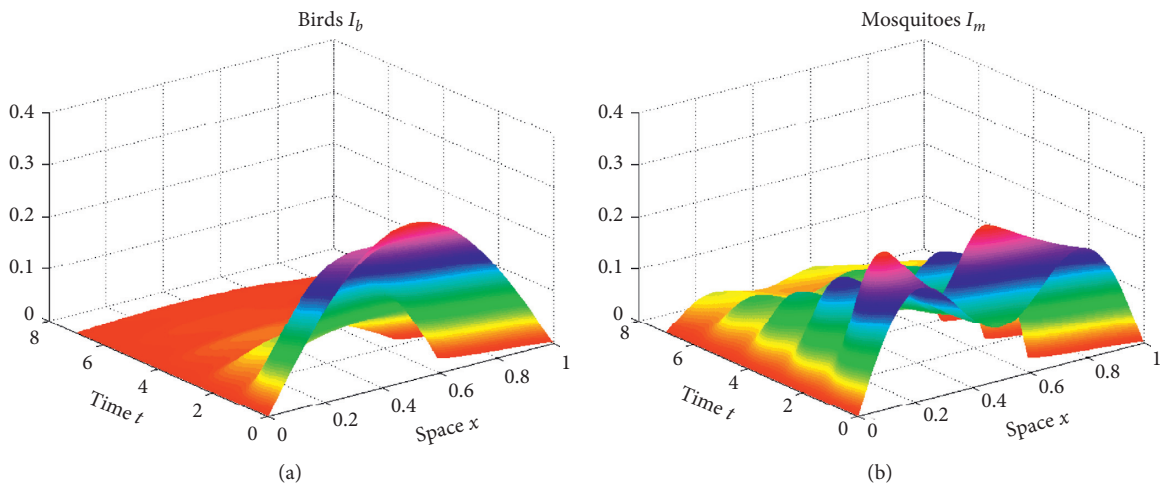


FIGURE 7:  $\rho(t) = e^{0.2(\cos(4t)-1)}$ ,  $\overline{\rho^{-2}} > 1$ ,  $R_0(\rho) < 1$ , which means that the solution  $(u, v)$  tends to zero.



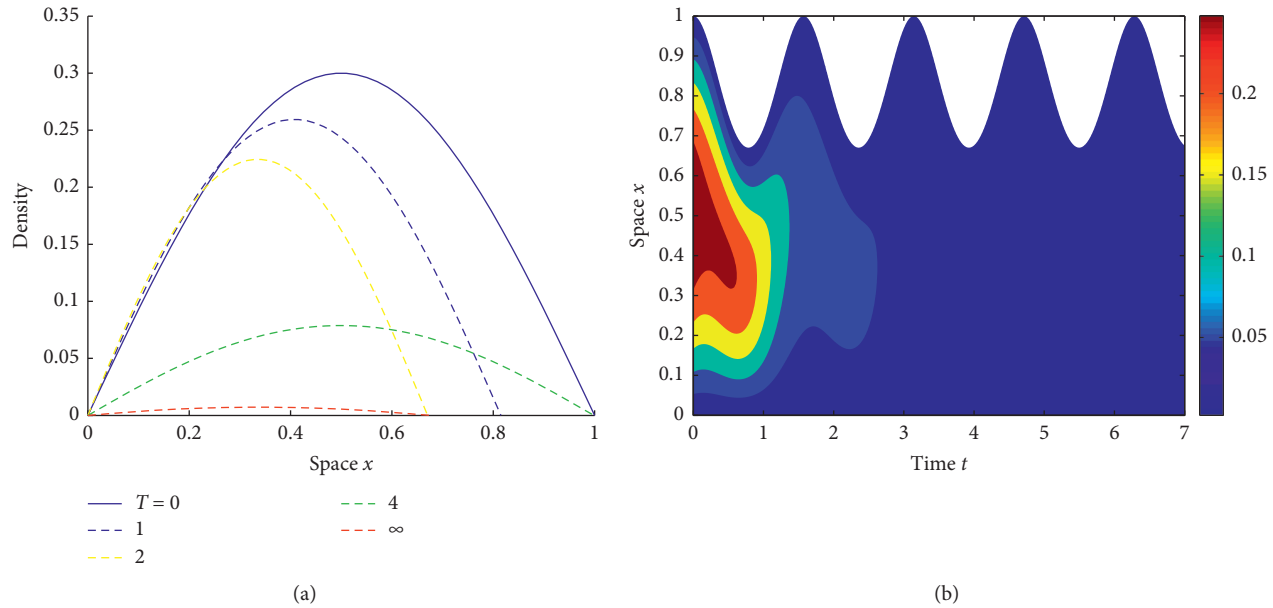


FIGURE 8: The corresponding cross-sectional view (a) and contour one (b) for the solution of problems (7) and (9), which implies that the domain is not periodically evolving when the evolution rate  $\rho(t) = e^{0.2(\cos(4t)-1)}$ .

means that the virus with periodically evolving domain will be extinct. Consequently, we can say that  $\overline{\rho^{-2}} > 1$  has negative effect on the persistence of WNV.

## 8. Conclusions

Recently, the impact of periodic evolution domain has been attracting considerable attention. In [31], Jiang and Wang studied the impact of periodic evolution on the single-species diffusion logistic model. Asymptotic profile of a mutualistic model on a periodically evolving domain has been investigated by Adam et al. in [33]. The diffusive model for *Aedes aegypti* mosquito on a periodically evolving domain has been considered by Zhang and Lin in [32]. Zhu et al. [34] constructed a dengue fever model and studied its asymptotic profile on a periodically evolving domain. These studies indicated that the periodic domain evolution has a significant impact on the dispersal of species and transmission of infectious diseases.

In this paper, we study a diffusive West Nile virus model with periodical and isotropic domain evolution. To circumvent the difficulty induced by the advection and dilution terms, we transform the model to a reaction-diffusion model in a fixed domain. We introduce the spatial-temporal basic reproduction number  $R_0(\rho)$  depending on the periodic evolution rate  $\rho(t)$ . In the case that all parameters are constants and  $\rho(t) \equiv 1$ , the explicit formula for the spatial-temporal basic reproduction number is presented (Theorem 1). Moreover, to better understand the impact of periodic evolution value on the persistence or extinction of the virus, we assume  $\rho(t) \equiv 1$ , that is, the periodic domain  $\Omega_t$  becomes a fixed domain  $\Omega_0$ . Furthermore, the notation  $\overline{\rho^{-2}} = (1/T) \int_0^T 1/\rho^2(t) dt$  is utilized as an average value. Our results show that if  $R_0(\rho) > 1$  depending on the evolution rate  $\rho(t)$ , then the virus will persist and all solutions possess

the attractor  $\langle(\underline{u}, \underline{v}), (\overline{u}, \overline{v})\rangle$ , which is the sector between the maximal and minimal  $T$ -periodic solutions  $(\overline{u}, \overline{v})$  and  $(\underline{u}, \underline{v})$  of problems (7) and (8) (Theorems 2–4) (a), whereas, if  $R_0(\rho) \leq 1$ , then any solution of problems (7) and (8) decays to  $(0, 0)$ , that is, the virus is in the case of extinction (Theorem 3 and 5) (b). In the case that  $\rho(t) \equiv 1$ , we introduce  $R_0^*$ . For this case, if  $R_0^* > 1$ , the model admits a maximal and minimal  $T$ -periodic solutions, while if  $R_0^* \leq 1$ , the model has no positive solution (Theorem 6 and 7). It is important to mention that numerical simulation in this paper is presented by using some parameters given in Lewis et al. [4], namely,  $A_m/N_b = 20$ ,  $\alpha_b = 0.88$ ,  $\alpha_m = 0.16$ ,  $\gamma_b = 0.01$ ,  $\beta_b = 0.3$ , and  $d_m = 0.029$ .

From our theoretical and numerical results, we believe that the periodic domain evolution has a significant impact on the transmission of WNV.

## Data Availability

All data are provided in full in the numerical simulation and discussion section of this article.

## Conflicts of Interest

The authors declare that they have no conflicts of interest.

## Authors' Contributions

All authors contributed equally and all of them read and approved the final manuscript.

## Acknowledgments

This research was supported by the National Natural Science Foundation of China (grant nos. 11872189 and 11472116).

## References

- [1] N. A. Maida and H. M. Yang, "Dynamic of West Nile virus transmission considering several coexisting avian populations," *Mathematical and Computer Modelling*, vol. 53, no. 5-6, pp. 1247-1260, 2011.
- [2] A. Abdelrazec, S. Lenhart, and H. Zhu, "Transmission dynamics of West Nile virus in mosquitoes and corvids and non-corvids," *Journal of Mathematical Biology*, vol. 68, no. 6, pp. 1553-1582, 2014.
- [3] D. S. Asnis, R. Conetta, A. A. Teixeira, G. Waldman, and B. A. Sampson, "The West Nile virus outbreak of 1999 in New York: the flushing hospital experience," *Clinical Infectious Diseases*, vol. 30, no. 3, pp. 413-418, 2000.
- [4] M. Lewis, J. Renclawowicz, and P. v. den Driessche, "Traveling waves and spread rates for a West Nile virus model," *Bulletin of Mathematical Biology*, vol. 68, no. 1, pp. 3-23, 2006.
- [5] D. Nash, F. Mostashari, A. Fine et al., "The outbreak of West Nile virus infection in the New York city area in 1999," *New England Journal of Medicine*, vol. 344, no. 24, pp. 1807-1814, 2001.
- [6] M. J. Wonham, T. de-Camino-Beck, and M. A. Lewis, "An epidemiological model for West Nile virus: invasion analysis and control applications," *Proceedings of the Royal Society of London. Series B: Biological Sciences*, vol. 271, no. 1538, pp. 501-507, 2004.
- [7] J. Chen, J. Huang, J. C. Beier et al., "Modeling and control of local outbreaks of West Nile virus in the United States," *Discrete and Continuous Dynamical Systems—Series B*, vol. 21, no. 8, pp. 2423-2449, 2016.
- [8] C. Bowman, A. Gumel, P. Vandendriessche, J. Wu, and H. Zhu, "A mathematical model for assessing control strategies against West Nile virus," *Bulletin of Mathematical Biology*, vol. 67, no. 5, pp. 1107-1133, 2005.
- [9] H. Wan and H. Zhu, "The backward bifurcation in compartmental models for West Nile virus," *Mathematical Biosciences*, vol. 227, no. 1, pp. 20-28, 2010.
- [10] N. A. Maida and H. M. Yang, "Spatial spreading of West Nile virus described by traveling waves," *Journal of Theoretical Biology*, vol. 258, no. 3, pp. 403-417, 2009.
- [11] R. Liu, J. Shuai, J. Wu, and H. Zhu, "Modeling spatial spread of west nile virus and impact of directional dispersal of birds," *Mathematical Biosciences and Engineering*, vol. 3, no. 1, pp. 145-160, 2006.
- [12] Z. Lin and H. Zhu, "Spatial spreading model and dynamics of West Nile virus in birds and mosquitoes with free boundary," *Journal of Mathematical Biology*, vol. 75, no. 6-7, pp. 1381-1409, 2017.
- [13] A. K. Tarboush, Z. Lin, and M. Zhang, "Spreading and vanishing in a West Nile virus model with expanding fronts," *Science China Mathematics*, vol. 60, no. 5, pp. 841-860, 2017.
- [14] O. Diekmann, J. A. P. Heesterbeek, and J. A. J. Metz, "On the definition and the computation of the basic reproduction ratio  $R_0$  in models for infectious diseases in heterogeneous populations," *Journal of Mathematical Biology*, vol. 28, pp. 365-382, 1990.
- [15] P. van den Driessche and J. Watmough, "Reproduction numbers and sub-threshold endemic equilibria for compartmental models of disease transmission," *Mathematical Biosciences*, vol. 180, no. 1-2, pp. 29-48, 2002.
- [16] L. J. Allen, B. M. Bolker, Y. Lou, and A. L. Nevai, "Asymptotic profiles of steady states for an SIS epidemic reaction-diffusion model," *Discrete & Continuous Dynamical Systems*, vol. 21, no. 1, pp. 1-20, 2008.
- [17] X. Q. Zhao, *Dynamical Systems in Population Biology*, Springer, Cham, Switzerland, 2nd edition, 2017.
- [18] A. K. Tarboush, J. Ge, and Z. G. Lin, "Coexistence of a cross-diffusive West Nile virus model in a heterogenous environment," *Mathematical Biosciences & Engineering*, vol. 15, no. 6, pp. 1479-1494, 2018.
- [19] A. K. Tarboush, J. Ge, and Z. Lin, "Asymptotic periodicity in a diffusive West Nile virus model in a heterogeneous environment," *International Journal of Biomathematics*, vol. 10, no. 8, p. 1750110, 2017.
- [20] Y. Du and Z. Lin, "The diffusive competition model with a free boundary: invasion of a superior or inferior competitor," *Discrete & Continuous Dynamical Systems-B*, vol. 19, no. 10, pp. 3105-3132, 2014.
- [21] J.-S. Guo and C.-H. Wu, "On a free boundary problem for a two-species weak competition system," *Journal of Dynamics and Differential Equations*, vol. 24, no. 4, pp. 873-895, 2012.
- [22] C. Lei, Z. Lin, and Q. Zhang, "The spreading front of invasive species in favorable habitat or unfavorable habitat," *Journal of Differential Equations*, vol. 257, no. 1, pp. 145-166, 2014.
- [23] M. Wang and Y. Zhang, "Two kinds of free boundary problems for the diffusive prey-predator model," *Nonlinear Analysis: Real World Applications*, vol. 24, pp. 73-82, 2015.
- [24] I. Ahn, S. Baek, and Z. Lin, "The spreading fronts of an infective environment in a man-environment-man epidemic model," *Applied Mathematical Modelling*, vol. 40, no. 15-16, pp. 7082-7101, 2016.
- [25] J. Ge, C. Lei, and Z. Lin, "Reproduction numbers and the expanding fronts for a diffusion-advection SIS model in heterogeneous time-periodic environment," *Nonlinear Analysis: Real World Applications*, vol. 33, pp. 100-120, 2017.
- [26] Z. Wang, H. Nie, and Y. Du, "Spreading speed for a West Nile virus model with free boundary," *Journal of Mathematical Biology*, vol. 79, no. 2, pp. 433-466, 2019.
- [27] E. J. Crampin, E. A. Gaffney, and P. K. Maini, "Mode-doubling and tripling in reaction-diffusion patterns on growing domains: a piecewise linear model," *Journal of Mathematical Biology*, vol. 44, no. 2, pp. 107-128, 2002.
- [28] A. Madzvamuse, "Time-stepping schemes for moving grid finite elements applied to reaction-diffusion systems on fixed and growing domains," *Journal of Computational Physics*, vol. 214, no. 1, pp. 239-263, 2006.
- [29] A. Madzvamuse and P. K. Maini, "Velocity-induced numerical solutions of reaction-diffusion systems on continuously growing domains," *Journal of Computational Physics*, vol. 225, no. 1, pp. 100-119, 2007.
- [30] Q. Tang and Z. Lin, "The asymptotic analysis of an insect dispersal model on a growing domain," *Journal of Mathematical Analysis and Applications*, vol. 378, no. 2, pp. 649-656, 2011.
- [31] D.-H. Jiang and Z.-C. Wang, "The diffusive Logistic equation on periodically evolving domains," *Journal of Mathematical Analysis and Applications*, vol. 458, no. 1, pp. 93-111, 2018.
- [32] M. Zhang and Z. Lin, "The diffusive model for Aedes Aegypti mosquito on a periodically evolving domain," *Discrete & Continuous Dynamical Systems B*, vol. 22, no. 11, pp. 1-18, 2017.
- [33] B. Adam, A. K. Tarboush, and Z. Lin, "Asymptotic profile of a mutualistic model on a periodically evolving domain," *International Journal of Biomathematics*, vol. 12, no. 7, 2019.
- [34] M. Zhu, Y. Xu, and J. Cao, "The asymptotic profile of a dengue fever model on a periodically evolving domain," *Applied Mathematics and Computation*, vol. 362, Article ID 124531, 2019.

- [35] D. Acheson, *Elementary Fluid Dynamics*, Oxford University Press, New York, NY, USA, 1990.
- [36] M. J. Baines, *Moving Finite Element, Monographs on Numerical Analysis*, Clarendon Press, Oxford, UK, 1994.
- [37] R. E. Baker and P. K. Maini, "A mechanism for morphogen-controlled domain growth," *Journal of Mathematical Biology*, vol. 54, no. 5, pp. 597–622, 2007.
- [38] W. Wang and X.-Q. Zhao, "Basic reproduction numbers for reaction-diffusion epidemic models," *SIAM Journal on Applied Dynamical Systems*, vol. 11, no. 4, pp. 1652–1673, 2012.
- [39] p Hess, "Periodic-parabolic boundary value problems and positivity," in *Pitman Research Notes in Mathematics*, Vol. 247, Longman Science and Technology., Harlow, UK, 1991.
- [40] P. A. Caudevilla and J. López-Gómez, "Asymptotic behaviour of principal eigenvalues for a class of cooperative systems," *Journal of Differential Equations*, vol. 244, pp. 1093–1113, 2008.
- [41] D. G. de Figueiredo and E. Mitidieri, "A maximum principle for an elliptic system and applications to semilinear problems," *SIAM Journal on Mathematical Analysis*, vol. 17, no. 4, pp. 836–849, 1986.
- [42] G. Sweers, "Strong positivity in  $C(\bar{\Omega})$  for elliptic systemsfor elliptic systems," *Mathematische Zeitschrift*, vol. 209, no. 1, pp. 251–271, 1992.
- [43] C. V. Pao, "Stability and attractivity of periodic solutions of parabolic systems with time delays," *Journal of Mathematical Analysis and Applications*, vol. 304, no. 2, pp. 423–450, 2005.

## Research Article

# Control of Near-Grazing Dynamics in the Two-Degree-of-Freedom Vibroimpact System with Symmetrical Constraints

Zihan Wang, Jieqiong Xu , Shuai Wu, and Quan Yuan

College of Mathematics and Information Science, Guangxi University, Nanning 530004, China

Correspondence should be addressed to Jieqiong Xu; xjq@gxu.edu.cn

Received 17 October 2019; Revised 16 February 2020; Accepted 2 March 2020; Published 10 April 2020

Guest Editor: Viet-Thanh Pham

Copyright © 2020 Zihan Wang et al. This is an open access article distributed under the Creative Commons Attribution License, which permits unrestricted use, distribution, and reproduction in any medium, provided the original work is properly cited.

The stability of grazing bifurcation is lost in three ways through the local analysis of the near-grazing dynamics using the classical concept of discontinuity mappings in the two-degree-of-freedom vibroimpact system with symmetrical constraints. For this instability problem, a control strategy for the stability of grazing bifurcation is presented by controlling the persistence of local attractors near the grazing trajectory in this vibroimpact system with symmetrical constraints. Discrete-in-time feedback controllers designed on two Poincaré sections are employed to retain the existence of an attractor near the grazing trajectory. The implementation relies on the stability criterion under which a local attractor persists near a grazing trajectory. Based on the stability criterion, the control region of the two parameters is obtained and the control strategy for the persistence of near-grazing attractors is designed accordingly. Especially, the chaos near codimension-two grazing bifurcation points was controlled by the control strategy. In the end, the results of numerical simulation are used to verify the feasibility of the control method.

## 1. Introduction

Grazing bifurcation, one type of discontinuity-induced bifurcations, has been extensively studied in vibroimpact system as it has complex dynamics and is widely encountered in many engineering examples. On analysis of the dynamics near grazing in a general class of impact oscillator systems, a classical concept of analysis is the so-called discontinuity-mapping approach initially conceived of by Nordmark [1, 2] (see [3, 4] for an overview). The analysis is usually carried out by finding an appropriate local map describing the system dynamics in neighborhood of the grazing event. The local map can then be combined with an analytic Poincaré map to give the so-called grazing normal form whose dynamics can be shown to be topologically equivalent to those of the underlying flow. The grazing normal form derived by the discontinuity-mapping approach is used to analyze the

local dynamics in the vicinity of a grazing trajectory. As shown in [5–8], the normal form map of the rigid impact oscillator contains a square-root term causing a singularity in the first derivative, which results in an abrupt loss of the stability. And different bifurcation scenarios associated with switching between impacting motions and nonimpacting motions near grazing were also described. In particular, the discontinuity-mapping approach was used by Fredriksson and Nordmark [9] to establish conditions for the persistence or disappearance of a local attractor in the vicinity of a grazing periodic trajectory. In addition, some conditions for the persistence of a local attractor in the immediate vicinity of quasiperiodic grazing trajectories in an impacting dynamical system were formulated by Thota and Dankowicz [10]. When the stability conditions of grazing bifurcation are degenerate, the codimension-two would occur, which is always a hot topic. Kowalczyk et al. [11] proposed a strategy for

classification of codimension-two discontinuity-induced bifurcations of limit cycles in piecewise smooth systems and studied their nonsmooth transitions. Foale [12] analyzed the results of a special codimension-two grazing bifurcation in a single-degree-of-freedom impact oscillator by using the impact surface as a Poincaré section. In addition, the study also shows that the bifurcation of the saddle node bifurcation and the flip bifurcation can meet at a certain codimension-two grazing points in the parameter plane. Thota et al. [13] studied the distribution of codimension-two grazing bifurcation point according to the discontinuous mapping in the single-degree-of-freedom collision oscillator and discussed the possible dynamic characteristics of the system response near this bifurcation point. Xu et al. [14] studied the codimension-two grazing bifurcation of  $n$ -degree-of-freedom vibrators with bilateral constraints and obtained and simplified the existence conditions of codimension-two grazing bifurcation. Similar phenomena about codimension-two grazing bifurcation can also be found in Refs. [15, 16]. Yin et al. [17] discussed the important role of some degenerated grazing bifurcation points in the transition between saddle node bifurcation and period doubling bifurcation. Dankowicz and Zhao [18, 19] studied the grazing bifurcations of the codimension-one and the codimension-two of a class of impact microactuators.

The loss of local attractors near grazing bifurcation may arise catastrophic changes of system response and lead to codimension-two or more complicated bifurcation; therefore, controlling near-grazing dynamics becomes necessary and significant. Dankowicz and Jerrelind [20] used the linear feedback control method to control the grazing bifurcation of the piece smooth dynamic system, so that the system has local attractors near the grazing orbit. Dankowicz and Svahn [21] presented for the existence of event-driven control strategies that guarantee the local persistence of system attractors with at most low-velocity contact in vibro impacting oscillators. Misra and Dankowicz [22] developed a rigorous control paradigm for regulating the near-grazing bifurcation behavior of limit cycles in piecewise-smooth dynamical systems. Yin et al. [23] analyzed the stability for near-grazing period-one impact motion to suppress grazing-induced instabilities. The bounded eigenvalues are further confined to the unit circle, and the continuous transition between the nonimpact motion and the controlled impact motion is obtained. Xu et al. [24] discussed the control problem of near-grazing dynamics in a two-degree-of-freedom vibroimpact system with a clearance.

Based on the concept of controlling the persistence of local attractors near the grazing trajectory in impact oscillator with unilateral constraints mentioned in [20–24], this paper aims to control the stability of grazing bifurcation or control the persistence of local attractors near the grazing trajectory in this vibroimpact system with symmetrical constraints. Compared with impact oscillator

with unilateral constraint, the instability problems near grazing trajectory become more complex for impact oscillator with symmetrical constraints as mentioned in [17]. The stability of double grazing motion bifurcation in the system is lost in three ways, and the existence conditions of the codimension-two grazing bifurcation occur in four different cases accordingly. For this complex unstable problem, analytic expressions of stability criterion are obtained in this paper. Based on the stability criterion, the stability control strategy of the persistence of near-grazing attractors is proposed. Furthermore, the chaos near codimension-two grazing bifurcation points was controlled by the control strategy. This paper is organized as follows. In Section 2, a two-degree-of-freedom vibroimpact system with symmetrical constraints is introduced. In Section 3, near-grazing bifurcation dynamics are analyzed. In Section 4, the discrete-in-time feedback control method is designed to maintain the persistence of the local attractor of double grazing period motion. In Section 5, numerical simulation is used to verify the feasibility of the control method. Finally, the conclusion is given in Section 6.

## 2. Mechanical Model and Double Grazing Periodic Motion

Figure 1 shows the schematic model of a two-degree-of-freedom impact oscillator with a clearance. Masses  $M_1$  and  $M_2$  are connected to linear viscous dampers  $C_1$  and  $C_2$  by linear springs with stiffness  $K_1$  and  $K_2$ , respectively. The harmonic forces of the amplitude  $P_1$  and  $P_2$  are applied to the masses  $M_1$  and  $M_2$ , respectively, and the harmonic force is applied only to the mass in the horizontal direction. The mass  $M_1$  moves between the symmetrical rigid stops  $A$  and  $C$ . When the mass  $M_1$  strikes rigid stop  $A$  or  $C$ , the motion becomes a nonlinear motion and the impact is described by the recovery factor  $R$ . Assuming that the damping in the mechanical model is the Rayleigh type proportional damping, it can be known that  $(C_1/K_1) = (C_2/K_2)$ .

The governing equation is described by

$$\begin{bmatrix} M_1 & 0 \\ 0 & M_2 \end{bmatrix} \begin{bmatrix} \ddot{X}_1 \\ \ddot{X}_2 \end{bmatrix} + \begin{bmatrix} C_1 & -C_1 \\ -C_1 & C_1 + C_2 \end{bmatrix} \begin{bmatrix} \dot{X}_1 \\ \dot{X}_2 \end{bmatrix} + \begin{bmatrix} K_1 & -K_1 \\ -K_1 & K_1 + K_2 \end{bmatrix} \begin{bmatrix} X_1 \\ X_2 \end{bmatrix} = \begin{bmatrix} P_1 \\ P_2 \end{bmatrix} \sin(\Omega T + \tau), \quad (|X_1| < D). \quad (1)$$

When  $|X_1| = D$ , the collision occurs. At this time, the collision equation is as follows:

$$\dot{X}_{1+} = -R\dot{X}_{1-}, \quad (|X_1| = D), \quad (2)$$

where  $\dot{X}$  and  $\ddot{X}$  represent the first and second derivatives of  $X$  with respect to time  $T$ , respectively.  $\dot{X}_{1+}$  indicates the instantaneous speed at which the mass  $M_1$  approaches the

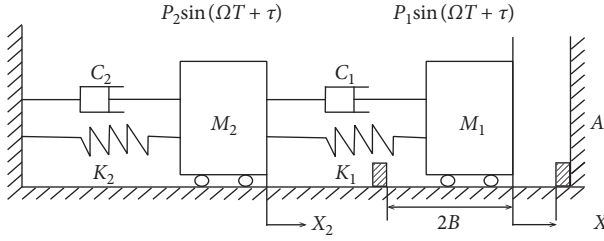


FIGURE 1: Schematic of the two-degree-of-freedom impact oscillator with symmetrical constraints.

rigid stop A or C.  $\dot{X}_{1-}$  indicates the instantaneous speed at which the mass  $M_1$  leaves the rigid stop A or C.

Introduce the nondimensional quantities as follows:

$$\begin{aligned}
 \mu_m &= \frac{M_2}{M_1}, \\
 \mu_k &= \frac{K_2}{K_1}, \\
 \mu_c &= \frac{C_2}{C_1}, \\
 \mu_c &= \mu_k, \\
 p &= \frac{P_2}{P_1 + P_2}, \\
 \omega &= \Omega \sqrt{\frac{M_1}{K_1}}, \\
 t &= T \sqrt{\frac{K_1}{M_1}}, \\
 \zeta &= \frac{C_1}{2\sqrt{K_1 M_1}}, \\
 d &= \frac{DK_1}{P_1 + P_2}, \\
 x_1 &= \frac{X_1 K_1}{P_1 + P_2}, \\
 x_2 &= \frac{X_2 K_1}{P_1 + P_2}.
 \end{aligned} \tag{3}$$

According to equations (1)–(3), the system can be transformed into nondimensional forms.

$$\begin{aligned}
 \begin{bmatrix} 1 & 0 \\ 0 & \mu_m \end{bmatrix} \begin{bmatrix} \ddot{x}_1 \\ \ddot{x}_2 \end{bmatrix} + \begin{bmatrix} 2\zeta & -2\zeta \\ -2\zeta & 2\zeta(1 + \mu_c) \end{bmatrix} \begin{bmatrix} \dot{x}_1 \\ \dot{x}_2 \end{bmatrix} \\
 + \begin{bmatrix} 1 & -1 \\ -1 & 1 + \mu_k \end{bmatrix} \begin{bmatrix} x_1 \\ x_2 \end{bmatrix} = \begin{bmatrix} 1 - p \\ p \end{bmatrix} \sin(\omega t + \tau), \quad (|x_1| < d),
 \end{aligned} \tag{4}$$

$$\dot{x}_{1+} = -R\dot{x}_{1-}, \quad (|x_1| = d), \tag{5}$$

where  $\dot{x}$  and  $\ddot{x}$  represent the first and second derivatives of  $x$  with respect to the nondimensional time  $t$ , respectively.

Suppose  $\Psi$  be the canonical modal matrix of equation (4), and coordinate transformation of equation (4). Let  $x = \Psi \xi$ .

$$I \ddot{\xi} + C \dot{\xi} + \Lambda \xi = P \sin(\omega t + \tau), \tag{6}$$

where  $\omega_1$  and  $\omega_2$  represent the eigenfrequencies of the system,  $x = (x_1, x_2)^T$ ,  $\xi = (\xi_1, \xi_2)^T$ ,  $I$  is the unit matrix,  $\Lambda$  and  $C$  are diagonal matrices,  $\Lambda = \text{diag}[\omega_1^2, \omega_2^2]$ ,  $C = 2\zeta\Lambda = \text{diag}[2\zeta\omega_1^2, 2\zeta\omega_2^2]$ , and  $P = \Psi^T(1 - p, p)^T$ . The general solution of equation (4) is given by

$$\begin{aligned}
 x_i &= \sum_{j=1}^2 \Psi_{ij} \left( e^{-\eta_j(t-t_0)} (a_j \cos \omega_{dj} t + b_j \sin \omega_{dj} t) \right. \\
 &\quad \left. + A_j \sin(\omega t + \tau) + B_j \cos(\omega t + \tau) \right), \\
 \dot{x}_i &= \sum_{j=1}^2 \Psi_{ij} \left( e^{-\eta_j(t-t_0)} ((b_j \omega_{dj} - a_j \eta_j) \cos \omega_{dj} t \right. \\
 &\quad \left. - (a_j \omega_{dj} + b_j \eta_j) \sin \omega_{dj} t) \right. \\
 &\quad \left. + A_j \omega \cos(\omega t + \tau) - B_j \omega \sin(\omega t + \tau) \right),
 \end{aligned} \tag{7}$$

where  $i = 1, 2$ ,  $t_0$  represents the time at which the mass  $M_1$  collides with the rigid stop A or C; we set the mass  $M_1$  to collide with the rigid stop A when  $t_0 = 0$ .  $\Psi_{ij}$  is an element of the canonical modal matrix  $\Psi$ ,  $\eta_j = \zeta \omega_j^2$ , and  $\omega_{dj} = \sqrt{\omega_j^2 - \eta_j^2}$ . The initial conditions and modal parameters of the system determine the integral constants  $a_j$  and  $b_j$ .  $A_j$  and  $B_j$  are amplitude parameters, and the expression is given by

$$\begin{aligned}
 A_j &= \frac{1}{2\omega_{dj}} \left( \frac{\omega + \omega_{dj}}{(\omega + \omega_{dj})^2 + \eta_j^2} - \frac{\omega - \omega_{dj}}{(\omega - \omega_{dj})^2 + \eta_j^2} \right) \bar{f}_j, \\
 B_j &= \frac{\eta_j}{2\omega_{dj}} \left( \frac{1}{(\omega + \omega_{dj})^2 + \eta_j^2} - \frac{1}{(\omega - \omega_{dj})^2 + \eta_j^2} \right) \bar{f}_j.
 \end{aligned} \tag{8}$$

According to the initial conditions and periodic conditions of the double grazing periodic-n motion, the existence conditions of two-degree-of-freedom impact oscillator double grazing periodic-n motion is as follows:



$$d = \sqrt{d_1^2 + d_2^2},$$

$$\tau = \arctan\left(\frac{d_1}{d_2}\right), \quad (9)$$

where  $d_1 = \Psi_{11}A_1 + \Psi_{12}A_2$  and  $d_2 = \Psi_{11}B_1 + \Psi_{12}B_2$ .

In addition, in order to ensure that the impacting cycle of the mass  $M_1$  does not adhere to rigid stop, the acceleration  $a^*$  of the mass  $M_1$  satisfies  $a^* < 0$  and the acceleration  $a^*$  of the mass  $M_2$  satisfies  $a^* > 0$ .

### 3. Near-Grazing Dynamics

*3.1. The Stability Criterion of Double Grazing Bifurcation.* Let  $p$  be a state vector, such that  $x = (x_1, v_1, x_2, v_2, p)^T \in \mathbb{R}^5$ , and it follows that

$$\frac{dx}{dt} = \dot{x} = f(x) = (v_1, a_1, v_2, a_2, 0)^T, \quad (10)$$

where  $a_i$  represents the acceleration of the oscillator as a function of  $x_i, v_i$ . Define  $\phi(x, t)$  as the local flow function associated with  $f(x)$ . Suppose that the movement of the oscillator is limited by symmetrical rigid constraints placed at  $|x_1| = d$  corresponding to state space discontinuity surfaces  $D_1$  and  $D_2$ , where

$$\begin{aligned} D_1 &= h^{D_1}(x, d) = d - x_1 = 0, \\ D_2 &= h^{D_2}(x, d) = -d - x_1 = 0. \end{aligned} \quad (11)$$

The oscillator moves between two rigid stops when  $h^{D_1}(x, d) > 0$  and  $h^{D_2}(x, d) < 0$ . When  $h^{D_1}(x, d) = 0$  or  $h^{D_2}(x, d) = 0$ , the oscillator collides with the rigid stop. In addition, let  $h^{P_1}(x) = h_x^{D_1}(x, d)f(x) = -v_1$ ,  $h_x^{D_2}(x) = h^{D_2}(x, d)f(x) = -v_1$ .

When the oscillator collides with the constraint, we establish a function  $R(x)$  with a characteristic restitution coefficient  $R$  to represent the jump map, i.e.,  $R(x)$  represents the instantaneous state after the collision and before the collision, where

$$R(x) = (x_1, -Rv_1, x_2, v_2, p)^T. \quad (12)$$

The state space trajectory and the grazing contact points of  $D_1$  and  $D_2$  are, respectively, corresponding to points  $x^{*1}$  and  $x^{*2}$ , so that

$$\begin{aligned} h^{D_1}(x^{*1}, d^*) &= 0, \\ h^{P_1}(x^{*1}) &= -v_1^{*1} = 0, \\ \frac{d}{dt}h^{P_1}(x) \Big|_{x=x^{*1}} &= h_x^{P_1}(x^{*1})f(x^{*1}) = -a_1^{*1} > 0, \\ h^{D_2}(x^{*2}, d^*) &= 0, \\ h^{P_2}(x^{*2}) &= -v_1^{*2} = 0, \\ \frac{d}{dt}h^{P_2}(x) \Big|_{x=x^{*2}} &= h_x^{P_2}(x^{*2})f(x^{*2}) = -a_1^{*2} < 0. \end{aligned} \quad (13)$$

Choose a constant phase angle  $\theta^*$  as a Poincaré section, and it has the following form:  $\Pi_1 = \{\hat{x} \in \mathbb{R}^5 \times S^1 \mid \theta = \theta^*\}$ , where  $\hat{x} = (x_1, \dot{x}_1, x_2, \dot{x}_2, p, \theta)^T$ ,  $\theta = \omega t + \tau$ . The modulus of  $\theta$  is  $2\pi$ ,  $\theta^* = \tau^*$ . Since the periodic trajectory of the system is symmetrical, we set another Poincaré section as  $\Pi_2 = \{\hat{x} \in \mathbb{R}^5 \times S^1 \mid \theta = \theta^* + \pi\}$ .

With  $d$  as the bifurcation parameter, we define the flow maps  $P_1(x)$  and  $P_2(x)$  by the evolution of the smooth flow  $\Phi(\cdot, T)$  on the Poincaré sections  $\Pi_1$  and  $\Pi_2$ ; the expressions of  $P_1(x)$  and  $P_2(x)$  are as follows:

$$P_1(x) = x^{*2} + N_1(x - x^{*1}) + M_1(d - d^*) + \text{h.o.t}, \quad (14)$$

where  $N_1 = (\partial/\partial x)P_1(x)|_{x=x^{*1}, d=d^*}$  and  $M_1 = (\partial/\partial d)P_1(x)|_{x=x^{*1}, d=d^*}$ .

$$P_2(x) = x^{*1} + N_2(x - x^{*2}) + M_2(d - d^*) + \text{h.o.t}, \quad (15)$$

where  $N_2 = (\partial/\partial x)P_2(x)|_{x=x^{*2}, d=d^*}$  and  $M_2 = (\partial/\partial d)P_2(x)|_{x=x^{*2}, d=d^*}$ .

The critical bifurcation value  $d^*$  can be obtained from expression (9). Since the vector field  $f(x)$  and the smooth flow function  $\Phi(\cdot, T)$  do not contain the bifurcation parameter  $d$ , the values of the matrices  $M_1 = M_2 = 0$ .

We use the discontinuous mapping method introduced by Nordmark to analyze the system; the two discontinuous maps  $DM_1$  and  $DM_2$  are introduced into the neighborhood of points  $x^{*1}$  and  $x^{*2}$  such that the surface  $P_1(x)$  is invariant under  $DM_1$ , i.e.,  $x \in P_1(x)$ ,  $DM_1(x) \in P_1(x)$ . The same surface  $P_2(x)$  is invariant under  $DM_2$ , i.e.,  $x \in P_2(x)$ ,  $DM_2(x) \in P_2(x)$ . According to the discontinuous mapping method, the discontinuous mapping of  $DM_1$  and  $DM_2$  is expressed by

$$DM_1 = \begin{cases} Id, & h^{D_1}(x, d) \geq 0, \\ x^{*1} + \beta_1 \sqrt{\frac{2}{h_x^{P_1}(x^{*1})f(x^{*1})}} \sqrt{-h^{D_1}(x, d)}, & h^{D_1}(x, d) < 0, \end{cases} \quad (16)$$

where

$$\beta_1 = f(x^{*1}) - g_x(x^{*1})f(x^{*1}),$$

$$DM_2 = \begin{cases} Id, & h^{D_2}(x, d) \leq 0, \\ x^{*2} + \beta_2 \sqrt{\frac{2}{h_x^{P_2}(x^{*2})f(x^{*2})}} \sqrt{-h^{D_2}(x, d)}, & h^{D_2}(x, d) > 0, \end{cases} \quad (17)$$

where

$$\beta_2 = f(x^{*2}) - g_x(x^{*2})f(x^{*2}). \quad (18)$$

According to (13)–(17), the composite maps  $\bar{P}_1 = P_1(x) \circ DM_1$  and  $\bar{P}_2 = P_2(x) \circ DM_2$  are written as

$$\tilde{P}_1 = \begin{cases} x^{*2} + N_1(x - x^{*1}) + \text{h.o.t}, & h^{D_1}(x, d) \geq 0, \\ x^{*2} + N_1\beta_1 \sqrt{\frac{2}{h_x^{P_1}(x^{*1})f(x^{*1})}} \sqrt{-h^{D_1}(x, d)} + \text{h.o.t}, & h^{D_1}(x, d) < 0, \end{cases} \quad (19)$$

$$\tilde{P}_2 = \begin{cases} x^{*1} + N_2(x - x^{*2}) + \text{h.o.t}, & h^{D_2}(x, d) \leq 0, \\ x^{*1} + N_2\beta_2 \sqrt{\frac{2}{h_x^{P_2}(x^{*2})f(x^{*2})}} \sqrt{-h^{D_2}(x, d)} + \text{h.o.t}, & h^{D_2}(x, d) > 0. \end{cases} \quad (20)$$

We will discuss the stability of double grazing bifurcation using the Poincaré map  $\tilde{P} = \tilde{P}_2 \circ \tilde{P}_1$ . Starting from the vicinity of the grazing point, whether it is at the impact side or the nonimpact side, if it is still close to the grazing point after the iterative mapping  $\tilde{P}$ , then the local attractor near the grazing trajectory exists; we refer to such scenario as a continuous grazing bifurcation or we say that the grazing bifurcation is stable. Otherwise, we refer to scenario as a discontinuous grazing bifurcation.

When point  $x$  starts from the impact side near the grazing point  $x^{*1}$ ,  $h^{D_1}(x, d) < 0$ . Here, we can think of the  $h^{D_1}(x, d)$  approximation as  $h_x^{D_1}(x^{*1})(x - x^{*1})$ . Similarly, we consider the  $h^{D_2}(x, d)$  approximation as  $h_x^{D_2}(x^{*2})(x - x^{*2})$ .

If

$$\begin{aligned} & h_x^{D_2}(x^{*2})(\tilde{P}_1(x) - x^{*2}) \\ &= h_x^{D_2}(x^{*2})N_1\beta_1 \sqrt{\frac{2}{h_x^{P_1}(x^{*1})f(x^{*1})}} \sqrt{-h^{D_1}(x, d)} \leq 0, \end{aligned} \quad (21)$$

it means  $\tilde{P}_1(x)$  is located at the nonimpact side near the grazing point  $x^{*2}$ .

After the iteration of the mapping  $\tilde{P}_2$ , if

$$\begin{aligned} & h_x^{D_1}(x^{*1})(\tilde{P}_2\tilde{P}_1(x) - x^{*1}) \\ &= h_x^{D_1}(x^{*1})N_2N_1\beta_1 \sqrt{\frac{2}{h_x^{P_1}(x^{*1})f(x^{*1})}} \sqrt{-h^{D_1}(x, d)} < 0, \end{aligned} \quad (22)$$

then,

$$h_x^{D_1}(x^{*1})N_2N_1\beta_1 < 0. \quad (23)$$

It means the impact point impacts discontinuity surface  $D_1$  again and the impact will be perpetuated, which results in a large stretching in a direction given by the image of the vector  $\beta_1$  under the Jacobian  $N_1$  and  $N_2$ . Therefore, the local attractor near the grazing trajectory does not exist. According to the analysis, the stability criterion of grazing bifurcation under which a local attractor persists near a grazing trajectory is formulated as follows:

$$h_x^{D_2}(x^{*2})N_1(N_2N_1)^{(n-1)}\beta_1 \leq 0, \quad (24)$$

and

$$h_x^{D_1}(x^{*1})(N_2N_1)^n\beta_1 \geq 0, \quad (25)$$

for all positive integer  $n$ .

According the same method, another stability criterion of grazing bifurcation under which a local attractor persists near a grazing trajectory is formulated as follows:

$$h_x^{D_1}(x^{*1})N_2(N_1N_2)^{(n-1)}\beta_2 \geq 0, \quad (26)$$

and

$$h_x^{D_2}(x^{*2})(N_1N_2)^n\beta_2 \leq 0, \quad (27)$$

for all positive integer  $n$ .

**3.2. Codimension-Two Grazing Bifurcation.** The local attractor near grazing trajectory is lost in there ways.

*Case 1.* If

$$\begin{aligned} & h^{D_2}(x^{*2})(\tilde{P}_1(x), d) \\ &= h_x^{D_2}(x^{*2})N_1\beta_1 \sqrt{\frac{2}{h_x^{P_1}(x^{*1})f(x^{*1})}} \sqrt{-h^{D_1}(x, d)} < 0, \end{aligned} \quad (28)$$

i.e.,  $h_x^{D_2}(x^{*2})N_1\beta_1 < 0$ , and

$$\begin{aligned} & h^{D_1}(x^{*1})(\tilde{P}_2(\tilde{P}_1(x)), d) \\ &= h_x^{D_1}(x^{*1})N_2N_1\beta_1 \sqrt{\frac{2}{h_x^{P_1}(x^{*1})f(x^{*1})}} \sqrt{-h^{D_1}(x, d)} < 0, \end{aligned} \quad (29)$$

i.e.,  $h_x^{D_1}(x^{*1})N_2N_1\beta_1 < 0$ , then it means that the point from the impact side near the grazing point  $x^{*1}$  will impact the discontinuous surface  $D_1$  again after the iteration of the mapping  $\tilde{P}$  and the impact will continue, which results in a large stretching in a direction given by the image of the vector  $\beta_1$  under the Jacobian  $N_1$  and  $N_2$ ; therefore, the local near-grazing attractor will lose, where discontinuous grazing bifurcation occurs.

If the impact point is followed by nonimpacting for some iterations but eventually impacts discontinuous surface  $D_1$ , the impact will be perpetuated which lead to the instability of grazing bifurcation or the loss of near-grazing attractors.

Therefore,

$$\begin{aligned} h_x^{D_2}(x^{*2})N_1(N_2N_1)^i\beta_1 &< 0, \\ h_x^{D_1}(x^{*1})(N_2N_1)^{i+1}\beta_1 &< 0, \end{aligned} \quad (30)$$

for any  $0 \leq i \leq j$ , the stability of grazing bifurcation will be lost, where  $i$  and  $j$  are positive integers.

*Case 2.* When the point  $x$  satisfying  $h_x^{D_1}(x - x^{*1}) < 0$  is from the impact side near the grazing point  $x^{*1}$ , if  $h_x^{D_2}(x^{*2})N_1\beta_1 > 0$  and  $h_x^{D_2}(x^{*2})N_1N_2\beta_2 > 0$ , it means that the impact point will impact with the discontinuous surface  $D_2$  again and the impact will continue, and the grazing bifurcation is discontinuous.

If the impact point is followed by nonimpacting for some iterations but eventually impacts discontinuous surface  $D_2$ , the impact will be perpetuated. Finally, the stability of grazing bifurcation will also be lost.

That is,

$$\begin{aligned} h_x^{D_2}(x^{*2})N_1(N_2N_1)^i\beta_1 &> 0, \\ h_x^{D_2}(x^{*2})(N_1N_2)^{i+1}\beta_2 &> 0, \end{aligned} \quad (31)$$

for any  $j \geq i \geq 0$ , the stability of grazing bifurcation will be lost.

*Case 3.* When the point  $x$  satisfying  $h_x^{D_1}(x - x^{*1}) < 0$  is from the impact side near the grazing point  $x^{*1}$ , if  $h_x^{D_2}(x^{*2})N_1\beta_1 > 0$  and  $h_x^{D_1}(x^{*1})N_2\beta_2 < 0$ , this means that the impact point will impact with the discontinuous surfaces  $D_1$  and  $D_2$  again and the impact will continue, and the grazing bifurcation is discontinuous. If the impact point is followed by non-impacting for some iterations but eventually impacts discontinuous surface  $D_1$  and  $D_2$  the impact will be perpetuated. Finally, the stability of grazing bifurcation will also be lost.

That is,

$$\begin{aligned} h_x^{D_2}(x^{*2})N_1(N_2N_1)^i\beta_1 &> 0, \\ h_x^{D_1}(x^{*1})N_2(N_1N_2)^j\beta_2 &< 0, \end{aligned} \quad (32)$$

for any  $j \geq i \geq 0$ , the stability of grazing bifurcation will be lost.

According to the above analysis, the conditions of codimension-two grazing bifurcation are obtained as follows (the definition of such points is seen in Ref. [10]):

$$\begin{aligned} h_x^{D_1}(x^{*1})(N_2N_1)^n\beta_1 &= 0, \\ h_x^{D_1}(x^{*1})N_2(N_1N_2)^n\beta_2 &= 0, \\ h_x^{D_2}(x^{*2})N_1(N_2N_1)^n\beta_1 &= 0, \\ h_x^{D_2}(x^{*2})(N_1N_2)^n\beta_2 &= 0, \end{aligned} \quad (33)$$

where  $n = 0, 1, 2, \dots$

## 4. Controlling the Persistence of Near-Grazing Attractors

As the lose of stability for grazing bifurcation may arise catastrophic changes of system response and codimension-two even more complicated bifurcation, it is necessary to control the stability of grazing bifurcation by controlling the persistence of the local near-grazing attractor. We use discrete-in-time feedback control to stabilize the grazing bifurcation. Two constant phase angles are defined as Poincaré sections, and two discrete-in-time feedback controllers on Poincaré sections are designed. After that, we obtain a new compound map and then control the stability of the grazing bifurcation by controlling the parameters on the controller.

We define the other two constant phase angles as Poincaré sections  $\Pi_3$  and  $\Pi_4$ , where  $\Pi_3 = \{\hat{x} \in R^5 \times S^1 \mid \theta = \theta^* + (\pi/2)\}$  and  $\Pi_4 = \{\hat{x} \in R^5 \times S^1 \mid \theta = \theta^* + (3\pi/2)\}$ .

According to  $P_1(x)$  and  $\Pi_3$ , we define the mappings  $P_3(x): \Pi_1 \rightarrow \Pi_3$  and  $P_4(x): \Pi_3 \rightarrow \Pi_2$ , and the resulting expansion is as follows:

$$\begin{aligned} P_3(x) &= x^{*3} + N_3(x - x^{*1}) + \text{h.o.t.}, \\ P_4(x) &= x^{*2} + N_4(x - x^{*3}) + \text{h.o.t.}, \end{aligned} \quad (34)$$

where  $x^{*3}$  is the fixed point of the grazing orbit on the Poincaré section  $\Pi_3$ ,  $N_3 = (\partial/\partial x)P_3(x)|_{x=x^{*3}}$ , and  $N_4 = (\partial/\partial x)P_4(x)|_{x=x^{*3}}$ .

In the same way, according to  $P_2(x)$  and  $\Pi_4$ , we define the mappings  $P_5(x): \Pi_2 \rightarrow \Pi_4$  and  $P_6(x): \Pi_4 \rightarrow \Pi_1$ , and the expansion is as follows:

$$\begin{aligned} P_5(x) &= x^{*4} + N_5(x - x^{*2}) + \text{h.o.t.}, \\ P_6(x) &= x^{*1} + N_6(x - x^{*4}) + \text{h.o.t.}, \end{aligned} \quad (35)$$

where  $x^{*4}$  is the fixed point of the grazing orbit on the Poincaré section  $\Pi_4$ ,  $N_5 = (\partial/\partial x)P_5(x)|_{x=x^{*2}}$ , and  $N_6 = (\partial/\partial x)P_6(x)|_{x=x^{*4}}$ .

Discrete-in-time feedback controllers are designed on the Poincaré sections  $\Pi_3$  and  $\Pi_4$ , respectively, as follows:

$$\begin{aligned} G_1(x) &= \begin{bmatrix} x_1 \\ v_1 \\ x_2 \\ v_2 \\ k_1(x_1 - x_1^{*3}) + k_2(v_1 - v_1^{*3}) + k_3(p - p^*) + p^* \end{bmatrix}, \\ G_2(x) &= \begin{bmatrix} x_1 \\ v_1 \\ x_2 \\ v_2 \\ k_4(x_1 - x_1^{*4}) + k_5(v_1 - v_1^{*4}) + k_6(p - p^*) + p^* \end{bmatrix}. \end{aligned} \quad (36)$$

We can calculate the expressions of maps  $G_1(x)$  and  $G_2(x)$  which have the following forms:

$$\begin{aligned} G_1(x) &= x_1^{*3} + G_{1x}(x - x_1^{*3}), \\ G_2(x) &= x_1^{*4} + G_{2x}(x - x_1^{*4}), \end{aligned} \quad (37)$$

where

$$\begin{aligned} G_{1x} &= \begin{bmatrix} 1 & 0 & 0 & 0 & 0 \\ 0 & 1 & 0 & 0 & 0 \\ 0 & 0 & 1 & 0 & 0 \\ 1 & 0 & 0 & 1 & 0 \\ k_1 & k_2 & 0 & 0 & k_3 \end{bmatrix}, \\ G_{2x} &= \begin{bmatrix} 1 & 0 & 0 & 0 & 0 \\ 0 & 1 & 0 & 0 & 0 \\ 0 & 0 & 1 & 0 & 0 \\ 1 & 0 & 0 & 1 & 0 \\ k_4 & k_5 & 0 & 0 & k_6 \end{bmatrix}. \end{aligned} \quad (38)$$

The combining the map  $G_1(x)$  and  $P_3(x)$ ,  $P_4(x)$ , obtain a controlled map as  $P_{g1}(x) = P_4(x) \circ G_1(x) \circ P_3(x)$ , expansion as follows:

$$\tilde{P}_{g1} = \begin{cases} x^{*2} + N_{g1}(x - x^{*1}) + \text{h.o.t.}, & h^{D_1}(x, d) \geq 0, \\ x^{*2} + N_{g1}\beta_1 \sqrt{\frac{2}{h_x^{D_1}(x^{*1})f(x^{*1})}} \sqrt{-h^{D_1}(x, d)} + \text{h.o.t.}, & h^{D_1}(x, d) < 0, \end{cases} \quad (42)$$

where  $N_{g1} = N_4 G_{1x} N_3$ .

$$\tilde{P}_{g2} = \begin{cases} x^{*1} + N_{g2}(x - x^{*2})\text{h.o.t.}, & h^{D_2}(x, d) \leq 0, \\ x^{*1} + N_{g2}\beta_2 \sqrt{\frac{2}{h_x^{D_2}(x^{*2})f(x^{*2})}} \sqrt{-h^{D_2}(x, d)} + \text{h.o.t.}, & h^{D_2}(x, d) > 0, \end{cases} \quad (43)$$

where  $N_{g2} = N_6 G_{2x} N_2$ .

According to the analysis in Section 3, there are three cases in which the grazing bifurcation is unstable, where discontinuous grazing bifurcation occurs. For Case 1, the impact point will impact with the discontinuous surface  $D_1$  again after some iterations and the impact will be perpetuated. Based on the stability criteria (24) and (25), we control  $k_1 - k_6$  on the controller to ensure that  $h_x^{D_2}(x^{*2})N_{g1}(N_{g2}N_{g1})^{n-1}\beta_1 \leq 0$  and  $h_x^{D_1}(x^{*1})(N_{g2}N_{g1})^n\beta_1 \geq 0$ , for

$$P_{g1}(x) = x^{*2} + N_4 G_{1x} N_3 (x - x^{*1}) + \text{h.o.t.}, \quad (39)$$

where  $G_{1x} = (\partial/\partial x)G_1(x)|_{x=x^{*3}}$ .

Similarly, combining the map  $G_2(x)$  with the map  $P_5(x)$ ,  $P_6(x)$ , the map under control  $P_{g2}(x) = P_6(x) \circ G_2(x) \circ P_5(x)$ , is obtained and its expansion has the following forms:

$$P_{g2}(x) = x^{*1} + N_6 G_{2x} N_5 (x - x^{*2}) + \text{h.o.t.}, \quad (40)$$

where  $G_{2x} = (\partial/\partial x)G_2(x)|_{x=x^{*4}}$ .

We can calculate the expressions of  $N_i$  as follows:

$$N_i = \begin{bmatrix} \Delta & \Delta & \Delta & \Delta & \Delta \\ \Delta & \Delta & \Delta & \Delta & \Delta \\ \Delta & \Delta & \Delta & \Delta & \Delta \\ \Delta & \Delta & \Delta & \Delta & \Delta \\ 0 & 0 & 0 & 0 & 1 \end{bmatrix}, \quad (41)$$

where  $i = 3, 4, 5, 6$  and the symbol  $\Delta$  refers to a nontrivial coefficient.

Combining (39) and (15), we construct a composite map of  $\tilde{P}_{g1} = P_{g1}(x) \circ DM_1$ ; the expressions are as follows:

Similarly, we can combine (40) and (17) to construct a composite map of  $\tilde{P}_{g2} = P_{g2}(x) \circ DM_2$ ; the expression is as follows:

positive integer  $n$ , such that the grazing bifurcation will be continuous.

For Case 2, the impact point will impact with the discontinuous surface  $D_2$  again after some iterations and the impact will be perpetuated. Based on the stability criteria (26) and (27), we control  $k_1 - k_6$  on the controller so that  $h_x^{D_2}(x^{*2})(N_{g1}N_{g2})^n\beta_2 \leq 0$  and  $h_x^{D_1}(x^{*1})N_{g2}(N_{g1}N_{g2})^{n-1}\beta_2 \geq 0$  for positive integer  $n$ . The grazing bifurcation will be continuous.

For Case 3, the impact point will impact with the discontinuous surfaces  $D_1$  and  $D_2$  again, and after some iterations, the impact will be perpetuated. Based on the stability criteria (24) and (25) or (26) and (27), the grazing bifurcation will be continuous by controlling parameters  $k_1 - k_6$  to ensure the local attractor near grazing bifurcation persists.

For the codimension-two grazing bifurcation point, the persistence of near-grazing attractors is also controlled by controlling  $k_1 - k_6$  based on the stability criteria (24) and (25) or (26) and (27). For example, if  $h_x^{D_1}(x^{*1})(N_2 N_1)^n \beta_1 = 0$ , we might let  $h_x^{D_2}(x^{*2})N_{g_1}(N_{g_2}N_{g_1})^{n-1}\beta_1 \leq 0$  and  $h_x^{D_1}(x^{*1})(N_{g_2}N_{g_1})^n \beta_1 \geq 0$  by controlling  $k_1 - k_6$ .

If  $h_x^{D_1}(x^{*1})N_2(N_1N_2)^n \beta_2 = 0$ , we might let  $h_x^{D_2}(x^{*2})(N_{g_1}N_{g_2})^n \beta_2 \leq 0$  and  $h_x^{D_1}(x^{*1})N_{g_2}(N_{g_1}N_{g_2})^{n-1}\beta_2 \geq 0$  by controlling  $k_1 - k_6$ .

## 5. Numerical Experiments

For this system, we take suitable parameters  $\mu_m = 6.0$ ,  $\mu_k = 3.0$ ,  $\omega = 0.63$ ,  $R = 0.82$ ,  $\zeta = 0.2$ , and  $p = 2.513$  as an example.  $d$  is supposed as the bifurcation parameter; the critical value  $d^* = 1.61139$  for grazing bifurcation is obtained from formula (9). According to the analysis of near-grazing dynamics in Section 3, under the set of fixed parameters,  $h_x^{D_2}(x^{*2})N_1\beta_1 = -0.128027 < 0$  and  $h_x^{D_1}(x^{*1})N_2N_1\beta_1 = -0.078865 < 0$ . The impact point will impact with the discontinuous surfaces  $D_1$  again and the impact will be perpetuated, which satisfies the instability conditions in Case 1. The bifurcation diagram as shown in Figure 2(a) is obtained through numerical simulation by discontinuity maps (19) and (20). It is clear that the grazing bifurcation is discontinuous because the discontinuous transition occurs at the bifurcation point  $d - d^* = 0$ . In addition, we take  $\Pi_2$  as the Poincaré section; the bifurcation diagram as shown in Figure 2(b) is obtained through direct numerical simulation by (4) and (5), and it is clear that the discontinuous jump also occurs at the grazing bifurcation point  $d - d^* = 0$ .

We use the control method in Section 4 to stabilize the unstable grazing bifurcation phenomena. When the parameters of  $k_1, k_3$  and  $k_4, k_6$  are fixed, the ranges of parameters  $k_2$  and  $k_5$  are calculated according to control strategy, which is named two-dimensional control region of  $k_2$  and  $k_5$ . Here, we select  $k_1 = -0.5$ ,  $k_3 = -1$ ,  $k_4 = -0.5$ , and  $k_6 = -1$  as the fixed parameters; a two-dimensional control region graph of  $k_2$  and  $k_5$  is obtained as shown in Figure 3(a), where  $k_2$  is  $x$ -axis,  $k_5$  is  $y$ -axis, and the blue region is the region of control parameters for ensuring the stability of the grazing bifurcation.

We select  $k_2 = -5.8$  and  $k_5 = -5.8$  to control the system and draw Figure 4(a) through the discontinuity maps (40) and (41). At the same time, we take  $\Pi_2$  as the Poincaré section and obtain Figure 4(b) by direct numerical simulation. As shown in Figures 4(a) and 4(b), there exists the local attractor near grazing bifurcation.

Take the set of parameters  $\mu_m = 6.0$ ,  $\mu_k = 3.0$ ,  $\omega = 0.48$ ,  $R = 0.82$ ,  $\zeta = 0.2$ ,  $p = 2.013$ , as an example.  $d^* = 0.65183$ , is obtained from equation (9). Without control,  $h_x^{D_2}(x^{*2})N_1N_2N_1\beta_1 = -0.00868998 < 0$  and  $h_x^{D_1}(x^{*1})(N_2N_1)^2\beta_1 = -0.00822255 < 0$ . are obtained under the above fixed parameters. It satisfies the instability conditions in case 1 according to expression (30). The bifurcation diagram as shown in Figure 2(c) is obtained through numerical simulation by discontinuity maps (19) and (20). It is clear that the grazing bifurcation is discontinuous because the discontinuous transition occurs at the bifurcation point  $d - d^* = 0$ . In addition, we take  $\Pi_2$  as the Poincaré section, and the bifurcation diagram as shown in Figure 2(d) is obtained through direct numerical simulation by (4) and (5); it is clear that the discontinuous jump also occurs at the grazing bifurcation point  $d - d^* = 0$ .

Based on the stability criterion mentioned in Section 4, we select  $k_1 = -0.6$ ,  $k_3 = -1$ ,  $k_4 = -0.6$ , and  $k_6 = -1$  as the fixed parameters; a two-dimensional control region graph of  $k_2$  and  $k_5$  is obtained as shown in Figure 3(b), where  $k_2$  is  $x$ -axis,  $k_5$  is  $y$ -axis, and the blue region is the region of control parameters for ensuring the stability of the grazing bifurcation. Then, we select  $k_2 = -5.8$  and  $k_5 = -5.8$  to control the system, and the bifurcation diagram is obtained as shown in Figure 4(c) by the discontinuity maps (40) and (41). In addition, we take  $\Pi_2$  as the Poincaré section and obtain Figure 4(d) by direct numerical simulation. As shown in Figures 4(c) and 4(d), there exists the local attractor near grazing bifurcation.

Fixed parameters  $\mu_m = 6.0$ ,  $\mu_k = 3.0$ ,  $\omega = 0.5649677$ ,  $R = 0.82$ ,  $\zeta = 0.2$ ,  $p = 0.813$ . the critical value  $d^* = 1.821554$ , such that  $h_x^{D_1}(x^{*1})(N_2N_1)^5\beta_1 = 0$ . It corresponds to the codimension-two grazing bifurcation. We obtain the bifurcation diagram Figure 2(e) through numerical simulation by the discontinuity maps (19) and (20). As shown in Figure 2(e), the system is in a complex chaotic state near the grazing point. Then, we take  $\Pi_2$  as the Poincaré section and obtain Figure 2(f) by direct numerical simulation.

Based on the control strategy mentioned in Section 4, we select  $k_1 = -0.6$ ,  $k_3 = -1$ ,  $k_4 = -0.6$ , and  $k_6 = -1$  as the fixed parameters; a two-dimensional control region graph of  $k_2$  and  $k_5$  is obtained as shown in Figure 3(c), where  $k_2$  is  $x$ -axis,  $k_5$  is  $y$ -axis, and the blue region is the region of control parameters for suppressing the chaos. Then, we select  $k_2 = -5.8$  and  $k_5 = -5.8$  to control the system, and the bifurcation diagram is obtained as shown in Figure 4(e) by the discontinuity maps (40) and (41). In addition, we take  $\Pi_2$  as the Poincaré section and obtain Figure 4(f) by direct numerical simulation.

Comparing Figure 2 with Figure 4, it is shown that the results obtained by mappings are in good agreement with the direct numerical simulation, and the control effect is further verified.

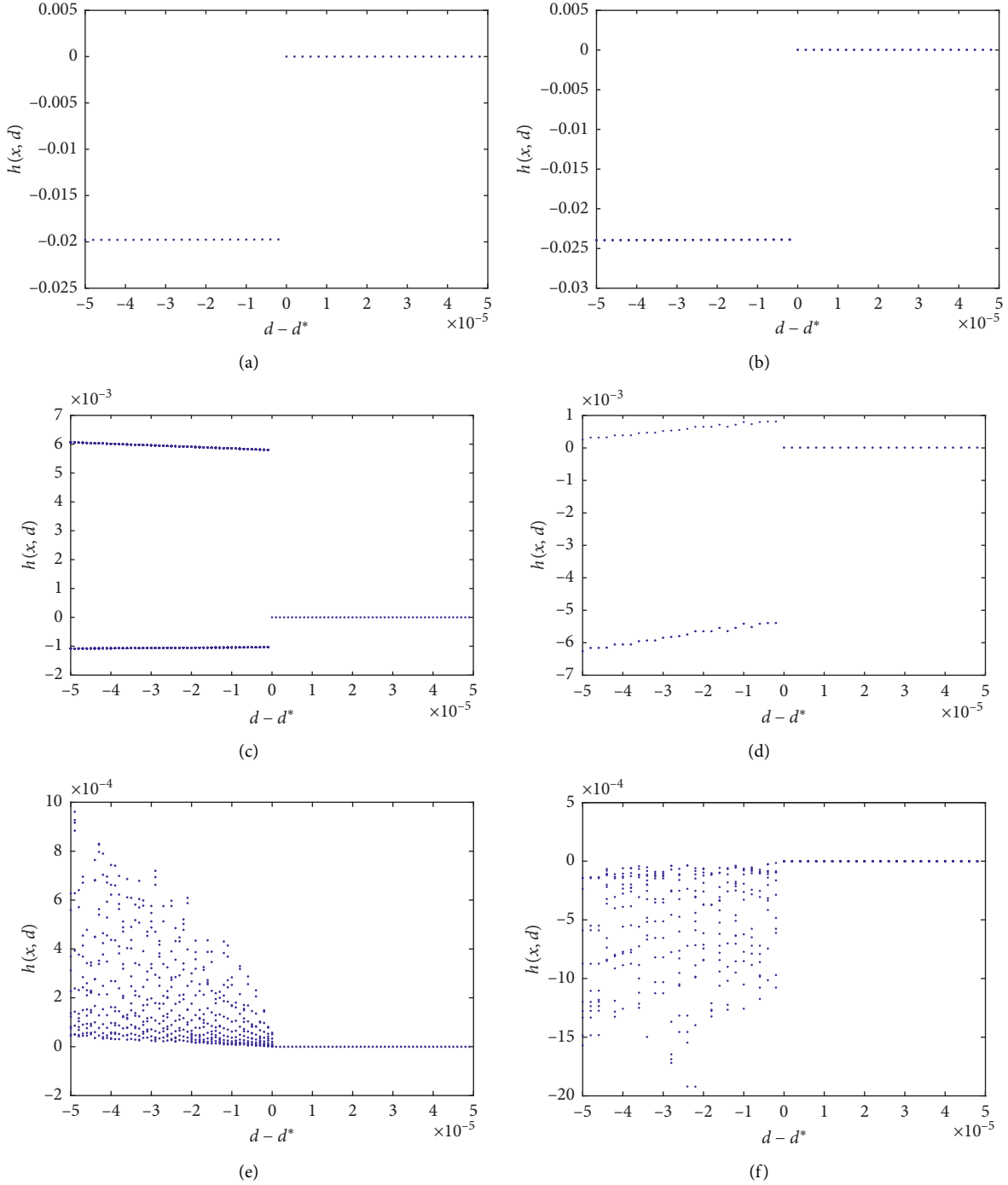


FIGURE 2: Bifurcation diagram from the grazing bifurcation. (a) (1/1) impact periodic motions based on the numerical simulation obtained by the discontinuity maps (19) and (20). (b) Direct numerical simulation on Poincaré section  $\Pi_2$  of (1/1) impact periodic motions. (c) (1/2) impact periodic motions based on the numerical simulation obtained by the discontinuity maps (19) and (20). (d) Direct numerical simulation on Poincaré section  $\Pi_2$  of (1/2) impact periodic motions. (e) The codimension-two grazing bifurcation points based on the numerical simulation obtained by the discontinuity maps (19) and (20). (f) Direct numerical simulation on Poincaré section  $\Pi_2$  of the codimension-two grazing bifurcation points.

## 6. Conclusions

The discontinuous grazing bifurcation is often accompanied by a jump phenomenon. In addition, complex chaotic regions occur near the codimension-two bifurcation points.

How to avoid the dramatic change of system response caused by jump phenomenon of grazing bifurcation or the codimension-two bifurcation point is an urgent requirement for the control mechanism of discontinuous grazing bifurcation. In this paper, a discrete-in-time feedback control



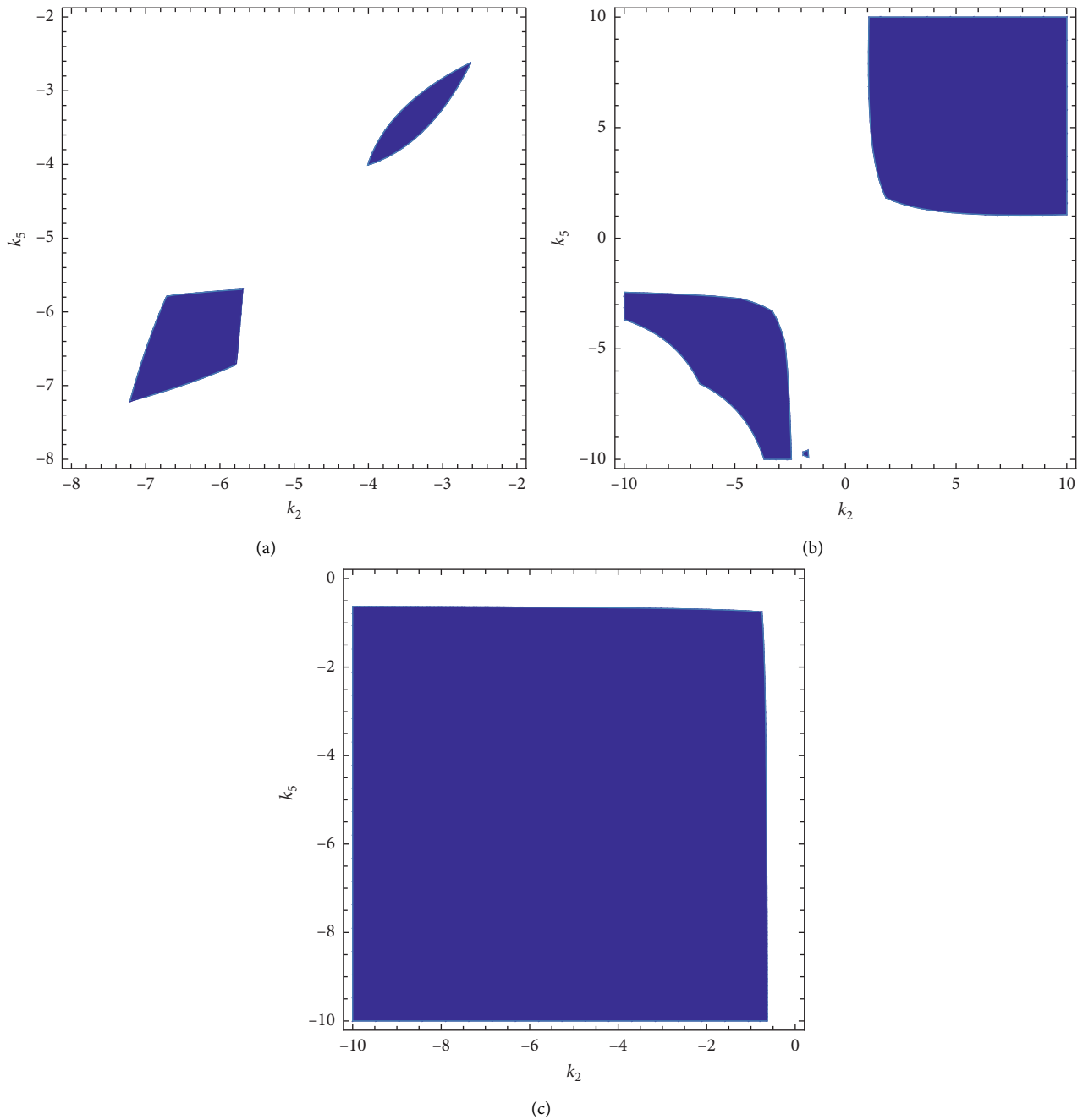


FIGURE 3: The parameters  $k_2$  and  $k_5$  control region. (a) The grazing bifurcation of  $(1/1)$  impact periodic motions. (b) The grazing bifurcation of  $(1/2)$  impact periodic motions. (c) The codimension-two grazing bifurcation points.

strategy is used to control the near-grazing dynamics of double grazing period motion in a two-degree-of-freedom vibroimpact system with symmetrical constraints. Compared to unilateral constrained systems, the stability criterion of double grazing period motion becomes more complex. Based on the stability criterion, the control strategy

is designed to control the near-grazing dynamics and the two parameters' control region is obtained. For the case of discontinuous grazing bifurcation, we take two jumping phenomena (jumping from nonimpact periodic motion to  $(1/1)$  and  $(1/2)$  impact periodic motion) as examples to stabilize grazing bifurcation by controlling the parameters

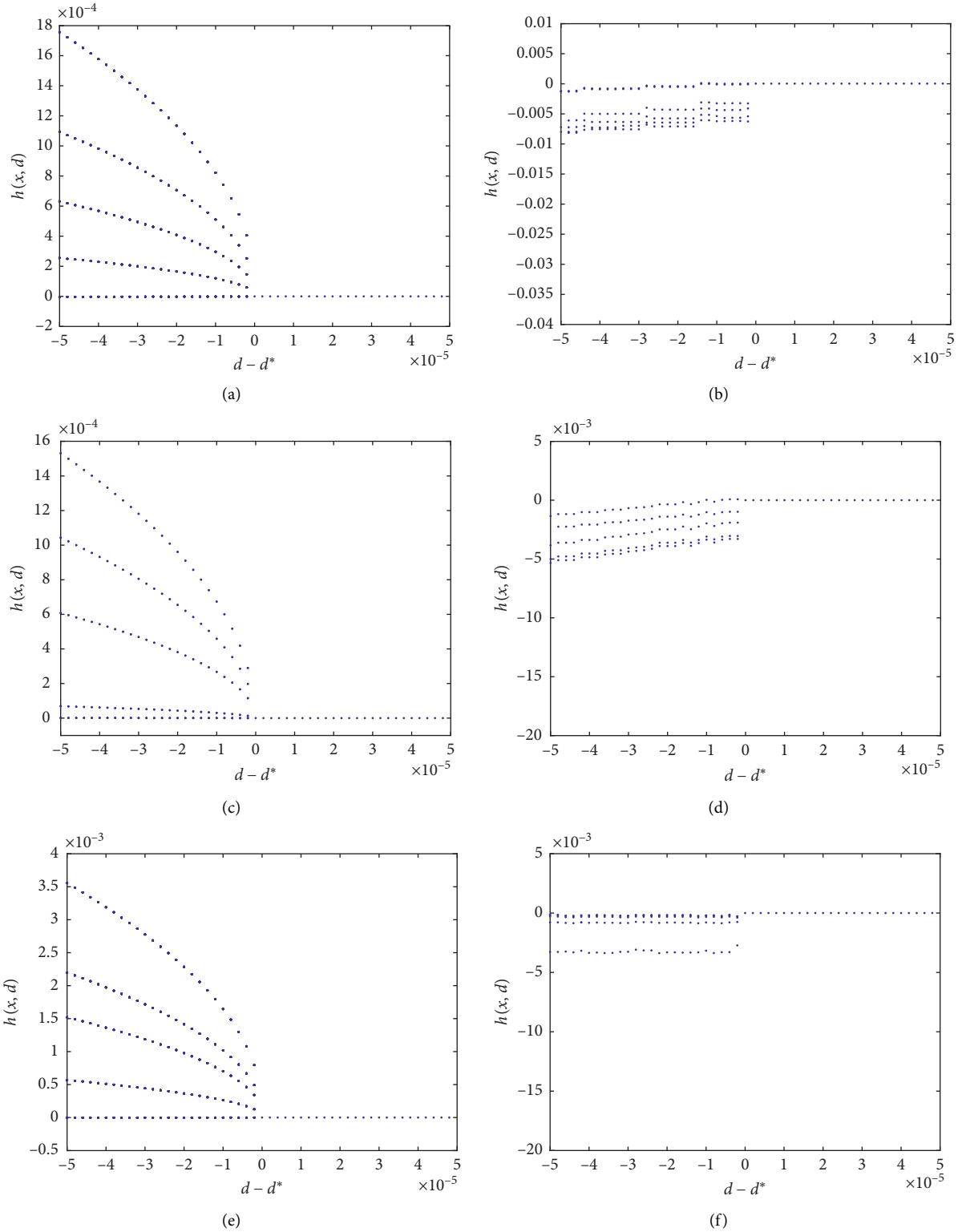


FIGURE 4: Bifurcation diagram of a stable grazing bifurcation after control. (a)  $(1/1)$  impact periodic motions based on the numerical simulation obtained by the discontinuity maps (38) and (39). (b) Direct numerical simulation on Poincaré section  $\Pi_2$  of  $(1/1)$  impact periodic motions. (c)  $(1/2)$  impact periodic motions based on the numerical simulation obtained by the discontinuity maps (38) and (39). (d) Direct numerical simulation on Poincaré section  $\Pi_2$  of  $(1/2)$  impact periodic motions. (e) The codimension-two grazing bifurcation points based on the numerical simulation obtained by the discontinuity maps (38) and (39). (f) Direct numerical simulation on Poincaré section  $\Pi_2$  of the codimension-two grazing bifurcation points.

on the controller. In addition, the chaos dynamics near codimension-two grazing bifurcation point is controlled by using this strategy. Finally, the feasibility of the control strategy is illustrated by comparing the numerical simulation of composite mapping with the direct numerical simulation of Poincaré section.

## Data Availability

The simulation data used to support the findings of this study are included within the article.

## Conflicts of Interest

The authors declare that they have no conflicts of interest.

## Acknowledgments

This study was supported by the project sponsored by the National Natural Science Foundation of China (nos. 11602059 and 11872154) and Guangxi Natural Science Foundation (no. 2018JJA110046).

## References

- [1] A. B. Nordmark, "Non-periodic motion caused by grazing incidence in an impact oscillator," *Journal of Sound and Vibration*, vol. 145, no. 2, pp. 279–297, 1991.
- [2] A. B. Nordmark, "Universal limit mapping in grazing bifurcations," *Physical Review E*, vol. 55, no. 1, pp. 266–270, 1997.
- [3] M. Bernardo, C. Budd, A. R. Champneys et al., *Piecewise-smooth Dynamical Systems: Theory and Applications*, Springer Science and Business Media, Berlin, Germany, 2008.
- [4] H. Dankowicz and M. Katzenbach, "Discontinuity-induced bifurcations in models of mechanical contact, capillary adhesion, and cell division: a common framework," *Physica D: Nonlinear Phenomena*, vol. 241, no. 22, pp. 1869–1881, 2012.
- [5] G. Wen, H. Xu, L. Xiao, X. Xie, Z. Chen, and X. Wu, "Experimental investigation of a two-degree-of-freedom vibro-impact system," *International Journal of Bifurcation and Chaos*, vol. 22, Article ID 1250110, 2012.
- [6] S. Banerjee, J. Ing, E. Pavlovskaya, M. Wiercigroch, and R. K. Reddy, "Invisible grazings and dangerous bifurcations in impacting systems: the problem of narrow-band chaos," *Physical Review E*, vol. 79, Article ID 037201, 2009.
- [7] D. R. J. Chillingworth, "Dynamics of an impact oscillator near a degenerate graze," *Nonlinearity*, vol. 23, no. 11, pp. 2723–2748, 2010.
- [8] N. Humphries and P. T. Piiroinen, "A discontinuity-geometry view of the relationship between saddle-node and grazing bifurcations," *Physica D: Nonlinear Phenomena*, vol. 241, no. 22, pp. 1911–1918, 2012.
- [9] M. H. Fredriksson and A. B. Nordmark, "Bifurcations caused by grazing incidence in many degrees of freedom impact oscillators," *Proceedings of the Royal Society of London. Series A: Mathematical, Physical and Engineering Sciences*, vol. 453, no. 1961, pp. 1261–1276, 1997.
- [10] P. Thota and H. Dankowicz, "Continuous and discontinuous grazing bifurcations in impacting oscillators," *Physica D: Nonlinear Phenomena*, vol. 214, no. 2, pp. 187–197, 2006.
- [11] P. Kowalczyk, M. di Bernardo, A. R. Champneys et al., "Two-parameter discontinuity-induced bifurcations of limit cycles: classification and open problems," *International Journal of Bifurcation and Chaos*, vol. 16, no. 03, pp. 601–629, 2006.
- [12] S. Foale, "Analytical determination of bifurcations in an impact oscillator," *Philosophical Transactions of the Royal Society of London. Series A: Physical and Engineering Sciences*, vol. 347, no. 1683, pp. 353–364, 1994.
- [13] P. Thota, X. Zhao, and H. Dankowicz, "Co-dimension-two grazing bifurcations in single-degree-of-freedom impact oscillators," *Journal of Computational and Nonlinear Dynamics*, vol. 1, no. 4, pp. 328–335, 2006.
- [14] J. Xu, P. Chen, and Q. Li, "Theoretical analysis of co-dimension-two grazing bifurcations in  $n$ -degree-of-freedom impact oscillator with symmetrical constraints," *Nonlinear Dynamics*, vol. 82, no. 4, pp. 1641–1657, 2015.
- [15] A. Colombo and F. Dercole, "Discontinuity induced bifurcations of nonhyperbolic cycles in nonsmooth systems," *SIAM Journal on Applied Dynamical Systems*, vol. 9, no. 1, pp. 62–83, 2010.
- [16] H. Jiang, A. S. E. Chong, Y. Ueda, and M. Wiercigroch, "Grazing-induced bifurcations in impact oscillators with elastic and rigid constraints," *International Journal of Mechanical Sciences*, vol. 127, pp. 204–214, 2017.
- [17] S. Yin, Y. Shen, G. Wen, and H. Xu, "Analytical determination for degenerate grazing bifurcation points in the single-degree-of-freedom impact oscillator," *Nonlinear Dynamics*, vol. 90, no. 1, pp. 443–456, 2017.
- [18] H. Dankowicz and X. Zhao, "Local analysis of co-dimension-one and co-dimension-two grazing bifurcations in impact microactuators," *Physica D: Nonlinear Phenomena*, vol. 202, no. 3–4, pp. 238–257, 2005.
- [19] X. Zhao and H. Dankowicz, "Unfolding degenerate grazing dynamics in impact actuators," *Nonlinearity*, vol. 19, no. 2, pp. 399–418, 2005.
- [20] H. Dankowicz and J. Jerrelind, "Control of near-grazing dynamics in impact oscillators," *Proceedings of the Royal Society A: Mathematical, Physical and Engineering Sciences*, vol. 461, no. 2063, pp. 3365–3380, 2005.
- [21] H. Dankowicz and F. Svahn, "On the stabilizability of near-grazing dynamics in impact oscillators," *International Journal of Robust and Nonlinear Control*, vol. 17, no. 15, pp. 1405–1429, 2007.
- [22] S. Misra and H. Dankowicz, "Control of near-grazing dynamics and discontinuity-induced bifurcations in piecewise-smooth dynamical systems," *International Journal of Robust and Nonlinear Control*, vol. 20, pp. 1836–1851, 2010.
- [23] S. Yin, G. Wen, and X. Wu, "Suppression of grazing-induced instability in single degree-of-freedom impact oscillators," *Applied Mathematics and Mechanics*, vol. 40, no. 1, pp. 97–110, 2019.
- [24] H. Xu, S. Yin, G. Wen, S. Zhang, and Z. Lv, "Discrete-in-time feedback control of near-grazing dynamics in the two-degree-of-freedom vibro-impact system with a clearance," *Nonlinear Dynamics*, vol. 87, no. 2, pp. 1127–1137, 2017.

## Research Article

# Data-Driven Learning-Based Fault Tolerant Stability Analysis

Lei Ge<sup>1</sup> and Shun Chen <sup>2</sup>

<sup>1</sup>*School of Finance, Southwestern University of Finance and Economics, Chengdu, Sichuan, China*

<sup>2</sup>*School of Economics, Huazhong University of Science and Technology, Wuhan, Hubei, China*

Correspondence should be addressed to Shun Chen; [shun6266@gmail.com](mailto:shun6266@gmail.com)

Received 20 December 2019; Accepted 16 March 2020; Published 9 April 2020

Guest Editor: Viet-Thanh Pham

Copyright © 2020 Lei Ge and Shun Chen. This is an open access article distributed under the Creative Commons Attribution License, which permits unrestricted use, distribution, and reproduction in any medium, provided the original work is properly cited.

In this paper, a new data-driven learning method is investigated based on the dynamical data of the system. A regularized regression wavelet (RRW) approach is proposed to optimize the learning result for the system fault. Based on the optimizing results, a fault tolerant stability scheme is given. Then, the efficiency of the proposed technique is verified by a vertical take-off and landing (VTOL) aircraft stability example.

## 1. Introduction

The analysis of the data-driven learning method in this paper aims at developing a reliable learning algorithm and applying the method to practical engineering systems. Specifically, we will show how the proposed data-driven learning technique is applied to the dynamical system.

Stability is a fundamental property in modern engineering systems. How to stabilize a system is well studied in the past decades. Plenty of stability controllers are proposed, for example, variable structure control [1], fuzzy control [2], sliding mode control [3], and adaptive neural control [4]. Various undesirable effects are always existed in many engineering applications, such as time-delay [4], fault [5, 6], and uncertainty [7]. In most cases, plenty of these effects can be observed by available measurement data; however in some cases, they are not easily described by existing mathematical models. In particular, these data contain meaningful features of the engineering applications. It is highly desirable to develop new techniques to learn the system data and generate a reliable algorithm based on the real data to cope with those fast changes in the complex systems directly. In this paper, we developed a learning model to address the issue of stabilizing dynamical systems from a different perspective.

During the last decade, data-driven innovation has become a hot topic across different research sectors and

provides new challenges associated with various network design, such as sensor networks and telecommunication networks. The network data constitute infrastructural information that could be used in many ways to produce different products and services. It provides additional information over the limitation of traditional system models and also enables creation of knowledge that is crucial for a new design. Recently, there are some data-driven control research studies available in the literature. For example, sampled data stabilization techniques for the T-S fuzzy system were proposed in [8]. A recurrent neural network-based data-driven control was constructed for the steady-state analysis in [9]. In addition, a lot of research studies have been undertaken to study the data-driven methods in industrial processes, see [10] for a survey. As one may know, the engineering systems are generally operated under different industrial environments. The classic model-based approach could be difficult to stabilize a real system in these types of applications. Hence, one may consider the data-driven approach to analyze the stability of the engineering system.

In particular, faulty issues in highly complexity dynamical systems always exist and are strongly reflected in the collected data. It has certainly a great effect on the safety requirement, and thus the fault reconstruction problem is one of the main concerns in the distributed network control design. The fault reconstruction problem was studied for sensor networks in

[11], and the results were used for the room temperature monitoring application. Recently, the fault tolerant consensus issue was researched in multiagent systems considering uncertainty in [12]. Data-driven methods for monitoring and fault diagnosis on the benchmark Tennessee Eastman process were investigated in [13].

In this paper, we propose a constructive data learning approach to analyze the effect of the fault. In addition, based on the learning result, the fault tolerant stability of the dynamical system is well studied. The method used in this paper is based on the RRW technique. It should be pointed out that the wavelet functions are used for nonlinear transformation function. Incorporating the time-frequency localization properties of wavelets, it has a strong learning ability for complex nonlinear system modelling. Especially, the wavelet approach has the advantage of dealing with rapid changes of data [14–16]. Inspired by the approach of multiresolution analysis, this paper provides a new data-driven approach for studying fault tolerant stability by applying this powerful wavelet tool. A detailed mathematical approach is constructed to deal with the effect of faults. In this paper, we aim to use the collected data from the dynamical system to stabilize the system. The novelties and advanced features of this paper are as follows:

- (1) Compared with the existing stability problem, this paper addresses the fault effect in the dynamical system. In addition, the designed technique used in this paper is a data-driven learning method which is based on a regularized regression wavelet neural network.
- (2) It is worth noting that most of the aforementioned literature is about data-driven stability analysis without considering to use a wavelet neural network. In this paper, we use the wavelet neural network-based learning control to stabilize the dynamical system which has the advantage of dealing with rapid changes of the sensor data and fault.
- (3) A detailed mathematical calculation for the reconstruction of the fault in this paper has been given, which potentially contributes to the real-world application of this paper.

The remainder of this paper is organized as follows: in Section 2, some preliminaries are proposed. In Section 3, data-driven fault tolerant stability is analyzed. In Section 4, a VTOL aircraft stability problem is analyzed to illustrate the effectiveness of the theoretical results. The final section concludes this paper.

## 2. Preliminaries

We consider a dynamical system described by the state equation:

$$\dot{x}(t) = Ax(t) + B(u(t) + \bar{g}(x(t))), \quad (1)$$

where  $x(t) \in \mathcal{R}^n$  is the state of the system,  $\bar{g}(x(t)) \in \mathcal{R}^q$  is the fault,  $u(t) \in \mathcal{R}^q$  is the actuator control input, and  $A \in \mathcal{R}^{n \times n}$  and  $B \in \mathcal{R}^{n \times q}$  are the known system parameters.

The sensor output of this system is taken to be the same as the state vector.

As is well known, for the fault  $\bar{g}(x(t))$ , the common assumption is that the uncertainty is norm bounded by a constant [12, 17]. In classical fault tolerant analysis for a dynamical system, one may use adaptive control to stabilize those faulty systems, see [12, 17]. In addition, the aforementioned fault assumptions in literature mostly require the fault to be differential, see [11] and the reference therein. However, due to the unpredictability of the fault, one cannot estimate the bound of the fault  $\bar{g}(x(t))$ , not to mention the differential requirement of the fault. In this paper, we released these assumptions by using a data-driven learning method based on the least-square regularized regression approach.

Before we propose the main results, we first focus on the initial data collecting procedure. Firstly, the system is assumed to be normal, i.e., this system is without fault. It is known that, to stabilize system (1) without fault, that is, to stabilize the following system:

$$\dot{x}(t) = Ax(t) + Bu(t). \quad (2)$$

One can define the feedback control as  $u(k) = -Kx(k)$ , with the matrix  $A - BK$  Hurwitz. Then, based on this construction, we initially collected the data with the feedback control  $u(k) = -Kx(k)$ . However, it should be pointed out that while the fault is considered, system (1) may be unstable. Next, based on the data generated by the faulty system, we will identify the fault by using the following results.

We let  $z(t)$  be the regression vector in the regression model,  $z(t) = x(t)$ . For the state sensor output  $x(t)$ , we calculate the derivative of state  $x(t)$  numerically, i.e.,  $\dot{x}(t) = (x(t+h) - x(t))/h$  mathematically, where  $h$  is the numerically sampling period. Then, we can obtain  $y(t)$  as  $\dot{x}(t) - Ax(t) - Bu(t)$  which is assumed to be the data output. We use this relation to evaluate data samples as  $\{z(t), y(t)\}_{t=0}^T$ .

## 3. Main Results

The data-driven learning problem is formulated as

$$\min_{g \in \mathcal{H}_T} \left[ \frac{1}{T} \sum_{t=1}^T \|y(t) - Bg(x(t))\|^2 + \nu \|g\|_T^2 \right], \quad (3)$$

where  $g = [g_1, g_2, \dots, g_q]^T$ ,  $\|g_i\|^2 = \langle g_i, g_i \rangle_{\mathcal{H}_T}$ , and the regularization constant  $\nu$  is used to make a trade-off between the empirical approximation error and the complexity of the model. The solution of the above optimization problem is expressed as

$$g_i(x_v) = \sum_{t=1}^T c_{g,t} K(x_v, x(t)). \quad (4)$$

Next, we shall consider the nonlinear function approximation method in this paper. The reproducing kernel Hilbert space (RKHS) is defined to be the closure of linear span of a set of functions, with the kernel functions used for approximation be nonlinear functions. In this paper, we use Morlet WNN kernel:

$$K_{\text{WNN}}(x, x') = \prod_{i=1}^n \cos\left(\omega_0 \frac{(x_i - x'_i)}{a_i}\right) \exp\left(-\frac{(x_i - x'_i)^2}{2a_i^2}\right). \quad (5)$$

The Morlet wavelet is a wavelet composed of a complex exponential (carrier) multiplied by a Gaussian window (envelope). The parameter  $\omega_0 > 0$  represents the dilation, and the parameter  $a_i > 0$  represents translation. These two parameters can be adjusted by users. One can find the theoretical analysis for optimal dilation and translation parameters selection in [15]. Then, the RKHS is a space of nonlinear functions and has good approximation performance. We solve the above optimization problem which is given by the following theorem.

**Theorem 1.** For the optimization problem (3), the solution is obtained by the following formula:

$$g_j(x) = \sum_{t=1}^T l_{jt} K_{\text{WNN}}(x(t), x), \quad (6)$$

where  $l_{jt}$  is the solution of the following equation:

$$(T\nu + (I_T \otimes B^T B) \bar{G} (I_q \otimes T_m) \bar{L}) l = (I_T \otimes B^T) y, \quad (7)$$

where

$$T_m = (T_{mij})_{T \times T}, T_{mij} = K_{\text{WNN}}(x(j), x(i)), \quad (8)$$

and  $\bar{G}$  and  $\bar{L}$  satisfy  $g_T = \bar{G} \bar{g}_T$  and  $\bar{l} = \bar{L} l$ , respectively, with

$$\begin{aligned} \bar{g}_{jT} &= [g_j(x(1)), g_j(x(2)), \dots, g_j(x(T))]^T \in \mathcal{R}^T, \\ \bar{g}_T &= [\bar{g}_{1T}, \bar{g}_{2T}, \dots, \bar{g}_{qT}]^T \in \mathcal{R}^{Tq}, \\ g_{iT} &= [g_1(x(t)), g_2(x(t)), \dots, g_q(x(t))]^T \in \mathcal{R}^q, \\ g_T &= [g_{1T}, g_{2T}, \dots, g_{qT}]^T \in \mathcal{R}^{Tq}, \\ \bar{l}_j &= [l_{j1}, l_{j2}, \dots, l_{jT}]^T \in \mathcal{R}^T, \\ \bar{l} &= [\bar{l}_1, \bar{l}_2, \dots, \bar{l}_q]^T \in \mathcal{R}^{Tq}, \\ l_t &= [l_{1t}, l_{2t}, \dots, l_{qt}]^T \in \mathcal{R}^q, \\ l &= [l_1, l_2, \dots, l_T]^T \in \mathcal{R}^{Tq}. \end{aligned} \quad (9)$$

*Proof.* Introduce an orthonormal wavelet  $\{\phi_{p,q}\}$  in  $L_p^2(X)$ . Their corresponding eigenvalues are  $\{\lambda_{p,q}\}$ . Then, we have  $g_i = \sum_{p,q=-\infty}^{\infty} c_{g_i p,q} \phi_{p,q}$  for any  $g_i \in \mathcal{H}_{\text{WNN}}$ . The parameters  $c_{g_i p,q}$  are to be chosen to minimize the objective function (3).

Let

$$\begin{aligned} P &= \frac{1}{T} \sum_{t=1}^T (y(t) - Bg(x(t)))^T (y(t) - Bg(x(t))) + \nu \|g\|_T^2 \\ &= \frac{1}{T} \sum_{t=1}^T \sum_{i=1}^n y_i(t) - \sum_{j=1}^q b_{ij} g_j(x(t))^2 + \nu \|g\|_T^2 g_j(x(t))^2 + \nu \|g\|_T^2. \end{aligned} \quad (10)$$

Then, one can obtain

$$\begin{aligned} \frac{\partial P}{\partial c_{g_j p,q}} &= -\frac{2}{T} \sum_{t=1}^T \sum_{i=1}^n \left( y_i(t) - \sum_{j=1}^q b_{ij} g_j(x(t)) \right) b_{ij} \phi_{p,q}(x(t)) \\ &\quad + 2 \frac{\nu c_{g_j p,q}}{\lambda_{p,q}} \\ &= -\frac{2}{T} \sum_{t=1}^T \sum_{i=1}^n \left( b_{ij} y_i(t) - b_{ij} \sum_{j=1}^q b_{ij} g_j(x(t)) \right) \phi_{p,q}(x(t)) \\ &\quad + 2 \frac{\nu c_{g_j p,q}}{\lambda_{p,q}}. \end{aligned} \quad (11)$$

Considering the minimum optimization problem, we have

$$c_{g_j p,q} = \lambda_{p,q} \frac{\sum_{t=1}^T \sum_{i=1}^n b_{ij} y_i(t) - b_{ij} \sum_{j=1}^q b_{ij} g_j(x(t)) \phi_{p,q}(x(t))}{T\nu}. \quad (12)$$

Using the fact that

$$K_{\text{WNN}}(x(t), x) = \sum_{p,q=-\infty}^{\infty} \lambda_{p,q} \phi_{p,q}(x(t)) \phi_{p,q}(x), \quad (13)$$

we can get

$$\begin{aligned} g_j(x) &= \sum_{p,q=-\infty}^{\infty} c_{g_j p,q} \phi_{p,q}(x) \\ &= \sum_{p,q=-\infty}^{\infty} \lambda_{p,q} \frac{\sum_{t=1}^T \sum_{i=1}^n (b_{ij} y_i(t) - b_{ij} \sum_{j=1}^q b_{ij} g_j(x(t))) \phi_{p,q}(x(t))}{T\nu} \phi_{p,q}(x) \\ &= \frac{\sum_{t=1}^T \sum_{i=1}^n (b_{ij} y_i(t) - b_{ij} \sum_{j=1}^q b_{ij} g_j(x(t))) K_{\text{WNN}}(x(t), x)}{T\nu} \\ &= \sum_{t=1}^T l_{jt} K_{\text{WNN}}(x(t), x). \end{aligned} \quad (14)$$



From (9),

$$\begin{aligned}\bar{g}_{jT} &= T_m \bar{l}_j, \\ \bar{g}_T &= (I_q \otimes T_m) \bar{l},\end{aligned}\quad (15)$$

we have

$$\begin{aligned}T\mathcal{V}_t &= B^T y(t) - B^T B g_{iT}, \\ T\mathcal{V} &= (I_T \otimes B^T) y - (I_T \otimes B^T B) g_T \\ &= (I_T \otimes B^T) y - (I_T \otimes B^T B) \bar{G} \bar{g}_T \\ &= (I_T \otimes B^T) y - (I_T \otimes B^T B) \bar{G} (I_q \otimes T_m) \bar{l} \\ &= (I_T \otimes B^T) y - (I_T \otimes B^T B) \bar{G} (I_q \otimes T_m) \bar{L}.\end{aligned}\quad (16)$$

The theorem is obtained.

The above optimization problem leads to the following approximation results:

$$g_i \in \mathcal{H}_T \|\min B\bar{g}(x(t)) - Bg(x(t))\|. \quad (17)$$

Then, by using the cross-validation method, we can estimate the approximation error  $\mathbf{e}$  in (17) which is not exactly known. In practice, define  $\zeta$  as the upper bound of the approximation error which can be computed by the data learning algorithm. In fact, one can find that a good approximation error at  $O(10^{-3})$  or even a smaller value can be obtained in simulations by using sufficiently large data samples for the learning. To ensure the control design to be robust under faulty data, the upper bound of the approximation error  $\zeta$  is set to be  $10\mathbf{e}$  in our data learning algorithm.

That is,  $\|B\bar{g}(x(t)) - Bg(x(t))\| \leq \zeta$ . This construction is explained based on the following facts: as one may know that the design of the control is based on future system process which is fully unknown. This makes the learning of future fault very difficult. Although the cross-validation method can estimate the error very well, there will still be some differences between the estimated fault and the true fault. That is to say, the learned fault obtained by approximating the trained data can reflect most of the parts of the fault function, but not the exactly true fault. Nevertheless, the parameter  $\zeta$  produced from training data can provide a good result and is used to estimate the approximate error.

In the following, we will give a theorem to design the fault tolerant control based on the approximation result.  $\square$

**Theorem 2.** *Considering the system with the fault given in (1), the system will be stabilized under the following control:*

$$u(t) = B^T Px(t) - \text{sign}(B^T Px(t)) \zeta - g(x(t)), \quad (18)$$

where  $P > 0$  is the unique solution to the algebraic Riccati equation (ARE):

$$A^T P + PA - PBB^T P + I = 0. \quad (19)$$

*Proof.* Introduce the following Lyapunov candidate:

$$V(t) = x^T(t) P x(t). \quad (20)$$

Then, the derivative of  $V(t)$  satisfies

$$\begin{aligned}\dot{V}(t) &= 2(Ax(t)n + qBh(B^T Px(t) - \text{sign}(B^T Px(t))\zeta - g(x(t)) + \bar{g}(x(t), k)))^T Px(t) \\ &= x^T(t)(A^T P + PA)x(t) + x^T(t)PBB^T Px(t) \\ &\quad - \zeta \text{sign}(B^T Px(t))B^T Px(t) + e_g^T(t)BB^T Px(t) \\ &\leq x^T(t)(A^T P + PA + PBB^T P)x(t).\end{aligned}\quad (21)$$

From (19), the theorem is obtained.  $\square$

*Remark 1.* In this paper, the data-driven learning method is proposed to identify the system fault. It should be pointed out that there exist some problems which remain to be solved: (i) since the data are collected for learning, it is well known that identification efficiency can be improved as more data samples are collected. The amount of data to be collected to improve the efficiency of the algorithm is still an open problem; (ii) from (3), one can find that there exists a regularization constant,  $\nu$  in (3), to reduce the model complexity and the learning error. The constant is always case dependent; (iii) the choice of the dilation  $\omega_0$  and violation  $a_i$  in the Morlet WNN kernel is also case dependent. One can refer to WNN for learning function in [14, 15].

*Remark 2.* In this paper, the data-driven learning method is given to analyze the system fault. This is different from the classic fault tolerant analysis in the networked system. Classically, the fault analysis used the model-based approach, see [17–19] and the reference therein, in which they solved the fault tolerant problem in a system basis. However, in this paper, we analyze the fault fully based on the historical data, and some useful data-based results are obtained. This makes a new insight in applying data learning strategies in the fault research area.

*Remark 3.* The results obtained in this paper aim to solve the stability problem in a dynamical system considering fault by using the WNN-based method. Through Theorem 1, we can obtain the detailed formula for the approximation of the system fault effect in (1). One can refer to (17) for details. In

addition, with the given equations (6)–(9), one can easily calculate the mathematical form of the control in (18). All these procedures contribute to the application of the obtained results in real-world engineering problems.

#### 4. Application

In this section, the VTOL aircraft stability problem is proposed to verify the method in Theorem 2. One typical VTOL aircraft model can be found in Yakovlev Yak-38 which is a Soviet Navy VTOL aircraft intended for their light carriers, cargo ships, and capital ships. The dynamical system is described by

$$\dot{x}(t) = Ax(t) + B(u(t) + \bar{g}(x(t))). \quad (22)$$

The parameter matrices  $A$  and  $B$  are given as follows:

$$A = \begin{pmatrix} -0.0366 & 0.0271 & 0.0188 & -0.4555 \\ 0.0482 & -1.01 & 0.0024 & -4.0208 \\ 0.1002 & 0.3681 & -0.707 & 1.42 \\ 0 & 0 & 1 & 0 \end{pmatrix}, \quad (23)$$

$$B = \begin{pmatrix} 0.4422 & 0.1761 \\ 3.5446 & -7.5922 \\ -5.52 & 4.49 \\ 0 & 0 \end{pmatrix}.$$

Based on the proposed method, we use the control  $u(t) = -B^T Px(t)$  to collect data in [5 s, 10 s], where

$$P = \begin{pmatrix} 2.2932 & 0.1056 & 0.0837 & -0.9103 \\ 0.1056 & 0.1940 & 0.1357 & -0.0156 \\ 0.0837 & 0.1357 & 0.2681 & 0.1683 \\ -0.9103 & -0.0156 & 0.1683 & 1.8079 \end{pmatrix}. \quad (24)$$

The fault considered in the first 10 seconds is given by

$$\bar{g}(x(t)) = \begin{pmatrix} \sin(x_1(t)) - 2\sin(x_3(t)) \\ 2\sin(x_2(t)) - \sin(x_4(t)) \end{pmatrix}. \quad (25)$$

Then, we can learn the fault effect  $B\bar{g}(x(t))$  numerically through the optimization (3) approach result in (7), see Figure 1. In Figure 1, it can be found that the dashed lines and solid lines are very close which means that the optimization problem in (3) is well solved by using the proposed Theorem 1. The fault considered in the system is given in (25). For illustration purpose, the parameter  $\nu$  in (3) is 0.8. The dilation and violation constants in (5) are set to be  $\omega_0 = 0.5$  and  $a_1 = a_2 = a_3 = a_4 = 2$ . The control proposed in (18) is applied at  $t = 10$  s with the  $\zeta$  equal to 0.3. The trajectory of the system is shown in Figure 2. In Figure 2, we aim to show the effectiveness of the proposed controller in (18). From the trajectory of  $x(t)$  in Figure 2, one can find that the system is stabilized since the value of  $x(t)$  goes to zero. One can see that the chattering phenomena is shown in this figure. This is due to the fact that the control (18) is based on the function sign. One may use other functions to replace

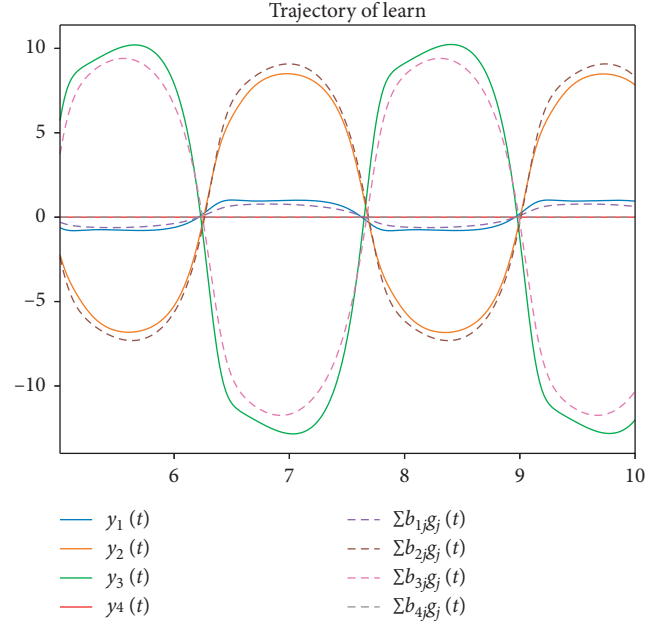


FIGURE 1: Learning result (this figure shows the learning result in (6) which is based on the optimization problem in (3).  $\sum b_{ij}g_j$ ,  $i = \{1, 2, 3, 4\}$  represents  $\sum_{j=1}^q b_{ij}g_j$ ,  $i = \{1, 2, 3, 4\}$ , see (10) for the detail calculation).

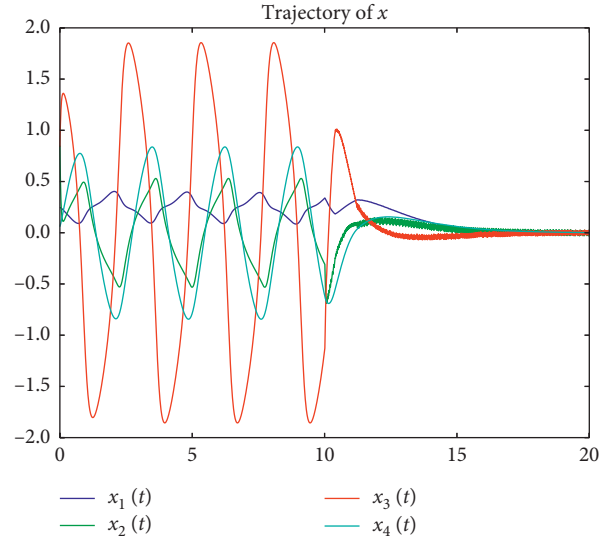


FIGURE 2: Trajectory of the state (this figure shows the trajectory of the dynamical system (22) with the given fault in (25) by using the proposed learning-based control in (18)).

the sign, which may lead to a bounded domain of the trajectory, see [12].

Next, we will consider different fault effects in [0 s, 50 s]. The fault of the aircraft in [0 s, 20 s] is

$$\bar{g}(x(t)) = \begin{pmatrix} \sin(x_2(t)) - 2\sin(x_3(t)) + \sin(x_4(t)) \\ \sin(x_1(t)) - 2\sin(x_2(t)) \end{pmatrix}. \quad (26)$$

The fault of this system in [20 s, 50 s] is

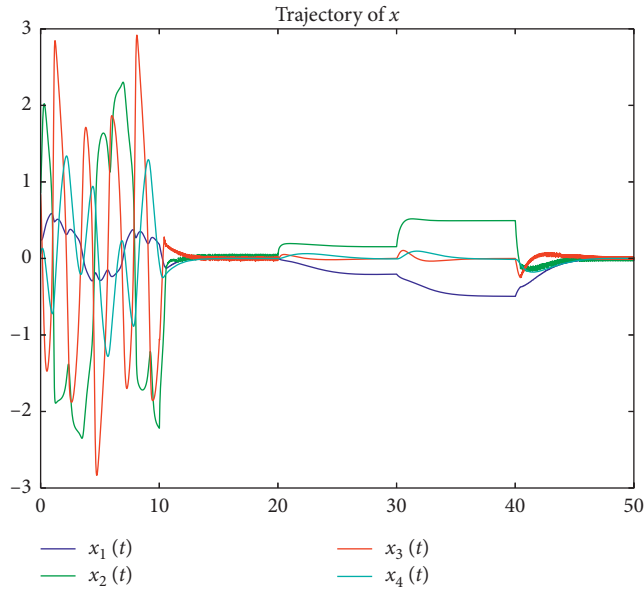


FIGURE 3: Trajectory of the state (this figure shows the trajectory of the dynamical system (22) with the given fault in (26) and (27) by using the proposed learning-based control in (18)).

$$\bar{g}(x(t)) = \begin{pmatrix} -0.5 \\ -0.5 \end{pmatrix}. \quad (27)$$

We analyze the whole process in the following sessions:

Session 1: observation time interval: [20 s, 35 s];

Session 2: data collection time intervals: [5 s, 10 s] and [35 s, 40 s];

Session 3: data-driven learning control time intervals: [10 s, 20 s] and [40 s, 50 s].

During the first 5 seconds, the operation system data are collected. One may observe that the system is not stable from the collected data. Then, we make the judgement that the system is faulty. In the next 5 seconds, we collect the data and use the proposed learning technique in Theorem 1 to identify the fault. From the data learned results, one may use the control in (18) to stabilize the system. From Figure 3, one can see that, after the controller is applied, the system is stabilized.

Considering the changing fault at 20 s, it can be observed that the previous control is failed to stabilize the system in the time interval [20 s, 30 s]. This makes us to remove the aforementioned controller and repeat the observation-collection learning progress. The details are given as following steps: (1) collect data in [35 s, 40 s]; (2) use the proposed learning technique to identify the fault; (3) apply the newly identified results into the controller (18).

From Figure 3, one can see that, after the controller is applied at 40 s, the system goes to the stability state during [40 s, 50 s]. In Figure 3, we consider different fault effects in different time intervals during the system operating. One can find that if two faults are observed at different time, we can always apply the proposed controller in (18) by using the collected data to stabilize the system in the time intervals [10 s, 20 s] and [40 s, 50 s].

## 5. Conclusion

In this paper, fault tolerant stability is given based on data-driven learning techniques. A regularized regression wavelet approach is proposed for the data-based fault identification. The data-driven scheme is investigated under the consideration to minimize the error between the fault effect and data samples. Based on the learning result, data-driven control is proposed to stabilize the system. Finally, a simulation example is exploited to show the effectiveness of the main result.

## Data Availability

The data used to support the findings of this study are available from the corresponding author upon request.

## Conflicts of Interest

The authors declare that they have no conflicts of interest.

## Acknowledgments

This work was supported by the Fundamental Research Funds for the Central Universities (220110004005040120 and 220110001002020043).










## References

- [1] B. Paden and S. Sastry, "A calculus for computing Filippov's differential inclusion with application to the variable structure control of robot manipulators," *IEEE Transactions on Circuits and Systems*, vol. 34, no. 1, pp. 73–82, 1987.
- [2] S. Chiu and S. Chand, "Fuzzy controller design and stability analysis for an aircraft model," in *Proceedings of the American Control Conference*, pp. 821–826, Boston, MA, USA, June 1991.
- [3] K. D. Young, V. I. Utkin, and U. Ozguner, "A control engineer's guide to sliding mode control," *IEEE Transactions on Control Systems Technology*, vol. 7, no. 3, pp. 328–342, 1999.
- [4] D. W. C. Ho, J. Li, and Y. Niu, "Adaptive neural control for a class of nonlinearly parametric time-delay systems," *IEEE Transactions on Neural Networks*, vol. 16, no. 3, pp. 625–635, 2005.
- [5] R. Isermann, R. Schwarz, and S. Stolzl, "Fault-tolerant drive-by-wire systems," *IEEE Control Systems*, vol. 22, no. 5, pp. 64–81, 2002.
- [6] Z. Chen, Q. Chen, X. He, and M. Sun, "Adaptive finite-time command filtered fault-tolerant control for uncertain spacecraft with prescribed performance," *Complexity*, vol. 2018, Article ID 4912483, 12 pages, 2018.
- [7] Y. Xiong and M. Saif, "Sliding mode observer for nonlinear uncertain systems," *IEEE Transactions on Automatic Control*, vol. 46, no. 12, pp. 2012–2017, 2001.
- [8] H. Gao and T. Chen, "Stabilization of nonlinear systems under variable sampling: a fuzzy control approach," *IEEE Transactions on Fuzzy Systems*, vol. 15, no. 5, pp. 972–983, 2007.
- [9] H. Zhang, L. Cui, X. Zhang, and Y. Luo, "Data-driven robust approximate optimal tracking control for unknown general nonlinear systems using adaptive dynamic programming method," *IEEE Transactions on Neural Networks*, vol. 22, no. 12, pp. 2226–2236, 2011.

- [10] S. Yin, S. X. Ding, X. Xie, and H. Luo, "A review on basic data-driven approaches for industrial process monitoring," *IEEE Transactions on Industrial Electronics*, vol. 61, no. 11, pp. 6418–6428, 2014.
- [11] S. Chen, D. W. C. Ho, and C. Huang, "Fault reconstruction and state estimator design for distributed sensor networks in multitarget tracking," *IEEE Transactions on Industrial Electronics*, vol. 62, no. 11, pp. 7091–7102, 2015.
- [12] S. Chen, D. W. C. Ho, L. Li, and M. Liu, "Fault-tolerant consensus of multi-agent system with distributed adaptive protocol," *IEEE Transactions on Cybernetics*, vol. 45, no. 10, pp. 2142–2155, 2015.
- [13] S. Yin, S. X. Ding, A. Haghani, H. Hao, and P. Zhang, "A comparison study of basic data-driven fault diagnosis and process monitoring methods on the benchmark Tennessee Eastman process," *Journal of Process Control*, vol. 22, no. 9, pp. 1567–1581, 2012.
- [14] D. W. C. Ho, P.-A. Ping-Au Zhang, and J. Jinhua Xu, "Fuzzy wavelet networks for function learning," *IEEE Transactions on Fuzzy Systems*, vol. 9, no. 1, pp. 200–211, 2001.
- [15] J. Xu and D. W. C. Ho, "A basis selection algorithm for wavelet neural networks," *Neurocomputing*, vol. 48, no. 1–4, pp. 681–689, 2002.
- [16] F. Wu and Y. Zhao, "Least squares support vector machine on Moret Wavelet kernel function," in *Proceedings of the 2005 International Conference on Neural Networks and Brain*, vol. 1, pp. 327–331, Beijing, China, October 2005.
- [17] M. Liu, D. W. C. Ho, and P. Shi, "Adaptive fault-tolerant compensation control for Markovian jump systems with mismatched external disturbance," *Automatica*, vol. 58, pp. 5–14, 2015.
- [18] S. X. Ding, *Model-based Fault Diagnosis Techniques: Design Schemes, Algorithms, and Tools*, Springer, Berlin, Germany, 2008.
- [19] M. Liu and P. Shi, "Sensor fault estimation and tolerant control for Itô stochastic systems with a descriptor sliding mode approach," *Automatica*, vol. 49, no. 5, pp. 1242–1250, 2013.

## Research Article

# Chaos-Based Application of a Novel Multistable 5D Memristive Hyperchaotic System with Coexisting Multiple Attractors

Fei Yu <sup>1</sup>, Li Liu <sup>1</sup>, Shuai Qian,<sup>1</sup> Lixiang Li <sup>1</sup>, Yuanyuan Huang <sup>1</sup>, Changqiong Shi <sup>1</sup>, Shuo Cai <sup>1</sup>, Xianming Wu <sup>2</sup>, Sichun Du <sup>3</sup>, and Qiuzhen Wan <sup>4</sup>

<sup>1</sup>School of Computer and Communication Engineering, Changsha University of Science and Technology, Changsha 410114, China

<sup>2</sup>School of Mechanical and Electrical Engineering, Guizhou Normal University, Guiyang 550025, China

<sup>3</sup>College of Computer Science and Electronic Engineering, Hunan University, Changsha 410082, China

<sup>4</sup>College of Information Science and Engineering, Hunan Normal University, Changsha 410081, China

Correspondence should be addressed to Fei Yu; [yufeyfyf@csust.edu.cn](mailto:yufeyfyf@csust.edu.cn), Yuanyuan Huang; [snailhyy@126.com](mailto:snailhyy@126.com), and Qiuzhen Wan; [waniuzhen@sina.com](mailto:waniuzhen@sina.com)

Received 23 November 2019; Revised 8 February 2020; Accepted 17 February 2020; Published 29 March 2020

Guest Editor: Sundarapandian Vaidyanathan

Copyright © 2020 Fei Yu et al. This is an open access article distributed under the Creative Commons Attribution License, which permits unrestricted use, distribution, and reproduction in any medium, provided the original work is properly cited.

Novel memristive hyperchaotic system designs and their engineering applications have received considerable critical attention. In this paper, a novel multistable 5D memristive hyperchaotic system and its application are introduced. The interesting aspect of this chaotic system is that it has different types of coexisting attractors, chaos, hyperchaos, periods, and limit cycles. First, a novel 5D memristive hyperchaotic system is proposed by introducing a flux-controlled memristor with quadratic nonlinearity into an existing 4D four-wing chaotic system as a feedback term. Then, the phase portraits, Lyapunov exponential spectrum, bifurcation diagram, and spectral entropy are used to analyze the basic dynamics of the 5D memristive hyperchaotic system. For a specific set of parameters, we find an unusual metastability, which shows the transition from chaotic to periodic (period-2 and period-3) dynamics. Moreover, its circuit implementation is also proposed. By using the chaoticity of the novel hyperchaotic system, we have developed a random number generator (RNG) for practical image encryption applications. Furthermore, security analyses are carried out with the RNG and image encryption designs.

## 1. Introduction

In recent years, chaos systems have become the subject of many studies in the fields of science and engineering. A large number of new chaotic systems have been proposed one after another, and their application scopes are more and more extensive [1–8]. With the progress of science and technology, chaos has been applied not only to communication [9–12], image processing [13–15], complex networks [16–21], synchronization [22–27], electronic circuits [28–30], and optimization [31–35] but also to encryption studies [36–41]. This is because chaotic signal has good pseudorandom, initial-value sensitive, and long-term unpredictable characteristics, which enhances the confusion and diffusion of encrypted data.

Due to the more complex structure and dynamic behavior of the hyperchaotic system, in order to better meet the needs

of secure communication and information hiding, people propose to construct hyperchaotic systems to improve the complexity of the systems. At present, hyperchaotic systems are usually constructed by loading feedback controller on 3D or 4D continuous chaotic systems [42–46]. The feedback controllers are divided into linear and nonlinear, among which the nonlinear-feedback term will further increase the complexity and unpredictability of the system, which is more suitable for the construction of hyperchaos [47–51].

Memristor is a kind of hardware implementation component of memory nonlinear electronic memristor chaotic circuit, which has research significance in chaotic secure communication, image encryption, neural networks, and other fields [52–56]. It describes the relationship between magnetic flux and charge. The concept of the memristor was proposed by Chua in 1971 [57], and it was not until 2008 that

HP laboratory realized the first real memristor [58]. Because of the nonlinear and memory characteristics of the memristor, as the feedback term of the hyperchaotic system, it can produce complex nonlinear dynamic phenomena, which provides a new development space for the design of the hyperchaotic system. At present, the main method is to use the memristor as the feedback term in typical chaotic systems to construct hyperchaotic systems. In [59], a novel 5D hyperchaotic four-wing memristive system (HFWMS) was proposed by introducing a flux-controlled memristor with quadratic nonlinearity into a 4D hyperchaotic system, the dynamic characteristics of the HFWMS were analyzed, and the FPGA realization of the 5D HFWMS was also reported. In [60], a new memristive system was presented by replacing the resistor in the circuit of modified Lü system with the flux-controlled memristor, respectively, which could exhibit a hyperchaotic multiwing attractor, and the values of two positive Lyapunov exponents were relatively large. The dynamical behaviors and the circuit implementation were also carried out.

Coexisting attractors depend on the symmetry of the systems and the initial condition of the systems [61]. Multistability refers to the phenomenon that the system shows different dynamic characteristics and different attractors coexist under same parameters [62]. In recent years, the study of multistability and coexistence attractors is a hot topic in nonlinear dynamics [63–70]. Lai et al. [63] showed the coexistence behavior of different attractors under different initial conditions and parameter values, such as four limit cycles, and two double-scroll attractors with a limit cycle. In [65], a new 4D fractional order chaotic system was proposed by adding a variable to the 3D chaotic system. This new system had no equilibrium point, but it could also show rich and complex hidden dynamics. Zhang et al. [66] introduced a state variable into a 3D chaotic system and then analyzed the dynamic characteristics of the new system under different initial conditions, proving that the new system has extreme multistability. In fact, various systems exhibiting multistability have been proposed. However, a review of literature revealed that this remarkable behavior is rare in 5D memristive hyperchaotic system with coexisting multiple attractors. Such systems cannot be ignored. Because of their complexity, the generated signals are usually used for secure communication and random number generation.

With the development of communication technology and the coming of information age, people are more and more aware of the important role of information security [71–76], and the research of various security protection has become the current research hotspot [77–82]. As an important part of information security transmission, random number generator (RNG) has been paid more and more attention. The unpredictable and unrepeatable random number sequence which can be produced by RNG plays an important role in information encryption. Based on Shannon information theory, in order to ensure the absolute security of communication, the RNG with high speed, unpredictability, and good randomness has great research value [83–89]. The chaotic system is a kind of complex nonlinear motion, which is highly sensitive to the initial

conditions, and its orbit is unpredictable for a long time. Therefore, the chaotic system shows very good cryptography characteristics.

In recent years, people are committed to the research and design of chaos-based RNGs [90–93]. Sometimes the key of generating random sequence by chaos is the choice of chaotic systems. However, most RNGs based on chaos have a typical disadvantage. That is to say, the limited precision of all processors may cause the chaotic system to degenerate into periodic function or fixed point [94]. In order to overcome this disadvantage, a generator based on hyperchaos was proposed in [94]. The self-shrinking generator was used to disturb the hyperchaotic sequence to reduce the period degradation and improve the sequence performance, which was superior to many other linear-feedback-shift register-based generators. Random numbers created in the chaotic systems are tested according to the randomness tests with the highest international standards such as AIS-31 and NIST 800 22 and then are ready to be used in encryption applications [95, 96]. In encrypted applications, it is not enough to encrypt data only. Encrypted data must also be equipped with the highest possible reliability. In order to prove the high level of reliability, some security analysis must be carried out according to the data type. Key space, sensitivity, floating frequency, histograms, correlation, and information entropy analysis are common security analysis in the literature [97–99].

Motivated by undiscovered features of systems with coexisting multiple attractors, we introduce a novel multistable 5D memristive hyperchaotic system with a line of equilibrium and its practical chaos-based application in the present work. The rest of this work is organized as follows. Section 2 describes the mathematical model of the novel multistable 5D memristive hyperchaotic system. Dynamical properties and circuit realization of the system are investigated in Sections 3 and 4, respectively. Section 5 presents a random number generation (RNG) using the chaoticity of the multistable 5D memristive hyperchaotic system, while security analyses are also carried out with the RNG designed. To validate the performance of the RNG, the application of image encryption is employed in Section 6, we also employ standard security analysis whose outcome is compared alongside available state-of-the-art methods. Finally, we conclude in Section 7.

## 2. A Novel Multistable 5D Memristive Hyperchaotic System

Recently, Yu and Wang [100] proposed a 4D four-wing chaotic system, and its mathematical model is

$$\begin{cases} \dot{x} = -ax + yz, \\ \dot{y} = by - xz, \\ \dot{z} = xy - cz + dw, \\ \dot{w} = xy - ew, \end{cases} \quad (1)$$

where  $x, y, z$ , and  $w$  are the state variables and  $a, b, c, d$ , and  $e$  are the system parameters. When  $a = 10, b = 12, c = 60, d = 2,$



and  $e = 3$ , system (1) can display a fully four-wing chaotic attractor under the initial conditions  $(2, 1, 1, 2)$ .

Memristor is a passive two terminal device which describes the relationship between flux  $\varphi$  and charge  $q$ . In this paper, the memristor is controlled by flux, and the relationship between the current flowing through the two terminal device and the port voltage can be expressed as follows:

$$i = W(\varphi)u, \dot{\varphi} = u, \quad (2)$$

where  $W(\varphi)$  is the memductance function of the flux-controlled memristor and defined as

$$W(\varphi) = f + 3g\varphi^2. \quad (3)$$

Based on system (1), by introducing the memristor model in (3) to the third equation of system (1), a novel 5D memristive hyperchaotic system is presented as follows:

$$\begin{cases} \dot{x} = -ax + yz, \\ \dot{y} = by - xz, \\ \dot{z} = xy - cz + dw(f + 3gu^2), \\ \dot{w} = xy - ew, \\ \dot{u} = -z, \end{cases} \quad (4)$$

where  $a, b, c, d, e, f$ , and  $g$  are the system parameters. When the typical parameters are fixed as  $a = 10, b = 12, c = 30, d = 2, e = 4, m = 0.1$ , and  $n = 0.01$  and the initial conditions are chosen as  $(2, 1, 1, 2, 2)$ , the memristive system (4) exhibits a four-wing hyperchaotic attractor, as shown in Figure 1, from which it can be seen that the system has topologically more complex attractor structure than system (1) presented by [100]. The memristive chaotic system (4) has the same symmetry as the original 4D chaotic system (1) and remains unchanged under the coordinate transformation  $(x, y, z, w, u) \rightarrow (\pm x, \mp y, -z, -w, -u)$ .

Equilibrium points of system (4) are obtained by setting its right-hand side to zero, that is,

$$\begin{cases} -ax + yz = 0, \\ by - xz = 0, \\ xy - cz + dw(f + 3gu^2) = 0, \\ xy - ew = 0, \\ -z = 0. \end{cases} \quad (5)$$

According to equation (5), it is easy to see that system (4) has a line equilibrium point  $O = \{(x, y, z, w, u) \mid x = y = z = w = 0, u = l\}$ , where  $l$  is any real constant. The Jacobian matrix at the online equilibrium point  $O$  of system (4) is

$$J_o = \begin{bmatrix} -a & z & y & 0 & 0 \\ -z & b & -x & 0 & 0 \\ y & x & -c & d(f + 3gu^2) & 6dwgu \\ y & x & 0 & -e & 0 \\ 0 & 0 & -1 & 0 & 0 \end{bmatrix}. \quad (6)$$

According to (6), the characteristic equation can be obtained as

$$\lambda(\lambda + e)(\lambda + c)(\lambda + a)(\lambda - b) = 0. \quad (7)$$

It is easy to get  $\lambda_1 = 0, \lambda_2 = -e, \lambda_3 = -a, \lambda_4 = -c$ , and  $\lambda_5 = b$  because the values of system parameters  $a, b, c$ , and  $e$  are greater than zero, so  $\lambda_2, \lambda_3$ , and  $\lambda_4$  are negative,  $\lambda_5$  is positive, so system (4) has unstable saddle point. The dissipativity of memristive chaotic system (4) can be described as

$$\nabla V = \frac{dx}{dx} + \frac{dy}{dy} + \frac{dz}{dz} + \frac{dw}{dw} + \frac{du}{du} = -a + b - c - e. \quad (8)$$

Since  $-a + b - c - e = -32$  satisfies  $\nabla V < 0$ , system (4) is dissipative.

### 3. Dynamic Analysis of the Novel 5D Memristive Chaotic System

In this section, we will use the tools of bifurcation diagram, Lyapunov exponent spectrum, time series, and phase diagram and use the fourth-order Runge–Kutta algorithm to study the complex dynamic behavior of system (4) through MATLAB. The proposed memristive chaotic system (4) has particularly complex dynamic characteristics, including coexistence attractors of the same type and different types, multistability, and transient transfer phenomena.

#### 3.1. Lyapunov Exponent Spectrum and Bifurcation Diagram.

It is very interesting that there are different dynamic behaviors (such as periodic phenomena, quasi-periodic, chaotic attractors, and hyperchaotic attractors), according to different differential equations of parameter values. The system parameters are set as  $b = 12, c = 30, d = 2, e = 4, m = 0.1$ , and  $n = 0.01$ , the initial conditions are chosen as  $x(0) = 2, y(0) = 1, z(0) = 1, w(0) = 2$ , and  $u(0) = 2$ , and the parameter  $a$  is the bifurcation parameter of the system. Figure 2(a) is the corresponding Lyapunov exponent spectrum (in order to make the graph display clear, the fifth Lyapunov index is omitted here), and Figure 2(b) is the bifurcation diagram when the parameter  $a$  of the system changes from 0 to 20 with the state variable  $x$ . It can be seen from Figure 2(b) that as the parameter  $a$  gradually increases in the range, the system leads from periodic state to chaos and then to period, with some quasi-periodic windows and transient transfer phenomena in the middle. Table 1 lists the dynamic behavior of parameter  $a$  in different ranges and its Lyapunov exponent. Therefore, it can be shown that system (4) has a very rich and complex dynamic behavior:

- (i) When  $0 \leq a \leq 1.6$ , the maximum Lyapunov exponent of system (4) is zero ( $\lambda_1 = 0, \lambda_{2,3,4,5} < 0$ ), so the system is in a multiperiod state.
- (ii) When  $1.6 \leq a < 2.2, 5.8 < a < 11.5$ , and  $12.4 < a < 13.1$ , the system has a positive Lyapunov exponent ( $\lambda_1 > 0, \lambda_2 = 0, \lambda_{3,4,5} < 0$ ) and is in a chaotic state.

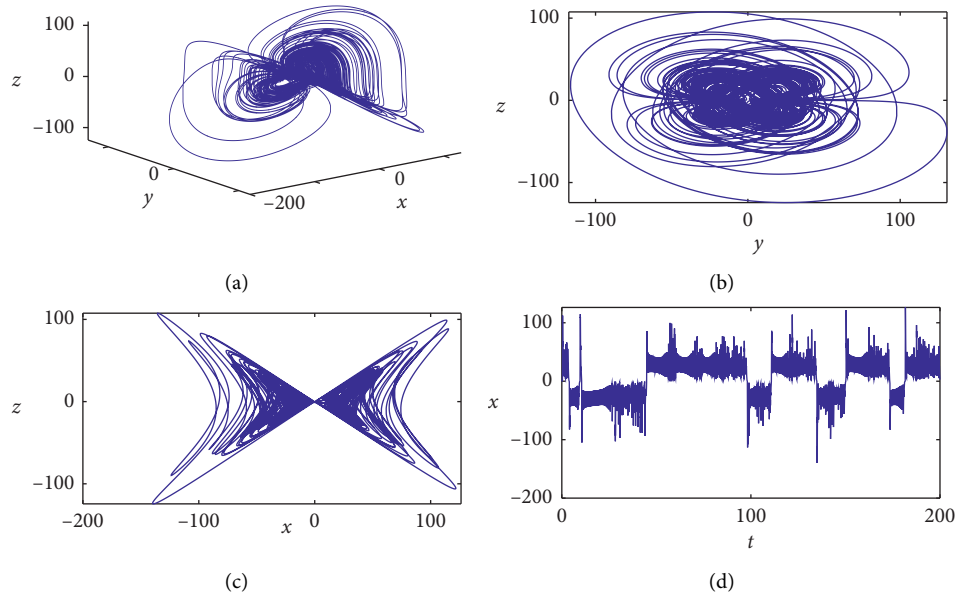


FIGURE 1: The four-wing chaotic attractor of system (4): (a) in the  $x - y - z$  plane, (b) in the  $y - z$  plane, (c) in the  $x - z$  plane, and (d) time-domain waveform of  $x$ .

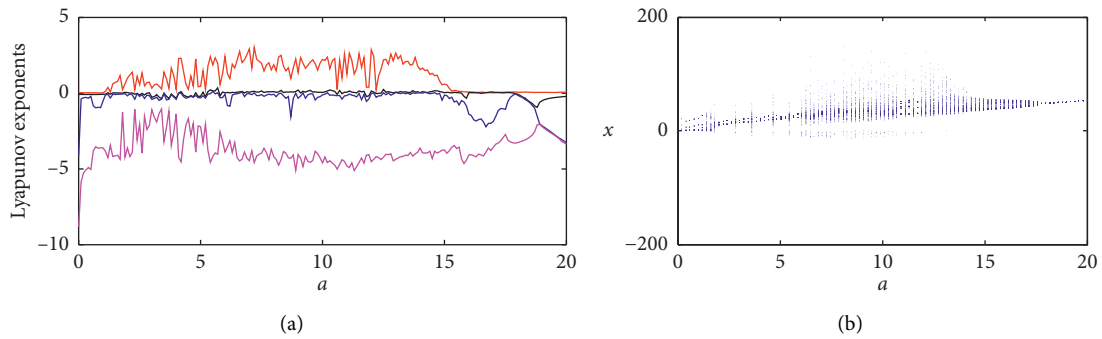


FIGURE 2: (a) Lyapunov exponent spectrum (the fifth LE is out of plot) and (b) bifurcation diagram for increasing parameter  $a \in [0, 20]$ .

TABLE 1: Dynamical behavior and Lyapunov exponents under different parameter ranges of  $a$ .

$a$	$(\lambda_1, \lambda_2, \lambda_3, \lambda_4, \lambda_5)$	Behavior of dynamics
$0 \leq a \leq 1.6$	$(0, -, -, -, -)$	Multiperiod
$1.6 \leq a < 2.2$	$(+, 0, -, -, -)$	Chaotic attractor
$2.2 \leq a \leq 5.8$	$(0, -, -, -, -)$	Transient chaos, stable state period-2
$5.8 < a < 11.5$	$(+, 0, -, -, -)$	Chaotic attractor
$11.5 \leq a \leq 12.4$	$(0, -, -, -, -)$	Transient chaos, stable state period-3
$12.4 < a < 13.1$	$(+, 0, -, -, -)$	Chaotic attractor
$13.1 \leq a \leq 14.8$	$(+, +, 0, -, -)$	Hyperchaotic attractor
$14.8 < a \leq 17.9$	$(0, 0, -, -, -)$	Quasi-periodic state
$17.9 < a \leq 20$	$(0, -, -, -, -)$	Limit cycle

(iii) When  $3.1 \leq a \leq 14.8$ , system (4) has two positive Lyapunov exponents ( $\lambda_{1,2} > 0, \lambda_3 = 0, \lambda_{4,5} < 0$ ), so the system is hyperchaotic.

(iv) When  $14.8 < a \leq 17.9$ , the Lyapunov exponent of the system has two zeros ( $\lambda_{1,2} = 0, \lambda_{3,4,5} < 0$ ), and the system is quasi-periodic.

(v) When  $17.9 < a \leq 20$ , the maximum Lyapunov exponent of system (4) is zero ( $\lambda_1 = 0, \lambda_{2,3,4,5} < 0$ ), which is different from that of the system in the multiperiod state ( $0 \leq a \leq 1.6$ ), but the parameter  $a$  is only in the limit cycle state in this range.

- (vi) When  $2.2 \leq a \leq 5.8$  and  $11.5 \leq a \leq 12.4$ , the most interesting and also very important is the existence of transient chaos and steady-state periodic phenomena. Firstly, the system has a positive Lyapunov exponent, but when it reaches a certain time range, the maximum Lyapunov exponent becomes zero.

### 3.2. Multistability in the 5D Memristive Chaotic System.

In order to study the coexistence attractors and other characteristics of the system better, it is necessary to give some disturbance to the initial conditions under the condition of keeping the system parameters constant. Figure 3 shows the dynamic behavior with coexistence bifurcation, in which the initial conditions of blue trajectory and red trajectory are  $(2, 1, 1, 2, 2)$  and  $(-2, -1, 1, 2, 2)$ , respectively. It can be seen from Figure 3 that, under these two initial conditions, the bifurcation mode of the system is almost the same, so the system has exactly the same coexistence attractor under these two conditions. Table 2 is a summary of the dynamic characteristics of different parameter values  $a$ . Figure 4 shows coexisting multiple attractors of system (4) for different parameter values  $a$ . Figure 4(a) shows that the system has the coexisting two-wing period-1 attractors for  $a = 1$ ; Figure 4(b) shows that the system has two-wing chaotic attractors coexisting when  $a = 2$ ; Figure 4(c) shows that the phenomenon is very rare, the system has transient chaos, and then transfers to stable state of period-2 for  $a = 3.2$ . When  $a = 8$ , Figure 4(d) is very similar to the two-wing chaotic attractors, as shown in Figure 4(b); The system has four-wing chaotic attractors coexisting for  $a = 10.1$  (see Figure 4(e)). It is very similar to the phenomenon in Figure 4(c), but it is different that Figure 4(f) has the coexistence of stable state of period-3 for  $a = 11.7$ . It is different from the previous two kinds of two-wing chaotic attractors; when  $a = 14.6$ , the system has the coexisting two-wing hyperchaotic attractors, as shown in Figure 4(g). Figure 4(h) shows that when  $a = 17$ , the system has coexistence quasi-periodic phenomenon. Figure 4(i) shows that when  $a = 18.2$ , the system has coexistence limit cycle with period-1 under two different initial conditions.

If a chaotic system has different states of coexistence attractors under different initial conditions, the system has better randomness and is more suitable for random number generation, image encryption, secure communication, and other fields. As shown in Figure 5, system (4) has coexistence of various types of attractors under the initial conditions  $(2, 1, 1, 2, 2)$  and  $(-2, 1, 1, 2, 2)$ , such as two-wing multiperiod and two-wing period-5 coexist (Figure 5(a)), different two-wing chaotic attractors coexist (Figure 5(b)), periodic-2 and two-wing chaotic attractors coexist (Figures 5(c) and 5(d)), two-wing chaotic attractors coexist with quasi-period (Figure 5(e)), and two-wing chaotic attractors coexist with four-wing chaotic attractors (Figure 5(f)).

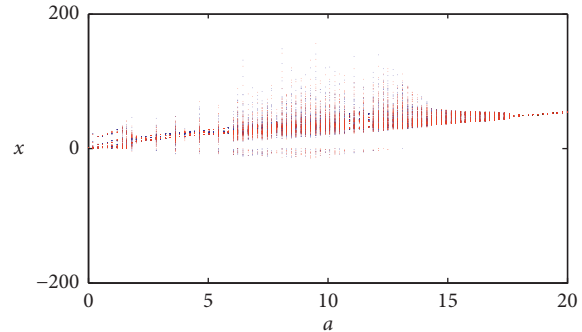


FIGURE 3: Bifurcation diagram with different initial values, the blue is  $(2, 1, 1, 2, 2)$  and the red is  $(-2, -1, 1, 2, 2)$ .

TABLE 2: Dynamical behavior under different parameter of  $a$  when  $b = 12$ ,  $c = 30$ ,  $d = 2$ ,  $e = 4$ ,  $m = 0.1$ , and  $n = 0.01$ .

$a$	Dynamics	Figure
1.0	Limit cycle with period-1	Figure 4(a)
2.0	Two-wing chaotic attractor	Figure 4(b)
3.2	Stable state period-2	Figure 4(c)
8.0	Two-wing chaotic attractor	Figure 4(d)
10.1	Four-wing chaotic attractor	Figure 4(e)
11.7	Stable state period-3	Figure 4(f)
14.6	Hyperchaotic attractor	Figure 4(g)
17.0	Quasi-periodic	Figure 4(h)
18.2	Limit cycle with period-1	Figure 4(i)

3.3. *Transient Chaos*. Due to the appearance of nonattractive saddle point in phase space, chaos appears in the system in a limited period of time. After a period of time, the system finally becomes a nonchaotic state, which is called transient chaos. In practice, transient chaos is more common than permanent chaos. A close observation of Figure 2 shows that, in the interval ranges  $[2.2, 5.8] \cup [11.5, 12.4]$  of system parameter  $a$ , a periodic window appears in Figure 2(b), but Figure 2(a) does indicate that the system is in a chaotic state in this range. This dynamic behavior with two different characteristics is called transient transfer behavior. With the evolution of time, system (4) changes from chaotic behavior to periodic behavior.

When  $a = 3$ , the time-domain waveform in the time interval  $[0, 200]$  is shown in Figure 6(a), and Figures 6(b)–6(e) are the phase portraits of the system in  $x$ - $z$  plane in different time intervals. It is clear from Figure 6(a) that the system is chaotic in  $t \in [0, 40]$  and periodic in  $t \in [40, 200]$ . From Figures 6(b)–6(e), it is verified that the system evolves from chaos to period gradually with time. Figure 7 also proves that the system does have transient chaos. Different from Figure 6, with the evolution of time, Figure 6 finally becomes a stable state period-2, while Figure 7 tends to a stable state period-3. The above-mentioned two cases show that the nonlinear phenomenon from transient chaos to stable state period is not a sudden phenomenon, and it needs a process like chaos bifurcation. For example, when  $t \in [0, 40]$  in Figure 6 is at a chaotic state but it is not just a stable state periodic

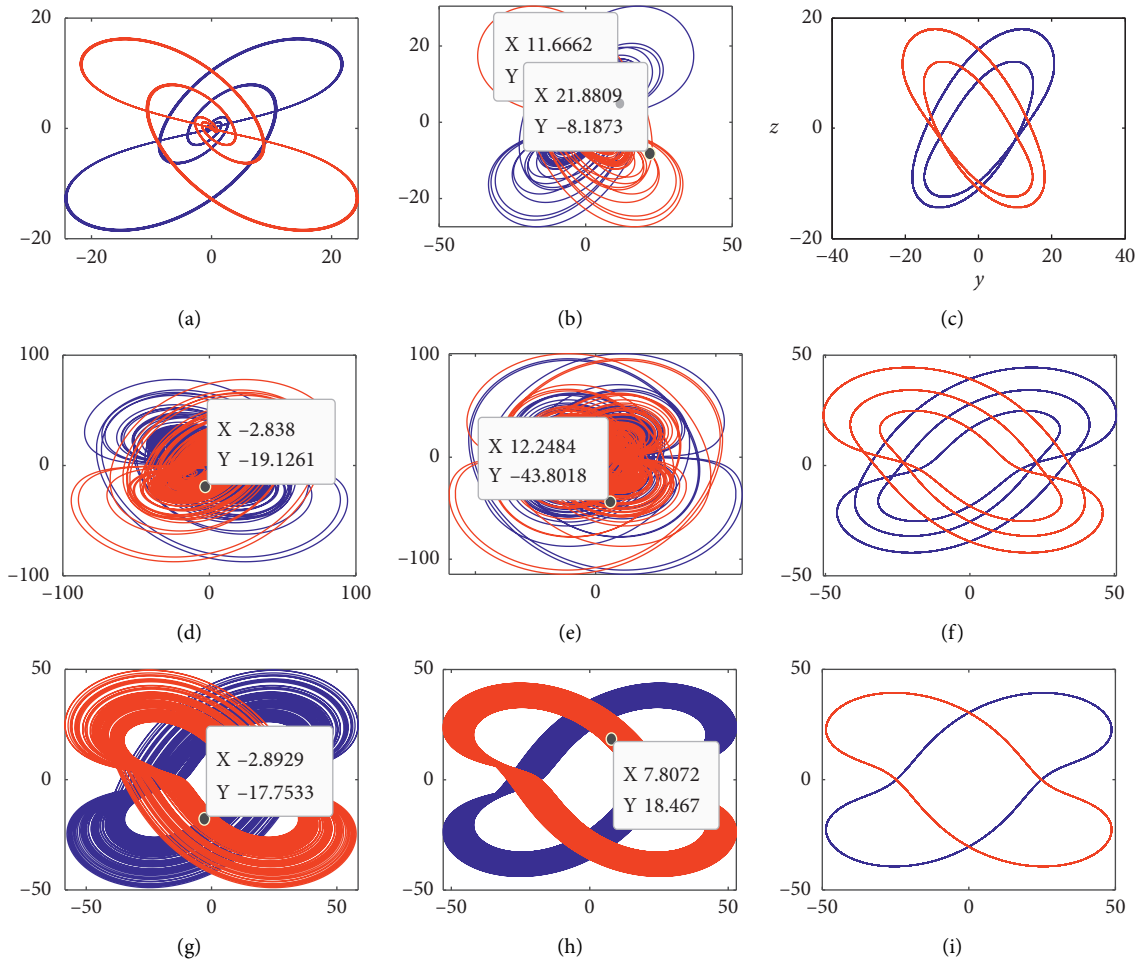


FIGURE 4: Various coexisting hidden attractors with different values of parameter  $a$  in the  $y$ - $z$  plane: (a)  $a = 1.0$ , (b)  $a = 2.0$ , (c)  $a = 3.2$ , (d)  $a = 8.0$ , (e)  $a = 10.1$ , (f)  $a = 11.7$ , (g)  $a = 14.6$ , (h)  $a = 17.0$ , and (i)  $a = 18.2$ . The blue one from the initial values  $(2, 1, 1, 2, 2)$  and the other from  $(-2, -1, 1, 2, 2)$ .

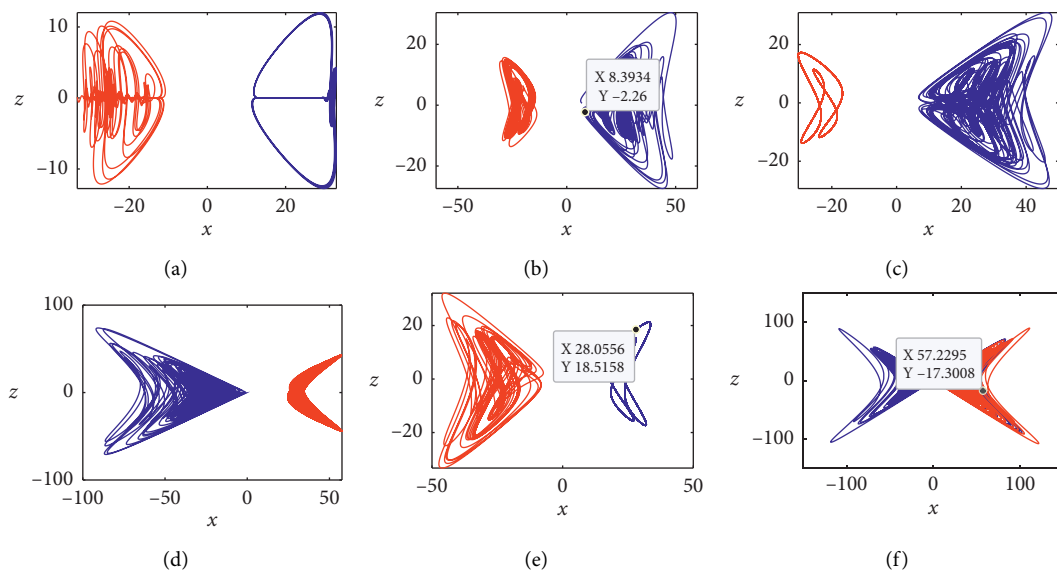


FIGURE 5: Various coexisting hidden attractors with different values of parameter  $a$  in the  $x$ - $z$  plane: (a)  $a = 0.2$ , (b)  $a = 2.0$ , (c)  $a = 3.0$ , (d)  $a = 4.2$ , (e)  $a = 6.75$ , and (f)  $a = 13.1$ . The blue one from the initial values  $(2, 1, 1, 2, 2)$  and the other from  $(-2, 1, 1, 2, 2)$ .

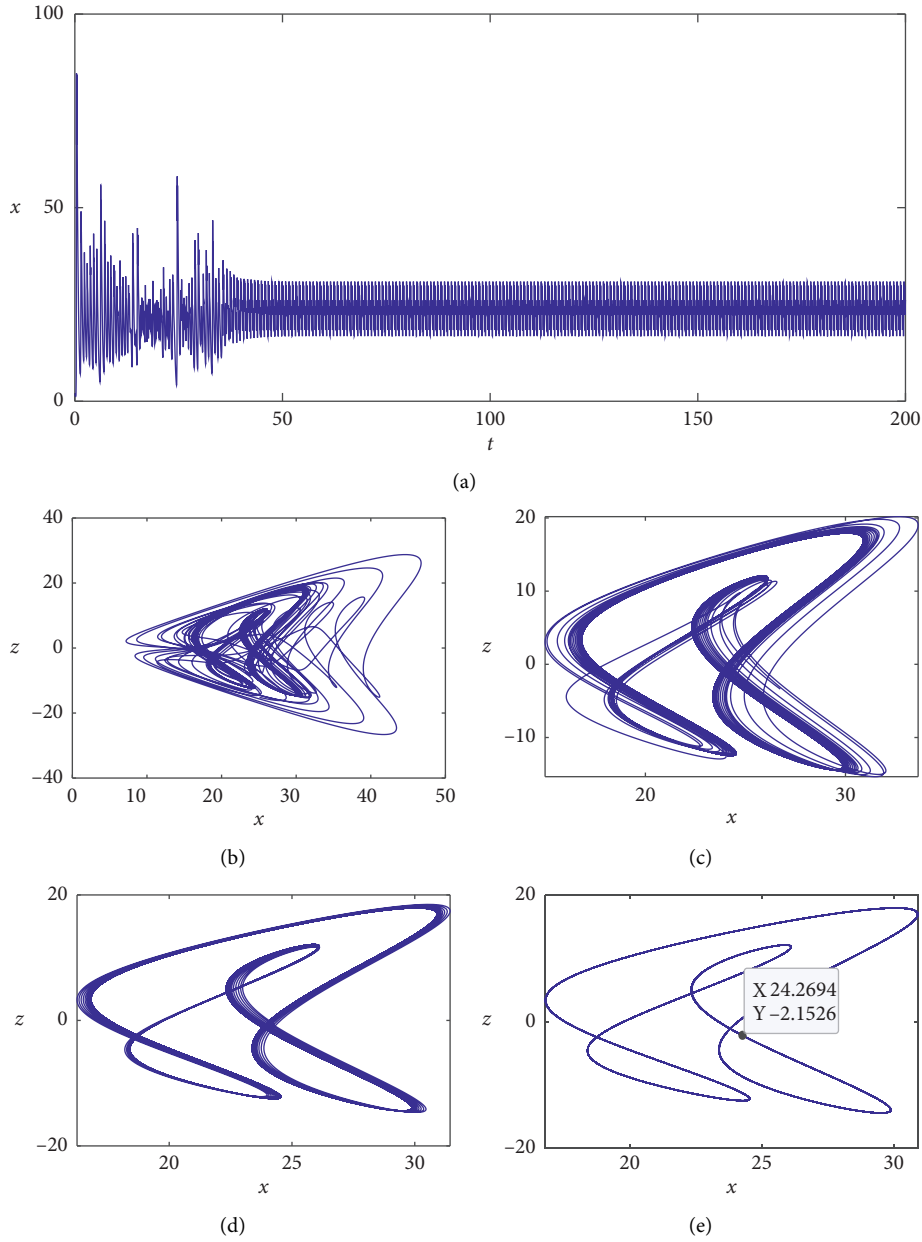


FIGURE 6: Transient chaos, steady-state period-2. (a) Time-domain waveform of  $x$  in the time interval  $[0, 200]$ , (b) phase portrait of the chaotic attractor in the  $x$ - $z$ , (c) chaotic attractor, (d) phase portrait of multiperiod, and (e) steady-state period-2. Under the initial values  $(2, 1, 1, 2, 2)$  and system parameter  $a = 3.2$ .

burning, the chaotic phase portraits will change from Figures 6(b)–6(e), which needs the same time interval (about  $[0, 100]$ ) to completely change from chaos to period. Figures 6(b) and 6(c) are transient chaotic attractors, and Figures 6(d) and 6(e) are steady-state periodic states. Figure 6(a) is the time-domain waveform of state variable  $x$ , which is different from the time series generated by the general chaotic system. Before  $t = 40$ , the system is in chaotic state, and then it will slowly convert to periodic state.

#### 4. Electronic Circuit Design

Using hardware circuit to realize the chaos mathematical model is a hot issue in practical application. The circuit design diagram of the 5D memristive hyperchaotic system (4) is shown in Figure 8. In the circuit design, LF347 is used as the operational amplifier, AD633JN is used as the multiplier chip, and the multiplication factor is  $0.1/V$ . The operating voltage of the operational amplifier is  $\pm E = \pm 15$  V, and the actual saturation voltage

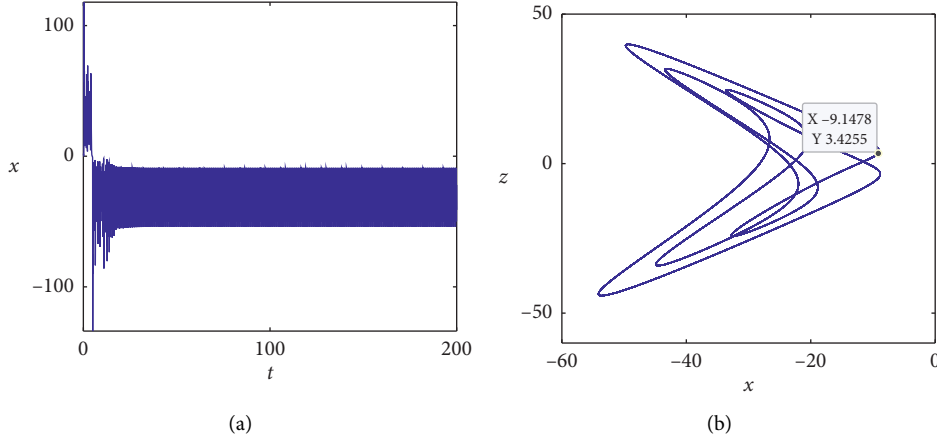


FIGURE 7: Transient chaos, stable state period-3. (a) Time-domain waveform of  $x$  in the time interval  $[0, 200]$  and (b) stable state period-3, under the initial values  $(2, 1, 1, 2, 2)$  and system parameter  $a = 11.5$ .

measured by the operational amplifier and multiplier is  $\pm|V_{\text{sat}}| \approx \pm 13.5 \text{ V}$ . Since the variables in the phase portraits shown in Figure 1 are beyond the linear dynamic range, we must scale the system, and the relevant circuit equations are as follows:

$$\begin{cases} \dot{v}_x = -\frac{1}{R_1 C_x} v_x + \frac{1}{10 \cdot R_2 C_x} v_y v_z, \\ \dot{v}_y = \frac{1}{R_3 C_y} v_y - \frac{1}{10 \cdot R_4 C_y} v_x v_z, \\ \dot{v}_z = \frac{1}{10 \cdot R_5 C_z} v_x v_y - \frac{1}{R_6 C_z} v_z - \frac{1}{C_z} \left( \frac{R v_w}{R_{11}} + \frac{R}{100 R_{12}} v_u^2 v_w \right), \\ \dot{v}_w = \frac{1}{10 \cdot R_8 C_w} v_x v_y - \frac{1}{R_9 C_w} v_w, \\ \dot{v}_u = \frac{1}{R_{10} C_u} v_z, \end{cases} \quad (9)$$

where  $R_1 = R/a$ ,  $R_3 = R/b$ ,  $R_6 = R/c$ ,  $R_9 = R/e$ ,  $R_{11} = R/dm$ , and  $R_{12} = R/(100 \cdot 3dn)$ . According to the parameters given in system (4),  $b = 12$ ,  $c = 30$ ,  $d = 2$ ,  $e = 4$ ,  $m = 0.1$ , and  $n = 0.01$ , we set  $C_x = C_y = C_z = C_w = C_u = C = 10 \text{ nF}$ ,  $R = 100 \text{ k}\Omega$ ,  $R_2 = R_4 = R_5 = R_8 = 10 \text{ k}\Omega$ ,  $R_3 = 8.25 \text{ k}\Omega$ ,  $R_6 = 3.32 \text{ k}\Omega$ ,  $R_9 = 25 \text{ k}\Omega$ ,  $R_{11} = 500 \text{ k}\Omega$ , and  $R_{12} = 16.5 \text{ k}\Omega$ . Figure 9 shows the phase portraits which are obtained by Multisim simulator. Compared with the MATLAB simulation Figure 4, it can be clearly seen that the phase portraits of Figure 9 and system (4) in initial condition  $(2, 1, 1, 2, 2)$  are exactly the same, which confirm the correctness of the proposed 5D memristive hyperchaotic system (4).

## 5. RNG Design with the Novel Multistable 5D Memristive Hyperchaotic System

**5.1. The Design of RNG.** Random numbers are widely used in image encryption, information security, computer, and other fields, so the research on RNGs is particularly

important. Because the chaotic system has high sensitivity and strong complexity to parameters and initial conditions, random numbers generated by using the chaotic system as an entropy source of RNG have strong randomness. Algorithm 1 is a pseudocode for designing a RNG. As shown in Algorithm 1, (1) the initial conditions of the chaotic system, step value  $\Delta h$ , and sampling interval are given; (2) the fourth-order Runge–Kutta algorithm (RK4) is used to solve the differential equation of the chaotic system to obtain the 32 bit output of the chaotic system, in which 0–21 bit are used for the design of the RNG; (3) XOR the output 22 bit  $x$ ,  $y$ ,  $z$ , and  $w$ , respectively, to improve the randomness; (4) the abovementioned two steps to obtain the test bit stream are combined

In order to better evaluate the performance of generating random numbers of chaotic systems, NIST 800.22 with international high standard is used for random test. NIST 800.22 includes 15 test methods: frequency test, run test, overlapping templates test, linear complexity test, etc. The 22 bit sequence generated from the chaotic system must be large enough for RNG test. If the  $p$  value<sub>T</sub> of NIST 800.22 is more than 0.0001, it shows that the  $p$  value<sub>T</sub> is uniformly distributed and the sequence is random. NIST test is carried out with 130 sample sequences of 1M bit length generated by the chaotic random number generator. The test results are shown in Table 3. All  $p$  value<sub>T</sub> are greater than the threshold value of 0.0001, so RNG passed the test. The lowest pass rate for each statistical test is about 0.975.

## 5.2. Security Analyses

**5.2.1. Key Space Analysis.** The main purpose of designing a random number sequence generator is encryption, and the size of key space determines the ability to withstand exhaustive attack. The larger the key space, the better the encryption effect. In order to ensure the security of encryption, the key space should be greater than  $2^{128}$ . In this paper, the proposed multistable 5D memristive hyperchaotic system is used to construct a RNG, which can effectively increase the size of the key space. Five 16 bit keys are used to



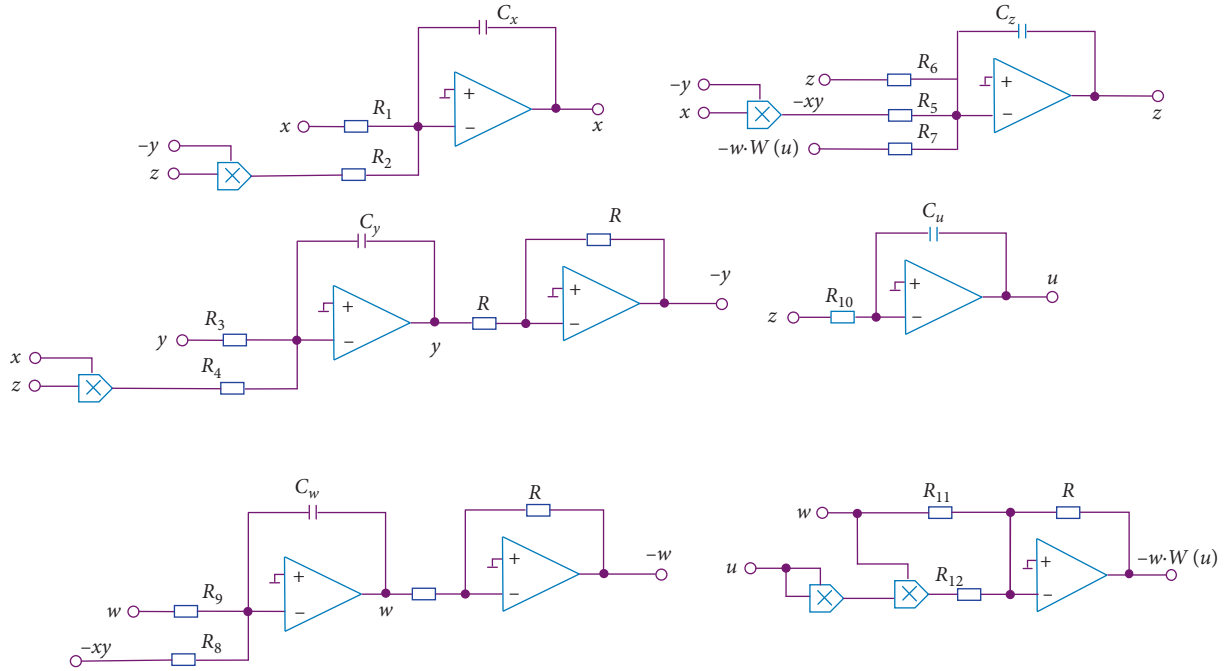


FIGURE 8: Circuit diagram of memristive chaotic system (4).

set the initial conditions  $(x_0, y_0, z_0, w_0, u_0)$  of the hyperchaotic system, and seven 16 bit keys are used to set the parameters  $a, b, c, d, e, f,$  and  $g$  of the hyperchaotic system. There are 192 bit keys in total, so the key space of this paper is  $2^{192} > 2^{128}$ , so the method used in this paper can effectively resist exhaustive attack.

**5.2.2. Key Sensitivity Analysis.** The chaos system is very sensitive to the initial value, so the random numbers generated by the chaotic system have good randomness. Generally, we make small changes to the initial value, and then judge the initial value sensitivity of the RNG by the bit change rate of two sequences. The closer the bit change rate is to 50%, the more sensitive it is to the initial value. Given  $x(0) = 2$ ,  $x(0)' = 2.00000001$ ,  $a = 10$ , and  $a' = 10.00000001$  and the length of random number sequence is 10120000 bits, the change rate of bit with initial value is shown in Table 4. It can be seen that when the random sequence changes only  $10^{-8}$ , the system's bit change rate is close to 50%, so the random sequence generator is very sensitive to the initial value of the 5D hyperchaotic system. Figure 10 is a time-domain waveform obtained by 50 iterations of the abovementioned two initial values. Figures 10(a) and 10(b) are time-domain oscillograms when the parameter value  $a$  and initial condition  $x$  change, respectively. The blue line represents the sequence generated when the system parameter value remains unchanged, and the red line represents the sequence generated by iteration when the initial value changes. As shown in Figure 10, when  $t \in [0, 8]$ , the sequence curves of two different initial values coincide completely. After  $t = 8$ , the sequence curves of different initial values begin to separate, and the difference is more obvious with the increase of time. All the above

show that the RNG is very sensitive to the initial value and small initial value changes will have a great impact on the sequence.

**5.2.3. Correlation Analysis.** Correlation is another important measure of randomness. For an ideal random number sequence, the autocorrelation function is  $\delta$ . The cross-correlation function is 0. Figure 11 is the correlation graph of two random sequences generated by the RNG, given the initial conditions  $x(0) = 2$  and  $x(0)' = 2.00000001$ . Figure 11(a) is the autocorrelation graph of the sequence, and Figure 11(b) is the crosscorrelation graph of the sequence. From these two figures, it can be seen that the random sequence generated by the RNG based on the 5D hyperchaotic system has strong randomness. In order to further verify the key sensitivity of the generated random number, two similar equal length sequences are generated by the RNG through small changes in the initial value of the system, and the correlation coefficient is used for testing. Correlation coefficient can measure the statistical relationship between sequences. If the correlation coefficient is zero, then there is no correlation between the two sequences. If it is  $\pm 1$ , then there is a strong correlation between the two sequences. In the experiment, one initial condition of the 5D chaotic system (4) changes  $10^{-8}$ , all system parameters remain unchanged, and two groups of random sequences with a length of 4048000 bits are generated. The correlation value is calculated by MATLAB, and Table 5 is obtained. It can be noted that the correlation values obtained by changing the five initial conditions are very close to zero, so there is almost no correlation between the two sequences. This shows that the random number produced in this paper is very sensitive to the initial value.

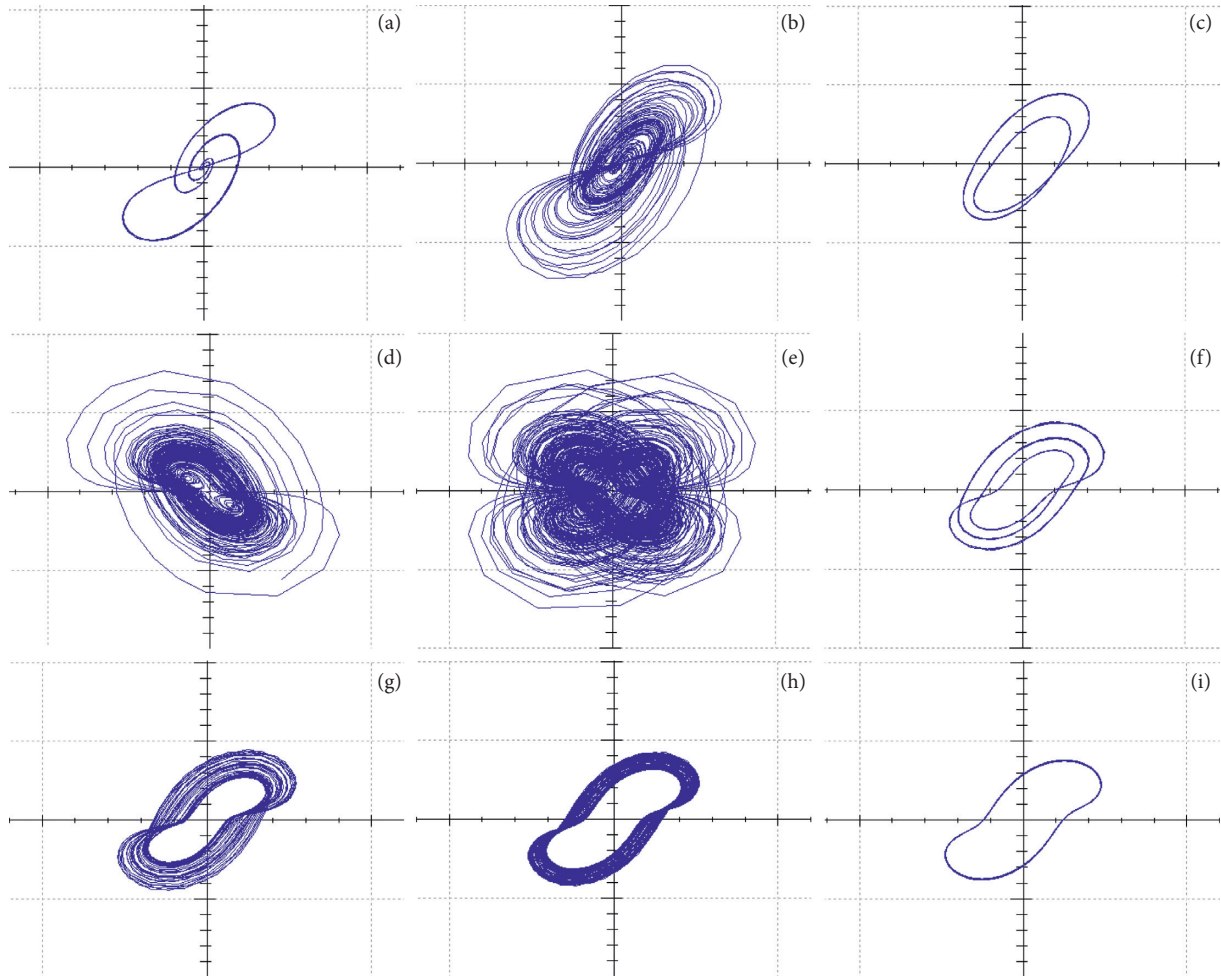


FIGURE 9: Various attractors with different values of resistance  $R_1$  in the  $y$ - $z$  plane observed from multisim simulation: (a)  $R_1 = 100 \text{ k}\Omega$ , (b)  $R_1 = 50 \text{ k}\Omega$ , (c)  $R_1 = 31.6 \text{ k}\Omega$ , (d)  $R_1 = 12.5 \text{ k}\Omega$ , (e)  $R_1 = 10 \text{ k}\Omega$ , (f)  $R_1 = 8.5 \text{ k}\Omega$ , (g)  $R_1 = 6.81 \text{ k}\Omega$ , (h)  $R_1 = 6.0 \text{ k}\Omega$ , and (i)  $R_1 = 5.5 \text{ k}\Omega$ .

```

(1) start
(2) Given the initial condition, parameter value, step value  $\Delta h$  and sampling interval of chaotic system (4);
(3) while (least 100 M. Bit data) do
(4) Using RK4 algorithm to solve chaotic system (4), 32 bit  $x, y, z, w, u$  has obtained;
(5) Select the last 22 bit number of 32 bit  $x, y, z,$  and  $w$ ;
(6) Obtain the bit stream of the chaotic system (4) by XOR  $x$  and  $y, z,$  and  $w$ ;
(7) Get test bit stream according to 5 and 6;
(8) end while
(9) End

```

ALGORITHM 1: RNG design algorithm pseudocode.

## 6. Image Encryption

With the rapid development of computer technology, image information acquisition, processing, transmission, and other related technologies have been rapidly developed and applied and have been widely studied by scholars [101–110]. Among them, image encryption plays an increasingly important role in the fields of information security, military, medicine, and meteorology and has become a hot issue of social concern. Chaotic systems show good randomness

because of their strong initial value and parameter sensitivity, and they are widely used in the field of image encryption [111–120]. In this section, as a typical application, we will use the random number generated by the proposed RNG for image encryption.

Suppose the size of the original image is  $m \times n$ , where  $m$  and  $n$  are the number of rows and columns of the image pixel matrix, respectively, and the pixel gray value is an integer between 0 and 255. The specific operation steps of encrypting image with random number are as follows:

TABLE 3: The results of RNG NIST 800.22 tests.

NIST statistical test	$p$ value $_T$	Proportion	Result
Frequency (monobit) test	0.037157	0.975	Successful
Block frequency test	0.706149	0.983	Successful
Cumulative sums test	0.287306/0.204076	0.983/0.983	Successful
Runs test	0.602458	0.983	Successful
Longest-run test	0.074177	1	Successful
Binary matrix rank test	0.422034	0.983	Successful
Discrete fourier transform test	0.392456	1	Successful
Nonoverlapping templates test	0.605808	0.9875	Successful
Overlapping templates test	0.804337	1	Successful
Maurer's universal statistical test	0.602458	0.975	Successful
Approximate entropy test	0.195163	0.9917	Successful
Random excursions test	0.407530	0.9844	Successful
Random excursions variant	0.455004	0.9861	Successful
Serial test 1	0.551026	0.975	Successful
Serial test 2	0.637119	1	Successful
Linear complexity test	0.985035	1	Successful

TABLE 4: Initial value sensitivity analysis of random sequences.

Initial value	Amount of change	Changed number of bits	$p$ (%)
$x(0)$	$10^{-8}$	5060283	50.0028
$a$	$10^{-8}$	5059553	49.9956

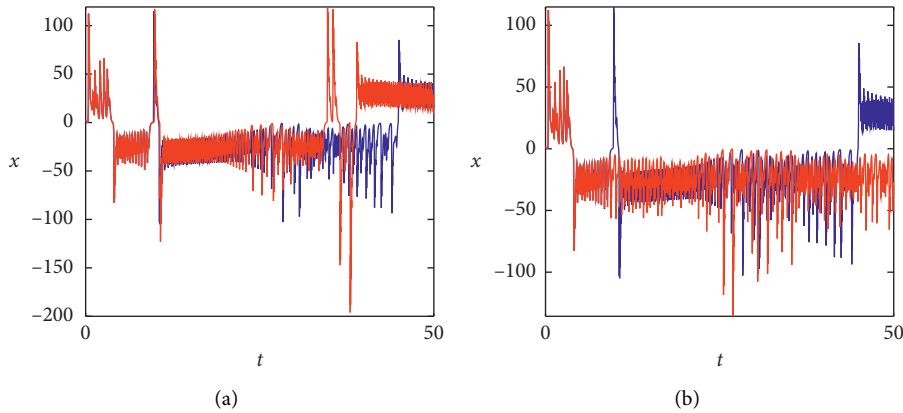


FIGURE 10: Time-domain waveform of  $x$  in the time interval  $[0, 50]$ . (a) parameters  $a = 10$  and  $a' = 10.00000001$  and (b) initial values  $x(0) = 2$  and  $x(0)' = 2.00000001$ .

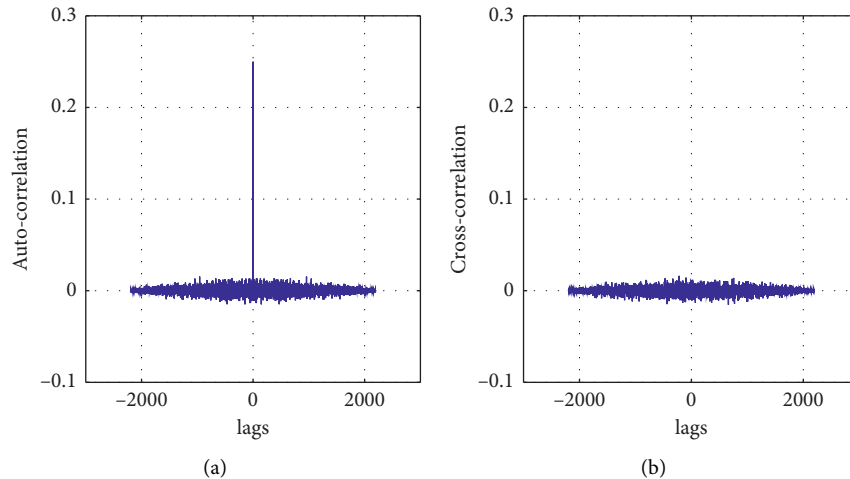


FIGURE 11: Correlation of random sequences: (a) autocorrelation and (b) crosscorrelation.

TABLE 5: Correlation value of random sequence.

Initial conditions	Amount of change	Changed value	Correlation value
$x(0) = 2$	$10^{-8}$	$x(0)' = 2.00000001$	0.00066917
$y(0) = 1$	$10^{-8}$	$x(0)' = 1.00000001$	-0.00047467
$z(0) = 1$	$10^{-8}$	$x(0)' = 1.00000001$	0.0017
$w(0) = 2$	$10^{-8}$	$x(0)' = 2.00000001$	0.00071957
$u(0) = 2$	$10^{-8}$	$x(0)' = 2.00000001$	-0.00069381

Step 1: using the proposed multistable 5D memristive hyperchaotic system, the random sequence is generated iteratively according to the given system parameters and initial conditions.

Step 2: transform the pixels in the image into a one-dimensional sequence  $I$  with a length of  $m \times n$  in the order of traversal hierarchy.

Step 3: ensure the randomness of the sequence and discard the previous  $n$  iterations. Continue the iteration to generate the binary sequence of  $m \times n \times 8$  bits. Then, we convert every 8 bits of binary sequence into an integer, ranging from 0 to 255. Finally, we get an integer sequence of length  $m \times n$ :  $i = 1, 2, \dots, M \times N$ .

Step 4: use the random sequence generated by the system to scramble all the pixel values in one-dimensional sequence  $I$  to get the scrambled sequence  $I'$ .

Step 5: store the generated image as the final encrypted image.

Decryption is the reverse of encryption.

**6.1. Simulation Results.** In this paper, the Lena image with the size of  $256 \times 256$  is used as the encrypted plain image (note that the same photo is used in all subsequent safety analysis comparisons with other references), and the keys are  $a = 10$ ,  $b = 12$ ,  $c = 30$ ,  $d = 2$ ,  $e = 4$ ,  $m = 0.1$ , and  $n = 0.01$  and  $(x_1(0), x_2(0), x_3(0), x_4(0), x_5(0)) = (2, 1, 1, 2, 2)$ . The results of encryption and decryption of Lena images are shown in Figure 12, where Figure 12(a) is the original plain image, Figure 12(b) is the encrypted image, and Figure 12(c) is the decrypted image successfully decrypted using the key. It can be seen that the encrypted image does not have the characteristics of the original plain image, and the decrypted image is exactly the same as the original plain image.

## 6.2. Security Analyses

**6.2.1. Histogram Analysis.** Histogram is used to display the distribution characteristics of pixels. In the encryption algorithm, changing the distribution characteristics is very important. If the probability of all intensity pixels generated is equal in the histogram of the encrypted image, the encryption has a high degree of symmetry and good uniformity. Figures 13(a) and 13(b), respectively, represent the histogram of the plain image and the encrypted image. It can be seen that the original plain image has obvious statistical characteristics, while the probability of each gray value of the

encrypted image is almost equal. Therefore, encrypted images can effectively resist statistical analysis attacks.

**6.2.2. Correlation Analysis.** There is usually a strong correlation between adjacent pixels in an image, so a good encryption algorithm should be able to produce cipher images with low correlation, so as to hide image information and resist statistical attacks. The correlation of adjacent pixels is determined by the following formula:

$$r_{x,y} = \frac{E((x - E(x))(y - E(y)))}{\sqrt{D(x)D(y)}}, \quad (10)$$

where

$$E(x) = \frac{1}{N} \sum_{i=1}^N x_i, \quad (11)$$

$$D(x) = \frac{1}{N} \sum_{i=1}^N (x_i - E(x))^2,$$

where  $E(x)$  and  $D(x)$  represent the expectation and variance of the variable  $x$ , and  $r_{x,y}$  is the correlation coefficient of adjacent pixels  $x$  and  $y$ . Figure 14 shows the phase diagrams of Lena plain text image and cipher text image with adjacent pixel points in all directions upward (where (a) and (b) are horizontal directions, (c) and (d) are vertical directions, and (e) and (f) are diagonal directions). It can be seen from these figures that the adjacent pixel values of the plain image are located near the line with slope 1, indicating that the two adjacent pixels are highly correlated. The pixel values of the cipher image are scattered throughout the region, indicating a low correlation between the adjacent pixels. Table 6 shows the test values of correlation in three directions: horizontal, vertical, and diagonal. It can be seen that the adjacent pixels of the plain image have high correlation ( $r_{x,y} \rightarrow 1$ ), and the adjacent pixels of the cipher image have low correlation ( $r_{x,y} \rightarrow 0$ ). At the same time, compared with the corresponding results of References [111–114], it shows that the proposed encryption algorithm has lower correlation between adjacent pixels and can more effectively resist statistical attacks.

**6.2.3. Information Entropy.** Information entropy is an important index to reflect the randomness of information. The more uniform the distribution of pixel gray value, the greater the information entropy, the greater the randomness, and the higher the security. The calculation formula is as follows:

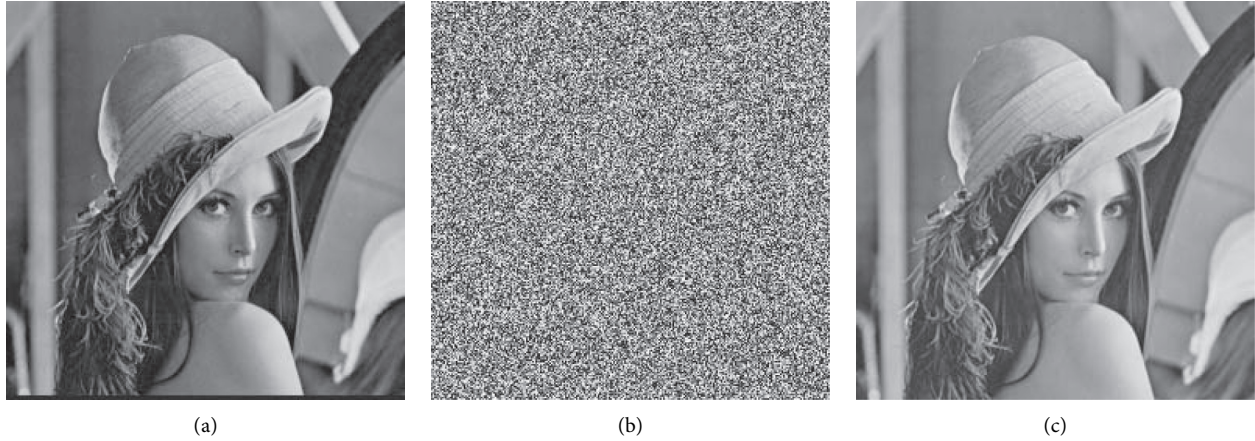


FIGURE 12: Image encryption and decryption. (a) Original plain image, (b) cipher image, and (c) decryption image.

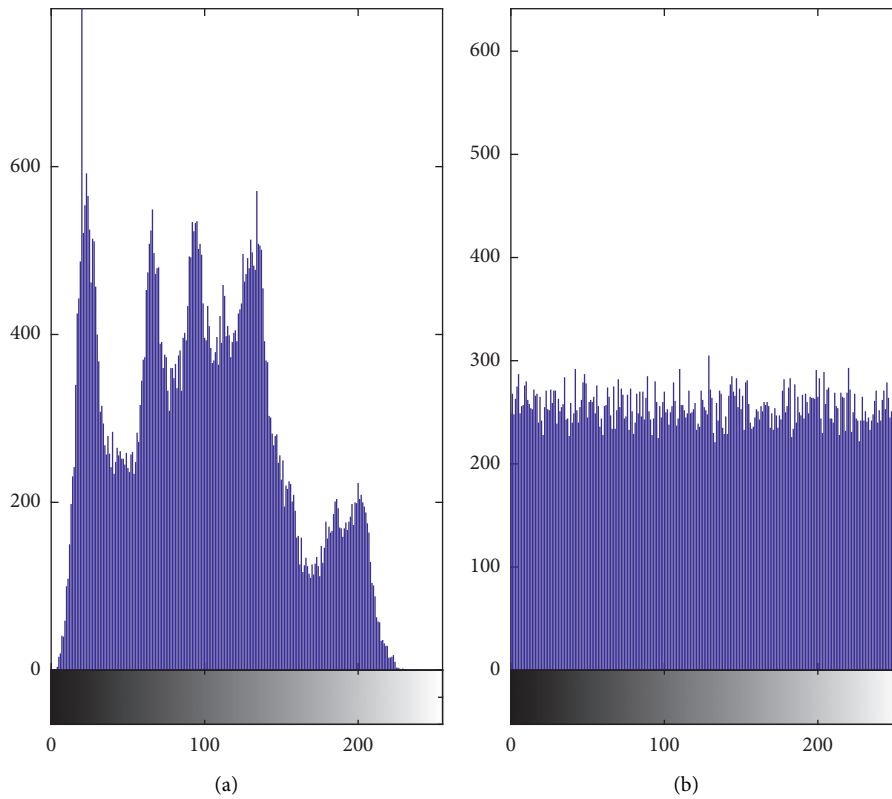


FIGURE 13: Histogram of (a) plain image and (b) cipher image.

$$H = \sum_{i=1}^{256} p_i \log_2 \frac{1}{p_i}, \quad (12)$$

where  $p_i$  is the probability of occurrence of pixel points with a pixel value of  $i$ . For grayscale images, the ideal value of information entropy is 8. As listed in Table 7, by comparing the information entropy of cipher and the cipher images in References [115–118], it can be concluded that the information entropy value of the encrypted images in the algorithm in this paper is closer to the ideal value 8, and the

encrypted images are closer to the random signal source, which can effectively resist the entropy attack.

**6.2.4. Differential Attack.** Pixels change rate (Number of Pixels Change Rate, NPCR) and normalized pixels flat change strong degree (Unified Average Changing Intensity, UACI) can be used to measure to express the sensitivity of the encryption algorithm, which is an important indicator of measuring algorithm ability to resist differential attack. NPCR and UACI, respectively, represent the proportion and



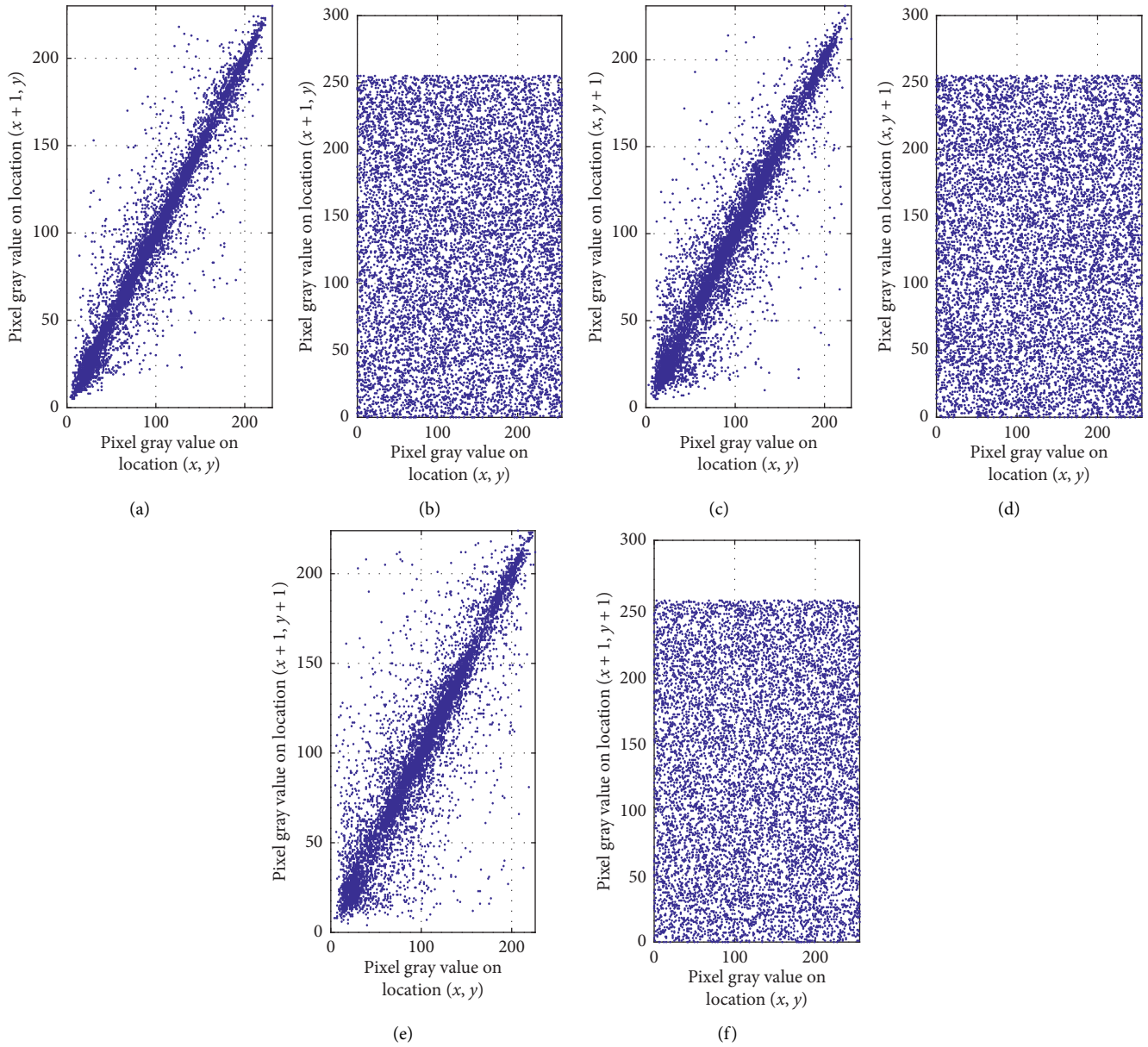


FIGURE 14: Correlation of two adjacent pixels of the plain image lena ( $256 \times 256$ ) and its cipher image. (a) Horizontal direction in plain image, (b) horizontal direction in cipher image, (c) vertical direction in plain image, (d) vertical direction in cipher image, (e) diagonal direction in plain image, and (f) diagonal direction in cipher image.

TABLE 6: Correlation coefficients of the plain and cipher images.

Image	Plain image			Cipher image		
	Horizontal	Vertical	Diagonal	Horizontal	Vertical	Diagonal
Ours	0.94505	0.96653	0.91917	0.00068299	-0.0007768	-0.0036362
Reference [111]	0.964227	0.982430	0.965609	-0.038118	-0.029142	0.002736
Reference [112]	0.812688	0.837959	0.782053	0.001251	-0.003543	0.001449
Reference [113]	0.91848	0.82921	0.80731	0.011899	0.018062	0.036784
Reference [114]	0.97165	0.98730	0.95440	0.00312	-0.00317	-0.00310



TABLE 7: The results of information entropy.

Image	Ours	Reference [115]	Reference [116]	Reference [117]	Reference [118]
Results	7.9974	7.9971	7.8232	7.9963	7.9951

TABLE 8: The results of NPCR and UACI compared to other state-of-the-art algorithms.

Image	Ours	Reference [111]	Reference [118]	Reference [119]	Reference [120]
NPCR	99.5956	99.6114	99.5511	99.57	99.58
UACI	33.4535	33.4523	33.3461	33.31	33.43

degree of change in the pixel value of the corresponding position. The larger the proportion and the higher the degree of change, the stronger the antiattack capability of the algorithm. The calculation formulas are as follows:

$$\left\{ \begin{array}{l} \text{NPCR} = \frac{\sum_{i=1}^M \sum_{j=1}^N D(i, j)}{M \times N} \times 100\%, \\ D(i, j) = \begin{cases} c1, & P_1(i, j) \neq P_2(i, j), \\ 0, & \text{otherwise,} \end{cases} \\ \text{UACI} = \frac{1}{M \times N} \frac{\sum_{i=1}^M \sum_{j=1}^N (P_1(i, j) - P_2(i, j))}{255} \times 100\%, \end{array} \right. \quad (13)$$

where  $M \times N$  is the size of the image,  $P_1(i, j)$  and  $P_2(i, j)$ , respectively, represent the pixel values of the positions corresponding to the plain and cipher. When the NPCR and UACI of the image are close to the ideal values of 99.6094070% and 33.4635070%, the algorithm has good safety [112, 121]. As listed in Table 8, the algorithm in this paper is more sensitive to the plain than the NPCR and UACI values in References [111–120] can meet the security requirements and have a good ability to resist differential attacks.

## 7. Conclusion

In this study, a novel multistable 5D memristive hyperchaotic system with line equilibrium is first introduced. Dynamical analysis is performed in terms of phase portraits, Lyapunov exponential spectrum, bifurcation diagram, and spectral entropy. Several interesting properties such as multistability and transient chaos have been revealed by using classical nonlinear analysis tools. Then, an electronic circuit is designed, and its accuracy is verified by Multisim simulation. As the engineering application, a new chaos-based RNG is designed and internationally accepted NIST 800.22 random tests are run. Security analyses are carried out and they have proved that the design can be used in cryptography applications. Finally, a chaotic image encryption is proposed based on the random number sequences; security analyses show that the algorithm has good security and can resist common attacks.

## Data Availability

The data used to support the findings of this study are available from the corresponding author upon request.

## Conflicts of Interest

The authors declare that they have no conflicts of interest.

## Acknowledgments

This work was supported by the National Natural Science Foundation of China under Grants 61504013, 61702052, 61772087, 61741104, 61674054, and 61901169, Natural Science Foundation of Hunan Province under Grants 2019JJ50648, 2016jj2005, 2017JJ2049, and 2019JJ40190, Scientific Research Fund of Hunan Provincial Education Department under Grant 18A137, National Key Research and Development Project under Grant 2018YFE0111200, Guizhou Provincial Science and Technology Foundation under Grant [2018]1115, and Guizhou Province Science and Technology Plan Project under Grant [2018]5769.

## References

- [1] F. Yu, C. H. Wang, J. W. Yin et al., "Novel four-dimensional autonomous chaotic system generating one-, two-, three- and four-wing attractors," *Chinese Physics B*, vol. 20, no. 11, Article ID 110505, 2011.
- [2] Q. Deng and C. Wang, "Multi-scroll hidden attractors with two stable equilibrium points," *Chaos*, vol. 29, no. 9, Article ID 093112, 2019.
- [3] X. Zhang, C. Wang, W. Yao, and H. Lin, "Chaotic system with bondorbital attractors," *Nonlinear Dynamics*, vol. 97, no. 4, pp. 2159–2174, 2019.
- [4] S. Çiçek, A. Ferikoğlu, and İ. Pehlivan, "A new 3D chaotic system: dynamical analysis, electronic circuit design, active control synchronization and chaotic masking communication application," *Optik*, vol. 127, no. 8, pp. 4024–4030, 2016.
- [5] F. Yu, L. Gao, K. Gu, B. Yin, Q. Wan, and Z. Zhou, "A fully qualified four-wing four-dimensional autonomous chaotic system and its synchronization," *Optik*, vol. 131, pp. 79–88, 2017.
- [6] M. Saleh, C. K. Volos, K. Sezgin et al., "A chaotic system with infinite number of equilibria located on an exponential curve and its chaos-based engineering application," *International Journal of Bifurcation and Chaos*, vol. 28, no. 9, Article ID 1850112, 2018.
- [7] F. Yu, P. Li, K. Gu, and B. Yin, "Research progress of multi-scroll chaotic oscillators based on current-mode devices," *Optik*, vol. 127, no. 13, pp. 5486–5490, 2016.

- [8] C. Wang, X. Liu, and H. Xia, "Multi-piecewise quadratic nonlinearity memristor and its  $2N$ -scroll and  $2N+1$ -scroll chaotic attractors system," *Chaos*, vol. 27, no. 3, Article ID 033114, 2017.
- [9] L. L. Zhou, F. Tan, and F. Yu, "A robust synchronization-based chaotic secure communication scheme with double-layered and multiple hybrid networks," *IEEE Systems Journal*, 2019.
- [10] L. Zhou and F. Tan, "A chaotic secure communication scheme based on synchronization of double-layered and multiple complex networks," *Nonlinear Dynamics*, vol. 96, no. 2, pp. 869–883, 2019.
- [11] F. Yu, Z. Zhang, L. Liu et al., "Secure communication scheme based on a new 5D multistable four-wing memristive hyperchaotic system with disturbance inputs," *Complexity*, vol. 2020, Article ID 5859273, 16 pages, 2020.
- [12] F. Yu, S. Qian, X. Chen et al., "A new 4D four-wing memristive hyperchaotic system: dynamical analysis, electronic circuit design, shape synchronization and secure communication," *International Journal of Bifurcation and Chaos*, 2020.
- [13] Q. Yin and C. H. Wang, "A new chaotic image encryption scheme using breadth-first search and dynamic diffusion," *International Journal of Bifurcation and Chaos*, vol. 28, no. 4, Article ID 1850047, 2018.
- [14] S. Wang, C. Wang, and C. Xu, "An image encryption algorithm based on a hidden attractor chaos system and the Knuth-Durstenfeld algorithm," *Optics and Lasers in Engineering*, vol. 128, Article ID 105995, 2020.
- [15] G. Cheng, C. Wang, and H. Chen, "A novel color image encryption algorithm based on hyperchaotic system and permutation-diffusion architecture," *International Journal of Bifurcation and Chaos*, vol. 29, no. 9, Article ID 1950115, 2019.
- [16] F. Yu, L. Liu, L. Xiao, K. Li, and S. Cai, "A robust and fixed-time zeroing neural dynamics for computing time-variant nonlinear equation using a novel nonlinear activation function," *Neurocomputing*, vol. 350, pp. 108–116, 2019.
- [17] L. Zhou, F. Tan, F. Yu, and W. Liu, "Cluster synchronization of two-layer nonlinearly coupled multiplex networks with multi-links and time-delays," *Neurocomputing*, vol. 359, pp. 264–275, 2019.
- [18] W. Yao, C. Wang, J. Cao, Y. Sun, and C. Zhou, "Hybrid multisynchronization of coupled multistable memristive neural networks with time delays," *Neurocomputing*, vol. 363, pp. 281–294, 2019.
- [19] J. Jin, L. Zhao, M. Li, F. Yu, and Z. Xi, "Improved zeroing neural networks for finite time solving nonlinear equations," *Neural Computing and Applications*, 2019.
- [20] F. Tan, L. Zhou, F. Yu, and J. Lu, "Fixed-time continuous stochastic synchronisation of two-layer dynamical networks," *International Journal of Systems Science*, vol. 51, no. 2, pp. 242–257, 2020.
- [21] H. Lin and C. Wang, "Influences of electromagnetic radiation distribution on chaotic dynamics of a neural network," *Applied Mathematics and Computation*, vol. 369, Article ID 124840, 2020.
- [22] X. Yang, Q. Zhu, and C. Huang, "Lag stochastic synchronization of chaotic mixed time-delayed neural networks with uncertain parameters or perturbations," *Neurocomputing*, vol. 74, no. 10, pp. 1617–1625, 2017.
- [23] Y.-Y. Huang, Y.-H. Wang, and Y. Zhang, "Shape synchronization of drive-response for a class of two-dimensional chaotic systems via continuous controllers," *Nonlinear Dynamics*, vol. 78, no. 4, pp. 2331–2340, 2014.
- [24] F. Yu and Y. Song, "Complete switched generalized function projective synchronization of a class of hyperchaotic systems with unknown parameters and disturbance inputs," *Journal of Dynamic Systems, Measurement, and Control-Transactions of the ASME*, vol. 136, no. 1, Article ID 014505, 2014.
- [25] Y. Huang, Y. Wang, H. Chen, and S. Zhang, "Shape synchronization control for three-dimensional chaotic systems," *Chaos, Solitons & Fractals*, vol. 87, pp. 136–145, 2016.
- [26] F. Yu, C. Wang, Q. Wan, and Y. Hu, "Complete switched chaotic function projective synchronization of a five-term chaotic system with uncertain parameters and disturbances," *Pramana*, vol. 80, no. 2, pp. 223–235, 2013.
- [27] F. Yu, C. H. Wang, Y. Hu, and J. W. Yin, "Anti-synchronization of a novel hyperchaotic system with parameter mismatch and external disturbances," *Pramana*, vol. 79, no. 1, pp. 81–93, 2012.
- [28] X. Zhang and C. Wang, "A novel multi-attractor period multi-scroll chaotic integrated circuit based on CMOS wide adjustable CCCII," *IEEE Access*, vol. 7, no. 1, pp. 16336–16350, 2019.
- [29] J. Jie and L. V. Zhao, "Low voltage low power fully integrated chaos generator," *Journal of Circuits Systems & Computers*, vol. 27, no. 10, Article ID 1850155, 2018.
- [30] J. Jin, "Programmable multi-direction fully integrated chaotic oscillator," *Microelectronics Journal*, vol. 75, pp. 27–34, 2018.
- [31] M. Long, F. Peng, and Y. Zhu, "Identifying natural images and computer generated graphics based on binary similarity measures of PRNU," *Multimedia Tools and Applications*, vol. 78, no. 1, pp. 489–506, 2019.
- [32] Y.-S. Huang and Z.-Y. Wang, "Decentralized adaptive fuzzy control for a class of large-scale MIMO nonlinear systems with strong interconnection and its application to automated highway systems," *Information Sciences*, vol. 274, pp. 210–224, 2014.
- [33] Q. Xie, X. Wang, Z. Han, Y. Zuo, and M. Tang, "Immersion and invariance control of a class of nonlinear cascaded discrete systems," *Neurocomputing*, vol. 171, pp. 1661–1665, 2016.
- [34] Y.-S. Huang and M. Wu, "Robust decentralized direct adaptive output feedback fuzzy control for a class of large-scale nonaffine nonlinear systems," *Information Sciences*, vol. 181, no. 11, pp. 2392–2404, 2011.
- [35] F. Wang, L. Zhang, S. Zhou, and Y. Huang, "Neural network-based finite-time control of quantized stochastic nonlinear systems," *Neurocomputing*, vol. 362, pp. 195–202, 2019.
- [36] V. T. Pham, S. Vaidyanathan, E. Tlelo-Cuautle et al., "Memory circuit elements: complexity, complex systems, and applications," *Complexity*, vol. 2019, Article ID 4936123, 4 pages, 2019.
- [37] W. S. Sayed, A. G. Radwan, A. A. Rezk, and H. A. H. Fahmy, "Finite precision logistic map between computational efficiency and accuracy with encryption applications," *Complexity*, vol. 2017, Article ID 8692046, 21 pages, 2017.
- [38] Z. Xiong, S. Qu, and J. Luo, "Adaptive multi-switching synchronization of high-order memristor-based hyperchaotic system with unknown parameters and its application in secure communication," *Complexity*, vol. 2019, Article ID 3827201, 18 pages, 2019.
- [39] N. Nesa, T. Ghosh, and I. Banerjee, "Design of a chaos-based encryption scheme for sensor data using a novel logarithmic

- chaotic map,” *Journal of Information Security and Applications*, vol. 47, pp. 320–328, 2019.
- [40] R. Montero-Canela, E. Zambrano-Serrano, E. I. Tamariz-Flores, J. M. Muñoz-Pacheco, and R. Torrealba-Melendez, “Fractional chaos based-cryptosystem for generating encryption keys in Ad Hoc networks,” *Ad Hoc Networks*, vol. 97, Article ID 102005, 2020.
- [41] W. Wang, M. Si, Y. Pang et al., “An encryption algorithm based on combined chaos in body area networks,” *Computers & Electrical Engineering*, vol. 65, pp. 282–291, 2018.
- [42] C. Volos, J.-O. Maaita, S. Vaidyanathan, V.-T. Pham, I. Stouboulos, and I. Kyprianidis, “A novel four-dimensional hyperchaotic four-wing system with a saddle-focus equilibrium,” *IEEE Transactions on Circuits and Systems II: Express Briefs*, vol. 64, no. 3, pp. 339–343, 2017.
- [43] X. Zhang and C. H. Wang, “Multiscroll hyperchaotic system with hidden attractors and its circuit implementation,” *International Journal of Bifurcation and Chaos*, vol. 29, no. 9, Article ID 1950117, 2019.
- [44] V.-T. Pham, S. Vaidyanathan, C. Volos, S. Jafari, and S. T. Kingni, “A no-equilibrium hyperchaotic system with a cubic nonlinear term,” *Optik*, vol. 127, no. 6, pp. 3259–3265, 2016.
- [45] P. Daltzis, S. Vaidyanathan, V. T. Pham, C. Volos, E. Nistazakis, and G. Tombras, “Hyperchaotic attractor in a novel hyperjerk system with two nonlinearities,” *Circuits, Systems, and Signal Processing*, vol. 37, no. 2, pp. 613–635, 2018.
- [46] V. T. Pham, F. Rahma, M. Frasca et al., “Dynamics and synchronization of a novel hyperchaotic system without equilibrium,” *International Journal of Bifurcation and Chaos*, vol. 24, no. 6, Article ID 1450087, 2014.
- [47] Z. Wan, C. Wang, X. Luo, Y. Lin, and T. Huang, “Generating variable number of wings from a novel four-dimensional hyperchaotic system with one equilibrium,” *Optik*, vol. 125, no. 3, pp. 1371–1376, 2014.
- [48] L. Zhou, C. Wang, and L. Zhou, “A novel no-equilibrium hyperchaotic multi-wing system via introducing memristor,” *International Journal of Circuit Theory and Applications*, vol. 46, no. 1, pp. 84–98, 2018.
- [49] J. Jin and L. Cui, “Fully integrated memristor and its application on the scroll-controllable hyperchaotic system,” *Complexity*, vol. 2019, Article ID 4106398, 8 pages, 2019.
- [50] L. Xiong, Z. Liu, and X. Zhang, “Dynamical analysis, synchronization, circuit design, and secure communication of a novel hyperchaotic system,” *Complexity*, vol. 2017, Article ID 4962739, 23 pages, 2017.
- [51] A. Lassoued and O. Boubaker, “Dynamic analysis and circuit design of a novel hyperchaotic system with fractional-order terms,” *Complexity*, vol. 2017, Article ID 3273408, 10 pages, 2017.
- [52] Q. Zhao, C. H. Wang, and X. Zhang, “A universal emulator for memristor, memcapacitor, and meminductor and its chaotic circuit,” *Chaos*, vol. 29, no. 1, Article ID 013141, 2019.
- [53] M. E. Sahin, Z. G. Cam Taskiran, H. Guler, and S. E. Hamamci, “Simulation and implementation of memristive chaotic system and its application for communication systems,” *Sensors and Actuators A: Physical*, vol. 290, pp. 107–118, 2019.
- [54] G. Peng, F. Min, and E. Wang, “Circuit implementation, synchronization of multistability, and image encryption of a four-wing memristive chaotic system,” *Journal of Electrical and Computer Engineering*, vol. 2018, Article ID 8649294, 13 pages, 2018.
- [55] C. Wang, L. Xiong, J. Sun, and W. Yao, “Memristor-based neural networks with weight simultaneous perturbation training,” *Nonlinear Dynamics*, vol. 95, no. 4, pp. 2893–2906, 2018.
- [56] A. G. Radwan, A. T. Azar, S. Vaidyanathan, J. M. Muñoz-Pacheco, and A. Ouannas, “Fractional-order and memristive nonlinear systems: advances and applications,” *Complexity*, vol. 2017, Article ID 3760121, 2 pages, 2017.
- [57] L. Chua, “Memristor—the missing circuit element,” *IEEE Transactions on Circuit Theory*, vol. 18, no. 5, pp. 507–519, 1971.
- [58] D. B. Strukov, G. S. Snider, D. R. Stewart, and R. S. Williams, “The missing memristor found,” *Nature*, vol. 453, no. 7191, pp. 80–83, 2008.
- [59] F. Yu, L. Liu, B. He et al., “Analysis and FPGA realization of a novel 5D hyperchaotic four-wing memristive system, active control synchronization and secure communication application,” *Complexity*, vol. 2019, Article ID 4047957, 18 pages, 2019.
- [60] L. Zhou, C. Wang, and L. Zhou, “Generating hyperchaotic multi-wing attractor in a 4D memristive circuit,” *Nonlinear Dynamics*, vol. 85, no. 4, pp. 2653–2663, 2016.
- [61] C. Li and J. C. Sprott, “Multistability in the Lorenz system: a broken butterfly,” *International Journal of Bifurcation and Chaos*, vol. 24, no. 10, Article ID 1450131, 2014.
- [62] C. Li and J. C. Sprott, “Finding coexisting attractors using amplitude control,” *Nonlinear Dynamics*, vol. 78, no. 3, pp. 2059–2064, 2014.
- [63] Q. Lai, A. Akgul, X. W. Zhao et al., “Various types of coexisting attractors in a new 4D autonomous chaotic system,” *International Journal of Bifurcation and Chaos*, vol. 27, no. 9, Article ID 1750142, 2017.
- [64] B. Bao, T. Jiang, Q. Xu, M. Chen, H. Wu, and Y. Hu, “Coexisting infinitely many attractors in active band-pass filter-based memristive circuit,” *Nonlinear Dynamics*, vol. 86, no. 3, pp. 1711–1723, 2016.
- [65] X. Zhang and Z. Li, “Hidden extreme multistability in a novel 4D fractional-order chaotic system,” *International Journal of Non-linear Mechanics*, vol. 111, pp. 14–27, 2019.
- [66] S. Zhang, Y. Zeng, Z. Li et al., “Generating one to four-wing hidden attractors in a novel 4D no-equilibrium chaotic system with extreme multistability,” *Chaos*, vol. 28, no. 1, Article ID 013113, 2018.
- [67] B. Bao, T. Jiang, G. Wang, P. Jin, H. Bao, and M. Chen, “Two-memristor-based Chua’s hyperchaotic circuit with plane equilibrium and its extreme multistability,” *Nonlinear Dynamics*, vol. 89, no. 2, pp. 1157–1171, 2017.
- [68] B. A. Mezatio, M. T. Motchongom, B. R. Wafo Tekam, R. Kengne, R. Tchitnga, and A. Fomethé, “A novel memristive 6D hyperchaotic autonomous system with hidden extreme multistability,” *Chaos, Solitons & Fractals*, vol. 120, pp. 100–115, 2019.
- [69] V.-T. Pham, C. Volos, S. Jafari, and T. Kapitaniak, “Coexistence of hidden chaotic attractors in a novel no-equilibrium system,” *Nonlinear Dynamics*, vol. 87, no. 3, pp. 2001–2010, 2017.
- [70] F. Yu, H. Shen, L. Liu et al., “CCII and FPGA realization: a multistable modified fourth-order autonomous Chua’s chaotic system with coexisting multiple attractors,” *Complexity*, vol. 2020, Article ID 5212601, 17 pages, 2020.
- [71] L. Xiang, Y. Li, W. Hao, P. Yang, and X. Shen, “Reversible natural language watermarking using synonym substitution and arithmetic coding,” *CMC: Computers, Materials & Continua*, vol. 55, no. 3, pp. 541–559, 2018.

- [72] K. Gu, N. Wu, B. Yin et al., "Secure data sequence query framework based on multiple fogs," *IEEE Transactions on Emerging Topics in Computing*, 2019.
- [73] L. Xiang, X. Shen, J. Qin, and W. Hao, "Discrete multi-graph hashing for large-scale visual search," *Neural Processing Letters*, vol. 49, no. 3, pp. 1055–1069, 2019.
- [74] K. Gu, X. Dong, and L. Wang, "Efficient traceable ring signature scheme without pairings," *Advances in Mathematics of Communications*, 2019.
- [75] M. Long, F. Peng, and H.-Y. Li, "Separable reversible data hiding and encryption for HEVC video," *Journal of Real-Time Image Processing*, vol. 14, no. 1, pp. 171–182, 2018.
- [76] K. Gu, K. Wang, and L. Yang, "Traceable attribute-based signature," *Journal of Information Security and Applications*, vol. 49, pp. 102400–102416, 2019.
- [77] S. He, W. Zeng, K. Xie et al., "PPNC: privacy preserving scheme for random linear network coding in smart grid," *KSII Transactions on Internet and Information Systems*, vol. 11, no. 3, pp. 1510–1533, 2017.
- [78] L. Xiang, G. Guo, J. Yu et al., "A convolutional neural network-based linguistic steganalysis for synonym substitution steganography," *Mathematical Biosciences and Engineering*, vol. 17, no. 2, pp. 1041–1058, 2020.
- [79] Z. Xia, Z. Fang, F. Zou et al., "Research on defensive strategy of real-time price attack based on multiperson zero-determinant," *Security and Communication Networks*, vol. 2019, Article ID 6956072, 13 pages, 2019.
- [80] K. Gu, N. Wu, B. Yin, and W. J. Jia, "Secure data query framework for cloud and fog computing," *IEEE Transactions on Network and Service Management*, 2019.
- [81] Z. Liu, Z. Lai, W. Ou et al., "Structured optimal graph based sparse feature extraction for semi-supervised learning," *Signal Processing*, vol. 170, Article ID 107456, 2020.
- [82] K. Gu, W. Zhang, S.-J. Lim, P. K. Sharma, Z. Al-Makhadmeh, and A. Tolba, "Reusable mesh signature scheme for protecting identity privacy of IoT devices," *Sensors*, vol. 20, no. 3, p. 758, 2020.
- [83] J. J. He and B. Xu, "Quick pseudo-random topology optimization design based on triangle element," *Journal of Vibroengineering*, vol. 19, no. 4, pp. 2822–2843, 2017.
- [84] A. R. Ahmed, H. M. Ahmed, G. R. Ahmed et al., "Reconfigurable chaotic pseudo random number generator based on FPGA," *AEU-international Journal of Electronics and Communications*, vol. 98, pp. 174–180, 2019.
- [85] M. Narek, S. Konstantin, and S. George, "Spectral test of the MIXMAX random number generators," *Chaos, Solitons & Fractals*, vol. 118, pp. 242–248, 2019.
- [86] H. Xu, N. Massari, L. Gasparini, A. Meneghetti, and A. Tomasi, "A SPAD-based random number generator pixel based on the arrival time of photons," *Integration*, vol. 64, pp. 22–28, 2019.
- [87] R. S. Hasan, S. K. Tawfeeq, N. Q. Mohammed, and A. I. Khaleel, "A true random number generator based on the photon arrival time registered in a coincidence window between two single-photon counting modules," *Chinese Journal of Physics*, vol. 56, no. 1, pp. 385–391, 2018.
- [88] M. M. Abutaleb, "A novel true random number generator based on QCA nanocomputing," *Nano Communication Networks*, vol. 17, pp. 14–20, 2018.
- [89] C. Wannaboon, M. Tachibana, and W. San-Um, "A 0.18- $\mu\text{m}$  CMOS high-data-rate true random bit generator through  $\Delta\Sigma$  modulation of chaotic jerk circuit signals," *Chaos*, vol. 28, no. 6, Article ID 063126, 2018.
- [90] F. Yu, Q. Wan, J. Jin et al., "Design and FPGA implementation of a pseudorandom number generator based on a four-wing memristive hyperchaotic system and Bernoulli map," *IEEE Access*, vol. 7, pp. 181884–181898, 2019.
- [91] F. Yu, L. Li, Q. Tang, S. Cai, Y. Song, and Q. Xu, "A survey on true random number generators based on chaos," *Discrete Dynamics in Nature and Society*, vol. 2019, Article ID 2545123, 10 pages, 2019.
- [92] R. A. Elmanfaloty and E. Abou-Bakr, "Random property enhancement of a 1D chaotic PRNG with finite precision implementation," *Chaos, Solitons & Fractals*, vol. 118, pp. 134–144, 2019.
- [93] O. Katz, D. A. Ramon, and I. A. Wagner, "A robust random number generator based on a differential current-mode chaos," *IEEE Transactions on Very Large Scale Integration (VLSI) Systems*, vol. 16, no. 12, pp. 1677–1686, 2008.
- [94] Y. Liu and X. Tong, "Hyperchaotic system-based pseudo-random number generator," *IET Information Security*, vol. 10, no. 6, pp. 433–441, 2016.
- [95] A. Akgul, H. Calgan, I. Koyuncu, I. Pehlivan, and A. Istanbulu, "Chaos-based engineering applications with a 3D chaotic system without equilibrium points," *Nonlinear Dynamics*, vol. 84, no. 2, pp. 481–495, 2016.
- [96] Z. Wang, A. Akgul, V. T. Pham et al., "Chaos-based application of a novel no-equilibrium chaotic system with coexisting attractors," *Nonlinear Dynamics*, vol. 89, no. 46, pp. 1877–1887, 2017.
- [97] M. O. Meranza-Castillón, M. A. Murillo-Escobar, R. M. López-Gutiérrez, and C. Cruz-Hernández, "Pseudo-random number generator based on enhanced Hénon map and its implementation," *AEU—International Journal of Electronics and Communications*, vol. 107, pp. 239–251, 2019.
- [98] L. G. D. L. Fraga, E. Torres-Perez, and E. Tlelo-Cuautle, "Hardware implementation of pseudo-random number generators based on chaotic maps," *Nonlinear Dynamics*, vol. 90, no. 2, pp. 1661–1670, 2017.
- [99] A. Akhshani, A. Akhavan, A. Mobaraki, S.-C. Lim, and Z. Hassan, "Pseudo random number generator based on quantum chaotic map," *Communications in Nonlinear Science and Numerical Simulation*, vol. 19, no. 1, pp. 101–111, 2014.
- [100] F. Yu and C. Wang, "Secure communication based on a four-wing chaotic system subject to disturbance inputs," *Optik*, vol. 125, no. 20, pp. 5920–5925, 2014.
- [101] Y. Chen, R. Xia, Z. Wang, J. Zhang, K. Yang, and Z. Cao, "The visual saliency detection algorithm research based on hierarchical principle component analysis method," *Multimedia Tools and Applications*, 2019.
- [102] W. Wang, Y. Li, T. Zou et al., "A novel image classification approach via dense-MobileNet models," *Mobile Information Systems*, vol. 2020, Article ID 7602384, 8 pages, 2020.
- [103] Y. Chen, J. Wang, S. Liu et al., "Multiscale fast correlation filtering tracking algorithm based on a feature fusion model," *Concurrency and Computation: Practice and Experience*, 2019.
- [104] D. Zhang, Z. Liang, G. Yang, Q. Li, L. Li, and X. Sun, "A robust forgery detection algorithm for object removal by exemplar-based image inpainting," *Multimedia Tools and Applications*, vol. 77, no. 10, pp. 11823–11842, 2018.
- [105] Y. Chen, J. Wang, R. Xia, Q. Zhang, Z. Cao, and K. Yang, "The visual object tracking algorithm research based on adaptive combination kernel," *Journal of Ambient Intelligence and Humanized Computing*, vol. 10, no. 12, pp. 4855–4867, 2019.

- [106] J. Zhang and C. Liu, "A study of a clothing image segmentation method in complex conditions using a features fusion model," *Automatika*, vol. 61, no. 1, pp. 150–157, 2020.
- [107] Y. Chen, J. Xiong, W. Xu, and J. Zuo, "A novel online incremental and decremental learning algorithm based on variable support vector machine," *Cluster Computing*, vol. 22, no. 3, pp. 7435–7445, 2019.
- [108] W. Wei, T. Can, W. Xin, L. Yanhong, H. Yongle, and L. Ji, "Image object recognition via deep feature-based adaptive joint sparse representation," *Computational Intelligence and Neuroscience*, vol. 2019, Article ID 8258275, 9 pages, 2019.
- [109] Y. Chen, J. Wang, X. Chen et al., "Single-image super-resolution algorithm based on structural self-similarity and deformation block features," *IEEE Access*, vol. 7, pp. 58791–58801, 2019.
- [110] Y. Chen, J. Wang, X. Chen, A. K. Sangaiah, K. Yang, and Z. Cao, "Image super-resolution algorithm based on dual-channel convolutional neural networks," *Applied Sciences*, vol. 9, no. 11, p. 2316, 2019.
- [111] M. Zhou and C. Wang, "A novel image encryption scheme based on conservative hyperchaotic system and closed-loop diffusion between blocks," *Signal Processing*, vol. 171, Article ID 107484, 2020.
- [112] H. Liu, Y. Zhang, A. Kadir, and Y. Xu, "Image encryption using complex hyper chaotic system by injecting impulse into parameters," *Applied Mathematics and Computation*, vol. 360, pp. 83–93, 2019.
- [113] Y. Xu, H. Wang, Y. Li, and B. Pei, "Image encryption based on synchronization of fractional chaotic systems," *Communications in Nonlinear Science and Numerical Simulation*, vol. 19, no. 10, pp. 3735–3744, 2014.
- [114] S. E. Assad and M. Farajallah, "A new chaos-based image encryption system," *Signal Processing Image Communication*, vol. 41, pp. 144–157, 2016.
- [115] X. Chai, Z. Gan, K. Yang, Y. Chen, and X. Liu, "An image encryption algorithm based on the memristive hyperchaotic system, cellular automata and DNA sequence operations," *Signal Processing: Image Communication*, vol. 52, no. 6, pp. 6–19, 2017.
- [116] Y. Li, C. Wang, and H. Chen, "A hyper-chaos-based image encryption algorithm using pixel-level permutation and bit-level permutation," *Optics and Lasers in Engineering*, vol. 90, pp. 238–246, 2017.
- [117] A. Belazi, A. A. Abd El-Latif, and S. Belghith, "A novel image encryption scheme based on substitution-permutation network and chaos," *Signal Processing*, vol. 128, pp. 155–170, 2016.
- [118] X. Wang, L. Liu, and Y. Zhang, "A novel chaotic block image encryption algorithm based on dynamic random growth technique," *Optics and Lasers in Engineering*, vol. 66, pp. 10–18, 2015.
- [119] X.-Y. Wang, Y.-Q. Zhang, and X.-M. Bao, "A colour image encryption scheme using permutation-substitution based on chaos," *Entropy*, vol. 17, no. 6, pp. 3877–3897, 2015.
- [120] H. Liu and X. Wang, "Color image encryption based on one-time keys and robust chaotic maps," *Computers & Mathematics with Applications*, vol. 59, no. 10, pp. 3320–3327, 2010.
- [121] M. A. B. Farah, R. Guesmi, A. Kachouri, and M. Samet, "A novel chaos based optical image encryption using fractional Fourier transform and DNA sequence operation," *Optics & Laser Technology*, vol. 121, Article ID 105777, 2020.

## Research Article

# Global Dynamics of the Chaotic Disk Dynamo System Driven by Noise

Chunsheng Feng <sup>1</sup>, Lijie Li <sup>2</sup>, Yongjian Liu <sup>2</sup> and Zhouchao Wei <sup>3</sup>

<sup>1</sup>School of Mathematics and Computational Science, Xiangtan University, Xiangtan 411105, China

<sup>2</sup>Guangxi Colleges and Universities Key Laboratory of Complex System Optimization and Big Data Processing, Yulin Normal University, Yulin 537000, China

<sup>3</sup>School of Mathematics and Physics, China University of Geosciences, Wuhan 430074, China

Correspondence should be addressed to Lijie Li; [lilijie1219@126.com](mailto:lilijie1219@126.com) and Zhouchao Wei; [weizhouchao@163.com](mailto:weizhouchao@163.com)

Received 24 December 2019; Revised 14 February 2020; Accepted 28 February 2020; Published 26 March 2020

Academic Editor: Hassan Zargarzadeh

Copyright © 2020 Chunsheng Feng et al. This is an open access article distributed under the Creative Commons Attribution License, which permits unrestricted use, distribution, and reproduction in any medium, provided the original work is properly cited.

The disk dynamo system, which is capable of chaotic behaviours, is obtained experimentally from two disk dynamos connected together. It models the geomagnetic field and is used to explain the reversals in its polarity. Actually, the parameters of the chaotic systems exhibit random fluctuation to a greater or lesser extent, which can carefully describe the disturbance made by environmental noise. The global dynamics of the chaotic disk dynamo system with random fluctuating parameters are concerned, and some new results are presented. Based on the generalized Lyapunov function, the globally attractive and positive invariant set is given, including a two-dimensional parabolic ultimate boundary and a four-dimensional ellipsoidal ultimate boundary. Furthermore, a set of sufficient conditions is derived for all solutions of the stochastic disk dynamo system being global convergent to the equilibrium point. Finally, numerical simulations are presented for verification.

## 1. Introduction

The magnetic field has reversed its polarity many times along geological history [1]. To geophysics, their fundamental goal is a coherent understanding of the structure and dynamics of the Earth's interior. A number of investigators worked hard in order to establish the state of the Earth's dynamo. Bullard studied a disk dynamo with the intention of discussing possible analogies between them and those of a homogeneous dynamo which is supposed to be the origin of the magnetic field of the Earth and other celestial bodies. Before long, Japanese geophysicist Rikitake [2] found that reversals of electric current generated by a circuit can often occur even in a very simple system such as the one with two disk dynamos. The behaviour of the system is far different from that of the single disk dynamo, which never has a reversal of the electric current. Then, a simple mechanical model used to study the reversals of the Earth's magnetic field is a two-disc

dynamo system idealized by Rikitake. The model consists of two identical single Faraday-disk dynamos of the Bullard type coupled together. For simplicity, we denote the angular velocities of their rotors by  $x_3$  and  $x_4$  and the currents generated by  $x_1$  and  $x_2$ , respectively. Then, with appropriate normalization of variables, the dynamical equations can be described by the following set of ordinary differential equations [3, 4]:

$$\begin{cases} \dot{x}_1 = -\mu_1 x_1 + x_2 x_3, \\ \dot{x}_2 = -\mu_2 x_2 + x_1 x_4, \\ \dot{x}_3 = q_1 - \epsilon_1 x_3 - x_1 x_2, \\ \dot{x}_4 = q_2 - \epsilon_2 x_4 - x_1 x_2. \end{cases} \quad (1)$$

where  $q_1$  and  $q_2$  are the torques applied to the rotors and  $\mu_1$ ,  $\mu_2$ ,  $\epsilon_1$ , and  $\epsilon_2$  are the positive constants representing dissipative effects of the disk dynamo system. Rather, from the physical meaning of the equation, the parameters  $\mu$  and  $\epsilon$



represent the power consumption and mechanical damping dissipation of disk dynamo, respectively. When the parameters are  $\mu_1 = 3$ ,  $\mu_2 = 1$ ,  $\epsilon_1 = 0.1$ ,  $\epsilon_2 = 0.2$ ,  $q_1 = 3$ , and  $q_2 = 1$  for initial states  $(x_1(0), x_2(0), x_3(0), x_4(0)) = (2.2, 2.0, 10.5, 20)$ , the numerical simulation shows that the corresponding Lyapunov exponents are 0.28, 0,  $-0.10$ , and  $-4.47$ . There exists one positive Lyapunov exponent suggest that system (1) has a chaotic attractor. The chaotic attractor's projections in the coordinate planes  $x_1 - x_2 - x_3$  and  $x_2 - x_3 - x_4$  are shown in Figure 1.

One the one hand, since the Lorenz system [5] was presented, there is a huge volume of the literature devoted to the studies of the Lorenz system and other classical chaotic systems, which are closely related but not topologically equivalent to the Lorenz system, such as Chen system [6], Lü system [7], and Yang system [8]. In a sense defined by Vaněček and Čelikovský [9, 10], the Chen system is a dual system to the Lorenz system and the Lü system and Yang system represent a transition between the Lorenz and the Chen systems. For the Lorenz family system, mathematicians, physicists, and engineers from various fields have studied the characteristics of systems, bifurcations, routes to chaos, essence of chaos, and chaos synchronization. By ignoring mechanical damping dissipation that parameters  $\epsilon_1 = \epsilon_2 = 0$  and setting  $q_1 = q_2 = 1$  and  $\mu_1 = \mu_2 = \mu$ , we can write  $x_3 = z$  and  $x_4 = z - \alpha$ , where  $\alpha$  is a constant of the motion. Finally, coupled dynamos (1) can be written in the following simple form [11]:

$$\begin{cases} \dot{x}_1 = -\mu x_1 + x_2 z, \\ \dot{x}_2 = -\mu x_2 + x_1 (z - \alpha), \\ \dot{z} = 1 - x_1 x_2. \end{cases} \quad (2)$$

System (2) has a three-dimensional attractor similar to the Lorenz attractor although both systems are obviously not topologically equivalent [11]. The chaotic behavior and other properties, synchronization and control of the disk dynamo system and disk dynamo-like chaotic systems (2), were extensively studied (see, for instance, [11–16] and their references).

On the other hand, Arnold [17] has pointed out that the parameters in the chaotic systems exhibit random fluctuation to a greater or lesser extent due to various environmental noise. Scholars usually estimate them by average values plus some error terms [18]. In general, by the well-known central limit theorem, the error terms follow normal distributions. For the best incorporate (natural) randomness into the mathematical description of the phenomena and to provide a more accurate description of it, we model the stochastic disk dynamo system by replacing the parameters  $\mu_1$ ,  $\mu_2$ ,  $\epsilon_1$ ,  $\epsilon_2$ ,  $q_1$ , and  $q_2$  by  $\mu_1 \rightarrow \mu_1 + \sigma_1 dW(t)$ ,  $\mu_2 \rightarrow \mu_2 + \sigma_2 dW(t)$ ,  $\epsilon_1 \rightarrow \epsilon_1 + \sigma_3 dW(t)$ ,  $\epsilon_2 \rightarrow \epsilon_2 + \sigma_4 dW(t)$ ,  $q_{100} \rightarrow q_1 + q_{10} dW(t)$ , and  $q_2 \rightarrow q_2 + q_{20} dW(t)$ , where  $W(t)$  are the mutually independent Brownian motions. Then, one gets the following system of stochastic differential equations:

$$\begin{cases} dx_1(t) = (-\mu_1 x_1 + x_2 x_3) dt + \sigma_1 x_1 dW(t), \\ dx_2(t) = (-\mu_2 x_2 + x_1 x_4) dt + \sigma_2 x_2 dW(t), \\ dx_3(t) = (q_1 - \epsilon_1 x_3 - x_1 x_2) dt + (\sigma_3 x_3 + q_{10}) dW(t), \\ dx_4(t) = (q_2 - \epsilon_2 x_4 - x_1 x_2) dt + (\sigma_4 x_4 + q_{20}) dW(t). \end{cases} \quad (3)$$

To illustrate the stochastic effects clearly, we performed simulations for the corresponding stochastic case of Figure 1. The corresponding stochastic case uses the same parameters and initial values. Let  $\mu_1 = 3$ ,  $\mu_2 = 1$ ,  $\epsilon_1 = 0.1$ ,  $\epsilon_2 = 0.2$ ,  $q_1 = 3$ , and  $q_2 = 1$  and initial states  $(x_1(0), x_2(0), x_3(0), x_4(0)) = (2.2, 2.0, 10.5, 20)$  additionally have the perturbed parameters  $\sigma_1 = 0.1$ ,  $\sigma_2 = 0.1$ ,  $\sigma_3 = 0.01$ ,  $\sigma_4 = 0.01$ ,  $q_{10} = 0.1$ , and  $q_{20} = 0.1$ . The projections in the coordinate planes  $x_1 - x_2 - x_3$  and  $x_2 - x_3 - x_4$  are shown in Figure 2. Comparing Figures 1 and 2, we can see the difference between the deterministic case and stochastic case. Actually, the behavior of system will change even if the parameters suffer small perturbation. Suppose that other parameters remain unchanged and only  $\epsilon_2$  change; let  $\mu_1 = 3$ ,  $\mu_2 = 1$ ,  $\epsilon_1 = 0.1$ ,  $\epsilon_2 = 0.2$ ,  $q_1 = 3$ , and  $q_2 = 1$ , initial states  $(x_1(0), x_2(0), x_3(0), x_4(0)) = (2.2, 2.0, 10.5, 20)$ , and the perturbed parameters  $\sigma_1 = 0$ ,  $\sigma_2 = 0$ ,  $\sigma_3 = 0$ ,  $\sigma_4 = 0.01$ ,  $q_{10} = 0$ , and  $q_{20} = 0$ . Time series  $x_1$  diagram of the deterministic case and stochastic case are shown in Figure 3.

Chaos synchronization is a very important topic in chaos theory. Enormous research activities have been carried out in chaos synchronization by many researchers from different disciplines, and lots of successful experiments have been reported. Many scholars, by using capacitor coupling [19], induction coil coupling [20], and resistance coupling [21] to realize the synchronization of chaotic systems, have obtained good results. In chaotic synchronization, the boundedness of the system is a very important prerequisite. In fact, ultimate boundedness of chaotic dynamical systems is always one of the fundamental concepts in dynamical systems. This plays an important role in investigating the stability of the equilibrium, estimating the Lyapunov dimension of attractors and the Hausdorff dimension of attractors, the existence of periodic solutions, chaos control, and chaos synchronization. Technically, to locate and estimate the relative position of the attractor is a difficult work even in a deterministic system [22–26]. For the deterministic system, Yu and Liao [27] give the concept of the exponential attractive set and estimate the globally attractive and positive invariant set of the typical Lorenz system. For the stochastic system, some results of the estimation global attractive set have also been obtained, for the stochastic Lorenz-Stenflo system [18], the stochastic Lorenz-Haken system [28], the stochastic Lorenz-84 system [29], the stochastic Lorenz system family [30], the stochastic Rabinovich system [31, 32], and other stochastic systems [33, 34].

In this paper, by using a technique combining the generalized Lyapunov function theory and optimization, globally exponential attractive set and a four-dimensional

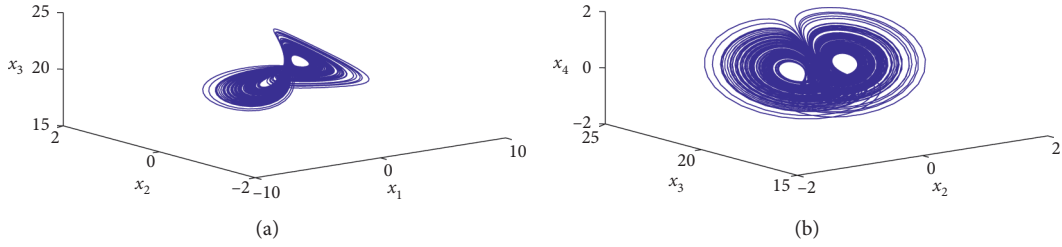


FIGURE 1: The disk dynamo system exhibits chaotic behavior of system parameters  $\mu_1 = 3, \mu_2 = 1, \epsilon_1 = 0.1, \epsilon_2 = 0.2, q_1 = 3,$  and  $q_2 = 1$  and initial values  $(x_0, y_0, z_0, u_0) = (2.2, 2.0, 10.5, 20)$ .

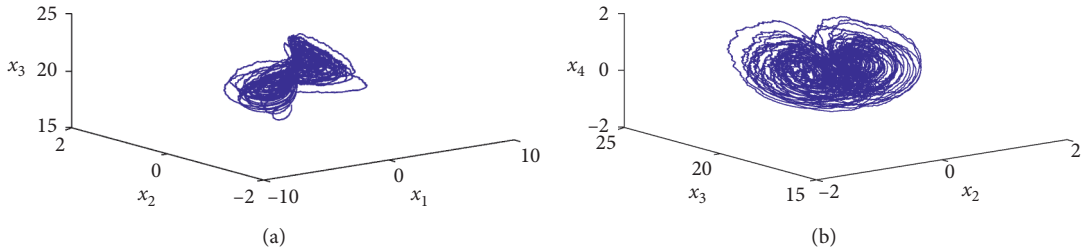


FIGURE 2: Simulated phase portraits of stochastic disk dynamo system (3) with parameters  $\mu_1 = 3, \mu_2 = 1, \epsilon_1 = 0.1, \epsilon_2 = 0.2, q_1 = 3, q_2 = 1,$   $\sigma_1 = 0.1, \sigma_2 = 0.1, \sigma_3 = 0.01, \sigma_4 = 0.01, q_{10} = 0.1, q_{20} = 0.1$  and initial values  $(x_0, y_0, z_0, u_0) = (2.2, 2.0, 10.5, 20)$ .

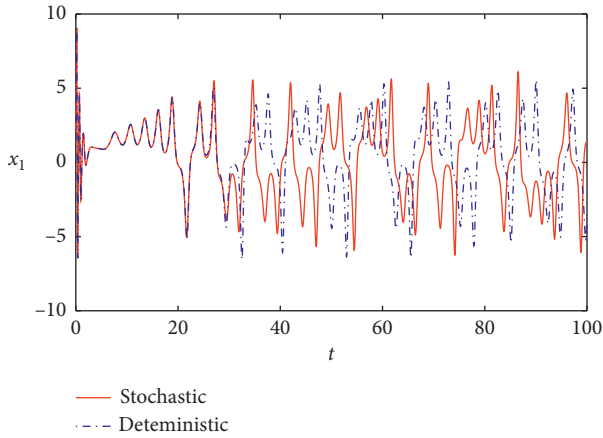


FIGURE 3: Time series diagrams of the deterministic and stochastic disk dynamo system with parameters  $\mu_1 = 3, \mu_2 = 1, \epsilon_1 = 0.1, \epsilon_2 = 0.2,$   $q_1 = 3, q_2 = 1, \sigma_1 = 0, \sigma_2 = 0, \sigma_3 = 0, \sigma_4 = 0$  (deterministic case),  $\sigma_4 = 0.01$  (stochastic case),  $q_{10} = 0, q_{20} = 0,$  and initial values  $(x_0, y_0, z_0, u_0) = (2.2, 2.0, 10.5, 20)$ .

ellipsoidal ultimate bound are derived, which can help us to locate the relative position of the attractor. The two-dimensional parabolic ultimate bound is also established. And numerical results to estimate the ultimate bound are also presented for verification. We hope that the investigation of this paper can help understanding the rich dynamic of the stochastic disk dynamo system and offer some enlightenments for the study of the reversals of the Earth's magnetic field.

This paper is organized as follows. In Section 2, the cylindrical bound of stochastic disk dynamo system (3) is presented. In Section 3, globally exponential attractive set

and positive invariant set of the system are derived. In Section 4, the stochastic stability of system (3) is studied. In each section, we also give corresponding numerical results, respectively. The conclusions are given in Section 5.

## 2. Cylindrical Bound

**Theorem 1.** Let  $l_{13} = \min\{2(\mu_1 - (1/2)\sigma_1^2), \epsilon_1 - (1/2)\sigma_3^2\}$  and  $l_{24} = \min\{2(\mu_2 - (1/2)\sigma_2^2), \epsilon_2 - (1/2)\sigma_4^2\}$ . Suppose that the parameters  $2\mu_1 > \sigma_1^2, 2\mu_2 > \sigma_2^2, 2\epsilon_1 > \sigma_3^2,$  and  $2\epsilon_2 > \sigma_4^2, \sigma_i \geq 0 (i = 1, 2, 3, 4)$ . Then, the set  $\Omega$  is the bound for system (3), in the sense that system (3) is the cylindrical bound, where

$$\Omega = \left\{ X \mid E[x_1^2 + x_3^2] \leq \frac{(q_1 + q_{10}\sigma_3)^2}{l_{13}(\epsilon_1 - (1/2)\sigma_3^2)} + \frac{q_{10}^2}{l_{13}}, E[x_2^2 + x_4^2] \leq \frac{(q_2 + q_{20}\sigma_4)^2}{l_{24}(\epsilon_2 - (1/2)\sigma_4^2)} + \frac{q_{20}^2}{l_{24}} \right\}. \quad (4)$$

*Proof*

*Step 1.* Construct a positive definite and radically unbounded Lyapunov function on  $\mathbb{R}^2$ :

$$V_{13}(x_1, x_3) = \frac{1}{2}(x_1^2 + x_3^2). \quad (5)$$

Applying Itô's formula, one has

$$\begin{aligned}
dV_{13} &= \left[ -\mu_1 x_1^2 - \epsilon_1 x_3^2 + q_1 x_3 + \frac{1}{2} (\sigma_1^2 x_1^2 + (\sigma_3 x_3 + q_{10})^2) \right] dt \\
&\quad + (\sigma_1 x_1^2 + \sigma_3 x_3^2 + q_{10} x_3) dW(t) \\
&\leq \left[ -\left( \mu_1 - \frac{1}{2} \sigma_1^2 \right) x_1^2 - \frac{1}{2} \left( \epsilon_1 - \frac{1}{2} \sigma_3^2 \right) x_3^2 + L_{13} \right] dt \\
&\quad + \left( \sigma_1 x_1^2 + 2\sigma_3 x_3^2 + \frac{q_{10}^2}{4\sigma_3} \right) dW(t) \\
&\leq (l_{13} V_{13} + L_{13}) dt + \left( l_3 V_{13} + \frac{q_{10}^2}{4\sigma_3} \right) dW(t),
\end{aligned} \tag{6}$$

where

$$\begin{aligned}
l_{13} &= \min \left\{ 2 \left( \mu_1 - \frac{1}{2} \sigma_1^2 \right), \epsilon_1 - \frac{1}{2} \sigma_3^2 \right\}, \\
l_3 &= \max \{ 2\sigma_1, 4\sigma_3 \}; \\
L_{13} &= \frac{(q_1 + q_{10}\sigma_3)^2}{2(\mu_1 - (1/2)\sigma_1^2)} + \frac{1}{2} q_{10}^2.
\end{aligned} \tag{7}$$

Similar to the proof of Theorem 1, we can obtain

$$E \left[ V_{13} - \frac{L_{13}}{l_{13}} \right] \leq \left[ V_{13}(x_1(t_0), x_3(t_0)) - \frac{L_{13}}{l_{13}} \right] \exp\{-l_{13}(t - t_0)\}. \tag{8}$$

Therefore, one has  $\lim_{t \rightarrow +\infty} EV_{13} \leq (L_{13}/l_{13})$ ; that is to say, the following inequality holds as  $t \rightarrow +\infty$ :

$$E[x_1^2 + x_3^2] \leq \frac{2L_{13}}{l_{13}}. \tag{9}$$

*Step 2.* Construct a positive definite and radically unbounded Lyapunov function on  $\mathbb{R}^2$ :

$$V_{24}(x_2, x_4) = \frac{1}{2} (x_2^2 + x_4^2). \tag{10}$$

Similar to the proof of Step 1, we can obtain

$$dV_{24} \leq (l_{24} V_{24} + L_{24}) dt + l_4 V_{24} dW(t), \tag{11}$$

where

$$\begin{aligned}
l_{24} &= \min \left\{ 2 \left( \mu_2 - \frac{1}{2} \sigma_3^2 \right), \epsilon_2 - \frac{1}{2} \sigma_4^2 \right\}, \\
l_1 &= \max \{ 2\sigma_3, 4\sigma_4 \}; \\
L_{24} &= \frac{(q_2 + q_{20}\sigma_4)^2}{2(\epsilon_2 - (1/2)\sigma_4^2)} + \frac{1}{2} q_{20}^2.
\end{aligned} \tag{12}$$

Therefore, the following inequality holds as  $t \rightarrow +\infty$ :

$$E[x_2^2 + x_4^2] \leq \frac{2L_{24}}{l_{24}}. \tag{13}$$

By Step 1 and Step 2, system (3) is the cylindrical bound.

*Remark 1.* Let  $\sigma_1 = \sigma_2 = \sigma_3 = \sigma_4 = 0$ ; then system (3) is deterministic. Theorem 2 contains the results given in [12] as special cases.

Let  $\mu_1 = 3$ ,  $\mu_2 = 1$ ,  $\epsilon_1 = 0.1$ ,  $\epsilon_2 = 0.2$ ,  $q_1 = 3$ ,  $q_2 = 1$ ,  $\sigma_1 = \sigma_2 = 0.1$ ,  $\sigma_3 = \sigma_4 = 0.01$ , and  $q_{10} = q_{20} = 0.1$ , and initial values  $(x_0, y_0, z_0, u_0) = (2.2, 2, 2.5, 3)$ . Calculate  $l_{13} = 0.099950$  and  $L_{24} = 0.199950$ . We give the following estimate of the ultimate boundary:

$$\Omega = \{X \mid E[x_1^2 + x_3^2] \leq 901.601426, E[x_2^2 + x_4^2] \leq 25.112567\}. \tag{14}$$

The corresponding projections of exponentially attractive sets are shown in Figure 4.

And we also have the following results:

$$\begin{aligned}
|\mathbf{E}x_1| &\leq 30.026679, \\
|\mathbf{E}x_2| &\leq 5.011244, \\
|\mathbf{E}x_3| &\leq 30.026679, \\
|\mathbf{E}x_4| &\leq 5.011244.
\end{aligned} \tag{15}$$

The numerical solutions, which are stochastic processes, of stochastic dynamo system (3) are obtained by the Euler–Maruyama method. All the stochastic processes' scopes and the ultimate boundary of the corresponding expectations are listed in Table 1. From Table 1, we are pleased to see that the simulation results and the theoretical results of (14) and (15) are consistent.

### 3. Globally Exponentially Attractive Set

**Theorem 2.** Let  $l_0 = \min\{\mu_1 - (1/2)\sigma_1^2, \mu_2 - (1/2)\sigma_2^2, \epsilon_1 - (1/2)\sigma_3^2, \epsilon_2 - (1/2)\sigma_4^2\}$ , and  $L = (L_1/l_0)$ . Suppose that the parameters  $2\mu_1 > \sigma_1^2$ ,  $2\mu_2 > \sigma_2^2$ ,  $2\epsilon_1 > \sigma_3^2$ , and  $2\epsilon_2 > \sigma_4^2$ . Then, for any constant  $\lambda > 0$ , the following estimate holds on system (3):

$$E[V(X) - L] \leq [V(X_0) - L] \exp\{-l_0(t - t_0)\}. \tag{16}$$

In particular,

$$\Omega = \{X \mid EV(X) \leq 2L\} = \{X \mid E[x_1^2 + \lambda x_2^2 + x_3^2 + \lambda x_4^2] \leq 2L\} \tag{17}$$

is a globally exponential attractive set of system (3), where

$$V(X) = \frac{1}{2} (x_1^2 + \lambda x_2^2 + x_3^2 + \lambda x_4^2),$$

$$L_1 = \frac{(q_1 + q_{10}\sigma_3)^2}{2(\epsilon_1 - (1/2)\sigma_3^2)} + \lambda \frac{(q_2 + q_{20}\sigma_4)^2}{2(\epsilon_2 - (1/2)\sigma_4^2)} + \frac{1}{2} q_{10}^2 + \frac{1}{2} \lambda q_{20}^2. \tag{18}$$

*Proof.* Define the Lyapunov on  $\mathbb{R}^4$ , where

$$V(X) = \frac{1}{2} (x_1^2 + \lambda x_2^2 + x_3^2 + \lambda x_4^2). \tag{19}$$

Applying Itô's formula to (19), one has

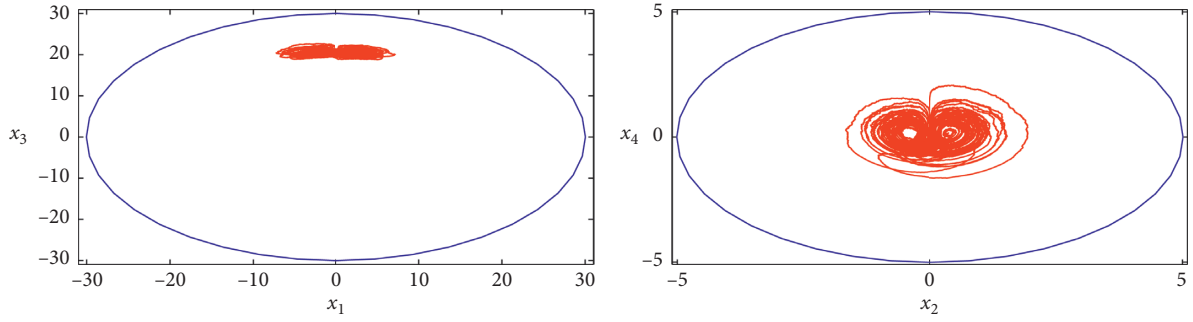


FIGURE 4: The projection of exponentially attractive set of the stochastic dynamo system with  $\mu_1 = 3, \mu_2 = 1, \epsilon_1 = 0.1, \epsilon_2 = 0.2, q_1 = 3, q_2 = 1, \sigma_1 = \sigma_2 = 0.1, \sigma_3 = \sigma_4 = 0.01$ , and  $q_{10} = q_{20} = 0.1$ , and initial values  $(x_0, y_0, z_0, u_0) = (2.2, 2, 2.5, 3)$ .

TABLE 1: Ultimate boundary for stochastic dynamo system.

Scopes of stochastic processes	Simulated results of expectation	Theoretical estimates of expectation
$-7.692934 \leq x_1 \leq 7.736921$	$\mathbf{E}x_1 = 0.104873$	$ \mathbf{E}x_1  \leq 30.026679$
$-1.484651 \leq x_2 \leq 2.785851$	$\mathbf{E}x_2 = 0.033916$	$ \mathbf{E}x_2  \leq 5.011244$
$1.160790 \leq x_3 \leq 22.686710$	$\mathbf{E}x_3 = 19.921792$	$ \mathbf{E}x_3  \leq 30.026679$
$-1.372995 \leq x_4 \leq 3.000000$	$\mathbf{E}x_4 = 0.248853$	$ \mathbf{E}x_4  \leq 5.011244$
$2.652947 \leq r_1 \leq 526.916239$	$\mathbf{E}r_1 = 410.415404$	$0 \leq \mathbf{E}r_1 \leq 901.601426$
$0.000000 \leq r_2 \leq 13.000000$	$\mathbf{E}r_2 = 0.525692$	$0 \leq \mathbf{E}r_2 \leq 25.112567$

$$r_1 = x_1^2 + x_3^2; r_2 = x_2^2 + x_4^2.$$

$$\begin{aligned}
dV(X) &= [x_1(-\mu_1 x_1 + x_2 x_3) + \lambda x_2(-\mu_2 x_2 + x_1 x_4) \\
&\quad + x_3(q_1 - \epsilon_1 x_3 - x_1 x_2) + \lambda x_4(q_2 - \epsilon_2 x_4 - x_1 x_2) \\
&\quad + \frac{1}{2}[\sigma_1^2 x_1^2 + \lambda \sigma_2^2 x_2^2 + (\sigma_3 x_3 + q_{10})^2 \\
&\quad + \lambda(\sigma_4 x_4 + q_{20})^2]] dt \\
&\quad + (\sigma_1 x_1^2 + \lambda \sigma_2 x_2^2 + \sigma_3 x_3^2 + q_{10} x_3 \\
&\quad + \lambda \sigma_4 x_4^2 + \lambda q_{20} x_4) dW(t) \\
&= \left[ -\left(\mu_1 - \frac{1}{2}\sigma_1^2\right)x_1^2 - \lambda\left(\mu_2 - \frac{1}{2}\sigma_2^2\right)x_2^2 - \left(\epsilon_1 - \frac{1}{2}\sigma_3^2\right)x_3^2 \right. \\
&\quad \left. - \lambda\left(\epsilon_2 - \frac{1}{2}\sigma_4^2\right)x_4^2 + (q_1 + q_{10}\sigma_3)x_3 \right. \\
&\quad \left. + \lambda(q_2 + q_{20}\sigma_4)x_4 + \frac{1}{2}(q_{10}^2 + \lambda q_{20}^2) \right] dt \\
&\quad + (\sigma_1 x_1^2 + \lambda \sigma_2 x_2^2 + \sigma_3 x_3^2 + q_{10} x_3 + \lambda \sigma_4 x_4^2 \\
&\quad + \lambda q_{20} x_4) dW(t) \\
&= \left[ -\frac{1}{2}\left(\mu_1 - \frac{1}{2}\sigma_1^2\right)x_1^2 - \frac{1}{2}\lambda\left(\mu_2 - \frac{1}{2}\sigma_2^2\right)x_2^2 \right. \\
&\quad \left. - \frac{1}{2}\left(\epsilon_1 - \frac{1}{2}\sigma_3^2\right)x_3^2 - \frac{1}{2}\lambda\left(\epsilon_2 - \frac{1}{2}\sigma_4^2\right)x_4^2 + F(X) \right] dt \\
&\quad + [2\sigma_1 x_1^2 + 2\lambda \sigma_2 x_2^2 + 2\sigma_3 x_3^2 + 2\lambda \sigma_4 x_4^2 + G(X)] dW(t),
\end{aligned} \tag{20}$$

where

$$\begin{aligned}
F(X) &= -\frac{1}{2}\left(\mu_1 - \frac{1}{2}\sigma_1^2\right)x_1^2 - \frac{1}{2}\lambda\left(\mu_2 - \frac{1}{2}\sigma_2^2\right)x_2^2 \\
&\quad - \frac{1}{2}\left(\epsilon_1 - \frac{1}{2}\sigma_3^2\right)x_3^2 - \frac{1}{2}\lambda\left(\epsilon_2 - \frac{1}{2}\sigma_4^2\right)x_4^2 \\
&\quad + (q_1 + q_{10}\sigma_3)x_3 + \lambda(q_2 + q_{20}\sigma_4)x_4 \\
&\quad + \frac{1}{2}(q_{10}^2 + \lambda q_{20}^2),
\end{aligned}$$

$$G(X) = -\sigma_1 x_1^2 - \lambda \sigma_2 x_2^2 - \sigma_3 x_3^2 + q_{10} x_3 - \lambda \sigma_4 x_4^2 + \lambda q_{20} x_4. \tag{21}$$

Then,

$$\begin{aligned}
F(X) \leq \sup_{x \in \mathbb{R}^4} F(X) &= \frac{(q_1 + q_{10}\sigma_3)^2}{2(\epsilon_1 - (1/2)\sigma_3^2)} + \lambda \frac{(q_2 + q_{20}\sigma_4)^2}{2(\epsilon_2 - (1/2)\sigma_4^2)} \\
&\quad + \frac{1}{2}q_{10}^2 + \frac{1}{2}\lambda q_{20}^2 = L_1,
\end{aligned} \tag{22}$$

$$G(X) \leq \sup_{x \in \mathbb{R}^4} G(X) = \frac{q_{10}^2}{4\sigma_3} + \frac{\lambda q_{20}^2}{4\sigma_4} = L_2. \tag{23}$$

From (22) and (23), we can obtain

$$dV(X) \leq [-l_0 V(X) + L_1] dt + [l_1 V(X) + L_2] dW(t). \tag{24}$$

where

$$l_0 = \min\left\{\mu_1 - \frac{1}{2}\sigma_1^2, \mu_2 - \frac{1}{2}\sigma_2^2, \mu_3 - \frac{1}{2}\sigma_3^2, \mu_4 - \frac{1}{2}\sigma_4^2\right\}, \quad (25)$$

$$l_1 = 4 \max\{\sigma_1, \sigma_2, \sigma_3, \sigma_4\}.$$

From (24) and the calculating the expectation, one obtains

$$EV(X) \leq V(X_0) + \int_{t_0}^t [-l_0 EV(X) + L_1] ds. \quad (26)$$

From above inequality, one can obtain

$$\begin{aligned} EV(X) &\leq V(X_0) \exp\{-l_0(t-t_0)\} + L_1 \int_{t_0}^t \exp\{-l_0(s-t_0)\} ds \\ &= V(X_0) \exp\{-l_0(t-t_0)\} + \frac{L_1}{l_0} \{1 - \exp\{-l_0(t-t_0)\}\}. \end{aligned} \quad (27)$$

Let  $L = (L_1/l_0)$ . When  $EV(X) - L > 0$ ,  $EV(X_0) - L > 0$ , the following estimate holds:

$$E[V(X) - L] \leq [V(X_0) - L] \exp\{-l_0(t-t_0)\}. \quad (28)$$

Thus,

$$\lim_{t \rightarrow \infty} EV(X) \leq L. \quad (29)$$

That is,

$$\Omega = \{X \mid EV(X) \leq 2L\} = \{X \mid E[x_1^2 + \lambda x_2^2 + x_3^2 + \lambda x_4^2] \leq 2L\}. \quad (30)$$

**Theorem 3.** Let  $l_0 = \min\{\mu_1 - (1/2)\sigma_1^2, \mu_2 - (1/2)\sigma_2^2, \epsilon_1 - (1/2)\sigma_3^2, \epsilon_2 - (1/2)\sigma_4^2\}$ , and  $L = (L_{\lambda\eta}/l_0)$ . Suppose that the parameters  $2\mu_1 > \sigma_1^2$ ,  $2\mu_2 > \sigma_2^2$ ,  $2\epsilon_1 > \sigma_3^2$ , and  $2\epsilon_2 > \sigma_4^2$ . Then, for any constant  $\lambda > 0$  and  $\eta \in \mathbb{R}$ , the following estimate holds on system (3):

$$E[V(X) - L] \leq [V(X_0) - L] \exp\{-l_0(t-t_0)\}. \quad (31)$$

In particular,

$$\begin{aligned} \Omega = \{X \mid EV(X) \leq 2L\} &= \{X \mid E[x_1^2 + \lambda x_2^2 + (x_3 + \lambda\eta)^2 \\ &\quad + \lambda(x_4 - \eta)^2] \leq 2L\} \end{aligned} \quad (32)$$

is a globally exponential attractive set of system (3), where

$$\begin{aligned} V(X) &= \frac{1}{2} [x_1^2 + \lambda x_2^2 + (x_3 + \lambda\eta)^2 + \lambda(x_4 - \eta)^2], \\ L_{\lambda\eta} &= \frac{(q_1 + q_{10}\sigma_3 - (1/2)\lambda\eta\sigma_3^2)^2}{2(\epsilon_1 - (1/2)\sigma_3^2)} + \frac{1}{2}\lambda^2\eta^2 \left( \epsilon_1 - \frac{1}{2}\sigma_3^2 \right) \\ &\quad + \lambda\eta q_1 + \frac{1}{2}q_{10}^2 \\ &\quad + \lambda \left[ \frac{(q_2 + q_{20}\sigma_4 - (1/2)\eta\sigma_4^2)^2}{2(\epsilon_2 - (1/2)\sigma_4^2)} + \frac{1}{2}\eta^2 \left( \epsilon_2 - \frac{1}{2}\sigma_4^2 \right) \right. \\ &\quad \left. - \eta q_2 + \frac{1}{2}q_{20}^2 \right]. \end{aligned} \quad (33)$$

*Proof.* The proof is the same as that for Theorem 2; we omit it here.

*Remark 2.* Let  $\sigma_1 = \sigma_2 = \sigma_3 = \sigma_4 = q_{10} = q_{20} = 0$ ; then, system (3) is deterministic. Theorem 3 contain the results given in [12] as special cases.

In Theorem 3, let  $\mu_1 = 3$ ,  $\mu_2 = 1$ ,  $\epsilon_1 = 0.1$ ,  $\epsilon_2 = 0.2$ ,  $q_1 = 3$ ,  $q_2 = 1$ ,  $\sigma_1 = \sigma_2 = 0.1$ ,  $\sigma_3 = \sigma_4 = 0.01$ ,  $q_{10} = q_{20} = 0.1$ , and initial values  $(x_0, y_0, z_0, u_0) = (2.2, 2, 10.5, 20)$ . We give the following estimate of the ultimate boundary:

$$\Omega = \{X \mid E[x_1^2 + x_2^2 + (x_3 + 1)^2 + (x_4 - 1)^2] \leq 1034.644495\}. \quad (34)$$

This is the globally exponential attractive set and positive invariant set of the stochastic disk dynamo system.

Then, we have the following results of the ultimate boundary about  $x_1 - x_2 - x_3$ ,  $x_1 - x_2 - x_4$ ,  $x_1 - x_3 - x_4$ , and  $x_2 - x_3 - x_4$ , which are the exponentially attractive sets of the stochastic disk dynamo system:

$$\begin{aligned} E[x_1^2 + x_2^2 + (x_3 + 1)^2] &\leq (32.165890)^2, \\ E[x_1^2 + x_2^2 + (x_4 - 1)^2] &\leq (32.165890)^2, \\ E[x_1^2 + x_2^2 + (x_3 + 1)^2 + (x_4 - 1)^2] &\leq (32.165890)^2, \\ E[x_2^2 + (x_3 + 1)^2 + (x_4 - 1)^2] &\leq (32.165890)^2. \end{aligned} \quad (35)$$

The numerical solutions, which are stochastic processes, of stochastic dynamo system (3) are obtained by the Euler-Maruyama method. The simulated time series about  $x_1^2 + x_2^2 + (x_3 + 1)^2 + (x_4 - 1)^2$  is displayed in Figure 5. In addition, the stochastic processes' scopes is

$$9.887650 \leq x_1^2 + x_2^2 + (x_3 + 1)^2 + (x_4 - 1)^2 \leq 580.748156, \quad (36)$$

and the corresponding expectation is

$$E[x_1^2 + x_2^2 + (x_3 + 1)^2 + (x_4 - 1)^2] = 457.015926. \quad (37)$$

It is nice to see that the simulation results and the theoretical results of (34) are consistent.

#### 4. Stochastic Stability

The purpose of this section is to seek condition for the asymptotic behavior of system (3).

**Theorem 4.** When perturbed parameters  $\sigma_3 = \sigma_4 = q_{10} = q_{20} = 0$ , suppose that the parameters  $2\mu_1 > \sigma_1^2$  and  $2\mu_2 > \sigma_2^2$ . If  $(q_1/\epsilon_1) + (q_2/\epsilon_2) < \sqrt{(2\mu_1 - \sigma_1^2)(2\mu_2 - \sigma_2^2)}$ , the equilibrium position  $(0, 0, (q_1/\epsilon_1), (q_2/\epsilon_2))$  of system (3) is stochastically asymptotically stable.

*Proof.* Let  $V(X) = (1/2)(x_1^2 + x_2^2 + (x_3 - (q_1/\epsilon_1))^2 + (x_4 - (q_2/\epsilon_2))^2)$ . Then,

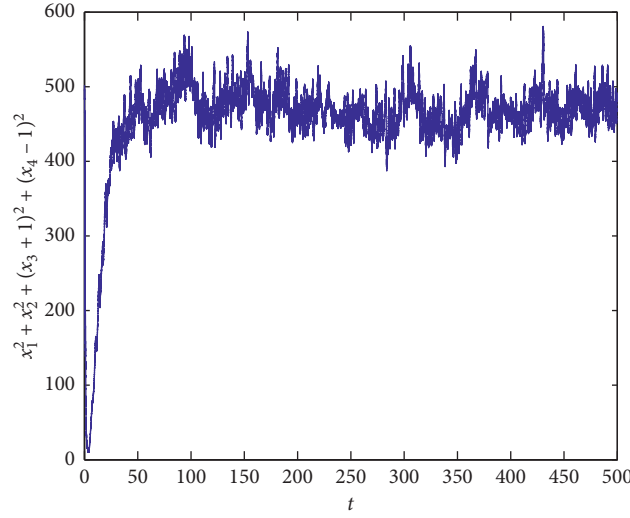


FIGURE 5: Time series diagrams of the stochastic dynamo system with  $u_1=0.2$ ,  $u_2=0.5$ ,  $\epsilon_1=0.5$ ,  $\epsilon_2=0.1$ ,  $q_1=5.9$ ,  $q_2=9.15$ ,  $\sigma_1=\sigma_2=\sigma_3=\sigma_4=0.1$ , and  $q_{10}=q_{20}=1$ , and initial values  $(x_0, y_0, z_0, u_0)=(2.2, 2, 10.5, 20)$ .

$$\begin{aligned}
LV &= x_1(-\mu_1 x_1 + x_2 x_3) + x_2(-\mu_2 x_2 + x_1 x_4) + \left(x_3 - \frac{q_1}{\epsilon_1}\right)(q_1 - \epsilon_1 x_3 - x_1 x_2) \\
&\quad + \left(x_4 - \frac{q_2}{\epsilon_2}\right)(q_2 - \epsilon_2 x_4 - x_1 x_2) + \frac{1}{2}(\sigma_1^2 x_1^2 + \sigma_2^2 x_2^2) \\
&= -\left(\mu_1 - \frac{1}{2}\sigma_1^2\right)x_1^2 - \left(\mu_2 - \frac{1}{2}\sigma_2^2\right)x_2^2 - \epsilon_1 \left(x_3 - \frac{q_1}{\epsilon_1}\right)^2 - \epsilon_2 \left(x_4 - \frac{q_2}{\epsilon_2}\right)^2 \\
&\quad - \left(x_1 x_2 x_3 - \frac{q_1}{\epsilon_1} x_4 - \frac{q_2}{\epsilon_2}\right) Q \begin{pmatrix} x_1 \\ x_2 \\ x_3 - \frac{q_1}{\epsilon_1} \\ x_4 - \frac{q_2}{\epsilon_2} \end{pmatrix}
\end{aligned} \tag{38}$$

When the parameters  $2\mu_1 > \sigma_1^2$ ,  $2\mu_2 > \sigma_2^2$ , and  $(q_1/\epsilon_1) + (q_2/\epsilon_2) < \sqrt{(2\mu_1 - \sigma_1^2)(2\mu_2 - \sigma_2^2)}$ , the matrix  $Q$  is positive-definite. Thus,  $LV$  is negative-definite. Then, from

Theorem 4.2.3 of [35], the equilibrium position  $(0, 0, (q_1/\epsilon_1), (q_2/\epsilon_2))$  of system (3) is stochastically asymptotically stable.



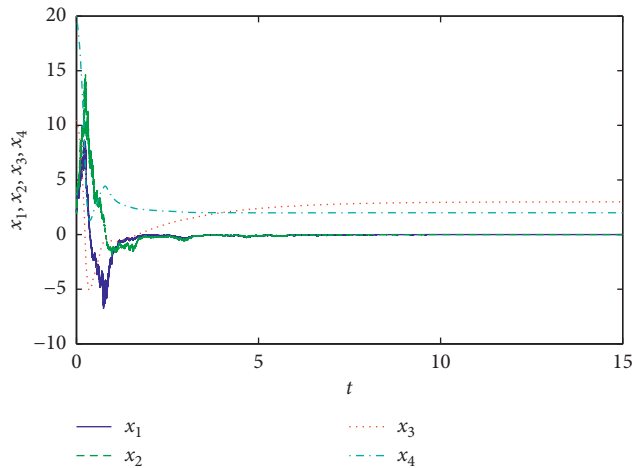


FIGURE 6: Time series diagrams of the stochastic dynamo system with  $u_1 = 2.5$ ,  $u_2 = 2.6$ ,  $\epsilon_1 = 0.5$ ,  $\epsilon_2 = 1$ ,  $q_1 = 1.5$ ,  $q_2 = 2$ ,  $\sigma_1 = 1$ ,  $\sigma_2 = 1$ , and  $\sigma_3 = \sigma_4 = q_{10} = q_{20} = 0$ , and initial values  $(x_0, y_0, z_0, u_0) = (2.2, 2, 10.5, 20)$ .

**Remark 3.** When the perturbed parameters  $\sigma_1 = \sigma_2 = \sigma_3 = \sigma_4 = q_{10} = q_{20} = 0$ , system (3) is deterministic. Suppose  $\mu_1 = \mu_2$ ,  $\epsilon_1 = \epsilon_2$ , and  $q_1 = q_2$ ; then, condition  $(q_1/\epsilon_1) + (q_2/\epsilon_2) < \sqrt{(2\mu_1 - \sigma_1^2)(2\mu_2 - \sigma_2^2)}$  is reduced to  $(q/\epsilon) < \mu$ . That is to say, the deterministic disk dynamo system is stable when  $(q/\epsilon) < \mu$ . That conclusion is coincident with the result of the literature [4].

**Remark 4.** Comparing the conditions of Theorem 3 and Theorem 4, the results show that the asymptotically stability of the stochastic disk dynamo system occurs when  $(q_1/\epsilon_1) + (q_2/\epsilon_2) < \sqrt{(2\mu_1 - \sigma_1^2)(2\mu_2 - \sigma_2^2)}$ , which means the stochastic disk dynamo system will not show chaotic behavior.

Let  $u_1 = 2.5$ ,  $u_2 = 2.6$ ,  $\epsilon_1 = 0.5$ ,  $\epsilon_2 = 1$ ,  $q_1 = 1.5$ ,  $q_2 = 2$ ,  $\sigma_1 = 1$ ,  $\sigma_2 = 1$ , and  $\sigma_3 = \sigma_4 = q_{10} = q_{20} = 0$ , and initial values  $(x_0, y_0, z_0, u_0) = (2.2, 2, 10.5, 20)$ . In Figure 6, the number results show that the trivial solution of system (3) is stochastically asymptotically stable.

## 5. Conclusions

The coupled dynamo system is a nonlinear dynamical system which is capable of chaotic behaviours. It models the geomagnetic field and is used to explain the reversals in its polarity. Actually, the parameters of the chaotic systems exhibit random fluctuation to a greater or lesser extent, which can carefully describe the disturbance made by environmental noise. The global dynamics of the chaotic disk dynamo system with random fluctuating parameters are concerned, and some new results are presented. Based on the generalized Lyapunov function, the globally attractive and positive invariant set is given, including a two-dimensional parabolic ultimate boundary and a four-dimensional ellipsoidal ultimate boundary. Furthermore, a set of sufficient conditions is derived for all solutions of the stochastic disk

dynamo system being global convergent to the equilibrium point. The stochastic disk dynamo system will not show chaotic behavior when the system is stable. Finally, numerical simulations are presented for verification.

## Data Availability

All data generated or analyzed during this study are included in this article.

## Conflicts of Interest

The authors declare that they have no conflicts of interest.

## Acknowledgments

This work was supported by the National Natural Science Foundation of China (Grant nos. 11961074 and 11971414), Natural Science Foundation of Guangxi Province (Grant nos. 2018GXNSFDA281028, 2017GXNSFAA198234, and 2016GXNSFBA380170), the Youth Project of Hunan Provincial Education Department (Grant nos. 18B518 and 18B082), the High Level Innovation Team Program from Guangxi Higher Education Institutions of China (Document no. [2018] 35), and the Fundamental Research Funds for the Central Universities, China University of Geosciences (CUGGC05).

## References

- [1] G. A. Glatzmaiers and P. H. Roberts, "A three-dimensional self-consistent computer simulation of a geomagnetic field reversal," *Nature*, vol. 377, no. 6546, pp. 203–209, 1995.
- [2] T. Rikitake, "Oscillations of a system of disk dynamos," *Mathematical Proceedings of the Cambridge Philosophical Society*, vol. 54, no. 1, pp. 89–105, 1958.
- [3] A. El-Gohary and R. Yassen, "Adaptive control and synchronization of a coupled dynamo system with uncertain parameters," *Chaos, Solitons & Fractals*, vol. 29, no. 5, pp. 1085–1094, 2006.
- [4] A. El-Gohary and R. Yassen, "Chaos and optimal control of a coupled dynamo with different time horizons," *Chaos, Solitons & Fractals*, vol. 41, no. 2, pp. 698–710, 2009.
- [5] E. N. Lorenz, "Deterministic nonperiodic flow," *Journal of the Atmospheric Sciences*, vol. 20, no. 2, pp. 130–141, 1963.
- [6] G. Chen and T. Ueta, "Yet another chaotic attractor," *International Journal of Bifurcation and Chaos*, vol. 9, no. 7, pp. 1465–1466, 1999.
- [7] J. Lü and G. Chen, "A new chaotic attractor coined," *International Journal of Bifurcation and Chaos*, vol. 12, no. 3, pp. 659–661, 2002.
- [8] Q. Yang and G. Chen, "A chaotic system with one saddle and two stable node-foci," *International Journal of Bifurcation and Chaos*, vol. 18, no. 5, pp. 1393–1414, 2008.
- [9] A. Vaněček and S. Čelikovský, *Control Systems: From Linear Analysis to Synthesis of Chaos*, Prentice-Hall, London, UK, 1996.
- [10] S. Čelikovský and G. Chen, "On a generalized Lorenz canonical form of chaotic systems," *International Journal of Bifurcation and Chaos*, vol. 12, pp. 1789–1812, 2002.
- [11] J. Llibre and M. Messias, "Global dynamics of the Rikitake system," *Physica D: Nonlinear Phenomena*, vol. 238, no. 3, pp. 241–252, 2009.

- [12] J. Jian and Z. Zhao, "New estimations for ultimate boundary and synchronization control for a disk dynamo system," *Nonlinear Analysis: Hybrid Systems*, vol. 9, pp. 56–66, 2013.
- [13] H. Yuan and F. Zhang, "Globally exponentially attractive set of disk dynamo system and its application," *Computer Engineering and Applications*, vol. 47, no. 33, pp. 226–228, 2011.
- [14] H. N. Agiza, "Controlling chaos for the dynamical system of coupled dynamos," *Chaos, Solitons & Fractals*, vol. 13, no. 2, pp. 341–352, 2002.
- [15] H. N. Agiza, "Chaos synchronization of two coupled dynamos systems with unknown system parameters," *International Journal of Modern Physics C*, vol. 15, no. 06, pp. 873–883, 2004.
- [16] S. Li and Y.-P. Tian, "Global stabilization of a coupled dynamo system," *Chaos, Solitons & Fractals*, vol. 16, no. 5, pp. 787–793, 2003.
- [17] L. Arnold, *Random Dynamical Systems*, Springer, New York, NY, USA, 1998.
- [18] Z. Huang, J. Cao, and T. Jiang, "Dynamics of stochastic Lorenz-Stenflo system," *Nonlinear Dynamics*, vol. 78, no. 3, pp. 1739–1754, 2014.
- [19] Z. Liu, C. Wang, W. Jin, and J. Ma, "Capacitor coupling induces synchronization between neural circuits," *Nonlinear Dynamics*, vol. 97, no. 4, pp. 2661–2673, 2019.
- [20] Z. Yao, J. Ma, Y. Yao, and C. Wang, "Synchronization realization between two nonlinear circuits via an induction coil coupling," *Nonlinear Dynamics*, vol. 96, no. 1, pp. 205–217, 2019.
- [21] Z. Yao, P. Zhou, A. Alsaedi, and J. Ma, "Energy flow-guided synchronization between chaotic circuits," *Applied Mathematics and Computation*, vol. 374, p. 124998, 2020.
- [22] D. Li, X. Wu, and J.-a. Lu, "Estimating the ultimate bound and positively invariant set for the hyperchaotic Lorenz-Haken system," *Chaos, Solitons & Fractals*, vol. 39, no. 3, pp. 1290–1296, 2009.
- [23] X. Liao, Y. Fu, S. Xie, and P. Yu, "Globally exponentially attractive sets of the family of Lorenz systems," *Science in China Series F: Information Sciences*, vol. 51, no. 3, pp. 283–292, 2008.
- [24] P. Yu and X. Liao, "New estimations for globally attractive and positive invariant set of the family of the Lorenz systems," *International Journal of Bifurcation and Chaos*, vol. 16, no. 11, pp. 3383–3390, 2006.
- [25] X. Liao, P. Yu, S. Xie, and Y. Fu, "Study on the global property of the smooth chua's system," *International Journal of Bifurcation and Chaos*, vol. 16, no. 10, pp. 2815–2841, 2006.
- [26] Z. Yan and P. Yu, "Globally exponential hyperchaos (lag) synchronization in a family of modified hyperchaotic rössler systems," *International Journal of Bifurcation and Chaos*, vol. 17, no. 5, pp. 1759–1774, 2007.
- [27] P. Yu and X. Liao, "Globally attractive and positive invariant set of the Lorenz system," *International Journal of Bifurcation and Chaos*, vol. 16, no. 3, pp. 757–764, 2006.
- [28] L. Li, Y. Feng, and Y. Liu, "Dynamics of the stochastic Lorenz-Haken system," *Chaos, Solitons & Fractals*, vol. 91, pp. 670–678, 2016.
- [29] Y. Liu, Z. Wei, C. Li, A. Liu, and L. Li, "Attractor and bifurcation of forced Lorenz-84 system," *International Journal of Geometric Methods in Modern Physics*, vol. 16, no. 1, p. 1950002, 2019.
- [30] Z. Huang, J. Cao, and T. Jiang, "Dynamics of stochastic Lorenz family of chaotic systems with jump," *Journal of Mathematical Chemistry*, vol. 52, no. 2, pp. 754–774, 2014.
- [31] Y. Liu, L. Li, and X. Wang, "Bifurcation and attractor of the stochastic Rabinovich system with jump," *International Journal of Geometric Methods in Modern Physics*, vol. 12, no. 09, p. 1550092, 2015.
- [32] A. Liu and L. Li, "Global dynamics of the stochastic Rabinovich system," *Nonlinear Dynamics*, vol. 81, no. 4, pp. 2141–2153, 2015.
- [33] Z. Huang, Q. Yang, and J. Cao, "A stochastic model for interactions of hot gases with cloud droplets and raindrops," *Nonlinear Analysis: Real World Applications*, vol. 12, no. 1, pp. 203–214, 2011.
- [34] Z. Huang, Q. Yang, and J. Cao, "Stochastic stability and bifurcation for the chronic state in Marchuk's model with noise," *Applied Mathematical Modelling*, vol. 35, no. 12, pp. 5842–5855, 2011.
- [35] X. Mao, *Stochastic Differential Equations and Applications*, Horwood Publishing, Chichester, UK, 2nd edition, 2007.

## Research Article

# CCII and FPGA Realization: A Multistable Modified Fourth-Order Autonomous Chua's Chaotic System with Coexisting Multiple Attractors

Fei Yu <sup>1</sup>, Hui Shen <sup>1</sup>, Li Liu <sup>1</sup>, Zinan Zhang <sup>1</sup>, Yuanyuan Huang <sup>1</sup>, Binyong He <sup>1</sup>, Shuo Cai <sup>1</sup>, Yun Song <sup>1</sup>, Bo Yin<sup>1</sup>, Sichun Du <sup>2</sup>, and Quan Xu <sup>3</sup>

<sup>1</sup>School of Computer and Communication Engineering, Changsha University of Science and Technology, Changsha 410114, China

<sup>2</sup>College of Computer Science and Electronic Engineering, Hunan University, Changsha 410082, China

<sup>3</sup>School of Information Science and Engineering, Changzhou University, Changzhou 213164, China

Correspondence should be addressed to Fei Yu; [yufeiyf@csust.edu.cn](mailto:yufeiyf@csust.edu.cn) and Yuanyuan Huang; [snailhy@126.com](mailto:snailhy@126.com)

Received 25 December 2019; Accepted 12 February 2020; Published 21 March 2020

Guest Editor: Viet-Thanh Pham

Copyright © 2020 Fei Yu et al. This is an open access article distributed under the Creative Commons Attribution License, which permits unrestricted use, distribution, and reproduction in any medium, provided the original work is properly cited.

In this paper, a multistable modified fourth-order autonomous Chua's chaotic system is investigated. In addition to the dynamic characteristics of the third-order Chua's chaotic system itself, what interests us is that this modified fourth-order autonomous Chua's chaotic system has five different types of coexisting attractors: double-scroll, single band chaotic attractor, period-4 limit cycle, period-2 limit cycle, and period-1 limit cycle. Then, an inductorless modified fourth-order autonomous Chua's chaotic circuit is proposed. The active elements as well as the synthetic inductor employed in this circuit are designed using second-generation current conveyors (CCIIs). The reason for using CCIIs is that they have high conversion rate and operation speed, which enable the circuit to work at a higher frequency range. The Multisim simulations confirm the theoretical estimates of the performance of the proposed circuit. Finally, using RK-4 numerical algorithm of VHDL 32-bit IQ-Math floating-point number format, the inductorless modified fourth-order autonomous Chua's chaotic system is implemented on FPGA for the development of embedded engineering applications based on chaos. The system is simulated and synthesized on Virtex-6 FPGA chip. The maximum operating frequency of modified Chua's chaotic oscillator based on FPGA is 180.180 MHz. This study demonstrates that the hardware-based multistable modified fourth-order autonomous Chua's chaotic system is a very good source of entropy and can be applied to various embedded systems based on chaos, including secure communication, cryptography, and random number generator.

## 1. Introduction

Nonlinear phenomena widely exist in natural science, engineering technology, and social science. Since 1960, the research and application of nonlinear systems have been more and more extensive. Many problems in complex networks [1–7], memristor [8–11], electronic circuits [12–15], image processing [16–21], economics [22], and other fields can be attributed to the study of nonlinear systems. Chaos is a special state of motion in a nonlinear system, which is a random-like behavior generated by a deterministic system and is extremely sensitive to initial values and highly dependent on them [23–28]. Entropy is

usually used to describe the complexity of chaotic systems. Therefore, it is of great significance to study the entropy of nonlinear systems [29–31].

With the rapid development of computer technology, the accompanying information security issues have attracted more and more attention and become a hot issue [32–42]. Chaos is widely used in cryptosystems, random numbers, and secure communications [43–49], and it has become a hot topic in nonlinear circuits and systems. In the realization of chaotic circuits, researchers have proposed many new methods to design different types of chaotic circuits [50–55]. Among them, Chua's chaotic circuit [56–58] has attracted wide attention because of its simple structure, bifurcation,

and chaotic complex dynamic characteristics. There are many research contents and achievements on this circuit, such as Chua's dual circuit [59], transformed Chua's circuit [60], multiscroll Chua's circuit [61], and hyperchaotic Chua's circuit [62, 63].

Multistability is a critical property of nonlinear dynamical systems, where a variety of behaviors such as coexisting attractors can appear for the same parameters, but different initial conditions. The flexibility in the system's performance can be archived without changing parameters [64, 65]. This has become a very popular research topic and some important research results have been achieved recently [11, 66–69]. In [66], a 4D memristor-based Colpitts system was proposed by employing an ideal memristor to substitute the exponential nonlinear term of original 3D Colpitts oscillator model, from which the initials-dependent extreme multistability was exhibited by phase portraits and local basins of attraction. In [67], an ideal voltage-controlled memristor emulator-based canonical Chua's circuit was investigated. With the voltage-current model, the initial condition-dependent extreme multistability was explored through analyzing the stability distribution of line equilibrium point and then the coexisting infinitely many attractors were numerically uncovered in such a memristive circuit by the attraction basin and phase portraits. In [69], a 5D multistable four-wing memristive hyperchaotic system (FWMHS) with linear equilibrium points was proposed by introducing a flux-controlled memristor model with absolute value function. A secure communication scheme based on the proposed 5D multistable FWMHS with disturbance inputs was also designed. To our best knowledge, fourth-order autonomous Chua's chaotic systems with multistability are rare in literature. Therefore, it is of great significance to study a fourth-order Chua's chaotic system with multistability.

In recent years, there exist several studies related to fourth-order autonomous Chua's chaotic circuits [70–73]. The design of a new fourth-order autonomous nonlinear electric circuit using two active elements, one linear negative conductance, and one nonlinear resistor has been proposed by Koliopoulos et al. to show rich dynamic behavior of Chua's circuit [71]. In the performed study by Liu et al., the design of fourth-order Chua's circuit has been proposed with a piecewise-linear nonlinearity and with a smooth cubic nonlinearity which could produce different kinds of attractors [72]. Wang et al. designed a fourth-order Chua's circuit using a capacitor, a resistance, and a controlled-source constituted by stair functions in the third-order Chua's circuit which could generate multidirectional multiscroll (MDMS) chaotic attractors [73]. However, the passive inductors are used in the circuits proposed in [70–73]. In fact, the parameters of passive inductor are not only difficult to control accurately in the actual Chua's circuit, but also very easy to be affected by frequency, environment, and other factors. Generally speaking, the internal resistance of the inductor will affect the oscillating circuit, and the larger the value of the inductor, the greater the internal resistance of the inductor, and the greater the impact on the circuit. In order to minimize the influence

of the internal resistance of the inductor on the circuit, the actual inductor can be replaced by the active inductor in the experiment. The active inductor can be equivalent to the ideal inductor without internal resistance consumption [74, 75].

Meanwhile, these modified Chua's circuits generally use ordinary voltage-mode operational amplifiers as active devices. Because the gain-bandwidth product of voltage-mode operational amplifiers is limited (usually several megahertz), it is necessary to balance the gain and bandwidth in the design of circuits. That is to say, in order to get a large circuit gain, the operating frequency of the circuit can only be reduced [76–79]. And the current-mode devices have good frequency gain characteristics. The bandwidth of these kind of devices is almost independent of gain, so there is no need to weigh the gain and bandwidth in the designed circuit, which can improve the working frequency of the circuit [80]. In recent years, the current-mode devices to realize Chua's circuit have gradually become a new research direction. In [81], active simulated inductor and piecewise nonlinear resistor in the circuit were all realized by second-generation current conveyors (CCII), so that the circuit was more stable and can work in higher frequency than does the usual Chua's circuit. The circuit also had the advantages in that the current waves and the corresponding phase diagrams could be tested easily. Jothimurugan et al. [82] reported an improved implementation of an inductorless third-order autonomous canonical Chua's circuit. The active elements as well as the synthetic inductor employed in this circuit were designed using current feedback operational amplifiers (CFOAs). The implementation of inductorless makes the experimental construction of Chua's circuit simple and compact.

Many analog implementations of chaotic systems in electronic circuits have been reported in recent decades, such as the well-known breadboard with discrete components [10, 13, 27, 28] and CMOS technology for integrated circuit (IC) design [12, 23, 24]. However, breadboard is not easy to carry, maintain, and store data, and IC design has a long cycle and high cost [83–87]. Meanwhile, in some chaotic information systems, digital implementation may be necessary, for example, in embedded chaos-based application areas and many other chaotic digital information systems. Digital chaotic generators have been implemented by varied structures such as Digital Signal Processor (DSP) [88, 89] and Field Programmable Gate Array (FPGA) [90–94]. In order to calculate complex mathematical operations, the DSP chips are optimized operations sequentially. Constant-time autonomous chaotic systems are characterized by at least three differential equations and at least three outputs. Therefore, it takes a long time for systems based on DSP to calculate the output signal values in turn. On the other hand, the FPGA chip can run in parallel and has a relatively flexible architecture. Therefore, the design and test cycle cost of the FPGA chip is extremely low. Moreover, because of its reprogrammability, high speed, and large capacity, the implementation of FPGA is of great significance in the fields of information security, encryption, cryptography, communication, and other applications [95, 96].



In recent years, the design of chaotic system based on FPGA has been extensively studied. In [90], by the help of fourth-order of RK4 method, Sundarapandian-Pehlivan chaotic system was proposed in VHDL 32-bit IEEE 754-1985 floating-point number standard on Virtex-6 FPGA chip. In [91], autonomous Lu-Chen chaotic system was implemented on Virtex-6 FPGA chip using Heun numerical algorithm in VHDL 32-bit IQ-Math fixed-point number format. In [92], with the method of Artificial Neural Networks, the design of Pehlivan-Uyaroglu chaotic system was implemented in VHDL IEEE 754 single precision floating-point number format on Virtex-6 FPGA chip. A 3D nonequilibrium chaotic system using RK4 numerical algorithm with IEEE 754-1985 floating-point number standard on Virtex-6 FPGA chip was designed in [93]. In [94], the implementation of multibutterfly chaotic system in FPGA by applying the Xilinx (Vivado) system generator was proposed.

The objective of this study is twofold. First, based on a multistable modified fourth-order autonomous Chua's chaotic circuit introduced in [70], an improved implementation of an inductorless modified fourth-order autonomous Chua's chaotic circuit is proposed. The active elements as well as the synthetic inductor employed in this circuit are designed using CCII's. The reason for employing CCII's is that, compared with circuits designed with voltage operational amplifiers, CCII's have better characteristics such as high conversion rate and high working speed, so that the circuit can work in higher frequency ranges. Second, the RK-4 method in a hardware description language (VHDL) is used to model the modified fourth-order autonomous Chua's chaotic system, and the model is tested comprehensively on Xilinx Virtex-6 FPGA chip. The phase portraits of the output result of the system based on FPGA are given. The design results of the modified Chua's chaotic oscillator based on FPGA are compared with those of computer, which verifies the correctness of the design based on digital circuit.

The structure of this paper is as follows: a multistable modified fourth-order autonomous Chua's chaotic system is investigated and the dynamic characteristics are discussed in Section 2. An inductorless modified fourth-order autonomous Chua's chaotic circuit is constructed by using CCII in Section 3. The Multisim simulation results of the inductorless modified Chua's chaotic circuit are also given. In Section 4, the FPGA-based model of the modified fourth-order autonomous Chua's chaotic system is introduced and simulation results of FPGA-based model are presented. Finally, conclusions are outlined in Section 5.

## 2. Multistable Modified Fourth-Order Autonomous Chua's Chaotic System

**2.1. Modified Fourth-Order Autonomous Chua's Chaotic Circuit.** By adding a linear resistor and a linear capacitor to the classical Chua's chaotic circuit, a modified fourth-order autonomous Chua's chaotic circuit is introduced in [70], as shown in Figure 1. According to Kirchhoff's law, the dynamics of this circuit is governed by the following equations:

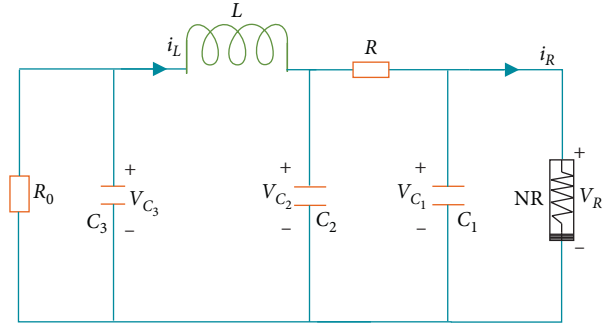


FIGURE 1: Modified fourth-order autonomous Chua's chaotic circuit.

$$\begin{cases} C_1 \frac{dV_{C_1}}{dt} = \frac{1}{R} (V_{C_2} - V_{C_1}) - f(V_{C_1}), \\ C_2 \frac{dV_{C_2}}{dt} = \frac{1}{R} (V_{C_1} - V_{C_2}) + i_L, \\ L \frac{di_L}{dt} = V_{C_3} - V_{C_2}, \\ C_3 \frac{dV_{C_3}}{dt} = -i_L - \frac{1}{R_0} V_{C_3}, \end{cases} \quad (1)$$

where  $V_{C_1}$ ,  $V_{C_2}$ ,  $V_{C_3}$ , and  $i_L$  are state variables which denote the voltage across  $C_1$ , the voltage across  $C_2$ , the voltage across  $C_3$ , and current through  $L$ , respectively. According to the principle of Chua's diode in classical Chua's chaotic circuit, the characteristic curve of Chua's diode NR in (1) can be graphically represented as in Figure 2 and is given by

$$f(V_{C_1}) = G_b V_{C_1} + \frac{1}{2} (G_a - G_b) \times (|V_{C_1} + E_a| - |V_{C_1} - E_a|), \quad (2)$$

where  $G_a$  and  $G_b$  are the slopes of the outer and inner regions, respectively, and  $\pm E_a$  denote the breakpoints.

### 2.2. Multistable Modified Fourth-Order Autonomous Chua's Chaotic System

**2.2.1. System Generation and Dynamics Analysis.** When  $x = V_{C_1}/E_a$ ,  $y = V_{C_2}/E_a$ ,  $z = i_L R/E_a$ ,  $w = V_{C_3}/E_a$ ,  $\alpha = C_2/C_1$ ,  $\beta = C_2 R^2/L$ ,  $\gamma_1 = R/R_0$ ,  $\gamma_2 = C_2/C_3$ , equation (1) can be expressed as follows:

$$\begin{cases} \dot{x} = \alpha [y - x - f(x)], \\ \dot{y} = x - y + z, \\ \dot{z} = -\beta (y - w), \\ \dot{w} = -\gamma_2 (z + \gamma_1 w). \end{cases} \quad (3)$$

When the parameters are selected as  $C_1 = 10$  nF,  $C_2 = 100$  nF,  $L = 17.64$  mH,  $R = 1.68$  k $\Omega$ ,  $C_3 = 2$   $\mu$ F,  $E_a = 1$ ,  $G_a = -1.28$  ms,  $G_b = -0.69$  ms, and  $R_0 = 60$   $\Omega$ , we can get  $\alpha = 10$ ,  $\beta = 16$ ,  $\gamma_1 = 28$ , and  $\gamma_2 = 0.05$ . A double-scroll chaotic

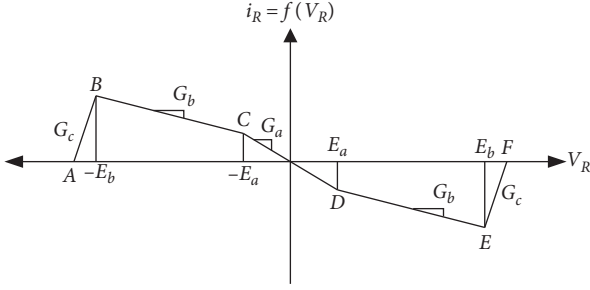


FIGURE 2: Five-segment piecewise linear  $V - I$  characteristic of the nonlinear resistor.

attractor is generated by MATLAB simulation under the initial condition  $[0, 0.1, 0, 0]$ , as shown in Figure 3. As can be seen from Figure 3, when the parameters of the system satisfy certain conditions, a self-excited oscillation attractor called double-scroll, like Chua's circuit, will also be generated. Chaotic orbits are currents circling around strange attractors [59]. The nonperiodicity of chaotic oscillation can be clearly seen from the time-domain waveforms, as shown in Figure 4.

The dynamic system described by differential equation (3) is symmetric with respect to origin and corresponds to the characteristics of Chua's diode NR. If the characteristics of Chua's diode NR are divided into three sections; that is,

$$f(x) = \begin{cases} G_b x + (G_a - G_b), & x > 1, \\ G_a x, & -1 \leq x \leq 1, \\ G_b x - (G_a - G_b), & x < -1, \end{cases} \quad (4)$$

$$= \begin{cases} -0.69x - 0.59, & x > 1, \\ -1.28x, & -1 \leq x \leq 1, \\ -0.69x + 0.59, & x < -1. \end{cases}$$

The three subspaces in the state space of (4) are

$$\begin{cases} D_1 = \{(x, y, z, w) \mid x > 1\}, \\ D_0 = \{(x, y, z, w) \mid -1 \leq x \leq 1\}, \\ D_{-1} = \{(x, y, z, w) \mid x < -1\}. \end{cases} \quad (5)$$

There are unique equilibrium points in three subspaces of the state space. The three unique equilibrium points are

$$\begin{aligned} P^+ &= (2.1388, 0.0738, -2.0650, 0.0738) \in D_1, \\ Q &= (0, 0, 0, 0) \in D_0, \\ P^- &= (-2.1388, -0.0738, 2.0650, -0.0738) \in D_{-1}. \end{aligned} \quad (6)$$

Linearization is carried out at the equilibrium point  $Q(0, 0, 0, 0)$ , and the linearization matrix is obtained as follows:

$$\begin{bmatrix} 2.8 & 10 & 0 & 0 \\ 1 & -1 & 1 & 0 \\ 0 & -16 & 0 & 16 \\ 0 & 0 & -0.05 & -1.4 \end{bmatrix}. \quad (7)$$

Four eigenvalues of the above matrix can be calculated:  $3.9298, -1.0103 + 3.3587i, -1.0103 - 3.3587i$ , and  $-1.5092$ ,

linearized at equilibrium points  $P^+$  and  $P^-$ , and the linearized matrix can be obtained as follows:

$$\begin{bmatrix} -3.1 & 10 & 0 & 0 \\ 1 & -1 & 1 & 0 \\ 0 & -16 & 0 & 16 \\ 0 & 0 & -0.05 & -1.4 \end{bmatrix}. \quad (8)$$

Four eigenvalues of the above matrix are calculated:  $-4.5531, 0.1295 + 3.4095i, 0.1295 - 3.4095i, -1.2060$ . Therefore, all equilibrium points  $P^+, Q$ , and  $P^-$  are saddle points. In the macroscopic view of chaotic attractors, holes are formed near  $P^+$  and  $P^-$ , respectively, which are like two whirlpools twisted together, showing a double-scroll chaotic strange attractor (Figure 3). This is the result of the combination of global stability and local instability. Chaotic orbits are the flow whirling around the strange attractor. The adjacent trajectories show a tendency of mutual exclusion and separation at an exponential rate [70].

There are many interesting chaotic phenomena when the system parameters are changed continuously. However, in order to debug the experimental circuit conveniently in the future, only the resistance  $R$  is changed to observe the  $x - y$  plane at the ends of  $C_1$  and  $C_2$ . In the simulation process, the  $x - y$  plane at the ends of  $C_1$  and  $C_2$  also shows that period-1 limit cycle, period-2 limit cycle, period-4 limit cycle, and single-band chaotic attractor are shown in Figure 5 and Table 1. It can be seen that the modified Chua's chaotic circuit exhibits abundant dynamic behavior of period doubling bifurcation sequence.

**2.2.2. Multistability Analysis.** Multistability allows flexibility of system performance without changing parameters, and appropriate control strategies can be used to induce switching behavior between different coexisting states. In order to study the complex dynamic characteristics of the system better, it is necessary to give some disturbance to the initial conditions, that is, to change the initial conditions of the system under the condition of keeping the system parameters unchanged. Figure 6 shows the coexistence phenomenon of the system under two different initial conditions. The initial condition of the blue trace is  $[0, 0.1, 0, 0]$  and the initial condition of the red trace is  $[0, -0.1, 0, 0]$ . It can be seen from Figure 6 that, under these two initial conditions, the attractors exhibited by the system are exactly the same, but the directions of the trajectories are different, which all depend on the symmetry of the system. Figure 6 shows the coexistence attractors for different parameter values  $\beta$  and  $\gamma_1$ . Figure 6(a) shows that the system has coexisting double-scroll chaotic attractors. Figure 6(b) shows that the system has coexisting single band chaotic attractors. Figure 6(c) shows that the system shows coexisting period-4 limit cycle. It is very interesting that Figure 6(d) shows that the system has a period-2 limit cycle coexistence phenomenon. Figure 6(e) shows that the system has a period-1 limit cycle coexistence phenomenon. Figure 6(f) is a time-domain waveform diagram of state  $x$ , and its parameter values are the same as period-1 limit cycle.



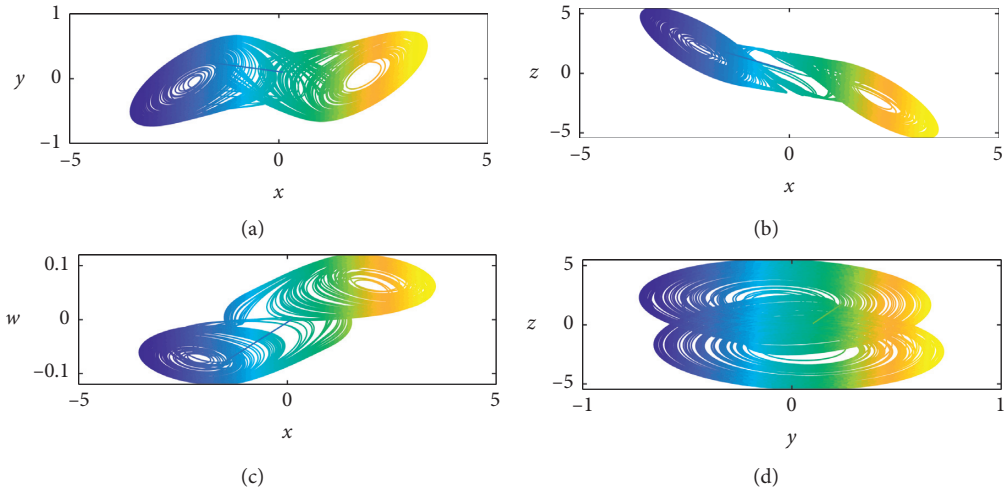


FIGURE 3: MATLAB simulation results of the modified Chua's chaotic circuit: (a) in  $x - y$  plane, (b) in  $x - z$  plane, (c) in  $x - w$  plane, and (d) in  $y - z$  plane.

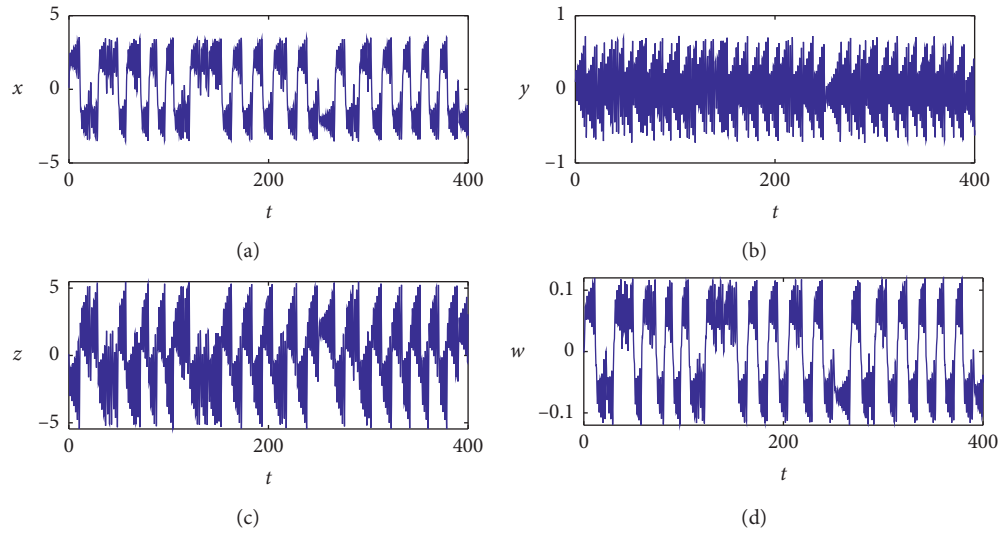


FIGURE 4: Time-domain waveforms of chaotic system (3).

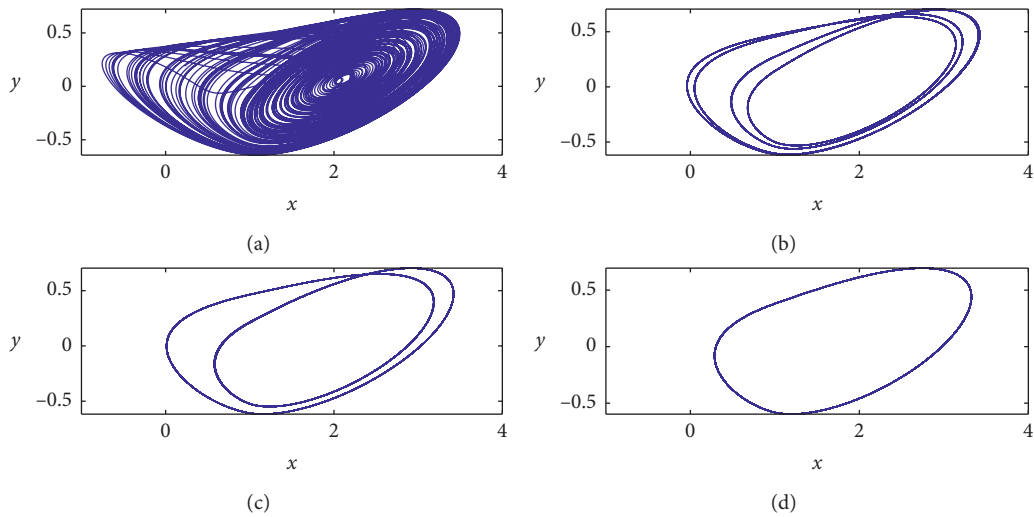


FIGURE 5: The period doubling scenario in the modified Chua's chaotic circuit shown in Figure 1: (a) single band chaotic attractor ( $R = 1734 \Omega$ ), (b) period-4 limit cycle ( $R = 1770 \Omega$ ), (c) period-2 limit cycle ( $R = 1775 \Omega$ ), and (d) period-1 limit cycle ( $R = 1801 \Omega$ ).

TABLE 1: Chaotic phenomena of the modified Chua's chaotic system by increasing resistance  $R$  values.

Chaotic phenomena	Range of $R$	$R$	$\alpha$	$\beta$	$\gamma_1$	$\gamma_2$	Figure
Single band chaotic attractor	1734 $\Omega$ –1769 $\Omega$	1734 $\Omega$	10	17.05	28.9	0.05	Figure 5(a)
Period-4 limit cycle	1770 $\Omega$ –1774 $\Omega$	1770 $\Omega$	10	17.76	29.5	0.05	Figure 5(b)
Period-2 limit cycle	1775 $\Omega$ –1800 $\Omega$	1775 $\Omega$	10	17.86	29.58	0.05	Figure 5(c)
Period-1 limit cycle	1801 $\Omega$ –1992 $\Omega$	1801 $\Omega$	10	18.39	30.02	0.05	Figure 5(d)

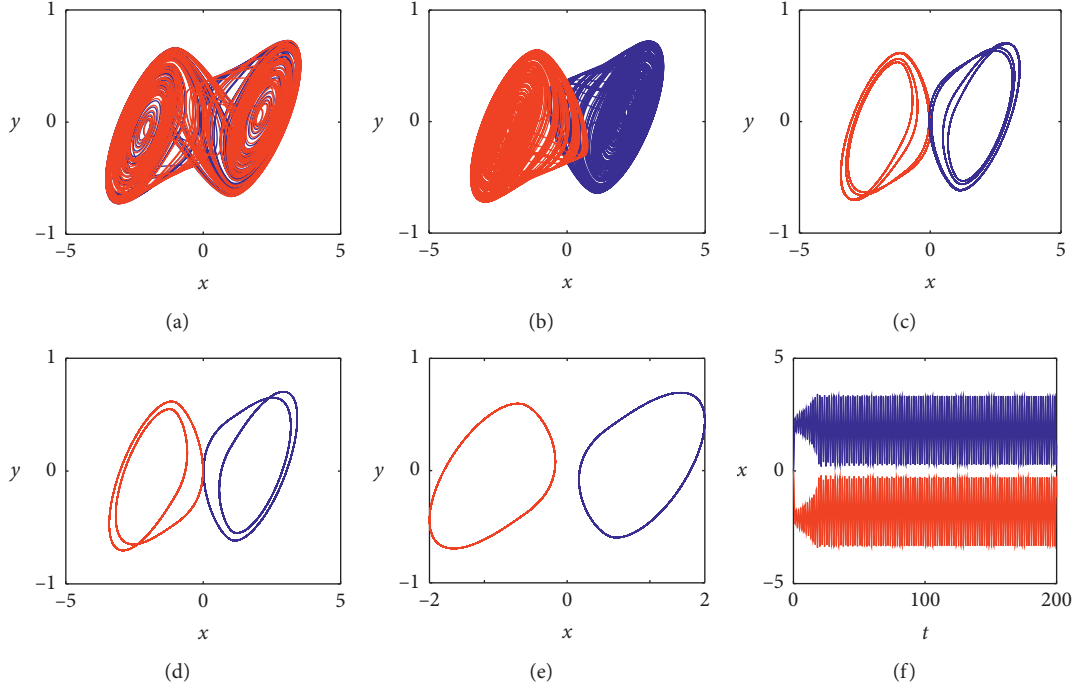


FIGURE 6: Coexisting attractors for the different parameter values  $\beta$  and  $\gamma_1$  and the initial conditions are  $[0, 0.1, 0, 0]$  and  $[0, -0.1, 0, 0]$  which are shown in blue and red, respectively: (a) coexisting double-scroll chaotic attractors, (b) coexisting single band chaotic attractors, (c) coexisting period-4 limit cycle, (d) coexisting period-2 limit cycle, (e) coexisting period-1 limit cycle, and (f) coexisting time-domain waveform diagram of state  $x$ .

### 3. Inductorless Modified Fourth-Order Autonomous Chua's Chaotic Circuit Based on CCII

3.1. *Inductorless Modified Chua's Chaotic Circuit Realized by CCII.* Current conveyor is a kind of electronic device with good high frequency performance, strong versatility, and flexibility, which has attracted wide attention of scholars [76–81]. In this part, a modified Chua's chaotic circuit realized by current conveyor is proposed. The key is to realize piecewise linear resistance  $NR$  and inductance  $L$  in Chua's chaotic circuit by using CCII commercial chip AD844 (current feedback operational amplifier) as the basic active device.

3.1.1. *CCII.* CCII is one of the most commonly used active devices in current-mode circuits. The symbolic representation of CCII is shown in Figure 7. Port relationship of CCII is

$$\begin{aligned} I_Y &= 0, \\ V_X &= V_Y, \\ I_Z &= KI_X, \end{aligned} \quad (9)$$

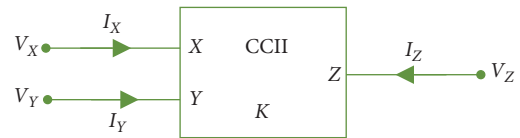


FIGURE 7: Symbolic representation of CCII.

where  $V_X$  and  $I_X$  are the voltage and current of  $X$ -terminal,  $V_Y$  and  $I_Y$  are the voltage and current of  $Y$ -terminal, and  $V_Z$  and  $I_Z$  are the voltage and current of  $Z$ -terminal, respectively.  $K$  is the transmission coefficient of the current conveyor. When  $K = 1$ , it is the in-phase current conveyor, and when  $K = -1$ , it is the reverse-phase current conveyor. The in-phase current conveyor can be implemented with one AD844, while the reverse-phase current conveyor needs two AD844. The implementation circuits are shown in Figures 8(a) and 8(b), respectively.

3.1.2. *Five-Segment Piecewise Nonlinear Resistance (NR).* Generally, when we use CCII to construct a nonlinear functional circuit, the five-segment piecewise nonlinear

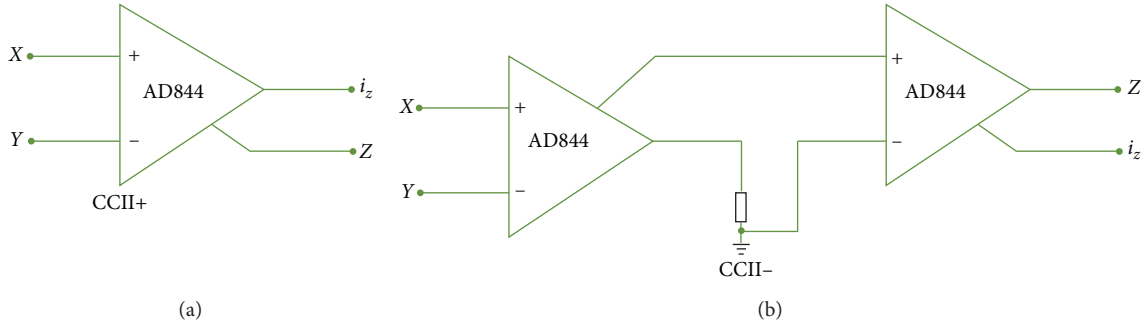


FIGURE 8: Implementation of the in-phase current conveyor (a) and the reverse-phase current conveyor (b).

resistance is employed. As shown in Figure 2, the input voltage is given to make it work in the middle of three BCDE segments. A five-piece nonlinear resistance [81] can be formed by parallel connection of two CCII, as shown in Figure 9(a). In Figure 2, the five-segment piecewise nonlinear resistance (NR)  $V$ - $I$  characteristic curve ABCDEF is generated by the circuit structure, the BCDE section has the characteristics of nonlinear negative resistance, and Chua's chaotic circuit mainly works in this curve section. The turning voltage and slope of the two circuits are  $E_a, E_b, G_a,$  and  $G_b,$  respectively. Therefore, the  $V$ - $I$  characteristic curve of the five-segment piecewise nonlinear resistance can be obtained as follows:

$$f(v) = \begin{cases} G_c v - (G_b - G_c)E_b - (G_a - G_b)E_a, & v < -E_b, \\ G_b v + (G_a - G_b)E_a, & -E_b \leq v < -E_a, \\ G_a v, & -E_a \leq v \leq E_a, \\ G_b v + (G_a - G_b)E_a, & E_a < v \leq E_b, \\ G_c v - (G_b - G_c)E_b - (G_a - G_b)E_a, & E_b < v. \end{cases} \quad (10)$$

According to the structure characteristics of the circuit shown in Figure 2, the slope expressions of each section are as follows:

$$\begin{aligned} E_a &= -R \left( \frac{1}{R_4} + \frac{1}{R_8} \right), \\ G_b &= R \left( \frac{1}{R_5} - \frac{1}{R_4} \right), \\ G_c &= R \left( \frac{1}{R_1} + \frac{1}{R_5} \right). \end{aligned} \quad (11)$$

The turning voltages of the circuit are

$$\begin{aligned} E_a &= \frac{R_8}{R_7 + R_8} V_{CC}, \\ E_b &= \frac{R_4}{R_3 + R_4} V_{CC}, \end{aligned} \quad (12)$$

where  $V_{CC}$  is the power supply voltage of the amplifier. Figure 9(b) shows the five-segment piecewise nonlinear resistance  $V$ - $I$  characteristic curve of Figure 9(a)'s circuit

which is simulated by Multisim. It can be seen that the curve is completely consistent with the performance of Figure 2.

**3.1.3. Lossless Grounded Active Inductor ( $L_{eq}$ ).** Although inductor is an important passive device in IC design, it is not easy to integrate because it cannot integrate itself. Therefore, spiral inductors are widely used in integrated circuits. Even so, there are some disadvantages, such as low adjustability, weight, large area, and high cost [82]. Therefore, in order to overcome these difficulties, inductance simulators are used as substitutes for spiral inductors in many circuit applications [97]. In this study, a lossless grounded active inductor based on CCII developed by Yang is used [81]. This is because CCII has proven to be very useful in either current or voltage-mode signal processing circuits. The principle circuit of the lossless grounded active inductor realized by CCII is shown in Figure 10.

In Figure 10, CCII-,  $Z_1,$  and  $Z_2$  form a voltage amplifier. CCII+,  $Z_2,$  and  $Z_3$  form a current amplifier. The input voltage  $v_i$  is added to the  $Y$ -terminal of CCII- and amplified by the voltage amplifier composed of CCII-,  $Z_1,$  and  $Z_2$ . According to the voltage-current relationship of CCII, if  $K = 1$ , the equivalent input impedance of the circuit shown in Figure 9(a) is

$$Z_{in} = \frac{Z_1 Z_2}{Z_3}. \quad (13)$$

It can be seen that the circuit shown in Figure 10 is an impedance converter, which can realize impedance conversion. By changing the properties of impedance  $Z_1, Z_2,$  and  $Z_3$ , different equivalent impedance can be obtained. If  $Z_1 = R_1, Z_2 = R_2,$  and  $Z_3 = 1/SC$ , the circuit can realize a lossless grounded active inductor, and the equivalent inductance value of the lossless grounded active inductor is

$$L_{eq} = R_1 R_2 C. \quad (14)$$

**3.1.4. Inductorless Modified Fourth-Order Autonomous Chua's Chaotic Circuit.** Figure 11 shows the modified Chua's chaotic circuit designed using CCII. The upper part inside the dash box of the circuit simulates a grounded inductor ( $L_{eq}$ ), the right part inside the dash box is piecewise five-segment linear NR designed using CCII, and the left

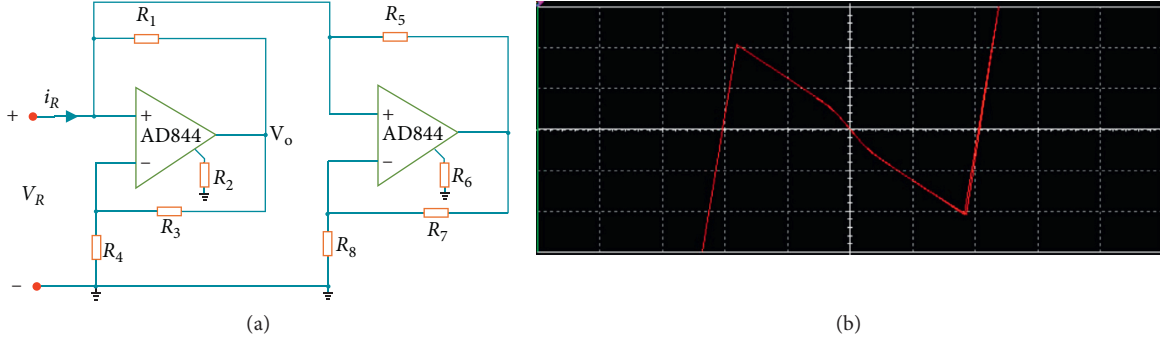


FIGURE 9: Five-segment piecewise nonlinear resistance implemented by two CCII: (a) circuit structure and (b)  $V$ - $I$  characteristic simulated by Multisim.

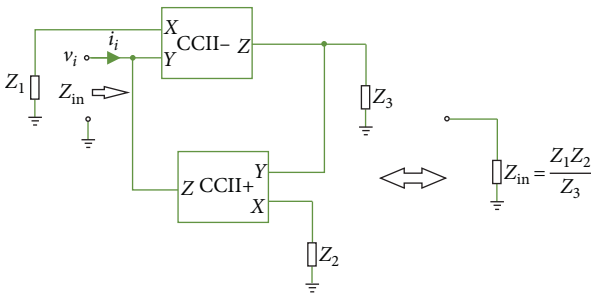


FIGURE 10: Lossless grounded active inductor circuit implemented by CCII.

part inside the dash box of the circuit is a linear RC network. The inspection of the present circuit configuration reveals that all the four state variables  $V_{C1}$ ,  $V_{C2}$ ,  $i_L$ , and  $V_{C3}$ , as stated in (1), are available from the circuit. The simulated inductance  $L_{eq}$  is composed of one CCII+, two CCII-, and one capacitor  $C_4$ . RC network is composed of  $C_1$ ,  $C_2$ ,  $C_3$ ,  $R_0$ , and  $R$ .  $C_2$ ,  $C_3$ , and  $L_{eq}$  constitute resonant circuit.  $C_1$  and piecewise linear resistance circuit are connected in parallel. Resistor  $R$  connects linear circuit and nonlinear circuit to form chaotic circuit. The values of components are taken in Table 2. This circuit is biased with  $\pm 15$  V supply. A double-scroll attractor is observed for  $R = 1680 \Omega$  as shown in Figure 12. Through the simulation of the circuit, we have also observed a variety of dynamic behaviors, such as single band chain attractor, period-4 limit cycle, period-2 limit cycle, period-1 limit cycle, steady state, and limit cycle, as shown in Figure 13. It can be seen that the Multisim simulation results are in good agreement with the theoretical analysis, which verifies the feasibility of the modified Chua's circuit.

#### 4. FPGA Implementation of the Multistable Modified Fourth-Order Autonomous Chua's Chaotic System

The multistable modified fourth-order autonomous Chua's chaotic system presented in this study is modeled on LabVIEW FPGA using Runge-Kutta (RK-4) algorithm, which is one of the most popular numerical differential equation decryption methods in the literature. According to the 32-bit IEEE 754-1985 floating-point number standard, the design is

coded on VHDL (Very-High-Speed High Speed Integrated Circuit Hardware Description Language) [98]. IP core generator developed by Vivado 2018.3 Design Tools system is used to design chaotic oscillator based on FPGA, such as multiplier, subtractor, and adder, which conform to IEEE 754-1985 standard.

**4.1. RK-4 Algorithm.** Runge-Kutta (RK) algorithm is a high precision one-step algorithm widely used in engineering. The theoretical basis of the algorithm is derived from Taylor's formula and the slope approximation to express the differential. It predicts the slope of several points several times in the integral interval, then carries out weighted averaging, which is used as the basis for the next point, and thus constructs a numerical integration calculation method with higher accuracy [90]. If the slopes of four points are calculated beforehand, it is the fourth-order Runge-Kutta (RK-4) algorithm. For differential equation  $\dot{y} = f(x, y)$ , the theoretical formula of RK-4 is as follows:

$$\begin{aligned}
 K1 &= f(x_k, y_k), \\
 K2 &= f\left(x_k + \frac{\Delta h}{2}, y_k + \frac{\Delta h}{2} K1\right), \\
 K3 &= f\left(x_k + \frac{\Delta h}{2}, y_k + \frac{\Delta h}{2} K2\right), \\
 K4 &= f(x_k + \Delta h, y_k + \Delta h K3), \\
 y_{k+1} &= y_k + \frac{\Delta h}{6} (K1 + 2K2 + 2K3 + K4),
 \end{aligned} \tag{15}$$

where  $K1, K2, K3, K4$  denote the first-order reciprocal of the output variable, that is, the differential at a point, expressed as the slope. The iteration step is  $\Delta h = 0.001$ . Figure 14 shows the block diagram of Chua's oscillator using RK-4 algorithm.  $x_0, y_0, z_0$ , and  $w_0$  signals are the initial conditions (IC) for the system to start running. In the design, they are defined as 32-bit symbolic floating-point numbers, which are determined internally by the user. The purpose of the multiplexer unit (MUX) is to select the external initial conditions at the

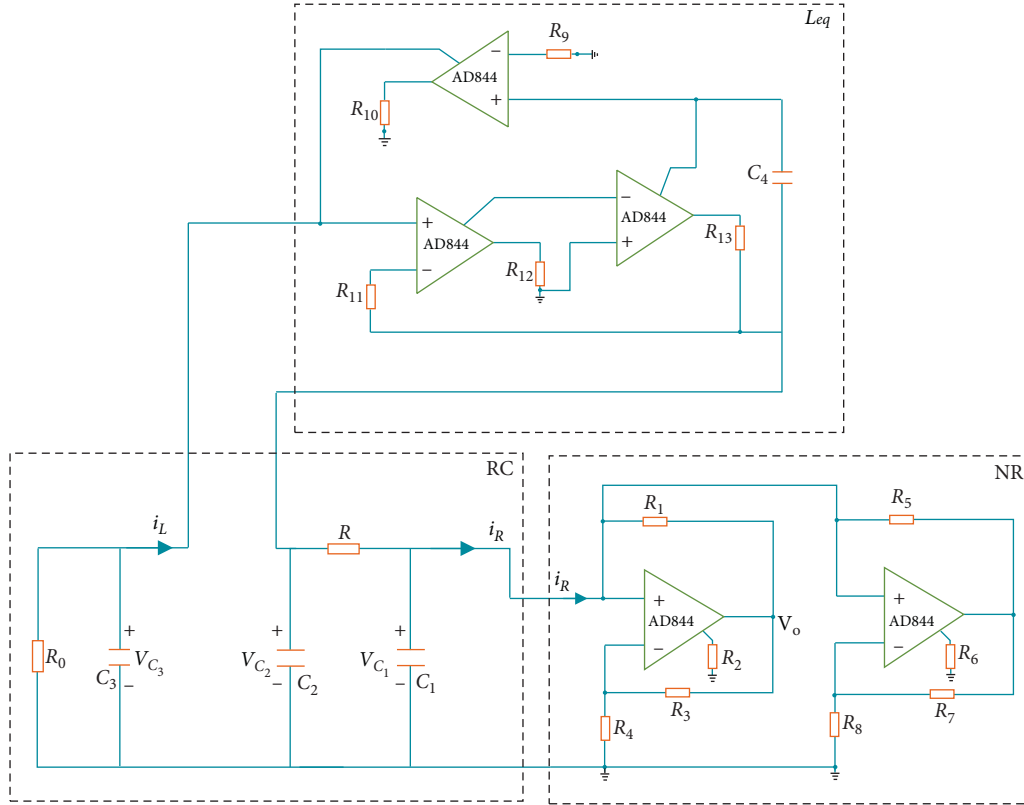


FIGURE 11: Inductorless modified Chua's chaotic circuit realized by CCII.

TABLE 2: Values of components used in the modified Chua's chaotic circuit.

Passive component	Value
$R_0$	60 $\Omega$
$R_1$	220 $\Omega$
$R_2$	220 $k\Omega$
$R_3$	220 $\Omega$
$R_4$	2.2 $k\Omega$
$R_5$	22 $k\Omega$
$R_6$	220 $k\Omega$
$R_7$	22 $k\Omega$
$R_8$	3.3 $k\Omega$
$R_9$	1 $k\Omega$
$R_{10}$	220 $k\Omega$
$R_{11}$	1 $k\Omega$
$R_{12}$	220 $k\Omega$
$R_{13}$	220 $k\Omega$
$R$	Variable
$C_1$	10 nF
$C_2$	100 nF
$C_3$	2 $\mu\text{F}$
$C_4$	17.64 nF

start or the internal values provided by the RK4-based oscillator unit in the successive steps. In the continuous steps after the start of operation, the  $x_{k+1}$ ,  $y_{k+1}$ ,  $z_{k+1}$ , and  $w_{k+1}$  signals generated by the oscillator unit are used as feedback inputs of the multiplexing unit, that is, the input signals of the next step, such as  $x_k$ ,  $y_k$ ,  $z_k$ , and  $w_k$ . The oscillator unit consists of six modules:  $K1$ ,  $K2$ ,  $K3$ ,  $K4$ ,  $ys$ , and filter, where

$K1$ ,  $K2$ ,  $K3$ ,  $K4$  modules are used to calculate the values of  $K1$ ,  $K2$ ,  $K3$ ,  $K4$  and  $ys$  module is used to calculate the value of  $x_{k+1}$ ,  $y_{k+1}$ ,  $z_{k+1}$ ,  $w_{k+1}$ . When  $ys$  does not produce the final required calculation results, the filter unit will prevent the intermediate value to reach the output.

**4.2. FPGA Implementation.** The top level block diagram of the modified fourth-order Chua's oscillator based on FPGA designed by RK-4 algorithm is shown in Figure 15. As can be seen from Figure 15, the design system has three inputs and five outputs. The input signal consists of a 1-bit clock signal (Clk), a 1-bit Reset, and a 32-bit  $\Delta h$ . Clk and Reset are used to ensure synchronization between the system and other modules. 32-bit  $\Delta h$  represents the step size, which is used to determine the sensitivity of the algorithm. The output signal consists of four 32-bit output signals  $X\_out$ ,  $Y\_out$ ,  $Z\_out$ ,  $W\_out$  and 1-bit flag signal  $XYZW\_ready$ . When the calculation generates  $X\_out$ ,  $Y\_out$ ,  $Z\_out$ ,  $W\_out$ , the flag signal  $XYZW\_ready$  is output.

The second level block diagram is composed of modified Chua's chaotic oscillator, floating-point to fixed-point unit, and digital-to-analog converter, as shown in Figure 16. The oscillator unit has three input signals, 1-bit Run, 1-bit Clk and 32-bit  $\Delta h$ , respectively. The 1-bit  $XYZW\_ready$  data signal provides the clock signal for the DAC unit. At the output of chaotic oscillator based on Rk-4, there are four floating-point standard 32-bit output signals ( $X\_out$ ,  $Y\_out$ ,  $Z\_out$ ,  $W\_out$ ). These signals are equivalent to the  $x$ ,  $y$ ,  $z$ , and  $w$  variables of the continuous-time chaotic system (3).



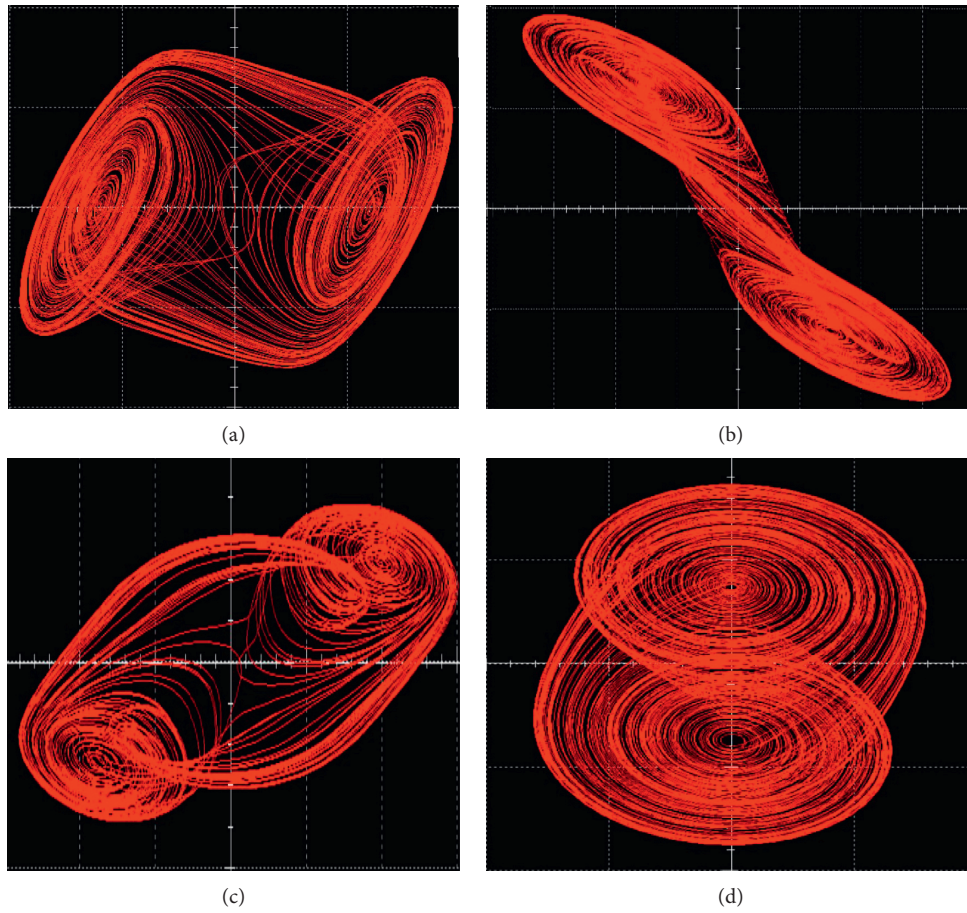


FIGURE 12: Multisim simulation of double-scroll phase portraits ( $R = 1680 \Omega$ ) of the inductorless modified Chua's chaotic circuit: (a) in  $x$ - $y$  plane, (b) in  $x$ - $z$  plane, (c) in  $x$ - $w$  plane, and (d) in  $y$ - $z$  plane.

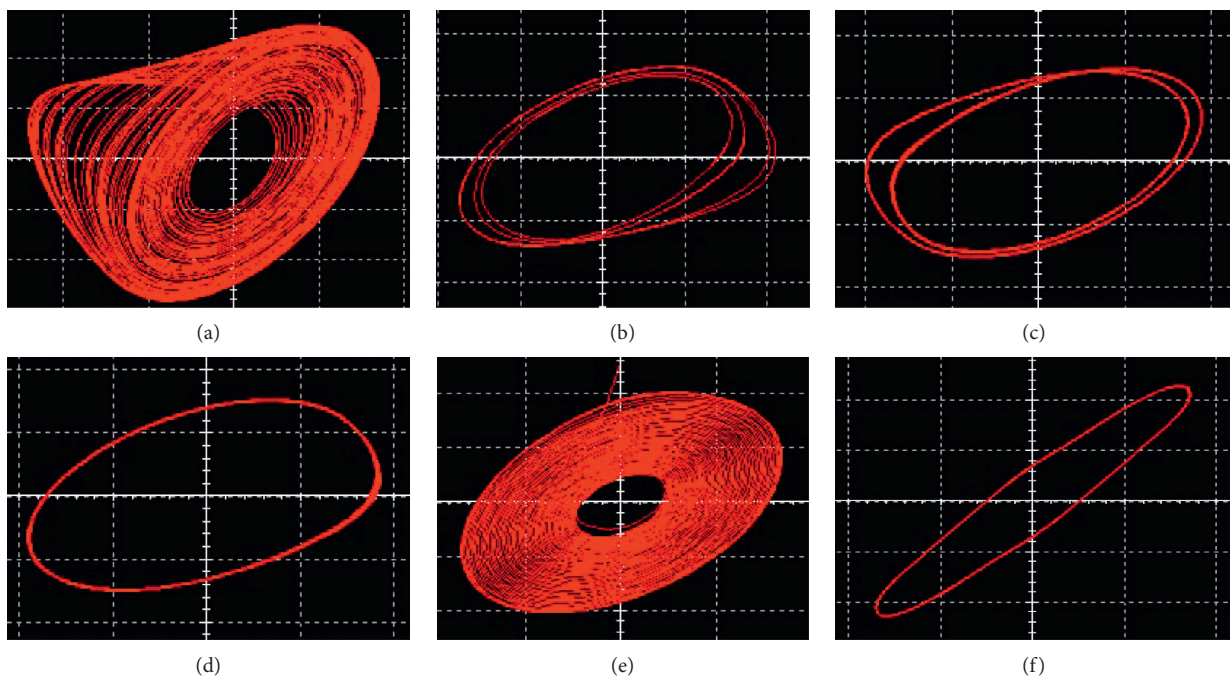


FIGURE 13: Multisim simulation of (a) single band chaotic attractor ( $R = 1950 \Omega$ ), (b) period-4 limit cycle ( $R = 1980 \Omega$ ), (c) period-2 limit cycle ( $R = 1990 \Omega$ ), (d) period-1 limit cycle ( $R = 2000 \Omega$ ), (e) steady state ( $R = 2040 \Omega$ ), and (f) limit cycle ( $R = 1100 \Omega$ ) in  $x$ - $y$  plane.



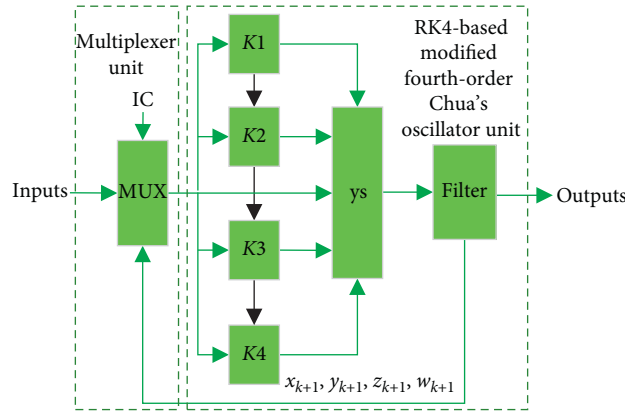


FIGURE 14: The block diagram of the FPGA-based multistable modified Chua's chaotic oscillator unit.

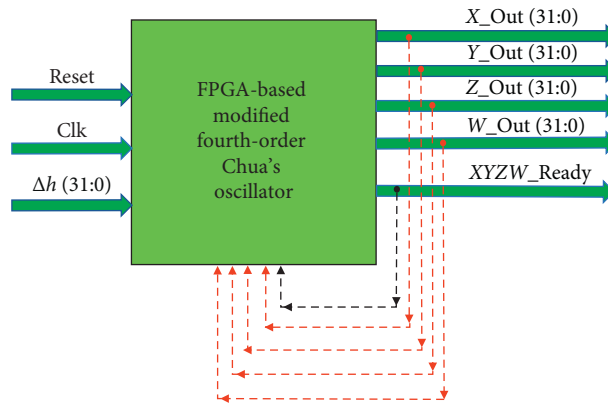


FIGURE 15: The top level block diagram of the FPGA-based multistable modified Chua's chaotic system.

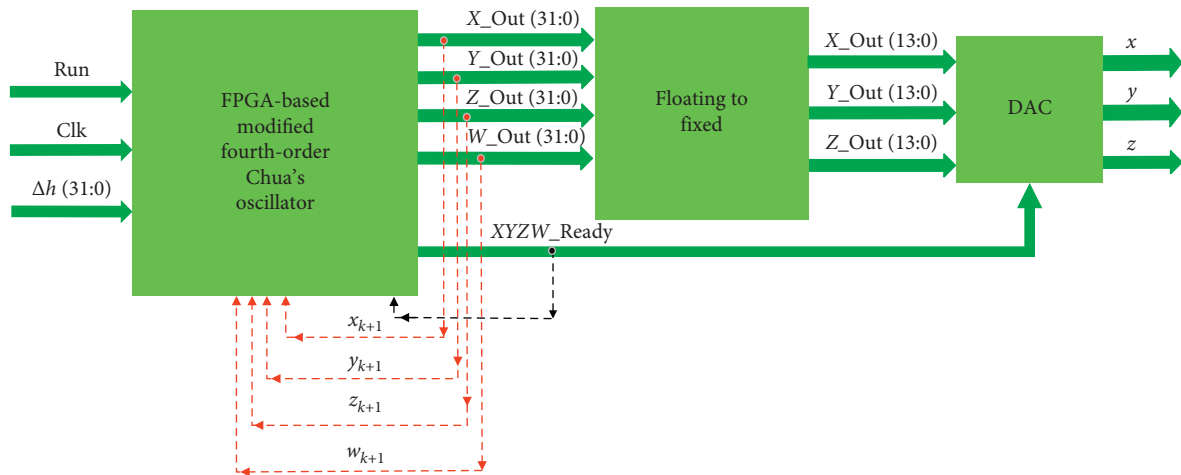


FIGURE 16: The second level block diagram of the FPGA-based multistable modified Chua's chaotic system.

The input of the floating-point to fixed-point unit is four 32-bit output signals of the oscillator unit, which converts the output of the former unit into 14-bit unsigned fixed-point. The DAC module converts the digital signal generated by the chaotic system into analog signal and outputs it to the oscilloscope. In the actual experiment, we choose

$X_{out}, Y_{out}$ , and  $Z_{out}$  to output the dual-channel DAC module and then the oscilloscope.

4.3. *FPGA Test Results.* The modified multistable fourth-order Chua's chaotic system based on RK-4 is synthesized on

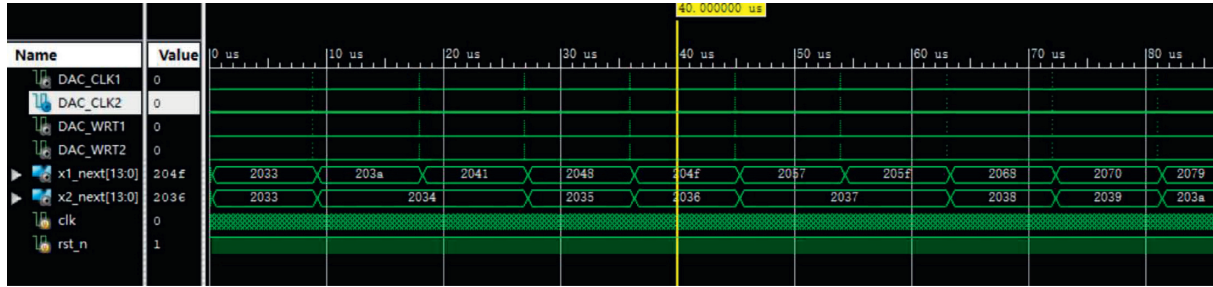


FIGURE 17: Xilinx ISim simulation results of the modified multistable fourth-order Chua's chaotic system based on FPGA.

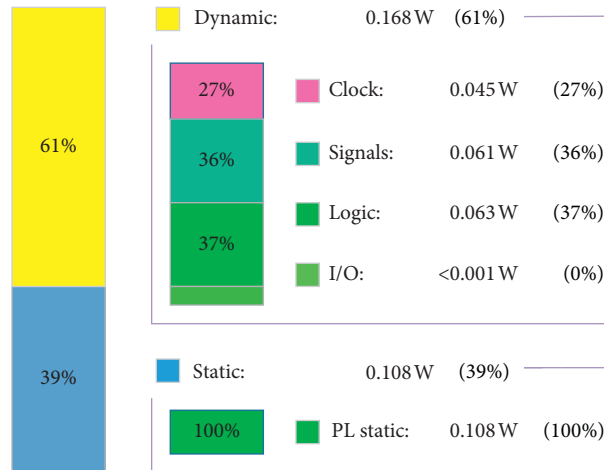


FIGURE 18: Power utilized by the system based on FPGA.

TABLE 3: The Xilinx ZYNQ-XC7Z020 chip statistics of FPGA-based multistable modified fourth-order Chua's chaotic system.

FPGA chip	Slice register number	LUTs number	Bonded IOBs number	Max. clock frequency (MHz)
ZYNQ-XC7Z020	21,711	16,430	34	180.180
Utilization (%)	20.01	30.88	27.20	—

Xilinx ZYNQ-XC7Z020 chip. The use of the chip source and the clock speed of the system are calculated. Using Vivado 2018.3 design tool, the data processing duration of the modified fourth-order Chua's chaotic system designed in this paper is determined. The  $X\_Out$ ,  $Y\_Out$ ,  $Z\_Out$ , and  $W\_Out$  signals are equivalent to the  $x$ ,  $y$ ,  $z$ , and  $w$  signals in the system. Although the 32-bit floating-point standard is adopted in the system design, which makes it easier to detect the time series values of these signals, the Vivado simulation results are displayed in hexadecimal digital format. The results of the Xilinx ISim simulator for the modified fourth-order Chua's chaotic system are shown in Figure 17 when  $\Delta h = 0.001$ . The system runs in pipeline mode and produces  $x$ ,  $y$ ,  $z$ , and  $w$  signals after every 320 clock cycles. Figure 18 shows the power utilized by the system. Table 3 shows the resources utilized by the chaotic oscillator implemented on FPGA including the clock frequency. The minimum working period of the modified fourth-order Chua's chaotic system signal generator based

on FPGA is 5.55 ns. Finally, the  $X\_Out$ ,  $Y\_Out$ , and  $Z\_Out$  signals obtained from the RK4-based FPGA design of the system are recorded in a file in the form of 32-bit floating-point hexadecimal number during the test step, which is given in Table 4. The phase portraits of the output signals are obtained using the data set generated in decimal format by the modified fourth-order Chua's chaotic system based on FPGA given in Table 4. Two pictures of the double-scroll chaotic attractors and single band chaotic attractor and period limit cycles obtained from the hardware implementation of the RK4-based modified fourth-order Chua's chaotic system on FPGA are shown in Figures 19 and 20, respectively. The results show that the phase portraits obtained by the model based on MATLAB and FPGA have good consistency. Although the implementation of FPGA has a reputation of being difficult to design, with the help of system methodology, the system can require less work than the traditional software-based implementation [99, 100].

TABLE 4: The conversion result from 32-bit floating-point number output by FPGA to decimal number.

FPGA output signals in 32-bit floating-point number with hexadecimal format			Decimal number values		
X_Out	Y_Out	Z_Out	$x(t)$	$y(t)$	$z(t)$
3ea6c5fa	3d8e688e	beb09da2	0.325729181065535	0.0695353589404750	-0.344952653576506
3eb5e9f5	3d8b58d6	beba7076	0.355300589372080	0.0680405320103716	-0.364139270662248
3ea6c5fa	3d8e688e	beb09da2	0.325729181065535	0.0695353589404750	-0.344952653576506
3f80921f	3db1af46	bf22ec49	1.00445926841886	0.0867600901838271	-0.636417953148042
3f818177	3db2d8e2	bf239408	1.01176345370630	0.0873277341857656	-0.638977523652504
400097f8	3e6cb53e	bfc2f4b9	2.00927537971617	0.231160129151098	-1.52309338070114
4002b408	3e70defb	bfca54f4	2.04223825024841	0.235225603385658	-1.58071756451930
4004bed6	3e748682	bfd1cf6d	2.07414771146939	0.238794362382855	-1.63914268012843
404d076a	3efe07f0	c0686855	3.20357746761604	0.496154299792244	-3.63136802769324
404de8cc	3ef5d30f	c06fb384	3.21733377662411	0.480125878954796	-3.74533166924290
404e9294	3eecea3c	c076ae83	3.22769634415875	0.462724565296702	-3.85440145110143
bf806354	bd80f4ae	400d650e	-1.00303124071647	-0.0629666870295447	2.20929280483211

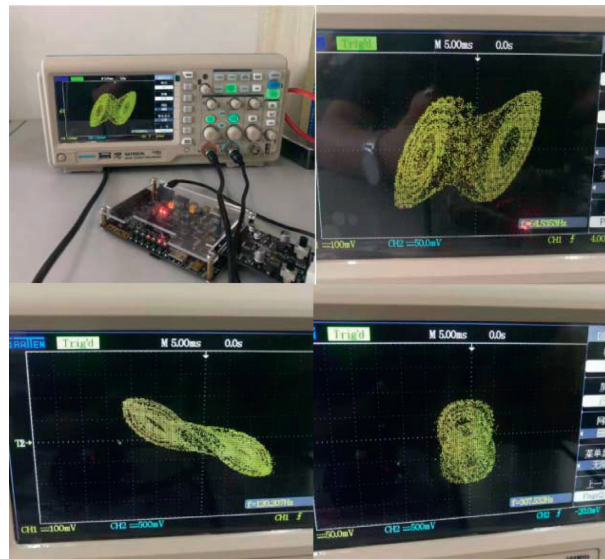


FIGURE 19: Implementation platform and exemplification of the double-scroll chaotic attractors generated by the FPGA implementation of the multistable modified fourth-order Chua's chaotic system.

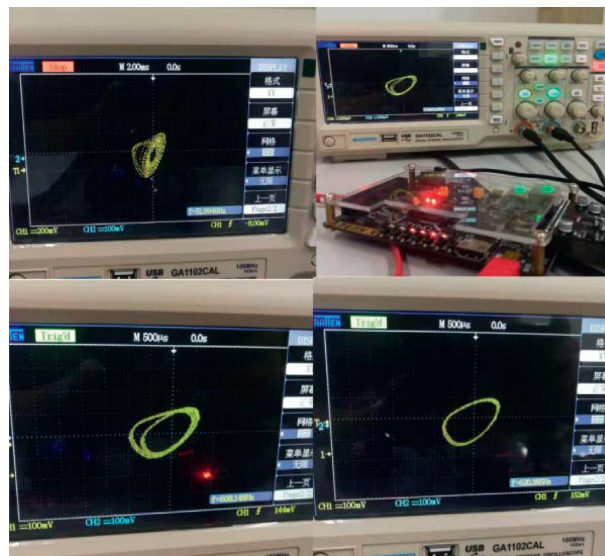


FIGURE 20: Implementation platform and exemplification of the single band chaotic attractor and period limit cycles generated by the FPGA implementation of the multistable modified fourth-order Chua's chaotic system.

## 5. Conclusion

A multistable modified fourth-order autonomous Chua's chaotic system is first investigated. Then the modified implementation of fourth-order autonomous Chua's chaotic circuit with CCII based active elements and synthetic inductor is reported. Synthetic inductor instead of the inductor coil makes the circuit more suitable for the fabrication of integrated circuits, which can be used for the study of coupled dynamics and spatiotemporal chaos. The modified Chua's circuit exhibits abundant dynamic behavior of period doubling bifurcation sequence. Finally, the design of multistable modified fourth-order autonomous Chua's chaotic system based on discrete-time FPGA is implemented on Xilinx Virtex-6 (ZYNQ-XC7Z020) chip using RK-4 algorithm. The maximum operating frequency of the designed chaotic system reaches 180.180 MHz. As can be observed from the results, the chaotic signal generator based on FPGA proposed in this paper can be used as a good entropy source in the applications of secure communication, cryptosystem, and random number generator.

## Data Availability

All data used to support the findings of this study are available from the corresponding authors upon request.

## Conflicts of Interest

The authors declare that they have no conflicts of interest.

## Acknowledgments

This work was partly supported by the National Natural Science Foundation of China under Grants 61504013, 61702052, 61772087, 61674054, and 61801054, the Natural Science Foundation of Hunan Province under Grants 2019JJ50648, 2016jj2005, 2017JJ2049, and 2017JJ3254, the Scientific Research Foundation of Hunan Provincial Education Department under Grants 18A137, 16B212, and 17C0048, and the National Key Research and Development Project under Grant 2018YFE0111200.

## References

- [1] H. Lin and C. Wang, "Influences of electromagnetic radiation distribution on chaotic dynamics of a neural network," *Applied Mathematics and Computation*, vol. 369, p. 124840, 2020.
- [2] F. Tan, L. Zhou, F. Yu, and J. Lu, "Fixed-time continuous stochastic synchronisation of two-layer dynamical networks," *International Journal of Systems Science*, vol. 51, no. 2, pp. 242–257, 2019.
- [3] J. Jin, L. Zhao, M. Li, F. Yu, and Z. Xi, "Improved zeroing neural networks for finite time solving nonlinear equations," *Neural Computing and Applications*, 2019.
- [4] F. Yu, L. Liu, L. Xiao, K. Li, and S. Cai, "A robust and fixed-time zeroing neural dynamics for computing time-variant nonlinear equation using a novel nonlinear activation function," *Neurocomputing*, vol. 350, pp. 108–116, 2019.
- [5] L. Zhou, F. Tan, F. Yu, and W. Liu, "Cluster synchronization of two-layer nonlinearly coupled multiplex networks with multi-links and time-delays," *Neurocomputing*, vol. 359, pp. 264–275, 2019.
- [6] F. Wang, L. Zhang, S. Zhou, and Y. Huang, "Neural network-based finite-time control of quantized stochastic nonlinear systems," *Neurocomputing*, vol. 362, pp. 195–202, 2019.
- [7] L. Xiang, G. Guo, and J. Yu, "A convolutional neural network-based linguistic steganalysis for synonym substitution steganography," *Mathematical Biosciences and Engineering*, vol. 17, no. 2, pp. 1041–1058, 2020.
- [8] C. Wang, L. Xiong, J. Sun, and W. Yao, "Memristor-based neural networks with weight simultaneous perturbation training," *Nonlinear Dynamics*, vol. 95, no. 4, pp. 2893–2906, 2019.
- [9] W. Yao, C. Wang, J. Cao, Y. Sun, and C. Zhou, "Hybrid multisynchronization of coupled multistable memristive neural networks with time delays," *Neurocomputing*, vol. 363, pp. 281–294, 2019.
- [10] L. Zhou, C. Wang, and L. Zhou, "A novel no-equilibrium hyperchaotic multi-wing system via introducing memristor," *International Journal of Circuit Theory and Applications*, vol. 46, no. 1, pp. 84–98, 2018.
- [11] F. Yu, L. Liu, S. Qian et al., "Chaos-based application of a novel multistable 5D memristive hyperchaotic system with coexisting multiple attractors," *Complexity*, vol. 2020, Article ID 8034196, 2020.
- [12] J. Jin, "Programmable multi-direction fully integrated chaotic oscillator," *Microelectronics Journal*, vol. 75, pp. 27–34, 2018.
- [13] L. Zhou, C. Wang, X. Zhang, and W. Yao, "Various attractors, coexisting attractors and antimonotonicity in a simple fourth-order memristive twin-T oscillator," *International Journal of Bifurcation and Chaos*, vol. 28, no. 4, Article ID 1850050, 2018.
- [14] Q. Zhao, C. H. Wang, and X. Zhang, "A universal emulator for memristor, memcapacitor, and meminductor and its chaotic circuit," *Chaos*, vol. 29, Article ID 013141, 2019.
- [15] F. Yu, S. Qian, X. Chen et al., "A new 4D four-wing memristive hyperchaotic system: dynamical analysis, electronic circuit design, shape synchronization and secure communication," *International Journal of Bifurcation and Chaos*, 2020.
- [16] G. Cheng, C. Wang, and H. Chen, "A novel color image encryption algorithm based on hyperchaotic system and permutation-diffusion architecture," *International Journal of Bifurcation and Chaos*, vol. 29, no. 9, Article ID 1950115, 2019.
- [17] Y. Chen, J. Wang, R. Xia, Q. Zhang, Z. Cao, and K. Yang, "The visual object tracking algorithm research based on adaptive combination kernel," *Journal of Ambient Intelligence and Humanized Computing*, vol. 10, no. 12, pp. 4855–4867, 2019.
- [18] Y. Chen, J. Xiong, W. Xu, and J. Zuo, "A novel online incremental and decremental learning algorithm based on variable support vector machine," *Cluster Computing*, vol. 22, no. S3, pp. 7435–7445, 2019.
- [19] F. Peng, X. W. Zhu, and M. Long, "An ROI privacy protection scheme for H.264 video based on FMO and chaos," *IEEE Transactions on Information Forensics and Security*, vol. 8, pp. 1688–1699, 2013.
- [20] Y. Chen, J. Wang, X. Chen et al., "Single-image super-resolution algorithm based on structural self-similarity and deformation block features," *IEEE Access*, vol. 7, pp. 58791–58801, 2019.



- [21] S. Wang, C. Wang, and C. Xu, "An image encryption algorithm based on a hidden attractor chaos system and the Knuth-Durstenfeld algorithm," *Optics and Lasers in Engineering*, vol. 128, Article ID 105995, 2020.
- [22] C. K. Volos, V. Sundarapandian, P. Viet-Thanh et al., "Discrete chaotic dynamics for economics and social science," *Discrete Dynamics in Nature and Society*, vol. 2016, no. 2, Article ID 3105084, 2016.
- [23] J. Jin and L. Zhao, "Low voltage low power fully integrated chaos generator," *Journal of Circuits, Systems and Computers*, vol. 27, no. 10, Article ID 1850155, 2018.
- [24] J. Jin and L. Cui, "Fully integrated memristor and its application on the scroll-controllable hyperchaotic system," *Complexity*, vol. 2019, no. 8, Article ID 4106398, 2019.
- [25] F. Yu, L. Gao, K. Gu, B. Yin, Q. Wan, and Z. Zhou, "A fully qualified four-wing four-dimensional autonomous chaotic system and its synchronization," *Optik*, vol. 131, pp. 79–88, 2017.
- [26] X. Zhang, C. Wang, W. Yao, and H. Lin, "Chaotic system with bondorbital attractors," *Nonlinear Dynamics*, vol. 97, no. 4, pp. 2159–2174, 2019.
- [27] C. Wang, X. Liu, and H. Xia, "Multi-piecewise quadratic nonlinearity memristor and its  $2N$ -scroll and  $2N + 1$ -scroll chaotic attractors system," *Chaos*, vol. 27, Article ID 033114, 2017.
- [28] X. Zhang and C. Wang, "Multiscroll hyperchaotic system with hidden attractors and its circuit implementation," *International Journal of Bifurcation and Chaos*, vol. 29, no. 9, Article ID 1950117, 2019.
- [29] K. Christos, S. J. Volos, K. Jacques et al., "Nonlinear dynamics and entropy of complex systems with hidden and self-excited attractors," *Entropy*, vol. 21, p. 370, 2019.
- [30] T. Hayat, F. Masood, S. Qayyum et al., "Entropy generation minimisation: nonlinear mixed convective flow of Sisko nanofluid," *Pramana*, vol. 93, p. 96, 2019.
- [31] M. Zhou and C. Wang, "A novel image encryption scheme based on conservative hyperchaotic system and closed-loop diffusion between blocks," *Signal Processing*, vol. 171, Article ID 107484, 2020.
- [32] K. Gu, X. Dong, and L. Wang, "Efficient traceable ring signature scheme without pairings," *Advances in Mathematics of Communications*, 2019.
- [33] Z. Xia, Z. Fang, F. Zou et al., "Research on defensive strategy of real-time price attack based on multiperson zero-determinant," *Security and Communication Networks*, vol. 2019, Article ID 6956072, 13 pages, 2019.
- [34] K. Gu, K. Wang, and L. Yang, "Traceable attribute-based signature, journal of information security and applications," *Journal of Information Security and Applications*, vol. 49, pp. 1–16, 2019.
- [35] L. Xiang, Y. Li, W. Hao, P. Yang, and X. Shen, "Reversible natural language watermarking using synonym substitution and arithmetic coding," *CMC: Computers, Materials & Continua*, vol. 55, pp. 541–559, 2018.
- [36] K. Gu, W. Jia, J. Zhang et al., "Identity-based multi-proxy signature scheme in the standard model," *Fundamenta Informaticae*, vol. 150, no. 2, pp. 179–210, 2017.
- [37] K. Gu, N. Wu, B. Yin et al., "Secure data sequence query framework based on multiple fogs," *IEEE Transactions on Emerging Topics in Computing*, 2019.
- [38] K. Gu, N. Wu, B. Yin et al., "Secure data query framework for cloud and fog computing," *IEEE Transactions on Network and Service Management*, 2019.
- [39] K. Gu, W. Jia, G. Wang, and S. Wen, "Efficient and secure attribute-based signature for monotone predicates," *Acta Informatica*, vol. 54, no. 5, pp. 521–541, 2017.
- [40] Y. Chen, J. Wang, S. Liu et al., "Multiscale fast correlation filtering tracking algorithm based on a feature fusion model," *Concurrency and Computation: Practice and Experience*, 2019.
- [41] K. Gu, W. Zhang, S.-J. Lim, P. K. Sharma, Z. Al-Makhadmeh, and A. Tolba, "Reusable mesh signature scheme for protecting identity privacy of IoT devices," *Sensors*, vol. 20, no. 3, p. 758, 2020.
- [42] Z. Liu, Z. Lai, W. Ou, W. Ou, K. Zhang, and R. Zheng, "Structured optimal graph based sparse feature extraction for semi-supervised learning," *Signal Processing*, vol. 170, Article ID 107456, 2020.
- [43] L. Zhou and F. Tan, "A chaotic secure communication scheme based on synchronization of double-layered and multiple complex networks," *Nonlinear Dynamics*, vol. 96, no. 2, pp. 869–883, 2019.
- [44] F. Yu and C. Wang, "Secure communication based on a four-wing chaotic system subject to disturbance inputs," *Optik*, vol. 125, no. 20, pp. 5920–5925, 2014.
- [45] F. Yu, L. Li, Q. Tang et al., "A survey on true random number generators based on chaos," *Discrete Dynamics in Nature and Society*, vol. 2019, Article ID 2545123, 10 pages, 2019.
- [46] F. Yu, Q. Wan, J. Jin et al., "Design and FPGA implementation of a pseudorandom number generator based on a four-wing memristive hyperchaotic system and Bernoulli map," *IEEE Access*, vol. 7, pp. 181884–181898, 2019.
- [47] L. Zhou, F. Tan, and F. Yu, "A robust synchronization-based chaotic secure communication scheme with double-layered and multiple hybrid networks," *IEEE Systems Journal*, 2019.
- [48] F. Yu, C. Wang, Q. Wan, and Y. Hu, "Complete switched modified function projective synchronization of a five-term chaotic system with uncertain parameters and disturbances," *Pramana*, vol. 80, no. 2, pp. 223–235, 2013.
- [49] F. Yu and Y. Song, "Complete switched generalized function projective synchronization of a class of hyperchaotic systems with unknown parameters and disturbance inputs," *Journal of Dynamic Systems, Measurement, and Control-Transactions of the ASME*, vol. 136, Article ID 014505, 2014.
- [50] B.-C. Lai and J.-J. He, "Dynamic analysis, circuit implementation and passive control of a novel four-dimensional chaotic system with multiscroll attractor and multiple coexisting attractors," *Pramana*, vol. 90, p. 33, 2018.
- [51] S. T. Kingni, J. R. M. Pone, G. F. Kuate et al., "Coexistence of attractors in integer- and fractional-order three-dimensional autonomous systems with hyperbolic sine nonlinearity: analysis, circuit design and combination synchronization," *Pramana*, vol. 93, p. 12, 2019.
- [52] Q. Deng and C. Wang, "Multi-scroll hidden attractors with two stable equilibrium points," *Chaos*, vol. 29, Article ID 093112, 2019.
- [53] F. Yu, C. Wang, and H. He, "Grid multiscroll hyperchaotic attractors based on Colpitts oscillator mode with controllable grid gradient and scroll numbers," *Journal of Applied Research and Technology*, vol. 11, no. 3, pp. 371–380, 2013.
- [54] F. Yu, L. Liu, B. He et al., "Analysis and FPGA realization of a novel 5D hyperchaotic four-wing memristive system, active control synchronization, and secure communication application," *Complexity*, vol. 2019, Article ID 4047957, 18 pages, 2019.
- [55] C. Wang, L. Zhou, and R. Wu, "The design and realization of a hyper-chaotic circuit based on a flux-controlled memristor with linear memductance," *Journal of Circuits, Systems and Computers*, vol. 27, no. 3, Article ID 1850038, 2018.
- [56] A. R. Vazquez and M. D. Restituto, "CMOS design of chaotic oscillator using state variables: a monolithic Chua's circuit,"

- IEEE Transactions on Circuits and Systems*, vol. 40, pp. 596–612, 1993.
- [57] Q. Xu, Y. Lin, B. Bao, and M. Chen, “Multiple attractors in a non-ideal active voltage-controlled memristor based Chua’s circuit,” *Chaos, Solitons & Fractals*, vol. 83, pp. 186–200, 2016.
- [58] L. O. Chua, M. Komuro, and T. Matsumoto, “The double scroll family,” *IEEE Transactions on Circuits and Systems*, vol. 33, pp. 1073–1118, 1986.
- [59] C. X. Liu, “Analysis of Chua’s dual chaotic circuit,” *Acta Physica Sinica*, vol. 51, pp. 1198–1202, 2002.
- [60] M. Z. D. I. Hoz, L. Acho, Y. Vidal et al., “A modified Chua chaotic oscillator and its application to secure communications,” *Applied Mathematics and Computation*, vol. 247, pp. 712–722, 2014.
- [61] D. Chen, Z. Sun, X. Ma, and L. Chen, “Circuit implementation and model of a new multi-scroll chaotic system,” *International Journal of Circuit Theory and Applications*, vol. 42, no. 4, pp. 407–424, 2014.
- [62] G. Gandhi, “An improved Chua’s circuit and its use in hyperchaotic circuit,” *Analog Integrated Circuits and Signal Processing*, vol. 46, no. 2, pp. 173–178, 2006.
- [63] B. Bao, T. Jiang, G. Wang, P. Jin, H. Bao, and M. Chen, “Two-memristor-based Chua’s hyperchaotic circuit with plane equilibrium and its extreme multistability,” *Nonlinear Dynamics*, vol. 89, no. 2, pp. 1157–1171, 2017.
- [64] A. T. Azar, N. M. Adele, K. S. T. Alain et al., “Multistability analysis and function projective synchronization in relay coupled oscillators,” *Complexity*, vol. 2018, Article ID 3286070, 12 pages, 2018.
- [65] M. Chen, Y. Feng, H. Bao et al., “Hybrid state variable incremental integral for reconstructing extreme multistability in memristive jerk system with cubic nonlinearity,” *Complexity*, vol. 2019, Article ID 8549472, 16 pages, 2019.
- [66] Y. Zhang, Z. Liu, M. Chen et al., “Dimensionality reduction reconstitution for extreme multistability in memristor-based Colpitts system,” *Complexity*, vol. 2019, Article ID 4308549, 12 pages, 2019.
- [67] H. Bao, T. Jiang, K. Chu et al., “Memristor-based canonical chuas circuit: extreme multistability in voltage-current domain and its controllability in flux-charge domain,” *Complexity*, vol. 2018, Article ID 5935637, 13 pages, 2018.
- [68] Y. Qian and W. Meng, “Mixed-mode oscillation in a class of delayed feedback system and multistability dynamic response,” *Complexity*, vol. 2020, Article ID 4871068, 18 pages, 2020.
- [69] F. Yu, Z. Zhang, L. Liu et al., “Secure communication scheme based on a new 5D multistable four-wing memristive hyperchaotic system with disturbance inputs,” *Complexity*, vol. 2019, Article ID 5859273, 16 pages, 2019.
- [70] X. Luo, L. Huo, and G. Zhang, “Chaos characteristics based on modified Chua’s circuit,” *Journal of Chongqing Technology and Business University (Natural Science Edition)*, vol. 24, pp. 65–68, 2007.
- [71] C. L. Koliopoulos, I. M. Kyprianidis, I. N. Stouboulos, A. N. Anagnostopoulos, and L. Magafas, “Chaotic behaviour of a fourth-order autonomous electric circuit,” *Chaos, Solitons & Fractals*, vol. 16, no. 2, pp. 173–182, 2003.
- [72] X. Liu, J. Wang, and L. Huang, “Attractors of fourth-order Chua’s circuit and chaos control,” *International Journal of Bifurcation and Chaos*, vol. 17, no. 8, pp. 2705–2722, 2007.
- [73] C. H. Wang, H. Xu, and F. Yu, “A novel approach for constructing high-order Chua’s circuit with multi-directional multi-scroll chaotic attractors,” *International Journal of Bifurcation and Chaos*, vol. 23, p. 50022, 2013.
- [74] R. Bhattacharya, A. Basu, and S. K. Koul, “A highly linear CMOS active inductor and its application in filters and power dividers,” *IEEE Microwave and Wireless Components Letters*, vol. 25, no. 11, pp. 715–717, 2015.
- [75] G. Leuzzi, V. Stornelli, and S. Del Re, “A tuneable active inductor with high dynamic range for band-pass filter applications,” *IEEE Transactions on Circuits and Systems II: Express Briefs*, vol. 58, no. 10, pp. 647–651, 2011.
- [76] X. Zhang and C. Wang, “A novel multi-attractor period multi-scroll chaotic integrated circuit based on CMOS wide adjustable CCCII,” *IEEE Access*, vol. 7, pp. 16336–16350, 2019.
- [77] L. Zhao and C. H. Wang, “A novel CMOSCCCII based on cross-coupled differential transistor pair and its application,” *Wireless Personal Communications*, vol. 85, no. 4, pp. 2295–2307, 2015.
- [78] Y. Lin, C. Wang, and H. He, “A simple multi-scroll chaotic oscillator employing CCII,” *Optik*, vol. 126, no. 7–8, pp. 824–827, 2015.
- [79] Y. Lin and C. Wang, “Current-mode multi-scroll chaos generator employing CCCII,” *Electronics Letters*, vol. 52, no. 15, pp. 1295–1297, 2016.
- [80] F. Yu, P. Li, K. Gu, and B. Yin, “Research progress of multi-scroll chaotic oscillators based on current-mode devices,” *Optik*, vol. 127, no. 13, pp. 5486–5490, 2016.
- [81] Z. M. Yang, J. Z. hang, and J. Y. Ma, “Design and realization of Chua’s circuit based on current conveyers, et al,” *Acta Physica Sinica*, vol. 59, pp. 3007–3016, 2010.
- [82] R. Jothimurugan, K. Suresh, P. M. Ezhilarasu, and K. Thamilmaran, “Improved realization of canonical Chua’s circuit with synthetic inductor using current feedback operational amplifiers,” *AEU—International Journal of Electronics and Communications*, vol. 68, no. 5, pp. 413–421, 2014.
- [83] F. Yu, Q. Tang, W. Wang, and H. Wu, “A 2.7 GHz low-phase-noise LC-QVCO using the gate-modulated coupling technique,” *Wireless Personal Communications*, vol. 86, no. 2, pp. 671–681, 2016.
- [84] F. Yu, “A low-voltage and low-power 3-GHz CMOS LC VCO for S-band wireless applications,” *Wireless Personal Communications*, vol. 78, no. 2, pp. 905–914, 2014.
- [85] J. Jin and M. Tan, “Low power quadrature voltage controlled oscillator,” *International Journal of RF and Microwave Computer-Aided Engineering*, vol. 29, no. 12, 2019.
- [86] Q. Wan, J. Dong, H. Zhou, and F. Yu, “A very low power quadrature VCO with modified current-reuse and back-gate coupling topology,” *Journal of Circuits, Systems and Computers*, vol. 26, no. 11, p. 1750184, 2017.
- [87] F. Yu, L. Gao, L. Liu, S. Qian, S. Cai, and Y. Song, “A 1 V, 0.53 ns, 59  $\mu$ W current comparator using standard 0.18  $\mu$ m CMOS technology,” *Wireless Personal Communications*, 2019.
- [88] S. Penaud, J. Guittard, PBouysse et al., “DSP implementation of self-synchronised chaotic encoder-decoder,” *Electronics Letters*, vol. 36, pp. 365–366, 2002.
- [89] R. M. Hidalgo, J. G. Fernández, R. R. Rivera, and H. A. Larrondo, “Versatile DSP-based chaotic communication system,” *Electronics Letters*, vol. 37, no. 19, pp. 1204–1205, 2001.
- [90] İ. Koyuncu and A. Turan Özcerit, “The design and realization of a new high speed FPGA-based chaotic true random number generator,” *Computers & Electrical Engineering*, vol. 58, pp. 203–214, 2017.
- [91] M. Tuna, M. Alçın, İ. Koyuncu, C. B. Fidan, and İ. Pehlivan, “High speed FPGA-based chaotic oscillator design,” *Microprocessors and Microsystems*, vol. 66, pp. 72–80, 2019.



- [92] M. Alcin, I. Pehlivan, I. Koyuncu et al., “Hardware design and implementation of a novel ANN-based chaotic generator in FPGA,” *Optik*, vol. 127, pp. 5500–5505, 2016.
- [93] A. Akgul, H. Calgan, I. Koyuncu, I. Pehlivan, and A. Istanbulu, “Chaos-based engineering applications with a 3D chaotic system without equilibrium points,” *Nonlinear Dynamics*, vol. 84, no. 2, pp. 481–495, 2016.
- [94] Q. Lai, X. W. Zhao, K. Rajagopa et al., “FPGA implementation and engineering applications of multi-butterfly chaotic attractors generated from generalized Sprott C system,” *Pramana*, vol. 90, p. 6, 2018.
- [95] J.-L. Zhang, W.-Z. Wang, X.-W. Wang, and Z.-H. Xia, “Enhancing security of FPGA-based embedded systems with combinational logic binding,” *Journal of Computer Science and Technology*, vol. 32, no. 2, pp. 329–339, 2017.
- [96] S. Afifi, H. GholamHosseini, and R. Sinha, “A system on chip for melanoma detection using FPGA-based SVM classifier,” *Microprocessors and Microsystems*, vol. 65, pp. 57–68, 2019.
- [97] A. K. Kushwaha and S. K. Paul, “Inductorless realization of Chua’s oscillator using DVCCTA,” *Analog Integrated Circuits and Signal Processing*, vol. 88, no. 1, pp. 137–150, 2016.
- [98] K. Rajagopal, A. Karthikeyan, D. Prakash, and H. Chameleon, “Fractional order FPGA implementation,” *Complexity*, vol. 2017, Article ID 8979408, 2017.
- [99] H. R. Abdolmohammadi, A. J. M. Khalaf, S. Panahi et al., “A new 4D chaotic system with hidden attractor and its engineering applications: analog circuit design and field programmable gate array implementation,” *Pramana*, vol. 90, p. 70, 2018.
- [100] A. Karthikeyan and K. Rajagopal, “FPGA implementation of fractional-order discrete memristor chaotic system and its commensurate and incommensurate synchronisations,” *Pramana*, vol. 90, p. 14, 2018.

## Research Article

# The Impact of Service and Channel Integration on the Stability and Complexity of the Supply Chain

Jianheng Zhou and Xingli Chen 

*Glorious Sun School of Business and Management, Donghua University, Shanghai 200051, China*

Correspondence should be addressed to Xingli Chen; [cxl\\_wlkq\\_666@163.com](mailto:cxl_wlkq_666@163.com)

Received 21 October 2019; Revised 1 February 2020; Accepted 12 February 2020; Published 20 March 2020

Guest Editor: Viet-Thanh Pham

Copyright © 2020 Jianheng Zhou and Xingli Chen. This is an open access article distributed under the Creative Commons Attribution License, which permits unrestricted use, distribution, and reproduction in any medium, provided the original work is properly cited.

This paper constructs a supply chain consisting of a manufacturer and a retailer. Considering channel integration and service cooperation, two dynamic Stackelberg game models are established: one without unit profit allocation ( $M$ ) and the other one with unit profit allocation ( $M^\epsilon$ ). In two dynamic models, we analyze the influence of relevant parameters on the stability and complexity of the dynamic system and system profit by nonlinear system theory and numerical simulation. We find that the higher adjustment parameters can cause the system to lose stability, showing double period bifurcation or wave-shape chaos. The stable region becomes larger with increase in service value and value of unit profit sharing. Besides, when the system is in chaotic state, we find that the profit of the system will fluctuate or even decline sharply; however, keeping the parameters in a certain range is helpful in maintaining the system stability and is conducive to decision-makers to obtain steady profits. In order to control the chaos phenomenon, the state feedback method is employed to control the chaotic system well. This study provides some valuable significance to supply chain managers in channel integration and service cooperation.

## 1. Introduction

In recent years, the development of e-commerce has brought a strong impact on offline stores [1]. Customer volume migrates from offline to online on a large scale. In 2018, Tmall platform “double eleven” shopping carnival achieved a total turnover of 12135 billion yuan. This phenomenon is not conducive to the development of offline stores. However, online shopping also brings a series of problems. For example, when buying clothes online, we cannot see the real thing, the clothes we buy often cannot meet our needs, and even the phenomenon of returns occurs. It can be seen that online shopping sometimes cannot bring consumers a perfect shopping experience. Under this background, the retail mode of online order delivery and offline store purchase emerges as the times require, namely, channel integration. At present, JD, Tmall, and Suning have arranged offline retailer outlets to achieve effective integration of online and offline channels. In addition, the international fast fashion brand: UNIQLO and Zara also provides a perfect

shopping experience for customers through channel integration. Relevant empirical research studies have proved that this mode not only meets the consumer’s shopping needs but also increases the flow of customers in offline stores [2, 3].

Over the past few years, many scholars have conducted in-depth research on dual-channel and multichannel supply chains [4–6] but rarely pay attention to online and offline integration. Because of the conflict between traditional channel and online channel and the change of consumer demand, channel integration as an important model of omnichannel has gained significant interest among academics and practitioners [3, 7]. Through a questionnaire survey, Lin et al. [8] revealed that the drivers of innovation in channel integration are positively correlated with supply performance. The development of channel integration is inseparable from the support of information technology. Based on survey data from 125 multichannel retailers in Singapore, Oh et al. [9] found that retail channel integration enables enterprises to not only provide current products

efficiently but also be innovative in creating future products through IT technology. Piotrowicz and Cuthbertson [10] discussed the influence of information technology on the development of channel integration from the technical level. On inventory research of channel integration, considering the randomness of demand, the inventory backlog cost, and the number of BOPS. Chen et al. [11] constructed and analyzed a stochastic equilibrium model. In an omnichannel supply chain, Du et al. [12] studied the impact of consumer disappointment and inventory on retailers' optimal pricing. Based on Gao and Su [13], Kusuda [14] considered the retailer's replenishment of inventory in an omnichannel strategy and found two types of equilibrium. Besides, in the omnichannel retailing, the characteristics of omnichannel retailers play an important role in consumers' response to cross-channel integration [15]. Jin et al. [16] analyzed the influence of orders from integration channels and customer arrival rate on the scale of offline service area.

The above research on channel integration focuses on the applicable conditions of information technology, channel inventory management, and adaptation scenario of channel integration and enriched the research of channel integration. In the channel operation, we find that consumers are increasingly demanding retail services during the shopping process. The relevant literature confirms that service factors have affected customer choice and shopping experience [17].

In the past few years, most of the research focuses on the impact of service factors on dual-channel and multichannel supply chains [18, 19]. In terms of channel coordination, retailers provide services to consumers in a dual-channel supply chain, which can reduce channel conflicts and improve the relationship with the manufacturer [20]. Channel competition is the inevitable result when a manufacturer adds a direct channel. Li and Li [21] discovered that retailers' value-added services help to alleviate this phenomenon, but when the retailer has fair concerns, the entire supply chain will conflict with fixed wholesale price. In supply chain decision making, Jena and Sarmah [22] constructed four price and service competition models consisting of two manufacturers and one retailer and analyzed the equilibrium decision and profit of each model. Considering service value, Zhang and Wang [23] studied the dynamic pricing strategy of dual-channel supply chain under centralized and decentralized conditions. It was found that, with increase in service value, the system stability decreases first and then increases. Considering price, service, and discount contracts, Sadjadi et al. [24] built a Stackelberg game model to analyze the equilibrium solution and found that service and price discounts can improve the performance of the supply chain. In addition, scholars have explored service competition and service contract issues [25]. When the manufacturer's warranty service competes with the retailer's value-added service, Dan et al. [26] found that when the manufacturer improves the level of warranty service, the competition of value-added service would be weakened. Considering the service factor, Li et al. [27] found that the stability of the low-carbon supply chain is related to sales service and player's behavior. Besides, Li et al. [28] established a dual-channel value chain and found that the channel service value and green innovation input would reduce the stability of supply chain.

The above research focuses on the research of the impact of services on the dual-channel supply chain. Few literature studies have been carried out on supply chain channel integration and service cooperation issues. In actual operation, the online and offline integration requires not only the support of information technology but also the close cooperation between members of the supply chain. In order to ensure that consumers get the corresponding services when picking up goods offline, manufacturers and retailers are required to cooperate with the service. In channel integration, how do manufacturer and retailer engage in service cooperation? How is the profit of the channel integration distributed?

It is worth noting that some scholars have recently employed nonlinear dynamics theory and numerical simulation to study supply chain problems and have obtained very good results [29, 30]. Ma and Xie [31] analyzed the dynamic behavior of dynamic game models under two scenarios and found that the stability of system depends on the channel type. Huang et al. [32] showed the smaller risk aversion attitude and fair concern coefficient will delay the occurrence of chaos in the system. In a closed-loop supply chain, Li et al. [33] analyzed the complexity entropy of the price game model with the recovery rate and service. Ma and Xie [34] focused on bundling goods and compared the dynamic price strategies under two different mechanisms. This paper also studies dynamic game models, which is a new model, with relatively little literature on integration channel service cooperation. Based on the nonlinear dynamic theory, this paper mainly focuses on the following issues: What impact does the different service cooperation model have on manufacturers and retailers? What impact does service value and unit profit sharing have on the dynamic behavior of the system?

Based on abovementioned factors, considering the channel integration and service factors, the main contributions of this paper are as follows:

- (1) Based on service cooperation, the paper proposes two distribution modes of profit from channel integration, discusses the stability and complexity of the two modes, and provides a reference for decision makers of the integration channel
- (2) The paper reveals the impact of service value and value of unit profit sharing on the dynamic evolution of the game model and the profits of decision-makers
- (3) The paper applies nonlinear dynamic theory to the study of channel fusion and enriches the research in this field

The rest of this paper is organized as follows. In Section 2, we present the model description and assumptions. In Section 3, we set up a decentralized model without unit profit sharing ( $M$ ) and give complexity analysis by numerical simulation. Section 4 sets up a decentralized model with unit profit sharing ( $M^e$ ) and performs the same dynamic analysis as in Section 3. In Section 5, we control the chaotic behavior of the system by employing the state feedback control method. Section 6 concludes this paper and proposes management insights.

## 2. Problem Description and Model Assumptions

**2.1. Model Description.** In this paper, we consider a supply chain consisting of one manufacturer and one retailer as shown in Figure 1, where three sales channels are described. On the one hand, the manufacturer sells the product to customers at  $p_1$  by online channel and also sells them to the retailer at the wholesale price  $w$ . Then, the retailer, by traditional channel, resells productions to customers at  $p_2$ . On the other hand, in order to increase sales and improve customer experience, the integrated channel is established by the manufacturer and retailer where customers can browse products and pay order at  $p_1$  online and pick up products at the retailer offline. Meanwhile, the retailer provides customer from traditional channel and integrated channel with service value  $s$ . In terms of profit from the integrated channel, there are two ways of distribution: one is the retailer obtains all the profits without unit profit sharing with the manufacturer and the other is the manufacturer obtains all the profit and shares unit profit  $\varepsilon$  with the retailer. Based on this, this paper builds two game models and carries out the complexity analysis of models.

**2.2. Model Assumptions.** Based on the real situation, the following hypothesizes are proposed in this paper:

- (1) Online channel and integrated channel adopt the same price strategy, and consumers have channel preferences.
- (2) There is a Stackelberg game with the manufacturer as the leader deciding on  $w$  and  $p_1$  and retailer as the follower deciding on  $p_2$ .
- (3) The service cost function of traditional channel can be described as  $C_s = \eta s^2$ , where  $\eta = \eta'/2$ . Due to the difference in service cost between the traditional channel and integrated channel, the service cost of the integrated channel can be described as  $\varphi C_s$ , where  $\varphi \in (0, 1)$  is the service cost consistency coefficient.

The related variables and parameters are reported in Table 1.

### 3. Model without Unit Profit Sharing (M)

**3.1. Static Model.** In this static model, the retailer obtains all the profits of the integration channel without unit profit sharing with the manufacturer. The manufacturer is the leader of the market, and the retailer is the follower. The manufacturer firstly decides  $w$  and  $p_1$ . Correspondingly, the retailer makes decisions  $p_2$  based on  $w$  and  $p_1$ .

Considering the service value and integration channel, based on the previous studies [26, 35], the demand functions for the three channels could be given as follows:

Online channel demand is

$$D_o = \theta_1 a - \rho_1 p_1 + \gamma_1 p_2. \quad (1)$$

Integration channel demand is

$$D_B = \theta_2 a - m_B (p_1 - s) + \gamma_1 p_2. \quad (2)$$

Traditional channel demand is

$$D_T = \theta_3 a - m_T (p_2 - s) + \gamma_1 p_1, \quad (3)$$

where  $\theta_i, i = 1, 2, 3$ , meet  $\sum_{i=0}^3 \theta_i = 1$ .  $m_B > n_1 \gamma_1, m_T > n_2 \gamma_1$  and  $\rho_1 > n_3 \gamma_1 (n_i > 2, i = 1, 2, 3)$  represent that the price elasticity coefficients are much larger than the cross price elasticity coefficients.

Therefore, the profit-maximizing functions of players can be expressed as follows:

$$\begin{aligned} \max_{p_1, w} \prod_m &= (w - c)[(\theta_2 + \theta_3)a - m_B(p_1 - s) \\ &\quad - m_T(p_2 - s) + \gamma_1(p_1 + p_2)] \\ &\quad + (p_1 - c)(\theta_1 a - \rho_1 p_1 + \gamma_1 p_2) \end{aligned} \quad (4)$$

s.t.  $w + \varphi \eta s^2 < p_1, c < w$ ,

$$\begin{aligned} \max_{p_2} \prod_r &= (p_2 - w - \eta s^2)[\theta_3 a - m_T(p_2 - s) + \gamma_1 p_1] \\ &\quad + (p_1 - w - \varphi \eta s^2)[\theta_2 a - m_B(p_1 - s) + \gamma_1 p_2] \end{aligned}$$

s.t.  $w + \eta s^2 < p_2$ . (5)

**Proposition 1.** *If the manufacturer and retailer pursue the profit maximizing in the supply chain with the integrated channel, their optimal decisions can be obtained as follows:*

$$\begin{cases} w^* = \frac{A_5 A_4 - A_2 A_6}{B_2^2 - B_3 B_5}, \\ p_1^* = \frac{A_3 A_6 - A_2 A_4}{A_2^2 - A_3 A_5}, \\ p_2^* = \frac{\gamma_1 (B_3 B_6 - B_2 B_4)}{m_T (B_2^2 - B_3 B_5)} + \frac{(m_T - \gamma_1) (B_5 B_4 - B_2 B_6)}{2m_T (B_2^2 - B_3 B_5)} + B_1, \end{cases} \quad (6)$$

where

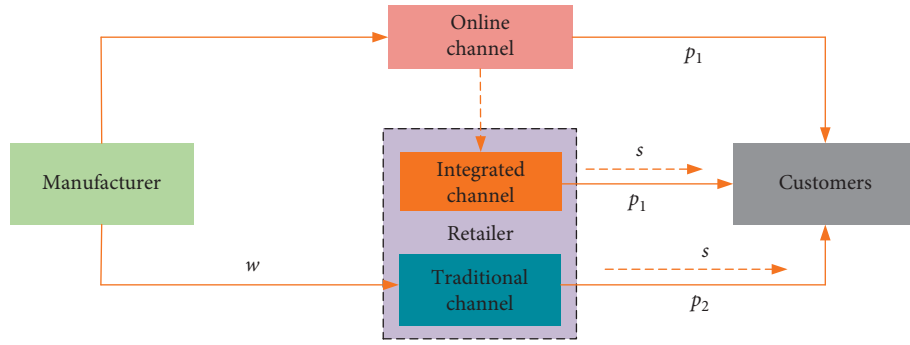


FIGURE 1: The supply model with the integrated channel.

TABLE 1: Key notations.

Variables	
$D_O$	Online channel demand
$D_B$	Integrated channel demand
$D_T$	Tradition channel demand
$a$	The potential market scale
$\theta_1$	The customer's loyalty to the online channel
$\theta_2$	The customer's loyalty to the integrated channel
$\theta_3$	The customer's loyalty to the tradition channel
$\rho_1$	The elasticity coefficient of the online channel demand for price
$m_B$	The elasticity coefficient of the integrated channel demand for price
$m_T$	The elasticity coefficient of the tradition channel demand for price
$\gamma_1$	Cross price elasticity coefficient
$w$	The wholesale price
$p_1$	Retail price of products in the online channel and integrated channel
$p_2$	Retail price of products in the tradition channel
$s$	Service value
$\varepsilon$	Value of unit profit sharing
$\varphi$	The service cost consistency coefficient
$\eta$	The service cost parameter of the traditional channel
$\alpha_1$	The limited rational adjustment parameter in model $M$
$\alpha_2$	The adaptive adjustment parameter in model $M$
$\beta_1$	The limited rational adjustment parameter in model $M^\varepsilon$
$\beta_2$	The adaptive adjustment parameter in model $M^\varepsilon$

$$\begin{aligned}
A_1 &= \frac{\theta_3 a + m_T s + m_T \eta s^2 - \gamma_1 \varphi \eta s^2}{2m_T}, \\
A_2 &= -m_B + \frac{\gamma_1}{2} + \frac{\gamma_1^2}{2m_T}, \\
A_3 &= -m_T + 2\gamma_1 - \frac{\gamma_1^2}{m_T}, \\
A_4 &= m_B s + m_T s - B_1 (m_T - \gamma_1) + \frac{c}{2} \left( m_T - 3\gamma_1 + \frac{2\gamma_1^2}{m_T} \right) + a\theta_2 + a\theta_3, \\
A_5 &= \frac{2\gamma_1^2 - 2m_T \rho_1}{m_T}, \\
A_6 &= \frac{A_1 m_T \gamma_1 + a m_T \theta_1 + c (m_B m_T - 2\gamma_1^2 + m_T \rho_1)}{m_T}.
\end{aligned} \tag{7}$$

*Proof.* See Appendix A.

Integrating equations (A.5) and (A.6) with equations (4) and (5), their estimated profit can be written as the following equation:

$$\begin{cases} \prod_m = (w^* - c)[(\theta_2 + \theta_3)a - m_B(p_1^* - s) - m_T(p_2^* - s) + \gamma_1(p_1^* + p_2^*)] + (p_1^* - c)(\theta_1 a - \rho_1 p_1^* + \gamma_1 p_2^*), \\ \prod_r = (p_1^* - w^* - \varphi\eta s^2)[\theta_2 a - m_B(p_1^* - s) + \gamma_1 p_2^*] + (p_2^* - w^* - \eta s^2)[\theta_3 a - m_T(p_2^* - s) + \gamma_1 p_1^*]. \end{cases} \quad (8)$$

**3.2. Dynamic Model.** The price game between competitors is a dynamic process. The changing market environment and product update will lead decision-makers to make new decisions for the next cycle, and each decision is not simply a repetition.

In reality, market participants are usually constrained by capital and other factors and cannot grasp the complete market information; therefore, their decisions are based on the bounded rationality and adaptive expectations in the current period. So, we build a dynamic price game model in which players employ different price adjustment strategies. The manufacturer adopts the limit rational expectation to

make the wholesale price decision:  $w_{t+1} = w_t + \alpha_1 w_t (\partial \prod_m(w_t, p_{1,t}) / \partial w_t)$ . If the marginal profit of the last period is negative, the manufacturer will reduce the price of the next period by adjusting  $\alpha_1$ , otherwise, increase it. The manufacturer makes retail price decision based on adaptive expectations:  $p_{1,t+1} = \alpha_2 p_{1,t} + (1 - \alpha_2) p_1^*$ . That is to say, the manufacturer adjusts the retail price of the next period on the basis of our period and the best reply function.

Therefore, the discrete dynamic system can be modeled as

$$\begin{cases} w_{t+1} = w_t + \alpha_1 w_t \left[ \left( -m_B + \frac{\gamma_1}{2} + \frac{\gamma_1^2}{2m_T} \right) p_{1,t} + \left( -m_T + 2\gamma_1 - \frac{\gamma_1^2}{m_T} \right) w_t + A_4 \right], \\ p_{1,t+1} = \alpha_2 p_{1,t} + (1 - \alpha_2) \frac{A_3 A_6 - A_2 A_4}{A_2^2 - A_3 A_5}, \end{cases} \quad (9)$$

where  $\alpha_1$  ( $\alpha_1 > 0$ ) is the limited rational adjustment parameter of the manufacturer and  $\alpha_2$  ( $0 < \alpha_2 < 1$ ) is the adaptive adjustment parameter.

It is easy to get the decision of retailer with  $w_{t+1} p_{1,t+1}$ :

$$p_{2,t+1} = \frac{\gamma_1}{m_T} p_{1,t+1} + \frac{m_T - \gamma_1}{2m_T} w_{t+1} + \frac{\theta_3 a + m_T s + m_T \eta s^2 - \gamma_1 \varphi \eta s^2}{2m_T}. \quad (10)$$

**3.2.1. Equilibrium Points and Local Stability.** This part discusses the stability of system (9) at equilibrium points. By setting  $w_{t+1} = w_t$  and  $p_{1,t+1} = p_{1,t}$ , there are two equilibrium points in the discrete system of equation (9):

$$\begin{aligned} e_1 &= \left( 0, \frac{A_3 A_6 - A_2 A_4}{A_2^2 - A_3 A_5} \right), \\ e_2 &= \left( \frac{A_5 A_4 - A_2 A_6}{A_2^2 - A_3 A_5}, \frac{A_3 A_6 - A_2 A_4}{A_2^2 - A_3 A_5} \right). \end{aligned} \quad (11)$$

Correspondingly, the retailer's decisions are expressed as

$$\begin{aligned} p_2^{e_1} &= \frac{\gamma_1 (A_3 A_6 - A_2 A_4)}{m_T (A_2^2 - A_3 A_5)} + A_1, \\ p_2^{e_2} &= \frac{\gamma_1 (A_3 A_6 - A_2 A_4)}{m_T (A_2^2 - A_3 A_5)} + \frac{A_4 (A_2^2 - A_3 A_5) (m_T - \gamma_1)}{2m_T A_2 A_3 (A_2 A_4 - A_3 A_6)} + A_1. \end{aligned} \quad (12)$$

In a discrete system, the stability of equilibrium points will be determined by the eigenvalues of Jacobian matrix at the corresponding equilibrium points. The Jacobian matrix of system (9) is defined as follows:

$$J(e_i) = \begin{bmatrix} 1 + \alpha_1 (A_2 p_1 + 2A_3 w + A_4) & A_2 \alpha_1 w \\ 0 & \alpha_2 \end{bmatrix}, \quad i = 1, 2. \quad (13)$$

Supposing that  $f(\lambda) = \lambda^2 - \xi_1 \lambda + \xi_2$  is the characteristic polynomial of  $J(e_i)$ , ( $i = 1, 2$ ); besides,  $\Delta = \xi_1^2 - 4\xi_2$  is its discriminant with  $\xi_1 = t_r$ , ( $j = 1 + \alpha_1 (A_2 p_1 + 2A_3 w + A_4) + \alpha_2$  and  $\xi_2 = \det(j) = \alpha_2 + \alpha_1 \alpha_2 (A_2 p_1 + 2A_3 w + A_4)$ ).

When  $\lambda = 1$ , the characteristic polynomial of Jacobian matrix is described as follows:  $F(1) = 1 - \text{tr}(J) + \det(J) = \alpha_1 (A_2 p_1 + 2A_3 w + A_4) (\alpha_2 - 1)$ .



**Lemma 1** (see [36]). *Defining the two values of  $f(\lambda) = 0$  as  $\lambda_1$  and  $\lambda_2$ , the eigenvalues of  $J(e_i)$  can be judged as follows by Lemma 1. Then,*

( $f_1$ )  $|\lambda_1| < 1$  and  $|\lambda_2| < 1$  if and only if  $f(-1) > 0$  and  $\det(J) < 1$

( $f_2$ )  $|\lambda_1| > 1$  and  $|\lambda_2| > 1$  if and only if  $f(-1) > 0$  and  $\det(J) < 1$

( $f_3$ )  $|\lambda_1| < 1$  and  $|\lambda_2| > 1$  or  $|\lambda_1| > 1$  and  $|\lambda_2| < 1$  if and only if  $f(-1) < 0$

( $f_4$ )  $\lambda_1 = -1$  and  $|\lambda_2| \neq 1$  if and only if  $f(-1) = 0$  and  $\det(J) \neq 0, 2$

( $f_5$ ) both roots are complex and  $|\lambda_1| = |\lambda_2| = 1$  if and only if  $\Delta < 0$  and  $\det(J) = 1$

*If all eigenvalues are smaller than one in modulus, this equilibrium point is asymptotically stable. Otherwise, bifurcation or chaos may occur in system (9).*

**Proposition 2.** *Obviously,  $e_1$  is an unstable equilibrium point, while  $e_2$  is the Stackelberg equilibrium point.*

*Proof.* See Appendix B.

According to Lemma 1, the jury stability criterion of system (9) at  $e_2$  can be expressed as follows:

$$\begin{cases} (g_1) = 1 + \text{tr}(J(e_2)) + \text{Det}(J(e_2)) > 0, \\ (g_2) = 1 - \text{tr}(J(e_2)) + \det(J(e_2)) > 0, \\ (g_3) = 1 - \det(J(e_2)) > 0, \end{cases} \quad (14)$$

where

$$\begin{aligned} \text{tr}(J(e_2)) &= 1 + \alpha_1 \left( A_2 \frac{A_3 A_6 - A_2 A_4}{A_2^2 - A_3 A_5} + \frac{2A_4(A_2^2 - A_3 A_5)}{A_2(A_2 A_4 - A_3 A_6)} + A_4 \right) + \alpha_2, \\ \det(J(e_2)) &= \alpha_2 + \alpha_2 \alpha_1 \left( A_2 \frac{A_3 A_6 - A_2 A_4}{A_2^2 - A_3 A_5} + \frac{2A_4(A_2^2 - A_3 A_5)}{A_2(A_2 A_4 - A_3 A_6)} + A_4 \right). \end{aligned} \quad (15)$$

By analyzing the above judgment conditions of equation (14),  $0 < \alpha_1 < (2/K)$  and  $0 < \alpha_2 < 1$  can be obtained, where  $K = A_2(A_3 A_6 - A_2 A_4) / (A_2^2 - A_3 A_5) + 2A_4(A_2^2 - A_3 A_5) / (A_2(A_2 A_4 - A_3 A_6) + A_4)$ . It can be known that adjustment parameters  $(\alpha_1, \alpha_2)$  are not related to the optimal decision  $e_2(w^*, p_1^*)$  but are the main factors that affect the stability of  $e_2$ . Service value  $s$  affects not only  $\alpha_1$  and  $\alpha_2$  but also  $e_2(w^*, p_1^*)$  and then affects the stability of system (9). When the decision parameters are not in this range ( $0 < \alpha_1 < 2/K$ ,  $0 < \alpha_2 < 1$ ), system (9) will be unstable at  $e_2(w^*, p_1^*)$  and show bifurcation or chaos. When the decision-maker chooses the adjustment coefficients  $(\alpha_1, \alpha_2)$  in the stable region ( $0 < \alpha_1 < (2/K)$ ,  $0 < \alpha_2 < 1$ ), the equilibrium point  $e_2(w^*, p_1^*)$  is stable. At this point, manufacturers and retailers in the supply chain can achieve maximum profits. From the point of view of management, managers should not only pay attention to their price adjustment parameters but focus on service value. Based on eigenvalues of the Jacobian matrix, the stability and bifurcation of system (9) will be studied in detail in the next section by numerical simulation.  $\square$

**3.3. Complexity Dynamics Analysis and Numerical Simulation.** Due to the existence of a large number of parameters, the complexity dynamics of system (9) will be studied intuitively by numerical simulation. Numerical values are assigned to the following letters:  $a = 180, \theta_1 = 0.3, \theta_2 = 0.3, \theta_3 = 0.4, \rho_1 = 2.6, m_B = 3, m_T = 6, \gamma_1 = 1, v = 2, \eta = 5, \varphi = 0.2$ , and  $c = 4$ . Thus, the Stackelberg equilibrium point can be expressed as  $e_2 = (7.342, 15.2)$ .

**3.3.1. Complexity Dynamics with respect to  $\alpha_i$ .** In this section, the bifurcation diagram is a powerful tool to analyze the

bifurcation phenomenon of system (9). Based on stability conditions equation (13), Figure 2 shows the 2D parameter bifurcation in the  $(\alpha_1, \alpha_2)$  plane, which shows the paths of system (9) to chaos. Different periods are represented by different colors: stable (green), period-2 (blue), period-3 (yellow), period-4 (Claret), period-5 (Cyan), period-6 (red), chaos (gray), and divergence (white). There are two ways to lead to chaos in system (9). The system enters chaos through periodic doubling bifurcation with  $\alpha_1$ ; when  $0 < \alpha_2 < 1$ , the system goes directly into chaos with  $\alpha_2$ . When  $0 < \alpha_1 < 0.065$ , we can know that flip bifurcation will happen when  $\alpha_1$  increases. In short, it can be judged that the stability of the system is not independent of  $\alpha_1$  and  $\alpha_2$ .

Figure 3 shows the bifurcation of prices  $(w, p_1, p_2)$  and the largest Lyapunov exponent (LLE) as  $\alpha_1$  increases with  $\alpha_2 = 0.5$ . In Figure 3(a), when  $\alpha_1 < 0.065$ ,  $w, p_1$ , and  $p_2$  do not fluctuate and system (9) is in a stable state. However,  $\alpha_1 > 0.065$ ,  $w$  and  $p_2$  show first the flip bifurcation. Due to limit, rational expectation has no effect on adaptive price expectation, and  $p_1$  does not show fluctuation. The LLE with respect to  $\alpha_1$  shown in Figure 3(b) is a powerful tool to identify the state of system (9). When  $\alpha_1 = 0.065$ , the LLE reaches the first zero, and  $w$  and  $p_2$  show the bifurcation phenomenon. After it, period doubling bifurcation continues to occur, and the system goes into chaos when LLE is more than zero.

When  $\alpha_1$  is set to 0.04, Figure 4 gives the bifurcation diagram of prices  $(w, p_1, p_2)$  and LLE of system (9) for  $\alpha_2$  varying from 0 to 1.1. We can see that as long as the parameter is in the stability region ( $\alpha_2 < 1$ ), the game will be stable at  $w = 7.342, p_1 = 15.2$ , and  $p_2 = 22.26$ . In this situation, manufacturers and retailers can obtain Stackelberg game's optimal profit. When  $\alpha_2 > 1$ , the system directly goes

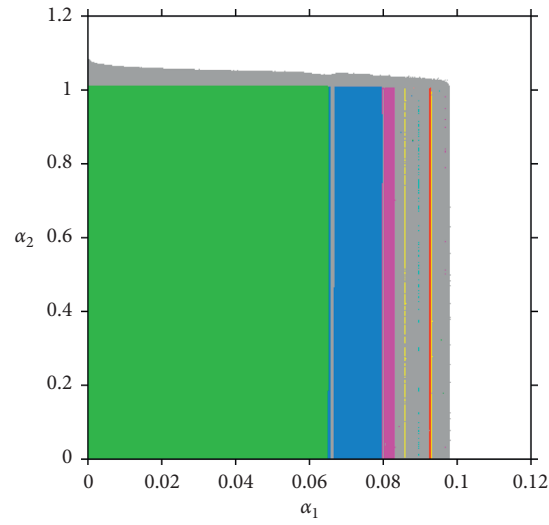


FIGURE 2: 2D bifurcation diagram with respect to  $\alpha_1$  and  $\alpha_2$ .

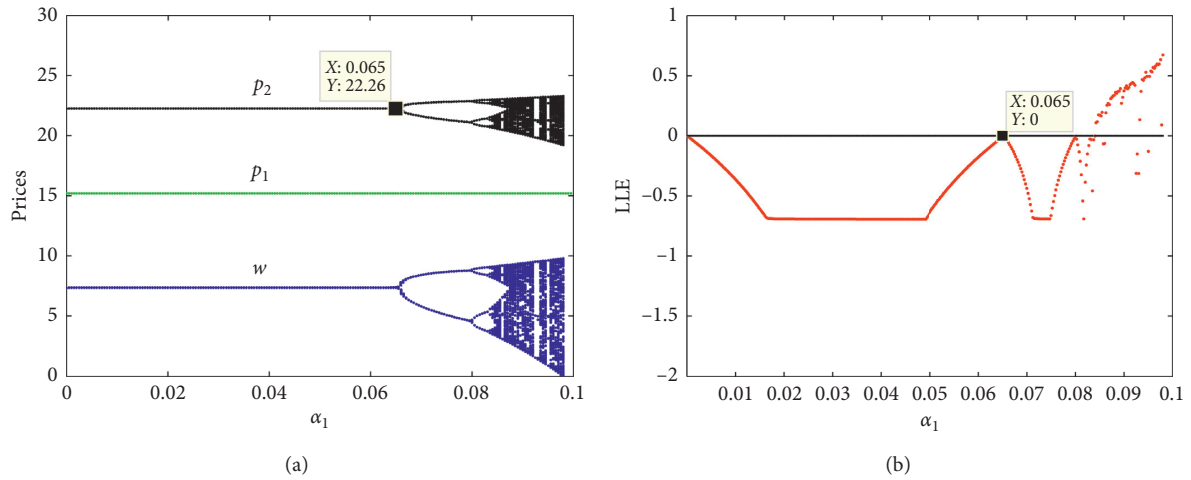


FIGURE 3: The behavior of dynamic system (9) with respect to  $\alpha_1$  when  $\alpha_2 = 0.5$ . (a) The bifurcation diagram. (b) The LLE diagram.

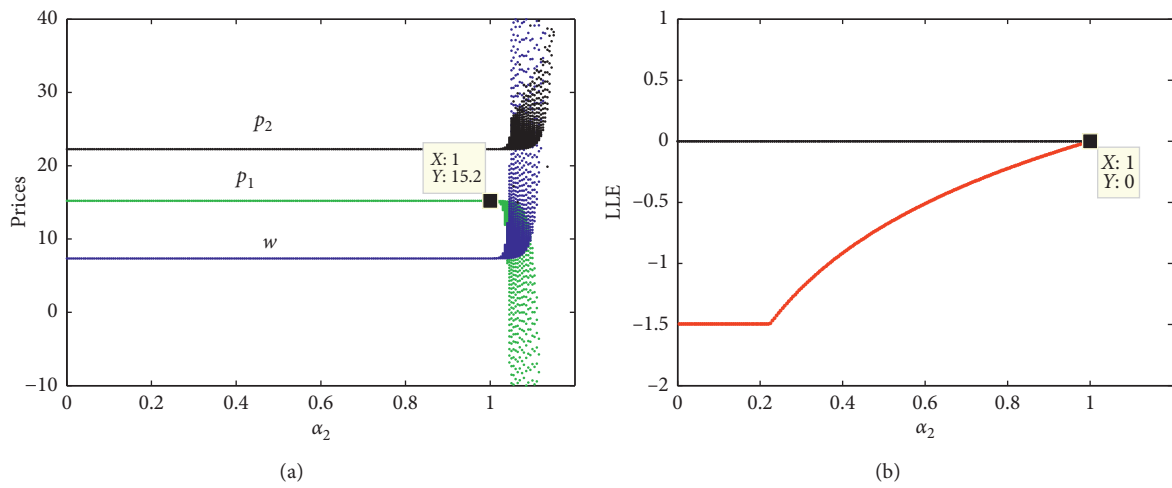


FIGURE 4: The behavior of dynamic system (9) with respect to  $\alpha_2$  when  $\alpha_1 = 0.04$ . (a) The wave shape bifurcation diagram. (b) The LLE diagram.

into the chaotic state without period doubling bifurcation; at this moment, the LLE is zero in Figure 4(b). Obviously, the influence of  $\alpha_2$  on the system dynamic behavior is different from that of  $\alpha_1$  on the system dynamic behavior.

Figure 5 is the 3D diagram for the chaos of system (9) corresponding to Figure 3(a). Red point represents the attractor when  $\alpha_1 = 0.04$  and  $\alpha_2 = 0.5$ , which indicates that the trajectory of the system is fixed. In Figure 5(b), the blue curve is the chaotic attractor of the system, when  $\alpha_1 = 0.094$  and  $\alpha_2 = 0.5$ , which vividly indicate the complexity and uncertainty of the system in chaotic state. Figure 6 shows the attractor of system (9) with respect to  $\alpha_1 = 0.04$  and  $\alpha_2 = 1.05$ . In the chaotic state,  $w$ ,  $p_1$ , and  $p_2$  are in disorder.

Besides, when  $\alpha_1 = 0.094$  and  $\alpha_2 = 0.5$  or  $\alpha_1 = 0.04$  and  $\alpha_2 = 1.05$ , chaotic system (9) also exhibits strong sensitivity to initial values. Here, fixing  $p_1 = 14$  and  $p_2 = 20$ , Figure 7(a) shows the sensitivity to initial value in stable state, when  $w$  is changed from 7 to 7.001. We can find that, at the beginning of iterations, there is a little difference, but after 5 iterations, the difference gradually reduces to zero. Conversely, in chaos, Figure 7(b) shows that small difference in initial values can cause a huge deviation after 10 iterations, which warns decision-makers to be cautious in choosing initial values when making decisions.

**3.3.2. Complexity Dynamics with respect to  $s$ .** When making price decisions, decision-makers should consider the impact of service value on optimal decision-making, as well as the impact of service value on the dynamic system. Figure 8 indicates the range of service values. It can be seen that  $w$  decreases with increase in  $s$ , but  $w$  must be above zero, which is in line with the actual situation of the market. Besides,  $p_1$  must be higher than  $w$ . Thus, it can be known that  $s \in (1.66, 2.42)$ .

Based on stability judgment conditions in equation (14), Figure 9 shows the 3D stable region with respect to  $s$ . When the value of  $(\alpha_1, \alpha_2, s)$  is in this region, system (9) is stable; otherwise, the system would not be stable. In Figure 9(b), increase in  $s$  improves the range of  $\alpha_1$ . Figure 10 shows the stability region composed of  $(\alpha_1, \alpha_2)$  with  $s$  fixed different values. We can see that the stable region is least when  $s = 2.2$  and becomes larger when  $s = 2.35$  and  $2.38$ . It is worth noting that  $s$  has no effect on the region of  $\alpha_2$ . The above analysis shows that the larger the  $s$  is, the larger the stable region of system (9) will be.

Next, the combined effects of  $s$  and  $\alpha_1$  on system's complexity are discussed. A 2D bifurcation diagram with respect to  $s$  and  $\alpha_1$ , when  $\alpha_2 = 0.5$ , is shown in Figure 11(a). Green represents the stable region consisting of  $(s, \alpha_1)$ . The range of  $\alpha_1$  increases significantly and then decreases with  $s$  increasing. For a given  $s$  belongs to  $(1.66, 2.20)$ , the system will experience a stable, series of period doubling bifurcations and fall into chaos with  $\alpha_1$  increasing. If  $s$  belongs to  $(1.66, 2.20)$ , the system will directly overflow. Figure 11(b) shows the 2D bifurcation diagram with respect to  $s$  and  $\alpha_2$  when  $\alpha_1 = 0.04$ . If given  $s$  belongs to  $(1.66, 1.694)$ , the

system goes into the period doubling region and shows period doubling bifurcation or chaos with  $\alpha_2$  varying in  $(0, 1)$ . If the given  $s$  belongs to  $(1.694, 2.42)$  and  $\alpha_1 \in (0, 1)$ , the system is in a stable state.

By comparing Figure 11(a) with Figure 11(b), it is found that service value  $s$  has little effect on  $\alpha_2$ . Besides, the retailer should reasonably choose the service value when providing services to customers; otherwise, the system will be in a chaotic state, which is not conducive to the retailer to get maximize profits.

**3.3.3. Impact of  $\alpha_i$  and  $s$  on Profits.** As the aim of enterprise in the market is to earn profit, the manufacturer and retailer have to pay attention to the result that whether they can get more profits or reduce losses by adjusting  $\alpha_1$ ,  $\alpha_2$ , and  $s$ . In this section, the influence of  $\alpha_1$ ,  $\alpha_2$ , and  $s$  on profits will be researched.

The bifurcation diagram of profits is shown in Figure 12 with  $\alpha_1$  varying from 0 to 0.1 and  $\alpha_2 = 0.5$ . In a stable state ( $\alpha_1 < 0.065$ ), the manufacturer and retailer can get stable returns and  $\prod_m > \prod_r$ . If  $\alpha_1 > 0.065$ , profits show the bifurcation and chaos phenomenon with  $\alpha_1$  increasing, which is consistent with Figure 3(a). Figure 13 shows the evolution diagram of the average profit with  $\alpha_1$ . It can be known that, in the periodic doubling bifurcation, the average profit of the manufacture and retailer decreases and shows a floating trend in chaotic state.

Figure 14 shows wave-shape chaos diagrams with respect to  $\alpha_2$  when  $\alpha_1 = 0.04$ . As  $\alpha_2$  increases ( $0 < \alpha_2 < 1$ ), system (9) remains stable. Once  $\alpha_2 > 1$ , system (9) will go into a fluctuant state, which causes a significant decline in profit.

Figure 15 shows the disordered evolution of system (9) as  $\alpha_1 = 0.094$  and  $\alpha_2 = 0.5$ . It can be found that the profit of system (9) changes irregularly in chaotic state, which is difficult for the manufacturer and retailer to predict future profits. In actual operation, decision-makers should avoid the appearance of this phenomenon.

Figure 16 shows the bifurcation diagram of  $\prod_r$  and  $\prod_m$  with respect to  $s$  as  $\alpha_1 = 0.04$  and  $\alpha_2 = 0.5$ . Obviously, the change of  $s$  has an impact on the dynamic evolution of system (9) and the profits of the manufacturer and retailer. It is shown in Figure 16 that when  $s$  is small ( $s < 1.8$ ), system (9) is in chaotic state. In this scenario,  $\prod_r$  and  $\prod_m$  are difficult to be measured. Further increase in  $s$  will lead to the appearance of period-4 state ( $1.8 < s < 1.848$ ), period-2 state ( $1.848 < s < 1.967$ ), and stable state ( $1.967 < s$ ). We can see that in stable state, increasing  $s$  is beneficial to the manufacturer and retailer. As  $s > 2.155$ ,  $\prod_r$  is greater than  $\prod_m$ . Table 2 shows the change of  $\prod_m$ ,  $\prod_r$ , and  $\prod_T$  with respect to  $s$ , where  $\prod_T$  is equivalent to  $\prod_m$  plus  $\prod_r$ . It can be found that the total profit of supply chain increases with  $s$  increasing.

Next, the combined effect of  $\alpha_1$ ,  $\alpha_2$ , and  $s$  on the profits of the manufacturer and retailer is to be explored in two situations.

*Situation 1.* System (9) falls into chaos with respect to  $\alpha_1$  and  $s$ .

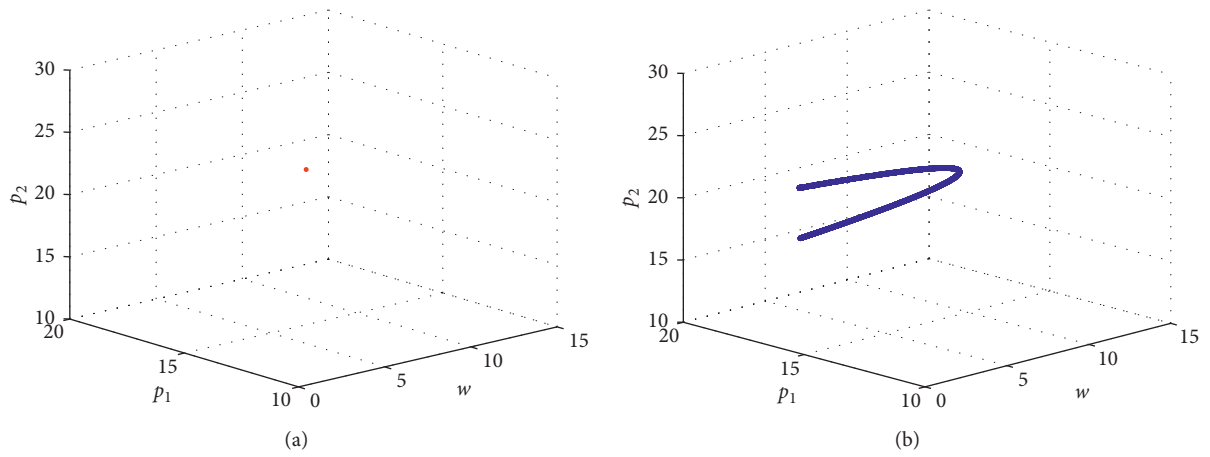


FIGURE 5: Chaos attractor of the dynamic system (9) with respect to  $\alpha_1$  and  $\alpha_2 = 0.5$ . (a)  $\alpha_1 = 0.04$ . (b)  $\alpha_1 = 0.094$ .

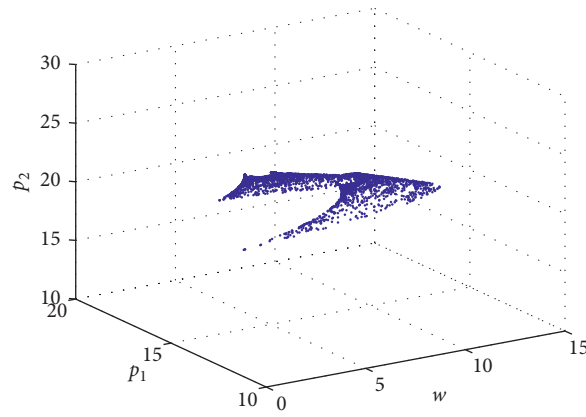
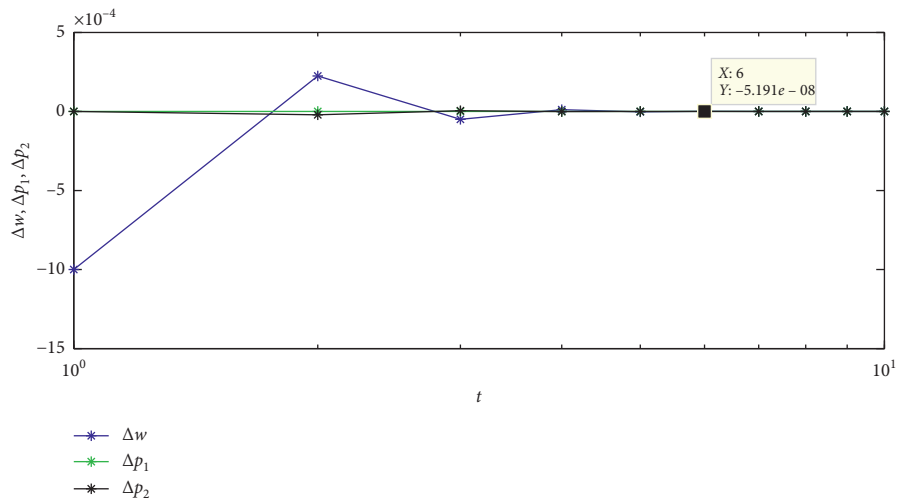


FIGURE 6: Chaos attractor of the dynamic system (9) with respect to  $\alpha_1 = 0.04$  and  $\alpha_2 = 1.05$ .



(a)  
FIGURE 7: Continued.

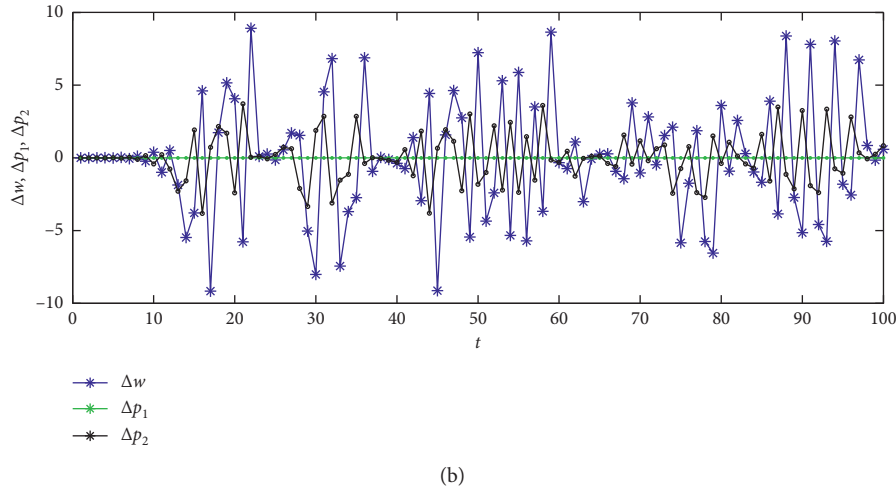


FIGURE 7: The sensitivity to initial value when  $(w, p_1, p_2) = (w = 7, p_1 = 14, p_2 = 20)$  and  $(w = 7.001, p_1 = 14, p_2 = 20)$ . (a)  $\alpha_1 = 0.04$  and  $\alpha_2 = 0.5$ . (b)  $\alpha_1 = 0.094$  and  $\alpha_2 = 0.5$ .

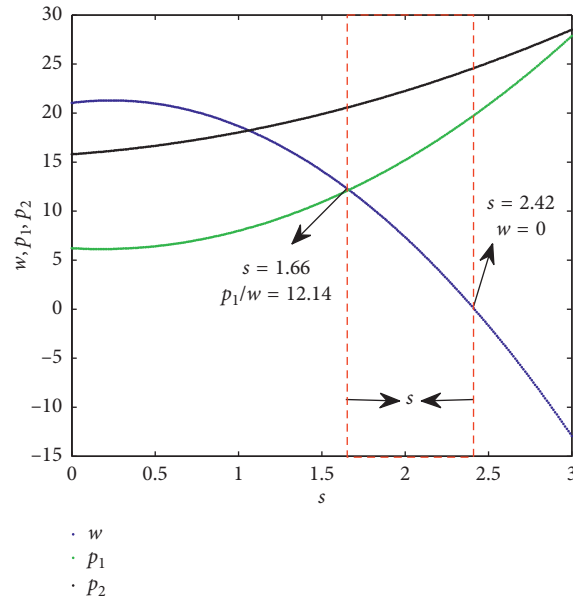


FIGURE 8: Nash equilibrium  $(w, p_1, p_2)$  with respect to  $s$ .

Figures 17 and 18 show the variation of  $\prod_m$  and  $\prod_r$  with  $\alpha_1$  and  $s$ . We can know that the smaller the service value is, the more easily the profit of the manufacturer and retailer fluctuates with  $\alpha_1$  increasing. On the contrary, the larger the service value, the chaotic phenomenon of system (9) will be delayed with  $\alpha_1$  increasing. The profits of the manufacturer and retailer will not be easily fluctuated. Meanwhile, the manufacturer and retailer can obtain stable profits. But too large  $\alpha_1$  will also cause the system to go into chaos.

*Situation 2.* System (9) falls into chaos with respect to  $\alpha_2$  and  $s$ .

As shown in Figures 19 and 20, as long as  $\alpha_2$  is less than 1, no matter how  $\alpha_2$  and  $s$  change, the profits of manufacturer and retailer will not fluctuate dramatically and the profit of manufacturer will slightly change with  $s$  increasing. However, the profit of retailer will increase with  $s$  increasing. Once  $\alpha_2$  is greater than 1, the profits of manufacturer and retailer will decline sharply.

With the variation of  $\alpha_1, \alpha_2,$  and  $s$ , system (9) probably loses stability and shows some complex behavior, meanwhile, which will lead to a decline in profits. Therefore, a management opinion given that manufacturer need to choose  $\alpha_1$  and  $\alpha_2$  carefully when making price decisions, in

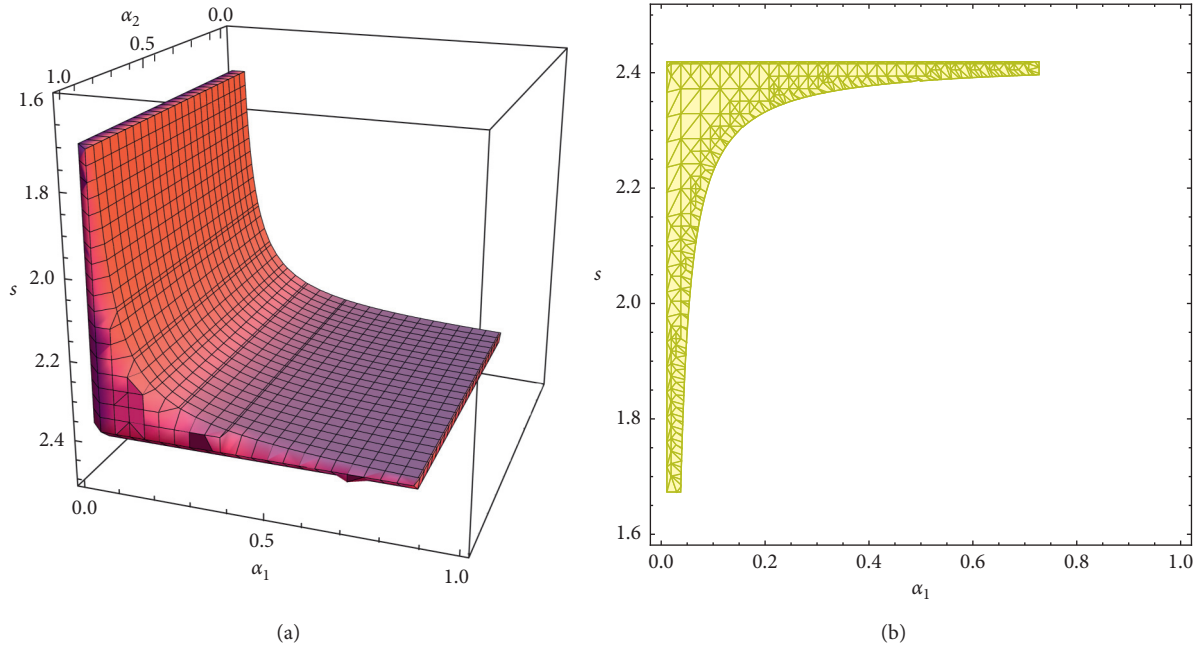


FIGURE 9: Stable region with respect to  $\alpha_1, \alpha_2$ , and  $s$ . (a) 3D stable region. (b) 2D stable region with  $\alpha_2 = 0.5$ .

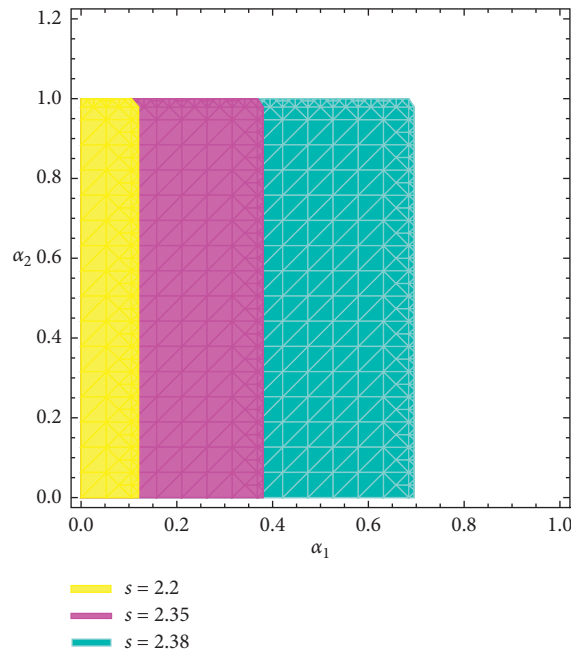


FIGURE 10: The stability region in the  $(\alpha_1, \alpha_2)$  plane with different  $s$ .

addition retailer need to cooperate with manufacturer to choose reasonable service value to ensure that the system is in a stable state and get maximize profits.

#### 4. Model with Unit Profit Sharing ( $M^\epsilon$ )

4.1. *Static Model.* In this section, the manufacturer controls the profit from the integration channel. The retailer provides

service value  $s$  for consumers from the integration channel and the traditional channel. Correspondingly, the manufacturer shares unit profit from the integration channel with the retailer. The manufacturer is the leader of the market, and the retailer is the follower.

Therefore, according to equations (1)–(3), the profit functions of the manufacturer and retailer can be described as follows:



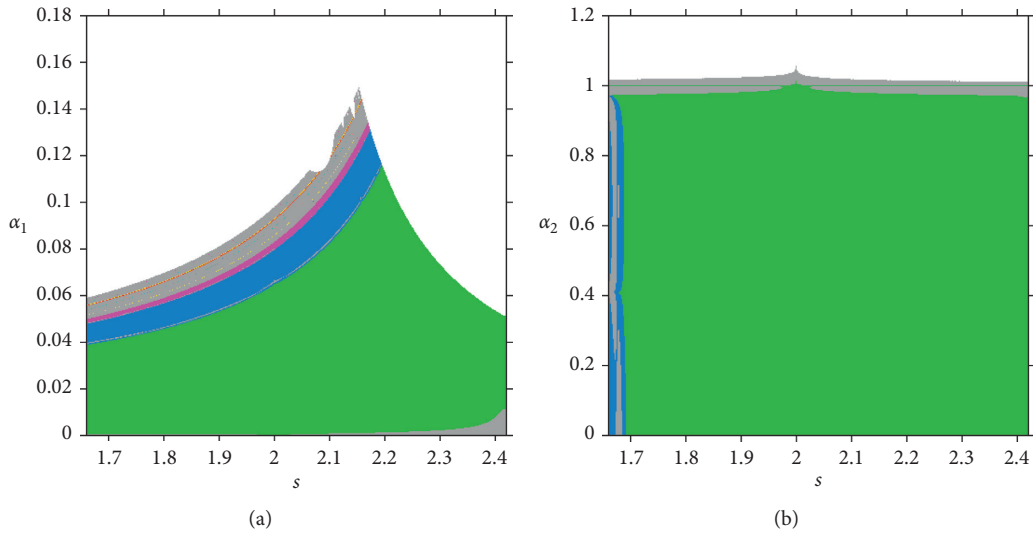


FIGURE 11: 2D bifurcation diagrams for periodic cycles. (a) 2D bifurcation with respect to  $\alpha_1$  and  $s$ . (b) 2D bifurcation with respect to  $\alpha_2$  and  $s$ .

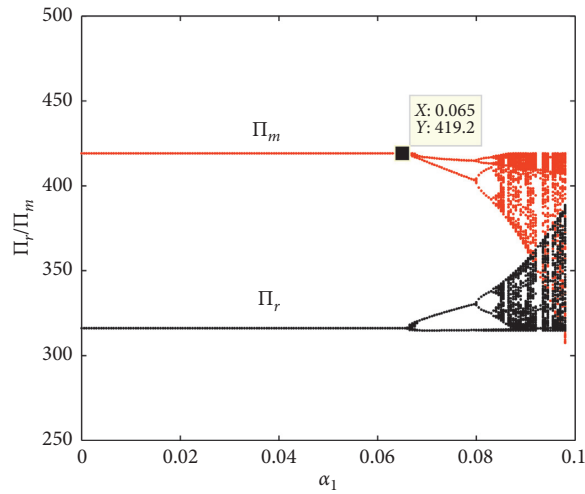


FIGURE 12: The bifurcation diagram of  $\Pi_r$  and  $\Pi_m$  with respect to  $\alpha_1$  as  $\alpha_2 = 0.5$ .

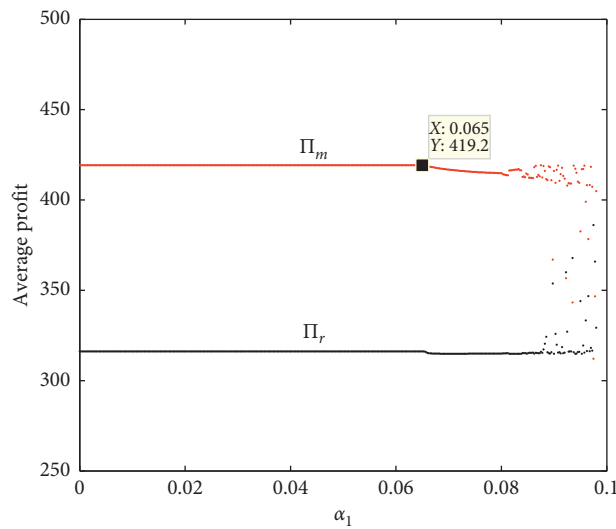


FIGURE 13: The average profit diagram with respect to  $\alpha_1$  and  $\alpha_2 = 0.5$ .

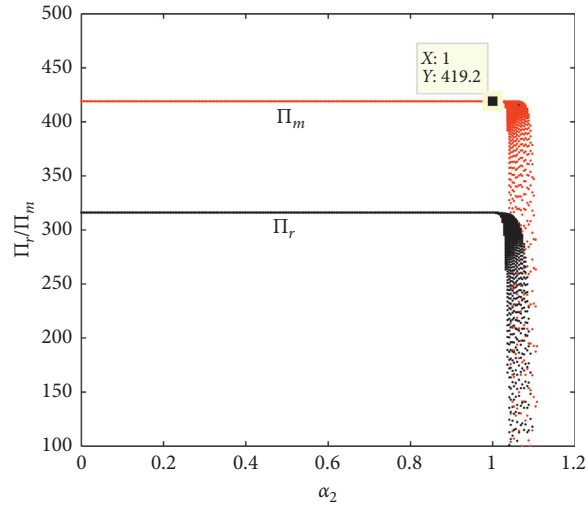


FIGURE 14: The wave-shape chaos diagram of  $\Pi_r$  and  $\Pi_m$  with respect to  $\alpha_2$  as  $\alpha_1 = 0.04$ .

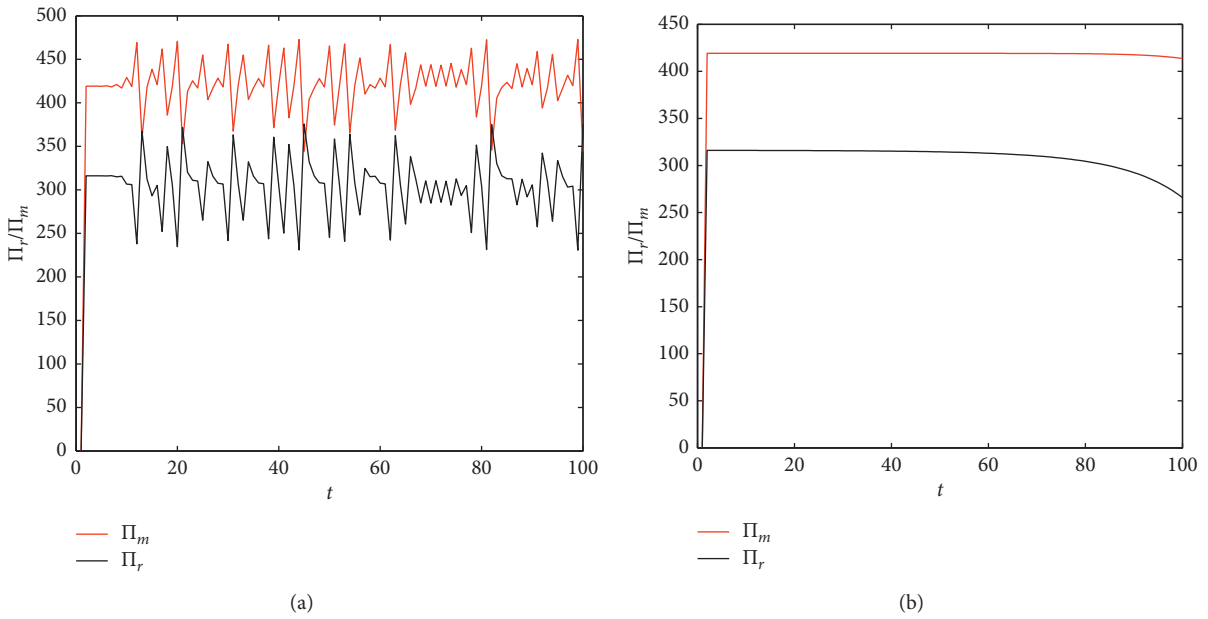


FIGURE 15: Time series of  $\Pi_r$  and  $\Pi_m$  with respect to  $\alpha_1$  and  $\alpha_2$ . (a)  $\alpha_1 = 0.094$  and  $\alpha_2 = 0.5$ . (b)  $\alpha_1 = 0.04$  and  $\alpha_2 = 1.05$ .

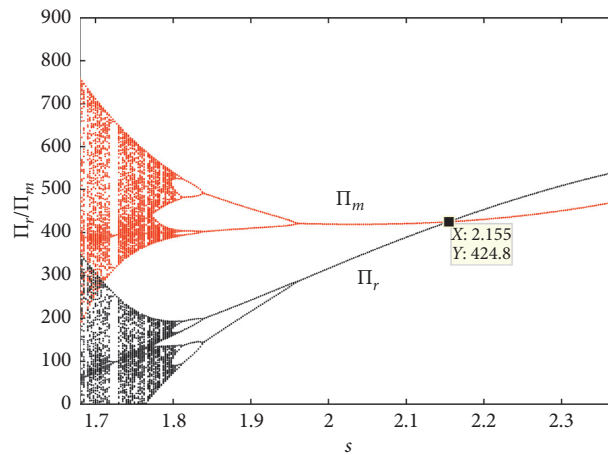


FIGURE 16: Profits change with  $s$  when  $\alpha_1 = 0.04$  and  $\alpha_2 = 0.5$ .

TABLE 2: The profits of system (9) for  $s$  ( $\alpha_1 = 0.06$  and  $\alpha_2 = 0.5$ ).

	$s = 1.967$	$s = 2.092$	$s = 2.155$	$s = 2.275$	$s = 2.36$
$\Pi_m$	420.4	420.1	424.8	444.5	468.1
$\Pi_r$	291.2	383.4	424.8	496.0	536.7
$\Pi_T$	711.6	803.5	849.6	940.5	1004.8

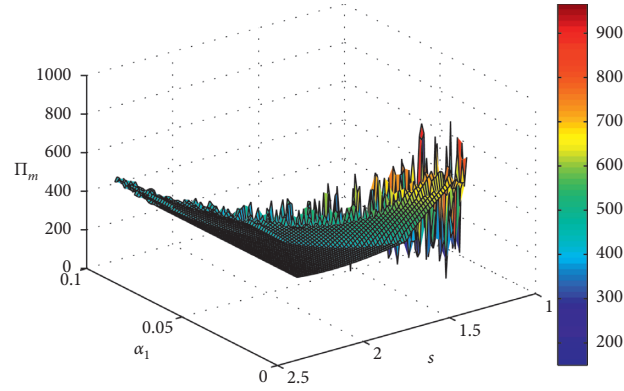


FIGURE 17: 3D profit diagram for the manufacturer with  $\alpha_1$  and  $s$ , as  $\alpha_2 = 0.5$ .

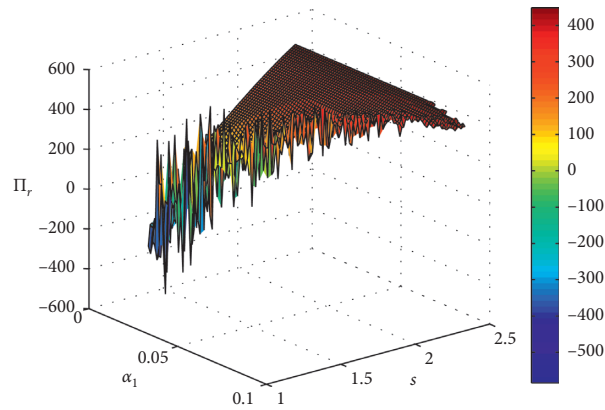


FIGURE 18: 3D profit diagram for the retailer with  $\alpha_1$  and  $s$ , as  $\alpha_2 = 0.5$ .

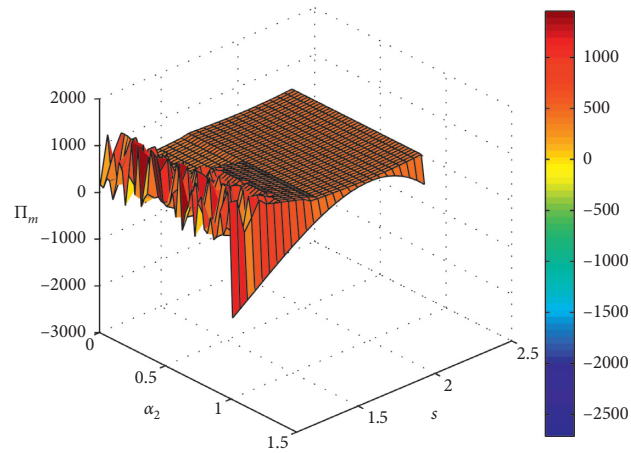
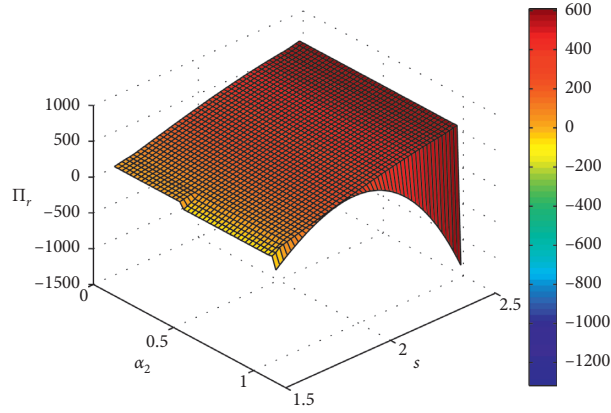


FIGURE 19: 3D profit diagram for the manufacturer with  $\alpha_2$  and  $s$ , as  $\alpha_1 = 0.04$ .

FIGURE 20: 3D profit diagram for the retailer with  $\alpha_2$  and  $s$ , as  $\alpha_1 = 0.04$ .

$$\begin{aligned}
 \max_{p_1, w} \prod_m^\varepsilon &= (p_1 - c)D_O + (w - c)D_T + (p_1 - c - \varepsilon)D_B \\
 &= (p_1 - c)(\theta_1 a - \rho_1 p_1 + \gamma_1 p_2) \\
 &\quad + (w - c)[\theta_3 a - m_T(p_2 - s) + \gamma_1 p_1] \\
 &\quad + (p_1 - c - \varepsilon)[\theta_2 a - m_B(p_1 - s) + \gamma_1 p_2] \\
 \text{s.t. } &c + \varepsilon < p_1, c < w,
 \end{aligned} \tag{16}$$

$$\begin{aligned}
 \max_{p_2} \prod_r^\varepsilon &= (p_2 - w - c_v)D_T + \varepsilon D_B - \varphi c_s D_B \\
 &= (p_2 - w - \eta s^2)[\theta_3 a - m_T(p_2 - s) + \gamma_1 p_1] \\
 &\quad + \varepsilon[\theta_2 a - m_B(p_1 - s) + \gamma_1 p_2] \\
 &\quad - \varphi \eta s^2 [\theta_2 a - m_B(p_1 - s) + \gamma_1 p_2] \\
 \text{s.t. } &w + \eta s^2 < p_2.
 \end{aligned} \tag{17}$$

To solve the Stackelberg equilibrium, we first find the optimal decision of the retailer. Given  $w$  and  $p_1$ , the retailer chooses  $p_2$  to maximize. Setting  $(\partial \prod_r^\varepsilon / \partial p_2) = 0$ ,

$$p_2 = \frac{\gamma_1 p_1}{2m_T} + \frac{w}{2} + \frac{s + \eta s^2}{2} + \frac{\varepsilon \gamma_1 + a\theta_3 - \varphi \eta \gamma_1 s^2}{2m_T}. \tag{18}$$

Submitting equation (18) into (16) and then taking the first-order partial derivatives of  $\prod_m^\varepsilon$  with respect to  $p_1$  and  $w$  can be shown as

$$\begin{cases}
 \frac{\partial \prod_m^\varepsilon}{\partial w} = \frac{3}{2}p_1\gamma_1 - m_T w + \frac{a\theta_3 + m_T s - \eta m_T s^2 + \varphi \eta \gamma_1 s^2 + m_T c - 2c\gamma_1 - 2\gamma_1 \varepsilon}{2} \\
 \frac{\partial \prod_m^\varepsilon}{\partial p_1} = \left(-2m_B - 2\rho_1 + \frac{3\gamma_1^2}{m_T}\right)p_1 + \frac{3\gamma_1 w}{2} - \frac{c\gamma_1}{2} + \frac{\gamma_1^2 \varepsilon}{2m_T} + m_B(c + \varepsilon + s) \\
 \quad + a\theta_1 + a\theta_2 - c\rho_1 + \frac{\gamma_1(m_T s + \eta m_T s^2 + a\theta_3 - \varphi \eta \gamma_1 s^2)}{m_T}.
 \end{cases} \tag{19}$$

Setting  $(\partial \prod_m^\varepsilon / \partial w) = 0$  and  $(\partial \prod_m^\varepsilon / \partial p_1) = 0$ , the solution of manufacturer can be obtained as

$$\begin{cases}
 w^* = \frac{4B_1 B_2 - 6B_3 \gamma_1}{4B_2 m_T + 9\gamma_1^3}, \\
 p_1^* = \frac{-4B_3 m_T - 6B_1 \gamma_1^2}{4B_2 m_T + 9\gamma_1^3},
 \end{cases} \tag{20}$$

where

$$\begin{aligned} B_1 &= \frac{a\theta_3 + m_T s - \eta m_T s^2 + \varphi \eta \gamma_1 s^2 + m_T c - 2c\gamma_1 - 2\gamma_1 \varepsilon}{2}, \\ B_2 &= -2m_B - 2\rho_1 + \frac{3\gamma_1^2}{m_T}, \\ B_3 &= -\frac{c\gamma_1}{2} + \frac{\gamma_1^2 \varepsilon}{2m_T} + m_B(c + \varepsilon + s) + a\theta_1 + a\theta_2 - c\rho_1 \\ &\quad + \frac{\gamma_1(m_T s + \eta m_T s^2 + a\theta_3 - \varphi \eta \gamma_1 s^2)}{m_T}. \end{aligned} \quad (21)$$

The Hessian matrix is

$$H^\varepsilon = \begin{bmatrix} -m_T & \frac{3}{2}\gamma_1 \\ \frac{3\gamma_1}{2} & -2m_B - 2\rho_1 + \frac{3\gamma_1^2}{m_T} \end{bmatrix}. \quad (22)$$

As  $\begin{vmatrix} -m_T & (3/2)\gamma_1 \\ (3/2)\gamma_1 & -2m_B - 2\rho_1 + (3\gamma_1^2/m_T) \end{vmatrix} = 2m_B m_T + 2\rho_1 m_T - 3\gamma_1^2 - (9/4)\gamma_1^2 > 16\gamma_1^2 - (9/4)\gamma_1^2 > 0$ , the Hessian matrix

$(w^*, p_1^*)$  is the optimal solution of the manufacturer.

Substituting equation (20) into (18), we obtain

$$\begin{aligned} p_2^* &= \frac{-4B_3 m_T \gamma_1 - 6B_1 \gamma_1^3}{8B_2 m_T^2 + 18m_T \gamma_1^3} + \frac{4B_1 B_2 - 6B_3 \gamma_1}{8B_2 m_T + 18\gamma_1^3} + \frac{s + \eta s^2}{2} \\ &\quad + \frac{\varepsilon \gamma_1 + a\theta_3 - \varphi \eta \gamma_1 s^2}{2m_T}. \end{aligned} \quad (23)$$

Substituting equations (20) and (23) into (16) and (17), the optimal profit functions of manufacturer and retailer can be described as follows:

$$\begin{cases} \Pi_m^\varepsilon = (p_1^* - c)(\theta_1 a - \rho_1 p_1^* + \gamma_1 p_2^*) + (w^* - c)[\theta_3 a - m_T(p_2^* - s) + \gamma_1 p_1^*] \\ \quad + (p_1^* - c - \varepsilon)[\theta_2 a - m_B(p_1^* - s) + \gamma_1 p_2^*], \\ \Pi_r^\varepsilon = (p_2^* - w^* - \eta s^2)[\theta_3 a - m_T(p_2^* - v) + \gamma_1 p_1^*] \\ \quad - \varphi \eta s^2 [\theta_2 a - m_B(p_1^* - s) + \gamma_1 p_2^*] + \varepsilon [\theta_2 a - m_B(p_1^* - s) + \gamma_1 p_2^*]. \end{cases} \quad (24)$$

**4.2. Dynamic Model.** In the changing market environment, we discuss that the situation of participants' dynamic decision and the influence of relevant parameters on the dynamic system are more in line with the actual market. Based on reality, this paper considers that the manufacturer employs different price adjustment strategies to make decisions of period  $t + 1$ . In dynamic periodic decision, the

manufacturer adopts the bounded rationality expectation to make the wholesale price decision:  $w_{t+1} = w_t [1 + \beta_1 (\partial \Pi_m^\varepsilon(w_t, p_{1,t}) / \partial w_t)]$  and make price decisions of integration channel and direct channel based on adaptive expectation:  $p_{1,t+1} = \beta_2 p_{1,t} + (1 - \beta_2) p_1^*$ .

Therefore, the dynamic process of the price game can be described as

$$w_{t+1} = w_t + \beta_1 w_t \left( \frac{3}{2} p_{1,t} \gamma_1 - m_T w_t + \frac{a\theta_3 + m_T s - \eta m_T s^2 + \varphi \eta \gamma_1 s^2 + m_T c - 2c\gamma_1 - 2\gamma_1 \varepsilon}{2} \right), \quad (25)$$

$$p_{1,t+1} = \beta_2 p_{1,t} + (1 - \beta_2) \frac{-4B_3 m_T - 6B_1 \gamma_1^2}{4B_2 m_T + 9\gamma_1^3}.$$

Here,  $\beta_1$  is the limited rational adjustment parameter and  $\beta_2$  ( $0 < \beta_2 < 1$ ) is the adaptive adjustment parameter.

In system (25), the manufacturer first makes the decisions:  $w_t$  and  $p_{1,t}$  by  $\beta_1$  and  $\beta_2$ , and the retailer are followers; his decision  $p_{2,t+1}$  is directly related to  $w_{t+1}$  and  $p_{1,t+1}$  as

$$p_{2,t+1} = \frac{\gamma_1}{2m_T} p_{1,t+1} + \frac{1}{2} w_{t+1} + \frac{s + \eta s^2}{2} + \frac{\varepsilon \gamma_1 + a\theta_3 - \varphi \eta \gamma_1 s^2}{2m_T}. \quad (26)$$

**4.2.1. Equilibrium Points and Local Stability.** According to the theory of the fixed point, setting  $w_{t+1} = w_t$  and  $p_{1,t+1} = p_{1,t}$ , there are two equilibrium points:  $e_1^\varepsilon$  and  $e_2^\varepsilon$ :

$$\begin{aligned} e_1^\varepsilon &= \left( 0, \frac{-4m_T B_3 - 6B_1 \gamma_1^2}{4m_T B_2 + 9\gamma_1^3} \right), \\ e_2^\varepsilon &= \left( \frac{4B_1 B_2 - 6B_3 \gamma_1}{4B_2 m_T + 9\gamma_1^3}, \frac{-4B_3 m_T - 6B_1 \gamma_1^2}{4B_2 m_T + 9\gamma_1^3} \right). \end{aligned} \quad (27)$$

Correspondingly, the retailer's decisions under two equilibrium points are, respectively,

$$p_2^{e_1^e} = \frac{-2m_T B_3 \gamma_1 - 3B_1 \gamma_1^3}{4m_T^2 B_2 + 9m_T \gamma_1^3} + \frac{s + \eta s^2}{2} + \frac{\varepsilon \gamma_1 + a \theta_3 - \varphi \eta \gamma_1 s^2}{2m_T},$$

$$p_2^{e_2^e} = \frac{-2m_T B_3 \gamma_1 - 3B_1 \gamma_1^3}{4m_T^2 B_2 + 9m_T \gamma_1^3} + \frac{2B_1 B_2 - 3B_3 \gamma_1}{4B_2 m_T + 9\gamma_1^3} + \frac{s + \eta s^2}{2} + \frac{\varepsilon \gamma_1 + a \theta_3 - \varphi \eta \gamma_1 s^2}{2m_T}. \quad (28)$$

**Proposition 3.** Obviously,  $e_1^e$  is the boundary equilibrium point, while  $e_2^e$  is the Stackelberg equilibrium point.

*Proof.* See Appendix C.

According to the analysis of equilibrium points in model M, we investigate the stability of  $e_2^e$  by using Jury conditions:

$$\begin{cases} (g_1) = 1 + \text{Tr}(J(e_2^e)) + \text{Det}(J(e_2^e)) > 0, \\ (g_2) = 1 - \text{tr}(J(e_2^e)) + \det(J(e_2^e)) > 0, \\ (g_3) = 1 - \det(J(e_2^e)) > 0, \end{cases} \quad (29)$$

where

$$\begin{aligned} \text{Tr}(J(e_2^e)) &= \beta_2 + 1 + \beta_1 \left( \frac{-6B_3 m_T \gamma_1 - 9B_1 \gamma_1^3}{4B_2 m_T + 9\gamma_1^3} - \frac{8m_T B_1 B_2 - 12m_T B_3 \gamma_1}{4B_2 m_T + 9\gamma_1^3} + B_1 \right), \\ \text{Det}(J(e_2^e)) &= \beta_2 \left[ 1 + \beta_1 \left( \frac{-6B_3 m_T \gamma_1 - 9B_1 \gamma_1^3}{4B_2 m_T + 9\gamma_1^3} - \frac{8m_T B_1 B_2 - 12m_T B_3 \gamma_1}{4B_2 m_T + 9\gamma_1^3} + B_1 \right) \right]. \end{aligned} \quad (30)$$

By above stability judgment conditions, we can know  $0 < \beta_1 < \vartheta$ ,  $0 < \beta_2 < 1$ , where  $\vartheta = 4B_2 m_T + 9\gamma_1^3 / (-6B_3 m_T \gamma_1 - 9B_1 \gamma_1^3 - 8m_T B_1 B_2 + 12m_T B_3 \gamma_1 + B_1 (4B_2 m_T + 9\gamma_1^3))$ . When the decision parameters are in this range ( $0 < \beta_1 < \vartheta$ ,  $0 < \beta_2 < 1$ ), system (25) will be stable at equilibrium point  $e_2^e(w^*, p_1^*)$ . Due to the existence of a large number of parameters in system (25), the stability and bifurcation of the system will be studied intuitively in the next part.  $\square$

**4.3. Complexity Dynamics Analysis and Numerical Simulation.** In this section, the same parameters are chosen as in Section 3.3 furthermore, given  $\varepsilon = 8$ . Correspondingly, the Stackelberg equilibrium is  $e_2^e = (6.1663, 15.9983)$ .

**4.3.1. Complexity Dynamics with respect to  $\beta_1$ .** First of all, we analyze the paths of system (25) going into chaos. Figure 21 shows the 2D parameter bifurcation in the  $(\beta_1, \beta_2)$  plane, where different colors represent different periods of system (25): stable (red), period-2 (yellow), period-3 (green), period-4 (blue), period-5 (cyan), period-6 (claret), chaos (gray), and divergence (white). It can be seen that system (25) can enter into chaos by two ways. In Path 1, we fix the value of  $\beta_2$  ( $0 < \beta_2 < 1$ ). Beginning in stable state, system (25) goes into chaos through a series of period doubling bifurcations. In Path 2, given  $\beta_1 \in (0, 0.054)$ , change the value of  $\beta_2$ . It can be seen that system (25) goes directly into chaos from the stable period. We can know the paths of system (25) into chaos is similar to system (9), but a difference is that system (25) enters the bifurcation period and chaos earlier than system (9).

Next, we investigate dynamic evolution of system (25). Figure 22 shows the behavior of dynamic system (25) with

respect to  $\beta_1$  when  $\beta_2 = 0.5$ .  $w$ ,  $p_1$ , and  $p_2$  do not fluctuate in Figure 22(a) when  $\beta_1 < 0.054$ . Compared with Figure 4(a),  $w$  and  $p_2$  are less than that in system (9). As  $\beta_1 = 0.054$ , the first flip bifurcation appears; meanwhile, the LLE showed in Figure 22(b) reaches the first zero. After it, with  $\beta_1$  increasing, system (25) goes through period doubling bifurcation and goes into chaos with LLE  $> 0$ .

The dynamic evolution of system (25) with respect to  $\beta_2$  is shown in Figure 23. As long as  $\beta_2 < 1$ , system (25) is always in the stable period. As  $\beta_2 > 1$  and the LLE is zero in Figure 23(b), system (25) directly goes into wave chaos without period doubling bifurcation, which is different from the dynamic evolution of system (25) with  $\beta_1$ . Obviously, wave chaos of system (25) is weaker than that of system (9) in Figure 4.

Figure 24 shows time series of  $w$ ,  $p_1$ , and  $p_2$  with  $t$  when  $\beta_1 = 0.08$  and  $\beta_2 = 0.4$ . We can see that  $w$  and  $p_2$  show violent and disorderly fluctuations once system (25) becomes unstable. But, because retailer adopts adaptive expectation when deciding retail price,  $p_1$  is not affected by bounded rationality adjustment parameter  $\beta_1$ . Figure 25 indicates the sensitivity to initial value of system (25) when  $\beta_1 = 0.08$  and  $\beta_2 = 0.4$ . It reveals that, in a chaotic system, small difference in initial values can cause a huge deviation after 10 iterations, which is similar to Figure 7(b). In the unstable system, it is very difficult for decision-maker to make the next-stage decision. Therefore, managers should rationally adjust price decisions and choose the initial values reasonably to keep the system stable.

**4.3.2. Influence of  $s$  and  $\varepsilon$  on the Stability of the System.** In the process of cooperation, the manufacturer and retailer have to determine service value  $s$  and value of unit profit sharing  $\varepsilon$  because service value and unit profit sharing will



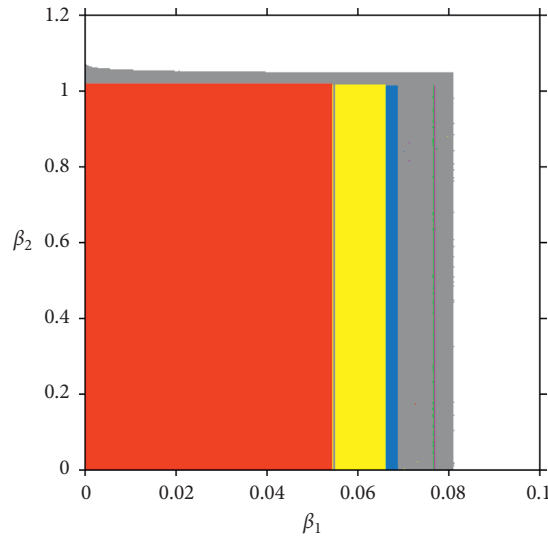


FIGURE 21: 2D parameter bifurcation in the  $(\beta_1, \beta_2)$  plane.

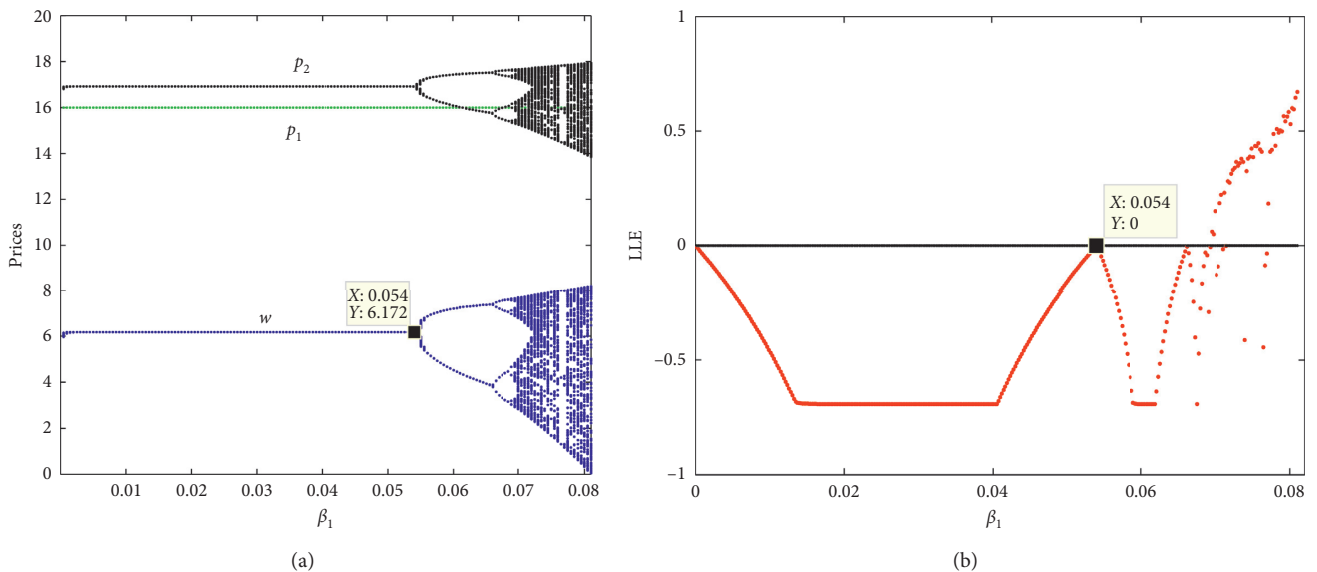


FIGURE 22: The behavior of dynamic system (25) with respect to  $\beta_1$  when  $\beta_2 = 0.5$ . (a) The bifurcation diagram. (b) The LLE diagram.

affect the stability of system (25). According to the actual operation of the market, the ranges of  $s$  and  $\varepsilon$  are shown in Figures 26 and 27, respectively. To ensure that  $p_2$  is greater than  $p_1$ , we can know  $s > 1.62$ . Meanwhile, in order to be meaningful,  $w$  must be greater than zero. Thus,  $s$  can be chosen in the range (1.62, 3.12). Similarly, only when  $\prod_r^\varepsilon > \prod_r$ , where  $\prod_r$  represents the profits of retailers without cooperating with the manufacturer, the retailer be willing to cooperate with the manufacturer. In addition, as  $\prod_r^\varepsilon > \prod_m^\varepsilon$ , the manufacturer will terminate its cooperation with the retailer. Therefore, we can know that  $\varepsilon$  can be chosen in (2, 15.38).

Figure 28(a) shows the 3D stable region of the parameters  $(\beta_1, \beta_2, s)$  when  $\varepsilon = 8$ . If  $\beta_1, \beta_2$ , and  $s$  are in this 3D stable region, system (25) is stable. Combining Figure 28(b) and Table 3, we can find that  $s$  changing in (1.62, 3.12) has a

significant effect on the stable region of the system. It can be concluded that if  $s$  is in (1.62, 3.12), the larger the service value  $s$  will be, the larger the stable region of system (25) will be, and service value  $s$  only affects the scope of  $\beta_1$  but does not affect the scope of  $\beta_2$ . The conclusion is similar to that of system (9).

Observing Figure 29 and Table 3, we can see that the effect of  $\varepsilon$  on the stable region is similar to that of  $s$ . But the sensitivity of  $\varepsilon$  to the stable region is weaker than that of  $s$ .

Figure 30 shows 2D bifurcation diagrams for periodic cycles. Different colors represent different periods of system (25), which is the same as Figure 20. In Figure 30(a), the stable range of  $\alpha_1$  increases significantly and then decreases with  $s$  increasing. For a given  $s$  belongs to (1.62, 2.42), system (25) will experience the stable period and a series of period doubling bifurcations and fall into chaos with  $\beta_1$  increasing. If

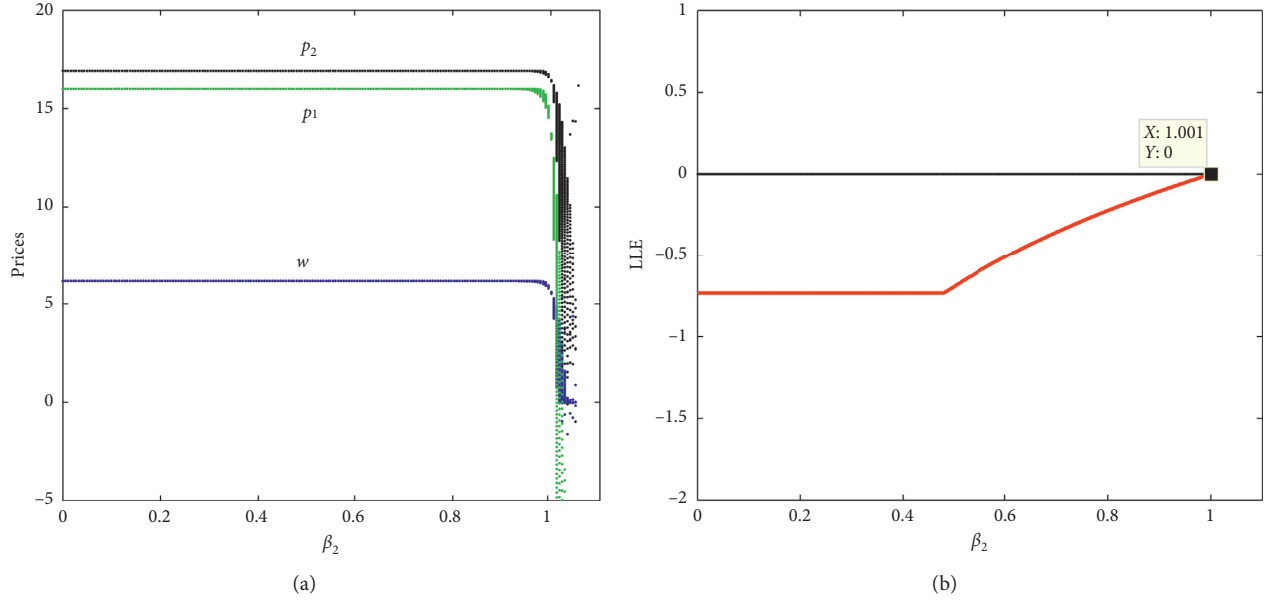


FIGURE 23: The behavior of dynamic system (25) with respect to  $\beta_2$  when  $\beta_1 = 0.04$ . (a) The bifurcation diagram. (b) The LLE diagram.

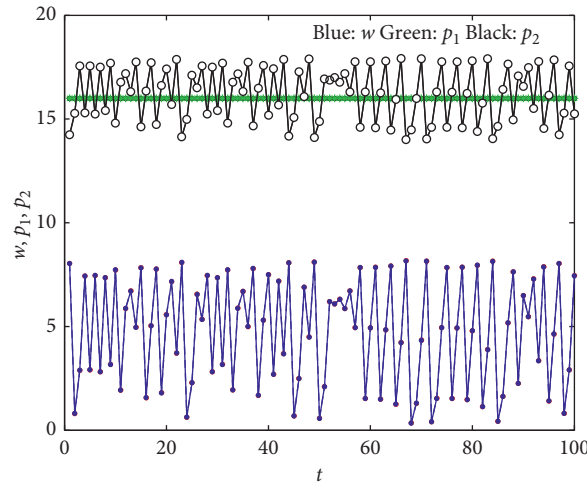


FIGURE 24: Time series of  $w$ ,  $p_1$ , and  $p_2$  with  $\beta_1 = 0.08$  and  $\beta_2 = 0.4$ .

$s$  belongs to  $(2.42, 3.12)$ , the system will directly overflow with  $\beta_1$  increases. In Figure 30(b), if  $\varepsilon$  increases in  $(2, 15.38)$ , bifurcation and chaos will occur belatedly in system (25). Thus, improving  $\varepsilon$  is beneficial to the stability of system (25). The manufacturer can delay the occurrence of bifurcation and chaos of system (25) by adjusting  $\varepsilon$ .

4.3.3. *Impact of  $\beta_i$ ,  $s$ , and  $\varepsilon$  on Profits.* Above all, we discuss the influence of  $\beta_i$ ,  $s$ , and  $\varepsilon$  on the stability and complexity of system (25). Due to system (25) stability affecting the profits of manufacturer and retailer, next, the influence of  $\beta_i$ ,  $s$ , and  $\varepsilon$  on profits will be investigated.

Figure 31(a) shows dynamic evolution of  $\prod_m^\varepsilon$  and  $\prod_r^\varepsilon$  with  $\beta_1$ ; we can know that as  $\beta_1 < 0.054$ , the manufacturer and retailer can get stable returns. However,  $\prod_m^\varepsilon$  and  $\prod_r^\varepsilon$  show the bifurcation and chaos phenomenon with  $\beta_1$  increasing. In Figure 31(b), in the bifurcation period,  $\prod_m^\varepsilon$  decreases while  $\prod_r^\varepsilon$  rises, which is different from system (9). As  $\beta_1$  increases, the average profit shows a floating trend in chaotic state.

Figure 32 shows wave-shape chaos diagrams with respect to  $\beta_2$  when  $\beta_1 = 0.04$ . As  $\beta_2$  changes in  $(0, 1)$ ,  $\prod_m$  and  $\prod_r$  remain stable. Once  $\beta_2 > 1$ ,  $\prod_m$  and  $\prod_r$  will go into a fluctuant state, which causes a significant decline in profit. It can be clearly seen that the impact of  $\beta_1$  on profits is significantly different from that of  $\beta_2$  on profits. That is to say,

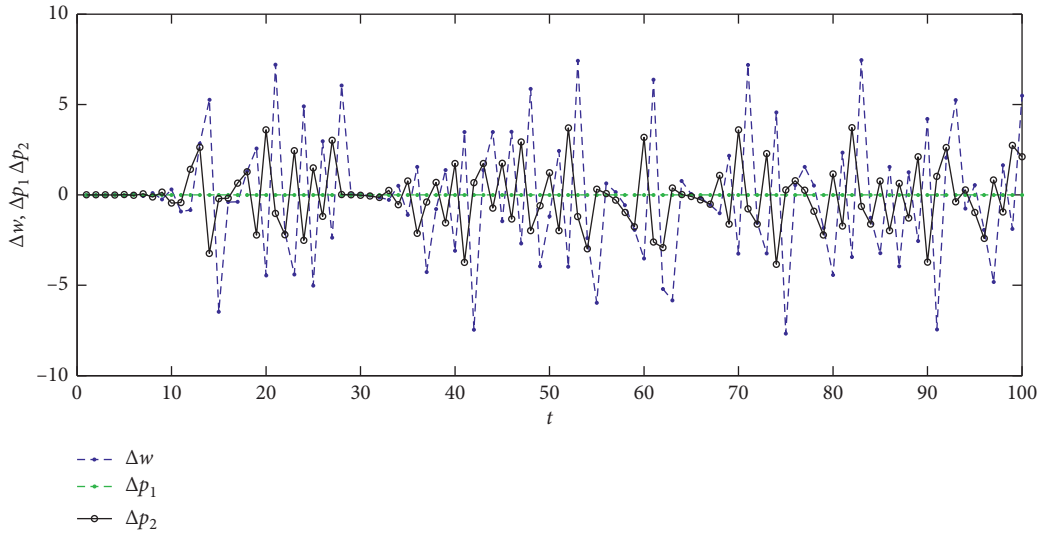


FIGURE 25: The sensitivity to initial value when  $(w, p_1, p_2) = (w = 7, p_1 = 14, p_2 = 20)$  and  $(w = 7.001, p_1 = 14, p_2 = 20)$ .

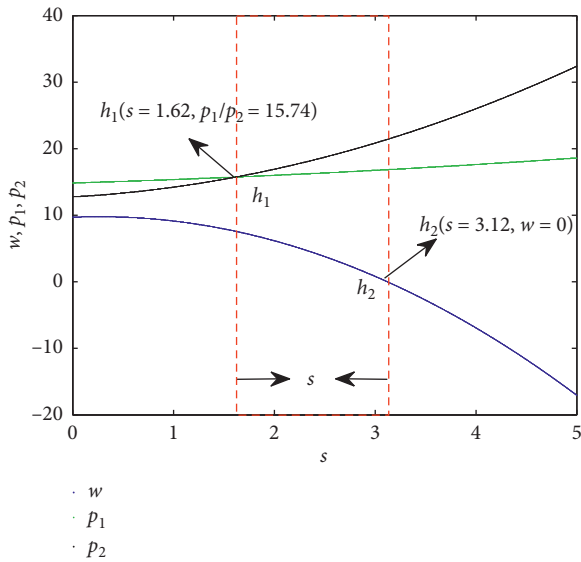


FIGURE 26: The Stackelberg equilibrium  $(w, p_1, \text{ and } p_2)$  with respect to  $s$ .

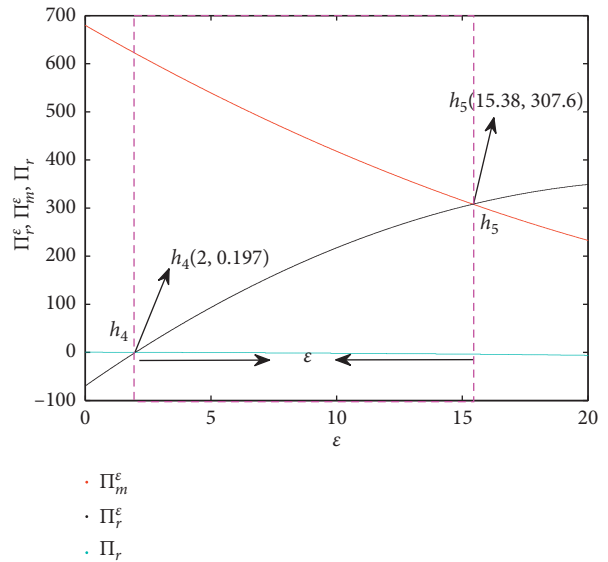


FIGURE 27: Profits of system  $(\Pi_r^\epsilon, \Pi_m^\epsilon, \text{ and } \Pi_r)$  with respect to  $\epsilon$ .

different price adjustment expectations have different effects on the profit of system (25).

Next, the combined effect of  $\beta_1, s,$  and  $\epsilon$  on the profits of the manufacturer and retailer is to be explored in two situations.

**Situation 3.** System (25) falls into chaos with respect to  $\beta_1$  and  $s$ .

Figure 33 shows the variation of  $\Pi_m$  and  $\Pi_r$  with  $\beta_1$  and  $s$ . It indicates that, with  $s$  increasing,  $\Pi_m$  increases while  $\Pi_r$  decreases. We can know that smaller  $s$  and bigger  $\beta_1$  can easily lead system (25) into chaotic state, causing  $\Pi_m$  and  $\Pi_r$  fluctuation. On the contrary, bigger  $s$  and smaller  $\beta_1$  are helpful to keep system (25) stable and help the manufacturer and retailer to obtain maximum profits.

**Situation 4.** System (25) falls into chaos with respect to  $\beta_1$  and  $\epsilon$ .

As shown in Figure 34,  $\Pi_m$  decreases while  $\Pi_r$  increases with  $\epsilon$  increasing. Meanwhile, it can be found that the larger  $\epsilon$  is, the less likely the system (25) goes into bifurcation and chaos. When  $\beta_1$  is less than a certain value, the system is in a stable state, and the profits of the manufacturer and retailer are also stable. In order to ensure the stability of system (25) and obtain stable profits, the manufacturer and retailer need to cooperate to make price decisions and service decisions.

### 5. Control of Complexity Dynamics

From the above numerical simulation and analysis, it can be seen that  $\alpha_i, \beta_i, s,$  and  $\epsilon$  affect the stability and complexity of the system. Once the system goes into chaos, the whole

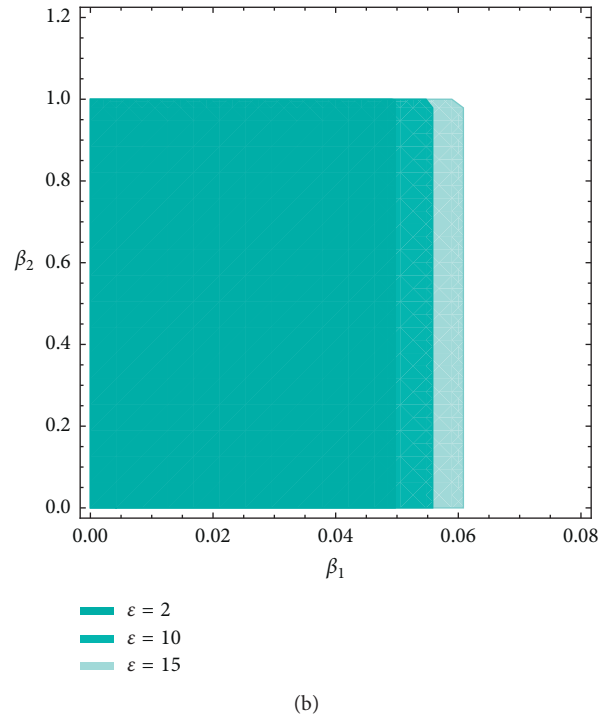
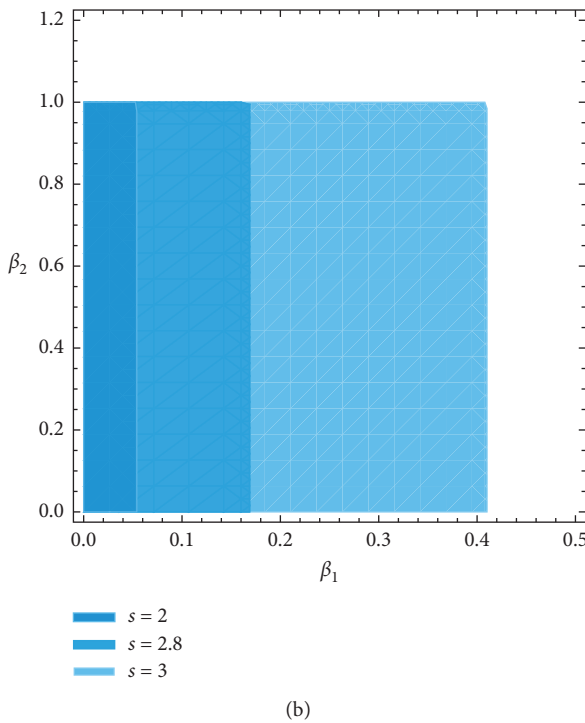
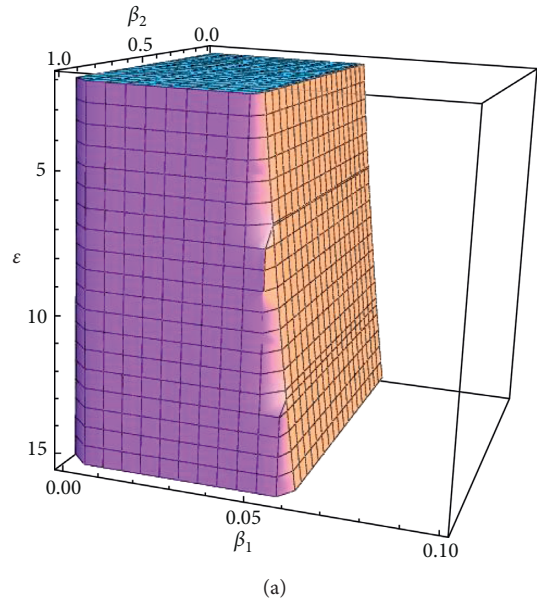
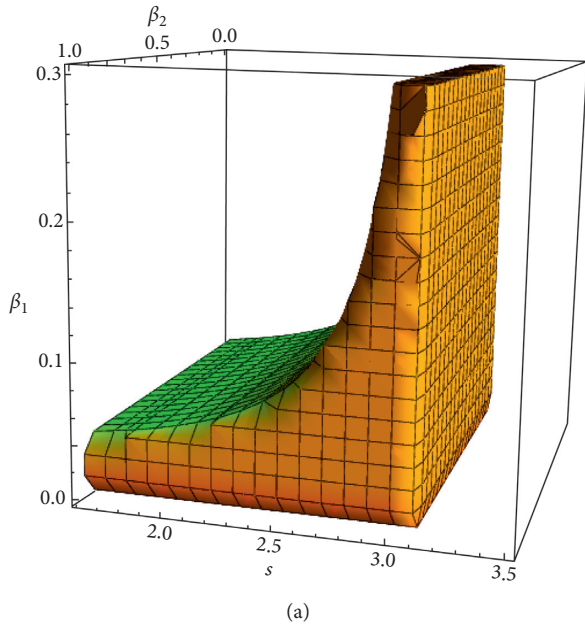


FIGURE 28: Stable region with respect to  $\beta_1$ ,  $\beta_2$ , and  $s$ . (a) 3D stable region. (b) 2D stable region in the  $(\beta_1, \beta_2)$  plane.

FIGURE 29: Stable region with respect to  $\beta_1$ ,  $\beta_2$ , and  $\epsilon$ . (a) 3D stable region. (b) 2D stable region in the  $(\beta_1, \beta_2)$  plane.

market becomes disordered and unpredictable, and profits of the supply chain fluctuate or even decline sharply. In this state, it is difficult for the manufacturer and retailer to make next price decisions based on current profit. Thus, controlling chaos is beneficial to the whole supply chain.

In chaos control, some scholars have studied the control methods of the chaotic system [27, 32, 37]. According to the characteristics of this paper, this paper takes system (25) as

TABLE 3: 2D stable region with respect to  $s$  and  $\epsilon$  in the  $(\beta_1, \beta_2)$  plane.

$s/\epsilon$	$\beta_1$	$\beta_2$
$s = 2.0$	(0, 0.0563)	(0, 1)
$s = 2.8$	(0, 0.1706)	(0, 1)
$s = 3.0$	(0, 0.4113)	(0, 1)
$\epsilon = 2.0$	(0, 0.0498)	(0, 1)
$\epsilon = 10$	(0, 0.0558)	(0, 1)
$\epsilon = 15$	(0, 0.0611)	(0, 1)

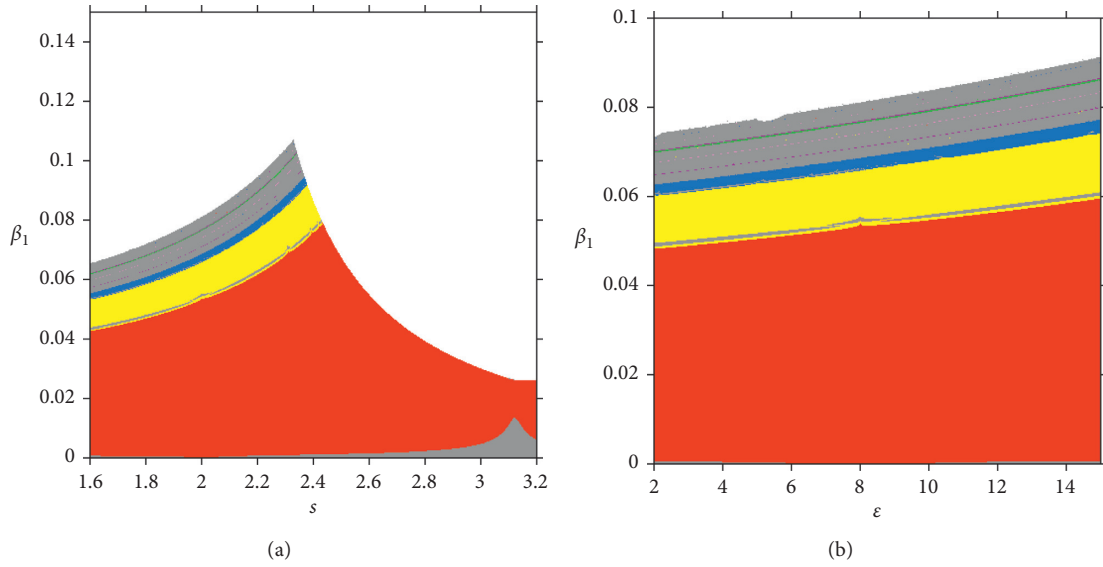


FIGURE 30: 2D bifurcation diagrams for periodic cycles. (a) 2D bifurcation with respect to  $\beta_1$  and  $s$ . (b) 2D bifurcation with respect to  $\beta_1$  and  $\epsilon$ .

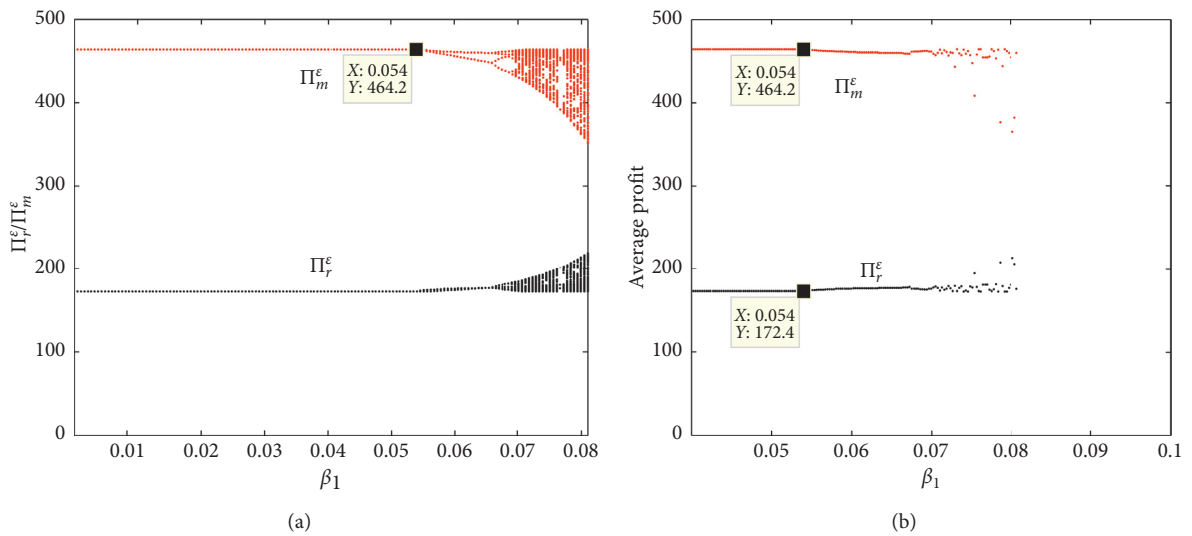


FIGURE 31: The bifurcation diagram and average profit diagram of  $\Pi_r$  and  $\Pi_m$  with respect to  $\beta_1$  as  $s = 2$  and  $\epsilon = 8$ . (a) The bifurcation diagram. (b) The average profit diagram.

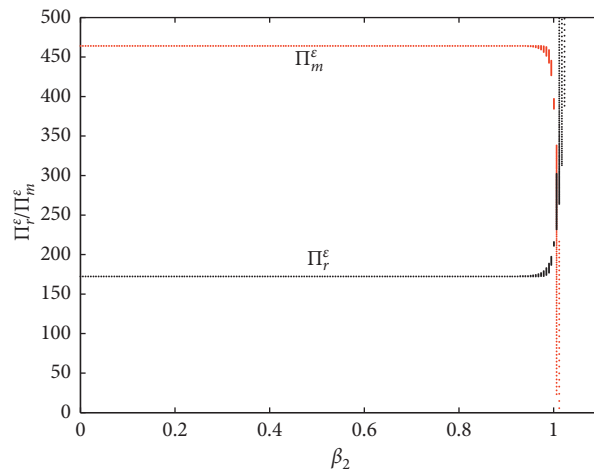


FIGURE 32: The bifurcation diagram of  $\Pi_r$  and  $\Pi_m$  with respect to  $\beta_2$ .

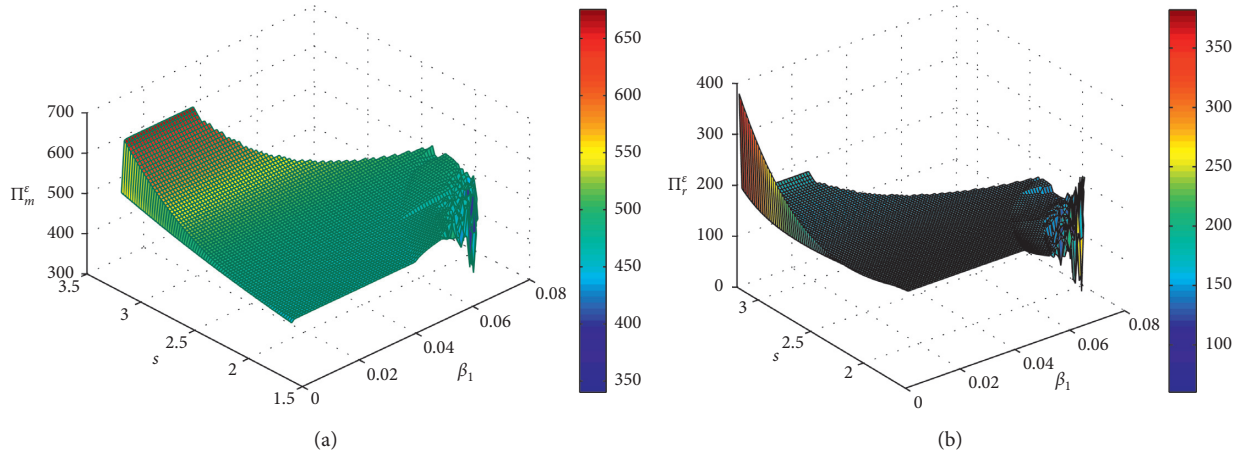


FIGURE 33: 3D profit diagrams of the manufacturer and retailer with  $\beta_1$  and  $s$ , as  $\beta_2 = 0.5$  and  $\varepsilon = 8$ . (a) 3D profit diagrams of the manufacturer. (b) 3D profit diagrams of the retailer.

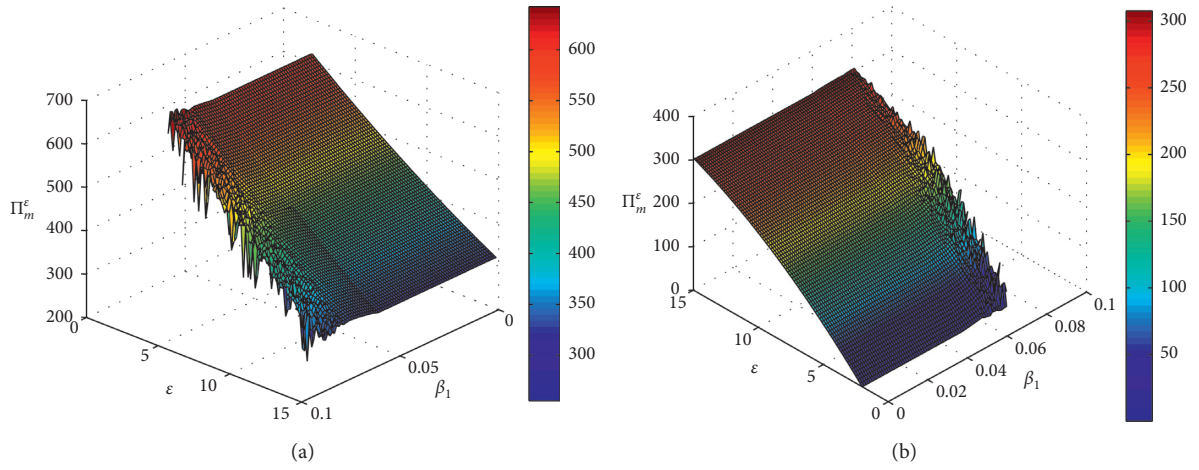


FIGURE 34: 3D profit diagrams of the manufacturer and retailer with  $\beta_1$  and  $\varepsilon$ , as  $\beta_2 = 0.5$  and  $s = 2$ . (a) 3D profit diagrams of the manufacturer. (b) 3D profit diagrams of the retailer.

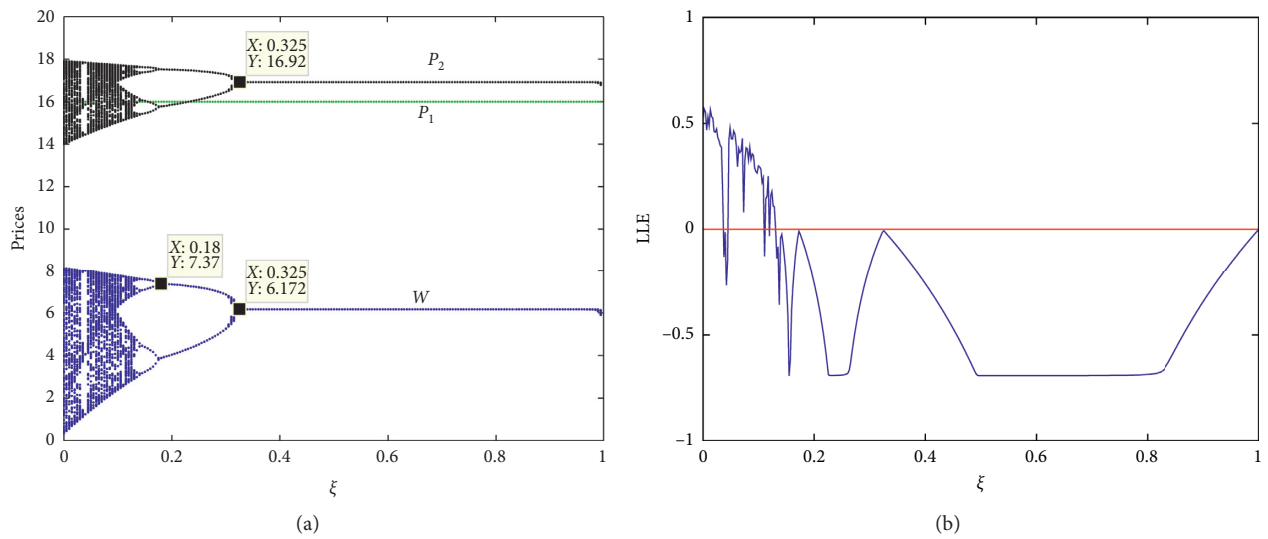


FIGURE 35: The price evolution process of system (32) with respect to  $\xi$ . (a) The bifurcation diagram. (b) The LLE diagram.



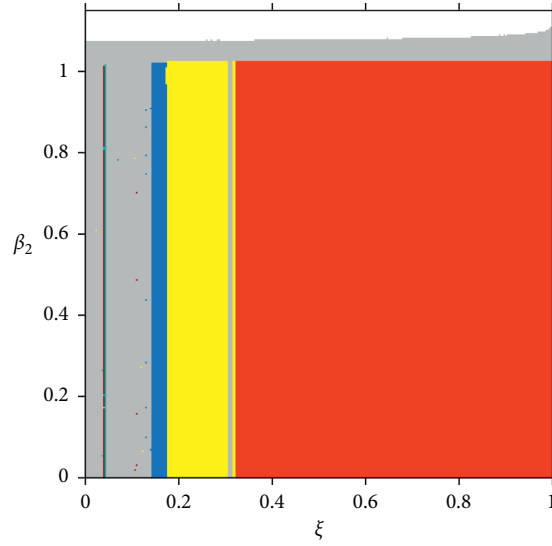


FIGURE 36: 2D bifurcation diagram with respect to  $\beta_2$  and  $\xi$ .

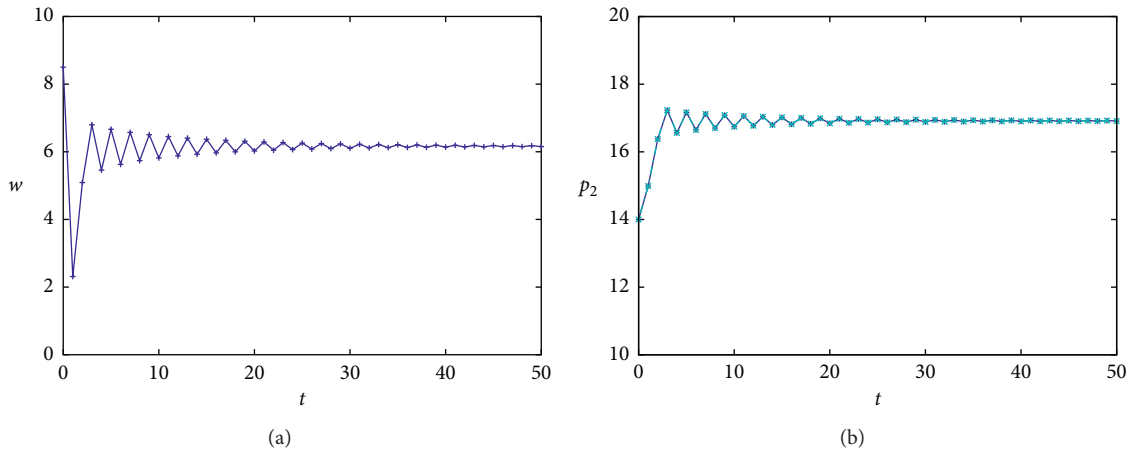


FIGURE 37: Initial value sensitivity of system (32) after being controlled as  $\xi = 0.35$ . (a) Initial value sensitivity of  $w$ . (b) Initial value sensitivity of  $p_2$ .

an example, and a chaos control method based on state feedback is adopted. Supposing system (25) is described as  $w_{t+1} = T_1(w_t, p_{1,t})$ ,  $p_{1,t+1} = T_2(p_{1,t})$ . Then, the control system can be obtained as follows:

Namely,

$$\begin{cases} w_{t+1} = (1 - \xi)T_1(w_t, p_{1,t}) + \xi w_t, \\ p_{1,t+1} = T_2(p_{1,t}). \end{cases} \quad (31)$$

$$\begin{cases} w_{t+1} = (1 - \xi) \left( w_t + \beta_1 w_t \left( \frac{3}{2} p_{1,t} \gamma_1 - m_T w_t + \frac{a\theta_3 + m_T v - \eta m_T v^2 + \varphi \eta \gamma_1 v^2 + m_T c - 2c\gamma_1 - 2\gamma_1 \varepsilon}{2} \right) \right) + \xi w_t, \\ p_{1,t+1} = \beta_2 p_{1,t} + (1 - \beta_2) \frac{-4F_3 m_T - 6F_1 \gamma_1^2}{4F_2 m_T + 9\gamma_1^3}, \end{cases} \quad (32)$$

where  $\xi$  is a feedback control parameter ( $0 < \xi < 1$ ). When  $\xi = 0$ , system (32) is in chaotic state.

The price evolution process of system (32) with respect to  $\xi$  is shown in Figure 35. When  $\xi > 0.18$ , in Figure 35(a), system (32) gets rid of chaos and four-period bifurcation and enters into two-period bifurcation state. Continuing to improve  $\xi$  to 0.325, system (32) goes into the stable state. In Figure 35(b), when  $\xi > 0.325$ , the LLE ( $LLE < 0$ ) confirms that the chaos of system has been controlled effectively.

Figure 36 shows 2D bifurcation diagram with respect to  $\beta_2$  and  $\xi$ . With  $\xi$  increasing, system (32) experiences chaos and double period bifurcation and goes into stable state. When  $\beta_2$  and  $\xi$  are in the red area, it is advantageous for the manufacturer and retailer to achieve business goals. The sensitivity of the system compared with Figure 25 can also be suppressed effectively in Figure 37.

## 6. Conclusions

In this paper, based on channel integration and service cooperation, we build two dynamic game models: one without unit profit allocation ( $M$ ) and the other one with unit profit allocation ( $M^\varepsilon$ ). In model  $M$ , first, we investigate the influence of adjusting parameters on the evolution of dynamic models and analyse the complex characteristics of the dynamic model. Second, we analyzed the influence of service value on the stability and complexity of the dynamic system. Finally, the combined effect of adjusting parameters and service value on the profit evolution of the dynamic model is explored. In model  $M^\varepsilon$ , we do similar research as model  $M$  and analyze and compare model  $M^\varepsilon$  with model  $M$ . Based on adaptive feedback, the dynamic game model is effectively controlled. The results show the following:

- (1) The dynamic system shows bifurcation and chaos with adjustment parameters ( $\alpha_1$  and  $\beta_1$ ) increasing, and the prices will fluctuate violently. Increase in adjustment parameters ( $\alpha_2$  and  $\beta_2$ ) will lead the system directly into wave chaos without bifurcation. The manufacturer can avoid occurrence of chaos phenomenon by reasonable price decisions.
- (2) Increasing service value  $s$  and profit distribution law  $\varepsilon$  will increase the stable region of the system. The larger distribution law will delay the system going into chaos.

- (3) In the two models, the effect of service value  $s$  on profit is different. In model  $M$ , the profits of the manufacturer and retailer increase with service value  $s$ . In model  $M^\varepsilon$ , the manufacturer's profit increases while the retailer's profit decreases.
- (4) When the system is in stable state, the manufacturer and retailer can get steady and persistent profits; once the system goes into chaos, their profits will suffer losses. Thus, keeping the relevant parameters in a certain range is profitable for the manufacturer and retailer to maintain the stability of the system.

However, this article does not take into account the behavior factors of the decision-makers, such as fairness concerns and altruistic preference. In the real market, these factors often affect the evolution and complexity of the dynamic system and profit of decision-makers. These problems will be studied in our future research.

## Appendix

### A. Proof of Proposition 1

To solve the Stackelberg equilibrium, we first consider the retailer's optimal decision. Given  $w$  and  $p_1$ , the retailer chooses  $p_2$  to maximize

$$\begin{aligned} \text{Max} \prod_r(p_2) &= (p_2 - w)D_T + (p_1 - w)D_B \\ &\quad - \eta s^2 D_T - \varphi \eta s^2 D_B \\ \text{s.t. } w + \varphi \eta s^2 &< p_1, c < w. \end{aligned} \quad (\text{A.1})$$

The solution can be solved by first-order equations ( $\partial \prod_r(p_2) / \partial p_2 = 0$ ):

$$\begin{aligned} p_2 &= \frac{\gamma_1}{m_T} p_1 + \frac{m_T - \gamma_1}{2m_T} w \\ &\quad + \frac{\theta_3 a + m_T s + m_T \eta s^2 - \gamma_1 \varphi \eta s^2}{2m_T} \end{aligned} \quad (\text{A.2})$$

$$\text{s.t. } w + \eta s^2 < p_2.$$

Submitting equation (A.2) into equation (4) and then taking the first-order partial derivatives of equation (4) with respect to  $p_1$  and  $w$  can be shown as

$$\left\{ \begin{aligned} \frac{\partial \prod_m(w, p_1)}{\partial w} &= \left( -m_B + \frac{\gamma_1}{2} + \frac{\gamma_1^2}{2m_T} \right) p_1 + \left( -m_T + 2\gamma_1 - \frac{\gamma_1^2}{m_T} \right) w + m_B s + m_T s \\ -A_1(m_T - \gamma_1) + \frac{c}{2} \left( m_T - 3\gamma_1 + \frac{2\gamma_1^2}{m_T} \right) + a\theta_2 + a\theta_3 \frac{\partial \prod_m(w, p_1)}{\partial p_1} & \\ = \frac{-2m_B m_T + m_T \gamma_1 + \gamma_1^2}{2m_T} w + \frac{2\gamma_1^2 - 2m_T \rho_1}{m_T} p_1 + \frac{A_1 m_T \gamma_1 + a m_T \theta_1 + c(m_B m_T - 2\gamma_1^2 + m_T \rho_1)}{m_T} & \end{aligned} \right. \quad (\text{A.3})$$

Taking the second-order derivatives, we can calculate the Hessian matrix as follows:

$$H^1 = \begin{bmatrix} -m_T + 2\gamma_1 - \frac{\gamma_1^2}{m_T} & -m_B + \frac{\gamma_1}{2} + \frac{\gamma_1^2}{2m_T} \\ -m_B + \frac{\gamma_1}{2} + \frac{\gamma_1^2}{2m_T} & \frac{2\gamma_1^2}{m_T} - 2\rho_1 \end{bmatrix}. \quad (\text{A.4})$$

Since  $m_B > n_1\gamma_1$ ,  $m_T > n_2\gamma_1$ , and  $\rho_1 > n_3\gamma_1$  ( $n_i > 2$ ,  $i = 1, 2, 3$ ),  $\left| \begin{matrix} -m_T + 2\gamma_1 - (\gamma_1^2/m_T) & -m_B + (m_T\gamma_1 + \gamma_1^2/2m_T) \\ -m_B + (m_T\gamma_1 + \gamma_1^2/2m_T) & (2\gamma_1^2/m_T) - 2\rho_1 \end{matrix} \right| > (3/2)\gamma_1^2 - (25/64)\gamma_1^2 > 0$ . Because the Hessian matrix  $H^1$  is negative definite. Setting  $(\partial \Pi_m(w, p_1)/\partial w) = 0$  and  $(\partial \Pi_m(w, p_1)/\partial p_1) = 0$ , the optimal solution of the manufacturer can be obtained as

$$\begin{cases} w^* = \frac{A_5A_4 - A_2A_6}{B_2^2 - B_3B_5}, \\ p_1^* = \frac{A_3A_6 - A_2A_4}{A_2^2 - A_3A_5}. \end{cases} \quad (\text{A.5})$$

Substituting equation (A.5) into (A.2), we obtain

$$p_2^* = \frac{\gamma_1(A_3A_6 - A_2A_4)}{m_T(A_2^2 - A_3A_5)} + \frac{(m_T - \gamma_1)(A_5A_4 - A_2A_6)}{2m_T(A_2^2 - A_3A_5)} + A_1. \quad (\text{A.6})$$

## B. Proof of Proposition 2

The Jacobian matrix at the equilibrium points  $e_1$  is

$$J(e_1) = \begin{bmatrix} 1 + \alpha_1 \left( \frac{A_2A_3A_6 - A_2^2A_4}{A_2^2 - A_3A_5} + A_4 \right) & 0 \\ 0 & \alpha_2 \end{bmatrix}. \quad (\text{B.1})$$

Correspondingly, let us define the characteristic polynomial of  $J(e_1)$ :  $f(\lambda) = \lambda^2 - \lambda \text{tr}(J(e_1)) + \det(J(e_1))$ . Its characteristic values satisfy

$$\begin{vmatrix} \lambda - \left( 1 + \alpha_1 \left( \frac{A_2A_3A_6 - A_2^2A_4}{A_2^2 - A_3A_5} + A_4 \right) \right) & 0 \\ 0 & \lambda - \alpha_2 \end{vmatrix} = 0. \quad (\text{B.2})$$

It can be deduced as  $\lambda_1 = \alpha_2$  and  $\lambda_2 = 1 + (A_3\alpha_1(A_2A_6 - A_4A_5)/A_2^2 - A_3A_5)$ , since  $0 < \alpha_1$ ,  $(A_3\alpha_1(A_2A_6 - A_4A_5)/A_2^2 - A_3A_5) > 0$ , and it is obvious that  $\lambda_2 > 1$ ; hence, the equilibrium point  $e_1$  is unstable.

## C. Proof of Proposition 3

The Jacobian matrix of system (25) can be expressed as follows:

$$J(e_i^\varepsilon) = \begin{pmatrix} 1 + \beta_1 \left( \frac{3}{2}p_1\gamma_1 - 2m_Tw + B_1 \right) & w + \frac{3}{2}\beta_1w\gamma_1 \\ 0 & \beta_2 \end{pmatrix}, \quad i = 1, 2. \quad (\text{C.1})$$

The Jacobian matrix at  $e_1^\varepsilon$  is  $J(e_1^\varepsilon) = \begin{pmatrix} 1 + \beta_1((-6m_TB_3\gamma_1 - 9B_1\gamma_1^3/4m_TB_2 + 9\gamma_1^3) + B_1) & 0 \\ 0 & \beta_2 \end{pmatrix}$ ; correspondingly, let us define the characteristic polynomial of  $J(e_1^\varepsilon)$  as

$$f(\lambda) = \lambda^2 - \lambda \text{tr}(J(e_1^\varepsilon)) + \det(J(e_1^\varepsilon)). \quad (\text{C.2})$$

Its characteristic values satisfy

$$\begin{vmatrix} \lambda - \left( 1 + \beta_1 \left( \frac{-6m_TB_3\gamma_1 - 9B_1\gamma_1^3}{4m_TB_2 + 9\gamma_1^3} + B_1 \right) \right) & 0 \\ 0 & \lambda - \beta_2 \end{vmatrix} = 0. \quad (\text{C.3})$$

It can be deduced that  $\lambda_1 = \beta_2$  and  $\lambda_2 = 1 + \beta_1((-6m_TB_3\gamma_1 - 9B_1\gamma_1^3/4m_TB_2 + 9\gamma_1^3) + B_1)$ , since  $0 < \beta_2 < 1$ ,  $p_1^* = (-4m_TB_3 - 6B_1\gamma_1^2/4m_TB_2 + 9\gamma_1^3) > 0$ , and  $B_1 > 0$ . So, it is obvious that  $\lambda_2 > 1$ ; hence, the equilibrium point  $e_1^\varepsilon$  is unstable and regarded as boundary equilibrium point.

## Data Availability

No data were used to support this study.

## Conflicts of Interest

The authors declare that they have no conflicts of interest.

## Acknowledgments

This research was supported in part by the National Natural Science Foundation of China (grant nos. 71872036 and 71832001), the Humanities and Social Sciences Foundation of Ministry of Education of China (grant no. 18YJA630153), and the Shanghai Social Science Foundation (grant no. 2017BGL018).

## References

- [1] M. Jehangir and M. Jehangir, *The Development of E-Commerce Capability and Its Impact on Business Performance: A Case of Malaysian Manufacturing Industries*, Universiti Teknologi PETRONAS, Seri Iskandar, Malaysia, 2012.
- [2] H. Li, "Omni-channel operations with showrooms and consumer returns," in *Proceedings of the 2018 15th International Conference on Service Systems and Service Management (ICSSSM)*, pp. 1–6, IEEE, Hang Zhou, China, July 2018.
- [3] S. Gallino and A. Moreno, "Integration of online and offline channels in retail: the impact of sharing reliable inventory availability information," *Management Science*, vol. 60, no. 6, pp. 1434–1451, 2014.

- [4] M. Radhi and G. Zhang, "Pricing policies for a dual-channel retailer with cross-channel returns," *Computers & Industrial Engineering*, vol. 119, pp. 63–75, 2018.
- [5] B. Li, P.-W. Hou, P. Chen, and Q.-H. Li, "Pricing strategy and coordination in a dual channel supply chain with a risk-averse retailer," *International Journal of Production Economics*, vol. 178, pp. 154–168, 2016.
- [6] J. Ma, W. Lou, and Y. Tian, "Bullwhip effect and complexity analysis in a multi-channel supply chain considering price game with discount sensitivity," *International Journal of Production Research*, vol. 57, no. 17, pp. 5432–5452, 2019.
- [7] Y. Liu and D. Zhou, "Is it always beneficial to implement BOPS? A comparative research with traditional dual channel," *Operations Research and Management Science*, vol. 2, p. 23, 2018.
- [8] Y. Lin, Y. Wang, and C. Yu, "Investigating the drivers of the innovation in channel integration and supply chain performance: a strategy orientated perspective," *International Journal of Production Economics*, vol. 127, no. 2, pp. 320–332, 2010.
- [9] L.-B. Oh, H.-H. Teo, and V. Sambamurthy, "The effects of retail channel integration through the use of information technologies on firm performance," *Journal of Operations Management*, vol. 30, no. 5, pp. 368–381, 2012.
- [10] W. Piotrowicz and R. Cuthbertson, "Introduction to the special issue information technology in retail: toward omnichannel retailing," *International Journal of Electronic Commerce*, vol. 18, no. 4, pp. 5–16, 2014.
- [11] X. Chen, Y. Liu, and Z. Wan, "Optimal decision making for online and offline retailers under BOPS mode," *The ANZIAM Journal*, vol. 58, no. 2, pp. 187–208, 2016.
- [12] S. Du, L. Wang, and L. Hu, "Omnichannel management with consumer disappointment aversion," *International Journal of Production Economics*, vol. 215, pp. 84–101, 2019.
- [13] F. Gao and X. Su, "Omnichannel retail operations with buy-online-and-pick-up-in-store," *Management Science*, vol. 63, no. 8, pp. 2478–2492, 2017.
- [14] Y. Kusuda, "Buy-online-and-pick-up-in-store in omnichannel retailing," 2019, <https://arxiv.org/abs/1909.00822>.
- [15] Y. Li, H. Liu, E. T. K. Lim, J. M. Goh, F. Yang, and M. K. O. Lee, "Customer's reaction to cross-channel integration in omnichannel retailing: the mediating roles of retailer uncertainty, identity attractiveness, and switching costs," *Decision Support Systems*, vol. 109, pp. 50–60, 2018.
- [16] M. Jin, G. Li, and T. C. E. Cheng, "Buy online and pick up in-store: design of the service area," *European Journal of Operational Research*, vol. 268, no. 2, pp. 613–623, 2018.
- [17] A. Dumrongsir, M. Fan, A. Jain, and K. Moinszadeh, "A supply chain model with direct and retail channels," *European Journal of Operational Research*, vol. 187, no. 3, pp. 691–718, 2008.
- [18] K. Du, "The impact of multi-channel and multi-product strategies on firms' risk-return performance," *Decision Support Systems*, vol. 109, pp. 27–38, 2018.
- [19] Y.-W. Zhou, J. Guo, and W. Zhou, "Pricing/service strategies for a dual-channel supply chain with free riding and service-cost sharing," *International Journal of Production Economics*, vol. 196, pp. 198–210, 2018.
- [20] Z. Pei and R. Yan, "Do channel members value supportive retail services? Why?" *Journal of Business Research*, vol. 68, no. 6, pp. 1350–1358, 2015.
- [21] Q.-H. Li and B. Li, "Dual-channel supply chain equilibrium problems regarding retail services and fairness concerns," *Applied Mathematical Modelling*, vol. 40, no. 15–16, pp. 7349–7367, 2016.
- [22] S. K. Jena and S. P. Sarmah, "Price and service co-opetition under uncertain demand and condition of used items in a remanufacturing system," *International Journal of Production Economics*, vol. 173, pp. 1–21, 2016.
- [23] F. Zhang and C. Wang, "Dynamic pricing strategy and coordination in a dual-channel supply chain considering service value," *Applied Mathematical Modelling*, vol. 54, pp. 722–742, 2018.
- [24] S. J. Sadjadi, H. Asadi, R. Sadeghian et al., "Retailer Stackelberg game in a supply chain with pricing and service decisions and simple price discount contract," *PLoS One*, vol. 13, no. 4, Article ID e0195109, 2018.
- [25] M. Protopappa-Sieke, M. A. Sieke, and U. W. Thonemann, "Optimal two-period inventory allocation under multiple service level contracts," *European Journal of Operational Research*, vol. 252, no. 1, pp. 145–155, 2016.
- [26] B. Dan, S. Zhang, and M. Zhou, "Strategies for warranty service in a dual-channel supply chain with value-added service competition," *International Journal of Production Research*, vol. 56, no. 17, pp. 5677–5699, 2018.
- [27] Q. Li, X. Chen, and Y. Huang, "The stability and complexity analysis of a low-carbon supply chain considering fairness concern behavior and sales service," *International Journal of Environmental Research and Public Health*, vol. 16, no. 15, p. 2711, 2019.
- [28] Q. Li, X. Chen, Y. Huang, H. Gui, and S. Liu, "The impacts of green innovation input and channel service in a dual-channel value chain," *International Journal of Environmental Research and Public Health*, vol. 16, no. 22, p. 4566, 2019.
- [29] Q. Li, Y. Zhuang, and Y. Huang, "The complexity analysis in dual-channel supply chain based on fairness concern and different business objectives," *Complexity*, vol. 2018, Article ID 4752765, 13 pages, 2018.
- [30] Z. Guo and J. Ma, "Dynamics and implications on a cooperative advertising model in the supply chain," *Communications in Nonlinear Science and Numerical Simulation*, vol. 64, no. 3, pp. 198–212, 2018.
- [31] J. Ma and L. Xie, "The comparison and complex analysis on dual-channel supply chain under different channel power structures and uncertain demand," *Nonlinear Dynamics*, vol. 83, no. 3, pp. 1379–1393, 2016.
- [32] Y. Huang, Q. Li, and Y. Zhang, "The complexity analysis for price game model of risk-averse supply chain considering fairness concern," *Complexity*, vol. 2018, Article ID 9216193, 15 pages, 2018.
- [33] Q. Li, M. Shi, Q. Deng, and Y. Huang, "The complexity entropy analysis of a supply chain system considering recovery rate and channel service," *Entropy*, vol. 21, no. 7, p. 659, 2019.
- [34] J. Ma and L. Xie, "The stability analysis of the dynamic pricing strategy for bundling goods: a comparison between simultaneous and sequential pricing mechanism," *Nonlinear Dynamics*, vol. 95, no. 2, pp. 1147–1164, 2019.
- [35] Y. C. Chen, S.-C. Fang, and U.-P. Wen, "Pricing policies for substitutable products in a supply chain with Internet and traditional channels," *European Journal of Operational Research*, vol. 224, no. 3, pp. 542–551, 2013.
- [36] X. Liu and D. Xiao, "Complex dynamic behaviors of a discrete-time predator-prey system," *Chaos, Solitons & Fractals*, vol. 32, no. 1, pp. 80–94, 2007.
- [37] J. Ma, H. Ren, M. Yu, and M. Zhu, "Research on the complexity and chaos control about a closed-loop supply chain with dual-channel recycling and uncertain consumer perception," *Complexity*, vol. 2018, Article ID 9853635, 13 pages, 2018.

## Research Article

# The Impacts of Fairness Concern and Different Business Objectives on the Complexity of Dual-Channel Value Chains

Qiuxiang Li <sup>1</sup>, Yuhao Zhang <sup>2,3</sup> and Yimin Huang <sup>4</sup>

<sup>1</sup>Institute of Management Science and Engineering, Henan University, Kaifeng, China

<sup>2</sup>School of Information Management and Engineering, Shanghai University of Finance and Economics, Shanghai, China

<sup>3</sup>School of Business, Henan University, Kaifeng 475004, China

<sup>4</sup>School of Management & Economics, North China University of Water Resources and Electric Power, Zhengzhou 450046, China

Correspondence should be addressed to Yuhao Zhang; [zyhydcg@163.com](mailto:zyhydcg@163.com) and Yimin Huang; [huang800526@163.com](mailto:huang800526@163.com)

Received 18 December 2019; Accepted 4 February 2020; Published 18 March 2020

Guest Editor: Sundarapandian Vaidyanathan

Copyright © 2020 Qiuxiang Li et al. This is an open access article distributed under the Creative Commons Attribution License, which permits unrestricted use, distribution, and reproduction in any medium, provided the original work is properly cited.

This paper considers a Stackelberg game model in a dual-channel supply chain, which is composed of a manufacturer and a retailer. The manufacturer and retailer consider fairness concern in the market competition, and the manufacturer takes market share and profit as his/her business objectives. The entropy complexity and dynamic characteristic of the dual-channel system are analyzed through mathematical analysis and numerical simulation, such as local stability, bifurcation, entropy, and chaos. The results show that, with the increase of price adjustment speed, the dual-channel supply chain is more complex and falls into a chaotic state in which system entropy increases; the stability of the dual-channel supply chain will be robust with the increase of weight of market share and weaken with the increase of the fairness concern level of the manufacturer and retailer. The high level of fairness concern of the manufacturer and retailer is always disadvantageous to the leading manufacturer but not always bad for the follower retailer. The performance of the dual-channel supply chain is improved with a high level of the manufacturer's fairness concern and reduced with a high level of the retailer's fairness concern. We also find the retailer will gain more profits in the chaotic state than the stable state in the Stackelberg game model. The variable feedback control method is applied to control the chaos of the dual-channel supply chain, and choosing appropriate control parameters can make the dual-channel supply chain system return to the stable state from the chaotic state, or delay the system to enter the bifurcation state. The research results can provide a guideline for enterprise decision-making.

## 1. Introduction

Nowadays, with the development of the e-commerce in China, many manufacturers or retailers establish online direct channels which make market competition become more and more tough and complex for participators. Therefore, choosing the proper sales strategies is vital to achieve business objectives for the players.

Firms are mainly concerned with different business objectives, such as maximizing revenues, market shares, sales, or even customer satisfaction [1, 2]. The previous literature assumed the decision-making only caring about profit maximization was an oversimplification view. In practice, a number of decision-makers not only concern on profit but also pay attention to extending the whole market

share as can as possible, especially in the oligarchic competitive market.

Business objectives, including profitability, market share, and revenues, have been discussed by many scholars. Tadic et al. [3] studied the effectiveness of business objectives and key performance indicators (KPIs) of the identified business objectives for different types of enterprises. Lohrmann and Reichert [4] developed and shortly evaluated a refined business objective modeling approach. Doyle [5] studied business objectives and explored the approach to measure performance. Keil et al. [6] introduced the impact of business objectives on the pricing behavior.

In addition, some researchers have concentrated on studying profitability and market share. Bell et al. [7] justified that the market share equals marketing efforts divided



by the total marketing effort under some assumptions. Szymanski et al. [8] pointed out that market share has a positive effect on business profitability by performing a meta-analysis on 276 market share-profitability findings. Jansen et al. [9] considered a two-stage market share delegation game with two competing firms and believed that if the firm owners choose to hire a manager, then the remuneration of the manager is weighted based on profits and sales or market share. The market share also has been studied extensively in the context of customer satisfaction and relative performance, respectively [10, 11]. Bischi and Kopel [12] established a bridge between gradient dynamics and market share and introduced a dynamic market share model where agents were bounded rational. Li and Ma [13] considered a dual-channel game model with bounded rationality and assumed retailers have different business objectives, and the dynamic behaviors of the system are investigated by numerical simulation. As far as we are concerned, there is no sufficient literature that explored the market share in dynamic scenarios in the dual-channel supply chain.

The researches in recent years focus on the behavior of the decision-maker in market competition. Fairness concern is widely studied by many scholars about the influence on the price decision-making and channel coordination in the supply chain. The fairness is modeled as inequity aversion such that the retailer is willing to give up some monetary payoff to move in the direction of more equitable outcomes. Cui et al. [14] showed that when fairness is concerned by the supply chain members, the manufacturer tends to make simple wholesale price contract to coordinate the supply chain rather than the elaborate one. Du et al. [15] studied how the retailer's fairness concern behaviors influence the coordination of the supply chain. Pavlov and Katok [16] analyzed the fairness concerns with the context of incomplete information and showed fairness would lower the efficiency of the supply chain. Zhang and Ma [17] considered two different pricing policies in a dual-channel supply chain with a fair caring retailer and found that the excessive fairness concern is not always benefit to the retailer. Chen et al. [18] modeled a Stackelberg game model to study the horizontal fairness concern influence on the backup supplier, and Qin [19] showed the fairness concerns of the supplier and retailer cannot change the coordination status of the supply chain in his paper. Tang et al. [20] established two pricing models to study the retailer's fairness concern in a closed-loop supply chain; the result showed that the system profit in a decentralized decision-making situation is less than that in a centralized decision-making situation. Ma et al. [21] investigated closed-loop supply chains under both the centralized and decentralized closed-loop supply chains and furnished the optimal marketing effort, collection rate, and pricing decisions for the supply chain members. Lin and Qin [22] compared the pricing strategies and profits in a two-level supply chain based on absolute fairness concern and relative fairness concern of the retailer. Li et al. [23] studied the impact of the manufacturer's fairness concern on cooperative advertising and analyzed equilibrium problems with retailer services as well as fairness concern in the dual-channel supply chain. Q. H. Li and B. Li [24] developed a game model assuming the private fairness concern is fuzzy and obtained the estimation model by fuzzy theory. Yang and Sun [25] considered the effect

of fairness concern in a closed-loop supply chain under two situations and found the result that a fair caring manufacturer or retailer would get more supply chain profits. Qin et al. [26] studied the dynamic evolution of fair preference under the demand of exponential function and pointed out the retailer utility and supply chain utility are increasing with fairness in exponential demand. Sharma et al. [27] developed a behavioral model of fairness in a two-echelon supply chain and found that the supply chain under the channel member's fairness concerns can be coordinated through option contract under certain conditions on the pricing parameters. Zheng et al. [28] investigated the optimal decisions and profits of closed-loop supply chains giving the retailer's distributional fairness concerns and focused on how to allocate maximum profit in a centralized setting. Zhang et al. [29] developed a supply chain system which includes one manufacturer and one retailer and studied how consumer environmental awareness and retailer's fairness concerns affected environmental quality, wholesale price, and retail price of the green product.

According to the research of behavior tendency, people pay attention to the fairness of income distribution quarterly in real life [30]. When the retailers such as Jing Dong, Tmall, and Uniqlo cooperate with their manufacturers, they are very concerned about the fairness of profits. However, few papers discussed the effect of fairness concern and different business objectives simultaneously on the dual-channel supply chain as well as analyzed the dynamic behavior of the complex system.

Complexity generates unpredictability in supply chain behavior, affects customer satisfaction, and increases cost. Relevant literature research attempted to use the optimizing strategy and entropy to enhance the supply chain performance in the system. Martínez-Olvera [31] proposed an entropy-based formulation for comparing different information sharing approaches in a supply chain environment and validated the usefulness of the proposed methodology. Mavi et al. [32] analyzed the problem of supplier selection in the context of supply chain risk management using Shannon entropy for weighing criteria. Raj and Lakshminarayanan [33] aimed to improve supply chain performance through entropy calculations. Qu and Hao [34] established the entropy model of the fractal supply chain network organization structure and showed that the fractal structure had prominent effect of dropping entropy. Meng-Gang et al. [35] built an entropy information diffusion theory model for agricultural flood and drought risk assessment. Zuo and Kajikawa [36] proposed a quantitative metric of entropy to measure the complexity and robustness of supply networks. In order to cope with complex combinatorial problems, Wang et al. [37] developed a cross-entropy algorithm for the first time in closed-loop supply chain design and planning. Kriheli and Levner [38] analyzed the complexity between the supply chain components under uncertainty using the information entropy. Levner and Ptuskin [39] presented the entropy-based optimization model for reducing the supply chain model size and assessing the economic loss. Some scholars analyzed the complexity of supply chain-based entropy theory [40, 41]. Lou et al. [42] analyzed the bullwhip effect in the supply chain with the sales game and consumer returns via the theory of entropy and complexity.



In this paper, a Stackelberg game model is established based on the manufacturer and retailer considering fairness concern and different business objectives. The features of the system are studied via nonlinear theory and entropy theory and investigated by numerical simulations, such as the stable domain, bifurcation, Lyapunov exponent, and entropy. Three-dimensional triangular meshes are carried out to describe the fluctuation of profits and average profits of the system.

This paper is organized as follows: Model assumptions and construction are presented in Section 2. Section 3 mainly analyzes the Stackelberg game model. The dynamic characteristics of the Stackelberg game model are presented in Section 4. Chaos control for the Stackelberg game model is made in Section 5. Section 6 presents the conclusion.

## 2. Model Assumptions and Construction

This paper considers a manufacturer and a retailer in a two-echelon supply chain; the manufacturer produces a single product and distributes the product through the online direct channel which is built by himself/herself and a traditional retailer channel in which the traditional retailer sells the product via his/her own traditional channel. It means customers not only can purchase the product in the traditional channel but also can buy in the online direct channel.

*2.1. Model Assumptions.* In order to make this study more realistic, we make the following assumptions:

- (1) The manufacturer and the retailer sell the same products from two different channels on the basis of price competition, and the marginal cost of the product is  $c$ .
- (2) The manufacturer and the retailer can only obtain part of market information and have limited rationality in decision-making [43].
- (3) Both manufacturer and the retailer consider fairness concern in the market competition [25].
- (4) The retailer only considers the objective of profit maximization, while the manufacturer not only considers the goal of profit maximization but also considers the market share goal under the price strategy [13].

*2.2. Model Construction.* Based on the previous assumptions and related research [13], the market demands of the manufacturer and the retailer are shown as follows:

$$\begin{cases} D_r = \alpha\theta - b_1 p_r + k p_m, \\ D_m = \alpha(1 - \theta) - b_2 p_m + k p_r, \end{cases} \quad (1)$$

where  $\alpha$  denotes the potential market size,  $\theta$  ( $0 < \theta < 1$ ) means the degree of customer loyalty to the traditional channel, and  $\alpha\theta$  represents the number of customers preferring the traditional retailer channel, while  $\alpha(1 - \theta)$  represents the number of customers preferring the online direct channel.  $b_1$  and  $b_2$  are the price elasticity coefficients of customer demands in different channels. The cross-price sensitivity of the manufacturer and retailer is the same and represented by  $k$ ,  $b_1 > k$ ,  $b_2 > k$ .

Furthermore, the profit functions of the manufacturer and retailer can be written as follows:

$$\begin{cases} \pi_r = (p_r - w)D_r, \\ \pi_m = D_m(p_m - c) + D_r(w - c). \end{cases} \quad (2)$$

Both the manufacturer and the retailer have fairness concern behavior on the profits gained of their own in the market. According to the literature [14], the retailer's utility function can be described as follows:

$$\begin{aligned} U(w, p) &= \pi(w, p) + f_r(w, p), \\ f_r(w, p) &= -\alpha \max(\gamma\Pi(w, p) - \pi(w, p), 0) \\ &\quad - \beta \max(\pi(w, p) - \gamma\Pi(w, p), 0), \end{aligned} \quad (3)$$

where  $\Pi(w, p)$  and  $\pi(w, p)$  denote the monetary payoff of the manufacturer and retailer, respectively, and  $\alpha$  and  $\beta$  represent the sensitivity coefficient of difference in payoff between  $\gamma\Pi(w, p)$  and  $\pi(w, p)$ . The retailer's fairness feeling depends on the comparison of relative profit of the manufacturer and retailer.

Du et al. [15] also give the retailer's utility function as

$$U_r = \pi_r - \lambda(\pi_m - \pi_r), \quad (4)$$

where  $\pi_m$  and  $\pi_r$  are the profits of the manufacturer and the retailer; the sensitive coefficients about profit and loss are the same and denoted by  $\lambda$ . The fair caring depends on the comparison of the absolute profit between the manufacturer and the retailer; the utility of the manufacturer and the retailer will change if there exists difference in both sides' profits and relative profits.

From the above conditions, the utility functions of the manufacturer and retailer in this paper are as follows:

$$\begin{cases} u_r = \pi_r - \lambda_1(\pi_{md} - \pi_r), \\ u_m = \mu\pi_m + (1 - \mu)L_m - \lambda_2(\pi_r - \gamma\pi_{md}), \end{cases} \quad (5)$$

where  $\lambda_1$  is the fairness concern coefficient of the retailer and  $\lambda_2$  is the fairness concern coefficient of the manufacturer ( $0 < \lambda_1 < 1$ ,  $0 < \lambda_2 < 1$ ),  $\pi_{md}$  is the manufacturer's profit which is gained from the traditional retailer channel, and  $\mu \in (0, 1)$  denotes the manufacturer's balance coefficient between profits and market share; the market share of the manufacturer is as follows:

$$L_m = \frac{D_m p_m}{D_m p_m + D_r p_r}. \quad (6)$$

Let  $e_1 = D_m p_m$  and  $e_2 = D_r p_r$ , then taking the partial derivative of  $L_m$  with respect to  $e_1$  yields

$$\frac{\partial L_m}{\partial e_1} = \frac{e_2}{(e_1 + e_2)^2} > 0. \quad (7)$$

Then, the change trends of sales revenue are the same as the market share; this paper uses sales revenue to replace the proportion of market share [8, 14].

## 3. The Stackelberg Model

In the market competition, the manufacturer is more powerful than the retailer in the dual-channel supply chain. Therefore, we

consider that the manufacturer is a game leader, the retailer is the follower, and the game equilibrium is called the Stackelberg equilibrium. In the game model, the manufacturer firstly makes decisions for his/her wholesale price ( $w$ ) and online direct sale price ( $p_m$ ), and then the retailer makes the price decision ( $p_r$ ) on the basis of the manufacturer's decision-making.

### 3.1. Single Period Game Model

**3.1.1. The Retailer's Decision.** The retailer's best response can be obtained via setting the wholesale price  $w$  and sale price  $p_m$  as fixed values, making the first derivative of  $u_r$  about  $p_r$  as

$$\begin{aligned} \frac{\partial u_r}{\partial p_r} &= a\theta(\lambda_1 + 1) + b_1(-c\lambda_1 - 2(\lambda_1 + 1)p_r + 2\lambda_1 w + w) \\ &\quad + k(\lambda_1 + 1)p_m. \end{aligned} \quad (8)$$

The second derivative of the retailer's utility function is  $(\partial^2 u_r / \partial p_r^2) = -2b_1(\lambda_1 + 1) < 0$ , and the retailer can get global optimal solutions. Letting  $(\partial u_r / \partial p_r) = 0$ , the retailer's best reply function is obtained as follows:

$$p_r^*(w, p_m) = \frac{a\theta(\lambda_1 + 1) - b_1 c \lambda_1 + (2b_1 \lambda_1 + b_1)w + k(\lambda_1 + 1)p_m}{2b_1(\lambda_1 + 1)}. \quad (9)$$

Then, we calculate the first-order partial derivatives of  $p_r^*(w, p_m)$  with respect to  $w$  and  $p_m$ , which can examine the influence of  $w$  and  $p_m$  on the retailer's best price strategy:

$$\begin{aligned} \frac{\partial p_r^*}{\partial w} &= \frac{1 + 2\lambda_1}{2 + 2\lambda_1} > \frac{1}{2}, \\ 0 < \frac{\partial p_r^*}{\partial p_m} &= \frac{k}{2b_1} < \frac{1}{2}. \end{aligned} \quad (10)$$

From above inequality equations, we know that the retailer's optimal price increases with the increasing  $w$  and  $p_m$ , respectively. Therefore, the price strategy of the retailer will be controlled by the manufacturer's price decision-

making. If  $w$  increases by one unit,  $p_r^*$  would increase more than 0.5 units; when  $p_m$  increases by one unit,  $p_r^*$  would increase less than 0.5 units.

Substituting formula (9) into  $u_r$  of formula (5), we obtain the retailer's optimal utility  $u_r^*$  which is represented by  $w$  and  $p_m$ .

**3.1.2. The Manufacturer's Decision.** Substituting formula (9) into  $u_m$  of formula (4), we obtain the manufacturer's optimal utility  $u_m^*(w, p_m)$  which is a function with respect to  $w$  and  $p_m$ . We take the first-order partial derivatives of  $u_m^*(w, p_m)$  with respect to  $w$  and  $p_m$ , respectively, and obtain the following equations:

$$\begin{aligned} \frac{\partial u_m^*}{\partial w} &= \frac{1}{2(1 + \lambda_1)^2} [a\theta(1 + \lambda_1)^2(\lambda_2 + \gamma\lambda_2 + \mu)] + A_0 + A_1, \\ \frac{\partial u_m^*}{\partial p_m} &= -\frac{1}{2(1 + \lambda_1)^2} \{k^2(1 + \lambda_1)[p_m(-2 + \lambda_2) + c\mu]\} \\ &\quad + A_2 + A_3 + A_4, \end{aligned} \quad (11)$$

where

$$\begin{aligned} A_0 &= b_1\{w(2\lambda_1 + 1)[2\gamma\lambda_2(\lambda_1 + 1) + \lambda_2 + 2\mu(\lambda_1 + 1)] \\ &\quad - c[\gamma\lambda_2(3\lambda_1^2 + 4\lambda_1 + 1) - \lambda_1^2(\lambda_2 - 3\mu) + 4\lambda_1\mu + \mu]\}, \\ A_1 &= k(\lambda_1 + 1)\{p_m[\lambda_1(\gamma\lambda_2 + \lambda_2 + \mu + 2) + \gamma\lambda_2 + \lambda_2 + \mu + 1] \\ &\quad - c\mu(2\lambda_1 + 1)\}, \\ A_2 &= a(1 + \lambda_1)[2b_1(\theta - 1) + k\theta(\lambda_2 - 1)], \\ A_3 &= -2b_2(1 + \lambda_1)(2p_m - c\mu) - ck[\gamma\lambda_2 + \mu \\ &\quad + \lambda_1(1 + \gamma\lambda_2 + \mu)], \\ A_4 &= w[\lambda_1(\gamma\lambda_2 + \lambda_2 + \mu + 2) + \gamma\lambda_2 + \lambda_2 + \mu + 1]. \end{aligned} \quad (12)$$

When the second-order derivative of the manufacturer's utility function is concave, the manufacturer can get global optimal solutions. The Hessian matrix of  $u_m$  is as follows:

$$H(u_m) = \begin{bmatrix} \frac{b_1(2\lambda_1 + 1)([2\gamma(\lambda_1 + 1) + 1] + 2(\lambda_1 + 1)\mu)}{2(\lambda_1 + 1)^2} & \frac{k[\lambda_1(\gamma\lambda_2 + \lambda_2 + \mu + 2) + \gamma\lambda_2 + \lambda_2 + \mu + 1]}{2(\lambda_1 + 1)} \\ \frac{k[\lambda_1(\gamma\lambda_2 + \lambda_2 + \mu + 2) + \gamma\lambda_2 + \lambda_2 + \mu + 1]}{2(\lambda_1 + 1)} & \frac{4b_1b_2 + k^2(\lambda_2 - 2)}{2b_1} \end{bmatrix}. \quad (13)$$

Obviously, the first-order principal minor of the Hessian matrix  $H(u_m)$  is

$$H(u_m) = \frac{b_1(2\lambda_1 + 1)\{\lambda_2[2\gamma(\lambda_1 + 1) + 1] + 2\mu(\lambda_1 + 1)\}}{2(\lambda_1 + 1)^2} < 0, \quad (14)$$

where  $b_1 = ((k^2\{(\lambda_1[(\gamma\lambda_2 + \lambda_2 + \mu + 2) + \gamma\lambda_2 + \lambda_2 + \mu + 1]\}^2 + A_5)/(4b_2(2\lambda_1 + 1)A_6))$ , in which

$$\begin{aligned} A_5 &= (2\lambda_1 + 1)(2 - \lambda_2)[2\gamma\lambda_2(\lambda_1 + 1) + 1] + 2\mu\lambda_2(\lambda_1 + 1), \\ A_6 &= \lambda_2 + 2(\mu + \gamma\lambda_2)(\lambda_1 + 1). \end{aligned} \quad (15)$$

Then, the second-order principal minor is bigger than zero, and  $H(u_m)$  is negative definite which indicates the manufacturer can reach the maximum value when making decisions. By solving  $(\partial u_m^*/\partial w) = 0$  and  $(\partial u_m^*/\partial p_m) = 0$ , the manufacturer's best reply function  $(w^*, p_m^*)$  can be obtained.

Because of the complexity of the model, the expressions of  $w^*$ ,  $p_m^*$ , and  $p_r^*$  are very complex, and we cannot see the interaction between variables and parameters. In the next section, in order to analyze and study the stability of the dynamic game model by numerical simulation, we assign parameters according to the actual operation of the market.

### 3.2. Dynamic Stackelberg Game Model

**3.2.1. Model Construction.** In this section, a dynamic Stackelberg game model is proposed. As a matter of fact, firms in the real market usually obtain limited information due to the objective condition restriction, and it indicates that decision-makers cannot get the whole market information and the system is not always in the Nash equilibrium state. In order to achieve maximum profit in every competition period, the manufacturer adopts bounded

rational expectation and the myopic adjustment mechanism to adjust price decisions dynamically based on partial estimation of the marginal utility of the current period; if the marginal utility in the current period is positive, the manufacturer will raise his/her price in the next period; otherwise, the manufacturer will reduce his/her price in the next period.

The dynamic model can be described as follows:

$$\begin{cases} w(t+1) = w(t) + \alpha_1 w(t) \frac{\partial u_m^*(t)}{\partial w(t)}, \\ p_m(t+1) = p_m(t) + \alpha_2 p_m(t) \frac{\partial u_m^*(t)}{\partial p_m(t)}, \end{cases} \quad (16)$$

where  $\alpha_i > 0$  ( $i = 1, 2$ ) represent the price adjustment speed of the manufacturer according to his/her marginal profits, which reflect the manufacturer's learning behavior and active managerial behavior.

Then, we can establish the discrete dynamic game model of the dual-channel supply chain considering fairness concern and different business objectives as follows:

$$\begin{cases} w(t+1) = w(t) + \alpha_1 w(t) \left\{ \frac{1}{2(1+\lambda_1)^2} [a\theta(1+\lambda_1)^2(\lambda_2 + \gamma\lambda_2 + \mu)] + A_0 + A_1 \right\}, \\ p_m(t+1) = p_m(t) + \alpha_2 p_m(t) \left\{ \frac{1}{2(1+\lambda_1)} [k^2(1+\lambda_1)[p_m(-2+\lambda_2) + c\mu]] + A_2 + A_3 + A_4 \right\}, \\ p_r^*(t) = \frac{a\theta\lambda_1 + a\theta - b_1c\lambda_1 + 2b_1\lambda_1w(t) + b_1w(t) + k\lambda_1p_m(t) + kp_m(t)}{2b_1(\lambda_1 + 1)}. \end{cases} \quad (17)$$

The manufacturer's price strategy is described by the dynamic system (17), and the retailer's price is directly related to  $w(t)$  and  $p_m(t)$ . The parameters  $\alpha_1$  and  $\alpha_2$  have a great impact on  $w(t)$  and  $p_m(t)$ .

**3.2.2. Model Analysis.** Firstly, making  $w(t) = w(t+1)$  and  $p_m(t) = p_m(t+1)$ , we can get four equilibrium solutions of the dynamic system (17):

$$E_1 = (0, 0),$$

$$E_2 = \left( 0, \frac{a(\lambda_1 + 1)[2b_1(\theta - 1) + \theta k(\lambda_2 - 1)] + A_7}{(\lambda_1 + 1)[k^2(2 - \lambda_1) - 4b_1b_2]} \right),$$

$$E_3 = \left( \frac{A_8 + A_9}{b_1(2\lambda_1 + 1)\{\lambda_2[2\gamma(\lambda_1 + 1) + 1] + 2\mu(\lambda_1 + 1)\}}, 0 \right),$$

$$E_4 = (w^*, p_m^*),$$

(18)

where

$$A_7 = c\{b_1[k(\gamma\lambda_1\lambda_2 + \gamma\lambda_2 + \lambda_1\mu + \lambda_1 + \mu) - 2b_2(\lambda_1 + 1)\mu] + \mu k^2(\lambda_1 + 1)\},$$

$$A_8 = (\lambda_1 + 1)[a\theta(\lambda_1 + 1)(\gamma\lambda_2 + \lambda_2 + \mu) - ck\mu(2\lambda_1 + 1)],$$

$$A_9 = b_1c(\gamma(3\lambda_1^2 + 4\lambda_1 + 1)\lambda_2 + \lambda_1^2[(3\mu - \lambda_2) + 4\lambda_1\mu + \mu]). \quad (19)$$

Then, we can get the retailer's equilibrium prices as  $p_r^{E_1}$ ,  $p_r^{E_2}$ ,  $p_r^{E_3}$ , and  $p_r^{E_4} = p_r^*$ .

Obviously,  $E_1$ ,  $E_2$ , and  $E_3$  are boundary unstable equilibrium solutions because they are partly or entirely zero, and the decision variables obviously are not allowed to be zero in economics for decision-makers. In contrast,  $E_4$  is the unique Stackelberg equilibrium solution. It is meaningless to study the unstable equilibrium solution, so we only analyze the characteristic of the Nash equilibrium solution in the following section.

3.2.3. *Stability of the Nash Equilibrium Solution.* The Jacobian matrix of the dynamic system (17) is given as

$$J = \begin{bmatrix} 1 + \alpha_1 f_1 & \frac{\alpha_1 w \{k[\lambda_1(\gamma\lambda_2 + \lambda_2 + \mu + 2) + \gamma\lambda_2 + \lambda_2 + \mu + 1]\}}{2(\lambda_1 + 1)} \\ \frac{\alpha_2 w \{k[\lambda_1(\gamma\lambda_2 + \lambda_2 + \mu + 2) + \gamma\lambda_2 + \lambda_2 + \mu + 1]\}}{2(\lambda_1 + 1)} & 1 + \alpha_2 f_2 \end{bmatrix}, \quad (20)$$

where

$$\begin{aligned} f_1 &= \frac{1}{2(1 + \lambda_1)^2} [a\theta(1 + \lambda_1)^2(\lambda_2 + \gamma\lambda_2 + \mu)] + A_{10} + A_1, \\ f_2 &= -\frac{1}{2(1 + \lambda_1)} \{k^2(1 + \lambda_1)[2p_m(-2 + \lambda_2) + c\mu]\} + A_2 \\ &\quad + A_{11} + A_4, \\ A_{10} &= 2b_1 w(2\lambda_1 + 1)\{2\gamma(\lambda_1 + 1) + 1\} + 2\mu(\lambda_1 + 1) \\ &\quad - cb_1[\gamma(3\lambda_1^2 + 4\lambda_1 + 1)\lambda_2 + \lambda_1^2(3\mu - \lambda_2) + 4\lambda_1\mu + \mu], \\ A_{11} &= -2b_2(1 + \lambda_1)(4p_m - c\mu) - ck[\gamma\lambda_2 + \mu \\ &\quad + \lambda_1(1 + \gamma\lambda_2 + \mu)]. \end{aligned} \quad (21)$$

The characteristic polynomial of the Jacobian matrix (20) is taken as follows:

$$F(\lambda) = \lambda^2 - B_0\lambda + B_1. \quad (22)$$

According to Jury's conditions, the necessary and sufficient condition of asymptotic stability of the system is that all the eigenvalues are inside the unit circle in the complex plane, so the stability of the dynamic system (17) should satisfy the following Jury's conditions:

$$\begin{cases} F(1) = 1 + B_0 + B_1 > 0, \\ F(-1) = 1 - B_0 + B_1 > 0, \\ F(0) = 1 - B_1 > 0, \end{cases} \quad (23)$$

where  $B_0$  and  $B_1$  are the trace and determinant of the Jacobian matrix, respectively. According to condition (23), we can give the stable region of the dynamic system (17) on the adjustment parameters  $\alpha_1$  and  $\alpha_2$ . Because the stable condition of the dynamic system (17) is too complicated, we will analyze the stable region and dynamic characteristic of the dynamic system (17) by numerical simulation in the next section.

## 4. Numerical Simulation

In this section, numerical simulations are carried out to show the influence of parameters on the dynamic characteristic of the dynamic system (17) via bifurcation diagrams, entropy diagrams, largest Lyapunov exponents (LLEs), chaotic attractors, and so on.

Here, we assign values to parameters according to the actual operation of the market in order to facilitate analysis:  $a = 100$ ,  $\theta = 0.6$ ,  $b_1 = 2$ ,  $b_2 = 1$ ,  $k = 0.5$ ,  $\gamma = 0.6$ , and  $c = 10$ .

### 4.1. Stability of the Dynamic System (17)

4.1.1. *The Influence of Parameters  $\mu$ ,  $\lambda_1$ , and  $\lambda_2$  on the Stable Region.* Figure 1 clearly presents the influence of the balance coefficient of business objectives on the system stability. When fixing  $\lambda_1 = \lambda_2 = 0.2$ , the stable region of the dynamic system (17) is the area enclosed by the red line with  $\mu = 0.9$ , the blue line with  $\mu = 0.6$ , and the green line with  $\mu = 0.4$ . It is easy to understand that market share, as one of the business objectives of the manufacturer, has significant impact on the stability of the dynamic system (17), and the stable region of the dynamic system (17) is decreasing with increasing  $\mu$ . Namely, with the increase of the weight of market share in business objectives, the stable range of the price adjustment speed ( $\alpha_1$ ,  $\alpha_2$ ) is extended, which indicates the manufacturer considering market share as part of business objectives makes the market competition more intense.

Fixing  $\mu = 0.6$  and  $\lambda_2 = 0.2$ , Figure 2(a) shows that the stable regions of system (17) are the areas enclosed by the blue line, green line, and red line when  $\lambda_1 = 0.2, 0.5$ , and  $0.9$ , respectively. Similarly, when  $\mu = 0.6$  and  $\lambda_1 = 0.2$  are fixed, Figure 2(b) shows the stable regions of the dynamic system (17) are the areas enclosed by the blue line, green line, and red line, respectively, with  $\lambda_2 = 0.2, 0.5$ , and  $0.9$ . We can see that, with the increasing level of fairness concern, the stable regions of the dynamic system (17) will decrease. The stable scope of  $\alpha_1$  is greatly influenced with increasing  $\lambda_2$  than with increasing  $\lambda_1$ , and the stable scope of  $\alpha_2$  is less affected by the change of  $\lambda_1$  and  $\lambda_2$ , which means that the influence of the manufacturer's fairness concerns on the scope of wholesale price adjustment is greater than that of the retailer's fairness concern behavior and the scope of online price adjustment is less affected by the fairness concern behavior of the manufacturer and the retailer.

4.2. *The Entropy Complexity Analysis of the Dynamic System (17) with Changing  $\alpha_2$ .* We know that entropy can measure the chaotic degree of the system, so it is not difficult to find that the entropy of the system is small when the system is in the stable state and the entropy of the system is large when the system is in the chaotic state. On the contrary, the entropy of the system shows the probability of the occurrence of some particular information; when the entropy of

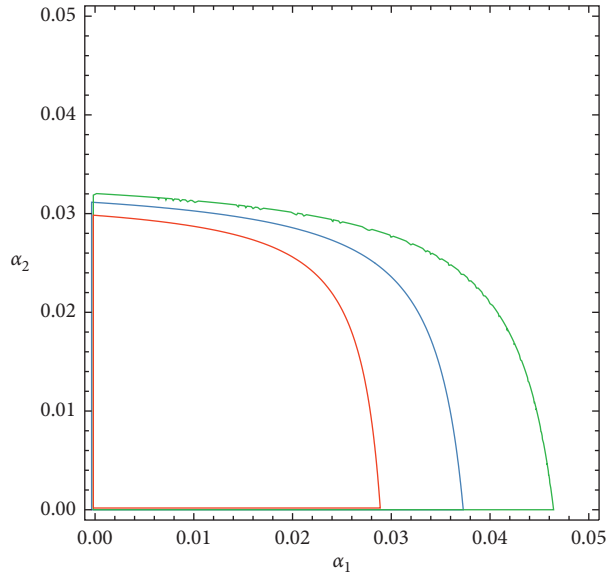


FIGURE 1: Stable regions of system (17) with different values of  $\mu$ .

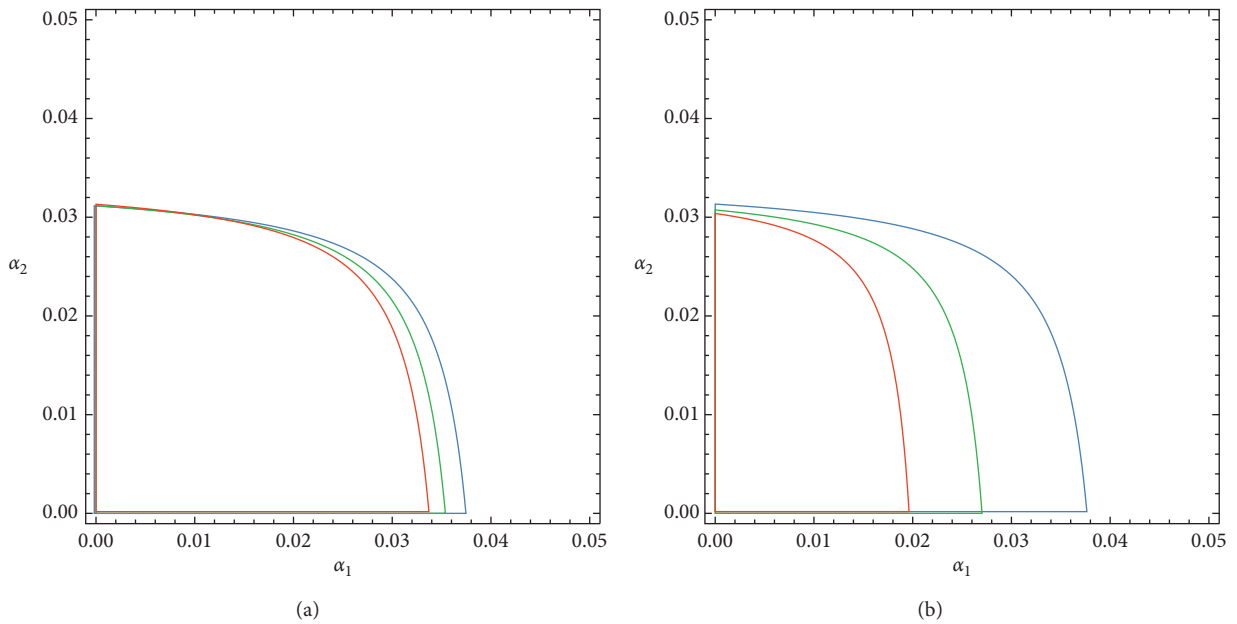


FIGURE 2: Stable regions of system (17) with different values of (a)  $\lambda_1$  and (b)  $\lambda_2$ .

the system is high, we need more information to make the system clear. In order to better study the influence of parameters on system stability, we use an entropy graph to show the change of the system's stability.

Figure 3 presents the dynamic evolution process of the dynamic system (17) with  $\alpha_1 = 0.02$ . From Figure 3(a), we can see that the dynamic system (17) is in the stable state at first, with increasing  $\alpha_2$ , and the dynamic system (17) has the first bifurcation at  $\alpha_2 = 0.028$  and then falls into chaos finally through a series of period doubling bifurcations. Figure 3(b) is the diagram of the LLE which can reflect the state of the dynamic system (17), and Figure 4 shows the entropy of the dynamic system (17) with  $\alpha_1 = 0.02$ . We can see from

Figures 3 and 4 that when the LLE is negative, the dynamic system (17) remains stable with lower entropy. When the LLE is positive, the dynamic system (17) falls into chaos with higher entropy. In other words, the larger the positive Lyapunov exponent is, the more chaotic the system is and the greater the entropy is.

So we can make a conclusion that irrational changes of price adjustment speed will lead to a large entropy to the system (17) and the manufacturers must get more market information to make a best decision and keep the dynamic system (17) in a stable state.

Figure 5 shows the bifurcation diagram and entropy of the dynamic system (17) with changing  $\alpha_2$  which is in

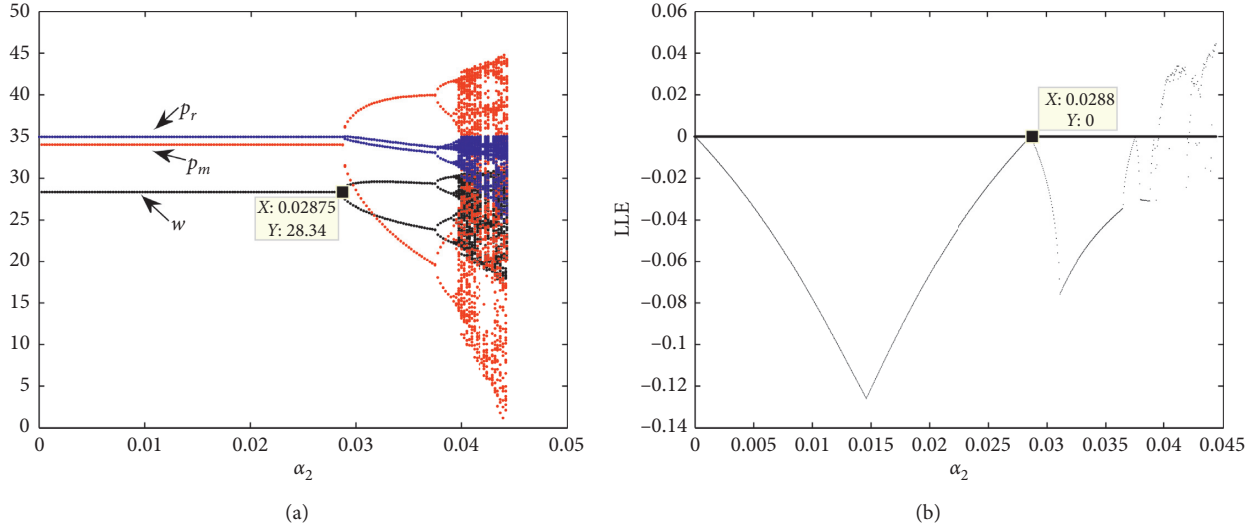


FIGURE 3: Bifurcation diagram and LLE of the system (17) with varying  $\alpha_2$  when  $\alpha_1 = 0.02$ . (a) Bifurcation diagram when  $\lambda_2 = 0.2$ . (b) LLE when  $\lambda_2 = 0.2$ .

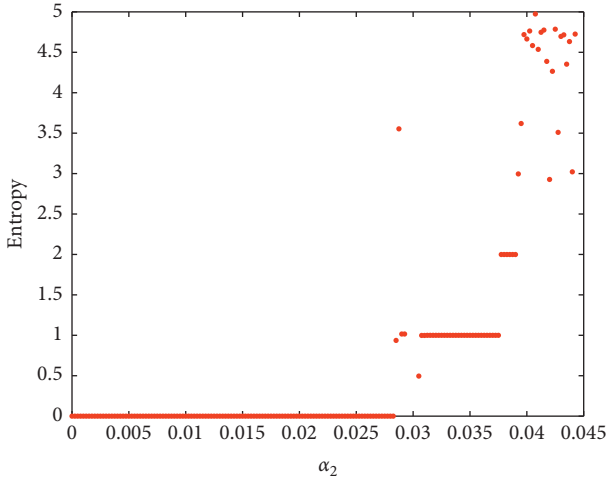


FIGURE 4: Entropy diagram of the system (17) with varying  $\alpha_2$  when  $\alpha_1 = 0.02$ .

accordance with Figure 2. When  $\lambda_2 = 0.6$ , the dynamic system (17) has first bifurcation at  $\alpha_2 = 0.0245$  and then falls into chaos through the flip bifurcation and N-S bifurcation shown in Figure 5(a), and the entropy of the dynamic system (17) is shown in Figure 5(b). When  $\lambda_2 = 0.9$ , the system (17) loses its stability at the beginning which is shown in Figure 5(c) and then falls into chaos finally through the N-S bifurcation, and its entropy is shown in Figure 5(d). We can see from Figure 5 that the system (17) remains stable with lower entropy and falls into chaos with higher entropy. In other words, the more chaotic the system (17) is, the greater the entropy is.

From this trend described above, we can draw a conclusion that a faster adjustment speed of direct price or wholesale price will pull the market into chaos through the slip bifurcation or N-S bifurcation; the higher the level of fairness concern from the manufacturer or retailer is, the

easier the market falls into chaos. Because the characteristic of the dynamic system (17) is the same as the one when  $\alpha_1$  changes, the characteristic of the dynamic system (17) with changing  $\alpha_1$  is not discussed in this paper.

The state of the system is fixed when stability stays, and the competitors in the market can make a profit in every time period via changing the price. Generally speaking, stability is beneficial for competitors to make the long-term strategies, and the market vibrates regularly in a certain period and returns to the same point in the periodic or limit cycle state; hence, the competitors can forecast the process of market and change their price strategies frequently to gain more profit. Chaos indicates that the market becomes unpredictable and irregular; it is so hard for competitors to achieve their business objectives just relying on the initial value sensitiveness in this situation. In most cases, chaos is an obstacle that the market operates orderly and efficiently.

Figure 6 shows the strange attractors of the dynamic system (17) from the four-period state to limit cycles, which are an important characteristic of the system. Figure 7(a) shows the price changes in the four-period state, and the manufacturer can forecast the tendency of direct price in the next period because the direct price is in a regular change. Figure 7(b) presents the price changes in the chaotic state, and the change of prices becomes irregular and unpredictable. Figure 8 shows the sensitiveness of system to the initial values with  $w$  and  $p_r$  being fixed and  $p_m$  change from 34.01 to 34.02. Figure 8(a) indicates the dynamic system (17) is in four-period bifurcation, and Figure 8(b) displays the dynamic system (17) is in the chaotic state, in which the black line, red line, and blue line represent the fluctuations of  $w$ ,  $p_m$ , and  $p_r$ , respectively. Although the difference of the initial value is quite small, the distance between two trajectories becomes large after several iterations. The manufacturer and retailer should pay more attention to the setting of the initial value and the price evolution when the system is in the chaotic state.



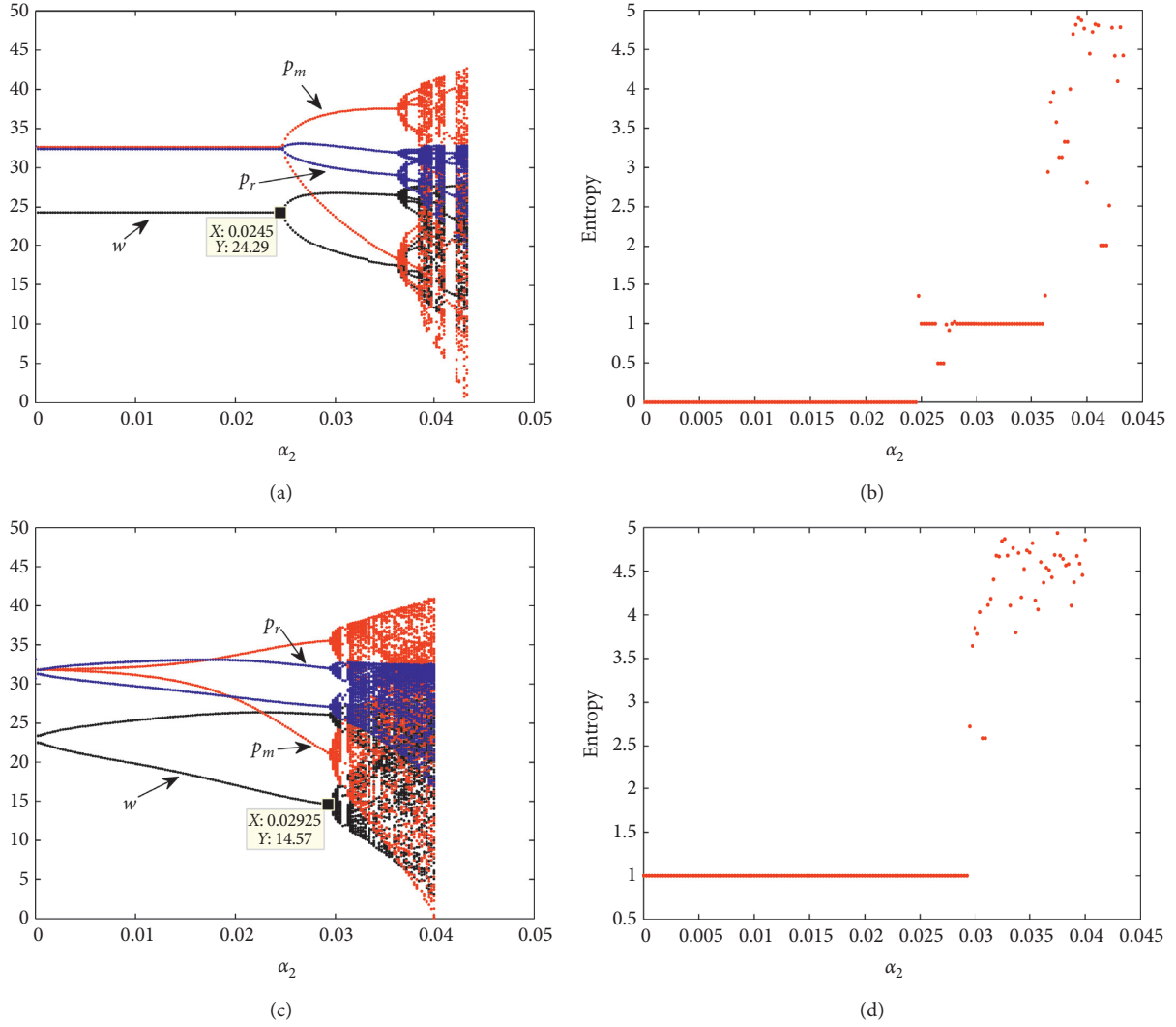


FIGURE 5: Bifurcation diagram and entropy of the dynamic system (17) with varying  $\alpha_2$  when  $\alpha_1 = 0.02$ . (a) Bifurcation diagram when  $\lambda_2 = 0.6$ . (b) Entropy diagram when  $\lambda_2 = 0.6$ . (c) Bifurcation diagram when  $\lambda_2 = 0.9$ . (d) Entropy diagram when  $\lambda_2 = 0.9$ .

**4.3. The Influence of Parameters on the Profits.** Figure 9 shows the average profits of the manufacturer and the retailer with the change of  $\alpha_1$  and  $\alpha_2$ . In the stable state, the average profits of the manufacturer and the retailer are 692.3 and 46.79, respectively; after that, the dynamic system (17) enters 2-period bifurcation and chaotic states eventually with the change of price adjustment speed, the average profit of the retailer increases with increasing  $\alpha_1$  and  $\alpha_2$ , but the manufacturer's average profit decreases sharply with increasing  $\alpha_1$  and  $\alpha_2$ . In Figure 10(a), the average profits of the manufacturer and the retailer are decreased with increasing  $\lambda_1$ . From Figure 10(b), it is seen that the average profits of the manufacturer and the retailer rise with increasing  $\lambda_2$  at the beginning, while the average profit of the retailer increases and that of manufacturer declines with increasing  $\lambda_2$ ; the performance of the dual-channel supply chain is improved with a high level of the manufacturer's fairness concern and declined with a high level of the retailer's fairness concern. We can obtain that chaos is unfavorable to the leading manufacturer and beneficial to the follower retailer, and the

high level of fairness concern of the manufacturer and retailer is always disadvantageous to the leading manufacturer but not always bad for the follower retailer.

Figure 11 shows the influence of  $\alpha_i$  and  $\lambda_i$  on the profits of the manufacturer and the retailer using the three-dimensional grid. From Figure 11(a), we obtain that when  $\alpha_1$  and  $\lambda_1$  are controlled in small values, the profit of the retailer almost remains stable; with fixed  $\lambda_1$  in a small region, the retailer's profit rises with increasing  $\alpha_1$ , but increasing  $\alpha_1$  and  $\lambda_1$  simultaneously to the larger value range, the dynamic system (17) falls into chaos and the retailer's profit changes violently and even has a great loss; chaos is a great disadvantage to achieving maximizing profit and making a long competition strategy for the retailer in the market.

Similarly, in Figure 11(b), keeping  $\lambda_2$  in small values, the manufacturer's profits increase with the increase of  $\alpha_1$  which indicates that the lower fairness concern of the manufacturer and the higher adjustment speed of wholesale price for the retailer are beneficial to the manufacturer. The lower level of fairness concern of the retailer and the

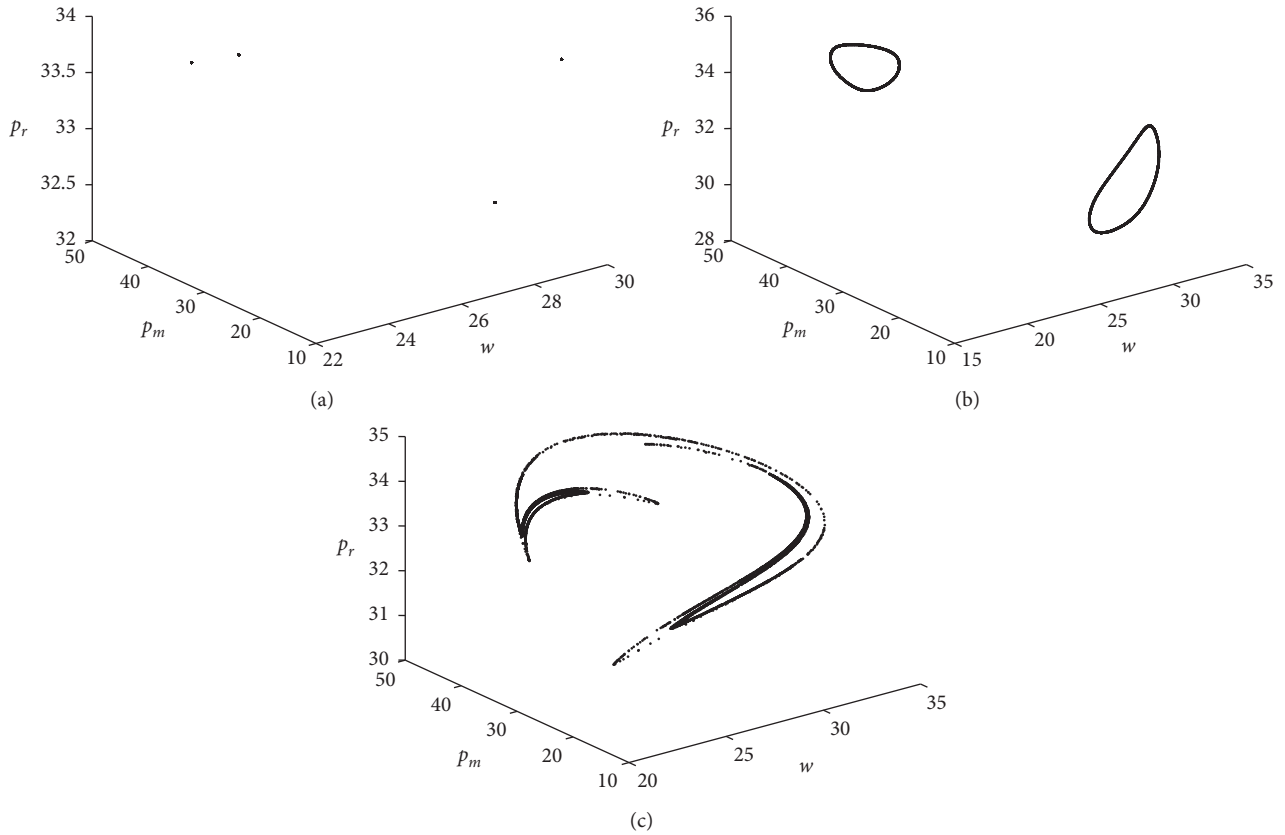


FIGURE 6: Chaos attractors of the system (17) with (a)  $\alpha_1 = 0.02, \alpha_2 = 0.038$ , (b)  $\alpha_1 = 0.03, \alpha_2 = 0.035$ , and (c)  $\alpha_1 = 0.02, \alpha_2 = 0.04$ .

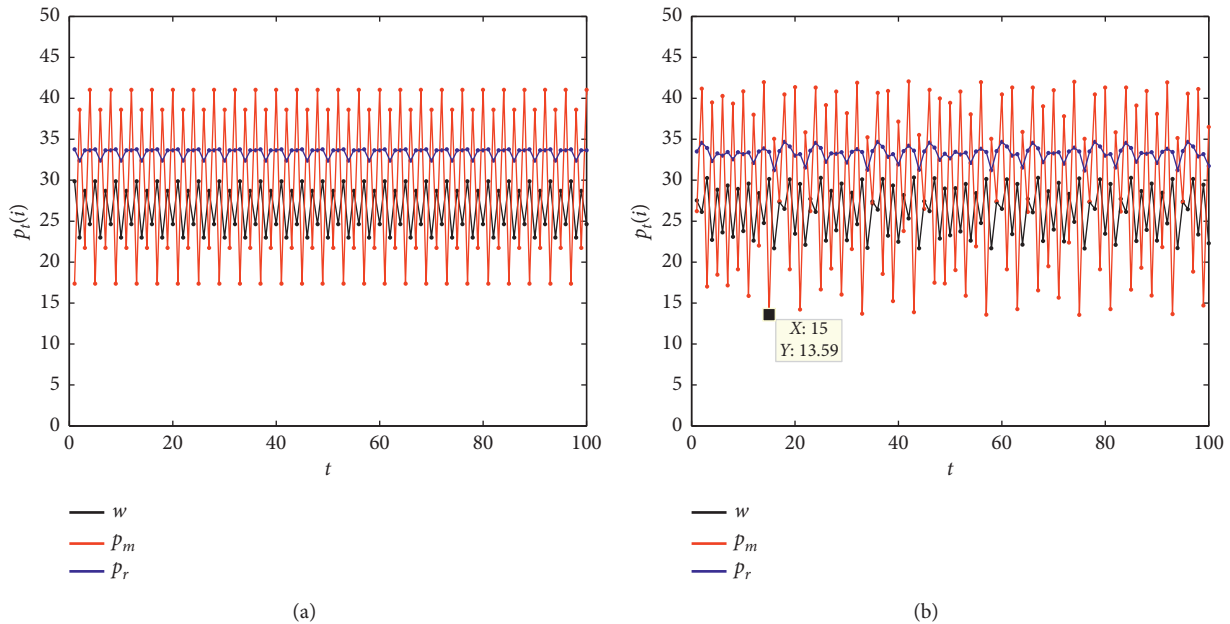


FIGURE 7: Wave plot of prices with the change of time. (a)  $\alpha_1 = 0.02, \alpha_2 = 0.038$ . (b)  $\alpha_1 = 0.02, \alpha_2 = 0.04$ .

higher adjustment speed of direct selling price for the manufacturer are beneficial to the retailer which is shown in Figure 11(c). Figure 11(d) shows the profit of the manufacturer influenced by  $\alpha_2$  and  $\lambda_2$ ; when  $\alpha_2$  stays in small values, the higher fairness concern of the

manufacturer is good for himself/herself to obtain the maximum profit. In the market competition, the competitors should pay attention to the range of parameters, and choosing proper values for parameters is indispensable for them to achieve business objectives.

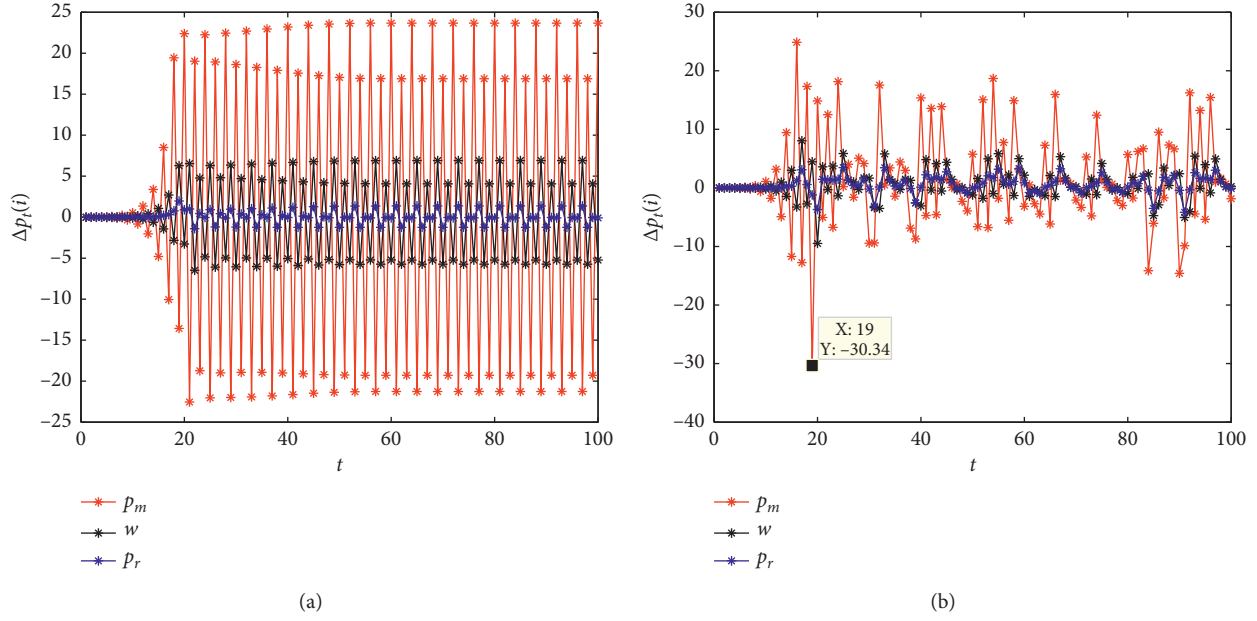


FIGURE 8: Sensitivity to initial values when  $w$ ,  $p_m$ , and  $p_r$  are 28.35, 34.01, and 34.95. (a)  $\alpha_1 = 0.02$ ,  $\alpha_2 = 0.038$ . (b)  $\alpha_1 = 0.02$ ,  $\alpha_2 = 0.04$ .

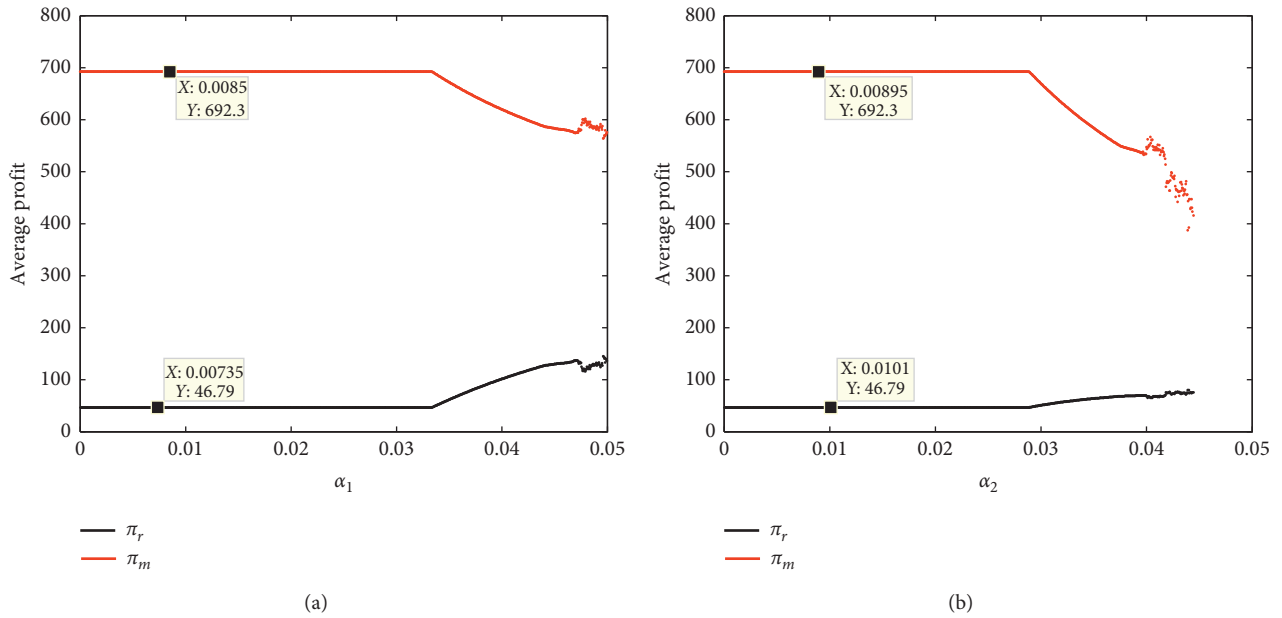


FIGURE 9: Change of average profit with respect to  $\alpha_i$  ( $i = 1, 2$ ). (a)  $\alpha_2 = 0.02$ . (b)  $\alpha_1 = 0.02$ .

## 5. Chaos Control

All the participants certainly want to achieve their own business objectives easily and adjust their price decision frequently to adapt the changes of market competition. Once the price adjustment speed is out of control, the market will go out of order and fall into chaos finally which is harmful to the stability of the supply chain. Therefore, some measures should be taken to delay or eliminate the occurrence of bifurcation and chaos.

As far as we are concerned, the method of variable feedback control is widely applied to control the chaos of the supply chain. Ma and Zhang [44] and Ma and Xie [45] have

used this method to control the chaos of the insurance market and the supply chain system. The dynamic system (17) under control can be rewritten as

$$\begin{cases} w(t+1) = w(t) + \alpha_1 w(t) \frac{\partial u_m^*(t)}{\partial w(t)} - vw(t), \\ p_m(t+1) = p_m(t) + \alpha_2 p_m(t) \frac{\partial u_m^*(t)}{\partial p_m(t)} - vp_m(t). \end{cases} \quad (24)$$

The controlled system (24) can be expressed as follows:

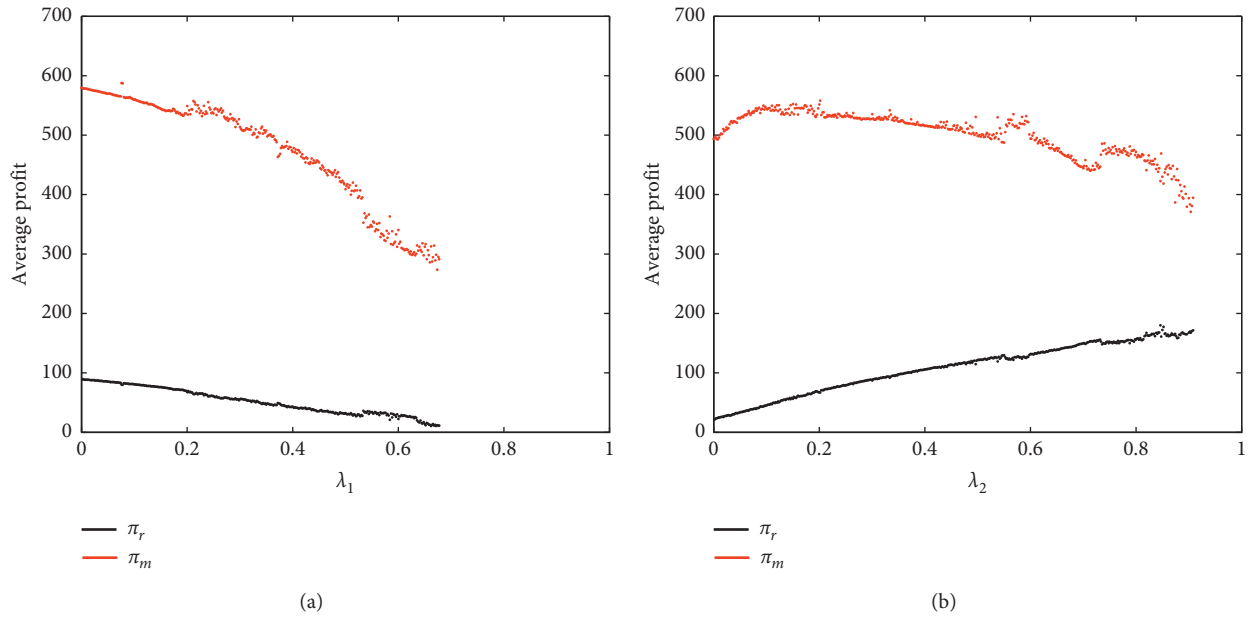


FIGURE 10: Change of the average profits when  $\alpha_1 = 0.02$  and  $\alpha_2 = 0.04$ .

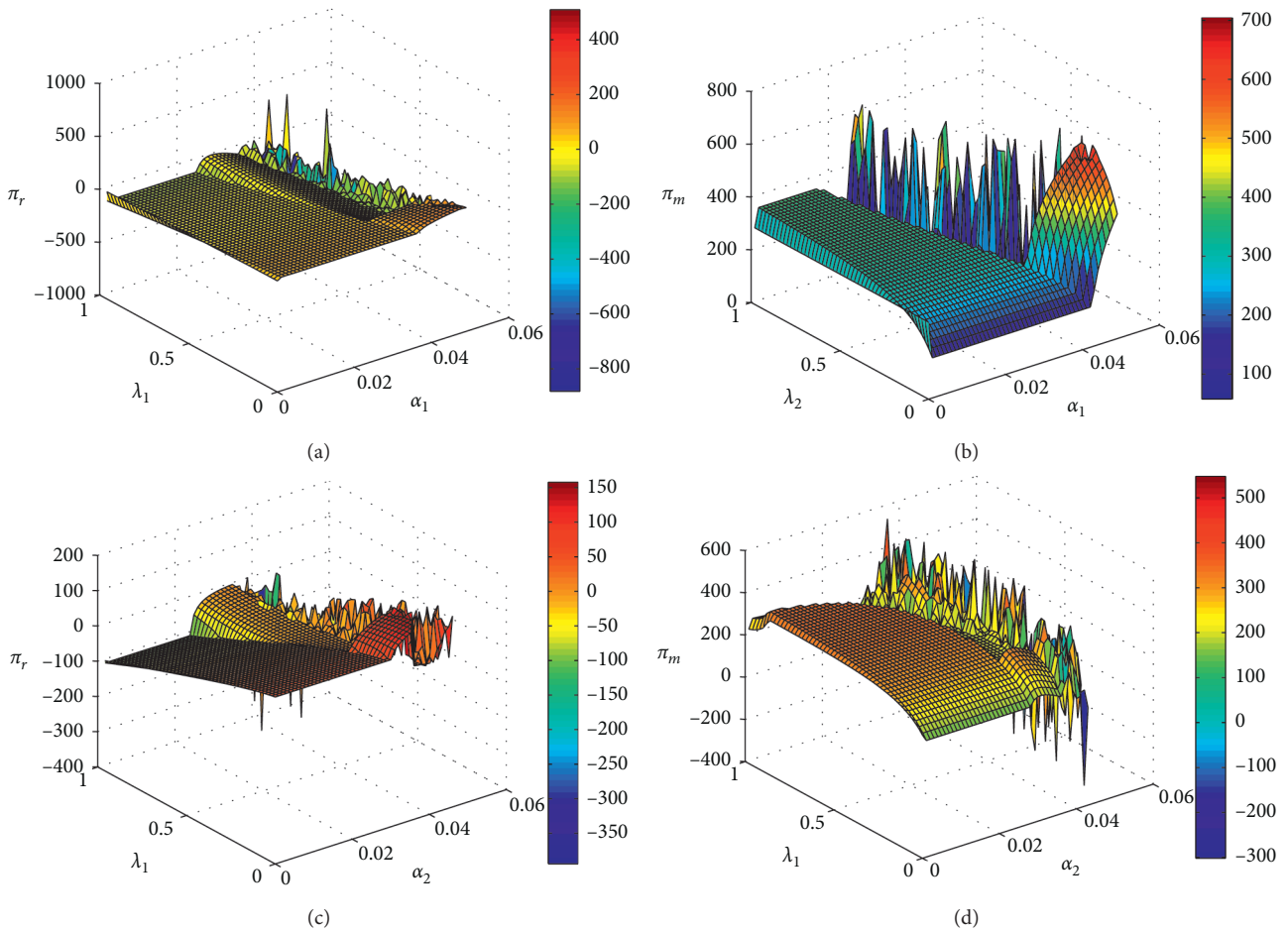


FIGURE 11: Change of profits with respect to  $\alpha_i$  ( $i = 1, 2$ ) and  $\lambda_i$  ( $i = 1, 2$ ). (a) Change of profit of the retailer with respect to  $\alpha_1$  and  $\lambda_1$ . (b) Change of profits of the retailer with respect to  $\alpha_1$  and  $\lambda_2$ . (c) Change of profit of the retailer with respect to  $\alpha_2$  and  $\lambda_1$ . (d) Change of profit of the manufacturer with respect to  $\alpha_2$  and  $\lambda_2$ .

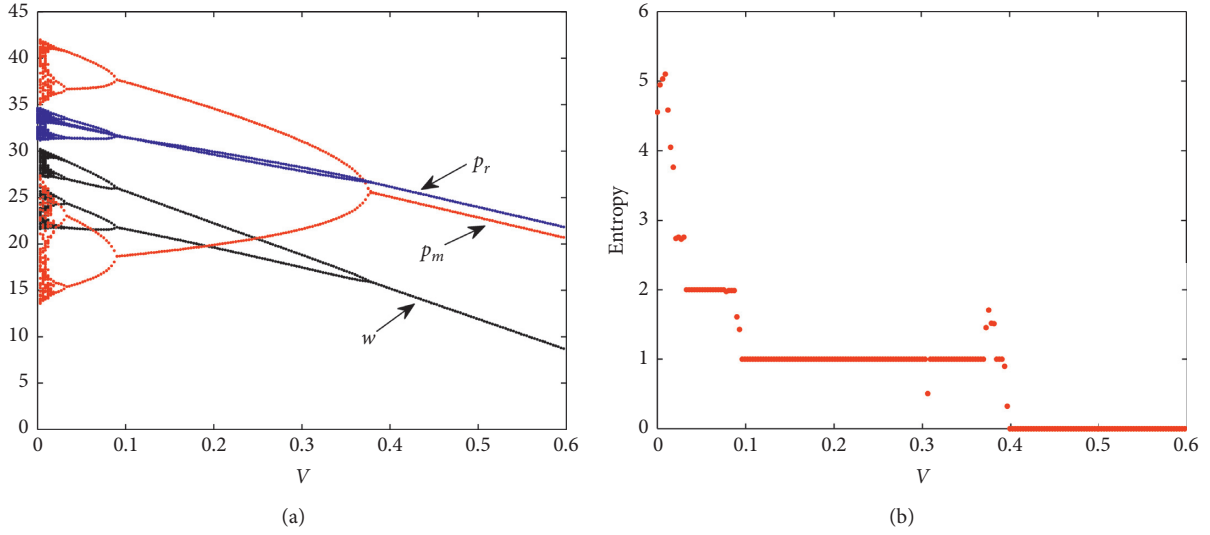


FIGURE 12: Bifurcation diagram and entropy with the change of  $\nu$  when  $\alpha_1 = 0.02$  and  $\alpha_2 = 0.04$ .

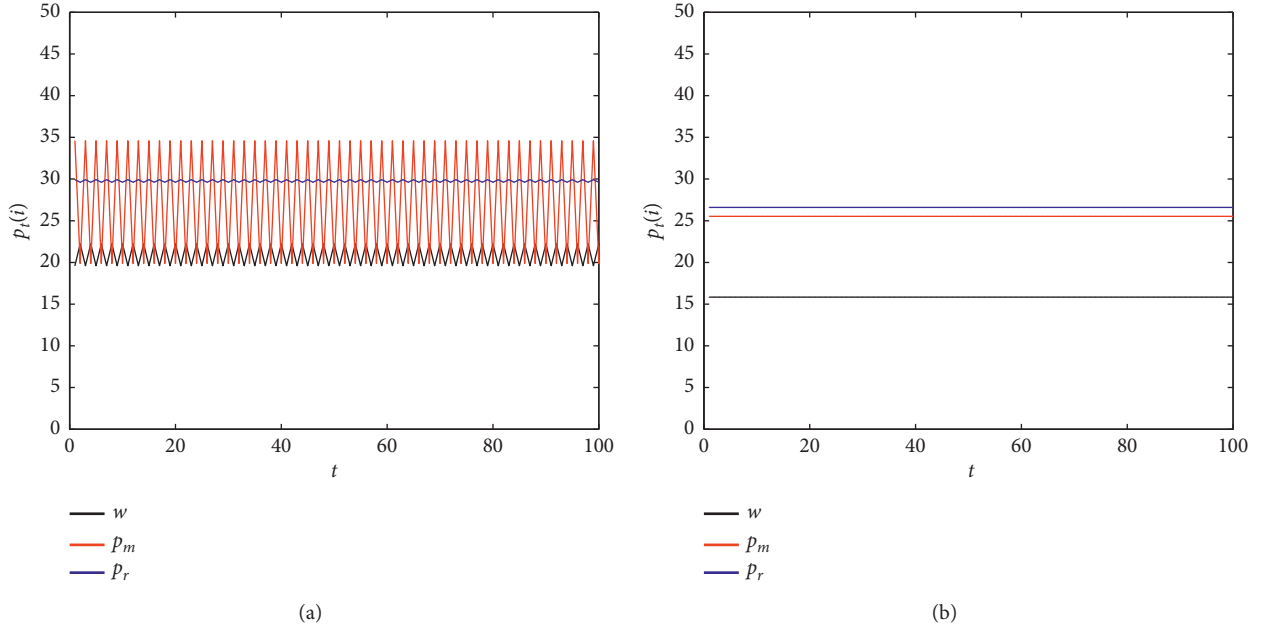


FIGURE 13: Price wave plot with the change of time when  $\alpha_1 = 0.02$  and  $\alpha_2 = 0.04$ . (a)  $\nu = 0.2$ . (b)  $\nu = 0.38$ .

$$\begin{cases} w(t+1) = w(t) + \alpha_1 w(t) \left\{ \frac{1}{2(1+\lambda_1)^2} [a\theta(1+\lambda_1)^2(\lambda_2 + \gamma\lambda_2 + \mu)] + A_0 + A_1 \right\} - \nu w(t), \\ P_m(t+1) = P_m(t) + \alpha_2 P_m(t) \left\{ -\frac{1}{2(1+\lambda_1)} [k^2(1+\lambda_1)(-2+\lambda_2)P_m + c\mu k^2(1+\lambda_1)P_m] + A_2 + A_3 + A_4 \right\} - \nu P_m(t), \end{cases} \quad (25)$$

where  $\nu$  represents the control parameter, and selecting an appropriate value for  $\nu$  is essential to delay bifurcation and make the supply chain system return to a stable state.

Next, we examine the influence of the parameter  $\nu$  on the stability of the system (25). Making  $\alpha_1 = 0.02$  and  $\alpha_2 = 0.04$ , Figure 12 shows the bifurcation diagram and entropy with the change of  $\nu$ , the controlled system (25) goes to the stable

state from the chaotic state with increasing  $\nu$ , and entropy of the controlled system (25) becomes smaller as the system's instability decreases. In Figure 13(a), when  $\nu = 0.2$  is fixed, the system vibrates in a two-period orbit; then adjusting the parameter  $\nu = 0.38$  (see in Figure 13(b)), the wave plot of prices remains at the determined value and the controlled system (25) returns to the stable state.

From Figure 12, it is seen that the control parameter  $\nu$  will affect the Stackelberg equilibrium value of the controlled system (25), so the manufacturer and retailer should make a good balance between the system's stability and profit maximization.

## 6. Conclusion

In this paper, we develop a Stackelberg game model in the dual-channel supply chain including a manufacturer and a retailer; both sides consider fairness concern, and the manufacturer has different business objectives. The entropy and complex characteristic of the dual-channel supply chain system are analyzed by nonlinear dynamics theory and entropy theory, such as the entropy diagram, bifurcation diagram, LLE, stable region, and chaos attractors. A three-dimensional triangular mesh is applied to describe the changes of profits of the manufacturer and retailer. The results show that, with the increase of price adjustment speed, the dual-channel supply chain is more complex and falls into a chaotic state in which system entropy increases; the stability of the dual-channel supply chain will be robust with the increase of the weight of market share and weaken with the increase of the fairness concern level of the manufacturer and retailer. The high level of fairness concern of the manufacturer and retailer is always disadvantageous to the leading manufacturer but not always bad for the follower retailer. The performance of the dual-channel supply chain is improved with a high level of the manufacturer's fairness concern and declined with a high level of the retailer's fairness concern. We also find the retailer will gain more profits in the chaotic state than in the stable state in the Stackelberg game model. In addition, the variable feedback control method can effectively control the chaotic behavior of the dual-channel supply chain.

## Data Availability

The data used to support the findings of this study are available from the corresponding author upon request.

## Conflicts of Interest

The authors declare that there are no conflicts of interest regarding the publication of this paper.

## Authors' Contributions

Qiuxiang Li provided research methods. Yuhao Zhang wrote the original draft. Yimin Huang revised the paper.

## Acknowledgments

This research was supported by Henan Province Soft Science Research Plan Project (no. 182400410054).

## References

- [1] W. J. Baumol, "On the theory of oligopoly," *Economica*, vol. 25, no. 99, pp. 187–198, 1958.
- [2] H. A. Simon, *Models of Man*, Wiley, New York, NY, USA, 1957.
- [3] D. Tadic, S. Arsovski, and P. Pravdic, "Determination of the effectiveness of the realization of enterprise business objectives and improvement strategies in an uncertain environment," *Expert Systems the Journal of Knowledge Engineering*, vol. 32, no. 4, pp. 494–506, 2015.
- [4] M. Lohrmann and M. Reichert, *Modeling Business Objectives for Business Process Management*, S-BPMONE-Scientific Research, Springer, Berlin, Germany, 2012.
- [5] P. Doyle, "Setting business objectives and measuring performance," *European Management Journal*, vol. 12, no. 2, pp. 123–132, 1994.
- [6] S. K. Keil, D. Reibstein, and D. R. Wittink, "The impact of business objectives and the time horizon of performance evaluation on pricing behavior," *International Journal of Research in Marketing*, vol. 18, no. 1-2, pp. 67–81, 2001.
- [7] D. E. Bell, R. L. Keeney, and J. D. C. Little, "A market share theorem," *Journal of Marketing Research*, vol. 12, no. 2, pp. 136–141, 1975.
- [8] D. M. Szymanski, S. G. Bharadwaj, and P. R. Varadarajan, "An analysis of the market share-profitability relationship," *Journal of Marketing*, vol. 57, no. 3, pp. 1–18, 1993.
- [9] T. Jansen, A. van Lier, and A. van Witteloostuijn, "A note on strategic delegation: the market share case," *International Journal of Industrial Organization*, vol. 25, no. 3, pp. 531–539, 2007.
- [10] L. L. Rego, N. A. Morgan, and C. Fornell, "Reexamining the market share-customer satisfaction relationship," *Journal of Marketing*, vol. 77, no. 5, pp. 1–20, 2013.
- [11] M. Nolan and P. Amit, "Relative performance as a strategic commitment mechanism," *Managerial & Decision Economics*, vol. 23, no. 2, pp. 51–68, 2002.
- [12] G.-I. Bischi and M. Kopel, "Multistability and path dependence in a dynamic brand competition model," *Chaos, Solitons & Fractals*, vol. 18, no. 3, pp. 561–576, 2003.
- [13] T. Li and J. Ma, "Complexity analysis of dual-channel game model with different managers' business objectives," *Communications in Nonlinear Science and Numerical Simulation*, vol. 20, no. 1, pp. 199–208, 2015.
- [14] T. H. Cui, J. S. Raju, and Z. J. Zhang, "Fairness and channel coordination," *Management Science*, vol. 53, no. 8, pp. 1303–1314, 2007.
- [15] S. Du, C. Du, and L. Liang, "Supply chain coordination considering fairness concerns," *Journal of Management Sciences in China*, vol. 13, no. 11, pp. 41–48, 2010.
- [16] V. Pavlov and E. Katok, *Fairness and Coordination Failures in Supply Chain Contracts*, Social Science Electronic Publishing, Rochester, NY, USA, 2011.
- [17] F. Zhang and J. Ma, "Research on the complex features about a dual-channel supply chain with a fair caring retailer," *Communications in Nonlinear Science & Numerical Simulation*, vol. 30, no. 1–3, pp. 151–167, 2016.
- [18] J. Chen, X. Zhao, and Z.-J. M. Shen, "The horizontal fairness concern of backup supplier in a triadic supply chain," *SSRN Electronic Journal*, vol. 4, 2012.



- [19] Y. Qin, "Supply chain coordination model under fairness concern of retailer and supplier," *Journal of Information and Computational Science*, vol. 11, no. 1, pp. 211–217, 2014.
- [20] F. Tang, M.-Z. Xu, and B. School, "Coordination of dual-channel closed-loop supply chain considering retailer's fairness concern," *Mathematics in Practice & Theory*, vol. 46, no. 8, pp. 63–73, 2016.
- [21] P. Ma, K. W. Li, and Z.-J. Wang, "Pricing decisions in closed-loop supply chains with marketing effort and fairness concerns," *International Journal of Production Research*, vol. 55, no. 22, pp. 6710–6731, 2017.
- [22] Q. Lin and Y. Qin, "Pricing decisions of supply chain under different fairness concern," *Industrial Engineering Journal*, vol. 19, no. 2, pp. 33–37, 2016.
- [23] B. Li, P. W. Hou, and Q. H. Li, "Cooperative advertising in a dual-channel supply chain with a fairness concern of the manufacturer," *IMA Journal of Management Mathematics*, vol. 28, no. 2, Article ID dpv025, 2017.
- [24] Q. H. Li and B. Li, "Dual-channel supply chain equilibrium problems regarding retail services and fairness concerns," *Applied Mathematical Modelling*, vol. 40, no. 15–16, pp. 7349–7367, 2016.
- [25] H. Yang and X. Sun, "A study on pricing decision of supply chain based on fairness concern," in *Proceedings of the Advances in Materials, Machinery, Electronics (AMME 2017)*, Shanghai, China, November 2017.
- [26] Y. H. Qin, X. U. Dan-Dan, G. Chen et al., "Dynamic evolution of supply chain fairness information under exponential demand," *Journal of Quantitative Economics*, vol. 34, no. 2, pp. 1–9, 2017.
- [27] A. Sharma, G. Dwivedi, and A. Singh, "Game-theoretic analysis of a two-echelon supply chain with option contract under fairness concerns," *Computers & Industrial Engineering*, vol. 137, Article ID 106096, 2019.
- [28] X.-X. Zheng, D.-F. Li, Z. Liu, F. Jia, and J.-B. Sheu, "Coordinating a closed-loop supply chain with fairness concerns through variable-weighted Shapley values," *Transportation Research Part E: Logistics and Transportation Review*, vol. 126, pp. 227–253, 2019.
- [29] L. Zhang, H. Zhou, Y. Liu, and R. Lu, "Optimal environmental quality and price with consumer environmental awareness and retailer's fairness concerns in supply chain," *Journal of Cleaner Production*, vol. 213, pp. 1063–1079, 2019.
- [30] E. Febr and K. M. Schmidt, "A theory of fairness, competition and cooperation," *Quarterly Journal of Economics*, vol. 114, no. 3, pp. 817–868, 1999.
- [31] C. Martínez-Olvera, "Entropy as an assessment tool of supply chain information sharing," *European Journal of Operational Research*, vol. 185, no. 1, pp. 405–417, 2008.
- [32] R. K. Mavi, M. Goh, and N. K. Mavi, "Supplier selection with Shannon entropy and fuzzy TOPSIS in the context of supply chain risk management," *Procedia—Social and Behavioral Sciences*, vol. 235, pp. 216–225, 2016.
- [33] T. S. Raj and S. Lakshminarayanan, "Entropy based optimization of decentralized supply chain networks," *IFAC Proceedings Volumes*, vol. 41, no. 2, pp. 10588–10593, 2008.
- [34] X. Qu and Z. Hao, "The entropy model of fractal supply chain network system based on fuzzy AHP," *Journal of Computers*, vol. 5, no. 8, pp. 1213–1218, 2010.
- [35] L. I. Meng-Gang, C. S. Zhou, and L. Lian, "Agricultural flood and drought risk assessment in China based on entropy information diffusion theory," *Journal of Natural Resources*, vol. 32, no. 4, pp. 620–631, 2017.
- [36] Y. Zuo and Y. Kajikawa, "Toward a theory of industrial supply networks: a multi-level perspective via network analysis," *Entropy*, vol. 19, no. 8, p. 382, 2017.
- [37] Z. Wang, H. Soleimani, D. Kannan, and L. Xu, "Advanced cross-entropy in closed-loop supply chain planning," *Journal of Cleaner Production*, vol. 135, pp. 201–213, 2016.
- [38] B. Kriheli and E. Levner, "Entropy-based algorithm for supply-chain complexity assessment," *Algorithms*, vol. 11, no. 4, p. 35, 2018.
- [39] E. Levner and A. Ptuskin, "Entropy-based model for the ripple effect: managing environmental risks in supply chains," *International Journal of Production Research*, vol. 56, no. 7, pp. 1–13, 2017.
- [40] E. Ekinici and A. Baykasoglu, "Modelling complexity in retail supply chains," *Kybernetes*, vol. 45, no. 2, pp. 297–322, 2016.
- [41] D. Ivanov, *Entropy-Based Supply Chain Structural Complexity Analysis*, Springer, Cham, Switzerland, 2018.
- [42] W. Lou, J. Ma, and X. Zhan, "Bullwhip entropy analysis and chaos control in the supply chain with sales game and consumer returns," *Entropy*, vol. 19, no. 2, p. 64, 2017.
- [43] Y. X. Cao, W. Zhou, T. Chu, and Y. X. Chang, "Global dynamics and synchronization in a duopoly game with bounded rationality and consumer surplus," *International Journal of Bifurcation and Chaos*, vol. 29, no. 11, 2019.
- [44] J. Ma and J. Zhang, "Price game and chaos control among three oligarchs with different rationalities in property insurance market," *Chaos*, vol. 22, no. 4, Article ID 043120, 2012.
- [45] J. Ma and L. Xie, "The comparison and complex analysis on dual-channel supply chain under different channel power structures and uncertain demand," *Nonlinear Dynamics*, vol. 83, no. 3, pp. 1379–1393, 2016.

## Research Article

# Dynamical Complexity and Multistability in a Novel Lunar Wake Plasma System

Bo. Yan,<sup>1</sup> Punam K. Prasad ,<sup>2</sup> Sayan Mukherjee,<sup>3</sup> Asit Saha ,<sup>2</sup> and Santo Banerjee <sup>4,5</sup>

<sup>1</sup>Department of Information Engineering, Shaoyang University, Shaoyang 422000, China

<sup>2</sup>Department of Mathematics, Sikkim Manipal Institute of Technology, Sikkim Manipal University, Majitar, Rangpo, East-Sikkim 737136, India

<sup>3</sup>Department of Mathematics, Sivanath Sastri College, Kolkata, India

<sup>4</sup>Institute for Mathematical Research, Universiti Putra Malaysia, Serdang, Malaysia

<sup>5</sup>Malaysia-Italy Centre of Excellence for Mathematical Science, Universiti Putra Malaysia, Serdang, Malaysia

Correspondence should be addressed to Santo Banerjee; santoban@gmail.com

Received 1 January 2020; Accepted 1 February 2020; Published 16 March 2020

Guest Editor: Viet-Thanh Pham

Copyright © 2020 Bo. Yan et al. This is an open access article distributed under the Creative Commons Attribution License, which permits unrestricted use, distribution, and reproduction in any medium, provided the original work is properly cited.

Dynamical complexity and multistability of electrostatic waves are investigated in a four-component homogeneous and magnetized lunar wake plasma constituting of beam electrons, heavier ions (alpha particles,  $\text{He}^{++}$ ), protons, and suprathermal electrons. The unperturbed dynamical system of the considered lunar wake plasma supports nonlinear and supernonlinear trajectories which correspond to nonlinear and supernonlinear electrostatic waves. On the contrary, the perturbed dynamical system of lunar wake plasma shows different types of coexisting attractors including periodic, quasiperiodic, and chaotic, investigated by phase plots and Lyapunov exponents. To confirm chaotic and nonchaotic dynamics in the perturbed lunar wake plasma, 0–1 chaos test is performed. Furthermore, a weighted recurrence-based entropy is implemented to investigate the dynamical complexity of the system. Numerical results show existence of chaos with variation of complexity in the perturbed dynamics.

## 1. Introduction

The Moon is nonconducting and has no atmosphere and intrinsic magnetic field, so the solar wind freely interacts with the Moon and forms a wake on the antisunward side of the Moon [1]. The magnetic field of solar wind enters the Moon easily compared with particles of solar wind. The variations in density across the boundary of lunar wake steer the solar wind plasma to replenish the void area by ambipolar diffusion [2, 3]. The presence of ion and electron beams with fluctuating temperature of solar wind plasma produces different kinds of waves. The wind satellite revealed ion beams [2] and different modes of nonlinear waves [4] in the tail region of lunar wake. A lunar orbiter SELENE revealed the existence of electrostatic waves which are generated due to the electrostatic instability driven by energetic solar wind particles in the lunar wake [5].

The particles of astrophysical plasmas such as solar wind plasma were generally found to follow non-Maxwellian distribution containing suprathermal particles with high-energy tails [6]. The kappa distribution appropriately defines the influence of suprathermal particles [7]. Recently, Saini [8] and Devanandhan et al. [9] investigated arbitrary nonlinear wave structures in two-temperature plasmas with suprathermal electrons and found the effect of suprathermal electrons on amplitude of solitons.

Some nonlinear systems can exhibit many solutions with specified parameters and distinct initial conditions [10]. This nonlinear behavior is termed as coexisting attractors or multistability. Multistability behaviors [11, 12] of the physical system act as important feature in the dynamics of nonlinear systems. Experimentally, multistability feature was firstly investigated in a Q-switched gas laser [13]; thereafter, various works [14, 15] were reported in different

complex systems exhibiting multistability features. In this study, we show multistability features of the lunar wake plasma system for the first time.

Recently, a new wave structure called supernonlinear wave was introduced in theoretical [16] and astrophysical plasmas [17]. The nonlinear Alfvén waves and solitons defined in the framework of derivative nonlinear Schrödinger equation [18] are found to support supernonlinear waves. Tamang and Saha [19] reported supernonlinear waves and chaotic motion in a non-Maxwellian plasma. Singh and Lakhina [20] investigated ion-acoustic supersolitons in multicomponent plasma. Streaming charged debris moving in space plasma may cause an external disturbance to the system. These disturbances can disrupt the motion of the system [21, 22]. To the best of our knowledge, the study on dynamical properties of nonlinear electrostatic waves in lunar wake plasma is not reported. So, in this work, we employ the concept of nonlinear dynamics to study dynamical properties nonlinear electrostatic structures in magnetized, collisionless, homogeneous plasma comprising of beam electrons, and heavier ions (alpha particles and  $\text{He}^{++}$ ), protons, and kappa distributed electrons.

The article is organized as follows. In Section 2, model equations for the lunar wake plasma system are considered. In Section 3, dynamics of the perturbed and unperturbed system are studied. It has been noticed that the novel system can produce coexisting attractors under the influence of an external forcing term. Variation of Lyapunov exponents shows the conservative nature of the system. To quantify chaos, Lyapunov exponents do not produce constructive information, since very small oscillations of the Lyapunov spectra are observed. To classify chaotic and nonchaotic regimes, 0 – 1 chaos test [23, 24] is then implemented. The analysis is given in Section 4. A dynamical complexity is also investigated by weighted recurrence entropy [25] in Section 5. Section 6 is the conclusion.

## 2. Model Equations

A homogeneous four-component magnetized lunar wake plasma constituting of protons ( $N_{p0}, T_p$ ), electron beams ( $N_{b0}, T_b$ ), heavier ions, such as alpha particles,  $\text{He}^{++}$  ( $N_{i0}, T_i$ ), and suprathermal electrons ( $N_{e0}, T_e$ ), where  $N_{j0}$  and  $T_j$  denote number densities at equilibrium state and temperature of  $j$ th species, where  $j = b, e, i$ , and  $p$  for beam electrons and suprathermal electrons, ions, and positrons, respectively. Here, nonlinear electrostatic waves and drift velocity of beam electron ( $V_{b0}$ ) are assumed to be propagating along the ambient magnetic field ( $B_0$ ).

The suprathermal electrons of the lunar wake plasma are assumed to follow the  $\kappa$ -distribution [26]:

$$f_e(v) = \frac{n_{e0}}{\pi^{(1/2)}\theta} \frac{\Gamma(k)}{\sqrt{\kappa}\Gamma(k - (1/2))} \left(1 + \frac{v^2}{\kappa\theta^2}\right)^{-(\kappa)}, \quad \kappa > \frac{3}{2}, \quad (1)$$

where  $\kappa$  represents spectral index,  $\Gamma(\kappa)$  stands for gamma function, and  $\theta$  denotes modified electron thermal velocity given by

$$\theta^2 = \left(2 - \frac{3}{\kappa}\right) \frac{T_e}{m_e}, \quad (2)$$

where  $T_e$  and  $m_e$  are electron temperature and mass, respectively. The kappa distribution tends to Maxwellian distribution, for  $\kappa \rightarrow \infty$ .

The suprathermal electron number density is given by [26]

$$n_e = \left[1 - \frac{\phi}{\kappa - (3/2)}\right]^{-\kappa + (1/2)}. \quad (3)$$

The normalized fluid equations for lunar wake plasma propagating parallel to  $B_0$  are given by

$$\frac{\partial n_j}{\partial t} + \frac{\partial(n_j v_j)}{\partial x} = 0, \quad (4)$$

$$\frac{\partial v_j}{\partial t} + v_j \frac{\partial v_j}{\partial x} + Z_j \mu_{pj} \frac{\partial \phi}{\partial x} + 3\mu_{pj} \sigma_j \frac{n_j}{(n_{j0})^2} \frac{\partial n_j}{\partial x} = 0, \quad (5)$$

$$\frac{\partial^2 \phi}{\partial x^2} = n_e + n_b - n_p - Z_i n_i, \quad (6)$$

where  $\mu_{pj} = (m_p/m_j)$  is the ratio of mass of proton to mass of  $j$ th species,  $n_0 = n_{e0} + n_{b0} = n_{p0} + Z_i n_{i0}$  is equilibrium number density, and  $Z_j$  denotes the electronic charge of the  $j$ th species with  $Z_p = 1$ ,  $Z_b = -1$ , and  $Z_i = 2$ . In equations (3)–(6), velocity ( $v_j$ ) is normalized by  $C_a = \sqrt{T_e/m_p}$ , time by  $\omega_{pp}^{-1} = (1/\sqrt{4\pi n_0 e^2/m_p})$ ,  $x$  by  $\lambda_D = \sqrt{T_e/4\pi n_0 e^2}$ ,  $\phi$  by  $(T_e/e)$ , and  $n_j$  by  $n_0$ . Furthermore, for one-dimensional case, we consider the adiabatic index,  $\gamma_j = 3$  for all species.

## 3. Dynamical Systems

**3.1. Unperturbed Dynamical System.** To analyze the dynamical properties of electrostatic waves in lunar wake plasma, we take transformation  $\xi = x - Vt$ , where  $V$  signifies wave speed. Employing  $\xi$  and imposing the conditions  $\phi \rightarrow 0$  and  $(d\phi/d\xi) = 0$  as  $\xi \rightarrow \pm\infty$  in equations (4)–(5), we obtain

$$n_p = \frac{n_{p0}}{2\sqrt{3}\sigma_p} \left\{ \left[ \left( (V + \sqrt{3}\sigma_p)^2 - 2\phi \right)^{1/2} - \left[ \left( (V - \sqrt{3}\sigma_p)^2 - 2\phi \right)^{1/2} \right] \right\}, \quad (7)$$

$$n_i = \frac{n_{i0}}{2\sqrt{3}\sigma_i} \left\{ \left[ \left( \frac{V}{\sqrt{\mu_{pi}}} + \sqrt{3\sigma_i} \right)^2 - 2Z_i\phi \right]^{1/2} - \left[ \left( \frac{V}{\sqrt{\mu_{pi}}} - \sqrt{3\sigma_i} \right)^2 - 2Z_i\phi \right]^{1/2} \right\}, \quad (8)$$

$$n_b = \frac{n_{b0}}{2\sqrt{3}\sigma_b} \left\{ \left[ \left( \frac{V - V_{b0}}{\sqrt{\mu_{pb}}} + \sqrt{3\sigma_b} \right)^2 + 2\phi \right]^{1/2} - \left[ \left( \frac{V - V_{b0}}{\sqrt{\mu_{pb}}} - \sqrt{3\sigma_b} \right)^2 + 2\phi \right]^{1/2} \right\}. \quad (9)$$

Again using equations (3), (7), (8), and (9) in equation (6), we obtain where

$$\frac{d^2\phi}{d\xi^2} = A\phi + B\phi^2 + C\phi^3 + D\phi^4, \quad (10)$$

$$\begin{aligned} A &= \frac{2\kappa-1}{2\kappa-3} - \frac{n_{p0}}{2\sqrt{3}\sigma_p} \left[ \frac{1}{(V + \sqrt{3\sigma_p})} + \frac{1}{(V - \sqrt{3\sigma_p})} \right] - \frac{n_{i0}}{\sqrt{3}\sigma_i} \left[ \frac{2}{((V/\sqrt{\mu_{pi}}) + \sqrt{3\sigma_i})} + \frac{2}{((V/\sqrt{\mu_{pi}}) - \sqrt{3\sigma_i})} \right] \\ &\quad + \frac{n_{b0}}{2\sqrt{3}\sigma_b} \left[ \frac{1}{(((V - V_{b0})/\sqrt{\mu_{pb}}) + \sqrt{3\sigma_b})} - \frac{1}{(((V - V_{b0})/\sqrt{\mu_{pb}}) - \sqrt{3\sigma_b})} \right], \\ B &= \frac{(2\kappa-1)(2\kappa+1)}{2(2\kappa-3)^2} - \frac{n_{p0}}{2\sqrt{3}\sigma_p} \left[ \frac{1}{2(V + \sqrt{3\sigma_p})^3} + \frac{1}{2(V - \sqrt{3\sigma_p})^3} \right] - \frac{n_{i0}}{\sqrt{3}\sigma_i} \left[ \frac{2}{(((V/\sqrt{\mu_{pi}}) + \sqrt{3\sigma_i})^3} + \frac{2}{(((V/\sqrt{\mu_{pi}}) - \sqrt{3\sigma_i})^3} \right] \\ &\quad + \frac{n_{b0}}{2\sqrt{3}\sigma_b} \left[ \frac{1}{2(((V - V_{b0})/\sqrt{\mu_{pb}}) + \sqrt{3\sigma_b})^3} + \frac{1}{2(((V - V_{b0})/\sqrt{\mu_{pb}}) - \sqrt{3\sigma_b})^3} \right], \\ C &= \frac{(2\kappa-1)(2\kappa+1)(2\kappa+3)}{6(2\kappa-3)^3} - \frac{n_{p0}}{2\sqrt{3}\sigma_p} \left[ \frac{1}{2(V + \sqrt{3\sigma_p})^5} + \frac{1}{2(V - \sqrt{3\sigma_p})^5} \right] - \frac{n_{i0}}{\sqrt{3}\sigma_i} \left[ \frac{4}{(((V/\sqrt{\mu_{pi}}) + \sqrt{3\sigma_i})^5} + \frac{4}{(((V/\sqrt{\mu_{pi}}) - \sqrt{3\sigma_i})^5} \right] \\ &\quad + \frac{n_{b0}}{2\sqrt{3}\sigma_b} \left[ \frac{1}{2(((V - V_{b0})/\sqrt{\mu_{pb}}) + \sqrt{3\sigma_b})^5} - \frac{1}{2(((V - V_{b0})/\sqrt{\mu_{pb}}) - \sqrt{3\sigma_b})^5} \right], \\ D &= \frac{(2\kappa-1)(2\kappa+1)(2\kappa+3)(2\kappa+5)}{24(2\kappa-3)^4} - \frac{n_{p0}}{2\sqrt{3}\sigma_p} \left[ \frac{5}{8(V + \sqrt{3\sigma_p})^7} + \frac{5}{8(V - \sqrt{3\sigma_p})^7} \right] - \frac{n_{i0}}{\sqrt{3}\sigma_i} \left[ \frac{10}{(((V/\sqrt{\mu_{pi}}) + \sqrt{3\sigma_i})^7} + \frac{10}{(((V/\sqrt{\mu_{pi}}) - \sqrt{3\sigma_i})^7} \right] \\ &\quad + \frac{n_{b0}}{2\sqrt{3}\sigma_b} \left[ \frac{5}{8(((V - V_{b0})/\sqrt{\mu_{pb}}) + \sqrt{3\sigma_b})^7} + \frac{5}{8(((V - V_{b0})/\sqrt{\mu_{pb}}) - \sqrt{3\sigma_b})^7} \right]. \end{aligned} \quad (11)$$

Equation (10) is represented as the following dynamical system:

$$\begin{cases} \frac{d\phi}{d\xi} = y, \\ \frac{dy}{d\xi} = A\phi + B\phi^2 + C\phi^3 + D\phi^4. \end{cases} \quad (12)$$

Here, equation (12) represents a dynamical system with physical parameters  $\kappa$ ,  $n_{b0}$ ,  $n_{e0}$ ,  $n_{i0}$ ,  $n_{p0}$ ,  $\sigma_b$ ,  $\sigma_i$ ,  $\sigma_p$ ,  $V_{bo}$ ,  $\mu_{pb}$ ,  $\mu_{pi}$ , and  $V$ .

Considering typical parametric values of lunar wake [3, 26], we set  $n_{b0} = 0.01$ ,  $n_{e0} = 0.99$ ,  $n_{i0} = 0.05$ ,  $n_{p0} \approx 0.9$ ,  $\sigma_b = 0.0025$ ,  $\sigma_i = 0.4$ ,  $\sigma_p = 0.2$ , and  $V_{bo} = 17.14$ .

In Figure 1, we present probable phase plots of system (12) for nonlinear electrostatic waves in lunar wake plasma. Based on the values of parameters  $\kappa$ ,  $n_{p0}$ ,  $n_{i0}$ ,  $n_{e0}$ ,  $n_{b0}$ ,  $\sigma_p$ ,  $\sigma_i$ ,  $\sigma_b$ ,  $V_{bo}$ ,  $\mu_{pb}$ ,  $\mu_{pi}$ , and  $V$ , we have four distinct types of phase plots. Each trajectory in a phase plane corresponds to a traveling wave solution. The phase plots presented in Figure 1 constitute different families of phase trajectories, such as superhomoclinic ( $SH_{3,1}$ ), superperiodic ( $SP_{3,1}$ ), periodic ( $P_{1,0}$ ), and homoclinic ( $H_{1,0}$ ) trajectories which correspond to supersolitary, superperiodic, periodic, and solitary wave solutions of system (12), respectively. Considering different speeds ( $V$ ) of the nonlinear wave with  $\kappa = 5$ ,  $n_{b0} = 0.01$ ,  $n_{e0} = 0.99$ ,  $n_{i0} = 0.05$ ,  $n_{p0} = 0.9$ ,  $\sigma_b = 0.0025$ ,  $\sigma_i = 0.4$ ,  $\sigma_p = 0.2$ ,  $V_{bo} = 17.14$ ,  $\mu_{pb} = 1836$ , and  $\mu_{pi} = 0.25187$ , all qualitatively distinct phase plots are depicted in Figures 1(a)–1(d). If we consider  $V = 1.1$  with specified values of other parameters, there exist only two fixed points at  $(\phi_0, 0)$  and  $(\phi_1, 0)$ , as shown in Figure 1(a), where  $\phi_0 = 0$  and  $\phi_1 < 0$ . The two fixed points  $(\phi_0, 0)$  and  $(\phi_1, 0)$  are the center and saddle point, respectively. The homoclinic trajectory ( $H_{1,0}$ ) at  $(\phi_1, 0)$  and a periodic trajectory ( $P_{1,0}$ ) at  $(\phi_0, 0)$  correspond to solitary and periodic wave solutions in lunar wake plasma. The phase portrait in Figure 1(b) is presented for  $V = 1.225$  with specified values of other parameters. In this case, we obtain a pair of saddle points and centers which occur at  $(\phi_0, 0)$ ,  $(\phi_3, 0)$ ,  $(\phi_1, 0)$ , and  $(\phi_2, 0)$ , respectively, where  $\phi_1 < 0$  and  $\phi_2, \phi_3 > 0$ . It shows signatures of superperiodic and supersolitary wave structures due to the presence of  $SH_{3,1}$  and  $SP_{3,1}$  trajectories. For  $V = 1.24$ , the existence of four fixed points can still be seen and there exist a pair of  $P_{1,0}$  and  $H_{1,0}$  trajectories but there is no superperiodicity as depicted in Figure 1(c). Figure 1(d) is obtained for  $V = 1.3$ . In this case, one saddle point at  $(\phi_0, 0)$  and a center at  $(\phi_1, 0)$  occur, where  $\phi_1 < 0$ . There also exist a class of  $P_{1,0}$  and  $H_{1,0}$  trajectories. Thus, the existence of supernonlinear waves (superperiodic and supersoliton) is confirmed in lunar wake for the first time.

**3.2. Perturbed Dynamical System.** Recently, effect of the Gaussian-shaped source term on nonlinear plasma waves is investigated [27]. But, the nonlinear source term as an external forcing can be of different types [28, 29]. In this work, we consider a source term or perturbation as  $f_0 \cos(\omega\xi)$ . In presence of the source  $f_0 \cos(\omega\xi)$ , the dynamical system (12) can be expressed in the following form:

$$\begin{cases} \frac{d\phi}{d\xi} = y, \\ \frac{dy}{d\xi} = A\phi + B\phi^2 + C\phi^3 + D\phi^4 + f_0 \cos(\omega\xi), \end{cases} \quad (13)$$

where  $f_0$  is the strength and  $\omega$  is the frequency of the external force.

In Figure 2, we depict possible phase plots of attractors corresponding to system (13) for nonlinear electrostatic structures of lunar wake. We display multistability for different values of  $\omega$  by varying the initial condition with  $\kappa = 5$ ,  $n_{b0} = 0.01$ ,  $n_{e0} = 0.99$ ,  $n_{i0} = 0.05$ ,  $n_{p0} = 0.9$ ,  $\sigma_b = 0.0025$ ,  $\sigma_i = 0.4$ ,  $\sigma_p = 0.2$ ,  $V_{bo} = 17.14$ ,  $\mu_{pb} = 1836$ ,  $\mu_{pi} = 0.25187$ ,  $V = 1.225$ , and  $f_0 = 0.01$ . For  $\omega = 0.08$ , we obtain Figure 2(a) which shows chaotic and quasiperiodic attractors in  $\phi y$  plane with initial conditions  $(0, -0.00161)$  (green curve) and  $(0, -0.00327)$  (red curve), respectively. In Figure 2(c), we set  $\omega = 2.09$  with specified values of other physical parameters and detect the presence of three kinds of attractors which are quasiperiodic, chaotic, and periodic-2 attractors. Quasiperiodic attractors are obtained for initial conditions  $(-0.049, 0.0021)$  (blue curve),  $(0, 0.011)$  (brown curve), and  $(0.049, 0)$  (ocean green curve). Chaotic and periodic-2 attractors are obtained for initial conditions  $(-0.049, -0.001897)$  (magenta curve) and  $(0.013, 0)$  (black curve), respectively. Here, Figure 2(b) is a part of attractors shown in Figure 2(c). For  $\omega = 1.08$ , we show chaotic and periodic-1 attractors with initial conditions  $(0, -0.0169)$  (red curve) and  $(0.21, 0)$  (blue curve), respectively, in Figure 2(d). Thus, multistability behaviors are confirmed in lunar wake plasma in presence of external periodic force.

Lyapunov exponent is an effective tool to check the chaotic motion of any system. For a system to be chaotic, there must be at least one positive Lyapunov exponent. In Figure 3, Lyapunov exponents are plotted against extent of the external periodic force  $f_0$  with specified values of other physical parameters as in Figure 2. Figures 3(a)–3(c) show the Lyapunov exponents corresponding to the chaotic phase trajectories shown in Figures 2(a)–2(d), respectively. From Figure 3, it can be also observed that the fluctuations of Lyapunov exponents are very small (near to 0) in all the cases. So, chaos in (13) cannot be confirmed strongly by the study of the Lyapunov exponent. A test of chaos is thus also performed which is given in the following section.

#### 4. Characterization of Chaos

In this section, we investigate chaos by 0 – 1 test method. In 0 – 1 test method, only one component, say  $x(n)_{k=1}^N$  ( $N$  being the length of the component), of a system is considered [23, 24]. Using the following transformation:

$$\begin{aligned} p(n, c) &= \sum_{j=1}^n x(j) \cos(jc), \\ q(n, c) &= \sum_{j=1}^n x(j) \sin(jc), \end{aligned} \quad (14)$$

$$c \in (0, \pi).$$

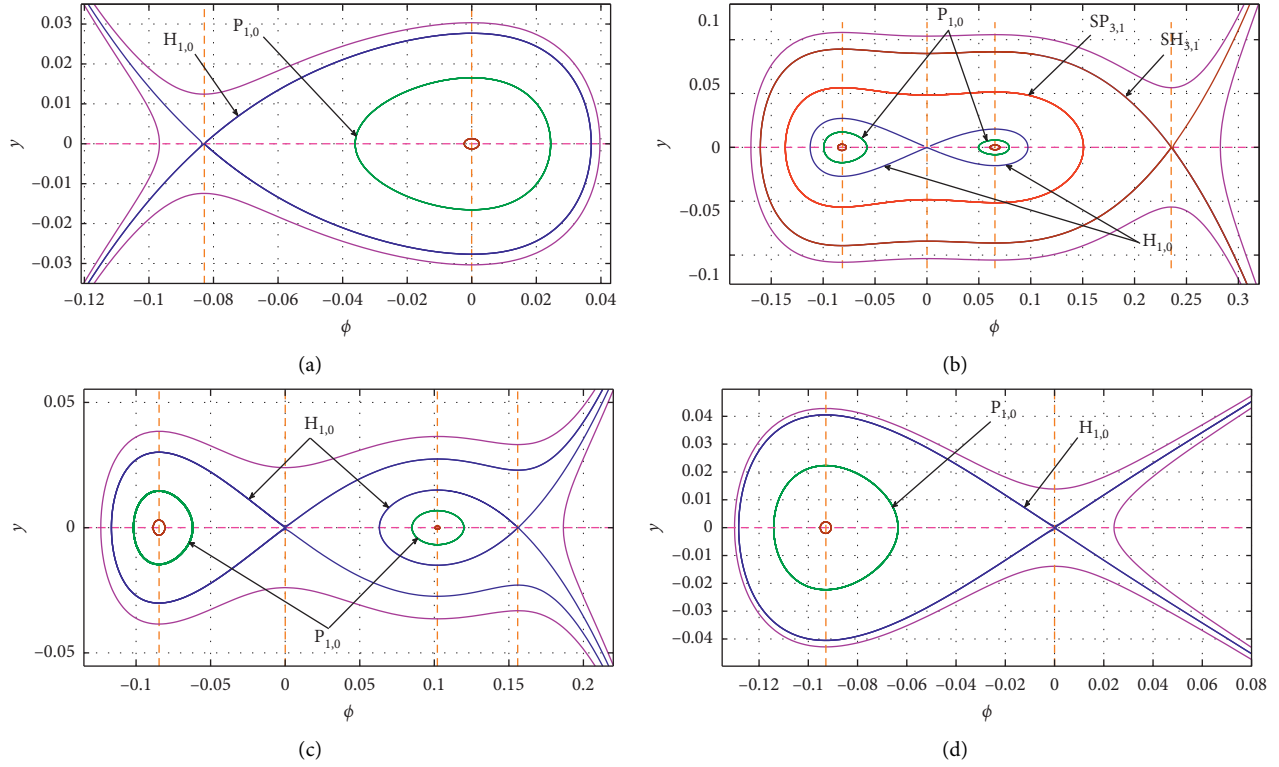


FIGURE 1: Probable phase plots of the dynamical system (12) for  $\kappa = 5$ ,  $n_{b0} = 0.01$ ,  $n_{c0} = 0.99$ ,  $n_{i0} = 0.05$ ,  $n_{p0} = 0.9$ ,  $\sigma_b = 0.0025$ ,  $\sigma_i = 0.4$ ,  $\sigma_p = 0.2$ ,  $V_{b0} = 17.14$ ,  $\mu_{pb} = 1836$ , and  $\mu_{pi} = 0.25187$  with (a)  $V = 1.1$ , (b)  $V = 1.225$ , (c)  $V = 1.24$ , and (d)  $V = 1.3$ .

The component  $x(n)_{k=1}^N$  is decomposed into two components  $p$  and  $q$ . In [23, 24], it has been established that the chaotic and nonchaotic behavior can be recognized by the respective regular and Brownian motion-like structure in the corresponding  $(p, q)$ -plots. So, we investigate nature of the  $(p, q)$ -plots for system (13) with the variation of  $f_0 \in [0, 0.012]$  and initial conditions  $I_k = (0, -k)$ ,  $k \in [0.00161, 0.00327]$ . Some of the plots are shown in Figure 4. It can be observed from Figures 4(a) and 4(b) that the corresponding  $(p, q)$  clouds are of regular and Brownian motion-like structures, respectively. It indicates nonchaotic and chaotic dynamics in system (13) for the respective  $f_0 = 0.001, 0.012$  with  $k = 0.00161$ . On the contrary, both Figures 4(c) and 4(d) show Brownian-like structure in the corresponding plots with  $k = 0.00161, 0.0261$  and  $f_0 = 0.012$ . Thus, Figure 4 shows chaotic as well as nonchaotic dynamics with the variation of  $f_0$  and  $k$ .

In the next, we compute fluctuation of  $K_c$  with the variations of  $f_0 \in [0, 0.012]$  and  $k \in [0.00161, 0.00327]$ , where  $K_c$  is defined by

$$K_c = \lim_{n \rightarrow \infty} \frac{\log M_c(n)}{\log n}, \quad (15)$$

where  $M_c(n)$  is defined as

$$M_c(n) = \lim_{N \rightarrow \infty} \frac{1}{N} \sum_{j=1}^N [p_c(j+n) - p_c(j)]^2 + [q_c(j+n) - q_c(j)]^2. \quad (16)$$

The values of  $K_c \approx 0$  and  $1$  correspond nonchaotic and chaotic dynamics of the system. Figures 5(a) and 5(b) show fluctuation of  $K_c$  over  $f_0 \in [0, 0.012]$  (fixed  $k = 0.0032$ ) and  $k \in [0.00161, 0.00327]$  (fixed  $f_0 = 0.012$ ), respectively. From Figure 5(a), it can be observed that the  $K_c \approx 1$  for  $f_0 \in [0, 0.0097]$ , except  $f_0 = 0.004, 0.005, 0.0055$ . It assures that chaos in system (13) can only be seen at  $f_0 = 0.004, 0.005, 0.0055$  when  $f_0 \in [0, 0.0097]$ . Furthermore,  $K_c \approx 1$  can be seen for  $f_0 \in [0.098, 0.12]$ . It confirms chaotic dynamics in perturbed system (13) over the region  $f_0 \in [0.098, 0.12]$ . On the contrary, Figure 5(b) shows  $K_c \approx 1$  for almost all values of  $k \in [0.00161, 0.00327]$  with fixed  $f_0 = 0.012$ . It confirms chaos in (13) over  $k \in [0.00161, 0.00327]$ . We also investigate fluctuation of  $K_c$  with the variation of  $(f_0, k) \in [0, 0.012] \times [0.00161, 0.00327]$ . The corresponding contour is given in Figure 5(c). In Figure 5(c), most of the region shows  $K_c \approx 1$ , except for few closed regions. It establishes chaotic dynamics of system (13) over  $[0, 0.012] \times [0.00161, 0.00327]$ , except few values of  $(f_0, k)$ .

In the following section, we have investigated dynamical complexity using weighted recurrence plot (WRP) [25].

## 5. Analysis of Dynamical Complexity

For a given  $n$ -dimensional phase space  $P = \{x_i \in R^n\}$ , weighted recurrence  $w(i, j)$  is defined by

$$w(i, j) = e^{-\|x_i - x_j\|}, \quad i, j = 1, 2, \dots, N, \quad (17)$$



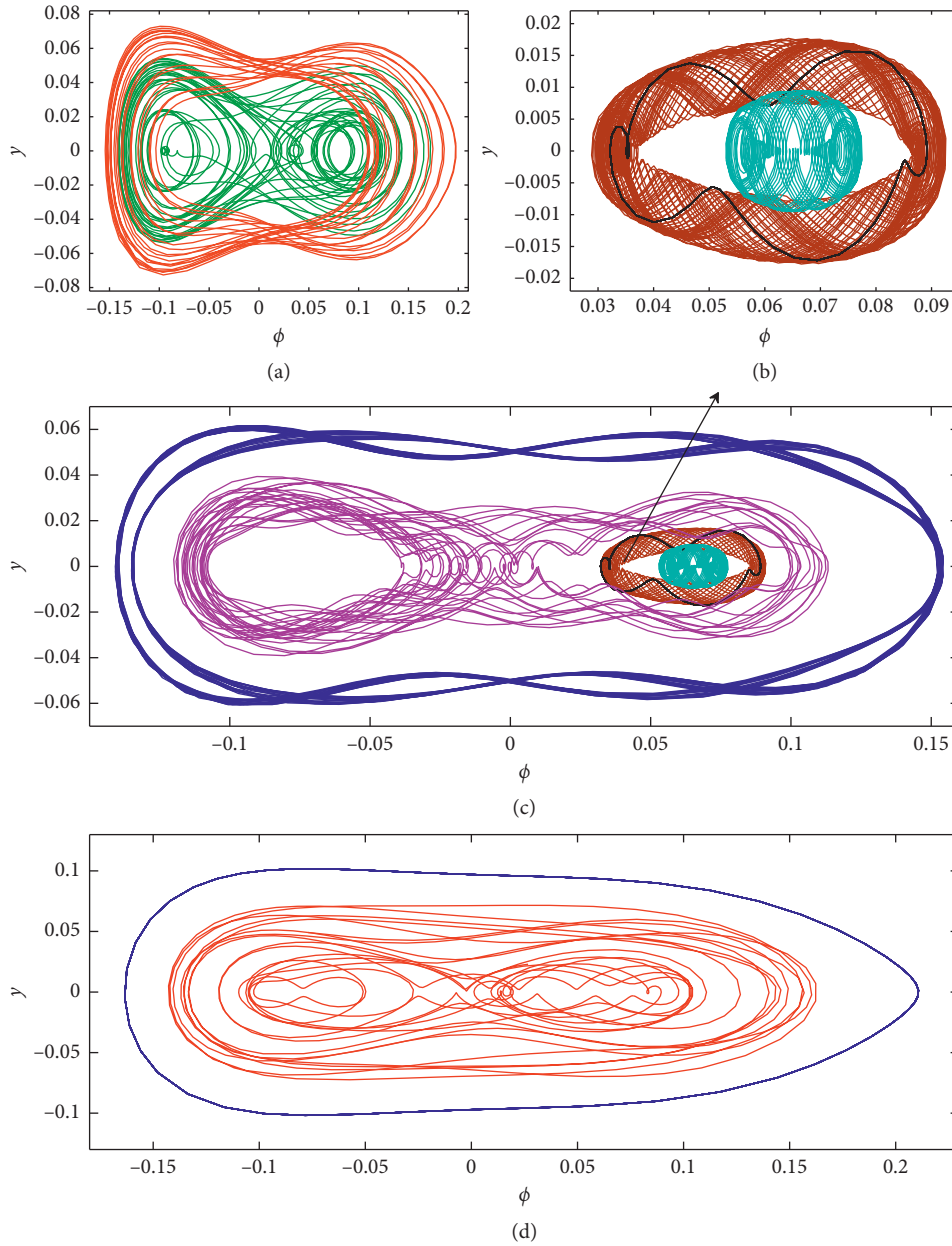


FIGURE 2: Coexisting attractors of system (13) for  $\kappa = 5$ ,  $n_{b0} = 0.01$ ,  $n_{e0} = 0.99$ ,  $n_{i0} = 0.05$ ,  $n_{p0} = 0.9$ ,  $\sigma_b = 0.0025$ ,  $\sigma_i = 0.4$ ,  $\sigma_p = 0.2$ ,  $V_{b0} = 17.14$ ,  $\mu_{pb} = 1836$ ,  $\mu_{pi} = 0.25187$ ,  $V = 1.225$ , and  $f_0 = 0.01$  and (a)  $\omega = 0.08$  with initial conditions  $(0, -0.00161)$  (green curve) and  $(0, -0.00327)$  (red curve), (b)  $\omega = 2.09$  with initial conditions  $(0, 0.011)$  (brown curve),  $(0.013, 0)$  (black curve), and  $(0.049, 0)$  (ocean green curve), (c) enlarged view of coexisting attractors enveloping attractors shown in Figure 2(c) with initial conditions  $(-0.049, -0.001897)$  (magenta curve) and  $(-0.049, 0.0021)$  (blue curve), and (d) for  $\omega = 1.08$  with initial conditions  $(0, -0.0169)$  (red curve) and  $(0.21, 0)$  (blue curve).

where  $N$  is the length of the trajectory of the phase space. As  $\|x_i - x_j\|$  indicates dispersion between  $x_i$  and  $x_j$ ,  $w(i, j)$  can measure exponential divergence between the trajectories. The corresponding matrix  $[w(i, j)]_{N \times N}$  can thus recognize disorder in the phase space. Figures 6(a) and 6(b) represent some of the weighted matrix plots for system (13) with  $f_0 = 0.001$  and  $0.012$  (fixed  $k = 0.0032$ ), respectively. From Figure 6(a), it can be seen that range of variation as well as its pattern in  $w(i, j)$  are very less as compared to same in Figure 6(b). It indicates that the

corresponding phase space of system (13) at  $f_0 = 0.012$  is more complex than the same at  $f_0 = 0.001$  for  $k = 0.001$ . Furthermore, similar investigation is carried out for  $k = 0.00161, 0.00261$  with fixed  $f_0 = 0.012$ . The corresponding weighted matrix plots are shown in Figures 6(c) and 6(d), respectively. As variation in the weights is almost similar between Figures 6(b) and 6(c), same kind of disorder can be observed in the respective phase spaces. On the contrary, completely different as well as various patterns in  $[w(i, j)]$  can be seen in Figure 6(d), which indicates higher

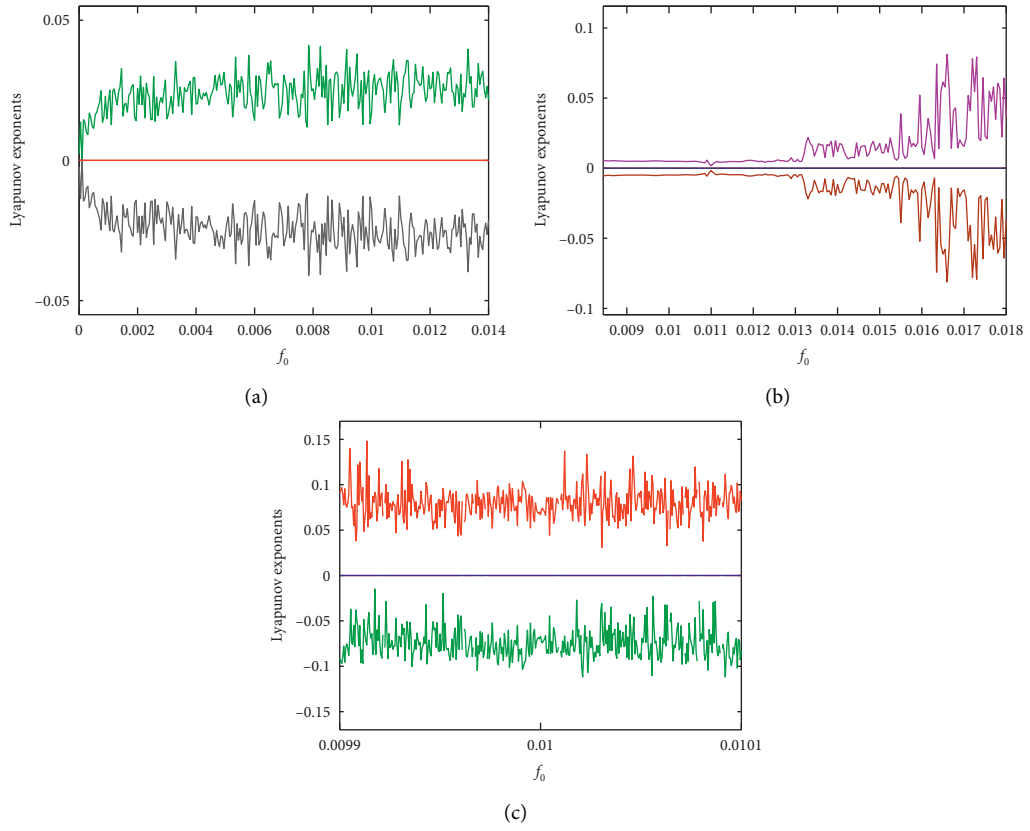


FIGURE 3: Lyapunov exponents of system (13) of chaotic attractors corresponding to (a) Figure 2(a), (b) Figure 2(c), and (c) Figure 2(d).

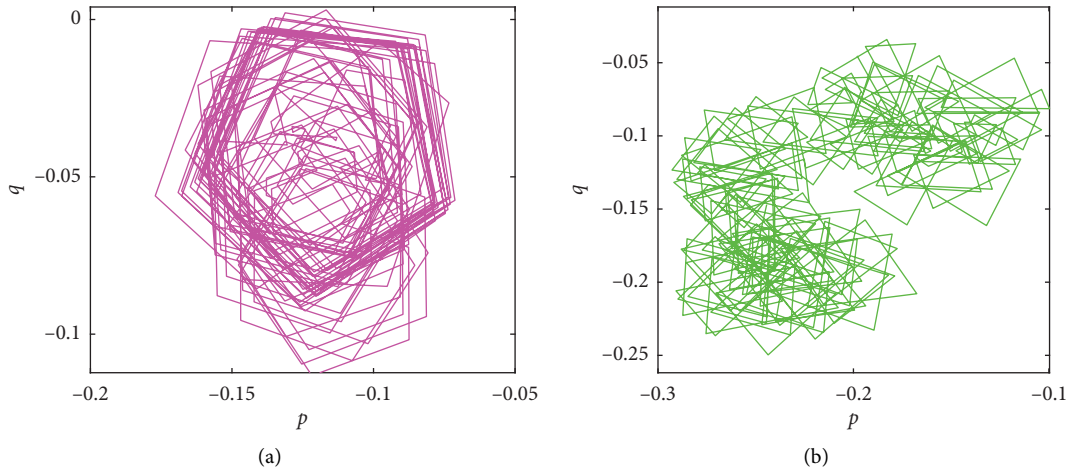


FIGURE 4: Continued.

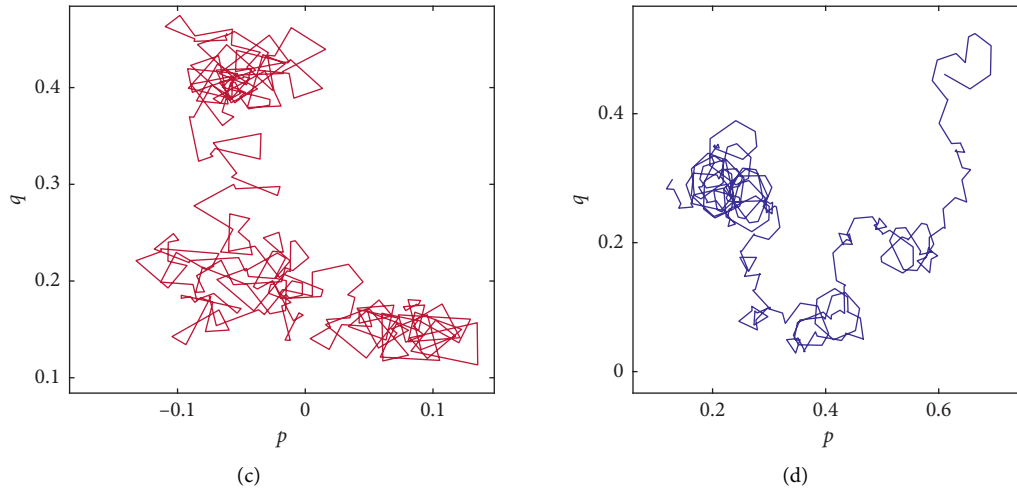


FIGURE 4: (a) and (b) represent  $(p, q)$ -plots for system (13) with  $f_0 = 0.001$  and  $0.012$ , respectively. In order to calculate  $p$  and  $q$ , we choose  $y$ -component of system (13) with the initial condition  $(0, -0.0032)$ . Same plots are represented in (c) and (d) with respect to the different initial conditions  $(0, -0.00161)$  and  $(0, -0.00261)$  for fixed  $f_0 = 0.012$ . In both the cases, the values of parameters are considered same as chosen in Figure 2. In each calculation, the value of (c) is considered as  $(2\pi/3)$ .

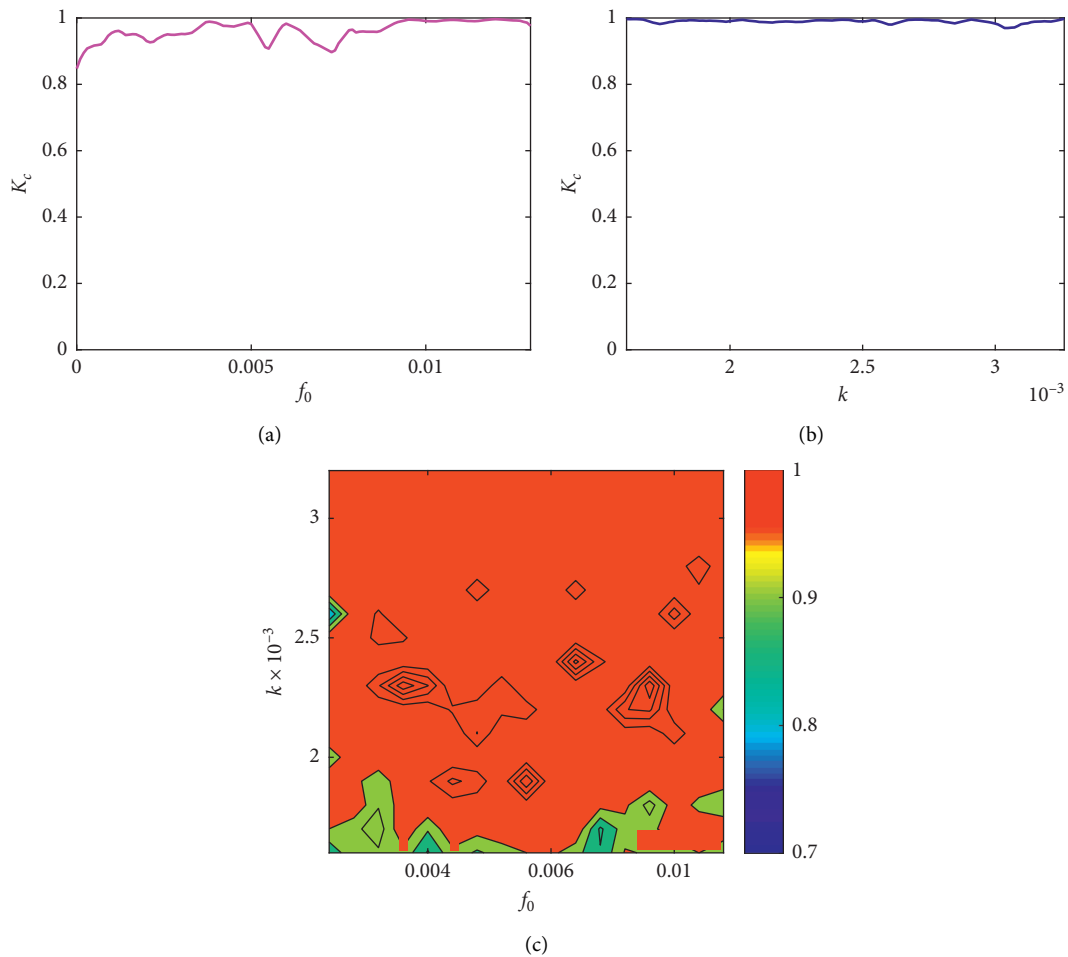


FIGURE 5: (a) represents  $K_c$  vs.  $f_0$  graph for system (13) with  $f_0 \in [0, 0.013]$  and  $k = 0.00161$ . (b) represents  $K_c$  vs.  $k$  for the same system with  $k \in [0.00161, 0.00327]$  and  $f_0 = 0.012$ . (c) represents  $[K_c(k, f_0)]$  matrix plot with  $k \in [0.00161, 0.00327]$ ,  $f_0 \in [0, 0.013]$ . The associated color bar indicates values of  $K_c$  over the region  $[0.00161, 0.00327] \times [0, 0.013]$ . In order to calculate  $K_c$ , we have taken  $n \ll n_{\text{cut}} = (N/10)$ .

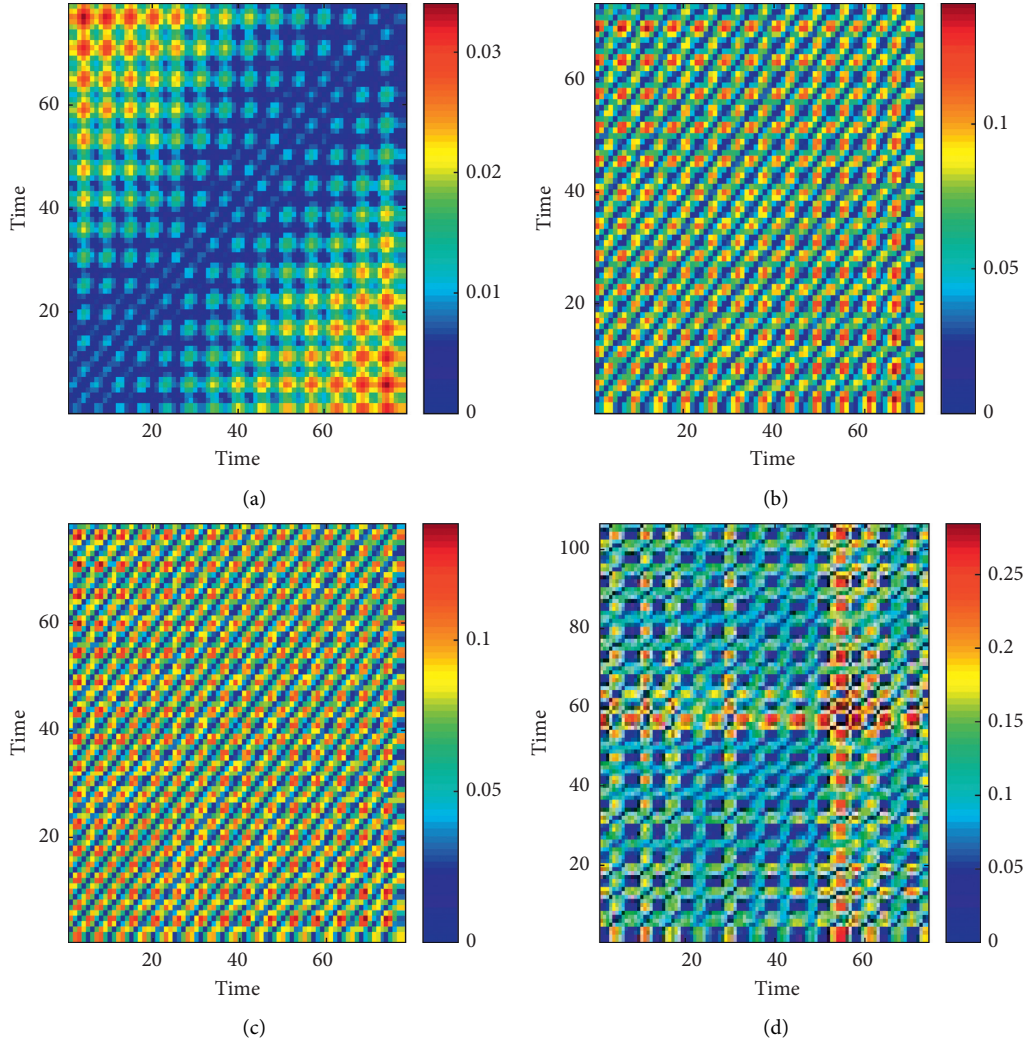


FIGURE 6: (a) and (b) represent  $[w(i, j)]$  matrix plots for system (13) with  $f_0 = 0.001$  and  $0.012$ , respectively. In order to calculate  $[w(i, j)]$  matrix, we solve system (13) with the initial condition  $(0, -0.0032)$ . Same plots are represented in (c) and (d) with respect to the different initial conditions  $(0, -0.00161)$ ,  $(0, -0.00261)$  for fixed  $f_0 = 0.012$ . In both the cases, the values of parameters are considered same, as chosen in Figure 2. In each calculation, we consider last 10,000 points on the trajectories.

complex structure in the corresponding phase space compared to the other cases.

However, the above mentioned analysis is not enough to understand the complexity for the whole range. This is why we utilize a complexity measure-weighted recurrence entropy measure to investigate how complexity varies with the variations of  $f_0$  and  $k$ . The weight recurrence entropy ( $S_w$ ) is defined as

$$S_w = - \sum_{s_k \in S} p(s_k) \log p(s_k), \quad (18)$$

where  $p(s_k)$  denotes probability of  $s_k \in S = \{s_k: s_k = (1/N) \sum_{j=1}^M \omega_{kj}, 1 \leq k \leq M\}$  ( $M$  being number of events). In our case, “events” means  $s_k$ s.

Using (18), we have computed fluctuation of  $S_w$  over  $f_0 \in [0, 0.012]$  and  $k \in [0.00161, 0.00327]$ . Corresponding oscillations are given in Figures 7(a) and 7(b), respectively. An increasing trend can be seen in Figure 7(a). It indicates increasing pattern in the complexity with the increasing

$f_0 \in [0, 0.012]$  (fixed  $k = 0.0032$ ). On the contrary, almost parallel trend exists in Figure 7(b). It assures that, variation in  $S_w$ s does not fluctuate abruptly. So, complexity does not differ significantly in system (13) with increasing  $k \in [-0.00161, -0.00327]$  (fixed  $f_0 = 0.012$ ).

We further investigate complexity of system (13) over the region  $(f_0, k) \in [0, 0.012] \times [0.00161, 0.00327]$ . The corresponding contour is shown in Figure 7(c). In Figure 7, it can be observed that higher complexity bounded regions are very fewer compared with its complement. However, some discrete increasing as well as decreasing patterns can be seen in the whole contour.

So, the analysis on the novel system reveals that the chaotic dynamics can be observed in system (13) for large regions of  $f_0$  and  $k$ , but higher complexity can be seen in the same system for small regions of  $f_0$  and  $k$ . Therefore, chaos with high complexity in system (13) for the interval  $(f_0, k) \in [0, 0.012] \times [0.00161, 0.00327]$  can be observed.

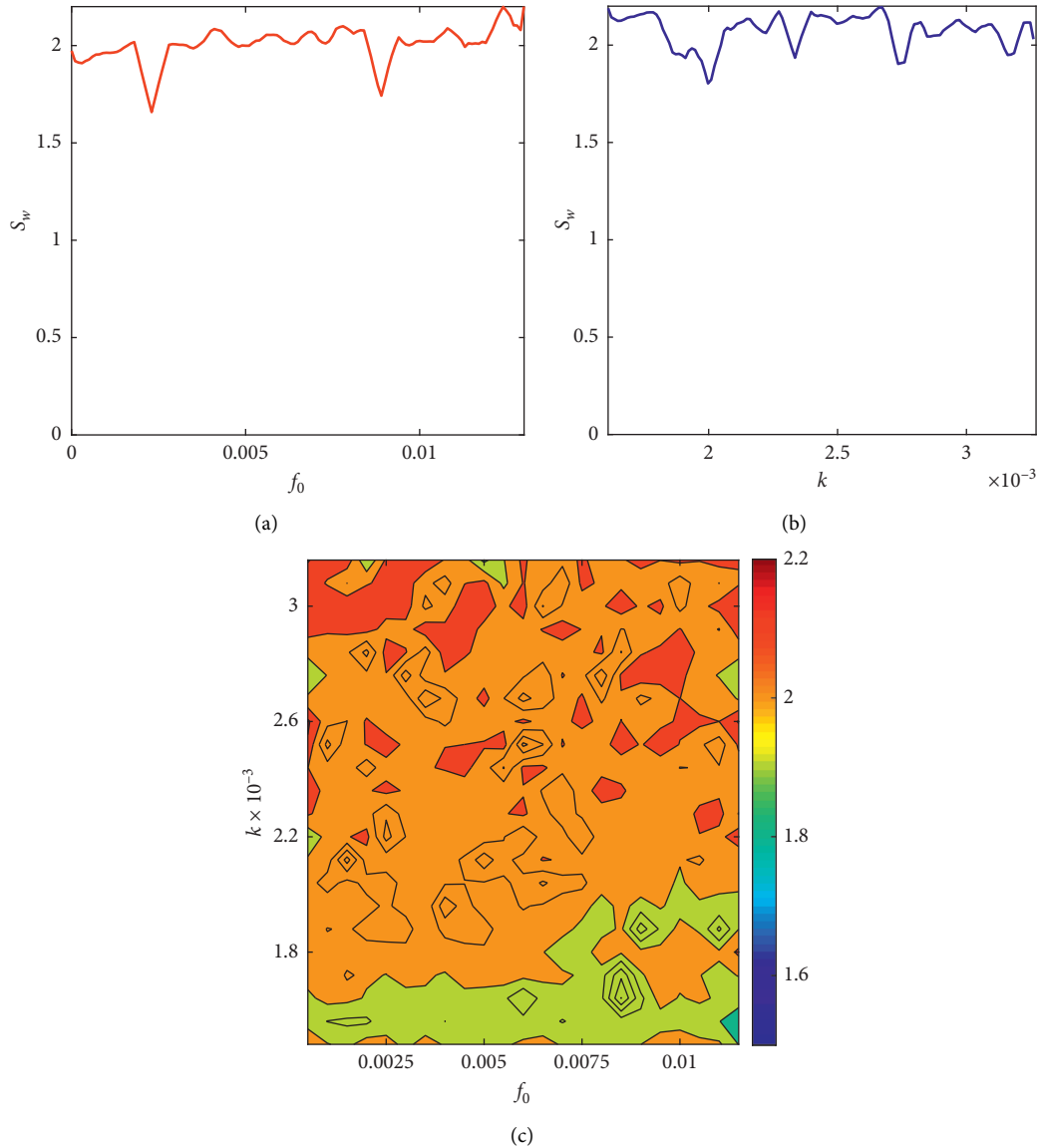


FIGURE 7: (a) and (b) represent  $[w(i, j)]$  matrix plots for system (13) with  $f_0 = 0.001$  and  $0.012$ , respectively. In order to calculate  $[w(i, j)]$  matrix, we solve system (13) with the initial condition  $(0, -0.0032)$ . Same plots are represented in (c) and (d) with respect to the different initial conditions  $(0, -0.00161)$  and  $(0, -0.00261)$ , for fixed  $f_0 = 0.012$ . In both the cases, the values of parameters are considered same, as chosen in Figure 2. In each calculation, we consider last 10,000 points on the trajectories.

## 6. Conclusions

Phase portrait analysis of a novel dynamical system corresponding to lunar wake has been performed in plasma constituting of beam electrons, heavier ions (alpha particles,  $\text{He}^{++}$ ), protons, and suprathermal electrons. Typical values of physical parameters of lunar wake [3, 26] have been applied in the unperturbed system to investigate qualitatively different phase portraits comprising of superperiodic, superhomoclinic, periodic, and homoclinic trajectories. These trajectories correspond to different types of nonlinear and supernonlinear wave solutions. For an external periodic perturbation due to the nonlinear source term, multistability features have been confirmed in a lunar wake plasma system.

The existence of multistability in such a plasma model is never been reported. We have also investigated that the system does not confirm chaos with the observations of Lyapunov exponents as the Lyapunov exponents are close to zero with conservative characteristics. To quantify the existence of chaos, we have constructed the 0 – 1 test. Furthermore, a detailed dynamical complexity analysis has been implemented by using weighted recurrence. The corresponding results assure that the perturbed system (13) has high complexity in some region inside the parametric space.

## Data Availability

No data were used to support this study.

## Conflicts of Interest

The authors declare that they have no conflicts of interest.

## Acknowledgments

Dr. Asit Saha is grateful to SMIT and SMU for research support funded by TMA Pai University Research Fund-Minor Grant (6100/SMIT/R&D/Project/05/2018).

## References

- [1] E. Kallio, "Formation of the lunar wake in quasi-neutral hybrid model," *Geophysical Research Letters*, vol. 32, no. 6, p. L06107, 2005.
- [2] K. W. Ogilvie, J. T. Steinberg, R. J. Fitzenreiter et al., "Observations of the lunar plasma wake from the WIND spacecraft on December 27, 1994," *Geophysical Research Letters*, vol. 23, no. 10, pp. 1255–1258, 1996.
- [3] J. B. Tao, R. E. Ergun, D. L. Newman et al., "Kinetic instabilities in the lunar wake: ARTEMIS observations," *Journal of Geophysical Research: Space Physics*, vol. 117, no. A3, p. A03106, 2012.
- [4] P. J. Kellogg, K. Goetz, S. J. Monson, J.-L. Bougeret, R. Manning, and M. L. Kaiser, "Observations of plasma waves during a traversal of the Moon's wake," *Geophysical Research Letters*, vol. 23, no. 10, pp. 1267–1270, 1996.
- [5] K. Hashimoto, M. Hashitani, Y. Kasahara et al., "Electrostatic solitary waves associated with magnetic anomalies and wake boundary of the Moon observed by KAGUYA," *Geophysical Research Letters*, vol. 37, no. 19, p. L19204, 2010.
- [6] M. M. Selim, A. El-Depsy, and E. F. El-Shamy, "Bifurcations of nonlinear ion-acoustic travelling waves in a multicomponent magnetoplasma with superthermal electrons," *Astrophysics and Space Science*, vol. 360, no. 66, 2015.
- [7] V. Pierrard and M. Lazar, "Kappa Distributions: theory and applications in space plasmas," *Solar Physics*, vol. 267, no. 1, p. 153174, 2010.
- [8] N. S. Saini, I. Kourakis, and M. A. Hellberg, "Arbitrary amplitude ion-acoustic solitary excitations in the presence of excess superthermal electrons," *Physics of Plasmas*, vol. 16, no. 6, Article ID 062903, 2009.
- [9] S. Devanandhan, S. V. Singh, and G. S. Lakhina, "Electron acoustic solitary waves with kappa-distributed electrons," *Physica Scripta*, vol. 84, no. 2, Article ID 025507, 2011.
- [10] H. Natiq, M. Said, M. Ariffin, S. He, L. Rondoni, and S. Banerjee, "Self-excited and hidden attractors in a novel chaotic system with complicated multistability," *The European Physical Journal Plus*, vol. 133, no. 12, p. 557, 2018.
- [11] H. Natiq, M. R. M. Said, N. M. G. Al-Saidi, and A. Kilicman, "Dynamics and complexity of a new 4d chaotic laser system," *Entropy*, vol. 21, no. 1, p. 34, 2019.
- [12] H. Natiq, S. Banerjee, A. P. Misra, and M. R. M. Said, "Degenerating the butterfly attractor in a plasma perturbation model using nonlinear controllers," *Chaos, Solitons & Fractals*, vol. 122, pp. 58–68, 2019.
- [13] F. T. Arecchi, R. Meucci, G. Puccioni, and J. Tredicce, "Experimental evidence of subharmonic bifurcations, multistability, and turbulence in aQ-switched gas laser," *Physical Review Letters*, vol. 49, no. 17, pp. 1217–1220, 1982.
- [14] H. Natiq, S. Banerjee, S. He, M. Said, and A. Kilicman, "Designing an m-dimensional nonlinear model for producing hyperchaos," *Chaos, Solitons & Fractals*, vol. 114, pp. 506–515, 2018.
- [15] H. Natiq, S. Banerjee, M. Ariffin, and M. Said, "Can hyperchaotic maps with high complexity produce multistability?" *Chaos: An Interdisciplinary Journal of Nonlinear Science*, vol. 29, no. 1, Article ID 011103, 2019.
- [16] A. E. Dubinov, D. Y. Kolotkov, and M. A. Sazonkin, "Supernonlinear waves in plasma," *Plasma Physics Reports*, vol. 38, no. 10, pp. 833–844, 2012.
- [17] A. E. Dubinov and D. Y. Kolotkov, "Above the weak nonlinearity: super-nonlinear waves in astrophysical and laboratory plasmas," *Reviews of Modern Plasma Physics*, vol. 2, no. 1, p. 2, 2018.
- [18] T. Hada, C. F. Kennel, and B. Buti, "Stationary nonlinear Alfvén waves and solitons," *Journal of Geophysical Research*, vol. 94, no. A1, p. 65, 1989.
- [19] J. Tamang and A. Saha, "Dynamical behavior of supernonlinear positron-acoustic periodic waves and chaos in non-extensive electron-positron-ion plasmas," *Zeitschrift für Naturforschung A*, vol. 74, no. 6, pp. 499–511, 2019.
- [20] S. V. Singh and G. S. Lakhina, "Ion-acoustic supersolitons in the presence of non-thermal electrons," *Communications in Nonlinear Science and Numerical Simulation*, vol. 23, no. 1–3, pp. 274–281, 2015.
- [21] A. Saha, P. Chatterjee, and C. S. Wong, "Dynamic motions of ion acoustic waves in plasmas with superthermal electrons," *Brazilian Journal of Physics*, vol. 45, no. 6, pp. 656–663, 2015.
- [22] L. Mandi, A. Saha, and P. Chatterjee, "Dynamics of ion-acoustic waves in Thomas-Fermi plasmas with source term," *Advances in Space Research*, vol. 64, no. 2, pp. 427–435, 2019.
- [23] G. A. Gottwald and I. Melbourne, "A new test for chaos in deterministic systems," *Proceedings of the Royal Society of London. Series A: Mathematical, Physical and Engineering Sciences*, vol. 460, no. 2042, pp. 603–611, 2004.
- [24] G. A. Gottwald and I. Melbourne, "Comment on 'reliability of the 0-1 test for chaos'," *Physical Review E*, vol. 77, no. 2, Article ID 028201, 2008.
- [25] D. Eroglu, T. K. D. M. Peron, N. Marwan et al., "Entropy of weighted recurrence plots," *Physical Review E*, vol. 90, no. 4, Article ID 042919, 2014.
- [26] R. Rubia, S. V. Singh, and G. S. Lakhina, "Occurrence of electrostatic solitary waves in the lunar wake," *Journal of Geophysical Research: Space Physics*, vol. 122, no. 9, pp. 9134–9147, 2017.
- [27] A. Sen, S. Tiwari, S. Mishra, and P. Kaw, "Nonlinear wave excitations by orbiting charged space debris objects," *Advances in Space Research*, vol. 56, no. 3, pp. 429–435, 2015.
- [28] P. Chatterjee, R. Ali, and A. Saha, "Analytical solitary wave solution of the dust ion acoustic waves for the damped forced Korteweg-de Vries equation in superthermal plasmas," *Zeitschrift für Naturforschung A*, vol. 73, no. 2, pp. 151–159, 2018.
- [29] H. Zhen, B. Tian, H. Zhong, W. Sun, and M. Li, "Dynamics of the Zakharov-Kuznetsov-Burgers equations in dusty plasmas," *Physics of Plasmas*, vol. 20, no. 8, Article ID 082311, 2013.



## Research Article

# Symmetry Breaking Soliton, Breather, and Lump Solutions of a Nonlocal Kadomtsev–Petviashvili System

Hong-Yu Wu <sup>1,2</sup>, Jin-Xi Fei,<sup>1</sup> Zheng-Yi Ma <sup>3,4</sup>, Jun-Chao Chen <sup>3</sup>  
and Wen-Xiu Ma <sup>2,5,6,7,8,9</sup>

<sup>1</sup>Department of Photoelectric Engineering, Lishui University, Lishui 323000, China

<sup>2</sup>Department of Mathematics and Statistics, University of South Florida, Tampa, FL 33620-5700, USA

<sup>3</sup>Institute of Nonlinear Analysis and Department of Mathematics, Lishui University, Lishui 323000, China

<sup>4</sup>Department of Mathematics, Zhejiang Sci-Tech University, Hangzhou 310018, China

<sup>5</sup>Department of Mathematics, Zhejiang Normal University, Jinhua 321004, China

<sup>6</sup>Department of Mathematics, King Abdulaziz University, Jeddah, Saudi Arabia

<sup>7</sup>School of Mathematics, South China University of Technology, Guangzhou 510640, China

<sup>8</sup>College of Mathematics and Systems Science, Shandong University of Science and Technology, Qingdao 266590, Shandong, China

<sup>9</sup>Department of Mathematical Sciences, North-West University, Mafikeng Campus, Private Bag X2046, Mmabatho 2735, South Africa

Correspondence should be addressed to Hong-Yu Wu; why160@126.com and Wen-Xiu Ma; mawx@cas.usf.edu

Received 26 September 2019; Accepted 18 November 2019; Published 10 March 2020

Guest Editor: Sundarapandian Vaidyanathan

Copyright © 2020 Hong-Yu Wu et al. This is an open access article distributed under the Creative Commons Attribution License, which permits unrestricted use, distribution, and reproduction in any medium, provided the original work is properly cited.

The Kadomtsev–Petviashvili equation is one of the well-studied models of nonlinear waves in dispersive media and in multicomponent plasmas. In this paper, the coupled Alice–Bob system of the Kadomtsev–Petviashvili equation is first constructed via the parity with a shift of the space variable  $x$  and time reversal with a delay. By introducing an extended Bäcklund transformation, symmetry breaking soliton, symmetry breaking breather, and symmetry breaking lump solutions for this system are presented through the established Hirota bilinear form. According to the corresponding constants in the involved ansatz function, a few fascinating symmetry breaking structures of the presented explicit solutions are shown.

## 1. Introduction

The localized excitations in nonlinear evolution equations have been studied widely, which were originated from many scientific fields, such as fluid dynamics, plasma physics, superconducting physics, condensed matter physics, and optical problems. Explicitly, the inverse scattering method [1], the Darboux transformation and the Bäcklund transformation [2, 3], the Painlevé analysis approach [4–6], the Hirota bilinear method [7, 8], and the generalized bilinear method [9] are among important approaches for studying these structures, especially solitary waves and solitons.

Owing to the idea of the parity-time reversal (PT) symmetry, the nonlinear Schrödinger (NLS) equation

$$\begin{aligned}iA_t + A_{xx} \pm A^2B &= 0, \\ B &= \hat{f}A = \hat{P}\hat{C}A = A^*(-x, t),\end{aligned}\tag{1}$$

(where the operators  $\hat{P}$  and  $\hat{C}$  are the usual parity and charge conjugation) was introduced and investigated [10]. Based on this, the revolutionary works, which named the Alice–Bob (AB) systems to describe two-place physical problems, were made by Lou recently [11, 12]. The technical approach originated from the so-called  $\hat{P}$ - $\hat{T}$ - $\hat{C}$  principle with  $\hat{P}$  (the parity),  $\hat{T}$  (time reversal), and  $\hat{C}$  (charge conjugation) [11–25]. From this, a general Nth Darboux transformation for the AB-mKdV equation was constructed [13]. By using this Darboux transformation, some types of  $\hat{P}\hat{T}$  symmetry

breaking solutions including soliton and rogue wave solutions were explicitly obtained. Combined with their Hirota bilinear forms, prohibitions caused by nonlocality for nonlocal Boussinesq-KdV type systems were investigated [14]. The two/four-place nonlocal Kadomtsev–Petviashvili (KP) equation were also explicitly solved for special types of multiple soliton solutions via a  $\widehat{P}\widehat{T}\widehat{C}$  symmetric-antisymmetric separation approach [15]. From the viewpoint of physical phenomena in climate disasters, a special approximate solution was applied to theoretically capture the salient features of two correlated dipole blocking events in atmospheric dynamical systems and the original two-vortex interaction was given to describe two correlated dipole blocking events with a lifetime through the models established from the nonlinear inviscid dissipative and equivalent barotropic vorticity equation in a  $b$ -plane [21, 22]. Also, a concrete AB-KdV system established from the nonlinear inviscid dissipative and barotropic vorticity equation in a  $\beta$ -plane channel was applied to the two correlated monopole blocking events, which were responsible for the snow disaster in the winter of 2007/2008 that happened in Southern China [18]. Meanwhile, the expression

$$f = \sum_{\{y\}} K_{\{y\}} \cosh\left(\frac{1}{2} \sum_{i=1}^N \nu_i \xi_i\right), \quad (2)$$

plays a crucial role in constructing analytical group invariant multisoliton solutions of the AB systems, including the KdV-KP-Toda type, mKdV-sG type, NLS type, and discrete  $H_1$  type AB systems [11–16, 18].

In this paper, we consider the KP equation (3) as an illustrative example, which is one of the well-studied models of nonlinear waves in dispersive media [26, 27] and in multicomponent plasmas [28]. In the immovable laboratory coordinate frame, it can be presented in the form

$$(u_t + cu_x + \alpha uu_x + \beta u_{xxx})_x + \frac{c}{2} u_{yy} = 0, \quad (3)$$

where  $c$  is the velocity of long linear perturbations and  $\alpha$  and  $\beta$  are the nonlinear and dispersive coefficients which are determined by specific types of wave and medium properties.

The rest of this paper is organized as follows. In Section 2, an AB-KP system is constructed based on equation (3) and its Hirota bilinear form is presented through an extended Bäcklund transformation. In Section 3, symmetry breaking soliton, symmetry breaking breather, and symmetry breaking lump solutions are generated through the established Hirota bilinear form, according to the corresponding constants of the involved ansatz function. Some conclusions are given in the final section.

## 2. An AB-KP System and Its Bäcklund Transformation and Bilinear Form

Based on the principle of the AB system in Refs. [11, 12], after substituting  $u = 1/2(A + B)$  into equation (3), the AB-KP initial equation is

$$\begin{aligned} A_{xt} + B_{xt} + \frac{1}{2}\alpha(A_x + B_x)^2 + \left[c + \frac{1}{2}\alpha(A + B)\right](A_{xx} + B_{xx}) \\ + \beta(A_{xxxx} + B_{xxxx}) + \frac{c}{2}(A_{yy} + B_{yy}) = 0, \end{aligned} \quad (4)$$

which can be split into the coupled equations

$$\begin{aligned} A_{xt} + \frac{\alpha}{4}(A_x + B_x)^2 + cA_{xx} + \frac{\alpha}{4}(A + B)(A_{xx} + B_{xx}) \\ + \beta A_{xxxx} + \frac{c}{2}A_{yy} + G(A, B) = 0, \end{aligned} \quad (5a)$$

$$\begin{aligned} B_{xt} + \frac{\alpha}{4}(A_x + B_x)^2 + cB_{xx} + \frac{\alpha}{4}(A + B)(A_{xx} + B_{xx}) \\ + \beta B_{xxxx} + \frac{c}{2}B_{yy} - G(A, B) = 0, \end{aligned} \quad (5b)$$

where  $B$  is related to  $A$  through  $B = \widehat{P}_s^x \widehat{T}_d A = A(-x + x_0, y, -t + t_0)$  ( $\widehat{P}_s^x \widehat{T}_d$  expresses parity with a shift of the space variable  $x$  and time reversal with a delay), and  $G(A, B)$  is an arbitrary function of  $A$  and  $B$ , but should be  $\widehat{P}_s^x \widehat{T}_d$  invariant. That is,  $G(A, B) = \widehat{P}_s^x \widehat{T}_d G(A, B)$ . Although there are infinitely many functions satisfying this, we take a nontrivial function  $G(A, B)$  as

$$G(A, B) = \frac{\alpha}{2}(A_x^2 + AA_{xx} - B_x^2 - BB_{xx}), \quad (6)$$

at present, and equation (5) is reduced to the following AB-KP system:

$$\begin{aligned} A_{xt} + \frac{\alpha}{4}(A_x + B_x)(3A_x - B_x) + \frac{\alpha}{4}(A - B)B_{xx} \\ + \left[\frac{\alpha}{4}(3A + B) + c\right]A_{xx} + \beta A_{xxxx} + \frac{c}{2}A_{yy} = 0, \end{aligned} \quad (7a)$$

$$\begin{aligned} B_{xt} - \frac{\alpha}{4}(A_x + B_x)(A_x - 3B_x) - \frac{\alpha}{4}(A - B)A_{xx} \\ + \left[\frac{\alpha}{4}(A + 3B) + c\right]B_{xx} + \beta B_{xxxx} + \frac{c}{2}B_{yy} = 0. \end{aligned} \quad (7b)$$

In fact, this AB-KP system can also be derived as a special reduction of the coupled KP system:

$$\begin{aligned} [A_t + (c_1 A + c_2 B)_x + (c_3 A + c_4 B)_{xxx} + (c_5 A + c_6 B)A_x \\ + (c_7 A + c_8 B)B_x]_x + c_9 A_{yy} = 0, \end{aligned} \quad (8a)$$

$$\begin{aligned} [B_t + (c_1 B + c_2 A)_x + (c_3 B + c_4 A)_{xxx} + (c_5 B + c_6 A)B_x \\ + (c_7 B + c_8 A)A_x]_x + c_9 B_{yy} = 0, \end{aligned} \quad (8b)$$

by taking the reduction condition  $B = \widehat{P}_s^x \widehat{T}_d A = A(-x + x_0, y, -t + t_0)$  and letting the arbitrary constants  $c_i$  ( $i = 1, 2, \dots, 9$ ) with

$$\begin{aligned}
c_1 &= c, \\
c_2 &= c_4 = 0, \\
c_3 &= \beta, \\
c_5 &= \frac{3\alpha}{4}, \\
c_6 &= c_7 = \frac{\alpha}{4}, \\
c_8 &= -\frac{\alpha}{4}, \\
c_9 &= \frac{c}{2}.
\end{aligned} \tag{9}$$

Now, we introduce an extended Bäcklund transformation:

$$\begin{aligned}
A &= \frac{12\beta}{\alpha}(\ln f)_{xx} + b_1(\ln f)_{xxx} + b_2(\ln f)_{xxt}, \\
B &= \frac{12\beta}{\alpha}(\ln f)_{xx} - b_1(\ln f)_{xxx} - b_2(\ln f)_{xxt},
\end{aligned} \tag{10}$$

where  $b_1$  and  $b_2$  are arbitrary constants and  $f \equiv f(x, y, t)$  is a new function of variables  $x, y$ , and  $t$ , satisfying the invariant condition

$$f(x, y, t) = \widehat{P}_s^x \widehat{T}_d f(x, y, t) = f(-x + x_0, y, -t + t_0). \tag{11}$$

When  $b_1 = 0$  and  $b_2 = 0$ , equation (10) becomes the standard Bäcklund transformation of equation (3). Substituting the transformation equation (10) into equation (7), we obtain a bilinear form of equation (7) as follows:

$$\left(D_x D_t + c D_x^2 + \beta D_x^4 + \frac{c}{2} D_y^2\right)(f \cdot f) = 0, \tag{12}$$

where  $D_x^4$  and  $D_y^2$  are the Hirota bilinear derivative operators defined by [7, 8]

$$\begin{aligned}
D_x^m D_y^n D_t^l (f \cdot g) &= \left(\frac{\partial}{\partial x} - \frac{\partial}{\partial x'}\right)^m \left(\frac{\partial}{\partial y} - \frac{\partial}{\partial y'}\right)^n \left(\frac{\partial}{\partial t} - \frac{\partial}{\partial t'}\right)^l \\
&\times f(x, y, t) g(x', y', t') \Big|_{x'=x, y'=y', t'=t}.
\end{aligned} \tag{13}$$

According to the properties of the Hirota bilinear operator, equation (12) reads

$$\begin{aligned}
2(ff_{xt} - f_x f_t) + 2c(ff_{xx} - f_x^2) \\
+ 2\beta(ff_{xxxx} - 4f_x f_{xxx} + 3f_{xx}^2) + c(ff_{yy} - f_y^2) = 0,
\end{aligned} \tag{14}$$

which is also the Hirota bilinear form of equation (3).

As we know, the Hirota bilinear method is direct and effective for constructing exact solutions, in which a given nonlinear equation is converted to a bilinear form through an appropriate transformation. With different types of ansatz for the auxiliary function, a variety of soliton, rational,

and periodic solutions of the nonlinear equation can be derived.

### 3. Symmetry Breaking Soliton, Breather, and Lump Solutions

In this section, we turn our attention to the Hirota bilinear form (12) of the AB-KP systems (7a) and (7b) to derive symmetry breaking soliton, symmetry breaking breather, and symmetry breaking lump solutions.

**3.1. Symmetry Breaking Soliton Solutions.** Based on the bilinear form (12), we can first determine symmetry breaking soliton solutions through the Bäcklund transformation (10) of the AB-KP systems (7a) and (7b) with the function  $f$  being written as a summation of some special functions [11–16, 18]:

$$\begin{aligned}
f &= f_N = \sum_{\{\nu\}} K_{\{\nu\}} \cosh\left(\frac{1}{2} \sum_{i=1}^N \nu_i \xi_i\right), \\
\xi_i &= k_i \left[ \left(x - \frac{x_0}{2}\right) + p_i y - \left(c + k_i^2 \beta + \frac{c p_i^2}{2}\right) \left(t - \frac{t_0}{2}\right) \right] + \eta_{i0},
\end{aligned} \tag{15}$$

where  $\{\nu\} = \{\nu_1, \nu_2, \dots, \nu_N\}$ , with  $\nu_i = \pm 1$ , and  $k_i, p_i, \eta_{i0}$  ( $i = 1, 2, \dots, N$ ),  $c, x_0$ , and  $t_0$  are undetermined constants, while

$$K_{\{\nu\}} = \prod_{i < j}^N \sqrt{c(p_i - p_j)^2 - 6\beta(k_i - \nu_i \nu_j k_j)^2}. \tag{16}$$

For  $N = 1$ , equation (15) takes the form

$$\begin{aligned}
f &= f_1 = \cosh\left(\frac{\xi_1}{2}\right), \\
\xi_1 &= k_1 \left[ \left(x - \frac{x_0}{2}\right) + p_1 y - \left(c + k_1^2 \beta + \frac{c p_1^2}{2}\right) \left(t - \frac{t_0}{2}\right) \right] + \eta_{10}.
\end{aligned} \tag{17}$$

However, the invariant condition (11) of this function  $f$  (17) is not satisfied for the constants  $k_1, p_1, c, x_0, t_0$ , and  $\eta_{10}$  being not all zero. It means that it is impossible to get any nontrivial symmetry breaking single soliton solution of equation (12) through (10).

The same circumstance happens when  $N = 3$ , in which the function  $f$  of equation (15) is

$$\begin{aligned}
f &= f_3 = K_{\emptyset} \cosh\left\{\frac{1}{2}(\xi_1 + \xi_2 + \xi_3)\right\} \\
&+ K_{\{1\}} \cosh\left\{\frac{1}{2}(\xi_1 - \xi_2 - \xi_3)\right\} \\
&+ K_{\{2\}} \cosh\left\{\frac{1}{2}(\xi_1 - \xi_2 + \xi_3)\right\} \\
&+ K_{\{3\}} \cosh\left\{\frac{1}{2}(\xi_1 + \xi_2 - \xi_3)\right\},
\end{aligned} \tag{18}$$

where

$$\begin{aligned} K_{\emptyset} &= a_{12}^- a_{13}^- a_{23}^-, \\ K_{\{1\}} &= a_{12}^+ a_{13}^+ a_{23}^-, \\ K_{\{2\}} &= a_{12}^+ a_{13}^- a_{23}^+, \\ K_{\{3\}} &= a_{12}^- a_{13}^+ a_{23}^+, \end{aligned} \quad (19a)$$

$$\begin{aligned} \xi_i &= k_i \left[ \left( x - \frac{x_0}{2} \right) + p_i y - \left( c + k_i^2 \beta + \frac{c p_i^2}{2} \right) \left( t - \frac{t_0}{2} \right) \right] + \eta_{i0}, \\ a_{ij}^\pm &= \sqrt{c(p_i - p_j)^2 - 6\beta(k_i \pm k_j)^2}, \quad i, j = 1, 2, 3. \end{aligned} \quad (19b)$$

Furthermore, one can verify that, for any odd  $N = 2n - 1$  ( $n$  is a positive integer), the function  $f$  (15) does not satisfy the invariant condition in equation (11). In other words, symmetry breaking soliton solutions of odd orders for the AB-KP systems (7a) and (7b) are prohibited.

For  $N = 2$ , equation (15) becomes

$$f = f_2 = K_{\emptyset} \cosh\left(\frac{\xi_1 + \xi_2}{2}\right) + K_{\{1\}} \cosh\left(\frac{\xi_1 - \xi_2}{2}\right), \quad (20)$$

where

$$\begin{aligned} K_{\emptyset} &= \sqrt{c(p_1 - p_2)^2 - 6\beta(k_1 - k_2)^2}, \\ K_{\{1\}} &= \sqrt{c(p_1 - p_2)^2 - 6\beta(k_1 + k_2)^2}. \end{aligned} \quad (21)$$

By fixing the real parameters,

$$\begin{aligned} k_2 &= \pm k_1, \\ p_2 &= -p_1, \\ \eta_{20} &= \mp \eta_{10}, \end{aligned} \quad (22)$$

the invariant condition in equation (11) is satisfied. Correspondingly, by writing

$$\begin{aligned} f = f_2 &= \sqrt{c p_1^2} \cosh\left\{ k_1 \left[ \left( x - \frac{x_0}{2} \right) - \left( c + k_1^2 \beta + \frac{c p_1^2}{2} \right) \left( t - \frac{t_0}{2} \right) \right] \right\} \\ &+ \sqrt{c p_1^2 - 6\beta k_1^2} \cosh(k_1 p_1 y + \eta_{10}), \end{aligned} \quad (23)$$

a symmetry breaking two-soliton solution of equations (7a) and (7b) are expressed as

$$\begin{aligned} A &= \frac{12\beta}{\alpha} (\ln f_2)_{xx} + b_1 (\ln f_2)_{xxx} + b_2 (\ln f_2)_{xxt}, \\ B &= \frac{12\beta}{\alpha} (\ln f_2)_{xx} - b_1 (\ln f_2)_{xxx} - b_2 (\ln f_2)_{xxt}. \end{aligned} \quad (24)$$

Figure 1 shows the symmetry breaking two-soliton structure of solution (24) with the parameters being taken as

$$\begin{aligned} \alpha &= k_1 = p_1 = 1, \\ \beta &= \frac{1}{6}, \\ c &= 4, \\ x_0 &= t_0 = \eta_{10} = 0. \end{aligned} \quad (25)$$

Meanwhile, Figure 1(a) describes a standard two-soliton structure ( $b_1 = b_2 = 0$ ) for solution (24) at time  $t = 0$ . Under this special condition, the solution  $A$  coincides with the solution  $B$  exactly. Figures 1(b) and 1(c) are two symmetry breaking two-soliton structures for solution (24) with the selected parameters  $b_1 = b_2 = 10$  at time  $t = 0$ . Obviously, Figure 1(c) depicts a reversal structure of Figure 1(b) by the solution  $B$  which is  $\widehat{P}_s^x \widehat{T}_d$  symmetry of the solution  $A$  for the AB-KP systems (7a) and (7b). This corresponds to the phenomenon that the shifted parity and delayed time reversal are applied to describe two-place events [11, 12]. These structures are realized via the symbolic computation software Maple efficiently.

For  $N = 4$ , the function  $f$  of equation (15) can be rewritten regularly as

$$\begin{aligned} f = f_4 &= K_{\emptyset} \cosh\left\{ \frac{1}{2} (\xi_1 + \xi_2 + \xi_3 + \xi_4) \right\} + K_{\{1\}} \cosh\left\{ \frac{1}{2} (-\xi_1 + \xi_2 + \xi_3 + \xi_4) \right\} \\ &+ K_{\{2\}} \cosh\left\{ \frac{1}{2} (\xi_1 - \xi_2 + \xi_3 + \xi_4) \right\} + K_{\{3\}} \cosh\left\{ \frac{1}{2} (\xi_1 + \xi_2 - \xi_3 + \xi_4) \right\} \\ &+ K_{\{4\}} \cosh\left\{ \frac{1}{2} (\xi_1 + \xi_2 + \xi_3 - \xi_4) \right\} + K_{\{23\}} \cosh\left\{ \frac{1}{2} (\xi_1 - \xi_2 - \xi_3 + \xi_4) \right\} \\ &+ K_{\{24\}} \cosh\left\{ \frac{1}{2} (\xi_1 - \xi_2 + \xi_3 - \xi_4) \right\} + K_{\{34\}} \cosh\left\{ \frac{1}{2} (\xi_1 + \xi_2 - \xi_3 - \xi_4) \right\}, \end{aligned} \quad (26)$$

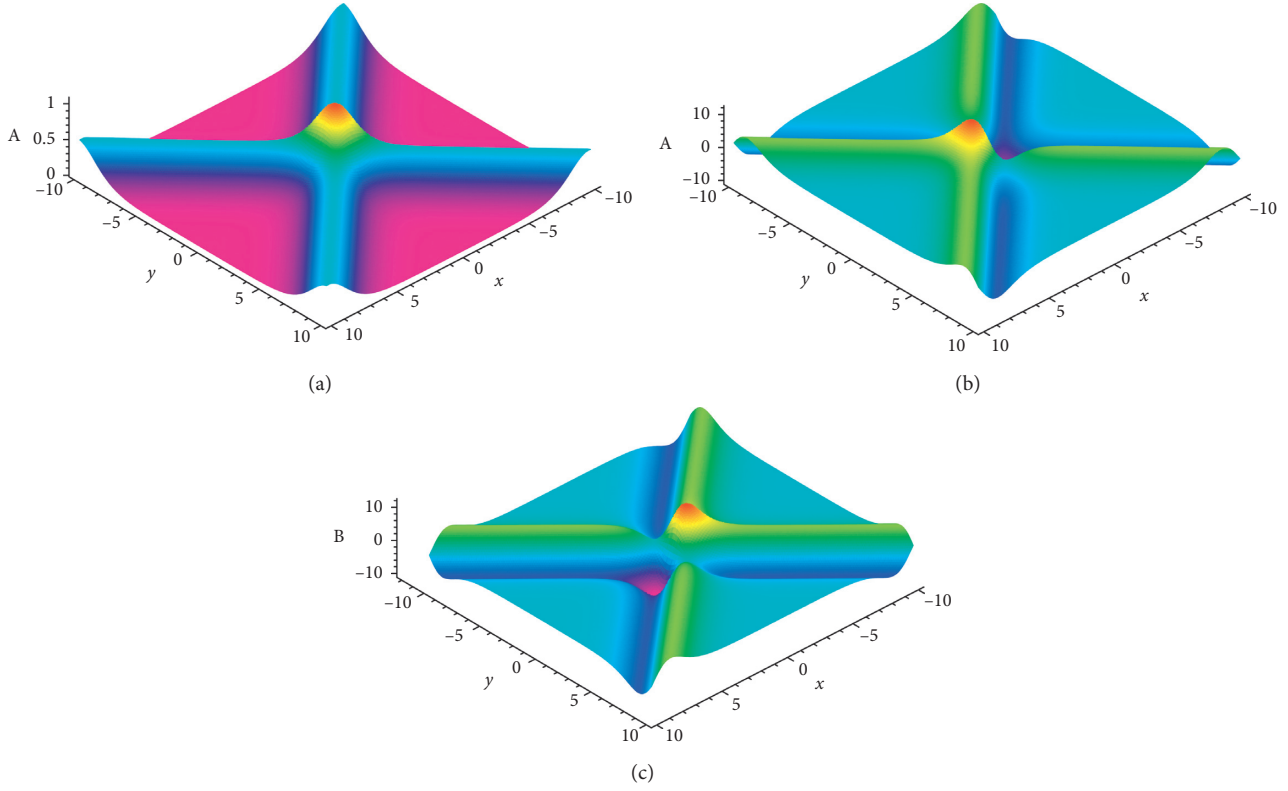


FIGURE 1: The symmetry breaking two-soliton solution (24) of the AB-KP systems (7a) and (7b), with the selecting parameters  $b_1$  and  $b_2$  are (a)  $b_1 = b_2 = 0$  and (b) and (c)  $b_1 = b_2 = 10$ , at time  $t = 0$ .

where

$$\begin{aligned}
 K_{\{\}} &= a_{12}^- a_{13}^- a_{14}^- a_{23}^- a_{24}^- a_{34}^-, \\
 K_{\{1\}} &= a_{12}^+ a_{13}^+ a_{14}^+ a_{23}^- a_{24}^- a_{34}^-, \\
 K_{\{2\}} &= a_{12}^+ a_{13}^- a_{14}^- a_{23}^+ a_{24}^+ a_{34}^-, \\
 K_{\{3\}} &= a_{12}^- a_{13}^+ a_{14}^- a_{23}^+ a_{24}^- a_{34}^+, \\
 K_{\{4\}} &= a_{12}^- a_{13}^- a_{14}^+ a_{23}^- a_{24}^+ a_{34}^+, \\
 K_{\{23\}} &= a_{12}^+ a_{13}^+ a_{14}^- a_{23}^+ a_{24}^+ a_{34}^+, \\
 K_{\{24\}} &= a_{12}^+ a_{13}^- a_{14}^+ a_{23}^+ a_{24}^- a_{34}^+, \\
 K_{\{34\}} &= a_{12}^- a_{13}^+ a_{14}^+ a_{23}^+ a_{24}^- a_{34}^-.
 \end{aligned}$$

$$\xi_i = k_i \left[ \left( x - \frac{x_0}{2} \right) + p_i y - \left( c + k_i^2 \beta + \frac{c p_i^2}{2} \right) \left( t - \frac{t_0}{2} \right) \right] + \eta_{i0},$$

$$a_{ij}^\pm = \sqrt{c(p_i - p_j)^2 - 6\beta(k_i \pm k_j)^2}, \quad i, j = 1, 2, 3, 4. \quad (27)$$

After finishing some detailed analysis, there are two independent real parameter selections of the symmetry breaking four-soliton solution for (7a) and (7b), which are

$$\begin{aligned}
 k_3 &= \pm k_1, \\
 k_4 &= \pm k_2, \\
 p_3 &= -p_1, \\
 p_4 &= -p_2, \\
 \eta_{30} &= \mp \eta_{10}, \\
 \eta_{40} &= \mp \eta_{20},
 \end{aligned} \quad (28)$$

with  $B = \widehat{P}_s \widehat{T}_d A = A(-x + x_0, y = y, -t + t_0)$ . Based on these restrictions in (28), we have

$$\begin{aligned}
 a_{23}^\pm &= a_{14}^\pm, \\
 a_{34}^\pm &= a_{12}^\pm, \\
 K_{\{3\}} &= K_{\{1\}}, \\
 K_{\{4\}} &= K_{\{2\}}.
 \end{aligned} \quad (29)$$

At this time, the symmetry breaking four-soliton solution of the AB-KP systems (7a) and (7b) is

$$A = \frac{12\beta}{\alpha} (\ln f_4)_{xx} + b_1 (\ln f_4)_{xxx} + b_2 (\ln f_4)_{xxt}, \quad (30)$$

$$B = \frac{12\beta}{\alpha} (\ln f_4)_{xx} - b_1 (\ln f_4)_{xxx} - b_2 (\ln f_4)_{xxt},$$

where

$$\begin{aligned}
f_4 = & K_{\{1\}} \cosh(\zeta_1^+ + \zeta_2^+) + K_{\{1\}} [\cosh(\zeta_1^- + \zeta_2^-) + \cosh(\zeta_1^- - \zeta_2^+)] \\
& + K_{\{2\}} [\cosh(\zeta_1^+ + \zeta_2^-) + \cosh(\zeta_1^+ - \zeta_2^-)] \\
& + K_{\{23\}} \cosh(\zeta_1^- - \zeta_2^-) + K_{\{24\}} \cosh(\zeta_1^+ - \zeta_2^+) \\
& + K_{\{34\}} \cosh(\zeta_1^- + \zeta_2^-),
\end{aligned} \tag{31}$$

with

$$\begin{aligned}
\zeta_1^\pm &= \frac{1}{2} (\xi_1 \pm \xi_3), \\
\zeta_2^\pm &= \frac{1}{2} (\xi_2 \pm \xi_4).
\end{aligned} \tag{32}$$

If setting  $\alpha = k_1 = p_1 = 1, \beta = 1/6, c = -5, k_2 = -p_2 = 6/5$ , and  $x_0 = t_0 = \eta_{10} = \eta_{20} = 0$ , we can depict the abovementioned symmetry breaking four-soliton structure in (Figure 2). The similar situation is as follows: Figure 2(a) is the standard four-soliton structure ( $b_1 = b_2 = 0$ ) for the solution  $A = B$  at time  $t = 0$ . Figures 2(b) and 2(c) are two symmetry breaking four-soliton structures for the solution  $A$  and  $B$ , respectively, with the selected parameters  $b_1 = b_2 = 10$  at time  $t = 0$ .

**3.2. Symmetry Breaking Breather Solutions.** When taking  $p_1 = p_0 I$  ( $p_0$  is a real constant and  $I$  is the imaginary unit,  $I^2 = -1$ ), a symmetry breaking breather solution of the AB-KP systems (7a) and (7b) can read

$$A = \frac{12\beta}{\alpha} (\ln f_b)_{xx} + b_1 (\ln f_b)_{xxx} + b_2 (\ln f_b)_{xxt}, \tag{33}$$

$$B = \widehat{P}_s^x \widehat{T}_d A = A(-x + x_0, y, -t + t_0),$$

with the ansatz function

$$\begin{aligned}
f = f_b = & \sqrt{-c p_0^2} \cosh \left\{ k_1 \left[ \left( x - \frac{x_0}{2} \right) - \left( c + k_1^2 \beta - \frac{c p_0^2}{2} \right) \left( t - \frac{t_0}{2} \right) \right] \right\} \\
& + \sqrt{-c p_0^2 - 6\beta k_1^2} \cosh(k_1 p_0 I y + \eta_{10}),
\end{aligned} \tag{34}$$

from equation (23).

By some constraints to the parameters in this solution, a family of analytical breather solutions can be generated. For example, when taking the real constants

$$\begin{aligned}
c &= -4, \\
\alpha &= k_1 = 1, \\
\beta &= \frac{1}{6}, \\
p_0 &= 2, \\
x_0 = t_0 = \eta_{10} &= 0,
\end{aligned} \tag{35}$$

equation (34) becomes

$$f = f_b = 4 \cosh \left( x - \frac{25}{6} t \right) + \sqrt{15} \cos(2y), \tag{36}$$

according to Euler's formula. This function indicates that the solution has two wave components, that is, a regular solitary wave with the propagating speed  $-25/6$  and a periodic wave with period  $\pi$ . Figure 3 is a density plot of the breathers defined by equation (36) with the parameters in (35). Figure 3(a) is the standard first-order breather structure ( $b_1 = b_2 = 0$ ) for the solution  $A = B = 8(\sqrt{15} \cos(2y) \cosh x + 4) / (4 \cosh x + \sqrt{15} \cos(2y))^2$  at time  $t = 0$ . Figures 3(b) and 3(c) are two symmetry breaking breather structures for the solution  $A, B = 8(\sqrt{15} \cos(2y) \cosh x + 4) / (4 \cosh x + \sqrt{15} \cos(2y))^2 \pm 95 \sinh x (32 + 4\sqrt{15} \cos(2y) \cosh x - 15 \cos^2(2y)) / (4 \cosh x + \sqrt{15} \cos(2y))^3$ , with the selected parameters  $b_1 = b_2 = 10$  at time  $t = 0$ . As these solutions combine the trigonometric cosine function with hyperbolic sine/cosine functions, the property of these functions describes the symmetry breaking breather structures [29, 30].

In the abovementioned situation, when taking the constants

$$\begin{aligned}
c &= -4, \\
\alpha &= 1, \\
\beta &= \frac{1}{6}, \\
k_1 &= I, \\
p_0 &= 2, \\
x_0 = t_0 = \eta_{10} &= 0,
\end{aligned} \tag{37}$$

equation (34) has the expression

$$f = f_b = \sqrt{16} \cos \left( x - \frac{23}{6} t \right) + \sqrt{17} \cosh(2y). \tag{38}$$

Figure 4 is a density plot of the breathers described according to equation (38) under the parameter selection (37). That is, when the parameter  $k_1$  also takes the imaginary unit  $I$ , the  $x$ -periodic symmetry breaking breathers of the AB-KP systems (7a) and (7b) are formed.

The abovementioned idea can be extended to solution (30). After setting the parameters

$$\begin{aligned}
c &= -5, \\
\alpha &= k_1 = 1, \\
\beta &= \frac{1}{6}, \\
k_2 &= \frac{1}{2}, \\
p_1 &= I, \\
p_2 &= -2I, \\
x_0 = t_0 = \eta_{10} = \eta_{20} &= 0, \\
c &= -4, \\
\alpha &= 1, \\
\beta &= \frac{1}{6}, \\
k_1 = p_1 = -p_2 &= I, \\
k_2 &= -2I, \\
x_0 = t_0 = \eta_{10} = \eta_{20} &= 0,
\end{aligned} \tag{39}$$



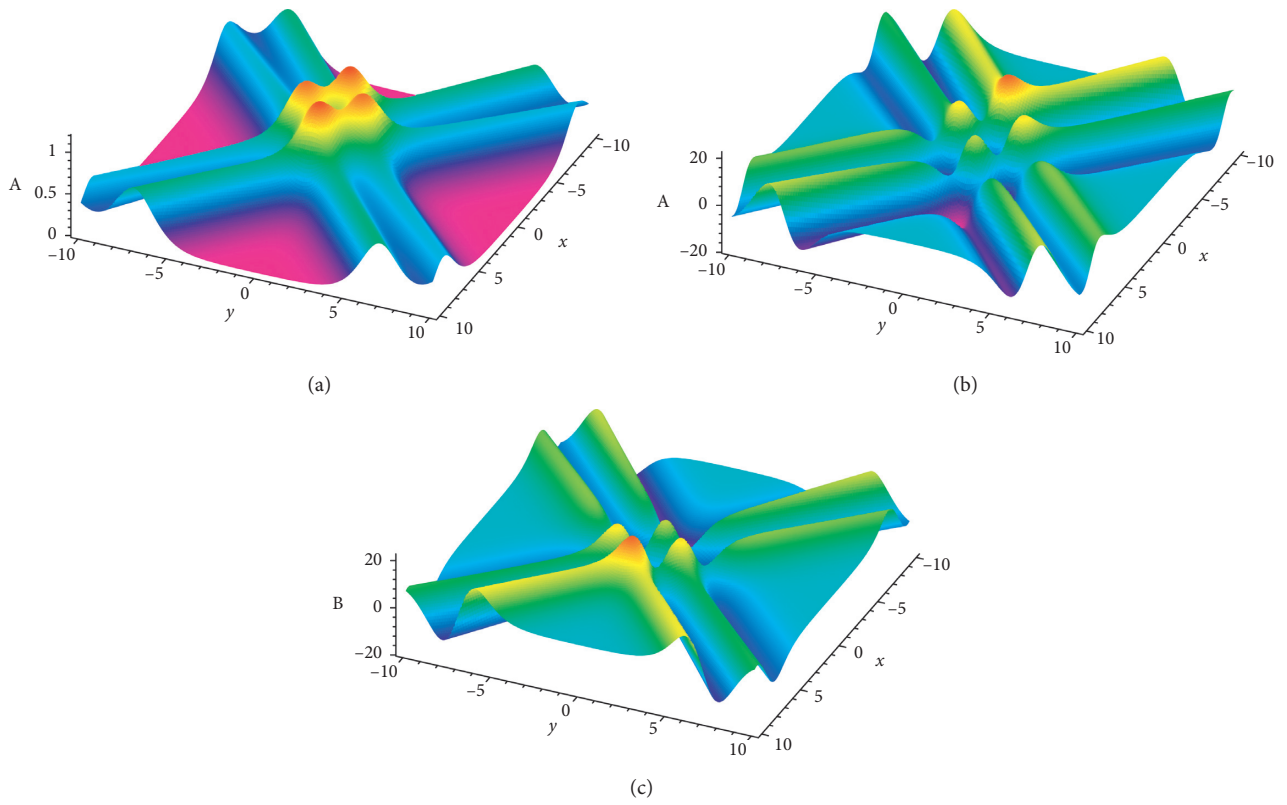


FIGURE 2: The symmetry breaking four-soliton solution (30) of the AB-KP systems (7a) and (7b), with the selecting parameters  $b_1$  and  $b_2$  are (a)  $b_1 = b_2 = 0$  and (b) and (c)  $b_1 = b_2 = 10$ , at time  $t = 0$ .

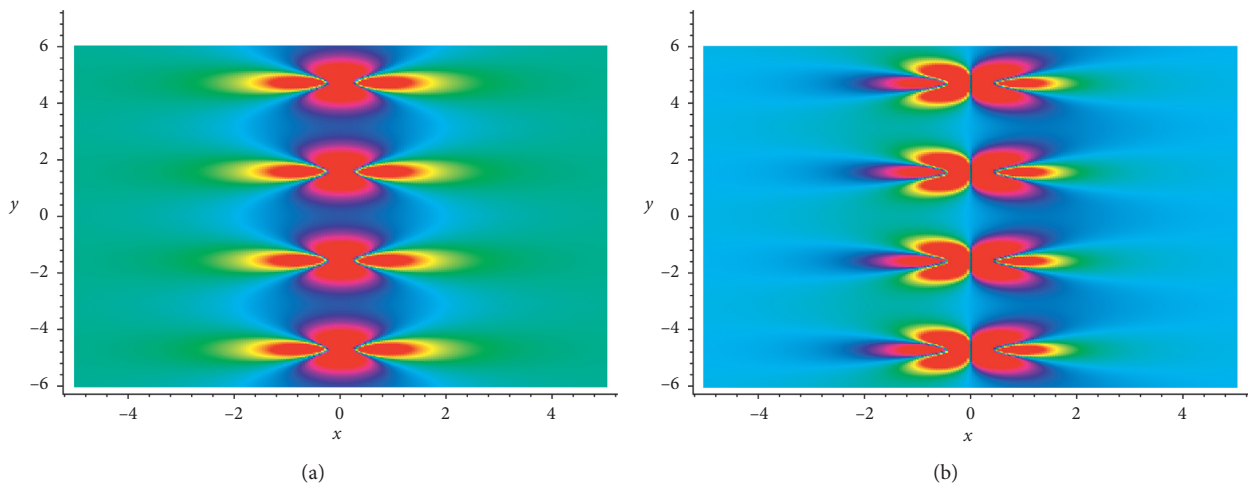


FIGURE 3: Continued.

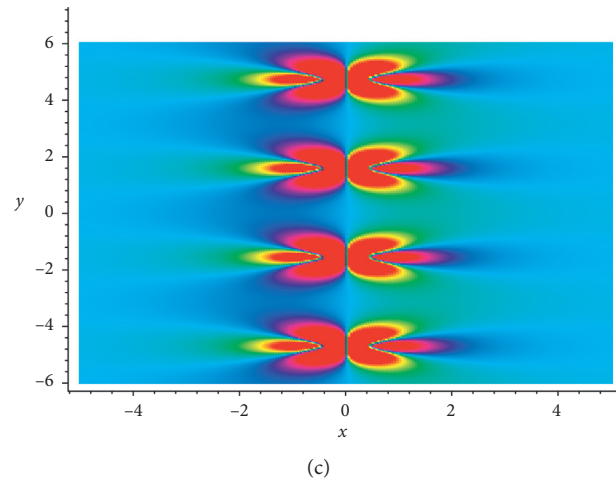


FIGURE 3: The density plot of the  $y$ -periodic symmetry breaking breathers of the AB-KP systems (7a) and (7b), with the selected parameters  $b_1$  and  $b_2$  are (a)  $b_1 = b_2 = 0$  and (b) and (c)  $b_1 = b_2 = 10$ , at time  $t = 0$ .

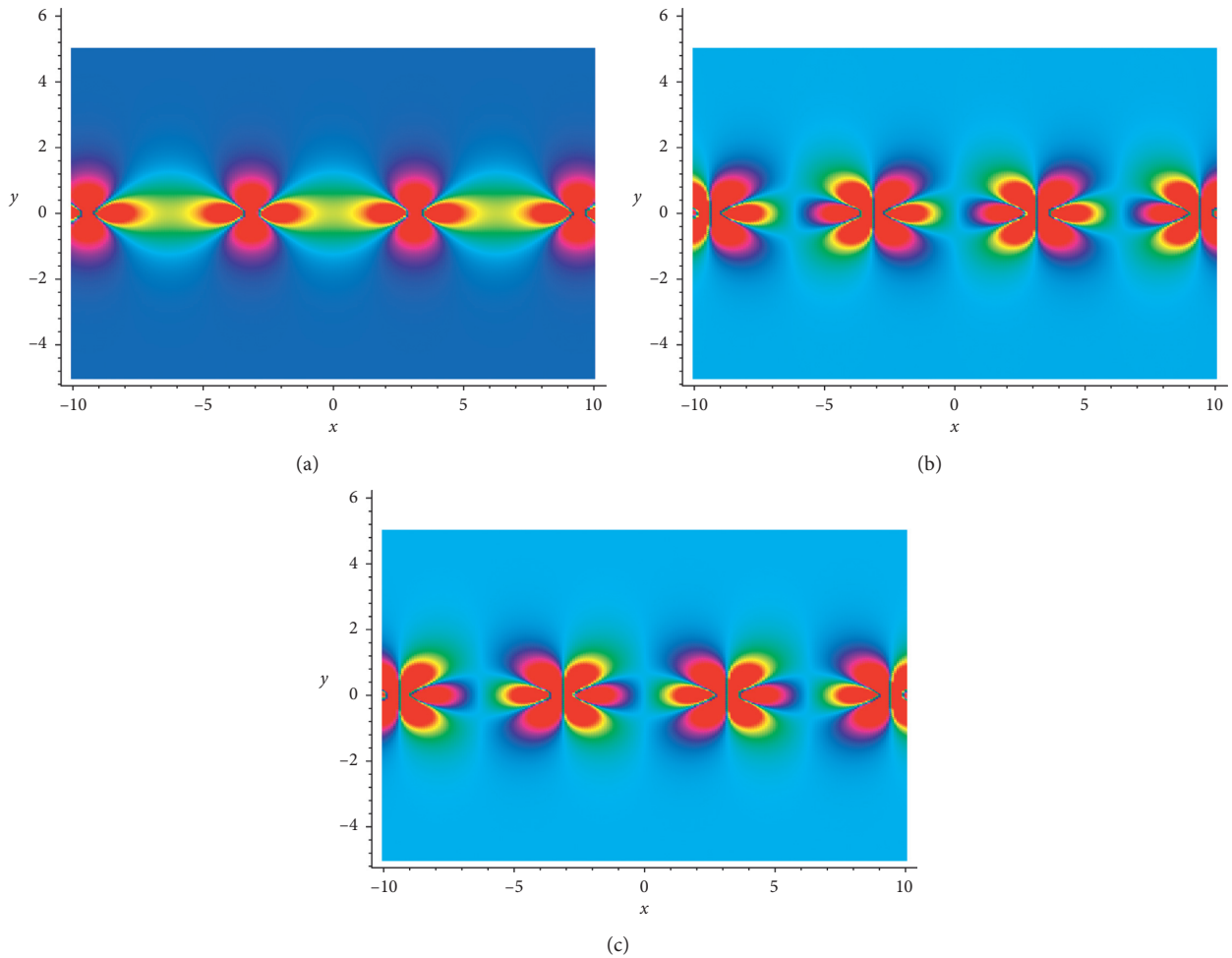


FIGURE 4: The density plot of the  $x$ -periodic symmetry breaking breather of the AB-KP systems (7a) and (7b), with the selected parameters  $b_1$  and  $b_2$  are (a)  $b_1 = b_2 = 0$  and (b) and (c)  $b_1 = b_2 = 10$ , at time  $t = 0$ .

the  $y$ -periodic and  $x$ -periodic second-order breather solutions can be derived, which are symmetry breaking (Figures 5 and 6, respectively).

**3.3. Symmetry Breaking Lump Solutions.** As we know, the lump solution is expressed by the rational function which is localized in all directions in the space. Based on the long-wave

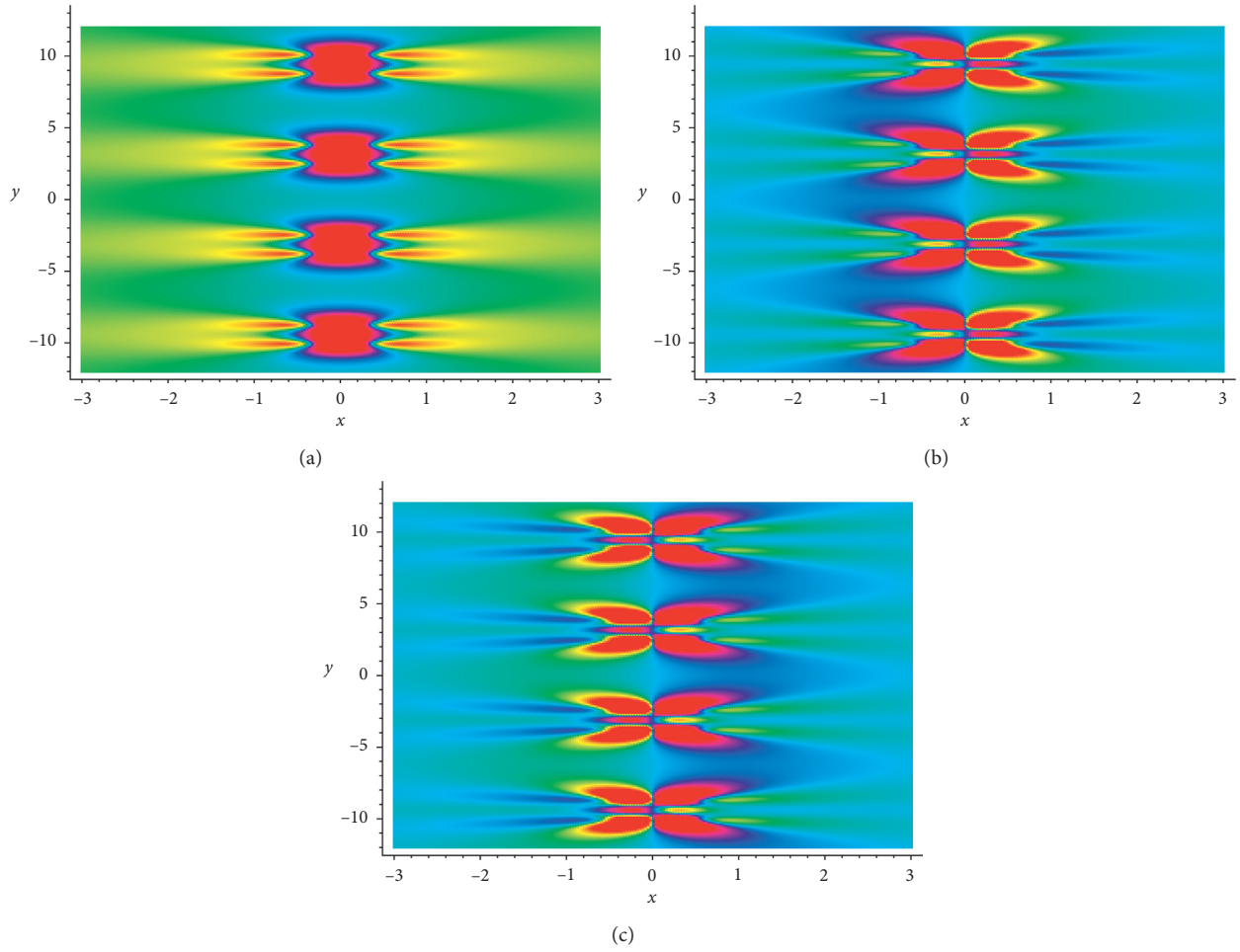


FIGURE 5: The  $y$ -periodic symmetry breaking density plot of the second-order breathers of the AB-KP systems (7a) and (7b), with the selected parameters  $b_1$  and  $b_2$  are (a)  $b_1 = b_2 = 0$  and (b) and (c)  $b_1 = b_2 = 10$ , at time  $t = 0$ .

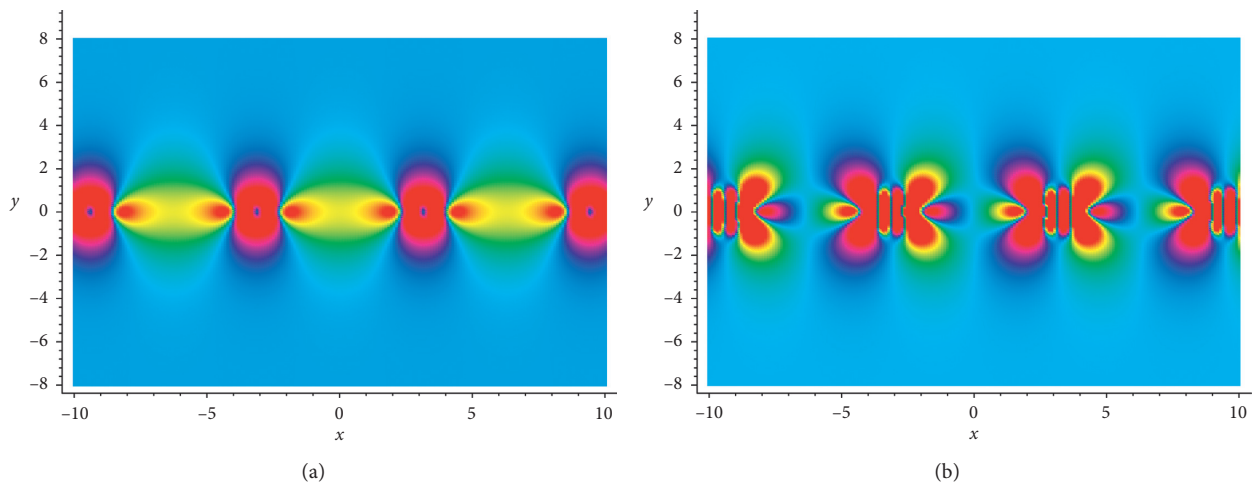


FIGURE 6: Continued.

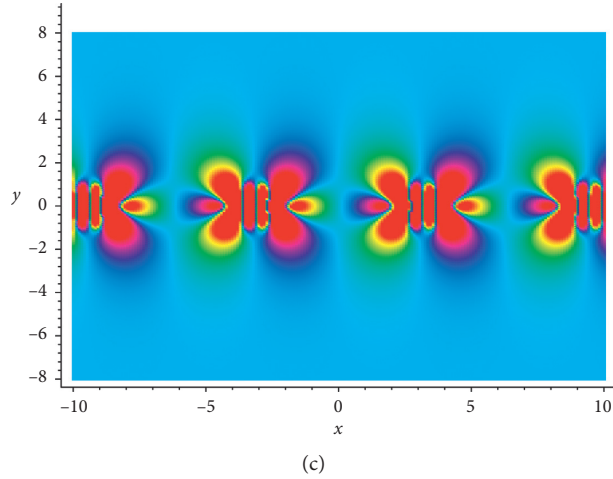


FIGURE 6: The  $x$ -periodic symmetry breaking density plot of the second-order breathers of the AB-KP systems (7a) and (7b), with the selected parameters  $b_1$  and  $b_2$  are (a)  $b_1 = b_2 = 0$  and (b) and (c)  $b_1 = b_2 = 10$ , at time  $t = 0$ .

limit idea of generating lump solutions to nonlinear equations, we derive this kind of solutions of the AB-KP systems (7a) and (7b) by taking a long-wave limit. After putting

$$\begin{aligned} k_1 &= \delta_1 \epsilon_1, \\ k_2 &= \delta_2 \epsilon_2, \\ \eta_{10} &= \eta_{20} = I\pi, \end{aligned} \quad (40)$$

into the bilinear function (20) and setting the limit  $\epsilon_1 \rightarrow 0, \epsilon_2 \rightarrow 0$ , the function  $f$  can be obtained:

$$\begin{aligned} f = f_l &= \delta_1 \delta_2 \left[ x - \frac{x_0}{2} + p_1 y - c \left( 1 + \frac{p_1^2}{2} \right) \left( t - \frac{t_0}{2} \right) \right] \\ &\cdot \left[ x - \frac{x_0}{2} + p_2 y - c \left( 1 + \frac{p_2^2}{2} \right) \left( t - \frac{t_0}{2} \right) \right] + \frac{24\delta_1 \delta_2 \beta}{c(p_1 - p_2)^2}. \end{aligned} \quad (41)$$

When letting

$$\begin{aligned} p_1 &= \frac{a_2 + a_5 I}{\delta_1}, \\ p_2 &= \frac{a_2 - a_5 I}{\delta_2}, \\ \delta_1 &= a_1 + a_4 I, \\ \delta_2 &= a_1 - a_4 I, \end{aligned} \quad (42)$$

equation (41) can be arranged in

$$\begin{aligned} f &= f_l = g^2 + h^2 + a_7, \\ g &= a_1 \left( x - \frac{x_0}{2} \right) + a_2 y + a_3 \left( t - \frac{t_0}{2} \right), \\ h &= a_4 \left( x - \frac{x_0}{2} \right) + a_5 y + a_6 \left( t - \frac{t_0}{2} \right), \end{aligned} \quad (43)$$

where  $a_i$  ( $1 \leq i \leq 7$ ) are all real parameters to be determined. Note that the function  $f$  in equation (43) is positive if the parameter  $a_7 > 0$ . Combining equation (43) with equations (11) and (12), the constraining relations of these parameters are

$$\begin{aligned} a_3 &= \frac{a_1 c (a_2^2 - 2a_4^2)}{2a_4^2}, \\ a_5 &= \frac{a_1 a_2}{a_4}, \\ a_6 &= \frac{c(a_2^2 - 2a_4^2)}{2a_4}, \\ a_7 &= \frac{6a_4^2 \beta (a_1^2 + a_4^2)}{a_2^2 c}, \end{aligned} \quad (44)$$

where all the denominators are nonzero.

This time, solution (10) becomes

$$\begin{aligned} A &= \frac{12\beta}{\alpha} \left[ \ln \left( g^2 + h^2 - \frac{6a_4^2 \beta (a_1^2 + a_4^2)}{a_2^2 c} \right) \right]_{xx} \\ &+ b_1 \left[ \ln \left( g^2 + h^2 - \frac{6a_4^2 \beta (a_1^2 + a_4^2)}{a_2^2 c} \right) \right]_{xxx} \end{aligned} \quad (45a)$$

$$\begin{aligned} &+ b_2 \left[ \ln \left( g^2 + h^2 - \frac{6a_4^2 \beta (a_1^2 + a_4^2)}{a_2^2 c} \right) \right]_{xxt}, \\ B &= \frac{12\beta}{\alpha} \left[ \ln \left( g^2 + h^2 - \frac{6a_4^2 \beta (a_1^2 + a_4^2)}{a_2^2 c} \right) \right]_{xx} \\ &- b_1 \left[ \ln \left( g^2 + h^2 - \frac{6a_4^2 \beta (a_1^2 + a_4^2)}{a_2^2 c} \right) \right]_{xxx} \\ &- b_2 \left[ \ln \left( g^2 + h^2 - \frac{6a_4^2 \beta (a_1^2 + a_4^2)}{a_2^2 c} \right) \right]_{xxt}, \end{aligned} \quad (45b)$$

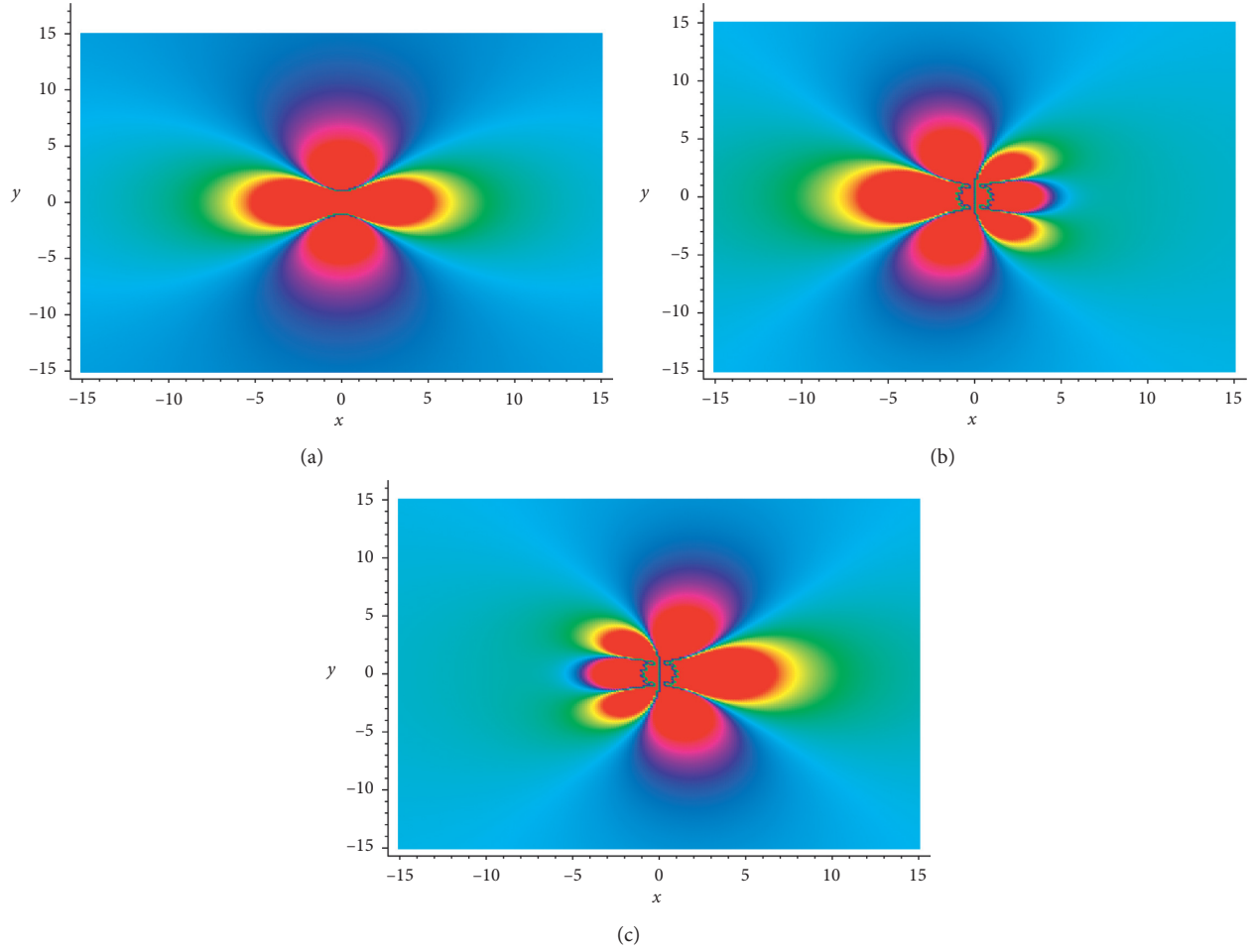


FIGURE 7: The density plot of the symmetry breaking lumps of the AB-KP systems (7a) and (7b), with the selected parameters  $b_1$  and  $b_2$  are (a)  $b_1 = b_2 = 0$  and (b) and (c)  $b_1 = b_2 = 10$ , at time  $t = 0$ .

where the functions  $g$  and  $h$  are given as follows:

$$g = a_1 \left( x - \frac{x_0}{2} \right) + a_2 y + \frac{a_1 c (a_2^2 - 2a_4^2)}{2a_4^2} \left( t - \frac{t_0}{2} \right), \quad (46)$$

$$h = a_4 \left( x - \frac{x_0}{2} \right) - \frac{a_1 a_2}{a_4} y + \frac{c (a_2^2 - 2a_4^2)}{2a_4} \left( t - \frac{t_0}{2} \right),$$

with  $c, a_1, a_2, a_4, x_0$ , and  $t_0$  being some free real constants. Obviously, this set of solution (45a) and (45b) represents solitary waves in the form of rational structures, which is a family of two-wave solutions with different velocities and directions due to the linear functions  $g$  and  $h$  of the three variables  $x, y$ , and  $t$ .

If the constants are taken as  $a_1 = a_4 = -1$ ,  $a_2 = c = \alpha = 1$ ,  $\beta = 1/6$ , and  $x_0 = t_0 = 0$ , equation (43) becomes

$$f = f_l = \left( x - y - \frac{t}{2} \right)^2 + \left( x + y - \frac{t}{2} \right)^2 - 2, \quad (47)$$

according to equation (44). Figure 7 is a density plot of the lumps by equation (36) under the abovementioned parameter selection. Figure 7(a) is a normal first-order lump structure ( $b_1 = b_2 = 0$ ) for the solution  $A = B = -4(x^2 -$

$y^2 + 1)/(x^2 + y^2 - 1)^2$  at time  $t = 0$ . Figures 7(b) and 7(c) are two symmetry breaking lump structures for the solution  $A, B = -4(x^2 - y^2 + 1)/(x^2 + y^2 - 1)^2 \pm 20x(x^2 + 3x - 3y^2)/(x^2 + y^2 - 1)^3$ , with the selected parameters  $b_1 = b_2 = 10$ , at time  $t = 0$ . As these solutions are all rational functions, the property of these functions describes symmetry breaking lump structures.

Furthermore, if we take  $k_i = \delta_i \epsilon_i$ ,  $\eta_{i0} = \pi I$ ,  $i = 1, 2, 3, 4$ , and

$$\begin{aligned} p_1 &= 1 + I, \\ p_2 &= 1 - I, \\ p_3 &= -p_1, \\ p_4 &= -p_2, \\ \delta_3 &= \delta_1, \\ \delta_4 &= \delta_2, \end{aligned} \quad (48)$$

after setting the limit  $\epsilon_i \rightarrow 0$ ,  $i = 1, 2, 3, 4$ , the function  $f$  (26) can be simplified into



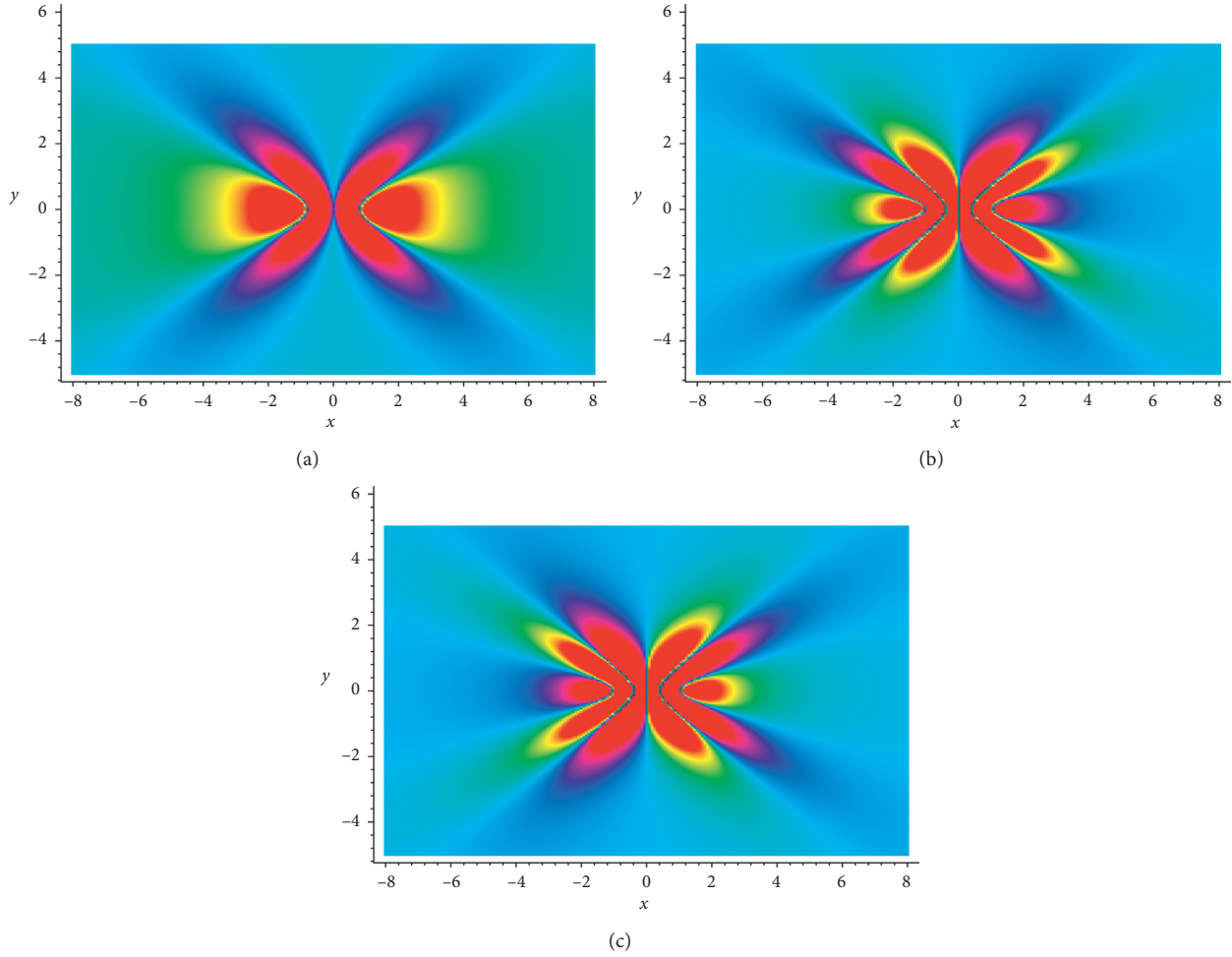


FIGURE 8: The symmetry breaking density plot of the second-order lumps of the AB-KP systems (7a) and (7b), with the selected parameters  $b_1$  and  $b_2$  are (a)  $b_1 = b_2 = 0$  and (b) and (c)  $b_1 = b_2 = 5$ , at time  $t = 0$ .

$$\begin{aligned}
 f = f_l = c^2 & \left[ \left( x - \frac{x_0}{2} \right)^4 + 4y^4 + 4c^4 \left( t - \frac{t_0}{2} \right)^4 \right] \\
 & - 4c^3 \left( x - \frac{x_0}{2} \right)^3 \left( t - \frac{t_0}{2} \right) + 8c^4 \left( x - \frac{x_0}{2} \right)^2 \left( t - \frac{t_0}{2} \right)^2 \\
 & - 4c^2 \left( x - \frac{x_0}{2} \right) \left( t - \frac{t_0}{2} \right) \left[ 2c^3 \left( t - \frac{t_0}{2} \right)^2 - 2cy^2 - 3\beta \right] \\
 & - 4c^3 (2cy^2 + 3\beta) \left( t - \frac{t_0}{2} \right)^2 - 36c\beta y^2 + 81\beta^2.
 \end{aligned} \tag{49}$$

Figure 8 shows the second-order lump structures when  $c = -4$ ,  $\alpha = 1$ ,  $\beta = 1/6$ , and  $x_0 = t_0 = \eta_{10} = \eta_{20} = 0$ , which are symmetry breaking.

#### 4. Conclusion

As everyone knows, the two-place correlated physical events widely exist in the field of natural science, and the discussed AB physics (two-place physics) has a profound influence on other scientific fields. In this work, by establishing a special

AB-KP system via the parity with a shift of the space variable  $x$  and time reversal with a delay, some group invariant solutions, such as symmetry breaking soliton, symmetry breaking breather, and symmetry breaking lump solutions have been presented through introducing an extended Bäcklund transformation and the established Hirota bilinear form. At the same time, the corresponding symmetry breaking structures of these explicit solutions are depicted according to the ansatz functions.

In fact, these are the following few open problems. Firstly, we may investigate more local and nonlocal symmetry breaking structures, such as the cnoidal wave and rogue wave through expression (2). Secondly, the arbitrary function  $G(A, B)$  of  $A$  and  $B$  (which should be  $\widehat{P}_s^x \widehat{T}_d$  invariant) is diverse, although we take  $G(A, B) = (\alpha/2)(A_x^2 + AA_{xx} - B_x^2 - BB_{xx})$  in this paper. Thirdly, algebraic structures involving the related Lie point symmetry and Lie-Bäcklund symmetry reductions, and Bäcklund transformations determined by residual symmetries may be discussed mathematically for the AB-KP systems (7a) and (7b). Finally, the  $\widehat{P}_s^x \widehat{T}_d$  symmetry of this paper could be generalized to other nonlinear systems by taking the specific elements of the larger  $\widehat{P}_s \widehat{T}_d \widehat{C}$  symmetry group [15].



## Data Availability

The data used to support the findings of this study are included within the article. For more details, the data are available from the corresponding author upon request.

## Conflicts of Interest

The authors declare that they have no conflicts of interest.

## Acknowledgments

The project was supported by the National Natural Science Foundation of China (nos. 11775104 and 11705077) and Scientific Research Foundation of the First-Class Discipline of Zhejiang Province (B) (no. 201601).

## References

- [1] W.-X. Ma, "The inverse scattering transform and soliton solutions of a combined modified Korteweg-de Vries equation," *Journal of Mathematical Analysis and Applications*, vol. 471, no. 1-2, pp. 796–811, 2019.
- [2] W.-M. Ma, "Darboux transformations for a Lax integrable system in  $2n$ -dimensions," *Letters in Mathematical Physics*, vol. 39, no. 1, pp. 33–49, 1997.
- [3] W.-X. Ma and Y.-J. Zhang, "Darboux transformations of integrable couplings and applications," *Reviews in Mathematical Physics*, vol. 30, no. 2, p. 1850003, 2018.
- [4] M. J. Ablowitz, A. Ramani, and H. Segur, "A connection between nonlinear evolution equations and ordinary differential equations of P-type. I, II," *Journal of Mathematical Physics*, vol. 21, no. 4, pp. 715–721, 1980.
- [5] J. Weiss, "Bäcklund transformation and the Painlevé property," *Journal of Mathematical Physics*, vol. 27, no. 5, pp. 1296–1305, 1986.
- [6] M. Musette and R. Conte, "Algorithmic method for deriving Lax pairs from the invariant Painlevé analysis of nonlinear partial differential equations," *Journal of Mathematical Physics*, vol. 32, no. 6, pp. 1450–1457, 1991.
- [7] R. Hirota, "Exact solution of the Korteweg-de Vries equation for multiple collisions of solitons," *Physical Review Letters*, vol. 27, no. 18, pp. 1192–1194, 1971.
- [8] R. Hirota, *The Direct Method in Soliton Theory*, Cambridge University Press, Cambridge, UK, 2004.
- [9] W. X. Ma, "Generalized bilinear differential equations," *Studies in Nonlinear Sciences*, vol. 2, pp. 140–144, 2011.
- [10] M. J. Ablowitz and Z. H. Musslimani, "Integrable nonlocal nonlinear Schrödinger equation," *Physical Review Letters*, vol. 110, no. 6, Article ID 064105, 2013.
- [11] S. Y. Lou, "Alice-Bob systems,  $\hat{P} - \hat{T} - \hat{C}$  symmetry invariant and symmetry breaking soliton solutions," *Journal of Mathematical Physics*, vol. 59, no. 8, Article ID 083507, 2018.
- [12] S. Y. Lou, "Alice-Bob systems,  $P_s - T_d - C$  principles and multi-soliton solutions," 2016, <https://arxiv.org/abs/1603.03975>.
- [13] C. Li, S. Y. Lou, and M. Jia, "Coherent structure of Alice-Bob modified Korteweg de-Vries equation," *Nonlinear Dynamics*, vol. 93, no. 4, pp. 1799–1808, 2018.
- [14] S. Y. Lou, "Prohibitions caused by nonlocality for nonlocal Boussinesq-KdV type systems," *Studies in Applied Mathematics*, vol. 143, no. 2, pp. 123–138, 2019.
- [15] S. Y. Lou, "Multi-place nonlocal systems," 2019, <https://arxiv.org/abs/1901.02828>.
- [16] M. Jia and S. Y. Lou, "Exact  $P_s T_d$  invariant and  $P_s T_d$  symmetric breaking solutions, symmetry reductions and Bäcklund transformations for an AB-KdV system," *Physics Letters A*, vol. 382, no. 17, pp. 1157–1166, 2018.
- [17] S.-Y. Lou and Z.-J. Qiao, "Alice-Bob peakon systems," *Chinese Physics Letters*, vol. 34, no. 10, Article ID 100201, 2017.
- [18] S. Y. Lou and F. Huang, "Alice-Bob physics: coherent solutions of nonlocal KdV systems," *Scientific Reports*, vol. 7, no. 1, 2017.
- [19] Z.-Y. Ma, J.-X. Fei, and J.-C. Chen, "Nonlocal symmetry and explicit solution of the Alice-Bob modified Korteweg-de Vries equation," *Communications in Theoretical Physics*, vol. 70, no. 1, pp. 031–037, 2018.
- [20] S. Y. Lou, "From nothing to something II: nonlinear systems via consistent correlated bang," *Chinese Physics Letters*, vol. 34, no. 6, Article ID 060201, 2017.
- [21] X.-Y. Tang, Z.-F. Liang, Z. F. Liang, and J. Y. Wang, "A general nonlocal variable coefficient KdV equation with shifted parity and delayed time reversal," *Nonlinear Dynamics*, vol. 92, no. 3, pp. 815–825, 2018.
- [22] X.-Y. Tang, Z.-F. Liang, and X.-Z. Hao, "Nonlinear waves of a nonlocal modified KdV equation in the atmospheric and oceanic dynamical system," *Communications in Nonlinear Science and Numerical Simulation*, vol. 60, pp. 62–71, 2018.
- [23] D.-J. Ding, D.-Q. Jin, and C.-Q. Dai, "Analytical solutions of differential-difference sine-Gordon equation," *Thermal Science*, vol. 21, no. 4, pp. 1701–1705, 2017.
- [24] Y.-Y. Wang, C.-Q. Dai, Y.-Q. Xu, J. Zheng, and Y. Fan, "Dynamics of nonlocal and localized spatiotemporal solitons for a partially nonlocal nonlinear Schrödinger equation," *Nonlinear Dynamics*, vol. 92, no. 3, pp. 1261–1269, 2018.
- [25] C.-Q. Dai, Y.-Y. Wang, Y. Fan, and D.-G. Yu, "Reconstruction of stability for Gaussian spatial solitons in quintic-septimal nonlinear materials under PT-symmetric potentials," *Nonlinear Dynamics*, vol. 92, no. 3, pp. 1351–1358, 2018.
- [26] M. J. Ablowitz and H. Segur, *Solitons and the Inverse Scattering Transform*, SIAM, Philadelphia, PA, USA, 1981.
- [27] V. I. Petviashvili and O. V. Pokhotelov, *Solitary Waves in Plasmas and in the Atmosphere*, Energoatomizdat, Moscow, Russia, 1989.
- [28] G. C. Das and J. Sarma, "Evolution of solitary waves in multicomponent plasmas," *Chaos, Solitons & Fractals*, vol. 9, no. 6, pp. 901–911, 1998.
- [29] Z. D. Dai, Z. J. Liu, and D. L. Li, "Exact periodic solitary-wave solution for KdV equation," *Chinese Physics Letters*, vol. 25, no. 5, pp. 1531–1533, 2008.
- [30] C. Wang, H. Fang, and X. Tang, "State transition of lump-type waves for the  $(2 + 1)$ -dimensional generalized KdV equation," *Nonlinear Dynamics*, vol. 95, no. 4, pp. 2943–2961, 2019.

## Research Article

# On a Thermoelastic Laminated Timoshenko Beam: Well Posedness and Stability

Baowei Feng 

Department of Economic Mathematics, Southwestern University of Finance and Economics, Chengdu 611130, China

Correspondence should be addressed to Baowei Feng; bwfeng@swufe.edu.cn

Received 7 January 2020; Accepted 3 February 2020; Published 28 February 2020

Guest Editor: Sundarapandian Vaidyanathan

Copyright © 2020 Baowei Feng. This is an open access article distributed under the Creative Commons Attribution License, which permits unrestricted use, distribution, and reproduction in any medium, provided the original work is properly cited.

In this paper, we are concerned with a linear thermoelastic laminated Timoshenko beam, where the heat conduction is given by Cattaneo's law. We firstly prove the global well posedness of the system. For stability results, we establish exponential and polynomial stabilities by introducing a stability number  $\chi$ .

## 1. Introduction

In this paper, we address the following thermoelastic laminated Timoshenko beam in  $(0, 1) \times (0, \infty)$ :

$$\begin{cases} \rho\omega_{tt} + G(\psi - \omega_x)_x + \delta\theta_x = 0, \\ I_p(3s - \psi)_{tt} - D(3s - \psi)_{xx} - G(\psi - \omega_x) = 0, \\ I_p s_{tt} - Ds_{xx} + G(\psi - \omega_x) + \frac{4}{3}\gamma s + \frac{4}{3}\beta s_t = 0, \\ \rho_3\theta_t + q_x + \delta\omega_{xt} = 0, \\ \tau q_t + \alpha q + \theta_x = 0, \end{cases} \quad (1)$$

which subject to the following boundary conditions:

$$\begin{cases} \omega_x(0, t) = \psi(0, t) = s(0, t) = \theta(0, t) = 0, & t \in (0, \infty), \\ \omega_x(1, t) = \psi(1, t) = s(1, t) = \theta(1, t) = 0, & t \in (0, \infty), \end{cases} \quad (2)$$

and initial conditions

$$\begin{cases} \omega(x, 0) = \omega_0(x), \psi(x, 0) = \psi_0(x), s(x, 0) = s_0(x), \theta(x, 0) = \theta_0(x), & x \in (0, 1), \\ q(x, 0) = q_0(x), \omega_t(x, 0) = \omega_1(x), \psi_t(x, 0) = \psi_1(x), s_t(x, 0) = s_1(x), & x \in (0, 1), \end{cases} \quad (3)$$

where  $\rho, G, I_p, D, \gamma, \beta, \rho_3, \delta, \tau$ , and  $\alpha$  are positive constants.  $\theta(x, t)$  represents the difference temperature and  $q(x, t)$  is the heat flux.

Laminated beam, which is a relevant research subject due to the high applicability of such materials in the industry, was firstly introduced by Hansen and Spies, see, for instance

[1, 2]. They introduced a mathematical model for two-layered beams with structural damping due to the interfacial slip which is given by

$$\begin{cases} \rho\omega_{tt} + G(\psi - \omega_x)_x = 0, \\ I_\rho(3s_{tt} - \psi_{tt}) - G(\psi - \omega_x) - D(3s_{xx} - \psi_{xx}) = 0, \\ I_\rho s_{tt} + G(\psi - \omega_x) + \frac{4}{3}\gamma s + \frac{4}{3}\beta s_t - Ds_{xx} = 0, \end{cases} \quad (4)$$

where the coefficients  $\rho, G, I_\rho, D, \gamma$ , and  $\beta$  are positive constants and represent density, shear stiffness, mass moment of inertia, flexural rigidity, adhesive stiffness, and adhesive damping parameter, respectively. The function  $\omega(x, t)$  denotes the transversal displacement,  $\psi(x, t)$  represents the rotational displacement, and  $s(x, t)$  is proportional to the amount of slip along the interface at time  $t$  and longitudinal

spatial variable  $x$ . The third equation describes the dynamics of the slip.

Up till now, there are some results concerning laminated beam equations, which are mainly concerned with global existence and stability of the related system. By adding suitable damping effects, such as internal damping, (boundary) frictional damping, and viscoelastic damping, it was shown that if the linear damping terms are added in two of the three equations, system (4) is exponentially stable under the “equal wave speeds” assumption  $(\rho/I_\rho) = (G/D)$ . But if the damping terms are added in the three equations, then the system decays exponentially without the equal wave speeds assumption, see, for example, [3–17]. For thermoelastic laminated Timoshenko beam, there are few published works, we can mention the results due to Liu and Zhao [18] and Apalara [19]. In [18], the authors considered the following laminated beams with past history

$$\begin{cases} \rho\varphi_{tt} + G(\psi - \varphi_x)_x + \theta_x = 0, \\ I_\rho(3\omega - \psi)_{tt} - D(3\omega - \psi)_{xx} + \int_0^\infty g(s)(3\omega - \psi)_{xx}(t-s)ds - G(\psi - \varphi_x) - \theta = 0, \\ I_\rho\omega_{tt} - D\omega_{xx} + G(\psi - \varphi_x) + \frac{4}{3}\gamma\omega + \frac{4}{3}\beta\omega_t = 0, \\ k\theta_t - \tau\theta_{xx} + \varphi_{xt} + (3\omega - \psi)_t = 0, \end{cases} \quad (5)$$

together with the following boundary conditions:

$$\begin{cases} \varphi_x(0, t) = \psi(0, t) = \omega(0, t) = \theta(0, t) = 0, & t \in (0, \infty), \\ \varphi(1, t) = \psi_x(1, t) = \omega_x(1, t) = \theta_x(1, t) = 0, & t \in (0, \infty). \end{cases} \quad (6)$$

They firstly proved the global well posedness of solutions to the system. The main results are the stability of the system. If  $\beta \neq 0$ , they proved the exponential and polynomial stabilities depending on the behavior of the kernel function  $g$  only. If  $\beta = 0$ , they established exponential stability in case of equal wave speeds assumption and lack of exponential stability in case of nonequal wave speeds assumption. Apalara [19] considered a laminated beam with second sound of the form

$$\begin{cases} \rho\omega_{tt} + G(\psi - \omega_x)_x = 0, \\ I_\rho(3s - \psi)_{tt} - D(3s - \psi)_{xx} - G(\psi - \omega_x) + \delta\theta_x = 0, \\ I_\rho s_{tt} - Ds_{xx} + G(\psi - \omega_x) + \frac{4}{3}\gamma s + \frac{4}{3}\beta s_t = 0, \\ \rho_3\theta_t + q_x + \delta(3s - \psi)_{xt} = 0, \\ \tau q_t + \alpha q + \theta_x = 0, \end{cases} \quad (7)$$

together with the following boundary conditions:

$$\begin{cases} \omega_x(0, t) = \psi(0, t) = s(0, t) = q(0, t) = 0, & t \in (0, \infty), \\ \omega(1, t) = \psi_x(1, t) = s_x(1, t) = \theta(1, t) = 0, & t \in (0, \infty), \end{cases} \quad (8)$$

and proved the global well posedness and established exponential and polynomial stabilities depending on the parameter

$$\chi_\tau = \left(1 - \frac{\tau\rho_3 G}{\rho}\right) \left(\frac{D}{I_\rho} - \frac{G}{\rho}\right) - \frac{\tau G \delta^2}{\rho I_\rho}. \quad (9)$$

One can also refer to two recent results of laminated beams with thermal damping in [20, 21], and a result of a coupled hyperbolic equations with a heat equation of second sound in [22].

When  $s = 0$ , system (4) reduces to the well-known Timoshenko system, which have been widely studied. There are so many papers on the Timoshenko system in the literature, most of those results recover the global well posedness, stability, and long-time dynamics by adding some kinds of damping. Here, we recall some works on the thermoelastic Timoshenko system. Muñoz Rivera and Racke [23] considered a Timoshenko system with thermoelastic dissipation and established exponential stability in case of equal wave speed assumption and polynomial stability if wave speeds are nonequal. Almeida Júnior et al. [24] studied

a thermoelastic Timoshenko beam acting on shear force. They obtained the same stability results as in [23]. In addition, they proved that the polynomial decay is optimal. Fernández Sare and Racke [25] considered a Timoshenko system with second sound. They proved that the system is not exponentially stable even if the propagation speeds are equal. The results were generalized by Guesmia et al. [26]. Recently, Santos et al. [27] introduced a stability number  $\chi_r$  for the system in [25] and established the exponential decay result for  $\chi_r = 0$  and polynomial decay for  $\chi_r \neq 0$  by using the semigroup method. One can also find a stability result for the Timoshenko system with second sound in Apalara et al. [28]. Feng [29] considered a Timoshenko-Coleman-Gurtin system and studied the long-time dynamics of the system. We at last mention the contribution of Hamadouche and Mes- saoudi [30] and Aouadi and Boulehmi [31], where the authors considered two classes of nonuniform thermoelastic Timoshenko systems and proved global well posedness and established some stability results.

Our goals in the present work are to study the global well posedness and stability of systems (1)–(3). The main points are summarized as follows:

- (i) We prove the global well posedness of systems (1)–(3) by using Lumer–Philips theorem. The main result is presented in Theorem 1.
- (ii) We introduce a new stability number denoted by

$$\chi = \tau \delta^2 D - (D\rho - GI_\rho) \left( \frac{\tau \rho_3 D}{I_\rho} - 1 \right), \quad (10)$$

and we show that the system is exponential stable when  $\chi = 0$  and polynomial stable when  $\chi \neq 0$ . The main results are presented in Theorems 1 and 2.

- (iii) The proof of stability results is based on the multiplier method. Since the boundary conditions here we considered are different from those in Apalara [19], so the multipliers we will define are greatly different from the multipliers in Apalara [19].

It follows, from (1), that

$$\begin{aligned} \frac{d^2}{dt^2} \int_0^1 \omega(x, t) dx &= 0, \\ \tau \frac{d}{dt} \int_0^1 q(x, t) dx + \alpha \int_0^1 q(x, t) dx &= 0. \end{aligned} \quad (11)$$

If we denote

$$\begin{aligned} \bar{\omega}(x, t) &= \omega(x, t) - \int_0^1 \omega_0(x) - t \int_0^1 \omega_1(x) dx, \\ \bar{q}(x, t) &= q(x, t) - e^{-(\alpha/\tau)t} \int_0^1 q_0(x) dx, \end{aligned} \quad (12)$$

we easily verify that  $(\bar{\omega}, \psi, s, \theta, \bar{q})$  satisfies (1) and in addition,

$$\begin{aligned} \int_0^1 \bar{\omega}(x, t) dx &= 0, \\ \int_0^1 \bar{q}(x, t) dx &= 0, \end{aligned} \quad (13)$$

$\forall t \geq 0.$

Hence, Poincaré's inequality holds for  $\bar{\omega}$ . In the following, we work with  $\bar{\omega}$  and  $\bar{q}$  but write  $\omega$  and  $q$  for convenience.

The remaining paper is planned as follows. In Section 2, we study the well posedness of the system. In Section 3, we establish the stability results. Throughout this paper,  $c > 0$  is a generic constant that changes from one inequality to another.

## 2. Well Posedness

We start by denoting the vector-valued function by  $U$ :

$$U = (\omega, \Phi, 3s - \psi, 3\Lambda - \Psi, s, \Lambda, \theta, q)^T, \quad (14)$$

with  $\Phi = \omega_t,$

$$\Psi = \psi_t, \text{ and } \Lambda = s_t.$$

Then, systems (1)–(3) can be written as

$$\begin{cases} \frac{d}{dt} U(t) = \mathcal{A}U, & t > 0, \\ U(0) = U_0 = (\omega_0, \omega_1, 3s_0 - \psi_0, 3s_1 - \psi_1, s_0, s_1, \theta_0, q_0)^T, \end{cases} \quad (15)$$

where the operator  $\mathcal{A}$  is defined by

$$\mathcal{A}U = \begin{pmatrix} \Phi \\ -\frac{G}{\rho}(\psi - \omega_x)_x - \frac{\delta}{\rho}\theta_x \\ 3\Lambda - \Psi \\ \frac{D}{I_\rho}(3s - \psi)_{xx} + \frac{G}{I_\rho}(\psi - \omega_x) \\ \Lambda \\ \frac{D}{I_\rho}s_{xx} - \frac{G}{I_\rho}(\psi - \omega_x) - \frac{4\gamma}{3I_\rho}s - \frac{4\beta}{3I_\rho}\Lambda \\ -\frac{1}{\rho_3}q_x - \frac{\delta}{\rho_3}\Phi_x \\ -\frac{\alpha}{\tau}q - \frac{1}{\tau}\theta_x \end{pmatrix}. \quad (16)$$

We consider the following spaces:

$$\begin{aligned}
L_*^2(0, 1) &= \left\{ v \in L^2(0, 1) : \int_0^1 v(x) dx = 0 \right\}, \\
H_*^1(0, 1) &= H^1(0, 1) \cap L_*^2(0, 1), \\
H_*^2(0, 1) &= \left\{ v \in H^2(0, 1) : v_x(0) = v_x(1) = 0 \right\}.
\end{aligned} \tag{17}$$

$$\begin{aligned}
\mathcal{H} &= H_*^1(0, 1) \times L_*^2(0, 1) \times H_0^1(0, 1) \times L^2(0, 1) \times H_0^1(0, 1) \\
&\quad \times L^2(0, 1) \times L^2(0, 1) \times L_*^2(0, 1)
\end{aligned} \tag{18}$$

be the Hilbert space equipped with the inner product

Let

$$\begin{aligned}
(U, \tilde{U})_{\mathcal{H}} &= \rho \int_0^1 \Phi \tilde{\Phi} dx + I_\rho \int_0^1 (3\Lambda - \Psi)(3\tilde{\Lambda} - \tilde{\Psi}) dx + 3I_\rho \int_0^1 \Lambda \tilde{\Lambda} dx \\
&\quad + \rho_3 \int_0^1 \theta \tilde{\theta} dx + \tau \int_0^1 q \tilde{q} dx + 4\gamma \int_0^1 s \tilde{s} dx + D \int_0^1 (3s - \psi)_x (3\tilde{s} - \tilde{\psi})_x dx \\
&\quad + G \int_0^1 (\psi - \omega_x)(\tilde{\psi} - \tilde{\omega}_x) dx + 3D \int_0^1 s_x \tilde{s}_x dx.
\end{aligned} \tag{19}$$

The domain of  $\mathcal{A}$  is given by

$$D\mathcal{A} = \left\{ U \in \mathcal{H} \left| \begin{array}{l} \omega \in H_*^2(0, 1) \cap H_*^1(0, 1), 3s - \psi, s \in H^2(0, 1) \cap H_0^1(0, 1), \\ \Phi, q \in H_*^1(0, 1), 3\Lambda - \Psi, \Lambda, \theta \in H_0^1(0, 1) \end{array} \right. \right\}. \tag{20}$$

The well posedness result can be stated in the following theorem.

**Theorem 1.** *Let  $U_0 \in \mathcal{H}$ , then problems (1)-(3) admit a unique weak solution  $U \in C(\mathbb{R}^+, \mathcal{H})$ . In addition, if  $U_0 \in D(\mathcal{A})$ , then  $U \in C(\mathbb{R}^+, D(\mathcal{A})) \cap C^1(\mathbb{R}^+, \mathcal{H})$ .*

*Proof.* It is easy to obtain that, for any  $U = (\omega, \Phi, 3s - \psi, 3\Lambda - \Psi, s, \Lambda, \theta, q)^T \in D(\mathcal{A})$ ,

$$(\mathcal{A}U, U)_{\mathcal{H}} = -4\beta \int_0^1 \Lambda^2 dx - \alpha \int_0^1 q^2 dx \leq 0, \tag{21}$$

which implies the operator  $\mathcal{A}$  is a dissipative operator.

In what follows, we shall show the operator  $Id - \mathcal{A}$  is surjective. In other words, given  $F = (f_1, f_2, f_3, f_4, f_5, f_6, f_7, f_8) \in \mathcal{H}$ , we will seek a solution  $V = (v_1, v_2, v_3, v_4, v_5, v_6, v_7, v_8) \in D(\mathcal{A})$  of

$$(Id - \mathcal{A})V = F. \tag{22}$$

We rewrite (21) as

$$\left\{ \begin{array}{l} v_1 - v_2 = f_1, \\ \rho v_2 - Gv_{1xx} - Gv_{3x} + 3Gv_{5x} + \delta v_{7x} = \rho f_2, \\ v_3 - v_4 = f_3, \\ I_\rho v_4 - Dv_{3xx} - 3Gv_5 + Gv_3 + Gv_{1x} = I_\rho f_4, \\ v_5 - v_6 = f_5, \\ \left( I_\rho + \frac{4}{3}\beta \right) v_6 - Dv_{5xx} - Gv_3 - Gv_{1x} + \left( 3G + \frac{4}{3}\gamma \right) v_5 = I_\rho f_6, \\ \rho_3 v_7 + v_{8x} + \delta v_{2x} = \rho_3 f_7, \\ (\tau + \alpha) v_8 + v_{7x} = \tau f_8, \end{array} \right. \tag{23}$$

which implies that

$$v_2 = v_1 - f_1, \quad (24)$$

$$v_4 = v_3 - f_3, \quad (25)$$

$$v_6 = v_5 - f_5, \quad (26)$$

$$v_{7x} = -(\tau + \alpha)v_8 + \tau f_8. \quad (27)$$

We infer from (27) that

$$v_7 = -(\tau + \alpha) \int_0^x v_8(y) dy + \tau \int_0^x f_8(y) dy. \quad (28)$$

Replacing (24)–(26) and (28) in (23), we see that

$$\begin{cases} \rho v_1 - Gv_{1xx} - Gv_{3x} + 3Gv_{5x} - \delta(\tau + \alpha)v_8 = \rho(f_1 + f_2) - \tau f_8, \\ I_\rho v_3 - Dv_{3xx} - 3Gv_5 + Gv_3 + Gv_{1x} = I_\rho(f_3 + f_4), \\ \left(I_\rho + 3G + \frac{4}{3}\beta + \frac{4}{3}\gamma\right)v_5 - Dv_{5xx} - Gv_3 - Gv_{1x} = I_\rho(f_5 + f_6) + \frac{4}{3}\beta f_5, \\ -\rho_3(\tau + \alpha) \int_0^x v_8(y) dy + v_{8x} + \delta v_{1x} = \rho_3 f_7 - \rho_3 \tau \int_0^x f_8(y) dy + \delta f_{1x}. \end{cases} \quad (29)$$

We multiply (29) by  $\tilde{v}_1, \tilde{v}_3, \tilde{v}_5,$  and  $(\tau + \alpha) \int_0^x \tilde{v}_8(y) dy,$  respectively, and integrate their sum over  $(0, 1)$  to get the following variational formulation:

$$\mathcal{B}((v_1, v_3, v_5, v_8), (\tilde{v}_1, \tilde{v}_3, \tilde{v}_5, \tilde{v}_8)) = \mathcal{L}(\tilde{v}_1, \tilde{v}_3, \tilde{v}_5, \tilde{v}_8), \quad (30)$$

where the bilinear form  $\mathcal{B}: [H_*^1(0, 1) \times H_0^1(0, 1) \times H_0^1(0, 1) \times L_*^2(0, 1)]^2 \rightarrow \mathbb{R}$  is given by

$$\begin{aligned} \mathcal{B}((v_1, v_3, v_5, v_8), (\tilde{v}_1, \tilde{v}_3, \tilde{v}_5, \tilde{v}_8)) &= G \int_0^1 (-v_{1x} - v_3 + 3v_5)(-\tilde{v}_{1x} - \tilde{v}_3 + 3\tilde{v}_5) dx + \rho \int_0^1 v_1 \tilde{v}_1 dx + I_\rho \int_0^1 v_3 \tilde{v}_3 dx \\ &+ (3I_\rho + 4\beta + 4\gamma) \int_0^1 v_5 \tilde{v}_5 dx + (\tau + \alpha) \int_0^1 v_8 \tilde{v}_8 dx + D \int_0^1 v_{3x} \tilde{v}_{3x} dx \\ &+ 3D \int_0^1 v_{5x} \tilde{v}_{5x} dx + \rho_3(\tau + \alpha)^2 \int_0^1 \left( \int_0^x v_8(y) dy \right) \left( \int_0^x \tilde{v}_8(y) dy \right) dx, \end{aligned} \quad (31)$$

and the linear form  $\mathcal{L}: [H_*^1(0, 1) \times H_0^1(0, 1) \times H_0^1(0, 1) \times L_*^2(0, 1)] \rightarrow \mathbb{R}$  is defined by

$$\begin{aligned} \mathcal{L}(\tilde{v}_1, \tilde{v}_3, \tilde{v}_5, \tilde{v}_8) &= \int_0^1 (\rho f_1 + \rho f_2 - \tau \delta f_8) \tilde{v}_1 dx + I_\rho \int_0^1 (f_3 + f_4) \tilde{v}_3 dx \\ &+ \int_0^1 [(3I_\rho + 4\beta) f_5 + 3I_\rho f_6] \tilde{v}_5 dx \\ &+ \delta(\tau + \alpha) \int_0^1 f_1 \tilde{v}_8 dx \\ &+ \int_0^1 \left[ \rho_3 \tau (\tau + \alpha) \int_0^x f_8(y) dy - \rho_3(\tau + \alpha) f_7 \right] \\ &\cdot \left( \int_0^x \tilde{v}_8(y) dy \right) dx. \end{aligned} \quad (32)$$

We denote the Hilbert space  $V$  by

$$V = H_*^1(0, 1) \times H_0^1(0, 1) \times H_0^1(0, 1) \times L_*^2(0, 1), \quad (33)$$

equipped with the norm

$$\begin{aligned} \|(v_1, v_3, v_5, v_8)\|_V^2 &= \|-v_{1x} - v_3 + 3v_5\|_2^2 + \|v_1\|_2^2 \\ &+ \|v_8\|_2^2 + \|v_{3x}\|_2^2 + \|v_{5x}\|_2^2. \end{aligned} \quad (34)$$

It is easy to get that  $\mathcal{B}(\cdot, \cdot)$  and  $\mathcal{L}(\cdot)$  are bounded. Moreover there exists a positive constant  $m$  such that

$$\begin{aligned} \mathcal{B}((v_1, v_3, v_5, v_8), (v_1, v_3, v_5, v_8)) &= G \int_0^1 (-v_{1x} - v_3 + 3v_5)^2 dx + \rho \int_0^1 v_1^2 dx + I_\rho \int_0^1 v_3^2 dx \\ &+ (3I_\rho + 4\beta + 4\gamma) \int_0^1 v_5^2 dx + (\tau + \alpha) \int_0^1 v_8^2 dx + D \int_0^1 v_{3x}^2 dx \\ &+ 3D \int_0^1 v_{5x}^2 dx + \rho_3(\tau + \alpha)^2 \int_0^1 \left( \int_0^x v_8(y) dy \right)^2 dx \\ &\geq G \int_0^1 (-v_{1x} - v_3 + 3v_5)^2 dx + \rho \int_0^1 v_1^2 dx \\ &+ (\tau + \alpha) \int_0^1 v_8^2 dx + D \int_0^1 v_{3x}^2 dx + 3D \int_0^1 v_{5x}^2 dx \\ &\geq m \|(v_1, v_3, v_5, v_8)\|_V^2. \end{aligned} \quad (35)$$



Thus,  $\mathcal{B}$  is coercive on  $V \times V$ . Consequently, using Lax–Milgram theorem, we conclude that (30) has a unique solution:

$$\begin{aligned} v_1 &\in H_*^1(0, 1), \\ v_3, v_5 &\in H_0^1(0, 1), \\ v_8 &\in L_*^2(0, 1). \end{aligned} \quad (36)$$

Substituting  $v_1, v_3, v_5$ , and  $v_8$  into (24)–(26) and (28), respectively, we have

$$\begin{aligned} v_2 &\in H_*^1(0, 1), \\ v_4, v_6 &\in H_0^1(0, 1), \\ v_7 &\in H_0^1(0, 1). \end{aligned} \quad (37)$$

Let  $\tilde{v}_1 \in H_0^1(0, 1)$  and denote

$$\widehat{v}_1(x) = \tilde{v}_1(x) - \int_0^1 \tilde{v}_1(s) ds, \quad (38)$$

which gives us  $\widehat{v}_1 \in H_*^1(0, 1)$ . Now we replace  $(\tilde{v}_1, \tilde{v}_3, \tilde{v}_5, \tilde{v}_8)$  by  $(\widehat{v}_1, 0, 0, 0)$  in (30) to obtain

$$\begin{aligned} G \int_0^1 (-v_{1x} - v_3 + 3v_5)(-\widehat{v}_{1x}) dx + \rho \int_0^1 v_1 \widehat{v}_1 dx \\ = \int_0^1 (\rho f_1 + \rho f_2 - \tau \delta f_8) \widehat{v}_1 dx, \end{aligned} \quad (39)$$

i.e.,

$$\begin{aligned} G \int_0^1 v_{1xx} \widehat{v}_1 dx = \rho \int_0^1 v_{1x} \widehat{v}_1 dx - G \int_0^1 v_{3x} \widehat{v}_1 dx + 3G \int_0^1 v_{5x} \widehat{v}_1 dx \\ - \int_0^1 (\rho f_1 + \rho f_2 - \tau \delta f_8) \widehat{v}_1 dx, \quad \forall \widehat{v}_1 \in H_0^1(0, 1), \end{aligned} \quad (40)$$

which yields

$$\begin{aligned} Gv_{1xx} = \rho v_{1x} - Gv_{3x} + 3Gv_{5x} \\ - (\rho f_1 + \rho f_2 - \tau \delta f_8) \in L^2(0, 1). \end{aligned} \quad (41)$$

Thus,

$$v_1 \in H^2(0, 1). \quad (42)$$

Moreover, (39) also holds for any  $\phi \in C^1([0, 1])$ . Then, by using integration by parts, we obtain

$$\begin{aligned} Gv_{1x}(1)\phi(1) - Gv_{1x}(0)\phi(0) - G \int_0^1 v_{1xx} \phi dx \\ + \rho \int_0^1 v_1 \phi dx - G \int_0^1 v_{3x} \phi dx \\ + 3G \int_0^1 v_{5x} \phi dx - \int_0^1 (\rho f_1 + \rho f_2 - \tau \delta f_8) \phi dx = 0. \end{aligned} \quad (43)$$

Then, we get for any  $\phi \in C^1([0, 1])$ ,

$$Gv_{1x}(1)\phi(1) - Gv_{1x}(0)\phi(0) = 0. \quad (44)$$

From (28), we obtain

$$v_7(0) = v_7(1) = 0. \quad (45)$$

Since  $\phi$  is arbitrary, we get that  $v_{1x}(0) = v_{1x}(1) = 0$ . Hence,  $v_1 \in H_*^2(0, 1)$ . Using similar arguments as above, we can obtain

$$\begin{aligned} v_3, v_5 &\in H^2(0, 1) \cap H_0^1(0, 1), \\ v_7 &\in H_0^1(0, 1), \\ v_8 &\in H_*^1(0, 1). \end{aligned} \quad (46)$$

Thus,  $V = (v_1, v_2, v_3, v_4, v_5, v_6, v_7, v_8) \in D(\mathcal{A})$  and  $\mathcal{A}$  is maximal. By using Lumer–Philips theorem, see, for example, Liu and Zheng [32] and Pazy [33], we end the proof of the theorem.  $\square$

### 3. Stability

In this section, we study the stability of systems (1)–(3). More precisely, we establish exponential and polynomial decay results depending on  $\chi$  defined by

$$\chi = \tau \delta^2 D - (D\rho - GI_\rho) \left( \frac{\tau \rho_3 D}{I_\rho} - 1 \right). \quad (47)$$

The energy functional of systems (1)–(3) is defined by

$$\begin{aligned} E(t) &= E(\omega, \psi, s, \theta, q) \\ &= \frac{1}{2} \int_0^1 [\rho \omega_t^2 + I_\rho [(3s - \psi)_t]^2 + 3I_\rho s_t^2 + \rho_3 \theta^2 \\ &\quad + \tau q^2 + 4\gamma s^2 + D[(3s - \psi)_x]^2 + G(\psi - \omega_x)^2 + 3Ds_x^2] dx. \end{aligned} \quad (48)$$

Now we give our stability results.

**Theorem 2** (exponential decay). *Suppose that  $\chi = 0$ . For any initial data  $U_0 \in \mathcal{H}$ , there exist two positive constants  $\mu$  and  $\eta$  such that the energy functional (48) satisfies*

$$E(t) \leq \mu e^{-\eta t}, \quad \forall t \geq 0. \quad (49)$$

**Theorem 3** (polynomial decay). *Suppose that  $\chi \neq 0$ . For any initial data  $U_0 \in D(\mathcal{A})$ , there exists positive constant  $\mu_0$  such that the energy functional (48) satisfies*

$$E(t) \leq \frac{\mu_0}{t}, \quad \forall t > 0. \quad (50)$$

To prove Theorems 1 and 2, we need the following technical lemmas.

#### 3.1. Technical Lemmas

**Lemma 1.** *It holds that the energy functional  $E(t)$  is non-increasing and satisfies*

$$E'(t) = -4\beta \int_0^1 s_t^2 dx - \alpha \int_0^1 q^2 dx \leq 0. \quad (51)$$

*Proof.* Multiplying (1) by  $\omega_t$ ,  $(3s - \psi)_t$ ,  $s_t$ ,  $\theta$ , and  $q$ , respectively, integrating the results by parts and using boundary condition (1), we easily get (51).  $\square$

**Lemma 2.** Define the functional  $F_1(t)$  by

$$F_1(t) = I_\rho \int_0^1 (3s - \psi)_t (3s - \psi) dx - \rho \int_0^1 \omega_t \int_0^x (3s - \psi)(y) dy dx. \quad (52)$$

Then, we have for any  $\varepsilon_1 > 0$ ,

$$F_1'(t) \leq -\frac{D}{2} \int_0^1 [(3s - \psi)_x]^2 dx + \varepsilon_1 \int_0^1 \omega_t^2 dx + c \left(1 + \frac{1}{\varepsilon_1}\right) \int_0^1 [(3s - \psi)_t]^2 dx + \frac{\delta^2 c_*^2}{2D} \int_0^1 \theta^2 dx, \quad (53)$$

where  $c_* > 0$  is the Poincaré constant.

*Proof.* It follows from (1) that

$$F_1'(t) = D \int_0^1 (3s - \psi)_{xx} (3s - \psi) dx + G \int_0^1 (\psi - \omega_x) (3s - \psi) dx + I_\rho \int_0^1 [(3s - \psi)_t]^2 dx + G \int_0^1 (\psi - \omega_x) \int_0^x (3s - \psi)(y) dy dx + \delta \int_0^1 \theta_x \int_0^x (3s - \psi)(y) dy dx - \rho \int_0^1 \omega_t \int_0^x (3s - \psi)_t(y) dy dx. \quad (54)$$

Using integration by parts and boundary condition (1), we arrive at

$$F_1'(t) = -D \int_0^1 [(3s - \psi)_x]^2 dx + I_\rho \int_0^1 [(3s - \psi)_t]^2 dx - \delta \int_0^1 \theta (3s - \psi) dx - \rho \int_0^1 \omega_t \int_0^x (3s - \psi)_t(y) dy dx. \quad (55)$$

Then, by using Hölder's, Young's, and Poincaré's inequalities, we can get (53) from (57).  $\square$

**Lemma 3.** The functional  $F_2(t)$  defined by

$$F_2(t) = \rho \int_0^1 (\psi - \omega_x) \int_0^x \omega_t(y) dy dx, \quad (56)$$

satisfies for any  $\varepsilon_2 > 0$ ,

$$F_2'(t) \leq -\frac{G}{2} \int_0^1 (\psi - \omega_x)^2 dx + \varepsilon_2 \int_0^1 \psi_t^2 dx + c \left(1 + \frac{1}{\varepsilon_2}\right) \int_0^1 \omega_t^2 dx + \frac{\delta^2}{2G} \int_0^1 \theta^2 dx. \quad (57)$$

*Proof.* Differentiating  $F_2(t)$  with respect to  $t$  and using (1), we see that

$$F_2'(t) = \rho \int_0^1 \psi_t \int_0^x \omega_t(y) dy dx - \rho \int_0^1 \omega_{xt} \int_0^x \omega_t(y) dy dx - G \int_0^1 (\psi - \omega_x) \int_0^x (\psi - \omega_y)_y dy dx - \delta \int_0^1 (\psi - \omega_x) \int_0^x \theta_y dy dx. \quad (58)$$

Using integration by parts, we obtain

$$F_2'(t) = \rho \int_0^1 \psi_t \int_0^x \omega_t(y) dy dx + \rho \int_0^1 \omega_t^2 dx - G \int_0^1 (\psi - \omega_x)^2 dx - \delta \int_0^1 \theta (\psi - \omega_x) dx. \quad (59)$$

Then, by using Young's inequality and Hölder's inequality, we can get (57).  $\square$

**Lemma 4.** Define the functional  $F_3(t)$  by

$$F_3(t) = \tau \rho_3 \int_0^1 \theta \int_0^x q(y) dy dx. \quad (60)$$

Then, we can get for any  $\varepsilon_3 > 0$ ,

$$F_3'(t) \leq -\frac{\rho_3}{2} \int_0^1 \theta^2 dx + \varepsilon_3 \int_0^1 \omega_t^2 dx + c \left(1 + \frac{1}{\varepsilon_3}\right) \int_0^1 q^2 dx. \quad (61)$$

*Proof.* Differentiating  $F_3$  with respect to  $t$  and using (1), we obtain

$$F_3'(t) = -\tau \int_0^1 q_x \int_0^x q(y) dy dx - \tau \delta \int_0^1 \omega_{xt} \int_0^x q(y) dy dx - \rho_3 \alpha \int_0^1 \theta \int_0^x q dy dx - \rho_3 \int_0^1 \theta \int_0^x \theta_y dy dx. \quad (62)$$

Integration by parts gives us

$$F_3'(t) = \tau \int_0^1 q^2 dy + \tau \delta \int_0^1 \omega_t q dx - \rho_3 \alpha \int_0^1 \theta \int_0^x q dy dx - \rho_3 \int_0^1 \theta^2 dx. \quad (63)$$

By using Young's inequality and Hölder's inequality, we can get (61).  $\square$

**Lemma 5.** The functional  $F_4(t)$  defined by

$$F_4(t) = -\rho\rho_3 \int_0^1 \theta \int_0^x \omega_t(y) dy dx, \quad (64)$$

satisfies for any  $\varepsilon_4 > 0$ ,

$$\begin{aligned} F_4'(t) &\leq -\frac{\rho\delta}{2} \int_0^1 \omega_t^2 dx + \varepsilon_4 \int_0^1 (\psi - \omega_x)^2 dx + c \left(1 + \frac{1}{\varepsilon_4}\right) \int_0^1 \theta^2 dx \\ &\quad + \frac{\rho}{2\delta} \int_0^1 q^2 dx. \end{aligned} \quad (65)$$

*Proof.* We take the derivative of  $F_4$  and use (1) and integrate by parts to obtain

$$\begin{aligned} F_4'(t) &= \rho \int_0^1 q_x \int_0^x \omega_t(y) dy dx + \rho\delta \int_0^1 \omega_{xt} \int_0^x \omega_t(y) dy dx \\ &\quad + \rho_3 G \int_0^1 \theta \int_0^x (\psi - \omega_y)_y(y) dy dx \\ &\quad + \rho_3 \delta \int_0^1 \theta \int_0^x \theta_y(y) \\ &= -\rho \int_0^1 q \omega_t dx - \rho\delta \int_0^1 \omega_t^2 dx \\ &\quad + \rho_3 G \int_0^1 \theta (\psi - \omega_x) dx + \rho_3 \delta \int_0^1 \theta^2 dx. \end{aligned} \quad (66)$$

Then, using Young's inequality, we can get (65).  $\square$

**Lemma 6.** Define the functional  $F_5(t)$  by

$$\begin{aligned} F_5(t) &= \tau G \delta I_\rho \int_0^1 (3s - \psi)_t (\psi - \omega_x) dx \\ &\quad - \tau \delta D \rho \int_0^1 \omega_t (3s - \psi)_x dx \\ &\quad + \tau \rho_3 (D\rho - GI_\rho) \int_0^1 \theta (3s - \psi)_t dx \\ &\quad - \tau (D\rho - GI_\rho) \int_0^1 q (3s - \psi)_x dx. \end{aligned} \quad (67)$$

Then, we have for any  $\varepsilon_5 > 0$ ,

$$\begin{aligned} F_5'(t) &\leq -\frac{\tau G \delta I_\rho}{2} \int_0^1 [(3s - \psi)_t]^2 dx + c_1 \int_0^1 s_t^2 dx \\ &\quad + c_2 \int_0^1 \theta^2 dx + c_3 \int_0^1 (\psi - \omega_x)^2 dx \\ &\quad + \varepsilon_5 \int_0^1 [(3s - \psi)_x]^2 dx + C_{\varepsilon_5} \int_0^1 q^2 dx \\ &\quad + \chi \int_0^1 \theta_x (3s - \psi)_x dx, \end{aligned} \quad (68)$$

where  $c_i$  ( $i = 1, 2, 3$ ) are positive constants.

*Proof.* By differentiating  $F_5$  with respect to  $t$ , we have

$$\begin{aligned} F_5'(t) &= \underbrace{\tau G \delta I_\rho \int_0^1 (3s - \psi)_{tt} (\psi - \omega_x) dx}_{:=I_1} + \tau G \delta I_\rho \int_0^1 (3s - \psi)_t (\psi - \omega_x)_t dx \\ &\quad - \underbrace{\tau \delta D \rho \int_0^1 \omega_{tt} (3s - \psi)_x dx - \tau \delta D \rho \int_0^1 \omega_t (3s - \psi)_{xt} dx}_{:=I_2} \\ &\quad + \underbrace{\tau \rho_3 (D\rho - GI_\rho) \int_0^1 \theta_t (3s - \psi)_t dx}_{:=I_3} + \underbrace{\tau \rho_3 (D\rho - GI_\rho) \int_0^1 \theta (3s - \psi)_{tt} dx}_{:=I_4} \\ &\quad - \underbrace{\tau (D\rho - GI_\rho) \int_0^1 q_t (3s - \psi)_x dx}_{:=I_5} - \underbrace{\tau (D\rho - GI_\rho) \int_0^1 q (3s - \psi)_{xt} dx}_{:=I_6}. \end{aligned} \quad (69)$$

Using equation (1) and integrating by parts, we see that

$$\begin{aligned} I_1 &= -\tau G \delta D \int_0^1 (3s - \psi)_x (\psi - \omega_x)_x dx \\ &\quad + \tau G^2 \delta \int_0^1 (\psi - \omega_x)^2 dx, \end{aligned} \quad (70)$$

$$\begin{aligned} I_2 &= \tau \delta D G \int_0^1 (\psi - \omega_x)_x (3s - \psi)_x dx \\ &\quad + \tau \delta^2 D \int_0^1 \theta_x (3s - \psi)_x dx, \end{aligned} \quad (71)$$

$$\begin{aligned} I_3 &= -\tau (D\rho - GI_\rho) \int_0^1 q_x (3s - \psi)_t dx \\ &\quad - \tau \delta (D\rho - GI_\rho) \int_0^1 \omega_{xt} (3s - \psi)_t dx, \end{aligned} \quad (72)$$

$$\begin{aligned} I_4 &= -\frac{\tau \rho_3 D}{I_\rho} (D\rho - GI_\rho) \int_0^1 \theta_x (3s - \psi)_x dx \\ &\quad + \frac{\tau \rho_3 G}{I_\rho} (D\rho - GI_\rho) \int_0^1 \theta (\psi - \omega_x) dx, \end{aligned} \quad (73)$$

$$I_5 = \alpha(D\rho - GI_\rho) \int_0^1 q(3s - \psi)_x dx + (D\rho - GI_\rho) \int_0^1 \theta_x(3s - \psi)_x dx, \quad (74)$$

$$I_6 = \tau(D\rho - GI_\rho) \int_0^1 q_x(3s - \psi)_t dx. \quad (75)$$

Inserting (70)–(75) into (69), we can obtain

$$\begin{aligned} F'_5(t) &= \tau G^2 \delta \int_0^1 (\psi - \omega_x)^2 dx + \tau G \delta I_\rho \int_0^1 \psi_t(3s - \psi)_t dx \\ &+ \frac{\tau \rho_3 G}{I_\rho} (D\rho - GI_\rho) \int_0^1 \theta(\psi - \omega_x) dx \\ &+ \alpha(D\rho - GI_\rho) \int_0^1 q(3s - \psi)_x dx \\ &+ \chi \int_0^1 \theta_x(3s - \psi)_x dx. \end{aligned} \quad (76)$$

Recalling  $\psi = (\psi - 3s) + 3s$  and using Young's inequality, we conclude that

$$\begin{aligned} &\tau G \delta I_\rho \int_0^1 \psi_t(3s - \psi)_t dx \\ &= -\tau G \delta I_\rho \int_0^1 [(3s - \psi)_t]^2 dx + 3\tau G \delta I_\rho \int_0^1 s_t(3s - \psi)_t dx \\ &\leq -\frac{\tau G \delta I_\rho}{2} \int_0^1 [(3s - \psi)_t]^2 dx + c_1 \int_0^1 s_t^2 dx, \end{aligned} \quad (77)$$

$$\begin{aligned} &\frac{\tau \rho_3 G}{I_\rho} (D\rho - GI_\rho) \int_0^1 \theta(\psi - \omega_x) dx \\ &\leq c_2 \int_0^1 \theta^2 dx + c_3 \int_0^1 (\psi - \omega_x)^2 dx, \end{aligned} \quad (78)$$

and for any  $\varepsilon_5 > 0$ ,

$$\begin{aligned} \alpha(D\rho - GI_\rho) \int_0^1 q(3s - \psi)_x dx &\leq \varepsilon_5 \int_0^1 [(3s - \psi)_x]^2 dx \\ &+ C_{\varepsilon_5} \int_0^1 q^2 dx, \end{aligned} \quad (79)$$

which, together with (76)–(78), gives us (68).  $\square$

**Lemma 7.** The functional  $F_6(t)$  defined by

$$F_6(t) = 3I_\rho \int_0^1 s_t s dx + 2\beta \int_0^1 s^2 dx, \quad (80)$$

satisfies

$$\begin{aligned} F'_6(t) &\leq -3\gamma \int_0^1 s^2 dx - 3D \int_0^1 s_x^2 dx \\ &+ c_4 \int_0^1 (\psi - \omega_x)^2 dx + 3I_\rho \int_0^1 s_t^2 dx, \end{aligned} \quad (81)$$

where  $c_4$  is a positive constant.

*Proof.* follows from (1) that

$$\begin{aligned} F'_6(t) &= -3D \int_0^1 s_x^2 dx - 3G \int_0^1 s(\psi - \omega_x) dx \\ &- 4\gamma \int_0^1 s^2 dx + 3I_\rho \int_0^1 s_t^2 dx. \end{aligned} \quad (82)$$

Young's inequality gives us (82).  $\square$

### 3.2. Exponential Stability: Proof of Theorem 1

*Proof.* We define the functional  $\mathcal{L}(t)$  by

$$\begin{aligned} \mathcal{L}(t) &= NE(t) + F_1(t) + N_2 F_2(t) + N_3 F_3(t) \\ &+ N_4 F_4(t) + N_5 F_5(t) + F_6(t), \end{aligned} \quad (83)$$

where  $N$  and  $N_i$  ( $i = 2, 3, 4, 5$ ) are positive constants that will be chosen later.

Note that

$$\begin{aligned} \int_0^1 \psi_t^2 dx &= \int_0^1 [(3s - \psi) - 3s]_t^2 dx \\ &\leq 2 \int_0^1 [(3s - \psi)_t]^2 dx + 18 \int_0^1 s_t^2 dx. \end{aligned} \quad (84)$$

Replacing (84) in (57) and then combining (51)–(53), (57)–(68), and (82), we obtain

$$\begin{aligned} \mathcal{L}'(t) &\leq -(4\beta N - c_1 N_5 - 18\varepsilon_2 N_2 - 3I_\rho) \int_0^1 s_t^2 dx \\ &- \left(\frac{D}{2} - \varepsilon_5 N_5\right) \int_0^1 [(3s - \psi)_x]^2 dx \\ &- \left[\alpha N - c N_3 \left(1 + \frac{1}{\varepsilon_3}\right) - \frac{\rho}{2\delta} N_4 - C_{\varepsilon_5} N_5\right] \int_0^1 q^2 dx \\ &- \left[\frac{\rho \delta}{2} N_4 - \varepsilon_1 - \varepsilon_3 N_3 - c N_2 \left(1 + \frac{1}{\varepsilon_2}\right)\right] \int_0^1 \omega_t^2 dx \\ &- \left[\frac{\tau G \delta I_\rho}{2} N_5 - 2\varepsilon_2 N_2 - c \left(1 + \frac{1}{\varepsilon_1}\right)\right] \int_0^1 [(3s - \psi)_t]^2 dx \\ &- \left(\frac{G}{2} N_2 - \varepsilon_4 N_4 - c_3 N_5 - c_4\right) \int_0^1 (\psi - \omega_x)^2 dx \\ &- \left[\frac{\rho_3 N_3}{2} - \frac{\delta^2 c^2}{2D} - \frac{\delta^2}{2G} N_2 - c N_4 \left(1 + \frac{1}{\varepsilon_4}\right) - c_2 N_5\right] \int_0^1 \theta^2 dx \\ &- 3D \int_0^1 s_x^2 dx - 3\gamma \int_0^1 s^2 dx. \end{aligned} \quad (85)$$

Taking

$$\begin{aligned}
\varepsilon_1 &= 1, \\
\varepsilon_2 &= \frac{\tau G \delta I_\rho}{8N_2} N_5, \\
\varepsilon_3 &= \frac{1}{N_3}, \\
\varepsilon_4 &= \frac{G}{4N_4} N_2, \\
\varepsilon_5 &= \frac{D}{4N_5},
\end{aligned} \tag{86}$$

we obtain

$$\begin{aligned}
\mathcal{L}'(t) &\leq -\left(4\beta N - c_1 N_5 - \frac{9}{4} \tau G \delta I_\rho N_5 - 3I_\rho\right) \int_0^1 s_t^2 dx \\
&\quad - \frac{D}{4} \int_0^1 [(3s - \psi)_x]^2 dx \\
&\quad - \left[\alpha N - cN_3(1 + N_3) - \frac{\rho}{2\delta} N_4 - C_{\varepsilon_5} N_5\right] \int_0^1 q^2 dx \\
&\quad - \left[\frac{\rho\delta}{2} N_4 - 2 - cN_2 \left(1 + \frac{8N_2}{N_5 \tau G \delta I_\rho}\right)\right] \int_0^1 \omega_t^2 dx \\
&\quad - \left(\frac{\tau G \delta I_\rho}{4} N_5 - 2c\right) \int_0^1 [(3s - \psi)_t]^2 dx \\
&\quad - \left(\frac{G}{4} N_2 - c_3 N_5 - c_4\right) \int_0^1 (\psi - \omega_x)^2 dx \\
&\quad - \left[\frac{\rho_3}{2} N_3 - \frac{\delta^2 c_*^2}{2D} - \frac{\delta^2}{2G} N_2\right. \\
&\quad \left. - cN_4 \left(1 + \frac{4N_4}{GN_2}\right) - c_2 N_5\right] \int_0^1 \theta^2 dx \\
&\quad - 3D \int_0^1 s_x^2 dx - 3\gamma \int_0^1 s^2 dx.
\end{aligned} \tag{87}$$

At this point, we first choose  $N_5 > 0$  large enough such that

$$\frac{\tau G \delta I_\rho}{4} N_5 - 2c > 0. \tag{88}$$

For fixed  $N_5$ , we take  $N_2 > 0$  so large that

$$\frac{G}{4} N_2 - c_3 N_5 - c_4 > 0. \tag{89}$$

Then, we pick  $N_4 > 0$  large so that

$$\frac{\rho\delta}{2} N_4 - 2 - cN_2 \left(1 + \frac{8N_2}{N_5 \tau G \delta I_\rho}\right) > 0. \tag{90}$$

And then we choose  $N_3$  so large that

$$\frac{\rho_3}{2} N_3 - \frac{\delta^2 c_*^2}{2D} - \frac{\delta^2}{2G} N_2 - cN_4 \left(1 + \frac{4N_4}{GN_2}\right) - c_2 N_5 > 0. \tag{91}$$

At last, we take  $N > 0$  large enough so that the functional  $\mathcal{L}(t)$  is equivalent to the energy functional  $E(t)$ , i.e., there exist two positive constants:

$$\beta_1 E(t) \leq \mathcal{L}(t) \leq \beta_2 E(t), \tag{92}$$

and further so that

$$\alpha N - cN_3(1 + N_3) - \frac{\rho}{2\delta} N_4 - C_{\varepsilon_5} N_5 > 0. \tag{93}$$

$$4\beta N - c_1 N_5 - \frac{9}{4} \tau G \delta I_\rho N_5 - 3I_\rho > 0,$$

Recalling (48), we infer that there exists a positive constant  $\beta_3$  such that, for any  $t > 0$ ,

$$\mathcal{L}'(t) \leq -\beta_3 E(t), \tag{94}$$

which, along with (92), implies

$$\mathcal{L}'(t) \leq -\frac{\beta_3}{\beta_2} \mathcal{L}(t). \tag{95}$$

Integrating (95) over  $(0, t)$ , we have, for any  $t > 0$ ,

$$\mathcal{L}(t) \leq \mathcal{L}(0) e^{-(\beta_3/\beta_2)t}, \tag{96}$$

which, using (95) again, gives us (49). The proof of Theorem 1 is done.  $\square$

**3.3. Polynomial Stability: Proof of Theorem 2.** In this section, we consider the case  $\chi \neq 0$  to prove Theorem 2.

Differentiating system (1) with respect to time, we obtain the following system:

$$\begin{cases}
\rho \omega_{ttt} + G(\psi - \omega_x)_{xt} + \delta \theta_{xt} = 0, \\
I_\rho (3s - \psi)_{ttt} - D(3s - \psi)_{xxt} - G(\psi - \omega_x)_t = 0, \\
I_\rho s_{ttt} - Ds_{xxt} + G(\psi - \omega_x)_t + \frac{4}{3} \gamma s_t + \frac{4}{3} \beta s_{tt} = 0, \\
\rho_3 \theta_{tt} + q_{xt} + \delta \omega_{xtt} = 0, \\
\tau q_{tt} + \alpha q_t + \theta_{xt} = 0,
\end{cases} \tag{97}$$

which subject to the following boundary conditions:

$$\begin{cases}
\omega_{xt}(0, t) = \psi_t(0, t) = s_t(0, t) = \theta_t(0, t) = 0, & t \in (0, \infty), \\
\omega_{xt}(1, t) = \psi_t(1, t) = s_t(1, t) = \theta_t(1, t) = 0, & t \in (0, \infty).
\end{cases} \tag{98}$$

For any initial data  $U_0 \in D(\mathcal{A})$ , system (97) is well posed. Next, we introduce second-order energy functional  $\bar{E}(t)$  by

$$\begin{aligned}
\bar{E}(t) &= E(\omega_t, \psi_t, s_t, \theta_t, q_t) \\
&= \frac{1}{2} \int_0^1 [\rho \omega_{tt}^2 + I_\rho [(3s - \psi)_{tt}]^2 + 3I_\rho s_{tt}^2 + \rho_3 \theta_t^2 + \tau q_t^2 + 4\gamma s_t^2 \\
&\quad + D[(3s - \psi)_{xt}]^2 + G[(\psi - \omega_x)_t]^2 + 3D s_{xt}^2] dx. \tag{99}
\end{aligned}$$

By using the same arguments as in Lemma 3, we can get the second-order energy  $\bar{E}(t)$  defined by (99) is nonincreasing and satisfies

$$\bar{E}'(t) = -4\beta \int_0^1 s_{tt}^2 dx - \alpha \int_0^1 q_t^2 dx \leq 0. \tag{100}$$

In Lemma 6, we have proved that, for any  $\varepsilon_5 > 0$ ,

$$\begin{aligned}
F_5'(t) &\leq -\frac{\tau G \delta I_\rho}{2} \int_0^1 [(3s - \psi)_t]^2 dx + c_1 \int_0^1 s_t^2 dx \\
&\quad + c_2 \int_0^1 \theta^2 dx + c_3 \int_0^1 (\psi - \omega_x)^2 dx \\
&\quad + \varepsilon_5 \int_0^1 [(3s - \psi)_x]^2 dx + C_{\varepsilon_5} \int_0^1 q^2 dx \\
&\quad + \chi \int_0^1 \theta_x (3s - \psi)_x dx. \tag{101}
\end{aligned}$$

Thanks to (1) and Young's inequality, we derive that

$$\int_0^1 \theta_x^2 dx \leq c \int_0^1 q^2 dx + c \int_0^1 q_t^2 dx. \tag{102}$$

Then, for any  $\varepsilon_5 > 0$ ,

$$\begin{aligned}
\chi \int_0^1 \theta_x (3s - \psi)_x dx &\leq \varepsilon_5 \int_0^1 [(3s - \psi)_x]^2 dx + C_{\varepsilon_5} \int_0^1 \theta_x^2 dx \\
&\leq \varepsilon_5 \int_0^1 [(3s - \psi)_x]^2 dx + C_{\varepsilon_5} \int_0^1 q^2 dx \\
&\quad + C_{\varepsilon_5} \int_0^1 q_t^2 dx. \tag{103}
\end{aligned}$$

Therefore, the derivative of  $F_5$  satisfies

$$\begin{aligned}
F_5'(t) &\leq -\frac{\tau G \delta I_\rho}{2} \int_0^1 [(3s - \psi)_t]^2 dx + c_1 \int_0^1 s_t^2 dx \\
&\quad + c_2 \int_0^1 \theta^2 dx + c_3 \int_0^1 (\psi - \omega_x)^2 dx \\
&\quad + 2\varepsilon_5 \int_0^1 [(3s - \psi)_x]^2 dx + C_{\varepsilon_5} \int_0^1 q^2 dx + C_{\varepsilon_5} \int_0^1 q_t^2 dx. \tag{104}
\end{aligned}$$

*Proof.* We define the functional  $\tilde{\mathcal{L}}(t)$  by

$$\begin{aligned}
\tilde{\mathcal{L}}(t) &= N(E(t) + \bar{E}(t)) + F_1(t) + N_2 F_2(t) \\
&\quad + N_3 F_3(t) + N_4 F_4(t) + N_5 F_5(t) + F_6(t). \tag{105}
\end{aligned}$$

It follows from (51)–(53), (57)–(65), and (100)–(104) that

$$\begin{aligned}
\tilde{\mathcal{L}}'(t) &\leq -(4\beta N - c_1 N_5 - 18\varepsilon_2 N_2 - 3I_\rho) \int_0^1 s_t^2 dx - \left(\frac{D}{2} - 2\varepsilon_5 N_5\right) \int_0^1 [(3s - \psi)_x]^2 dx \\
&\quad - \left[\alpha N - c N_3 \left(1 + \frac{1}{\varepsilon_3}\right) - \frac{\rho}{2\delta} N_4 - C_{\varepsilon_5} N_5\right] \int_0^1 q^2 dx \\
&\quad - \left[\frac{\rho \delta}{2} N_4 - \varepsilon_1 - \varepsilon_3 N_3 - c N_2 \left(1 + \frac{1}{\varepsilon_2}\right)\right] \int_0^1 \omega_t^2 dx \\
&\quad - \left[\frac{\tau G \delta I_\rho}{2} N_5 - 2\varepsilon_2 N_2 - c \left(1 + \frac{1}{\varepsilon_1}\right)\right] \int_0^1 [(3s - \psi)_t]^2 dx \\
&\quad - \left(\frac{G}{2} N_2 - \varepsilon_4 N_4 - c_3 N_5 - c_4\right) \int_0^1 (\psi - \omega_x)^2 dx \\
&\quad - \left[\frac{\rho_3}{2} N_3 - \frac{\delta^2 c^2}{2D} - \frac{\delta^2}{2G} N_2 - c N_4 \left(1 + \frac{1}{\varepsilon_4}\right) - c_2 N_5\right] \int_0^1 \theta^2 dx \\
&\quad - 3D \int_0^1 s_x^2 dx - 3\gamma \int_0^1 s^2 dx - (\alpha N - C_{\varepsilon_5}) \int_0^1 q_t^2 dx. \tag{106}
\end{aligned}$$



With the same choice of constants as in Section 3.2, we further take  $N > 0$  so large that

$$\alpha N - C_{\varepsilon_s} > 0. \quad (107)$$

Noting that (48), we know that there exists a positive constant  $\mu_1$  such that, for any  $t > 0$ ,

$$\tilde{\mathcal{L}}'(t) \leq -\mu_1 E(t). \quad (108)$$

Since the energy functional  $E(t)$  is positive and non-increasing, we infer (108) that, for any  $t > 0$ ,

$$tE(t) \leq \int_0^t E(s)ds \leq \frac{1}{\mu_1} (\tilde{\mathcal{L}}(0)t - n\tilde{\mathcal{L}}q(t)) \leq \frac{\tilde{\mathcal{L}}(0)}{\mu_1}, \quad (109)$$

which gives us

$$E(t) \leq \frac{\mu_0}{t}, \quad \forall t > 0. \quad (110)$$

Here,  $\mu_0 = (\tilde{\mathcal{L}}(0)t/\mu_1) = (E(0) + \tilde{E}(0)/\mu_1)$ . The proof is complete.  $\square$

*Remark 1.* We point out that the functional  $\tilde{\mathcal{L}}(t)$  is inequivalent to the energy functional  $E(t)$ . That is to say, (92) does not hold true.

## Data Availability

No data were used during this study.

## Conflicts of Interest

The author declares that there are no conflicts of interest regarding the publication of this paper.

## Acknowledgments

This work was supported by the National Natural Science Foundation of China (Grant no. 11701465).



## References

- [1] S. W. Hansen, "A model for a two-layered plate with interfacial slip," in *Control and Estimation of Distributed Parameter Systems: Nonlinear Phenomena*, pp. 143–170, Birkhauser, Basel, Switzerland, 1994.
- [2] S. W. Hansen and R. D. Spies, "Structural damping in laminated beams due to interfacial slip," *Journal of Sound and Vibration*, vol. 204, no. 2, pp. 183–202, 1997.
- [3] M. S. Alves and R. N. Monteiro, "Exponential stability of laminated Timoshenko beams with boundary/internal controls," *Journal of Mathematical Analysis and Applications*, vol. 482, Article ID 123516, 2020.
- [4] X.-G. Cao, D.-Y. Liu, and G.-Q. Xu, "Easy test for stability of laminated beams with structural damping and boundary feedback controls," *Journal of Dynamical and Control Systems*, vol. 13, no. 3, pp. 313–336, 2007.
- [5] Z. Chen, W. Liu, and D. Chen, "General decay rates for a laminated beam with memory," *Taiwanese Journal of Mathematics*, vol. 23, no. 5, pp. 1227–1252, 2019.
- [6] B. Feng, "Well-posedness and exponential decay for laminated Timoshenko beams with time delays and boundary feedbacks," *Mathematical Methods in the Applied Sciences*, vol. 41, no. 3, pp. 1162–1174, 2018.
- [7] B. Feng, T. F. Ma, R. N. Monteiro, and C. A. Raposo, "Dynamics of laminated Timoshenko beams," *Journal of Dynamics and Differential Equations*, vol. 30, no. 4, pp. 1489–1507, 2018.
- [8] G. Li, X. Kong, and W. Liu, "General decay for a laminated beam with structural damping and memory: the case of non-equal wave speeds," *Journal of Integral Equations and Applications*, vol. 30, no. 1, pp. 95–116, 2018.
- [9] A. Lo and N.-e. Tatar, "Stabilization of a laminated beam with interfacial slip," *Electronic Journal of Differential Equations*, vol. 129, p. 14, 2015.
- [10] A. Lo and N.-e. Tatar, "Uniform stability of a laminated beam with structural memory," *Qualitative Theory of Dynamical Systems*, vol. 15, no. 2, pp. 517–540, 2016.
- [11] A. Lo and N.-e. Tatar, "Exponential stabilization of a structure with interfacial slip," *Discrete and Continuous Dynamical Systems*, vol. 36, no. 11, pp. 6285–6306, 2016.
- [12] M. I. Mustafa, "Laminated Timoshenko beams with viscoelastic damping," *Journal of Mathematical Analysis and Applications*, vol. 466, no. 1, pp. 619–641, 2018.
- [13] M. I. Mustafa, "On the stabilization of viscoelastic laminated beams with interfacial slip," *Zeitschrift für Angewandte Mathematik und Physik*, vol. 69, p. 33, 2018.
- [14] M. I. Mustafa, "Boundary control of laminated beams with interfacial slip," *Journal of Mathematical Physics*, vol. 59, Article ID 051508, p. 9, 2018.
- [15] C. A. Raposo, "Exponential stability for a structure with interfacial slip and frictional damping," *Applied Mathematics Letters*, vol. 53, pp. 85–91, 2016.
- [16] C. A. Raposo, D. A. Z. Villanueva, S. D. M. Borjas, and D. C. Pereira, "Exponential stability for a structure with interfacial slip and memory," *Poincare Journal of Analysis and Application*, vol. 2, pp. 1–18, 2017.
- [17] C. A. Raposo, O. V. Villagrán, J. E. Muñoz Rivera, and M. S. Alves, "Hybrid laminated Timoshenko beam," *Journal of Mathematical Physics*, vol. 58, Article ID 101512, 11 pages, 2017.
- [18] W. Liu and W. Zhao, "Stabilization of a thermoelastic laminated beam with past history," *Applied Mathematics & Optimization*, vol. 80, no. 1, pp. 103–133, 2019.
- [19] T. A. Apalara, "Uniform stability of a laminated beam with structural damping and second sound," *Zeitschrift für Angewandte Mathematik und Physik*, vol. 68, p. 41, 2017.
- [20] W. Liu, Y. Luan, Y. Liu, and G. Li, "Well-posedness and asymptotic stability to a laminated beam in thermoelasticity of type III," *Mathematical Methods in the Applied Sciences*, p. 19, 2019.
- [21] L. Seghour, N. e. Tatar, and A. Berkani, "Stability of a thermoelastic laminated system subject to a neutral delay," *Mathematical Methods in the Applied Sciences*, vol. 43, no. 1, pp. 281–304, 2020.
- [22] M. Afilal, S. Messaoudi, and A. Soufyane, "Stabilization of a coupled hyperbolic equations with a heat equation of second sound," *Mediterranean Journal of Mathematics*, vol. 14, no. 2, p. 39, 2017.
- [23] J. E. Muñoz Rivera and R. Racke, "Mildly dissipative nonlinear Timoshenko systems-global existence and exponential stability," *Journal of Mathematical Analysis and Applications*, vol. 276, no. 1, pp. 248–278, 2002.
- [24] D. d. S. Almeida Júnior, M. L. Santos, and J. E. Muñoz Rivera, "Stability to 1-D thermoelastic Timoshenko beam acting on

- shear force,” *Zeitschrift für angewandte Mathematik und Physik*, vol. 65, no. 6, pp. 1233–1249, 2014.
- [25] H. D. Fernández Sare and R. Racke, “On the stability of damped Timoshenko systems: Cattaneo versus Fourier law,” *Archive for Rational Mechanics and Analysis*, vol. 194, no. 1, pp. 221–251, 2009.
- [26] A. Guesmia, S. A. Messaoudi, and A. Soufyane, “Stabilization of a linear Timoshenko system with infinite history and applications to the Timoshenko-heat systems,” *Electronic Journal of Differential Equations*, vol. 2012, no. 193, pp. 1–45, 2012.
- [27] M. L. Santos, D. S. Almeida Júnior, and J. E. Muñoz Rivera, “The stability number of the Timoshenko system with second sound,” *Journal of Differential Equations*, vol. 253, no. 9, pp. 2715–2733, 2012.
- [28] T. A. Apalara, S. A. Messaoudi, and A. A. Keddi, “On the decay rates of Timoshenko system with second sound,” *Mathematical Methods in the Applied Sciences*, vol. 39, no. 10, pp. 2671–2684, 2016.
- [29] B. Feng, “On a semilinear Timoshenko-Coleman-Gurtin system: quasi-stability and attractors,” *Discrete & Continuous Dynamical Systems—A*, vol. 37, no. 9, pp. 4729–4751, 2017.
- [30] T. Hamadouche and S. A. Messaoudi, “Existence and energy decay of a nonuniform Timoshenko system with second sound,” *Zeitschrift für Angewandte Mathematik und Physik*, vol. 69, pp. 1–18, 2018.
- [31] M. Aouadi and K. Boulehmi, “Asymptotic behavior of non-uniform Timoshenko beam acting on shear force with feedback controller,” *ZAMM—Journal of Applied Mathematics and Mechanics/Zeitschrift für Angewandte Mathematik und Mechanik*, vol. 97, no. 12, pp. 1579–1599, 2017.
- [32] Z. Liu and S. Zheng, *Semigroups Associated with Dissipative Systems*, Vol. 398, Chapman Hall/CRC, London, UK, 1999.
- [33] A. Pazy, *Semigroups of Linear Operators and Applications to Partial Differential Equations*, Springer, New York, NY, USA, 1983.

## Research Article

# Hopf Bifurcation and Dynamic Analysis of an Improved Financial System with Two Delays

G. Kai,<sup>1,2,3</sup> W. Zhang ,<sup>4,5</sup> Z. Jin ,<sup>6</sup> and C. Z. Wang<sup>1</sup>

<sup>1</sup>School of Statistics and Mathematics, Inner Mongolia University of Financial and Economics, Hohhot 010070, China

<sup>2</sup>School of Materials Science and Engineering, Inner Mongolia University of Technology, Hohhot 010051, China

<sup>3</sup>Inner Mongolia Key Laboratory of Economic Data Analysis and Mining, Hohhot 010070, China

<sup>4</sup>Beijing Key Laboratory of Nonlinear Vibrations and Strength of Mechanical Structures, College of Mechanical Engineering, Beijing University of Technology, Beijing 100124, China

<sup>5</sup>Department of Mechanics, Inner Mongolia University of Technology, Hohhot 010051, China

<sup>6</sup>School of Finance, Inner Mongolia University of Financial and Economics, Hohhot 010070, China

Correspondence should be addressed to W. Zhang; sandyzhang0@yahoo.com and Z. Jin; jinzhuang@sina.com

Received 24 September 2019; Accepted 18 October 2019; Published 27 February 2020

Guest Editor: Viet-Thanh Pham

Copyright © 2020 G. Kai et al. This is an open access article distributed under the Creative Commons Attribution License, which permits unrestricted use, distribution, and reproduction in any medium, provided the original work is properly cited.

The complex chaotic dynamics and multistability of financial system are some important problems in micro- and macroeconomic fields. In this paper, we study the influence of two-delay feedback on the nonlinear dynamics behavior of financial system, considering the linear stability of equilibrium point under the condition of single delay and two delays. The system undergoes Hopf bifurcation near the equilibrium point. The stability and bifurcation directions of Hopf bifurcation are studied by using the normal form method and central manifold theory. The theoretical results are verified by numerical simulation. Furthermore, one feature of the proposed financial chaotic system is that its multistability depends extremely on the memristor initial condition and the system parameters. It is shown that the nonlinear dynamics of financial chaotic system can be significantly changed by changing the values of time delays.

## 1. Introduction

It is widely recognized that chaos can be obtained in some mathematically simple systems of nonlinear differential equations. With the advent of computers, it is now possible to study the entire parameter space of these systems that result in some desired characteristics of the system. Recently, there has been increasing attention to some unusual examples and application of such systems [1–8]. The financial system is an extremely complex nonlinear dynamical system composed of many elements. The study of the complex nonlinear dynamics behavior of the financial system is an important problem in the fields of micro- and macroeconomy [9]. The uncertain factors bring very important influence to the description of the financial system and make analysis of the financial systems become a very important problem.

Researchers try to explain the core characteristics of economic data: irregular microeconomic fluctuations, unstable macroeconomic fluctuations, irregular growth, and syntax changes [10–13]. However, some inappropriate combination of parameters in the financial system may lead to financial markets in trouble or out of control. Therefore, it is necessary to make a systematic and deep study on the internal syntax characteristics of the complicated financial system. The results will reveal the bifurcation phenomena under different parameter combinations, probe into the causes of the complicated nonlinear dynamics phenomena, and predict and control the complicated financial systems [14, 15]. In addition, multistability is a critical property of nonlinear dynamical systems when coexisting attractors can be obtained for the same parameters, but different initial conditions [16–19]. The flexibility in the systems' performance can be archived without changing parameters.

Wang et al. [20] studied the bifurcation topology and the global complexity of a class of nonlinear financial systems. Ishiyama and Saiki [21] established the macroeconomic growth cycle model and solved the qualitative- and quantitative-related unstable periodic solutions embedded in the chaotic attractor. By using Lyapunov stability theory and Routh–Hurwitz criterion, Zhao et al. [22] studied the global synchronization of the three-dimensional chaotic financial system. Yu et al. [23] used numerical simulation to analyze the Lyapunov exponents and bifurcation diagram of chaotic financial system. Cantore and Levine [24] studied the reparameterized model with evaluation parameters. Gao et al. [25] gave the final bounded estimator set and chaotic synchronization analysis of the financial risks system.

Until now, one of the nonlinear economic and financial dynamic models confirmed by economists comes from a financial system model composed of four subblocks (production, money, security, and labor) [15, 24, 26].

$$\dot{x} = z + (y - a)x, \quad (1a)$$

$$\dot{y} = 1 - by - x^2, \quad (1b)$$

$$\dot{z} = -x - cz, \quad (1c)$$

where  $x$  represents the interest rate,  $y$  represents the investment demand,  $z$  represents the price index,  $a$  represents the saving amount,  $b$  represents the unit investment cost, and  $c$  represents the elasticity of commodity demand;  $a, b$ , and  $c$  are all normal numbers.

In real life, with the development of economy, there are more and more factors that restrict the development of economy. Some classical chaotic financial systems can not reflect the laws and changes of economic development well. For example, the factors that affect the change of interest rate are related to the average profit rate besides investment demand and price index, and the average profit rate is proportional to the interest rate. Therefore, we construct the following improved chaotic financial system model:

$$\dot{x} = z + (y - a)x, \quad (2a)$$

$$\dot{y} = 1 - by - x^2 - bxy, \quad (2b)$$

$$\dot{z} = -x - cz, \quad (2c)$$

where  $x$  is the interest rate,  $y$  is the investment demand,  $z$  is the price index,  $a$  is the saving amount,  $b$  is the unit investment cost, and  $c$  is the elasticity of commodity demand;  $a, b$ , and  $c$  are all normal numbers. When the parameters  $a = 3$ ,  $b = 0.1$ , and  $c = 1$  and initial values are at points  $(0.1, 2, 0.1)$ , system (2a)–(2c) generates chaotic attractors, as shown in Figure 1.

With the development and innovation of financial markets, scholars have found that it will be better to add time delay factor for describing the actual economic markets [27–30]. Chen [31] analyzed the complex nonlinear dynamics, such as periodicity, quasiperiodicity, and chaotic behavior in the delayed feedback of financial systems. Ma

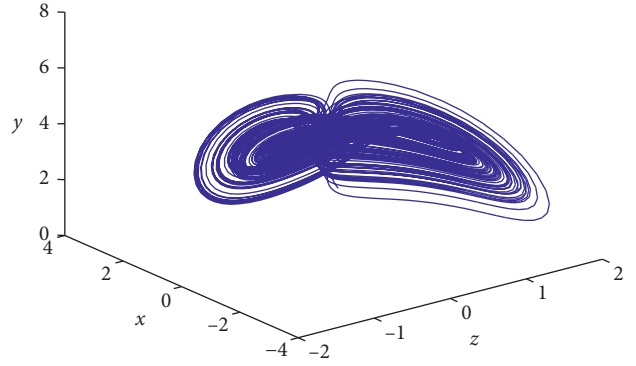


FIGURE 1: Chaotic attractor for the 3D chaotic system ((2a)–(2c)).

and Tu [32] established a class of complex dynamic macroeconomic systems and studied the effect of time delay on savings rate and dynamic financial stability. Holyst and Urbanowicz [33] have shown that the chaotic attractor of the financial model can be stabilized in a periodic track by using Pyragas delayed feedback control. In addition, Ma and Chen [14] added the delayed feedback to the three variables of financial system and gave some results on the existence of Hopf bifurcation and the effect of delayed feedback. Based on political events and other human factors, some scholars have considered the impact of delay and feedback items (see [28, 34]). In practice, financial behaviour is not only affected by a single time delay but often seems to be affected by multiple external shocks. These various external influences embody multiple delays and can be reflected in all variables, i.e., by introducing various delayed feedback items into interest rates  $x$  of change of interest rate, they will also have a significant impact on system (2a)–(2c). Therefore, we further consider the double-delay system.

$$\dot{x} = z + (y - a)x + k_1(x(t) - x(t - \tau_1)) + k_2(x(t) - x(t - \tau_2)), \quad (3a)$$

$$\dot{y} = 1 - by - x^2 - bxy, \quad (3b)$$

$$\dot{z} = -x - cz. \quad (3c)$$

where  $\tau_1$  and  $\tau_2$  are the two time delays and  $k_1$  and  $k_2$  are the feedback control intensities.

In this paper, we study the Hopf bifurcation and nonlinear dynamics of an improved financial system with two delays. Firstly, we study the distribution of the roots of the characteristic equations at the equilibrium point. Sufficient conditions for the local stability of the equilibrium point and the existence of Hopf bifurcation are obtained. Secondly, taking two delays as bifurcation parameters and using the canonical form method and the central manifold theorem, we determine the bifurcation direction of the periodic solution and the explicit algorithm for the stability of the bifurcation periodic solution. Under the premise of the existence of local bifurcation, the existence of the bifurcation periodic solution of this system is discussed by using the theory of functional differential equations. Finally, the

correctness of the conclusion is verified by numerical simulation.

## 2. Existence of Hopf Bifurcation in Financial System

In order to study the influence of time delays on nonlinear dynamic system, the three equilibrium points of the system are obtained as follows:

$$\left(-1, \frac{1+ac}{c}, \frac{1}{c}\right), \quad (4a)$$

$$\left(0, \frac{1}{b}, 0\right), \quad (4b)$$

$$\left(\frac{-b+c-abc}{c}, \frac{1+ac}{c}, \frac{b-c+abc}{c^2}\right). \quad (4c)$$

Here, we only analyze the following equilibrium point:

$$(x_0, y_0, z_0) = \left(0, \frac{1}{b}, 0\right). \quad (5)$$

Linear transformations are given as

$$u_1 = x - x_0, \quad (6a)$$

$$u_2 = y - y_0, \quad (6b)$$

$$u_3 = z - z_0. \quad (6c)$$

System (2a)–(2c) becomes the following equations:

$$\dot{u}_1 = u_3 + \left(u_2 - a + \frac{1}{b}\right)u_1 + k_1(u_1(t) - u_1(t - \tau_1)) \quad (7a)$$

$$+ k_2(u_1(t) - u_1(t - \tau_2)),$$

$$\dot{u}_2 = -u_1 - bu_2 - u_1^2 - bu_1, \quad (7b)$$

$$\dot{u}_3 = -u_1 - cu_3. \quad (7c)$$

The characteristic equation of equations (7a) and (7b) at  $(0, 0, 0)$  is

$$\begin{aligned} & b - c + abc + ab\lambda + ac\lambda - \frac{c\lambda}{b} + bc\lambda + a\lambda^2 - \frac{\lambda^2}{b} + b\lambda^2 + c\lambda^2 + \lambda^3 \\ & + e^{-\lambda\tau_1}(-bck_1 - bk_1\lambda - ck_1\lambda - k_1\lambda^2) + e^{-\lambda\tau_2}(-bck_2 - bk_2\lambda - ck_2\lambda - k_2\lambda^2) = 0. \end{aligned} \quad (8)$$

Since the dynamics of differential equations with two delays are very complex, we first discuss the case of  $\tau_1 = \tau_2 = 0$ , then discuss the case of  $\tau_1 > 0, \tau_2 = 0$  with single delay, and finally discuss the case of  $\tau_1 > 0, \tau_2 > 0$ .

*Case 1.*  $\tau_1 = \tau_2 = 0$ .

The characteristic equation (5) becomes

$$b - c + abc + \left(ab + ac - \frac{c}{b} + bc\right)\lambda + \left(a - \frac{1}{b} + b + c\right)\lambda^2 + \lambda^3 = 0. \quad (9)$$

Let

$$p_1 = a - \frac{1}{b} + b + c, \quad (10a)$$

$$p_2 = ab + ac - \frac{c}{b} + bc, \quad (10b)$$

$$p_3 = b - c + abc, \quad (10c)$$

and assume

$$H_1: p_1 > 0, p_3 > 0, p_1 p_2 - p_3 > 0. \quad (11)$$

According to Routh–Hurwitz criterion, if  $H_1$  holds, the equilibrium point  $(0, 0, 0)$  of system (7a)–(7c) is locally asymptotically stable.

*Case 2.*  $\tau_1 > 0, \tau_2 = 0$ .

The characteristic equation (5) becomes

$$\begin{aligned} & b - c + abc - bck_1 + ab\lambda + ac\lambda - \frac{c\lambda}{b} + bc\lambda - bk_1\lambda - ck_1\lambda + a\lambda^2 - \frac{\lambda^2}{b} \\ & + b\lambda^2 + c\lambda^2 - k_1\lambda^2 + \lambda^3 + e^{-\lambda\tau_1}(bck_1 + bk_1\lambda + ck_1\lambda + k_1\lambda^2) = 0. \end{aligned} \quad (12)$$

If  $\lambda = iw$  is a solution of equation (12), then the real part and imaginary part are separated and made equal to zero. We can obtain

$$\begin{aligned} & w^2 + b^2(1 + ac + ck_1(-1 + m) + k_1nw - w^2) \\ & + b(-(a + k_1(-1 + m))w^2 + c(-1 + k_1mw - w^2)) = 0, \end{aligned} \quad (13a)$$

$$\begin{aligned} & -cw + bw(ac + ck_1(-1 + m) + (k_1n - w)w) \\ & + b^2((a + k_1(-1 + m))w + c(-k_1n + w)) = 0, \end{aligned} \quad (13b)$$

where  $m = \cos(\omega\tau_1)$  and  $n = \sin(\omega\tau_1)$ .

From formulas (13a) and (13b),

$$\begin{aligned} & b^2w^4 + (1 - 2ab - 2b^2 + a^2b^2 + b^2c^2 + 2bk_1 - 2ab^2k_1)w^2 + b^2 - 2bc + 2ab^2c \\ & + c^2 - 2abc^2 + a^2b^2c^2 - 2b^2ck_1 + 2bc^2k_1 - 2ab^2c^2k_1 = 0. \end{aligned} \quad (14)$$

If all the parameters in system (3a)–(3c) are given, it is easy to calculate the numerical solution of equation (14) by computer. Thus, the following assumptions are given.

Suppose  $H_2$  that equation (14) has at least one positive real root.

If  $H_2$  is assumed to be true and equation (14) has two positive real roots  $\omega_k$  ( $k = 1, 2$ ), we have

$$\tau_1(k, j) = \frac{1}{\omega_k} [\arccos(p) + 2j\pi], \quad Q \geq 0, \quad (15a)$$

$$\tau_1(k, j) = \frac{1}{\omega_k} [2\pi - \arccos(p) + 2j\pi], \quad Q \leq 0, \quad k = 1, 2, \quad j = 0, 1, \dots, \quad (15b)$$

where

$$P = \frac{bc - c^2 + abc^2 - bc^2k_1 - w^2 + abw^2 - bk_1w^2}{bk_1(c^2 + w^2)}, \quad (16a)$$

$$Q = \frac{w - c^2w - w^3}{k_1(c^2 + w^2)}. \quad (16b)$$

$\pm i\omega_k$  is a pair of pure virtual root under  $\tau_1 = \tau_1(k, j)$  of equation (12). Let us take

$$\tau_1^0 = \min\{\tau_1(k, j), k = 1, 2; j = 0, 1, \dots\}. \quad (17)$$

Let  $\lambda(\tau) = \nu(t) + i\omega(\tau)$  be the virtual root of equation (12) near  $\tau_1 = \tau_1(k, j)$ . By differential degeneracy of equation (12) with respect to  $\tau$ , we can obtain

$$\begin{aligned} \left[ \frac{d\lambda}{d\tau_1} \right]^{-1} &= \frac{e^{\lambda\tau_1} [ab^2 - c + abc + b^2c - (b^2 - bc)k_1 + 2(ab + b^2 + bc - 1)\lambda]}{bk_1\lambda(b + \lambda)(c + \lambda)} \\ &+ \frac{3b\lambda^2 + b^2k_1 + bck_1 - b^2ck_1\tau_1 - b^2k_1\lambda\tau_1 - bck_1\lambda^2\tau_1}{bk_1\lambda(b + \lambda)(c + \lambda)}. \end{aligned} \quad (18)$$

When  $\lambda = i\omega$  is substituted into equation (18), we have

$$\left[ \frac{d(\operatorname{Re}\lambda)}{d\tau_1} \right]^{-1} = \frac{f(\omega_k)}{\Lambda}. \quad (19)$$

Among them,

$$\begin{aligned} f(\omega_k) &= a^2b^2c^2 + b^4c^2 + 2b^3k_1 - 2ab^4k_1 - 2b^2ck_1 + 2bc^2k_1 \\ &+ (2 - 4ab - 4b^2 + 2a^2b^2 + 2b^4 + 2b^2c^2 \\ &+ 4bk_1 - 4ab^2k_1)\omega k^2 \\ &+ 2b^2 - 2ab^3 - 2b^4 + a^2b^4 - 2bc + 2ab^2c \\ &+ c^2 - 2abc^2 - 2ab^2c^2k_1 + 3b^2\omega k^4, \end{aligned} \quad (20a)$$

$$\Lambda = b^2k_1^2(b^2 + \omega k^2)(c^2 + \omega k^2). \quad (20b)$$

*Hypothesis 1.*  $H_3$ :

$$\left[ \frac{d(\operatorname{Re}\lambda)}{d\tau_1} \right]^{-1} \neq 0. \quad (21)$$

Therefore, there are the following theorems.

**Theorem 1.** *If  $(H_1)$ ,  $(H_2)$ , and  $(H_3)$  are assumed to be true, then the equilibrium  $(0, (1/b), 0)$  is locally stable for  $\tau_1 \in (0, \tau_1^0)$ . When  $\tau_1 > \tau_1^0$  equilibrium  $(0, (1/b), 0)$  is unstable and Hopf bifurcation occurs in system (3a)–(3c) at  $\tau_1 = \tau_1^0$ .*

*Case 3.*  $\tau_1 > 0, \tau_2 > 0$ .

The corresponding characteristic equation of system (3a)–(3c) is (8). Now, let delay  $\tau_1 \in (0, \tau_1^0)$ , and  $\tau_2$  is taken as a parameter. Assuming  $\lambda = i\sigma$  is the characteristic root under the two delays in the characteristic equation (5), then



$$\begin{aligned} \lambda^3 + \left(a - \frac{1}{b} + b + c - k_1 - k_2\right)\lambda^2 + \left(ab + ac - \frac{c}{b} + bc - bk_1 - ck_1 - bk_2 - ck_2\right)\lambda \\ + b - c + abc - bck_1 - bck_2 + (\cos(\sigma\tau_1) - \sin(\sigma\tau_1))(bck_1 + bk_1\lambda + ck_1\lambda + k_1\lambda^2) \\ + (\cos(\sigma\tau_2) - \sin(\sigma\tau_2))(bck_2 + bk_2\lambda + ck_2\lambda + k_2\lambda^2) = 0. \end{aligned} \quad (22)$$

From (22),

$$\cos(\sigma\tau_2) = -\frac{1}{bk_2(c^2 + \sigma^2)} \left( \begin{array}{l} bc - c^2 + abc^2 - bc^2k_1 - bc^2k_2 + bc^2k_1 \cos(\sigma\tau_1) \\ -\sigma^2 + ab\sigma^2 - bk_1\sigma^2 - bk_2\sigma^2 + bk_1 \cos(\sigma\tau_1)\sigma^2 \end{array} \right), \quad (23a)$$

$$\sin(\sigma\tau_2) = -\frac{c^2k_1 \sin(\sigma\tau_1) + \sigma - c^2\sigma + k_1 \sin(\sigma\tau_1)\sigma^2 - \sigma^3}{k_2(c^2 + \sigma^2)}. \quad (23b)$$

Therefore, the equation about  $\sigma$  can be obtained:

$$\begin{aligned} b^2 - 2bc + 2ab^2c + c^2 - 2abc^2 + a^2b^2c^2 - 2b^2ck_1 + 2bc^2k_1 - 2ab^2c^2k_1 + c^2b^2k_1 - 2b^2ck_2 \\ + 2bc^2k_2 - 2ab^2c^2k_2 + 2b^2c^2k_1k_2 + 2b^2ck_1 \cos(\sigma\tau_1) - 2bc^2k_1 \cos(\sigma\tau_1) \\ + 2ab^2c^2k_1 \cos(\sigma\tau_1) - 2b^2c^2k_1^2 \cos(\sigma\tau_1) - 2b^2c^2k_1k_2 \cos(\sigma\tau_1) + b^2c^2k_1^2 \\ + 2b^2k_1 \sin(\sigma\tau_1)(1 - c^2)\sigma + (1 - 2ab - 2b^2 + a^2b^2 + b^2c^2 + 2bk_1 - 2ab^2k_1 \\ + b^2k_1^2 + 2bk_2 - 2ab^2k_2 + 2b^2k_1k_2 - 2bk_1 \cos(\sigma\tau_1) + 2ab^2k_1 \cos(\sigma\tau_1) \\ - 2b^2k_1^2 \cos(\sigma\tau_1) - 2b^2k_1k_2 \cos(\sigma\tau_1) + b^2k_1^2)\sigma^2 - 2b^2k_1 \sin(\sigma\tau_1)\sigma^3 + b^2\sigma^4 = 0. \end{aligned} \quad (24)$$

Obviously, equation (24) has at most a positive real root of  $N$  ( $N \leq 4$ ), which is denoted as  $\sigma_h$  ( $h = 1, 2, \dots, N$ ). Similarly, the following can be obtained:

$$\tau_2(h, j) = \frac{1}{\sigma_h} [\arccos(\bar{p}) + 2j\pi], \quad \bar{Q} \geq 0, \quad (25a)$$

$$\tau_2(h, j) = \frac{1}{\sigma_h} [2\pi - \arccos(\bar{p}) + 2j\pi], \quad \bar{Q} < 0, \quad (25b)$$

where

$$\bar{p} = -\frac{1}{bk_2(c^2 + \sigma^2)} \left( \begin{array}{l} bc - c^2 + abc^2 - bc^2k_1 - bc^2k_2 \\ +bc^2k_1 \cos(\sigma\tau_1) - \sigma^2 + ab\sigma^2 \\ -bk_1\sigma^2 - bk_2\sigma^2 + bk_1 \cos(\sigma\tau_1)\sigma \end{array} \right), \quad (26a)$$

$$\bar{Q} = \frac{c^2k_1 \sin(\sigma\tau_1) + \sigma - c^2\sigma + k_1 \sin(\sigma\tau_1)\sigma^2 - \sigma^3}{k_2(c^2 + \sigma^2)}, \quad h = 1, 2, \dots, N; j = 0, 1, \dots \quad (26b)$$

Then, there is a point column  $\tau_2 = \tau_2(h, j)$  satisfying equation (26a) and (26b),

$$\tau_2^0 = \min\{\tau_2(h, j)\}, \quad h = 1, 2, \dots, N; j = 0, 1, \dots \quad (27)$$

Correspondingly,  $h = h_0 \in \{1, 2, \dots, N\}$  and  $\sigma = \sigma_{h_0}$ .

When  $\tau_1 \in (0, \tau_1^0)$  and  $\tau_2 \in \tau_2^0$ , equation (8) has a pair of pure virtual root.

*Hypothesis 2*

$$H_4: \left[ \frac{d(\operatorname{Re}\lambda)}{d\tau_2} \right]^{-1} \neq 0. \quad (28)$$

In this way, by using the general Hopf bifurcation theorem [35–40] for functional differential equations, the results on the stability and bifurcation of system (3a)–(3c) are obtained.

**Theorem 2.** Assuming  $(H_4)$  holds and  $\tau_1 \in (0, \tau_1(2, 0))$  holds, the equilibrium  $(0, (1/b), 0)$  of system (3a)–(3c) is asymptotically stable at  $\tau_2 \in (0, \tau_2^0)$ . When  $\tau_2 \in \tau_2^0$  occurs, Hopf bifurcation occurs in system (3a)–(3c).

### 3. Period Solution and Stability of Hopf Bifurcation

In this section, we study the relevant properties of Hopf bifurcation in financial system (3a)–(3c) under the condition of delays  $\tau_1 > 0$ ,  $\tau_2 > 0$ .

Using the ideas of Hassard et al. [36], the exact expression of Hopf bifurcation property of system (3a)–(3c) is considered by using central manifold theorem. Here, we consider the Hopf bifurcation of system (4a)–(4c) at the

equilibrium point  $(0, 0, 0)$  for  $\tau_2 = \tau_2^0$ . The financial system can be converted to the following equation:

$$\dot{u}(t) = L_u(u_t) + f(\mu, u_t), \quad (29)$$

where

$$u(t) = (u_1(t), u_2(t), u_3(t))^T \in R^3, \quad (30)$$

$$L_\mu: C \longrightarrow R^3, f: R \times C \longrightarrow R^3, u_t(\theta) = u(t + \theta) \in C, \quad (31a)$$

$$L_\mu(\phi) = A(0) + B_1(-\tau_1) + B_2(-(\tau_2^0 + \mu)). \quad (31b)$$

According to systems (3a)–(3c) and (7a)–(7c), it can be seen that

$$A = \begin{pmatrix} \frac{1}{(b-a)} + k_1 = k_2 & 0 & 1 \\ -1 & -b & 0 \\ -1 & 0 & -c \end{pmatrix}, \quad (32a)$$

$$B_1 = \begin{pmatrix} -k_1 & 0 & 0 \\ 0 & 0 & 0 \\ 0 & 0 & 0 \end{pmatrix}, \quad (32b)$$

$$B_2 = \begin{pmatrix} -k_2 & 0 & 0 \\ 0 & 0 & 0 \\ 0 & 0 & 0 \end{pmatrix}. \quad (32c)$$

Let

$$\phi(t) = (\phi_1(t), \phi_2(t), \phi_3(t))^T. \quad (33)$$

Then,

$$f(\mu, u_t) = (\mu + \tau_k) \begin{pmatrix} \varphi_1(0)\varphi_2(0) \\ -\varphi_1^2(0) \\ 0 \end{pmatrix}. \quad (34)$$

When the equilibrium point  $(0, 0, 0)$  of system (29) passes Hopf bifurcation at  $\mu = 0$ , the characteristic equation has a pair of pure virtual root  $i\sigma_h$  and  $-i\sigma_h$ . According to Ritz representation theorem, there is a matrix function of bounded variation

$$L_\mu(\phi) = \int_{-\tau_1}^0 d\eta(\theta, \mu)\phi(\theta), \quad \phi \in C. \quad (35)$$

In fact, we can choose

$$\eta(\theta, \mu) = \begin{cases} A + B_1 + B_2, & \theta = 0, \\ B_1 + B_2, & \theta \in (-\tau_2, 0), \\ B_1, & \theta \in (-\tau_1, -\tau_2), \\ 0, & \theta \in -\tau_1. \end{cases} \quad (36)$$

For  $\phi = C([- \tau_1, 0], R^3)$ , we define

$$A(\mu)\phi = \frac{d\phi(\theta)}{d\theta}, \quad \theta \in [-\tau_1, 0], \quad (37a)$$

$$A(\mu)\phi = \int_{-\tau_1}^0 d\eta(\xi, \mu)\phi\xi, \quad \theta = 0, \quad (37b)$$

$$R(\mu)\phi = 0, \quad \theta \in [-\tau_1, 0], \quad (38a)$$

$$R(\mu)\phi = f(\mu, \phi), \quad \theta = 0. \quad (38b)$$

To simplify, equation (29) can be written in the following form:

$$\dot{u}(t) = A(\mu)u_t + R(\mu)u_t, \quad (39)$$

in which

$$u_t = u(t + \theta), \quad \theta \in [-\tau_1, 0]. \quad (40)$$

The adjoint operator  $A^*$  that defines  $A$  for  $\psi \in C^1([0, \tau_1], (R^3)^*)$  is as follows:

$$A^*\psi(s) = -\frac{d\psi(s)}{ds}, \quad s \in (0, \tau_1), \quad (41a)$$

$$A^*\psi(s) = \int_{-\tau_1}^0 d\eta^T(t, 0)\psi(-t), \quad s = 0. \quad (41b)$$

In addition, we define a bilinear form

$$\langle \psi, \phi \rangle = \bar{\psi}(0)\phi(0) - \int_{-\tau_1}^0 \int_{s=0}^\theta \bar{\psi}(\xi - \theta)d\eta(\theta)\phi(\xi)d\xi, \quad (42a)$$

$$\eta(\theta) = \eta(\theta, 0). \quad (42b)$$

According to the above analysis,  $\sigma_h$  and  $-i\sigma_{h_0}$  are the eigenvalues of  $A(0)$  and  $A^*(0)$ . Let  $q(\theta)$  be the eigenvector corresponding to the eigenvalue  $i\sigma_{h_0}$  of  $A(0)$  and  $q^*(\theta)$  be the eigenvector corresponding to the eigenvalue  $-i\sigma_{h_0}$  of  $A^*(0)$ . There are

$$A(0)q(\theta) = i\sigma_{h_0}q(\theta), \quad (43a)$$

$$A^*(0)q^*(\theta) = -i\sigma_{h_0}q^*(\theta). \quad (43b)$$

Through simple calculation, we can get

$$q(0) = (1, \alpha, \beta)^T = \left(1, \frac{1}{-b - \sigma_{h_0}i}, \frac{1}{-c - \sigma_{h_0}i}\right)^T, \quad (44a)$$

$$\begin{aligned} q^*(s) &= D(1, \alpha, \beta)e^{is\sigma_{h_0}} = D\left(1, 0, \frac{1}{-c - \sigma_{h_0}i}\right)e^{is\sigma_{h_0}} \\ &= \bar{D}(1, \bar{\alpha}^*, \bar{\beta}^*)(1, \alpha, \beta)^T - \int_{-\tau_1}^0 \int_{\xi=0}^\theta \bar{D}(1, \bar{\alpha}^*, \bar{\beta}^*) \\ &\quad \cdot e^{-i(\xi-\theta)\sigma_{h_0}}d\eta(\theta)(1, \alpha, \beta)^T e^{is\sigma_{h_0}}d\xi \\ &= \bar{D}\{1 + \alpha\bar{\alpha}^* + \beta\bar{\beta}^* - k_1\tau_1 e^{-i\sigma_{h_0}} - k_2\tau_2^0 e^{-i\sigma_{h_0}}\}, \end{aligned} \quad (44b)$$

where  $D$  is a constant, making  $\langle q^*(s), q(\theta) \rangle = 1$  valid.

Therefore, we have

$$D = \frac{1}{1 + \alpha\bar{\alpha}^* + \beta\bar{\beta}^* - k_1\tau_1 e^{i\sigma_{h_0}} - k_2\tau_2 e^{i\sigma_{h_0}}}. \quad (45)$$

Using the same notation of Ruan et al. [37], we can calculate the center popularity of  $\mu = 0$ . Let  $\mu_1$  be the solution of equation (29) when  $\mu = 0$ , defining

$$z(t) = \langle q^*, u_t \rangle, \quad (46a)$$

$$W(t, \theta) = W(z(t), \bar{z}(t), \theta) = W_{20}(\theta) \frac{z^2}{2} + W_{11}(\theta) z\bar{z} + W_{02}(\theta) \frac{\bar{z}^2}{2} + W_{30}(\theta) \frac{z^3}{6} + \dots, \quad (46b)$$

where  $z$  and  $\bar{z}$  are the local coordinates of the central epidemic. When  $\mu = 0$ ,

$$\begin{aligned} \bar{z}(t) &= i\sigma_k \tau_k z + \langle q^*(\theta), f(0, W(z(t), \bar{z}(t), \theta) + 2R_e\{z(t)q(\theta)\}) \rangle \\ &= i\sigma_{h_0} z + \bar{q}^*(0) (f(0, W(z(t), \bar{z}(t), 0)) + 2R_e\{z(t)q(0)\}). \end{aligned} \quad (47)$$

Make

$$f(0, W(z(t), \bar{z}(t), 0) + 2R_e\{z(t)q(0)\}) = f_0(z, \bar{z}). \quad (48)$$

Then,

$$\dot{z}(t) = i\sigma_{h_0} z + \bar{q}^*(0) f_0(z, \bar{z}) = i\sigma_{h_0} z + g(z, \bar{z}), \quad (49a)$$

$$g(z, \bar{z}) = g_{20} \frac{z^2}{2} + g_{11} z\bar{z} + g_{02}(\theta) \frac{\bar{z}^2}{2} + g_{21}(\theta) \frac{z^2 \bar{z}}{2} + \dots \quad (49b)$$

Because

$$q(\theta) = (1, \alpha, \beta)^T e^{i\theta\sigma_{h_0}}, \quad (50a)$$

$$\begin{aligned} u_t(\theta) &= (u_{1t}(\theta), u_{2t}(\theta), u_{3t}(\theta)) \\ &= W(t, \theta) + z(t)q(\theta) + \bar{z}(t)\bar{q}(\theta), \end{aligned} \quad (50b)$$

we can obtain

$$u_{1t}(0) = z + \bar{z} + W_{20}^{(1)} \frac{z^2}{2} + W_{11}^{(1)} z\bar{z} + W_{02}^{(1)} \frac{\bar{z}^2}{2} + \dots, \quad (51a)$$

$$u_{2t}(0) = \alpha z + \bar{\alpha} \bar{z} + W_{20}^{(2)} \frac{z^2}{2} + W_{11}^{(2)} z\bar{z} + W_{02}^{(2)} \frac{\bar{z}^2}{2} + \dots, \quad (51b)$$

$$u_{3t}(0) = \beta z + \bar{\beta} \bar{z} + W_{20}^{(3)} \frac{z^2}{2} + W_{11}^{(3)} z\bar{z} + W_{02}^{(3)} \frac{\bar{z}^2}{2} + \dots. \quad (51c)$$

Based on the above formula (49b), it can be seen that

$$\begin{aligned} g(z, \bar{z}) &= q^*(0) f_0(z, \bar{z}) \\ &= \bar{D} (1, \bar{\alpha}^*, \bar{\beta}^*) \begin{pmatrix} u_{1t}(0) \\ -u_{1t}^2(0) - bu_{1t}(0)u_{2t}(0) \\ 0 \end{pmatrix} \\ &= D \left( z + \bar{z} + W_{20}^{(1)} \frac{z^2}{2} + W_{11}^{(1)} z\bar{z} + W_{02}^{(1)} \frac{\bar{z}^2}{2} + \dots \right) \\ &= \left( \alpha z + \bar{\alpha} \bar{z} + W_{20}^{(2)} \frac{z^2}{2} + W_{11}^{(2)} z\bar{z} + W_{02}^{(2)} \frac{\bar{z}^2}{2} + \dots \right). \end{aligned} \quad (52)$$

By using the method of comparison coefficient, we obtain

$$g_{20} = 2\alpha\bar{D}, \quad (53a)$$

$$g_{21} = 2\bar{D} \left[ \frac{1}{2} W_{20}^{(1)}(0) \bar{\alpha} + \frac{1}{2} W_{20}^{(1)}(0) + W_{11}^{(2)}(0) + W_{11}^{(1)}(0) \alpha \right], \quad (53b)$$

$$g_{02} = 2\bar{\alpha}\bar{D}, \quad (53c)$$

$$g_{11} = (\alpha + \bar{\alpha})\bar{D}. \quad (53d)$$

In order to calculate  $W_{20}(\theta)$  and  $W_{11}(\theta)$ , we use

$$\begin{aligned} \dot{W} &= \dot{u}_t - \dot{z}q - \dot{\bar{z}}\bar{q} \\ &= \begin{cases} A(0)W - 2R_e\{\bar{q}^*(0)f_0q(\theta)\}, & \theta \in [-\tau_1, 0], \\ A(0)W - 2R_e\{\bar{q}^*(0)f_0q(\theta)\} + f_0, & \theta = 0, \end{cases} \end{aligned} \quad (54)$$

Make

$$H(z, \bar{z}, \theta) = \begin{cases} 2R_e\{\bar{q}^*(0)f_0q(\theta)\}, & \theta \in [-\tau_1, 0], \\ 2R_e\{\bar{q}^*(0)f_0q(\theta)\} + f_0, & \theta = 0, \end{cases} \quad (55)$$

We rewrite (54):

$$\dot{W} = A(0)W + H(z, \bar{z}, \theta), \quad (56)$$

$$H(z, \bar{z}, \theta) = H_{20}(\theta) \frac{\bar{z}^2}{2} + H_{11}(\theta) z\bar{z} + H_{02}(\theta) \frac{z^2}{2} + \dots \quad (57)$$

Using (54) and (55), one can obtain

$$(A(0) - 2i\sigma_{h_0})W_{20}(\theta) = -H_{20}, \quad (58a)$$

$$A(0)W_{11}(\theta) = -H_{11}(\theta), \quad (58b)$$

$$\begin{aligned} \theta \in [-\tau_1, 0], \quad H(z, \bar{z}, \theta) &= -\bar{q}^*(0)f_0q(\theta) - q^*(0)\bar{f}_0\bar{q}(\theta) \\ &= -g(z, \bar{z})q(\theta) - \bar{g}(z, \bar{z})\bar{q}(\theta). \end{aligned} \quad (59a)$$

The combination formula (57) is obtained:

$$H_{20}(\theta) = -g_{20}q(\theta) - \bar{g}_{02}\bar{q}(\theta), \quad (60a)$$

$$H_{11}(\theta) = -g_{11}q(\theta) - \bar{g}_{11}\bar{q}(\theta). \quad (60b)$$

Using equations (58a) and (58b) and (60a) and (60b), it is easy to obtain

$$W_{20} = 2i\sigma_{h_0}W_{20}(\theta) + g_{20}q(\theta) + \bar{g}_{02}\bar{q}(\theta), \quad (61a)$$

$$W_{20} = \frac{ig_{20}}{\sigma_{h_0}}q(0)e^{i\theta\sigma_{h_0}} + \frac{i\bar{g}_{02}}{3\sigma_{h_0}}\bar{q}(0)e^{-i\theta\sigma_{h_0}} + Ee^{2i\theta\sigma_{h_0}}, \quad (61b)$$

$$W_{11} = \frac{ig_{11}}{\sigma_{h_0}}q(0)e^{i\theta\sigma_{h_0}} + \frac{i\bar{g}_{11}}{\sigma_{h_0}}\bar{q}(0)e^{-i\theta\sigma_{h_0}} + E_2. \quad (62)$$

Make

$$E_1 = (E_1^{(1)}, E_1^{(2)}, E_1^{(3)})^T \in R^3, \quad (63a)$$

$$E_2 = (E_2^{(1)}, E_2^{(2)}, E_2^{(3)})^T \in R^3. \quad (63b)$$

Combine formulas (58a) and (58b) again to obtain

$$\dot{W}_{20}(\theta) = \int_{-\tau_1}^0 d\eta(\theta)W_{20}(\theta) = 2i\theta\sigma_{h_0}W_{20}(\theta) - H_{20}(\theta), \quad (64a)$$

$$\dot{W}_{11}(\theta) = \int_{-\tau_1}^0 d\eta(\theta)W_{11}(\theta) = -H_{11}(\theta), \quad (64b)$$

$$H_{20}(0) = -g_{20}q(0) - \bar{g}_{02}\bar{q}(0) + 2(\alpha, -1 - b\alpha, 0), \quad (65a)$$

$$H_{11}(0) = -g_{11}q(0) - \bar{g}_{11}\bar{q}(0) + (\alpha + \bar{\alpha}, -2 - b(\bar{\alpha} + \alpha))^T, \quad (65b)$$

$$\left(i\sigma_{h_0} - \int_{-\tau_1}^0 e^{i\theta\sigma_{h_0}}d\eta(\theta)\right)q(0) = 0, \quad (65c)$$

$$\left(-i\sigma_{h_0} - \int_{-\tau_1}^0 e^{-i\theta\sigma_{h_0}}d\eta(\theta)\right)\bar{q}(0) = 0. \quad (65d)$$

Substituting equations (62) and (65a)–(65d) into (64a) and (64b), there is

$$\left(2i\sigma_{h_0}I - \int_{-\tau_1}^0 e^{i\theta\sigma_{h_0}}d\eta(\theta)\right)E_1 = 2(\alpha, -1 - b\alpha, 0)^T. \quad (66)$$

Therefore,

$$\begin{pmatrix} 2i\sigma_{h_0} + \Pi & 0 & -1 \\ 1 & 2i\sigma_{h_0} + b & 0 \\ 1 & 0 & 2i\sigma_{h_0} + c \end{pmatrix} E_1 = 2 \begin{pmatrix} \alpha \\ -1 - b\alpha \\ 0 \end{pmatrix}, \quad (67)$$

where

$$\Pi = a - \frac{1}{b} - k_1 - k_2 + k_2e^{-2i\sigma_{h_0}\tau_2^0}, \quad (68a)$$

$$f(\tau_1, \tau_2^0) = k_1e^{-2i\sigma_{h_0}\tau_1} + k_2e^{-2i\sigma_{h_0}\tau_2^0}. \quad (68b)$$

Let

$$E_1^{(1)} = \frac{\Delta_{11}}{\Delta_1}, E_1^{(2)} = \frac{\Delta_{12}}{\Delta_1}, E_1^{(3)} = \frac{\Delta_{13}}{\Delta_1}, \quad (69)$$

in which

$$\Delta_{11} = \begin{vmatrix} 2\alpha & 0 & -1 \\ -2 - 2b\alpha & 2i\sigma_{h_0} & 0 \\ 0 & 0 & 2i\sigma_{h_0} + c \end{vmatrix}, \quad (70a)$$

$$\Delta_{12} = \begin{vmatrix} 2i\sigma_{h_0} + \Pi & 2\alpha & -1 \\ 1 & -2 - 2b\alpha & 0 \\ 1 & 0 & 2i\sigma_{h_0} + c \end{vmatrix}, \quad (70b)$$

$$\Delta_{13} = \begin{vmatrix} 2i\sigma_{h_0} + \Pi & 0 & 2\alpha \\ 1 & 2i\sigma_{h_0} + b & -b - 2b\alpha \\ 1 & 0 & 0 \end{vmatrix}, \quad (70c)$$

$$\Delta_1 = \begin{vmatrix} \frac{2i\sigma_{h_0} + a - 1}{b - k_1 - k_2 + f(\tau_1, \tau_2^0)} & 0 & -1 \\ 1 & 2i\sigma_{h_0} + b & 0 \\ 1 & 0 & 2i\sigma_{h_0} + c \end{vmatrix}. \quad (70d)$$

Similarly, we can also have

$$\begin{pmatrix} \frac{a-1}{b-k_1-k_2} & 0 & -1 \\ 1 & b & 0 \\ 1 & b & c \end{pmatrix} E_2 = \begin{pmatrix} \alpha + \bar{\alpha} \\ -2 - b(\bar{\alpha} + \alpha) \\ 0 \end{pmatrix}. \quad (71)$$

Let

$$E_2^{(1)} = \frac{\Delta_{21}}{\Delta_2}, E_2^{(2)} = \frac{\Delta_{22}}{\Delta_2}, E_2^{(3)} = \frac{\Delta_{23}}{\Delta_2}, \quad (72)$$

where

$$\Delta_{21} = \begin{vmatrix} \alpha + \bar{\alpha} & 0 & -1 \\ -2 - b(\bar{\alpha} + \alpha) & b & 0 \\ 1 & 0 & c \end{vmatrix}, \quad (73a)$$

$$\Delta_{22} = \begin{vmatrix} \frac{a-1}{b-k_1-k_2} & \alpha + \bar{\alpha} & 0 \\ 1 & -2 - b(\bar{\alpha} + \alpha) & 0 \\ 1 & 0 & c \end{vmatrix}, \quad (73b)$$

$$\Delta_{23} = \begin{vmatrix} \frac{a-1}{b-k_1-k_2} & 0 & \alpha + \bar{\alpha} \\ 1 & b & -2 - b(\bar{\alpha} + \alpha) \\ 1 & 0 & 0 \end{vmatrix}, \quad (73c)$$

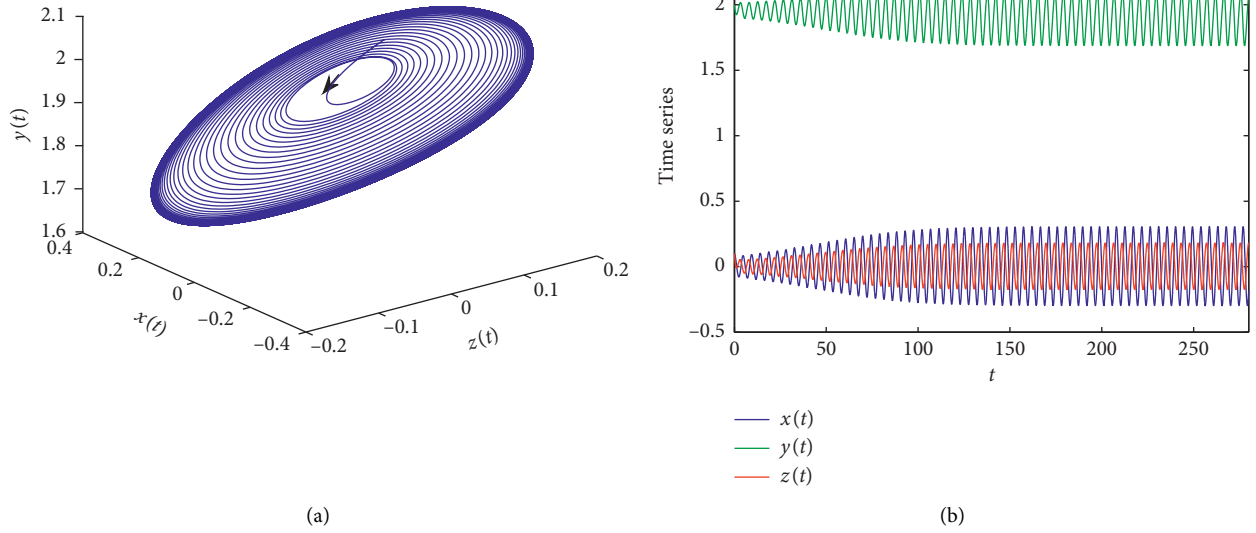


FIGURE 2: The phase diagram (a) and the time series diagram (b) of system (3a)–(3c) with initial value  $(0.1, 2, 0.1)$  for  $\tau_1 = 1.5 > \tau_1^0$  and  $\tau_2 = 0$ .

$$\Delta_2 = \begin{vmatrix} a - 1/b - k_1 - k_2 & 0 & -1 \\ & 1 & b & 0 \\ & 1 & 0 & c \end{vmatrix}. \quad (73d)$$

Furthermore,  $g_{ij}$  can be determined by the coefficients and time delays of system (7a)–(7c). Thus, the following values can be calculated using the method in [37]:

$$C_1(0) = \frac{i}{2\sigma_{h_0}} \left( g_{20}g_{11} - 2|g_{11}|^2 - \frac{1}{3}|g_{02}|^2 \right) + \frac{g_{21}}{2}, \quad (74a)$$

$$\mu_2 = \frac{\text{Re}\{C_1(0)\}}{e\{d\lambda/d\tau_2^0\}}, \quad (74b)$$

$$T_2 = -\frac{\text{Im} C_1(0) + \mu_2 \text{Im}\{d\lambda/d\tau_2^0\}}{\sigma_{h_0}}, \quad (74c)$$

$$\beta_2 = 2R_e\{C_1(0)\}. \quad (74d)$$

Formulas (74a)–(74d) determine the critical point above the central flow  $\tau_2^0$ . Now, the properties of periodic solutions of system (3a)–(3c) could be obtained. Therefore, we obtain the following theorem.

**Theorem 3.** For system (3a)–(3c), when  $\tau_1 \in (0, \tau_1^0)$ ,

- (1) The symbol  $\mu_2$  determines the orientation of Hopf bifurcation. If  $\mu_2 > 0$  ( $\mu_2 < 0$ ), then the Hopf bifurcation is supercritical (subcritical). If  $\tau_2 > \tau_2^0$  ( $\tau_2 < \tau_2^0$ ), the bifurcation period solution exists.
- (2) The sign of  $\beta_2$  determines the stability of the bifurcation period solution: if  $\beta_2 < 0$  ( $\beta_2 > 0$ ), the period solution is stable (unstable).

- (3) The symbol  $T_2$  determines the period of bifurcation period solution. If  $T_2 > 0$  ( $T_2 < 0$ ), the period solution is increased (decreased).

#### 4. Numerical Results and Analysis

In this section, we will give numerical simulations on the theoretical results of Hopf bifurcation with two delays.

Given the parameters  $a = 3, b = 0.51, c = 1.0, k_1 = 1$ , and  $k_2 = 5$ , it is verified that at that time  $\tau_1 = \tau_2 = 0$ , the parameters satisfy the assumption  $H_1$  that the equilibrium point  $(0, (1/b), 0)$  of system (3a)–(3c) without time delay is asymptotically stable.

- (1)  $\tau_1 > 0, \tau_2 = 0$

If equation (8) has a pair of pure virtual root  $iw$  and  $-iw$ , there are two positive roots  $w_1 = 0.20211$  and  $w_2 = 1.39915$ . Substituting  $w_1$  and  $w_2$  into equations (15a) and (15b), we can obtain

$$\tau_1(1, j) = 15.5044 + 31.0872j, \quad (75a)$$

$$\tau_1(2, j) = 1.39921 + 4.49073j, \quad (j = 0, 1, 2, \dots). \quad (75b)$$

That is,  $\tau_1^0 = 1.39921$ , and we have the following result for  $\tau_1 = \tau_1^0$ :

$$H_3 : \frac{d(R_e\lambda)}{d\tau_1} = 0.23975 > 0. \quad (76)$$

According to Theorem 1, equilibrium point  $(0, (1/b), 0)$  of system (3a)–(3c) is asymptotically

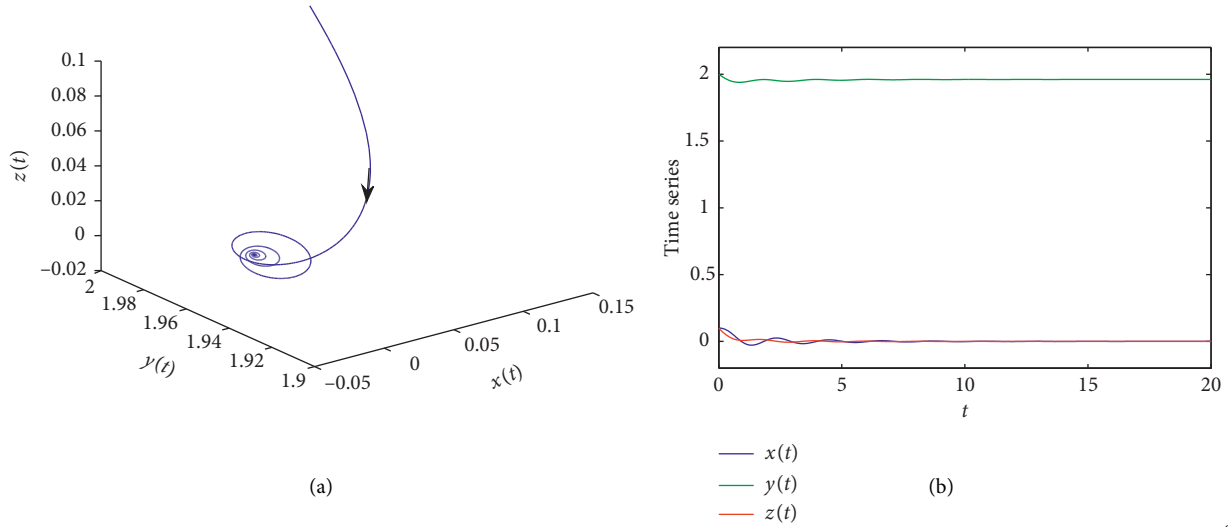


FIGURE 3: Phase diagram (a) and time sequence diagram (b) of system (3a)–(3c) with initial value  $(0.1, 2, 0.1)$  for  $\tau_1 = 0.45 < \tau_1^0$  and  $\tau_2 = 0.1 < \tau_2^0$ .

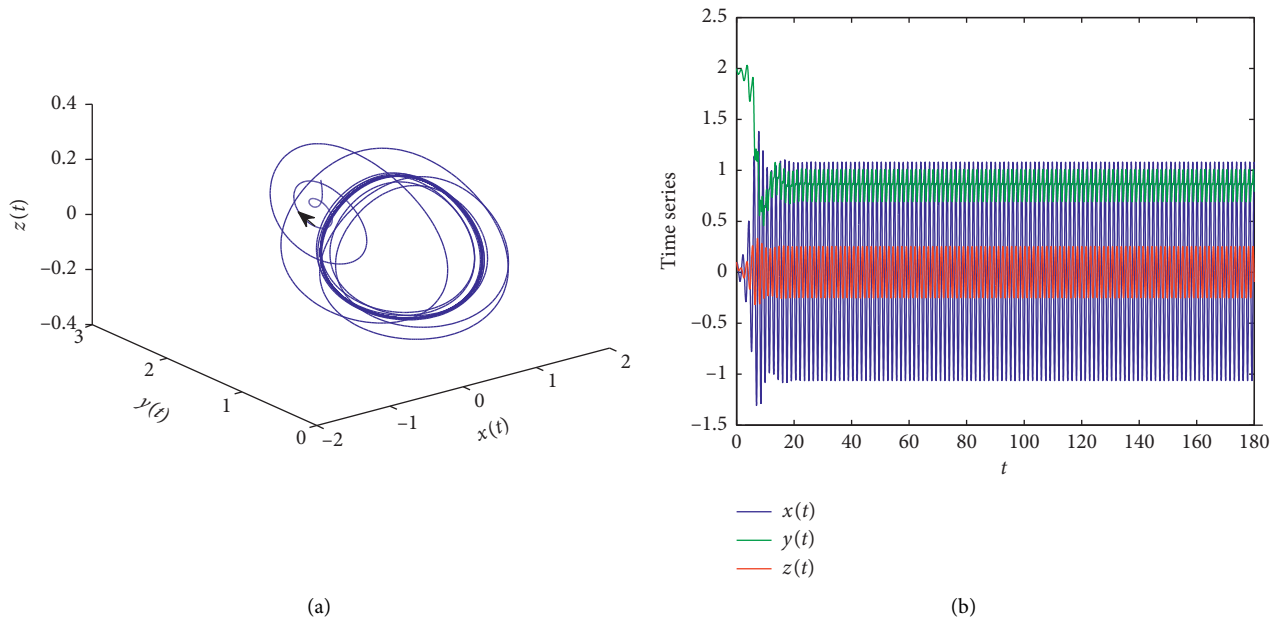


FIGURE 4: Phase space (a) and time series (b) of system (3a)–(3c) with initial value  $(0.1, 2, 0.1)$  for  $\tau_1 = 0.45 < \tau_1^0$  and  $\tau_2 = 0.1 < \tau_2^0$ .

stable for  $\tau_1 \in (0, \tau_1^0)$ . Hopf bifurcation occurs when  $\tau_1 = \tau_1^0$ ,  $\tau_2 = 0$ , and a stable period solution is obtained. The time series diagram and phase diagram are shown in Figure 2.

(2)  $\tau_1 > 0$ ,  $\tau_2 > 0$

Let  $\tau_1 = 0.45 < \tau_1^0$  and consider  $\tau_2 > 0$ . Suppose that equation (22) has a pair of pure virtual root  $i\sigma$  and  $-i\sigma$ . Then, according to equation (24), it is found that  $N = 1$ . There is  $\sigma_1 = 3.05932$ . Substituting  $\sigma_1$  into equations (25a) and (25b), we can obtain

$$\tau_2(2, j) = 0.11917 + 2.05378j, \quad (j = 0, 1, 2, \dots). \quad (77)$$

That is,  $\tau_2^0 = 0.11917$  and

$$\frac{d(R_e\lambda)}{d\tau_2} = 0.227516 > 0. \quad (78)$$

According to Theorem 2, we know when  $\tau_2 \in (0, \tau_2^0)$ , the equilibrium point  $(0, (1/b), 0)$  is asymptotically stable (as shown in Figure 3:  $\tau_1 = 0.45 < \tau_1^0$  and  $\tau_2 = 0.1 < \tau_2^0$ ).

When  $\tau_1 = 0.45$  and  $\tau_2 = \tau_2^0$ , Hopf bifurcation occurs and we can have



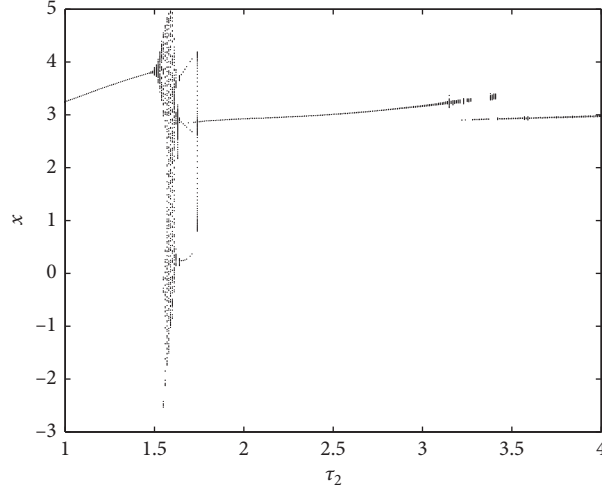


FIGURE 5: Bifurcation diagram of system (3a)–(3c) with initial value (0.1, 2, 0.1) and  $\tau_1 = 0.45 < \tau_1^0$  and  $\tau_2 \in [1, 4]$ .

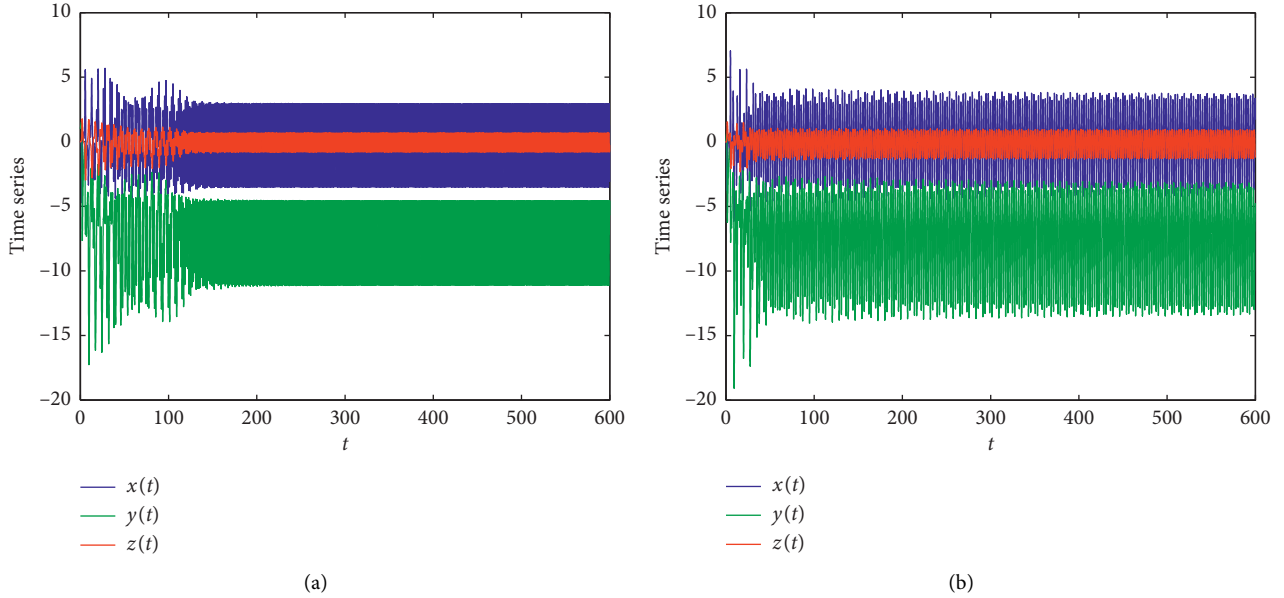


FIGURE 6: Time series of system (3a)–(3c) with  $\tau_1 = 0.45 < \tau_1^0$  and  $\tau_2 = 3.8$ : (a) initial value (0.01, 1, 0.01) and periodic orbit; (b) initial value (0.1, 0, 0) and means chaos.

$$C_1(0) = -2.29734 + 4.10025i, \quad (79a)$$

$$\mu_2 = 0.92535 > 0, \quad (79b)$$

$$\beta_2 = -4.59468 < 0. \quad (79c)$$

Therefore, the bifurcation direction is  $\tau_2 > \tau_2^0$ , and the period solution is stable, as shown in Figure 4:  $\tau_1 = 0.45$  and  $\tau_2 = 0.15$ . In addition, the complex dynamics of system (3a)–(3c) could be shown from the bifurcation diagram in Figure 5.

### 5. Multistability in the Improved Financial System (3a)–(3c) with Two Delays

When  $\tau_1 = 0.45$  and  $\tau_2 = 3.8$ , we will find the multistability in the systems without changing parameters. Given the parameters  $a = 3$ ,  $b = 0.51$ ,  $c = 1.0$ ,  $k_1 = 1$ , and  $k_2 = 5$ , we have obtained the periodic attractor with initial value (0.01, 1, 0.01) in Figure 6(a). However, we also obtain chaos for same parameters' values but different initial values (0.1, 0, 0) in Figure 6(b). Therefore, when different initial conditions are taken, the coexisting and different attractors

are exhibited. We know multistability is a critical property of nonlinear dynamical systems [41–44]. Since the crisis of the financial system is subject to various factors, the nature of the multi-steady state plays an important role in making correct decisions for government workers.

## 6. Conclusion

Time delay is a very sensitive factor in financial systems with multistability. Financial systems with multiple time delays have richer dynamic characteristics than those with single time delay. Two-delay feedback can effectively control the unstable behavior of financial markets. In this paper, Hopf bifurcation of an improved financial model with two time delays is studied in detail. The existence of the bifurcation period solution of this system is discussed by using the theory of functional differential equations. Complexity of the proposed financial chaotic system is studied from the bifurcation diagram that its multistability depends extremely on the memristor initial condition and the system parameters. In summary, time delay is one of the effective methods to control the stability of the financial market, so it can provide a theoretical reference for relevant departments to regulate economic behavior.

## Data Availability

The data used to support the findings of this study are available from the corresponding author upon request.

## Conflicts of Interest

The authors declare that there are no conflicts of interest regarding the publication of this research work.

## Acknowledgments

The authors gratefully acknowledge the support of National Natural Science Foundation of China (nos. 11902163, 11832002, 71763021, and 11427801), the National Social Science Foundation of China (no. BMA180038), Science and Technology Research Project of Universities in Inner Mongolia Autonomous Region (no. NJZY20159), China Postdoctoral Science Foundation funded project (no. 2019M660003XB), and the Funding Project for Academic Human Resources Development in Institutions of Higher Learning under the Jurisdiction of Beijing Municipality (PHRIHLB).

## References

- [1] S. I. Batool and H. M. Waseem, “A novel image encryption scheme based on Arnold scrambling and Lucas series,” *Multimedia Tools and Applications*, vol. 78, no. 19, pp. 27611–27637, 2019.
- [2] K. M. Ali and M. Khan, “Application based construction and optimization of substitution boxes over 2D mixed chaotic maps,” *International Journal of Theoretical Physics*, vol. 58, no. 9, pp. 3091–3117, 2019.
- [3] M. Khan and F. Masood, “A novel chaotic image encryption technique based on multiple discrete dynamical maps,” *Multimedia Tools and Applications*, vol. 78, pp. 26203–26222, 2019.
- [4] I. Younas and M. Khan, “A new efficient digital image encryption based on inverse left almost semi group and lorenz chaotic system,” *Entropy*, vol. 20, no. 12, p. 913, 2018.
- [5] M. Khan, “A novel image encryption scheme based on multiple chaotic S-boxes,” *Nonlinear Dynamics*, vol. 82, no. 1–2, pp. 527–533, 2015.
- [6] Z. Wei, Y. Li, B. Sang et al., “Complex dynamical behaviors in a 3D simple chaotic flow with 3D stable or 3D unstable manifolds of a single equilibrium,” *International Journal of Bifurcation and Chaos*, vol. 29, no. 07, p. 1950095, 2019.
- [7] Z. C. Liu, I. Moroz, J. C. Sprott et al., “Hidden hyperchaos and electronic circuit application in a 5D self-exciting homopolar disc dynamo,” *Chaos*, vol. 27, no. 3, Article ID 033101, 2017.
- [8] Z. Wei, I. Moroz, J. C. Sprott et al., “Detecting hidden chaotic regions and complex dynamics in the self-exciting homopolar disc dynamo,” *International Journal of Bifurcation and Chaos*, vol. 27, no. 2, p. 1730008, 2017.
- [9] R. Wang, *Economic Dynamics*, Cambridge University Press, Cambridge, England, 2002.
- [10] A. C.-L. Chian, “Nonlinear dynamics and chaos in macroeconomics,” *International Journal of Theoretical and Applied Finance*, vol. 3, no. 3, p. 601, 2000.
- [11] S. Radelet, J. D. Sachs, R. N. Cooper, and B. P. Bosworth, “The east asian financial crisis: diagnosis, remedies, prospects,” *Brookings Papers on Economic Activity*, vol. 1998, no. 1, pp. 1–74, 1998.
- [12] A. Bosworth, “Is there chaos in economic series?,” *Canadian Journal of Economics*, vol. 29, pp. 210–212, 1996.
- [13] Y. Wang and Y. H. Zhai, “Chaos and Hopf bifurcation of a finance system with distributed time delay,” *International Journal of Applied Mathematics and Mechanics*, vol. 6, no. 20, pp. 1–13, 2010.
- [14] J. H. Ma and Y. Chen, “Study for the bifurcation topological structure and the global complicated character of a kind of non-linear finance system (I),” *Applied Mathematics and Mechanics*, vol. 22, pp. 1240–1251, 2010.
- [15] C. Ma and X. Wang, “Hopf bifurcation and topological horseshoe of a novel finance chaotic system,” *Communications in Nonlinear Science and Numerical Simulation*, vol. 17, no. 2, pp. 721–730, 2012.
- [16] Z. Wei, P. Yu, W. Zhang et al., “Study of hidden attractors, multiple limit cycles from Hopf bifurcation and boundedness of motion in the generalized hyperchaotic Rabinovich system,” *Nonlinear Dynamics*, vol. 82, no. 1–2, pp. 131–141, 2015.
- [17] K. Yao, S. Jafari, V.-T. Pham et al., “Antimonotonicity, bifurcation and multistability in the vallis model for el niño,” *International Journal of Bifurcation and Chaos*, vol. 29, no. 3, p. 1950032, 2019.
- [18] K. Wei, A. J. M. Khalaf, Z. Wei et al., “Hyperchaos and coexisting attractors in a modified van der Pol-Duffing oscillator,” *International Journal of Bifurcation and Chaos*, vol. 29, no. 5, p. 1950067, 2019.
- [19] Z. Pham, V.-T. Pham, T. Kapitaniak et al., “Bifurcation analysis and circuit realization for multiple-delayed Wang-Chen system with hidden chaotic attractors,” *Nonlinear Dynamics*, vol. 85, no. 3, pp. 1635–1650, 2016.
- [20] Y. Wang, W. Jiang, and H. Wang, “Delayed feedback control and bifurcation analysis of Rossler chaotic system,” *Nonlinear Dynamics*, vol. 61, no. 4, pp. 707–715, 2010.
- [21] K. Ishiyama and Y. Saiki, “Unstable periodic orbits and chaotic economic growth,” *Chaos, Solitons & Fractals*, vol. 26, no. 8, pp. 33–42, 2005.

- [22] X. S. Zhao, Z. B. Li, and S. Li, "Synchronization of a chaotic finance system," *Applied Mathematics and Computation*, vol. 217, no. 2, pp. 6031–6039, 2011.
- [23] H. J. Yu, G. L. Cai, and Y. X. Li, "Dynamic analysis and control of a new hyperchaotic finance system," *Nonlinear Dynamics*, vol. 67, no. 23, pp. 2171–2182, 2012.
- [24] C. Cantore and P. Levine, "Getting normalization right: dealing with 'dimensional constants' in macroeconomics," *Journal of Economic Dynamics and Control*, vol. 36, no. 2, pp. 1931–1949, 2012.
- [25] W. Gao, L. Yan, M. Saeedi et al., "Ultimate bound estimation set and chaos synchronization for a financial risk system," *Mathematics and Computers in Simulation*, vol. 154, pp. 19–33, 2018.
- [26] W. Saberi Nik, "Integrability analysis of chaotic and hyperchaotic finance systems," *Nonlinear Dynamics*, vol. 94, no. 1, pp. 443–459, 2018.
- [27] L. Zhang, G. Cai, and X. Fang, "Stability for a novel time-delay financial hyperchaotic system by adaptive periodically intermittent linear control," *Journal of Applied Analysis and Computation*, vol. 7, no. 1, pp. 79–91, 2017.
- [28] W. Zhang, J. Cao, A. Alsaedi et al., "Synchronization of time delayed fractional order chaotic financial system," *Discrete Dynamics in Nature and Society*, vol. 2017, no. 29–32, pp. 1–5, 2017.
- [29] Y. Alsaadi and J. Cao, "Bifurcation analysis and chaos switchover phenomenon in a nonlinear financial system with delay feedback," *International Journal of Bifurcation and Chaos*, vol. 25, no. 12, pp. 2671–2691, 2015.
- [30] Z. Wei, B. Zhu, J. Yang, M. Perc, and M. Slavinec, "Bifurcation analysis of two disc dynamos with viscous friction and multiple time delays," *Applied Mathematics and Computation*, vol. 347, pp. 265–281, 2019.
- [31] W. C. Chen, "Dynamics and control of a financial system with time-delayed feedbacks," *Chaos, Solitons & Fractals*, vol. 37, no. 5, pp. 1198–1207, 2008.
- [32] J. Ma and H. Tu, "Analysis of the stability and Hopf bifurcation of money supply delay in complex macroeconomic models," *Nonlinear Dynamics*, vol. 76, no. 1, pp. 497–508, 2014.
- [33] J. A. Holyst and K. Urbanowicz, "Chaos control in economical model by time-delayed feedback method," *Physica A*, vol. 287, no. 3–4, pp. 587–598, 2000.
- [34] Y. Ding, W. Jiang, and H. Wang, "Hopf-pitchfork bifurcation and periodic phenomena in nonlinear financial system with delay," *Chaos, Solitons & Fractals*, vol. 45, no. 8, pp. 1048–1057, 2012.
- [35] J. Hale, *Theory of Functional Differential Equations*, Springer, New York, NY, USA, 1977.
- [36] B. Hassard, D. Kazarino, and Y. Wan, *Theory and Applications of Hopf Bifurcation*, Cambridge University Press, Cambridge, England, 1981.
- [37] S. Ruan and J. Wei, "On the zero of some transcendental functions with applications to stability of delay differential equations with two delays," *Dynamics of Continuous, Discrete and Impulsive Systems*, vol. 10, pp. 863–874, 2003.
- [38] Q. Shi, J. Shi, and Y. Song, "Hopf bifurcation in a reaction-diffusion equation with distributed delay and Dirichlet boundary condition," *Journal of Differential Equations*, vol. 263, no. 10, pp. 6537–6575, 2017.
- [39] Z. Wang, X. Wang, Y. Li et al., "Stability and Hopf bifurcation of fractional-order complex-valued single neuron model with time delay," *International Journal of Bifurcation and Chaos*, vol. 27, no. 13, p. 1750209, 2017.
- [40] G. Huang, W. Zhang, Z. C. Wei et al., "Hopf bifurcation, positively invariant set and physical realization of a new four-dimensional hyperchaotic financial system," *Mathematical Problems in Engineering*, vol. 2017, Article ID 2490580, 2017.
- [41] J. P. Singh and B. K. Roy, "The simplest 4-D chaotic system with line of equilibria, chaotic 2-torus and 3-torus behaviour," *Nonlinear Dynamics*, vol. 89, no. 3, pp. 1845–1862, 2017.
- [42] J. P. Singh and B. K. Roy, "Hidden attractors in a new complex generalised Lorenz hyperchaotic system, its synchronisation using adaptive contraction theory, circuit validation and application," *Nonlinear Dynamics*, vol. 92, no. 2, pp. 373–394, 2018.
- [43] J. P. Singh, K. Lochan, N. V. Kuznetsov et al., "Coexistence of single- and multi-scroll chaotic orbits in a single-link flexible joint robot manipulator with stable spiral and index-4 spiral repeller types of equilibria," *Nonlinear Dynamics*, vol. 90, no. 2, pp. 1277–1299, 2017.
- [44] C. B. Roy, W. J. C. Thio, J. C. Sprott et al., "Constructing Infinitely many attractors in a programmable chaotic circuit," *IEEE Access*, vol. 6, pp. 29003–29012, 2018.

## Research Article

# Navigating Deeply Uncertain Tradeoffs in Harvested Predator-Prey Systems

Antonia Hadjimichael <sup>1</sup>, Patrick M. Reed,<sup>1</sup> and Julianne D. Quinn<sup>2</sup>

<sup>1</sup>School of Civil and Environmental Engineering, Cornell University, Ithaca, NY, USA

<sup>2</sup>Department of Engineering Systems and the Environment, University of Virginia, Charlottesville, VA, USA

Correspondence should be addressed to Antonia Hadjimichael; ah986@cornell.edu

Received 14 October 2019; Accepted 21 November 2019; Published 27 February 2020

Guest Editor: Viet-Thanh Pham

Copyright © 2020 Antonia Hadjimichael et al. This is an open access article distributed under the Creative Commons Attribution License, which permits unrestricted use, distribution, and reproduction in any medium, provided the original work is properly cited.

Multiple fisheries have collapsed as a result of overfishing and strong limitations in our knowledge of system conditions and consequential ecological interactions. Fishery managers need to establish harvesting strategies that balance economic benefits against ecological objectives, including avoiding unintended catastrophic consequences. Our results show that classical assumptions for fisheries management can yield severe instabilities in our quantified views of socioecological tradeoffs, making their ability to inform stakeholder preferences questionable. The complex ecological interactions implied by different parameterizations of such systems yield highly complex and nonlinear dynamic properties with multiple distinct basins of attraction. We show that small changes in our deeply uncertain representations of predator-prey systems can fundamentally shift their dynamics and the validity of candidate management strategies for harvest. Insights from this study highlight the importance of ensuring models capture deep uncertainties, as well as a breadth of financial and ecological criteria when searching for robust management options for resilient fisheries.

## 1. Introduction

One in four fisheries has collapsed in the latter half of the 20<sup>th</sup> century [1]. In the northwest Atlantic, most Atlantic cod (*Gadus morhua*) stocks collapsed in the early 1990s in a decline that was considered to be sudden and unexpected at the time [2]. The collapse has since been attributed to the decades-long overexploitation of the system at unsustainable levels [3] and changes in ocean climate conditions [4]. Overlooked changes in environmental conditions and system interactions led to the collapse of the sardine (*Sardinops sagax*) and anchovy (*Engraulis encrasicolus*) fisheries in the northern Benguela ecosystem off the coast of Namibia in the 1970s. As both species are energy-rich prey, their collapse culminated in significant population declines for their predators as well [5]. In the Volga River, the construction of dams has interrupted spawning migrations and reduced habitat sizes, resulting in the collapse of inconnu (*Stenodus leucichthys*), beluga (*Huso huso*), Russian sturgeon (*A.*

*gueldenstaedtii*), and herrings (*Clupea harengus*) [6]. These catastrophic events have been attributed to imprudent human action on marine and freshwater ecosystems and to deep uncertainty in system conditions and poorly understood interactions [7, 8]. Deep uncertainty refers to situations where parameters and relationships describing the system can be complex and difficult to estimate from empirical data, and experts cannot agree on probability density functions to describe them or on the relationships themselves [9, 10].

Such is the case for predator-prey theory in the trophic ecology field. The standard theory of predator-prey interactions has largely been based on the Lotka–Volterra equations that describe a system of two differential equations with a simple relation of proportionality between prey consumption and predator growth. The core assumptions of this model (prey growth and trophic function) have been challenged by multiple authors on both empirical and theoretical bases (e.g., [11–13]). Arditi and Ginzburg [14]

argued that the trophic function should account for the intricacies of the predation process at the macroscale (i.e., that the predators need to share the prey available to them). This proposition (the “ratio-dependent” trophic function) sparked a strong debate [15–18] that appeared to come to its conclusion with the general agreement that a range of predator interference levels can be found in nature (i.e., a predator-dependent trophic function with case-specific levels of interference, [19]).

In this study, we consider a fishery management problem where a fleet must develop a harvesting strategy that balances profits with the ecological stability of a predator-prey system. We use the predator-dependent predator-prey system of equations, proposed by Arditi and Akçakaya [20], that includes parameter  $m$  for the level of predator interference. Accounting for predator interaction ( $m$ ) and time adaptive human prey harvesting ( $z_t$ ), the following discrete-time forms of the predator-prey system equations are defined:

$$\begin{aligned} x_{t+1} &= \left[ x_t + bx_t \left( 1 - \frac{x_t}{K} \right) - \frac{\alpha x_t y_t}{y_t^m + \alpha h x_t} - z_{t+1} x_t \right] \cdot e^{\epsilon_x}, \\ y_{t+1} &= \left[ y_t + \frac{c \alpha x_t y_t}{y_t^m + \alpha h x_t} - d y_t \right] \cdot e^{\epsilon_y}, \end{aligned} \quad (1)$$

where  $x$  is prey abundance,  $y$  is predator abundance,  $z$  is the fraction of harvested prey, and  $t \in \{1, 2, \dots\}$  is the time index in years.  $b$  is the prey growth rate and  $K$  is its environmental carrying capacity.  $\alpha$  represents the rate at which the predator encounters the prey,  $h$  is the time it needs to consume the prey, and  $c$  is the rate at which it converts the consumed prey to new predators.  $d$  is the predator death rate and  $m$  is the level of predator interference. Parameterizing the level of predator interference in this way, allows us to move between the two contested equation forms (predator dependence versus not) and examine the effects of this type of parametric uncertainty on management tradeoffs. Furthermore, this is the first study to use this specific form of predator-prey relationships and pair it with adaptive human harvesting of prey. Environmental stochasticity is included using “process noise” factors  $\epsilon_x$  and  $\epsilon_y$ , modeled as coming from a log-normal distribution,  $\epsilon_i \sim \text{Normal}(0.0, \sigma_i^2)$  [21–23]. Additional information on the model and its parameterization is provided in Section 2; detailed parameter descriptions, units, and default values are listed in Table 1.

Different system parameterizations can have profound implications on the ways the system behaves. Even in systems without human disruption ( $z_t = 0$ ), the parameter values and population interactions can affect system dynamics in complex ways, changing, for example, the presence and stability of equilibria between the species (Figure 1). Focusing on the zero isoclines (i.e., the black lines designating the prey and predator population levels that result in either of the species having a zero growth rate), we can identify equilibria (at the intersection of the two zero isoclines). For the prey-dependent model, if the nontrivial (coexistence) equilibrium is stable, it is also a global attractor, which is the specific value that the system tends to

evolve toward, irrespective of initial conditions (Figure 1(a)). If the equilibrium is unstable then the global attractor of the system is a stable limit cycle (Figure 1(d)) (i.e., a closed trajectory in the phase space with at least one other trajectory spiraling into it, [24]). For the generalized predator-dependent model, when the nontrivial (coexistence) equilibrium is stable, it is also a global attractor (Figure 1(b)). For this model, if the nontrivial equilibrium is unstable, it can either lead to stable limit cycles (Figure 1(c)) or deterministic extinction (Figure 1(e)). When predator interference is high ( $m > 1$ ) and there is sufficient carrying capacity ( $K$ ), there are two nontrivial equilibria, only one of which is stable (Figure 1(f)). The instability of the nontrivial equilibrium can therefore lead to sustained population oscillations or extinction, depending on the model parameters and the initial conditions [24]. As a result, the complex ecological interactions implied by each model formulation are nonlinear and yield highly complex dynamical impacts on the ecosystem, leading to distinct basins of attraction [25, 26]. The complex dynamics of these systems can be further seen in the bifurcation diagrams in Figure S1 of the Supplementary Material, for all respective systems presented in Figure 1. The diagrams are plotted with respect to parameter  $m$  and demonstrate both the fixed points and the periodic orbits possible under different parameterizations. Specifically, for the systems presented in Figures 1(b)–1(d), decreasing values of  $m$  change the stability of the equilibrium point, resulting in periodic behavior.

Precise estimates of predator interference, predation, and growth and death rates are difficult to estimate from empirical data, especially for nonartificial environments [19, 20]. As a result, the form of functional responses for a large number of species remains unknown [27]. This is concerning, as the modern ecological paradigm highlights the significance of species interactions to the management of populations, communities, and ecosystems [28–30]. The consequences of such deeply uncertain ecological dynamics on the management objectives can therefore be significant, potentially leading to unattained harvesting profits, or worse, unintentional population collapse.

In this study, we quantify and analyze the tradeoffs of managing (harvesting) a two-species fishery governed by a predator-prey relationship and assess how deep uncertainty in population interactions can affect the management tradeoffs. This application expands on the work by [31, 32] and [33] that also sought to identify management tradeoffs resulting from a socioecological system, as well as the implications of deep uncertainty in the system’s parameters. As illustrated in Figure 1, the system investigated in this application exhibits a much richer variety of dynamics, in ways that may potentially alter the topological characteristics of the attained tradeoffs (e.g., if the parameterization shifts in a manner that changes the stability of an equilibrium, Figures 1(b) and 1(c)). Furthermore, the system considered here includes an additional dimension, increasing the complexity of maximizing economic benefits without inadvertently driving either of the species to collapse. The prey can be overconsumed by the predator and harvester; the predator can collapse if there is not enough available prey.

TABLE 1: Description, values in the assumed state of the world (SOW), and ranges of sampled uncertain model parameters. The fishery harvesting plans are optimized to a system assumed to be described by the base values and then re-evaluated in 4,000 alternative SOWs generated by a Latin Hypercube Sample across the parameter ranges listed in the table (minimum and maximum).

Parameter	Description	Unit	Base value	Minimum	Maximum
$\alpha$	Rate at which the prey is available to the predator	1/time	0.005	0.002	2
$b$	Prey growth rate	1/time	0.5	0.005	1
$c$	Rate with which consumed prey is converted to predator abundance	mass/mass*	0.5	0.2	1
$d$	Predator death rate	1/time	0.1	0.05	0.2
$h$	Handling time (time each predator needs to consume the caught prey)	time	0.1	0.001	1
$K$	Prey carrying capacity given its environmental conditions	mass*	2000	100	5000
$m$	Predator interference parameter	mass/mass*	0.7	0.1	1.5
$\sigma_x$	Standard deviation of stochastic noise in prey population	mass <sup>2</sup> *	0.004	0.001	0.01
$\sigma_y$	Standard deviation of stochastic noise in predator population	mass <sup>2</sup> *	0.004	0.001	0.01

\*The units of these parameters depend on the units used to measure prey ( $x$ ) and predator ( $y$ ) abundance. If prey and predator abundance is measured in volume then these units would equivalently change.

Finally, we demonstrate how the concept of multiobjective robustness can be valuable for selecting harvesting policies that avoid triggering potentially catastrophic consequences in harvested fisheries.

This study aims to bridge and complement the two intellectual threads shaping the management of fisheries: economics and biology. As recounted by [34], seminal work by [35, 36] helped ground a biological rationale for the management of fisheries by illuminating the connections between fishing effort, mortality, and dynamics. From the economic perspective, early work by [37, 38] established an operational foundation for the management of fisheries, based on capital theory and investment concepts, that addressed resource conservation by establishing an objective that ought to be pursued by management. Optimal control theory methods [39, 40] complemented these efforts by describing optimal action paths to achieve this objective. In recent decades, progressive discoveries on the importance of complex multispecies relationships, trophic connectivity, and ecosystem interactions have questioned the traditional and, to this day, predominant view of fisheries management: that of a single-species- and single-objective-based control that establishes a “maximum sustainable yield” or an “allowable biological catch” [29, 41, 42]. Work by [43, 44] and others demonstrated that single-species assessments and management controls may indeed produce misleading predictions and destructive impacts on ecosystems with multispecies interactions, and in marine environments, all species have predator-prey relationships with other species in their ecosystem.

On these grounds, ecosystem-based fishery management [29, 45] has been promoted as the new paradigm for fisheries management, advocating for the consideration of multiple species and values. However, explicit incorporation of nonharvesting values has been limited in fisheries management studies. In cases where multispecies interactions are considered [46, 47], the inclusion of nonharvesting values has been hindered by the fact that

these commodities are not typically traded in markets. This might lead to the underappreciation or even complete omission of the nonmarket values of environmental and ecosystem goods and services from studies aiming to provide support for socioecological systems management [48]. Such formulations might consequently result in the inappropriate suggestion of strategies that promote resource exploitation and degrade the ecosystem and its provisions [49, 50]. Broadening the set of fishery management objectives to include nonharvesting values could result in fundamentally different management strategies [47, 51, 52]. The latest review of fisheries’ decision-making applications using multiple criteria [53] identified several studies that considered either several species or several objectives (including nonharvesting). However, all of the presented approaches (multiattribute utility, linear and nonlinear goal programming, and weighted goal programming) collapsed these multiple objectives into one, using an a-priori formulation of the preferences of the stakeholders to be included in the model in the form of weights. These weights may not accurately reflect the true stakeholder preferences, especially before exploring the wider set of possible options, and in cases of nonlinear, threshold responses in the objective space [54–56]. Furthermore, specifying specific goals or weights before the search may miss potential solutions that are of interest by unnecessarily limiting the search space [57]. To the best of the authors’ knowledge, there has been one study that applied heuristic global optimization for the identification of management strategies for a fishery without collapsing objectives into one, Mardle et al. [58]. The application used the GENOCOP III genetic algorithm [59], albeit inappropriately, with a search population and number of function evaluations that were too small for the problem at hand. This work aims to expand on the current literature by optimizing state-dependent, adaptive harvesting strategies that explicitly consider a broad range of objectives



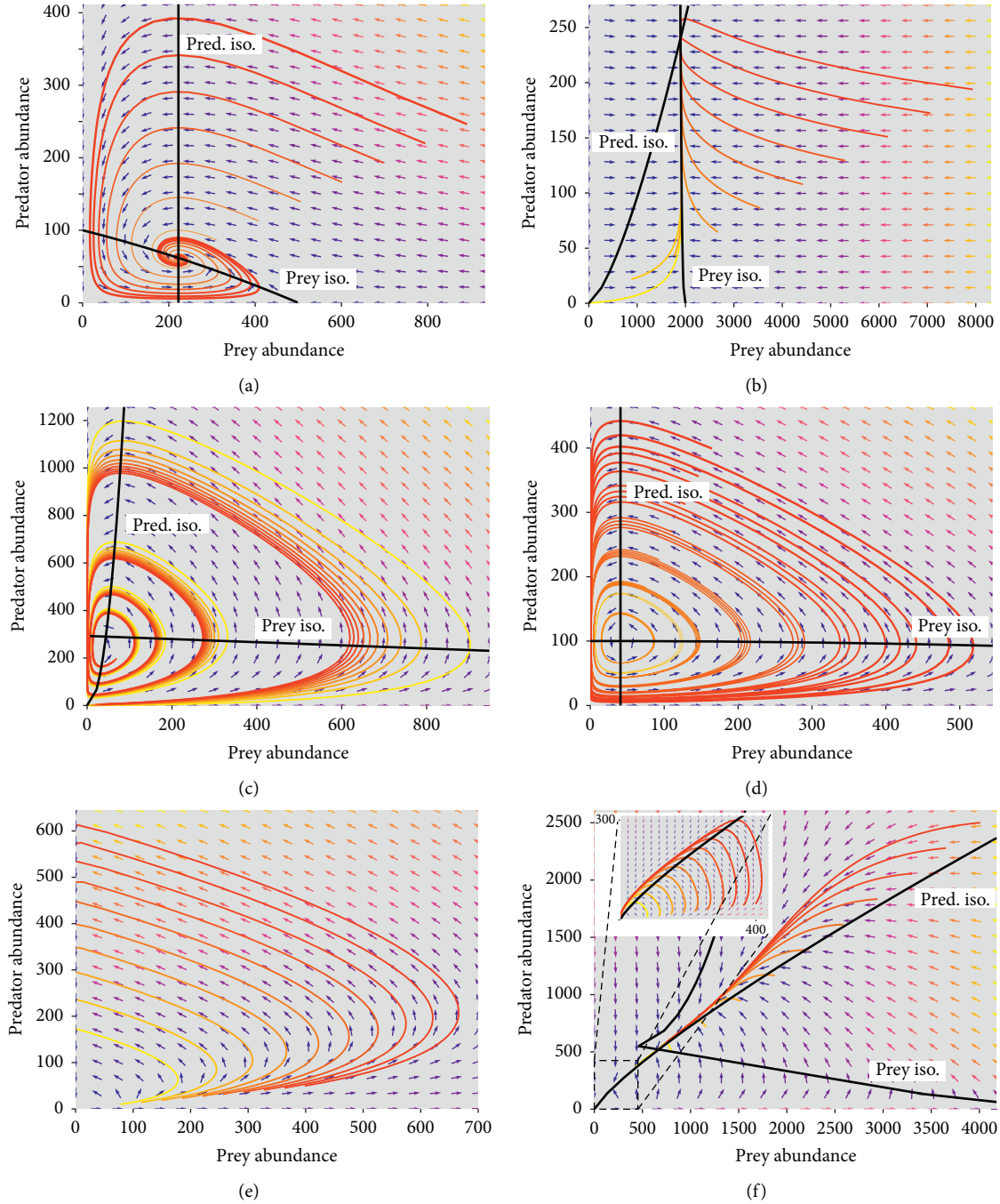


FIGURE 1: Direction fields and trajectories for different parameterizations of the predator-prey system. Black lines indicate zero-isoclines; their intersections indicate nontrivial equilibria. (a) Prey-dependent system with a global attractor stable equilibrium ( $\alpha = 0.005, b = 0.5, c = 0.5, d = 0.5, h = 0.1, K = 500, m = 0$ ). (b) Predator-dependent system with a global attractor stable equilibrium ( $\alpha = 0.005, b = 0.5, c = 0.5, d = 0.1, h = 0.1, K = 2000, m = 0.7$ ). (c) Predator-dependent system with unstable equilibrium and limit cycles as the global attractor ( $\alpha = 0.047, b = 0.877, c = 0.666, d = 0.094, h = 0.306, K = 1893.72, m = 0.465$ ). (d) Prey-dependent system with unstable equilibrium and limit cycles as the global attractor ( $\alpha = 0.005, b = 0.5, c = 0.5, d = 0.1, h = 0.1, K = 2000, m = 0$ ). (e) Predator-dependent system with unstable equilibrium and deterministic extinction ( $\alpha = 1.775, b = 0.389, c = 0.441, d = 0.083, h = 0.941, K = 4465.07, m = 0.107$ ). (f) Predator-dependent system with two equilibria and no global attractor ( $\alpha = 0.796, b = 0.215, c = 0.565, d = 0.137, h = 0.472, K = 4858.48, m = 1.21$ ). All systems assume no process noise.

(including nonharvesting), in a multiobjective optimization framework. We believe this is the first application of stochastic multiobjective control for the identification of robust harvesting strategies for a fishery.

The rest of this manuscript is organized as follows. In Section 2 we first explain the system under study and discuss the presence and stability of equilibria. We then detail how we used multiobjective optimization to identify candidate

harvesting strategies for five management objectives, while constraining strategies to avoid predator collapse. Finally, we explain how the robustness of each candidate strategy was assessed using several satisficing criteria. In Section 3, we present the potential values achieved in each objective by each of the candidate management strategies and demonstrate the significant instability of these tradeoffs, when considering uncertainty in parameter values. We then explore how interactions between parameters affect system stability and, consequently, the attainment of management objectives, including avoiding predator collapse. Lastly, we show how alternative preferences in management strategy may affect the system and potentially avoid population collapse in unstable systems.

## 2. Methods

**2.1. System Equilibria and Stability.** A generalized predator-dependent predator-prey system of equations has been modified for the purposes of this study to account for human action by means of harvesting:

$$\begin{aligned} \frac{dx}{dt} &= bx \left(1 - \frac{x}{K}\right) - \frac{axy}{y^m + ahx} - zx, \\ \frac{dy}{dt} &= \frac{caxy}{y^m + ahx} - dy, \end{aligned} \quad (2)$$

where  $z$  describes the harvesting effort performed by the fleet. The parameter values describing the system are listed in Table 1 and represent our best current state of knowledge. Since the system in this study represents a stylistic example, these values were not derived from a specific empirical system, but were based on values and ranges that appear in multiple literature sources (e.g., [21–24]). In an unharvested system, for the nontrivial (coexistence) equilibrium to exist, the following equation must hold [24]:

$$c > hd. \quad (3)$$

A mathematical proof of how this condition also holds for a system with harvested prey is provided in the Supplementary Material. In an unharvested system, for the nontrivial equilibrium to be stable, the following equation must hold:

$$\alpha(hK)^{1-m} < (b)^m. \quad (4)$$

Biologically, when (3) holds, predators convert the consumed prey to new predators at a higher rate than the rate of their death  $d$  and handling time  $h$  (i.e., their losses in time and energy). When (4) holds, the prey isocline (detailed in the Supplementary Material) decreases as a function of  $x$ , stabilizing the system [24]. For a system where prey is harvested (i.e., the additional parameter  $z$  only decreases the prey level), the condition must also hold as the prey isocline can only further decrease as a function of  $x$ . This is also demonstrated experimentally by our study.

We use the stochastic, closed loop control method direct policy search (DPS) [60], also known as parameterization-simulation-optimization, to identify harvesting policies. This

allows for the use of a state-aware control rule that maps the prey population level ( $x_t$ ) to the harvesting effort at the next time step ( $z_{t+1}$ ), instead of optimizing all individual harvesting efforts. The following sections describe this approach in detail, beginning with the management objectives, the policies that were optimized, and the algorithm used.

**2.2. Optimization of Harvesting Strategies.** The optimization is aimed at determining dynamic harvesting policies that describe how much prey to harvest over time in order to optimize five objectives and meet the specified constraint. The objectives are designed to address financial goals and to ensure that the fish population is maintained at natural levels; this gives rise to tradeoffs between candidate harvesting strategies. We identify a set of “nondominated” solutions, which is comprised of the harvesting strategies that perform better than any other strategy in at least one of the five objectives. The nondominated solutions compose optimal tradeoffs where improvement in any single objective comes at the cost of degraded performance in one or more of the remaining objectives. The objectives and constraint are described in more detail below.

**2.2.1. Maximize Harvesting Discounted Profits (Net Present Value).** The net present value of harvesting profits for each realization of environmental stochasticity is given by  $\sum_{t=0}^{T-1} z_{t+1,i} x_{t,i} / (1 + \delta)^t$  for  $T$  years, where  $\delta$  is the discount rate used to convert future benefits to present value,  $x_{t,i}$  is prey abundance at the  $t$ th year of the  $i$ th realization, and  $z_{t+1,i}$  is the harvesting effort performed for that prey. The expected harvesting discounted profits  $O_1$  are estimated as the average across  $N$  realizations:

$$O_1 = \frac{1}{N} \sum_{i=1}^N \left( \sum_{t=0}^{T-1} \frac{z_{t+1,i} x_{t,i}}{(1 + \delta)^t} \right), \quad (5)$$

where  $\delta = 0.05$ .

**2.2.2. Minimize Prey Population Deficit.** The prey population deficit for each realization of environmental stochasticity is given by  $(K - x_{t,i})/K$ , where  $K$  is the prey carrying capacity (i.e., the maximum population abundance that can be achieved if the prey is not subjected to predation or harvest). The expected prey population deficit  $O_2$  is estimated as the average deficit over all time steps, averaged across  $N$  realizations:

$$O_2 = \frac{1}{N} \sum_{i=1}^N \left( \frac{1}{T} \sum_{t=1}^T \left( \frac{K - x_{t,i}}{K} \right) \right). \quad (6)$$

When policies are re-evaluated or reoptimized in systems with different parameter combinations (as elaborated in Section 2.6), the respective value of  $K$  is adjusted accordingly, so as to reflect the deficit of population as it relates to the carrying capacity implied by the new set of parameters.

**2.2.3. Minimize Longest Duration of Consecutive Low Harvest.** Given operational costs, the fishery managers would like to avoid long durations of consecutively low harvest, defined by a minimum harvest limit. The max duration of low harvest is given by both  $z_t < \text{limit}$  and  $z_{t+1} < \text{limit}$  holding for all  $t$  in a realization of  $T$  years. The expected worst case of consecutive low harvest  $O_3$  is defined as the average of the max duration across  $N$  realizations:

$$O_3 = \frac{1}{N} \sum_{i=1}^N (\max_T(\phi_{t,i})),$$

where:

$$\phi_{t,i} = \begin{cases} \phi_{t-1,i} + 1, & \text{if } z_t < \text{limit}, \\ 0, & \text{otherwise,} \end{cases} \quad (7)$$

$$\phi_{1,i} = \begin{cases} 1, & \text{if } z_1 < \text{limit}, \\ 0, & \text{otherwise,} \end{cases}$$

where  $\text{limit} = 5\%$ .

**2.2.4. Maximize Worst Harvest Instance.** Given operational costs, the fishery managers would like to avoid exposure to financial risks. Variance-minimizing strategies have been widely employed in the literature to model behavior under risk; authors have noted, however, that the costs of risks associated with uncertainty often depend on higher order moments, such as skewness and kurtosis (tail events in the distribution) [61]. This was approximated in this analysis by maximizing the worst harvest instance as well as minimizing the variance of harvest in every realization ( $O_5$ , explained in the next section). The worst harvest instance is approximated here by the 1st percentile of harvest for every  $T$ -year realization. The expected worst harvest instance is calculated as the average 1st percentile across  $N$  realizations:

$$O_4 = \frac{1}{N} \sum_{i=1}^N (\text{percentile}_T(z_{t+1,i} x_{t,i}, 1)). \quad (8)$$

**2.2.5. Minimize Harvest Variance.** More traditionally encountered in the literature is the minimization of the variance of deviations from the expected profits [61, 62]. This objective has been approximated by estimating the variance of the obtained harvest in every  $T$  year realization and averaging across all  $N$  realizations:

$$O_5 = \frac{1}{N} \sum_{i=1}^N (\text{Var}_T(z_{t+1,i} x_{t,i})). \quad (9)$$

**2.3. Avoid Collapse of Predator Population.** Considering the unharvested predator population as a valuable species, the

population of which the managers would like to maintain, the optimization is also subject to a constraint:

$$\frac{1}{N} \sum_{i=1}^N (\psi_{t,i}) = 0,$$

where:

$$\psi_{t,i} = \begin{cases} 1, & \text{if } y_{t,i} < 1, \\ 0, & \text{otherwise,} \end{cases} \quad (10)$$

$$\forall t \in T \text{ and } \forall i \in N.$$

**2.4. Formulation of Harvesting Policy.** For the purposes of this study, candidate DPS control rules were used to map the current levels of prey population ( $x_t$ ) to the harvesting effort at the next time step ( $z_{t+1}$ ). The optimization was aimed at identifying the parameters describing the control rules, instead of the harvesting efforts themselves, allowing for state-based feedback control strategies. The control rules were in the form of Gaussian radial basis functions (RBFs), following the formulation by [63]. The optimization problem was formulated as follows:

$$\text{Minimize } F(z_x) = (-O_1, O_2, O_3, -O_4, O_5),$$

$$z = (z_1, z_2, \dots, z_T),$$

(11)

$$z_{t+1} = \sum_{i=1}^n w_i \left[ \exp \left[ - \left( \frac{(x_t) - c_i}{b_i} \right)^2 \right] \right],$$

where  $i = 1, 2, \dots, n$  and  $n$  is the number of RBFs used in the function mapping; in this study  $n = 2$ .  $w_i$  is the weight of the  $i$ th RBF and the weights are formulated so as to be positive (i.e.,  $w_i > 0 \forall i$ ) and sum to one (i.e.,  $\sum_{i=1}^n w_i = 1$ ).  $c_i$  and  $b_i$  are the center and radius of the  $i$ th RBF. All  $w_i, c_i$  and  $b_i \in [0, 1]$ . We used two RBFs and one input in this study, resulting in six decision variables that need to be optimized for the control rule mapping current prey population to next harvest. More inputs can be used in the policy formulation, but were omitted from equation (10) for the purposes of simplicity. Note that with the application of these control rules, the harvesting effort  $z_{t+1}$  will not necessarily be the same in each of the  $N$  realizations as the harvesting action is informed by the respective level of prey,  $x_t$ , which is subject to the environmental stochasticity at each realization. Furthermore, this formulation assumes a perfectly accurate measurement of the prey level at all times, as well as a perfectly accurate execution of the harvesting strategy. These simplifying assumptions have the benefit in this study of demonstrating the severe difficulty of the class of fisheries management problems even in optimistic formulations of available information.

**2.5. Optimization Algorithm.** The multiobjective formulation was solved for  $N = 100$  realizations of randomly

generated environmental stochasticity, with each realization spanning  $T = 100$  years. Initial prey and predator population values were assumed to be  $x_0 = 2000$  and  $y_0 = 250$ . The parameter values for the assumed state of the world (SOW) are listed in Table 1. The default SOW is assumed to have a single stable equilibrium that is a global attractor. The parameters of the formulated policy were optimized using the Borg multiobjective evolutionary algorithm (MOEA). MOEAs are heuristic optimization algorithms that follow an iterative search procedure to adapt and evolve a population of possible solutions toward an optimized set. To do so, MOEAs apply various probabilistic operators for mutation, mating, archiving, and selection [64].

The Borg MOEA has been designed for the optimization of a wide array of many-objective, multimodal problems [65]. The Borg MOEA is a stochastic population-based search algorithm. Multiple diagnostic studies have demonstrated its capacity to perform consistently well across multiple challenging applications [64]. Its success in identifying high quality Pareto-approximate solution sets has been attributed to its use of  $\epsilon$ -dominance archiving,  $\epsilon$ -progress, and its autoadaptive exploitation of multiple search operators based on their success in generating high quality solutions [65]. The numerical precision required for evaluating each objective,  $\epsilon$ , is specified by the decision maker, creating multidimensional  $\epsilon$ -boxes for ranking and archiving solutions as the algorithm completes its search [65]. Additionally,  $\epsilon$ -values provide a control on the resolution of the Pareto-approximate set (e.g., [66]). The standard means of specifying  $\epsilon$ -values is to consider the significance of precision in each objective. The  $\epsilon$ -values for the five objectives were set as follows:  $O_1: \epsilon = 5$ ,  $O_2: \epsilon = 0.005$ ,  $O_3: \epsilon = 1$ ,  $O_4: \epsilon = 1$ , and  $O_5: \epsilon = 5$ . The Borg MOEA was implemented using its default parameter values, as recommended by [65]. Since Borg is a stochastic optimization algorithm, its search is affected by the random seed that initializes the population and impacts its stochastic operators. The optimization problem was hence solved with 20 random seed runs, each of which exploited 3,000 function evaluations.

**2.6. Robustness Analysis.** As illustrated in Figure 1, the parameters describing the predator-prey system can fundamentally shift its dynamics and, by extension, the harvesting strategy one should choose to employ. Given the limitations of our knowledge of the parameters describing the modeled system [19, 20, 27], decision makers may consider identifying potential policies that continue to perform satisfactorily when operated under a broad range of alternative system characteristics, also referred to as SOWs. Such policies are termed “robust” and can be identified using various metrics available in the decision analysis literature [67–69]. The domain criterion satisficing measure [70] quantifies the fraction of potential SOWs, in which a solution meets a desired performance (e.g., a set of criteria), and has been widely used in the robustness literature. When compared against other satisficing- and regret-based measures, this metric has been found to identify solutions in line with the stakeholders’ performance criteria [67]. We generated 4,000 alternative SOWs using a Latin Hypercube Sample across the ranges of the deeply uncertain parameters listed in Table 1,

assuming uniform parameter distributions. The prey population at each SOW was initialized at the respective sampled  $K$ -simulated unharvested population trajectories of both prey and predator for all SOWs can be found in Figure S3 in the Supplementary Material. The purpose of the exploratory parameter ranges is to encompass the best available nominal estimates, while sampling broadly enough in their feasible ranges to discover consequential impacts. The intent of this approach is to shift focus from predicting system conditions to, instead, discovering scenarios that are consequential to the decision makers [71–73]. Our multivariate satisficing robustness measure quantifies the percentage (%) of the SOWs in which harvest management is possible (i.e., there is no deterministic extinction) that meet the following requirements:

- (1) Net Present Value (NPV)  $\geq 1,500$
- (2) Prey population deficit (Prey Deficit)  $\leq 0.5$
- (3) Longest duration of low harvest (Low Harvest Duration)  $\leq 5$
- (4) Worst harvest instance (Worst Harvest)  $\geq 50$
- (5) Harvest variance  $\leq 2300$
- (6) Duration of predator population collapse (Predator Collapse)  $\leq 1$

These performance criteria should be elicited by relevant stakeholders in a real world application. In this exploratory work, they are set so as to reflect possible performance levels expected by decision makers managing this system. Criteria 1, 3, 4, and 5 are each met by at least 75% of the solutions in the assumed SOW. Criterion 2 was set based on critical fish biomass levels for sustainable yields, as reported in the literature [74]. Criterion 6 was met by all solutions in the assumed SOW as it was defined as a constraint.

Even though more robust solutions may be discovered if the optimization is conducted over a large ensemble of deeply uncertain SOWs, said robustness might also result in increased losses (regrets) in the assumed SOW as well as in SOWs that are never encountered [31]. Instead, in this study, we aim to establish a baseline of performance in the assumed SOW, representing our best current state of knowledge, and then re-evaluate this performance across a subjective and wide enough range of SOWs. This allows us to both minimize regret in the assumed SOW and also highlight the existence of areas in the parametric space where management plans might fail, despite their highly adaptive and optimistic design, due to their ignorance of a fundamental shift in system dynamics. Lastly, this intentionally broad ensemble of parameter combinations produces SOWs where extinction of one or both species is unavoidable (detailed in the following section). Such SOWs were omitted from the robustness analysis of the candidate solutions, so as to only evaluate them in contexts where the choice of strategy actually matters and affects the outcomes.

### 3. Results and Discussion

This section is organized as follows, with Figure 2 summarizing the motivation and main findings of each section.

In Section 3.1, we first present and discuss the objective values attained in the assumed SOW, presented in Figure 3, highlighting the strong tradeoffs between NPV and Prey Deficit objectives. In Section 3.2, we explore the impacts of deep uncertainty on the inferred tradeoffs for four other potential SOWs. Figures 4 and 5 demonstrate severe instabilities in these objective values when strategies are re-evaluated in different SOWs. Further, Figure 5 shows that when compared with solutions identified assuming perfect knowledge of the SOW, there are significant losses in the populations of the two species, despite the highly adaptive harvesting policies. In Section 3.3, we explore how system stability is generally affected by parametric uncertainty, by looking at the SOWs leading to predator population collapse. In Figure 6, we show that there is a multidimensional threshold surface dividing sustained harvesting and recovery from fishery collapse, where there are no management tradeoffs to be attained. Finally, in Section 3.4, we posit that the concept of multiobjective robustness can be a valuable driver for selecting management strategies that meet necessary system performance and avoid system collapse. We present the robustness values of each candidate management strategy in Figure 7, and the implications of choosing two of them for the two fish populations in Figure 8. Figure 2 summarizes the methodological approach of this study, with the motivation and main findings of each section.

*3.1. Fishery Management Tradeoffs in Assumed State of the World.* The general challenge considered by fishery management is how to best exploit the system through harvesting while balancing multiple societal objectives with respect to environmental sustainability and profit. Figure 3 presents a parallel axis plot of the objective values achieved by each optimized solution in the assumed SOW (i.e., the set of model parameters describing the system, to which the policies were optimized). The performance on each objective is represented by a vertical axis. The points where each line crosses a vertical axis represent the average performance value for that objective across 100 realizations of environmental stochasticity. An upward shift in one of the vertical axes indicates increased preference in the equivalent objective performance. All lines have been shaded according to their performance on the NPV objective. The plot is oriented such that the ideal solution would be a dark horizontal line crossing the top of each vertical axis. Diagonal, intersecting lines indicate pairwise tradeoffs between two objectives, where improving the performance in one objective is only possible with reduced performance in the other. One should note that the identified solutions carry no stakeholder preference (or weight) towards the objectives but have been instead identified by searching the space of possibilities as widely as possible. Presenting objective performance and tradeoffs in such a format allows and facilitates an a-posteriori elicitation and negotiation of preferences by the decision makers [76]. For example, in systems or decision-making contexts, where species conservation is valued more than harvest profits, one can express such weighting by imposing upward moving limits on the respective axes. This

## Main study findings

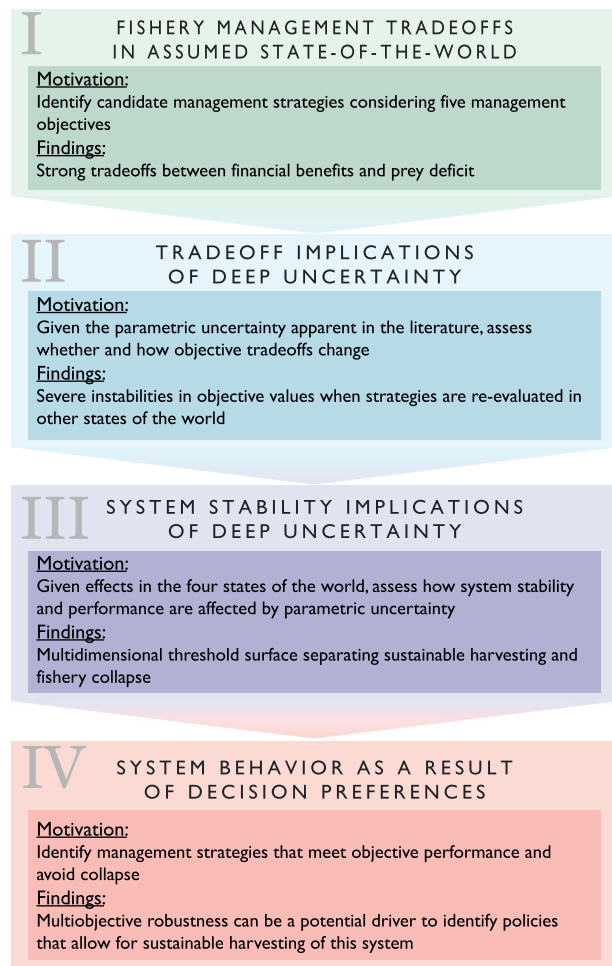


FIGURE 2: Main findings on the implications of deep uncertainty on this predator-prey system. Latin numerals indicate the Results and Discussion sections in which each step is presented. See the main text for further description.

preference elicitation process should be iterative, allowing for stakeholders with diverging preferences to evaluate the performance and appropriateness of the candidate solutions for the system at hand.

As indicated by the intersecting lines and the switch in the color gradient, there appears to be strong tradeoffs between the NPV and Prey Deficit objectives, as well as between the Prey Deficit and the Low Harvest Duration objectives. NPV-maximizing policies do so by harvesting large parts of the available prey population, depleting it from its natural levels by 58.2% on average, across all realizations. Similarly, policies that minimize the Low Harvest Duration to zero (i.e., harvesting at least 5% of the available prey at all times) also severely deplete the prey population. In contrast, policies that minimize the Prey Deficit to 5%, achieve very low values in the NPV objective (indicated by their very light color), as well as in the Low Harvest Duration objective. Looking at the two objectives incorporated to minimize financial risk, Worst Harvest and Harvest Variance, one may note that some solutions ranking poorly with regards to their



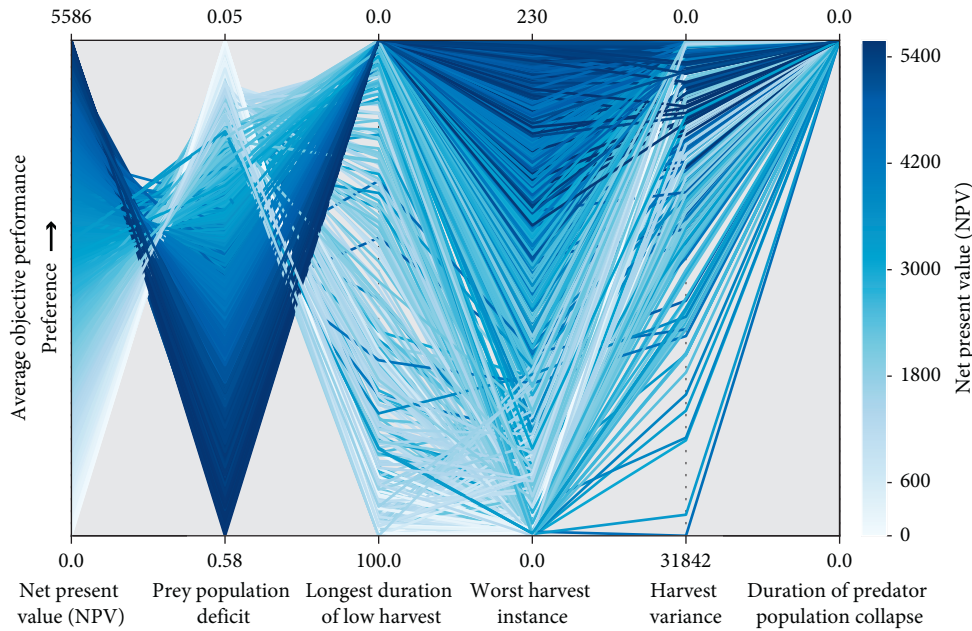


FIGURE 3: Parallel axis plot of the average objective values of solutions optimized in the assumed SOW. The points where each line (solution) intersects with a vertical axis represent the average performance value across 100 realizations of environmental stochasticity. The plot is oriented such that the ideal solution would be a horizontal line crossing the top of each vertical axis. Diagonal lines indicate pairwise tradeoffs between two objectives. The color gradient is based on the performance of each solution in the NPV objective, with darker colors representing a higher NPV.

Worst Harvest perform very well in minimizing Harvest Variance. These solutions also achieve low NPVs (as indicated by their light color), suggesting that the low variance is achieved by simply consistently harvesting very little at every time step. This observation is consistent with past robust optimization studies (e.g., [77, 78]) that have found variance-minimizing objectives penalizing outcomes both above and below the mean (i.e., both higher and lower profits when only lower profits are of concern).

The identified solutions have been optimized under the assumption that the abstracted harvesting agent has access to an accurate reading of the prey population at each timestep (i.e., “error-free information”). Furthermore, the solutions and tradeoffs that arise as a result of this formulation only take into account uncertainty in the form of environmental stochasticity ( $\epsilon_i$ ), which is traditionally assumed to be well characterized. These assumptions are commonly employed in the literature [52, 79, 80] and are highlighted here to emphasize the highly optimistic nature of such optimized strategies, even when they account for standard sources of environmental uncertainty. In addition, the harvesting policies assume no incidental by-catch of the predator. Our intent is to illustrate that even in a highly optimistic harvested predator-prey management context, with a well-informed and highly adaptive harvesting agent, deep uncertainties that are traditionally neglected pose severe challenges.

**3.2. Tradeoff Implications of Deep Uncertainty.** Figure 3 presents the objective values achieved by each policy under

a SOW representing our best knowledge of the system, a predator-dependent system with a stable global attractor, the dynamics of which are presented in Figure 1(b). As previously elaborated, precise estimates of growth and death rates, predation, and interference are often difficult to estimate from empirical data [19, 20]. Given this uncertainty in the parameter estimates, Figure 1(c) presents the dynamics of a predator-dependent system with a now unstable equilibrium, resulting from slight shifts in our best estimates of the system’s parameter values. Figures 1(a)–1(f) illustrate the wide variety of dynamic behavior that can occur as a result of uncertainty in the system parameterization, in absence of any human disturbance (harvesting). Having identified the Pareto-approximate set of solutions for the assumed SOW (Figure 3), Figure 4 presents the same set of optimized solutions with their performance in a three-dimensional objective space. The solutions in the assumed SOW are presented in blue, and, in light red, light orange, light green, and brown, the plot shows how their objective values change when re-evaluated in four other SOWs. The parameter values for the four SOWs presented in Figure 4 are provided in Table 2.

When policies are re-evaluated in a SOW with deterministic extinction (dynamics presented in Figure 1(e)), the Pareto front collapses (brown points). Population collapse is deterministic in this SOW and occurs even without any harvest. Deterministic extinction has been the focus of several studies [13, 24, 81], particularly in the context of the prey- versus ratio-dependent predator-prey theory. Deterministic extinction behavior was routinely observed [24], but could not be described by the classic prey-dependent model. The



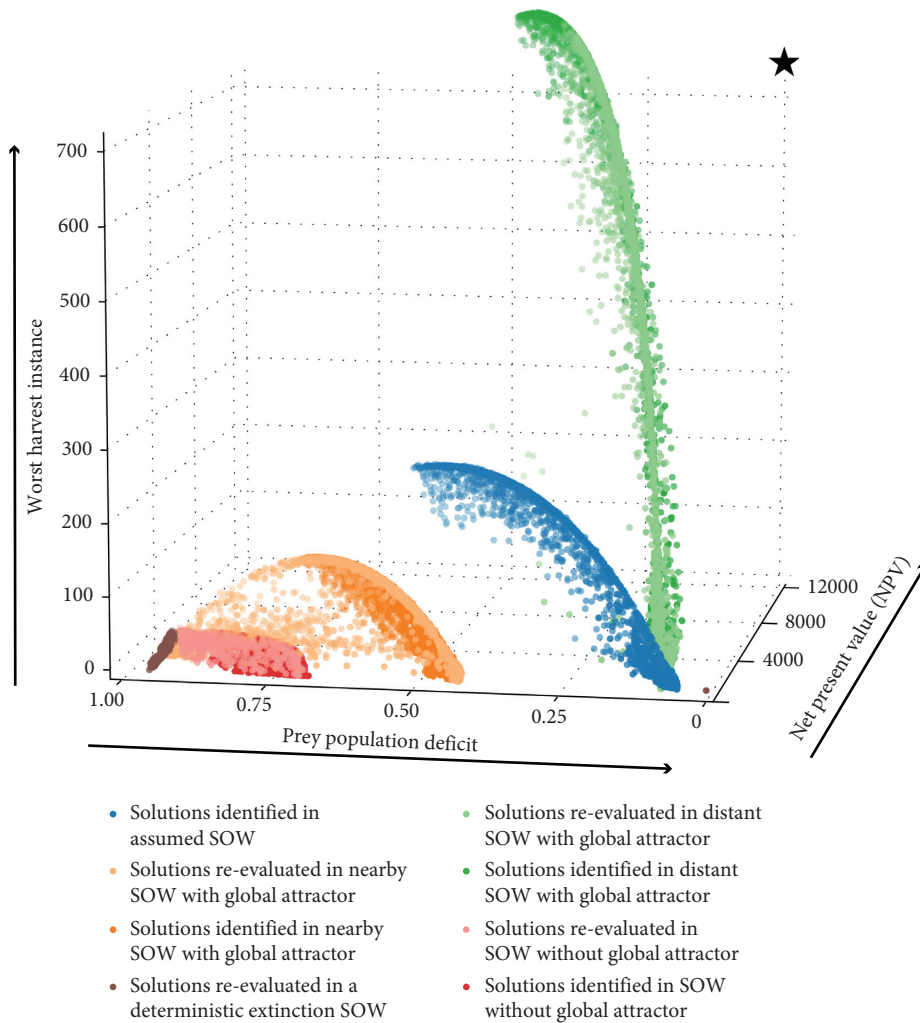


FIGURE 4: Solutions as points in a 3D objective space. Blue: as identified in the assumed SOW; brown: re-evaluated in a SOW with deterministic extinction; light red: re-evaluated in nearby SOW without a global attractor; light orange: re-evaluated in nearby SOW with global attractor; light green: re-evaluated in distant SOW with global attractor. Dark red, dark green, and dark orange represent the solutions identified when optimizing to those SOWs. The parameter values for each SOW are provided in Table 2.

behavior is explained by predators becoming more efficient (higher  $\alpha$  and  $c$  and lower  $h$  values) and dying out after exhausting the prey.

The policies were also re-evaluated in a parametrically nearby SOW with a global attractor (light orange) and in a parametrically distant SOW with a global attractor (light green), both of which exhibit dynamic behavior akin to that in the assumed SOW (presented in Figure 1(b)). Both re-evaluations examine situations where the decision makers find themselves managing a system exhibiting similar dynamic behavior to that assumed, but having different parameter values from their best estimates. In the nearby SOW (light orange), a subset of candidate harvesting policies cause significant losses in the prey population numbers (increased values in prey population deficit) and predator population collapse (Figure 4). In the distant SOW (light green), the conditions for prey growth are more favorable: higher  $K$  allows for larger prey population and higher  $m$  stabilizes the system. In this SOW, no significant losses are exhibited in

either of the two populations and the adaptive control policies that had been identified appear to outperform the expected objective values achieved in the assumed SOW. However, this is a stable SOW favorable to higher growth and a decision maker might be inclined to inquire into what objective values could have been achieved having had perfect information about the SOW being managed. In other words, if the optimization was performed, having the accurate reading of the parameters describing the system each time, how would the performance of those solutions differ?

Points in dark orange and dark green in Figure 4 present the objective values achieved by the solutions identified when re-optimizing to the equivalent nearby and distant SOWs. In the nearby stable SOW (light and dark orange), the significant losses in prey population numbers are reduced by the solutions identified through optimization with perfect information. This is more clearly seen in the equivalent parallel axis plot (Figure 5(a)). Here, the solutions identified in the assumed SOW and re-evaluated in the one

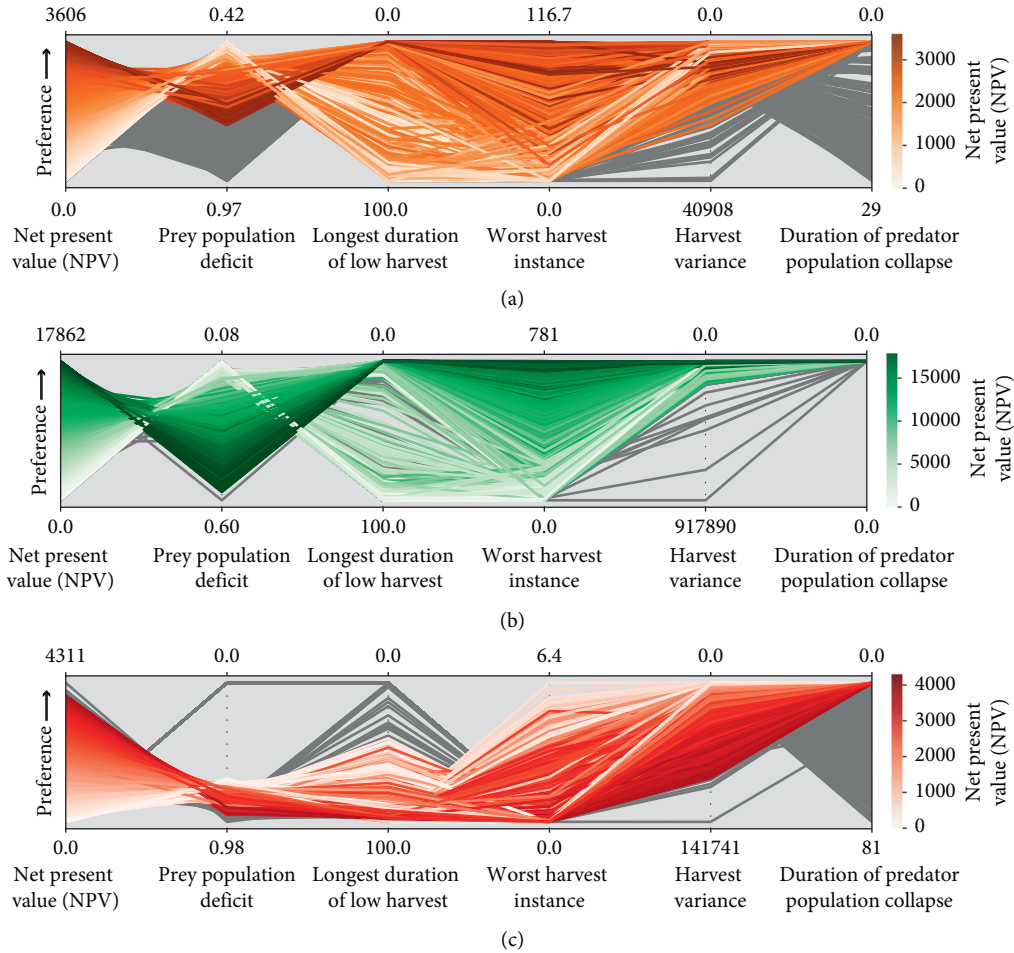


FIGURE 5: Solutions re-evaluated in three SOWs and solutions optimized to those SOWs, in a parallel coordinate form. (a) Nearby SOW with a global attractor. Orange: solutions optimized in this SOW and grey: solutions identified in assumed SOW and re-evaluated in this SOW. (b) Distant SOW with a global attractor. Green: solutions optimized in this SOW and grey: solutions identified in assumed SOW and re-evaluated in this SOW. (c) Nearby SOW without a global attractor. Red: solutions optimized in this SOW and grey: solutions identified in assumed SOW and re-evaluated in this SOW. The parameter values for each SOW are provided in Table 2.

nearby (presented in grey) are contrasted with those achieved in the nearby SOW, having had perfect information during the optimization (presented in shades of orange). The regrets are significant in the Prey Deficit objective, where the value of the worst-performing policy could have been reduced from 97% to 75% with perfect information about the SOW parameterization. More importantly, many of the policies re-evaluated in this SOW fail to meet the Predator Collapse constraint, with the worst-performing among them failing 29.34% of the time. Conversely, all the policies identified with perfect information about the SOW meet that constraint. Looking at the distant stable SOW (light and dark green in Figure 4), even though the state-aware control policies manage to avoid significant prey losses, the regrets in this case come in the form of lower values in the NPV and Worst Harvest objectives. This is despite the fact that the harvesting agent is highly adaptive and has a perfect reading of the prey population at each timestep.

When solutions are re-evaluated in a nearby SOW without a global attractor (light red in Figure 4), multiple basins of attraction exist and changes in initial conditions

can lead to different equilibria (as depicted in Figure 1(f)). In this SOW, the predators are more efficient (higher  $\alpha$  and  $c$  values), but also exhibit high interference ( $m > 1$ ) which has a stabilizing effect on their population [24]. In such a system, the decision maker harvesting the prey competes with more efficient predators and the solutions re-evaluated in this SOW end up significantly depleting the prey (light red in Figure 4), as well as collapsing the predator population in most instances (grey lines in Figure 5(c)). Even if the system dynamics are less favorable in this SOW, predator population collapse could have been entirely avoided by all solutions if the optimization had perfect information about the SOW parameters (red lines in Figure 5(c)).

**3.3. System Stability Implications of Deep Uncertainty.** Figures 4 and 5 present how the initial perceptions of tradeoffs in the original SOW would be misleading if the fishery was actually described by the parameterizations of the four other distinct SOWs, selected here for the purpose of demonstration. As knowledge limits may yield broad

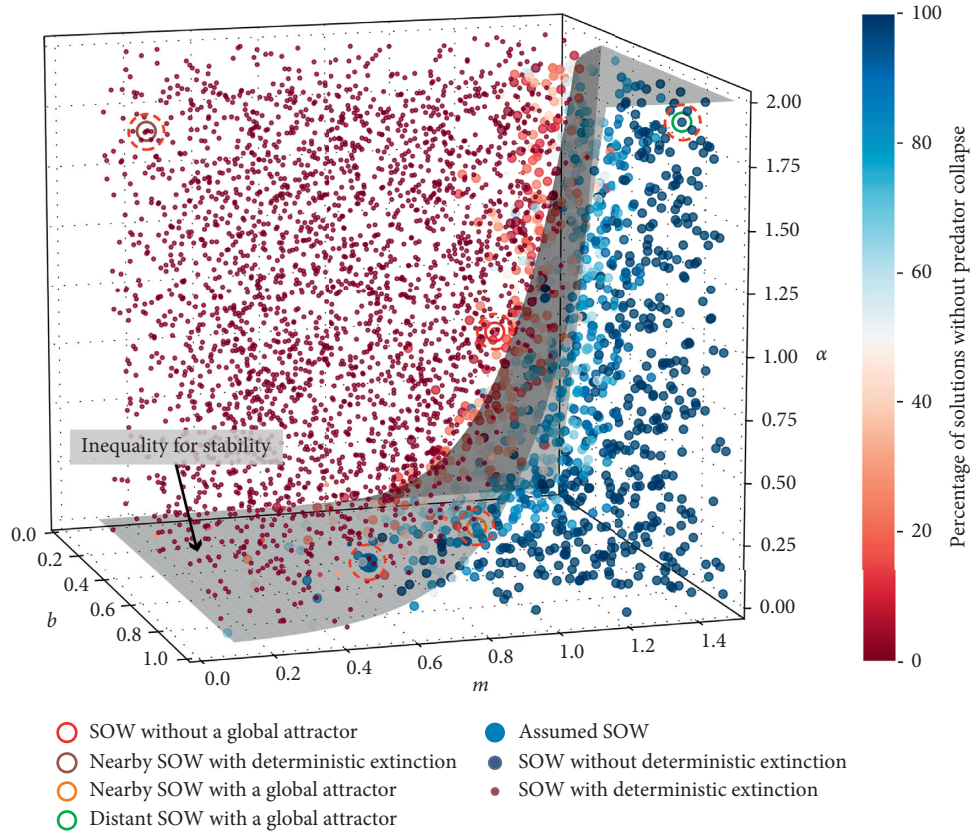


FIGURE 6: All the sampled SOWs, as they fall in the  $\alpha$ ,  $b$ , and  $m$  parametric space (all other parameters kept constant). The percentage of solutions that do not lead to any predator collapse when applied in each SOW is represented by the color at each point. Small points and large points indicate SOWs with and without deterministic extinction, respectively. The shaded surface indicates the inequality for stability (4), with all other parameters held constant at the default values and harvesting  $z$  assumed to be zero. The SOWs presented in Figure 4 are also contextualized in the parametric space.

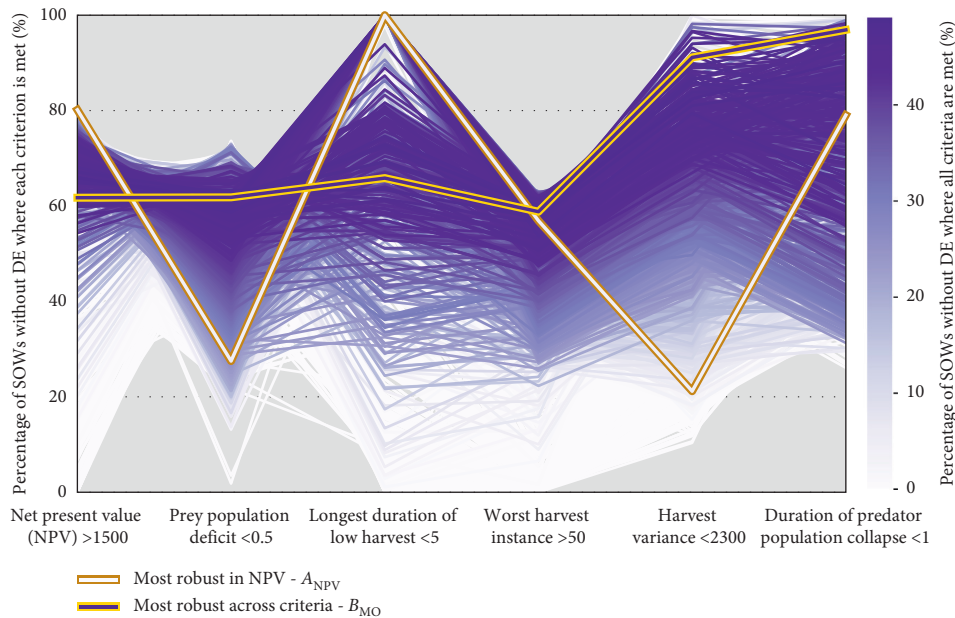


FIGURE 7: Parallel coordinate plot of satisfying tradeoffs for all identified solutions when applied in the alternative SOWs without deterministic extinction. Each vertical axis represents the percentage of SOWs in which each solution fulfills each criterion. Each solution is colored based on the percentage of SOWs in which it fulfills all criteria. The two highlighted solutions,  $A_{NPV}$  and  $B_{MO}$ , were identified using two robustness definitions, meeting criterion 1 and meeting all criteria, respectively.

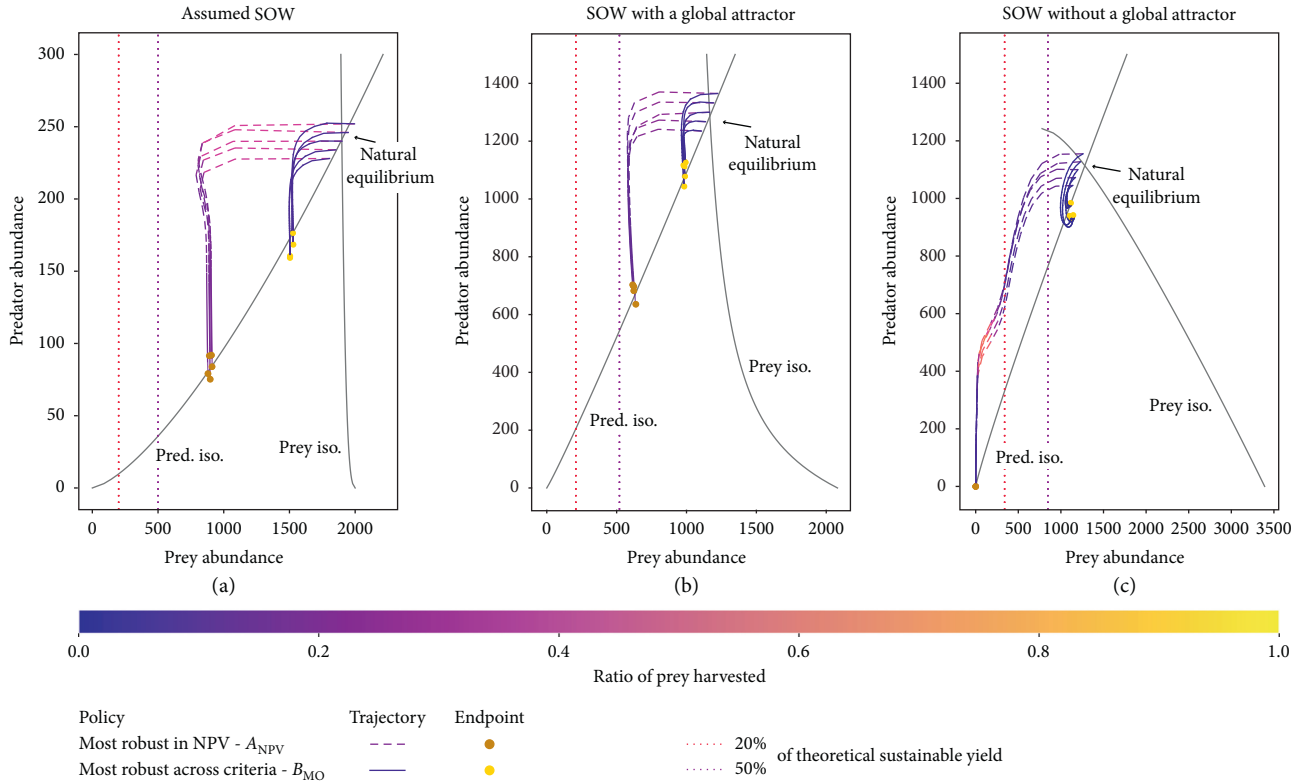


FIGURE 8: Fish population trajectories as a result of two harvesting policies applied in the assumed SOW and two alternative SOWs. The two applied solutions,  $A_{NPV}$  and  $B_{MO}$ , were identified using two robustness definitions, meeting criterion 1 and meeting all criteria, respectively. Each line is a system trajectory starting near the unharvested equilibrium. The color at each point of the trajectory indicates harvesting effort. Critical prey population levels, 50% and 20% of the biomass for theoretical sustainable yield indicate overfishing and endangerment, respectively [74, 75].

TABLE 2: Parameter values for the assumed SOW and four distinct SOWs. The fishery harvesting policies are optimized to the assumed SOW (in blue). The performance of the solutions in four distinct SOWs is highlighted in Figures 4–6.

Parameters	Assumed (blue)	Nearby and stable (orange)	Distant and stable (green)	Nearby and unstable (red)	Deterministic extinction (brown)
$\alpha$	0.005	0.208	1.867	0.796	1.775
$b$	0.5	0.663	0.830	0.215	0.389
$c$	0.5	0.361	0.542	0.565	0.441
$d$	0.1	0.095	0.197	0.137	0.083
$h$	0.1	0.372	0.949	0.472	0.941
$K$	2000	2080.58	4610.48	4858.48	4465.07
$m$	0.7	0.93	1.442	1.21	0.107
$\sigma_x$	0.004	0.004	0.002	0.008	0.003
$\sigma_y$	0.004	0.003	0.005	0.009	0.007

parameter ranges, it is a decision relevant concern to assess how consequential performance changes may be for the tradeoff solutions across a broader sample of the deeply uncertain parametric space. We therefore have explored the impacts of 4,000 SOWs. Figure 6 presents the sampled SOWs in the  $\alpha$ ,  $b$ , and  $m$  parametric space, with all other parameter values kept constant. The color of each point indicates the percentage of the original set of tradeoff solutions (%) that do not lead to inadvertent predator collapse within each sampled SOW. Certain parameter combinations cause deterministic extinction, as populations collapse even in the absence of harvest; these SOWs are indicated by the

smaller dark red points in Figure 6. Even though the model used in this study is in a discrete-time form, the continuous-time model (equation (2) in Section 2) can be used to study the underlying dynamics of the system. The necessary condition for a stable global attractor equilibrium, as derived for this generalized system with harvest (equation (4) in Section 2) and applied to the parametric space, is represented by the shaded surface shown in Figure 6.

The underlying dynamics of the system can shift such that the coexistence of the two species is deterministically impossible. In other words, a multidimensional threshold surface exists that separates sustained harvesting and

recovery from fishery collapse, where there are no management tradeoffs to be attained. Even though this exploratory analysis sampled the parametric space uniformly, its intent has not been to assign equal probabilities to all outcomes, including the deterministic extinction cases, but rather to explore broadly to discover said threshold surface in the parametric space. With regards to the parametric plausibility of such a region, it could be the side effect of permanent change in one or more critical components in the environment of a species. Such changes may be progressive (e.g., climate change [4] or habitat loss [6]) and lead to permanent changes in the growth or death rates of a species, such that it inevitably moves towards extinction [82]. When collapse is not prescribed by the underlying dynamics, it is evident that it can be avoided by some of the optimized strategies, and, as a result, value preference in the objective space becomes the most decisive consideration. When feasible, we hypothesize that the concept of multiobjective robustness [76, 83], achieved through compromise, can be a valuable driver in selecting a strategy that can avoid the collapse of the two species.

### 3.4. System Behavior as a Result of Decision Preferences.

Exploiting knowledge of the deterministic extinction threshold, we shift focus to reevaluating the candidate harvesting strategies in SOWs, where management tradeoffs exist, and assess their robustness. To do so, we re-evaluate each of the Pareto-approximate solutions presented in Figure 3 in the alternative sampled SOWs and compute their robustness using the domain criterion satisficing measure. This measure includes minimum performance requirements defined by six satisficing criteria for the management problems' objectives and predator population collapse constraint (detailed in Section 2). We then calculate the percentage of SOWs where each solution meets each of the criteria, as well as the percentage of SOWs where each solution meets all criteria. Extinction of the two species is deterministic in some of the SOWs, and thus the domain criterion satisficing measure was only applied in SOWs in which human action (and choice thereof) matters. Figure 7 presents the percentage of SOWs where each of the optimized solutions meets each of the six criteria (placed on a vertical axis). Each line is shaded according to the percentage of SOWs where it meets all specified criteria. As with Figure 3, diagonal, intersecting lines indicate pairwise tradeoffs in the robustness of the equivalent criteria. For example, there appears to be a strong tradeoff between meeting the NPV criterion in many SOWs and meeting the Prey Deficit criterion in many SOWs. Furthermore, solutions most robust in either of those two criteria (top-most lines crossing the vertical axes) fail to meet at least one of the other specified criteria (indicated by their white color).

Two solutions are highlighted in this figure,  $A_{NPV}$  and  $B_{MO}$ , illustrating two different robustness definitions. The  $A_{NPV}$  solution meets criterion 1 ( $NPV \geq 1500$ ) in the most SOWs (leftmost vertical axis in Figure 7). NPV-maximizing criteria (or similar metrics of discounted profits) are very common in the bioeconomics literature (e.g., [34, 84–86]),

typically considered as the only system objective. The  $B_{MO}$  solution meets all of the specified satisficing criteria in the most SOWs, meaning that it exhibits the highest multiobjective robustness (indicated by the line color and color bar on the right of Figure 7). This solution is more in line with newer paradigms in fisheries management, with experts calling for multiobjective perspectives and values [29, 45]. The concept of multiobjective robustness builds on that perspective, by identifying policies that are successful in meeting a specified level of performance in all objectives. The solution most robust in NPV performs poorly in the prey population deficit and the harvest variance criteria. The solution most robust across all criteria achieves robustness by compromising individual robustness for the NPV and low harvest duration criteria, as well as performance in the objective space (see Supplementary Material Figure S2).

With regards to the entire set of optimized solutions and their application in other SOWs, Figure 7 highlights that assumptions on their stability are tenuous even in SOWs where species coexistence and harvesting are possible (i.e., without deterministic extinction). Looking at criterion 2 in particular, the most robust of the solutions in meeting that criterion (topmost line crossing the axis) only does so in fewer than 50% of the considered SOWs without deterministic extinction and, in doing so, it harvests at very low rates and fails to ever meet the other criteria (as indicated by its color). Solution  $A_{NPV}$  (most robust in criterion 1) harvests at very high rates and fails to meet the prey deficit criterion. Finally, solution  $B_{MO}$  (meeting all criteria in the most SOWs) only performs acceptably in fewer than 50% of the sampled SOWs. In other words, out of the original set of optimized solutions, all of which adapting their harvest given a perfect reading of the prey population at each timestep, most fail to meet all the criteria in other SOWs, and the most robust among them only does so in less than half of the sampled SOWs without deterministic extinction. At the same time, when looking at criteria 1 and 2, the equivalent objectives of which are conflicting (maximizing NPV and minimizing prey population deficit), increasing robustness preference for any of the two inevitably reduces robustness in the other.

Linking our observations for this socioecological system to the broader concept of resilience, we draw from its definition as proposed by [87]: “*the capacity of a system to absorb disturbance and reorganize while undergoing change so as to retain essentially the same function, structure, identity, and feedbacks.*” While robustness is a related term, it is defined as the ability of the strategies to maintain an acceptable performance (as measured by some criteria) and it more closely pertains to the decision space of the system, as shaped by the decision-makers' value preferences. As such, the concept can be used to link complex system dynamics, persistence, and transformation to performance measures (albeit in a more narrow sense—that of feedback and control) [88]. With the application of the concept of multiobjective robustness in this paper, the identified strategy is also more resilient across the sampled SOWs.

This is more explicitly demonstrated in Figure 8, where we present the trajectories of the predator-prey system as a



result of the two harvesting strategies in the assumed SOW and two alternative SOWs. We include five trajectories in each of the subplots, aiming to capture imperfect readings of the initial population levels, each starting near the natural (unharvested) equilibrium of the system. Figure 8(a) presents the trajectories of the two populations as they result from the implementation of the two policies in the assumed SOW. Solution  $A_{NPV}$  appears to harvest at significantly higher levels (indicated by the color of each line segment) and reduce the prey population, resulting in a reduction in the predator population as well. Solution  $B_{MO}$  harvests at significantly lower levels and reduces both populations as well, albeit to levels much closer to the natural equilibrium. When applied in a nearby SOW with a global attractor (Figure 8(b)), the harvesting actions behave similarly, shifting the prey isocline, and as a result, the equilibrium moves to lower population levels for the two species (the dynamics of the unharvested system are presented in Figure 1(b)). Figure 8(c) shows the two policies applied in a SOW, where the coexistence equilibrium (trajectory starting point) is not a global attractor. Here, the harvesting can shift the system to a different basin of attraction so as to lead to the collapse of the two populations. This is avoided by the strategy selected for being robust across the multiple objectives ( $B_{MO}$ ).

#### 4. Conclusions

Progressive discoveries in the ecological literature have highlighted the importance of multispecies relationships and trophic connectivity in fisheries management, resulting in a new proposed paradigm, that of ecosystem-based fishery management [29, 45]. Within this new direction, multiple species and objective values need to be taken into account. This simple exploratory experiment was designed with the specific aim of complementing the current fisheries management literature with the inclusion of a multiobjective perspective for the management of a two-species fishery. The formulation of the system in such a manner allows us to demonstrate the potentially catastrophic consequences of deep uncertainty, as manifested in our parameterized mathematical representations of predator-prey systems that are coupled with human actions (harvesting) and human preferences (multiobjective tradeoffs). For this purpose, the isoclines, equilibria, and conditions for stability were analytically derived for the harvested system and used to discover regions of the deeply uncertain parametric space that lead to system instability and fundamentally impact the estimated tradeoffs. The impacts of deep uncertainty on such a system are significant as distinct basins of attraction can be present and also shift with only marginal changes in assumed mathematical parameterizations. Human action, manifested in the form of harvest, can move the populations into basins of attraction where the attractor is a collapsed system.

As a result, harvesting strategies able to navigate the dynamic complexities of such a system need to be identified. We demonstrate that multiobjective robustness can be valuable as a driver for identifying fishery harvest policies

that can navigate deep uncertainties in system parameters and relationships. It is important to note here that the concept of multiobjective robustness is not treated as entirely equivalent to resilience, but rather as an alternative principle by which one can operationalize the identification of such policies in a systematic manner. The principle is applied here with the specific aim of achieving acceptable performance, as measured by explicit criteria, that are defined subjectively and specifically for the system at hand. The broader concept of resilience includes a wider array of aspects and spatial and temporal scales, as well as system boundaries [88], that multiobjective robustness (as applied here) does not claim to consider. Nevertheless, management policies that are not robust fail to meet their decision-relevant criteria and, by extension, lead to a system that is also not resilient. For these reasons, we believe that the findings have broader implications for socioecological management in general, where balancing conflicting economic and ecological objectives is an essential yet complex task that is further impeded by severe uncertainties in determining tipping points and the consequences of crossing them [89].

The system used in the study is specifically formulated at a reduced complexity relative to those found in the mathematical biology literature, where multispecies systems are typical, or in resource economics, where operational costs and more complex financial accounting take place. However, the more complex models in the respective fields are not typically paired with each other and the impacts of deep uncertainty in the ecological system are not manifested through to the decision space, to assess its social implications. The socioecological model employed in this study pairs the two perspectives to demonstrate significant implications for the decision maker even when management is operating in the optimistic context of adaptive, perfectly informed, and perfectly implemented policies. Furthermore, the harvesting policies assume no incidental by-catch nor intentional harvest of the predator, as the aim has been to highlight the implications of deep uncertainty for such a system.

Be that as it may, this simplicity in design bears certain limitations that future work should aim to address. First, the information used by the state-aware control rules is limited to the current levels of the prey fish population. In the interest of avoiding crossing tipping points critical to the recovery and sustainability of a fishery, additional information can be incorporated, for example, predator population levels. This would be particularly valuable for system parameterizations that exhibit multistability (for example, in Figure 1(f)), where remaining with the basin of attraction of the preferred equilibrium is a vital concern. In a real application, this would likely be accompanied by additional costs borne by sensing and measurements. Secondly, the control rules mapping system state to action could take different forms to more realistically represent the harvesting actions performed by fisheries, for example, to avoid significantly shifting the prescribed harvest between sequential time steps, or accidentally harvesting other species (by-catch). Lastly, the study assumes a perfect reading of the prey population at each time step as well as a perfect execution of



the prescribed harvesting effort. These are common assumptions in the literature [52, 79, 80], but result in highly optimistic quantifications of the tradeoffs and should be addressed in future applications. Inclusion of a learning procedure about system parameters and dynamics, in the form of a probabilistic approach with sequentially updated estimates [90, 91], would also be a valuable next step.

## Data Availability

The predator-prey harvesting optimization code, re-evaluation code, robustness analysis, and identified solutions are available on Github at [https://github.com/antonia-had/Generalized\\_fish\\_game](https://github.com/antonia-had/Generalized_fish_game). The optimization and Pareto-sorting can be replicated using the software code available for the Borg MOEA (<http://borgmoea.org/>), `pareto.py` (<https://github.com/matthewjwoodruff/pareto.py>), and the MOEA framework (<http://moeaframework.org/>).

## Disclosure

Any opinions, findings, and conclusions or recommendations expressed in this material are those of the authors and do not necessarily reflect the views of the funding entities.

## Conflicts of Interest

The authors declare no conflicts of interest.

## Acknowledgments

This study was partially supported by the National Science Foundation (NSF) through the Network for Sustainable Climate Risk Management (SCRiM) under NSF cooperative agreement GEO-1240507 and the Penn State Center for Climate Risk Management.

## Supplementary Materials

S1 Appendix: derivation of condition (3). S2 Appendix: derivation of the prey isocline. S1 Figure: bifurcation diagrams for systems presented in Figure 1, with regard to predator interference parameter  $m$ . S2 Figure: population trajectories for prey and predator populations under all sampled SOWs. S3 Figure: parallel axis plot of the objective values achieved by each optimized solution in the assumed SOW. (*Supplementary Materials*)

## References

- [1] C. Mullon, P. Freon, and P. Cury, "The dynamics of collapse in world fisheries," *Fish and Fisheries*, vol. 6, no. 2, pp. 111–120, 2005.
- [2] W. H. Lear and L. S. Parsons, "History and management of the fishery for northern cod in NAFO Divisions 2J, 3K and 3L," in *Perspectives on Canadian Marine Fisheries Management*, W. H. Lear and L. S. Parsons, Eds., vol. 226, pp. 55–90, Canadian Bulletin of Fisheries and Aquatic Sciences, Ottawa, Canada, 1993.
- [3] J. A. Hutchings and R. A. Myers, "What can be learned from the collapse of a renewable resource? Atlantic Cod, *Gadus morhua*, of newfoundland and labrador," *Canadian Journal of Fisheries and Aquatic Sciences*, vol. 51, no. 9, pp. 2126–2146, 1994.
- [4] C. Möllmann and R. Diekmann, "Chapter 4—marine ecosystem regime shifts induced by climate and overfishing: a review for the northern hemisphere," in *Advances in Ecological Research (Global Change in Multispecies Systems Part 2)*, G. Woodward, U. Jacob, and E. J. O’Gorman, Eds., vol. 47, pp. 303–347, Academic Press, Cambridge, MA, USA, 2012.
- [5] K. Ludynia, J.-P. Roux, R. Jones, J. Kemper, and L. G. Underhill, "Surviving off junk: low-energy prey dominates the diet of African penguins *Spheniscus demersus* at Mercury island, Namibia, between 1996 and 2009," *African Journal of Marine Science*, vol. 32, no. 3, pp. 563–572, 2010.
- [6] J. F. Craig, *Freshwater Fisheries Ecology*, John Wiley & Sons, Chichester, UK, 2015.
- [7] J. Travis, F. C. Coleman, P. J. Auster et al., "Integrating the invisible fabric of nature into fisheries management," *Proceedings of the National Academy of Sciences*, vol. 111, no. 2, pp. 581–584, 2014.
- [8] M. L. Pinsky and D. Byler, "Fishing, fast growth and climate variability increase the risk of collapse," *Proceedings of the Royal Society B: Biological Sciences*, vol. 282, no. 1813, Article ID 20151053, 2015.
- [9] R. J. Lempert and M. T. Collins, "Managing the risk of uncertain threshold responses: comparison of robust, optimum, and precautionary approaches," *Risk Analysis*, vol. 27, no. 4, pp. 1009–1026, 2007.
- [10] F. H. Knight, *Risk, Uncertainty and Profit*, Courier Dover Publications, Mineola, NY, USA, 1921.
- [11] M. P. Hassell and G. C. Varley, "New inductive population model for insect parasites and its bearing on biological control," *Nature*, vol. 223, no. 5211, pp. 1133–1137, 1969.
- [12] J. R. Beddington, "Mutual interference between parasites or predators and its effect on searching efficiency," *The Journal of Animal Ecology*, vol. 44, no. 1, pp. 331–340, 1975.
- [13] Y. Kuang and E. Beretta, "Global qualitative analysis of a ratio-dependent predator-prey system," *Journal of Mathematical Biology*, vol. 36, no. 4, pp. 389–406, 1998.
- [14] R. Arditi and L. R. Ginzburg, "Coupling in predator-prey dynamics: ratio-Dependence," *Journal of Theoretical Biology*, vol. 139, no. 3, pp. 311–326, 1989.
- [15] G. D. Ruxton and W. S. C. Gurney, "The interpretation of tests for ratio-dependence," *Oikos*, vol. 65, no. 2, pp. 334–335, 1992.
- [16] P. A. Abrams, "The fallacies of "ratio-dependent" predation," *Ecology*, vol. 75, no. 6, pp. 1842–1850, 1994.
- [17] O. Sarnelle, "Inferring process from pattern: trophic level abundances and imbedded interactions," *Ecology*, vol. 75, no. 6, pp. 1835–1841, 1994.
- [18] H. R. Akçakaya, R. Arditi, and L. R. Ginzburg, "Ratio-dependent predation: an abstraction that works," *Ecology*, vol. 76, no. 3, pp. 995–1004, 1995.
- [19] P. A. Abrams and L. R. Ginzburg, "The nature of predation: prey dependent, ratio dependent or neither?" *Trends in Ecology & Evolution*, vol. 15, no. 8, pp. 337–341, 2000.
- [20] R. Arditi and H. R. Akçakaya, "Underestimation of mutual interference of predators," *Oecologia*, vol. 83, no. 3, pp. 358–361, 1990.
- [21] S. R. Carpenter, K. L. Cottingham, and C. A. Stow, "Fitting predator-prey models to time series with observation errors," *Ecology*, vol. 75, no. 5, pp. 1254–1264, 1994.
- [22] C. Jost and R. Arditi, "Identifying predator-prey processes from time-series," *Theoretical Population Biology*, vol. 57, no. 4, pp. 325–337, 2000.

- [23] J. L. Sabo, "Stochasticity, predator-prey dynamics, and trigger harvest of nonnative predators," *Ecology*, vol. 86, no. 9, pp. 2329–2343, 2005.
- [24] R. Arditi, J.-M. Callois, Y. Tyutyunov, and C. Jost, "Does mutual interference always stabilize predator-prey dynamics? A comparison of models," *Comptes Rendus Biologies*, vol. 327, no. 11, pp. 1037–1057, 2004.
- [25] Y.-M. Bozec, S. O'Farrell, J. H. Bruggemann, B. E. Luckhurst, and P. J. Mumby, "Tradeoffs between fisheries harvest and the resilience of coral reefs," *Proceedings of the National Academy of Sciences*, vol. 113, no. 16, pp. 4536–4541, 2016.
- [26] J. A. Estes, J. Terborgh, J. S. Brashares et al., "Trophic downgrading of planet earth," *Science*, vol. 333, no. 6040, pp. 301–306, 2011.
- [27] D. B. Stouffer, "All ecological models are wrong, but some are useful," *Journal of Animal Ecology*, vol. 88, no. 2, pp. 192–195, 2019.
- [28] S. Murawski, "Definitions of overfishing from an ecosystem perspective," *ICES Journal of Marine Science*, vol. 57, no. 3, pp. 649–658, 2000.
- [29] E. K. Pikitch, C. Santora, E. A. Babcock et al., "ECOLOGY: ecosystem-based fishery management," *Science*, vol. 305, no. 5682, pp. 346–347, 2004.
- [30] W. J. Sutherland, R. P. Freckleton, H. C. J. Godfray et al., "Identification of 100 fundamental ecological questions," *Journal of Ecology*, vol. 101, no. 1, pp. 58–67, 2013.
- [31] J. D. Quinn, P. M. Reed, and K. Keller, "Direct policy search for robust multi-objective management of deeply uncertain socio-ecological tipping points," *Environmental Modelling & Software*, vol. 92, pp. 125–141, 2017.
- [32] R. Singh, P. M. Reed, and K. Keller, "Many-objective robust decision making for managing an ecosystem with a deeply uncertain threshold response," *Ecology and Society*, vol. 20, no. 3, pp. 1–32, 2015.
- [33] D. Hadka, J. Herman, P. Reed, and K. Keller, "An open source framework for many-objective robust decision making," *Environmental Modelling & Software*, vol. 74, pp. 114–129, 2015.
- [34] J. E. Wilen, "Renewable resource economists and policy: what differences have we made?" *Journal of Environmental Economics and Management*, vol. 39, no. 3, pp. 306–327, 2000.
- [35] M. B. Schaefer, "Some considerations of population dynamics and economics in relation to the management of the commercial marine fisheries," *Journal of the Fisheries Research Board of Canada*, vol. 14, no. 5, pp. 669–681, 1957.
- [36] R. J. H. Beverton and S. J. Holt, "On the dynamics of exploited fish populations," *Fisheries Investigations Series*, Vol. 19, Ministry of Agriculture, FAO, Rome, Italy, 1957.
- [37] A. Scott, *Natural Resources: The Economics of Conservation*, University of Toronto Press, Toronto, Canada, 1955.
- [38] H. S. Gordon, "The economic theory of a common-property resource: the fishery," *Journal of Political Economy*, vol. 62, no. 2, pp. 124–142, 1954.
- [39] L. S. Pontryagin, V. S. Boltyanskii, R. V. Gamkrelidze, and E. F. Mishchenko, *Mathematical Theory of Optimal Processes*, Wiley-Interscience, Hoboken, NJ, USA, 1962.
- [40] R. Dorfman, "An economic interpretation of optimal control theory," *The American Economic Review*, vol. 59, no. 5, pp. 817–831, 1969.
- [41] H. Matsuda and P. A. Abrams, "Maximal yields from multispecies fisheries systems: rules for systems with multiple trophic levels," *Ecological Applications*, vol. 16, no. 1, pp. 225–237, 2006.
- [42] J. Morishita, "What is the ecosystem approach for fisheries management?" *Marine Policy*, vol. 32, no. 1, pp. 19–26, 2008.
- [43] A. Hollowed, N. Bax, R. Beamish et al., "Are multispecies models an improvement on single-species models for measuring fishing impacts on marine ecosystems?" *ICES Journal of Marine Science*, vol. 57, no. 3, pp. 707–719, 2000.
- [44] C. J. Walters, V. Christensen, S. J. Martell, and J. F. Kitchell, "Possible ecosystem impacts of applying MSY policies from single-species assessment," *ICES Journal of Marine Science*, vol. 62, no. 3, pp. 558–568, 2005.
- [45] S. M. Garcia, A. Zerbi, C. Aliaume, T. Do Chi, and G. Lasserre, "The ecosystem approach to fisheries: issues, terminology, principles, institutional foundations, implementation and outlook," Food & Agriculture Organization (FAO), Rome, Italy, No. 443 in FAO Fisheries Technical Paper, 2003.
- [46] J. Hoekstra and J. C. J. M. van den Bergh, "Harvesting and conservation in a predator-prey system," *Journal of Economic Dynamics and Control*, vol. 29, no. 6, pp. 1097–1120, 2005.
- [47] J. B. Kellner, J. N. Sanchirico, A. Hastings, and P. J. Mumby, "Optimizing for multiple species and multiple values: tradeoffs inherent in ecosystem-based fisheries management," *Conservation Letters*, vol. 4, no. 1, pp. 21–30, 2011.
- [48] R. J. Johnston, T. A. Grigalunas, J. J. Opaluch, M. Mazzotta, and J. Diamantedes, "Valuing estuarine resource services using economic and ecological models: the peconic estuary system study," *Coastal Management*, vol. 30, no. 1, pp. 47–65, 2002.
- [49] J. P. Hoehn and A. Randall, "Too many proposals pass the benefit cost test," *The American Economic Review*, vol. 79, no. 3, pp. 544–551, 1989.
- [50] D. Holland, J. Sanchirico, R. Johnston et al., *Economic Analysis for Ecosystem-Based Management: Applications to Marine and Coastal Environments*, Routledge, Abingdon, UK, 2012, <https://www.taylorfrancis.com/books/9781936331246>.
- [51] J. N. Sanchirico, D. K. Lew, A. C. Haynie, D. M. Kling, and D. F. Layton, "Conservation values in marine ecosystem-based management," *Marine Policy*, vol. 38, pp. 523–530, 2013.
- [52] E. Tromeur and N. Loeuille, "Balancing yield with resilience and conservation objectives in harvested predator-prey communities," *Oikos*, vol. 126, no. 12, pp. 1780–1789, 2017.
- [53] P. S. Leung, "Multiple-criteria decision-making (MCDM) applications in fishery management," *International Journal of Environmental Technology and Management*, vol. 6, no. 1–2, pp. 96–110, 2006.
- [54] M. Zeleny, "Cognitive equilibrium: a new paradigm of decision making?" *Human Systems Management*, vol. 8, no. 3, pp. 185–188, 1989.
- [55] R. Lahdelma, J. P. Salminen, and Hokkanen, "Using multi-criteria methods in environmental planning and management," *Environmental Management*, vol. 26, no. 6, pp. 595–605, 2000.
- [56] M. Franssen, "Arrow's theorem, multi-criteria decision problems and multi-attribute preferences in engineering design," *Research in Engineering Design*, vol. 16, no. 1–2, pp. 42–56, 2005.
- [57] C. Coello Coello, G. B. Lamont, and D. A. Van Veldhuizen, *Evolutionary Algorithms for Solving Multi-Objective Problems*, Springer US, New York, USA, 2007.
- [58] S. J. Mardle, S. Pascoe, and M. Tamiz, "An investigation of genetic algorithms for the optimization of multi-objective fisheries bioeconomic models," *International Transactions in Operational Research*, vol. 7, no. 1, pp. 33–49, 2000.

- [59] Z. Michalewicz and G. Nazhiyath, "Genocop III: a co-evolutionary algorithm for numerical optimization problems with nonlinear constraints," in *Proceedings of 1995 IEEE International Conference on Evolutionary Computation*, vol. 2, pp. 647–651, Pittsburgh, PA, USA, July 1995.
- [60] M. T. Rosenstein and A. G. Barto, "Robot weightlifting by direct policy search," in *Proceedings of the 17th International Joint Conference on Artificial Intelligence (IJCAI'01)*, vol. 2, pp. 839–846, Seattle, WA, USA, August 2001.
- [61] L. Eeckhoudt, C. Gollier, and H. Schlesinger, *Economic and Financial Decisions under Risk*, Princeton University Press, Princeton, NJ, USA, 2005.
- [62] S. A. Sethi, T. A. Branch, and R. Watson, "Global fishery development patterns are driven by profit but not trophic level," *Proceedings of the National Academy of Sciences*, vol. 107, no. 27, pp. 12163–12167, 2010.
- [63] M. Giuliani, A. Castelletti, F. Pianosi, E. Mason, and P. Reed, "Curses, tradeoffs, and scalable management: advancing evolutionary multiobjective direct policy search to improve water reservoir operations," *Journal of Water Resources Planning and Management*, vol. 142, no. 2, Article ID 04015050, 2016.
- [64] P. M. Reed, D. Hadka, J. D. Herman, J. R. Kasprzyk, and J. B. Kollat, "Evolutionary multiobjective optimization in water resources: the past, present, and future," *Advances in Water Resources*, vol. 51, pp. 438–456, 2013.
- [65] D. Hadka and P. Reed, "Borg: an auto-adaptive many-objective evolutionary computing framework," *Evolutionary Computation*, vol. 21, no. 2, pp. 231–259, 2013.
- [66] J. B. Kollat and P. M. Reed, "A computational scaling analysis of multiobjective evolutionary algorithms in long-term groundwater monitoring applications," *Advances in Water Resources*, vol. 30, no. 3, pp. 408–419, 2007.
- [67] J. D. Herman, P. M. Reed, H. B. Zeff, and G. W. Characklis, "How should robustness be defined for water systems planning under change?" *Journal of Water Resources Planning and Management*, vol. 141, no. 10, Article ID 04015012, 2015.
- [68] M. Giuliani and A. Castelletti, "Is robustness really robust? How different definitions of robustness impact decision-making under climate change," *Climatic Change*, vol. 135, no. 3–4, pp. 409–424, 2016.
- [69] C. McPhail, H. R. Maier, J. H. Kwakkel, M. Giuliani, A. Castelletti, and S. Westra, "Robustness metrics: how are they calculated, when should they be used and why do they give different results?" *Earth's Future*, vol. 6, no. 2, pp. 169–191, 2018.
- [70] M. K. Starr, *Product Design and Decision Theory: Prentice-Hall Series in Engineering Design*, Prentice-Hall, Englewood Cliffs, NJ, USA, 1962.
- [71] S. Bankes, "Exploratory modeling for policy analysis," *Operations Research*, vol. 41, no. 3, pp. 435–449, 1993.
- [72] B. P. Bryant and R. J. Lempert, "Thinking inside the box: a participatory, computer-assisted approach to scenario discovery," *Technological Forecasting and Social Change*, vol. 77, no. 1, pp. 34–49, 2010.
- [73] D. G. Groves and R. J. Lempert, "A new analytic method for finding policy-relevant scenarios," *Global Environmental Change*, vol. 17, no. 1, pp. 73–85, 2007.
- [74] B. Worm, R. Hilborn, J. K. Baum et al., "Rebuilding global fisheries," *Science*, vol. 325, no. 5940, pp. 578–585, 2009.
- [75] M. L. Pinsky, O. P. Jensen, D. Ricard, and S. R. Palumbi, "Unexpected patterns of fisheries collapse in the world's oceans," *Proceedings of the National Academy of Sciences*, vol. 108, no. 20, pp. 8317–8322, 2011.
- [76] J. R. Kasprzyk, S. Nataraj, P. M. Reed, and R. J. Lempert, "Many objective robust decision making for complex environmental systems undergoing change," *Environmental Modelling & Software*, vol. 42, pp. 55–71, 2013.
- [77] D. W. Watkins and D. C. McKinney, "Finding robust solutions to water resources problems," *Journal of Water Resources Planning and Management*, vol. 123, no. 1, pp. 49–58, 1997.
- [78] J. D. Quinn, P. M. Reed, M. Giuliani, and A. Castelletti, "Rival framings: a framework for discovering how problem formulation uncertainties shape risk management trade-offs in water resources systems," *Water Resources Research*, vol. 53, no. 8, pp. 7208–7233, 2017.
- [79] M. R. Kelly, Y. Xing, and S. Lenhart, "Optimal fish harvesting for a population modeled by a nonlinear parabolic partial differential equation," *Natural Resource Modeling*, vol. 29, no. 1, pp. 36–70, 2015.
- [80] A. O. Shelton, J. F. Samhoury, A. C. Stier, and P. S. Levin, "Assessing trade-offs to inform ecosystem-based fisheries management of forage fish," *Scientific Reports*, vol. 4, no. 1, p. 7110, 2014.
- [81] C. Jost, O. Arino, and R. Arditi, "About deterministic extinction in ratio-dependent predator-prey models," *Bulletin of Mathematical Biology*, vol. 61, no. 1, pp. 19–32, 1999.
- [82] B. Rieman, D. Lee, J. McIntyre, K. Overton, and R. Thurow, *Consideration of Extinction Risks for Salmonids: Fish Habitat Relationships Technical Bulletin 14 Boise, ID*, US Department of Agriculture, Forest Service, Intermountain Research Station, Washington, DC, USA, 1993.
- [83] K. Deb and H. Gupta, "Introducing robustness in multi-objective optimization," *Evolutionary Computation*, vol. 14, no. 4, pp. 463–494, 2006.
- [84] J. J. Deroba and J. R. Bence, "A review of harvest policies: understanding relative performance of control rules," *Fisheries Research*, vol. 94, no. 3, pp. 210–223, 2008.
- [85] F. K. Diekert, D. Ø. Hjermmann, E. Nævdal, and N. C. Stenseth, "Spare the young fish: optimal harvesting policies for north-east arctic cod," *Environmental and Resource Economics*, vol. 47, no. 4, pp. 455–475, 2010.
- [86] T. Kumar Kar, "Modelling and analysis of a harvested prey-predator system incorporating a prey refuge," *Journal of Computational and Applied Mathematics*, vol. 185, no. 1, pp. 19–33, 2006.
- [87] C. Folke, S. Carpenter, B. Walker et al., "Regime shifts, resilience, and biodiversity in ecosystem management," *Annual Review of Ecology, Evolution, and Systematics*, vol. 35, no. 1, pp. 557–581, 2004.
- [88] J. Anderies, C. Folke, B. Walker, and E. Ostrom, "Aligning key concepts for global change policy: robustness, resilience, and sustainability," *Ecology and Society*, vol. 18, no. 2, p. 8, 2013.
- [89] T. M. Lenton, "Environmental tipping points," *Annual Review of Environment and Resources*, vol. 38, no. 1, pp. 1–29, 2013.
- [90] R. M. Dorazio and F. A. Johnson, "Bayesian inference and decision theory—a framework for decision making in natural resource management," *Ecological Applications*, vol. 13, no. 2, pp. 556–563, 2003.
- [91] R. Singh, J. D. Quinn, P. M. Reed, and K. Keller, "Skill (or lack thereof) of data-model fusion techniques to provide an early warning signal for an approaching tipping point," *PLoS One*, vol. 13, no. 2, Article ID e0191768, 2018.

## Research Article

# Mixed-Mode Oscillation in a Class of Delayed Feedback System and Multistability Dynamic Response

**Youhua Qian**  and **Wenjing Meng**

*College of Mathematics and Computer Science, Zhejiang Normal University, Jinhua, Zhejiang 321004, China*

Correspondence should be addressed to Youhua Qian; [qyh2004@zjnu.cn](mailto:qyh2004@zjnu.cn)

Received 8 November 2019; Accepted 6 January 2020; Published 6 February 2020

Guest Editor: Viet-Thanh Pham

Copyright © 2020 Youhua Qian and Wenjing Meng. This is an open access article distributed under the Creative Commons Attribution License, which permits unrestricted use, distribution, and reproduction in any medium, provided the original work is properly cited.

In this paper, a class of two-parameter mixed-mode oscillation with time delay under the action of amplitude modulation is studied. The investigation is from four aspects. Firstly, a parametric equation is considered as a slow variable. By the time-history diagram and phase diagram, we can find that the system generates a cluster discovery image. Secondly, the Euler method is used to discretize the system and obtain the discrete equation. Thirdly, the dynamic characteristics of the system at different time scales are discussed when the ratio of the natural frequency and the excitation frequency of the system is integer and noninteger. Fourthly, we discuss the influence of time delay on the discovery of clusters of this kind of system. The research shows that the time lag does not interfere with the influence of the cluster image, but the dynamics of the upper and lower parts of the oscillation in each period will be delayed. So, we can improve peak performance by adjusting the time lag and obtain the desired peak. Finally, we explore the multistate dynamic response of a two-dimensional nonautonomous Duffing system with higher order. According to bifurcation diagram and time-history curve, bistable state will appear in the system within the critical range. With the gradual increase of parameters, the chaotic attractor will suddenly disappear which will lead to the destruction of the bistable state.

## 1. Introduction

In recent years, with the rapid development of science and technology, the nonlinear problems of the actual power systems in various fields have become more and more prominent. In the national economy, national defense industry, and engineering technology, a large number of practical problems urgently need to be processed by nonlinear dynamics theory and methods, which will promote the development of nonlinear dynamics into a more comprehensive and in-depth development period.

The researcher can conduct a comprehensive analysis and discussion from two important aspects of amplitude and frequency. For example, when we focus on low-frequency forces, i.e., the external excitation frequency is much smaller than the natural frequency of the original system, and the oscillator can exhibit a typical fast-slow dynamic called mixed-mode oscillation (MMO). Sadhu [1] researched the

canards and mixed-mode oscillations in a singularly perturbed two predators-one prey model. Upadhyay et al. [2] studied mixed-mode oscillations and the synchronous activity in the noise-induced modified Morris-Lecar neural system. Kingston and Thamilmaran [3] discussed the bursting oscillations and mixed-mode oscillations in the driven Lienard system. Shimizu et al. [4] made a thorough exploration of mixed-mode oscillations and chaos from a simple second-order oscillator under weak periodic perturbation. The oscillating behavior appeared in the above four articles is generally expressed as a periodic state characterized by a combination of a relatively large amplitude (spike state) close to the harmonics and a small-amplitude oscillation (stationary state). Due to its complexity and diversity, the system with delayed feedback has a wide range of practical backgrounds which are always an inevitable hysteresis when studying the laws of the motion of the objective. Therefore, it has important theoretical significance and practical value in the research of delayed

feedback system. Inaba et al. [5] studied the feedback control problem of network systems with discrete delay and distributed delay. Thus, unlimited distributed delays were first introduced in discrete network domains. Weicker et al. [6] focused on the rapid transition layers among the plateaus and demonstrated their contribution to the total cycle. Porte et al. [7] experimentally characterized the mechanism of strong chaos in semiconductor lasers with delayed feedback. Sun et al. [8] proposed a method for time delay identification in a multidegree-of-freedom (MDOF) linear system with multiple feedbacks. Dmitrishin et al. [9] studied the robust stability problem of the linear delayed feedback control (DFC) mechanism.

As one of the research directions of nonlinear dynamics, the multitime scale plays the nonlinear essential characteristics in the perspective of dynamics. Its theoretical method has been widely applied to neuroscience, chemistry, physics, bioscience, and other fields. Therefore, nonlinear systems with multiple time scales have attracted attention of many scholars at home and abroad. The effects of slow variables on the rupture of pancreatic cells were investigated [10] on the basis of the Chay–Keizer model with three time scales. Izumiet al. [11] discussed the relationship between fast scale bifurcation and slow scale bifurcation in the discontinuous circuit. Yu et al. [12] studied the delayed feedback control problem of bursting synchronization in the small-world neural network presented by the neural network in some areas of the cerebral cortex. Yu et al. [13] studied the generation of complex cluster patterns in the Duffing oscillator with delayed feedback and proposed the symmetric fold-fold and symmetric Hopf-Hopf bursting patterns. Cornforth and Lipson [14] introduced the fast and slow analysis method and applied it to the study of multitime scale problems in nonlinear systems. Han et al. [15] proposed a general method for analyzing the mixed-mode vibration of a system with two excitation frequencies. The validity of this method was verified by the Duffing and van der Pol equations. Yang et al. [16] discussed the influence of delay coupling on bursting synchronous differential feedback control in the modularized neural network. Meng et al. [17] presented and analyzed two different types of bursting in a two-compartment neuron model with the current feedback control due to totally different generation mechanisms. Li et al. [18] investigated the Brusselator with different time scales, which behave in the classical slow-fast effect. Zhou et al. [19] established a 3D discrete system featuring a new series of complex fast-slow behaviors caused by different bursters. Ding and Li [20] studied the Rulkov model with self-inhibiting synapses and time delays and compared them with the Rulkov model without self-inhibiting synapses. Fan and Wang [21] studied the effects of different time delays and coupling intensities on the synchronization and cluster transition of Hindmarsh–Rose neuron system. Bertram and Rubin [22] described the fast-slow analysis technique and applied it to relaxation oscillations, neuronal bursting oscillations, canard oscillations, and mixed-mode oscillations. Han et al. [23] studied the dynamics of the bursting by Duffing

system with multifrequency excitation. Qian and Yan [24] studied a two-degree-of-freedom nonlinear-coupled Duffing system with an external excitation and two external excitations by the fast-slow analysis method. Han et al. [25] proposed two new bursting modes, fork-shaped delay, and multifrequency excitation of the Duffing system. Different patterns of electrical bursting were proposed, and the types and generation mechanisms of these bursting oscillations were analyzed by using fast-slow dynamics. For instance, Shen et al. [26] introduced the fast and slow analysis method and applied it to the study of multitime scale problems in nonlinear systems. Yu et al. [27] studied the generation of some new cluster modes in multidelay-controlled oscillators. The bifurcation condition of the fast subsystem and its stability related to time delay were calculated. Zhang et al. [28] analyzed the effects of time scales on the dynamic behavior of the system. McKenna and Bertram [29] explained the mechanism behind the oscillation in cells by using the fast-slow analysis method. Han et al. [30] proposed an approximate frequency-truncation fast-slow analysis method to analyze the dynamics of a fast-slow system with two incommensurate excitation frequencies. Yu and Wang [31] analyzed the dynamics involving different waves in a double-well potential oscillator coupling amplitude modulation control of low frequency. Zhou et al. [32] investigated the bursting in Spratt B system with a single excitation and showed that Hopf bifurcation delay may exhibit due to the effect of slow passage through the supercritical Hopf bifurcation. Wang et al. [33] dealt with transitions through Melnikov thresholds and the corresponding fast-slow dynamics in a family of biparametric mechanical oscillators.

From nature to humanity society, the phenomenon of time delay is everywhere. In natural and social phenomena, the changes and development of many systems are not only related to the current state of the system but also depend on some past state of the system. In other words, time delay is inevitable in the system. Plaut and Hsich [34] discussed parametric excitation systems with time delay, through numerical simulation, and they found that the system had very complicated dynamics. Then, through the method of multiple scales, they studied the weak nonlinear time-delay system which is only in damping and discussed the main resonance, the harmonic resonance, superharmonic resonance, and time-delayed effect on the steady-state motion frequency amplitude curve. Raghothama and Narayanan [35] used the incremental harmonic equilibrium (IHB) method to analyze the dynamic response of systems with quadratic and cubic nonlinear time-delay parameters, studied the stability of the periodic solution of the system by Floquet theory, and obtained the bifurcation diagram of the system by combining the stability analysis with the path-following algorithm with arc-length parametric continuation. Maccari [36] studied dynamic response with a time-delay state feedback of van der Pol by using the asymptotic perturbation (asymptotic perturbation) method to get the system amplitude and frequency equation of two groups of slowly varying. Ji and Leung [37] considered a parametric



excitation of Duffing time-delay feedback problems through the multiscale method to study the main parameters of the resonance system and analyzed the stability of the steady-state solution. It is found that saddle bifurcation and subcritical fork bifurcation exist in the system equilibrium point.

It is also an important part in the field of nonlinear dynamics to study the multistability problem of systems. Multistability means that a system is neither stable nor completely unstable but switches between two or more mutually exclusive states over time. Multistable systems are also susceptible to noise, initial conditions, or system parameters. The methods of solving the problem include the analytical method, numerical analysis method, and experimental method. In the fields of chemistry, electricity, ecology, neuroscience and so on, the characteristic of the multistable state has been widely applied and has produced the vital influence to the research and development of these disciplines. Therefore, the system containing the multistable state has been paid attention by many scholars at home and abroad. Loukaides et al. [38] verified that the multistable structure could be produced by single additive manufacturing operation through analyzing examples, numerical simulation, and physical prototype of selective laser sintering production of titanium alloy. Yang and Ma [39] systematically studied the mechanical responses of two new two-dimensional (2D) mechanical metamaterials and realized phase transition/shape reconstruction and zero Poisson's ratio on the basis of the multistable mechanism, achieving great morphological changes. Huang and Xü [40] obtained the mathematical model by introducing time-delay feedback to a plane autonomous nonlinear system, and the results showed that time delay can not only make the system Hopf bifurcation and produce periodic vibration but also make the system appear multistable periodic motion or periodic attractor. Schmitz et al. [41] discussed an example of the application of the multistable state to chemistry, showing that the phenomenon of the multistable state is usually described by discussing the steady-state solution of a nonlinear process, which is given by an abstract mathematical model of single variable  $x$  and evolves according to the differential equation. Lai et al. [42] studied the dynamic behaviors such as multistability and bifurcation of a class of neural network systems with time delay. The results show that the system has 16 kinds of stable states and its own attractive region. Huang et al. [43] discussed the phenomenon of multistable synchronization in the synchronous region of the Kuramoto phase oscillator on a one-dimensional closed loop under the action of asymmetric coupling and further theoretically analyzed its steady-state law and steady-state stability.

Here, we describe analytical and numerical studies of a class of two-parameter mechanical systems with delayed feedback:

$$\ddot{x} + \dot{x} - \alpha\dot{x} - ax(t - \tau) + bx^3 = (f_1 + f_2 \cos(\omega_1 t))\cos(\omega_2 t), \quad (1)$$

where  $a$  is the linear restoring parameter and  $\alpha > 0$  is the nonlinear damping coefficient.  $f_1 > 0$  is the unmodulated amplitude,  $f_2$  is the degree of forcing modulation,  $\omega_1$  is the modulation frequency, and  $\omega_2$  is the forcing frequency.

First of all, we analyze the case for  $f_2 = 0$ . By the singular perturbation methods, equation (1) can be given by

$$\ddot{x} + \dot{x} - \alpha\dot{x} - ax(t - \tau) + bx^3 = f_1 \cos(\omega_2 t). \quad (2)$$

Let  $\gamma = f_1 \cos \omega_2 t$ , and use the Euler method obtained the following discrete systems:

$$\begin{aligned} x_{n+1} &= k_n, \\ k_{n+1} &= a_1 x_n + c_1 k_n - b_1 (x_n)^3 - d_1 x_n - e_1 k_n + \gamma, \end{aligned} \quad (3)$$

where  $a_1 = (\Delta t)^2 + \tau \Delta t$ ,  $b_1 = b(\Delta t)^6$ ,  $c_1 = 2 + \alpha \Delta t$ ,  $d_1 = 1 + \alpha(\Delta t)^2$ , and  $e_1 = \tau \Delta t$ . Set  $a = b = 1$ ,  $\alpha = 1$ ,  $\omega_2 = 0.01$ , and  $f_1 = 1$ . Figure 1 shows the time-history curve and phase portraits of the system when  $\tau = 0.3$ . As shown in the figure, we can found that the trajectory of system (2) undergoes symmetrical folding bifurcation, and it is a typical fast and slow oscillation system.

From the previous developments, this paper focuses on a class of two-parameter mixed-mode vibrations with time delay under the action of amplitude modulation. The structure of this paper is as follows. In Section 2, the bifurcation of the undisturbed model will be investigated. In Section 3, we will discuss the oscillating dynamics when the natural frequency is equal to the excitation frequency. In Section 4, we will study the mixed-mode oscillation dynamics reflected by the system when the natural frequency and the resonant frequency are not equal. In Section 5, the influence of the time delay is discussed. In Section 6, we explore the multistate dynamic response of a two-dimensional nonautonomous Duffing system with higher order. In Section 7, further conclusions are presented.

## 2. Representation and Local Bifurcation of the Unperturbed Model

We consider the left side of equation (1). When  $\tau = 0.3$ , the unperturbed form

$$\begin{aligned} \dot{x} &= y, \\ \dot{y} &= \alpha y + ax(t - \tau) - bx^3 - y^3. \end{aligned} \quad (4)$$

Using Taylor's expansion, we have  $x(t - \tau) \approx x(t) - \tau x'(t)$ ,

$$\begin{aligned} \dot{x} &= y, \\ \dot{y} &= \alpha y + ax - a\tau y - bx^3 - y^3. \end{aligned} \quad (5)$$

By calculation, the system has three equilibrium points:  $E_{\pm} (\pm \sqrt{a/b}, 0)$  and  $E_0 = (0, 0)$ . With  $\alpha > 0$  and  $a > 0$ , from the stability analysis, we know,  $E_{\pm}$  are unstable and  $E_0$  is a saddle point. In order to improve the bifurcation analysis of system (5), we employ the Melnikov method. Using the following transformations,



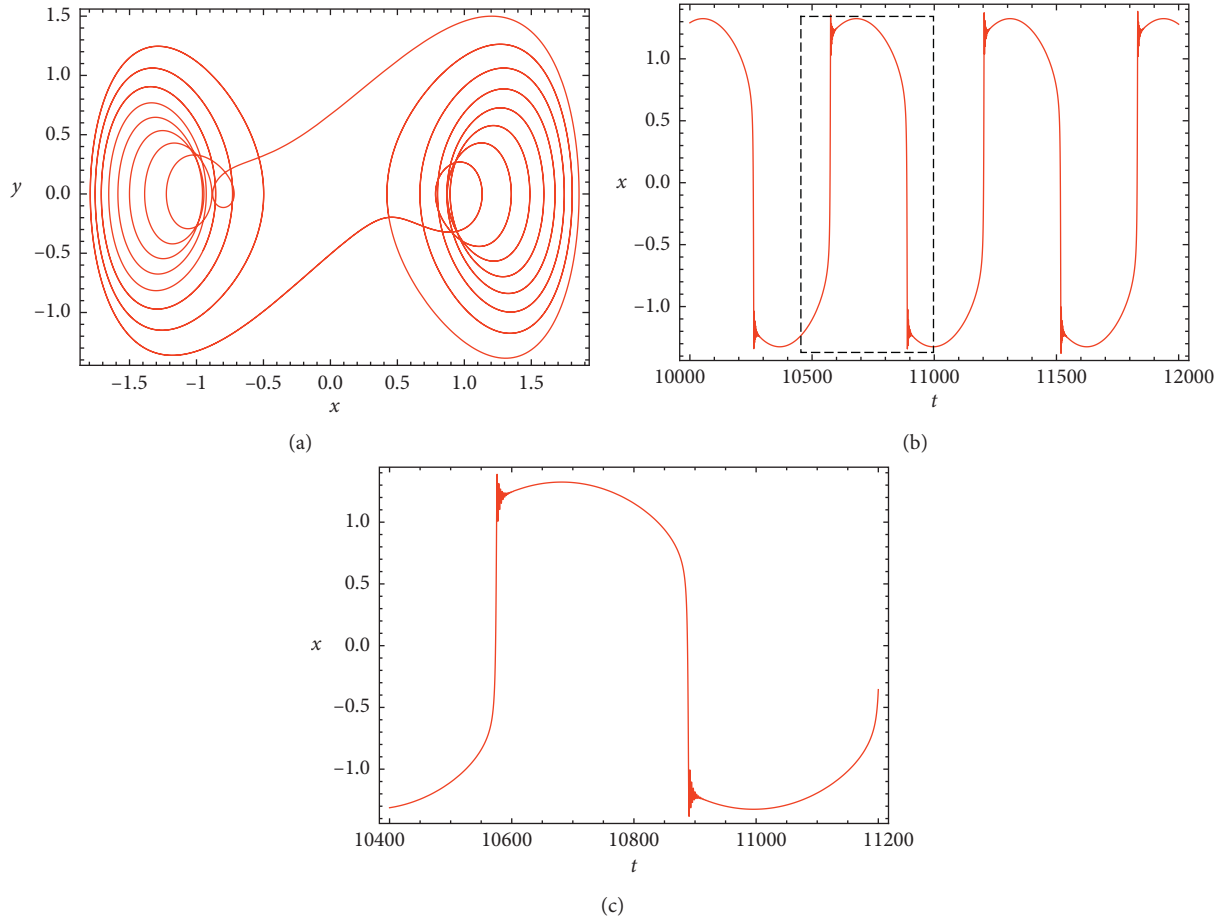


FIGURE 1: Phase portraits (a) and time series (b, c) of fast-slow system (2) for  $a = b = \alpha = 1$ ,  $\omega_2 = 0.01$ ,  $f_1 = 1$ , and  $\tau = 0.3$ .

$$\begin{aligned}
 x &= \varepsilon^{1/3} X, \\
 y &= \varepsilon^{2/3} Y, \\
 t &= \varepsilon^{1/3} t_1, \\
 a &= \varepsilon^{2/3} \xi_1, \\
 \tau &= \varepsilon^{2/3} \tau_1, \\
 \alpha &= \varepsilon^{4/3} \xi_2,
 \end{aligned} \tag{6}$$

so system (5) turns into

$$\begin{aligned}
 \dot{X} &= Y, \\
 \dot{Y} &= \xi_1 X - bX^3 + \varepsilon(\xi_2 Y - Y^3 - \tau \xi_1 Y).
 \end{aligned} \tag{7}$$

Setting  $\xi_1 = 1$  and  $\varepsilon = 0$ , we get the integrable Hamiltonian system as follows:

$$\begin{aligned}
 \dot{X} &= Y, \\
 \dot{Y} &= X - bX^3.
 \end{aligned} \tag{8}$$

And the corresponding Hamiltonian function is  $H(X, Y) = 1/2Y^2 - 1/2X^2 + b/4Y^4$ . As shown in Figure 2, the phase portraits can express the homoclinic trajectories for  $H(X, Y) = 0$ .

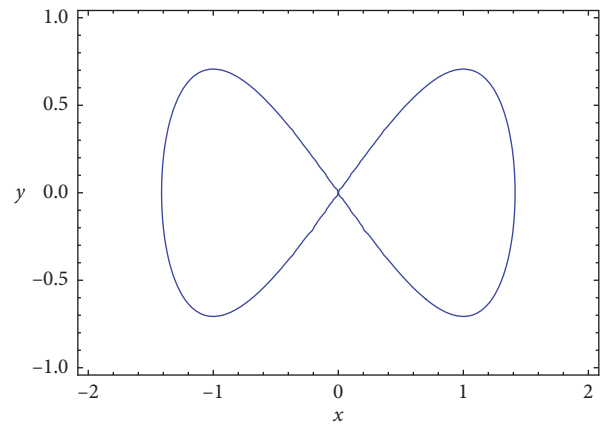


FIGURE 2: The phase portraits of Hamiltonian function.

In order to discuss the value of parameters, we set

$$x_0(t) = \pm \sqrt{\frac{2}{b}} \sec(t), \tag{9}$$

$$y_0(t) = \mp \sqrt{\frac{2}{b}} \sec(t) \tanh(t).$$

The Melnikov functions

$$M_{\pm}(\xi_2) = \xi_2 \int_{-\infty}^{+\infty} y_0^2(t) dt - \int_{-\infty}^{+\infty} y_0^4(t) dt \quad (10)$$

are given to verify the existence of Hamiltonian bifurcations. By calculating, we get the Melnikov function as

$$M_{\pm}(\xi_2) = \frac{4\xi_2}{3b} - \frac{16}{35b^2}. \quad (11)$$

From Melnikov function theory, when  $M_{\pm}(\xi_2) = 4\xi_2/3b - 16/35b^2 = 0$ , that is,  $\xi_2 = 12/35b$ , we get the approximate bifurcation of homoclinic orbits. Let  $\xi_1 = 1$ , and then according to transformation equation (7), the Melnikov threshold  $\alpha = 12a^2/35b$ . To illustrate the existence of saddle-node bifurcations in limit cycles at this time, we lead into a periodic orbit  $\gamma(e)$  by the level energy of  $e$  and period of  $T(e)$ . In the case of  $e \in (-1/4, 0)$ , there is a small-amplitude period; if  $e > 0$ ,  $\gamma(e)$ , there becomes a large-amplitude period. Therefore, the Melnikov function for cyclic orbits is

$$M_{\pm}(\xi_2, e) = \xi_2 \int_0^{T(e)} y_0^2(t) dt - \int_0^{T(e)} y_0^4(t) dt. \quad (12)$$

Through numerical simulation, it can be seen that the saddle-node bifurcations of the two periodic orbits are very close to the Melnikov threshold. Figure 3 shows that when the parameter enters region 2 from region 1 through the saddle junction, the system transits from the equilibrium state of the two small-amplitude limit cycles to a larger amplitude periodic orbit. It also indicates that the Melnikov threshold curve leads to the disappearance of the two limit cycles, resulting in a stable large-amplitude limit cycle. In order to facilitate the expansion discussed below, we only consider the parameters of the region where there are two small-amplitude periods and the unstable saddle point of the ordinary equilibrium point. Therefore, the numerical simulation parameter values given in this paper are fixed at  $\alpha = a = b = 1$ .

### 3. Oscillatory Dynamics with Equal Frequencies

This section focuses on the oscillating dynamics when the natural frequency is equal to the excitation frequency. We discuss the case when  $f_2 = 0$  and  $f_1$  is a variable. Then, the case where both  $f_2$  and  $f_1$  are variables is discussed.

**3.1. Oscillation Mechanism of MMOs for  $f_2 = 0$ .** For  $f_2 = 0$ , we set  $\beta = \cos(\omega_2 t)$ , and the fast system is driven by

$$\ddot{x} + \dot{x}^3 - \alpha\dot{x} - ax(t - \tau) + bx^3 = f_1\beta. \quad (13)$$

We obtain its perturbed form by scale transformation as follows:

$$\begin{aligned} \dot{X} &= Y, \\ \dot{Y} &= \xi_1 X - bX^3 + \varepsilon(\xi_2 Y - Y^3 - \tau\xi_1 Y + f_1\beta). \end{aligned} \quad (14)$$

By further calculating the Melnikov function, we have

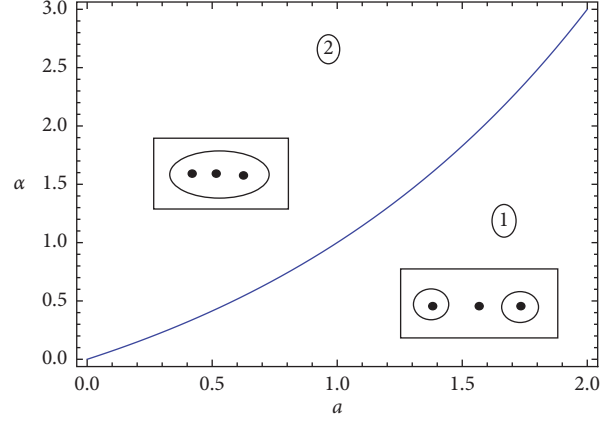


FIGURE 3: Melnikov threshold curve of the unperturbed model and the qualitative branching at  $b = 1$ .

$$M_{\pm}(\xi_2) = \xi_2 \int_{-\infty}^{+\infty} y_0^2(t) dt - \int_{-\infty}^{+\infty} y_0^4(t) dt + f_1\beta \int_{-\infty}^{+\infty} y_0(t) dt. \quad (15)$$

Thus, the Melnikov function of the local periodic orbit can be expressed as

$$M_{\pm}(\xi_2, e) = \xi_2 \int_0^{T(e)} y_0^2(t) dt - \int_0^{T(e)} y_0^4(t) dt + f_1\beta \int_0^{T(e)} y_0(t) dt. \quad (16)$$

In equation (16), these basic integrals are constants. When the value of  $y_0(t)$  is given by a determined value, we can get the critical threshold of the function. With the change of  $\beta$ ,  $f_1\beta$  will periodically affect the saddle-junction bifurcation, which leads to the phase trajectory transition from a small-amplitude periodic orbit to a large-amplitude periodic orbit, which further determines the oscillation phenomenon.

Given the parameter value  $a = b = \alpha = 1, \omega_2 = 0.1, \tau = 0.3$ , and  $f_1 = 1$ , Figure 4 shows the trajectory phase diagram and time-history curve of the system. The transition of the system between two small-amplitude periodic orbits can be seen from Figure 4. This excitation oscillation can be expressed as a closed singular orbit formed by two fast and slow motion trajectories.

**3.2. Oscillation Mechanism of MMOs as Varying  $f_1$  and  $f_2$ .** When  $f_1 \neq 0, f_2 \neq 0$ , and  $\omega_1 = \omega_2$ , set  $\beta = \cos(\omega_1 t) = \cos(\omega_2 t)$ , and we assume

$$\ddot{x} + \dot{x}^3 - \alpha\dot{x} - ax(t - \tau) + bx^3 = (f_1 + f_2\beta)\beta. \quad (17)$$

Use the scale change to obtain its perturbed form as

$$\begin{aligned} \dot{X} &= Y, \\ \dot{Y} &= \xi_1 X - bX^3 + \varepsilon[\xi_2 Y - Y^3 - \tau\xi_1 Y + (f_1 + f_2\beta)\beta]. \end{aligned} \quad (18)$$

Then, we get the Melnikov function

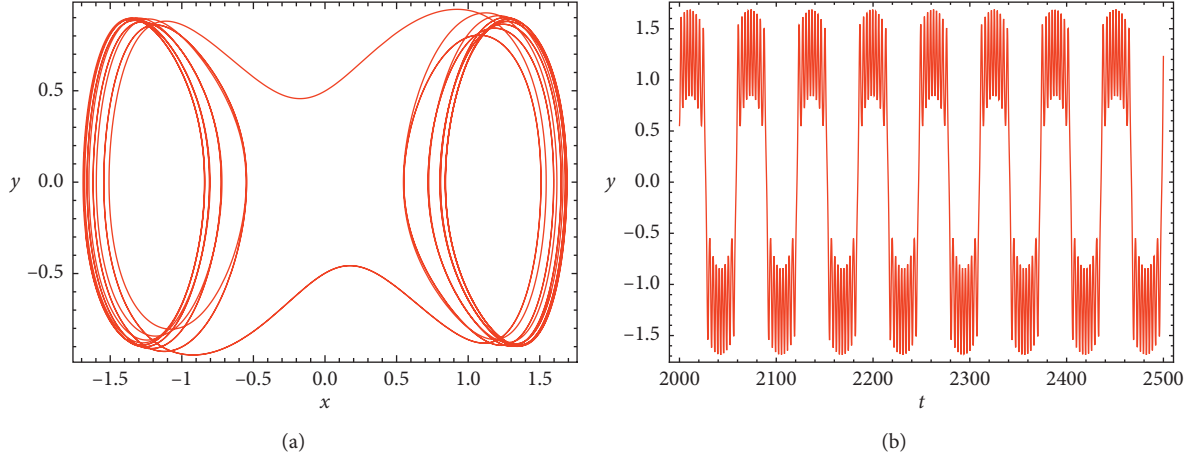


FIGURE 4: The phase trajectory (a) and time series (b) for the parameters  $a = b = \alpha = 1$ ,  $\omega_2 = 0.1$ ,  $f_1 = 1$ ,  $f_2 = 0$ , and  $\tau = 0.3$ .

$$M_{\pm}(\xi_2) = \xi_2 \int_{-\infty}^{+\infty} y_0^2(t) dt - \int_{-\infty}^{+\infty} y_0^4(t) dt + (f_1 + f_2\beta)\beta \int_{-\infty}^{+\infty} y_0(t) dt. \quad (19)$$

And the Melnikov function of the local periodic orbit can be written as

$$M_{\pm}(\xi_2, e) = \xi_2 \int_0^{T(e)} y_0^2(t) dt - \int_0^{T(e)} y_0^4(t) dt + (f_1 + f_2\beta)\beta \int_0^{T(e)} y_0(t) dt. \quad (20)$$

Once the value of  $y_0(t)$  is determined in equation (20), we can obtain the critical threshold of the function. With the change of  $\beta$ ,  $(f_1 + f_2\beta)\beta$  will periodically affect the saddle-junction bifurcation, which leads to the phase trajectory transit from a small-amplitude periodic orbit to a large-amplitude periodic orbit, which determines the oscillation phenomenon.

Take the parameter value  $a = b = \alpha = 1$ ,  $\omega_2 = \omega_1 = 0.01$ ,  $\tau = 0.3$ ,  $f_1 = 1$ , and  $f_2 = 0.5$ . The time-history curve of the system is seen in Figure 5. From the figures, we can observe that the mixed-mode oscillation at this time has two asymmetric small-amplitude periodic orbits and a set of independent large-amplitude periodic orbits in each period.

#### 4. Oscillatory Dynamics with Two Resonant Frequencies

This section mainly discusses the mixed-mode oscillation dynamics reflected by the system when the natural frequency and the resonant frequency are not equal. Without loss of generality, assume that the two frequencies are proportional, and  $\omega_1$  is a positive integer multiple of  $\omega_2$ , i.e.,  $\omega_1 = n\omega_2$ ,  $n$  is an integer greater than 1, or  $\omega_1$  is a noninteger multiple of  $\omega_2$ , i.e.,  $n$  is an irrational number, and then system (1) can be turned into

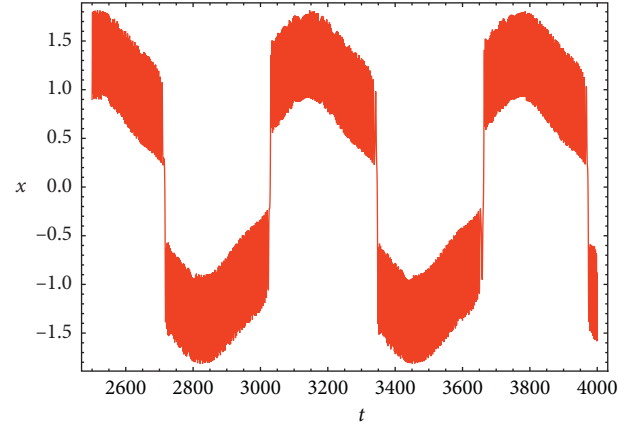


FIGURE 5: The time series for the parameters  $a = b = \alpha = 1$ ,  $\omega_2 = \omega_1 = 0.01$ ,  $f_2 = 0.5$ ,  $f_1 = 1$ , and  $\tau = 0.3$ .

$$\ddot{x} + \dot{x}^3 - \alpha\dot{x} - ax(t - \tau) + bx^3 = (f_1 + f_2 \cos(n\omega_2))\cos(\omega_2). \quad (21)$$

Then, we will discuss three cases: (1) the dynamics of the system with  $n$  being a small positive integer; (2) the oscillation behavior with  $n$  being a large positive integer; and (3) the coupling of time-delay systems with  $n$  being an irrational number.

**4.1. Oscillation Mechanism of MMOs for a Relatively Small  $n$ .** Since  $n$  is a small real number, then the natural frequency  $\omega_1$  is still a low frequency. Thus,  $\omega_1$  and  $\omega_2$  can be treated as a fast and slow form with a single slow variable. Borrowing De Moivre's formula, we arrive at

$$\begin{aligned} \cos(nx) &= C_n^0 \cos^n x + C_n^2 \cos^{n-2} x (i \sin x)^2 + \dots \\ &+ C_n^m \cos^{n-m} x (i \sin x)^m, \end{aligned} \quad (22)$$

where  $m$  is the maximum value not greater than  $n$ . Let us see some simple examples. When  $n$  takes 2 and 3, respectively, we can get  $\cos(2x) = 2 \cos^2 x - 1$  and  $\cos(3x) = 4 \cos^3 x - 3 \cos x$ . Let  $n = 2$ , the oscillation behavior of the system is

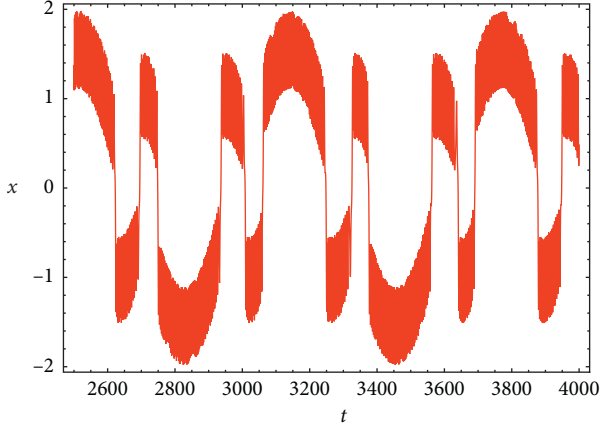


FIGURE 6: The time history of fast-slow system (1) at  $\omega_1 = 2\omega_2$ , where the parameters are  $a = b = 1, \alpha = 0.1, \omega_1 = 0.02, \omega_2 = 0.01, \tau = 0.3, f_1 = 0.1$ , and  $f_2 = 2$ .

shown in Figure 6, and the values of the parameters are  $a = b = 1, \alpha = 0.1, \omega_1 = 0.02, \omega_2 = 0.01, \tau = 0.5, f_1 = 0.5$ , and  $f_2 = 2$ , respectively.

From Figure 6, the oscillation mode can be clearly divided into different parts, and the upper and lower oscillations are connected by the jump connection. And compared with previous Figure 6, the number of different oscillations is significantly increased in the gentle region and the peak region in each cycle.

Now, considering the situation of divergence when  $n = 2$  and setting  $\beta = \cos(\omega_1 t)$  and  $\cos(\omega_2 t) = 2\beta^2 - 1A$ , we have

$$\ddot{x} + \dot{x}^3 - \alpha\dot{x} - ax(t - \tau) + bx^3 = f_1\beta^2 + f_2\beta^3 - f_2\beta. \quad (23)$$

Perturbation form by reference to the scale change method is

$$\begin{aligned} \dot{X} &= Y, \\ \dot{Y} &= \xi_1 X - bX^3 + \varepsilon[\xi_2 Y - Y^3 - \tau\xi_1 Y + f_1\beta^2 + f_2\beta^3 - f_2\beta]. \end{aligned} \quad (24)$$

Then, we obtain the Melnikov function

$$\begin{aligned} M_{\pm}(\xi_2) &= \xi_2 \int_{-\infty}^{+\infty} y_0^2(t)dt - \int_{-\infty}^{+\infty} y_0^4(t)dt + (f_1\beta^2 + f_2\beta^3 \\ &\quad - f_2\beta) \int_{-\infty}^{+\infty} y_0(t)dt. \end{aligned} \quad (25)$$

The Melnikov function of the local periodic orbit can be written as

$$\begin{aligned} M_{\pm}(\xi_2, e) &= \xi_2 \int_0^{T(e)} y_0^2(t)dt - \int_0^{T(e)} y_0^4(t)dt + (f_1\beta^2 \\ &\quad + f_2\beta^3 - f_2\beta) \int_0^{T(e)} y_0(t)dt. \end{aligned} \quad (26)$$

If  $y_0(t)$  in equation (26) is given, the critical threshold of the function can be determined. With the change of  $\beta$ ,  $f_1\beta^2 + f_2\beta^3 - f_2\beta$  periodically affects the saddle-junction

bifurcation, causing the phase trajectory to change from a small-amplitude periodic orbit to a large-amplitude periodic orbit and generating oscillation behavior.

**4.2. Oscillation Mechanism of MMOs for a Relatively Large  $n$ .** When  $n$  is a sufficiently large integer, there is a large step gap between the natural frequency and the excitation frequency. Since there are many oscillatory components in each oscillation mode, the De Moivre's formula cannot be used for analysis. Now, in this example, we discuss the following.

Letting  $\beta = \cos(\omega_2 t)$ , then system (1) can be described as

$$\ddot{x} + \dot{x} - \alpha\dot{x} - ax(t - \tau) + bx^3 = (f_1 + f_2 \cos(\omega_1 t))\beta. \quad (27)$$

Accordingly, its perturbation form is

$$\begin{aligned} \dot{X} &= Y, \\ \dot{Y} &= \xi_1 X - bX^3 + \varepsilon[\xi_2 Y - Y^3 - \tau\xi_1 Y + (f_1 + f_2 \cos(\omega_1 t))\beta]. \end{aligned} \quad (28)$$

So, the Melnikov function of the system becomes

$$\begin{aligned} M_{\pm}(\xi_2) &= \xi_2 \int_{-\infty}^{+\infty} y_0^2(t)dt - \int_{-\infty}^{+\infty} y_0^4(t)dt + (f_1 \\ &\quad + f_2 \cos(\omega_1 t)) \int_{-\infty}^{+\infty} y_0(t)dt. \end{aligned} \quad (29)$$

Thus, we obtain the Melnikov function of the periodic orbit as follows:

$$\begin{aligned} M_{\pm}(\xi_2, e) &= \xi_2 \int_0^{T(e)} y_0^2(t)dt - \int_0^{T(e)} y_0^4(t)dt + (f_1 \\ &\quad + f_2 \cos(\omega_1 t)) \int_0^{T(e)} y_0(t)dt. \end{aligned} \quad (30)$$

If we can determine the value of  $y_0(t)$  in equation (30), then we also can get the critical threshold of the function. The value of the natural frequency  $\omega$  also affects the function  $M_{\pm}(\xi_2, e)$ . In this case, as  $\beta$  changes, the system periodically crosses the saddle-junction of the limit cycle, resulting in more complex oscillatory behavior.

Through numerical simulation, we use Figure 7 to illustrate the dynamic behavior of the mixed-mode oscillation when there is a gap between the natural frequency and the excitation frequency. Here, we set the parameters of the system  $a = b = 1, \alpha = 0.1, \omega_1 = 2, \omega_2 = 0.01, \tau = 0.3$ , and  $f_1 = f_2 = 0.5$ . From Figure 7, we can find the transition between two local limit cycles.

**4.3. Oscillation Mechanism of MMOs for an Irrational Number  $n$ .** In this section, we consider the coupled Duffing equation with multiple-frequency external forces and delayed feedbacks as follows:

$$\begin{aligned} x'' + \delta_1 x' - y(t - \tau) + x^3 &= \beta_1 \cos(\omega_1 t) + \beta_3 \cos(\omega_2 t), \\ y'' + \delta_2 y' - x(t - \tau) + y^3 &= \beta_2 \cos(\omega_1 t) + \beta_4 \cos(\omega_2 t), \end{aligned} \quad (31)$$

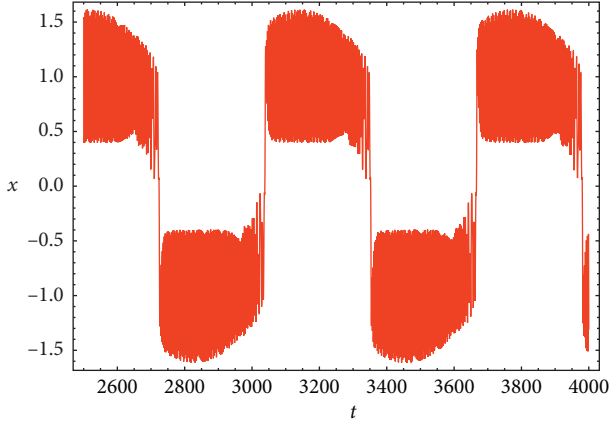


FIGURE 7: The time history of fast-slow system (1) at  $\omega_1 = 200\omega_2$ , where the parameters are  $a = b = 1$ ,  $\alpha = 0.1$ ,  $\omega_1 = 2$ ,  $\omega_2 = 0.01$ ,  $\tau = 0.3$ , and  $f_1 = f_2 = 0.5$ .

where  $\delta_i$  ( $i = 1, 2$ ) ( $\delta > 0$ ) are the dampings,  $\beta_i$  ( $i = 1, 2, 3, 4$ ) are the excitation amplitudes, and  $\omega_i$  ( $i = 1, 2$ ) are the corresponding excitation frequencies.  $\tau$  ( $\tau \geq 0$ ) is the time delay and  $\omega_1 = O(\varepsilon)$ , where  $\varepsilon \ll 1$ .

**4.3.1. General Method.** We study the dynamic behavior of fast-slow system (31) with two slow variables by using the fast-slow analysis method. The two slow variables can be represented by functions containing  $\gamma(t)$ , that is,  $\cos(\omega_1 t) = f_1(\gamma(t))$  and  $\cos(\omega_2 t) = f_2(\gamma(t))$ , and the system can be transformed into a fast-slow system with only one slow variable  $\gamma(t)$ . Therefore, the system can be studied by the traditional fast-slow analysis method.

According to Taylor series expansion, we obtain

$$\cos(nt) = f_n^*(\cos(t)), \quad (32)$$

where

$$\begin{aligned} f_n^*(x) = & C_n^0 x^n - C_n^2 x^{n-2} (1-x^2) + C_n^4 x^{n-4} (1-x^2)^2 - \dots \\ & + i^m C_n^m x^{n-m} (1-x^2)^{m/2}. \end{aligned} \quad (33)$$

Set  $\omega_2 = n\omega_1$  ( $n$  is a positive integer), and then equation (32) becomes

$$\begin{aligned} x'' + \delta_1 x' - y(t-\tau) + x^3 &= \beta_1 \gamma(t) + \beta_3 f_n^*(\gamma(t)), \\ y'' + \delta_2 y' - x(t-\tau) + y^3 &= \beta_2 \gamma(t) + \beta_4 f_n^*(\gamma(t)), \end{aligned} \quad (34)$$

where  $\gamma(t) = \cos(\omega_1 t)$ . Furthermore, the fast subsystem can be regarded as

$$\begin{aligned} x'' + \delta_1 x' - y(t-\tau) + x^3 &= \beta_1 \gamma + \beta_3 f_n^*(\gamma), \\ y'' + \delta_2 y' - x(t-\tau) + y^3 &= \beta_2 \gamma + \beta_4 f_n^*(\gamma). \end{aligned} \quad (35)$$

**4.3.2. The Duffing System with Commensurate Excitation Frequencies.** We begin our analysis by considering the case when  $\omega_1 = 0.01$  and  $\omega_2 = 0.03$ , name  $\omega_2 = 3\omega_1$ .

Setting  $\delta_1 = 2$ ,  $\delta_2 = 1$ ,  $\beta_1 = \beta_2 = 1.2$ ,  $\beta_3 = 0.5$ , and  $\beta_4 = 0.555$ . Figure 8 shows the time-history curve of the system when  $\tau = 0$ ,  $\tau = 1$ , and  $\tau = 2$ . As shown in the figure, periodic oscillations occur in these states. Each periodic oscillation is composed of large-amplitude oscillations and small-amplitude oscillations. When appearing small-amplitude oscillation, the system is said to be in a resting state. When the system trajectory passes through the bifurcation point, it loses its equilibrium state and shows a large oscillation. At this point, the system moves from the resting state to the excited state. When the orbit of the system jumps back and forth between the resting state and the excited state, it is called bursting. The two frequencies are engaged in the bursting of the system. It is seen that each bursting pattern can be divided into two parts, i.e., the upper and lower oscillations which are connected by catastrophic jumps.

To further study the dynamic behavior in Figure 8, the equilibrium curve and the transformation phase diagram of fast subsystem (32) were drawn by setting  $\omega_1 = 0.01$ ,  $\omega_2 = 0.03$ ,  $\delta_1 = 2$ ,  $\delta_2 = 1$ ,  $\beta_1 = \beta_2 = 1.2$ ,  $\beta_3 = 0.5$  and  $\beta_4 = 0.555$  (see Figure 8). So, we have the fast subsystem

$$\begin{aligned} x'' + \delta_1 x' - y(t-\tau) + x^3 &= \beta_1 \gamma + \beta_3 f_3^*(\gamma), \\ y'' + \delta_2 y' - x(t-\tau) + y^3 &= \beta_2 \gamma + \beta_4 f_3^*(\gamma), \end{aligned} \quad (36)$$

where  $\gamma(t) = \cos(0.01t)$  is the control parameter. Figure 9 shows the equilibrium curve and the transformation phase diagram  $\tau = 0$ . It leads to an S-shaped equilibrium curve. The solid line represents the stable equilibrium point, and the dotted line represents the unstable equilibrium point; FB indicates the fold bifurcation point, and it can be seen from the figure that there are two stable equilibrium points and two fold bifurcation points in the fast subsystem. With the change of  $\gamma$ , the system trajectory moves to the right along the stable equilibrium and loses the balance after meeting the fold bifurcation point and then jumps to the lower part of the balance curve. The system is excited from a static state. Due to the attraction of the lower balance, the rail line tends to be stable and exits the excited state into the static state until  $\gamma$  attains its maximum value, and then the rail line moves to the left. By this way, two jumps are completed in a cycle.

Figures 9(c)–9(f) are the equilibrium curve and the transformation phase diagram when  $\tau = 1$  and  $\tau = 2$ . The solid line represents the stable equilibrium point, while the dotted line represents the unstable equilibrium point; FB indicates the fold bifurcation point. The similar fold bifurcation occurred in Figures 9(a) and 9(b), and almost the same rail line was drawn. Combining the equilibrium curve and the transformation phase diagram, we found that the occurrence of bursting is not significantly disturbed even if the time delay increased, and the dynamic behavior of the system do not lose its typical characteristics with the change of time delay.

To further study the influence of time delay on the bursting, Figure 10 shows the plot of the peak parts of Figures 8(a)–8(c). We find that the time delay causes the dynamic changes in the upper and lower parts of the oscillation within each period.

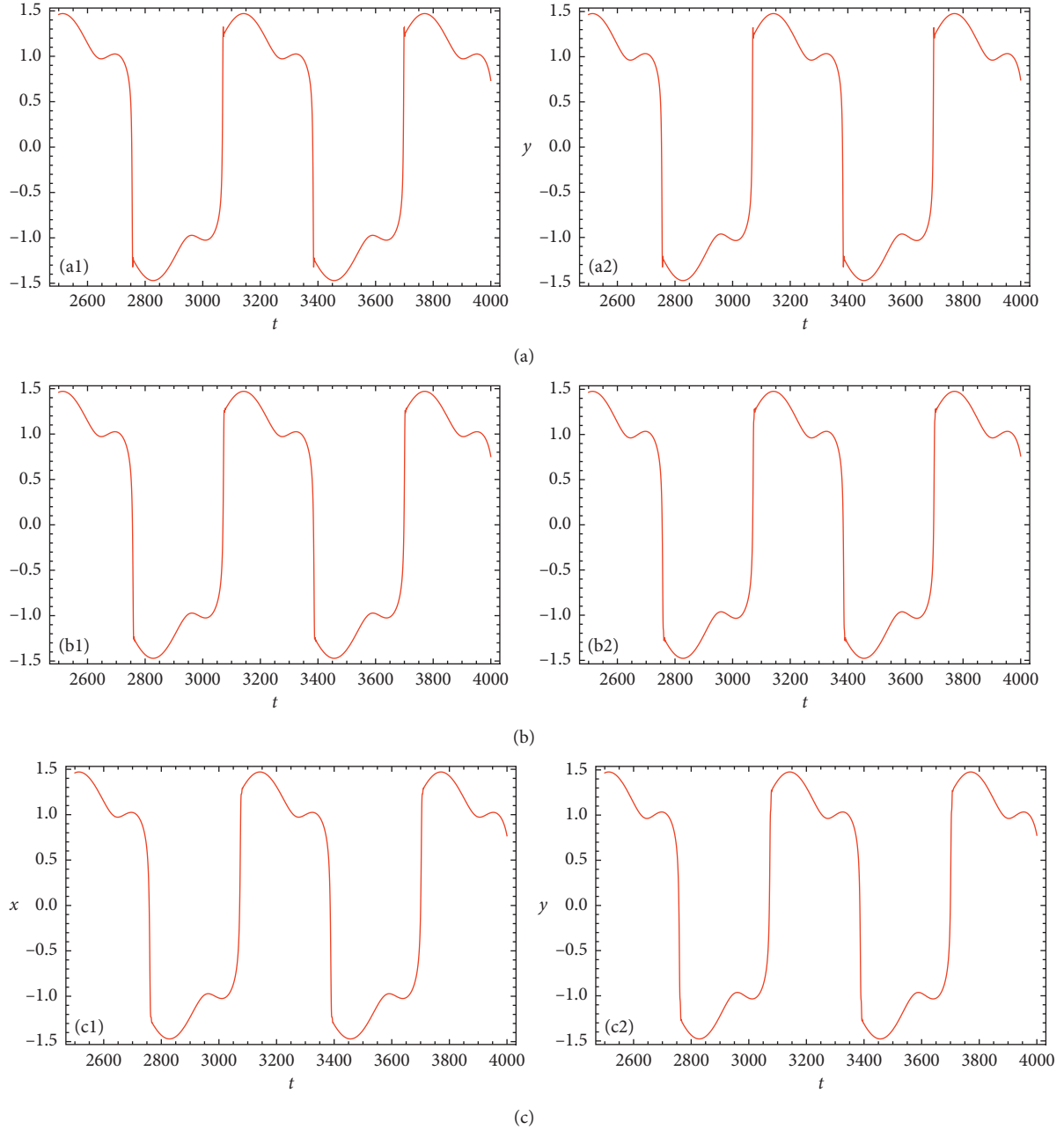


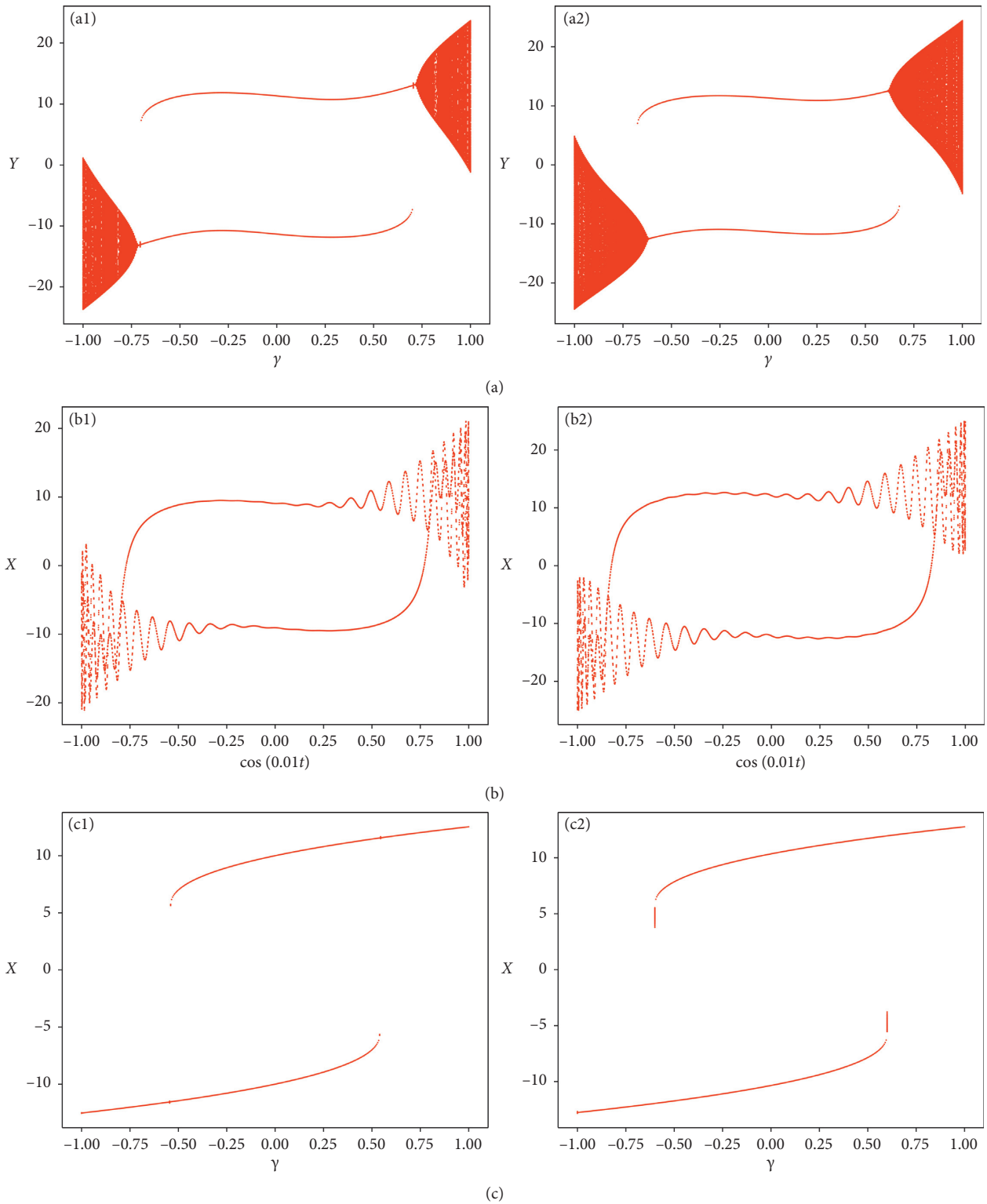
FIGURE 8: Time series of the bursting for  $\delta_1 = 2, \delta_2 = 1, \beta_1 = \beta_2 = 1.2, \beta_3 = 0.5, \beta_4 = 0.555, \omega_1 = 0.01, \omega_2 = 0.03$ . (a<sub>1</sub>, a<sub>2</sub>)  $\tau = 0$ , (b<sub>1</sub>, b<sub>2</sub>)  $\tau = 1$ , and (c<sub>1</sub>, c<sub>2</sub>)  $\tau = 2$ .

**4.3.3. The Duffing System with Incommensurate Excitation Frequencies.** Now, we consider that the ratio of two frequencies is not the ratio of two integers, i.e., there is at least one of the two excitation frequencies which is irrational. We assume that, in system (31),  $\omega_1$  is a rational frequency, while  $\omega_2$  is an irrational frequency, e.g.,  $\omega_2 = \pi/100$ . Then, the irrational frequency  $\omega_2$  leads to a rational sequence  $\Omega_n = \pi/100$ , in which  $\pi_n$  denotes the  $10^{-n}$ -grade truncated  $\pi$ , i.e., an approximation of  $\pi$ . For example,  $\pi_3 = 3.141$  and  $\pi_6 = 3.141592$ . Set  $\delta_1 = 2, \delta_2 = 1, \beta_1 = \beta_2 = 1.2, \beta_3 = 0.5, \beta_4 = 0.555$ , and  $\tau = 1$ . Figure 11 shows the time-history curve of the system when  $\omega_1 = 0.01, \omega_2 = \pi/100, \omega_1 = 0.01$ ,

$\omega_2 = \sqrt{3}/100, \omega_1 = \pi/100, \omega_2 = 0.01$ , and  $\omega_1 = \sqrt{3}/100, \omega_2 = 0.01$ . The complex bursting behavior in the system with delayed feedback is universal. Compared with Figure 8, the upper and lower vibration of each bursting curve is more intense.

Since the ratio of two excitation frequencies is not the ratio of two integers, we cannot directly use the traditional fast and slow analysis method to analyze the behavior of the system with incommensurate excitation frequencies. So, we try to use the numerical simulation to draw the overlap of the bursting with incommensurate excitation frequencies and the one with truncated and commensurate excitation





(c)  
FIGURE 9: Continued.

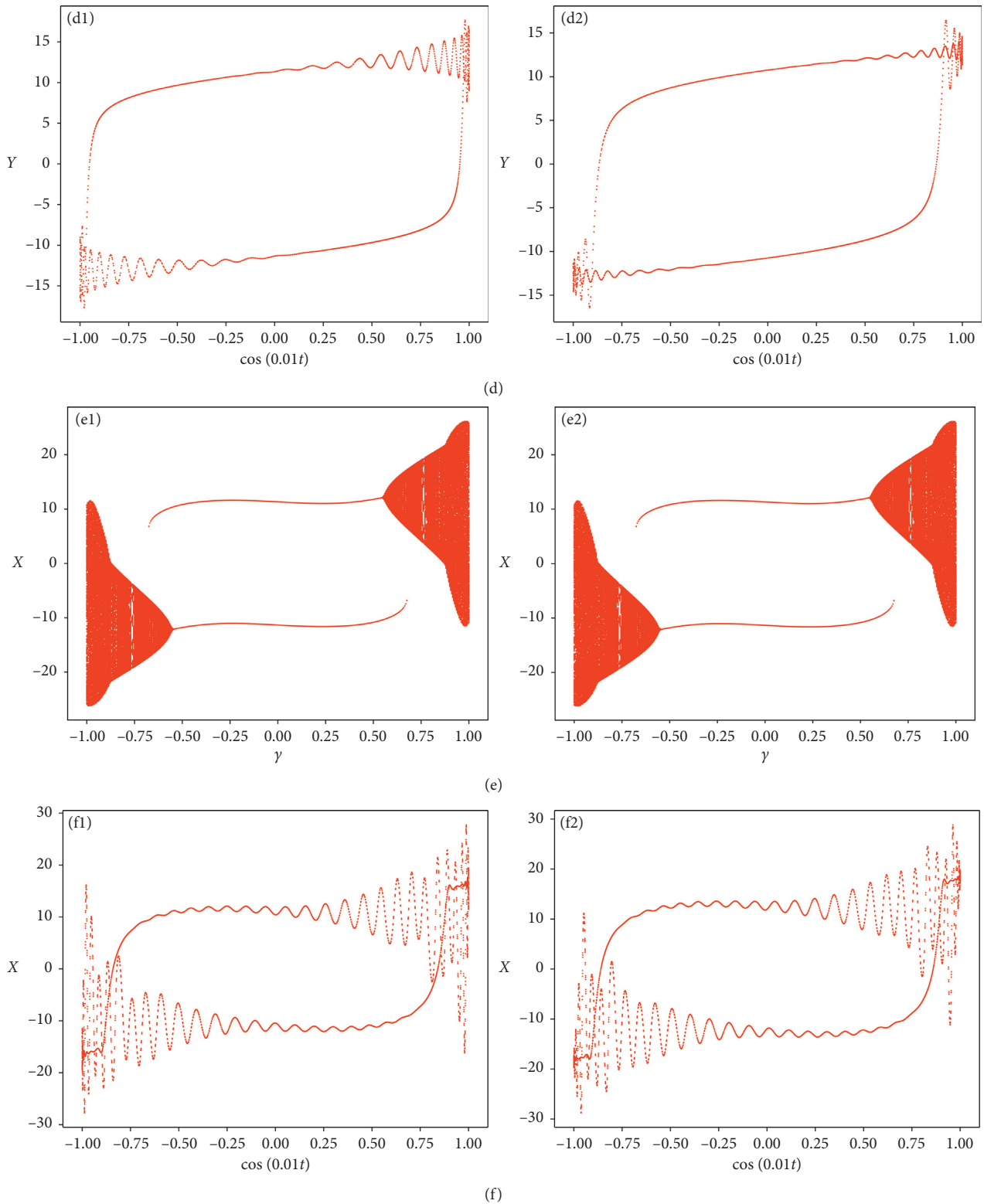


FIGURE 9: Fast-slow analysis of the bursting  $(a_1, b_1, a_2, b_2)$ ,  $(c_1, d_1, c_2, d_2)$ , and  $(e_1, f_1, e_2, f_2)$  is related to the bursting patterns in Figure 8  $(a_1, a_2)$ ,  $(b_1, b_2)$ , and  $(c_1, c_2)$ .

frequency (see Figure 12). It is shown that the yellow curve agrees well with the red curve, i.e., the bursting pattern in Figure 12(a) with  $10^{-2}$ -grade truncated frequency agrees

well with the one in Figure 11(a), and the bursting pattern in Figure 12(b) with  $10^{-3}$ -grade truncated frequency agrees well with the one in Figure 11(b). Therefore, we can conclude

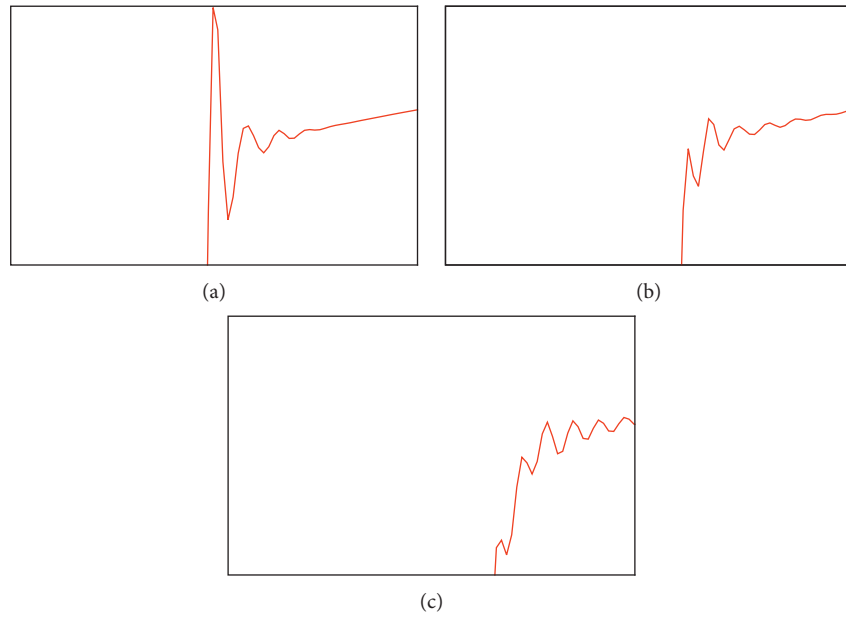


FIGURE 10: The plot of the peak part of Figures 8(a)–8(c).

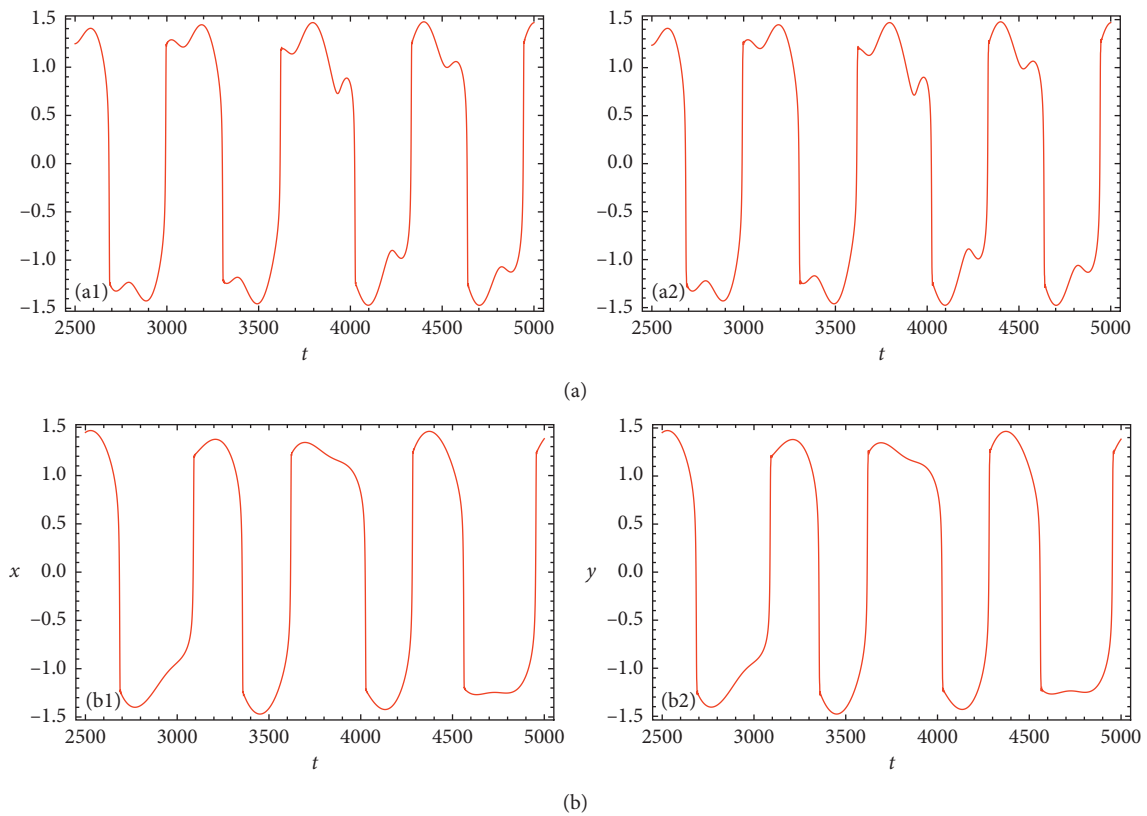


FIGURE 11: Continued.

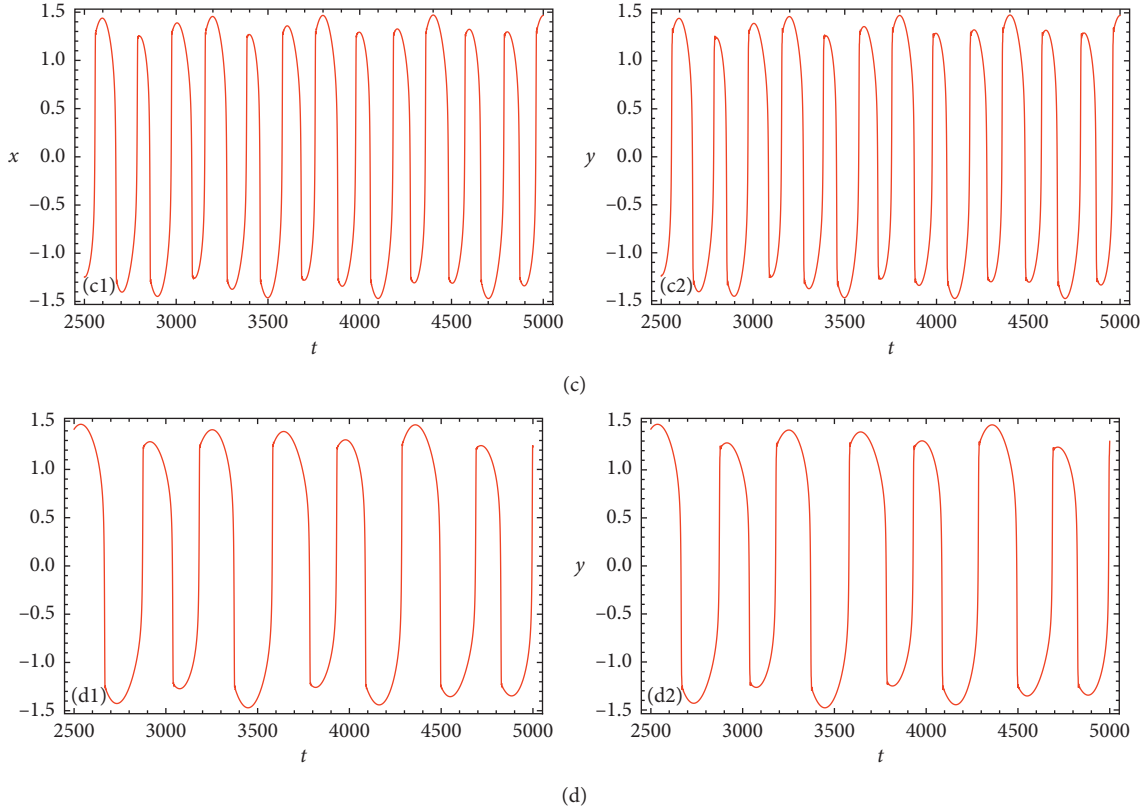


FIGURE 11: Time series of the bursting for  $\delta_1 = 2$ ,  $\delta_1 = 1$ ,  $\beta_1 = \beta_2 = 1.2$ ,  $\beta_3 = 0.5$ ,  $\beta_4 = 0.555$ , and  $\tau = 1$ .  $(a_1, a_2)$   $\omega_1 = 0.01$ ,  $\omega_2 = \pi/100$  and  $(b_1, b_2)$   $\omega_1 = 0.01$ ,  $\omega_2 = \sqrt{3}/100$ .  $(c_1, c_2)$   $\omega_1 = \pi/100$ ,  $\omega_2 = 0.01$  and  $(d_1, d_2)$   $\omega_1 = \sqrt{3}/100$ ,  $\omega_2 = 0.01$ .

that the bursting mode related to the incommensurate excitation frequency can be well approximated to the  $10^{-n}$ -grade truncated excitation frequency.

Then, the bursting in Figure 10(a) can be used to analyze the following system:

$$\begin{aligned} x'' + \delta_1 x' - y(t - \tau) + x^3 &= \beta_1 f_{50}^*(\gamma) + \beta_3 f_{157}^*(\gamma), \\ y'' + \delta_2 y' - x(t - \tau) + y^3 &= \beta_2 f_{50}^*(\gamma) + \beta_4 f_{157}^*(\gamma), \end{aligned} \quad (37)$$

where  $\gamma(t) = \cos(0.0002t)$  is the control parameter so that we can continue to study the fast subsystem by the fast-slow analysis method.

## 5. The Effect of Time Delay on Cluster Discovery

Time delay is an important parameter of time-delay systems, which affects the dynamic bifurcation and stability of the system. This section mainly discusses the influence of time lag on the occurrence and development of cluster discovery before and after approximation and then confirms the effective time lag range by numerical simulation to reduce the error size and obtain the desired peak dynamics. Here, we mainly consider the system

$$\ddot{x} + \dot{x} - a\dot{x} - ax(t - \tau) + bx^3 = f_1 \cos(\omega_2 t). \quad (38)$$

Set  $x(t - \tau) \approx x(t) - \tau x'(t)$  in the numerical simulation of the two cases before and after the approximation of the time lag which is performed.

Now, we take the parameters  $a = b = \alpha = 1$ ,  $\omega_2 = 0.01$ ,  $f_1 = 1$ ,  $\tau = 1$ ,  $\tau = 0.6$ ,  $\tau = 0.5$ , and  $\tau = 0.3$ . Figures 13–16 compare the time-history curves of the system before and after approximation. From the comparison of these figures, the time lag does not affect the generation of cluster images, respectively. By comparing the preapproximation and the approximation of the system delay, it is found that the approximation of the system in Figures 13 and 14 causes the dynamics of the upper and lower portions of the oscillation to change in each cycle. Figures 15 and 16 show the approximation of the system is almost consistent with the dynamic behavior before the approximation. Therefore, the effective time range of the system should be 0~0.3. In the above sections, we generally take  $\tau = 0.3$ .

## 6. The Multistate Dynamic Response of the System

In dynamic systems, multistability is the property that there are multiple stable equilibrium points in the vector space spanned by the state of the system. According to the mathematical, there must also be points of instability between the stable points. Near the unstable equilibrium point, any system will be sensitive to noise, initial conditions, and system parameters, which will lead to the development of the system in many different directions. Here, we mainly consider the system

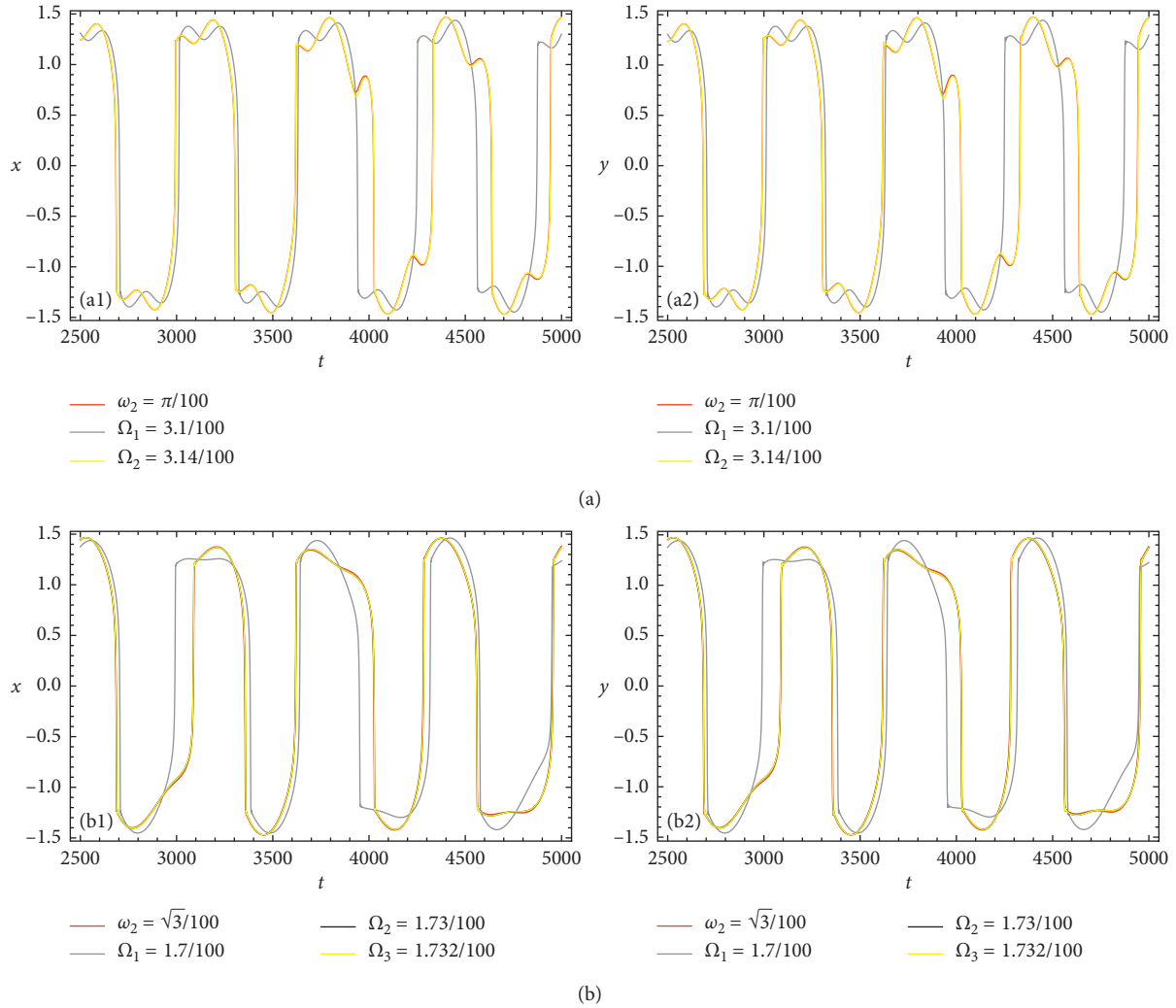


FIGURE 12: Bursting pattern with incommensurate excitation frequencies (red curve) agrees well with the one with truncated, commensurate excitation frequencies (yellow curve).

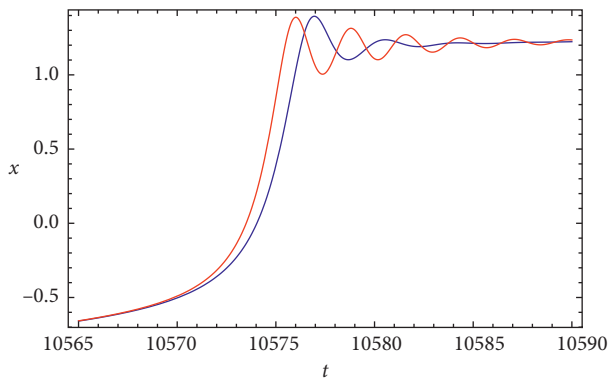


FIGURE 13: Time history of system (36). The red line represents the curve before time-delay approximation, and the blue line represents the curve after time-delay approximation when the parameters are  $a = b = \alpha = 1$ ,  $\omega_2 = 0.01$ ,  $f_1 = 1$ , and  $\tau = 1$ .

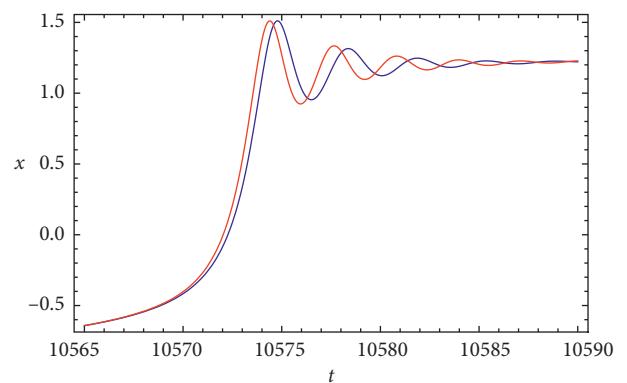


FIGURE 14: Time history of system (36). The red line represents the curve before time-delay approximation, and the blue line represents the curve after time-delay approximation when the parameters are  $a = b = \alpha = 1$ ,  $\omega_2 = 0.01$ ,  $f_1 = 1$ , and  $\tau = 0.6$ .

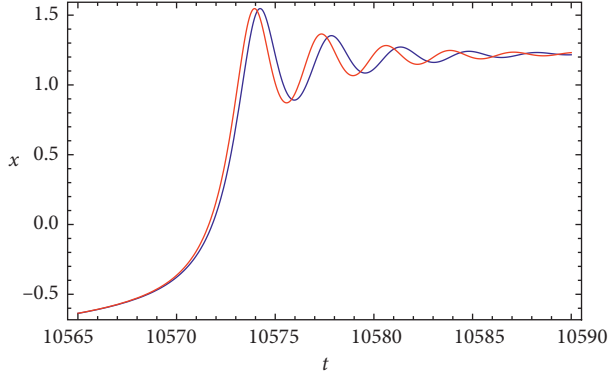


FIGURE 15: Time history of system (36). The red line represents the curve before time-delay approximation, and the blue line represents the curve after time-delay approximation when the parameters are  $a = b = \alpha = 1$ ,  $\omega_2 = 0.01$ ,  $f_1 = 1$ , and  $\tau = 0.5$ .

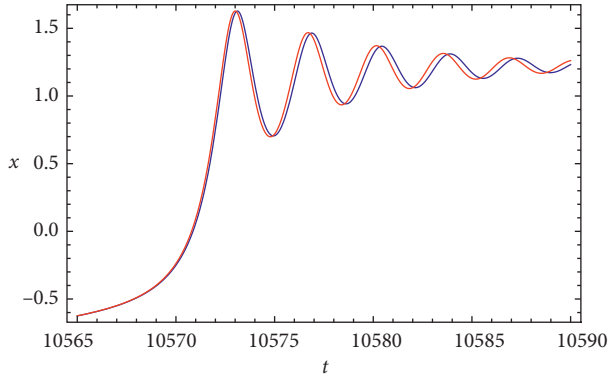


FIGURE 16: Time history of system (36). The red line represents the curve before time-delay approximation, and the blue line represents the curve after time-delay approximation when the parameters are  $a = b = \alpha = 1$ ,  $\omega_2 = 0.01$ ,  $f_1 = 1$ , and  $\tau = 0.3$ .

$$\begin{aligned} \dot{x} &= y, \\ \dot{y} &= -a_1 x + a_2 y + y^5 - f \cos \Omega t, \end{aligned} \quad (39)$$

where  $x(t)$  and  $y(t)$  are the real function.  $f > 0$  is the amplitude, and  $\omega$  is the frequencies.  $a_1$  and  $a_2$  are the physical parameters.

Use the Euler method to obtain the following discrete systems:

$$\begin{aligned} x_{n+1} &= y_n, \\ y_{n+1} &= a y_n - b(x_n) - c y_n^5 + \beta, \end{aligned} \quad (40)$$

where  $a = 2 - a_2(\Delta t)$ ,  $b = a_1(\Delta t)^2 + a_2(\Delta t) + 1$ ,  $c = (\Delta t)^5$ , and  $\beta = f \cos \Omega t$ . Next, we will study the multistate dynamic response of the above discrete system. Set  $a$  and  $b$  as the real parameter and  $\beta$  as the control parameter. Controllable slow periodic motion is expressed as  $Z_n = f \cos \Omega t$ , in which the external excitation frequency is taken as 0.001. For convenience of calculation, we set  $c = 1$ .

Now, we take  $\beta$  as the bifurcation parameter to explore the coexistence of chaotic attractors, periodic attractors, and chaotic attractors or the occurrence of numbers and sizes when parameters  $a$  and  $b$  take different values.

*Case 1.* Dynamic response without jumping phenomenon.

According to Figures 17 and 18, when  $a = 1.2$  and  $\beta = 0.24$ , the system is in a single periodic motion. When  $-0.6 < \beta < -0.5$  and  $0.5 < \beta < 0.6$ , the system is in double periodic motion. And there is no jump occurring at  $\beta = 0$ .

*Case 2.* When  $a = 1.2$  and  $b = 0.23$ , dynamic occurs in the jumping phenomenon at  $\beta = 0$ .

From Figures 19 and 20, we know, when  $-0.53 < \beta < -0.43$  and  $0.43 < \beta < 0.53$ , the system is in double periodic motion. When  $-0.43 < \beta < 0.43$ , the system is in a single periodic motion. But, there appear jumping phenomenon when  $\beta$  is near 0.

*Case 3.* The transition of the system from the bistable state to the chaotic attractor to the monoperciodic attractor.

As shown in Figure 21, when  $\beta_c^\pm = \pm 0.91$ , the system is in a state of bistable, and chaotic attractor and haploid cycle attractor coexist. When  $\beta > 0.91$  and  $\beta < -0.91$ , the system enters into haploid periodic motion, and the bistable state disappears. And we also found that as  $\beta$  increases or decreases, namely, more than the critical value, the system of the chaotic attractor suddenly disappeared.

*Case 4.* The transition of the system from the bistable state to the chaotic attractor to the double periodic attractor.

When  $a = 1.9$  and  $b = 0.17$ , from Figure 22, we obtain  $\beta_c^\pm = \pm 0.042$ , and the system is in a state of bistable, and chaotic attractor and double period attractor coexist. When  $\beta > 0.042$  and  $\beta < -0.042$ , the system enters into double periodic motion, and the bistable state disappears. And as  $\beta$  increases or decreases, namely, more than the critical value, the system of the chaotic attractor disappeared.

*Case 5.* The transition of the system from the bistable state to the chaotic attractor to the quadruple periodic attractor.

When  $a = 1.9$  and  $b = 0.23$ , from Figure 23, we obtain  $\beta_c^\pm = \pm 0.026$ , and the system is in a state of bistable, and chaotic attractor and haploid cycle attractor coexist. When  $\beta > 0.026$  and  $\beta < -0.026$ , the system enters into quadruple periodic motion, and the bistable state disappears. And as  $\beta$  increases or decreases, namely, more than the critical value, the system of the chaotic attractor disappeared.

*Case 6.* The transition of the system from the bistable state to the chaotic attractor to the chaotic attractor.

From Figure 24, we obtain  $\beta_c^\pm = \pm 0.026$ , and when  $a = 1.9$  and  $b = 0.14$ , the system is in a state of bistable, and chaotic attractor and haploid cycle attractor coexist. When  $\beta > 0.026$  and  $\beta < -0.026$ , the system enters into quadruple periodic motion, and the bistable state disappears. And as  $\beta$  increases or decreases, namely, more than the critical value, the system of the chaotic attractor disappeared.



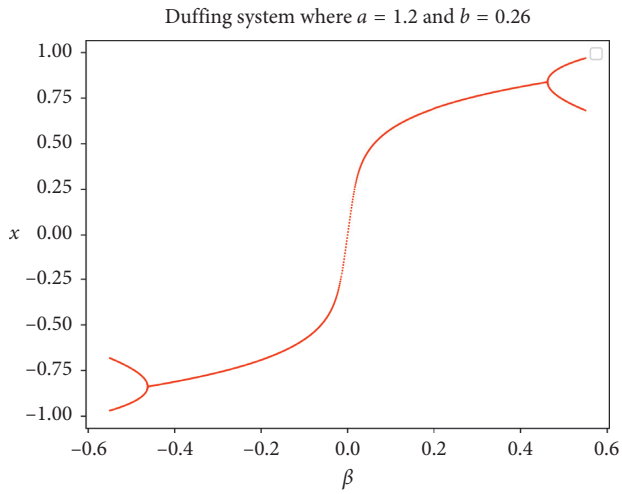


FIGURE 17: Bifurcation diagram of  $\beta$ .

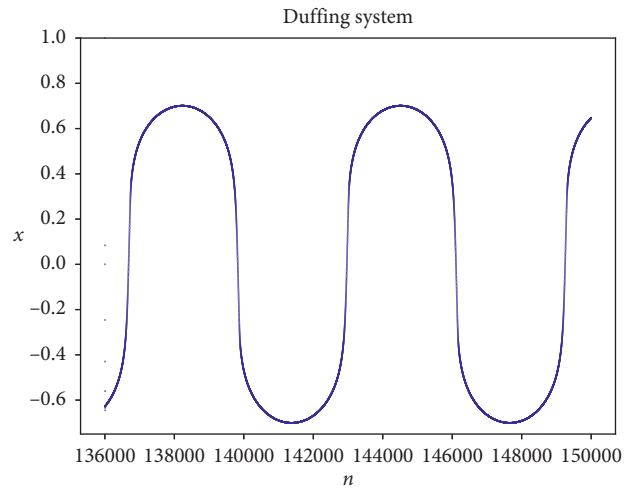


FIGURE 20: Time series diagram.

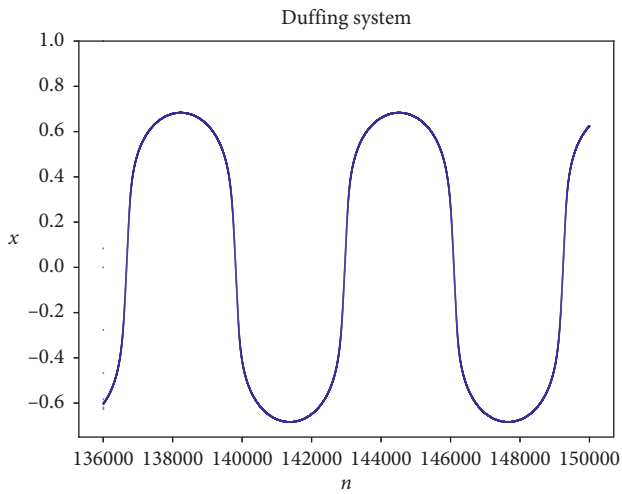


FIGURE 18: Time series diagram.

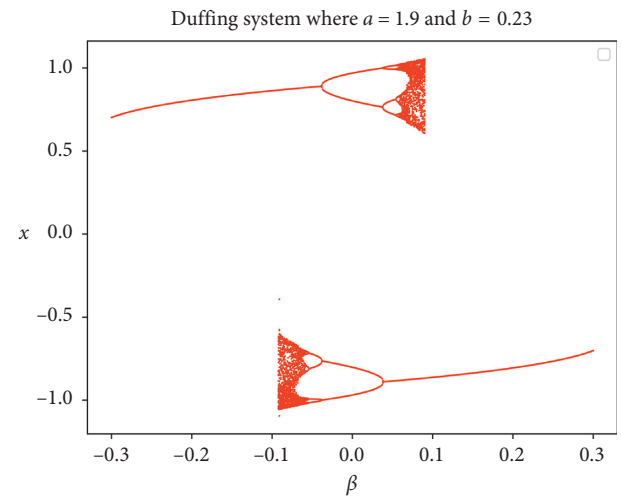


FIGURE 21: Bifurcation diagram of  $\beta$ .

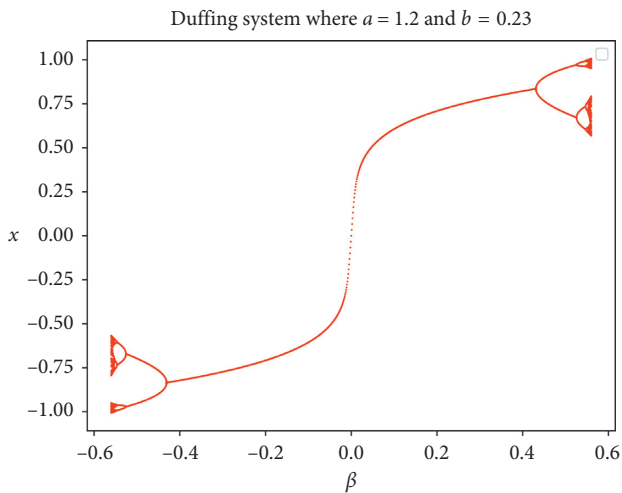


FIGURE 19: Bifurcation diagram of  $\beta$ .

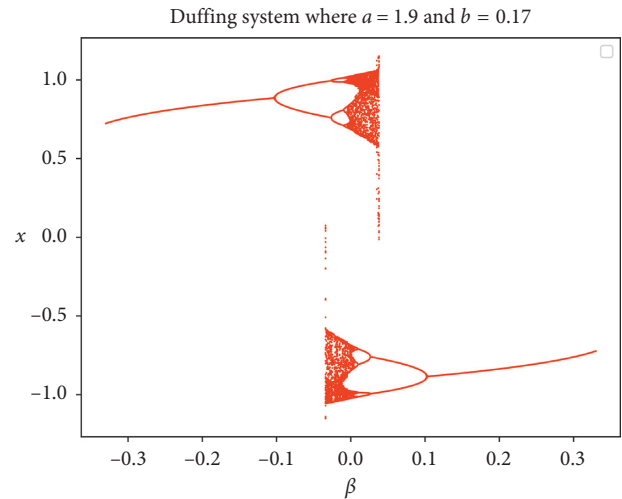


FIGURE 22: Bifurcation diagram of  $\beta$ .

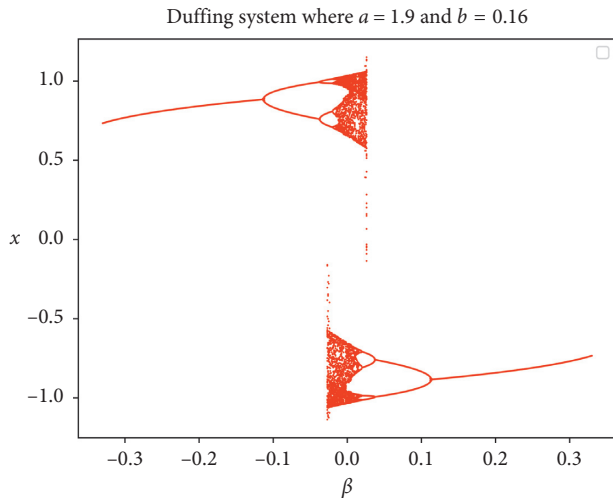


FIGURE 23: Bifurcation diagram of  $\beta$ .

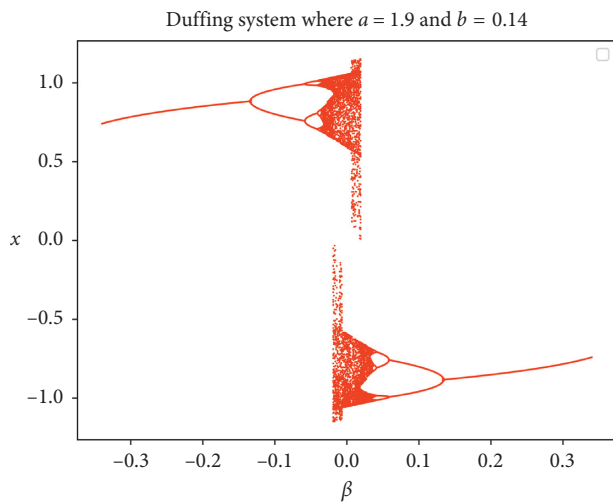


FIGURE 24: Bifurcation diagram of  $\beta$ .

## 7. Conclusion

In this paper, we study the mixed-mode dynamics of a class of oscillators with time-delay modulated amplitude. Combine theoretical analysis and numerical simulation to make time-history graphs and phase diagrams to explain when the natural frequency and excitation frequency are the same or proportional. We use the Melnikov method to explore the influence of threshold parameters on the bifurcation. We also discuss the coupled time-delay Duffing system to illustrate the dynamic behavior when the frequency ratio is irrational. Meanwhile, we analyze the effect of time-delay approximation before and after the delay approximation on the system clustering phenomenon. Finally, we explore the bifurcation behavior of the fast subsystem. The numerical simulation results show that, near the critical value  $\beta_c$ , the chaotic attractor will coexist with multiple periodic orbits or chaos. By studying the bifurcation of stability and multistability of these systems with parameter excitation, these results have certain practicability and interest for the

mathematical modeling of the systems studied in the fields of physics, chemistry, and mechanics. We can also idealize the required systems in more fields.

## Data Availability

The data used to support the findings of this study are included within the article.

## Conflicts of Interest

The authors declare that there are no conflicts of interest regarding the publication of this paper.

## Acknowledgments

The authors gratefully acknowledge the support of the National Natural Science Foundation of China (NNSFC) through grant no. 11572288 and the Natural Science Foundation of Zhejiang through grant no. LY20A020003.

## References

- [1] S. Sadhu, "Canards mixed-mode oscillations in a singularly perturbed two predators-one prey model," *Dynamic Systems and Applications*, vol. 7, pp. 211–219, 2016.
- [2] R. K. Upadhyay, A. Mondal, and W. W. Teka, "Mixed-mode oscillations and synchronous activity in noise induced modified Morris–Lecar neural system," *International Journal of Bifurcation and Chaos*, vol. 27, no. 5, Article ID 1730019, 2017.
- [3] S. L. Kingston and K. Thamilmaran, "Bursting oscillations and mixed-mode oscillations in driven Liénard system," *International Journal of Bifurcation and Chaos*, vol. 27, 2017.
- [4] K. Shimizu, M. Sekikawa, and N. Inaba, "Mixed-mode oscillations and chaos from a simple second-order oscillator under weak periodic perturbation," *Physics Letters A*, vol. 375, no. 14, pp. 1566–1569, 2011.
- [5] S. Y. Inaba, W. Pan, L. S. Yan et al., "Time-delay signature of chaotic vertical-cavity surface-emitting lasers with polarization-rotated optical feedback," *Chinese Physics Letters (English Edition)*, vol. 28, no. 1, Article ID 014203, pp. 98–101, 2011.
- [6] L. Weicker, T. Erneux, O. D. Huys et al., "Slow-fast dynamics of a time-delayed electro-optic oscillator," *Philosophical Transactions of the Royal Society A: Mathematical, Physical and Engineering Sciences*, vol. 371, no. 1999, Article ID 20120459, pp. 1–14, 2013.
- [7] X. P. Porte, C. S. Miguel, and I. Fischer, "Similarity properties in the dynamics of delayed-feedback semiconductor lasers," *Physical Review A*, vol. 89, no. 2, 2014.
- [8] Y.-Q. Sun, M.-S. Jin, H.-W. Song, and J. Xu, "Time-delay identification for vibration systems with multiple feedback," *Acta Mechanica Sinica*, vol. 32, no. 6, pp. 1138–1148, 2016.
- [9] D. Dmitrishin, P. Hagelstein, A. Khamitova, and A. Stokolos, "Limitations of robust stability of a linear delayed feedback control," *SIAM Journal on Control and Optimization*, vol. 56, no. 1, pp. 148–157, 2018.
- [10] P. Khamitova, Q. Lu, and Q. Wang, "Dynamical analysis of bursting oscillations in the Chay-Keizer model with three time scales," *Science China Technological Sciences*, vol. 54, no. 8, pp. 2024–2032, 2011.
- [11] Y. Izumi, H. Asahara, K. Aihara, and T. Kousaka, "Analysis of an interrupted circuit with fast-slow bifurcation," in

- Proceedings of the IEEE Asia Pacific Conference on Circuits and Systems (APCCAS)*, pp. 96–99, Kaohsiung, Taiwan, December 2012.
- [12] H. Yu, J. Wang, Q. Liu, B. Deng, and X. Wei, “Delayed feedback control of bursting synchronization in small-world neuronal networks,” *Neurocomputing*, vol. 99, pp. 178–187, 2013.
  - [13] Y. Yu, H. Tang, X. Han, and Q. Bi, “Bursting mechanism in a time-delayed oscillator with slowly varying external forcing,” *Communications in Nonlinear Science and Numerical Simulation*, vol. 19, no. 4, pp. 1175–1184, 2014.
  - [14] T. W. Cornforth and H. Lipson, “A hybrid evolutionary algorithm for the symbolic modeling of multiple-time-scale dynamical systems,” *Evolutionary Intelligence*, vol. 8, no. 4, pp. 149–164, 2015.
  - [15] X. J. Han, Q. S. Bi, P. Ji, and J. Kurths, “Fast-slow analysis for parametrically and externally excited systems with two slow rationally related excitation frequencies,” *Physical Review E: Statistical, Nonlinear Soft Matter Physics*, vol. 92, no. 1, 2015.
  - [16] X. L. Yang, L. P. Hu, and Z. K. Sun, “Bursting and delay behavior in the Belousov-Zhabotinsky reaction with external excitation,” *European Physical Journal Plus*, vol. 86, no. 3, pp. 1797–1806, 2016.
  - [17] P. Meng, Q. B. Ji, H. X. Wang, and Q. S. Lu, “Bursting and synchronization in a two-compartment model with current-feedback control,” *International Journal of Bifurcation and Chaos*, vol. 26, no. 13, 2016.
  - [18] X. Li, J. Hou, and Y. Shen, “Slow-fast effect and generation mechanism of Brusselator based on coordinate transformation,” *Open Physics*, vol. 14, no. 1, pp. 261–268, 2016.
  - [19] R. D. Zhou, S. Y. Wang, and Q. Wu, “An analysis of bursting oscillations and its experimental confirmation,” *Revista Tecnica De La Facultad De Ingenieria Universidad Del Zulia*, vol. 39, no. 8, pp. 359–364, 2016.
  - [20] X. L. Ding and Y. Y. Li, “Period-adding bifurcation of neural firings induced by inhibitory autapses with time-delay,” *Acta Physica Sinica*, vol. 65, no. 21, 2016.
  - [21] D. Fan and Q. Wang, “Synchronization and bursting transition of the coupled Hindmarsh-Rose systems with asymmetrical time-delays,” *Science China Technological Sciences*, vol. 60, no. 7, pp. 1019–1031, 2016.
  - [22] R. Bertram and J. E. Rubin, “Multi-timescale systems and fast-slow analysis,” *Mathematical Biosciences*, vol. 287, pp. 105–121, 2017.
  - [23] X. Han, Y. Yu, C. Zhang, F. Xia, and Q. Bi, “Turnover of hysteresis determines novel bursting in Duffing system with multiple-frequency external forcings,” *International Journal of Non-Linear Mechanics*, vol. 89, pp. 69–74, 2017.
  - [24] Y. H. Qian and D. M. Yan, “Fast-slow dynamics analysis of a coupled Duffing system with periodic excitation,” *International Journal of Bifurcation and Chaos*, vol. 28, no. 12, Article ID 1850148, 2018.
  - [25] X. J. Han, Y. Zhang, Q. S. Bi, and J. Kurths, “Two novel bursting patterns in the Duffing system with multiple-frequency slow parametric excitations,” *Chaos*, vol. 28, no. 4, Article ID 043111, 2018.
  - [26] Y.-J. Shen, S.-F. Wen, S.-P. Yang, S.-Q. Guo, and L.-R. Li, “Analytical threshold for chaos in a Duffing oscillator with delayed feedbacks,” *International Journal of Non-Linear Mechanics*, vol. 98, pp. 173–179, 2018.
  - [27] Y. Yu, Z. Zhang, and Q. Bi, “Multistability and fast-slow analysis for van der Pol-Duffing oscillator with varying exponential delay feedback factor,” *Applied Mathematical Modelling*, vol. 57, pp. 448–458, 2018.
  - [28] H. Zhang, D. Chen, C. Wu, and X. Wang, “Dynamics analysis of the fast-slow hydro-turbine governing system with different time-scale coupling,” *Communications in Nonlinear Science and Numerical Simulation*, vol. 54, pp. 136–147, 2018.
  - [29] J. P. McKenna and R. Bertram, “Fast-slow analysis of the integrated oscillator model for pancreatic  $\beta$ -cells,” *Journal of Theoretical Biology*, vol. 457, pp. 152–162, 2018.
  - [30] X. Han, Y. Liu, Q. Bi, and J. Kurths, “Frequency-truncation fast-slow analysis for parametrically and externally excited systems with two slow incommensurate excitation frequencies,” *Communications in Nonlinear Science and Numerical Simulation*, vol. 72, pp. 16–25, 2019.
  - [31] Y. Yu and Q. Q. Wang, “Multiple-shaped critical manifold and jump phenomena in low frequency forced vibration with amplitude modulation,” *International Journal of Bifurcation and Chaos*, vol. 20, no. 5, pp. 0218–1274, 2019.
  - [32] C. Y. Zhou, Z. J. Li, and F. Xie, “Bursting oscillation in Sprott B system with multi-frequency slow excitation: two novel Hopf/Hopf-hysteresis-induced bursting and complex AMB rhythms,” *Nonlinear Dynamic*, vol. 97, no. 4, pp. 2700–2811, 2019.
  - [33] Q. Wang, Y. Yu, Z. Zhang, and X. Han, “Melnikov-threshold-triggered mixed-mode oscillations in a family of amplitude-modulated forced oscillator,” *Journal of Low Frequency Noise, Vibration and Active Control*, vol. 38, no. 2, pp. 377–387, 2019.
  - [34] R. H. Plaut and J.-C. Hsieh, “Chaos in a mechanism with time delays under parametric and external excitation,” *Journal of Sound and Vibration*, vol. 114, no. 1, pp. 73–90, 1987.
  - [35] A. Raghobama and S. Narayanan, “Periodic response and chaos in nonlinear systems with parametric excitation and time delay,” *Nonlinear Dynamics*, vol. 27, no. 4, pp. 341–365, 2002.
  - [36] A. Maccari, “The response of a parametrically excited van der Pol oscillator to a time delay state feedback,” *Nonlinear Dynamics*, vol. 26, pp. 105–109, 2001.
  - [37] J. C. Ji and A. Y. T. Leung, “Bifurcation control of a parametrically excited Duffing system,” *Nonlinear Dynamics*, vol. 27, no. 4, pp. 411–417, 2002.
  - [38] E. G. Loukaides, R. W. C. Lewis, and C. R. Bowen, “Additive manufacture of multistable structures,” *Smart Materials and Structures*, vol. 28, no. 2, pp. 0964–1726, 2019.
  - [39] H. Yang and L. Ma, “Multi-stable mechanical metamaterials by elastic buckling instability,” *Materials Science and Engineering*, vol. 54, no. 4, 2019.
  - [40] Y. Huang and J. Xü, “Multiple state-steady motion and chaos in a class of planar autonomous nonlinear system with delayed control,” *Chinese Quarterly of Mechanics*, vol. 26, no. 4, pp. 660–672, 2005.
  - [41] G. Schmitz, S. Anic, Z. Cupic, and L. Kolar-Anic, “The illustration of multistability,” *Journal of Chemical Education*, vol. 77, no. 1, pp. 1502–1505, 2000.
  - [42] Q. Lai, B. Hu, Z.-H. Guan, T. Li, D.-F. Zheng, and Y.-H. Wu, “Multistability and bifurcation in a delayed neural network,” *Neurocomputing*, vol. 207, pp. 785–792, 2016.
  - [43] X. Huang, C. Xu, Y. T. Sun, and Z. G. Zheng, “Multiple synchronous states in a ring of coupled phase oscillators,” *Acta Physica Sinica*, vol. 17, pp. 53–63, 2015.

## Research Article

# Stability and Hopf Bifurcation of Three-Species Prey-Predator System with Time Delays and Allee Effect

F. A. Rihan <sup>1</sup>, H. J. Alsakaji <sup>1</sup> and C. Rajivganthi<sup>2</sup>

<sup>1</sup>Department of Mathematical Sciences, College of Science, United Arab Emirates University, Al-Ain 15551, UAE

<sup>2</sup>School of Applied Mathematics, Getulio Vargas Foundation, Rio de Janeiro, RJ 22250-900, Brazil

Correspondence should be addressed to H. J. Alsakaji; heba.sakaji@uaeu.ac.ae

Received 27 September 2019; Revised 22 December 2019; Accepted 2 January 2020; Published 31 January 2020

Guest Editor: Viet-Thanh Pham

Copyright © 2020 F. A. Rihan et al. This is an open access article distributed under the Creative Commons Attribution License, which permits unrestricted use, distribution, and reproduction in any medium, provided the original work is properly cited.

Allee effect is one of the important factors in ecology, and taking it into account can cause significant impacts in the system dynamics. In this paper, we study the dynamics of a two-prey one-predator system, where the growth of both prey populations is subject to Allee effects, and there is a direct competition between the two-prey species having a common predator. Two discrete time delays  $\tau_1$  and  $\tau_2$  are incorporated into the model to represent reaction time of predators. Sufficient conditions for local stability of positive interior equilibrium and existence of Hopf bifurcations in terms of threshold parameters  $\tau_1^*$  and  $\tau_2^*$  are obtained. A Lyapunov functional is deduced to investigate the global stability of positive interior equilibrium. Sensitivity analysis to evaluate the uncertainty of the state variables to small changes in the Allee parameters is also investigated. Presence of Allee effect and time delays in the model increases the complexity of the model and enriches the dynamics of the system. Some numerical simulations are provided to illustrate the effectiveness of the theoretical results. The model is highly sensitive to small changes in Allee parameters at the early stages and with low population densities, and this sensitivity decreases with time.

## 1. Introduction

The dynamical relationship between prey and their predators has long been and will continue to be one of the dominant themes in ecology due to its universal existence and importance (see, e.g., [1–5]). This relationship/interaction between two or more species has been essential in theoretical ecology since the famous Lotka–Volterra equations [6, 7], which are a system of first order, nonlinear differential equations that describe the dynamics and interactions between two or more species of biological systems. Of course, the qualitative properties of a prey-predator system such as stability of the steady states, bifurcation analysis, and oscillation of the solutions usually depend on the system parameters (see [8]).

Suppose that  $N(t)$  is the size of prey population and  $P(t)$  is the size of the predator population at time  $t$ , then

the Lotka–Volterra model is given by the following equations:

$$\begin{aligned}\frac{dN(t)}{dt} &= N(t)[\beta_1 - \gamma_1 - g_1N(t)] - eN(t)P(t), \\ \frac{dP(t)}{dt} &= P(t)[- \gamma + eN(t)],\end{aligned}\tag{1}$$

with  $N(0) > 0$  and  $P(0) > 0$ . Here,  $\beta_1$  is the per capita maximum filtering rate and  $\gamma_1$  is the death rate of the prey  $N(t)$ , while the parameter  $g_1$  denotes the strength of intraspecific competition. The predator death rate and predation rate are, respectively, denoted by  $\gamma$  and  $e$ . In the above model, it is assumed that prey population is subjected to logistic growth rate and the exponential type functional response.

We should also mention here that one important component of prey-predator relationships is the functional

response of predators to their prey(s)' densities. The response of predators to different prey densities depends on the feeding behavior of individual predators. In [9], Holling discussed three different types of functional responses: Holling type I (linear), type II, and type III, etc. These responses are used to model the phenomena of predation, which captures the usual properties, for instance, positivity and increase (see also [10–13]).

The authors believe that Allee effect and time delays greatly increase the likelihood of local and global extinction and can produce a rich variety of dynamic effects. It is a natural question that how the introduction of Allee effect in the prey growth function changes the system dynamics of the prey-predator system. However, before we introduce the final model, we give brief preliminaries about Allee effects and time delays in the prey-predator model (see [14, 15]).

*1.1. Allee Effect.* Allee effect was firstly reported by the American ecologist Allee [16], when he asked “*what minimal numbers are necessary if a species is to maintain itself in nature?*” Allee, in [16], shows that the growth rate is not always positive for small densities, and it may not be decreasing as in the logistic model either. In general, Allee effect mechanisms arise from cooperation or facilitation among individuals in the species [17]. A population is said to have an Allee effect if the growth rate per capita is initially an increasing function for the low density. It can be classified into two types: strong and weak. A strong Allee effect takes place when the population density is less than the specified threshold population considered, resulting in the species dying out. However, if the population density is greater than the threshold, the growth rate will remain positive [18], while a weak Allee effect means that the per capita growth rate cannot go below zero and remains positive.

Now, we show how an Allee effect can be modelled, and how the per capita growth rate is affected with a weak Allee effect or a strong Allee effect throughout the simple examples:  $(dN/dt) = rN^2(1 - (N/K))$  for a weak Allee effect and  $(dN/dt) = rN(1 - (N/K))((N/A) - 1)$  for a strong Allee effect.

Figure 1 shows a per capita growth rate  $(1/N)(dN/dt)$  of the population with strong and weak Allee effects. The straight line shows the logistic growth, and the red curve displays a weak Allee effect, while the blue curve shows a strong Allee effect. The negative density dependence at low population sizes is described as a strong Allee effect, where there exists a threshold population level  $A$ , such that for  $N < A$ ,  $(1/N)(dN/dt) < 0$  (the species will die out) and for  $N > A$ ,  $(1/N)(dN/dt) > 0$ , the growth will remain positive [18]. However, when the growth rate remains positive at low population densities, it is considered as a weak Allee effect.

For multispecies models, there are flexible ways to formulate the Allee effects. For example, due to difficulties in finding mates when prey population density becomes low, Allee effect takes place in prey species. Herein, we propose and incorporate an additive Allee effect of the form  $b(N) \equiv (N/\alpha_1 + N)$  in the prey growth function of model

(1), which is considered as the probability of finding a mate (see [19]), so that

$$\begin{aligned} \frac{dN(t)}{dt} &= N(t) \left[ \frac{\beta_1 N(t)}{\alpha_1 + N(t)} - \gamma_1 - gN(t) \right] - eN(t)P(t), \\ \frac{dP(t)}{dt} &= P(t)[- \gamma + eN(t)]. \end{aligned} \quad (2)$$

The parameter  $\alpha_1$  is the strength of Allee effect,  $\alpha_1 = 1/R$ , where  $R$  is the average area that can be searched by an individual [20]. We may notice that  $b(0) = 0$  and  $b'(N) > 0$  if  $N \in [0, \infty)$ , i.e., Allee effect decreases as density increases, and  $\lim_{N \rightarrow \infty} b(N) = 1$  means that Allee effect disappears at high densities. Therefore, the term  $b(N)$  is considered as a weak Allee effect function in a rectangular hyperbola form, known as Michaelis–Menten-like function [21].

*1.2. Time Delays.* Usually, the individuals of the prey and predator species usually pass through various life stages during their entire life span and the involved morphology differs from one stage to another. Construction of delay differential equation models is a well-known modelling strategy to take care of the stage-specific activities which are responsible for significant change in the dynamics of interacting populations. In various existing literature studies, the biological processes like incubation, gestation, maturation, and reaction time, are taken care of by introducing relevant time-delay parameters to the models for prey predator and other types of interacting populations. Incorporating time lags (or time delays) in biological models makes the systems much more realistic, as it can destabilize the equilibrium points and give rise to a stable limit cycle, causing oscillations to grow and enriching the dynamics of the model. Time delays have been considered and extremely studied by many authors in prey-predator models and biological systems (see [21–25]).

Motivation to what we mentioned above, it is interesting and important to study the impact of time delays and Allee effect on the dynamics of three-species prey-predator models. In this paper, we extend the work in [26] and study the dynamics of a two-prey one-predator system, where the growth of both prey populations is subject to Allee effects, and there exists a direct competition between the two-prey species having a common predator. Two discrete time delays  $\tau_1$  and  $\tau_2$  are incorporated into the predator growth equation to represent the reaction time with each prey. Sensitivity analysis to evaluate the uncertainty of the state variables to small changes in the Allee parameters is also considered.

The rest of this paper is organized as follows: Model formulation is presented in Section 2. Local stability and bifurcation analysis of the steady states are discussed in Section 3, and global asymptotic stability of interior steady state is discussed in Section 4. We also utilize sensitivity functions to evaluate the sensitivity (uncertainty) of the state variables (preys and predator populations) to small changes in the severity Allee parameters through Section 5. Some numerical simulations are presented in Section 6 to show the effectiveness of the theoretical results. Finally, Section 7



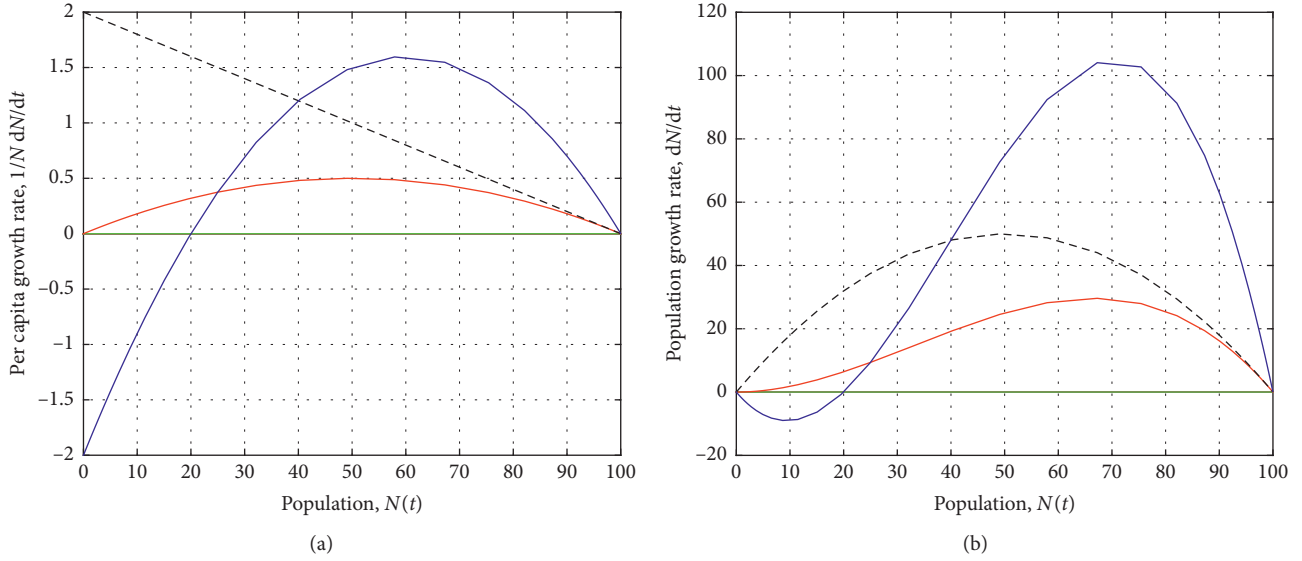


FIGURE 1: (a) The per-capita growth rate  $(1/N)(dN/dt)$  vs. population  $N(t)$  with logistic (black dashes), strong (blue curve), and weak (red curve) Allee effects. (b) The population growth rate  $(dN/dt)$  vs. population  $N(t)$ . For the strong Allee effect, the y-intercept of the per capita growth rate is less than zero at zero density, while in weak Allee effect, the y-intercept cannot go below zero.

concludes the study with a summary of the reported findings and future recommendations.

## 2. Delayed Model with Allee Effect for the Two-Prey One-Predator System

Many studies have been done on multispecies prey-predator systems, including local and global bifurcations and different types of chaos (see, e.g., [26–29]). Sen et al. [26] discussed the Allee effect on two-preys' growth function, where the predator is generalized. They explained how the Allee effect can suppress the chaotic dynamics and the route to chaos in prey growth by comparing it with a model without the Allee effect. In [27], the authors studied dynamics of three species (two preys and one predator) delayed prey-predator model with cooperation among the preys against predation. The growth rate for preys is thought to be logistic. Delays are taken just in the growth components for each of the species. Takeuchi and Adachi [28] considered two preys with logistic growth rates and an exponential functional response, where the predator survives on two-prey populations. Their results showed that the apparent chaotic behavior is a result of the periodic solution when one of the two-prey has greater competitive strength than the other. Song and Li [29] explored the dynamic behaviors of a Holling II two-prey one-predator system by introducing constant periodic releases of predators through periodically spraying a pesticide on the prey. They were then able to show that the system remains permanent under certain conditions.

Herein, we generalize model (2) to a multispecies prey-predator system (two-preys one-predator). The model consists of two teams of preys with densities  $x(t)$  and  $y(t)$ , interacting with one team of predator with density  $z(t)$ . We also incorporate Allee effects in the growth functions of the

two-prey populations, and there exists a direct competition between the two-prey species having a common predator.

The model takes the general form:

$$\begin{aligned} \frac{dx(t)}{dt} &= x(t) \left[ \frac{\beta_1 x(t)}{\alpha_1 + x(t)} - \gamma_1 - g_1 x(t) \right] \\ &\quad - \alpha x(t)y(t) - ex(t)z(t), \\ \frac{dy(t)}{dt} &= y(t) \left[ \frac{\beta_2 y(t)}{\alpha_2 + y(t)} - \gamma_2 - g_2 y(t) \right] - \beta x(t)y(t) \\ &\quad - \frac{\delta y(t)z(t)}{1 + cy(t)}, \\ \frac{dz(t)}{dt} &= -\beta_3 z(t) + \varepsilon ex(t - \tau_1)z(t - \tau_1) \\ &\quad + \frac{\varepsilon \delta y(t - \tau_2)z(t - \tau_2)}{1 + cy(t - \tau_2)}, \end{aligned} \quad (3)$$

with initial conditions

$$\begin{aligned} x(\theta) &= \phi_1(\theta) > 0, \\ y(\theta) &= \phi_2(\theta) > 0, \\ z(\theta) &= \phi_3(\theta) > 0, \\ \theta &\in [-\tau, 0], \\ \tau &= \max\{\tau_1, \tau_2\}. \end{aligned} \quad (4)$$

Here,  $\phi_i(\theta)$  ( $i = 1, 2, 3$ ) are smooth initial functions. The coefficients  $\alpha$  and  $\beta$  represent the coefficients of competition of two preys  $x$  and  $y$ , in the absence of predator. The description of rest of model parameters along with their symbols is presented in Table 1.



TABLE 1: One biological meaning for the parameters of model (3).

Parameter	Description
$\alpha_1, \alpha_2$	Strength of Allee effect
$\beta_1, \beta_2$	Per capita maximum filtering rate of population
$g_1, g_2$	Strength of intracompetition
$\gamma_1, \gamma_2$	Death rate for preys
$\alpha, \beta$	Coefficient of competition
$e, \delta$	Decrease rate of $x(t)$ and $y(t)$ due to predation by $z(t)$
$\beta_3$	Predator death rate
$c$	Magnitude of interference between the second type of prey
$\epsilon$	An equal transformation rate of predator to preys $x(t)$ and $y(t)$

It is reasonable to assume that the death (predation) of preys is instantaneous when attacked by their predator but their contribution to the growth of predator population must be delayed by some time delay. Therefore, we incorporated two discrete time delays  $\tau_1$  and  $\tau_2$  in the reaction response functionals in the predator growth to represent the reaction time. The interaction between first species of prey and predator is assumed to be governed by Holling type I. While the interaction between the second species of prey and predator is assumed to be governed by Holling type II (cyrtoid functional)  $\delta y(t)z(t)/(1 + cy(t))$ , response indicates that it is a hard-to-capture prey compared to the first species (see Figure 2).

To investigate the role of time delay and Allee effect on the dynamics of the system, we first discuss the boundedness and positivity of the solutions of system (3) with the given positive initial conditions (4).

**2.1. Positivity and Boundedness of the Solution.** The positivity of the solutions indicates the existence of the population, while the boundedness explains the natural control of growth due to the restriction of resources. We arrive at the following lemma.

**Lemma 1.** *Every solution of system (3) corresponding to initial conditions (4) defined on  $[0, \infty)$  remains positive for all  $t \geq 0$ , which satisfies*

$$\begin{aligned} \limsup_{t \rightarrow \infty} (x(t) + y(t)) &\leq \kappa, \\ \limsup_{t \rightarrow \infty} z(t) &\leq N, \end{aligned} \quad (5)$$

where  $\kappa = \min\{\beta_1, \beta_2\}$  and  $N > 0$ .

*Proof.* Model (3) can be represented in a matrix form

$$\dot{U}(t) = F(U), \quad (6)$$

where  $U = (x, y, z)^T \in \mathbb{R}^3$  and

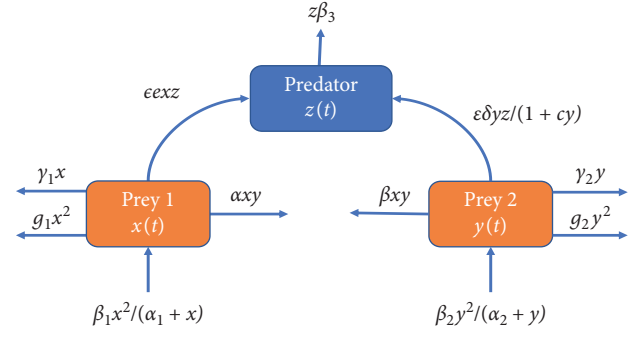


FIGURE 2: Mathematic scheme of the three-species predator-prey system (3).

$$F(U) = \begin{bmatrix} F_1(U) \\ F_2(U) \\ F_3(U) \end{bmatrix} = \begin{bmatrix} x \left( \frac{\beta_1 x}{\alpha_1 + x} - \gamma_1 - g_1 x \right) - \alpha xy - \epsilon xz \\ y \left( \frac{\beta_2 y}{\alpha_2 + y} - \gamma_2 - g_2 y \right) - \beta xy - \frac{\delta yz}{1 + cy} \\ -\beta_3 z + \epsilon xz(t - \tau_1)z(t - \tau_1) \\ + \frac{\epsilon \delta y(t - \tau_2)z(t - \tau_2)}{1 + cy(t - \tau_2)} \end{bmatrix}. \quad (7)$$

Let  $\mathbb{R}_+^3 = [0, \infty)^3$ , since the right-hand side of system (3) is locally Lipschitz on  $C: \mathbb{R}_+^{3+1} \rightarrow \mathbb{R}^3$ , such that  $F_i(U)|_{u_i(t)=0, U \in \mathbb{R}_+^3} \geq 0$ , where  $u_1 = x$ ,  $u_2 = y$ , and  $u_3 = z$ . According to [30], the solutions of (6) with initial conditions (4) exist uniquely on the interval  $[0, \xi)$ , where  $0 < \xi \leq \infty$ ; therefore, all solutions exist on the first quadrant of the  $xy$  plane.

To prove the boundedness of solutions for system (3), let us first consider the case when the predator is absent, so that

$$\frac{dx}{dt} = x \left( \frac{\beta_1 x}{\alpha_1 + x} - \gamma_1 - g_1 x \right) - \alpha xy \equiv G_1(x, y), \quad (8)$$

$$\frac{dy}{dt} = y \left( \frac{\beta_2 y}{\alpha_2 + y} - \gamma_2 - g_2 y \right) - \beta xy \equiv G_2(x, y),$$

with initial conditions  $x(0) > 0$  and  $y(0) > 0$ ; we can easily show that  $G_1(x, y) \geq 0$  for  $y = 0$  and  $x < (\beta_1 - \gamma_1)/g_1$ , such that  $\beta_1 > \gamma_1$  and  $G_2(x, y) \geq 0$  for  $x = 0$  and  $y < (\beta_2 - \gamma_2)/g_2$ , where  $\beta_2 > \gamma_2$ . Adding the two equations of (8) yields

$$\begin{aligned} \frac{d}{dt} (x + y) &= x \left( \frac{\beta_1 x}{\alpha_1 + x} - \gamma_1 - g_1 x \right) + y \left( \frac{\beta_2 y}{\alpha_2 + y} - \gamma_2 - g_2 y \right) \\ &\quad - xy(\alpha + \beta) \\ &\leq x(\beta_1 - \gamma_1 - g_1 x) + y(\beta_2 - \gamma_2 - g_2 y) \\ &\leq \beta_1 x + \beta_2 y \leq \kappa(x + y), \end{aligned} \quad (9)$$

where  $\kappa = \min\{\beta_1, \beta_2\}$ . If we integrate both sides of (9), we get

$$(x(t) + y(t)) \leq (x(0) + y(0))e^{-\kappa t}. \quad (10)$$

Since  $(x(0) + y(0)) > 0$ , the solutions are bounded, which clearly shows that  $\lim_{t \rightarrow \infty} \sup (x(t) + y(t)) \leq \kappa$ .

To extend the analysis to (3), let us consider  $0 < \phi_1(\theta) + \phi_2(\theta) + \phi_3(0) < M$ ,  $\theta \in [-\tau, 0]$ . Also assume that  $W(t) = \varepsilon x(t - \tau_1) + \varepsilon \delta y(t - \tau_2) + z$  and choose  $0 < \rho < \beta_3$ . By considering the derivative of  $W$ , for  $t > T + \tau$  for some fixed positive time  $T$ , we have

$$\begin{aligned} \frac{dW}{dt} + \rho W &\leq \varepsilon x(t - \tau_1)(\beta_1 + \rho - x(t - \tau_1)) \\ &+ \varepsilon \delta y(t - \tau_2)(\beta_2 + \rho - y(t - \tau_2)) + (\rho - \beta_3)z. \end{aligned} \quad (11)$$

Since  $x$  and  $y$  are nonnegative and bounded by  $\kappa$ ,

$$\frac{dW}{dt} + \rho W \leq (\varepsilon + \varepsilon \delta)\kappa + (\rho - \beta_3)z \leq M. \quad (12)$$

Due to the positivity of  $z$  and since the parametric condition exists for  $\rho$ , the differential inequality is bounded above, such that  $(dW/dt) \leq M - \rho W$ , i.e., there exists  $N$  where  $0 < W(t) < N$  for all  $t > T$ , which implies the boundedness of  $z$ , such that  $\lim_{t \rightarrow \infty} \sup z(t) \leq N$ .  $\square$

### 3. Local Stability and Hopf Bifurcation

In this section, we investigate the qualitative behaviour of system (3) by studying the local stability of positive equilibrium points and Hopf bifurcation analysis, which provides a deeper insight into the model to address the behavioral change of solutions as a response to changes in a particular parameter. Since time lags  $\tau_1$  and  $\tau_2$  have a significant impact in the complexity and dynamics of the model, we consider them as bifurcation parameters.

**3.1. Existence of Interior Equilibrium Points.** System (3) has some boundary and interior equilibrium points. However, we only focus on the dynamic analysis of interior equilibrium points. In order to obtain the attainable equilibrium points for system (3), the zero growth isoclines of the system are given by  $x((\beta_1 x / (\alpha_1 + x)) - \gamma_1 - g_1 x) - \alpha x y - \varepsilon x z = 0$ ,  $y((\beta_2 y / (\alpha_2 + y)) - \gamma_2 - g_2 y) - \beta x y - (\delta y z / (1 + c y)) = 0$ , and  $-\beta_3 z + \varepsilon \varepsilon x z + (\varepsilon \delta y z / (1 + c y)) = 0$ , in  $\mathbb{R}_+^3 = \{(x, y, z) \in \mathbb{R}^3: x, y, z \geq 0\}$ . Therefore, the equilibria are the points of intersection of these zero growth isoclines regardless of the parameter values.

An interior equilibrium point  $\mathcal{E}^* \equiv (x^*, y^*, z^*)$  exists with  $((\beta_1 x^* / (\alpha_1 + x^*)) - \gamma_1 - g_1 x^*) - \alpha y^* - \varepsilon z^* = 0$ ,  $((\beta_2 y^* / (\alpha_2 + y^*)) - \gamma_2 - g_2 y^*) - \beta x^* - (\delta z^* / (1 + c y^*)) = 0$ , and  $-\beta_3 z^* + \varepsilon \varepsilon x^* + (\varepsilon \delta y^* / (1 + c y^*)) = 0$  such that  $x^* = (1/\varepsilon e)(\beta_3 - (\varepsilon \delta y^* / (1 + c y^*))) > 0$  and  $z^* = (1/e)((\beta_1(\beta_3(1 + c y^*) - \varepsilon \delta y^*) / (1 + c y^*)(\varepsilon e + \beta_3)) + g_1(\beta_3 - (\varepsilon \delta y^* / (1 + c y^*))) - \gamma_1 - \alpha y^*) > 0$ , where  $y^*$  is the root(s) the following equation:

$$G(y) = \sigma_1 y^4 + \sigma_2 y^3 + \sigma_3 y^2 + \sigma_4 y + \sigma_5 = 0. \quad (13)$$

The coefficients  $\sigma_i$ ,  $i = 1, \dots, 5$ , are defined by

$$\begin{aligned} \sigma_1 &= \alpha_2 c^2, \\ \sigma_2 &= c \left( 2\alpha_2 + \alpha_2 c g_2 + \frac{\beta \beta_2 c}{\varepsilon e} - \frac{\beta \delta}{e} - \delta \alpha + c \gamma_2 \right), \\ \sigma_3 &= \frac{\beta_1 \delta^2 \varepsilon - c \delta \beta_1 \beta_2}{\varepsilon e + \beta_3} + \frac{\alpha_2 \beta \delta \varepsilon c - \beta \beta_2 \alpha_2 c^2 - \beta \delta \varepsilon}{\varepsilon e} \\ &\quad - \delta^2 \varepsilon g_1 + c \beta_2 + c^2 \beta_2 + c g_1 \delta \beta_3 + c \delta \gamma_1 + \alpha_2 - \delta \alpha, \\ \sigma_4 &= \frac{\beta \beta_2 - \alpha_2 \beta \delta \varepsilon}{\varepsilon e} + \frac{\delta \beta_1 \beta_2 + c \delta \beta_1 \beta_3 \alpha_2 + \beta_1 \alpha_2 \delta^2}{\varepsilon e + \beta_3} \\ &\quad - g_1 \alpha_2 \delta^2 \varepsilon + c \alpha_2 \delta \beta_3 g_1 + c \alpha_2 \delta \gamma_1 + c \alpha_2 \gamma_2 - \beta_2 - \beta_2 c \\ &\quad + \alpha_2 g_2 - \delta \beta_2 g_1 - \delta \gamma_1 + \gamma_2, \\ \sigma_5 &= \frac{\delta \beta_1 \beta_3 \alpha_2}{\varepsilon e + \beta_3} - \frac{\alpha_2 \beta_2 \beta}{\varepsilon e} - \alpha_2 \delta \beta_3 g_1 - \alpha_2 \delta \gamma_1 + \alpha_2 \gamma_2. \end{aligned} \quad (14)$$

The nature of the roots for (13) is determined by noting the sign of its discriminant [31]. Therefore, a sufficient condition that guarantees that (13) has at least one positive root is  $\sigma_5 < 0$ , which leads to  $(\delta \beta_1 \beta_3 \alpha_2 / (\varepsilon e + \beta_3)) + \alpha_2 \gamma_2 < (\alpha_2 \beta_2 \beta / \varepsilon e) + \alpha_2 \delta \beta_3 g_1 + \alpha_2 \delta \gamma_1$ . Thus, system (3) can have at most four interior equilibria in the presence of the Allee effect. However, in the absence of Allee effect, we arrive at the following remark.

*Remark 1.* In the absence of the Allee effect ( $\alpha_1 = \alpha_2 = 0$ ), the interior equilibria for system (3) are reduced to at most three interior equilibria. Consequently, Allee effect can generate or eradicate interior equilibria. It may stabilize or destabilize the system.

**3.1.1. Existence of Bistability.** The phenomenon of bistability has been recognized experimentally in some biological situations but much more commonly in theoretical models, such as the dynamics of animal populations [32]. The co-existence between two stable attractors can be determined by increasing or decreasing the value of some control parameters. Therefore, the system pursues one branch of equilibrium points when increasing a control parameter until a threshold limit point is reached at which the system jumps to another branch of stable equilibrium points. Bistability occurs when the system can converge to two different equilibrium points, depending on the variation of the initial conditions in the same parametric region. Or the system is able to evolve into either one of two equilibrium points by increasing or decreasing the level of one of the system's parameters.

The underlying model (3) displays bistability of two interior equilibria, which is based on the variation of the coefficient of competition  $\alpha$  (see Figure 3). Both equilibria are locally asymptotically stable.

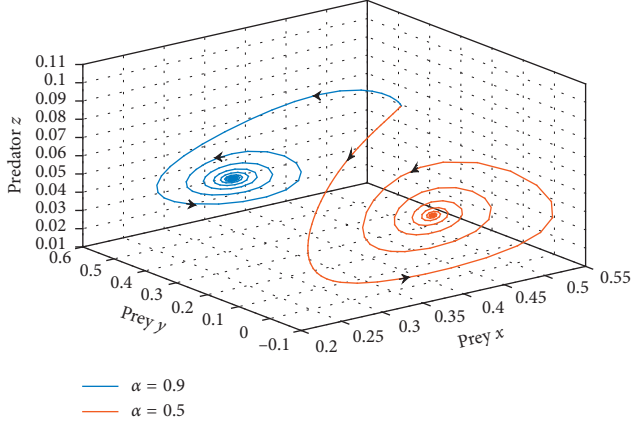


FIGURE 3: Bistability of two interior equilibria for the delayed system (3), with  $\alpha = 0.9$  and  $\alpha = 0.5$ . Both equilibria are locally asymptotically stable; other parameter values are given in (45).

3.2. *Stability and Bifurcation Analysis of the Interior Equilibrium  $\mathcal{E}^*$ .* Now, we study the stability of the interior equilibrium  $\mathcal{E}^* \equiv (x^*, y^*, z^*)$ , at which the Jacobian matrix is

$$J = \begin{bmatrix} F_1 & F_2 & F_3 \\ F_4 & F_5 & F_6 \\ I_1 e^{-\lambda\tau_1} & I_2 e^{-\lambda\tau_2} & F_7 + I_3 e^{-\lambda\tau_1} + I_4 e^{-\lambda\tau_2} \end{bmatrix}. \quad (15)$$

Here,

$$\begin{aligned} F_1 &= \frac{\beta_1 x^*}{(\alpha_1 + x^*)} \left( 1 + \frac{\alpha_1}{(\alpha_1 + x^*)} \right) - 2g_1 x^* - \gamma_1 \\ &\quad - \alpha y^* - ez^* < 0, \\ F_2 &= -\alpha x^*, \\ F_3 &= -ex^*, \\ F_4 &= -\beta y^*, \\ F_5 &= \frac{\beta_2 y^*}{(\alpha_2 + y^*)} \left( 1 + \frac{\alpha_2}{(\alpha_2 + y^*)} \right) - 2g_2 y^* - \gamma_2 \\ &\quad - \beta x^* - \frac{\delta z^*}{(1 + cy^*)^2} < 0, \\ F_6 &= -\frac{\delta y^*}{1 + cy^*}, F_7 = -\beta_3, \\ I_1 &= \epsilon ez^*, \\ I_2 &= \frac{\epsilon \delta z^*}{(1 + cy^*)^2}, \\ I_3 &= \epsilon ex^*, \\ I_4 &= \frac{\epsilon \delta y^*}{1 + cy^*}. \end{aligned} \quad (16)$$

The characteristic equation for the interior point  $\mathcal{E}^* \equiv (x^*, y^*, z^*)$  is then given by

$$A(\lambda) + B(\lambda)e^{-\lambda\tau_1} + C(\lambda)e^{-\lambda\tau_2} = 0. \quad (17)$$

Here,

$$\begin{aligned} A(\lambda) &= \lambda^3 + R_1 \lambda^2 + R_2 \lambda + R_3, \\ B(\lambda) &= N_1 \lambda^2 + N_2 \lambda + N_3, \\ C(\lambda) &= M_1 \lambda^2 + M_2 \lambda + M_3, \end{aligned} \quad (18)$$

such that

$$\begin{aligned} R_1 &= -F_1 - F_5 - F_7, \\ R_2 &= F_1 F_5 + F_1 F_7 + F_5 F_7 - F_2 F_4, \\ R_3 &= F_2 F_4 F_7 - F_1 F_5 F_7, \\ N_1 &= -I_3, \\ N_2 &= (F_1 + F_5)I_3 - F_3 I_1, \\ N_3 &= F_2 F_4 I_3 + F_3 F_5 I_1 - F_2 F_6 I_1 - F_1 F_5 I_3, \\ M_1 &= -I_4, \\ M_2 &= (F_1 + F_5)I_4 - F_6 I_2, \\ M_3 &= F_2 F_4 I_4 + F_1 F_6 I_2 - F_3 F_4 I_2 - F_1 F_5 I_4. \end{aligned} \quad (19)$$

To gain insight regarding interior equilibrium  $\mathcal{E}^*$ , we discuss the stability of interior steady states and Hopf bifurcation conditions of the threshold parameters  $\tau_1$  and  $\tau_2$  by considering the following different cases.

*Case 1.* When  $\tau_1 = \tau_2 = 0$ , equation (17) becomes

$$\begin{aligned} \lambda^3 + (R_1 + N_1 + M_1)\lambda^2 + (R_2 + N_2 + M_2)\lambda \\ + (R_3 + N_3 + M_3) = 0. \end{aligned} \quad (20)$$

Therefore, the interior equilibrium  $\mathcal{E}^*$  is locally asymptotically stable if

(i)  $(H_1)R_1 + N_1 + M_1 > 0$ ,  $R_3 + N_3 + M_3 > 0$  and  $(R_1 + N_1 + M_1)(R_2 + N_2 + M_2) > R_3 + N_3 + M_3$  holds

Thus, based on Routh–Hurwitz Criteria, all the roots of (20) have negative real parts.

*Case 2.* For  $\tau_1 = 0$ ,  $\tau_2 > 0$ , then equation (17) becomes

$$\begin{aligned} \lambda^3 + (R_1 + N_1)\lambda^2 + (R_2 + N_2)\lambda + (R_3 + N_3) \\ + (M_1 \lambda^2 + M_2 \lambda + M_3)e^{-\lambda\tau_2} = 0. \end{aligned} \quad (21)$$

We assume for some values of  $(\tau_2 > 0)$ , there exists a real number  $\omega$  such that  $\lambda = i\omega$  is a root of (21); then, we get

$$\begin{aligned} -(R_1 + M_1)\omega^2 + (R_3 + N_3) \\ = (M_1 \omega^2 - M_3)\cos \omega\tau_2 - M_2 \omega \sin \omega\tau_2, \\ -\omega^3 + (R_2 + N_2)\omega \\ = (M_3 - M_1 \omega^2)\sin \omega\tau_2 - M_2 \omega \cos \omega\tau_2. \end{aligned} \quad (22)$$

Squaring and adding both of the equations yield

$$\omega^6 + a_1\omega^4 + a_2\omega^2 + a_3 = 0, \quad (23)$$

where

$$\begin{aligned} a_1 &= (R_1 + M_1)^2 - 2(R_2 + N_2) - M_1^2, \\ a_2 &= (R_2 + N_2)^2 - 2(R_1 + M_1)(R_3 + N_3) + 2M_1M_3 - M_2^2, \\ a_3 &= (R_3 + N_3)^2 - M_3^2. \end{aligned} \quad (24)$$

By Descartes' rule of signs, equation (22) has at least one positive root  $\omega_1$  if

$$(i) \quad (H_2)R_1^2 + 2R_1M_1 > 2(R_2 + N_2) \text{ and } (R_3 + N_3)^2 < M_3^2 \text{ holds}$$

Eliminating  $\sin \omega_1 \tau_2$  from (22) yields

$$\tau_{2,j} = \frac{1}{\omega_1} \arccos \left[ \frac{((R_3 + N_3) - (R_1 + N_1)\omega_1^2)(M_1\omega_1^2 - M_3) + M_2(R_2 + N_2)\omega_1^2 - M_2\omega_1^4}{(M_3 - M_1\omega_1^2)^2 - (M_2\omega_1)^2} \right] + \frac{2j\pi}{\omega_1}, \quad (25)$$

where  $j = 0, 1, 2, \dots$

By differentiating (21) with respect to  $\tau_2$  such that  $\omega = \omega_1$  and  $\tau_2 = \tau_{2,j}$ , the transversality condition can be obtained in this form:

$$\Re e \left( \frac{d\lambda}{d\tau_2} \right)^{-1} = \frac{A_1A_4 - A_2A_3}{A_2A_4}. \quad (26)$$

Here,

$$\begin{aligned} A_1 &= [(R_2 + N_2) - 3\omega_1^2][(R_2 + N_2)\omega_1^2 - \omega_1^4] \\ &\quad + 2(R_1 + N_1)\omega_1[(R_3 + N_3)\omega_1 - (R_1 + N_1)\omega_1^3], \\ A_2 &= (\omega_1^4 - (R_2 + N_2)\omega_1^2)^2 + ((R_3 + N_3)\omega_1 - (R_1 + N_1)\omega_1^3)^2, \\ A_3 &= M_2^2\omega_1^2 + 2(M_1\omega_1^3 - M_3\omega_1)M_1\omega_1, \\ A_4 &= (M_2\omega_1^2)^2 + (M_3\omega_1 - M_1\omega_1^3)^2. \end{aligned} \quad (27)$$

Then, a Hopf bifurcation occurs for  $\tau_2$  if  $\Re e(d\lambda/d\tau_2)^{-1} > 0$ ; i.e.,  $A_1A_4 > A_2A_3$ . We arrive at the following theorem.

**Theorem 1.** *Let  $(H_1)$  and  $(H_2)$  hold, where  $\tau_1 = 0$ ; then, there exists  $\tau_2 > 0$  such that  $\mathcal{E}^*$  remains stable for  $\tau_2 < \tau_2'$  and unstable for  $\tau_2 > \tau_2'$ , where  $\tau_2' = \min\{\tau_{2,j}\}$  defined by (25). Moreover, system (3) undergoes a Hopf bifurcation at  $\mathcal{E}^*$  when  $\tau_2 = \tau_2'$ .*

*Case 3.* When  $\tau_2 = 0$  and  $\tau_1 > 0$ , in the same manner of the pervious case, we arrive at the following theorem.

**Theorem 2.** *For system (3), with  $\tau_2 = 0$ , there exists a positive number  $\tau_1$ , such that the equilibrium point  $\mathcal{E}^*$  is locally asymptotically stable for  $\tau_1 < \tau_1'$  and unstable for  $\tau_1 > \tau_1'$ , where  $\tau_1' = \min\{\tau_{1,j}\}$ . Furthermore, Hopf bifurcation occurs at  $\tau_1 = \tau_1'$ .*

$$\tau_{1,j} = \frac{1}{\omega_0} \arccos \left[ \frac{((R_3 + M_3) - (R_1 + M_1)\omega_2^2)(N_1\omega_2^2 - N_3) - N_2(R_2 + M_2)\omega_2^2 + N_2\omega_2^4}{(N_1\omega_2^2 - N_3)^2 + (N_2\omega_2)^2} \right] + \frac{2j\pi}{\omega_2}, \quad (28)$$

where  $j = 0, 1, 2, \dots$

*Case 4.* When  $\tau_1 > 0$  and  $\tau_2 > 0$ , we assume that  $\tau_1$  as a variable parameter and  $\tau_2$  as fixed on its stable interval. Let  $\lambda = iw$  as a root of (17); separating real and imaginary parts implies

$$\begin{aligned} -w^3 + R_2w + (M_1w^2 - M_3)\sin w\tau_2 + M_2w \cos w\tau_2 \\ = (N_3 - N_1w^2)\sin w\tau_1 - N_2w \cos w\tau_1, \end{aligned} \quad (29)$$

$$\begin{aligned} -R_1w^2 + R_3 + (M_3 - M_1w^2)\cos w\tau_2 + M_2w \sin w\tau_2 \\ = (N_1w^2 - N_3)\cos w\tau_1 - N_2w \sin w\tau_1. \end{aligned} \quad (30)$$

Thus, eliminating the trigonometric functions ( $\sin \omega\tau_1$  and  $\cos \omega\tau_1$ ) from (29) and (30) yields

$$\omega^6 + \xi_4\omega^5 + \xi_3\omega^4 + \xi_2\omega^3 + \xi_1\omega^2 + \xi_0 = 0, \quad (31)$$

where

$$\begin{aligned} \xi_4 &= -2M_1 \sin w\tau_2, \\ \xi_3 &= R_1 + M_1^2 - 2R_2 - N_1^2 - 2M_2 \cos w\tau_2, \\ \xi_2 &= 2(M_1R_2 + M_3)\sin w\tau_2 - 2M_3R_1 \cos w\tau_2, \\ \xi_1 &= -2M_3R_2 \sin w\tau_2, \\ \xi_0 &= R_3^2 + M_3^2 - N_3^2 + (2M_3R_3 + R_1M_1)\cos w\tau_2. \end{aligned} \quad (32)$$

Equation (31) is a preternatural equation in a complicated form; it is quite difficult to predict the nature of its roots. Thus, by applying Descartes rule of signs, we can say that (31) has at least one positive root  $\omega_0$  if

(i)  $(H_3)\xi_4 > 0$  since  $M_1 < 0$  and  $\xi_0 < 0$ ; therefore, we have

$$\tau_{1,j} = \frac{1}{\omega_0} \arccos \left[ \frac{AD + CB}{A^2 + C^2} \right] + \frac{2j\pi}{\omega_0}, \quad j = 0, 1, 2, \dots \quad (33)$$

Here,

$$\begin{aligned} A &= N_1 w_0^2 - N_3, \\ B &= -w_0^3 + R_2 w_0 + (M_3 - M_1 w_0^2) \sin w_0 \tau_2 + \cos w_0 \tau_2, \\ C &= N_2 w_0, \\ D &= -R_1 w_0^2 + R_3 + (M_1 w_0^2 - M_3) \cos w_0 \tau_2 \\ &\quad + M_2 w_0 \sin w_0 \tau_2. \end{aligned} \quad (34)$$

To study the Hopf bifurcation analysis, we fix  $\tau_2$  in its stable interval and differentiate equations (29) and (30) with respect to  $\tau_1$ . Then, substitute  $\tau_1 = \tau_{1,0}$  and  $w = w_0$ , we have

$$Q_2 \left( \frac{d(\Re \lambda)}{d\tau_1} \Big|_{\tau_1 = \tau_{1,0}} \right) + Q_1 \left( \frac{d(w)}{d\tau_1} \Big|_{\tau_1 = \tau_{1,0}} \right) = Q_3, \quad (35)$$

$$-Q_1 \left( \frac{d(\Re \lambda)}{d\tau_1} \Big|_{\tau_1 = \tau_{1,0}} \right) + Q_2 \left( \frac{d(w)}{d\tau_1} \Big|_{\tau_1 = \tau_{1,0}} \right) = Q_4$$

where

$$\begin{aligned} Q_1 &= -3w_0^2 + R_2 + (2N_1 w_0 - N_2 w_0 \tau_{1,0}) \sin w_0 \tau_{1,0} \\ &\quad + (N_2 + N_1 \tau_1 w_0^2 - N_3 \tau_{1,0}) \cos w_0 \tau_{1,0} \\ &\quad + (2w_0 M_1 - M_2 \tau_2 w_0) \sin w_0 \tau_2 \\ &\quad + (M_1 \tau_2 w_0^2 - M_3 \tau_2 + M_2) \cos w_0 \tau_2, \\ Q_2 &= -2R_1 w_0 + (N_1 w_0^2 \tau_{1,0} - N_3 \tau_{1,0} + N_2) \sin w_0 \tau_{1,0} \\ &\quad + (N_2 w_0 \tau_1 - 2N_1 w_0) \cos w_0 \tau_{1,0} \\ &\quad + (M_2 + M_1 w_0^2 \tau_2 - M_3 \tau_2) \sin w_0 \tau_2 \\ &\quad + (M_2 w_0 \tau_2 - 2M_1 w_0) \cos w_0 \tau_2, \\ Q_3 &= N_2 w_0^2 \sin w_0 \tau_{1,0} + (N_3 w_0 - N_1 w_0^3) \cos w_0 \tau_{1,0}, \\ Q_4 &= N_2 w_0^2 \cos w_0 \tau_{1,0} + (N_1 w_0^3 - N_3 w_0) \sin w_0 \tau_{1,0}. \end{aligned} \quad (36)$$

From (35), we get

$$\left( \frac{d(\Re \lambda)}{d\tau_1} \Big|_{\tau_1 = \tau_{1,0}} \right) = \frac{Q_2 Q_3 - Q_1 Q_4}{Q_2^2 + Q_1^2}. \quad (37)$$

As  $Q_2 Q_3 > Q_1 Q_4$ , then Hopf bifurcation occurs for  $\tau_1 = \tau_{1,0}$ .

Therefore, we arrive at the following theorem.

**Theorem 3.** *If  $\mathcal{E}^*$  exists, such that  $(H_1)$  and  $(H_3)$  hold, with  $\tau_2 \in (0, \tau_2')$ , then there exists a positive threshold parameter  $\tau_1^*$  such that the interior equilibrium  $\mathcal{E}^*$  is locally asymptotically stable for  $\tau_1 < \tau_1^*$  and unstable  $\tau_1 > \tau_1^*$ , where  $\tau_1^* = \min\{\tau_{1,j}\}$  as in (38). Additionally, system (3) undergoes Hopf bifurcation at  $\mathcal{E}^*$  when  $\tau_1 = \tau_1^*$ .*

*Remark 2.* Similarly, for  $\tau_1 \in (0, \tau_1')$ , there exists a threshold parameter  $\tau_2^*$  such that the interior equilibrium  $\mathcal{E}^*$  is locally asymptotically stable for  $\tau_2 < \tau_2^*$  and unstable  $\tau_2 > \tau_2^*$ . Also, Hopf bifurcation occurs for system (3) as  $\tau_2 = \tau_2^*$ , where  $\tau_2^* = \min\{\tau_{2,j}\}$  is given by

$$\tau_{2,j} = \frac{1}{w_3} \arccos \left[ \frac{A_1 D_1 + C_1 B_1}{A_1^2 + C_1^2} \right] + \frac{2j\pi}{w_3}, \quad j = 0, 1, 2, \dots, \quad (38)$$

with

$$\begin{aligned} A_1 &= M_1 w_3^2 - M_3, \\ B_1 &= w_3^3 - R_2 w_3 + (N_3 - N_1 w_3^2) \sin w_3 \tau_1 - N_2 w_3 \cos w_3 \tau_1, \\ C_1 &= M_2 w_3, \\ D_1 &= -R_1 w_3^2 + R_3 + \cos w_3 \tau_1 + N_2 w_3 \sin w_3 \tau_1. \end{aligned} \quad (39)$$

The proofs are obtained in the same manner of the above analysis.

#### 4. Global Stability of Interior Steady State $\mathcal{E}^*$

In this section, we study the global stability of system (3) around interior steady state  $\mathcal{E}^* \equiv (x^*, y^*, z^*)$ .

**Theorem 4.** *If  $\beta_1 \alpha_1 < g_1(\alpha_1 + x^*)(\alpha_1 + x)$  and  $\beta_2 \alpha_2(1 + cy^*)(1 + cy) + \delta cz^*(\alpha_2 + y^*)(\alpha_2 + y) < g_2(\alpha_2 + y^*)(\alpha_2 + y)(1 + cy^*)(1 + cy)$ , then system (3) is globally asymptotically stable at the interior equilibrium point  $\mathcal{E}^*$ .*

*Proof.* We suggest the Lyapunov function at  $\mathcal{E}^* \equiv (x^*, y^*, z^*)$  of the form:

$$\begin{aligned} V(t) &= \varrho_1 \left( x(t) - x^* - x^* \ln \frac{x(t)}{x^*} \right) \\ &\quad + \varrho_2 \left( y(t) - y^* - y^* \ln \frac{y(t)}{y^*} \right) \\ &\quad + \varrho_3 \left( z(t) - z^* - z^* \ln \frac{z(t)}{z^*} \right), \end{aligned} \quad (40)$$

where  $\varrho_1, \varrho_2$ , and  $\varrho_3$  are nonnegative constants. Take derivative  $V$  with respect to time  $t$ , yielding to

$$\begin{aligned}
\dot{V}(t) &= \varrho_1 \frac{x-x^*}{x} \dot{x}(t) + \varrho_2 \frac{y-y^*}{y} \dot{y}(t) + \varrho_3 \frac{z-z^*}{z} \dot{z}(t) \\
&= \varrho_1 (x-x^*) \left( \frac{\beta_1 x}{\alpha_1+x} - \gamma_1 - g_1 x - \alpha y - e z \right) \\
&\quad + \varrho_2 (y-y^*) \left( \frac{\beta_2 y}{\alpha_2+y} - \gamma_2 - g_2 y - \beta x - \frac{\delta y z}{y(1+cy)} \right) \\
&\quad + \varrho_3 (z-z^*) \left( -\beta_3 + \frac{\varepsilon \varepsilon x(t-\tau_1) z(t-\tau_1)}{z} + \frac{\varepsilon \delta y(t-\tau_2) z(t-\tau_2)}{z(1+cy(t-\tau_2))} \right) \\
&\leq \varrho_1 (x-x^*) \left( \frac{\beta_1 x}{\alpha_1+x} - \frac{\beta_1 x^*}{\alpha_1+x^*} - g_1 (x-x^*) - \alpha (y-y^*) - e (z-z^*) \right) \\
&\quad + \varrho_2 (y-y^*) \left( \frac{\beta_2 y}{\alpha_2+y} - \frac{\beta_2 y^*}{\alpha_2+y^*} - g_2 (y-y^*) - \beta (x-x^*) + \frac{\delta y^* z^*}{y^*(1+cy^*)} - \frac{\delta y z}{y(1+cy)} \right) \\
&\quad + \varrho_3 (z-z^*) \left( \frac{\varepsilon \varepsilon x(t-\tau_1) z(t-\tau_1)}{z} + \frac{\varepsilon \delta y(t-\tau_2) z(t-\tau_2)}{z(1+cy(t-\tau_2))} - \left( \varepsilon \varepsilon x^* + \frac{\varepsilon \delta y^*}{1+cy^*} \right) \right) \\
&\leq -\varrho_1 g_1 (x-x^*)^2 - \varrho_2 g_2 (y-y^*)^2 - (\varrho_1 \alpha + \varrho_2 \beta) (x-x^*) (y-y^*) \\
&\quad + (\varepsilon \varepsilon \varrho_3 - e \varrho_1) (x-x^*) (z-z^*) + \varrho_1 (x-x^*) \left( \frac{\beta_1 x}{\alpha_1+x} - \frac{\beta_1 x^*}{\alpha_1+x^*} \right) \\
&\quad + \varrho_2 (y-y^*) \left( \frac{\beta_2 y}{\alpha_2+y} - \frac{\beta_2 y^*}{\alpha_2+y^*} \right) + \varrho_2 (y-y^*) \left( \frac{\delta y^* z^*}{y^*(1+cy^*)} - \frac{\delta y z}{y(1+cy)} \right) \\
&\quad + \varrho_3 (z-z^*) \left( \frac{\varepsilon \delta y}{1+cy} - \frac{\varepsilon \delta y^*}{1+cy^*} \right) \\
&\leq -\varrho_1 g_1 (x-x^*)^2 - \varrho_2 g_2 (y-y^*)^2 - (\varrho_1 \alpha + \varrho_2 \beta) (x-x^*) (y-y^*) \\
&\quad + (\varepsilon \varepsilon \varrho_3 - e \varrho_1) (x-x^*) (z-z^*) + \beta_1 \varrho_1 (x-x^*)^2 \left( \frac{\alpha_1}{(\alpha_1+x^*)(\alpha_1+x)} \right) \\
&\quad + \beta_2 \varrho_2 (y-y^*)^2 \left( \frac{\alpha_2}{(\alpha_2+y^*)(\alpha_2+y)} \right) + \delta \varrho_2 (y-y^*) \left( \frac{-(z-z^*)}{1+cy} + \frac{cz^*(y-y^*)}{(1+cy^*)(1+cy)} \right) \\
&\quad + \varepsilon \delta \varrho_3 (y-y^*) (z-z^*) \left( \frac{1}{1+cy} - \frac{cy}{(1+cy^*)(1+cy)} \right).
\end{aligned} \tag{41}$$

Thus, based on the assumptions:  $\beta_1 \alpha_1 < g_1 (\alpha_1 + x^*)(\alpha_1 + x)$ ,  $\beta_2 \alpha_2 (1 + cy^*)(1 + cy) + \delta c z^* (\alpha_2 + y^*)$   $(\alpha_2 + y) < g_2 (\alpha_2 + y^*)(\alpha_2 + y)(1 + cy^*)(1 + cy)$ , and  $\varepsilon \varrho_3 < \max\{\varrho_1, \varrho_2\}$ , we can get



$$\begin{aligned}
\dot{V}(t) \leq & \left( \frac{\varrho_1 \alpha_1 \beta_1}{(\alpha_1 + x^*)(\alpha_1 + x)} - \varrho_1 g_1 \right) (x - x^*)^2 \\
& + \left( \frac{\varepsilon \delta \varrho_3 - \delta \varrho_2}{1 + cy} \right) (y - y^*)(z - z^*) \\
& + \left( \frac{\delta \varrho_2 cz^*}{(1 + cy^*)(1 + cy)} + \frac{\varrho_2 \alpha_2 \beta_2}{(\alpha_2 + y^*)(\alpha_2 + y)} - \varrho_2 g_2 \right) \\
& \cdot (y - y^*)^2 + (\varepsilon \varrho_3 - \varrho_1 e)(x - x^*)(z - z^*) \\
& - (\varrho_1 \alpha + \varrho_2 \beta)(x - x^*)(y - y^*) - \frac{\varepsilon \delta \varrho_3 cy}{(1 + cy^*)(1 + cy)} \\
& \cdot (z - z^*)(y - y^*) \leq 0.
\end{aligned} \tag{42}$$

Hence, the proof is complete.  $\square$

## 5. Sensitivity Analysis to Severity of Allee Effect

Here, we study the sensitivity of model solution of (3), with respect to the parameters  $\alpha_1$  and  $\alpha_2$  (strength Allee effect). It is quite common for a model to exhibit high sensitivity to small variations in some parameters, while showing robustness to variation in other parameters. There are different ways to find the sensitivity functions of DDEs [33]. Nevertheless, we utilize the so-called “direct approach” to find sensitivity functions of model (3). The sensitivity functions with respect to Allee parameters  $\alpha_i$  ( $i = 1, 2$ ) are denoted by

$$\begin{aligned}
S_{x_{\alpha_i}}(t) &:= \frac{\partial}{\partial \alpha_i} x(t), \\
S_{y_{\alpha_i}}(t) &:= \frac{\partial}{\partial \alpha_i} y(t), \\
S_{z_{\alpha_i}}(t) &:= \frac{\partial}{\partial \alpha_i} z(t).
\end{aligned} \tag{43}$$

Hence, sensitivity functions due to small perturbations in Allee parameter  $\alpha_1$  are given by a system of DDEs:

$$\begin{aligned}
S'_{x_{\alpha_1}}(t) &= S_{x_{\alpha_1}}(t) \left[ \frac{\beta_1 x(t)}{\alpha_1 + x(t)} - \gamma_1 - 2g_1 x(t) - \alpha y(t) - ez(t) \right] - \alpha S_{y_{\alpha_1}}(t) x(t) \\
&\quad - e S_{z_{\alpha_1}}(t) x(t) + \beta_1 x(t) \left( \frac{\alpha_1 S_{x_{\alpha_1}}(t) - x(t)}{(\alpha_1 + x(t))^2} \right), \\
S'_{y_{\alpha_1}}(t) &= S_{y_{\alpha_1}}(t) \left[ \frac{\beta_2 y(t)}{\alpha_2 + y(t)} - \gamma_2 - 2g_2 y(t) - \beta x(t) \right] + y(t) \left[ -\beta S_{x_{\alpha_1}}(t) + \frac{\alpha_2 \beta_2 S_{y_{\alpha_1}}(t)}{(\alpha_2 + y(t))^2} \right] \\
&\quad - \delta \left[ \frac{S_{y_{\alpha_1}}(t) z(t)}{(1 + cy(t))^2} + \frac{S_{z_{\alpha_1}}(t) y(t)}{1 + cy(t)} \right], \\
S'_{z_{\alpha_1}}(t) &= -\beta_3 S_{z_{\alpha_1}}(t) + \varepsilon e \left[ S_{x_{\alpha_1}}(t - \tau_1) z(t - \tau_1) + S_{z_{\alpha_1}}(t - \tau_1) x(t - \tau_1) \right] \\
&\quad + \varepsilon \delta \left[ \frac{S_{y_{\alpha_1}}(t - \tau_2) z(t - \tau_2)}{(1 + cy(t - \tau_2))^2} + \frac{S_{z_{\alpha_1}}(t - \tau_2) y(t - \tau_2)}{1 + cy(t - \tau_2)} \right].
\end{aligned} \tag{44}$$

To estimate the sensitivity functions  $S_{x_{\alpha_1}}(t)$ ,  $S_{y_{\alpha_1}}(t)$ , and  $S_{z_{\alpha_1}}(t)$ , we have to solve the system of sensitivity equations (44) together with the original system (3).

Similarly, the sensitivity functions due to small changes in Allee coefficient  $\alpha_2$  satisfy the system of DDEs:

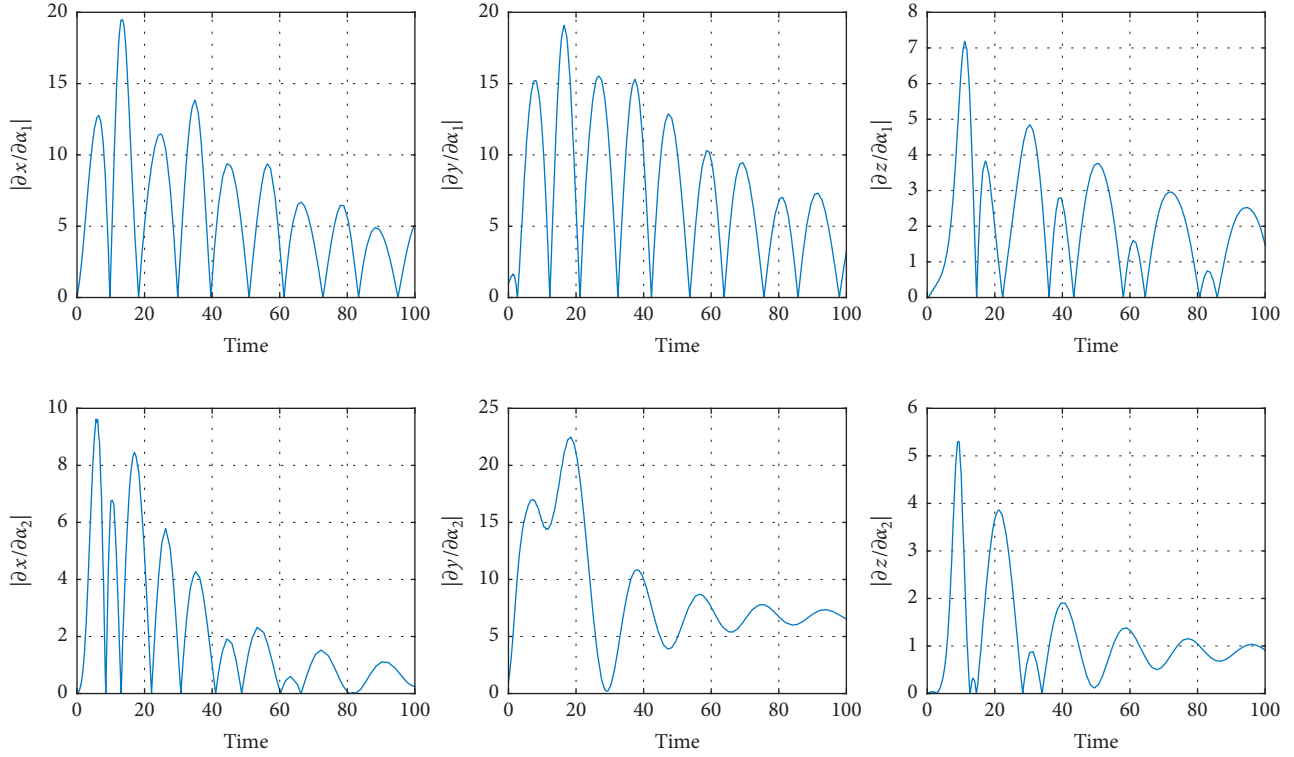


FIGURE 4: Sensitivity functions of model solution of system (3) with respect to Allee parameters  $\alpha_1$  and  $\alpha_2$ . The top banners show the sensitivity functions for  $x(t)$ ,  $y(t)$  and  $z(t)$  with respect to small changes in Allee parameter  $\alpha_1$ . However, the bottom banners display the sensitivity with respect to  $\alpha_2$ . They show that the model is very sensitive to the small perturbations of Allee parameters in early time intervals and the sensitivity decreases by time. The two parameters  $\alpha_1$  and  $\alpha_2$  are significant in the model and cause high impact in early stages of interactions.

$$\begin{aligned}
S'_{x\alpha_2}(t) &= S_{x\alpha_2}(t) \left[ \frac{\beta_1 x(t)}{\alpha_1 + x(t)} - \gamma_1 - 2g_1 x(t) - \alpha y(t) - ez(t) \right] \\
&\quad + \beta_1 x(t) \left( \frac{\alpha_1 S_{x\alpha_2}(t)}{(\alpha_1 + x(t))^2} \right) - \alpha S_{y\alpha_2}(t) x(t) \\
&\quad - e S_{z\alpha_2}(t) x(t), \\
S'_{y\alpha_2}(t) &= S_{y\alpha_2}(t) \left[ \frac{\beta_2 y(t)}{\alpha_2 + y(t)} - \gamma_2 - 2g_2 y(t) - \beta x(t) \right] \\
&\quad - \beta S_{x\alpha_2}(t) y(t) \\
&\quad + \beta_2 y(t) \left[ \frac{\alpha_2 S_{y\alpha_2}(t) - y(t)}{(\alpha_2 + y(t))^2} \right] \\
&\quad - \delta \left[ \frac{S_{y\alpha_2}(t) z(t)}{(1 + cy(t))^2} + \frac{S_{z\alpha_2}(t) y(t)}{1 + cy(t)} \right], \\
S'_{z\alpha_2}(t) &= -\beta_3 S_{z\alpha_2}(t) + \varepsilon e \left[ S_{x\alpha_2}(t - \tau_1) z(t - \tau_1) \right. \\
&\quad \left. + S_{z\alpha_2}(t - \tau_1) x(t - \tau_1) \right] \\
&\quad + \varepsilon \delta \left[ \frac{S_{y\alpha_2}(t - \tau_2) z(t - \tau_2)}{(1 + cy(t - \tau_2))^2} + \frac{S_{z\alpha_2}(t - \tau_2) y(t - \tau_2)}{1 + cy(t - \tau_2)} \right].
\end{aligned} \tag{45}$$

We then solve (45) along with (3) to evaluate  $S_{x\alpha_2}(t)$ ,  $S_{y\alpha_2}(t)$ , and  $S_{z\alpha_2}(t)$  (see Figure 4).

## 6. Numerical Simulations

Some numerical simulations of system (3) are carried out, using Matlab package DDE23, to confirm our theoretical results. We first investigate the behavior of the model around  $\mathcal{E}^*$  with parameter values:

$$\begin{aligned}
\alpha &= 0.9, \\
\alpha_1 &= 0.001, \\
\alpha_2 &= 0.001, \\
\beta &= 1.35, \\
\gamma_2 &= 1, \\
\gamma_1 &= 1, \\
\beta_1 &= 2, \\
\beta_2 &= 2, \\
\beta_3 &= 1, \\
\varepsilon &= 0.5, \\
e &= 5, \\
\delta &= 1.
\end{aligned} \tag{46}$$

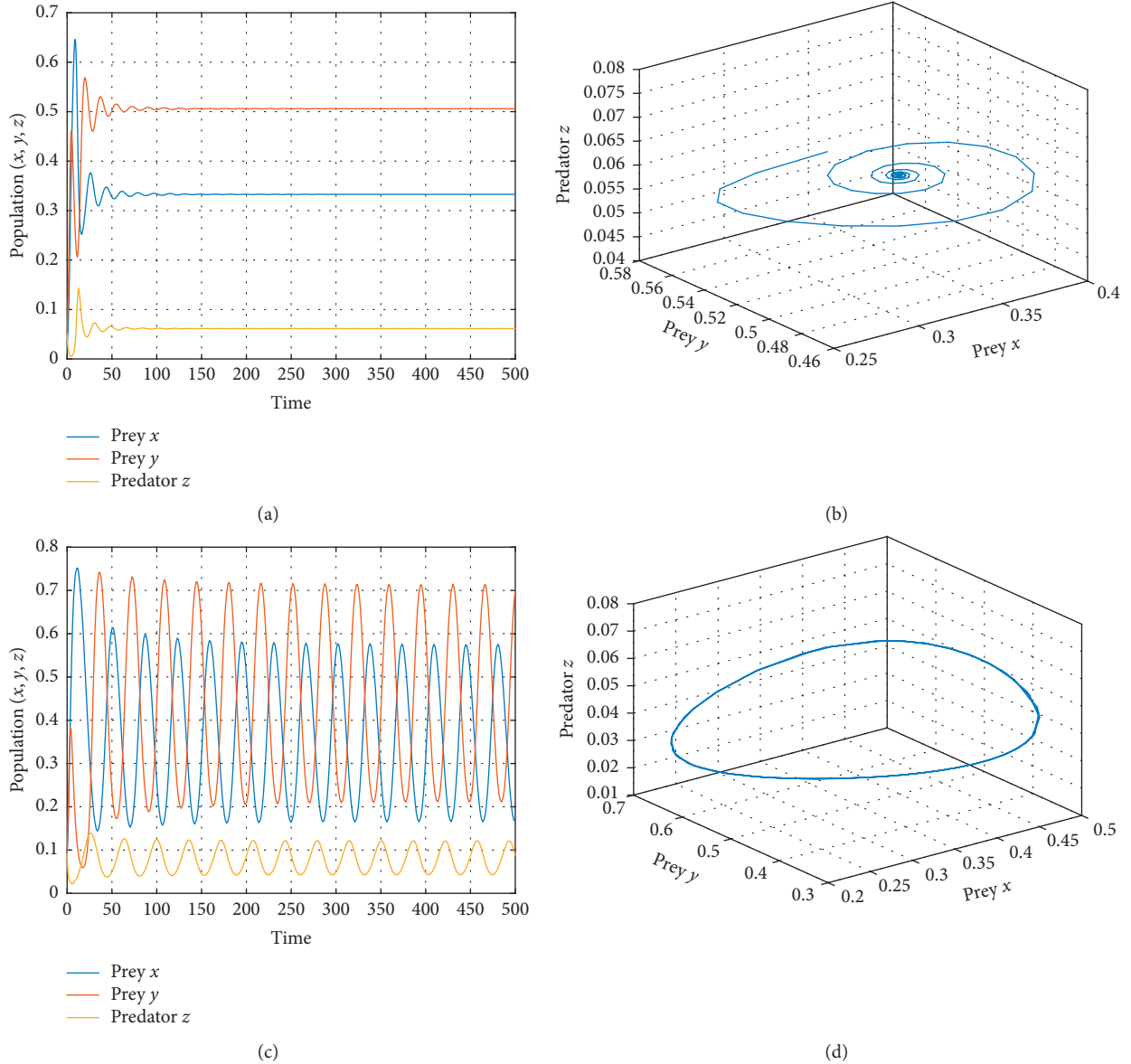


FIGURE 5: Numerical simulations of system (3) around the steady state  $\mathcal{E}^*$ . Top banners show that  $\mathcal{E}^*$  is asymptotically stable when  $\tau_1 = 5.54 < \tau_1^*$  and  $\tau_2 \in (0, \tau_2^*)$ . Bottom banners display a Hopf bifurcation when  $\tau_1 = \tau_1^* = 4.34$  and  $\tau_2 < \tau_2^* = 5.34$ ; the other parameter values are given in (45).

Figure 5 shows the numerical simulations of the delayed system (3) around the steady state  $\mathcal{E}^*$ . The interior steady state  $\mathcal{E}^*$  is asymptotically stable when  $\tau_1 < \tau_1^*$  and  $\tau_2 \in (0, \tau_2^*)$ . The model undergoes a Hopf bifurcation when  $\tau_1 = \tau_1^* = 4.34$  and  $\tau_2 < \tau_2^* = 5.33$ . Figure 6 displays the Hopf bifurcation diagrams of  $\tau_1$  and  $\tau_2$  which are obtained numerically by maximum and minimum amplitudes of  $z(t)$ . The left banner displays the threshold parameter  $\tau_1^* = 4.34$  with  $\tau_2 < \tau_2^*$ , while right banner shows that the threshold parameter  $\tau_2^* = 5.54$  with  $\tau_1 < \tau_1^*$ .

Figure 5 displays a bistability of two interior equilibrium points, for the DDEs model (3), when parameter  $\alpha$  varies from  $\alpha = 0.5$  to  $\alpha = 0.9$ . If the interior equilibria exist, any trajectory starting from the interior of  $\mathcal{R}_+^3$  converges to one of the interior equilibria.

Figure 7 shows the sensitivity of the dynamics of system (3) due to small changes in the severity of Allee effects  $\alpha_1$  and  $\alpha_2$ . The left banners show the numerical simulations with different values of  $\alpha_1$  ( $0.001 \leq \alpha_1 \leq 0.02$ ) and fixed value of  $\alpha_2 = 0.001$ , while right banners display the simulations with different values of  $\alpha_2$  ( $0.01 \leq \alpha_2 \leq 0.02$ ) and fixed value of  $\alpha_1 = 0.01$ . The phase portrait gets stretched over time as  $\alpha_1$  is reduced, while low values of  $\alpha_2$  increases the oscillations over time. The presence of Allee effect in the model enriches the dynamics of the system, while Figure 4 exhibits the absolute values of sensitivity functions:  $\partial x(t)/\partial \alpha_{1,2}$ ,  $\partial y(t)/\partial \alpha_{1,2}$ , and  $\partial z(t)/\partial \alpha_{1,2}$  to evaluate the sensitivity of the state variables due to a small perturbation in  $\alpha_1$  and  $\alpha_2$ . The oscillation behaviour indicates that the species population is very sensitive to small changes in the parameter. It is clear

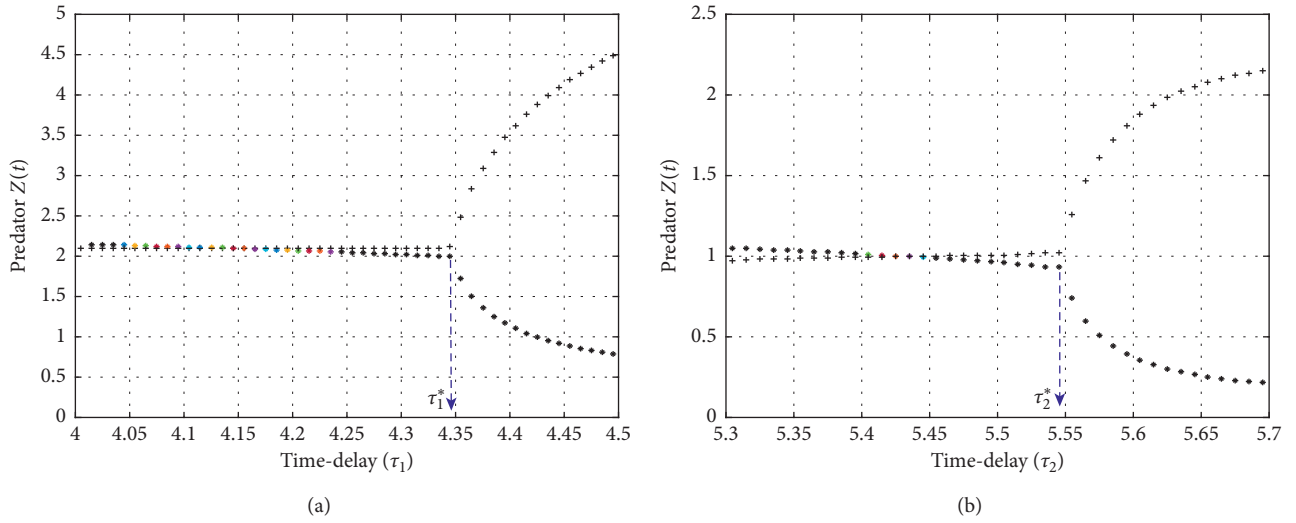


FIGURE 6: The Hopf bifurcation diagrams of  $\tau_1$  and  $\tau_2$  which are obtained numerically by maximum and minimum amplitudes of  $z(t)$ . (a) The threshold parameter  $\tau_1^* = 4.34$  with  $\tau_2 < \tau_2^*$ . (b) The threshold parameter  $\tau_2^* = 5.54$  with  $\tau_1 < \tau_1^*$ .

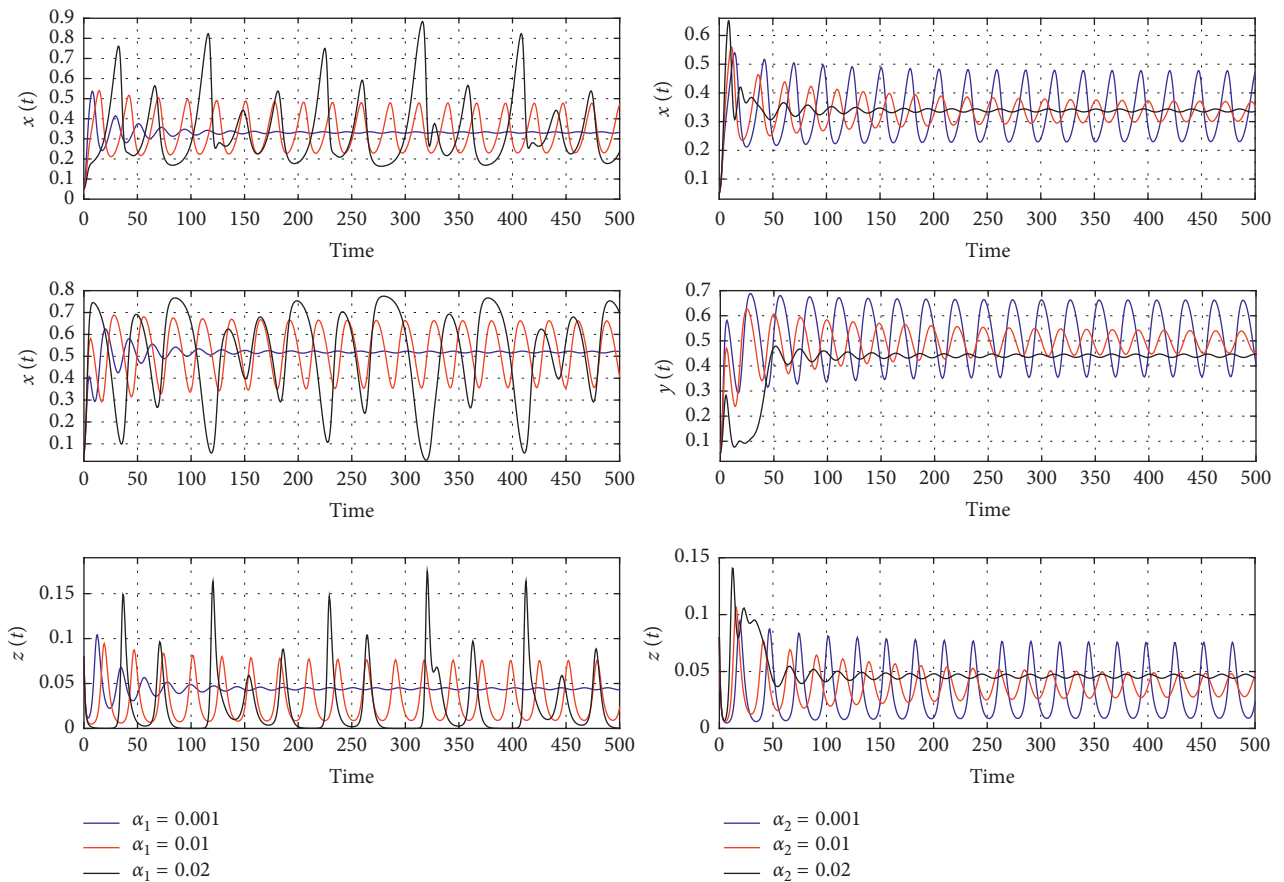


FIGURE 7: The sensitivity of the dynamics of system (3) due to small changes in the severity of Allee effect  $\alpha_1$  and  $\alpha_2$ . The left banners show the numerical simulations with different values of  $\alpha_1$  ( $0.001 \leq \alpha_1 \leq 0.02$ ) and fixed value of  $\alpha_2 = 0.001$ . The right banners display the simulations with different values of  $\alpha_2$  ( $0.01 \leq \alpha_2 \leq 0.02$ ) and fixed value of  $\alpha_1 = 0.01$ . The phase portrait gets stretched over time as  $\alpha_1$  reduced, while low values of  $\alpha_2$  increase the oscillations over time. The presence of Allee effect in the model enriches the dynamics of the system.

that  $\alpha_1$  and  $\alpha_2$  are important in the model and have a significant impact in the dynamics, specially in the early stages of time. However, the sensitivity to these parameters decreases with time.

## 7. Conclusion

In this paper, we established the two-prey one-predator mode with time delays and a weak Allee effect in the preys' growth functions, where there is a direct competition between prey populations. Although the model is simple, the system exhibits rich dynamic behaviour such as bistability of equilibria, Hopf bifurcation, and period doubling chaos. Nonnegativity and boundedness of the solutions have been investigated. Some new sufficient conditions for local and global asymptotic stability of interior steady states have been deduced. In addition, Hopf bifurcation with respect to time delay threshold parameters  $\tau_1^*$  and  $\tau_2^*$  has been studied. The model undergoes a Hopf bifurcation when time delays pass through its critical values. We also investigated the sensitivity of model solutions to small perturbations in the severity Allee effects  $\alpha_1$  and  $\alpha_2$ . The obtained results confirm that Allee effect has a significant impact in the dynamics in the early stages of interaction. It has been seen by the numerical simulations that time delay and Allee effects play an important role in the dynamics of prey-predator systems. Introduction of time delay and Allee effects, in the model, improves the stability results, enriches the dynamics of the system, keeps the population densities in balance, and makes the model closer to reality.

As part of future work, more sophisticated models with harvesting terms, control variables, and effect of environmental noise can be studied. Fractional derivatives, instead of integer-order derivatives in the same or similar model, to consider the long-term memory effect, with a saturating functional response, will also be our future goal.

## Data Availability

No data were used to support this study.

## Conflicts of Interest

The authors declare that they have no conflicts of interest.

## Acknowledgments

This study was supported by PhD project, United Arab Emirates University (UAE).

## References

- [1] M. Kot, *Elements of Mathematical Ecology*, Cambridge University Press, Cambridge, UK, 2001.
- [2] S. Li and W. Liu, "A delayed holling type III functional response predator-prey system with impulsive perturbation on the prey," *Advances in Difference Equations*, vol. 2016, no. 1, p. 42, 2016.
- [3] Z. Liu and R. Tan, "Impulsive harvesting and stocking in a monod-haldane functional response predator-prey system," *Chaos, Solitons & Fractals*, vol. 34, no. 2, pp. 454–464, 2007.
- [4] J. D. Murray, *Mathematical Biology*, Springer, New York, NY, USA, 1993.
- [5] G. Tang, S. Tang, and R. A. Cheke, "Global analysis of a Holling type II predator-prey model with a constant prey refuge," *Nonlinear Dynamics*, vol. 76, no. 1, pp. 635–647, 2014.
- [6] A. J. Lotka, *Elements of Physical Biology*, Williams & Wilkins Co., Baltimore, MD, USA, 1925.
- [7] V. Volterra, "Fluctuations in the abundance of a species considered mathematically," *Nature*, vol. 118, no. 2972, pp. 558–560, 1926.
- [8] Y. Kuang, *Delay Differential Equations: with Applications in Population Dynamics*, Vol. 191, Academic Press, Cambridge, MA, USA, 1993.
- [9] C. S. Holling, "The components of predation as revealed by a study of small-mammal predation of the european pine sawfly," *The Canadian Entomologist*, vol. 91, no. 5, pp. 293–320, 1959.
- [10] M. Bandyopadhyay and C. G. Chakrabarti, "Deterministic and stochastic analysis of a nonlinear prey-predator system," *Journal of Biological Systems*, vol. 11, no. 2, pp. 161–172, 2003.
- [11] R. Khoshsiar Ghaziani and J. Alidousti, "Stability analysis of a fractional order prey-predator system with nonmonotonic functional response," *Computational Methods for Differential Equations*, vol. 4, no. 2, pp. 151–161, 2016.
- [12] K. Nosrati and M. Shafiee, "Dynamic analysis of fractional-order singular Holling type-ii predator-prey system," *Applied Mathematics and Computation*, vol. 313, pp. 159–179, 2017.
- [13] P. D. N. Srinivasu, B. S. R. V. Prasad, and M. Venkatesulu, "Biological control through provision of additional food to predators: a theoretical study," *Theoretical Population Biology*, vol. 72, no. 1, pp. 111–120, 2007.
- [14] Y. Cai, C. Zhao, W. Wang, and J. Wang, "Dynamics of a Leslie-Gower predator-prey model with additive Allee effect," *Applied Mathematical Modelling*, vol. 39, no. 7, pp. 2092–2106, 2015.
- [15] H. Liu, Z. Li, M. Gao, H. Dai, and Z. Liu, "Dynamics of a host-parasitoid model with Allee effect for the host and parasitoid aggregation," *Ecological Complexity*, vol. 6, no. 3, pp. 337–345, 2009.
- [16] W. C. Allee, "Animal aggregations: a study in general sociology," *The Quarterly Review of Biology*, vol. 2, no. 3, pp. 367–398, 1927.
- [17] D. Hadjiavgousti and S. Ichtiaroglou, "Allee effect in a prey-predator system," *Chaos, Solitons & Fractals*, vol. 36, no. 2, pp. 334–342, 2008.
- [18] P. J. Pal, T. Saha, M. Sen, and M. Banerjee, "A delayed predator-prey model with strong Allee effect in prey population growth," *Nonlinear Dynamics*, vol. 68, no. 1-2, pp. 23–42, 2012.
- [19] J. Zu and M. Mimura, "The impact of Allee effect on a predator-prey system with Holling type II functional response," *Applied Mathematics and Computation*, vol. 217, no. 7, pp. 3542–3556, 2010.
- [20] I. Scheuring, "Allee effect increases the dynamical stability of populations," *Journal of Theoretical Biology*, vol. 199, no. 4, pp. 407–414, 1999.
- [21] F. A. Rihan, S. Lakshmanan, A. H. Hashish, R. Rakkiyappan, and E. Ahmed, "Fractional-order delayed predator-prey systems with Holling type-II functional response," *Nonlinear Dynamics*, vol. 80, no. 1-2, pp. 777–789, 2015.
- [22] J. J. Batzel and H. T. Tran, "Stability of the human respiratory control system i. analysis of a two-dimensional delay state-

- space model,” *Journal of Mathematical Biology*, vol. 41, no. 1, pp. 45–79, 2000.
- [23] G. A. Bocharov and F. A. Rihan, “Numerical modelling in biosciences using delay differential equations,” *Journal of Computational and Applied Mathematics*, vol. 125, no. 1-2, pp. 183–199, 2000.
- [24] F. A. Rihan, A. A. Azamov, and H. J. Al-Sakaji, “An inverse problem for delay differential equations: parameter estimation, nonlinearity, sensitivity,” *Applied Mathematics & Information Sciences*, vol. 12, no. 1, pp. 63–74, 2018.
- [25] M. Banerjee and Y. Takeuchi, “Maturation delay for the predators can enhance stable coexistence for a class of prey–predator models,” *Journal of Theoretical Biology*, vol. 412, pp. 154–171, 2017.
- [26] M. Sen, M. Banerjee, and Y. Takeuchi, “Influence of Allee effect in prey populations on the dynamics of two-prey-one-predator model,” *Mathematical Biosciences & Engineering*, vol. 15, no. 4, pp. 883–904, 2018.
- [27] S. Kundu and S. Maitra, “Dynamical behaviour of a delayed three species predator–prey model with cooperation among the prey species,” *Nonlinear Dynamics*, vol. 92, no. 2, pp. 627–643, 2018.
- [28] Y. Takeuchi and N. Adachi, “Existence and bifurcation of stable equilibrium in two-prey, one-predator communities,” *Bulletin of Mathematical Biology*, vol. 45, no. 6, pp. 877–900, 1983.
- [29] X. Song and Y. Li, “Dynamical complexities of a Holling II two-prey one predator system with impulsive effect,” *Chaos Solitons & Fractals*, vol. 33, no. 2, pp. 463–478, 2007.
- [30] H.-F. Huo, “Permanence and global attractivity of delay diffusive prey-predator systems with the michaelis-menten functional response,” *Computers & Mathematics with Applications*, vol. 49, no. 2-3, pp. 407–416, 2005.
- [31] R. Garver, “On the nature of the roots of a quartic equation,” *Mathematics News Letter*, vol. 7, no. 4, pp. 6–8, 1933.
- [32] A. Goldbeter, “Dissipative structures in biological systems: bistability, oscillations, spatial patterns and waves,” *Philosophical Transactions of the Royal Society A: Mathematical, Physical and Engineering Sciences*, vol. 376, no. 2124, Article ID 20170376, 2018.
- [33] F. A. Rihan, “Sensitivity analysis for dynamic systems with time-lags,” *Journal of Computational and Applied Mathematics*, vol. 151, no. 2, pp. 445–462, 2003.



## Research Article

# A New Proof of Existence of Positive Weak Solutions for Sublinear Kirchhoff Elliptic Systems with Multiple Parameters

Salah Mahmoud Boulaaras <sup>1,2</sup>, Rafik Guefaïfa <sup>3</sup>, Bahri Cherif <sup>1</sup>,  
and Sultan Alodhaibi <sup>1</sup>

<sup>1</sup>Department of Mathematics, College of Sciences and Arts in Al-Rass, Qassim University, Buraidah, Saudi Arabia

<sup>2</sup>Laboratory of Fundamental and Applied Mathematics of Oran (LMFAO), University of Oran 1, Ahmed Benbella, Algeria

<sup>3</sup>Department of Mathematics, Faculty of Exact Sciences, University of Tebessa, Tébessa 12002, Algeria

Correspondence should be addressed to Salah Mahmoud Boulaaras; s.boulaaras@qu.edu.sa

Received 8 November 2019; Accepted 19 December 2019; Published 25 January 2020

Guest Editor: Sundarapandian Vaidyanathan

Copyright © 2020 Salah Mahmoud Boulaaras et al. This is an open access article distributed under the Creative Commons Attribution License, which permits unrestricted use, distribution, and reproduction in any medium, provided the original work is properly cited.

This paper deals with the study of the existence of weak positive solutions for sublinear Kirchhoff elliptic systems with zero Dirichlet boundary condition in bounded domain  $\Omega \subset \mathbb{R}^N$  by using the subsuper solutions method.

## 1. Introduction

In this paper, we consider the following system of differential equations:

$$\begin{cases} -A\left(\int_{\Omega} |\nabla u|^2 dx\right)\Delta u = \lambda_1 u^a + \mu_1 v^b \text{ in } \Omega, \\ -B\left(\int_{\Omega} |\nabla u|^2 dx\right)\Delta v = \lambda_2 u^c + \mu_2 v^d \text{ in } \Omega, \\ u = v = 0 \text{ on } \partial\Omega, \end{cases} \quad (1)$$

where  $\Omega \subset \mathbb{R}^N$  ( $N \geq 3$ ) is a bounded smooth domain with  $C^2$  boundary  $\partial\Omega$ ,  $A, B: \mathbb{R}^+ \rightarrow \mathbb{R}^+$  are continuous functions, and  $\lambda_1, \lambda_2, \mu_1$ , and  $\mu_2$  are positive parameters, where  $a + c < 1$  and  $b + d < 1$ . The peculiarity of this type of problem, and by far the most important, is that it is not local. This is based on the presence of the operator

$$-A\left(\int_{\Omega} |\nabla u|^2 dx\right)\Delta u \left(\text{respectively } -B\left(\int_{\Omega} |\nabla u|^2 dx\right)\Delta u\right), \quad (2)$$

which contains an integral on all the fields and implies that the equation is not a specific identity. It is clear that these problems contribute to the transition from academia to application. Indeed, very popular for its physical

motivations, problem (1) is none other than a stationary version of the following model which regulates the behavior of elastic whose ends are fixed and which is subjected to nonlinear vibrations:

$$\begin{cases} u_{tt} - M\left(\int_{\Omega} |\nabla u|^2 dx\right)\Delta u = h(x, u), \text{ in } \Omega \times (0, T), \\ u = 0, \text{ in } \partial\Omega \times (0, T), \\ u(x, 0) = u_0(x), u_t(x, 0) = u_1(x), \end{cases} \quad (3)$$

where  $T$  is a positive constant and  $u_0$  and  $u_1$  are given functions. In such problems,  $u$  expresses the displacement,  $h(x, u)$  the extreme force,  $M(r) = a_1 r + b_1$ ,  $b_1$  the initial tension, and  $a_1$  relates to the intrinsic properties of the wire material (such as Young's modulus). For more details, see [1], as well as their references. Basically, this is a generalization to larger dimensions of the model originally proposed in one dimension by Kirchhoff [2] in (1883):

$$\frac{\partial^2 u}{\partial t^2} - \left(\rho_0 + \rho_1 \int_0^L \left|\frac{\partial u}{\partial x}\right|^2 dx\right) \frac{\partial u}{\partial x} = 0, \quad (4)$$

where  $\rho_0$  is the initial tension,  $\rho_1$  represents Young's modulus of the material of the wire, and  $L$  its length. The

latter is known to be an extension of the equation of D'Alembert waves. Indeed, Kirchhoff took into account the changes caused by transverse oscillations along the length of the wire. With their implications in other disciplines, and given the breadth of their fields of application, nonlocal problems will be used to model several physical phenomena, and they also intervene in biological systems or describe a process dependent on its average, such as particle density population. Moreover, With this significant impact strengthening the field of applications, this type of problem has caught the interest of mathematicians and a lot of work on the existence of solutions has emerged, particularly after the coup de force provided by the famous Lions article [3], where the latter has adopted an approach based on functional analysis. Nevertheless, in most of these articles, the benefit method is purely topological. It is only in the last decades that this approach has been removed from variational methods when Alves and his colleagues [4] obtained for the first time the results of their existence through these methods. Since then, a very fruitful development has given rise to many works based on this advantageous axis (see [1, 3, 5]).

In recent years, problems relating to Kirchhoff operators have been studied in several papers (we refer to [6]), where the authors used different methods to obtain solutions (1) in the case of single equation (see [6]). The concept of weak sub- and supersolutions was first formulated by Hess and Deuel in [7, 8] to obtain existence results for weak solutions of semilinear elliptic Dirichlet problems and was subsequently continued by several authors (see, e.g., [9–18]).

In our recent paper [19], we have discussed the existence of weak positive solution for the following Kirchhoff elliptic systems:

$$\begin{cases} -A\left(\int_{\Omega} |\nabla u|^2 dx\right) \Delta u = \lambda' f(v) + \mu_1' h(u) \text{ in } \Omega, \\ -B\left(\int_{\Omega} |\nabla v|^2 dx\right) \Delta v = \lambda_2' g(u) + \mu_2' \tau(v) \text{ in } \Omega, \\ u = v = 0 \text{ on } \partial\Omega. \end{cases} \quad (5)$$

Motivated by the ideas of [20], which the authors considered a system (1) in the case  $A(t) = B(t) = 1$ , more precisely, under suitable conditions on  $f, g$ , we will prove that the problem which is defined in (1) admits a positive solution. In current paper, motivated by previous works in ([19, 20]), we discuss the existence of weak positive solution for sublinear Kirchhoff elliptic systems in bounded domains by using subsupersolutions method combined with comparison principle (see Lemma 2.1 in [4]).

The outline of the paper is as follows. In the second section, we give some assumptions and definitions related to problem (1). In Section 3, we prove our main result.

## 2. Assumptions and Definitions

Let us assume the following assumption.

(H1) Assume that  $A, B: \mathbb{R}^+ \rightarrow \mathbb{R}^+$  are two continuous and increasing functions and there exists  $a_i, b_i > 0, i = 1, 2$ , such that

$$\begin{aligned} a_1 &\leq A(t) \leq a_2, \\ b_1 &\leq B(t) \leq b_2, \end{aligned} \quad (6)$$

for all  $t \in \mathbb{R}^+$ .

(H2) Suppose that  $a, d \geq 0, b, c > 0, a + c < 1$  and  $b + d < 1$ .

Now, in order to discuss our main result of problem (1), we need the following two definitions.

*Definition 1.* Let  $(u, v) \in (H_0^1(\Omega) \times H_0^1(\Omega))$ ;  $(u, v)$  is said to be a weak solution of (1) if it satisfies

$$\begin{aligned} A(\|u\|^2) \int_{\Omega} \nabla u \nabla \phi dx &= \lambda_1 \int_{\Omega} u^a \phi dx + \mu_1 \int_{\Omega} v^b \phi dx \text{ in } \Omega, \\ B(\|v\|^2) \int_{\Omega} \nabla v \nabla \psi dx &= \lambda_2 \int_{\Omega} u^c \psi dx + \mu_2 \int_{\Omega} v^d \psi dx \text{ in } \Omega, \end{aligned} \quad (7)$$

for all  $(\phi, \psi) \in (H_0^1(\Omega) \times H_0^1(\Omega))$ .

*Definition 2.* A pair of nonnegative functions  $(\underline{u}, \underline{v}), (\bar{u}, \bar{v})$  in  $(H_0^1(\Omega) \times H_0^1(\Omega))$  is called a weak subsolution and supersolution of (1) if they satisfy  $(\underline{u}, \underline{v}), (\bar{u}, \bar{v}) = (0, 0)$  on  $\partial\Omega$ :

$$\begin{aligned} A(\|\bar{u}\|^2) \int_{\Omega} \nabla \bar{u} \nabla \phi dx &\leq \lambda_1 \int_{\Omega} \bar{u}^a \phi dx + \mu_1 \int_{\Omega} \bar{v}^b \phi dx \text{ in } \Omega, \\ B(\|\bar{v}\|^2) \int_{\Omega} \nabla \bar{v} \nabla \psi dx &\leq \lambda_2 \int_{\Omega} \bar{u}^c \psi dx + \mu_2 \int_{\Omega} \bar{v}^d \psi dx \text{ in } \Omega, \\ A(\|\underline{u}\|^2) \int_{\Omega} \nabla \underline{u} \nabla \phi dx &\geq \lambda_1 \int_{\Omega} \underline{u}^a \phi dx + \mu_1 \int_{\Omega} \underline{v}^b \phi dx \text{ in } \Omega, \\ B(\|\underline{v}\|^2) \int_{\Omega} \nabla \underline{v} \nabla \psi dx &\geq \lambda_2 \int_{\Omega} \underline{u}^c \psi dx + \mu_2 \int_{\Omega} \underline{v}^d \psi dx \text{ in } \Omega, \end{aligned} \quad (8)$$

for all  $(\phi, \psi) \in (H_0^1(\Omega) \times H_0^1(\Omega))$ .

**Lemma 1 [4].** Assume that  $M: \mathbb{R}^+ \rightarrow \mathbb{R}^+$  is a continuous and nonincreasing function satisfying

$$M(s) > m_0, \quad \text{for all } s \geq s_0, \quad (9)$$

where  $m_0$  is a positive constant and assume that  $u, v$  are two nonnegative functions such that

$$\begin{cases} -M(\|u\|^2) \Delta u \geq -M(\|v\|^2) \Delta v \text{ in } \Omega, \\ u = v = 0 \text{ on } \partial\Omega, \end{cases} \quad (10)$$

and then  $u \geq v$  a.e. in  $\Omega$ .

## 3. Main Result

In this section, we shall state and prove the main result of this paper.

**Theorem 1.** Suppose that (H1)-(H2) hold and  $M$  is a nonincreasing function satisfying (9). Then, problem (1) has a large positive weak solution for each positive parameters  $\lambda_1, \lambda_2, \mu_1$ , and  $\mu_2$ .

*Proof of Theorem 1.* Let  $\sigma$  be the first eigenvalue of  $-\Delta$  with Dirichlet boundary conditions and  $\phi_1$  the corresponding eigenfunction with  $\|\phi_1\| = 1$  satisfying  $\phi_1 > 0$  in  $\Omega$  and  $|\nabla\phi_1| > 0$  on  $\partial\Omega$ .

Since  $bc < (1-a)(1-d)$ , we can take  $k$  such that

$$\frac{c}{1-d} < k < \frac{b}{1-a}. \quad (11)$$

We shall verify that  $(\underline{u}, \underline{v}) = (\varepsilon\phi_1^2, \varepsilon^k\phi_1^2)$  is a subsolution of problem (1), where  $\varepsilon > 0$  is small and specified later.

A simple calculation:

$$\begin{aligned} A(\|\underline{u}\|^2) \int_{\Omega} \nabla \underline{u} \cdot \nabla \phi dx &= 2\varepsilon A(\|\underline{u}\|^2) \int_{\Omega} \phi_1 \nabla \phi_1 \cdot \nabla \phi dx \\ &= 2\varepsilon A(\|\underline{u}\|^2) \times \left\{ \int_{\Omega} \nabla \phi_1 \nabla (\phi_1 \cdot \phi) dx \right. \\ &\quad \left. - \int_{\Omega} |\nabla \phi_1|^2 \phi dx \right\} \\ &= 2\varepsilon A(\|\underline{u}\|^2) \int_{\Omega} (\sigma\phi_1^2 - |\nabla\phi_1|^2) \phi dx \\ &\leq 2a_2\varepsilon \int_{\Omega} (\sigma\phi_1^2 - |\nabla\phi_1|^2) \phi dx. \end{aligned} \quad (12)$$

Similarly,

$$\begin{aligned} B(\|\underline{v}\|^2) \int_{\Omega} \nabla \underline{v} \cdot \nabla \psi dx &= 2\varepsilon^k B(\|\underline{v}\|^2) \int_{\Omega} (\sigma\phi_1^2 - |\nabla\phi_1|^2) \phi dx \\ &\leq 2b_2\varepsilon^k \int_{\Omega} (\sigma\phi_1^2 - |\nabla\phi_1|^2) \phi dx. \end{aligned} \quad (13)$$

Let  $\eta > 0$ ,  $\mu > 0$  be such that

$$\begin{aligned} \sigma\phi_1^2 - |\nabla\phi_1|^2 &\leq 0, \\ x &\in \overline{\Omega}_\eta, \end{aligned} \quad (14)$$

and  $\mu \leq \phi_1 \leq 1$  on  $\Omega \setminus \overline{\Omega}_\eta$  where  $\overline{\Omega}_\eta = \{x \in \Omega : d(x, \partial\Omega) \leq \eta\}$ .

We have from (14) that

$$A\left(\int_{\overline{\Omega}_\eta} |\nabla \underline{u}|^2 dx\right) \int_{\overline{\Omega}_\eta} \nabla \underline{u} \cdot \nabla \phi dx \leq 0 \leq \lambda_1 \int_{\overline{\Omega}_\eta} \underline{u}^a \phi dx + \mu_1 \int_{\overline{\Omega}_\eta} \underline{v}^b \phi dx, \quad (15)$$

$$B\left(\int_{\overline{\Omega}_\eta} |\nabla \underline{v}|^2 dx\right) \int_{\overline{\Omega}_\eta} \nabla \underline{v} \cdot \nabla \psi dx \leq 0 \leq \lambda_2 \int_{\overline{\Omega}_\eta} \underline{u}^c \psi dx + \mu_2 \int_{\overline{\Omega}_\eta} \underline{v}^d \psi dx. \quad (16)$$

On the other hand, in  $\Omega \setminus \overline{\Omega}_\eta$ , let

$$\begin{aligned} r_1 &= \frac{1-a}{c}, \\ r_2 &= \frac{1-a}{1-a-c}, \\ s_1 &= \frac{1-d}{b}, \\ s_2 &= \frac{1-d}{1-d-b}. \end{aligned} \quad (17)$$

Note that

$$\frac{1}{r_1} + \frac{1}{r_2} = 1, \quad (18)$$

$$\frac{1}{s_1} + \frac{1}{s_2} = 1.$$

We have from (11) that

$$1 - \frac{a}{r_1} - \frac{kb}{r_2} \geq 1 - a - kb > 0, \quad (19)$$

$$k\left(1 - \frac{d}{s_2}\right) - \frac{c}{s_1} \geq k(1-d) - c > 0.$$

Thus, we choose  $\varepsilon > 0$  such that

$$\begin{aligned} 2a_2\varepsilon^{1-(a/r_1)-(kb/r_2)}\sigma\phi_1^2 &\leq \lambda_1^{1/r_1}\mu_1^{1/r_2}\mu^{2+a\delta}, \quad x \in \Omega \setminus \overline{\Omega}_\eta, \\ 2b_2\varepsilon^{k(1-(d/s_2))-(c/s_1)}\sigma\phi_1^2 &\leq \lambda_2^{1/s_1}\mu_2^{1/s_2}\mu^{2+\gamma d}, \quad x \in \Omega \setminus \overline{\Omega}_\eta, \end{aligned} \quad (20)$$

where  $\delta = 2/(1-a)$ ,  $\gamma = 2/(1-d)$ . Furthermore,

$$\begin{aligned} a\delta r_1 &= \frac{2a}{1-a-c} \geq 2a, \\ \gamma d s_2 &= \frac{2d}{1-d-b} \geq 2d, \\ 2s_1 &= 2\left(\frac{1-d}{b}\right) > 2\left(\frac{c}{1-a}\right) \geq 2c, \\ 2r_2 &= 2\left(\frac{1-a}{c}\right) > 2\left(\frac{b}{1-d}\right) \geq 2b. \end{aligned} \quad (21)$$

These relations and Young inequality show that

$$\begin{aligned} 2a_2\varepsilon \int_{\Omega \setminus \overline{\Omega}_\eta} (\sigma\phi_1^2 - |\nabla\phi_1|^2) \phi dx &\leq 2a_2\varepsilon \int_{\Omega \setminus \overline{\Omega}_\eta} \sigma\phi_1^2 \cdot \phi dx \\ &\leq \int_{\Omega \setminus \overline{\Omega}_\eta} (\lambda_1^{1/r_1} \varepsilon^{a/r_1} \mu^{a\delta}) (\mu_1^{1/r_2} \varepsilon^{kb/r_2} \mu^2) \phi dx \\ &\leq \int_{\Omega \setminus \overline{\Omega}_\eta} \left[ \frac{(\lambda_1^{1/r_1} \varepsilon^{a/r_1} \mu^{a\delta})^{r_1}}{r_1} + \frac{(\mu_1^{1/r_2} \varepsilon^{kb/r_2} \mu^2)^{r_2}}{r_2} \right] \phi dx \\ &\leq \int_{\Omega \setminus \overline{\Omega}_\eta} \left[ (\lambda_1^{1/r_1} \varepsilon^{a/r_1} \mu^{a\delta})^{r_1} + (\mu_1^{1/r_2} \varepsilon^{kb/r_2} \mu^2)^{r_2} \right] \phi dx \\ &= \int_{\Omega \setminus \overline{\Omega}_\eta} (\lambda_1 \varepsilon^a \mu^{a\delta r_1} + \mu_1 \varepsilon^{kb} \mu^{2r_2}) \phi dx \\ &\leq \int_{\Omega \setminus \overline{\Omega}_\eta} (\lambda_1 \varepsilon^a \phi_1^{2a} + \mu_1 \varepsilon^{kb} \phi_1^{2b}) \phi dx \\ &= \int_{\Omega \setminus \overline{\Omega}_\eta} (\lambda_1 \underline{u}^a + \mu_1 \underline{v}^b) \phi dx, \end{aligned} \quad (22)$$

$$\begin{aligned}
& 2b_2\varepsilon^k \int_{\Omega \setminus \bar{\Omega}_\eta} (\sigma\phi_1^2 - |\nabla\phi_1|^2) \psi \, dx \leq 2b_2\varepsilon^k \int_{\Omega \setminus \bar{\Omega}_\eta} \sigma\phi_1^2 \cdot \psi \, dx \\
& \leq \int_{\Omega \setminus \bar{\Omega}_\eta} (\lambda_2^{1/s_1} \varepsilon^{c/s_1} \mu^2) (\mu_2^{1/s_2} \varepsilon^{kd/s_2} \mu^{\gamma d}) \psi \, dx \\
& \leq \int_{\Omega \setminus \bar{\Omega}_\eta} \left[ \frac{(\lambda_2^{1/s_1} \varepsilon^{c/s_1} \mu^2)^{s_1}}{s_1} + \frac{(\mu_2^{1/s_2} \varepsilon^{kd/s_2} \mu^{\gamma d})^{s_2}}{s_2} \right] \psi \, dx \\
& \leq \int_{\Omega \setminus \bar{\Omega}_\eta} \left[ (\lambda_2^{1/s_1} \varepsilon^{c/s_1} \mu^2)^{s_1} + (\mu_2^{1/s_2} \varepsilon^{kd/s_2} \mu^{\gamma d})^{s_2} \right] \psi \, dx \\
& = \int_{\Omega \setminus \bar{\Omega}_\eta} (\lambda_2 \varepsilon^c \mu^{2s_1} + \mu_2 \varepsilon^{kd} \mu^{\gamma ds_2}) \psi \, dx \\
& \leq \int_{\Omega \setminus \bar{\Omega}_\eta} (\lambda_2 \varepsilon^c \mu^{2c} + \mu_2 \varepsilon^{kd} \mu^{2d}) \psi \, dx \\
& \leq \int_{\Omega \setminus \bar{\Omega}_\eta} (\lambda_2 \varepsilon^c \phi_1^{2c} + \mu_2 \varepsilon^{kd} \phi_1^{2d}) \psi \, dx \\
& = \int_{\Omega \setminus \bar{\Omega}_\eta} \left( \lambda_2 \underline{\mu}^c + \mu_2 \underline{\nu}^d \right) \psi \, dx.
\end{aligned} \tag{23}$$

Hence, from (15)–(23), it follows that

$$\begin{aligned}
& A \left( \int_{\Omega} |\nabla \underline{u}|^2 \, dx \right) \left[ \int_{\Omega_\eta} \nabla \underline{u} \nabla \phi \, dx + \int_{\Omega \setminus \bar{\Omega}_\eta} \nabla \underline{u} \nabla \phi \, dx \right] \\
& = A \left( \int_{\Omega} |\nabla \underline{u}|^2 \, dx \right) \int_{\Omega} \nabla \underline{u} \nabla \phi \, dx \leq (\lambda_1 \underline{\mu}^a + \mu_1 \underline{\nu}^b) \phi \, dx,
\end{aligned} \tag{24}$$

$$\begin{aligned}
& B \left( \int_{\Omega} |\nabla \underline{v}|^2 \, dx \right) \left[ \int_{\Omega_\eta} \nabla \underline{v} \nabla \psi \, dx + \int_{\Omega \setminus \bar{\Omega}_\eta} \nabla \underline{v} \nabla \psi \, dx \right] \\
& = B \left( \int_{\Omega} |\nabla \underline{v}|^2 \, dx \right) \int_{\Omega} \nabla \underline{v} \nabla \psi \, dx \leq (\lambda_2 \underline{\mu}^c + \mu_2 \underline{\nu}^d) \psi \, dx.
\end{aligned} \tag{25}$$

Then, by (24) and (25),  $(\underline{u}, \underline{v})$  is a subsolution of (1).

Next, we shall construct a supersolution of problem (1).

Let  $\omega$  be the solution of the following problem:

$$\begin{cases} -\Delta e = 1 \text{ in } \Omega, \\ e = 0 \text{ on } \partial\Omega. \end{cases} \tag{26}$$

Let

$$\begin{aligned}
\bar{u} &= C_1 e, \\
\bar{v} &= C_2 e,
\end{aligned} \tag{27}$$

where  $e$  is given by (26) and  $C_1, C_2 > 0$  are large positive real numbers to be chosen later. We shall verify that  $(\bar{u}, \bar{v})$  is a supersolution of problem (1). Let  $\phi \in H_0^1(\Omega)$  with  $\phi \geq 0$  in  $\Omega$ . Then, we obtain from (26) and the condition (H1) that

$$\begin{aligned}
A \left( \int_{\Omega} |\nabla \bar{u}|^2 \, dx \right) \int_{\Omega} \nabla \bar{u} \cdot \nabla \phi \, dx &= A \left( \int_{\Omega} |\nabla \bar{u}|^2 \, dx \right) C_1 \int_{\Omega} \nabla e \cdot \nabla \phi \, dx \\
&= A \left( \int_{\Omega} |\nabla \bar{u}|^2 \, dx \right) C_1 \int_{\Omega} \phi \, dx \\
&\geq a_1 C_1 \int_{\Omega} \phi \, dx \\
B \left( \int_{\Omega} |\nabla \bar{v}|^2 \, dx \right) \int_{\Omega} \nabla \bar{v} \cdot \nabla \psi \, dx &= B \left( \int_{\Omega} |\nabla \bar{v}|^2 \, dx \right) C_2 \int_{\Omega} \nabla e \cdot \nabla \psi \, dx \\
&= B \left( \int_{\Omega} |\nabla \bar{v}|^2 \, dx \right) C_2 \int_{\Omega} \psi \, dx \\
&\geq b_1 C_2 \int_{\Omega} \psi \, dx.
\end{aligned} \tag{28}$$

Let  $l = \|e\|_{\infty}$ . Since  $a < 1$ ,  $d < 1$ , these imply that there exist positive large constants  $\alpha = a_1 C_1, \beta = b_1 C_2$  such that

$$\begin{aligned}
\alpha &\geq \lambda_1 (\alpha l)^a + \mu_1 (\beta l)^b, \\
\beta &\geq \lambda_2 (\alpha l)^c + \mu_2 (\beta l)^d.
\end{aligned} \tag{29}$$

Thus,

$$a_1 C_1 \int_{\Omega} \phi \, dx \geq \int_{\Omega} (\lambda_1 \bar{u}^a + \mu_1 \bar{v}^b) \phi \, dx, \tag{30}$$

$$b_1 C_2 \int_{\Omega} \psi \, dx \geq \int_{\Omega} (\lambda_2 \bar{u}^c + \mu_2 \bar{v}^d) \psi \, dx. \tag{31}$$

From (26) and (30), we can deduce that the couple  $(\bar{u}, \bar{v})$  is a subsolution of problem (1) with  $\underline{u} \leq \bar{u}$  and  $\underline{v} \leq \bar{v}$  for  $C_1, C_2$  large.

In order to obtain a weak solution of problem (1) we shall use the arguments by Azouz and Bensedik [19]. For this purpose, we define a sequence  $\{(u_n, v_n)\} \subset (H_0^1(\Omega) \times H_0^1(\Omega))$  as follows:  $u_0 := \bar{u}, v_0 := \bar{v}$  and  $(u_n, v_n)$  is the unique solution of the system

$$\begin{cases} -A \left( \int_{\Omega} |\nabla u_n|^2 \, dx \right) \Delta u_n = \lambda_1 u_{n-1}^a + \mu_1 v_{n-1}^b \text{ in } \Omega, \\ -B \left( \int_{\Omega} |\nabla v_n|^2 \, dx \right) \Delta v_n = \lambda_2 u_{n-1}^c + \mu_2 v_{n-1}^d \text{ in } \Omega, \\ u_n = v_n = 0 \text{ on } \partial\Omega. \end{cases} \tag{32}$$

Problem (32) is  $(A, B)$ -linear in the sense that if  $(u_{n-1}, v_{n-1}) \in (H_0^1(\Omega) \times H_0^1(\Omega))$  is given, the right hand sides of (32) are independent of  $u_n, v_n$ .

Set  $A(t) = tA(t^2), B(t) = tB(t^2)$ . Then, since  $A(\mathbb{R}) = \mathbb{R}, B(\mathbb{R}) = \mathbb{R}, f(u_{n-1}) = u_{n-1}^a, h(v_{n-1}) = v_{n-1}^b, g(u_{n-1}) = u_{n-1}^c$ , and  $\tau(v_{n-1}) = v_{n-1}^d \in L^2(\Omega)$ .

We deduce from a result in [4] that system (32) has a unique solution  $(u_n, v_n) \in (H_0^1(\Omega) \times H_0^1(\Omega))$ .

By using (32) and the fact that  $(u_0, v_0)$  is a supersolution of (1), we have

$$\begin{cases} -A \left( \int_{\Omega} |\nabla u_0|^2 \, dx \right) \Delta u_0 \geq \lambda_1 u_0^a + \mu_1 v_0^b = -A \left( \int_{\Omega} |\nabla u_1|^2 \, dx \right) \Delta u_1, \\ -B \left( \int_{\Omega} |\nabla v_0|^2 \, dx \right) \Delta v_0 \geq \lambda_2 u_0^c + \mu_2 v_0^d = -B \left( \int_{\Omega} |\nabla v_1|^2 \, dx \right) \Delta v_1, \end{cases} \tag{33}$$

and by Lemma 1,  $u_0 \geq u_1$  and  $v_0 \geq v_1$ . Also, since  $u_0 \geq \underline{u}$ ,  $v_0 \geq \underline{v}$  and the monotonicity of  $f, h, g$ , and  $\tau$  one has

$$\begin{aligned} -A\left(\int_{\Omega} |\nabla u_1|^2 dx\right) \Delta u_1 &= \lambda_1 u_0^a + \mu_1 v_0^b \geq \lambda_1 \underline{u}^a + \mu_1 \underline{v}^b \geq \\ &\quad -A\left(\int_{\Omega} |\nabla \underline{u}|^2 dx\right) \Delta \underline{u}, \\ -B\left(\int_{\Omega} |\nabla v_1|^2 dx\right) \Delta v_1 &= \lambda_2 u_0^c + \mu_2 v_0^d \geq \lambda_2 \underline{u}^c + \mu_2 \underline{v}^d \geq \\ &\quad -B\left(\int_{\Omega} |\nabla \underline{v}|^2 dx\right) \Delta \underline{v}, \end{aligned} \quad (34)$$

from which, rding to Lemma 1,  $u_1 \geq \underline{u}$ ,  $v_1 \geq \underline{v}$  for  $u_2, v_2$  we write

$$\begin{aligned} -A\left(\int_{\Omega} |\nabla u_1|^2 dx\right) \Delta u_1 &= \lambda_1 u_0^a + \mu_1 v_0^b \geq \lambda_1 u_1^a + \mu_1 v_1^b \\ &= -A\left(\int_{\Omega} |\nabla u_2|^2 dx\right) \Delta u_2, \\ -B\left(\int_{\Omega} |\nabla v_1|^2 dx\right) \Delta v_1 &= \lambda_2 u_0^c + \mu_2 v_0^d \geq \lambda_2 u_1^c + \mu_2 v_1^d \\ &= -B\left(\int_{\Omega} |\nabla v_2|^2 dx\right) \Delta v_2, \end{aligned} \quad (35)$$

and then  $u_1 \geq u_2$ ,  $v_1 \geq v_2$ . Similarly,  $u_2 \geq \underline{u}$  and  $v_2 \geq \underline{v}$  because

$$\begin{aligned} -A\left(\int_{\Omega} |\nabla u_2|^2 dx\right) \Delta u_2 &= \lambda_1 u_0^a + \mu_1 v_0^b \geq \lambda_1 \underline{u}^a + \mu_1 \underline{v}^b \geq \\ &\quad -A\left(\int_{\Omega} |\nabla \underline{u}|^2 dx\right) \Delta \underline{u}, \\ -B\left(\int_{\Omega} |\nabla v_2|^2 dx\right) \Delta v_2 &= \lambda_2 u_1^c + \mu_2 v_1^d \geq \lambda_2 \underline{u}^c + \mu_2 \underline{v}^d \geq \\ &\quad -B\left(\int_{\Omega} |\nabla \underline{v}|^2 dx\right) \Delta \underline{v}. \end{aligned} \quad (36)$$

Repeating this argument, we get a bounded monotone sequence  $\{(u_n, v_n)\} \subset (H_0^1(\Omega) \times H_0^1(\Omega))$  satisfying

$$\bar{u} = u_0 \geq u_1 \geq u_2 \geq \dots \geq u_n \geq \dots \geq \underline{u} > 0, \quad (37)$$

$$\bar{v} = v_0 \geq v_1 \geq v_2 \geq \dots \geq v_n \geq \dots \geq \underline{v} > 0. \quad (38)$$

Using the continuity of the functions  $f, h, g$ , and  $t$  and the definition of the sequences  $\{u_n\}, \{v_n\}$ , there exist constants  $C_i > 0$ ,  $i = 1, \dots, 4$  independent of  $n$  such that

$$\begin{aligned} |f(v_{n-1})| &\leq C_1, \\ |h(u_{n-1})| &\leq C_2, \end{aligned} \quad (39)$$

$$\begin{aligned} |g(u_{n-1})| &\leq C_3, \\ |\tau(u_{n-1})| &\leq C_4, \text{ for all } n. \end{aligned} \quad (40)$$

From (39), multiplying the first equation of (32) by  $u_n$  and integrating using the Holder inequality and Sobolev embedding, we can show that

$$\begin{aligned} a_1 \int_{\Omega} |\nabla u_n|^2 dx &\leq A \left( \int_{\Omega} |\nabla u_n|^2 dx \right) \int_{\Omega} |\nabla u_n|^2 dx \\ &= \lambda_1 \int_{\Omega} f(v_{n-1}) u_n dx + \mu_1 \int_{\Omega} h(u_{n-1}) u_n dx \\ &\leq \lambda_1 \int_{\Omega} |f(v_{n-1})| |u_n| dx + \mu_1 \int_{\Omega} |h(u_{n-1})| |u_n| dx \\ &\leq C_1 \lambda_1 \int_{\Omega} |u_n| dx + C_2 \mu_1 \int_{\Omega} |u_n| dx \\ &\leq C_5 \|u_n\|_{H_0^1(\Omega)}, \end{aligned} \quad (41)$$

or

$$\|u_n\|_{H_0^1(\Omega)} \leq C_5, \quad \forall n, \quad (42)$$

where  $C_5 > 0$  is a constant independent of  $n$ . Similarly, there exists  $C_6 > 0$  independent of  $n$  such that

$$\|v_n\|_{H_0^1(\Omega)} \leq C_6, \quad \forall n. \quad (43)$$

From (42) and (43), we infer that  $\{(u_n, v_n)\}$  has a subsequence which weakly converges in  $H_0^1(\Omega, \mathbb{R}^2)$  to a limit  $(u, v)$  with the properties  $u \geq \underline{u} > 0$  and  $v \geq \underline{v} > 0$ . Being monotone and also using a standard regularity argument,  $\{(u_n, v_n)\}$  converges itself to  $(u, v)$ . Now, letting  $n \rightarrow +\infty$  in (32), we deduce that  $(u, v)$  is a positive solution of system (1). The proof of theorem is now completed.  $\square$

## 4. Conclusion

In this work, we study the existence of weak positive solutions for a sublinear Kirchhoff elliptic systems in bounded domains by using the subsuper solutions method (SSM) combined with comparison principle which have been widely applied in many work (see for example [4, 19, 21–25]). Validity of the comparison principle and of the SSM for local and nonlocal problems as the stationary Kirchhoff Equation was an important subject in the last few years (see, for example, [26] and [23]). Moreover, the two conditions that  $M$  is nonincreasing and  $H$  is increasing turn out to be necessary and sufficient, at least for the validity of the comparison principle. It is worth to notice that in [4], Alves and Correa developed a new SSM for problem (1) to deal with the increasing  $M$  case. The result is obtained by using a kind of Minty–Browder theorem for a suitable pseudomonotone operator, but instead of constructing a subsolution, the authors assumed the existence of a whole family of functions which satisfy a stronger condition than just being subsolutions; the inconvenience is that these stronger conditions restrict the possible right hand sides in (1). Another SSM for nonlocal problems is obtained in [4] for a problem involving a nonlocal term with a Lebesgue norm, instead of the Sobolev norm appearing in (1). In our next study, we will try to apply an alternative approach using the variational principle which has been presented in [27–29].



## Data Availability

The data used to support the findings of the study are available from the corresponding author upon request.

## Conflicts of Interest

The authors declare that there are no conflicts of interest regarding the publication of this article.

## Authors' Contributions

All authors contributed equally to this article. They have all read and approved the final manuscript.

## References

- [1] P. D'Ancona and S. Spagnolo, "Global solvability for the degenerate Kirchhoff equation with real analytic data," *Inventiones Mathematicae*, vol. 108, pp. 247–262, 1992.
- [2] H. Medekhel, S. Boulaaras, K. Zennir, and A. Allahem, "Existence of positive solutions and its asymptotic behavior of  $(p(x), q(x))$ -Laplacian parabolic system," *Symmetry*, vol. 11, no. 3, p. 332, 2019.
- [3] J. L. Lions, "On some questions in boundary value problems of mathematical physics," *Contemporary Developments in Continuum Mechanics and Partial Differential Equations, Proceedings of the International Symposium on Continuum Mechanics and Partial Differential Equations*, vol. 30, pp. 284–346, 1978.
- [4] C. O. Alves and F. J. S. A. Correa, "On existence of solutions for a class of problem involving a nonlinear operator," *Communications on Applied Nonlinear Analysis*, vol. 8, pp. 43–56, 2001.
- [5] Y. Li, F. Li, and J. Shi, "Existence of positive solutions to Kirchhoff type problems with zero mass," *Journal of Mathematical Analysis and Applications*, vol. 410, no. 1, pp. 361–374, 2014.
- [6] B. Ricceri, "On an elliptic Kirchhoff-type problem depending on two parameters," *Journal of Global Optimization*, vol. 46, no. 4, pp. 543–549, 2010.
- [7] J. Deuel and P. Hess, "Inequations variationnelles elliptiques non coercives," *C. R. Acad. Sci. Paris*, vol. 279, pp. 719–722, 1974.
- [8] P. Hess, "On the solvability of nonlinear elliptic boundary value problems," *Indiana University Mathematics Journal*, vol. 25, no. 5, pp. 461–466, 1976.
- [9] S. Carl, V. K. Le, and D. Motreanu, "The sub-supersolution method and extremal solutions for quasilinear hemivariational inequalities," *Differential and Integral Equations*, vol. 17, pp. 165–178, 2004.
- [10] E. N. Dancer and G. Sweers, "On the existence of a maximal weak solution for a semilinear elliptic equation," *Differential and Integral Equations*, vol. 2, pp. 533–540, 1989.
- [11] T. Kura, "The weak supersolution-subsolution method for second order quasilinear elliptic equations," *Hiroshima Mathematical Journal*, vol. 19, p. 136, 1989.
- [12] B. Mairi, R. Guefaïfia, S. Boulaaras, and T. Bouali, "Existence of positive solutions for a new class of nonlocal  $p(x)$ -Kirchhoff elliptic systems via sub-super solutions concept," *Applied Science APPS*, vol. 20, pp. 117–128, 2018.
- [13] S. Boulaaras, R. Guefaïfia, and K. Zennir, "Existence of positive solutions for nonlocal  $p(x)$ -Kirchhoff elliptic systems," *Advances in Pure and Applied Mathematics*, vol. 10, no. 1, pp. 1867–1152, 2019.
- [14] V. K. Le and K. Schmitt, "Some general concepts of sub- and supersolutions for nonlinear elliptic problems," *Topological Methods in Nonlinear Analysis*, vol. 28, pp. 87–103, 2006.
- [15] N. Mezouar and S. Boulaaras, "Global existence and decay of solutions for a class of viscoelastic Kirchhoff equation," *Bulletin of the Malaysian Mathematical Sciences Society*, vol. 43, no. 1, pp. 725–755, 2018.
- [16] V. K. Le, "Subsolution-supersolution method in variational inequalities," *Nonlinear Analysis*, vol. 45, pp. 775–800, 2001.
- [17] V. K. Le, "Subsolution-supersolutions and the existence of extremal solutions in noncoercive variational inequalities," *Journal of Inequalities in Pure and Applied Mathematics*, vol. 2, p. 116, 2001.
- [18] S. Boulaaras, D. Ouchenane, and F. Mesloub, "General decay for a viscoelastic problem with not necessarily decreasing kernel," *Applicable Analysis*, vol. 98, no. 9, pp. 1677–1693, 2019.
- [19] N. Azouz and A. Bensedik, "Existence result for an elliptic equation of Kirchhoff-type with changing sign data," *Funkcialaj Ekvacioj*, vol. 55, no. 1, pp. 55–66, 2012.
- [20] D. D. Hai and R. Shivaji, "An existence result on positive solutions for a class of  $p$ -Laplacian systems," *Nonlinear Analysis: Theory, Methods & Applications*, vol. 56, no. 7, pp. 1007–1010, 2004.
- [21] S. Boulaaras and R. Guefaïfia, "Existence of positive weak solutions for a class of Kirchhoff elliptic systems with multiple parameters," *Mathematical Methods in the Applied Sciences*, vol. 41, no. 13, pp. 5203–5210, 2018.
- [22] S. Boulaaras, R. Guefaïfia, and S. Kabli, "An asymptotic behavior of positive solutions for a new class of elliptic systems involving of  $(p(x), q(x))$ -Laplacian systems," *Boletín de la Sociedad Matemática Mexicana*, vol. 25, no. 1, pp. 145–162, 2019.
- [23] F. J. S. A. Correa and G. M. Figueiredo, "On an elliptic equation of  $p$ -Kirchhoff type via variational methods," *Bulletin of the Australian Mathematical Society*, vol. 74, no. 2, pp. 263–277, 2006.
- [24] R. Guefaïfia and S. Boulaaras, "Existence of positive solution for a class of  $(p(x), q(x))$ -Laplacian systems," *Rendiconti del Circolo Matematico di Palermo Series 2*, vol. 67, pp. 93–103, 2018.
- [25] S. Boulaaras and A. Allahem, "Existence of positive solutions of nonlocal  $p(x)$ -Kirchhoff evolutionary systems via sub-super solutions concept," *Symmetry*, vol. 11, no. 2, p. 253, 2019.
- [26] M. Chipot and B. Lovat, "Some remarks on non local elliptic and parabolic problems," *Nonlinear Analysis: Theory, Methods & Applications*, vol. 30, no. 7, pp. 4619–4627, 1997.
- [27] S. Boulaaras, "Some existence results for elliptic Kirchhoff equation with changing sign data and a logarithmic non-linearity," *Journal of Intelligent and Fuzzy Systems*, vol. 37, no. 6, pp. 1–10, 2019.
- [28] S. Boulaaras, "A well-posedness and exponential decay of solutions for a coupled lamé system with viscoelastic term and logarithmic source terms," *Applicable Analysis*, pp. 1–19, 2019.
- [29] J.-H. He, "Variational principle for the generalized KdV-burgers equation with fractal derivatives for shallow water waves," *Journal of Applied and Computational Mechanics*, vol. 6, no. 4, [http://jacm.scu.ac.ir/article\\_14813.html](http://jacm.scu.ac.ir/article_14813.html), 2020.



## Research Article

# Existence of Positive Solutions for a Class of $(p(x), q(x))$ -Laplacian Elliptic Systems with Multiplication of Two Separate Functions

Youcef Bouizem <sup>1</sup>, Salah Mahmoud Boulaaras <sup>2,3</sup>, and Ali Allahem <sup>4</sup>

<sup>1</sup>Department of Mathematics, Faculty of Mathematics and Informatics,

University of Science and Technology of Oran Mohamed Boudiaf El Mnaouar, Bir El'Djir, Oran 31000, Algeria

<sup>2</sup>Department of Mathematics, College of Sciences and Arts, Qassim University, Al-Rass, Saudi Arabia

<sup>3</sup>Laboratory of Fundamental and Applied Mathematics of Oran (LMFAO), University of Oran 1, Ahmed Benbella, Algeria

<sup>4</sup>Department of Mathematics, College of Sciences, Qassim University, Buraydah, Saudi Arabia

Correspondence should be addressed to Salah Mahmoud Boulaaras; s.boulaaras@qu.edu.sa

Received 5 November 2019; Accepted 6 December 2019; Published 20 January 2020

Guest Editor: Viet-Thanh Pham

Copyright © 2020 Youcef Bouizem et al. This is an open access article distributed under the Creative Commons Attribution License, which permits unrestricted use, distribution, and reproduction in any medium, provided the original work is properly cited.

The paper deals with the study of the existence of weak positive solutions for a new class of the system of elliptic differential equations with respect to the symmetry conditions and the right hand side which has been defined as multiplication of two separate functions by using the sub-supersolutions method (1991 Mathematics Subject Classification: 35J60, 35B30, and 35B40).

## 1. Introduction

Elliptic systems of differential equations are of crucial importance in modelization and description of a wide variety of phenomena such as fluid dynamics, quantum physics, sound, heat, electrostatics, diffusion, gravitation, chemistry, biology, simulation of airplane, calculator charts, and time prediction. PDEs are equations involving functions of several variables and their derivatives and model multidimensional systems generalizing ODEs (ordinary differential equations), which deal with functions of a single variable and their derivatives (see, for example, [1–15]).

In contrary to ODEs, there is no general result such as the Picard–Lindelöf theorem for PDEs to settle the existence and uniqueness of solutions. Malgrange–Ehrenpreis theorem states that linear partial differential equations with constant coefficients always have at least one solution; another powerful and general result in case of polynomial coefficients is the Cauchy–Kovalevskaya theorem ensuring the existence and uniqueness of a locally analytic solution

for PDEs with coefficients that are analytic in the unknown function and its derivatives; otherwise, the existence of solutions is not guaranteed at all for nonanalytic coefficients even if they have derivatives of all orders (see [16]). Given the rich variety of PDEs, there is no general theory of solvability. Instead, research focuses on particular PDEs that are important for applications. It would be desirable when solving a PDE to prove the existence and uniqueness of a regular solution that depends on the initial data given in the problem, but perhaps we are asking too much. A solution with enough smoothness is called a classical solution, but in most cases as for conservation laws, we cannot achieve that much and allow generalized or weak solutions. The point is this: looking for weak solutions allows us to investigate a larger class of candidates, so it is more reasonable to consider as separate the existence and the regularity problems. For various PDEs, this is the best that can be done, and naturally nonlinear equations are more difficult than linear ones. Overall, we know too much about linear PDEs and in best cases, we can express their

solutions but too little about nonlinear equations. For linear PDEs, various methods and techniques can be used for separation of variables, method of characteristics, integral transform, change of variables, superposition principle, or even finding a fundamental solution and taking a convolution product to obtain the solution. Variational theory is the most accessible and useful of the methods for nonlinear PDEs, but there are other non-variational techniques of use for nonlinear elliptic and parabolic PDEs such as monotonicity and fixed point methods, semigroup theory, and sub-supersolutions method that played an important role in the study of nonlinear boundary value problems for a long time. Scorza-Dragnoni's work in [17] was one of the earliest papers using a pair of ordered solutions of differential inequalities to establish the existence of solution to a given boundary value problem for a nonlinear second-order ordinary differential equation; his work was followed later by Nagumo in [18, 19] which inspired much work on both ordinary and PDEs during the decade of the sixties. Knobloch in [20] introduced the sub-supersolution method to the study of periodic boundary value problems for nonlinear second-order ordinary differential equations using Cesari's method; similar problems and techniques were studied in [21, 22] and still the sub-supersolutions and supersolutions are assumed to be smooth solutions of differential inequalities. Then, the SSM were also used to study Dirichlet and Neumann boundary value problems for semilinear elliptic problems in [23, 24], and even for nonlinear boundary value problems in [25–27] and also for systems of nonlinear ordinary differential equations in [28–30]. The concept of weak sub-supersolutions and supersolutions was first formulated by Hess and Deuel in [31, 32] to obtain existence results for weak solutions of semilinear elliptic Dirichlet problems and was subsequently continued by several authors (see, e.g., [33–43]).

The study of differential equations and variational problems with nonstandard  $p(x)$ -growth conditions is a new and interesting topic. It arises from nonlinear elasticity theory, electrorheological fluids, etc (see [44]). Many existence results have been obtained on this kind of problems (see, for example, [44–57]) and in [45] a new class of anisotropic quasilinear elliptic equations with a power-like variable reaction term has been investigated.

In the last few years in [51, 58–60], the regularity and existence of solutions for differential equations with nonstandard  $p(x)$ -growth conditions have been studied and  $p$ -Laplacian elliptic systems with  $p(x) = q(x) = p$  (a constant) have been archived. In this work, we study the existence of weak positive solutions for a new class of the system of differential equations with respect to the symmetry conditions by using sub-supersolution method.

## 2. Preliminaries, Assumptions, and Statement of the Problem

*2.1. Plate Problems and Its History.* In this paper, we consider the system of differential equations:

$$\begin{cases} -\Delta_{p(x)}u = \lambda^{p(x)}[a(x)f(u)h(v)] \text{ in } \Omega, \\ -\Delta_{q(x)}v = \lambda^{q(x)}[b(x)g(u)\tau(v)] \text{ in } \Omega, \\ u = v = 0 \text{ on } \partial\Omega, \end{cases} \quad (1)$$

where  $\Omega \subset \mathbb{R}^N$  is a bounded smooth domain with  $C^2$  boundary  $\partial\Omega$  and  $1 < p(x), q(x) \in C^1(\overline{\Omega})$  are functions with  $1 < p^- := \inf_{\Omega} p(x) \leq p^+ := \sup_{\Omega} p(x) < \infty$ ,  $1 < q^- := \inf_{\Omega} q(x) \leq q^+ := \sup_{\Omega} q(x)$ , and  $\Delta_{p(x)}$  is a  $p(x)$ -Laplacian defined as

$$\Delta_{p(x)}u = \operatorname{div}(|\nabla u|^{p(x)-2}\nabla u), \quad (2)$$

and  $a, b: \overline{\Omega} \rightarrow \mathbb{R}^+$  are continuous functions, while  $f, g, h$ , and  $\tau$  are monotone functions in  $\mathbb{R}^+$  such that

$$\begin{aligned} \lim_{u \rightarrow +\infty} f(u) &= +\infty, \\ \lim_{u \rightarrow +\infty} g(u) &= +\infty, \\ \lim_{u \rightarrow +\infty} h(u) &= +\infty, \\ \lim_{u \rightarrow +\infty} \tau(u) &= +\infty, \end{aligned} \quad (3)$$

satisfying some natural growth condition at  $u = \infty$ .

We point out that the extension from  $p$ -Laplace operator to  $p(x)$ -Laplace operator is not trivial, since the  $p(x)$ -Laplacian has a more complicated structure than the  $p$ -Laplace operator, such as it is nonhomogeneous. Moreover, many results and methods for  $p$ -Laplacians are not valid for the  $p(x)$ -Laplacian; for example, if  $\Omega$  is bounded, then the Rayleigh quotient

$$\lambda_{p(x)} = \inf_{u \in W_0^{1,p(x)}(\Omega) \setminus \{0\}} \frac{\int_{\Omega} (1/p(x)) |\nabla u|^{p(x)} dx}{\int_{\Omega} (1/p(x)) |u|^{p(x)} dx}, \quad (4)$$

is zero in general, and only under some special conditions,  $\lambda_{p(x)}$  is positive (see [53]). Maybe the first eigenvalue and the first eigenfunction of the  $p(x)$ -Laplacian do not exist, but the fact that the first eigenvalue  $\lambda_p$  is positive and the existence of the first eigenfunction are very important in the study of  $p$ -Laplacian problem. There are more difficulties in discussing the existence of solutions of variable exponent problems. In [59], the authors considered the existence of positive weak solutions for the following  $p$ -Laplacian problem:

$$\begin{cases} -\Delta_p u = \lambda f(v) \text{ in } \Omega, \\ -\Delta_p u = \lambda g(u) \text{ in } \Omega, \\ u = v = 0 \text{ on } \partial\Omega, \end{cases} \quad (5)$$

where the first eigenfunction has been used to construct the subsolution of  $p$ -Laplacian problem. Under the condition that for all  $M > 0$ ,

$$\lim_{u \rightarrow +\infty} \frac{f(M(g(u))^{1/p-1})}{u^{p-1}} = 0, \quad (6)$$

the authors gave the existence of positive solutions for problem (5) provided that  $\lambda$  is large enough.

In [48], the existence and nonexistence of positive weak solutions to the following quasilinear elliptic system:

$$\begin{cases} -\Delta_p u = \lambda u^\alpha v^\gamma \text{ in } \Omega, \\ -\Delta_q u = \lambda u^\delta v^\beta \text{ in } \Omega, \\ u = v = 0 \text{ on } \partial\Omega, \end{cases} \quad (7)$$

has been considered where the first eigenfunction has been used to construct the subsolution of problem (7) and the following results were obtained:

- (i) If  $\alpha, \beta \geq 0, \gamma, \delta > 0, \theta = (p-1-\alpha)(q-1-\beta) - \gamma\delta > 0$ , then problem (7) has a positive weak solution for each  $\lambda > 0$ .
- (ii) If  $\theta = 0$  and  $p\gamma = q(p-1-\alpha)$ , then there exists  $\lambda_0 > 0$  such that for  $0 < \lambda < \lambda_0$ , problem (7) has no nontrivial nonnegative weak solution. For further generalizations of system (7), we refer to [49, 50].

As already discussed before, on the  $p(x)$ -Laplacian problems, maybe the first eigenvalue and the first eigenfunction of the  $p(x)$ -Laplacian do not exist even if the first eigenfunction of the  $p(x)$ -Laplacian exists. Because of the nonhomogeneous property of the  $p(x)$ -Laplacian, the first eigenfunction cannot be used to construct the subsolutions of  $p(x)$ -Laplacian problems. Moreover, in [47, 61], the authors studied the existence of solutions for problem (5), where some symmetry conditions are imposed. Then, in [46], the existence of positive solutions of the system was investigated:

$$\begin{cases} -\Delta_{p(x)} u = \lambda^{p(x)} f(v) \text{ in } \Omega, \\ -\Delta_{p(x)} u = \lambda^{p(x)} g(u) \text{ in } \Omega, \\ u = v = 0 \text{ on } \Omega, \end{cases} \quad (8)$$

without any symmetry conditions. Motivated by the ideas introduced in [47], the authors proved the existence of a positive solution when  $\lambda$  is large enough and satisfies condition (6) and they did not assume any symmetric condition and did not assume any sign condition on  $f(0)$  and  $g(0)$ . Also the authors proved the existence of positive solutions with multiparameters; in this paper, we extend this given system of differential equations, where we establish the existence of a positive solution for a new class of this system with respect to the symmetry conditions by constructing a positive subsolution and supersolution and  $p, q \in C^1(\overline{\Omega})$  are functions,  $\lambda, \lambda_1, \lambda_2, \mu_1$ , and  $\mu_2$  are positive parameters, and  $\Omega \subset \mathbb{R}^N$  is a bounded domain and we did not assume any sign condition on  $f(0)$ ,  $g(0)$ ,  $h(0)$ , and  $\tau(0)$ .

**2.2. Preliminary Results.** In order to discuss problem (1), we need some theories on  $W_0^{1,p(x)}(\Omega)$  which we call variable exponent Sobolev space. Firstly, we state some basic properties of spaces  $W_0^{1,p(x)}(\Omega)$  which will be used later (for details, see [54]).

Let us define

$$L^{p(x)}(\Omega) = \left\{ u: u \text{ is a measurable real - valued function such that } \int_{\Omega} |u(x)|^{p(x)} dx < \infty \right\}. \quad (9)$$

We introduce the norm on  $L^{p(x)}(\Omega)$  by

$$\|u\|_{p(x)} = \inf \left\{ \lambda > 0: \int_{\Omega} \left| \frac{u(x)}{\lambda} \right|^{p(x)} dx \leq 1 \right\}, \quad (10)$$

$$W^{1,p(x)}(\Omega) = \{u \in L^{p(x)}(\Omega); |\nabla u| \in L^{p(x)}(\Omega)\},$$

with the norm

$$\|u\| = \|u\|_{p(x)} + \|\nabla u\|_{p(x)}, \forall u \in W^{1,p(x)}(\Omega). \quad (11)$$

We denote by  $W_0^{1,p(x)}(\Omega)$  the closure of  $C_0^\infty(\Omega)$  in  $W^{1,p(x)}(\Omega)$ .

**Proposition 1** (see [59]). *The spaces  $L^{p(x)}(\Omega)$ ,  $W^{1,p(x)}(\Omega)$ , and  $W_0^{1,p(x)}(\Omega)$  are separable and reflexive Banach spaces.*

Throughout the paper, we will assume that

$$(H1) \quad p, q \in C^1(\overline{\Omega}) \text{ and } 1 < p^- \leq p^+, 1 < q^- \leq q^+$$

(H2)  $f, g, h, \tau: \mathbb{R}^+ \rightarrow \mathbb{R}$  are  $C^1$  monotone functions such that

$$\begin{aligned} \lim_{u \rightarrow +\infty} f(u) &= +\infty, \\ \lim_{u \rightarrow +\infty} g(u) &= +\infty; \\ \lim_{u \rightarrow +\infty} h(u) &= +\infty, \\ \lim_{u \rightarrow +\infty} \tau(u) &= +\infty. \end{aligned} \quad (12)$$

(H3)  $\exists r > 0$  such that

$$\lim_{u \rightarrow +\infty} \frac{f(u)h(cu^{r/q-1})}{u^{p-1}} = 0, \quad (13)$$

for all  $c > 0$ ,

$$\lim_{u \rightarrow +\infty} \frac{g(u)\tau(ku^{r/q-1})}{u^r} = 0, \quad (14)$$

for all  $k > 0$ .

(H4)  $a, b: \overline{\Omega} \rightarrow \mathbb{R}^+$  are continuous functions, such that

$$\begin{aligned} a_1 &= \min_{x \in \overline{\Omega}} a(x), \\ b_1 &= \min_{x \in \overline{\Omega}} b(x), \\ a_2 &= \max_{x \in \overline{\Omega}} a(x), \\ b_2 &= \max_{x \in \overline{\Omega}} b(x). \end{aligned} \quad (15)$$

We define

$$\langle L(u), v \rangle = \int_{\Omega} |\nabla u|^{p(x)-2} \nabla u \nabla v \, dx, \quad \forall u, v \in W_0^{1,p(x)}(\Omega). \quad (16)$$

Then,  $L: W_0^{1,p(x)}(\Omega) \rightarrow (W_0^{1,p(x)}(\Omega))^*$  is a continuous, bounded, and strictly monotone operator, and it is a homeomorphism (see [61], Theorem 3.1).

Define  $A: W_0^{1,p(x)}(\Omega) \rightarrow (W_0^{1,p(x)}(\Omega))^*$  as for all  $u, \varphi \in W_0^{1,p(x)}(\Omega)$ ,

$$\langle A(u), \varphi \rangle = \int_{\Omega} (|\nabla u|^{p(x)-2} \nabla u \nabla \varphi + h(x, u) \varphi) \, dx, \quad (17)$$

where  $h(x, u)$  is continuous on  $\overline{\Omega} \times \mathbb{R}$  and  $h(x)$  is increasing. It is easy to check that  $A$  is a continuous bounded mapping. Copying the proof of [44], we have the following lemma:

**Lemma 1** (see [45]) (comparison principle). *Let  $u, v \in W_0^{1,p(x)}(\Omega)$  satisfy*

$$\begin{aligned} Au - Av &\geq 0 \text{ in } (W_0^{1,p(x)}(\Omega))^*, \\ \varphi(x) &= \min\{u(x) - v(x), 0\}. \end{aligned} \quad (18)$$

If

$$\varphi(x) \in W_0^{1,p(x)}(\Omega), \quad (\text{i.e. } u \geq v \text{ on } \partial\Omega), \quad (19)$$

then  $u \geq v$  a.e. in  $\Omega$ .

**Definition 1.** Let  $(u, v) \in (W_0^{1,p(x)}(\Omega) \times W_0^{1,q(x)}(\Omega))$ ; the couple  $(u, v)$  is said to be a weak solution of (1) if it satisfies

$$\begin{cases} \int_{\Omega} |\nabla u|^{p(x)-2} \nabla u \cdot \nabla \varphi \, dx = \int_{\Omega} \lambda^{p(x)} [a(x) f(u) h(v)] \varphi \, dx, \\ \int_{\Omega} |\nabla v|^{q(x)-2} \nabla v \cdot \nabla \varphi \, dx = \int_{\Omega} \lambda^{q(x)} [b(x) g(u) \tau(v)] \psi \, dx, \end{cases} \quad (20)$$

for all  $(\varphi, \psi) \in (W_0^{1,p(x)}(\Omega) \times W_0^{1,q(x)}(\Omega))$  with  $(\varphi, \psi) \geq 0$ .

Here, and hereafter, we will use the notation  $d(x, \partial\Omega)$  to denote the distance of  $x \in \Omega$  to denote the distance of  $\Omega$ . Denote  $d(x) = d(x, \partial\Omega)$  and  $\partial\Omega_{\varepsilon} = \{x \in \Omega: d(x, \partial\Omega) < \varepsilon\}$ .

Since  $\partial\Omega$  is  $C^2$  regularly, there exists a constant  $\delta \in (0, 1)$  such that  $d(x) \in C^2(\overline{\partial\Omega_{3\delta}})$  and  $|\nabla d(x)| = 1$ .

Denote

$$v_1(x) = \begin{cases} \gamma d(x), d(x) < \delta, \\ \gamma \delta + \int_{\delta}^{d(x)} \gamma \left( \frac{2\delta - t}{\delta} \right)^{2/p-1} (a_2)^{2/p-1} dt, \\ \delta \leq d(x) < 2\delta, \\ \gamma \delta + \int_{\delta}^{2\delta} \gamma \left( \frac{2\delta - t}{\delta} \right)^{2/p-1} (a_2)^{2/p-1} dt, \\ 2\delta \leq d(x). \end{cases} \quad (21)$$

$$v_2(x) = \begin{cases} \gamma d(x), d(x) < \delta, \\ \gamma \delta + \int_{\delta}^{d(x)} \gamma \left( \frac{2\delta - t}{\delta} \right)^{2/p-1} (b_2)^{2/p-1} dt, \\ \delta \leq d(x) < 2\delta, \\ \gamma \delta + \int_{\delta}^{2\delta} \gamma \left( \frac{2\delta - t}{\delta} \right)^{2/p-1} (b_2)^{2/p-1} dt, \\ 2\delta \leq d(x). \end{cases}$$

Obviously,  $0 \leq v_1(x), v_2(x) \in C^1(\overline{\Omega})$ . Considering

$$\begin{cases} -\Delta_{p(x)} \omega = \eta \text{ in } \Omega, \\ \omega = 0 \text{ on } \partial\Omega, \end{cases} \quad (22)$$

we have the following result

**Lemma 2** (Lemma 2.1 in [52]). *If positive parameter  $\eta$  is large enough and  $\omega$  is the unique solution of (22), then we have*

(i) *For any  $\theta \in (0, 1)$ , there exists a positive constant  $C_1$  such that*

$$C_1 \eta^{1/p^+ - 1 + \theta} \leq \max_{x \in \overline{\Omega}} \omega(x), \quad (23)$$

(ii) *and, there exists a positive constant  $C_2$  such that*

$$\max_{x \in \overline{\Omega}} \omega(x) \leq C_2 \eta^{1/p^- - 1}. \quad (24)$$

### 3. Main Result

In the following, when there is no misunderstanding, we always use  $C_i$  to denote positive constants.

**Theorem 1.** *Assume that the conditions (H1) – (H4) are satisfied. Then problem (1) has a positive solution when  $\lambda$  is large enough.*

*Proof.* We shall establish Theorem 1 by constructing a positive subsolution  $(\phi_1, \phi_2)$  and supersolution  $(z_1, z_2)$  of (1) such that  $\phi_1 \leq z_1$  and  $\phi_2 \leq z_2$ , that is,  $(\phi_1, \phi_2)$  and  $(z_1, z_2)$  satisfy

$$\begin{aligned}
& \int_{\Omega} |\nabla \phi_1|^{p(x)-2} \nabla \phi_1 \cdot \nabla \varphi \, dx \leq \int_{\Omega} \lambda^{p(x)} [a(x)f(\phi_1)h(\phi_2)] \varphi \, dx, \\
& \int_{\Omega} |\nabla \phi_2|^{q(x)-2} \nabla \phi_2 \cdot \nabla \psi \, dx \leq \int_{\Omega} \lambda^{q(x)} [b(x)g(\phi_1)\tau(\phi_2)] \psi \, dx, \\
& \left\{ \begin{aligned} \int_{\Omega} |\nabla z_1|^{p(x)-2} \nabla z_1 \cdot \nabla \varphi \, dx &\geq \int_{\Omega} \lambda^{p(x)} [a(x)f(z_1)h(z_2)] \varphi \, dx, \\ \int_{\Omega} |\nabla z_2|^{q(x)-2} \nabla z_2 \cdot \nabla \psi \, dx &\geq \int_{\Omega} \lambda^{q(x)} [b(x)g(z_1)\tau(z_2)] \psi \, dx, \end{aligned} \right.
\end{aligned} \tag{25}$$

for all  $(\varphi, \psi) \in (W_0^{1,p(x)}(\Omega) \times W_0^{1,q(x)}(\Omega))$  with  $(\varphi, \psi) \geq 0$ . According to the sub-supersolution method for  $p(x)$ -Laplacian equations (see [52]), problem (1) has a positive solution.

*Step 1.* We will construct a subsolution of (1). Let  $\sigma \in (0, \delta)$  be small enough. Denote

$$\begin{aligned}
\phi_1(x) &= \begin{cases} e^{kd(x)} - 1, & d(x) < \sigma, \\ e^{k\sigma} - 1 + \int_{\sigma}^{d(x)} ke^{k\sigma} \left( \frac{2\delta - t}{2\delta - \sigma} \right)^{2/p^- - 1} (a_1)^{2/p^- - 1} dt, & \sigma \leq d(x) < 2\delta, \\ e^{k\sigma} - 1 + \int_{\sigma}^{2\delta} ke^{k\sigma} \left( \frac{2\delta - t}{2\delta - \sigma} \right)^{2/p^- - 1} (a_1)^{2/p^- - 1} dt, & 2\delta \leq d(x), \end{cases} \\
\phi_2(x) &= \begin{cases} e^{kd(x)} - 1, & d(x) < \sigma, \\ e^{k\sigma} - 1 + \int_{\sigma}^{d(x)} ke^{k\sigma} \left( \frac{2\delta - t}{2\delta - \sigma} \right)^{2/p^- - 1} (b_1)^{2/q^- - 1} dt, & \sigma \leq d(x) < 2\delta, \\ e^{k\sigma} - 1 + \int_{\sigma}^{2\delta} ke^{k\sigma} \left( \frac{2\delta - t}{2\delta - \sigma} \right)^{2/p^- - 1} (b_1)^{2/q^- - 1} dt, & 2\delta \leq d(x). \end{cases}
\end{aligned} \tag{26}$$

It is easy to see that  $\phi_1, \phi_2 \in C^1(\overline{\Omega})$ .

Denote

$$\begin{aligned}
\alpha &= \min \left\{ \frac{\inf p(x) - 1}{4(\sup |\nabla p(x)| + 1)}, \frac{\inf q(x) - 1}{4(\sup |\nabla q(x)| + 1)}, 1 \right\}, \\
\zeta &= \begin{cases} \min \left[ \left( \frac{-\alpha}{a_1 f(0)h(0)} \right)^{1/p^+}; \left( \frac{-\alpha}{a_1 f(0)h(0)} \right)^{1/p^-}; \left( \frac{-\alpha}{b_1 g(0)\tau(0)} \right)^{1/q^+}; \left( \frac{-\alpha}{b_1 g(0)\tau(0)} \right)^{1/q^-} \right], & \text{if } f(0)h(0) < 0, g(0)\tau(0) < 0, \\ \min \left[ \left( \frac{-\alpha}{a_1 f(0)h(0)} \right)^{1/p^+}; \left( \frac{-\alpha}{a_1 f(0)h(0)} \right)^{1/p^-} \right], & \text{if } f(0)h(0) < 0, g(0)\tau(0) > 0, \\ \min \left[ \left( \frac{-\alpha}{b_1 g(0)\tau(0)} \right)^{1/q^+}; \left( \frac{-\alpha}{b_1 g(0)\tau(0)} \right)^{1/q^-} \right], & \text{if } f(0)h(0) > 0, g(0)\tau(0) < 0, \\ 1, & \text{if } f(0)h(0) > 0, g(0)\tau(0) > 0. \end{cases}
\end{aligned} \tag{27}$$

By some simple computations, we can obtain

$$\begin{aligned}
-\Delta_{p(x)}\phi_1 &= \begin{cases} -k(e^{kd(x)})^{p(x)-1} \times \left[ (p(x)-1) + \left( d(x) + \frac{\ln k}{k} \right) \nabla p \nabla d + \frac{\Delta d}{k} \right], & d(x) < \sigma, \\ \frac{1}{2\delta - \sigma} \frac{2(p(x)-1)}{p^- - 1} - \left( \frac{2\delta - d}{2\delta - \sigma} \right) \times \left[ (\ln k e^{k\sigma}) \times \left( \frac{2\delta - d}{2\delta - \sigma} \right)^{2/p^- - 1} \nabla p \nabla d + \Delta d \right] \\ \times (K e^{k\sigma})^{p(x)-1} \left( \frac{2\delta - d}{2\delta - \sigma} \right)^{2(p(x)-1)/p^- - 1} (a_1), & \sigma \leq d(x) < 2\delta, \\ 0, & 2\delta \leq d(x), \end{cases} \\
-\Delta_{q(x)}\phi_2 &= \begin{cases} -k(e^{kd(x)})^{q(x)-1} \times \left[ \begin{array}{l} (q(x)-1) \\ + \left( d(x) + \frac{\ln k}{k} \right) \nabla q \nabla d + \frac{\Delta d}{k} \end{array} \right], & d(x) < \sigma, \\ \left\{ \frac{1}{2\delta - \sigma} \frac{2(q(x)-1)}{q^- - 1} - \left( \frac{2\delta - d}{2\delta - \sigma} \right) \times \left[ (\ln k e^{k\sigma}) \times \left( \frac{2\delta - d}{2\delta - \sigma} \right)^{2/q^- - 1} \nabla q \nabla d + \Delta d \right] \right\} \\ \times (K e^{k\sigma})^{q(x)-1} \left( \frac{2\delta - d}{2\delta - \sigma} \right)^{(2(q(x)-1)/q^- - 1)} (b_1), & \sigma \leq d(x) < 2\delta, \\ 0, & 2\delta \leq d(x). \end{cases} \tag{28}
\end{aligned}$$

From (H2), there exists a positive constant  $M > 1$  such that

$$\begin{aligned}
f(M-1)h(M-1) &\geq 1, \\
g(M-1)\tau(M-1) &\geq 1. \tag{29}
\end{aligned}$$

Let  $\sigma = (1/k)\ln M$ , then

$$\sigma k = \ln M. \tag{30}$$

If  $k$  is sufficiently large, from (30), we have

$$-\Delta_{p(x)}\phi_1 \leq -k^{p(x)}\alpha, \quad d(x) < \sigma. \tag{31}$$

Let  $\lambda = \zeta k$ . We claim that

$$-k^{p(x)}\alpha \leq a_1 f(0)h(0)\lambda^{p(x)}, \quad \forall x \in \Omega, \tag{32}$$

Indeed, by definition of  $\lambda$ , the last inequality is obvious when  $f(0)h(0) > 0$ .

When  $f(0)h(0) < 0$ , we can notice that

$$\frac{\lambda}{k} \leq \left( \frac{-\alpha}{a_1 f(0)h(0)} \right)^{1/p(x)}, \quad \forall x \in \Omega, \tag{33}$$

Then, we have

$$-\Delta_{p(x)}\phi_1 \leq -k^{p(x)}\alpha \leq \lambda^{p(x)}(a_1 f(\phi_1)h(\phi_2)), \quad d(x) < \sigma. \tag{34}$$

Since  $d(x) \in C^2(\overline{\partial\Omega_{3\delta}})$ , there exists a positive constant  $C_3$  such that

$$\begin{cases} -\Delta_{p(x)}\phi_1 \leq (K e^{k\sigma})^{p(x)-1} \times \left( \frac{2\delta - d}{2\delta - \sigma} \right)^{(2(p(x)-1)/p^- - 1)} a_1 \\ \times \left| \frac{1}{2\delta - \sigma} \frac{2(p(x)-1)}{p^- - 1} - \left( \frac{2\delta - d}{2\delta - \sigma} \right) \times \left[ (\ln k e^{k\sigma}) \times \left( \frac{2\delta - d}{2\delta - \sigma} \right)^{2/p^- - 1} \nabla p \nabla d + \Delta d \right] \right|, \\ \leq C_3 (K e^{k\sigma})^{p(x)-1} a_1 \ln k, \\ \sigma \leq d(x) < 2\delta. \end{cases} \tag{35}$$

If  $k$  is sufficiently large, we have

$$C_3 (k e^{k\sigma})^{p(x)-1} (a_1) \ln k = C_3 (kM)^{p(x)-1} a_1 \ln k \leq \lambda^{p(x)} a_1. \tag{36}$$



Then,

$$\begin{aligned} -\Delta_{p(x)}\phi_1 &\leq \lambda^{p(x)}a_1, \\ \sigma &\leq d(x) < 2\delta. \end{aligned} \quad (37)$$

Since  $\phi_1(x)$ ,  $\phi_2(x)$ , and  $f, h$  are monotone, when  $\lambda$  is large enough, we have

$$\begin{aligned} -\Delta_{p(x)}\phi_1 &\leq \lambda^{p(x)}(a_1f(\phi_1)h(\phi_2)), \\ \sigma &\leq d(x) < 2\delta, \end{aligned} \quad (38)$$

$$\begin{aligned} -\Delta_{p(x)}\phi_1 &= 0 \leq \lambda^{p(x)}a_1 \leq \lambda^{p(x)}(a_1f(\phi_1)h(\phi_2)), \\ 2\delta &\leq d(x). \end{aligned} \quad (39)$$

Combining (34), (38), and (39), we can deduce that

$$-\Delta_{p(x)}\phi_1 \leq \lambda^{p(x)}(a(x)f(\phi_1)h(\phi_2)), \quad \text{a.e. on } \Omega. \quad (40)$$

Similarly,

$$-\Delta_{q(x)}\phi_2 \leq \lambda^{q(x)}(b(x)g(\phi_1)\tau(\phi_2)), \quad \text{a.e. on } \Omega. \quad (41)$$

From (40) and (41), we can see that  $(\phi_1, \phi_2)$  is a sub-solution of problem (1).

*Step 2.* We will construct a supersolution of problem (1); we consider

$$\begin{cases} -\Delta_{p(x)}z_1 = \lambda^{p^+}a_2\mu \text{ in } \Omega, \\ -\Delta_{q(x)}z_2 = \lambda^{q^+}b_2\beta^r \text{ in } \Omega, \\ z_1 = z_2 = 0 \text{ on } \partial\Omega, \end{cases} \quad (42)$$

where  $r > 0$  is the positive number that verifies (H3) and  $\beta = \max_{x \in \overline{\Omega}} z_1(x)$ . We shall prove that  $(z_1, z_2)$  is a supersolution of problem (1).

For  $\psi \in W_0^{1,q(x)}(\Omega)$  with  $\psi \geq 0$ , it is easy to see that

$$\int_{\Omega} |\nabla z_2|^{q(x)-2} \nabla z_2 \cdot \nabla \psi \, dx = \int_{\Omega} \lambda^{q^+} b_2 \beta^r \psi \, dx. \quad (43)$$

By (H4), for a  $\mu$  large enough, using Lemma 2, we have

$$\beta^r \geq g(\beta)\tau(C_2(\lambda^{q^+}b_2\beta^r)^{1/q^-}). \quad (44)$$

Hence,

$$\begin{aligned} \int_{\Omega} |\nabla z_2|^{q(x)-2} \nabla z_2 \cdot \nabla \psi \, dx &\geq \int_{\Omega} \lambda^{q^+} b_2 g(\max z_1) \tau(\max z_2) \psi \, dx, \\ &\geq \int_{\Omega} \lambda^{q(x)} b(x) g(z_1) \tau(z_2) \psi \, dx. \end{aligned} \quad (45)$$

Also, for  $\varphi \in W_0^{1,p(x)}(\Omega)$  with  $\varphi \geq 0$ , it is easy to see that

$$\int_{\Omega} |\nabla z_1|^{p(x)-2} \nabla z_1 \cdot \nabla \varphi \, dx = \int_{\Omega} \lambda^{p^+} a_2 \mu \varphi \, dx. \quad (46)$$

By (H3) and Lemma 2, when  $\mu$  is sufficiently large, we have

$$a_2 \lambda^{p^+} \mu \geq \left[ \frac{1}{C_2} \beta \right]^{p^- - 1} \geq a_2 \lambda^{p^+} f(\beta) h(C_2(\lambda^{q^+} b_2 \beta^r)^{1/q^- - 1}). \quad (47)$$

Then,

$$\int_{\Omega} |\nabla z_1|^{p(x)-2} \nabla z_1 \cdot \nabla \varphi \, dx \geq \int_{\Omega} \lambda^{p(x)} a(x) f(z_1) h(z_2) \varphi \, dx. \quad (48)$$

According to (45) and (48), we can conclude that  $(z_1, z_2)$  is a supersolution of problem (1). It only remains to prove that  $\phi_1 \leq z_1$  and  $\phi_2 \leq z_2$ .

In the definition of  $v_1(x)$ , let

$$\gamma = \frac{2}{\delta} \left( \max_{\overline{\Omega}} \phi_1(x) + \max_{\overline{\Omega}} |\nabla \phi_1|(x) \right). \quad (49)$$

We claim that

$$\phi_1(x) \leq v_1(x), \quad \forall x \in \Omega. \quad (50)$$

From the definition of  $v_1$ , it is easy to see that

$$\begin{aligned} \phi_1(x) &\leq 2 \max_{\overline{\Omega}} \phi_1(x) \leq v_1(x), \quad \text{when } d(x) = \delta, \\ \phi_1(x) &\leq 2 \max_{\overline{\Omega}} \phi_1(x) \leq v_1(x), \quad \text{when } d(x) \geq \delta, \\ \phi_1(x) &\leq v_1(x), \quad \text{when } d(x) < \delta. \end{aligned} \quad (51)$$

Since  $v_1 - \phi_1 \in C^1(\overline{\partial\Omega_\delta})$ , there exists a point  $x_0 \in \overline{\partial\Omega_\delta}$  such that

$$v_1(x_0) - \phi_1(x_0) = \min_{x_0 \in \partial\Omega_\delta} (v_1(x_0) - \phi_1(x_0)). \quad (52)$$

If  $v_1(x_0) - \phi_1(x_0) < 0$ , it is easy to see that  $0 < d(x) < \delta$  and then

$$\nabla v_1(x_0) - \nabla \phi_1(x_0) = 0. \quad (53)$$

From the definition of  $v_1$ , we have

$$\begin{aligned} |\nabla v_1(x_0)| &= \gamma = \frac{2}{\delta} \left( \max_{\overline{\Omega}} \phi_1(x_0) + \max_{\overline{\Omega}} |\nabla \phi_1|(x_0) \right) \\ &> |\nabla \phi_1|(x_0). \end{aligned} \quad (54)$$

It is a contradiction to

$$\nabla v_1(x_0) - \nabla \phi_1(x_0) = 0. \quad (55)$$

Thus, (50) is valid.

Obviously, there exists a positive constant  $C_3$  such that  $\gamma \leq C_3 \lambda$ .

Since  $d(x) \in C^2(\overline{\partial\Omega_{3\delta}})$ , according to the proof of Lemma 2, there exists a positive constant  $C_4$  such that

$$\begin{aligned} -\Delta_{p(x)} v_1(x) &\leq C_* \gamma^{p(x)-1+\theta} \leq C_4 \lambda^{p(x)-1+\theta}, \\ &\text{a.e. in } \Omega, \text{ where } \theta \in (0, 1). \end{aligned} \quad (56)$$

When  $\eta \geq \lambda^{p^*}$  is large enough, we have  $-\Delta_{p(x)} v_1(x) \leq \eta$ . According to the comparison principle, we have

$$v_1(x) \leq \omega(x). \quad (57)$$

From (50) and (57), when  $\eta \geq \lambda^{p^*}$  and  $\lambda \geq 1$  are sufficiently large, we have, for all  $x \in \Omega$ ,

$$\phi_1(x) \leq v_1(x) \leq \omega(x). \quad (58)$$

According to the comparison principle, when  $\mu$  is large enough, we have, for all  $x \in \Omega$ ,

$$v_1(x) \leq \omega(x) \leq z_1(x). \quad (59)$$

Combining the definition of  $v_1(x)$  and (58), it is easy to see that, for all  $x \in \Omega$ ,

$$\phi_1(x) \leq v_1(x) \leq \omega(x) \leq z_1(x). \quad (60)$$

When  $\mu \geq 1$  and  $\lambda$  is large enough, from Lemma 2, we can see that  $\beta$  is large enough, and then  $\lambda^{4+} b_2 \beta^r$  is a large enough. Similarly, we have  $\phi_2 \leq z_2$ . This completes the proof.

#### 4. Conclusion

Validity of the comparison principle and of the SSM for local and nonlocal problems as the stationary and evolutionary Kirchhoff Equation was an important subject in the last few years (see, for example, [44, 53, 58, 62–66]), where the authors showed by giving different counterexamples that the simple assumption  $M$  increasing somewhere is enough to make the comparison principle and SSM hold false contradiction and clear up some results in the literature. Moreover, the two conditions that  $M$  is nonincreasing and  $H$  is increasing turn out to be necessary and sufficient, at least for the validity of the comparison principle. It is worth to note that in [45, 67], C. O. Alves and F. J. S. A. Correa developed a new SSM for problem (1) to deal with the increasing  $M$  case. The result is obtained by using a kind of Minty–Browder theorem for a suitable pseudomonotone operator, but instead of constructing a subsolution, the authors assumed the existence of a whole family of functions which satisfy a stronger condition than just being subsolutions; the inconvenience is that these stronger conditions restrict the possible right hand sides in (1). Another SSM for nonlocal problems is obtained in [45] for a problem involving a nonlocal term with a Lebesgue norm, instead of the Sobolev norm appearing in (1).

#### Data Availability

No data were used to support this study.

#### Conflicts of Interest

The authors declare that there are no conflicts of interest regarding the publication of this manuscript.

#### Authors' Contributions

The authors contributed equally in this article. All authors read and approved the final manuscript.

#### Acknowledgments

This work was sponsored by the Deanship of Scientific Research at Qassim University in the Kingdom of Saudi Arabia.

#### References

- [1] G. A. Afrouzi, N. T. Chung, and S. Shakeri, "Existence of positive solutions for Kirchhoff type equations," *Electronic Journal of Differential Equations*, vol. 180, pp. 1–8, 2013.
- [2] Y. Güldü and S. Gülyaz, "On integral representation for solution of generalized sturm-liouville equation with discontinuity conditions," *Boletim da Sociedade Paranaense de Matemática*, vol. 33, no. 2, pp. 95–109, 2015.
- [3] O. Kavian, *Introduction a la theorie des points critiques et applications aux problemes elliptiques*, Springer-Verlag, France, Paris, 1993.
- [4] S. Boulaaras and M. Haiour, " $L^\infty$ -asymptotic behavior for a finite element approximation in parabolic quasi-variational inequalities related to impulse control problem," *Applied Mathematics and Computation*, vol. 217, no. 14, pp. 6443–6450, 2011.
- [5] S. Boulaaras and M. Haiour, "The finite element approximation of evolutionary Hamilton–Jacobi–Bellman equations with nonlinear source terms," *Indagationes Mathematicae*, vol. 24, no. 1, pp. 161–173, 2013.
- [6] S. Boulaaras and M. Haiour, "The maximum norm analysis of an overlapping Shwarz method for parabolic quasi-variational inequalities related to impulse control problem with the mixed boundary conditions," *Applied Mathematics & Information Sciences*, vol. 7, no. 1, pp. 343–353, 2013.
- [7] J. L. Lions, "On some questions in boundary value problems of mathematical physics," *North-Holland Mathematics Studies*, vol. 30, pp. 284–346, 1978.
- [8] K. Bartkowski and P. Górka, "One-dimensional Klein-Gordon equation with logarithmic nonlinearities," *Journal of Physics A: Mathematical and Theoretical*, vol. 41, no. 35, p. 355201, 2008.
- [9] N. Mezouar and S. Boulaaras, "Global existence of solutions to a viscoelastic non-degenerate Kirchhoff equation," *Applicable Analysis*, 2018.
- [10] A. Zarai, A. Draifia, and S. Boulaaras, "Blow-up of solutions for a system of nonlocal singular viscoelastic equations," *Applicable Analysis*, vol. 97, no. 13, pp. 2231–2245, 2018.
- [11] Q. Zhang, "Existence and asymptotic behavior of positive solutions for variable exponent elliptic systems," *Nonlinear Analysis: Theory, Methods & Applications*, vol. 70, no. 1, pp. 305–316, 2009.
- [12] M. Ruzicka, *Electrorheological Fluids: Modeling and Mathematical Theory*, Springer-Verlag, Berlin, Germany, 2002.
- [13] M. Mihailescu, P. Pucci, and V. Radulescu, "Eigenvalue problems for anisotropic quasi-linear elliptic equations with variable exponent," *Journal of Mathematical Analysis and Applications*, vol. 3401, pp. 687–698, 2008.
- [14] Q. H. Zhang, "A strong maximum principle for differential equations with nonstandard  $p(x)$ -growth conditions," *Journal of Mathematical Analysis and Applications*, vol. 312, pp. 24–32, 2005.
- [15] L. Evans, *Partial Differential Equations*, American Mathematical Society, Providence, RI, USA, 2010.
- [16] H. Lewy, "An example of a smooth linear partial differential equation without solution," *The Annals of Mathematics*, vol. 66, no. 1, pp. 155–158, 1957.

- [17] G. S. Dragoni, "Il problema dei valori ai limiti studiato in grande per le equazioni differenziali del secondo ordine," *Mathematische Annalen*, vol. 105, no. 1, pp. 133–143, 1931.
- [18] M. Nagumo, "Über die Differentialgleichung  $y''=f(x, y, y')$ ," *Proceedings of the Physico-Mathematical Society of Japan*, vol. 19, pp. 861–866, 1937.
- [19] Y. Bouizm, S. Boulaaras, and B. Djebbar, "Some existence results for an elliptic equation of Kirchhoff-type with changing sign data and a logarithmic nonlinearity," *Mathematical Methods in the Applied Sciences*, vol. 42, no. 7, pp. 2465–2474, 2019.
- [20] H.-W. Knobloch, "Eine neue methode zur approximation periodischer Lösungen nicht-linearer differentialgleichungen zweiter ordnung," *Mathematische Zeitschrift*, vol. 82, no. 3, pp. 177–197, 1963.
- [21] J. Mawhin, *Nonlinear Functional Analysis and Periodic Solutions of Ordinary Differential Equations, Summer School on Ordinary Differential Equations*, 1974.
- [22] K. Schmitt, "Periodic solutions of nonlinear second order differential equations," *Mathematische Zeitschrift*, vol. 98, no. 3, pp. 200–207, 1967.
- [23] H. Amann and M. Crandall, "On some existence theorems for semilinear elliptic equations," *Indiana University Mathematics Journal*, vol. 27, no. 5, pp. 779–790, 1978.
- [24] D. Sattinger, "Monotone methods in nonlinear elliptic and parabolic boundary value problems," *Indiana University Mathematics Journal*, vol. 21, no. 11, pp. 979–1000, 1972.
- [25] H. Medekhel, S. Boulaaras, K. Zennir, and A. Allahem, "Existence of positive solutions and its asymptotic behavior of  $(p(x), q(x))$ -Laplacian parabolic system," *Symmetry*, vol. 11, no. 3, p. 332, 2019.
- [26] L. H. Erbe, "Nonlinear boundary value problems for second order differential equations," *Journal of Differential Equations*, vol. 7, no. 3, pp. 459–472, 1970.
- [27] J. Mawhin and K. Schmitt, "Upper and lower solutions and semilinear second order elliptic equations with non-linear boundary conditions," *Proceedings of the Royal Society of Edinburgh: Section A Mathematics*, vol. 97, pp. 199–207, 1984.
- [28] J. W. Bebernes and K. Schmitt, "Periodic boundary value problems for systems of second order differential equations," *Journal of Differential Equations*, vol. 13, no. 1, pp. 32–47, 1973.
- [29] H. Medekhel and S. Boulaaras, "Existence of positive solutions for a class of Kirchhoff parabolic systems with multiple parameters," *Applied Mathematics E-Notes*, vol. 18, pp. 295–306, 2018.
- [30] H. W. Knobloch and K. Schmitt, "Non-linear boundary value problems for systems of differential equations," *Proceedings of the Royal Society of Edinburgh: Section A Mathematics*, vol. 78, no. 1-2, pp. 139–159, 1977.
- [31] J. Deuel and P. Hess, "Inequations variationnelles elliptiques non coercives," *Comptes rendus de l'Académie des Sciences*, vol. 279, pp. 719–722, 1974.
- [32] P. Hess, "On the solvability of nonlinear elliptic boundary value problems," *Indiana University Mathematics Journal*, vol. 25, no. 5, pp. 461–466, 1976.
- [33] C. Chen, "On positive weak solutions for a class of quasilinear elliptic systems," *Nonlinear Analysis: Theory, Methods & Applications*, vol. 62, no. 4, pp. 751–756, 2005.
- [34] S. Carl, V. K. Le, and D. Motreanu, "The sub-supersolution method and extremal solutions for quasilinear hemivariational inequalities," *Differential and Integral Equations*, vol. 17, pp. 165–178, 2004.
- [35] E. N. Dancer and G. Sweers, "On the existence of a maximal weak solution for a semilinear elliptic equation," *Differential and Integral Equations*, vol. 2, pp. 533–540, 1989.
- [36] T. Kura, "The weak supersolution-subsolution method for second order quasilinear elliptic equations," *Hiroshima Mathematical Journal*, vol. 19, no. 1, p. 136, 1989.
- [37] B. Mairi, R. Guefaifia, S. Boulaaras, and T. Bouali, "Existence of positive solutions for a new class of nonlocal  $p(x)$ -Kirchhoff elliptic systems via sub-super solutions concept," *Applied Science APPS*, vol. 20, pp. 117–128, 2018.
- [38] S. Boulaaras, R. Guefaifia, and K. Zennir, "Existence of positive solutions for nonlocal  $p(x)$ -Kirchhoff elliptic systems," *Advances in Pure and Applied Mathematics*, vol. 10, no. 1, pp. 1867–1152, 2019.
- [39] V. K. Le and K. Schmitt, "Some general concepts of sub- and supersolutions for nonlinear elliptic problems," *Topological Methods in Nonlinear Analysis*, vol. 28, pp. 87–103, 2006.
- [40] N. Mezouar and S. Boulaaras, "Global existence and decay of solutions for a class of viscoelastic Kirchhoff equation," *Bulletin of the Malaysian Mathematical Sciences Society*, vol. 43, no. 1, pp. 725–755, 2018.
- [41] V. K. Le, "Subsolution-supersolution method in variational inequalities," *Nonlinear Analysis*, vol. 45, no. 6, pp. 775–800, 2001.
- [42] V. K. Le, "Subsolution-supersolutions and the existence of extremal solutions in noncoercive variational inequalities," *Journal of Inequalities in Pure and Applied Mathematics (Electronic)*, vol. 2, p. 116, 2001.
- [43] S. Boulaaras, D. Ouchenane, and F. Mesloub, "General decay for a viscoelastic problem with not necessarily decreasing kernel," *Journal of Applied Mathematics and Computing*, vol. 43, no. 1, pp. 725–755, 2018.
- [44] F. Júlio, S. A. Correa, and G. M. Figueiredo, "On an elliptic equation of  $p$ -Kirchhoff type via variational methods," *Bulletin of the Australian Mathematical Society*, vol. 74, no. 2, pp. 263–277, 2006.
- [45] C. O. Alves and F. J. S. A. Correa, "On existence of solutions for a class of problem involving a nonlinear operator," *Communications on Applied Nonlinear Analysis*, vol. 8, pp. 43–56, 2001.
- [46] S. Boulaaras and R. Guefaifia, "Existence of positive weak solutions for a class of Kirchhoff elliptic systems with multiple parameters," *Mathematical Methods in the Applied Sciences*, vol. 41, no. 13, pp. 5203–5210, 2018.
- [47] S. Boulaaras, R. Guefaifia, and S. Kabli, "An asymptotic behavior of positive solutions for a new class of elliptic systems involving of  $(p(x), q(x))$ -Laplacian systems," *Boletín de la Sociedad Matemática Mexicana*, vol. 25, no. 1, pp. 145–162, 2019.
- [48] D. D. Hai and R. Shivaji, "An existence result on positive solutions for a class of  $p$ -Laplacian systems," *Nonlinear Analysis: Theory, Methods & Applications*, vol. 56, no. 7, pp. 1007–1010, 2004.
- [49] R. Guefaifia and S. Boulaaras, "Existence of positive radial solutions for  $(p(x), q(x))$ -Laplacian systems," *Applied Mathematics E-Notes*, vol. 18, pp. 209–218, 2018.
- [50] R. Guefaifia and S. Boulaaras, "Existence of positive solution for a class of  $(p(x), q(x))$ -Laplacian systems," *Rendiconti del Circolo Matematico di Palermo Series 2*, vol. 67, pp. 93–103, 2018.
- [51] G. Kirchhoff, *Mechanik*, Teubner, Leipzig, Germany, 1883.
- [52] S. Boulaaras, "Some existence results for elliptic Kirchhoff equation with changing sign data and a logarithmic

- nonlinearity,” *Journal of Intelligent and Fuzzy Systems*, vol. 37, no. 6, pp. 8335–8344, 2019.
- [53] B. Ricceri, “On an elliptic Kirchhoff-type problem depending on two parameters,” *Journal of Global Optimization*, vol. 46, no. 4, pp. 543–549, 2010.
- [54] S. Boulaaras, “Existence of positive solutions for a new class of Kirchhoff parabolic systems,” *Rocky Mountain Journal of Mathematics*, 2019, <https://projecteuclid.org/euclid.rmjm/1572836541>.
- [55] J. P. Garcia Azorero and I. Peral Alonso, “Existence and nonuniqueness for the  $p$ -Laplacian: nonlinear eigenvalues,” *Communications in Partial Differential Equations*, vol. 12, pp. 1389–1430, 1987.
- [56] K. Schmitt and I. Sim, “Bifurcation problems associated with generalized Laplacians,” *Advances in Difference Equations*, vol. 9, pp. 797–828, 2004.
- [57] S. Boulaaras, R. Guefaïfia, and T. Bouali, “Existence of positive solutions for a class of quasilinear singular elliptic systems involving Caffarelli-Kohn-Nirenberg exponent with sign-changing weight functions,” *Indian Journal of Pure and Applied Mathematics*, vol. 49, no. 4, pp. 705–715, 2018.
- [58] M. Chipot and B. Lovat, “Some remarks on non local elliptic and parabolic problems,” *Nonlinear Analysis: Theory, Methods & Applications*, vol. 30, no. 7, pp. 4619–4627, 1997.
- [59] S. Boulaaras, “A well-posedness and exponential decay of solutions for a coupled lamé system with viscoelastic term and logarithmic source terms,” *Applicable Analysis*, 2019.
- [60] A. El Hamidi, “Existence results to elliptic systems with nonstandard growth conditions,” *Journal of Mathematical Analysis and Applications*, vol. 300, no. 1, pp. 30–42, 2004.
- [61] N. Azouz and A. Bensedik, “Existence result for an elliptic equation of Kirchhoff -type with changing sign data,” *Funkcialaj Ekvacioj*, vol. 55, pp. 55–66, 2012.
- [62] S. Boulaaras and A. Allahem, “Existence of positive solutions of nonlocal  $p(x)$ -Kirchhoff evolutionary systems via sub-super solutions concept,” *Symmetry*, vol. 11, no. 2, p. 253, 2019.
- [63] M. Maizi, S. Boulaaras, M. Haiour, and A. Mansour, “Existence of positive solutions of Kirchhoff hyperbolic systems with multiple parameters,” *Boletim Sociedade Paranaense de Matematica*, 2019.
- [64] L. Iturriaga and E. Massa, “On necessary conditions for the comparison principle and the sub and supersolutions method for the stationary Kirchhoff equation,” *Journal of Mathematical Physics*, vol. 59, Article ID 011506, 2018.
- [65] J. García-Melián and L. Iturriaga, “Some counterexamples related to the stationary Kirchhoff equation,” *Proceedings of the American Mathematical Society*, vol. 144, no. 8, pp. 3405–3411, 2016.
- [66] X. Hanand and G. Dai, “On the sub-supersolution method for  $p(x)$ -Kirchhoff type equations,” *Journal of Inequalities and Applications*, vol. 283, pp. 1–11, 2012.
- [67] C. Azizieh, P. Clément, and E. Mitidieri, “Existence and a priori estimates for positive solutions of  $p$ -Laplace systems,” *Journal of Differential Equations*, vol. 184, no. 2, pp. 422–442, 2002.



## Research Article

# Secure Communication Scheme Based on a New 5D Multistable Four-Wing Memristive Hyperchaotic System with Disturbance Inputs

Fei Yu <sup>1</sup>, Zinan Zhang <sup>1</sup>, Li Liu <sup>1</sup>, Hui Shen <sup>1</sup>, Yuanyuan Huang <sup>1</sup>,  
Changqiong Shi <sup>1</sup>, Shuo Cai <sup>1</sup>, Yun Song <sup>1</sup>, Sichun Du <sup>2</sup> and Quan Xu <sup>3</sup>

<sup>1</sup>School of Computer and Communication Engineering, Changsha University of Science and Technology, Changsha 410114, China

<sup>2</sup>College of Computer Science and Electronic Engineering, Hunan University, Changsha 410082, China

<sup>3</sup>School of Information Science and Engineering, Changzhou University, Changzhou 213164, China

Correspondence should be addressed to Fei Yu; [yufeiyf@csust.edu.cn](mailto:yufeiyf@csust.edu.cn) and Yuanyuan Huang; [snailhy@126.com](mailto:snailhy@126.com)

Received 9 October 2019; Revised 12 November 2019; Accepted 22 November 2019; Published 10 January 2020

Guest Editor: Viet-Thanh Pham

Copyright © 2020 Fei Yu et al. This is an open access article distributed under the Creative Commons Attribution License, which permits unrestricted use, distribution, and reproduction in any medium, provided the original work is properly cited.

By introducing a flux-controlled memristor model with absolute value function, a 5D multistable four-wing memristive hyperchaotic system (FWMHS) with linear equilibrium points is proposed in this paper. The dynamic characteristics of the system are studied in terms of equilibrium point, perpetual point, bifurcation diagram, Lyapunov exponential spectrum, phase portraits, and spectral entropy. This system is of the group of systems that have coexisting attractors. In addition, the circuit implementation scheme is also proposed. Then, a secure communication scheme based on the proposed 5D multistable FWMHS with disturbance inputs is designed. Based on parametric modulation theory and Lyapunov stability theory, synchronization and secure communication between the transmitter and receiver are realized and two message signals are recovered by a convenient robust high-order sliding mode adaptive controller. Through the proposed adaptive controller, the unknown parameters can be identified accurately, the gain of the receiver system can be adjusted continuously, and the disturbance inputs of the transmitter and receiver can be suppressed effectively. Thereafter, the convergence of the proposed scheme is proven by means of an appropriate Lyapunov functional and the effectiveness of the theoretical results is testified via numerical simulations.

## 1. Introduction

Chaotic signals are naturally invisible because of their non-periodic continuous bandwidth spectrum, similar noise, and extreme sensitivity to initial values. Therefore, in the past decade, chaos has attracted more and more scientists' interest and research in the fields of complex networks [1–3], electronic circuits [4–6], image encryption [7–9], synchronization [10–11], random number generator [12, 13], and secure communications [14–16]. In chaotic communication systems, how to generate chaotic signals suitable for modulation and spread spectrum has become an issue of concern [17, 18]. Several methods for generating complex chaotic signals are proposed, among which the generations of four-wing [19–21], multiwing [22–24], and multiscroll [25–29] chaotic attractors are the important achievements in recent years. Compared

with chaotic systems, hyperchaotic systems have two or more positive Lyapunov exponents, and their motion orbits are separated in many directions, showing more complex dynamic behavior [30–34]. Complex hyperchaotic signals can improve the security of chaotic secure communication and chaotic information encryption, so hyperchaos will have a very broad application prospect in the field of information engineering.

Memristor has the advantages of nanometer size, automatic memory, and nonlinear characteristics. Compared with the traditional chaotic circuit system, a memristor chaotic circuit has more complex chaotic characteristics because the system is sensitive to circuit parameters and depends on the initial value of the memristor [35–39]. Chaotic signals generated by memristor chaotic systems have stronger pseudorandomness, which makes them have a broader application prospect in traditional chaotic applications.

Therefore, it is of great practical significance to design a chaotic system and circuit based on a memristor by combining the memristor with a nonlinear chaotic system. The generation of new multiwing hyperchaotic attractors based on memristors has become a research hotspot, and many such hyperchaotic systems have been introduced in recent years. In [39], by introducing a flux-controlled memristor into a multiwing system, no equilibrium hyperchaotic multiwing attractors are observed in the memristive system. A flux-controlled memristor with linear memductance is proposed in [40]; then, a new hyperchaotic system is presented by adding the proposed memristor into the Lorenz system, and the memristive system exhibits complex dynamic characteristics such as four-wing hyperchaotic attractors.

Multistability is one of the most important phenomena in dynamic systems [41–50], which occurs in many fields such as physics, biology, chemistry, economics, and electronics. Multistability allows flexibility of system performance without changing parameters, and appropriate control strategies can be used to induce switching behavior between different coexisting states [41]. For chaotic systems, hidden attractors [42–46] and infinite attractors [47–50] can exhibit multistability. For example, complex dynamic behaviors of coexisting attractors [51], transient chaos [52], and limit cycle [53] can be observed from hidden attractors. Recently, various multistable memristive hyperchaotic systems have been proposed in many literatures. In [52], by introducing a flux-controlled memristor model into an existing 5D hyperchaotic autonomous system, a 6D hyperchaotic autonomous system with hidden extreme multistability is proposed. Some attractive dynamics are observed like transient chaos, bursting, and offset boosting phenomenon. In [53], by utilizing a memristor to substitute a coupling resistor in the realization circuit of a 3D chaotic system having one saddle and two stable node-foci, a novel memristive hyperchaotic system with coexisting infinite hidden attractors is presented. The memristive system does not show any equilibrium but can exhibit hyperchaos, chaos, periodic dynamics, and transient hyperchaos.

With the application of network information technology, people attach great importance to the security and confidentiality of information [54–66]. Researchers are constantly looking for new methods of confidentiality [54–66]. Secure communication and chaotic encryption based on chaotic synchronization have become one of the research hotspots in the field of information security in recent years. In recent years, the secure communication scheme based on chaotic synchronization control has attracted extensive attention. People have made a thorough study on it and proposed various effective chaotic control methods, such as adaptive control [67–68], active control [69], linear feedback control [70, 71], and sliding mode control [72, 73]. In [69], the synchronization of 3D chaotic systems with the same structure is realized by using active control and adaptive control law. In the developed secure communication system, information signal sent over noisy channel is successfully retrieved at the receiver. In [72], a secure communication mechanism based on a four-wing 4D chaotic system is designed. Using high-order sliding mode control synchronization technology,

parameter modulation method, and Lyapunov stability theory, two useful signals are encrypted and recovered and the external interference is suppressed.

Based on the above studies, a 5D multistable FWMHS is proposed based on the flux-controlled memristor model with absolute value function, from which the coexisting phenomenon of many hidden attractors are observed. Hyperchaos is exhibited with a line of equilibria. After that, circuitry implementation of the proposed system is investigated. Then, an adaptive asymptotic method is proposed to identify the 5D multistable FWMHS with several unknown parameters and to apply chaotic parameter modulation in secure communication. By this method, chaotic synchronization can be realized, unknown parameters can be identified, message signals can be recovered, and disturbance inputs can be suppressed simultaneously via a high-order sliding mode adaptive controller, whose adaptive parameters are adjusted according to the proposed adaptive algorithm. By using Lyapunov functional and Barbalat's lemma, the convergence of the proposed scheme is analyzed. Finally, two triangular wave signals are taken as examples for numerical simulation. The results show the effectiveness and feasibility of the proposed secure communication scheme.

## 2. New 5D Multistable FWMHS and Its Dynamics

*2.1. System Description.* A simple 5D chaotic oscillator with five parameters and five nonlinearities is proposed, and a flux-controlled memristor model with absolute value function is introduced to establish the mathematical model of the system:

$$\begin{cases} \dot{x}_1 = -ax_1 + x_2x_3, \\ \dot{x}_2 = bx_2 - x_1x_3, \\ \dot{x}_3 = x_1x_2 - cx_3 + dx_4W(x_5), \\ \dot{x}_4 = x_1x_2 - ex_4, \\ \dot{x}_5 = -x_3, \end{cases} \quad (1)$$

where  $a, b, c, d$ , and  $e$  are the parameters of the system and  $x_1, x_2, x_3, x_4$ , and  $x_5$  are state variables. The memductance function  $W(\psi) = 1 - \beta|\psi|$  [52],  $\psi$  and  $\beta$  being its flux variable and positive constant parameter, respectively. It is easy to see that system (1) is invariant under the transformation  $(x_1, x_2, x_3, x_4, x_5) \rightarrow (\pm x_1, \mp x_2, x_3, x_4, x_5)$ . Thus, if  $(x_1, x_2, x_3, x_4, x_5)$  is a solution for a specific set of parameters, then  $(\pm x_1, \mp x_2, x_3, x_4, x_5)$  is also a solution for the same parameters set. So, the appearances of multiple coexisting symmetric attractors are expected in the new system.

When the parameters are chosen as  $a = 10, b = 12, c = 30, d = 2, e = 3$ , and  $\beta = 0.2$ , the Lyapunov exponents of system (1) are calculated as  $LE1 = 3.5610, LE2 = 0.3092, LE3 = 0, LE4 = -2.0660$ , and  $LE5 = -23.4708$ . It can be seen that there are two positive Lyapunov exponents which means system (1) can exhibit hyperchaotic dynamics. A typical four-wing hyperchaotic attractor from system (1) is shown in Figure 1, while the initial conditions are selected as  $[0.1, 0.1, 0.1, 0.1, 0.1]$ .



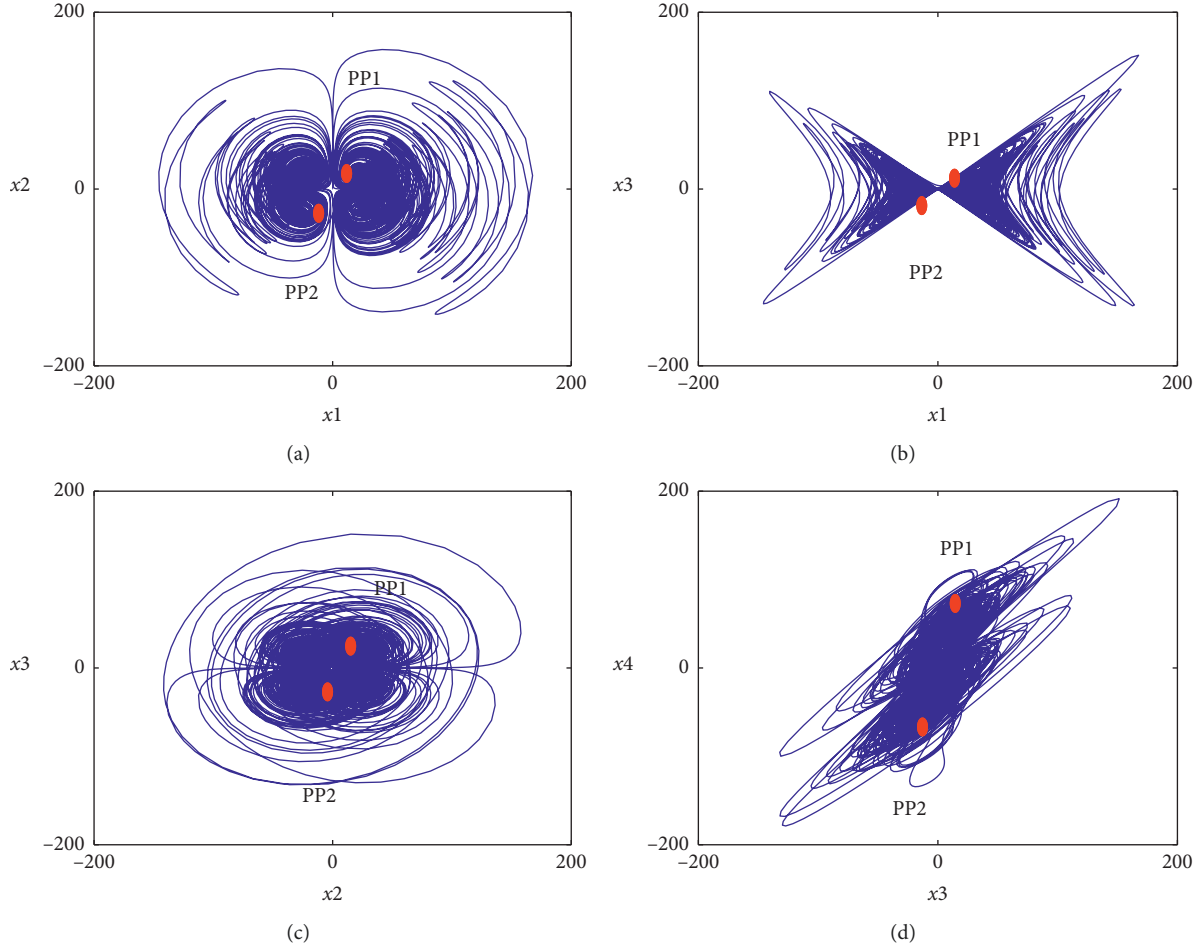


FIGURE 1: A typical four-wing hyperchaotic attractor of the 5D FWMHS (1) and perpetual points (red) in the (a)  $x_1 - x_2$  plane, (b)  $x_1 - x_3$  plane, (c)  $x_2 - x_3$  plane, and (d)  $x_3 - x_4$  plane.

**2.2. Dissipativity.** The volume contraction rate of system (1) is given by the following Lie derivatives:

$$\nabla V = \frac{\partial \dot{x}_1}{\partial x_1} + \frac{\partial \dot{x}_2}{\partial x_2} + \frac{\partial \dot{x}_3}{\partial x_3} + \frac{\partial \dot{x}_4}{\partial x_4} + \frac{\partial \dot{x}_5}{\partial x_5} = -a + b - c - e. \quad (2)$$

Equation (2) shows that divergence is negative when  $-a + b - c - e < 0$ . In this case, the set of system trajectories is ultimately limited to a specific zero volume limit set and the asymptotic motion of the new four-wing hyperchaotic system (1) falls on the attractor.

**2.3. Equilibrium Points and Stability.** Equilibrium points play an important role in the study of nonlinear systems because they allow the system response to be characterized as self-excited oscillation or hidden oscillation. These oscillations originate around the equilibrium point obtained from system (1), by setting the left-hand side to zero as follows:

$$\begin{cases} 0 = -ax_1 + x_2x_3, \\ 0 = bx_2 - x_1x_3, \\ 0 = x_1x_2 - cx_3 + dx_4W(x_5), \\ 0 = x_1x_2 - ex_4, \\ 0 = -x_3. \end{cases} \quad (3)$$

It can be seen that the equilibrium states of system (3) only depends on  $x_1, x_2, x_3,$  and  $x_4$ , but independent of  $x_5$ . System (3) has the abnormal characteristics of linear equilibrium in  $(0, 0, 0, 0, x_5)$ . Since  $x_5$  in equilibrium can be any constant, assuming that  $l$  is a real constant, the equilibrium of system (3) can be described as follows:

$$O = \{(x_1, x_2, x_3, x_4, x_5) \mid x_1 = x_2 = x_3 = x_4 = 0, x_5 = l\}. \quad (4)$$

The Jacobian matrix of system (3) at this line equilibrium is

$$J_O = \begin{bmatrix} -a & 0 & 0 & 0 & 0 \\ 0 & b & 0 & 0 & 0 \\ 0 & 0 & -c & d(1 - \beta|l|) & 0 \\ 0 & 0 & 0 & -e & 0 \\ 0 & 0 & 0 & -1 & 0 \end{bmatrix}. \quad (5)$$

According to Jacobian matrix (5), the characteristic equation of system (1) can be expressed as follows:

$$\lambda(\lambda + e)(\lambda + a)(\lambda - b)(\lambda + c) = 0. \quad (6)$$

Five eigenvalues of system (1) can be obtained from equation (6):  $\lambda_1 = 0, \lambda_2 = -e, \lambda_3 = -a, \lambda_4 = b$ , and  $\lambda_5 = -c$ . When  $a = 10, b = 12, c = 30$ , and  $e = 3$ , it is obvious that there are  $\lambda_1 = 0, \lambda_{2,3,5} < 0$ , and  $\lambda_4 > 0$ . Therefore, regardless of the parameter values, when system (1) has a line equilibrium, there is one zero eigenvalue, one positive eigenvalue, and three negative eigenvalues, so system (1) has unstable saddle points.

**2.4. Perpetual Points.** In this paper, we study the new kind of critical points proposed by Prasad in [74], which are called perpetual points. They are defined as points where the acceleration of the system becomes zero and the velocity remains nonzero. According to the number of zero derivatives, permanent points can belong to any regular point set except  $R^0$ . The various interesting properties and uses of these points can be found in [74–76]. According to the definition of perpetual points in [74], system (1) possesses two permanent points:  $PP1 = (\sqrt{bce/(e+d)}, \sqrt{ace/(e+d)}, \sqrt{ab}, c(\sqrt{ab}/(e+d)), 0)$  and  $PP2 = (-\sqrt{bce/(e+d)}, -\sqrt{ace/(e+d)}, -\sqrt{ab}, -c(\sqrt{ab}/(e+d)), 0)$ . When  $a = 10, b = 12, c = 30, d = 2$ , and  $e = 3$ , the two permanent points are  $(\pm 14.697, \pm 13.416, \pm 10.954, \pm 65.727, 0)$ , which are shown in Figure 1, while perpetual points are denoted by red dots. We can see that the trajectories of the attractors pass through the perpetual points, so coexistence attractors can also be located using perpetual points.

**2.5. Bifurcation Diagram and Lyapunov Exponent Spectrum.** Bifurcation diagram and Lyapunov exponent spectrum are suitable tools for visualizing different scenes to chaos/hyperchaos in dynamic systems. When the system parameters change, this is achieved by the expression of the local maximum or minimum of the state variables. In order to study the dynamic behavior of the 5D FWMHS with parameters, we discuss the bifurcation diagram and Lyapunov exponent spectrum of the system with increasing parameter  $d$  by using Wolf's algorithm and maximum method, respectively. Figures 2 and 3 show the bifurcation diagram of the state  $|X|$  and the corresponding Lyapunov exponents' spectrum with the range of the parameter  $d$  taken as  $[0, 15]$ , respectively, under the initial conditions of  $[0.1, 0.1, 0.1, 0.1, 0.1]$ . It can be seen that the bifurcation diagram is in good agreement with the Lyapunov exponent spectrum. When  $0 \leq d \leq 7.52$ , the system has two positive Lyapunov exponents and the system is in the hyperchaotic state; when  $7.52 < d \leq 10.1$ , the system is in the periodic state; when  $10.1 < d \leq 15$ , the system has one positive Lyapunov exponent, so the system is in the chaotic state.

**2.6. The Complexity of Spectral Entropy.** The complexity of spectral entropy reflects the disorder in the Fourier domain. We usually measure the complexity of a system by calculating its spectral entropy. The larger the spectral entropy is, the higher the complexity is, and vice versa

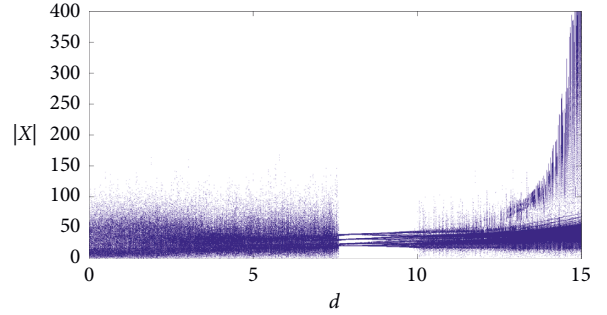


FIGURE 2: Bifurcation diagram for increasing parameter  $d$ .

[77–79]. In this part, the complexity of chaotic system (1) in the parameter range is analyzed by using spectral entropy complexity algorithm. Figure 4 is the complexity curve of the parameter  $d \in [0, 12]$ , which is very consistent with the Lyapunov exponents spectrum of system (1). When the parameter  $d \in [0, 7.52]$ , the Lyapunov exponents show that the system is hyperchaos. Similarly, Figure 4 also shows that the waveform changes steeply in this region, which means that the more complex the spectrum, the higher the complexity. When  $d \in (7.52, 10.1]$ , the waveform changes gently, so the spectrum is simple and the complexity is low; when  $d \in (10.1, 12]$ , the system is in the chaos state, and the spectral entropy complexity curve of the system changes greatly, so the complexity is very high.

**2.7. Multistability Analysis.** Multistability, the result of coexistence of many kinds of nonlinear attractors, is the inherent property of many nonlinear dynamic systems. In recent years, it has become a very important research topic and has attracted much attention [41–50]. Multistability is rich in the diversity of stable states of nonlinear dynamic systems, which makes the system flexible. In particular, when the number of coexisting attractors from a dynamic system tends to infinite, the coexistence of infinite attractors depending on the initial conditions of a state variable is called extreme multistability [80].

In order to investigate the possible multistability in this 5D FWMHS, we first consider random initial conditions while all the parameters are fixed. These coexisting attractors exist in different values of all parameters, and Figure 5 shows some symmetric coexisting attractors in state space of system (1) for different values of the parameter  $d$ . Figure 6 shows some coexisting multiwing attractors in state space of system (1) for different values of the parameter  $d$  with different initial conditions. As can be seen in Figure 6, the occurrence of chaos/hyperchaos, period, and quasi-period attractors coexist with each other for selected initial conditions.

### 3. Circuit Design

The above conclusions can be verified by the analog circuit. The analog circuit is a method that can really present the chaotic motion state, which is more convincing than

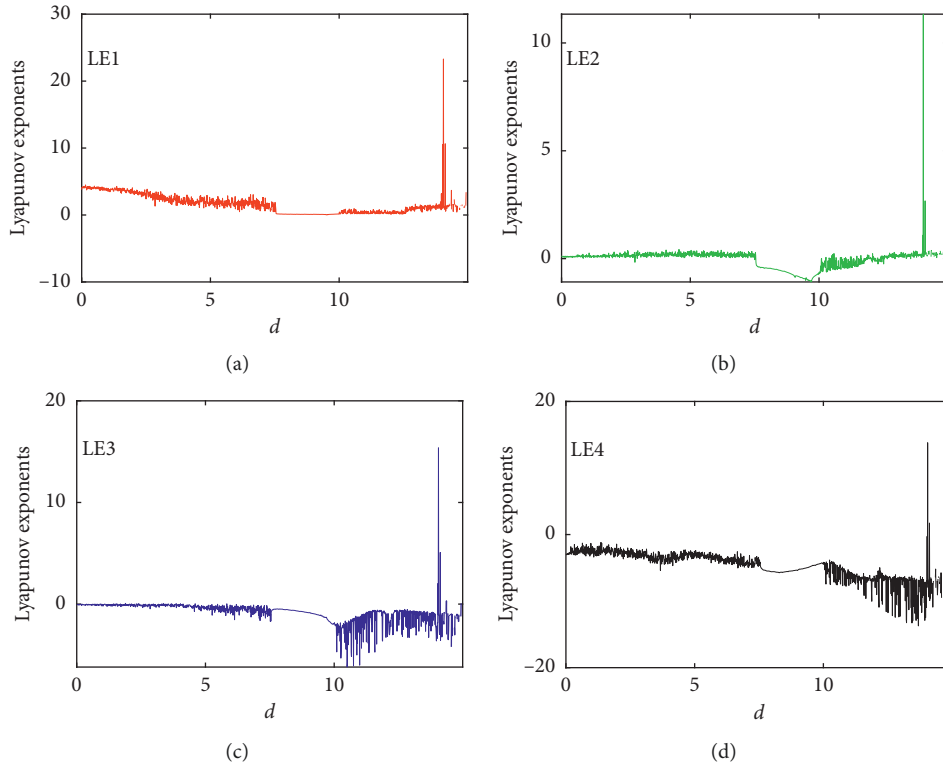


FIGURE 3: Lyapunov exponents' spectrum for increasing parameter  $d$  (the fifth LE is out of plot).

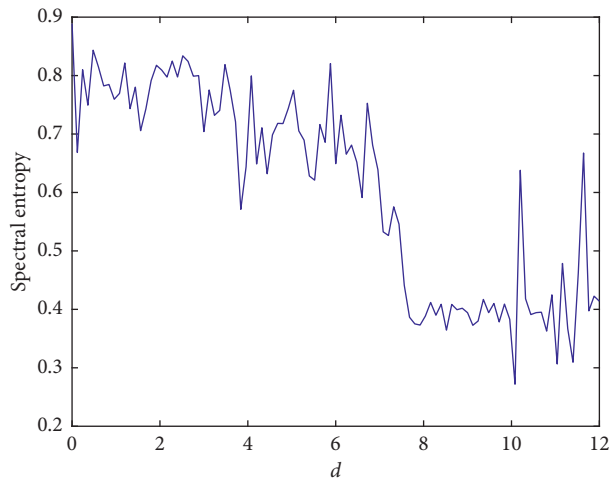


FIGURE 4: The complexity of spectral entropy for increasing parameter  $d$ .

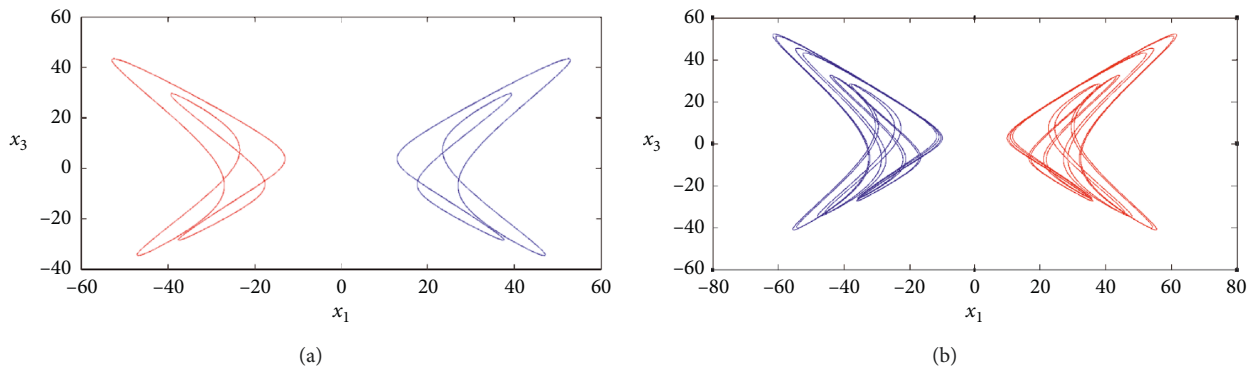


FIGURE 5: Continued.

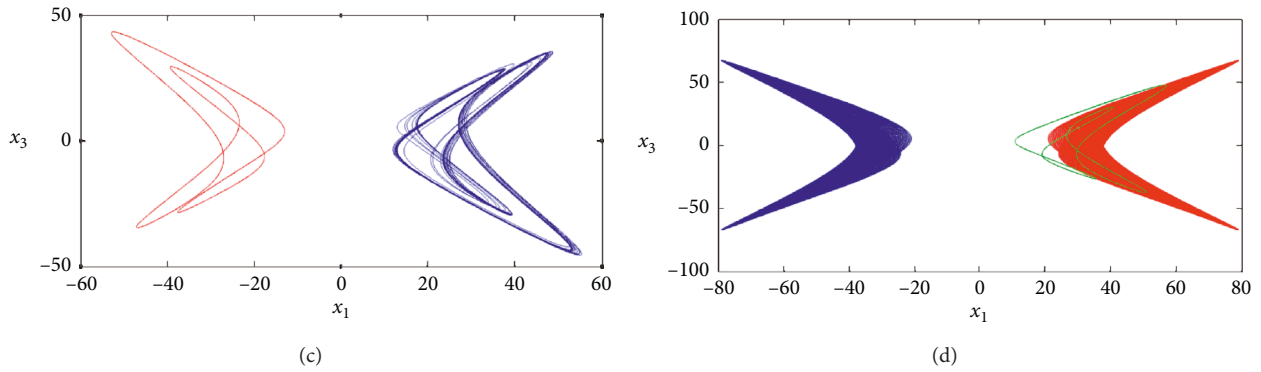


FIGURE 5: Symmetric coexisting attractors for parameters: (a)  $d = 9$  and the initial conditions are  $[0.1, \pm 0.1, 0.1, 0.1, 0.1]$  (red and blue), (b)  $d = 12.5$  and the initial conditions are  $[0.1, -0.1, 0.1, 0.1, 0.1]$  and  $[-0.1, 0.1, 0.1, 0.1, 0.1]$  (red and blue), (c)  $d = 9$  and the initial conditions are  $[0.1, -0.1, 0.1, 0.1, 0.1]$  and  $[2, 1, 1, 2, 2]$  (red and blue), and (d)  $d = 11.9$  and the initial conditions are  $[-0.1, 0.1, 0.1, 0.1, 0.1]$ ,  $[0.1, -0.1, 0.1, 0.1, 0.1]$  and  $[0.1, 0.1, 0.1, 0.1, 0.1]$  (blue, red, and green).

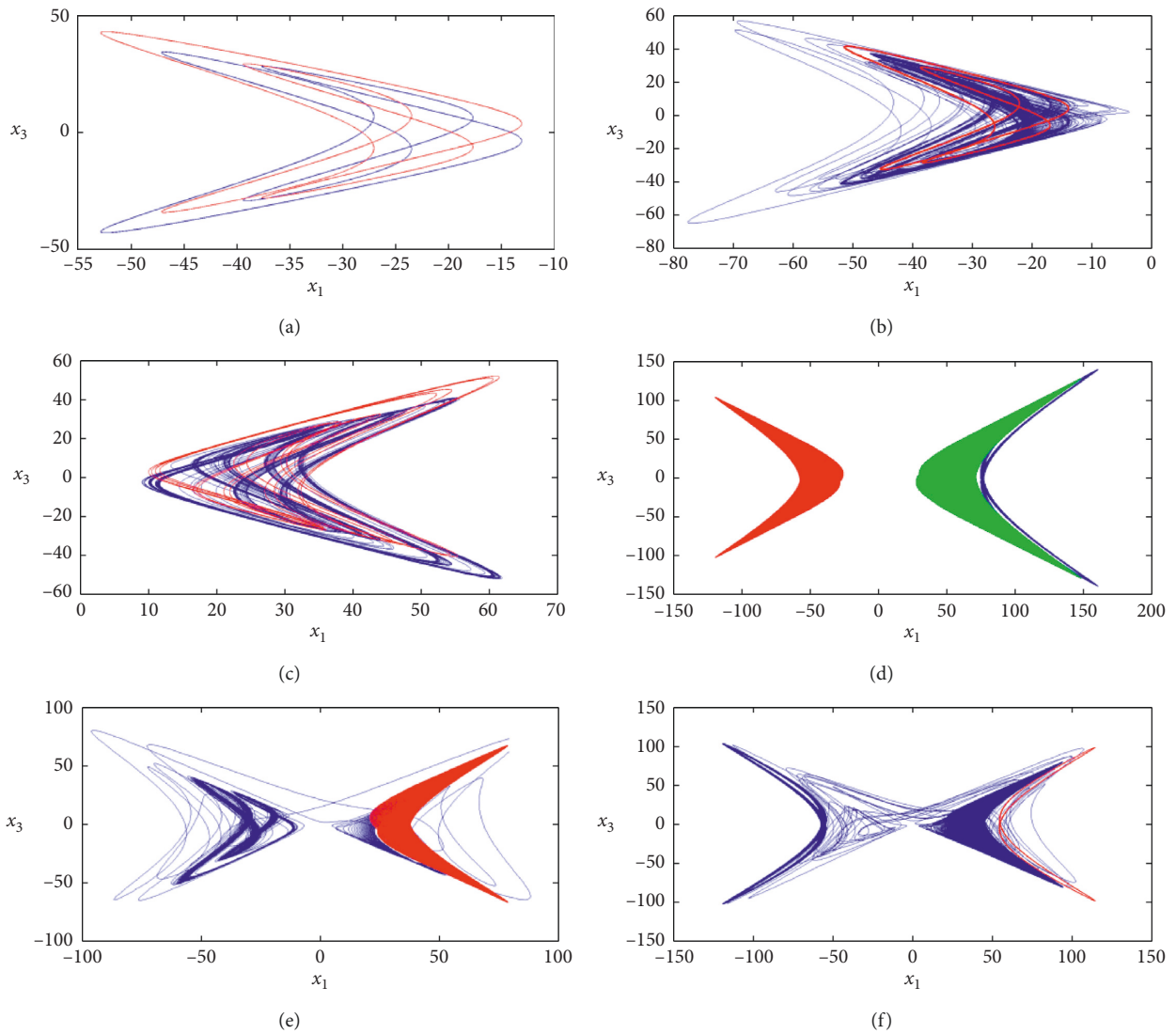


FIGURE 6: Coexisting multiwing attractors for parameters: (a)  $d = 9$  and the initial conditions are  $[0.1, -0.1, 0.1, 0.1, 0.1]$  and  $[20, 1, 1, 2, 2]$  (red and blue), (b)  $d = 8$  and the initial conditions are  $[0.1, -0.1, 0.1, 0.1, 0.1]$  and  $[20, 1, 1, 2, 2]$  (red and blue), (c)  $d = 12.5$  and the initial conditions are  $[0.1, -0.1, 0.1, 0.1, 0.1]$  and  $[1, 0.1, 0.1, 0.1, 0.1]$  (red and blue), (d)  $d = 13.5$  and the initial conditions are  $[0.1, \pm 0.1, 0.1, 0.1, 0.1]$  and  $[2, 1, 1, 2, 2]$  (blue, red, and green), (e)  $d = 11.9$  and the initial conditions are  $[0.1, -0.1, 0.1, 0.1, 0.1]$  and  $[2, 1, 1, 2, 2]$  (red and blue), and (f)  $d = 13$  and the initial conditions are  $[0.1, 1, 0.1, 0.1, 0.1]$  and  $[2, 1, 1, 2, 2]$  (red and blue).

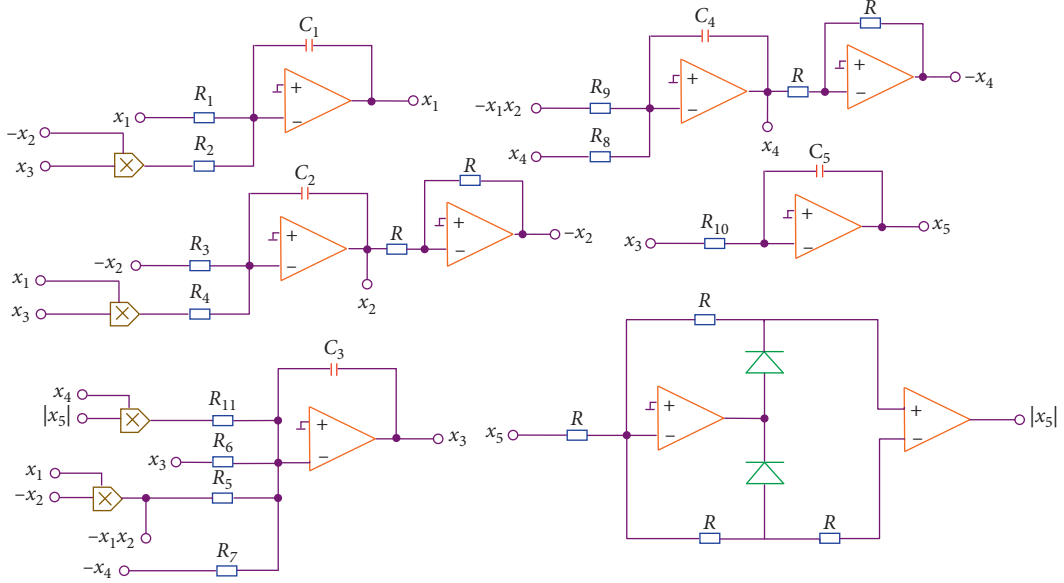


FIGURE 7: Hardware circuit implementation of the four-wing memristive hyperchaotic system (1).

numerical simulation. The operational amplifiers and multipliers are LF347 and AD633JN, respectively. Diode uses 1N1199C when all active components are powered with  $\pm 15$  V. The schematic diagram of the circuit is designed with Multisim 14.0 software platform, as shown in Figure 7.

The simulation circuit designed according to the mathematical equation of each state of equation (1) is

shown in Figure 7. In the simulation circuit, capacitors, resistors, analog multipliers, and integrated operational amplifiers are used (the memristor model has been split into two parts). According to the characteristics of the nonlinear circuit and the basic theory of the circuit, the mathematical equations of the states in the simulation circuit shown in Figure 7 are obtained as shown in the following equation:

$$\begin{cases} \frac{dx_1}{dt} = \frac{1}{R_1 C_1} x_1 - \frac{1}{10 R_2 C_1} x_2 x_3, \\ \frac{dx_2}{dt} = \frac{1}{R_3 C_2} x_2 - \frac{1}{10 R_4 C_2} x_1 x_3, \\ \frac{dx_3}{dt} = \frac{1}{10 R_5 C_3} x_1 x_2 - \frac{1}{R_6 C_3} x_3 + \frac{1}{R_7 C_3} \left( 1 - \frac{R_{12}}{R_{13}} |x_5| \right) x_4, \\ \frac{dx_4}{dt} = -\frac{1}{R_8 C_4} x_4 + \frac{1}{10 R_9 C_4} x_1 x_2, \\ \frac{dx_5}{dt} = -\frac{1}{R_{10} C_5} x_2. \end{cases} \quad (7)$$

According to the given parameters, the resistance value in (7) can be calculated as follows:

$$\left. \begin{aligned}
 \frac{R}{R_1} &= 10, & R_1 &= 10 \text{ k}\Omega, \\
 \frac{R}{10R_2} &= 1, & R_2 &= 10 \text{ k}\Omega, \\
 \frac{R}{R_3} &= 12, & R_3 &= 8.33 \text{ k}\Omega, \\
 \frac{R}{10R_4} &= 1, & R_4 &= 10 \text{ k}\Omega, \\
 \frac{R}{10R_5} &= 1, & R_5 &= 10 \text{ k}\Omega, \\
 \frac{R}{R_6} &= 30, & R_6 &= 3.33 \text{ k}\Omega, \\
 \frac{R}{R_7} &= 2, & R_7 &= 50 \text{ k}\Omega, \\
 \frac{R}{R_8} &= 3, & R_8 &= 33.33 \text{ k}\Omega, \\
 \frac{R}{10R_9} &= 1, & R_9 &= 10 \text{ k}\Omega, \\
 \frac{R}{R_{10}} &= 1, & R_{10} &= 100 \text{ k}\Omega.
 \end{aligned} \right\} \quad (8)$$

The other parameters of each component in the circuit are set as follows:  $R = 100 \text{ k}\Omega$  and  $C_1 = C_2 = C_3 = C_4 = 0.01 \mu\text{F}$ . Under the above parameters setting conditions, the hyperchaotic phase portraits are obtained, as shown in Figure 8(a)–8(d), respectively. From these diagrams, it can be seen that the circuit implementation results are basically consistent with the numerical simulation results.

#### 4. Secure Communication Scheme Based on the New 5D Multistable FWMHS

In this section, based on the proposed 5D multistable FWMHS, a chaotic secure communication scheme with two inputs and two outputs is proposed. By using high-order sliding mode control synchronization technology, parameter modulation method, and Lyapunov stability theory, the encryption and recovery of two message signals are realized, the gain of the receiver can be continuously adjusted, the unknown parameters can be accurately identified, and the disturbance inputs can be suppressed simultaneously.

**4.1. Higher-Order Sliding Mode Control Theory.** The sliding order  $r$  of the traditional sliding mode ( $r$  refers to the number of continuous full derivatives of the sliding mode variable  $s$  which are zero on the sliding mode surface  $s = 0$ ) is 1. Because  $s = 0$  on the sliding mode surface,  $s$  is discontinuous, the traditional sliding mode is also called the first-order sliding mode. Traditional sliding mode control is essentially a discontinuous control input acting on the first derivative of the sliding mode, which makes the traditional sliding mode control have discontinuous and serious chattering problems. In order to restrain such problems, the theory of high-order sliding mode control is proposed. In the sense of Filippov, high-order sliding mode is actually a kind of motion on a special type of integral manifold of a discontinuous dynamic system [81]. It can be characterized by the convergence of switching function  $s(x)$  and derivatives up to a certain order to zero. The order sliding set of sliding surface  $s = 0$  is described as follows:

$$s = \dot{s} = \ddot{s} = \dots = s^{(r-1)} = 0. \quad (9)$$

When the  $r$ -order sliding set (9) is nonempty and assumes that it is a local integral set in the sense of Filippov, the related motion satisfying the above formula is called “ $r$ -order sliding mode,” with respect to the sliding surface  $s = 0$ . At present, there is a popular design method for high-order sliding mode variable structure control, i.e., gain-adjustable switching control. Its structure is as follows:

$$u = k \text{sgn}(s(x))s^r(x), \quad (10)$$

where the constant  $k$  is the control gain and can be adjusted. It can be seen that the high-order sliding mode control is to apply discontinuous control inputs to the high-order derivatives of the sliding mode, which can not only greatly weaken the chattering during system switching but also realize the high-order dynamic characteristics of the system [82]. Therefore, the high-order sliding mode maintains the advantages of the traditional sliding mode, suppresses the chattering, eliminates the restriction of relative order, and improves the control accuracy.

**4.2. Some Definitions and Assumptions.** *Definition 1.* Consider the following form of smooth nonlinear chaotic systems:

$$\begin{aligned}
 \dot{X} &= f(X, Q), \\
 \dot{Y} &= h(X),
 \end{aligned} \quad (11)$$

where  $X = (x_1, x_2, \dots, x_n)^T \in R^n$  is the state variable,  $Y = (y_1, y_2, \dots, y_m)^T \in R^m$  is the output state variable, and  $m \leq n$ .  $f(\circ)$  and  $h(\circ)$  are smooth nonlinear functions and  $Q \in R^l$  are state vectors satisfying  $l \leq n$ . Let  $\alpha^{(j)}$  be the reciprocal of  $j$  times of vector  $\alpha$ . If  $X$  can be uniquely expressed by equation (12), we think that the state variable  $X$  can be observed by the algebraic method:



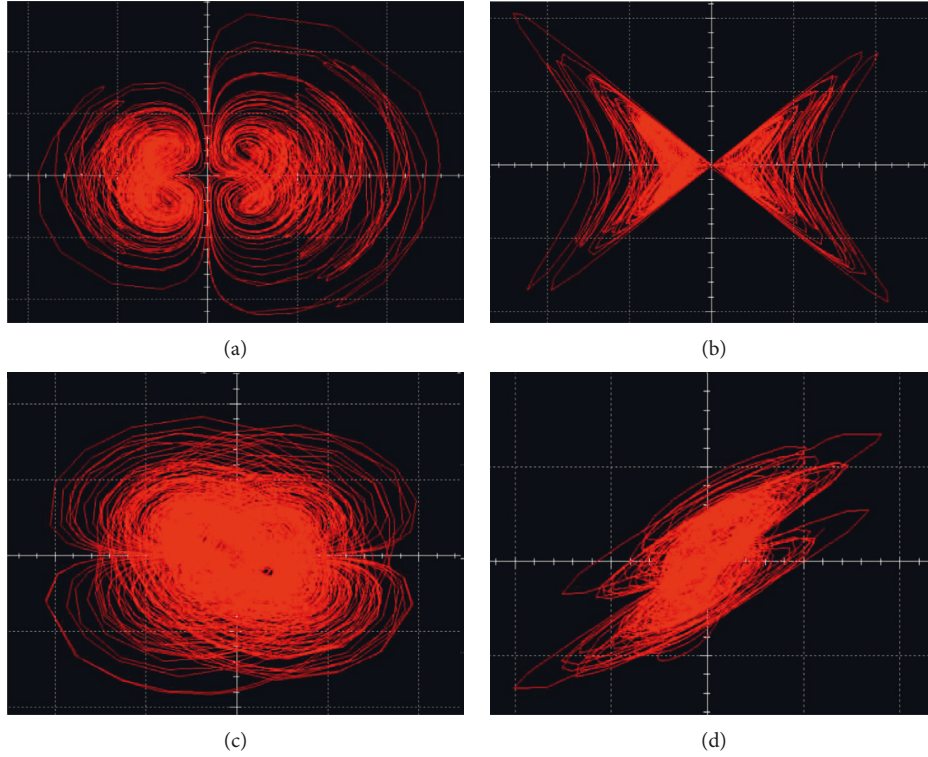


FIGURE 8: Four-wing memristive hyperchaotic phase portraits obtained by Multisim simulations in the (a)  $x_1 - x_2$  plane, (b)  $x_1 - x_3$  plane, (c)  $x_2 - x_3$  plane, and (d)  $x_3 - x_4$  plane.

$$X = \psi(\alpha, \alpha^{(1)}, \dots, \alpha^{(j)})^T, \quad (12)$$

where  $j$  is an integer and  $\psi$  is a smooth function.

*Definition 2.* Under the same conditions as Definition 1, when  $Q$  satisfies the following relationship:

$$\varphi_1(\alpha, \alpha^{(1)}, \dots, \alpha^{(j)}) = \varphi_2(\alpha, \alpha^{(1)}, \dots, \alpha^{(j)})Q, \quad (13)$$

where  $\varphi_1(\circ)$  and  $\varphi_2(\circ)$  are smooth matrices of  $n \times 1$  and  $n \times n$ , respectively,  $Q$  is considered to be observable with the algebraic method for output vector matrix  $\alpha$ .

*Assumption 1.* The 5D multistable FWMHS (1) proposed above is selected as the transceiver system of the communication scheme. It is clear from Figures 1 and 2 that the five state variables of the system oscillate within a certain range. In fact, for most of the initial conditions and system parameters, the five state variables of system (1) are bounded in most cases.

*Assumption 2.* It is assumed that both transmitter and receiver systems of secure communication mechanism are subject to disturbance inputs of  $d_{1i}$ ,  $i = 1, 2, 3, 4, 5$  and  $d_{2i}$ ,  $i = 1, 2, 3, 4, 5$ , respectively, and are bounded and satisfy  $|d_{1i}| \leq \rho_{1i}$ ,  $i = 1, 2, 3, 4, 5$  and  $|d_{2i}| \leq \rho_{2i}$ ,  $i = 1, 2, 3, 4, 5$ , of which  $\rho_{2i}, \rho_{1i}$  are known positive constants and satisfy  $\rho_{2i} \geq \rho_{1i}$ .

Now, we rewrite the second difference equation of system (1) as follows:

$$x_3 = \frac{bx_2 - \dot{x}_2}{x_1}, \quad (14)$$

then equation (14) is substituted into the first equation of system (1) to obtain

$$x_1 \dot{x}_1 + x_2 \dot{x}_2 = bx_2^2 - ax_1^2. \quad (15)$$

According to Definitions 1 and 2, it is obvious that system (1) is observable by the algebraic method with respect to two outputs  $x_1$  and  $x_2$ . According to equation (15), it is further shown that the state parameter vector  $Q = [a, b]^T$  of system (1) can be observed algebraically with respect to the two outputs  $x_1$  and  $x_2$ . Therefore, invalid states  $x_3, x_4$ , and  $x_5$  and parameter vector  $Q$  can be recovered by the two output variables at the same time.

*4.3. Transceiver Design.* At the transmitter, we choose the 5D multistable FWMHS (1) as the drive system. The algebraic equation with some uncertain parameters and disturbance inputs is described as follows:

$$\begin{cases} \dot{x}_1 = -a(t)x_1 + x_2x_3 + d_{11}, \\ \dot{x}_2 = b(t)x_2 - x_1x_3 + d_{12}, \\ \dot{x}_3 = x_1x_2 - 30x_3 + 2x_4(1 - 0.2|x_5|) + d_{13}, \\ \dot{x}_4 = x_1x_2 - 3x_4 + d_{14}, \\ \dot{x}_5 = -x_3 + d_{15}, \end{cases} \quad (16)$$

where  $x_1, x_2, x_3, x_4$ , and  $x_5$  are the state variables of the 5D multistable FWMHS, and the uncertain parameters are defined as follows:

$$a(t) = a + s_a(t), b(t) = b + s_b(t), \quad (17)$$

where  $s_a(t)$  and  $s_b(t)$  are two useful message signals, and the state parameter vector is  $Q = [a, b]^T$ .  $d_{1i}$ ,  $i = 1, 2, 3, 4, 5$ , are disturbance inputs and satisfy Assumption 2.

At the receiver, we define the 5D multistable FWMHS (1) with partial uncertainties and disturbance inputs as a response system. The response system has two effective output variables  $x_1$  and  $x_2$ , whose algebraic equation is described as follows:

$$\begin{cases} \dot{x}_6 = -\hat{a}(t)x_1 + x_2x_8 + d_{21} + u_1, \\ \dot{x}_7 = \hat{b}(t)x_2 - x_1x_8 + d_{22} + u_2, \\ \dot{x}_8 = x_1x_2 - 30x_8 + 2x_9(1 - 0.2|x_{10}|) + d_{23} + u_3, \\ \dot{x}_9 = x_1x_2 - 3x_9 + d_{24} + u_4, \\ \dot{x}_{10} = -x_8 + d_{25} + u_5, \end{cases} \quad (18)$$

where  $x_6, x_7, x_8, x_9$ , and  $x_{10}$  are the state variables of the system, and the uncertain parameters are defined as follows:

$$\hat{a}(t) = \hat{a} + \hat{s}_a(t), \hat{b}(t) = \hat{b} + \hat{s}_b(t), \quad (19)$$

where  $\hat{s}_a(t)$  and  $\hat{s}_b(t)$  are two useful message signals after decryption.  $d_{2i}$ ,  $i = 1, 2, 3, 4, 5$ , are disturbance inputs and satisfy Assumption 2,  $U = [u_1, u_2, u_3, u_4, u_5]^T$  are controllers, and  $\hat{Q} = [\hat{a}, \hat{b}]^T$ . Figure 9 shows the proposed secure communication scheme based on two-input two-output with partial uncertainties and disturbance inputs.

**4.4. Error Dynamics System Design.** By subtracting system (16) from system (18), the following error dynamics system is obtained:

$$\dot{e} = \begin{bmatrix} \dot{e}_1 \\ \dot{e}_2 \\ \dot{e}_3 \\ \dot{e}_4 \\ \dot{e}_5 \end{bmatrix} = \begin{bmatrix} -\tilde{a}x_1 - \tilde{s}_a(t)x_1 + x_2e_3 + d_{11} - d_{21} - u_1 \\ \tilde{b}x_2 + \tilde{s}_b(t)x_2 - x_1e_3 + d_{12} - d_{22} - u_2 \\ -30e_3 + 2e_4 - 0.4(x_4|x_5| - x_9|x_{10}|) + d_{13} - d_{23} - u_3 \\ -3e_4 + d_{14} - d_{24} - u_4 \\ -e_3 + d_{15} - d_{25} - u_5 \end{bmatrix}, \quad (20)$$

where

$$\begin{aligned} e &= \begin{bmatrix} e_1 \\ e_2 \\ e_3 \\ e_4 \\ e_5 \end{bmatrix} = \begin{bmatrix} x_1 - x_6 \\ x_2 - x_7 \\ x_3 - x_8 \\ x_4 - x_9 \\ x_5 - x_{10} \end{bmatrix}, \\ Q &= \begin{bmatrix} a \\ b \end{bmatrix}, \\ \tilde{Q} &= \begin{bmatrix} \tilde{a} \\ \tilde{b} \end{bmatrix} = \begin{bmatrix} a - \hat{a} \\ b - \hat{b} \end{bmatrix}, \\ s(t) &= \begin{bmatrix} s_a(t) \\ s_b(t) \end{bmatrix}, \\ \tilde{s}(t) &= \begin{bmatrix} \tilde{s}_a(t) \\ \tilde{s}_b(t) \end{bmatrix} = \begin{bmatrix} s_a(t) - \hat{s}_a(t) \\ s_b(t) - \hat{s}_b(t) \end{bmatrix}. \end{aligned} \quad (21)$$

It can be seen that the synchronization between system (16) and system (18) can be achieved as long as the appropriate controller  $U = [u_1, u_2, u_3, u_4, u_5]^T$  and the corresponding parameter identification law are designed to make the error system approach zero gradually.

**4.5. High-Order Sliding Mode Controller Design.** Based on the idea of high-order sliding mode control proposed in the previous section, we present the following corresponding theory.

**Theorem 1.** *If the following high-order sliding mode adaptive controller is designed,*

$$U = \begin{bmatrix} u_1 \\ u_2 \\ u_3 \\ u_4 \\ u_5 \end{bmatrix} = \begin{bmatrix} k_1 \text{sign}(e_1)e_1^\lambda + \rho_{11} \text{sign}(e_1) - \rho_{21} \text{sign}(e_1) \\ k_2 \text{sign}(e_2)e_2^\lambda + \rho_{12} \text{sign}(e_2) - \rho_{22} \text{sign}(e_2) \\ x_2e_1 - x_1e_2 - 30e_3 - 0.4(x_4|x_5| - x_9|x_{10}|) + \rho_{13} \text{sign}(e_3) - \rho_{23} \text{sign}(e_3) \\ 2e_3 - 3e_4 + \rho_{14} \text{sign}(e_4) - \rho_{24} \text{sign}(e_4) \\ -e_3 + \rho_{15} \text{sign}(e_5) - \rho_{25} \text{sign}(e_5) \end{bmatrix}, \quad (22)$$

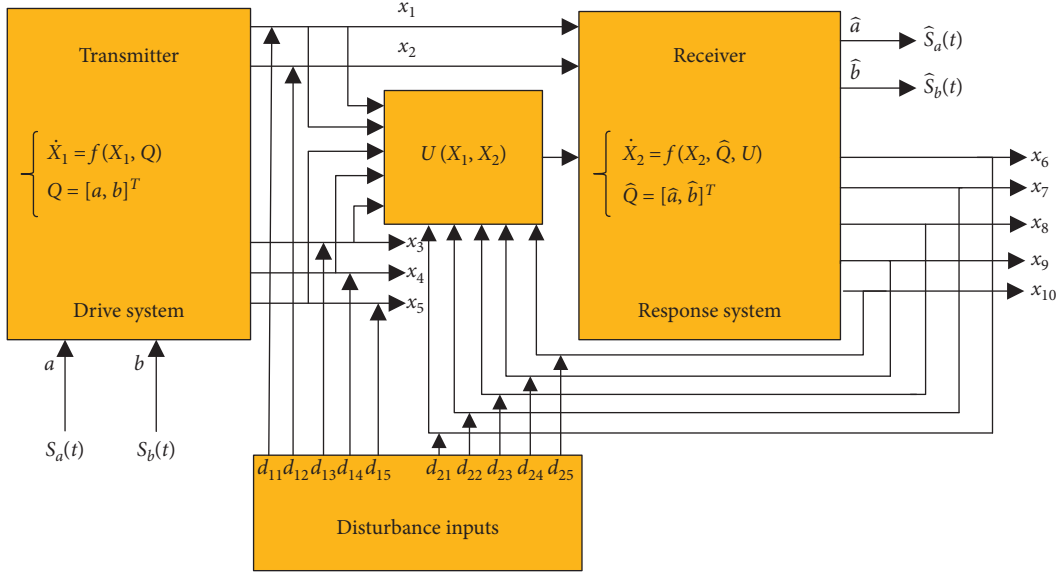


FIGURE 9: Secure communication scheme based on two-input and two-output with partial uncertainty parameters and disturbance inputs.

where  $k = [k_1, k_2]^T$  is the controller gain,  $\lambda \in \mathbb{Z}^+, \lambda > 1$ , and  $\text{sign}(\circ)$  is symbolic function. The adaptive parameter identification law and the useful message signal law are designed as follows:

$$\begin{aligned} \dot{\hat{Q}} &= \begin{bmatrix} \dot{\hat{a}} \\ \dot{\hat{b}} \end{bmatrix} = \begin{bmatrix} -x_1 e_1 \\ x_2 e_2 \end{bmatrix}, \\ \dot{\hat{s}}(t) &= \begin{bmatrix} \dot{\hat{s}}_a(t) \\ \dot{\hat{s}}_b(t) \end{bmatrix} = \begin{bmatrix} -x_1 e_1 \\ x_2 e_2 \end{bmatrix}, \end{aligned} \quad (23)$$

where  $\hat{a}$  and  $\hat{b}$  are the estimates of unknown parameters and  $a$  and  $b$  are useful message signals for decryption. The response system (18) and the drive system (16) can be synchronized

globally and asymptotically with disturbance inputs, any normal number  $k_1$  and  $k_2$ , and any positive integer  $\lambda$ . By modulation laws (17), (19), and (22), the receiver system (18) can accurately recover useful message signals  $s_a(t)$  and  $s_b(t)$ , respectively.

*Proof.* Consider the following Lyapunov function:

$$V(t) = \frac{1}{2} \left[ e^T e + \tilde{Q}^T \tilde{Q} + \tilde{s}^T(t) \tilde{s}(t) \right]. \quad (24)$$

By calculating the derivative of  $V(t)$  along the trajectories of the error system (19) and using equations (21) and (22), we can obtain

$$\begin{aligned} \dot{V}(t) &= e_1 \dot{e}_1 + e_2 \dot{e}_2 + e_3 \dot{e}_3 + e_4 \dot{e}_4 + e_5 \dot{e}_5 + \tilde{a} \dot{\tilde{a}} + \tilde{b} \dot{\tilde{b}} + \tilde{s}_a(t) \dot{\tilde{s}}_a(t) + \tilde{s}_b(t) \dot{\tilde{s}}_b(t) \\ &= -e_1 \tilde{a} x_1 - e_1 \tilde{s}_a(t) x_1 + e_1 x_2 e_3 + e_1 d_{11} - e_1 d_{21} - e_1 k_1 \text{sign}(e_1) e_1^\lambda - \rho_{11} e_1 \text{sign}(e_1) \\ &\quad + \rho_{21} e_1 \text{sign}(e_1) + \rho_{21} e_1 \text{sign}(e_1) + e_2 \tilde{b} x_2 + e_2 \tilde{s}_b(t) x_2 - e_2 x_1 e_3 + e_2 d_{12} - e_2 d_{22} - e_2 k_2 \text{sign}(e_2) e_2^\lambda \\ &\quad - p_{12} e_2 \text{sign}(e_2) + p_{22} e_2 \text{sign}(e_2) - 30e_3^2 + 2e_3 e_4 - 0.4e_4(x_4|x_5| - x_9|x_{10}|) + e_3 d_{13} - e_3 d_{13} - e_3 d_{23} \\ &\quad - e_3 x_2 e_1 + x_1 e_3 e_2 + 30e_3^2 + 0.4e_4(x_4|x_5| - x_9|x_{10}|) - p_{13} e_3 \text{sign}(e_3) + p_{23} e_3 \text{sign}(e_3) + p_{23} e_3 \text{sign}(e_3) - 3e_4^2 \\ &\quad + e_4 d_{14} - e_4 d_{24} - 2e_4 e_3 + 3e_3^2 - p_{14} e_4 \text{sign}(e_4) + p_{24} e_4 \text{sign}(e_4) - e_3 e_5 + e_5 d_{15} - e_5 d_{25} + e_3 e_5 \\ &\quad - p_{15} e_5 \text{sign}(e_5) + p_{25} e_5 \text{sign}(e_5) + \tilde{a} x_1 e_1 - \tilde{b} x_2 e_2 + x_1 e_1 \tilde{s}_a(t) - x_2 e_2 \tilde{s}_b(t) \\ &= -k_1 e_1 \text{sign}(e_1) e_1^\lambda - k_2 e_2 \text{sign}(e_2) e_2^\lambda + e_1 d_{11} - p_{11} e_1 \text{sign}(e_1) - [e_1 d_{21} - p_{21} e_1 \text{sign}(e_1)] \\ &\quad + e_2 d_{12} - p_{12} e_2 \text{sign}(e_2) - [e_2 d_{22} - p_{22} e_2 \text{sign}(e_2)] + e_3 d_{13} - p_{13} e_3 \text{sign}(e_3) - [e_3 d_{23} - p_{23} e_3 \text{sign}(e_3)] \\ &\quad + e_4 d_{14} - p_{14} e_4 \text{sign}(e_4) - [e_4 d_{24} - p_{24} e_4 \text{sign}(e_4)] + e_5 d_{15} - p_{15} e_5 \text{sign}(e_5) \\ &\quad - [e_5 d_{25} - p_{25} e_5 \text{sign}(e_5)]. \end{aligned} \quad (25)$$

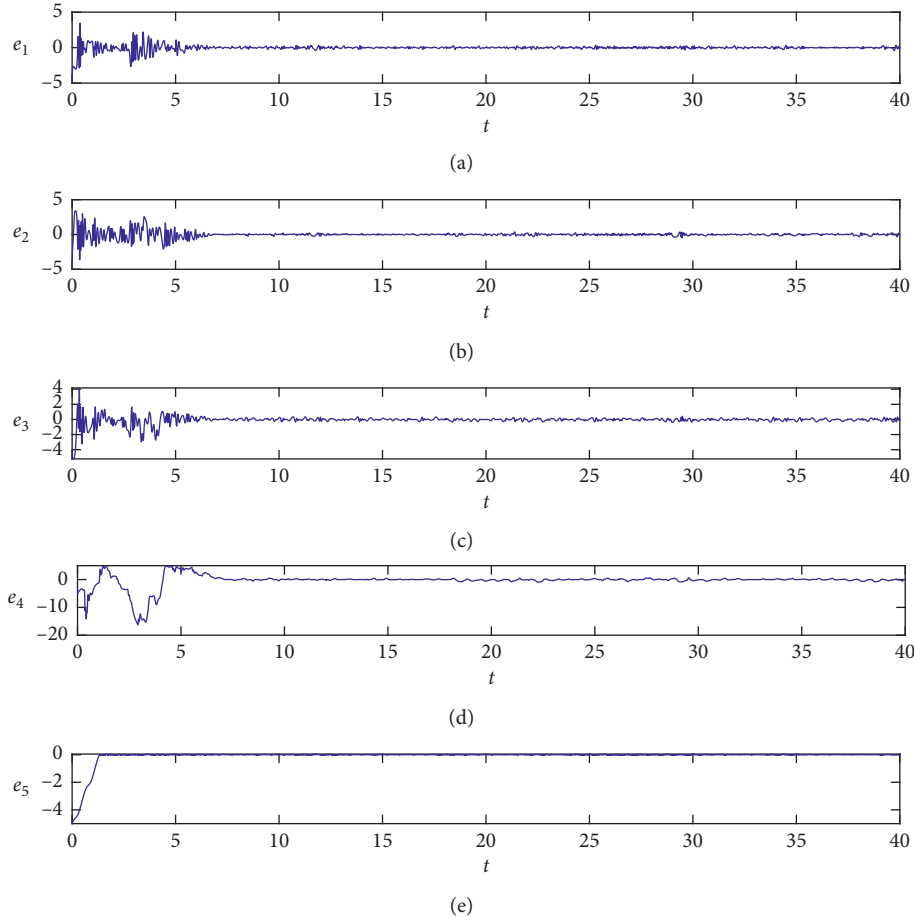


FIGURE 10: The trajectories of the synchronization errors  $e_1, e_2, e_3, e_4$ , and  $e_5$ .

When

$$\begin{cases} \psi_{1i} = e_i d_{1i} - \rho_{1i} e_i \text{sign}(e_i), \\ \psi_{2i} = e_i d_{2i} - \rho_{2i} e_i \text{sign}(e_i), \end{cases} \quad (26)$$

where  $\psi_{1i}, \psi_{2i}$ , ( $i = 1, 2, 3, 4, 5$ )  $\in \mathbb{R}$  are the compensators for eliminating disturbance inputs. According to the definitions and assumptions of  $d_{1i}$  and  $d_{2i}$  and  $\rho_{1i}$  and  $\rho_{2i}$ ,  $\psi_{1i} \leq \psi_{2i}$  can be guaranteed, so (24) can be changed to

$$\begin{aligned} \dot{V}(t) &= -[k_1 e_1 \text{sign}(e_1) e_1^\lambda + k_2 e_2 \text{sign}(e_2) e_2^\lambda] + \sum_{i=1}^4 (\psi_{1i} - \psi_{2i}) \\ &\leq -[k_1 e_2 \text{sign}(e_2) e_2^\lambda + k_2 e_2 \text{sign}(e_2) e_2^\lambda] \\ &= -(k_1 |e_1| e_1^\lambda + k_2 |e_2| e_2^\lambda). \end{aligned} \quad (27)$$

So,  $\dot{V}(t)$  is negative definite. In fact, because of  $\dot{V}(t) < 0$ , there are  $e_1, e_2 \in L_{\mathbb{Y}}$ . The error equation (19) shows that  $\dot{e}_1, \dot{e}_2 \in L_{\mathbb{Y}}$ . Integrating both sides of equation (27), it can be obtain:

$$\int_0^t (k_1 |e_1(t)| e_1^\lambda(t) + k_2 |e_2(t)| e_2^\lambda(t)) dt \leq V(0). \quad (28)$$

According to Barbalat's lemma, when  $t \rightarrow \mathbb{Y}$ , there are  $\dot{e} \rightarrow \mathbb{Y}$ . Therefore, the response system (18) with

disturbance inputs and the drive system (16) with disturbance inputs achieve global asymptotic synchronization.

As shown in Figure 2, the state variables  $x_1$  and  $x_2$  oscillate aperiodically around the zero. From the above discussion, we can conclude that  $\dot{e}$  is bounded, which means that  $e$  is continuous. According to Barbalat's lemma, when  $t \rightarrow \mathbb{Y}$ , there are  $\dot{e} \rightarrow \mathbb{Y}$ . By differentiating equation (19), we also get that  $\ddot{e}$  is bounded, and when  $t \rightarrow \mathbb{Y}$ , there is  $\ddot{e} \rightarrow \mathbb{Y}$ . Since when  $t \rightarrow \mathbb{Y}$ ,  $V(t)$  is convergent, it is obtained that when  $t \rightarrow \mathbb{Y}$ , two uncertain parameter errors  $\bar{Q}$  and two useful message signal errors  $\bar{s}(t)$  are convergent. From equation (22), when  $t \rightarrow \mathbb{Y}$ ,  $\bar{Q}s$  and  $\bar{s}(t)$  converge to zero. Therefore, the uncertain parameters  $a(t)$  and  $b(t)$  at the receiver can be identified and the useful message signals  $s_a(t)$  and  $s_b(t)$  can be accurately recovered at the same time.

**4.6. Numerical Simulations.** In this section, the fourth-order Runge-Kutta method is used to simulate and verify the theoretical analysis with the step size 0.001. At the transmitter, the uncertain parameters of the system are selected as  $a = 10$  and  $b = 12$  and the initial conditions of the system are set to  $x_1(0) = 1, x_2(0) = 2, x_3(0) = 3, x_4(0) = 4$ , and  $x_5(0) = 5$ . At the receiver side, the initial conditions of the system are set to  $x_6(0) = 6, x_7(0) = 7, x_8(0) = 8, x_9(0) = 9$ , and

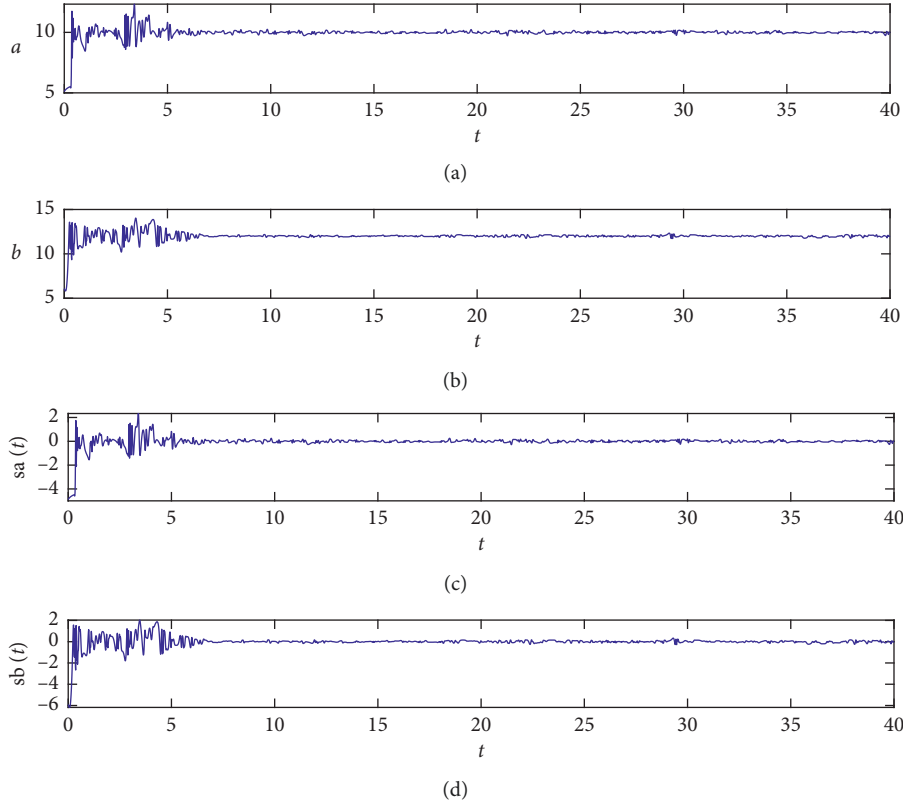


FIGURE 11: Estimation of uncertain parameters (a) and (b) and the recovered signal errors (c) and (d).

$x_{10}(0) = 10$ . The initial conditions of uncertain parameters and useful message signals are set to  $\hat{Q}(0) = [\hat{a}(0), \hat{b}(0)]^T =$

$[0.1, 0.1]^T$  and  $\hat{s}(0) = [\hat{s}_a(0), \hat{s}_b(0)]^T = [0.1, 0.1]^T$ , respectively. The disturbance inputs are set as follows:

$$\begin{cases} [d_{11}, d_{12}, d_{13}, d_{14}, d_{15}]^T = [-0.3 \cos(20t), 0.2 \sin(10t), 0.2 \sin(10t), 0.2 \cos(20t), 0.2 \cos(20t)]^T, \\ [d_{21}, d_{22}, d_{23}, d_{24}, d_{25}]^T = [4 \sin(20t), -3 \cos(10t), 3 \sin(20t), 2 \sin(10t), 2 \sin(10t)]^T. \end{cases} \quad (29)$$

Assuming that the useful message signals  $s_a(t)$  and  $s_b(t)$  are triangular function signals, and the frequencies of both triangular function signals are 90 Hz, we have

$$\begin{cases} s_a(t) = 0.6 \sin(180\pi t), \\ s_b(t) = 0.5 \cos(180\pi t). \end{cases} \quad (30)$$

At the same time, the gains of the receiver system are chosen as  $k = [k_1, k_2]^T = [0.6, 0.8]^T$  and sliding order  $\lambda = 4$ . Figure 10 shows the synchronization error of the response system (18) and the drive system (16), indicating that the error tends to zero rapidly and gradually with time. Figures 11(a) and 11(b) show that when  $t \rightarrow \infty$ , the estimated values of unknown parameters  $\hat{a}(t)$  and  $\hat{b}(t)$  gradually tend to  $a = 10$  and  $b = 12$  over time, respectively. As shown in Figures 11(c) and 11(d), it is easy to see that both useful message signals  $s_a(t)$  and  $s_b(t)$  are accurately recovered.

## 5. Conclusion

In this work, a new 5D four-wing hyperchaotic system having a flux-controlled memristor model with absolute

value function is introduced. Dynamical analysis is performed in terms of equilibrium point, perpetual point, phase portraits, Lyapunov exponents, bifurcations, and spectral entropy. In particular, the phenomenon of extreme multistability with hidden oscillation is revealed and the coexistence of infinite hidden attractors is observed. Then, the 5D multistable FWMHS circuit is designed. Finally, a secure chaotic communication scheme of the 5D multistable FWMHS with disturbance inputs based on parametric modulation theory and Lyapunov stability theory is implemented by a convenient robust high-order sliding mode adaptive controller. The proposed adaptive controller can accurately identify unknown parameters, continuously adjust the gain of the receiver system, and effectively suppress the disturbance inputs of the transmitter and receiver. Numerical simulations are given to demonstrate the validity of the theories and the chaotic secure communication scheme. Our future work is to apply the system to image encryption, random number generator, and other fields.



## Data Availability

The data used to support the findings of this study are included within the article.

## Conflicts of Interest

The authors declare that they have no conflicts of interest.

## Acknowledgments

This work was supported by the National Natural Science Foundation of China under Grant nos. 61504013, 61702052, 61772087, 61674054, and 61801054, Natural Science Foundation of Hunan Province under Grant nos. 2019JJ50648, 2016JJ2005, and 2017JJ2049, and Scientific Research Fund of Hunan Provincial Education Department under Grant no. 18A137.

## References

- [1] J. Jin, L. Zhao, M. Li, Z. Yu, and F. Xi, "Improved zeroing neural networks for finite time solving nonlinear equations," *Neural Computing and Applications*, 2009.
- [2] F. Yu, L. Liu, L. Xiao, K. Li, and S. Cai, "A robust and fixed-time zeroing neural dynamics for computing time-variant nonlinear equation using a novel nonlinear activation function," *Neurocomputing*, vol. 350, pp. 108–116, 2019.
- [3] L. Zhou, F. Tan, F. Yu, and W. Liu, "Cluster synchronization of two-layer nonlinearly coupled multiplex networks with multi-links and time-delays," *Neurocomputing*, vol. 359, pp. 264–275, 2019.
- [4] V.-T. Pham, S. Vaidyanathan, E. Tlelo-Cuautle, and T. Kapitaniak, "Memory circuit elements: complexity, complex systems, and applications," *Complexity*, vol. 2019, p. 4, 2019.
- [5] X. Zhang and C. Wang, "A novel multi-atttractor period multi-scroll chaotic integrated circuit based on CMOS wide adjustable CCCII," *IEEE Access*, vol. 7, no. 1, pp. 16336–16350, 2019.
- [6] J. Jie and L. V. Zhao, "Low voltage low power fully integrated chaos generator," *Journal of Circuits Systems & Computers*, vol. 27, no. 10, Article ID 1850155, 2018.
- [7] Q. Yin and C. Wang, "A new chaotic image encryption scheme using breadth-first search and dynamic diffusion," *International Journal of Bifurcation and Chaos*, vol. 28, no. 4, Article ID 1850047, 2018.
- [8] Y. Li, C. Wang, and H. Chen, "A hyper-chaos-based image encryption algorithm using pixel-level permutation and bit-level permutation," *Optics and Lasers in Engineering*, vol. 90, pp. 238–246, 2017.
- [9] G. Cheng, C. Wang, and H. Chen, "A novel color image encryption algorithm based on hyperchaotic system and permutation-diffusion architecture," *International Journal of Bifurcation and Chaos*, vol. 29, no. 9, Article ID 1950115, 2019.
- [10] X. Yang, Q. Zhu, and C. Huang, "Lag stochastic synchronization of chaotic mixed time-delayed neural networks with uncertain parameters or perturbations," *Neurocomputing*, vol. 74, no. 10, pp. 1617–1640, 2017.
- [11] B. Vaseghi, M. A. Pourmina, and S. Mobayen, "Finite-time chaos synchronization and its application in wireless sensor networks," *Transactions of the Institute of Measurement and Control*, vol. 40, no. 13, pp. 3788–3799, 2017.
- [12] F. Yu, L. Li, B. He et al., "Design and FPGA implementation of a pseudorandom number generator based on a four-wing memristive hyperchaotic system and Bernoulli map," *IEEE Access*, vol. 7, pp. 181884–181898, 2019.
- [13] F. Yu, L. Li, Q. Tang, S. Cai, Y. Song, and Q. Xu, "A survey on true random number generators based on chaos," *Discrete Dynamics in Nature and Society*, vol. 2019, Article ID 2545123, 2019.
- [14] L. L. Zhou, F. Tan, and F. Yu, "A robust synchronization-based chaotic secure communication scheme with double-layered and multiple hybrid networks," *IEEE Systems Journal*, 2019.
- [15] L. Zhou and F. Tan, "A chaotic secure communication scheme based on synchronization of double-layered and multiple complex networks," *Nonlinear Dynamics*, vol. 96, no. 2, pp. 869–883, 2019.
- [16] B. Vaseghi, M. A. Pourmina, and S. Mobayen, "Secure communication in wireless sensor networks based on chaos synchronization using adaptive sliding mode control," *Nonlinear Dynamics*, vol. 89, no. 3, pp. 1689–1704, 2017.
- [17] X. Zhang, C. Wang, W. Yao, and H. Lin, "Chaotic system with bondorbital attractors," *Nonlinear Dynamics*, vol. 97, no. 4, pp. 2159–2174, 2019.
- [18] M. Saleh, C. K. Volos, K. Sezgin, Ü. Çavuşoğlu, and B. Vaseghi, "A chaotic system with infinite number of equilibria located on an exponential curve and its chaos-based engineering application," *International Journal of Bifurcation and Chaos*, vol. 28, no. 9, Article ID 1850112, 2018.
- [19] F. Yu, L. Gao, K. Gu, B. Yin, Q. Wan, and Z. Zhou, "A fully qualified four-wing four-dimensional autonomous chaotic system and its synchronization," *Optik*, vol. 131, pp. 79–88, 2017.
- [20] C. Volos, J.-O. Maaita, S. Vaidyanathan, V.-T. Pham, I. Stouboulos, and I. Kyprianidis, "A novel four-dimensional hyperchaotic four-wing system with a saddle-focus equilibrium," *IEEE Transactions on Circuits and Systems II: Express Briefs*, vol. 64, no. 3, pp. 339–343, 2017.
- [21] F. Yu, C.-H. Wang, J.-W. Yin, and H. Xu, "Novel four-dimensional autonomous chaotic system generating one-, two-, three- and four-wing attractors," *Chinese Physics B*, vol. 20, no. 11, Article ID 110505, 2011.
- [22] X. Zhou, C. H. Wang, and X. R. Guo, "A new grid multi-wing chaotic system and its circuit implementation," *Acta Physica Sinica*, vol. 61, no. 20, Article ID 200506, 2012.
- [23] L. Zhou, C. Wang, and L. Zhou, "Generating hyperchaotic multi-wing attractor in a 4D memristive circuit," *Nonlinear Dynamics*, vol. 85, no. 4, pp. 2653–2663, 2016.
- [24] X. Luo, C. Wang, and Z. Wan, "Grid multi-wing butterfly chaotic attractors generated from a new 3-D quadratic autonomous system," *Nonlinear Analysis: Modelling and Control*, vol. 19, no. 2, pp. 272–285, 2014.
- [25] F. Yu, P. Li, K. Gu, and B. Yin, "Research progress of multi-scroll chaotic oscillators based on current-mode devices," *Optik*, vol. 127, no. 13, pp. 5486–5490, 2016.
- [26] Q. Deng and C. Wang, "Multi-scroll hidden attractors with two stable equilibrium points," *Chaos: An Interdisciplinary Journal of Nonlinear Science*, vol. 29, no. 9, Article ID 093112, 2019.
- [27] X. Zhang and C. Wang, "Multiscroll hyperchaotic system with hidden attractors and its circuit implementation," *International Journal of Bifurcation and Chaos*, vol. 29, no. 9, Article ID 1950117, 2019.
- [28] J. Jin, "Programmable multi-direction fully integrated chaotic oscillator," *Microelectronics Journal*, vol. 75, pp. 27–34, 2018.



- [29] J. Jin and L. Cui, "Fully integrated memristor and its application on the scroll-controllable hyperchaotic system," *Complexity*, vol. 2019, p. 8, 2019.
- [30] F. Yu, L. Liu, B. He et al., "Analysis and FPGA realization of a novel 5D hyperchaotic four-wing memristive system, active control synchronization and secure communication application," *Complexity*, vol. 2019, p. 18, 2019.
- [31] V.-T. Pham, S. Vaidyanathan, C. Volos, S. Jafari, and S. T. Kingni, "A no-equilibrium hyperchaotic system with a cubic nonlinear term," *Optik*, vol. 127, no. 6, pp. 3259–3265, 2016.
- [32] P. Daltzis, S. Vaidyanathan, V. T. Pham, C. Volos, E. Nistazakis, and G. Tombras, "Hyperchaotic attractor in a novel hyperjerk system with two nonlinearities," *Circuits, Systems, and Signal Processing*, vol. 37, no. 2, pp. 613–635, 2018.
- [33] V.-T. Pham, F. Rahma, M. Frasca, and L. Fortuna, "Dynamics and synchronization of a novel hyperchaotic system without equilibrium," *International Journal of Bifurcation and Chaos*, vol. 24, no. 6, Article ID 1450087, 2014.
- [34] C. H. Wang, H. Xia, and L. Zhou, "Implementation of a new memristor-based multiscroll hyperchaotic system," *Pramana-Journal of Physics*, vol. 88, no. 2, p. 34, 2017.
- [35] H. Lin and C. Wang, "Influences of electromagnetic radiation distribution on chaotic dynamics of a neural network," *Applied Mathematics and Computation*, vol. 369, Article ID 124840, 2020.
- [36] C. Wang, L. Xiong, J. Sun, and W. Yao, "Memristor-based neural networks with weight simultaneous perturbation training," *Nonlinear Dynamics*, vol. 95, no. 4, pp. 2893–2906, 2019.
- [37] Q. Zhao, C. Wang, and X. Zhang, "A universal emulator for memristor, memcapacitor, and meminductor and its chaotic circuit," *Chaos*, vol. 29, no. 1, Article ID 013141, 2019.
- [38] W. Yao, C. Wang, J. Cao, Y. Sun, and C. Zhou, "Hybrid multisynchronization of coupled multistable memristive neural networks with time delays," *Neurocomputing*, vol. 363, pp. 281–294, 2019.
- [39] L. Zhou, C. Wang, and L. Zhou, "A novel no-equilibrium hyperchaotic multi-wing system via introducing memristor," *International Journal of Circuit Theory and Applications*, vol. 46, no. 1, pp. 84–98, 2018.
- [40] C. Wang, L. Zhou, and R. Wu, "The design and realization of a hyper-chaotic circuit based on a flux-controlled memristor with linear memductance," *Journal of Circuits, Systems and Computers*, vol. 27, no. 3, Article ID 1850038, 2018.
- [41] E. Dong, M. Yuan, S. Du, and Z. Chen, "A new class of Hamiltonian conservative chaotic systems with multistability and design of pseudo-random number generator," *Applied Mathematical Modelling*, vol. 73, pp. 40–71, 2019.
- [42] V. Sundarapandian, J. Sajad, and V. T. Pham, "A 4-D chaotic hyperjerk system with a hidden attractor, adaptive backstepping control and circuit design," *Archives of Control Sciences*, vol. 28, no. 2, pp. 239–254, 2018.
- [43] V.-T. Pham, S. Jafari, C. Volos, and T. Kapitaniak, "Different families of hidden attractors in a new chaotic system with variable equilibrium," *International Journal of Bifurcation and Chaos*, vol. 27, no. 9, Article ID 1750138, 2017.
- [44] V.-T. Pham, C. Volos, S. Jafari, and T. Kapitaniak, "A novel cubic-equilibrium chaotic system with coexisting hidden attractors: analysis, and circuit implementation," *Journal of Circuits, Systems and Computers*, vol. 27, no. 4, Article ID 1850066, 2018.
- [45] V. T. Pham, C. Volos, S. T. Kingni, T. Kapitaniak, and S. Jafari, "Bistable hidden attractors in a novel chaotic system with hyperbolic sine equilibrium," *Circuits Systems and Signal Processing*, vol. 37, no. 19, pp. 1028–1043, 2017.
- [46] V.-T. Pham, X. Wang, S. Jafari, C. Volos, and T. Kapitaniak, "From wang-chen system with only one stable equilibrium to a new chaotic system without equilibrium," *International Journal of Bifurcation and Chaos*, vol. 27, no. 6, Article ID 1750097, 2017.
- [47] Z. Wang, H. R. Abdolmohammadi, F. E. Alsaadi, T. Hayat, and V.-T. Pham, "A new oscillator with infinite coexisting asymmetric attractors," *Chaos, Solitons & Fractals*, vol. 110, pp. 252–258, 2018.
- [48] V. T. Pham, S. Jafari, C. Volos, and T. Kapitaniak, "A gallery of chaotic systems with an infinite number of equilibrium points," *Chaos, Solitons & Fractals*, vol. 93, pp. 58–63, 2016.
- [49] V. T. Pham, S. Jafari, C. Volos, T. Gotthans, X. Wang, and D. V. Hoang, "A chaotic system with rounded square equilibrium and with no-equilibrium," *Optik*, vol. 130, pp. 365–371, 2016.
- [50] V.-T. Pham, S. Jafari, X. Wang, and J. Ma, "A chaotic system with different shapes of equilibria," *International Journal of Bifurcation and Chaos*, vol. 26, no. 4, Article ID 1650069, 2016.
- [51] L. Zhou, C. Wang, X. Zhang, and W. Yao, "Various attractors, coexisting attractors and antimonotonicity in a simple fourth-order memristive twin- $T$  oscillator," *International Journal of Bifurcation and Chaos*, vol. 28, no. 4, Article ID 1850050, 2018.
- [52] B. A. Mezatio, M. T. Motchongom, B. R. Wafo Tekam, R. Kengne, R. Tchitnga, and A. Fomethe, "A novel memristive 6D hyperchaotic autonomous system with hidden extreme multistability," *Chaos, Solitons & Fractals*, vol. 120, pp. 100–115, 2019.
- [53] A. Bayani, K. Rajagopal, A. J. M. Khalaf, S. Jafari, G. D. Leutcho, and J. Kengne, "Dynamical analysis of a new multistable chaotic system with hidden attractor: antimonotonicity, coexisting multiple attractors, and offset boosting," *Physics Letters A*, vol. 383, no. 13, pp. 1450–1456, 2019.
- [54] K. Xie, X. Ning, X. Wang et al., "An efficient privacy-preserving compressive data gathering scheme in WSNs," *Information Sciences*, vol. 390, no. 2, pp. 702–715, 2016.
- [55] K. Gu, W. Jia, G. Wang, and S. Wen, "Efficient and secure attribute-based signature for monotone predicates," *Acta Informatica*, vol. 54, no. 5, pp. 521–541, 2017.
- [56] M. Long, F. Peng, and H.-Y. Li, "Separable reversible data hiding and encryption for HEVC video," *Journal of Real-Time Image Processing*, vol. 14, no. 1, pp. 171–182, 2018.
- [57] K. Gu, N. Wu, B. Yin, and W. Jia, "Secure data sequence query framework based on multiple fogs," *IEEE Transactions on Emerging Topics in Computing*, 2019.
- [58] K. Gu, X. Dong, and L. Wang, "Efficient traceable ring signature scheme without pairings," *Advances in Mathematics of Communications*, 2019.
- [59] S. He, W. Zeng, K. Xie et al., "PPNC: privacy preserving scheme for random linear network coding in smart grid," *KSII Transactions on Internet and Information Systems*, vol. 11, pp. 1510–1533, 2017.
- [60] Z. Xia, Z. Fang, F. Zou, J. Wang, and A. K. Sangaiah, "Research on defensive strategy of real-time price attack based on multiperson zero-determinant," *Security and Communication Networks*, vol. 2019, p. 13, 2019.
- [61] K. Gu, K. M. Wang, and L. Yang, "Traceable attribute-based signature," *Journal of Information Security and Applications*, vol. 49, pp. 1–16, 2019.

- [62] M. Long, F. Peng, and Y. Zhu, "Identifying natural images and computer generated graphics based on binary similarity measures of PRNU," *Multimedia Tools and Applications*, vol. 78, pp. 489–506, 2019.
- [63] K. Gu, N. Wu, B. Yin, and W. Jia, "Secure data query framework for cloud and fog computing," *IEEE Transactions on Network and Service Management*, 2019.
- [64] J.-L. Zhang, W.-Z. Wang, X.-W. Wang, and Z.-H. Xia, "Enhancing security of FPGA-based embedded systems with combinational logic binding," *Journal of Computer Science and Technology*, vol. 32, no. 2, pp. 329–339, 2017.
- [65] K. Gu, W. Jia, and C. Jiang, "Efficient identity-based proxy signature in the standard model," *The Computer Journal*, vol. 58, no. 4, pp. 792–807, 2015.
- [66] L. Xiang, G. Guo, J. Yu, V. S. Sheng, and P. Yang, "A convolutional neural network-based linguistic steganalysis for synonym substitution steganography," *Mathematical Biosciences and Engineering*, vol. 17, no. 2, pp. 1041–1058, 2020.
- [67] Y.-Y. Huang, Y.-H. Wang, and Y. Zhang, "Shape synchronization of drive-response for a class of two-dimensional chaotic systems via continuous controllers," *Nonlinear Dynamics*, vol. 78, no. 4, pp. 2331–2340, 2014.
- [68] Y. Huang, Y. Wang, H. Chen, and S. Zhang, "Shape synchronization control for three-dimensional chaotic systems," *Chaos, Solitons & Fractals*, vol. 87, pp. 136–145, 2016.
- [69] S. Çiçek, A. Ferikoğlu, and İ. Pehlivan, "A new 3D chaotic system: dynamical analysis, electronic circuit design, active control synchronization and chaotic masking communication application," *Optik*, vol. 127, no. 8, pp. 4024–4030, 2016.
- [70] J. M. V. Grzybowski, M. Rafikov, and J. M. Balthazar, "Synchronization of the unified chaotic system and application in secure communication," *Communications in Nonlinear Science and Numerical Simulation*, vol. 14, no. 6, pp. 2793–2806, 2009.
- [71] J. He and J. Cai, "Parameter modulation for secure communication via the synchronization of Chen hyperchaotic systems," *Systems Science & Control Engineering*, vol. 2, no. 1, pp. 718–726, 2014.
- [72] F. Yu and C. Wang, "Secure communication based on a four-wing chaotic system subject to disturbance inputs," *Optik*, vol. 125, no. 20, pp. 5920–5925, 2014.
- [73] J. L. Mata-Machuca, R. Martínez-Guerra, R. Aguilar-López, and C. Aguilar-Ibañez, "A chaotic system in synchronization and secure communications," *Communications in Nonlinear Science and Numerical Simulation*, vol. 17, no. 4, pp. 1706–1713, 2012.
- [74] A. Prasad, "Existence of perpetual points in nonlinear dynamical systems and its applications," *International Journal of Bifurcation and Chaos*, vol. 25, no. 2, Article ID 1530005, 2015.
- [75] D. Dudkowski, A. Prasad, and T. Kapitaniak, "Perpetual points and hidden attractors in dynamical systems," *Physics Letters A*, vol. 379, no. 40–41, pp. 2591–2596, 2015.
- [76] D. Dudkowski, A. Prasad, and T. Kapitaniak, "Describing chaotic attractors: regular and perpetual points," *Chaos*, vol. 28, no. 3, Article ID 033604, 2018.
- [77] S. He, K. Sun, and H. Wang, "Complexity analysis and DSP implementation of the fractional-order Lorenz hyperchaotic system," *Entropy*, vol. 17, no. 12, pp. 8299–8311, 2015.
- [78] S. He, K. Sun, and S. Banerjee, "Dynamical properties and complexity in fractional-order diffusionless Lorenz system," *European Physical Journal Plus*, vol. 131, p. 254, 2016.
- [79] S. He, K. Sun, X. Mei, B. Yan, and S. Xu, "Numerical analysis of fractional-order chaotic system based on conformable fractional-order derivative," *European Physical Journal Plus*, vol. 132, p. 36, 2017.
- [80] B. C. Bao, H. Bao, N. Wang, M. Chen, and Q. Xu, "Hidden extreme multistability in memristive hyperchaotic system," *Chaos, Solitons & Fractals*, vol. 94, pp. 102–111, 2017.
- [81] S. Laghrouche, F. Plestan, and A. Glumineau, "Higher order sliding mode control based on integral sliding mode," *Automatica*, vol. 43, no. 3, pp. 531–537, 2007.
- [82] A. Levant, "Homogeneity approach to high-order sliding mode design," *Automatica*, vol. 41, no. 5, pp. 823–830, 2005.

## Research Article

# Investigations of Nonlinear Triopoly Models with Different Mechanisms

S. S. Askar <sup>1,2</sup> and A. Al-khedhairi <sup>1</sup>

<sup>1</sup>Department of Statistics and Operations Researches, College of Science, King Saud University, P.O. Box 2455, Riyadh 11451, Saudi Arabia

<sup>2</sup>Department of Mathematics, Faculty of Science, Mansoura University, Mansoura 35516, Egypt

Correspondence should be addressed to S. S. Askar; [s.e.a.askar@hotmail.co.uk](mailto:s.e.a.askar@hotmail.co.uk)

Received 5 September 2019; Accepted 21 November 2019; Published 19 December 2019

Guest Editor: Viet-Thanh Pham

Copyright © 2019 S. S. Askar and A. Al-khedhairi. This is an open access article distributed under the Creative Commons Attribution License, which permits unrestricted use, distribution, and reproduction in any medium, provided the original work is properly cited.

This paper studies the dynamic characteristics of triopoly models that are constructed based on a 3-dimensional Cobb–Douglas utility function. The paper presents two parts. The first part introduces a competition among three rational firms on which their prices are isoelastic functions. The competition is described by a 3-dimensional discrete dynamical system. We examine the impact of rationality on the system's steady state point. Studying the stability/instability of this point, which is Nash equilibrium and is unique in those models, is illustrated. Numerically, we give some global analysis of Nash point and its stability. The second part deals with heterogeneous scenarios. It consists of two different models. In the first model, we assume that one competitor adopts the local monopolistic approximation mechanism (LMA) while the other opponents are rational. The second model assumes two heterogeneous players with LMA mechanism against one rational firm. Studies show that the stability of NE point of those models is not guaranteed. Furthermore, simulation shows that when firms behave rational with symmetric costs, the stability of NE point is achievable.

## 1. Introduction

Oligopolistic competition in economic market structure has got much attention recently. It is more complex and perfect competition when one compares it with the monopolistic one. When tackling this kind of competition, a wide range of different outcomes can arise, and therefore it is reasonable to use the theory of game. Game theory has been used heavily to model the behavior of such oligopolistic competitors.

Fully rational firms involved in oligopolistic competition are provided with cognitive and computational skills so that they can perfectly identify the demand curve of produced commodity, and therefore, the expectation of their competitors' production in the next period is achieved. Knowing such skills makes firms ready to solve a one period optimization problem. Recent works [1–6] have investigated the influence of reducing rationality in terms of computational and informational capabilities. Those works have yielded an

important conclusion; that is, reducing such rationality leads to the appearance of complex dynamic characteristics of firms' behaviors. In [1], some triopolistic games have been introduced and studied using quasiconcave utility function. The complex behavior of a Cournot duopoly game has been investigated in [2]. Using heterogeneous expectations, a nonlinear duopoly game has been introduced and discussed in [4]. Askar et al. [5] have studied the dynamic characteristics of Cournot duopoly models based on unknown inverse demand function. With nonlinear demand function, whose inflection points do not exist, Askar has proposed and investigated the complex dynamic behavior of a Cournot duopoly game.

Puu [7] has constructed a duopolistic model on which he has used a unimodal reaction function accompanying Cobb–Douglas consumer's preferences. Studies carried out by Puu have shown that the firms' outputs are evolved through a chaotic scenario which in turn leads to chaos.

Since Puu's work, several studies have made by researchers to look into different decisional and adjustment mechanisms such as bounded rationality and LMA (local monopolistic approximation) mechanisms. The bounded rationality mechanism requires from the competitors some local knowledge in order to improve their outputs according to the variations in the marginal profit. Indeed, this mechanism makes the competitors unaware of any information or knowledge about the demand and cost functions. Only the competitors need to be aware of any change that occurs in market due to small changes in the produced quantities by estimating the marginal profit. For more details about this mechanism, readers are advised to refer to the literature [4, 8, 9]. The LMA mechanism was first introduced by Tuinstra [10]. Oligopolistic players adopting the LMA mechanism do not have any information or knowledge about the demand function of the market. Even though it is unknown for the competitors, they conjecture it in linear. Therefore, with local knowledge about the true demand curve and the current market state in terms of quantities produced and their prices, they estimate this linear function.

The literature has reported several works that have adopted such rationality and LMA mechanisms. For instance, Pecora and Sodini have analyzed a Cournot duopoly game whose demand function was isoelastic in continuous time periods [11]. In [12], the LMA and the gradient rule have been used to analyze the complex dynamic behavior of a duopoly model. A discrete duopolistic fishery model with two agents who adopt heterogeneous expectations has been investigated in [13]. Both the monopolistic approximation and the gradient approach have been used in [14] to study an evolutionary oligopoly competition. For more related works and simulation approaches, readers are advised to refer to [15, 16].

The current paper discusses the influences of some adjustment mechanisms on the stability of Nash equilibrium point. Here, we propose and investigate different types of triopoly games on which firms use bounded rationality and LMA mechanisms. Our obtained results show that the repeated triopoly game based on rationality mechanism converges at Nash point and implies more stability region. On the other two games where LMA mechanism is adopted by competed firms, the results show that the repeated games based on that mechanism or based on a mixed type of both rationality and LMA do not converge at Nash point due to the complicated behaviors of systems described those games and due to the negative quantities obtained which have no meaning in economic market.

Briefly, the current paper is described as follows. In Section 2, we introduce the Cobb–Douglas production function for three oligopolistic firms. After that, the first scenario of a rational game is constructed, and then an investigation on its complex dynamic characteristics is presented. After that, a heterogeneous game is introduced and studied in details. Finally, conclusion is provided in Section 3.

## 2. Model

In 1927, the first formulation of Cobb–Douglas function was described. In that time, Douglas sought for a functional form

by which he could use to present the data he calculated for workers and capital. Economists today widely use this production function to study the relationship between the amount of two or more inputs and the amount of outputs that can be produced by those inputs. The current paper assumes that the market structure consists of three firms whose preferences are derived from Cobb–Douglas. It takes the following form:

$$U = \prod_{i=1}^3 q_i^{\alpha_i}, \sum_{i=1}^3 \alpha_i = 1. \quad (1)$$

Indeed, firms want to maximize their preferences due to a budget constraint  $\sum_{i=1}^3 p_i q_i = 1$ , where  $p_i$ ,  $i = 1, 2, 3$  is a commodity price supplied by firm  $i$ . According to this constraint, the following maximization problem is constructed:

$$\begin{aligned} \text{Max } & \sum_{i=1}^3 \alpha_i \log q_i \\ & \sum_{i=1}^3 p_i q_i = 1. \end{aligned} \quad (2)$$

Equation (2) has the following solution:

$$q_j = \frac{\alpha_j}{p_j}, \quad j = 1, 2, 3. \quad (3)$$

If we sum the above for all firms, we get

$$p(Q) = \frac{1}{Q}, \quad (4)$$

$$Q = \sum_{i=1}^3 q_i.$$

This kind of demand is called an isoelastic function. Now, we suppose that the firms' costs are

$$C_i(q_i) = c_i q_i, \quad i = 1, 2, 3, \quad (5)$$

where  $c_i > 0$  is a constant marginal cost for each firm. Using (4) and (5), each firm has its own profit as follows:

$$\begin{aligned} \pi_1 &= \frac{q_1}{q_1 + q_2 + q_3} - c_1 q_1, \\ \pi_2 &= \frac{q_2}{q_1 + q_2 + q_3} - c_2 q_2, \\ \pi_3 &= \frac{q_3}{q_1 + q_2 + q_3} - c_3 q_3. \end{aligned} \quad (6)$$

Game theory can be used to study the above scenario on which the firms are three oligopolists. The game feasible space will be constructed with all strategies  $q_i > 0$ ,  $i = 1, 2, 3$  and the payoff functions that are given in (6). Only one Nash equilibrium point for this game is given by



$$\begin{aligned} \text{NE} &= (\bar{q}_1, \bar{q}_2, \bar{q}_3) \\ &= \left( \frac{2(c_2 + c_3 - c_1)}{(c_1 + c_2 + c_3)^2}, \frac{2(c_1 + c_3 - c_2)}{(c_1 + c_2 + c_3)^2}, \frac{2(c_1 + c_2 - c_3)}{(c_1 + c_2 + c_3)^2} \right). \end{aligned} \quad (7)$$

It is positive under the conditions  $c_2 + c_3 > c_1$ ,  $c_1 + c_3 > c_2$  and  $c_1 + c_2 > c_3$ . In an oligopolistic competition, information that should be available for each player about its opponent is important and limited. The gradient mechanism which is important and intensively used in literature is a rule of thumb. It requires only local knowledge about the player's marginal profit. It depends on some thoughts each player should know about variations in the amount  $q_{i,t+1} - q_{i,t}$  that in turn gives exact estimation of the marginal profit  $\partial\pi_i/\partial q_{i,t}$ . Firms in such competition are always seeking for a good estimation of the current marginal profit in order to see whether it increases or decreases its output level depending on the information given by the marginal profit in the previous time step. This is governed by a positive parameter called the speed of adjustment. The mechanism is described by the following discrete map:

$$q_{i,t+1} = q_{i,t} + k_i \phi_i, \quad i = 1, 2, 3, \quad (8)$$

where,  $k_i > 0$  is the speed of adjustment and  $\phi_i = \partial\pi_i/\partial q_{i,t}$ . Here, we study two different scenarios: the first scenario assumes that the three oligopolistic firms adopt this mechanism, while in the other we suppose that one of the firms adopts the so-called Local Monopolistic Approximation (LMA) that is described later. Let us now construct the

first scenario. Using (6), the marginal profit of each firm is given by

$$\phi_i = \frac{Q - q_i}{Q^2} - c_i, \quad i = 1, 2, 3. \quad (9)$$

Substituting (9) in (8), the resulting oligopolistic game is presented by the following discrete dynamical system:

$$\begin{aligned} q_{1,t+1} &= q_{1,t} + k \left[ \frac{Q - q_1}{Q^2} - c_1 \right], \\ q_{2,t+1} &= q_{2,t} + k \left[ \frac{Q - q_2}{Q^2} - c_2 \right], \\ q_{3,t+1} &= q_{3,t} + k \left[ \frac{Q - q_3}{Q^2} - c_3 \right]. \end{aligned} \quad (10)$$

*2.1. Local Analysis.* This subsection provides a discussion on the steady state of the game and the local stability of system (10). We investigate under what conditions should system (10) be stable and where complex dynamic can influence the stabilization of the steady states. The following proposition is given.

*Proposition 1.* The Nash equilibrium (7) is a steady state of the system (10) and is locally asymptotically stable provided that  $k < (4/(c_1 + c_2 + c_3))^2$ .

*Proof.* System (10) at NE point has the following Jacobian matrix:

$$J = \begin{bmatrix} 1 - c_1 k (c_1 + c_2 + c_3) & \frac{-k}{4} (c_1 + c_2 + c_3) (3c_1 - c_2 - c_3) & \frac{-k}{4} (c_1 + c_2 + c_3) (3c_1 - c_2 - c_3) \\ \frac{-k}{4} (c_1 + c_2 + c_3) (3c_2 - c_1 - c_3) & 1 - c_2 k (c_1 + c_2 + c_3) & \frac{-k}{4} (c_1 + c_2 + c_3) (3c_2 - c_1 - c_3) \\ \frac{-k}{4} (c_1 + c_2 + c_3) (3c_3 - c_1 - c_2) & \frac{-k}{4} (c_1 + c_2 + c_3) (3c_3 - c_1 - c_2) & 1 - c_3 k (c_1 + c_2 + c_3) \end{bmatrix}. \quad (11)$$

When games described are by discrete dynamic systems, then studying the stability of the NE point of those systems depends on the eigenvalues of the Jacobian matrix. This makes us to impose the condition  $|\lambda_i| < 1, i = 1, 2, 3$  that means that all the eigenvalues must be in the unit circle. This can be carried by recalling the following Jury conditions:

$$\begin{aligned} \text{(i): } & 1 + a_1 + a_2 + a_3 > 0, \\ \text{(ii): } & 1 - a_1 + a_2 - a_3 > 0, \\ \text{(iii): } & 1 + a_2 - a_1 a_3 - a_3^2 > 0, \\ \text{(iv): } & 1 - a_3^2 > 0, \end{aligned} \quad (12)$$

where  $f(\lambda) = \lambda^3 + a_1 \lambda^2 + a_2 \lambda + a_3$  is the characteristic polynomial of the above Jacobian and

$$\begin{aligned} a_1 &= -(\lambda_1 + \lambda_2 + \lambda_3) = -\text{Trace}(J), \\ a_2 &= \lambda_1 \lambda_2 + \lambda_1 \lambda_3 + \lambda_2 \lambda_3, \\ a_3 &= (-1)^3 \lambda_1 \lambda_2 \lambda_3 = -\text{Determinant}(J). \end{aligned} \quad (13)$$

From the above Jacobian and with simple calculations, we deduce

$$\begin{aligned}
a_1 &= -(3 - 2\ell), \\
a_2 &= \left(1 - \frac{1}{2}\ell\right)\left(3 - \frac{5}{2}\ell\right), \\
a_3 &= -(1 - \ell)\left(1 - \frac{1}{2}\ell\right)^2, \\
\ell &= \frac{1}{2}k(c_1 + c_2 + c_3)^2.
\end{aligned} \tag{14}$$

This makes Jury conditions become

$$\begin{aligned}
\text{(i): } & \frac{1}{4}\ell^3 > 0, \\
\text{(ii): } & \frac{1}{4}(2 - \ell)(4 - \ell)^2 > 0, \\
\text{(iii): } & \frac{1}{16}\ell(128 - 208\ell + 140\ell^2 - 49\ell^3 + 10\ell^4 - \ell^5) > 0, \\
\text{(iv): } & \frac{1}{16}\ell(8 - 5\ell + \ell^2)(8 - 8\ell + 5\ell^2 - \ell^3) > 0.
\end{aligned} \tag{15}$$

Simple calculations show that the first condition (i) is always fulfilled, the condition (ii) is fulfilled under  $0 < \ell < 2$  (this is equivalent  $k < (4/(c_1 + c_2 + c_3)^2)$ ), and the other two conditions hold providing that (ii) holds. The second condition (ii) becomes zero at  $\ell = 2$  or  $\ell = 4$  which means period-doubling bifurcation (flip bifurcation) may occurs. Furthermore, the condition (iv) can not be zero and hence Neimark–Sacker bifurcation does not exist for the system (10). In addition, one can easily get the eigenvalues as follows:

$$\begin{aligned}
\lambda_1 &= 1 - \frac{k}{2}(c_1 + c_2 + c_3)^2, \\
\lambda_{2,3} &= 1 - \frac{k}{4}(c_1 + c_2 + c_3)^2.
\end{aligned} \tag{16}$$

Those eigenvalues are real and  $|\lambda_i| < 1, i = 1, 2, 3$  if  $k < (4/(c_1 + c_2 + c_3)^2)$  which completes the proof.  $\square$

**2.2. Simulation.** In this section, we perform some numerical simulation to investigate the complex behavior of system (10). This includes the influences of the system's parameters on the stability of Nash point. We start our simulation by assuming the following parameter values:  $(q_{0,1}, q_{0,2}, q_{0,3}) = (0.11, 0.12, 0.13)$  and  $c_1 = 0.20, c_2 = 0.30$  and  $c_3 = 0.25$ . We assume different values for the firms' costs as we study first the asymmetric case. This makes Nash point equal  $(1.2444, 0.53333, 0.88889)$ . As shown in Figure 1(a) Nash point is asymptotically stable for any values for the parameter  $k$  till  $k$  approaches 7.11 on where birth of period 2-cycle arises. After that a period-doubling bifurcation (flip

bifurcation) exists. Only flip bifurcation exists in this case as we have only two different real eigenvalues. Here, we should highlight on the values of the costs' parameters that must be selected in such a way that the conditions  $c_2 + c_3 > c_1, c_1 + c_3 > c_2$  and  $c_1 + c_2 > c_3$  are satisfied and at the same time, positivity of the quantities is preserved. Those costs parameters have a great impact on the system behavior as shown in Figure 1(b). Simulation shows that choosing values for the costs' parameters above 0.25 preserves positivity of quantities but does not guarantee stability of NE point. Figures 2(a) and 2(b) show the influence of  $c_2$  and  $c_3$  on the behavior of system (10). Now, we investigate more the influence of the parameter  $k$  on the stability of Nash point. It is confirmed by simulation that when increasing  $k$  above 7.11, different types of period cycles are obtained. For example, when  $k = 8.85$  and the other parameter values are fixed, a birth of stable period 2-cycle is emerged. The time series for this cycle is given in Figure 3(a); besides that, we give the phase portrait of it in Figure 3(b). This means that the system (10) jumps to these two cycles and around the stable Nash point during the period of competition. Fixing the quantity produced by the third firm to 0.13, the size and shape of the period 2-cycle basin of attraction are depicted in Figure 4. The red color refers to the basin of attraction of Nash point while the blue one denotes the basin of attraction of the period 2-cycle.

Increasing the parameter  $k$  slightly to the value of 9, we get a stable period 4-cycle. However, those cycles are stable but one can observe that there are negative quantities which have no economic meaning. Figure 5(a) shows the phase portrait of this cycle. Figure 5(b) shows the basin of attraction of this cycle. The basin of attraction given in Figure 5(b) seems more complicated than that of the period 2-cycle. The gray color is for the Nash point which in this case includes negative values while the other colors are for the basin of attraction of the period 4-cycle. Furthermore, we increase the parameter  $k$  to the value of 9.33, and hence, we get a stable period 8-cycle. Figures 6(a) and 6(b) show the phase portrait and the basin of attraction of this cycle, respectively. This figure contains fractal structure with different colors that are embedded with the colors of the basin of attraction of period 8-cycle. The white color is for nonconvergent points.

Now, we end this section by studying the symmetric case. This case is obtained when we set  $c_1 = c_2 = c_3 = c$ . It makes Nash equilibrium point become  $NE = (2/9c, 2/9c, 2/9c)$ . One can easily prove that this point is locally stable if  $k < (4/9c^2)$ . Numerical simulation shows that NE point is locally stable for values of  $k$  less than 11.22. Therefore, an increase in  $k$  more than that value makes the Nash point unstable via period-doubling bifurcation which is given in Figure 7(a) (the corresponding maximum Lyapunov exponent is plotted in Figure 7(b)). Moreover, the coexistence of period 2-cycle is detected at those parameters and for value of  $k = 12$ . Figures 8(a) and 8(b) show this period with its time series. This makes us to investigate more to see whether there are more cycles.



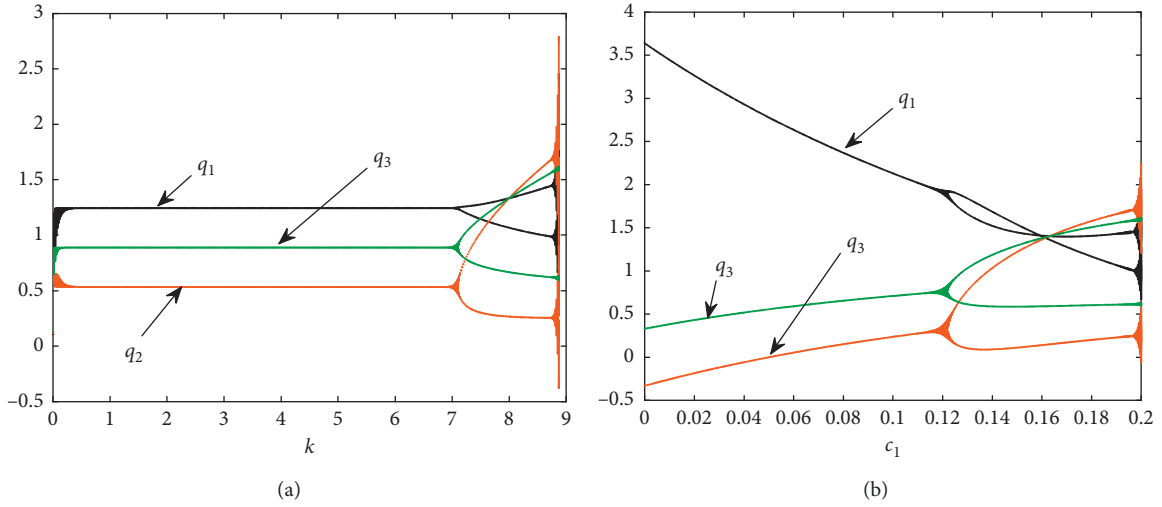


FIGURE 1: (a) Bifurcation diagram of system (10) with respect to  $k$  at  $(q_{0,1}, q_{0,2}, q_{0,3}) = (0.11, 0.12, 0.13)$ ,  $c_1 = 0.2, c_2 = 0.3, c_3 = 0.25$ . (b) Bifurcation diagram of system (10) with respect to  $c_1$  at  $(q_{0,1}, q_{0,2}, q_{0,3}) = (0.11, 0.12, 0.13)$ ,  $k = 8.85, c_2 = 0.3, c_3 = 0.25$ .

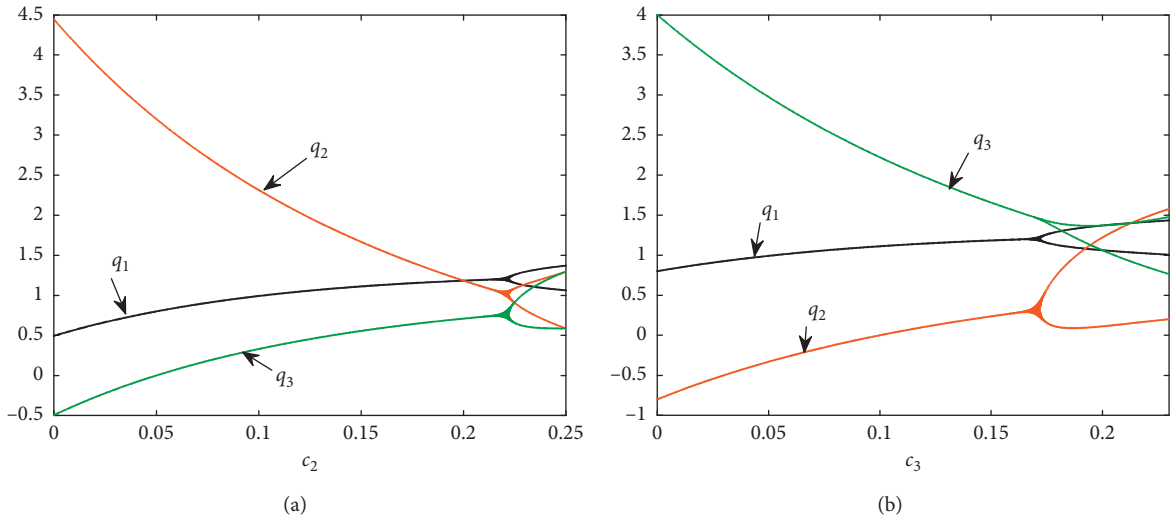


FIGURE 2: (a) Bifurcation diagram of system (10) with respect to  $c_2$  at  $(q_{0,1}, q_{0,2}, q_{0,3}) = (0.11, 0.12, 0.13)$ ,  $k = 8.85, c_1 = 0.2, c_3 = 0.25$ . (b) Bifurcation diagram of system (10) with respect to  $c_3$  at  $(q_{0,1}, q_{0,2}, q_{0,3}) = (0.11, 0.12, 0.13)$ ,  $k = 8.85, c_1 = 0.2, c_2 = 0.3$ .

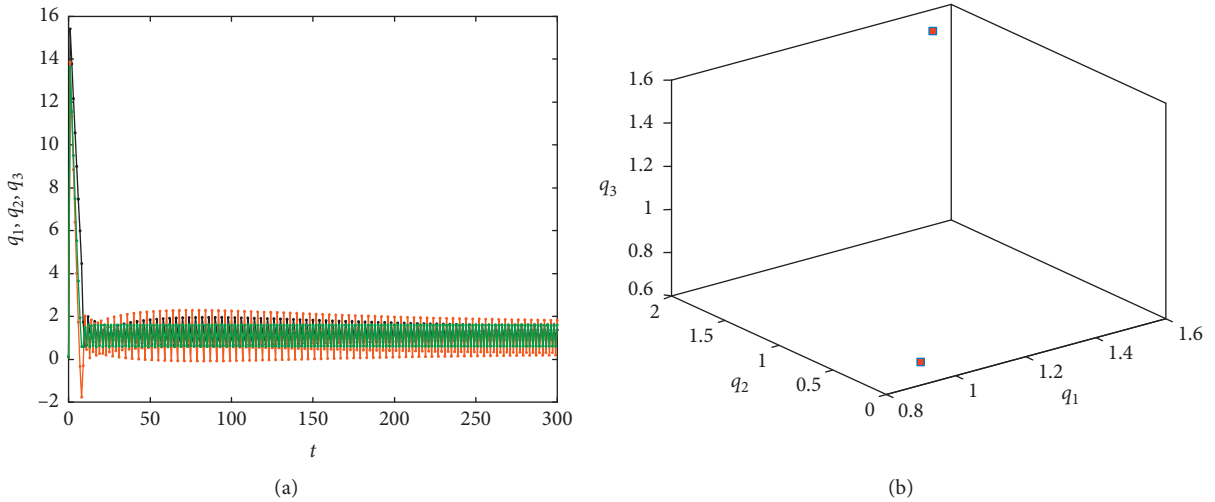


FIGURE 3: (a) Time series of system (10) at  $(q_{0,1}, q_{0,2}, q_{0,3}) = (0.11, 0.12, 0.13)$ ,  $k = 8.85, c_1 = 0.2, c_2 = 0.3, c_3 = 0.25$ . (b) Phase space of the period 2-cycle of system (10) with respect to  $c_3$  at  $(q_{0,1}, q_{0,2}, q_{0,3}) = (0.11, 0.12, 0.13)$ ,  $k = 8.85, c_1 = 0.2, c_2 = 0.3$ .

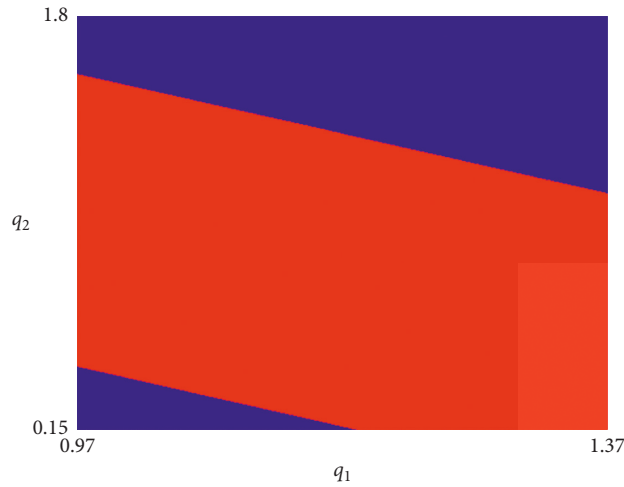


FIGURE 4: Basin of attraction of the period 2-cycle at  $q_{0,3} = 0.13, k = 8.85, c_1 = 0.2, c_2 = 0.3, c_3 = 0.25$ .

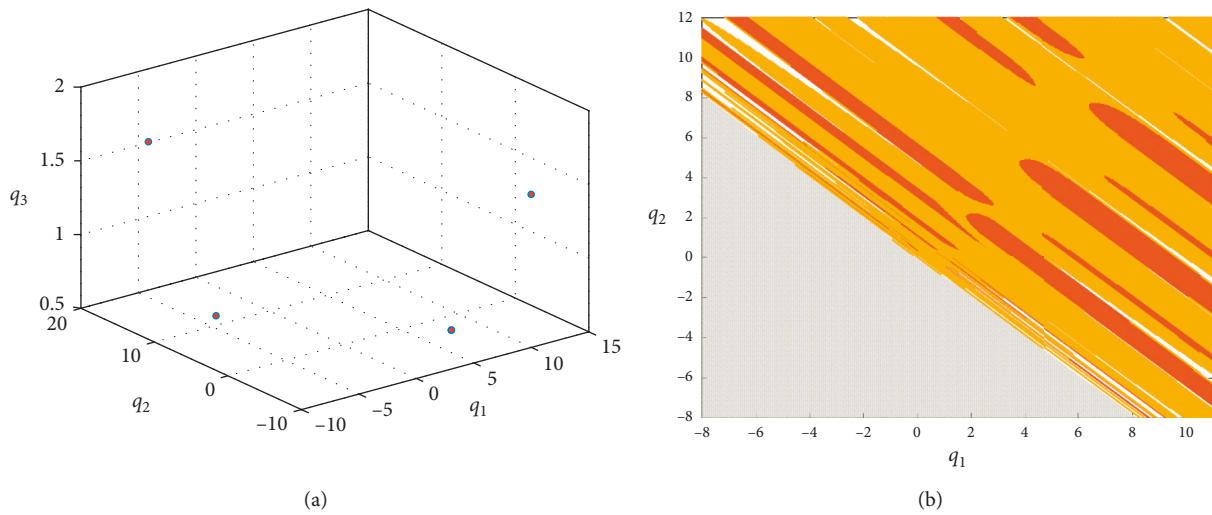


FIGURE 5: (a) Phase space of the period 4-cycle of system (10) at  $(q_{0,1}, q_{0,2}, q_{0,3}) = (0.11, 0.12, 0.13), k = 9, c_1 = 0.2, c_2 = 0.3, c_3 = 0.25$ . (b) Basin of attraction of the period 4-cycle at  $q_{0,3} = 0.13, k = 9, c_1 = 0.2, c_2 = 0.3, c_3 = 0.25$ .

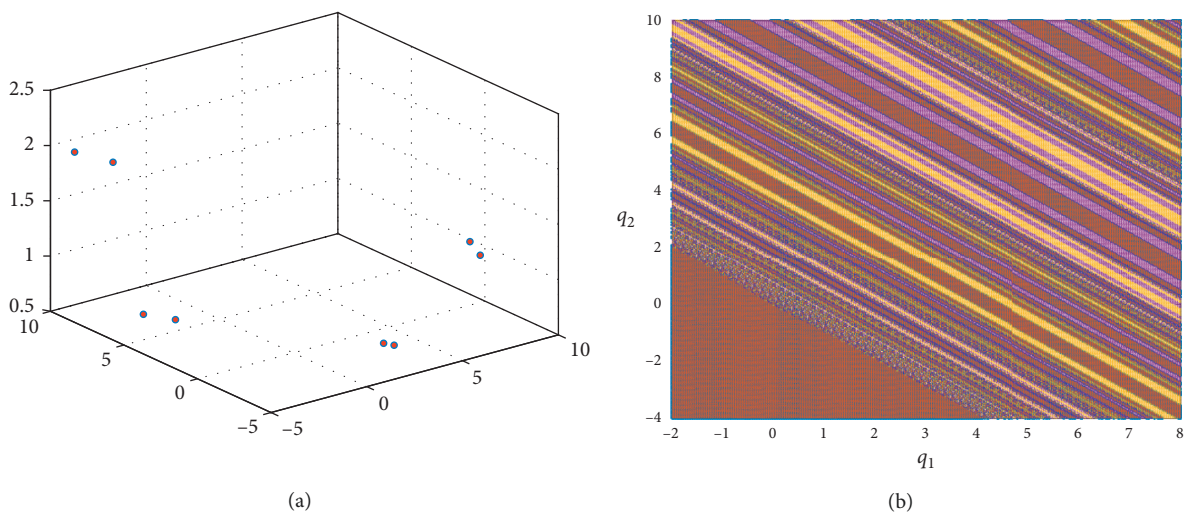


FIGURE 6: (a) Phase space of the period 8-cycle of system (10) at  $(q_{0,1}, q_{0,2}, q_{0,3}) = (0.11, 0.12, 0.13), k = 9.33, c_1 = 0.2, c_2 = 0.3, c_3 = 0.25$ . (b) Basin of attraction of the period 8-cycle at  $q_{0,3} = 0.13, k = 9.33, c_1 = 0.2, c_2 = 0.3, c_3 = 0.25$ .

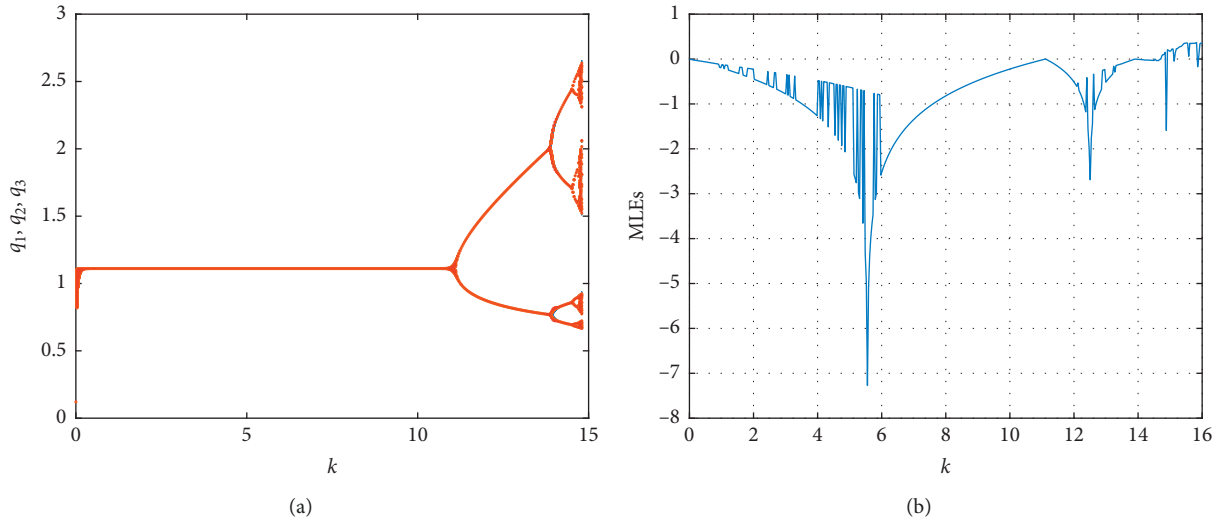


FIGURE 7: (a) Bifurcation diagram of system (10) with respect to  $k$  at  $(q_{0,1}, q_{0,2}, q_{0,3}) = (0.11, 0.12, 0.13)$ ,  $c = 0.2$ . (b) Lyapunov exponents with respect to  $k$  at  $(q_{0,1}, q_{0,2}, q_{0,3}) = (0.11, 0.12, 0.13)$ ,  $c = 0.2$ .

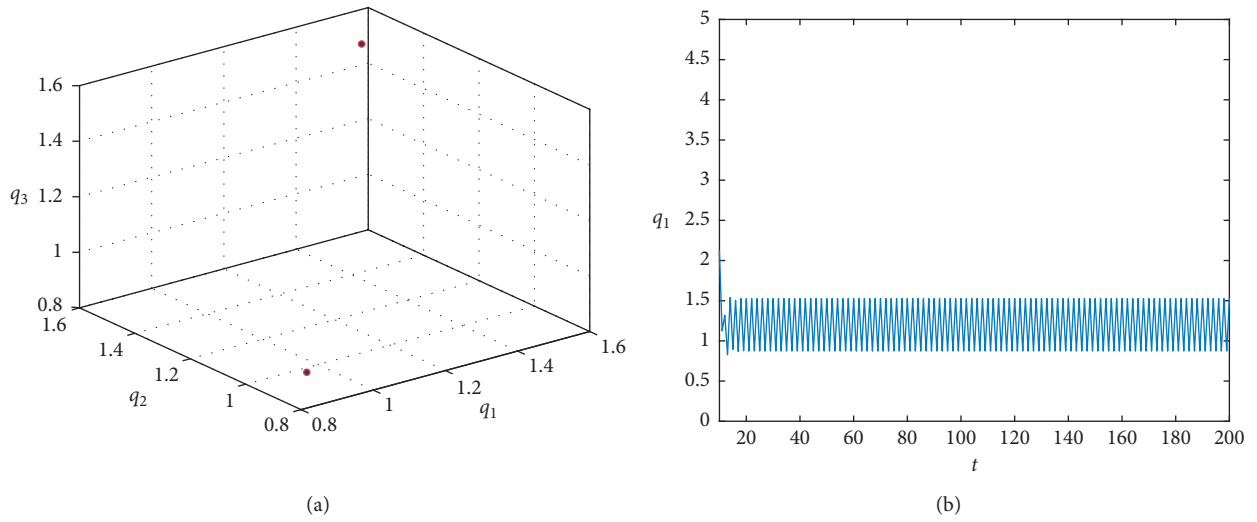


FIGURE 8: (a) Phase space of the period 2-cycle of system (10) at  $(q_{0,1}, q_{0,2}, q_{0,3}) = (0.11, 0.12, 0.13)$ ,  $k = 12$ ,  $c = 0.25$ . (b) Time series for  $q_1$  at  $k = 12$ ,  $c = 0.2$ .

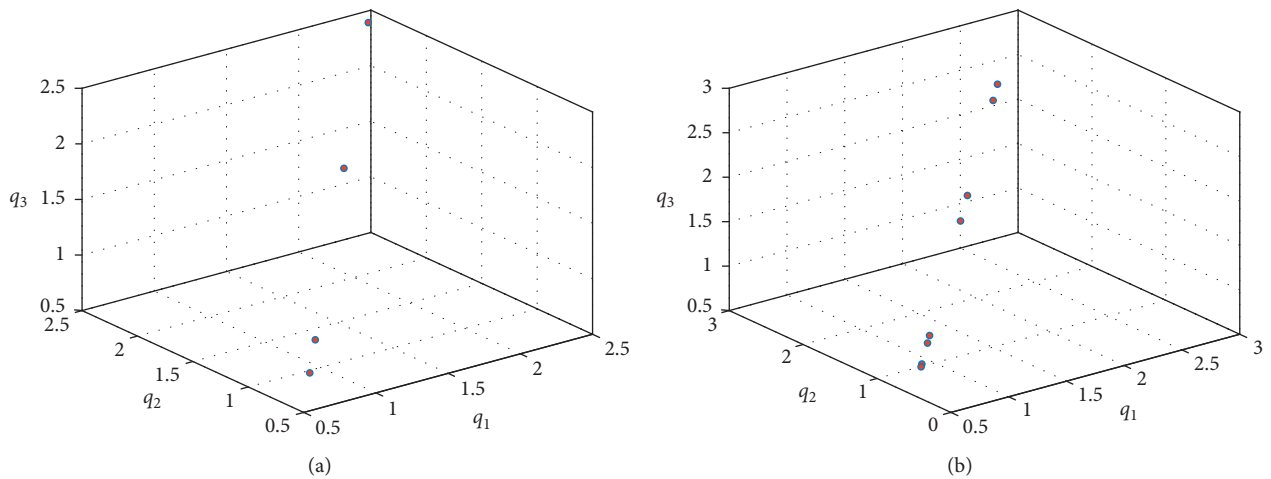


FIGURE 9: (a) Phase space of the period 4-cycle of system (10) at  $(q_{0,1}, q_{0,2}, q_{0,3}) = (0.11, 0.12, 0.13)$ ,  $k = 14.4$ ,  $c = 0.25$ . (b) Phase space of the period 8-cycle of system (10) at  $(q_{0,1}, q_{0,2}, q_{0,3}) = (0.11, 0.12, 0.13)$ ,  $k = 14.6$ ,  $c = 0.2$ .

Figures 9(a) and 9(b) present the phase portrait of period 4-cycle and period 8-cycle at  $k = 14.4$  and  $k = 14.6$  respectively. We give the basin of attraction of period 8-cycle that is described by two colors in Figure 10. We conclude based on these obtained results that this case is better than the previous case and the region of stability of Nash point is bigger than that of the asymmetric case and positivity of quantities are guaranteed.

**2.3. Heterogeneous Effect.** The competition described here includes heterogeneous competitors. We assume that two firms behave rational while the other adopts the LMA mechanism. In [10], the definition of the LMA mechanism has been introduced. It requires no global information about the demand function, yet it needs the players knowing market price  $p_t$  and the corresponding produced quantity  $Q_t$ . This can be called local information of the price function for  $(p_t, Q_t)$  only. Through some experiences on the market, the player may be able to estimate the price function for market values within a neighborhood of  $(p_t, Q_t)$  and then compute properly the following derivative:

$$\partial_{q_1} f(q_{1,t}, q_{2,t}) = f'(Q_t). \quad (17)$$

*Scenario 1.* We assume that the first oligopolist is adopting the LMA mechanism. It has been discussed that such mechanism can be calculated by the effect of small quantity and price variations which make the firm (the player) evaluates the price function at each time for the total supply  $Q_t$ . Therefore, equation (17) with the price of the first player  $p_{1,t}$  gives the following price function:

$$p_{1,t+1}^e = p_{1,t} + p'(Q_t)[Q_{t+1}^e - Q_t], \quad (18)$$

where  $Q_{t+1}^e = q_{1,t+1}^e + q_{2,t+1}^e + \dots + q_{3,t+1}^e$  and  $q_{2,t+1}^e, q_{3,t+1}^e$  are the expected outputs, i.e., the outputs which the first oligopolist expects from its opponents at time  $t + 1$ . Now, we consider static expectations for the second and third oligopolists ( $q_{2,t+1}^e = q_{2,t}, q_{3,t+1}^e = q_{3,t}$ ); then (18) takes the form

$$p_{1,t+1}^e = \frac{1}{(q_1 + q_2 + q_3)} - \frac{1}{(q_1 + q_2 + q_3)^2} [q_{1,t+1} - q_{1,t}], \quad (19)$$

where  $p'(Q_t) = 1/Q^2$ . Now, the first oligopolist chooses its next period strategy according to the following:

$$q_{1,t+1} = \arg \max_{q_{2,t+1}} [p_{1,t+1}^e q_{1,t+1} - c_1 q_{1,t+1}], \quad (20)$$

namely,

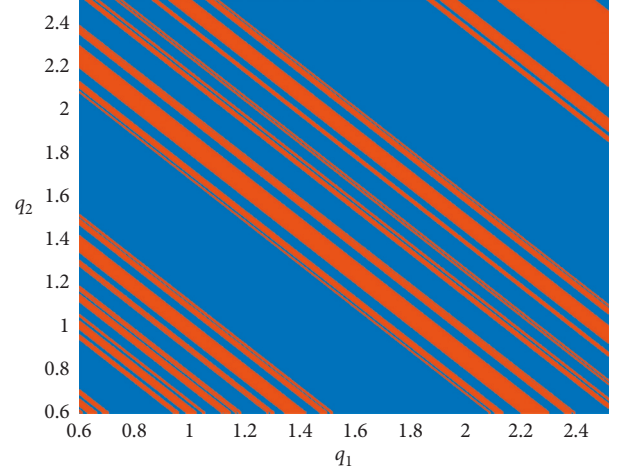


FIGURE 10: Basin of attraction of the period 8-cycle at  $q_{0,3} = 0.13, k = 14.6, c = 0.2$ .

$$q_{1,t+1} = \frac{1}{2} q_{1,t} + \frac{Q}{2} (1 - c_1 Q), \quad (21)$$

$$Q = q_1 + q_2 + q_3.$$

Then the resulting oligopolistic game is now described by

$$\begin{aligned} q_{1,t+1} &= \frac{1}{2} q_{1,t} + \frac{Q}{2} [1 - c_1 Q], \\ q_{2,t+1} &= q_{2,t} + k \left[ \frac{Q - q_2}{Q^2} - c_2 \right], \\ q_{3,t+1} &= q_{3,t} + k \left[ \frac{Q - q_3}{Q^2} - c_3 \right]. \end{aligned} \quad (22)$$

The above system is a nonlinear discrete dynamic system which consists of one LMA player against two rational competitors.

**2.3.1. Local Analysis.** As previously done, we calculate here the steady state of system (22) and study its stability and the corresponding complex characteristics. Simple calculations yield the NE described in (7) as the steady state of system (22). Even though the heterogeneousness is carried out by the first oligopolist, the steady state of system (22) is the same steady state of system (10) where all the oligopolists adopt the bounded rationality mechanism. The following proposition is given.

*Proposition 2.* The Nash equilibrium (7) is a steady state of system (22) and it is locally asymptotically stable if the following conditions are satisfied.

$$\begin{aligned} & \frac{1}{16\bar{c}} \left[ (3\bar{c} - 8c_1)\bar{c}^4 k^2 + 8(5\bar{c} - 11c_1)\bar{c}^2 k + 16(c_1 + 3c_2 + 5c_3) \right] > 0, \\ & \frac{-1}{64} \left[ k^4 \bar{c}^6 (2c_1 - \bar{c}) + 12k^3 \bar{c}^4 (2c_1 - \bar{c})^2 + 8k\bar{c}^2 (3c_1 - 3c_2 - 5c_3)(2c_1 - \bar{c}) + 32((2c_1 - \bar{c})(2c_2 + c_3) - 2c_1 c_3) \right] > 0, \\ & \frac{-1}{16\bar{c}} \left[ k^2 \bar{c}^4 (8c_1 - 5\bar{c}) + 24k\bar{c}^2 (\bar{c} - c_1) + 16c_3 - 16c_2 - 48c_1 \right] > 0, \end{aligned} \quad (23)$$

$$\bar{c} = c_1 + c_2 + c_3.$$

System (22) at NE point has the following Jacobian matrix:

$$\begin{bmatrix} \frac{c_2 + c_3 - c_1}{c_1 + c_2 + c_3} & \frac{c_2 + c_3 - 3c_1}{2(c_1 + c_2 + c_3)} & \frac{c_2 + c_3 - 3c_1}{2(c_1 + c_2 + c_3)} \\ 1 - \frac{k}{4}(c_1 + c_2 + c_3)(3c_2 - c_1 - c_3) & -c_2 k (c_1 + c_2 + c_3) & \frac{-k}{4}(c_1 + c_2 + c_3)(3c_2 - c_1 - c_3) \\ 1 - \frac{k}{4}(c_1 + c_2 + c_3)(3c_3 - c_1 - c_2) & \frac{-k}{4}(c_1 + c_2 + c_3)(3c_3 - c_1 - c_2) & -c_3 k (c_1 + c_2 + c_3) \end{bmatrix}. \quad (24)$$

For NE to be asymptotically stable, all the roots of the following characteristic equation must have magnitudes of eigenvalues less than one:

$$\lambda^3 + \theta_1 \lambda + \theta_2 \lambda + \theta_3 = 0, \quad (25)$$

where

$$\begin{aligned} \theta_1 &= \frac{k(c_2 + c_3)(c_1 + c_2 + c_3)^2 + (c_1 - c_2 + c_3)}{(c_1 + c_2 + c_3)}, \\ \theta_2 &= -\frac{[k(c_1 + c_2 + c_3)^2 (k(c_1 + c_2 + c_3)^2 (c_1 - 3c_2 - 3c_3) - 12c_1 + 12c_2 + 12c_3) - 48c_1 + 16c_2 + 16c_3]}{16(c_1 + c_2 + c_3)}, \\ \theta_3 &= \frac{k}{8} [k(c_1 - c_2 - c_3)(c_1 + c_2 + c_3)^3 + 2(c_1 + c_2 + c_3)(3c_1 - c_2 - c_3)]. \end{aligned} \quad (26)$$

This can be achieved if and only if the following Jury conditions are satisfied:

$$\begin{aligned} \ell_1 &:= 3 + \theta_1 - \theta_2 - 3\theta_3 > 0, \\ \ell_2 &:= 1 - \theta_2 + \theta_3(\theta_1 - \theta_3) > 0, \\ \ell_3 &:= 1 - \theta_1 + \theta_2 - \theta_3 > 0. \end{aligned} \quad (27)$$

Substituting (26) in (27) completes the proof. In order to get more insights about the above proposition, we perform some numerical simulations.

**2.3.2. Simulation and Global Analysis.** This simulation handles the complex characteristics of system (22). It is

devoted to investigate the results obtained by Proposition 2 and to see whether NE is stable or not. We set the parameter values to  $c_1 = 0.12$ ,  $c_2 = 0.33$  and  $c_3 = 0.25$ . Figure 11(a) shows that the Nash point is locally stable whenever varying the parameter  $k$  until the system (22) starts bifurcating around Nash point and then high period cycles are formed. Comparing this case with the previous case, we see that the previous case is more stable in terms of the stability region with respect to the parameter  $k$ . This means that adopting LMA mechanism does not help the firm to be more stable against its rational competitors. Figure 11(a) shows the stability of Nash point when we increase  $k$ . We should highlight here that choosing the costs' parameters should satisfy the

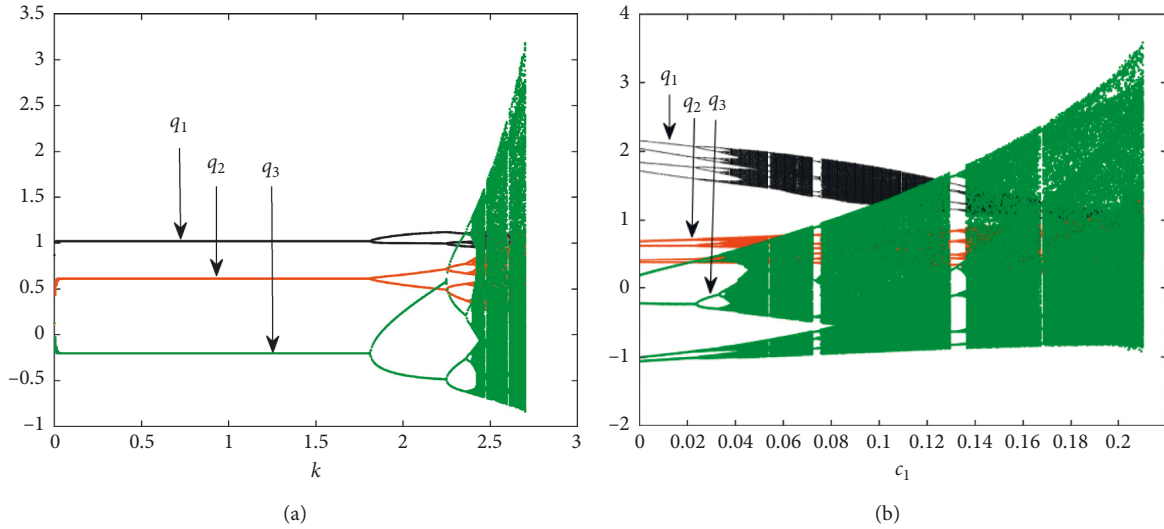


FIGURE 11: (a) Bifurcation diagram of system (22) with respect to  $k$  at  $(q_{0,1}, q_{0,2}, q_{0,3}) = (0.11, 0.12, 0.13)$ ,  $c_1 = 0.2, c_2 = 0.4, c_3 = 0.8$ . (b) Bifurcation diagram of system (22) with respect to  $c_1$  at  $(q_{0,1}, q_{0,2}, q_{0,3}) = (0.11, 0.12, 0.13)$ ,  $k = 2.7, c_2 = 0.4, c_3 = 0.8$ .

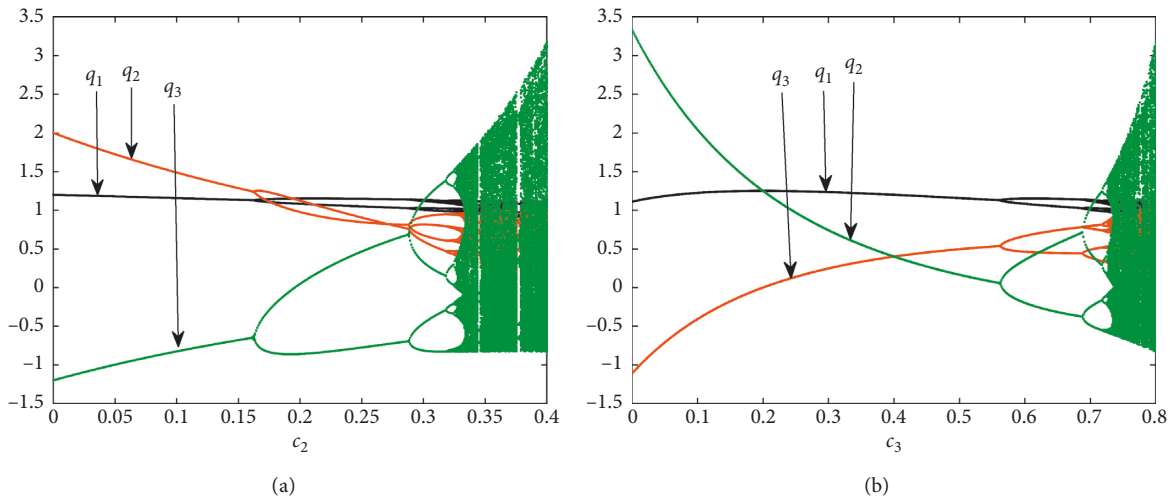


FIGURE 12: (a) Bifurcation diagram of system (22) with respect to  $c_2$  at  $(q_{0,1}, q_{0,2}, q_{0,3}) = (0.11, 0.12, 0.13)$ ,  $c_1 = 0.2, k = 2.7, c_3 = 0.8$ . (b) Bifurcation diagram of system (22) with respect to  $c_3$  at  $(q_{0,1}, q_{0,2}, q_{0,3}) = (0.11, 0.12, 0.13)$ ,  $k = 2.7, c_1 = 0.2, c_2 = 0.4$ .

conditions,  $c_2 + c_3 > c_1, c_1 + c_3 > c_2$  and  $c_1 + c_2 > c_3$ . Choosing very small values of cost parameters extends the region of stability of Nash point. Figures 11(b) and 12(a) and 12(b) show the influences of costs on the stability of Nash point. As one can see, only small values of costs should be selected; otherwise, chaotic behavior may arise. The corresponding Lyapunov exponent for those costs and  $k$  is given in Figures 13(a) and 13(b). Other interesting chaotic behaviors are given in Figures 14 and 15. Figure 14(a) gives the phase portrait of a chaotic attractor of system (22) at the parameters:  $k = 2.7, c_1 = 0.2, c_2 = 0.4, c_3 = 0.8$ . The time series of quantities at those pa-

rameters is shown in Figure 14(b). Figures 15(a) and 15(b) present different chaotic attractors of the system. Period 2-cycle and period 5-cycle are obtained in Figure 16. The basin of attraction of period 5-cycle is represented by many colors and is given in Figure 17. All these periods are unstable.

*Scenario 2.* In this scenario, we assume that two monopolists (firm 1 and firm 2) adopt the LMA mechanism while the other uses bounded rationality. This means that system (22) can be rewritten in the form



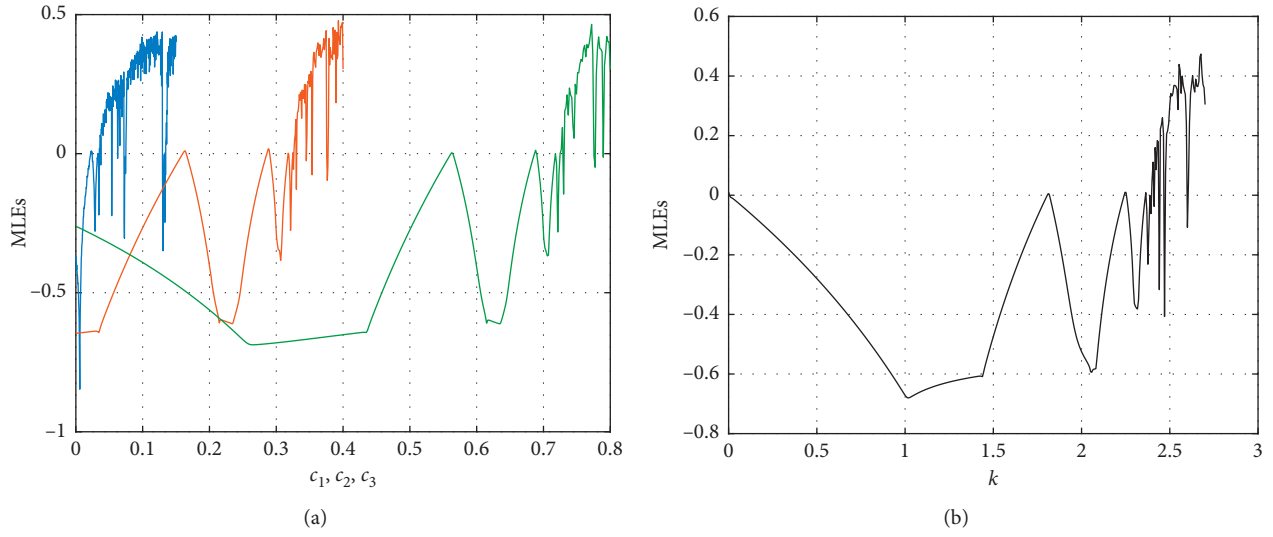


FIGURE 13: (a) Lyapunov exponents with respect to  $c_1, c_2, c_3$  at  $k = 2.7$ . (b) Lyapunov exponents with respect to  $k = 2.7, c_1 = 0.2, c_2 = 0.4, c_3 = 0.8$ .

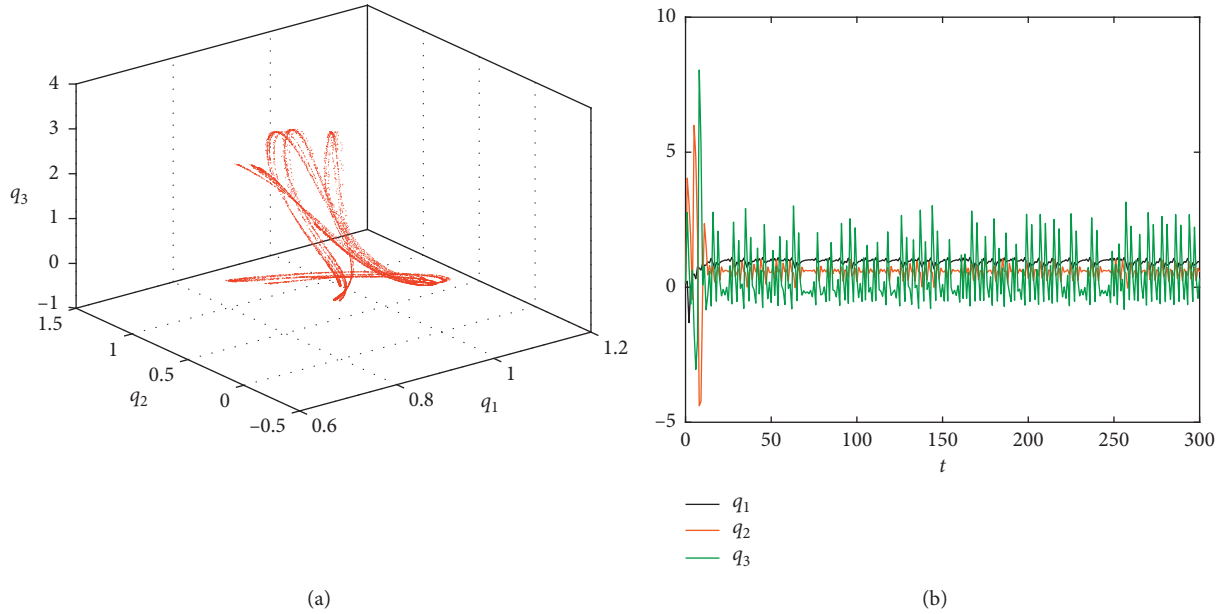


FIGURE 14: (a) Chaotic attractor of system (22) at  $(q_{0,1}, q_{0,2}, q_{0,3}) = (0.11, 0.12, 0.13), k = 2.7, c_1 = 0.2, c_2 = 0.4, c_3 = 0.8$ . (b) Time series for  $q_1, q_2, q_3$  at  $k = 2.7, c_1 = 0.2, c_2 = 0.4, c_3 = 0.8$ .

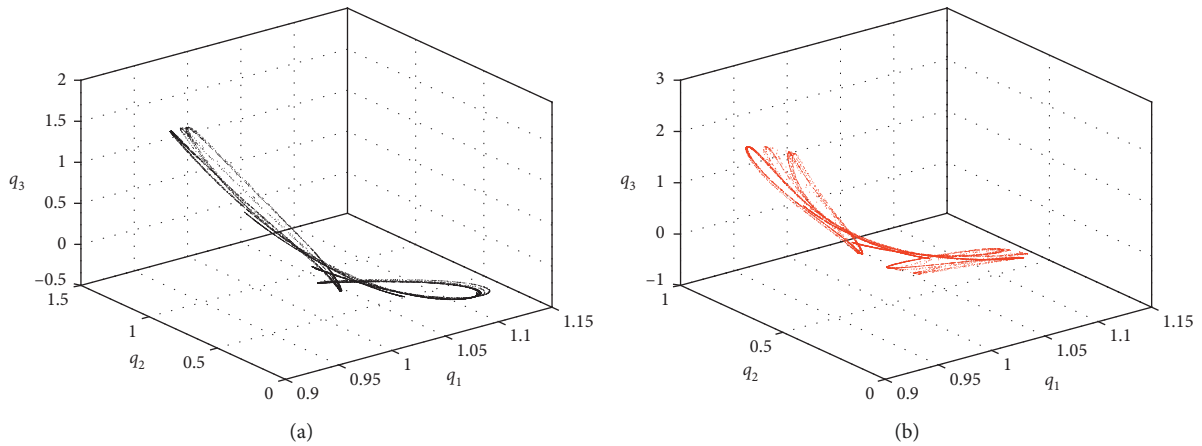


FIGURE 15: (a) Chaotic attractor of system (22) at  $(q_{0,1}, q_{0,2}, q_{0,3}) = (0.11, 0.12, 0.13), k = 2.55, c_1 = 0.2, c_2 = 0.5, c_3 = 0.7$ . (b) Chaotic attractor of system (22) at  $(q_{0,1}, q_{0,2}, q_{0,3}) = (0.11, 0.12, 0.13), k = 2.55, c_1 = 0.2, c_2 = 0.4, c_3 = 0.8$ .

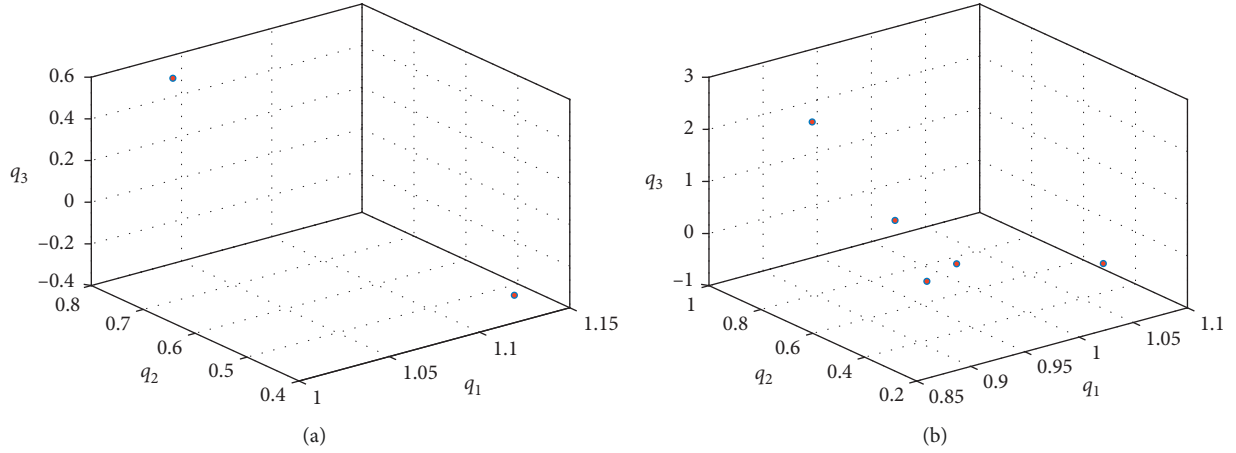


FIGURE 16: (a) Phase space of the period 2-cycle of system (22) at  $(q_{0,1}, q_{0,2}, q_{0,3}) = (0.11, 0.12, 0.13)$ ,  $k = 2.55$ ,  $c_1 = 0.2$ ,  $c_2 = 0.4$ ,  $c_3 = 0.7$ . (b) Phase space of the period 8-cycle of system (22) at  $(q_{0,1}, q_{0,2}, q_{0,3}) = (0.11, 0.12, 0.13)$ ,  $k = 14.6$ ,  $c = 0.2$ .

$$\begin{aligned}
 q_{1,t+1} &= \frac{1}{2}q_{1,t} + \frac{Q}{2}[1 - c_1Q], \\
 q_{2,t+1} &= \frac{1}{2}q_{2,t} + \frac{Q}{2}[1 - c_2Q], \\
 q_{3,t+1} &= q_{3,t} + k \left[ \frac{Q - q_3}{Q^2} - c_3 \right].
 \end{aligned} \tag{28}$$

*Proposition 3.* The Nash equilibrium (7) is a steady state of system (32).

Now, the stability of Nash point is as previously obtained, and we get Jacobian matrix as follows:

$$\begin{bmatrix}
 \frac{c_2 + c_3 - c_1}{c_1 + c_2 + c_3} & \frac{c_2 + c_3 - 3c_1}{2(c_1 + c_2 + c_3)} & \frac{c_2 + c_3 - 3c_1}{2(c_1 + c_2 + c_3)} \\
 \frac{c_1 + c_3 - 3c_2}{2(c_1 + c_2 + c_3)} & \frac{c_1 + c_3 - c_2}{c_1 + c_2 + c_3} & \frac{c_1 + c_3 - 3c_2}{2(c_1 + c_2 + c_3)} \\
 \frac{k}{4}(c_1 + c_2 + c_3)(c_1 + c_2 - 3c_3) & \frac{k}{4}(c_1 + c_2 + c_3)(c_1 + c_2 - 3c_3) & 1 - c_3k(c_1 + c_2 + c_3)
 \end{bmatrix}, \tag{29}$$

whose characteristic equation is given by

$$\lambda^3 + \Lambda_1\lambda + \Lambda_2\lambda + \Lambda_3 = 0, \tag{30}$$

where

$$\begin{aligned}
 \Lambda_1 &= \frac{c_3k(c_1 + c_2 + c_3)^2 - (c_1 + c_2 + 3c_3)}{c_1 + c_2 + c_3}, \\
 \Lambda_2 &= \frac{k(c_1 + c_2 - 5c_3)(c_1 + c_2 + c_3)^2 - (c_1 + c_2 - 11c_3)}{4(c_1 + c_2 + c_3)}, \\
 \Lambda_3 &= -\frac{k(c_1 + c_2 - 3c_3)(c_1 + c_2 + c_3)^2 - 2(c_1 + c_2 - 3c_3)}{8(c_1 + c_2 + c_3)}.
 \end{aligned} \tag{31}$$

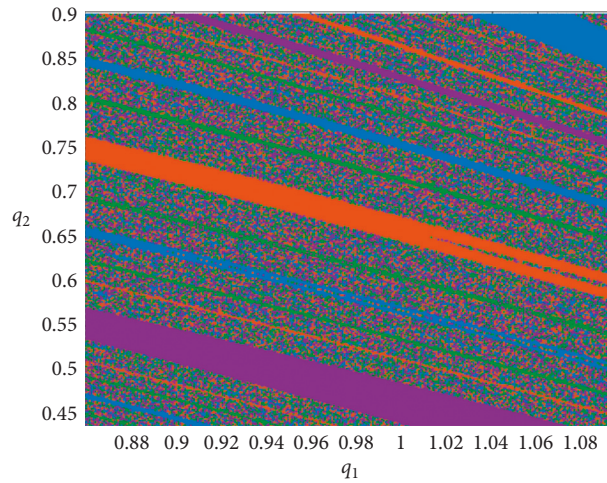


FIGURE 17: Basin of attraction of the period 5-cycle at  $q_{0,3} = 0.13, k = 2.6, c_1 = 0.2, c_2 = 0.4, c_3 = 0.8$ .

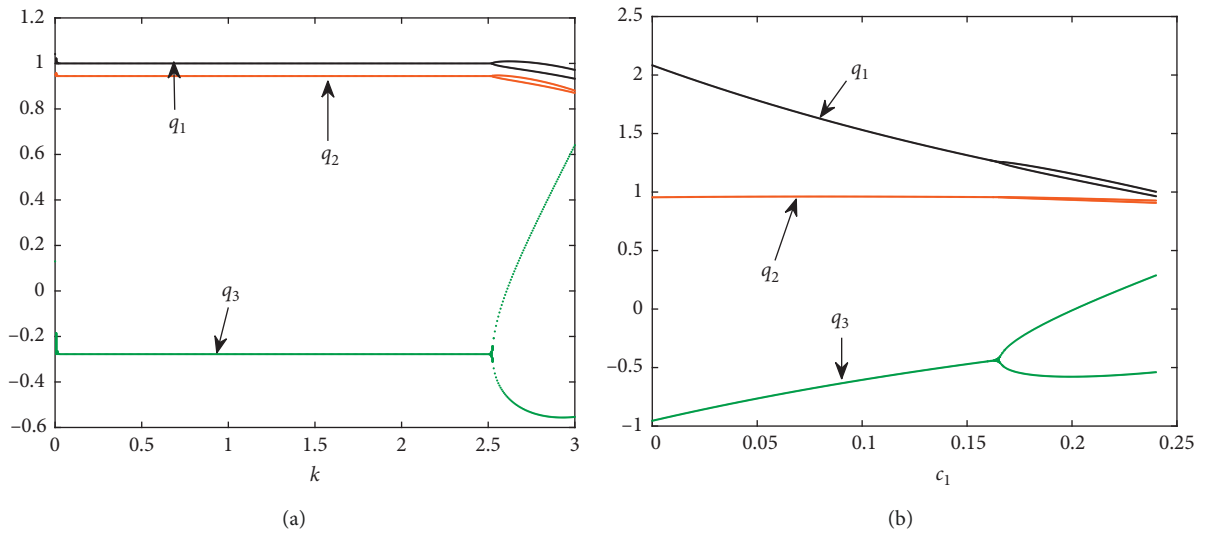


FIGURE 18: (a) Bifurcation diagram of system (32) with respect to  $k$  at  $(q_{0,1}, q_{0,2}, q_{0,3}) = (0.11, 0.12, 0.13), c_1 = 0.24, c_2 = 0.26, c_3 = 0.785$ . (b) Bifurcation diagram of system (32) with respect to  $c_1$  at  $(q_{0,1}, q_{0,2}, q_{0,3}) = (0.11, 0.12, 0.13), k = 2.77, c_2 = 0.26, c_3 = 0.785$ .

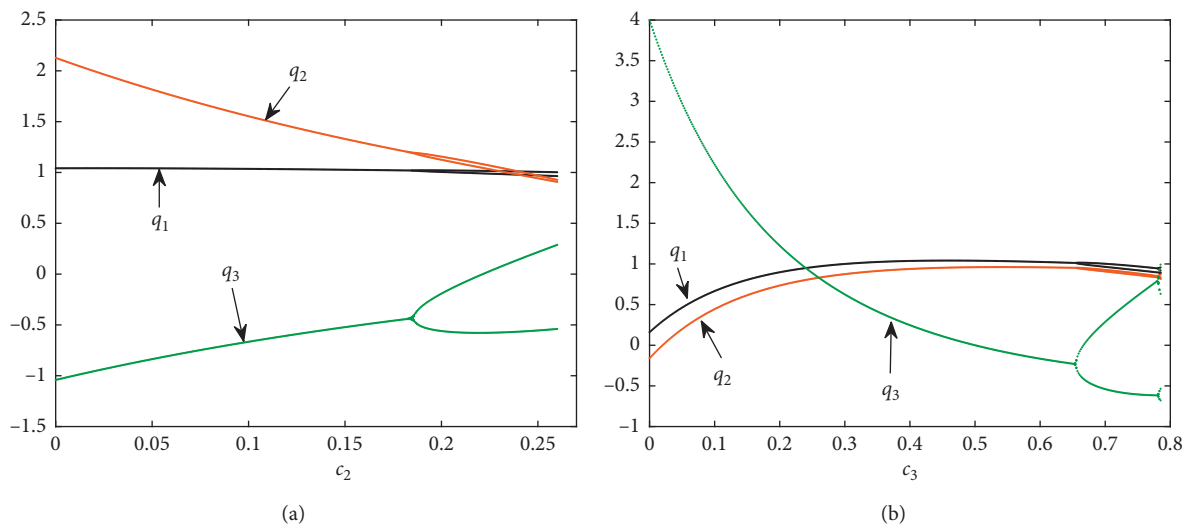


FIGURE 19: (a) Bifurcation diagram of system (32) with respect to  $c_2$  at  $(q_{0,1}, q_{0,2}, q_{0,3}) = (0.11, 0.12, 0.13), c_1 = 0.24, k = 2.77, c_3 = 0.785$ . (b) Bifurcation diagram of system (32) with respect to  $c_3$  at  $(q_{0,1}, q_{0,2}, q_{0,3}) = (0.11, 0.12, 0.13), k = 2.77, c_1 = 0.24, c_2 = 0.26$ .

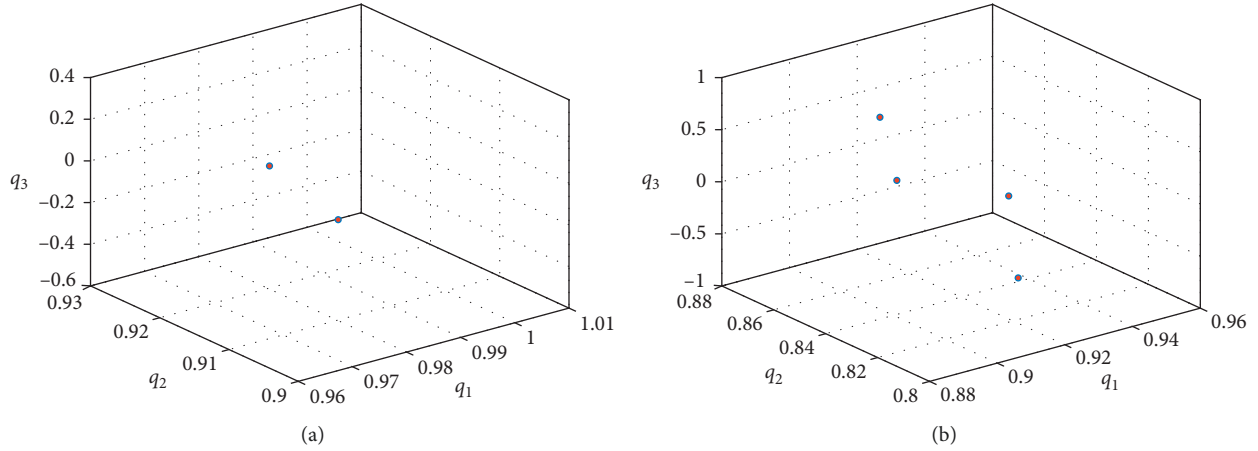


FIGURE 20: (a) Phase space of the period 2-cycle of system (32) at  $(q_{0,1}, q_{0,2}, q_{0,3}) = (0.11, 0.12, 0.13)$ ,  $k = 2.77$ ,  $c_1 = 0.24$ ,  $c_2 = 0.26$ ,  $c_3 = 0.785$ . (b) Phase space of the period 4-cycle of system (32) at  $(q_{0,1}, q_{0,2}, q_{0,3}) = (0.11, 0.12, 0.13)$ ,  $k = 2.77$ ,  $c_1 = 0.24$ ,  $c_2 = 0.26$ ,  $c_3 = 0.785$ .

Using Jury conditions and (31) we get

$$\begin{aligned} \ell_1 &= \frac{k(c_1 + c_2 + 9c_3)(c_1 + c_2 + c_3)^2 + 4(3c_1 + 3c_2 - c_3)}{c_1 + c_2 + c_3}, \\ \ell_2 &= \frac{[k(c_1 + c_2 + c_3)^2(k(c_1 + c_2 + 5c_3)(c_1 + c_2 - 3c_3)(c_1 + c_2 + c_3)^2 + 4(c_1 + c_2)^2 - 4c_3(14c_1 + 14c_2 - c_3)) - 4(5c_1 + 5c_2 + c_3)(3c_1 + 3c_2 - c_3)]}{64(c_1 + c_2 + c_3)^2}, \\ \ell_3 &= \frac{3[k(c_1 + c_2 - 7c_3)(c_1 + c_2 + c_3)^2 + 4(c_1 + c_2 + 5c_3)]}{8(c_1 + c_2 + c_3)}. \end{aligned} \quad (32)$$

Therefore, the Nash point system (32) is asymptotically stable if  $\ell_i > 0$ ,  $i = 1, 2, 3$ . The eigenvalues and Jury conditions take complicated forms, and then some simulations are carried out to investigate the conditions (32). We observe that when  $c_i = c$ ,  $i = 1, 2, 3$ , both  $\ell_1$  and  $\ell_2$  are positive while  $\ell_3 > 0$  provided that  $kc^2 < 0.62$ , and hence, Nash point is asymptotically stable. On the other hand, when we take different values of costs, i.e.,  $c_1 = 0.24$ ,  $c_2 = 0.26$ , and  $c_3 = 0.785$ , bifurcated behaviors of the system appear and then the local stability of Nash point does not exist. Figure 18(a) shows different bifurcated behaviors with respect to the parameter  $k$ . It seems that all firms get unstable due to the bad influences of those cost parameters and the negative quantities that appear which are nonsense in any economic context. Figures 18(b) and 19 give the influence of costs on the stability of Nash point. As one can see, those costs affect the system's behavior even if they have taken small values. This is also clear from Figures 20(a) and 20(b) where the period 2-cycle and period 4-cycle appear.

### 3. Conclusion

The current paper has investigated an oligopolistic game that consists of three competitors. Different complicated dynamic routes have been raised due to the adoption of two

different adjustment mechanisms, bounded rationality and the LMA mechanism. The demand function used to build this game and its corresponding dynamical systems has been derived from Cobb–Douglas production function. The obtained results have shown that the stability of Nash equilibrium loses its stability due to the appearance of bifurcated behaviors of those discussed systems in the manuscript. We have concluded from the obtained results that bounded rationality mechanism when it is adopted by firms has given better stability for the Nash point in comparison with the results of stability given by the LMA mechanism. Our obtained results extend results existed in literature. Furthermore, we have detected several fractal structures which require more analysis and investigations that will be addressed in future research works. The limitation of the current work lies in the application of only two types of mechanisms; the bounded rationality and LMA mechanism. Other types of mechanisms should be considered in comparison, and this might include expected cooperation among firms.

### Data Availability

The availability of data is carried out by the corresponding author.

## Conflicts of Interest

The authors declare that they have no conflicts of interest.

## Acknowledgments





The authors would like to extend their sincere appreciation to the Deanship of Scientific Research at King Saud University for its financial support (RG-1435-054).

## References

- [1] S. S. Askar and M. Abouhawwash, "Quantity and price competition in a differentiated triopoly: static and dynamic investigations," *Nonlinear Dynamics*, vol. 91, no. 3, pp. 1963–1975, 2018.
- [2] D. Rand, "Exotic phenomena in games and duopoly models," *Journal of Mathematical Economics*, vol. 5, no. 2, pp. 173–184, 1978.
- [3] T. Poston and I. Stewart, *Catastrophe Theory and its Applications*, Pitman Ltd., London, UK, 1978.
- [4] H. N. Agiza and A. A. Elsadany, "Chaotic dynamics in nonlinear duopoly game with heterogeneous players," *Applied Mathematics and Computation*, vol. 149, no. 3, pp. 843–860, 2004.
- [5] S. S. Askar, A. M. Alshamrani, and K. Alnowibet, "Dynamic Cournot duopoly games with nonlinear demand function," *Applied Mathematics and Computation*, vol. 259, pp. 427–437, 2015.
- [6] S. Askar, "The rise of complex phenomena in Cournot duopoly games due to demand functions without inflection points," *Communications in Nonlinear Science and Numerical Simulation*, vol. 19, no. 6, pp. 1918–1925, 2014.
- [7] T. Puu, "Chaos in duopoly pricing," *Chaos, Solitons & Fractals*, vol. 1, no. 6, pp. 573–581, 1991.
- [8] H. N. Agiza and A. A. Elsadany, "Nonlinear dynamics in the Cournot duopoly game with heterogeneous players," *Physica A: Statistical Mechanics and its Applications*, vol. 320, pp. 512–524, 2003.
- [9] S. S. Askar and A. Alshamrani, "The dynamics of economic games based on product differentiation," *Journal of Computational and Applied Mathematics*, vol. 268, pp. 135–144, 2014.
- [10] J. Tuinstra, "A price adjustment process in a model of monopolistic competition," *International Game Theory Review*, vol. 6, no. 3, pp. 417–442, 2004.
- [11] N. Pecora and M. Sodini, "A heterogeneous Cournot duopoly with delay dynamics: hopf bifurcations and stability switching curves," *Communications in Nonlinear Science and Numerical Simulation*, vol. 58, pp. 36–46, 2018.
- [12] F. Cavalli and A. Naimzada, "A Cournot duopoly game with heterogeneous players: nonlinear dynamics of the gradient rule versus local monopolistic approach," *Applied Mathematics and Computation*, vol. 249, pp. 382–388, 2014.
- [13] E.-G. Gu, "Complex dynamics analysis on fish stock harvested by two players with heterogeneous rationality," *Chaos, Solitons & Fractals*, vol. 42, no. 2, pp. 964–974, 2009.
- [14] L. C. Baiardi, F. Lamantia, and D. Radi, "Evolutionary competition between boundedly rational behavioral rules in oligopoly games," *Chaos, Solitons & Fractals*, vol. 79, pp. 204–225, 2015.
- [15] S. Vaidyanathan, A. T. Azar, K. Rajagopal, A. Sambas, S. Kacar, and U. Cavusoglu, "A new hyperchaotic temperature fluctuations model, its circuit simulation, FPGA implementation and an application to image encryption," *International Journal of Simulation and Process Modelling*, vol. 13, no. 3, pp. 281–296, 2018.
- [16] S. Vaidyanathan, A. Sambas, S. Kacar, and Ü. Çavuşoğlu, "A new three-dimensional chaotic system with a cloud-shaped curve of equilibrium points, its circuit implementation and sound encryption," *International Journal of Modelling, Identification and Control*, vol. 30, no. 3, pp. 184–196, 2018.

## Research Article

# Abundant Coexisting Multiple Attractors' Behaviors in Three-Dimensional Sine Chaotic System

Huagan Wu <sup>1</sup>, Han Bao <sup>2</sup>, Quan Xu <sup>1</sup>, and Mo Chen <sup>1</sup>

<sup>1</sup>School of Information Science and Engineering, Changzhou University, Changzhou 213164, China

<sup>2</sup>College of Automation Engineering, Nanjing University of Aeronautics and Astronautics, Nanjing 211106, China

Correspondence should be addressed to Mo Chen; [mchen@cczu.edu.cn](mailto:mchen@cczu.edu.cn)

Received 15 October 2019; Revised 2 November 2019; Accepted 15 November 2019; Published 6 December 2019

Guest Editor: Viet-Thanh Pham

Copyright © 2019 Huagan Wu et al. This is an open access article distributed under the Creative Commons Attribution License, which permits unrestricted use, distribution, and reproduction in any medium, provided the original work is properly cited.

This paper presents a novel and simple three-dimensional (3-D) chaotic system by introducing two sine nonlinearities into a simple 3-D linear dynamical system. The presented sine system possesses nine equilibrium points consisting of five index-2 saddle foci and four index-1 saddle foci which allow the coexistence of various types of disconnected attractors, also known as multistability. The coexisting multiple attractors are depicted by the phase plots and attraction basins. Coexisting bifurcation modes triggered by different initial values are numerically simulated by two-dimensional bifurcation and complexity plots under two sets of initial values and one-dimensional bifurcation plots under three sets of initial values, which demonstrate that the abundant coexisting multiple attractors' behaviors in the presented sine system are related not only to the system parameters but also to the initial values. A simulation-oriented circuit model is synthesized, and PSIM (power simulation) screen captures well validate the numerical simulations.

## 1. Introduction

Recently, numerous nonlinear dynamical systems have been reported that they present the coexistence of two or more disconnected attractors with their isolated attraction basins. The coexisting phenomena of two or more attractors have been encountered in nonlinear oscillating circuits [1–5], biological neuron models [6, 7], Hopfield neural networks [8–11], vibroimpact system [12], superconducting quantum interference device oscillators [13], pure mathematical systems [14–17], and so on. This striking phenomenon, also known as multistability, demonstrates that the system initial values do play an important role in the emergence of complex coexisting attractors' behaviors [18, 19]. For a multistable dynamical system, it is usually challenging to predict the final steady state to which the dynamical system will tend for a given initial value since a small disturbance in the initial value can alter the steady state of such dynamical systems [20–23]. Multistability has great application potentials in the chaos-based secure communication and information encryption [24–27], but efficient prediction and

control methods should be employed to make these dynamical systems in the desired oscillating modes [28–32].

Usually, an effective method for implementing the initial-related multistability is to lead one, two, or more generic or extended memristors in various existing circuits and systems [15–17, 33–36]. Memristor-based circuits and systems with different types of equilibrium points are easy to exhibit coexisting attractors' behaviors of multistability. Comparatively speaking, another beneficial and simple method for generating initial value offset-boosted coexisting attractors is to put periodic trigonometric functions into specific offset-boostable dynamical systems [37–41]. When the cyclic periods for the periodic functions are identical, any attractor will be copied by periodic offset boosting the initial values [37]. However, due to the reported offset-boostable dynamical systems with self-contained nonlinearities, the newly constructing multistable dynamical systems become relatively complicated [38–41], not convenient for theoretical analyses and hardware circuit implementations. The algebraic simplicity of system's structure and topological complexity of chaotic attractors are benefits for developing chaos-based



cryptosystems [42]. In this paper, based on a simple 3-D linear dynamical system and two newly introduced sine nonlinearities, a novel and extremely simple 3-D sine chaotic system is readily constructed, from which abundant coexisting multiple attractors' behaviors are observed [43].

The rest is organized as follows. In Section 2, a novel and simple 3-D sine chaotic system is presented. It has nine equilibrium points consisting of five index-2 saddle foci and four index-1 saddle foci, resulting in the coexistence of up to six types of disconnected attractors. In Section 3, by two-dimensional bifurcation and complexity plots under two sets of initial values and one-dimensional bifurcation plots under three sets of initial values, coexisting bifurcation modes are numerically simulated to demonstrate the abundant coexisting multiple attractors' behaviors. In Section 4, with the simulation-oriented circuit model, PSIM screen captures validate the numerical simulations. The conclusion is summarized in Section 5.

## 2. System Model and Its Coexisting Multiple Attractors

By introducing two sine nonlinearities with two coupling coefficients into a simple 3-D linear dynamical system, a novel 3-D sine chaotic system with simple algebraic equations is easily achieved, which is modeled by

$$\begin{aligned}\dot{x} &= y + z - k_1 \sin(y), \\ \dot{y} &= -x + z, \\ \dot{z} &= -x - z + k_2 \sin(x),\end{aligned}\quad (1)$$

where  $x$ ,  $y$ , and  $z$  are the three state variables and  $k_1$  and  $k_2$  are the two positive constants.

The presented sine system in (1) is symmetric about the origin and dissipative. The symmetric property can be demonstrated by the invariance of system (1) with respect to the transformation  $(x, y, z) \longleftrightarrow (-x, -y, -z)$ . The dissipativity is explained by

$$\nabla V = \frac{\partial \dot{x}}{\partial x} + \frac{\partial \dot{y}}{\partial y} + \frac{\partial \dot{z}}{\partial z} = -1 < 0. \quad (2)$$

Thus, the orbits are finally confined to a specific subset with zero volume and its asymptotic motion settles onto a standalone attractor.

The equilibrium points of the presented sine system in (1) are obtained by solving the following equations:

$$\begin{aligned}0 &= y + z - k_1 \sin(y), \\ 0 &= -x + z, \\ 0 &= -x - z + k_2 \sin(x),\end{aligned}\quad (3)$$

which is expressed as

$$E = (\delta, \sigma, \delta). \quad (4)$$

The values  $\delta$  and  $\sigma$  can be yielded by solving the following transcendental functions:

$$h_1 = 2\delta - k_2 \sin(\delta) = 0 \quad (5)$$

$$h_2 = \sigma + \delta - k_1 \sin(\sigma) = 0, \quad (6)$$

respectively.

The Jacobian matrix  $\mathbf{J}$  at  $E$  is given as

$$\mathbf{J} = \begin{bmatrix} 0 & 1 - k_1 \cos(\sigma) & 1 \\ -1 & 0 & 1 \\ -1 + k_2 \cos(\delta) & 0 & -1 \end{bmatrix}, \quad (7)$$

so that the characteristic polynomial is derived as

$$P(\lambda) = \lambda^3 + c_1 \lambda^2 + c_2 \lambda + c_3 = 0, \quad (8)$$

where

$$\begin{aligned}c_1 &= 1, \\ c_2 &= 2 - k_1 \cos(\sigma) - k_2 \cos(\delta), \\ c_3 &= [1 - k_1 \cos(\sigma)][2 - k_2 \cos(\delta)].\end{aligned}\quad (9)$$

The above characteristic polynomial implies that Jacobian matrix (7) has three nonzero roots. For these roots, Routh–Hurwitz conditions are given as

$$\begin{aligned}c_1 &> 0, \\ c_3 &> 0, \\ c_1 c_2 - c_3 &> 0,\end{aligned}\quad (10)$$

i.e.,

$$\begin{aligned}[1 - k_1 \cos(\sigma)][2 - k_2 \cos(\delta)] &> 0, \\ k_1 \cos(\sigma)[1 - k_2 \cos(\delta)] &> 0.\end{aligned}\quad (11)$$

If the conditions in (11) are satisfied, i.e.,  $k_1 \cos(\sigma) < 1$  and  $k_2 \cos(\delta) < 1$ ,  $E$  is stable, leading to the existence of the point attractor. Otherwise, if any one of the conditions in (11) is not satisfied, i.e.,  $k_1 \cos(\sigma) < 1$  or  $k_2 \cos(\delta) < 1$ ,  $E$  is unstable, resulting in that unstable behaviors may be triggered in the presented sine system.

Denote  $k_1 = k_2 = k$  and take  $k = 3.6$  and  $5$  as two examples. The values  $\delta$  and  $\sigma$  of the equilibrium point  $E$  in (4) are the intersection points of two function curves  $h_1$  and  $h_2$  described by (5) and (6), as shown in Figures 1(a) and 1(b), respectively, from which nine pairs of  $\delta$  and  $\sigma$  are obtained by inspecting the intersection points, indicating the existence of nine equilibrium points in the presented sine system. With these equilibrium points, the three nonzero eigenvalues are calculated from the Jacobian matrix  $\mathbf{J}$  in (7) and the corresponding stabilities can be determined, as listed in Table 1. The calculation results illustrate that five index-2 saddle foci (Index-2 USF, for short) and four index-1 saddle foci (Index-1 USF, for short) can be found, which could emerge five disconnected attracting regions when these attracting regions cannot be linked with each other, leading to the coexistence of disconnected attractors.

For  $k = 3.6, 5$ , and several sets of the initial values (labeled in Figure 2), the phase plots of coexisting multiple attractors projected on the  $x$ - $y$  plane are depicted in Figures 2(a) and 2(b), respectively. In Figure 2(a), a chaotic attractor coexisted with twin small-size period-1 limit cycles, twin large-size

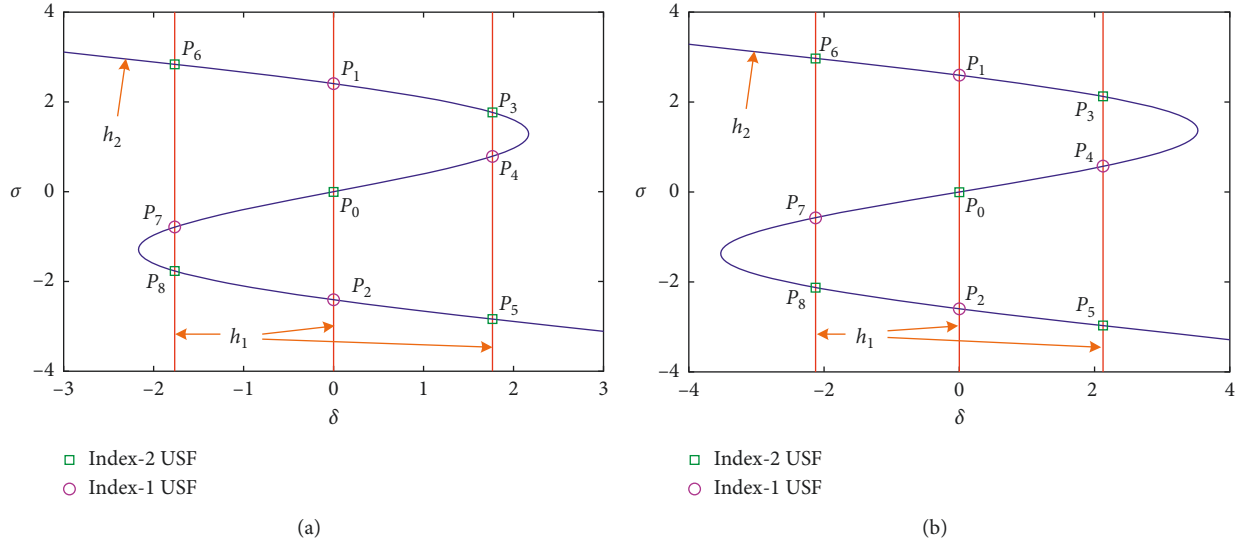


FIGURE 1: Values  $\delta$  and  $\sigma$  of the equilibrium points by inspecting the intersections of two function curves  $h_1$  and  $h_2$  described by (5) and (6). (a)  $k=3.6$ . (b)  $k=5$ .

TABLE 1: Equilibrium points, eigenvalues, and stabilities for  $k=3.6$  and 5.

$k$	Equilibrium points	Eigenvalues	Stabilities
3.6	$P_0: (0, 0, 0)$	$1.0528 \pm j0.4807, -3.1057$	Index-2 USF
	$P_{1,2}: (0, \pm 2.4074, 0)$	$1.3656, -1.1828 \pm j1.7041$	Index-1 USF
	$P_{3,8}: (\pm 1.7659, \pm 1.7668, \pm 1.7659)$	$0.1205 \pm j1.9193, -1.2410$	Index-2 USF
	$P_{4,7}: (\pm 1.7659, \pm 0.7858, \pm 1.7659)$	$1.3103, -1.1551 \pm j1.3587$	Index-1 USF
	$P_{5,6}: (\pm 1.7659, \pm 2.8378, \pm 1.7659)$	$0.3285 \pm j2.6672, -1.6569$	Index-2 USF
5	$P_0: (0, 0, 0)$	$1.4346 \pm j1.0215, -3.8692$	Index-2 USF
	$P_{1,2}: (0, \pm 2.5976, 0)$	$2.0719, -1.5359 \pm j2.2986$	Index-1 USF
	$P_{3,8}: (\pm 2.1253, \pm 2.1271, \pm 2.1253)$	$0.4429 \pm j2.9575, -1.8857$	Index-2 USF
	$P_{4,7}: (\pm 2.1253, \pm 0.5756, \pm 2.1253)$	$2.1115, -1.5558 \pm j2.1419$	Index-1 USF
	$P_{5,6}: (\pm 2.1253, \pm 2.9680, \pm 2.1253)$	$0.6154 \pm j3.4532, -2.2309$	Index-2 USF

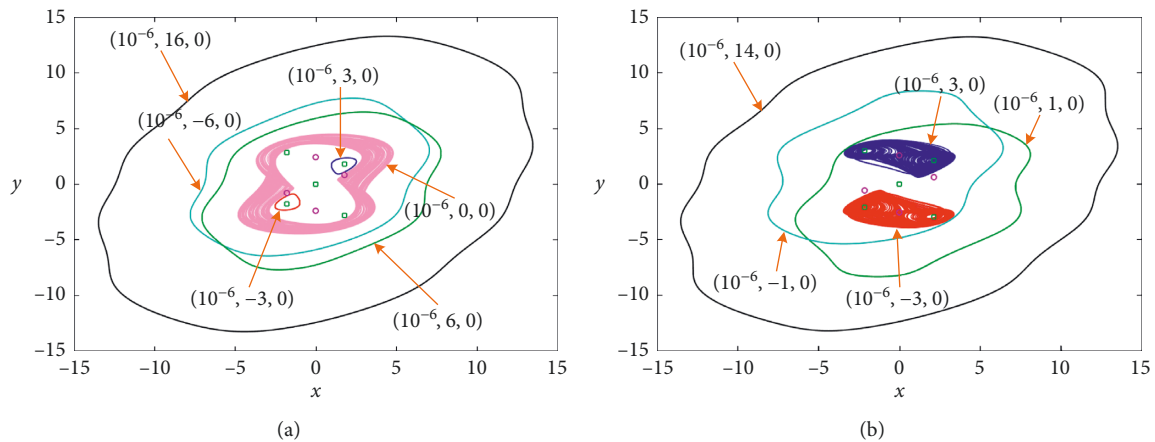


FIGURE 2: Phase plots of coexisting multiple attractors projected on the  $x$ - $y$  plane for different initial values. (a) For  $k=3.6$ , six types of coexisting multiple attractors. (b) For  $k=5$ , five types of coexisting multiple attractors.

period-1 limit cycles, and a relatively larger size period-1 limit cycle. By contrast, in Figure 2(b), two chaotic attractors coexisted with twin large-size period-1 limit cycles and a relatively larger size period-1 limit cycle. Therefore, up to six

types of coexisting multiple attractors are numerically disclosed in the 3-D sine chaotic system because of the attracting and repelling interactions between the five index-2 saddle foci and four index-1 saddle foci.

To detect the attracting regions of the coexisting multiple attractors given in Figure 2, the attraction basins in the initial value plane are used to classify different dynamical behaviors [44]. For the two coupling coefficients used in Figure 2, the attraction basins in the  $x(0)$ - $y(0)$  plane with  $z(0) = 10^{-6}$  are depicted in Figure 3. The attracting regions painted by different colors represent the initial value regions corresponding to different long-term oscillating states, i.e., coexisting multistable states, which are identical with the colored trajectories appearing in Figure 2. Thus, the attraction basins show the relatively complicated manifold structures along with basin boundaries. Meanwhile, the numerical results in Figure 3 demonstrate the emergence of multistability in the presented sine system.

It can be concluded that due to the appearance of five index-2 saddle foci and four index-1 saddle foci and their interactions with each other, some disconnected attracting regions are thereby formed in the neighborhoods around these unstable saddle foci, resulting in the generation of coexisting multiple disconnected attractors.

### 3. Initial Values-Related Coexisting Multiple Bifurcation Modes

Because the presented sine system in (1) is symmetric about the origin, the disconnected attracting regions have locally symmetric behaviors, which are well exhibited in Figures 2 and 3. For this reason and convenient analysis, three sets of the initial values  $(10^{-6}, 0, 0)$ ,  $(10^{-6}, 3, 0)$ , and  $(10^{-6}, -3, 0)$  are considered in next numerical plots. The fourth-order Runge–Kutta algorithm with the 0.01 s time step and (700 s, 800 s) time interval is used for depicting the phase plots and bifurcation plots, whereas the fourth-order Runge–Kutta-based Wolf's method with the 0.01 s time step and 20 ks time end is adopted for calculating the Lyapunov exponents.

Firstly, two-dimensional bifurcation plots (bifurcation diagrams and dynamical maps) [23] are employed to show complex dynamical behaviors in the presented sine system intuitively, as shown in Figures 4 and 5. Here, both the coupling coefficients  $k_1$  and  $k_2$  are simultaneously increased in the region [2, 8] and two sets of initial values  $(10^{-6}, 0, 0)$  and  $(10^{-6}, 3, 0)$  are chosen. Note that the exhibited two-dimensional bifurcation behaviors are similar to each other for the initial values  $(10^{-6}, 3, 0)$  and  $(10^{-6}, -3, 0)$  due to the system symmetry.

As shown in Figure 4, the two-dimensional bifurcation diagrams in the  $k_1$ - $k_2$  parameter plane are obtained by calculating the periodicities of state variable  $x$ , which demonstrate rich and complex coexisting dynamical behaviors related to system parameters and initial values. The stable points and chaotic attractors distribute in the black- and red-colored regions, respectively, and the periodic attractors with different periodicities situate in the other colored regions. Comparing Figure 4(b) with Figure 4(a), there is a big difference between the two dynamical behaviors in the lower right regions, which is triggered by the initial values-dependent multistability in the presented sine system, leading to the coexistence of multiple bifurcation modes.

As shown in Figure 5, the two-dimensional dynamical maps in the  $k_1$ - $k_2$  parameter plane under two sets of initial values are depicted by evaluating the values of the largest Lyapunov exponent. The yellow-red-white colored regions with different positive values of the largest Lyapunov exponent represent different chaotic behaviors, the black-colored regions with different negative values of the largest Lyapunov exponent only stand for stable point behaviors, and the black-yellow colored regions with the zero largest Lyapunov exponent represent different periodic behaviors. In a similar manner, the dynamical behaviors described by the dynamical maps in Figures 5(a) and 5(b) are of great difference, which manifest how coexisting dynamical behaviors evolve for different initial values.

Similarly, the two-dimensional spectral entropy-based complexity plots in the  $k_1$ - $k_2$  parameter plane are displayed in Figure 6, where two sets of initial values  $(10^{-6}, 0, 0)$  and  $(10^{-6}, 3, 0)$  are employed. On the basis of the Fourier transform [32, 45], the complexity values are obtained by calculating the spectral entropy of the time sequence of the variable  $x$ . The relatively large complexity value in Figure 6 indicates the appearance of an irregularly chaotic sequence, whereas the relatively small complexity value in Figure 6 represents the occurrence of a regularly periodic sequence. For the two sets of different initial values, there are some differences in the complexity plots between Figures 6(a) and 6(b), implying that the system initial values have great effects on the dynamical behaviors of the presented sine system.

Therefore, the dynamical maps shown in Figure 5 and complexity plots shown in Figure 6 can reflect the dynamical evolutions with the variations of the system parameters and initial values, which are the effective supplements to confirm the coexisting dynamical behaviors depicted by the bifurcation diagrams in Figure 4.

To visualize the coexisting multiple bifurcation modes related to the initial values, three sets of initial values  $(10^{-6}, 0, 0)$ ,  $(10^{-6}, 3, 0)$ , and  $(10^{-6}, -3, 0)$  are considered and both the coupling coefficients  $k_1$  and  $k_2$  are simultaneously increased in the region [2, 8]. Denote  $k_1 = k_2 = k$  as a bifurcation parameter. The one-dimensional bifurcation plots with the variation of the system parameter  $k$  are shown in Figure 7. In Figure 7(a), the bifurcation diagrams drawn by the black, blue, and red trajectories correspond to those initiated from the initial values  $(10^{-6}, 0, 0)$ ,  $(10^{-6}, 3, 0)$ , and  $(10^{-6}, -3, 0)$ , respectively. And in Figure 7(b), the first two Lyapunov exponents associated with three sets of initial values are drafted in the upper, middle, and bottom of Figure 7(b), which entirely match with the bifurcation diagrams in Figure 7(a). Therefore, when more initial values are considered, more complicated coexisting multiple bifurcation modes can be revealed in the presented sine system.

Observed from Figure 7, abundant coexisting multiple attractors' behaviors related to the initial values are exhibited, including stable points, periodic oscillations, and chaotic oscillations along with period-doubling bifurcations, tangent bifurcations, and crisis scenarios. When two sets of initial values  $(10^{-6}, 3, 0)$  and  $(10^{-6}, -3, 0)$  are chosen, both the depicted dynamical behaviors in Figure 7 are basically identical over the entire parameter region, with only slight

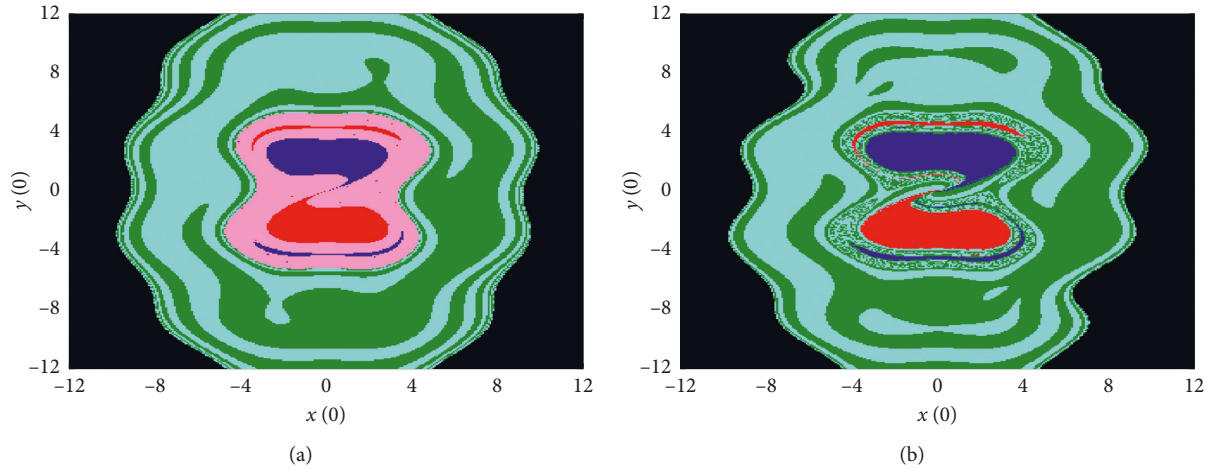


FIGURE 3: Two attraction basins in the  $x(0)$ - $y(0)$  plane with  $z(0) = 10^{-6}$  and the painted colors correspond to the colored motion orbits shown in Figure 2. (a) Attraction basin for  $k = 3.6$ . (b) Attraction basin for  $k = 5$ .

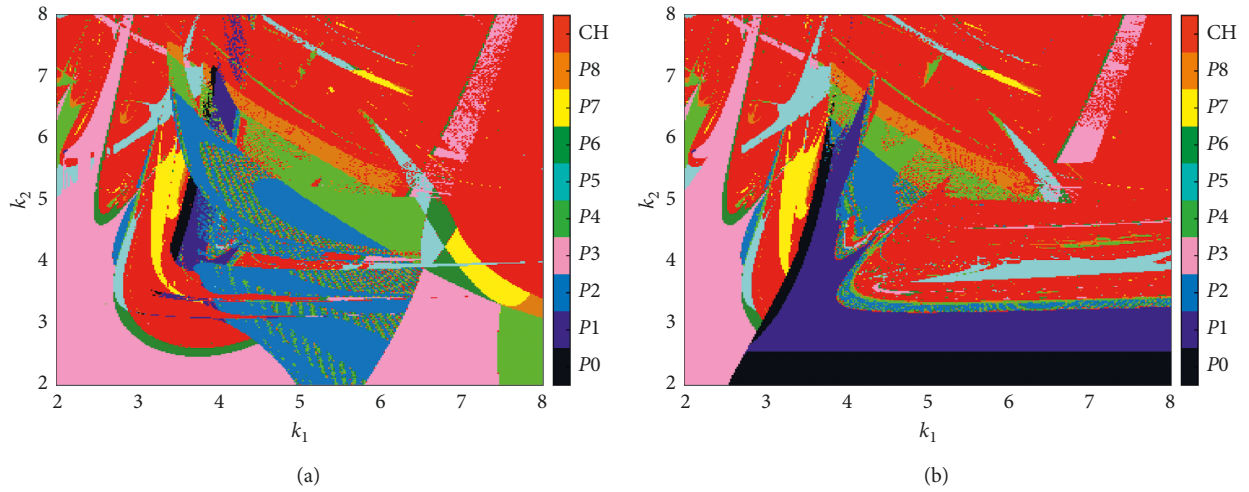


FIGURE 4: Two-dimensional bifurcation diagrams in the  $k_1$ - $k_2$  parameter plane through calculation of the periodicities of the state variable  $x$  under two sets of initial values. (a) Initial values  $(10^{-6}, 0, 0)$ . (b) Initial values  $(10^{-6}, 3, 0)$ .

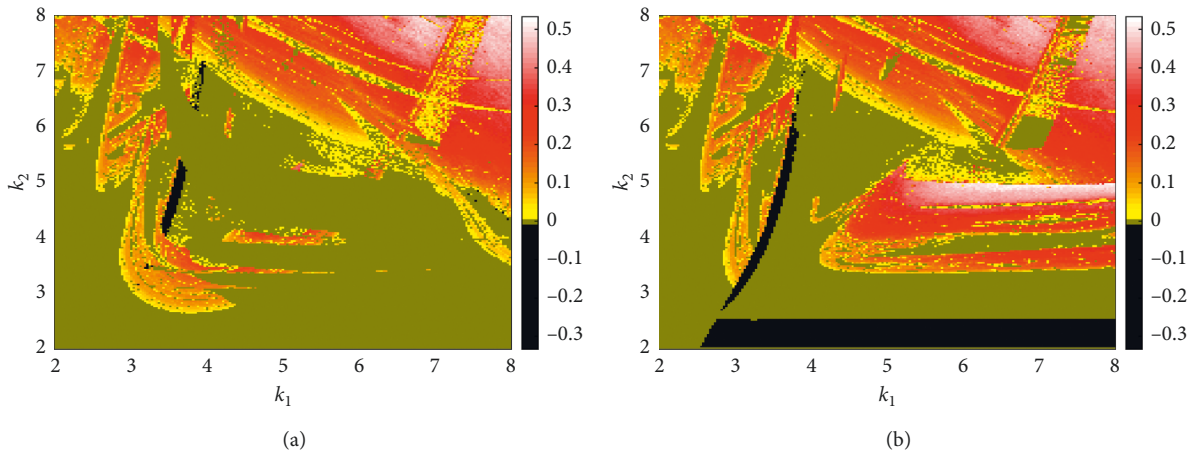


FIGURE 5: Two-dimensional dynamical maps in the  $k_1$ - $k_2$  parameter plane by evaluating the values of the largest Lyapunov exponent under two sets of initial values. (a) Initial values  $(10^{-6}, 0, 0)$ . (b) Initial values  $(10^{-6}, 3, 0)$ .



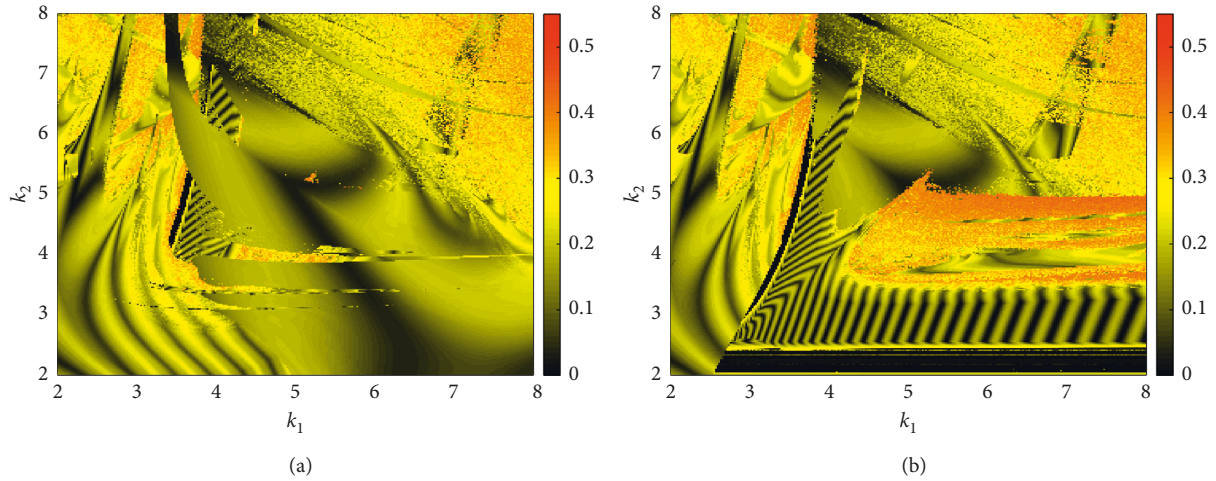


FIGURE 6: Two-dimensional spectral entropy-based complexity plots for the variable  $x$  sequence in the  $k_1$ - $k_2$  parameter plane under two sets of initial values. (a) Initial values  $(10^{-6}, 0, 0)$ . (b) Initial values  $(10^{-6}, 3, 0)$ .

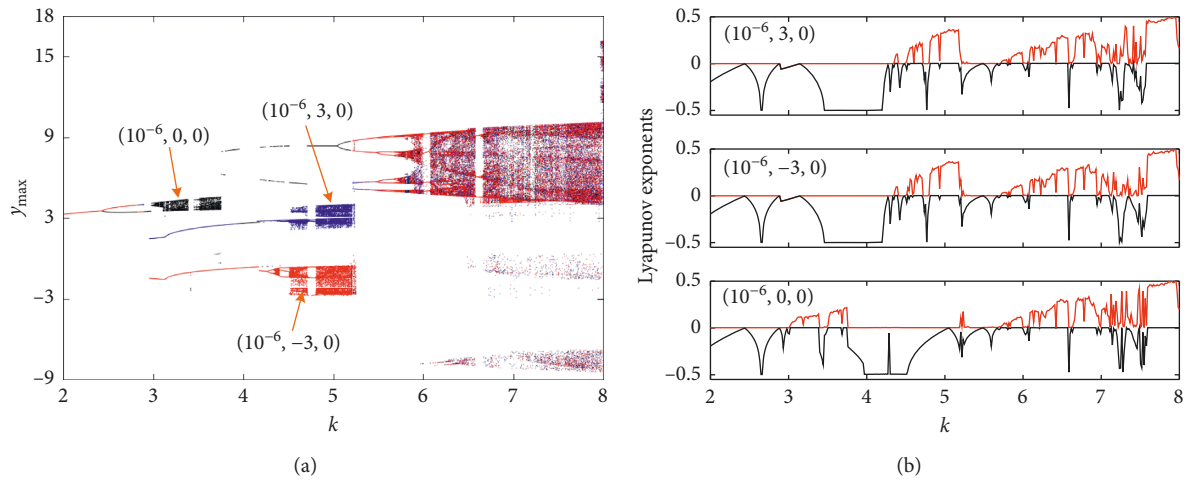


FIGURE 7: For three sets of initial values  $(10^{-6}, 0, 0)$ ,  $(10^{-6}, 3, 0)$ , and  $(10^{-6}, -3, 0)$ , one-dimensional bifurcation plots with the variation of the system parameter  $k$ . (a) Bifurcation diagrams of the maxima  $y_{\max}$  of the variable  $y$ . (b) First two Lyapunov exponents.

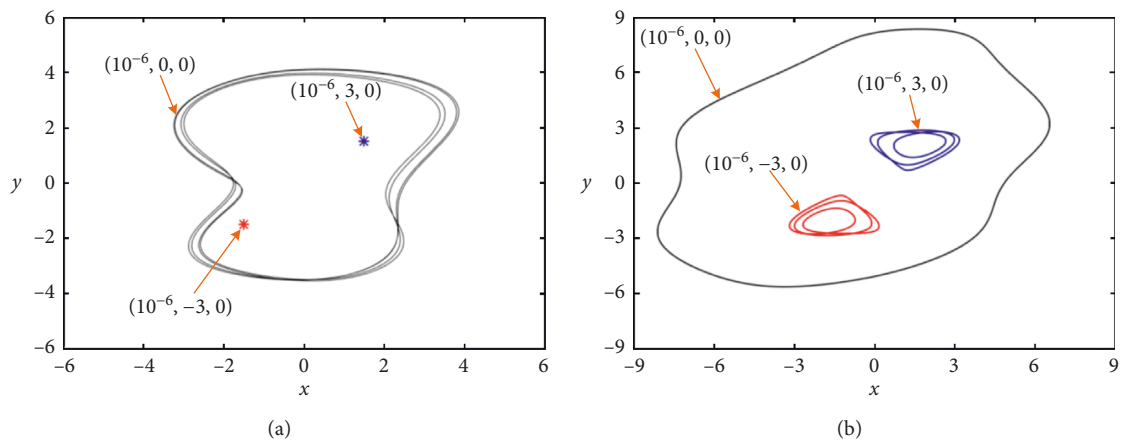


FIGURE 8: Continued.

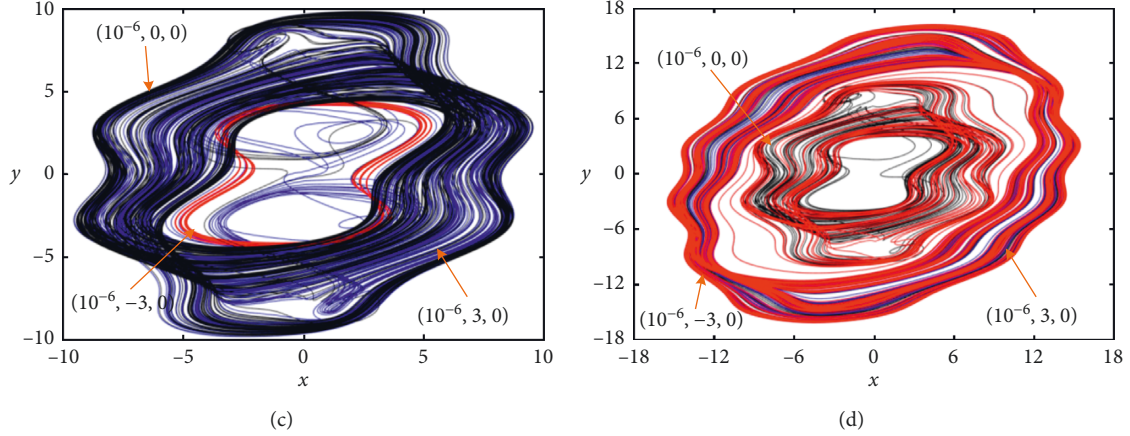


FIGURE 8: Phase plots of coexisting attractors in the  $x$ - $y$  plane for different values of the parameter  $k$ . (a) Period-4 limit cycle coexisted with a pair of symmetric points at  $k=3$ . (b) Large-size period-1 limit cycle coexisted with a pair of symmetric period-3 limit cycles at  $k=4.5$ . (c) Chaotic attractor coexisted with period-5 limit cycle at  $k=7$ . (d) Coexisting chaotic attractors with two topologies at  $k=8$ .

differences in the parameter region (6.94, 7.58). However, when the other two sets of initial values  $(10^{-6}, 0, 0)$  and  $(10^{-6}, 3, 0)$  are chosen, both the depicted dynamical behaviors in Figure 7 have big differences in the parameter region (2.96, 5.24). As the parameter  $k$  is increased in this parameter region, the moving orbit for  $(10^{-6}, 0, 0)$  goes into chaotic oscillating state at  $k=3.01$  via period-doubling bifurcation route and mutates into periodic oscillating state at  $k=3.76$  via chaos crisis, whereas the moving orbit for  $(10^{-6}, 3, 0)$  turns into periodic oscillating state from stable resting state at  $k=3.14$  and enters into chaotic oscillating state at  $k=4.34$  via period-doubling bifurcation route with two relatively larger periodic windows. Of course, in the parameter region (6.94, 7.58), some slight differences between the depicted dynamical behaviors under two sets of initial values  $(10^{-6}, 0, 0)$  and  $(10^{-6}, 3, 0)$  can be seen for the presented sine system as well.

Except for the two examples in Figure 2, other examples to exhibit coexisting multiple attractors' behaviors are given in Figure 8, where four sets of phase plots in the  $x$ - $y$  plane are provided together for the initial values  $(10^{-6}, 0, 0)$ ,  $(10^{-6}, 3, 0)$ , and  $(10^{-6}, -3, 0)$ . When  $k=3$ , the coexistence of a period-4 limit cycle and a pair of symmetric points is exhibited in Figure 8(a). When  $k=4.5$ , the coexistence of a large size period-1 limit cycle and a pair of symmetric period-3 limit cycles is demonstrated in Figure 8(b). When  $k=7$ , the coexistence of a chaotic attractor and a period-5 limit cycle is illustrated in Figure 8(c). However, when  $k=8$ , the coexistence of two chaotic attractors with different topologies is disclosed in Figure 8(d). Consequently, various types of coexisting attractors' behaviors can be found in the presented sine system.

#### 4. Validations by the Simulation-Oriented Circuit Model

By employing PSIM Version 9.0.3 software, the simulation-oriented circuit model for implementation of the presented sine system is synthesized and its screen shot is given in Figure 9, in which three operation channels containing three

integrators, three inverters and two sine function converters are used to implement three state variables  $x$ ,  $y$ , and  $z$ , respectively.

Based on the simulation-oriented circuit model shown in Figure 9, the state equations for the capacitor voltages  $v_x$ ,  $v_y$ , and  $v_z$  are described by

$$\begin{aligned} RC \frac{dv_x}{dt} &= v_y + v_z - \frac{R}{R_{k1}} \sin(v_y), \\ RC \frac{dv_y}{dt} &= -v_x + v_z, \\ RC \frac{dv_z}{dt} &= -v_x - v_z - \frac{R}{R_{k2}} \sin(v_x). \end{aligned} \quad (12)$$

where  $C_1 = C_2 = C_3 = C$ ,  $R_{k1} = R/k_1$ , and  $R_{k2} = R/k_2$ . When  $RC = 10 \text{ k}\Omega \times 10 \text{ nF} = 100 \mu\text{s}$ , i.e.,  $R = 10 \text{ k}\Omega$  and  $C = 10 \text{ nF}$ , the circuit parameters  $R_{k1}$  and  $R_{k2}$  for PSIM circuit simulations can be conveniently determined.

According to the system parameters  $k_1$  and  $k_2$  and the initial values used in Figure 2, the circuit parameters  $R_{k1}$  and  $R_{k2}$  have the same values, i.e.,  $R_{k1} = R_{k2}$ . When  $R_{k1} = R_{k2} = 2.78 \text{ k}\Omega$  and  $2 \text{ k}\Omega$ , respectively, PSIM screen captures are obtained in Figure 10, where the initial voltages  $v_x(0)$  and  $v_z(0)$  of the capacitors  $C_1$  and  $C_3$  are always fixed as  $1 \mu\text{V}$  and  $0 \text{ V}$ , respectively, and only the initial voltage  $v_y(0)$  of the capacitor  $C_2$  is adjusted as different initial values.

Similarly, based on the system parameters  $k_1$  and  $k_2$  and three sets of initial values used in Figure 8, the circuit parameters are selected as  $R_{k1} = R_{k2} = 3.33 \text{ k}\Omega$ ,  $2.22 \text{ k}\Omega$ ,  $1.43 \text{ k}\Omega$ , and  $1.25 \text{ k}\Omega$ , respectively. The corresponding PSIM screen captures are attached in Figure 11, where the initial voltages  $v_x(0)$ ,  $v_y(0)$ , and  $v_z(0)$  of the capacitors  $C_1$ ,  $C_2$ , and  $C_3$  are assigned as  $v_x(0) = 1 \mu\text{V}$ ,  $v_y(0) = 3 \text{ V}$  (or  $0 \text{ V}$  and  $-3 \text{ V}$ ), and  $v_z(0) = 0 \text{ V}$ , respectively.

PSIM circuit simulations in Figure 11(d) are slightly different from MATLAB numerical simulations in Figure 8(d), which are mainly caused by the inconsistently



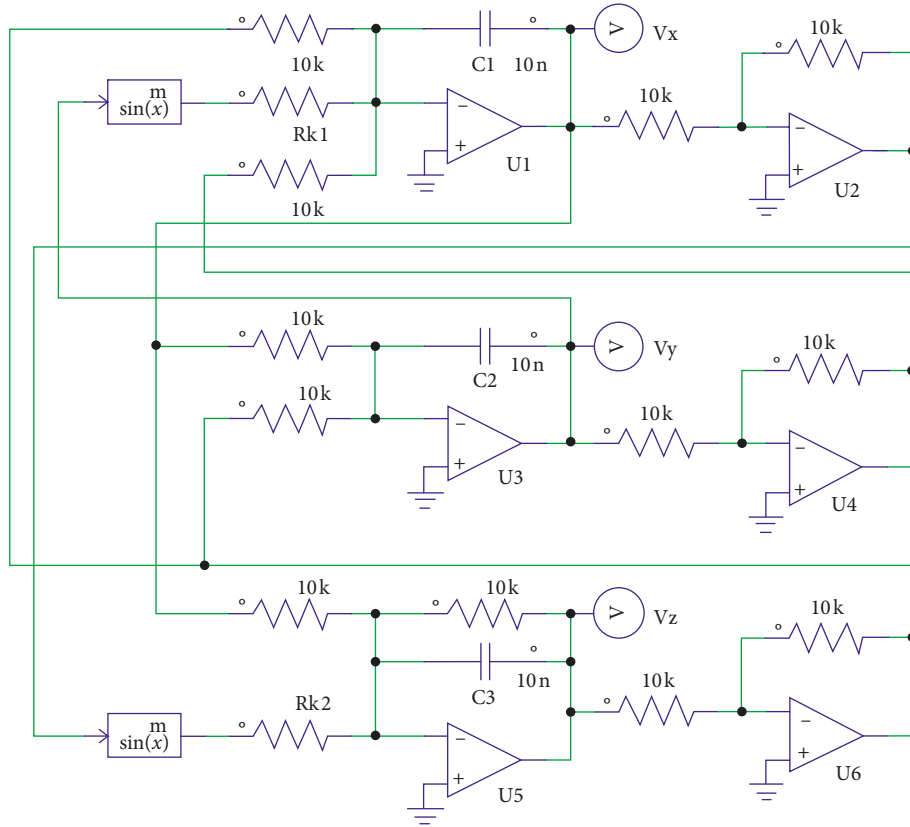


FIGURE 9: Screen shot of PSIM simulation-oriented circuit model for implementation of the presented sine system.

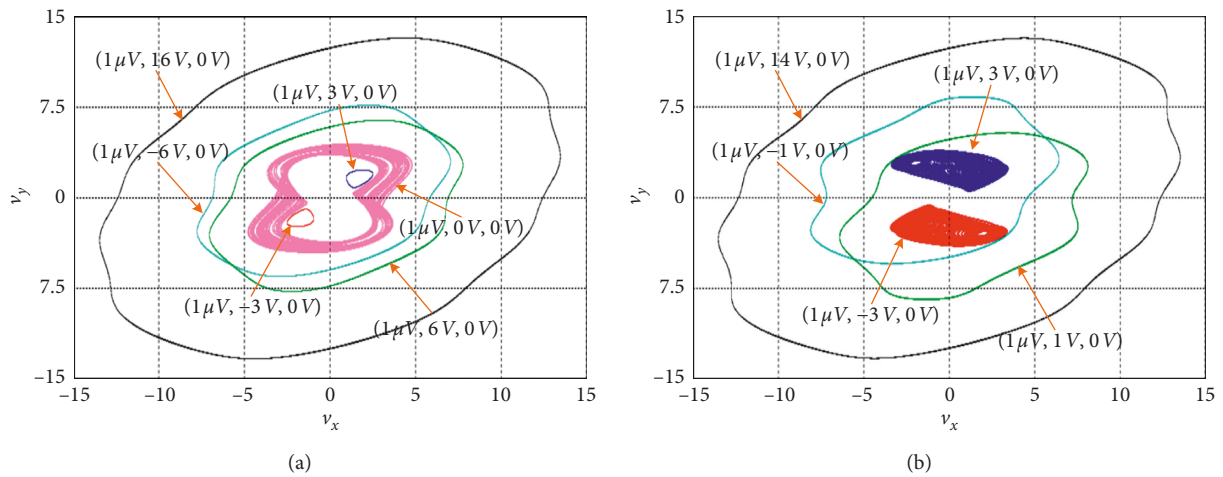


FIGURE 10: PSIM screen captures of coexisting multiple attractors in the  $v_x$ - $v_y$  plane for different initial values. (a) For  $R_{k1} = R_{k2} = 2.78 \text{ k}\Omega$ , six types of coexisting multiple attractors. (b) For  $R_{k1} = R_{k2} = 2 \text{ k}\Omega$ , five types of coexisting multiple attractors.

transient behaviors due to the existence of simulation errors [46]. Ignoring the tiny differences between MATLAB numerical simulations and PSIM circuit simulations, the results in Figures 10 and 11 effectively validate the coexisting attractors' behaviors disclosed in Figures 2 and 8.

Besides, it should be mentioned that the sine function terms are the two key units for realizing the proposed 3-D sine chaotic system. In the analog circuit experiments [47], the sine function terms can be physically implemented using

two AD639AD trigonometric function converters. But the system initials, corresponding to the initial capacitor voltages, are hardly set in the experimental measurements. In contrast, in the digital circuit experiments [48], the sine function terms can be directly achieved by calling IP cores in CORDIC library of FPGA and the system initials can be readily preset. Therefore, a feasible way to realize the proposed 3-D sine chaotic system could be implemented on the FPGA, which is addressed in our future paper.

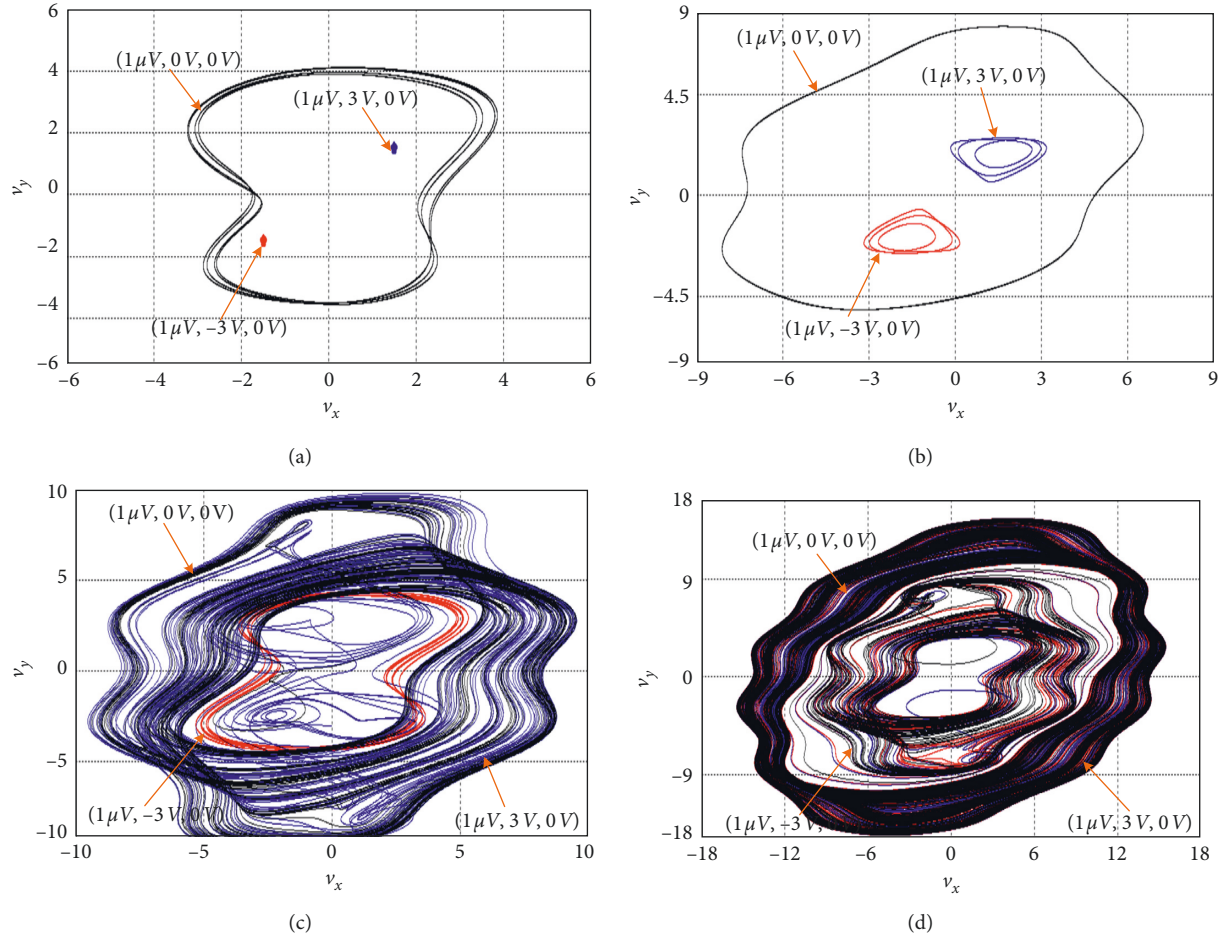


FIGURE 11: PSIM screen captures of coexisting attractors in the  $v_x - v_y$  plane for different values of  $R_{k1}$  and  $R_{k2}$ . (a) Period-4 limit cycle coexisted with a pair of symmetric points at  $R_{k1} = R_{k2} = 3.33 \text{ k}\Omega$ . (b) Large-size period-1 limit cycle coexisted with a pair of symmetric period-3 limit cycles at  $R_{k1} = R_{k2} = 2.22 \text{ k}\Omega$ . (c) Chaotic attractor coexisted with period-5 limit cycle at  $R_{k1} = R_{k2} = 1.43 \text{ k}\Omega$ . (d) Coexisting chaotic attractors with two topologies at  $R_{k1} = R_{k2} = 1.25 \text{ k}\Omega$ .

## 5. Conclusion

The autonomous chaotic systems can generate the conventional self-excited attractors as their oscillations are excited from the unstable determined equilibrium points. The mechanism for constructing chaotic systems with coexisting multiple attractors is based on the fact that the system equilibrium points can be reinstalled by newly introduced sine nonlinearities, leading to the great variations of their number, characteristics, and distributions [49]. Therefore, by introducing two sine nonlinearities into a simple 3-D linear dynamical system, this paper presented a novel and simple 3-D sine chaotic system with the reinstalled five index-2 saddle foci and four index-1 saddle foci, from which the abundant coexisting multiple attractors' behaviors were thereby revealed by numerical simulations, such as phase plots, attraction basins, two-dimensional bifurcation and complexity plots, and one-dimensional bifurcation plots, and finally validated by PSIM circuit simulations. The

algebraic simplicity of system structure and topological complexity of chaotic attractor are a long-term goal for seeking a new chaotic system with coexisting behaviors, which could acquire wide interest for its chaos-based engineering applications [42, 50].

## Data Availability

The data used to support the findings of this study are available from the corresponding author upon request.

## Conflicts of Interest

The authors declare that they have no conflicts of interest.

## Acknowledgments

This research was supported by the grants from the National Natural Science Foundations of China under Grant nos.

51607013, 61601062, and 61801054 and Natural Science Foundation of Jiangsu Province, China, under Grant no. BK20191451.

## References

- [1] G. H. Kom, J. Kengne, J. R. Mboupda Pone, G. Kenne, and A. B. Tiedeu, "Asymmetric double strange attractors in a simple autonomous jerk circuit," *Complexity*, vol. 2018, Article ID 4658785, 16 pages, 2018.
- [2] L. Zhou, C. H. Wang, X. Zhang, and W. Yao, "Various attractors, coexisting attractors and antimonotonicity in a simple fourth-order memristive Twin-T oscillator," *International Journal of Bifurcation and Chaos*, vol. 28, no. 4, Article ID 1850050, 2018.
- [3] M. Chen, Q. Xu, Y. Lin, and B. Bao, "Multistability induced by two symmetric stable node-foci in modified canonical Chua's circuit," *Nonlinear Dynamics*, vol. 87, no. 2, pp. 789–802, 2017.
- [4] A. T. Azar, N. M. Adele, T. Alain, R. Kengne, and F. H. Bertrand, "Multistability analysis and function projective synchronization in relay coupled oscillators," *Complexity*, vol. 2018, Article ID 3286070, 12 pages, 2018.
- [5] N. Stankevich and E. Volkov, "Multistability in a three-dimensional oscillator: tori, resonant cycles and chaos," *Nonlinear Dynamics*, vol. 94, no. 4, pp. 2455–2467, 2018.
- [6] B. C. Bao, A. H. Hu, H. Bao, Q. Xu, M. Chen, and H. G. Wu, "Three-dimensional memristive Hindmarsh-Rose neuron model with hidden coexisting asymmetric behaviors," *Complexity*, vol. 2018, Article ID 3872573, 11 pages, 2018.
- [7] H. Bao, W. Liu, and A. Hu, "Coexisting multiple firing patterns in two adjacent neurons coupled by memristive electromagnetic induction," *Nonlinear Dynamics*, vol. 95, no. 1, pp. 43–56, 2019.
- [8] Z. T. Njitacke and J. Kengne, "Complex dynamics of a 4D Hopfield neural networks (HNNs) with a nonlinear synaptic weight: coexistence of multiple attractors and reemerging Feigenbaum trees," *AEU—International Journal of Electronics and Communications*, vol. 93, pp. 242–252, 2018.
- [9] B. C. Bao, H. Qian, Q. Xu, M. Chen, J. Wang, and Y. J. Yu, "Coexisting behaviors of asymmetric attractors in hyperbolic-type memristor based Hopfield neural network," *Frontiers in Computational Neuroscience*, vol. 11, no. 81, pp. 1–14, 2017.
- [10] K. Rajagopal, J. M. Munoz-Pacheco, V.-T. Pham, D. V. Hoang, F. E. Alsaadi, and F. E. Alsaadi, "A Hopfield neural network with multiple attractors and its FPGA design," *The European Physical Journal Special Topics*, vol. 227, no. 7–9, pp. 811–820, 2018.
- [11] C. Chen, J. Chen, H. Bao, M. Chen, and B. Bao, "Coexisting multi-stable patterns in memristor synapse-coupled Hopfield neural network with two neurons," *Nonlinear Dynamics*, vol. 95, no. 4, pp. 3385–3399, 2019.
- [12] Y. Zhang and G. Luo, "Multistability of a three-degree-of-freedom vibro-impact system," *Communications in Nonlinear Science and Numerical Simulation*, vol. 57, pp. 331–341, 2018.
- [13] J. Hizanidis, N. Lazarides, and G. P. Tsironis, "Flux bias-controlled chaos and extreme multistability in SQUID oscillators," *Chaos: An Interdisciplinary Journal of Nonlinear Science*, vol. 28, no. 6, Article ID 063117, 2018.
- [14] Q. Lai, P. D. K. Kuate, F. Liu, and H. H. C. Iu, "An extremely simple chaotic system with infinitely many coexisting attractors," *IEEE Transactions on Circuits and Systems II: Express Briefs*, 2019.
- [15] M. Chen, Y. Feng, H. Bao et al., "State variable mapping method for studying initial-dependent dynamics in memristive hyper-jerk system with line equilibrium," *Chaos, Solitons & Fractals*, vol. 115, pp. 313–324, 2018.
- [16] Z. T. Njitacke, J. Kengne, R. W. Tapche, and F. B. Pelap, "Uncertain destination dynamics of a novel memristive 4D autonomous system," *Chaos, Solitons & Fractals*, vol. 107, pp. 177–185, 2018.
- [17] H. Bao, N. Wang, B. Bao, M. Chen, P. Jin, and G. Wang, "Initial condition-dependent dynamics and transient period in memristor-based hypogenetic jerk system with four line equilibria," *Communications in Nonlinear Science and Numerical Simulation*, vol. 57, pp. 264–275, 2018.
- [18] A. N. Pisarchik and U. Feudel, "Control of multistability," *Physics Reports*, vol. 540, no. 4, pp. 167–218, 2014.
- [19] P. R. Sharma, M. D. Shrimali, A. Prasad, N. V. Kuznetsov, and G. A. Leonov, "Control of multistability in hidden attractors," *The European Physical Journal Special Topics*, vol. 224, no. 8, pp. 1485–1491, 2015.
- [20] M. Chen, M. Sun, B. Bao, H. Wu, Q. Xu, and J. Wang, "Controlling extreme multistability of memristor emulator-based dynamical circuit in flux-charge domain," *Nonlinear Dynamics*, vol. 91, no. 2, pp. 1395–1412, 2018.
- [21] F. Hegedűs, W. Lauterborn, U. Parlitz, and R. Mettin, "Non-feedback technique to directly control multistability in nonlinear oscillators by dual-frequency driving," *Nonlinear Dynamics*, vol. 94, no. 1, pp. 273–293, 2018.
- [22] K. Yadav, A. Prasad, and M. D. Shrimali, "Control of coexisting attractors via temporal feedback," *Physics Letters A*, vol. 382, no. 32, pp. 2127–2132, 2018.
- [23] M. Chen, M. X. Sun, H. Bao, Y. H. Hu, and B. C. Bao, "Flux-charge analysis of two-memristor-based Chua's circuit: dimensionality decreasing model for detecting extreme multistability," *IEEE Transactions on Industrial Electronics*, vol. 67, no. 3, pp. 2197–2206, 2019.
- [24] Z. Wang, A. Akgul, V.-T. Pham, and S. Safari, "Chaos-based application of a novel no-equilibrium chaotic system with coexisting attractors," *Nonlinear Dynamics*, vol. 89, no. 3, pp. 1877–1887, 2017.
- [25] Q. Lai, B. Norouzi, and F. Liu, "Dynamic analysis, circuit realization, control design and image encryption application of an extended Lü system with coexisting attractors," *Chaos, Solitons & Fractals*, vol. 114, pp. 230–245, 2018.
- [26] G. Peng and F. Min, "Multistability analysis, circuit implementations and application in image encryption of a novel memristive chaotic circuit," *Nonlinear Dynamics*, vol. 90, no. 3, pp. 1607–1625, 2017.
- [27] C. Li, F. H. Min, Q. S. Jin, and H. Y. Ma, "Extreme multistability analysis of memristor-based chaotic system and its application in image decryption," *AIP Advances*, vol. 7, no. 12, Article ID 125204, 2017.
- [28] F. Yuan, G. Y. Wang, and X. W. Wang, "Chaotic oscillator containing memcapacitor and meminductor and its dimensionality reduction analysis," *Chaos: An Interdisciplinary Journal of Nonlinear Science*, vol. 27, no. 3, Article ID 033103, 2017.
- [29] M. Chen, Y. Feng, H. Bao, B. C. Bao, H. G. Wu, and Q. Xu, "Hybrid state variable incremental integral for reconstructing extreme multistability in memristive jerk system with cubic nonlinearity," *Complexity*, vol. 2019, Article ID 8549472, 16 pages, 2019.
- [30] H. Bao, T. Jiang, K. B. Chu, M. Chen, Q. Xu, and B. C. Bao, "Memristor-based canonical Chua's circuit: extreme multistability in voltage-current domain and its controllability in

- flux-charge domain,” *Complexity*, vol. 2018, Article ID 5935637, 13 pages, 2018.
- [31] M. Chen, B. C. Bao, T. Jiang et al., “Flux-Charge analysis of initial state-dependent dynamical behaviors of a memristor emulator-based chua’s circuit,” *International Journal of Bifurcation and Chaos*, vol. 28, no. 10, Article ID 1850120, 2018.
- [32] H. Bao, W. Liu, and M. Chen, “Hidden extreme multistability and dimensionality reduction analysis for an improved non-autonomous memristive FitzHugh-Nagumo circuit,” *Nonlinear Dynamics*, vol. 96, no. 3, pp. 1879–1894, 2019.
- [33] Q. Xu, Y. Lin, B. Bao, and M. Chen, “Multiple attractors in a non-ideal active voltage-controlled memristor based Chua’s circuit,” *Chaos, Solitons & Fractals*, vol. 83, pp. 186–200, 2016.
- [34] B. Bao, T. Jiang, G. Wang, P. Jin, H. Bao, and M. Chen, “Two-memristor-based Chua’s hyperchaotic circuit with plane equilibrium and its extreme multistability,” *Nonlinear Dynamics*, vol. 89, no. 2, pp. 1157–1171, 2017.
- [35] L. Wang, S. Zhang, Y.-C. Zeng, and Z.-J. Li, “Generating hidden extreme multistability in memristive chaotic oscillator via micro-perturbation,” *Electronics Letters*, vol. 54, no. 13, pp. 808–810, 2018.
- [36] J. Kengne, Z. T. Njitacke, and H. B. Fotsin, “Dynamical analysis of a simple autonomous jerk system with multiple attractors,” *Nonlinear Dynamics*, vol. 83, no. 1-2, pp. 751–765, 2016.
- [37] C. Li and J. C. Sprott, “An infinite 3-D quasiperiodic lattice of chaotic attractors,” *Physics Letters A*, vol. 382, no. 8, pp. 581–587, 2018.
- [38] J. Sun, X. Zhao, J. Fang, and Y. Wang, “Autonomous memristor chaotic systems of infinite chaotic attractors and circuitry realization,” *Nonlinear Dynamics*, vol. 94, no. 4, pp. 2879–2887, 2018.
- [39] C. Li, Y. Xu, G. Chen, Y. Liu, and J. Zheng, “Conditional symmetry: bond for attractor growing,” *Nonlinear Dynamics*, vol. 95, no. 2, pp. 1245–1256, 2019.
- [40] Q. Lai, C. Chen, X.-W. Zhao, J. Kengne, and C. Volos, “Constructing chaotic system with multiple coexisting attractors,” *IEEE Access*, vol. 7, pp. 24051–24056, 2019.
- [41] C. Li, W. Joo-Chen Thio, J. C. Sprott, H. H.-C. Iu, and Y. Xu, “Constructing infinitely many attractors in a programmable chaotic circuit,” *IEEE Access*, vol. 6, pp. 29003–29012, 2018.
- [42] G. Alvarez and S. Li, “Some basic cryptographic requirements for chaos-based cryptosystems,” *International Journal of Bifurcation and Chaos*, vol. 16, no. 8, pp. 2129–2151, 2006.
- [43] T. F. Fonzin, K. Srinivasan, J. Kengne, and F. B. Pelap, “Coexisting bifurcations in a memristive hyperchaotic oscillator,” *AEÜ—International Journal of Electronics and Communications*, vol. 90, pp. 110–122, 2018.
- [44] C. C. Streliaoff and A. W. Hübler, “Medium-term prediction of chaos,” *Physical Review Letters*, vol. 96, no. 4, Article ID 044101, 2006.
- [45] H. Bao, M. Chen, H. Wu, and B. Bao, “Memristor initial-boosted coexisting plane bifurcations and its extreme multistability reconstitution in two-memristor-based dynamical system,” *Science China Technological Sciences*, 2019.
- [46] N. V. Kuznetsov, G. A. Leonov, M. V. Yuldashev, and R. V. Yuldashev, “Hidden attractors in dynamical models of phase-locked loop circuits: limitations of simulation in MATLAB and SPICE,” *Communications in Nonlinear Science and Numerical Simulation*, vol. 51, pp. 39–49, 2017.
- [47] Q. Lai, A. Akgul, C. Li, G. Xu, and Ü. Çavuşoğlu, “A new chaotic system with multiple attractors: dynamic analysis, circuit realization and S-Box design,” *Entropy*, vol. 20, no. 1, p. 12, 2018.
- [48] B. C. Bao, Q. F. Yang, L. Zhu et al., “Chaotic bursting dynamics and coexisting multistable firing patterns in 3D autonomous Morris–Lecar model and microcontroller-based validations,” *International Journal of Bifurcation and Chaos*, vol. 29, no. 10, Article ID 1950134, 2019.
- [49] V. T. Pham, C. Volos, T. Kapitaniak, S. Jafari, and X. Wang, “Dynamics and circuit of a chaotic system with a curve of equilibrium points,” *International Journal of Electronics*, vol. 105, no. 3, pp. 385–397, 2018.
- [50] Z. Y. Hua, Y. C. Zhou, and B. C. Bao, “Two-dimensional sine chaotification system with hardware implementation,” *IEEE Transactions on Industrial Informatics*, 2019.